

HANDBOOK OF PHOTOVOLTAIC SCIENCE AND ENGINEERING

Edited by Antonio Luque and Steven Hegedus

**Handbook of
Photovoltaic Science
and Engineering**

This Page Intentionally Left Blank

Handbook of Photovoltaic Science and Engineering

Edited by

Antonio Luque

Instituto de Energía Solar, Universidad Politécnica de Madrid, Spain

and

Steven Hegedus

Institute of Energy Conversion, University of Delaware, USA



WILEY

Some images in the original version of this book are not available for inclusion in the eBook.

Copyright © 2003 John Wiley & Sons Ltd, The Atrium, Southern Gate, Chichester, West Sussex PO19 8SQ, England

Telephone (+44) 1243 779777

Email (for orders and customer service enquiries): cs-books@wiley.co.uk
Visit our Home Page on www.wileyurope.com or www.wiley.com

All Rights Reserved. No part of this publication may be reproduced, stored in a retrieval system or transmitted in any form or by any means, electronic, mechanical, photocopying, recording, scanning or otherwise, except under the terms of the Copyright, Designs and Patents Act 1988 or under the terms of a licence issued by the Copyright Licensing Agency Ltd, 90 Tottenham Court Road, London W1T 4LP, UK, without the permission in writing of the Publisher. Requests to the Publisher should be addressed to the Permissions Department, John Wiley & Sons Ltd, The Atrium, Southern Gate, Chichester, West Sussex PO19 8SQ, England, or emailed to permreq@wiley.co.uk, or faxed to (+44) 1243 770620.

This publication is designed to provide accurate and authoritative information in regard to the subject matter covered. It is sold on the understanding that the Publisher is not engaged in rendering professional services. If professional advice or other expert assistance is required, the services of a competent professional should be sought.

Other Wiley Editorial Offices

John Wiley & Sons Inc., 111 River Street, Hoboken, NJ 07030, USA

Jossey-Bass, 989 Market Street, San Francisco, CA 94103-1741, USA

Wiley-VCH Verlag GmbH, Boschstr. 12, D-69469 Weinheim, Germany

John Wiley & Sons Australia Ltd, 33 Park Road, Milton, Queensland 4064, Australia

John Wiley & Sons (Asia) Pte Ltd, 2 Clementi Loop #02-01, Jin Xing Distripark, Singapore 129809

John Wiley & Sons Canada Ltd, 22 Worcester Road, Etobicoke, Ontario, Canada M9W 1L1

Wiley also publishes its books in a variety of electronic formats. Some content that appears in print may not be available in electronic books.

Library of Congress Cataloging-in-Publication Data

Handbook of photovoltaic science and engineering / edited by Antonio Luque and Steven Hegedus.
p. cm.

Includes bibliographical references and index.

ISBN 0-471-49196-9 (alk. paper)

1. Photovoltaic cells. 2. Photovoltaic power generation. I. Luque, A. (Antonio) II. Hegedus, Steven.

TK8322 .H33 2003
621.31'244 – dc21

2002191033

British Library Cataloguing in Publication Data

A catalogue record for this book is available from the British Library

ISBN 0-471-49196-9

Typeset in 10/12 Times by Laserwords Private Limited, Chennai, India
Printed and bound in Great Britain by Antony Rowe Ltd, Chippenham, Wiltshire
This book is printed on acid-free paper responsibly manufactured from sustainable forestry in which at least two trees are planted for each one used for paper production.

We dedicate this book to all those who have worked so hard for half a century to bring solar electricity to where it is today, and to our colleagues present and future who must work even harder in the next half century to make sure that it fulfills its potential as a widely available clean energy source.

The editors also owe much appreciation to the authors of the chapters contained in this book. Their long hours spent writing the best possible chapter covering their field of expertise, and then suffering through a storm of editorial criticisms, has hopefully made this a high-quality publication of lasting value.

Finally, we want to express our gratitude to our loved ones (Carmen, Ignacio, Sofia, Victoria, Inés, and Debbie, Jordan, Ariel) for the many hours stolen from family life while working on this book.

AL & SH

December 2, 2002

This Page Intentionally Left Blank

Contents

List of Contributors

xxiii

1 Status, Trends, Challenges and the Bright Future of Solar Electricity from Photovoltaics	1
<i>Steven S. Hegedus and Antonio Luque</i>	
1.1 The Big Picture	1
1.2 What Is Photovoltaics?	3
1.3 Six Myths of Photovoltaics	5
1.4 History of Photovoltaics	11
1.5 PV Costs, Markets and Forecasts	15
1.6 What Are the Goals of Today's PV Research and Manufacturing?	19
1.7 Global Trends in Performance and Applications	20
1.8 Crystalline Silicon Progress and Challenges	23
1.9 Thin Film Progress and Challenges	27
1.10 Concentration PV Systems	31
1.11 Balance of Systems	32
1.12 Future of Emerging PV Technologies	37
1.13 Conclusions	39
References	41
2 Motivation for Photovoltaic Application and Development	45
<i>Joachim Luther</i>	
2.1 Characteristics of Photovoltaic Energy Conversion	45
2.2 A Long-term Substitute for Today's Conventional Electricity Production – The Ecological Dimension of Photovoltaics	48
2.2.1 In Summary	54
2.3 A Technological Basis for Off-grid Electricity Supply – The Development Dimension of Photovoltaics	54
2.3.1 In Summary	57
2.4 Power Supply for Industrial Systems and Products – The Professional Low Power Dimension	57
2.5 Power for Spacecraft and Satellites – the Extraterrestrial Dimension of Photovoltaics	59
References	60

3 The Physics of the Solar Cell	61
<i>Jeffery L. Gray</i>	
3.1 Introduction	61
3.2 Fundamental Properties of Semiconductors	64
3.2.1 Crystal Structure	64
3.2.2 Energy Band Structure	65
3.2.3 Conduction-band and Valence-band Densities of State	66
3.2.4 Equilibrium Carrier Concentrations	67
3.2.5 Light Absorption	70
3.2.6 Recombination	74
3.2.7 Carrier Transport	78
3.2.8 Semiconductor Equations	81
3.2.9 Minority-carrier Diffusion Equation	82
3.3 <i>PN</i> -Junction Diode Electrostatics	83
3.4 Solar Cell Fundamentals	87
3.4.1 Solar Cell Boundary Conditions	87
3.4.2 Generation Rate	89
3.4.3 Solution of the Minority-carrier Diffusion Equation	89
3.4.4 Terminal Characteristics	89
3.4.5 Solar Cell $I-V$ Characteristics	92
3.4.6 Properties of Efficient Solar Cells	95
3.4.7 Lifetime and Surface Recombination Effects	96
3.4.8 An Analogy for Understanding Solar Cell Operation: A Partial Summary	98
3.5 Additional Topics	99
3.5.1 Efficiency and Band gap	99
3.5.2 Spectral Response	100
3.5.3 Parasitic Resistance Effects	102
3.5.4 Temperature Effects	104
3.5.5 Concentrator Solar Cells	106
3.5.6 High-level Injection	107
3.5.7 <i>p-i-n</i> Solar Cells	109
3.5.8 Detailed Numerical Modeling	109
3.6 Summary	110
References	111
4 Theoretical Limits of Photovoltaic Conversion	113
<i>Antonio Luque and Antonio Martí</i>	
4.1 Introduction	113
4.2 Thermodynamic Background	114
4.2.1 Basic Relationships	114
4.2.2 The Two Laws of Thermodynamics	116
4.2.3 Local Entropy Production	116
4.2.4 An Integral View	117
4.2.5 Thermodynamic Functions of Radiation	117
4.2.6 Thermodynamic Functions of Electrons	119
4.3 Photovoltaic Converters	120

4.3.1	The Balance Equation of a PV Converter	120
4.3.2	The Monochromatic Cell	124
4.3.3	Thermodynamic Consistence of the Shockley–Queisser Photovoltaic Cell	126
4.3.4	Entropy Production in the Whole Shockley–Queisser Solar Cell	129
4.4	The Technical Efficiency Limit for Solar Converters	131
4.5	Very High Efficiency Concepts	132
4.5.1	Multijunction Solar Cells	132
4.5.2	Thermophotovoltaic Converters	135
4.5.3	Thermophotonic Converters	136
4.5.4	Higher-than-one Quantum Efficiency Solar Cells	140
4.5.5	Hot Electron Solar Cells	141
4.5.6	Intermediate Band Solar Cell	144
4.6	Conclusions	148
	References	149
5	Solar Grade Silicon Feedstock	153
	<i>Bruno Ceccaroli and Otto Lohne</i>	
5.1	Introduction	153
5.2	Silicon	154
5.2.1	Physical Properties of Silicon Relevant to Photovoltaics	154
5.2.2	Chemical Properties Relevant to Photovoltaics	156
5.2.3	Health Factors	156
5.2.4	History and Applications of Silicon	157
5.3	Production of Metallurgical Grade Silicon	161
5.3.1	The Carbothermic Reduction of Silica	161
5.3.2	Refining	163
5.3.3	Casting and Crushing	166
5.3.4	Economics	167
5.4	Production of Semiconductor Grade Silicon (Polysilicon)	167
5.4.1	The Siemens Process	168
5.4.2	The Union Carbide Process	172
5.4.3	The Ethyl Corporation Process	173
5.4.4	Economics and Business	175
5.5	Current Silicon Feedstock to Solar Cells	175
5.6	Requirements of Silicon for Crystalline Solar Cells	179
5.6.1	Solidification	179
5.6.2	Effect of Crystal Imperfections	182
5.6.3	Effect of Various Impurities	186
5.7	Routes to Solar Grade Silicon	193
5.7.1	Crystallisation	193
5.7.2	Upgrading Purity of the Metallurgical Silicon Route	194
5.7.3	Simplification of the Polysilicon Process	198
5.7.4	Other Methods	201
5.8	Conclusions	201
	References	202

6 Bulk Crystal Growth and Wafering for PV	205
<i>W. Koch, A. L. Endrös, D. Franke, C. Häßler, J. P. Kalejs and H. J. Möller</i>	
6.1 Introduction	205
6.2 Bulk Monocrystalline Material	206
6.2.1 Cz Growth of Single-crystal Silicon	207
6.2.2 Tri-crystalline Silicon	211
6.3 Bulk Multicrystalline Silicon	214
6.3.1 Ingot Fabrication	214
6.3.2 Doping	216
6.3.3 Crystal Defects	217
6.3.4 Impurities	219
6.4 Wafering	223
6.4.1 Multi-wire Wafering Technique	224
6.4.2 Microscopic Process of Wafering	226
6.4.3 Wafer Quality and Saw Damage	229
6.4.4 Cost and Size Considerations	230
6.5 Silicon Ribbon and Foil Production	230
6.5.1 Process Description	232
6.5.2 Productivity Comparisons	238
6.5.3 Manufacturing Technology	239
6.5.4 Ribbon Material Properties and Solar Cells	240
6.5.5 Ribbon/Foil Technology – Future Directions	243
6.6 Numerical Simulations of Crystal Growth Techniques	244
6.6.1 Simulation Tools	245
6.6.2 Thermal Modelling of Silicon Crystallisation Techniques	245
6.6.3 Simulation of Bulk Silicon Crystallisation	247
6.6.4 Simulation of Silicon Ribbon Growth	249
6.7 Conclusions	251
6.8 Acknowledgement	252
References	252
7 Crystalline Silicon Solar Cells and Modules	255
<i>Ignacio Tobías, Carlos del Cañizo and Jesús Alonso</i>	
7.1 Introduction	255
7.2 Crystalline Silicon as a Photovoltaic Material	257
7.2.1 Bulk Properties	257
7.2.2 Surfaces	257
7.3 Crystalline Silicon Solar Cells	259
7.3.1 Cell Structure	259
7.3.2 Substrate	260
7.3.3 The Front Surface	263
7.3.4 The Back Surface	266
7.3.5 Size Effects	266
7.3.6 Cell Optics	268
7.3.7 Performance Comparison	270

7.4	Manufacturing Process	271
7.4.1	Process Flow	271
7.4.2	Screen-printing Technology	276
7.4.3	Throughput and Yield	279
7.5	Variations to the Basic Process	280
7.5.1	Thin Wafers	280
7.5.2	Back Surface Passivation	281
7.5.3	Improvements to the Front Emitter	281
7.5.4	Rapid Thermal Processes	282
7.6	Multicrystalline Cells	283
7.6.1	Gettering in mc Solar Cells	283
7.6.2	Passivation with Hydrogen	283
7.6.3	Optical Confinement	285
7.7	Other Industrial Approaches	288
7.7.1	Silicon Ribbons	288
7.7.2	Heterojunction with Intrinsic Thin Layer	288
7.7.3	Buried Contact Technology	289
7.8	Crystalline Silicon Photovoltaic Modules	291
7.8.1	Cell Matrix	291
7.8.2	The Layers of the Module	292
7.8.3	Lamination and Curing	293
7.8.4	Postlamination Steps	294
7.8.5	Special Modules	294
7.9	Electrical and Optical Performance of Modules	295
7.9.1	Electrical and Thermal Characteristics	295
7.9.2	Fabrication Spread and Mismatch Losses	297
7.9.3	Local Shading and Hot Spot Formation	297
7.9.4	Optical Properties	300
7.10	Field Performance of Modules	301
7.10.1	Lifetime	301
7.10.2	Qualification	301
7.11	Conclusions	302
	References	303
8	Thin-film Silicon Solar Cells	307
	<i>Bhushan Sopori</i>	
8.1	Introduction	307
8.2	A Review of Current Thin-film Si Cells	310
8.2.1	Single-crystal Films Using Single-crystal Si Substrates	317
8.2.2	Multicrystalline-Si Substrates	320
8.2.3	Non-Si Substrates	321
8.3	Design Concepts of TF-Si Solar Cells	324
8.3.1	Light-trapping in Thin Si Solar Cells	326
8.3.2	Description of PV Optics	327
8.3.3	Electronic Modeling	333
8.3.4	Methods of Making Thin-Si Films for Solar Cells	341

8.3.5	Methods of Grain Enhancement of a-Si/ μ c-Si Thin Films	343
8.3.6	Processing Considerations for TF-Si Solar Cell Fabrication	350
8.4	Conclusion	353
	References	354
9	High-Efficiency III-V Multijunction Solar Cells	359
	<i>J. M. Olson, D. J. Friedman and Sarah Kurtz</i>	
9.1	Introduction	359
9.2	Applications	363
9.2.1	Space Solar Cells	363
9.2.2	Terrestrial Energy Production	363
9.3	Physics of III-V Multijunction and Single-junction Solar Cells	363
9.3.1	Wavelength Dependence of Photon Conversion Efficiency	363
9.3.2	Theoretical Limits to Multijunction Efficiencies	364
9.3.3	Spectrum Splitting	364
9.4	Cell Configuration	365
9.4.1	Four-terminal	365
9.4.2	Three-terminal Voltage-matched Interconnections	366
9.4.3	Two-terminal Series-connected (Current Matched)	366
9.5	Computation of Series-Connected Device Performance	366
9.5.1	Overview	366
9.5.2	Top and Bottom Subcell QE and J_{SC}	367
9.5.3	Multijunction $J-V$ Curves	368
9.5.4	Efficiency versus Band Gap	370
9.5.5	Top-cell Thinning	372
9.5.6	Current-matching Effect on Fill Factor and V_{OC}	373
9.5.7	Spectral Effects	374
9.5.8	AR Coating Effects	375
9.5.9	Concentration	376
9.5.10	Temperature Dependence	380
9.6	Materials Issues Related to GaInP/GaAs/Ge Solar Cells	382
9.6.1	Overview	382
9.6.2	MOCVD	382
9.6.3	GaInP Solar Cells	383
9.6.4	GaAs Cells	393
9.6.5	Ge Cells	395
9.6.6	Tunnel-junction Interconnects	396
9.6.7	Chemical Etchants	397
9.6.8	Materials Availability	398
9.7	Troubleshooting	398
9.7.1	Characterization of Epilayers	398
9.7.2	Transmission Line Measurements	400
9.7.3	$I-V$ Measurements of Multijunction Cells	400
9.7.4	Evaluation of Morphological Defects	401
9.7.5	Device Diagnosis	401

9.8	Future-generation Solar Cells	403
9.8.1	Refinements to the GaInP/GaAs/Ge Cell	403
9.8.2	Mechanical Stacks	404
9.8.3	Growth on Other Substrates	405
9.8.4	Spectrum Splitting	406
9.9	Implementation into Terrestrial Systems	406
9.9.1	Economic Issues	406
9.9.2	Concentrator Systems	406
9.9.3	Terrestrial Spectrum	407
	References	407
10	Space Solar Cells and Arrays	413
	<i>Sheila Bailey and Ryne Raffaele</i>	
10.1	The History of Space Solar Cells	413
10.1.1	Vanguard I to Deep Space I	413
10.2	The Challenge for Space Solar Cells	416
10.2.1	The Space Environment	417
10.2.2	Thermal Environment	420
10.2.3	Solar Cell Calibration and Measurement	424
10.3	Silicon Solar Cells	425
10.4	III-V Solar Cells	426
10.4.1	Thin-film Solar Cells	428
10.5	Space Solar Arrays	431
10.5.1	Body-mounted Arrays	432
10.5.2	Rigid Panel Planar Arrays	432
10.5.3	Flexible Fold-out Arrays	433
10.5.4	Thin-film or Flexible Roll-out Arrays	435
10.5.5	Concentrating Arrays	436
10.5.6	High-temperature/Intensity Arrays	438
10.5.7	Electrostatically Clean Arrays	439
10.5.8	Mars Solar Arrays	440
10.5.9	Power Management and Distribution (PMAD)	441
10.6	Future Cell and Array Possibilities	441
10.6.1	Low Intensity Low Temperature (LILT) Cells	441
10.6.2	Quantum Dot Solar Cells	442
10.6.3	Integrated Power Systems	442
10.6.4	High Specific Power Arrays	443
10.6.5	High-radiation Environment Solar Arrays	443
10.7	Power System Figures of Merit	444
	References	446
11	Photovoltaic Concentrators	449
	<i>Richard M. Swanson</i>	
11.1	Introduction	449
11.1.1	The Concentrator Dilemma	450
11.2	Basic Types of Concentrators	452
11.2.1	Types of Optics	452
11.2.2	Concentration Ratio	455

11.2.3	Types of Tracking	456
11.2.4	Static Concentrators	456
11.3	Historical Overview	460
11.3.1	The Sandia National Laboratories Concentrator Program (1976 to 1993)	461
11.3.2	The Martin Marietta Point-focus Fresnel System	462
11.3.3	The Entech Linear-focus Fresnel System	463
11.3.4	Other Sandia Projects	465
11.3.5	The Concentrator Initiative	465
11.3.6	Early Demonstration Projects	466
11.3.7	The EPRI High-concentration Program	467
11.3.8	Other Concentrator Programs	471
11.3.9	History of Performance Improvements	472
11.4	Optics of Concentrators	474
11.4.1	Basics	474
11.4.2	Reflection and Refraction	478
11.4.3	The Parabolic Concentrator	479
11.4.4	The Compound Parabolic Concentrator	482
11.4.5	The V-trough Concentrator	483
11.4.6	Refractive Lenses	485
11.4.7	Secondary Optics	489
11.4.8	Static Concentrators	491
11.4.9	Innovative Concentrators	492
11.4.10	Issues in Concentrator Optics	494
11.5	Current Concentrator Activities	495
11.5.1	Amonix	496
11.5.2	Australian National University	496
11.5.3	BP Solar and the Polytechnical University of Madrid	496
11.5.4	Entech	497
11.5.5	Fraunhofer-Institut für Solare Energiesysteme	497
11.5.6	Ioffe Physical-Technical Institute	498
11.5.7	National Renewable Energy Laboratory	498
11.5.8	Polytechnical University of Madrid	498
11.5.9	Solar Research Corporation	499
11.5.10	Spectrolab	499
11.5.11	SunPower Corporation	499
11.5.12	University of Reading	500
11.5.13	Tokyo A&T University	500
11.5.14	Zentrum für Sonnenenergie und Wasserstoff Forschung Baden Württemberg (ZSW)	500
	References	500
12	Amorphous Silicon-based Solar Cells	505
	<i>Xunming Deng and Eric A. Schiff</i>	
12.1	Overview	505
12.1.1	Amorphous Silicon: The First Bipolar Amorphous Semiconductor	505

12.1.2	Designs for Amorphous Silicon Solar Cells: A Guided Tour	508
12.1.3	Staebler–Wronski Effect	511
12.1.4	Synopsis of this Chapter	512
12.2	Atomic and Electronic Structure of Hydrogenated Amorphous Silicon	513
12.2.1	Atomic Structure	513
12.2.2	Defects and Metastability	514
12.2.3	Electronic Density-of-states	515
12.2.4	Bandtails, Bandedges, and Band Gaps	516
12.2.5	Defects and Gap States	517
12.2.6	Doping	518
12.2.7	Alloying and Optical Properties	518
12.3	Depositing Amorphous Silicon	520
12.3.1	Survey of Deposition Techniques	520
12.3.2	RF Glow Discharge Deposition	521
12.3.3	Glow Discharge Deposition at Different Frequencies	523
12.3.4	Hot-wire Chemical Vapor Deposition	525
12.3.5	Other Deposition Methods	526
12.3.6	Hydrogen Dilution	526
12.3.7	Alloys and Doping	528
12.4	Understanding a-Si <i>pin</i> Cells	528
12.4.1	Electronic Structure of a <i>pin</i> Device	528
12.4.2	Photocurrent Drift in Absorber Layers	530
12.4.3	Absorber Layer Design of a <i>pin</i> Solar Cell	533
12.4.4	The Open-circuit Voltage	534
12.4.5	Optical Design of a-Si:H Solar Cells	537
12.4.6	Cells under Solar Illumination	540
12.4.7	Light-soaking Effects	541
12.5	Multiple-Junction Solar Cells	542
12.5.1	Advantages of Multiple-junction Solar Cells	542
12.5.2	Using Alloys for Cells with Different Band Gaps	544
12.5.3	a-Si/a-SiGe Tandem and a-Si/a-SiGe/a-SiGe Triple-junction Solar Cells	546
12.5.4	Microcrystalline Silicon Solar Cells	551
12.5.5	Micromorph and Other μ c-Si-based Multijunction Cells	552
12.6	Module Manufacturing	553
12.6.1	Continuous Roll-to-roll Manufacturing on Stainless Steel Substrates	553
12.6.2	a-Si Module Production on Glass Superstrate	555
12.6.3	Manufacturing Cost, Safety, and Other Issues	556
12.6.4	Module Performance	557
12.7	Conclusions and Future Projections	558
12.7.1	Status and Competitiveness of a-Si Photovoltaics	558
12.7.2	Critical Issues for Further Enhancement and Future Potential	559
12.8	Acknowledgments	559
	References	560

13 Cu(InGa)Se₂ Solar Cells	567
<i>William N. Shafarman and Lars Stolt</i>	
13.1 Introduction	567
13.2 Material Properties	570
13.2.1 Structure and Composition	571
13.2.2 Optical Properties	574
13.2.3 Electrical Properties	574
13.2.4 The Surface and Grain Boundaries	576
13.2.5 Substrate Effects	578
13.3 Deposition Methods	578
13.3.1 Substrates	579
13.3.2 Back Contact	580
13.3.3 Coevaporation of Cu(InGa)Se ₂	580
13.3.4 Two-step Processes	583
13.3.5 Other Deposition Approaches	584
13.4 Junction and Device Formation	584
13.4.1 Chemical Bath Deposition	585
13.4.2 Interface Effects	586
13.4.3 Other Deposition Methods	587
13.4.4 Alternative Buffer Layers	588
13.4.5 Transparent Contacts	590
13.4.6 Buffer Layers	591
13.4.7 Device Completion	592
13.5 Device Operation	592
13.5.1 Light-generated Current	593
13.5.2 Recombination	595
13.5.3 The Cu(InGa)Se ₂ /CdS Interface	599
13.5.4 Wide and Graded Band Gap Devices	600
13.6 Manufacturing Issues	602
13.6.1 Processes and Equipment	602
13.6.2 Module Fabrication	604
13.6.3 Module Performance	604
13.6.4 Production Costs	607
13.6.5 Environmental Concerns	608
13.7 The Cu(InGa)Se ₂ Outlook	609
References	611
14 Cadmium Telluride Solar Cells	617
<i>Brian E. McCandless and James R. Sites</i>	
14.1 Introduction	617
14.2 CdTe Properties and Thin-film Fabrication Methods	621
14.2.1 Condensation/Reaction of Cd and Te ₂ Vapors on a Surface	628
14.2.2 Galvanic Reduction of Cd and Te Ions at a Surface	629
14.2.3 Precursor Reaction at a Surface	630
14.3 CdTe Thin-Film Solar Cells	631
14.3.1 Window Layers	631
14.3.2 CdTe Absorber Layer and CdCl ₂ Treatment	633

14.3.3 CdS/CdTe Intermixing	637
14.3.4 Back Contact	642
14.3.5 Solar Cell Characterization	644
14.3.6 Summary of CdTe-cell Status	650
14.4 CdTe Modules	651
14.5 The Future of CdTe-based Solar Cells	653
14.6 Acknowledgments	657
References	657
15 Dye-sensitized Solar Cells	663
<i>Kohjiro Hara and Hironori Arakawa</i>	
15.1 Introduction to Dye-Sensitized Solar Cells (DSSC)	663
15.1.1 Background	663
15.1.2 Structure and Materials	664
15.1.3 Mechanism	670
15.1.4 Charge-transfer Kinetics	673
15.1.5 Characteristics	678
15.2 DSSC Fabrication ($\eta = 8\%$)	678
15.2.1 Preparation of TiO ₂ Colloid	678
15.2.2 Preparation of the TiO ₂ Electrode	679
15.2.3 Dye Fixation onto the TiO ₂ Film	680
15.2.4 Redox Electrolyte	681
15.2.5 Counter Electrode	681
15.2.6 Assembling the Cell and Cell Performance	681
15.3 New Developments	682
15.3.1 New Oxide Semiconductor Film Photoelectrodes	683
15.3.2 New Dye Photosensitizers	683
15.3.3 New Electrolytes	688
15.3.4 Quasi-solid-state and Solid-state DSSCs	689
15.4 Approach to Commercialization	691
15.4.1 Stability of the DSSC	691
15.4.2 Module Fabrication and Other Subjects for Commercialization	694
15.5 Summary and Prospects	695
References	696
16 Measurement and Characterization of Solar Cells and Modules	701
<i>Keith Emery</i>	
16.1 Introduction	701
16.2 Rating PV Performance	701
16.2.1 Standard Reporting Conditions	702
16.2.2 Alternative Peak Power Ratings	715
16.2.3 Energy-based Performance Rating Methods	716
16.2.4 Translation Equations to Reference Conditions	719
16.3 Current Versus Voltage Measurements	721
16.3.1 Measurement of Irradiance	721
16.3.2 Simulator-based $I-V$ Measurements: Theory	722

16.3.3	Primary Reference Cell Calibration Methods	723
16.3.4	Uncertainty Estimates in Reference Cell Calibration Procedures	726
16.3.5	Intercomparison of Reference Cell Calibration Procedures	727
16.3.6	Multijunction Cell Measurement Procedures	728
16.3.7	Cell and Module $I-V$ Systems	731
16.3.8	Solar Simulators	736
16.4	Spectral Responsivity Measurements	738
16.4.1	Filter-based Systems	739
16.4.2	Grating-based Systems	741
16.4.3	Spectral Responsivity Measurement Uncertainty	742
16.5	Module Qualification and Certification	745
	Acknowledgements	746
	References	747
17	Photovoltaic Systems	753
	<i>Klaus Preiser</i>	
17.1	Introduction to PV Systems and Various Forms of Application	753
17.2	Principles of photovoltaic Power System Configuration and their Application	755
17.2.1	Grid-independent Photovoltaic Systems for Small Devices and Appliances	755
17.2.2	Photovoltaic Systems for Remote Consumers of Medium and Large Size	761
17.2.3	Decentralised Grid-connected Photovoltaic Systems	774
17.2.4	Central Grid-connected Photovoltaic Systems	779
17.2.5	Space Application	780
17.3	Components for PV Systems	784
17.3.1	Battery Storage	784
17.3.2	Charge Controller	787
17.3.3	Inverters	788
17.3.4	Auxiliary Generators	790
17.3.5	System Sizing	791
17.3.6	Energy-saving Domestic Appliances	793
17.4	Future Developments in Photovoltaic System Technology	794
17.4.1	Future Developments in Off-grid Power Supply with Photovoltaics	794
17.4.2	Future Developments in Grid-connected Photovoltaic Systems	796
	References	797
18	Electrochemical Storage for Photovoltaics	799
	<i>Dirk Uwe Sauer</i>	
18.1	Introduction	799
18.2	General Concept of Electrochemical Batteries	801
18.2.1	Fundamentals of Electrochemical Cells	801

18.2.2	Batteries with Internal and External Storage	807
18.2.3	Commonly Used Technical Terms and Definitions	809
18.2.4	Definitions of Capacity and State of Charge	811
18.3	Typical Operation Conditions of Batteries in PV Applications	812
18.3.1	An Example of an Energy Flow Analysis	812
18.3.2	Classification of Battery-operating Conditions in PV Systems	813
18.4	Secondary Electrochemical Accumulators with Internal Storage	817
18.4.1	Overview	817
18.4.2	NiCd Batteries	818
18.4.3	Nickel-metal Hydride (NiMH) Batteries	821
18.4.4	Rechargeable Alkali Mangan (RAM) Batteries	822
18.4.5	Lithium-ion and Lithium-polymer Batteries	822
18.4.6	Double-layer Capacitors	824
18.4.7	The Lead Acid Battery	826
18.5	Secondary Electrochemical Battery Systems with External Storage	849
18.5.1	Redox-flow Batteries	850
18.5.2	Hydrogen/Oxygen Storage Systems	852
18.6	Investment and Lifetime Cost Considerations	857
18.7	Conclusion	859
	References	860
19	Power Conditioning for Photovoltaic Power Systems	863
	<i>Jürgen Schmid, Heribert Schmidt</i>	
19.1	Charge Controllers and Monitoring Systems for Batteries in PV Power Systems	864
19.1.1	Charge Controllers	864
19.1.2	Charge Equaliser for Long Battery Strings	877
19.2	Inverters	881
19.2.1	General Characteristics of PV Inverters	881
19.2.2	Inverters for Grid-connected Systems	881
19.2.3	Inverters for Stand-alone Operation	883
19.2.4	Inverter Principles	884
19.2.5	Power Quality of Inverters	896
19.2.6	Active Quality Control in the Grid	900
19.2.7	Safety Aspects with Grid-connected Inverters	900
19.3	Acknowledgement	902
	References	902
20	Energy Collected and Delivered by PV Modules	905
	<i>Eduardo Lorenzo</i>	
20.1	Introduction	905
20.2	Movement between Sun and Earth	906
20.3	Solar Radiation Components	912
20.4	Solar Radiation Data and Uncertainty	915
20.4.1	Clearness Index	920
20.5	Radiation on Inclined Surfaces	920

20.5.1	Estimation of the Direct and Diffuse Components of Horizontal Radiation, Given the Global Radiation	920
20.5.2	Estimation of the Hourly Irradiation from the Daily Irradiation	925
20.5.3	Estimation of the Radiation on Surfaces on Arbitrary Orientation, Given the Components Falling on a Horizontal Surface	927
20.6	Diurnal Variations of the Ambient Temperature	933
20.7	Effects of the Angle of Incidence and of the Dirt	934
20.8	Some Calculation Tools	937
20.8.1	Generation of Daily Radiation Sequences	937
20.8.2	The Reference Year	937
20.8.3	Shadows and Trajectory Maps	939
20.9	Irradiation on Most Widely Studied Surfaces	940
20.9.1	Fixed Surfaces	943
20.9.2	Sun-tracking Surfaces	945
20.9.3	Concentrators	946
20.10	PV Generator Behaviour under Real Operation Conditions	947
20.10.1	The Selected Methodology	949
20.10.2	Second-order Effects	953
20.11	Reliability and Sizing of Stand-alone PV Systems	956
20.12	The Case of Solar Home Systems	962
20.13	Energy Yield of Grid-connected PV Systems	964
20.14	Conclusions	966
	Acknowledgements	967
	References	967
21	Economic Analysis and Environmental Aspects of Photovoltaic Systems	971
	<i>Richard A. Whisnant, Stephen A. Johnston and James H. Hutchby</i>	
21.1	Background	972
21.2	Economic Analysis	973
21.2.1	Key Concepts	973
21.2.2	General Methodology	980
21.2.3	Case Studies	984
21.3	Energy Payback and Air Pollution Reduction	997
21.4	Prospects for the Future	999
	References	1003
22	PV in Architecture	1005
	<i>Tjerk H. Reijenga</i>	
22.1	Introduction	1005
22.1.1	Photovoltaics (PV) as a Challenge for Architects and Engineers	1005
22.1.2	Definition of Building Integration	1006

22.2	PV in Architecture	1008
22.2.1	Architectural Functions of PV Modules	1008
22.2.2	PV as Part of “Green Design”	1011
22.2.3	PV Integrated as Roofing Louvres, Facades and Shading	1011
22.2.4	Well-integrated Systems	1014
22.2.5	Integration of PV Modules in Architecture	1019
22.2.6	Brundtland Centre, Toftlund (DK) – a Case Study	1022
22.3	BIPV Basics	1026
22.3.1	Categories and Type of Buildings	1026
22.3.2	Cells and Modules	1029
22.4	Steps in the Design Process with PV	1036
22.4.1	Urban Aspects	1036
22.4.2	Practical Rules for Integration	1037
22.4.3	Step-by-step Design	1038
22.4.4	Design Process: Strategic Planning	1039
22.5	Conclusions	1040
	References	1041
	Further Reading	1042
23	Photovoltaics and Development	1043
	<i>Jorge M. Huacuz and Lalith Gunaratne</i>	
23.1	Electricity and Development	1043
23.1.1	Energy and the Early Man	1043
23.1.2	Let There be Electricity	1044
23.1.3	One Third of Humanity Still in Darkness	1044
23.1.4	The Centralized Electrical System	1045
23.1.5	Rural Electrification	1045
23.1.6	The Rural Energy Scene	1046
23.2	Breaking the Chains of Underdevelopment	1046
23.2.1	Electricity Applications in the Rural Setting	1046
23.2.2	Basic Sources of Electricity	1047
23.3	The PV Alternative	1048
23.3.1	PV Systems for Rural Applications	1049
23.3.2	Barriers to PV Implementation	1051
23.3.3	Technical Barriers	1052
23.3.4	Nontechnical Issues	1055
23.3.5	Trained Human Resources	1059
23.4	Four Examples of PV Rural Electrification	1061
23.4.1	Argentina	1061
23.4.2	Bolivia	1061
23.4.3	Brazil	1063
23.4.4	Mexico	1064
23.4.5	Sri Lanka	1065
23.4.6	Water Pumping in the Sahel	1067
23.5	Toward a New Paradigm for Rural Electrification	1068
	References	1069

24 Financing PV Growth	1073
<i>Michael T. Eckhart, Jack L. Stone and Keith Rutledge</i>	
24.1 Historical Development of PV Financing	1073
24.2 Capital Requirements	1075
24.2.1 Market Drivers	1075
24.2.2 Growth Outlook	1075
24.2.3 Capital Requirements	1076
24.3 Financial Characteristics of PV	1077
24.4 Financing PV for Grid-connected Residences	1079
24.4.1 Impact of Loan Terms on End-user Cost	1079
24.4.2 Types of Residential Financing	1080
24.4.3 Lender's Issues	1081
24.4.4 Borrowers' Experience	1081
24.4.5 Example Calculation	1082
24.4.6 Improving the Financing of Residential PV	1082
24.5 Financing PV in Rural Areas of Developing Countries	1083
24.5.1 Rural Applications	1083
24.5.2 Impact of Financing on Market Demand	1084
24.5.3 Examples of PV Financing in Rural Areas	1085
24.6 Sources of International Financing	1086
24.6.1 International Aid and Donor Funding	1086
24.6.2 United Nations	1087
24.6.3 World Bank Solar Home System Projects	1088
24.6.4 International Finance Corporation (IFC)	1089
24.6.5 Global Environment Facility	1089
24.7 Financing the PV Industry	1091
24.7.1 Financing Working Capital in the Distribution Channels	1092
24.8 Government Incentives and Programs	1092
24.8.1 Potential Impact of Financing as a Government Policy Option	1092
24.8.2 Direct Subsidies ("Buy-downs")	1094
24.8.3 Soft Loans (Interest Subsidies)	1095
24.8.4 Income Tax Deductions and Credits	1096
24.9 Funding Government Research and Development	1096
24.9.1 PV Programs in the United States	1096
24.9.2 PV Programs in Japan	1097
24.9.3 PV Programs in Europe	1097
24.9.4 Future PV R&D Programs	1099
24.9.5 Sources of R&D Funding	1099
Annex	1100
References	1114
Index	1117

List of Contributors

Jesús Alonso

Departamento de I+D
ISOFOTON
C/Caleta de Velez, 52
Pol. Ind. Santa Teresa
29006 Malaga
Spain
Phone: +3495 224 3790
Fax: +3495 224 3449
email: *j.alonso@isofoton.es*

Hironori Arakawa

National Institute of Advanced
Industrial Science and Technology
(AIST)
1-1-1 Higashi, Tsukuba, Ibaraki
305-8565, Japan
Phone: 29-861-4410
Fax: 29-856-3445
email: *h.arakawa@aist.go.jp*

Sheila Bailey

NASA Lewis Research Center
MS 302-1, 21000 Brookpark Road
Cleveland, OH 44135
USA
Phone: +1 216 433 2228
Fax: +1 216 433 6106
email: *Sheila.bailey@lerc.nasa.gov*

Carlos del Cañizo

Instituto de Energía Solar
Universidad Politécnica de Madrid

E.T.S.I. Telecomunicación
28040 Madrid
Spain
Phone: +34 91 544 1060
Fax: +34 91 544 6341
email: *canizo@ies-def.upm.es*

Bruno Ceccaroli

Silicon Technologies AS
P.O. Box 8309 Vaagsbygd
N-4676 Kristiansand
Norway
Phone: +47 38 08 58 81
Fax: +47 38 11 99 61
email: *br-c@online.no*

Xunming Deng

Department of Physics and
Astronomy
University of Toledo
Toledo, OH 43606
USA
Phone: +1 419 530 4782
Fax: +1 419 530 2723
email: *dengx@physics.utoledo.edu*

Michael T. Eckhart

Solar Bank Program
Solar International
Management Inc.
1825 I Street, NW, Suite 400
Washington, DC 20006 USA
USA

Phone: +1 202-429-2030
Fax: +1 202-429-5532
email: *eckhart@solarbank.com*

Keith Emery
NREL
1617 Cole Boulevard
Golden, CO 80401-3393
USA
Phone: +1 303 384 6632
Fax: +1 303 384 6604
email: *keith_emery@nrel.gov*

Arthur Endrös
Corporate R&D department
Siemens and Shell Solar GmbH
Siemens AG
Munich, Germany

Dieter Franke
ACCESS e.V.
Aachen
Germany

D. J. Friedman
NREL
1617 Cole Boulevard
Golden, CO 80401-3393
USA

Jeffery L. Gray
Purdue University
West Lafayette
Indiana
USA
email: *grayj@ecn.purdue.edu*

Lalith Gunaratne
Solar Power & Light Co, Ltd
338 TB Jayah Mawatha
Colombo 10
Sri Lanka

Phone: +94 014 818395
Fax: + 94 014 810824
email: *laithq@sri.lanka.net*

Christian Haessler
Central Research Physics
Bayer AG Krefeld
Germany
email: *christian.haessler@
bayerpolymers.com*

Steven S. Hegedus
Institute of Energy Conversion
University of Delaware
Newark DE 19716
USA
email: *ssh@udel.edu*

Jorge Huacuz
Unidad de Energías no
Convencionales
Instituto de Investigaciones
Eléctricas
P.O. Box 1-475
Cuernavaca, Morelos
62490 Mexico
Phone/Fax: +52 73 182 436
email: *jhuacuz@iie.org.mx*

J. A. Hutchby
Semiconductor Research
Corporation
P.O. Box 12053
Research Triangle Park
North Carolina 27709
USA

S. A. Johnston
P.O. Box 12194
Research Triangle Park
North Carolina 27709
USA

Juris Kalejs

RWE Schott Solar Inc.
4 Suburban Park Drive
Billerica, MA 01821 USA
Phone: 978-947-5993
Fax: 978-663-2868
email: *jkalejs@asepv.com*

Department of Materials
Technology
N-7491 Trondheim
Norway
Phone: +47 73 59 27 94
Fax: +47 43 59 48 89
email: *Otto.Lohne@sintef.no*

Wolfgang Koch

Central Research, Physics
(ZF-FPM), Photonic Materials
Chemicals-Bayer Solar, (CH-BS),
Projects
Bayer AG
Geb.R82, PF111107
D-47812 Krefeld
Germany
Phone: +492151-883370
Fax: +492151-887503
email: *wolfgang.koch.wk2@bayer-ag.de*

Eduardo Lorenzo

Instituto de Energía Solar
Universidad Politécnica de Madrid
E.T.S.I. Telecomunicación
Ciudad Universitaria
28040 Madrid
Spain
Phone: +3491 366 7228
Fax: +3491 544 6341
email: *lorenzo@ies-def.upm.es*

Hara Kohjiro

National Institute of Advanced
Industrial Science and Technology
(AIST)
1-1-1 Higashi, Tsukuba, Ibaraki
305-8565, Japan
Phone: 29-861-4494
Fax: 29-861-6771
email: *k-hara@aist.go.jp*

Antonio Luque

Instituto de Energía Solar
Universidad Politécnica de Madrid
E.T.S.I. Telecomunicación
28040 Madrid
Spain
Phone: +34 91 336 7229
Fax: +34 91 544 6341
email: *luque@ies-def.upm.es*

Sarah Kurtz

NREL
1617 Cole Boulevard
Golden, CO 80401-3393
USA
Phone: +1 303 384 6475
Fax: +1 303 384 6531
email: *sarah_kurtz@nrel.gov*

Joachim Luther

Fraunhofer Institute for Solar
Energy Systems ISE
Heidenhofstrasse 2
79110 Freiburg
Germany
Phone: +49 (0) 761 4588-5120
Fax: +49 (0) 761 4588-9120
email: *luther@ise.fhg.de*

Otto Lohne

Norwegian University of Science
and Technology

Antonio Martí

Instituto de Energía Solar
Universidad Politécnica de Madrid
E.T.S.I. Telecomunicación

28040 Madrid
Spain
Phone: +34 91 544 1060
Fax: +34 91 544 6341
email: *amarti@etsit.upm.es*

Brian McCandless
Institute of Energy Conversion
University of Delaware
Newark, DE 19716
USA
Phone: +1 302 831 6240
Fax: +1 302 831 6226
email: *bem@udel.edu*

H. J. Moeller
Institut für Experimentelle Physik
TU Bergakademie Freiberg
Silbermannstr. 1
09599 Freiberg
Germany
Phone: +493731-392896
Fax: +493731-394314
email: *moeller@physik.tu-freiberg.de*

J. M. Olson
NREL
1617 Cole Boulevard
Golden, CO 80401-3393
USA

Klaus Preiser
Produktion Energie badenova
AG & Co. KG
Tullastraße 61
79108 Freiburg i.Br.
Telefon 0761/279-2207
Telefax 0761/279-2731
Mobil 0160/7154879
email: *klaus.preiser@badenova.de*
www.badenova.de

Ryne Raffaele
Rochester Institute of Technology

84 Lomb Memorial Drive
Rochester, NY 14623-5603
USA

Tjerk Reijenga
BEAR Architecten
Gravin Beatrixstraat 34
NL 2805 PJ Gouda
The Netherlands
Phone: +31 182 529 899
Fax: +31 182 582 599
email: *Tjerk@bear.nl*

Keith Rutledge
Renewable Energy Development
Institute
Willits, CA 95490
USA

Dirk Uwe Sauer
Electrical Energy Systems -
Storage Systems
Fraunhofer Institut für Solare
Energiesysteme ISE
Heidenhofstrasse 2
D-79110 Freiburg
Germany
Phone: +49 761 4588 5219
Fax: +49 761 4588 9217
email: *sauer@ise.fhg.de*

Eric A. Schiff
Department of Physics
Syracuse University
Syracuse, New York 13244-1130
USA
http://physics.syr.edu/~schiff

Jürgen Schmid
ISET–Institut für Solare
Energieversorgungstechnik e.V.,
Universität Kassel
Königstor 59

34119 Kassel
Germany
Phone: +49 (0)5 61/72 94-3 45
Fax: +49 (0)5 61/72 94-3 00
email: *jschmid@iset.uni-kassel.de*

Heribert Schmidt
Fraunhofer Institut für Solare
Energiesysteme ISE, Freiburg
Heidenhofstr. 2
79110 Freiburg
Germany
Phone: +49 (0)7 61/45 88-52 26
Fax: +49 (0)7 61/45 88-92 26
email: *heri@ise.fhg.de*

William Shafarman
Institute of Energy Conversion
University of Delaware
Newark, DE 19716
USA
Phone: 1 302 831 6215
Fax: 1 302 831 6226
email: *wms@udel.edu*

James Sites
Department of Physics
Colorado State University
Fort Collins, CO 80523-1875
USA
Phone: +1 970 491 5850
Fax: +1 970 491 7947
email: *sites@lamar.colostate.edu*

Bushan Sopori
NREL
1617 Cole Boulevard
Golden, CO 80401-3393
USA
Phone: +1 303 384 6683
Fax: +1 303 384 6684
email: *bsopori@nrel.gov*

Lars Stolt
Ångström Solar Center
Uppsala University
P.O. Box 534
SE-751 21 Uppsala
Sweden
Phone: +46 18 471 3039
Fax: +46 18 555 095
email: *Lars.Stolt@angstrom.uu.se*

Jack L. Stone
NREL
1617 Cole Boulevard
Golden, CO 80401-3393
USA

Richard Swanson
SUNPOWER Corporation
435 Indio Way
Sunnyvale, CA 94086
USA
Phone: +1 408 991 0900
Fax: +1 408 739 7713
email: *Rswanson@sunpowercorp.com*

Ignacio Tobías
Instituto de Energía Solar
Universidad Politécnica de Madrid
ETSI Telecomunicación
Ciudad Universitaria
28040 Madrid
Spain
Phone: +3491 5475700-282
Fax: +3491 5446341
email: *Tobias@ies-def.upm.es*

Richard A. Whisnant
Parameters, Inc.
1505 Primrose Lane
Cary, NC 27511
(919) 467-8710 (phone, fax)
(919) 523-0456 (cell phone)

This Page Intentionally Left Blank

1

Status, Trends, Challenges and the Bright Future of Solar Electricity from Photovoltaics

Steven S. Hegedus¹ and Antonio Luque²

¹*Institute of Energy Conversion, University of Delaware, Newark, Delaware, USA,* ²*Universidad Politecnica de Madrid, Madrid, Spain*

1.1 THE BIG PICTURE

Congratulations! You are reading a book about a technology that has changed the way we think about energy. Solar electricity, also known as photovoltaics (PV), has shown since the 1970s that the human race can get a substantial portion of its electrical power without burning fossil fuels (coal, oil or natural gas) or creating nuclear fission reactions. Photovoltaics helps us avoid most of the threats associated with our present techniques of electricity production and also has many other benefits. Photovoltaics has shown that it can generate electricity for the human race for a wide range of applications, scales, climates, and geographic locations. Photovoltaics can bring electricity to a rural homemaker who lives 100 kilometers and 100 years away from the nearest electric grid connection in her country, thus allowing her family to have clean, electric lights instead of kerosene lamps, to listen to a radio, and to run a sewing machine for additional income. Or, photovoltaics can provide electricity to remote transmitter stations in the mountains allowing better communication without building a road to deliver diesel fuel for its generator. It can help a major electric utility in Los Angeles, Tokyo, or Madrid to meet its peak load on hot summer afternoons when air conditioners are working full time. It allows homes and businesses a new level of guaranteed energy availability and security, and photovoltaics has been powering satellites orbiting the Earth or flying to Mars for over 30 years.

Photovoltaics is an empowering technology that allows us to do totally new things, as well as, do old things better. It allows us to look at whole new modes of supplying

electricity to different markets around the world and out of the world (in outer space). It also allows us to do what we already do (generate electricity, which is distributed over the transmission grid) but to do it in a sustainable, pollution-free, equitable fashion. Why is photovoltaics equitable? Because nearly every one has access to sunlight!

Electricity is the most versatile form of energy we have. It is what allows citizens of the developed countries to have nearly universal lighting on demand, refrigeration, hygiene, interior climate control in their homes, businesses and schools, and widespread access to various electronic and electromagnetic media. Access to and consumption of electricity is closely correlated with quality of life. Figure 1.1 shows the Human Development Index (HDI) for over 60 countries, which includes over 90% of the Earth's population, versus the annual per capita electricity use (adapted from ref 1). The HDI is compiled by the UN and calculated on the basis of life expectancy, educational achievement, and per capita Gross Domestic Product. To improve the quality of life in many countries, as measured by their HDI, will require increasing their electricity consumption by factors of 10 or more, from a few hundred to a few thousand kilowatt-hrs (kWh) per year. How will we do it? Our choices are to continue applying the answers of the last century such as burning more fossil fuels (and releasing megatons of CO_2 , SO_2 , and NO_2) or building more nuclear plants (despite having no method of safely disposing of the high-level radioactive waste) or to apply the new millennium's answer of renewable, sustainable, nonpolluting, widely available clean energy like photovoltaics and wind. (Wind presently generates over a thousand times more electricity than photovoltaics but it is very site-specific, whereas photovoltaics is generally applicable to most locations.)

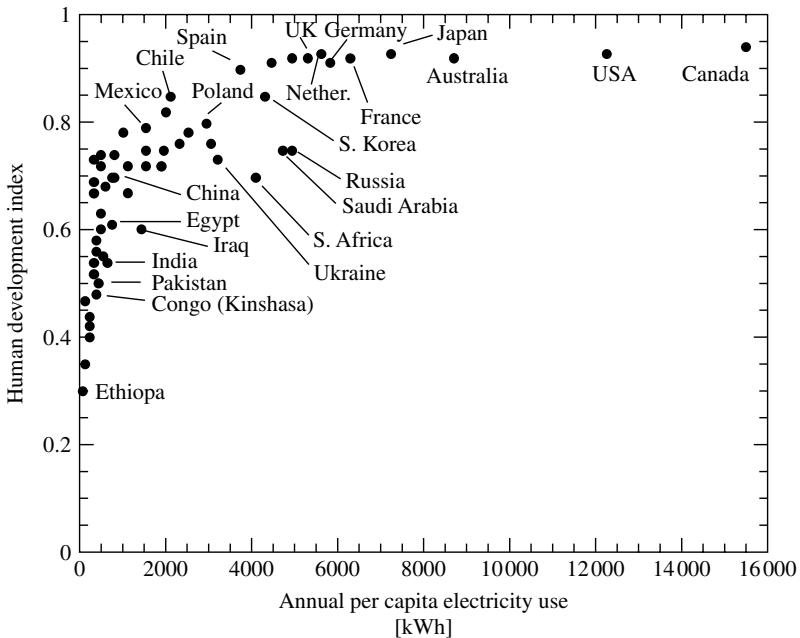


Figure 1.1 Human development index (HDI) vs. per capita kW usage [1]

1.2 WHAT IS PHOTOVOLTAICS?

Photovoltaics is the technology that generates direct current (DC) electrical power measured in Watts (W) or kiloWatts (kW) from semiconductors when they are illuminated by photons. As long as light is shining on the solar cell (the name for the individual PV element), it generates electrical power. When the light stops, the electricity stops. Solar cells never need recharging like a battery. Some have been in continuous outdoor operation on Earth or in space for over 30 years.

Table 1.1 lists some of the advantages and disadvantages of photovoltaics. Note, that they include both technical and nontechnical issues. Often, the advantages and disadvantages of photovoltaics are almost completely opposite of conventional fossil-fuel power plants. For example, fossil-fuel plants have disadvantages of: a wide range of environmentally hazardous emissions, parts which wear out, steadily increasing fuel costs, they are not modular (deployable in small increments), and they suffer low public opinion (no one wants a coal burning power plant in their neighborhood). Photovoltaics suffers none of these problems. The two common traits are that both PV and fossil fueled power plants are very reliable but lack the advantage of storage.

Notice that several of the disadvantages are nontechnical but relate to economics and infrastructure. They are partially compensated for by a very high public acceptance and awareness of the environmental benefits. During the late 1990s, the average growth rate of PV production was over 33% per annum.

What is the physical basis of PV operation? Solar cells are made of materials called semiconductors, which have weakly bonded electrons occupying a band of energy

Table 1.1 Advantages and disadvantages of photovoltaics

Advantages of photovoltaics	Disadvantages of photovoltaics
Fuel source is vast and essentially infinite	Fuel source is diffuse (sunlight is a relatively low-density energy)
No emissions, no combustion or radioactive fuel for disposal (does not contribute perceptibly to global climate change or pollution)	
Low operating costs (no fuel)	High installation costs
No moving parts (no wear)	
Ambient temperature operation (no high temperature corrosion or safety issues)	
High reliability in modules (>20 years)	Poorer reliability of auxiliary (balance of system) elements including storage
Modular (small or large increments)	
Quick installation	
Can be integrated into new or existing building structures	
Can be installed at nearly any point-of-use	Lack of widespread commercially available system integration and installation so far
Daily output peak may match local demand	Lack of economical efficient energy storage
High public acceptance	
Excellent safety record	

called the *valence band*. When energy exceeding a certain threshold, called the *band gap energy*, is applied to a valence electron, the bonds are broken and the electron is somewhat “free” to move around in a new energy band called the *conduction band* where it can “conduct” electricity through the material. Thus, the free electrons in the conduction band are separated from the valence band by the band gap (measured in units of electron volts or eV). This energy needed to free the electron can be supplied by photons, which are particles of light. Figure 1.2 shows the idealized relation between energy (vertical axis) and the spatial boundaries (horizontal axis). When the solar cell is exposed to sunlight, photons hit valence electrons, breaking the bonds and pumping them to the conduction band. There, a specially made selective contact that collects conduction-band electrons drives such electrons to the external circuit. The electrons lose their energy by doing work in the external circuit such as pumping water, spinning a fan, powering a sewing machine motor, a light bulb, or a computer. They are restored to the solar cell by the return loop of the circuit via a second selective contact, which returns them to the valence band with the same energy that they started with. The movement of these electrons in the external circuit and contacts is called the *electric current*. The potential at which the electrons are delivered to the external world is slightly less than the threshold energy that excited the electrons; that is, the band gap. Thus, in a material with a 1 eV band gap, electrons excited by a 2 eV photon or by a 3 eV photon will both still have a potential of slightly less than 1 V (i.e. the electrons are delivered with an energy of 1 eV). The electric power produced is the product of the current times the voltage; that is, power is the number of free electrons times their potential. Chapter 3 delves into the physics of solar cells in much greater detail.

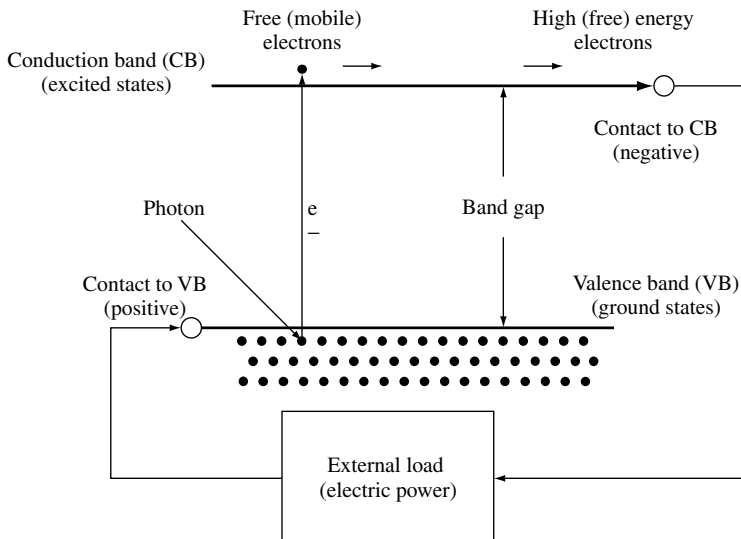


Figure 1.2 Schematic of a solar cell. Electrons are pumped by photons from the valence band to the conduction band. There they are extracted by a contact selective to the conduction band (an *n*-doped semiconductor) at a higher (free) energy and delivered to the outside world via wires, where they do some useful work, then are returned to the valence band at a lower (free) energy by a contact selective to the valence band (a *p*-type semiconductor)

Sunlight is a spectrum of photons distributed over a range of energy. Photons whose energy is greater than the band gap energy (the threshold energy) can excite electrons from the valence to conduction band where they can exit the device and generate electrical power. Photons with energy less than the energy gap fail to excite free electrons. Instead, that energy travels through the solar cell and is absorbed at the rear as heat. Solar cells in direct sunlight can be somewhat (20–30°C) warmer than the ambient air temperature. Thus, PV cells can produce electricity without operating at high temperature and without mobile parts. These are the salient characteristics of photovoltaics that explain safe, simple, and reliable operation.

At the heart of any solar cell is the *pn* junction. Modeling and understanding is very much simplified by using the *pn* junction concept. This *pn* junction results from the “doping” that produces conduction-band or valence-band selective contacts with one becoming the *n*-side (lots of negative charge), the other the *p*-side (lots of positive charge). The role of the *pn* junction and of the selective contacts will be explained in detail in Chapters 3 and 4. Here, *pn* junctions are mentioned because this term is often present when talking of solar cells, and is used occasionally in this chapter.

Silicon (Si), one of the most abundant materials in the Earth’s crust, is the semiconductor used in crystalline form (c-Si) for 90% of the PV applications today (Chapter 5). Surprisingly, other semiconductors are better suited to absorb the solar energy spectrum. This puzzle will be explained further in Section 1.10. These other materials are in development or initial commercialization today. Some are called thin-film semiconductors, of which amorphous silicon (a-Si) (Chapter 12), copper indium gallium diselenide (Cu(InGa)Se₂ or CIGS) (Chapter 13), and cadmium telluride (CdTe) (Chapter 14) receive most of the attention. Solar cells may operate under concentrated sunlight (Chapter 11) using lenses or mirrors as concentrators allowing a small solar cell area to be illuminated with the light from larger area. This saves the expensive semiconductor but adds complexity to the system, since it requires tracking mechanisms to keep the light focused on the solar cells when the sun moves in the sky. Silicon and III-V semiconductors (Chapter 9), made from compounds such as gallium arsenide (GaAs) and gallium indium phosphide (GaInP) are the materials used in concentrator technology that is still in its demonstration stage.

For practical applications, a large number of solar cells are interconnected and encapsulated into units called PV modules, which is the product usually sold to the customer. They produce DC current that is typically transformed into the more useful AC current by an electronic device called *an inverter*. The inverter, the rechargeable batteries (when storage is needed), the mechanical structure to mount and aim (when aiming is necessary) the modules, and any other elements necessary to build a PV system are called the *balance of the system* (BOS). These BOS elements are presented in Chapters 17 to 19.

1.3 SIX MYTHS OF PHOTOVOLTAICS

Borrowing a format for discussing photovoltaics from Kazmerski [2], in this section, we will briefly present and then dispel six common myths about photovoltaics. In the following sections, we identify serious challenges that remain despite 40 years of progress in photovoltaics.

The six myths are as follows:

1. *Photovoltaics will require too much land area to ever meet significant fraction of world needs:*

Solar radiation is a rather diffuse energy source. What area of PV modules is needed to produce some useful amounts of power? Let's make some very rough estimates to give answers that will be accurate within a factor of 2. Using methods described in detail in Chapter 20 (especially equations 20.50 and 20.51 and Table 20.5), one can calculate how much sunlight falls on a square meter, anywhere in the world, over an average day or a year. We will use an average value of 4 kilowatt-hrs (kWh) per m^2 per day to represent a conservative worldwide average. Now, a typical PV module is approximately 10% efficient in converting the sunlight into electricity, so every square meter of PV module produces, on average, $4 \times 0.1 = 0.4$ kWh of electrical energy per day. We can calculate the area in m^2 needed for a given amount of electrical energy E in kWh by dividing E by 0.4 kWh/m^2 . (Chapter 20 contains much more detailed methods to calculate the incident sunlight and the PV module output as a function of time of day, month of year, etc.)

Let us consider three different-sized PV applications: a family's house in an industrialized country, replacing a 1000 MW (megawatt) coal or nuclear powered generating plant, or providing all the electricity used in the USA.

First, for a typical family, let us assume that there are four people in the house. Figure 1.1 shows a range of electricity usage for the industrialized countries. Let us use 6000 kWh/person/year as an average. But, this includes all their electrical needs including at work, at school, as well as the electricity needed for manufacturing the products they buy, powering their street lights, pumping water to their homes, and so on. Since people spend about a third of the day awake in their home, let us assume that a third of their electrical needs are to be supplied in their home, or 2000 kWh/person/year. Dividing this by 365 days in a year gives about 5 kWh/person/day, or 20 kWh/day per family of four. This is consistent with household data from various sources for the US and Europe. Thus, they would need $20 \text{ kWh}/0.4 \text{ kWh/m}^2$ or 50 m^2 of solar modules to provide their electrical power needs over the year. Thus, a rectangular area of solar modules of 5 by 10 meters will be sufficient. In fact, many roofs are about this size, and many homes have sunny areas of this size around them, so it is possible for a family of four, with all the conveniences of a typical modern home, to provide all their power from PV modules on their house or in their yard.

Next, how much land would it take to replace a 1000 MW coal or nuclear power plant that operates 24 hours/day and might power a large city? This would require $10^6 \text{ kW} \times 24 \text{ hr}/(0.4 \text{ kWh/m}^2)$ or $6 \times 10^7 \text{ m}^2$. So, with 60 km^2 (or 24 square miles) of photovoltaics we could replace one of last century's power plants with one of this century's power plants. This is a square 8 km (or 5 miles) on a side. For the same electricity production, this is equivalent to the area for coal mining during the coal powered plant's life cycle, if it is surface mining, or three times the area for a nuclear plant, counting the uranium mining area [3]. This is also the same area required to build a 600 km (373 miles) long highway (using a 100 m wide strip of land).

Finally, we can calculate how much land is needed to power the entire US with photovoltaics (neglecting the storage issue). The US used about 3.6×10^{12} kWh of electricity in 2000. This could be met with $2 \times 10^{10} \text{ m}^2$. If we compare with the area of paved roads across the country, of about $3.6 \times 10^6 \text{ km}^2$ and assume an average width

of 10 m this leads to $3.6 \times 10^{10} \text{ m}^2$. It is to be concluded that all the electricity needed in the US can be met by covering the paved roads with PV modules. Of course, no one is seriously proposing this action. We use the road analogy to show that if society wanted, it could establish land use priorities favorable to photovoltaics just as it has done to accommodate the ubiquitous automobile. We are certain that each state could find areas of unused land around airports, parking spaces, rooftops, highway dividing strips, or desert land that could be used for photovoltaics.

These simplistic “back-of-the-envelope” calculations show that having enough area for PV modules is not a limit for a homeowner or a large city. Certainly, there are sunny places in every country that could be used for generating significant amounts of PV power. As will be evident in other chapters, it is the initial cost of the photovoltaics, not the amount of land that is the primary barrier to be overcome.

2. *Photovoltaics can meet all of the world's needs today if we would just pass laws requiring photovoltaics and halting all fossil and nuclear plants:*

Besides the difficulty of convincing the people's representatives to pass such a law, the first technical problem faced would be the intermittent nature of the solar radiation, available only during the day and strongly reduced in overcast skies. Energy storage would solve this problem but no cheap storage method appears on the horizon. Nevertheless, well-developed electric grids may accept large amounts of PV electricity by turning off some conventional power plants when PV plants are delivering power. Adequate grid management would allow up to 20 to 30% of the electric production to be intermittent [4].

But now for a dose of reality. The cumulative production of PV modules up to the year 2002 is about 2000 MW. Thus, if you took all of the PV panels that were ever made up to and including the year 2002, and put them all in the same sunny place at the same time, they would generate enough electricity to displace about one of last century's 500 MW smoke- or radioactive-waste-producing power plants. (This assumes that the solar plant would operate at full output for an equivalent of six hours per day owing to the daily variation in sunlight). Clearly, if we want photovoltaics to make any meaningful contribution to the world's energy supply, very massive increases in manufacturing capacity are needed. Additionally, PV electricity is very expensive, presently between 5 to 10 times more expensive than conventional alternatives. Mass use of PV electricity today could produce significant negative distortion of the economic system.

Thus, requesting the immediate and exclusive use of photovoltaics is not feasible technically or, probably, economically. It would also be socially unacceptable.

3. *Photovoltaics cannot meet any significant fraction of world needs. It will remain a small-scale “cottage” industry that will only meet the needs of specialty markets like remote homes in developing countries or space satellites:*

Figure 1.3 shows the evolution of markets associated with different applications [5]. Some used to be considered as *specialty* markets, for example, the category of “world off-grid power” which is trying to supply power to the $\sim 1/3$ of the world's citizens who lack it. The grid-connected market, whose growth has been meteoric in the past decade, is by no means a small market. Ironically it is the large-scale (recently awakened) centralized power plant market which is the smallest “specialty” application in today's world. Thus, evidence from the recent past tends to refute

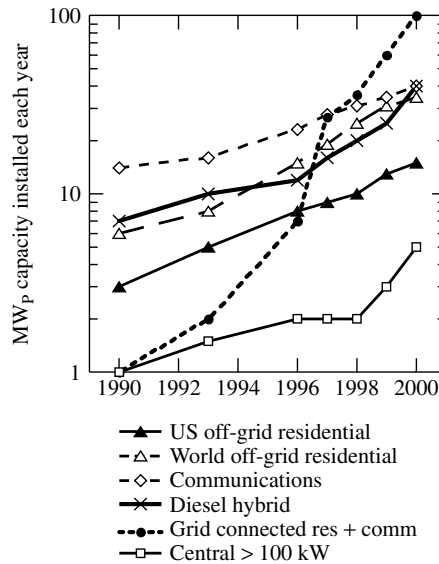


Figure 1.3 Trend in worldwide PV applications (From Reference [5] Maycock P, *Renewable Energy World* 3, 59–74 (2000))

the modest forecasts that some attribute to photovoltaics. We shall come to this point again.

4. *No more R/D is needed since PV technology has demonstrated the technical capability to perform, so we should stop all public funding and let the economic markets decide if it is worthwhile:*

The present cost of photovoltaics is affordable for certain markets but it is still too high to actually compete with conventional electricity. If PV technology is to be promoted for environmental or social reasons, public subsidy to R&D and to installation will be necessary to stimulate production and thereby reduce costs. Without continued subsidies, photovoltaics will probably remain as a specialty cottage industry for the next half century.

Public support for photovoltaics is one of the major factors compelling politicians to fund R&D. This funding had been comparable to PV sales in the 1980s, as shown in Figure 1.4. Private funding has doubled this public support so that PV companies themselves have also heavily supported the development of photovoltaics. After two decades of constant investment in a promising market that was slow to actually start, the market finally awoke and became one of the fastest growing in the world by the beginning of the twentieth century, with sales now greatly exceeding public investment.

But, this fast growing market is still dependent on public/government funding. As with many goods and services (e.g. military hardware, commercial air travel), photovoltaics is partly publicly financed. In Germany or in Japan, for instance, significant public support is being given to grid-connected installations. If photovoltaics is going to become a major energy contender, the countries where the support has been lacking will remain technologically inferior with respect to those, where the support has

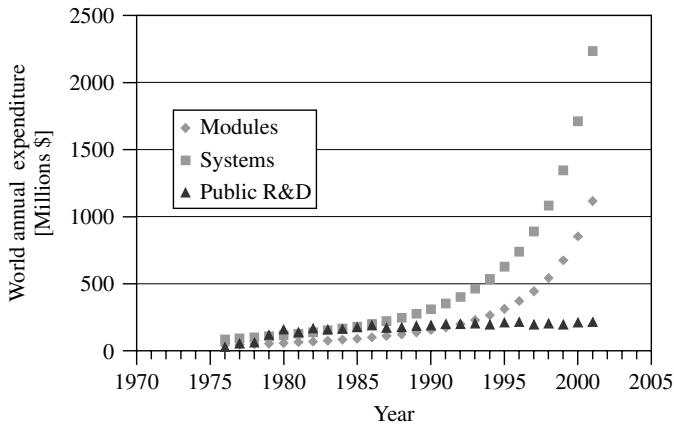


Figure 1.4 Public funding for R&D (triangles) compared to module (diamonds) and system (squares) sales. (This curve is drawn from the data of Eckhart *et al.* in Chapter 24, “Financing PV Growth”, in this book)

been stronger. This should be taken into account while making decisions about energy policy and public or private financing.

The critical question then is: Should the support be focused in R&D, or is PV technology already mature enough (as many claim) to focus on the cost reduction via the economy of scale permitted by the larger volume of production required by a subsidized market? This point will be discussed later in this chapter.

5. *Photovoltaics is polluting just like all high-technology or high-energy industries only with different toxic emissions:*

One of the most valuable characteristics of photovoltaics is its well-deserved image as an environmentally clean and “green” technology. This healthy image obviously results from the cleaner operation of a PV electricity generator compared to a fossil-fuel fired generator, but this must also extend to the manufacturing process itself as well as the recycling of discarded modules. Manufacturing of PV modules on a large scale requires the handling of large quantities of hazardous or potentially hazardous materials (e.g. heavy metals, reactive chemical solutions, toxic gases). Let it be stated at the beginning that the present Si-based PV technology which dominates the market has few environmental concerns and is considered totally safe to the public.

The PV industry is very aware of the value of its clean “green” image and has worked hard over the years to establish and maintain high standards of environmental responsibility [6, 7]. Conferences on PV Safety and Environmental Issues have been held since the late 1980s and their proceedings have been published [8, 9]; the PV Environmental Health Safety Assistance Center at Brookhaven National Laboratory in New York, USA provides worldwide leadership in risk analysis and safety recommendations for the PV industry [10].

Safe handling procedures for some of the materials and processes were already well established from the integrated circuit or glass coating industries. But in the case of unique materials and processes, safety procedures had to be developed by the PV industry. This is especially true of the thin-film technologies [11]. The PV industry recognized early that being proactive and designing safety into the process, from the

beginning, was the responsible thing to do and would ultimately result in reduced costs. The international nature of the PV industry introduces some variability in the standards which must be met.

Hazards can be classified by whether they affect workers at a PV manufacturing plant, customers with photovoltaics on or near their homes, or the public who consumes air and water near the PV plant. The population with greatest potential health risks are employees in PV manufacturing. Very little risk is associated with the public or the PV owner or installer. Among the most heavily studied issues unique to the PV industry is the potential toxicity of semiconductor CdTe and the safe usage of hydride gases AsH₃, SiH₄, GeH₄, PH₃, B₂H₆, and H₂Se, which are used in the growth of GaAs, a-Si, a-SiGe, and Cu(InGa)Se₂ layers. There has been considerable research and risk analysis of CdTe as a PV material [12–14]. The general conclusion is that CdTe in modules does not pose a risk to the public. Similarly, procedures and hardware ensuring safe usage of the hydride gases listed above have been well established in both the electronics and PV industries [15].

Environmental monitoring of the workplace for hazardous levels in the air or on surfaces, and biological monitoring of the employee for evidence of exposure should be routine. Once the module is manufactured, the only way for the public to be exposed to hazardous materials existing in some kind of modules is by absorbing them via ingestion or inhalation. Accordingly, accidental human absorption is not at all likely. Even in event of a house fire, studies have shown that PV modules do not release any potentially hazardous materials [16].

A related issue is what to do with thin film PV modules at the end of their projected 25- to 30-year life. An excellent strategy is to recycle the modules. This solves two problems at once, namely, keeping potentially hazardous materials out of the environment and reducing the need for additional mining and/or refining of new materials. Semiconductor vendors have indicated a willingness to accept used modules, and to extract and purify the CdTe, CdS, or Cu(InGa)Se₂ for resale and reuse [17, 18].

Thus, we can say with confidence that photovoltaics is nearly the cleanest and safest technology with which to generate electricity. It is especially true of the present Si technology.

6. *PV modules never recover all of the energy required in making them, thus they represent a net energy loss:*

The focus of photovoltaics is on generating energy (specifically electrical energy) with many beneficial characteristics as noted in Table 1.1. Among those who envision photovoltaics having an increasingly larger role in producing the world's electricity, there is awareness that photovoltaics must produce much more energy than was required to produce the PV system. Otherwise, it would be a net energy loss not a net energy source. The "energy payback" has been widely studied. It is described in terms of how many years the PV system must operate to produce the energy required for its manufacture. After the payback time, all of the energy produced is truly new energy.

This topic is discussed in Chapter 21. An excellent review has been given by Alsema [19]. In general, results of several studies have arrived at some general conclusions. Specific payback times have ranged from 3 to 5 years for crystalline Si and 1 to 4 years for thin films. For crystalline Si, forming the crystalline Si wafers is

the major energy requirement. For thin films, the semiconductor layers are 100 times thinner, and deposited at $\sim 1000^\circ\text{C}$ lower temperature, so their energy requirement is negligible, in comparison. Instead, it is the energy embodied in the glass or stainless steel substrate, which is the major energy sink. Also, a seemingly insignificant component, the cosmetic Al frame around the module, is responsible for a surprisingly large fraction of energy. In fact, this can be the dominant energy sink for thin-film a-Si or Cu(InGa)Se₂ modules [20, 21]. Although thin-film modules have a shorter energy payback, they also have lower efficiency, which means a larger BOS is needed to support the larger number of modules. Thus, a larger amount of energy is embodied in the BOS for thin-film photovoltaics compared to crystalline Si photovoltaics.

The case of concentrators is less studied, but again the use of semiconductor is reduced and the BOS becomes more important than even for the thin films because the concentrating structures are very massive. However, their efficiency is higher. In summary, we can guess that in this case the situation will be similar to the case of thin films.

1.4 HISTORY OF PHOTOVOLTAICS

The history of photovoltaics goes back to the nineteenth century, as shown in Table 1.2. The first functional, intentionally made PV device was by Fritts [22] in 1883. He melted Se into a thin sheet on a metal substrate and pressed a Au-leaf film as the top contact. It was nearly 30 cm² in area. He noted, “the current, if not wanted immediately, can be either stored where produced, in storage batteries, . . . or transmitted a distance and there used.” This man foresaw today’s PV technology and applications over a hundred years ago. The modern era of photovoltaics started in 1954 when researchers at Bell Labs in the USA accidentally discovered that *pn* junction diodes generated a voltage when the room lights were on. Within a year, they had produced a 6% efficient Si *pn* junction solar cell [23]. In the same year, the group at Wright Patterson Air Force Base in the US published results of a thin-film heterojunction solar cell based on Cu₂S/CdS also having 6% efficiency [24]. A year later, a 6% GaAs *pn* junction solar cell was reported by RCA Lab in the US [25]. By 1960, several key papers by Prince [26], Loferski [27], Rappaport and Wysoski [28], Shockley (a Nobel laureate) and Queisser [29], developed the fundamentals of *pn* junction solar cell operation including the theoretical relation between band gap, incident spectrum, temperature, thermodynamics, and efficiency. Thin films of CdTe were also producing cells with 6% efficiency [30]. By this time, the US space program was utilizing Si PV cells for powering satellites. Since space was still the primary application for photovoltaics, studies of radiation effects and more radiation-tolerant devices were made using Li-doped Si [31]. In 1970, a group at the Ioffe Institute led by Alferov (a Nobel laureate), in the USSR, developed a heteroface GaAlAs/GaAs [32] solar cell which solved one of the main problems that affected GaAs devices and pointed the way to new device structures. GaAs cells were of interest due to their high efficiency and their resistance to the ionizing radiation in outer space. The year 1973 was pivotal for photovoltaics, in both technical and nontechnical areas. A significant improvement in performance occurring in 1973 was the “violet cell” having an improved short wavelength response leading to a 30% relative increase in efficiency over state-of-the-art Si cells [33]. GaAs heterostructure cells were also developed at IBM in

Table 1.2 Notable events in the history of photovoltaics

-
- 1839 Becquerel (FR) discovered photogalvanic effect in liquid electrolytes
 - 1873 Smith (UK) discovered photoconductivity of solid Se
 - 1877 Adams and Day (UK) discover photogeneration of current in Se tubes; the first observation of PV effect in solids
 - 1883 Fritts (US) makes first large area solar cell using Se film
 - 1954 First 6% efficient solar cells reported: Si (Bell Lab, USA) and $\text{Cu}_2\text{S}/\text{CdS}$ (Air Force, USA)
 - 1955 Hoffman Electronics (USA) offers 2% efficient Si PV cells at \$1500/W
 - 1958 NASA Vanguard satellite with Si backup solar array
 - 1959 Hoffman Electronics (USA) offers 10% efficient Si PV cells
 - 1963 Sharp Corp (JP) produces first commercial Si modules
 - 1966 NASA Orbiting Astronomical Observatory launched with 1 kW array
 - 1970 First GaAs heterostructure solar cells by Alferov, Andreev *et al.* in the USSR
 - 1972 First PV conference to include a session on terrestrial applications (IEEE)
 - 1973 A big year in photovoltaics: Worldwide oil crisis spurs many nations to consider renewable energy including photovoltaics; Cherry Hill Conference in USA (established photovoltaics' potential and legitimacy for government research funding); World's first solar powered residence (University of Delaware, USA) built with Cu_2S (not c-Si!) solar modules
 - 1974 Project Sunshine initiated in Japan to foster growth of PV industry and applications; Tyco (USA) grows 2.5 cm wide Si ribbon for photovoltaics, first alternative to Si wafers
 - 1975 First book dedicated to PV science and technology by Hovel (USA)
 - 1980 First thin-film solar cell >10% using $\text{Cu}_2\text{S}/\text{CdS}$ (USA)
 - 1981 350 kW Concentrator array installed in Saudi Arabia
 - 1982 First 1 MW utility scale PV power plant (CA, USA) with Arco Si modules on 2-axis trackers
 - 1984 6 MW array installed in Carrisa Plains CA, USA [35]
 - 1985 A big year for high-efficiency Si solar cells: Si solar cell >20% under standard sunlight (UNSW, Australia) [36] and >25% under 200X concentration (Stanford Univ. USA) [37]
 - 1986 First commercial thin-film power module, the a-Si G4000 from Arco Solar (USA)
 - 1987 Fourteen solar powered cars complete the 3200 km World Solar Challenge race (Australia) with the winner averaging 70 kph
 - 1994 GaInP/GaAs 2-terminal concentrator multijunction >30% (NREL, USA) [38]
 - 1995 "1000 roofs" German demonstration project to install photovoltaics on houses, which triggered the present favorable PV legislation in Germany, Japan and other countries
 - 1996 Photoelectrochemical "dye-sensitized" solid/liquid cell achieves 11% (EPFL, Switzerland) [39]
 - 1997 Worldwide PV production reaches 100 MW per year
 - 1998 $\text{Cu}(\text{InGa})\text{Se}_2$ thin-film solar cell reaches 19% efficiency (NREL, US) [40] comparable with multicrystalline Si. First concentrating array for space launched on Deep Space 1 by US (5 kW using high efficiency GaInP/GaAs/Ge triple junction cells)
 - 1999 Cumulative worldwide installed photovoltaics reaches 1000 MW
 - 2000 Olympics in Australia highlight wide range of PV applications, and the awarding of the first Bachelor of Engineering degrees in Photovoltaics and Solar Engineering (UNSW, Australia)
 - 2002 Cumulative worldwide installed photovoltaics reaches 2000 MW. It took 25 years to reach the first 1000 MW and only 3 years to double it; production of crystalline Si cells exceeds 100 MW per year at Sharp Corp. (Japan). BP Solar ceases R&D and production of a-Si and CdTe thin-film modules in USA ending >20 years of effort
-

the USA having 13% efficiency [34]. Also in 1973, a crucial nontechnical event occurred called the *Cherry Hill Conference*, named after the town in New Jersey, USA, where a group of PV researchers and heads of US government scientific organizations met to evaluate the scientific merit and potential of photovoltaics. The outcome was the decision that photovoltaics was worthy of government support, resulting in the formation of the US Energy Research and Development Agency, the world's first government group whose mission included fostering research on renewable energy, which ultimately became the US Dept. of Energy. Finally, in October 1973, the first World Oil Embargo was instituted by the Persian Gulf oil producers. This sent shock waves through the industrialized world, and most governments began programs to encourage renewable energy especially solar energy. Some would say this ushered in the modern age of photovoltaics and gave a new sense of urgency to research and application of photovoltaics in terrestrial applications.

In the 1980s, the industry began to mature, as emphasis on manufacturing and costs grew. Manufacturing facilities for producing PV modules from Si wafer *pn* junction solar cells were built in the USA, Japan, and Europe. New technologies began to move out of the government, university and industrial laboratories, and into precommercialization or "pilot" line production. Companies attempted to scale up the thin-film PV technologies like a-Si and CuInSe₂, which had achieved >10% efficiency for small area (1 cm²) devices made with carefully controlled laboratory scale equipment. Much to their disappointment, they found that this was far more complicated than merely scaling the size of the equipment. Most large US semiconductor companies, gave up their R/D efforts (IBM, General Electric, Motorola) lacking large infusions of private or government support to continue. One common result was the purchase of American companies and their technologies by foreign companies. In 1990, the world's largest solar manufacturer was Arco Solar (CA, USA), owned by oil company Atlantic Richfield, which had c-Si and thin-film a-Si in production and thin-film CuInSe₂ in precommercialization. They were sold to the German firm Siemens and renamed Siemens Solar (in 2001, the Dutch company Shell Solar would buy Siemens, becoming another large internationally based company with multiple PV technologies in production). Also in 1990, Energy Conversion Devices (MI, USA) formed a joint venture called United Solar Systems Corp. with the Japanese manufacturer Canon to commercialize ECD's roll-to-roll triple-junction a-Si technology. In 1994, Mobil Solar Energy (MA, USA), which had developed a process for growing solar cells on Si ribbon (called the Edge defined film growth or EFG process) instead of more costly wafers, was sold to the German company ASE and renamed ASE Americas. The British solar company BP Solar acquired patents to electrodeposition of thin-film CdTe solar cells in 1989, when its parent company purchased the American oil giant Standard Oil of Ohio. At the same time, it acquired the patents of the University of New South Wales (Australia) to fabricate the Laser-Grooved Buried-Grid (LGBG) cells, which became the most efficient silicon cells in fabrication. In 1996, it signed a license agreement with the Polytechnic University of Madrid (Spain) to exploit the Euclides concentration technology that used their LGBG cells as concentrator cells. In 1999, BP Solar acquired Solarex from Enron (another huge fossil-fuel energy company) that had crystalline and amorphous Si solar cell technology. Thus, BP Solar established themselves with manufacturing interests in all three technology options (standard Si wafers, thin films

and concentrators).¹ Meanwhile, the Japanese PV industry began to take off. Production of c-Si modules and intensive research on thin-film technology in Japan led to many innovative device designs, improved materials processing, and growing dominance in the world PV market.

Along with the maturing of the solar cell technology, the BOS needed to grow. Many products like inverters, which convert the DC power into AC power, and sun trackers had only limited application outside of a PV power system, so once again there was only limited technical and financial resources for development. In many system evaluations, the inverter was repeatedly identified as the weak link in terms of reliability and AC power quality [41]. Their costs have not fallen nearly as fast as those for the PV modules. While much effort and resources had been focused on the solar cell cost and performance, little attention had been paid to installation and maintenance costs. It was quickly discovered that there was room for much improvement.

An early development that helped many companies was to sell PV cells for consumer-sized, small-scale power applications. The solar-powered calculator, pioneered by Japanese electronics companies as a replacement for battery-powered calculators in the early 1980s, is the best-known example. This led to the early use of thin-film a-Si PV cells for various applications. Another example was solar-powered outdoor lighting. These novel consumer applications, where portability and convenience were more valued than low price, allowed the PV companies to maintain some small income while continuing to develop power modules.

Another application was the rural electrification of remote villages in an attempt to help roughly one-third of the world's citizens to gain access to a modest amount of modern communication and lighting. Most of these PV installations were very small, on the order of 10 to 40 W per household (100 times smaller than the "needs" of a modern home in the developed world.) Most of these installations were funded by some international aid agency. Reviews and follow-up studies of these programs have indicated very large failure rates, primarily due to lack of technical infrastructure [42], training, cultural misunderstandings, design of the payment structure, and other nontechnical reasons [43]. Rarely have the PV modules failed. Even with subsidies from the international agencies, the high initial cost of ownership (\$100–1000) was still a major barrier in much of the world where this represents a year's income for a family [44].

On the opposite end of the size scale were the MW-size PV plants installed by utilities in developed countries in the 1980s to evaluate their potential in two applications: as a peak-load-reduction technology, where the photovoltaics provides additional power primarily to meet the peak demand during the afternoon [45]; or as distributed generators, to reduce transmission and distribution losses [46]. Several American utilities investigated these applications, to assess the technical as well as financial benefits for photovoltaics in utility scale applications. Other novel configurations of grid-tied PV

¹ While this book was going to press in November 2002, BP Solar suddenly announced the closure of its two thin-film manufacturing efforts in the United States (a-Si in Virginia and CdTe in California) in order to focus more resources on its multicrystalline Si wafer PV production. This was a great disappointment to all those who worked so hard to establish these thin-film technologies and facilities, which were among the most advanced thin-film PV products in the world.

systems were evaluated as so-called “demand side management” options where the on-site distributed photovoltaics is used to reduce demand rather than increase supply [47]. Although American utilities lost interest in PV in the late 90s due to deregulation, grid-connected applications in Europe and Japan began to grow rapidly, primarily owing to strong government support. Both small- and large-scale grid connected PV installations are blossoming in these countries [48, 49].

Yet another important development in the application of PV in the late 1990s, was building integrated PV (BIPV [50]), where PV cells are incorporated into a standard building product, such as a window or a roof shingle, or into an architectural feature like an exterior sun awning or semitransparent skylight. In this way, the cost of the PV is partially offset by the cost of the building materials, which would have been required anyway, so the incremental cost of the photovoltaics is much lower. BIPV is discussed in Chapter 22. The success of grid-connected residential or BIPV commercial applications has been possible because several countries led by Germany have established high rates to pay for the PV electricity produced by solar installations in private houses. In this scheme, the installation owner receives \$0.5/kWh for the electricity they feed into the public electric grid (as of 2001). But the owner buys the electricity consumed in their own house at the normal cost of ~\$0.1/kWh from the grid. Additionally, German banks provided generous loans for purchasing the installation. Similar concepts are used in Spain, the Netherlands, and other countries in Europe. But, the success has been still bigger in Japan where homebuilders receive a rebate from the government for about 30% of the PV system cost. Then, their electric bill is determined by the utility using the “net metering” where the customer pays only the net difference between what they used and what they generated. Rebates and net metering are available in some, but not all, states in the USA as of 2002. Interestingly, government support of photovoltaics in Japan has been decreasing while the market for PV homes has continued showing an impressive growth rate.

1.5 PV COSTS, MARKETS AND FORECASTS

In the first 20 years of PV research, from the mid 1960s to the mid 1980s, the main focus was to make the product more efficient so it produced more power. Impressive gains in cell and module efficiency were made. Costs also fell dramatically as solar cells moved from pilot scale to semiautomated production.

Although the important figure of merit for cost is \$/kWh, typically $\$/W_p$ is often used. Modules are rated in Watts of peak power (W_p). This is the power the module would deliver to a perfectly matched load when the module is illuminated with 1 kW/m² of luminous power of a certain standard spectrum while the cell temperature is fixed at 25°C. (By the way, these “standard test conditions” or STC rarely occur in real outdoor applications! See Chapter 16 for a complete discussion of testing conditions and Chapter 20 for real outdoor conditions.).

Figure 1.5 shows costs ($\$/W_p$) and production measured in MW_p over the commercial history of photovoltaics. Up until about year 2000, these values represent mostly c-Si solar cell technology. These two curves are typical of most new technologies. Initially, prices are high since volume production is low, so development and start-up

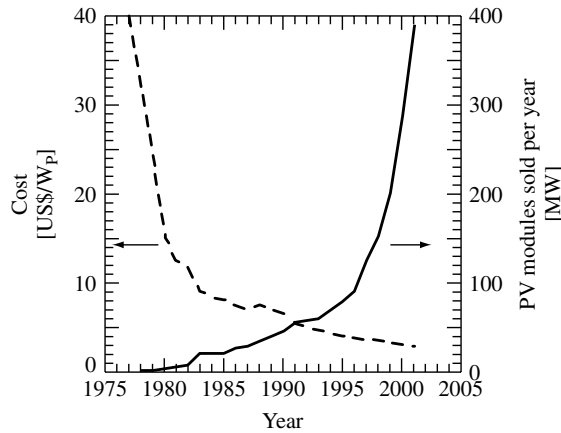


Figure 1.5 Historical trends of cost per Watt for solar cells and volume of production. Data from various sources. Beware: these costs are for PV modules not completed systems, which typically increase by a factor of 2 to 3

costs are spread over the relatively few units sold. The high price excludes most buyers except unique niche applications (i.e. remote telecommunications transmitters, where the unique properties of photovoltaics makes it the most appropriate source of electricity) government-sponsored programs (i.e. satellites, weather monitoring stations, military outposts and also human development programs in remote areas including water pumping), and curious wealthy pioneers (i.e. private homes in the mountains for environmentally concerned millionaires). As volume production increases, costs fall as economies of scale take over. The technology is now within economic reach of wider markets and demand grows rapidly as people with moderate incomes can afford the product. Eventually, the decrease in price slows, and it becomes harder to improve the cost and performance of a given product. But each small decrease in cost opens up larger markets and applications. Once a certain price is reached, a massive new market will open up with ample opportunity for investors to finance new manufacturing capacity.

This relation between cumulative production of PV modules in MW_P (M) and price in $\$/W_P$ (p) can be described by an experience curve, which is characterized by a parameter E called the experience exponent [51, 52] or

$$\frac{p(t)}{p_0} = \left[\frac{M(t)}{M_0} \right]^{-E} \quad (1.1)$$

where M_0 and p_0 are the cumulative market and the price at an arbitrary initial time $t = 0$ (that we can take at the beginning of the early commercialization). The experience curve for photovoltaics is shown in Figure 1.6 where lowest price per W_P for a given year is plotted against the cumulative module production up to that year. When graphed as a log-log plot, it is the slope that is of significance since it defines the experience factor given as $1 - 2^{-E}$. This quantity indicates how much costs are reduced for every doubling of cumulative production. Figure 1.6 presents an exponent $E = 0.30$ which gives an experience factor of 0.19. Thus, prices have fallen 19% for every doubling in

cumulative production over the past 30 years. If the trend continues, the price of $\$1/W_p$ will be reached when the cumulative production reaches 10^5 MW_p.

It should be said that while the annual growth in sales of photovoltaics is quite spectacular, averaging 33% per year from 1995 to 2000, the experience factor of 0.19 is rather mediocre. For example, for semiconductor memories it is about 0.32, although for wind power it is only 0.15. PV technology has not reduced prices very effectively. This supports the idea that R&D must be supported to look for innovative options able to reduce prices beyond the safe path of the experience curve (additional argument for myth 4).

When this cumulative market will be reached can be determined, if we know the demand elasticity S . Technically, this is the logarithmic derivative of the annual market with respect to the price (changed of sign) and shows that one percent of price decrement will produce S percent of market increase. This parameter allows us to determine when in the future a certain level of price is reached [52].

Based on this, the installed PV power is given in Figure 1.7 for reasonable values of the demand elasticity. We can observe a fast initial growth, followed by a period of moderate growth. This second period is determined by the investment that society is willing to invest in this expensive energy technology. Extreme curves of the shaded area correspond to the expenditure for photovoltaics of the case that 0.05% (lower curve) and the 0.2% (upper curve) of the GDP of the industrialized countries is invested every year in PV electricity. As a reference, about 0.3% of the industrialized countries GNP is being given today as aid for development.

In 1992, a study (the RIGES scenario [54]) was presented to the Rio Summit analyzing the possibility of reducing the CO₂ emissions while maintaining a high economic growth rate in the developing countries. The dots represent the amount of photovoltaics to attain the RIGES requirements. In other words, the dots are the amount of installed photovoltaics required to be environmentally relevant and socially advanced. Note that

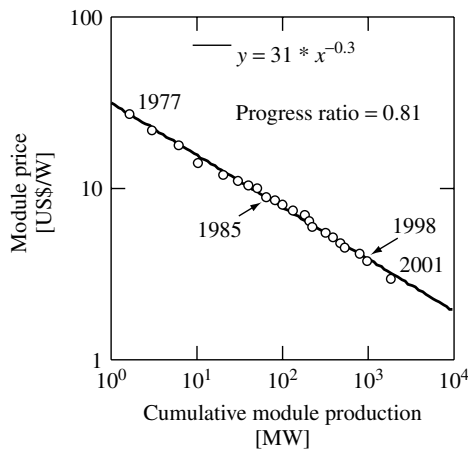


Figure 1.6 Experience curve for photovoltaics from 1976 until 1998 [53]. Straight line is fit indicating an experience factor of $1 - 2^{-0.3} = 0.19$

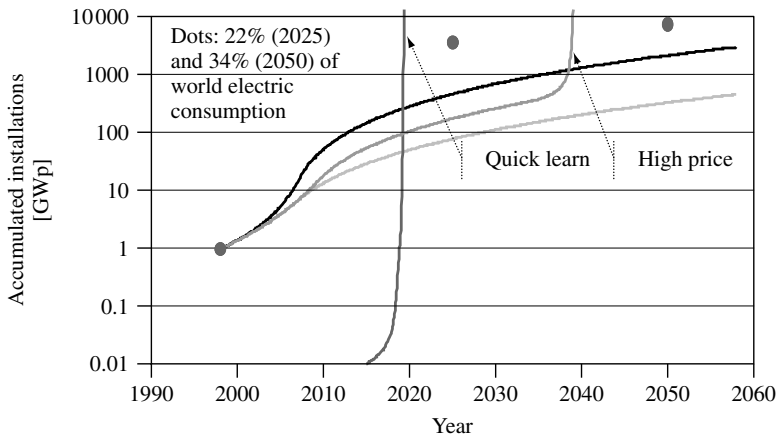


Figure 1.7 Long-term forecast of cumulative installed peak PV power. The dashed area represents the expected cumulative installed capacity for a range of assumptions associated with the demand elasticity. PV prices (not shown) will not be competitive in the period shown unless the conventional electricity doubles in price (in constant dollars). However, photovoltaics will be competitive if some innovation develops and is commercialized with a “quick learn” experience factor like that of the microelectronic memories (0.32). Dots represent the level of electricity penetration to reach environmental goals (see text)

the goal for 2050 is to produce the 34% of the total world electricity production; by no means a niche market to be produced by a cottage industry!

It is observed that with the present low experience factor, the environmental goals are not achieved. Nevertheless, this forecast predicts that the PV industry will be very large by the middle of the century.

The curve labeled high price refers to the case where conventional electricity prices are doubled. In this case, photovoltaics will reach price competitiveness with the existing electricity before the middle of the century (the almost-vertical line means photovoltaics is cheaper than conventional electricity but realistic growth will occur more slowly). Perhaps a hidden but practical conclusion of this analysis is that support to the PV industry will result in an additional element of security in the supply of electricity. Energy security is of increasing interest for the public officials as well as for citizens.

The preceding cases correspond to the situation governed by a constant experience factor. No technological breakthrough is considered. What would be the situation if a breakthrough were produced? A breakthrough technology would be characterized by a higher experience factor and should be able to reduce costs by experience faster than present PV technology. The curve labeled quick learning in Figure 1.7 shows the case of a technology with the experience factor of the microelectronic memories. Note that in very few years (after real commercialization starts) it would be able to reach competition with conventional electricity.

However, note that this success is based on reaching a certain cumulative market (in this exercise 10,000 MW) despite the higher price of this technology at its early stage as compared to the competing PV technology. This is a commonly occurring situation and

must be taken into account by investors. Comparison must not be made between prices of different alternatives at the same moment in time but for equal cumulated market. In other words, we must compare the price of an option today with that of its more mature competitor in some moment of the past and we must also consider the experience factor. In other words, sometimes a product that at a given moment is more expensive than its competition can become cheaper sooner because it bears internally the seed for lower cost and comparable performance. But, of course, not every more-expensive novel product bears this seed. This is the risky nature of entrepreneurship.

We conclude, and this is our position concerning the controversy pointed out in myth 4, that basic R&D in photovoltaics must be looking for breakthroughs if we want photovoltaics to fulfill the goals that society requests. At the same time, support to the market will help create a sizeable industry that will be able to commercialize breakthroughs worldwide. In any case we are not talking of a cottage industry. The PV industry has the potential of becoming a major electricity supplier in the twenty-first century and to constitute a powerful industry able to abate environmental stresses, to facilitate the human development of the poorest, and to constitute an element of safety in our electric supply.

1.6 WHAT ARE THE GOALS OF TODAY'S PV RESEARCH AND MANUFACTURING?

Chapters 5 to 15 in this book focus on individual technologies and will give specific examples of where the research and manufacturing effort is concentrating to reduce costs and improve performance. But several trends are common to all. These are listed in Table 1.3.

Since the overall goal is to produce a low cost PV *system*, we need more than low-cost-efficient solar cells, we need a low cost efficient system including mounting hardware, power conditioning electronics, fuses, cables, storage, tracking, and so on. Less research and development has gone into these areas than into PV solar cells and modules.

Table 1.3 Goals of current solar cell research and manufacturing

-
- Use less semiconductor material by making thinner cells or
 - Use less expensive semiconductor materials. These tend to be less pure and less perfect.
 - Improve solar cell performance with less expensive, less perfect semiconductors
 - Even with this poorer material keep a high production yield, that is, reduce the number of cells or modules rejected by the quality control.
 - Increase material utilization by reducing waste in semiconductor and cell fabrication
 - Increase solar cell flux on the solar cells by using concentrators without increasing cost or optical losses too much. In this way, less semiconductor material is used.
 - Increase solar radiation utilization by absorbing more of the spectrum efficiently
 - Increase speed and throughput of manufacturing processes
 - Simplify processing steps (this reduces fabrication costs and increases the yield) and reduce equipment costs
 - Reduce costs and improve reliability of BOS (auxiliary elements).
-

1.7 GLOBAL TRENDS IN PERFORMANCE AND APPLICATIONS

Figure 1.8 shows the trends in efficiency achieved over the past 20 years for all the major PV technologies. These results are for small area “champion cells”, the one-of-a-kind result that establishes the potential of a given material system and device technology. The highest efficiency is for the most expensive and complex devices, based on III–V technologies like GaAs and GaInP, consisting of multiple devices with different optical and electrical properties, grown on top of each other. They are discussed in Chapter 9. These multijunction (MJ) cells outperform other cell technologies for three reasons. They are made from very perfect and high-purity crystalline materials, they can capture either a wider range of the solar spectrum or the same range more efficiently than other devices, and they are operated with high concentration factors, using lenses, which increases the efficiency for reasons discussed in Chapter 3. Not surprisingly, they are also extremely expensive.

The workhorse of the PV industry is still Si as discussed in Chapters 5, 6, and 7. Si wafers in the form of either single crystal Si or multicrystalline (also called polycrystalline) Si accounts for 90% of the PV market. Although champion single crystal (c-Si) and multicrystalline Si (multi-Si) cells have been recorded with 25% and 20% efficiency, respectively (both made at UNSW in Australia), the difference in module performance between the two Si-wafer technologies is much smaller. They have typically 14% and 12% efficiency in commercial modules, respectively. Despite three decades of research and manufacturing, clever scientists and engineers are still finding ways to improve the performance of Si-wafer photovoltaics. They are also finding ways of reducing the cost.

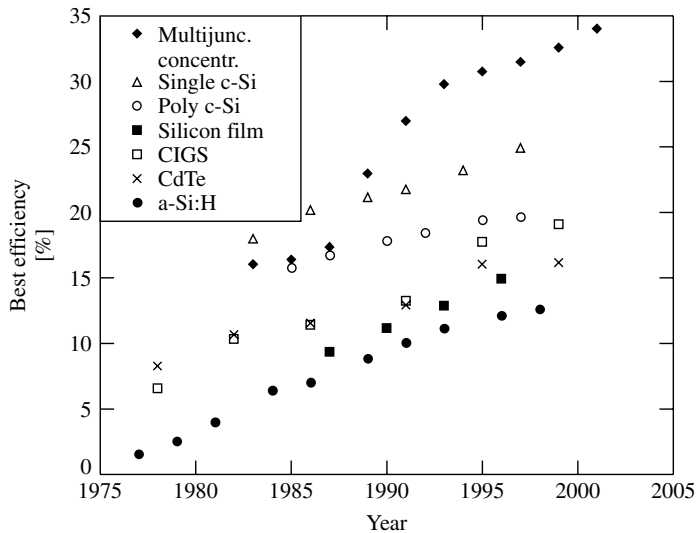


Figure 1.8 Best small area (0.5–5 cm²) efficiency for various cell technologies measured under standard laboratory test conditions. MJ concentrators are double junctions before 1995, and triple junctions after. a-Si represents stabilized efficiency after extended light soaking and are MJ after 1990 (see Chapter 12)

Among these attempts are the developments of silicon sheets, which avoid the wafering of bulky Si ingots, a very expensive and wasteful process. Ribbon sheets have already reached a noticeable fraction of the market with two companies: RWE in Germany/USA (leading) and Evergreen Solar in the USA.

Continuing down the efficiency axis we come to the three leading thin-film PV contenders, Cu(InGa)Se₂ (CIGS) (Chapter 13), CdTe (Chapter 14), and a-Si (Chapter 12), in that order. The main motivation for interest in thin-film photovoltaics has always been the possibility of lower cost, not higher performance. Their champion cell performance has always been a factor of about 2 lower than Si-wafer technologies until ~2000, when Cu(InGa)Se₂ cells with efficiencies of 19% were reported, putting them in potentially close competition with multi-Si, although there are vast differences in the manufacturing experience base between Cu(InGa)Se₂ (no base) and multi-Si (large base). The benefits and challenges of thin-film PV technologies are discussed in detail in Section 1.9. Finally, we note that the category of “Si film” solar cells in Figure 1.8 is a special case of solar cells developed entirely by one company (Astropower in the USA), in which they are attempting to achieve the high performance of polycrystalline Si with the low-cost approach of thin films. More information about thin-film Si technology is given in Chapter 8.

The results in Figure 1.8 clearly show that there are many promising technologies in terms of their possibility of achieving rather high efficiency. But the reality is that, as seen in Figure 1.9, almost 90% of the world’s PV power modules are either single c-Si or multi c-Si. The evolution shows a trend away from c-Si towards the multicrystalline-Si technology with the market share of Si sheet also increasing. About 10% of worldwide PV sales are a-Si/a-Si or a-Si/a-SiGe multijunctions and the remaining <1% is Cu(InGa)Se₂, CdTe, and concentrators. The multijunction concentrators based on GaInP/GaAs cells have yet to find commercial application on Earth but nonconcentrating GaInP/GaAs cells are commonly used for space missions where their high efficiency is more important than their high cost. High performance GaInP-based technology is discussed in Chapter 9 and PV space power is described in Chapter 10.

Who is making all the PV modules? Figure 1.10 shows the breakdown by the three major geographic regions of Europe, Japan, and the United States. Note that this is a logarithmic scale, indicating very steady growth for the past decade of 20 to 30%. Production in 2001 was actually 36% higher than in 2000. The USA has had steady growth and led the world in photovoltaics between 1992 and 1998 when Europe and Japan

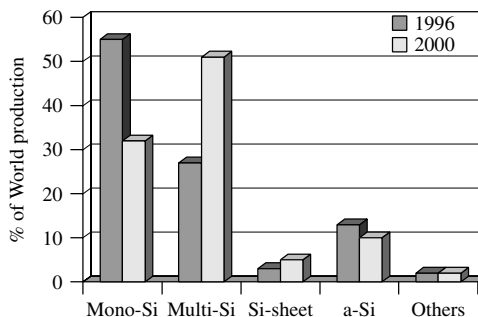


Figure 1.9 Distribution of the PV market by technologies

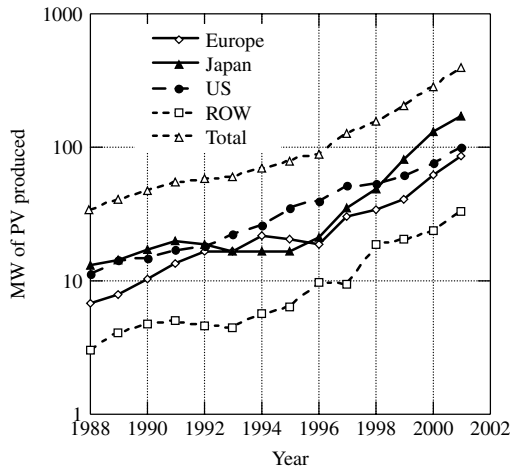


Figure 1.10 World production of PV modules

had static manufacturing growth. Then in 1998, progressive and supportive government policies in many European countries and in Japan resulted in a substantial increase in production. These policies were driven partly by a strong commitment to CO_2 reduction as proscribed by the Kyoto Protocol. European production is dominated by Spain closely followed by Germany, and to a lesser extent France, Italy, and The Netherlands. Note that these figures do not indicate the final residence of the PV module, only its place of birth. For example, a large fraction of PV modules made in the US (~70%) and Spain (~80%) are in fact exported.

We present in Figure 1.11 the top ten PV manufacturers in 2001 [55]. The list is headed by the Japanese electronics company, Sharp, followed in the third position

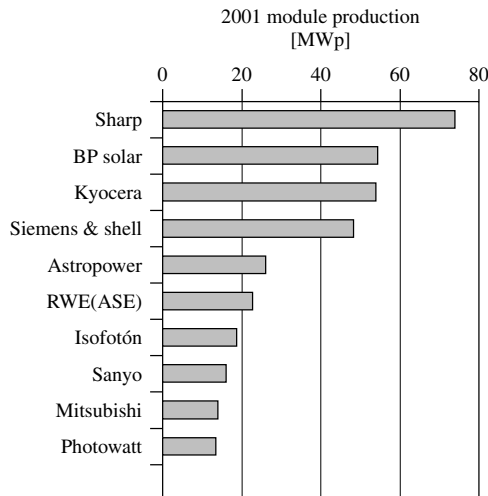


Figure 1.11 The top ten PV cell manufacturers in 2001

by Kyocera, another Japanese company. The second place is held by the UK-based oil multinational BP Solar with c-Si and multi-Si plants in United States, Spain, Australia, and India. BP Solar also had two thin-film technologies in commercialization in the United States, namely a-Si and CdTe, (see footnote in Section 1.4). The biggest PV manufacturer in the USA today is Shell Solar (formerly Siemens Solar) but is held by European capital. As of this writing, of all the companies in Figure 1.11, only Astropower (US), Isofoton (Spanish), and Photowatt (French but held by Canadian investors) focus their business exclusively on photovoltaics. The others are either divisions or subsidiaries of large companies with diverse manufacturing interests.

Figure 1.3 showed the worldwide trend for various applications. Growth has been driven by distributed, grid-connected PV applications since 1996, mostly in Europe and Japan, as discussed above. There is steady growth in use of photovoltaics for diesel hybrid and communication. These are off-grid applications, typically in remote locations. Previously, operating a diesel generator 24 h a day or replacing large battery packs was the only alternative. PV diesel hybrids can be cost-effective in these cases [56].

Note that Figure 1.3 shows that large-scale, centralized solar power plants are almost nonexistent. These huge “solar electric farms” were envisioned in the early days of photovoltaics to be built in sunny arid deserts, where land was essentially worthless for other uses (note, that photovoltaics operates without water in contrast to conventional thermal power plants). These huge facilities would replace conventional power plants, at least for daytime power. The world’s largest centralized PV power plant to date was installed in central California between 1984 and 1985. The operation and performance over several years was reported [57], including operation and maintenance costs [58]. After several years of operation, the installation was disassembled and the modules were sold individually on the market. Presently, the largest centralized PV power plant is 3 MW in Serre, Italy [59]. There have been several other large-scale PV installations, and their installation techniques, labor, and operation costs have been well documented. In particular, the 0.4 MW a-Si plant in California, USA [60] and the 0.48 MW concentration plant [61] in Tenerife, Spain are notable because they do not use the ubiquitous unconcentrated c-Si technology.

1.8 CRYSTALLINE SILICON PROGRESS AND CHALLENGES

Figure 1.9 showed that c-Si, as either single or multicrystalline wafers or ribbons, was responsible for almost 90% of worldwide PV production in 2001. How did its dominance occur?

First, there was a tremendous worldwide scientific and technical infrastructure for Si starting in the 1960s. Huge government and industrial investments were made in programs for understanding the chemical and electronic properties of Si, how to grow it with the required purity and crystalline structure, and to create the equipment needed to perform all the processing steps. The motivation was not just idle scientific curiosity, but rather the competitive drive to manufacture increasingly complex integrated circuit chips, which created first the analog then the digital electronic revolutions leading to our current information, entertainment, and telecommunications industries. The promise of wealth and market dominance led public and private organizations to unlock many

secrets of Si technology. The silicon band gap, of 1.1 eV, is almost optimum to make a good solar converter, as explained in Chapters 3 and 4. The PV industry could utilize the preceding gains for their own application without having to re-create this scientific and technological infrastructure. In addition, Si is one of the most abundant minerals in the Earth's crust. Thus, there was no physical limitation to providing a huge fraction of the Earth's electricity needs with the known Si reserves.

However, for mechanical reasons (it is brittle), silicon requires relatively thick cells, with a typical wafer thickness of about 300 μm . Therefore, some of the electrons pumped by the photons to the conduction band have to travel large distances, on the order of the thickness, to be extracted by the front face through the selective contact to this band (the *pn* junction). Consequently, a good material with high chemical purity and structural perfection is required to fight the natural tendency of the conduction-band electrons to return to the valence band. This loss process is called *recombination*. To avoid this loss, the electrons must be highly mobile, as they are in perfect silicon. Impurities and imperfections must be avoided as they can absorb the extra energy of the conduction-band electrons and convert it into heat, thus eliminating the free electron from traveling through the circuit by immediately restoring it to the valence band energy. Producing heat, which is desirable in solar thermal panels, where this heat is transferred to a fluid, is undesirable in PV modules, where we try to recover the solar energy as electricity, of much higher value.

Metallurgical Grade (MG) Silicon is obtained by reduction of quartz with coke in an arc furnace. Then it is strongly purified by a method developed by and named after the Siemens Company consisting of the fractional distillation of chlorosilanes, which are obtained from the reaction of HCl with Si. Finally, silanes are reduced with hydrogen at high temperatures to produce hyperpure silicon, usually called *Semiconductor Grade (SG) Silicon* or just *polysilicon* (it is called *polysilicon* because it has many grains of crystalline Si, typically of about 1 mm).

The polysilicon now has the desired chemical purity (unwanted impurities below the parts per billion (ppb) level, or less than one impurity atom for every 10^{12} Si atoms, for some impurity atoms), but its structural quality is deficient. The structural quality is improved by melting the polysilicon ($>1400^\circ\text{C}$) and "freezing" or allowing it to solidify very slowly around a rotating crystalline seed, usually by the Czochralski (Cz) method. In this way, a cylindrical single crystalline ingot is obtained of about 25 cm diameter and of 100 cm length. In this step, a very small number of atoms of boron are introduced in the melt to allow the appropriate metallic contacts deposited later to be selective to the valence-band electrons. This forms the *p*-type side of the *pn* junction.

The ingot is now cut in wafers with a saw. For this a very long wire (up to 500 Km) is wound many times on rotating drums cuts with slurry the silicon ingot into wafers. However, the process is slow and about half of the silicon is lost in the sawdust. The challenge here is to cut the wafers thinner so as to make more profit from the silicon. Wafers of 150 μm instead of the standard 300 μm are used in some companies. The techniques and challenges related to crystal growth and sawing are described in detail in Chapter 6.

The wafer is now etched slightly to remove the saw damage and to condition (texture) the surface for better light absorption. Then the conduction-band selective contacts

are made by introducing atoms of phosphorus to one surface of the wafer, making it the *n*-type partner in the *pn* junction. This is done by locating the wafers in a phosphorus rich atmosphere at high temperature so that these atoms penetrate slightly ($\sim 0.2 \mu\text{m}$) into the silicon wafer.

Then metallic grids are printed on the boron and phosphorus-doped zones (some tricks, sometimes proprietary, are used to separate boron- and phosphorus-doped regions properly) and the solar cell is thus finished. The grids make it easier to collect the electricity without resistance losses and are commonly applied with low cost screen-printing methods. But a solar cell is brittle and produces low voltage (about 0.5 V) so that some 36 cells (or multiples of this number) are interconnected with tinned copper ribbons and encapsulated in a sandwich formed of a sheet of tempered glass, an embedding polymer that surrounds the solar cells, and a back sealing plastic layer. The reason for multiples of 36 cells is so that their output voltage $\sim 15 \text{ V}$ will be compatible with most DC battery charging applications.

The lowest (publicly offered) module selling prices in 2002 were about $\$3/W_p$. The breakdown of costs, as given in Chapter 6 are presented in Figure 1.12. The wafer itself represents about 65% of the module cost, approximately equally divided between purification, crystallization, and sawing. This hyperpure silicon is found today as a scrap or waste product from the microelectronics industry at a price of $\sim \$50/\text{kg}$. The increase of the PV market in the 1990s has nearly exhausted this market. Additional supplies are coming from the former Soviet Union, whose microelectronic industry has disappeared due to western competition. The Siemens method is considered ultimately too expensive for photovoltaics, but the purity it provides seems necessary for the fabrication of solar cells. Attempts in the 1980s to fabricate a low-cost solar silicon (SolSil) did not succeed due in part to the scarce interest generated by the small markets of the time. Today, new attempts are being made. These might include purification in the MG silicon production steps and in the crystal growth steps avoiding the expensive chlorination procedure and using the molten step of the crystal growth for further purification, or alternately, reducing the chlorosilanes in the molten phase prior to the crystal growth. It is not clear whether they can achieve the needed purity level. Even if feasible it is uncertain whether such wafers would be less expensive than the standard Siemens process or some simplified versions of it. There are fears that a shortage of hyperpure polycrystalline silicon availability might seriously hinder the growth in cell production demanded by the market. Chapter 5

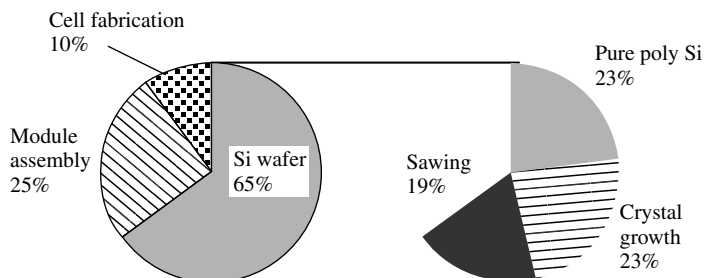


Figure 1.12 Breakdown of costs in the fabrication of a Si-wafer-based PV module. The right side presents the wafer costs

describes in detail the problems and challenges associated with silicon production and purification.

An important advance in solar cell fabrication was the demonstration that solar cells with high efficiency can be fabricated from wafers containing hundreds of large-grain (1–10 mm) multicrystals, called multicrystalline (multi-Si) or polycrystalline (poly-Si), although this later term is less favored because it may cause confusion with the feedstock (polysilicon). The multi-Si growth procedure is much faster and the wafer is cheaper. The loss of efficiency of a few percent (absolute) caused by the random orientation of crystalline grains in a multi-Si wafer compared to a single c-Si wafer is balanced by the lower cost so that the price per watt peak is the same on a module basis. But the simplicity of the multi-Si wafer-growing equipment and process is producing a clear trend towards the use of the multicrystalline option as seen in Figure 1.9.

An interesting option in Si solar cell manufacturing is the growth of ribbons [62, 63]. Ribbons do not require the expensive sawing process. However, the growth of the ribbon crystal is slower because they usually grow in the plane perpendicular to the ribbon surface, with very small area (the ribbon width times the thickness). In contrast, wafers grow in the plane of the wafer surface whose area is the wafer area. The standard ingot solidification process is a very effective purification process due to the preferential segregation of impurities to the molten silicon. However, in ribbon Si the plane of solidification moves faster (although with very small area), so the segregation is less effective. In summary, the ribbon cells are almost as good as the multicrystalline bulk-grown cells and possibly cheaper. Challenges lie in increasing the growth speed and the resulting cell efficiency.

Although the solar cell manufacturing process represents a relatively small fraction of the total cell cost, it strongly affects the overall cost in $\$/W_p$ because it determines the cell and module efficiency. This efficiency depends on the quality of the wafer or ribbon utilized but it also greatly depends on the cell process itself.

As a matter of fact, an efficiency of 25% has been achieved for laboratory cells in a long complex process where every possible efficiency-improving detail has been implemented to produce a complicated but nearly ideal device structure. This is explained in Chapter 7. However, most factories use some variation of the wafer and cell fabrication process described above, including the screen-printing process, that leads to 15% single crystal cells or 13% multicrystal cells. In modules, these efficiencies are reduced to 14% or 12%, mainly due to the redefinition of area that now includes the module frame. This process is considered the best compromise between costs and performance.

The existence of the large efficiency gap between laboratory and commercial cells, together with the increasing markets, suggest that novel, high efficiency commercial cell processes will appear in the next years. Some companies (BP Solar or Sanyo, for instance) are already on this path and have different processes leading to 17 to 18% cells in production. It is worth noting, that the ribbon technology is incompatible (see Chapter 7) with the ubiquitous screen-printing processing, so that a new processing, which may not be so cheap, is required to fabricate cells with this material.

An additional factor very seriously affecting the cell cost is the production yield. In the fabrication of any semiconductor device, not every unit introduced into the production

line is successfully completed. In good single crystal Si cells, the manufacturing yield is 95%. Many supposedly cheap technologies find their Achilles' heel in the low yield.

Finally, the module fabrication requires interconnecting and encapsulating the cells. These steps also have room for some cost reduction. The use of cheaper materials may help somewhat, as well as better automation, better module interconnection, and integration designs.

1.9 THIN FILM PROGRESS AND CHALLENGES

One might ask “why develop a totally different semiconductor technology for photovoltaics when Si is so well established?”. The simplest answer is “to achieve lower cost and improved manufacturability at larger scales than could be envisioned for Si wafer-based modules.” In fact, we have already defended our belief that Si technology, very important in the next decades, will not be able to reach the ultimate goals required for mass worldwide penetration of photovoltaics (Section 1.5). What were the disadvantages of c-Si that led to the early investigation and eventual commercialization of alternatives? It was recognized early in the development of photovoltaics that Si crystals were expensive and slow to grow. It was also recognized that of all the viable semiconductors, Si would require the greatest thickness to absorb sunlight, due to its unique optical properties. Si is the most weakly absorbing semiconductor used for solar cells because it has an indirect band gap while most of the other semiconductors have a direct band gap (see Chapter 3 for a more complete explanation of direct and indirect band gaps). Therefore, at least ten times more crystalline Si is needed to absorb a given fraction of sunlight compared to other semiconductors like GaAs, CdTe, Cu(InGa)Se₂, and even other forms of Si such as a-Si. Thicker semiconductor material means higher material volume but also a higher quality material because of the longer paths that the high-energy electrons excited by the photons must travel before they are delivered to the external circuit to produce useful work. All this leads, as seen before, to high material cost. In addition, we mention that, presently, much of the Si-PV industry relies on buying scrap material from the electronics industry. As photovoltaics' demand grows, the supply of scrap material might become insufficient (see Chapter 5).

It was recognized almost as early as c-Si PV cells were developed in the 1950s that other semiconductors could make good solar cells. Most of them exist in a form called thin films. When they are fabricated into useful devices, they are so thin that they must be deposited on a foreign material called a substrate for mechanical support like a layer of paint on a piece of wood or the reflective metal coating on glass to form a mirror. A framework for analyzing the material properties, device structures, and manufacturing issues unique to thin-film solar cells (TFSC) was developed [64] since they differ considerably from Si wafers. Throughout the 1970s, progress in Cu₂S/CdS solar cells led to the development of new theories to explain the device performance, new methods of materials processing, and new concepts in semiconductor device manufacturing [65, 66]. Between 1981 and 82, four thin-film technologies demonstrated the ability to cross the magical 10% efficiency barrier, thus becoming candidates for serious consideration: Cu₂S/CdS [67], a-Si [68], CuInSe₂/CdS [69], and CdTe/CdS [70]. (It is an inexplicable fact in this business that 10% efficiency seems to suddenly confer respectability and status to any PV technology.) Of these four TFSC technologies, Cu₂S/CdS would soon be

rejected for commercialization due to fundamental and fatal stability problems related to electrochemical decomposition [71]. In contrast, a-Si has a minor stability problem that is not catastrophic and has not been a major barrier to further development and production as discussed in Chapter 12. No fundamental stability problem has been found with Cu(InGa)Se₂ and CdTe modules. Consequently, significant industrial and government-sponsored research and development resources have been directed worldwide at TFSC technology. This has led to steady progress in champion cell efficiencies as seen in Figure 1.8.

The main advantage of TFSC is that they will eventually have lower costs than c-Si-wafer PV technology when they are produced in sufficiently large volumes to offset the initial capital investment. The lower costs of TFSC derive from the following characteristics: they are typically 100 times thinner than Si wafers ($\sim 1\text{--}3\ \mu\text{m}$ for all the semiconductor layers) deposited onto relatively low-cost substrates such as glass, metal foils, and plastics; they are deposited continuously over large areas at much lower temperature (200 to 500°C vs $\sim 1400^\circ\text{C}$ for c-Si); they can tolerate higher impurities (thus needing less expensive purification of raw materials); and they are easily integrated into a monolithic interconnected module. For a reference, the semiconductors in typical TFSC are 10 times thinner than a human hair. TFSC are either polycrystalline with small $\sim 1\ \mu\text{m}$ sized grains such as Cu(InGa)Se₂ or CdTe, or else amorphous like a-Si. This is a consequence of being deposited at temperatures too low to allow perfect crystalline bond formation. TFSCs typically consist of 5 to 10 different layers whose functions include reducing resistance, forming the *pn* junction, reducing reflection losses, and providing a robust layer for contacting and interconnection between cells. Some of the layers are only ~ 20 atoms thick (10 nm), yet they may be a meter wide! This requires excellent process control. The manufacturing process is designed such that they are deposited sequentially on moving substrates as in a continuous process line. This minimizes handling and facilitates automation, including laser scribing, to isolate and interconnect individual cells on the module, called monolithic integration.

With all the advantages of TFSCs, why does c-Si or multi-Si still dominate 90% of the world market? This brings us to the disadvantages of TFSC: they have lower efficiencies (so far), and they have a much less-developed knowledge and technology base compared to c-Si. Consequently, under-capitalized companies have had to struggle to develop not only an understanding of the materials and devices but also the equipment and processing to manufacture them. The thin-film PV industry has had to develop the technologies all by itself with considerably less financial resources than the Si industry had. They were not able to adopt a mature technology like the Si PV community did from the Si electronics industry.

What are the strengths and remaining challenges for the TFSC industry? We will review the salient characteristics of the three leaders: a-Si, Cu(InGa)Se₂/CdS, and CdTe/CdS.

Amorphous Si (Chapter 12) is deposited from hydride gases such as SiH₄ using plasma to decompose the gas. This is called *plasma-enhanced CVD* (PECVD) and allows for large areas to be coated rather uniformly and with excellent control. However, the utilization of gases is only around 10 to 30%, meaning much of the source material is

wasted. The material has 1 to 10% hydrogen bonded to the Si, and is often designated as *a-Si:H*. The H atoms passivate a large number of the defects resulting from the incomplete bonding of the Si atoms. The atomic structure has no long-range order like all other crystalline or polycrystalline materials. This can be an advantage. Films are typically deposited between 150 to 300°C, the lowest temperature of any of the TFSC materials, allowing the use of lower-cost, low-temperature substrates. *a-Si* solar cells are deposited on glass, stainless steel foil, or plastic. The last two substrates are flexible allowing for “roll-to-roll” manufacturing where all the layers are deposited as the roll moves through their process zone. The *pn* junction is formed by doping the thin contact layers as they grow with dopant gases containing the boron or phosphorous atoms. All practical *a-Si* modules contain multiple junction devices where two or three junctions are grown on top of each other. This allows for more efficient utilization of the sunlight. The total thickness, including multiple junctions and all the contact layers, is less than 1 μm excluding the substrate. The highest reported efficiency was 15% for a triple junction, which degraded to about 13% before stabilizing. While *a-Si* TFSCs cells may have slightly poorer performance compared to other TFSCs when tested under laboratory conditions (Figure 1.8), they have a unique feature that improves their relative performance outside in real conditions; namely, their efficiency is temperature-independent while for all other PV technologies, *c-Si* or thin-film, the efficiency decreases as the module heats up as in real outdoor conditions. This can result in those other modules losing 2 to 4% (absolute) of their rated output in the summer time and helps *a-Si* look more favorable. The three major challenges for *a-Si* technology are: 1) to improve the efficiency from today’s 6 to 8% up to 10 to 12%; 2) minimize or eliminate the self-limited degradation which reduces efficiency by 2 to 3% (absolute); and 3) to increase the deposition rate of the layers and the utilization of the gases to allow for faster, lower-cost manufacturing.

Polycrystalline layers of Cu(InGa)Se_2 (Chapter 13) alloys have produced the highest efficiency TFSC devices and modules. TFSCs based on CuInSe_2 (no Ga) achieved 12 to 15% efficiency but were limited by the low band gap. Alloying with Ga and/or S increases the band gap and increases the efficiency of delivering the electrons to the circuit (as discussed in Section 1.2). While many deposition methods have been explored in the laboratory, there are two different processes under commercial development. Co-evaporation forms the alloy by simultaneous evaporation of the Cu, In, Ga, and Se from sources onto a heated substrate. The other process is called *selenization*, because layers of Cu, In, and Ga are deposited by various means onto a substrate, then heated in the presence of Se from a gas such as H_2Se or a Se vapor, thus contributing the fourth constituent of the alloy. Substrate temperatures typically reach 500 to 600°C during some stage of the growth. Substrates of Mo-coated glass are typically used although metal foils or plastic are being investigated. The Cu(InGa)Se_2 -films are *p*-type, typically 1 to 3 μm thick and have crystallites or grains on the order of 1 μm . The *pn* junction is formed by depositing an *n*-type layer of CdS, ZnO, or other new materials under development to replace the CdS. The highest reported cell efficiency is presently 19% and several companies have reported modules with >10% efficiency. However, progress has been largely empirical since little fundamental understanding of the materials or devices is available. A very active area of research is developing methods to incorporate other alloys to increase the band gap even further. The three major challenges for Cu(InGa)Se_2 -related technology are: 1) to control the composition (Ga, S, Se, or Na) of the alloy through the film in a

manufacturing environment on a moving substrate; 2) to find alternative junction partners to replace CdS; and 3) to find new alloys or new deposition methods to give high performance devices with higher band gap alloys.

Polycrystalline layers of CdTe (Chapter 14) have been investigated for photovoltaics since the 1970s. In contrast to limited process options for a-Si or Cu(InGa)Se₂, there are over 10 methods to deposit the CdTe films that have produced CdTe solar cells exceeding 10% efficiency. Four have reached precommercialization: spray pyrolysis (SP), electrodeposition (ED), vapor deposition (VD) and close spaced sublimation (CSS). Some take place in liquid baths that are barely warm $\sim 50^{\circ}\text{C}$ with CdTe deposition rates of $\mu\text{m/hr}$ (ED) while others take place in vacuum systems at temperatures high enough to soften glass $\sim 600^{\circ}\text{C}$ with CdTe deposition rates of $\mu\text{m/min}$ (CSS). There seem to be three critical steps, however, that all efficient CdTe solar cells require. First, they need a post-deposition anneal in the presence of Cl and O₂ at around 400°C . This chemical/thermal treatment enlarges the grains, passivates the grain boundaries, and improves the electronic quality of the CdTe. Second, all CdTe layers need a surface treatment before applying a contact. This treatment can be a wet or dry process and prepares the CdTe surface by etching away unwanted oxides and leaving a Te-rich layer needed to make a low-resistance contact. Third, all high efficiency devices have a Cu-containing material somewhere in their CdTe contact process but again, there are many ways this can be achieved. Whichever process is used to deposit the CdTe, it has been found that the entire device process is highly coupled since processing steps strongly influence previous layers. This is partially due to the CdTe grain boundaries which act like paths for interdiffusion.

The *pn* junction is formed by first depositing an *n*-type layer of CdS on a transparent conductive oxide substrate followed by the CdTe layer and appropriate chemical annealing. Once the solar cell is made, the CdTe films are slightly *p*-type, typically, 2 to 8 μm thick and have crystallites or grains on the order of 1 μm . The highest reported efficiency for a CdTe/CdS device is presently 16%. Some CdTe modules have been in outdoor field-testing for over five years with negligible degradation, yet other CdTe devices degrade during accelerated life testing indoors. Of the three leading TFSC technologies, CdTe may have the most challenges. The dual role of Cu must be resolved; it seems to be required to produce a high-efficiency device but it is also implicated in long-term stability problems. The various optimizing treatments need to be better understood so they can be simplified and transferred into production. CdTe modules may be more sensitive to atmospheric interaction (O₂, H₂O) requiring better encapsulation methods. Finally, safe and cost-effective Cd usage in the workplace followed by recycling at the end of the module's life need to be determined.

In fact, technically astute investors know that other factors can be more important than efficiency in selecting a technology for development. This point is made loud and clear by examining the relative performance of the three major TFSC technologies – Cu(InGa)Se₂, CdTe, and a-Si – in Figure 1.8. Note that a-Si has always had the lowest efficiency. Yet, of the three, it was a-Si that has been commercialized much earlier and more widely. It enjoys by far a much greater manufacturing capacity. As of 2001 [72], a-Si accounted for almost 9% (34 MW) of the world PV power module production, while CdTe and Cu(InGa)Se₂ power modules together accounted for less than 0.3% (1 MW), despite a-Si champion-cell-stabilized efficiency lagging the others by several percent. In

reality, typical production modules of a-Si and CdTe are in the 7 to 8% range while Cu(InGa)Se₂ is 9 to 10%.

Why has so much capital been invested to develop a-Si technology over CdTe and Cu(InGa)Se₂? A major factor was that a-Si had a stronger worldwide scientific research base, which ensured that the relation between deposition conditions and fundamental material and device properties were well characterized. In contrast, CdTe and Cu(InGa)Se₂ are “orphans” because they have no real application outside of photovoltaics. Therefore, the entire knowledge base and technical infrastructure had to be developed mostly by underfunded industrial groups and a small number of university and government research labs. This shows that translating research-grade champion cell performance into production modules coming off-the-line day after day is a very challenging task. Figure 13.23 in Chapter 13 shows the time delay in translating efficiency achieved in the lab for a small area cell to a prototype large area module for the Cu(InGa)Se₂ technology. Delays of six to eight years are typical. To conclude, the highest efficiency technology is not always going to be the best choice for a low-cost, high-yield process, at least not until much of the technical background is in place.

Recognizing that the ideal PV technology would have some of the merits of c-Si but be deposited as a thin film a few microns thick, several groups have elected to try to achieve the “best of both worlds” by developing thin films of multi-Si deposited on a substrate. This is the subject of Chapter 8. At present, the best thin-film multi-Si solar cells have the same efficiency as their CuInGaSe₂, CdTe, or a-Si based predecessors. This is partly because multi-Si thin-film photovoltaics also inherits some of the problems of both c-Si and thin films. In particular, passivation of grain boundaries and surfaces seems to be a major problem, yet many of the well-established passivation methods from c-Si are not applicable to multi-Si thin films.

But there are new thin-film technologies such as the dye-sensitized solar cell that operate on a very different principle than an all-solid-state solar cell, almost more like photosynthesis than photovoltaics. This fascinating new solid–liquid technology, not free of challenges either, is described in Chapter 15.

1.10 CONCENTRATION PV SYSTEMS

If solar cells are expensive, focusing concentrated sunlight onto fewer solar cells was considered from the earliest times as a way of reducing costs. For example, instead of a typical 100 cm² solar cell absorbing 100 cm² worth of sunlight, one could focus the sunlight from 100 cm² onto a 1 cm² of solar cell, thus reducing the solar cell cost by 99% while still utilizing the same amount of sunlight. This neglects the cost of the optical focusing elements and other special equipment needed for concentrator technology. Of course, two conditions were required. One is that the optical surface collecting the light and redirecting it to the cells had to be cheaper than the cell area it replaced and the second is that the efficiency of the cells under concentrated sunlight should not decrease substantially. The first condition is generally fulfilled if we consider only the optical surfaces. However, keeping the cells constantly in focus requires a moving structure to keep the optics pointing at the sun as it moves across the sky, which adds cost to the system. As for the cell efficiency, there are fundamental reasons (see Chapter 3) why

it should increase with increasing luminous flux. However, in practice, ohmic resistance losses caused by the handling of large currents limits the efficiency increase. Thus, cells for concentrator applications must be carefully designed to minimize such losses and therefore they become more expensive. Yet, the small area of cells used in a concentration system, or alternatively, the large amount of electric power produced by each cell, allows for paying higher costs for the cells, and therefore allows them to incorporate many refinements in order to make such cells very efficient.

One factor that reduces the system efficiency is the loss associated with the optical hardware used to concentrate the light. Additionally, only the direct sunbeam is collected since scattered (diffuse) light is not focused. This again reduces the electric output by at least 15%. However, this last reduction is compensated for in many sunny locations by the fact that the tracking system always aims the cell directly at the sun (at least for two-axis tracking systems). In contrast, with the more typical stationary modules, the output power varies like the cosine of the angle of the sun, so this is very low in morning and late afternoon, when the sun is at an oblique shallow angle relative to the module (equations describing the sun's motion and the relative illumination on a module versus time of day or time of year is given in Chapter 20). Accounting for these gains and losses, it is generally found that concentrator efficiency today tends to be somewhat higher than flat module efficiency and this tendency will increase in the future with the adoption of higher efficiency cells. It is also believed that concentrators should ultimately be cheaper than flat module silicon solar cells. However, this statement has not been confirmed in practice due to the lack of a real market, apart from a few purchases for demonstration purposes.

Actually, concentrators are appropriate for relatively large installations while the PV market has evolved so far in smaller installations such as grid-connected houses, remote homes, or telecommunication applications whose size is seldom bigger than 5 kW. Therefore, only very few companies fabricate concentrator cells today, and their prices are very high because they have large general costs for very small production volumes. However, the situation may change. The general increase of the PV markets will probably stimulate the appearance of niches better adapted to concentrators.

The difficulty of developing concentrators must not be underestimated. Combining the requirement for high performance with the low cost is a formidable challenge. In particular, the optics must be low cost, yet permit highly accurate focussing, high optical efficiency, and equal illumination in all cells. The tracking structure must be cheap and accurate, cells must be efficient and not too expensive, and finally the cooling and current extraction must be effective and cheap. Chapter 11 deals in detail with concentrator issues.

1.11 BALANCE OF SYSTEMS

A photovoltaic system consists of more than PV modules composed of solar cells. In addition, it requires elements that are generically known together as "*Balance Of System*" (BOS). The BOS is, typically, composed of the battery, the control unit and the inverter, the mechanical support structure, the electric cabling, and protection devices such as fuses, grounding rods, and disconnect switches. We present in Figure 1.13 the cost of a PV stand-alone installation with storage, as presented in Chapter 2.

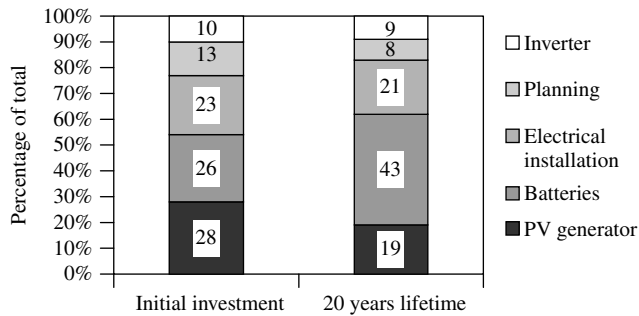


Figure 1.13 Breakdown of costs of a stand-alone PV installation with an optimum size storage. Differences in the initial investment and the life cycle investment are due to replacement of batteries during the 20 year life

We can see that in this case the PV modules represent approximately a quarter of the cost, while the cost of the batteries exceed that of the PV modules, especially when their periodic replacement over 20 years is included. This makes a very important and little appreciated point: even if we could make PV modules for free, the life cycle cost of the stand-alone system in Figure 1.13 would only be reduced by 25%! Clearly, batteries must be examined more closely. It is fortunate that many important applications do not require battery storage and therefore are free from this major cost burden.

Batteries are in most cases the lead-acid type. While automobile batteries are optimized for providing strong current for a short period to start the car, the ideal batteries for PV systems are so-called “deep cycle” batteries that can yield a large fraction of their charge (deep discharge cycle) and must operate with high efficiency and long duration. Yet, many PV applications use standard “shallow discharge” auto batteries due to their ubiquitous availability and lower initial cost (due to massive worldwide markets and applications) to the detriment of the long-term PV system cost. Some of the modern batteries such as those based on lithium ion or lithium polymer used in laptop computers or mobile phones could be used in solar applications but they are too expensive and are not significantly better than properly managed lead-acid batteries. This is studied in detail in Chapter 18. As said before, the relatively high cost of the batteries is further increased when we consider the costs over the PV system’s life cycle since the batteries have to be replaced every four to eight years due to their relatively short lifetime. Therefore, good maintenance procedures to increase the battery lifetime are important but not always applied. Alternative methods of storage exist but they will not replace lead-acid battery, at least, not in the next ten years.

The battery charge controller is essential for the long life of the battery. It is an electronic device that prevents overcharging and excessive discharging, both of which can dramatically shorten the battery’s life. In large systems, equilibration of the battery charging (so that all battery cells charge equally) should also be incorporated. In hybrid systems, which combine photovoltaics and a diesel or wind generator, the control unit must connect and disconnect the different generators according to a plan. Also, loads can be categorized, so that in case of low battery charge and low PV output, some loads can be disconnected while some essential ones are maintained active.

In many cases, battery storage is not necessary. For PV-powered water pumping, the water is pumped and stored while the sun is shining. For the grid-connected homes (one the fastest growing applications) and office buildings, the photovoltaics produces energy during the day and the grid supplies the energy during the night or on cloudy days, thus eliminating the need for batteries, simplifying system design, and reducing BOS costs. In PV-powered generating plants, the electricity is produced while the sun shines. The success of grid-connected PV applications is very sensitive to price competition with conventional electricity (even if the PV electricity is subsidized, as it occurs in Europe and Japan). Luckily the expensive batteries do not hamper this competition.

PV modules produce direct current (DC) which is suitable for directly charging batteries or powering a small number of special products. However, most appliances run on alternating current (AC). Consequently, an inverter must be used to convert the DC into AC. Inverters are widely used for many industrial applications. They are fabricated in large quantities as uninterruptible power supplies (UPS), to convert the DC electricity stored in batteries into AC electricity in the case of grid failure. They are used in hospitals and other installations where electricity failure is not tolerable. Small UPSs are often used in computers that must operate continuously. The PV inverter has an additional and important role: to vary the electrical operating point of the PV array to maintain its output at the maximum value, that is, the variable bias point at which the PV array produces highest power extraction. Changes of temperature and insolation change the voltage where maximum power extraction occurs. The electronics of the inverter typically include maximum power tracking. The inverters used in photovoltaics and the rest of the power conditioning electronics are explained in Chapter 19. Inverters have often been the source of poor reliability in early systems. Feedback to manufacturers and more robust components has greatly reduced these problems.

Because of the cost, the electronics for power conditioning is sometimes considered as a serious hindrance in the development of photovoltaics. However, we think the appearance of a significant market will reduce costs to reasonable limits. One fresh approach is to have a small inverter on the back of every module instead of a centralized inverter for the entire system. This modular approach has many advantages and is being put into production in USA [73] and Germany [74], but at present it is more expensive and will be so unless mass production reduces costs with respect to the theoretically cheaper bigger inverters.

The system-mounting structure is also important, in particular, in concentrating systems. In fact, this is the second most important cost element in concentrating PV systems, after the modules. In contrast, the power conditioning cost is comparable to many other small costs associated with the plant construction. This can be seen in Figure 1.14, where we present the breakdown of costs for a TFSC (CuInSe_2 , an ancestor of today's $\text{Cu}(\text{InGa})\text{Se}_2$) flat module central plant and a concentrating central plant. Both sets of calculations are based on the same criteria for the two technologies involved (but based on realistic but futuristic assumptions) and presented in Chapter 21.

The plant cost is about twice the module cost: more for concentrators, less for "flat-plate" modules. Notice, that the cost of land is absolutely negligible land (provided the plant is built where land prices are low). It has to be stressed again that modules at the costs in the figure are not yet achievable.

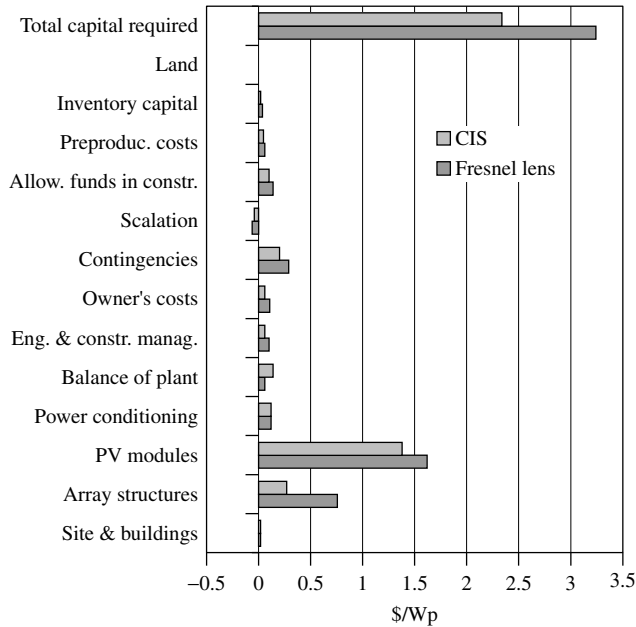


Figure 1.14 Calculated breakdown of costs of the construction of a PV central plant based on two anticipated technologies. Above, CIS flat module cells; below, Fresnel lens concentrator with Si cells operating at 500 suns. (Data from Whisnant *et al.* in Chapter 21)

We present in Figure 1.15 a calculation of costs of different types of modules in an advanced manufacturing process calculated with the same procedure. Again, the origin of this is Chapter 21, devoted to cost calculations. Although cost calculations for the $\text{Cu}(\text{InGa})\text{Se}_2$ technology is not available, their costs are not expected to be too different to those of a-Si. Indeed, the cost model in Chapter 21 includes many more parameters and assumptions and the results depend on such choices. Nevertheless, according to the model, the common c-Si Cz module (with efficiency of about 14 to 15%) is clearly more expensive than any one of the other options (provided they have a minimal efficiency of 5 to 7%). Dendritic web technology refers to one form of Si ribbon technology that is starting to find a place in the market.

Using again the cost model in Chapter 21 we can calculate the cost of the electricity generated. Table 1.4 shows the difference of electric output of the two equally rated plants.² Obviously, the yearly efficiency (referred to as the *module aperture area*) is different. Furthermore, they both present different capacity factors as defined by the ratio of the produced energy (in kWh or MWh) to the rated power (in kWp or MWp) times the total number of hours in a year (365×24). To calculate the electricity cost (in \$/kWh), one term is the financial cost of all the expenditures and another much smaller one is the operation and maintenance costs (very small as stated at the beginning). The price per kWh must be compared to the typical average price of \$0.05/kWh for conventional

² Figure 1.15 and Table 1.4 present cost data scaled to 1985 or 1990 equivalent dollars, as does discussion and results in Chapter 21. Although quantitatively “out of date”, they are still quite useful for relative comparison.

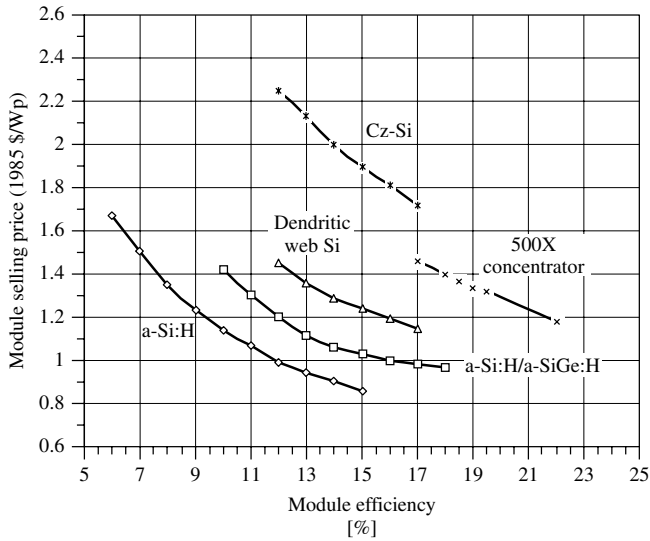


Figure 1.15 Effect of cell technology and efficiency on module price. (Source: Whisnant *et al.* in Chapter 21)

Table 1.4 Annual performance and energy cost summary for central station plants. Calculations for constant 1990\$, for a 50 Mw_p plant in Central California, USA. Source Whisnant *et al.*, Chapter 21

	Fresnel lens concentrator	CIS Flat-plate
Energy output (MWh)	140 100	112 000
Capacity factor	32.0%	25.8%
Annual energy efficiency	18.8%	9.9%
Annual expenses (\$10 ⁶)		
Capital charge	16.69	11.95
Operation & maintenance expense	0.61	0.18
Total	17.30	12.13
30-YR Levelized energy cost (\$/kWh)		
Capital charge	0.119	0.106
Operation & maintenance costs	0.004	0.002
Total (\$/kWh)	0.123	0.106

electricity. Photovoltaics is more than twice as expensive. However, this cost can be attractive for a part of the electricity generated by a utility, such as when it meets peak power demand.

For the end-user, the cost of the conventional electricity can be very similar to the one in the table. The cost of installing a PV grid-connected system in a house or building is not much more expensive than the centralized power plant presented in the table but the marketing cost of this distributed residential product will increase the final installation cost. It is to be stressed, that the costs used here are merely an indication

of the relative significance of various factors. These assumptions and model parameters may not apply to some immature or as-yet undeveloped technologies. Yet, these exercises can be useful to decision makers, especially if complemented by sensitivity studies (as in Chapter 21).

As a final comment, the costs presented in this section are final costs calculated by a detailed account of all the elements utilized in a plant or module and an estimation of the performances achieved. In contrast, the costs in Section 1.5 are based on fundamental economic laws that are found empirically to occur regardless of technological details, yielding costs as a function of the time. Thus, the costs, as calculated in the present section, may be considered as a point of that curve, to occur somewhere in the future.

Of course, all components in the system have some parasitic power loss. Yearly average AC efficiencies of 10% are common in a well-managed grid-connected system with modules starting at 14%. Much of this loss can be attributed to temperature: cells operate at 20 to 30°C over the ambient which reduces their efficiency and output since efficiency decreases with temperature (except for a-Si). Additionally, 8 to 10% relative losses are expected for the DC–AC conversion in the inverter. Round trip battery losses (charge–discharge) in stand-alone applications can be an additional relative 10 to 20%.

1.12 FUTURE OF EMERGING PV TECHNOLOGIES

The solar resource is huge although its energy density is rather low. However, it is not so low as to lose any hope of massive utilization but it is not high enough to make it easy.

Obviously, the proper strategy for recovering a dispersed resource is to do it with high efficiency at a low cost per area. But the standard PV-effect, as described in this chapter, only delivers to the external circuit with high efficiency those charge carriers generated by the few photons with energy close to the band gap. The excess energy of photons whose energy is greater than the band gap is typically wasted as heat. Even worse, all of the energy of the photons whose energy is below the band gap is wasted since they are not absorbed and therefore generate no charge carriers.

Thus, as described in detail in Chapter 4, the maximum efficiency that can be obtained under the best conditions from a single junction solar cell is in the range of 40%. The best efficiency so far obtained for single-junction solar cells is 27.6%, with GaAs research-type cells [75] under concentrated sunlight of 255 suns, that is, of 255 times the unconcentrated standard power density (i.e. at 255 kW/m²). Typical commercial silicon cell efficiency is ~15% measured at standard conditions (input optical power density of 1 kW/m², 25°C and standard terrestrial solar spectrum).

One way of extracting more power from the sun is to use stacks of cells of semiconductors having different band gaps. Higher band gap semiconductors are located on top of the stack allowing photons of energy less than their band gap to pass through, where they can be absorbed by inner cells of lower band gap. The limit efficiency of these stacks, as presented in Chapter 4, with infinite number of cells of different band gap is 86%, as compared with the 40% of the single band gap cells. Efficiencies up to 32% (under standard unconcentrated terrestrial solar spectrum) have been achieved for a monolithic three band gap stacked cells of GaInP/GaAs/Ge [76].

The interest in multijunction cells has been reawakened by the requirements of space cells, where price is less relevant than the performance in many cases (Chapter 10). However, they can be used in terrestrial applications provided they are operating at very high concentration. There is a trend to develop cells operating at 1000 suns. Efficiencies up to 26% with a single band gap GaAs solar cell [77] and of over 29% with a double band gap GaInP/GaAs cells [78] have been achieved (Chapter 9). Also, the development of low-cost concentrators able to operate at 1000 suns is a subject of current research [79]. The prospects are very promising because such technologies predict in the long-term to produce electricity competitive with conventional sources. A cost estimate is presented in Table 1.5. In the 1-J no learning case, the costs are similar to those in Table 1.4. However, in the learning case the costs are, in extremely good locations (EGL), very competitive with conventional electricity, provided that we achieve very high efficiencies. In this calculation, the experience factor for the cells is the same as in microelectronics; for the rest of the elements the learning curve is same as the present one for modules [80].

The role of the experience factor has been stressed when describing Figures 1.6 and 1.7. Conventional cells have a relatively low experience factor, we think, because they are limited in the maximum efficiency they can reach. Multijunction cells, in contrast, have a much higher efficiency limit and therefore they can progress in efficiency for a longer time. This is one reason to attribute to them a faster experience factor.

Multijunction cells are also crucial to the success of the thin-film photovoltaics. In the a-Si thin-film PV technology, the highest cell and module efficiencies being reported for the past decade are for triple junctions as described in Chapter 12. The use of multijunction cells in thin films might lead to a faster learning curve and hence reduced costs. The band gap of various polycrystalline alloys of Cu(InGa)Se₂, Cu(InAl)Se₂, Cu(InGa)(SeS), or CdZnTe can be varied with alloying. The theoretical efficiency of a tandem device with a 1.6 to 1.8 eV band gap top cell and a 1.0 to 1.2 eV band gap bottom cell exceeds 30%. In all cases, the top cell must provide the majority of the power.

Table 1.5 Costs for very high-efficiency 1000 suns-concentrating systems [80] for one junction (1-J) and four junctions (4-J) cells. NDI stands for Normal Direct Irradiation. EGL stands for extremely good location with NDI = 2700 W·m⁻²·year⁻¹. “No learning” means with present costs (2002) while “learning” means they are reduced by a learning curve with experience factor of 0.32

Cost element	1-J, no learning	4-J, learning
Cells (\$ per cm ² cell area)	13.4	4.43
Module (\$ per aperture area)	265	113
Cell efficiency (%)	23.1	45
Module efficiency (%)	19.0	37.1
Plant price (\$ per m ² aperture area)	526	271
Madrid NDI (W·m ⁻² ·year ⁻¹)	1826	1826
Performance ratio	0.606	0.606
Electricity costs in Madrid (\$ per kWh)	0.186	0.050
Electricity costs in EGL (\$ per kWh)	0.131	0.035

Yet, in all these alloy systems, material quality and device performance degrades substantially for band gaps exceeding 1.4 to 1.6 eV, depending on the materials (see Chapter 13). A very productive area for research will be to either improve these materials when they are produced with high band gaps or to develop new alloys. Any multijunction process must be sequentially compatible from beginning to end.

Besides the multijunction effort, other concepts are in place for attempting a better utilization of the solar spectrum, such as the Intermediate Band (IB) concept [81], which is described further in Chapter 4. A band, with electron states in the center of the band gap, would permit the passage of electrons from the valence band to the conduction band by means of two low-energy photons, one pumping electrons from the valence to the intermediate band and the other pumping the electron from this band to the conduction band. This concept presents a potential behavior which is somewhat better than the multijunction cell stack with two semiconductors. Nanotechnology is a means of producing this intermediate band [82], and the basic effect sketched above seems to have been proved already by using quantum dots [83]. Quantum dots are droplets of one material in a host of another material of higher band gap. The droplets are very small and exhibit quantum effects among which is the appearance of intermediate bands or levels. Alloys might also be found with intermediate band [84], but no practical realization of this concept has been shown so far. Other new type devices, although not easy to realize today, are also envisioned. The theoretical basis of all these new devices can be found in Chapter 4.

Finally, solar cells have been constructed which do not operate on the photovoltaic effect but on charge transfer between molecular orbitals, as in photosynthesis. Their potential for efficient absorption of the spectrum depends on “tuning” the chemistry of organic dyes, as described in Chapter 15. Presently the subject of much research, dye-sensitized solar cells have achieved >10% efficiency but have many challenges regarding stability and manufacturability.

1.13 CONCLUSIONS

Photovoltaics constitutes a new form of producing electric energy that is environmentally clean and very modular. In stand-alone installations, it must use storage or another type of generator to provide electricity when the sun is not shining. In grid-connected installations storage is not necessary: in the absence of sunlight, electricity is provided from other (conventional) sources.

PV electricity is highly appreciated by the public. It is unique for many applications of high social value such as providing electricity to people who lack it in remote areas. Often, international donor agencies are providing the funding, as many of the users are very poor. Photovoltaics is very suitable as the power supply for remote communication equipment. Its use is increasing rapidly to produce electricity in grid-connected houses and buildings in industrialized countries, despite a 5 to 10 times higher cost than conventional electricity. Often, publicly funded programs are required to enable photovoltaics to compete by partially offsetting its higher costs.

Largely, because of grid-connected PV applications such as homes and businesses, the expansion of the PV market has been very rapid in the last years of the twentieth

century and it is expected to continue during the next few years of the twenty-first century. Then, the growth will probably continue at a slower pace unless new technological advances are developed and commercialized. In that case, growth could accelerate.

Photovoltaics is poised to become a large global high-tech industry, manufacturing and selling modules in nearly every country. Governments and entrepreneurs should be aware of this. Public R&D support has always been generous. It must continue to be so for those countries that want to maintain leadership in this technology. Partial subsidization of PV installations is permitting an unprecedented development of the PV industry and will also help the industry of the countries involved in this endeavor to take the lead.

Crystalline Si technology, both monocrystalline and multicrystalline is today clearly dominant, with about 90% of the market. It will remain dominant at least for the next ten years. The trend is towards the multicrystalline option. Si is one of the most abundant elements in the Earth's crust but the purified Si used in today's solar cells is obtained primarily as off-grade poly-Si and scrap wafers from the microelectronic industry. Soon it will not be enough for the growing PV industry. Thus, some concerns exist regarding a shortage of the purified silicon for the PV industry. However, it is doubtful that Si technology will be able to reach competition with conventional electricity. Consequently, low-cost alternatives and high-efficiency novel concepts, many already in development, are needed.

Thin-film technology is one of the candidates to take over from Si technology in the long-term. There are many technological options regarding thin-film materials and methods of deposition but their primary claim to the throne currently occupied by Si is that they can be ultimately produced at much lower cost.

Concentration of sunlight is another candidate for mass penetration of photovoltaics, although it will not be easily accepted for the grid-connected houses, one of the most promising applications today. Concentrators will probably find incipient niche markets in big stand-alone applications or as small, central-power plants during the present decade.

Finally, new materials and device designs based on III-V semiconductor alloys, such as GaInP allowing more efficient use of the solar spectrum are now being developed for space applications. With the use of concentrators, they may be of interest for terrestrial applications, with the potential of reaching competitive costs with conventional electricity. Other options, such as quantum dots and dye-sensitized solar cells, are still in the initial research phase. They must compete not only with the ubiquitous Si but also with the other options, mentioned above for funding for further development.

Thus, photovoltaics possesses a panoply of novel technologies that almost ensures that alternatives will be available when the current Si wafer technology cannot reach prices low enough to compete with conventional electricity. If this happens, a strong industry and infrastructure – first developed for the Si technology – will be able to seamlessly take this new PV technology and apply it worldwide. In any case, the present “subsidies” to research or application must be considered as public investment in a policy with strong public support and long-term human benefits.

The widespread contribution of PV electricity in electric grids will require a new type of grid management that can accept small generators as well as small consumers. On

the other hand, hybrid forms of electricity generation, including photovoltaics, will play an important role in the future development of stand-alone applications and minigrids. The general cost reduction will make photovoltaics available to more and more people in developing countries helping their development with little degradation of air quality associated with fossil-fuel generators.

In summary, it is very likely that photovoltaics will become in the next half century an important source of world electricity. Public support and global environmental concerns will keep photovoltaics viable, visible, and vigorous both in new technical developments and user applications. Nations which encourage photovoltaics will be leaders in this shining new technology, leading the way to a cleaner, more equitable twenty-first century, while those that ignore or suppress photovoltaics will be left behind in the green, economic energy revolution.

REFERENCES

1. Benka S, *Phys. Today* 38, 39 (2002); adapted from Pasternak A, Lawrence Livermore Natl. Lab report UCRL_ID_140773 (October 2000).
2. We acknowledge Dr. Larry Kazmerski of NREL, and coauthor of Chap. 24, for developing the “myths of PV” concept as a way of dispelling common misunderstandings and issues in PV. See his paper *Renewable Energy World*, August 2002, 175–183.
3. “*Energy System Emissions and Material Requirements*”, Meridian Corporation (Alexandria VA) report prepared for the Deputy Assistant Secretary for Renewable Energy of the USA (1989).
4. Kelly H, Weinberg C, in Johansson T *et al.* (Eds), *Renewable Energy*, 1011–1069, Island Press, Washington, DC (1993).
5. Maycock P, *Renewable Energy World* 3, 59–74 (2000).
6. Fthenakis V, Moskowitz P, *Prog. Photovolt.* 8, 27–38 (2000).
7. Tsou Y *et al.*, *Proc. 2nd World Conf. Photovoltaic Energy Conversion*, 1199–1204 (1998).
8. See Papers contained in Proc. of Photovoltaic Safety Conf., *Sol. Cells* 19, 189–397 (1987).
9. See Papers contained in Proc. of Workshop on Environmental Aspects of PV Systems, *Prog. Photovolt.* 6, 87–146 (1998).
10. www.pv.bnl.gov.
11. Fthenakis V, Moskowitz P, *Prog. Photovolt.* 3, 295–306 (1995).
12. Patterson M, Turner A, Sadeghi M, Marshall R, *Proc. 12th Euro Photovoltaic Solar Energy Conf.*, 951–953 (1994).
13. Fthenakis V *et al.*, *Prog. Photovolt.* 7, 489–497 (1999).
14. Bohland J, Smigielski K, *Proc. 28th IEEE Photovoltaic Specialist Conf.*, 575–578 (2000).
15. Moskowitz P, Fthenakis V, *Sol. Cells* 31, 513–525 (1993).
16. Moskowitz P, Fthenakis V, *Sol. Cells* 29, 63–71 (1990).
17. Fthenakis V, Eberspacher C, Moskowitz P, *Prog. Photovolt.* 4, 447–456 (1996).
18. Bohland J, Dapkus T, Kamm K, *Proc. 2nd IEEE World Photovoltaic Specialists Conf.*, 716–719 (1998).
19. Alsema E, *Prog. Photovolt.* 8, 17–25 (2000).
20. Keoleian G, Lewis G, *Prog. Photovolt.* 5, 287–300 (1997).
21. Knapp K, Jester T, *16th Euro Photovoltaic Solar Energy Conf.*, 2053–2056 (2000).
22. Fritts C, *Proc. Am. Assoc. Adv. Sci.* 33, 97 (1883).
23. Chapin D, Fuller C, Pearson G, *J. Appl. Phys.* 25, 676, 677 (1954).
24. Reynolds D, Leies G, Antes L, Marburger R, *Phys. Rev.* 96, 533, 534 (1954).
25. Jenny D, Loferski J, Rappaport P, *Phys. Rev.* 101, 1208, 1209 (1956).
26. Prince M, *J. Appl. Phys.* 26, 534–540 (1955).

27. Loferski J, *J. Appl. Phys.* **27**, 777–784 (1956).
28. Wysocki J, Rappaport P, *J. Appl. Phys.* **31**, 571–578 (1960).
29. Shockey W, Queisser H, *J. Appl. Phys.* **32**, 510–519 (1961).
30. Cusano D, *Solid State Electron.* **6**, 217–232 (1963).
31. Wysocki J *et al.*, *Appl. Phys. Lett.* **9**, 44–46 (1966).
32. Alferov ZhI, *Fiz. Tekh. Poluprovodn.* **4**, 2378 (1970).
33. Lindmayer J, Allsion J, *COMSAT Tech. Rev.* **3**, 1–22 (1973).
34. Hovel H, Woodall J, *Proc. 10th IEEE Photovoltaic Specialist Conf.*, 25–30 (1973).
35. Sumner D, Whitaker C, Schlueter L, *Proc. 20th IEEE Photovoltaic Specialist Conf.*, 1289–1292 (1988).
36. Green M *et al.*, *Proc. 18th IEEE Photovoltaic Specialist Conf.*, 39–42 (1985).
37. Sinton R, Kwark Y, Gruenbaum P, Swanson R, *Proc. 18th IEEE Photovoltaic Specialist Conf.*, 61–65 (1985).
38. Friedman D *et al.*, *Prog. Photovolt.* **3**, 47 (1995).
39. Gratzel M, *Prog. Photovolt.* **8**, 171–186 (2000).
40. Contreras M *et al.*, *Prog. Photovolt.* **7**, 311–316 (1999).
41. Bower W, *Prog. Photovolt.* **8**, 113–126 (2000).
42. Fitzgerald M, Mrohs M, *Proc. 26th IEEE Photovoltaic Specialist Conf.*, 1225–1229 (1997).
43. Nieuwenhout F *et al.*, *Prog. Photovolt.* **9**, 455–474 (2001).
44. Cabraal A, Cosgrove-Davies M, Schaeffer L, *Proc. 25th IEEE Photovoltaic Specialist Conf.*, 1357–1362 (1996).
45. Hoff T, Jennings C, *Proc. 18th IEEE Photovoltaic Specialist Conf.*, 235–240 (1985).
46. Shugar D, Hoff T, *Prog. Photovolt.* **1**, 233–250 (1993).
47. Byrne J, Hegedus S, Wang Y, *Prog. Photovolt.* **2**, 235–248 (1994).
48. Yordi B, Gillett W, *Prog. Photovolt.* **5**, 175–185 (1997).
49. Iuchi M, *2nd World Conference and Exhibition on Photovoltaic Solar Energy Conversion*, 3304–3307 (1998).
50. Strong S, *Proc. 25th IEEE Photovoltaic Specialist Conf.*, 1197–1202 (1996).
51. Cody G, Tiedje T, *Proc. 25th IEEE Photovoltaic Specialist Conf.*, 1521–1524 (1996).
52. Luque A, *Prog. Photovolt.* **9**, 303–312 (2001).
53. Parente V, Goldemberg J, Zilles R, *Prog. Photovolt.* **10**, 571–574 (2002).
54. Johansson T, Kelly H, Reddy A, Williams R, *Renewable Energy*, Chap. 1, Island Press, Washington, DC, 1–71 (1993).
55. *Photon Int.* 38–43 (March 2002).
56. Aulich H, Raptis F, Schmid J, *Prog. Photovolt.* **6**, 325–340 (1998).
57. Sumner D, Whitaker C, Schlueter L, *Proc. 20th IEEE Photovoltaic Specialist Conf.*, 1289–1292 (1988).
58. Wenger H, Jennings C, Ianucci J, *Proc. 21st IEEE Photovoltaic Specialist Conf.*, 844–849 (1990).
59. Iliceto A, Belli G, Lambri L, Toninelli F, *Proc. 14th Euro. Photovoltaic Solar Energy Conf.*, 2670–2674 (1997).
60. Matlin R, Shugar D, *Proc. 12th Euro Photovoltaic Solar Energy Conf.*, 842–845 (1994).
61. Sala G *et al.*, *2nd World Conference and Exhibition on Photovoltaic Solar Energy Conversion*, 1963–1968 (1998).
62. Kardauskas M, Rosenblum M, Mackintosh B, Kalejs J, *Proc. 25th IEEE Photovoltaic Specialist Conf.*, 383–388 (1996).
63. Schmidt W, Woesten B, Kalejs J, *Prog. Photovolt.* **10**, 129–140 (2002).
64. Barnett A, Rothwarf A, *IEEE Trans. Electron Devices* **27**, 615–630 (1980).
65. Hewig G *et al.*, *Proc. 16th IEEE Photovoltaic Specialist Conf.*, 713–718 (1982).
66. Bragagnolo J *et al.*, *IEEE Trans. Electron Devices* **27**, 645–650 (1980).
67. Hall R, Birkmire R, Phillips J, Meakin J, *Appl. Phys. Lett.* **38**, 925, 926 (1981).
68. Catalano A *et al.*, *Proc. 16th IEEE Photovoltaic Specialist Conf.*, 1421, 1422 (1982).

69. Mickelson R, Chen W, *Proc. 16th IEEE Photovoltaic Specialist Conf.*, 781–785 (1982).
70. Tyan Y, Perez-Albuerne E, *Proc. 16th IEEE Photovoltaic Specialist Conf.*, 794–799 (1982).
71. Phillips J, Birkmire R, Lasswell P, *Proc. 16th IEEE Photovoltaic Specialist Conf.*, 719–722 (1982).
72. Maycock P, *PV NEWS* **21**(4), 1 (April 2002).
73. Wills R, Hall F, Strong S, Wohlgemuth J, *Proc. 25th IEEE Photovoltaic Specialist Conf.*, 1231–1234 (1996).
74. Knaupp W *et al.*, *Proc. 25th IEEE Photovoltaic Specialist Conf.*, 1235–1238 (1996).
75. Vernon S *et al.*, *Proc. 22nd IEEE Photovoltaic Specialist Conf.*, 353–357 (1991).
76. Cotal H *et al.*, *Proc. 28th IEEE Photovoltaic Specialist Conf.*, 955 (2000).
77. Algora C *et al.*, *IEEE Trans. Electron Devices* **48**, 840–844 (2001).
78. Bett A *et al.*, *Proc. 28th IEEE Photovoltaic Specialist Conf.*, 961 (2000).
79. Miñano J, González J, Benítez P, *Appl. Opt.* **34**, 7850 (1995).
80. Yamaguchi M, Luque A, *IEEE Trans. Electron Devices* **46**(10), 2139–2144 (1999).
81. Luque A, Martí A, *Phys. Rev. Lett.* **78**(26), 5014–5017 (1997).
82. Martí A, Cuadra L, Luque A, *Proc. 28th IEEE Photovoltaic Specialist Conf.*, 940–943 (2000).
83. Cassaboisa G *et al.*, *Physica* **E13**, 105–108 (2002).
84. Wahnou P, Tablero C, *Phys. Rev. B* **65**, 165115-1–165115-10 (2002).

This Page Intentionally Left Blank

2

Motivation for Photovoltaic Application and Development

Joachim Luther

*Fraunhofer Institut für Solare Energiesysteme, Heidenhofstr 2 D-79110
Freiburg, Germany*

Photovoltaics is the technological symbol for a future sustainable energy supply system in many countries. A considerable amount of money is invested in research, development and demonstration; several governments set up substantial market introduction programs and industry invests in larger production facilities. No other renewable energy technology receives such a strong appreciation by the public and to an increasing extent also by the politicians and the industrial and financial sectors. This is a remarkable situation since at the same time photovoltaic (PV) electricity is regarded as much too expensive compared to conventional grid electricity. The high and justified recognition of photovoltaics may be understood on the basis of a description of the main positive features of this kind of solar electricity conversion.

2.1 CHARACTERISTICS OF PHOTOVOLTAIC ENERGY CONVERSION

Photovoltaics aims at two areas of application. One is the power supply for off-grid professional devices and supply systems (e.g. telecommunication equipment, solar home systems) and the other is large-scale electricity generation as a substitute for and a complement to today's non-sustainable energy processes. With respect to the latter, the global potential of PV electricity is of key importance. Figure 2.1 shows the technical and the theoretical potential of several renewable energy sources. The theoretical potential does not take into account land use restrictions, conversion efficiencies, storage requirements and so on. The technical potential on the other hand must not be confused with short-term economic potentials, since price situations and capital requirements for activating these energy sources on a large scale are not considered.

Resource	Current use	Technical potential	Theoretical potential
Hydropower	9	50	147
Biomass energy	50	>276	2900
Solar energy	0.1	>1575	3900000
Wind energy	0.12	640	6000

Units: exajoule per year

Figure 2.1 Current use and current potentials of selected renewable energy sources [1]. For comparison: global primary energy demand 402 exajoule/annum (1998). The electricity part of “current use” has been converted to primary energy utilising an efficiency factor of 0.385

Nevertheless, two important conclusions may be drawn from Figure 2.1: (1) even under strong area restrictions (e.g. utilisation of a small percentage of the land area) and guarded assumptions of overall technical efficiencies, solar energy conversion alone could in principle produce considerably more technical energy than is consumed today and (2) compared to other renewable sources, solar radiation is by far the largest. A sustainable global energy system that is strongly based on renewable sources will in the long run mainly be a solar energy system. With respect to the technology of solar electricity production, this means solar thermal power plants and photovoltaics. The application of thermal power plants is restricted to areas with high and direct insulation; flat-plate (standard) PV modules may be applied practically everywhere in the world since they convert diffuse and direct (beam) radiation with approximately the same efficiency.

Photovoltaic energy conversion meets the important requirements of a sustainable energy production in an obvious way. During operation there is no harmful emission or transformation of matter (generation of pollutants), nor any production of noise or other by-products. PV energy conversion is a technologically elegant one-step process avoiding conventional thermodynamic or mechanical intermediate steps. On the other hand, production of PV modules and system components will – as any industrial device production – include material transformation and the production of wastes. Thus, it is extremely important to realise PV conversion technologies that comply with the requirements of environmentally benign production schemes.

Though characterised by the high global potential given in Figure 2.1, the area-specific power density of solar radiation is relatively low, that is, approximately 100 W/m² on the average. This means that the global harvesting of solar resources necessarily requires a large-area production of energy converters. Appropriate recycling strategies will thus be essential for the energy-relevant application of photovoltaics. Already today standard silicon-wafer PV-technology meets in principle the requirements with respect to recycling and sustainable production.

Photovoltaic energy conversion is highly modular. Installations may vary between milliwatts for consumer products (watches) to megawatts in the case of grid-connected power plants. From a market point of view, this gives rise to a broad variety of PV applications. For the professional energy supply business, modularity is especially important with

respect to the development of electricity supply systems in many rural and remote areas where grid extension is economically not feasible. Starting from low power installations, PV modules may be gradually added to suitable systems in order to cope with the growing energy demands. In this way electricity supplies can be realised avoiding too high initial investments. In the context of rural electrification and also for the professional energy supply of off-grid electronic devices, the low maintenance characteristic of photovoltaics is regarded as a considerable advantage. The absence of moving parts, the robustness against harsh environment and the lack of fuel supply requirements (exception: hybrid systems) make photovoltaics a well-suited energy supply technique for a vast area of stand-alone energy supplies.

Another positive characteristic of PV is that it may be seen as part of the rapidly growing semiconductor industry/market. This relation facilitates a strong technology transfer from a mature industry to the emerging PV industry. Parallel to this the affinity opens the prospect of new big industries creating considerable business and employment opportunities.

The strong market growth of photovoltaics over the last two decades (Figure 2.2) and the high recognition of this technology could not be understood if there had not been a continuous and strong reduction in PV system and module prices.

Figure 2.3 shows the price-experience curve (learning curve) until 2000. Each doubling of the module shipment resulted on the average in a market price reduction of 20%. It is generally accepted that it is possible to cut down the prices by another factor of two utilising mass production lines based on today's crystalline silicon-wafer technology. Considerable further cost reduction seems feasible since new and most probably least costly PV technologies are already in the state of pilot production (thin-film cells) or under investigation in laboratories: cells based on III/V materials and optical concentration, cells using dyes or organic compounds for energy conversion and so on. Thus, there is a good

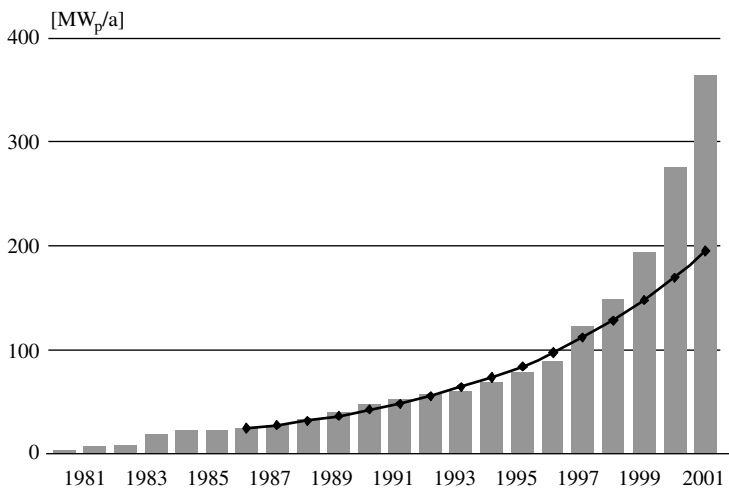


Figure 2.2 Evolution of the global photovoltaic market [2]. Until 1996 the growth rate was approximately 15%/annum. Today's growth rates are in the order of 30%/annum

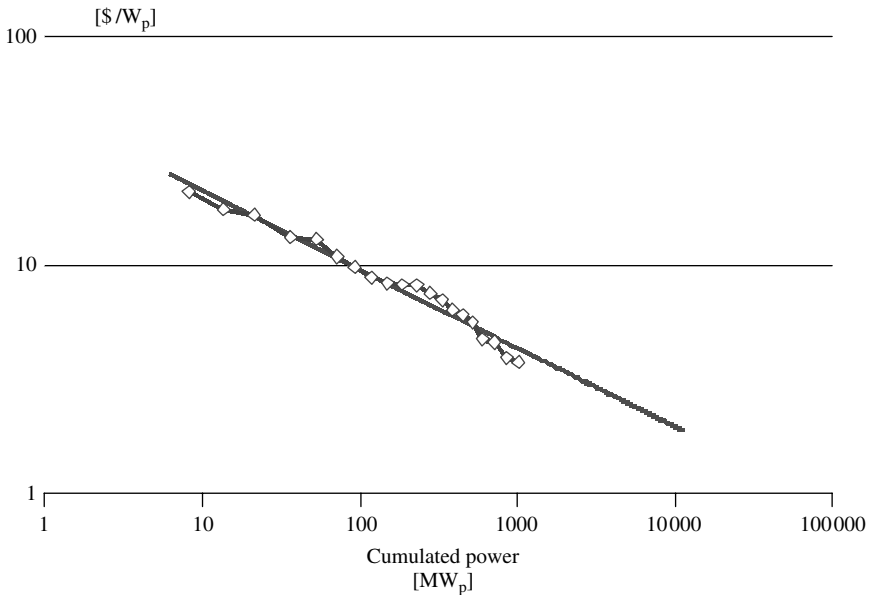


Figure 2.3 Price-experience curve of the photovoltaic market until 2000 [2]. Scale: double logarithmic. The slope of the curve is characterised by a factor $f = 0.8$. This means that a doubling of the photovoltaic shipment resulted in a price reduction down to 80%

chance of at least a break even between PV electricity and conventional electricity prices, given that the external (social) costs of non-sustainable electricity are properly taken into account.

2.2 A LONG-TERM SUBSTITUTE FOR TODAY'S CONVENTIONAL ELECTRICITY PRODUCTION – THE ECOLOGICAL DIMENSION OF PHOTOVOLTAICS

A sustainable development has to respect certain guard rails. With respect to the energy supply system, these are mainly determined by the global warming/ CO_2 problem (Figure 2.4). A global warming of more than 2°C (with respect to the pre-industrialised period) and a warming rate of 0.2°C per decade seems to be the upper limits for a development that may be kept under control. These settings are in accordance with the results of recent studies of the International Panel on Climate Change [3].

Since preservation and expansion and especially the transformation of energy systems require important investments, a strategy of large stopping-distances seems reasonable. For example, the German Advisory Council on Global Change proposes a continuous CO_2 reduction rate of 1% per year over the next 150 years [3]. If one strives for a fair and rational distribution of the worldwide reduction obligations, the highly industrialised nations have to reduce their CO_2 emissions until 2050 by almost 80% relative to the 1990 level [3]. This reduction mainly affects the energy sector including fuels for transportation.

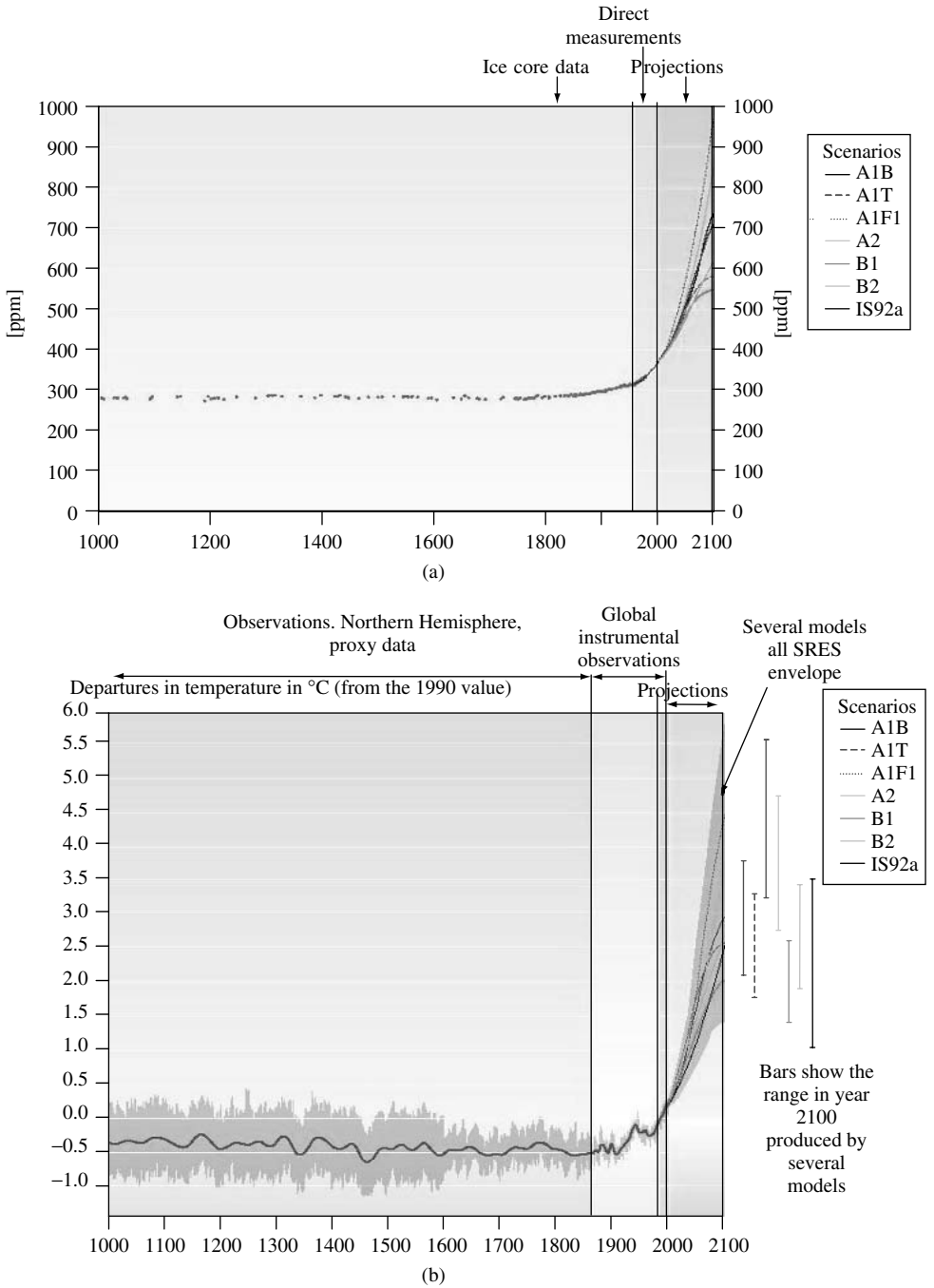


Figure 2.4 Past and future CO₂ atmospheric concentrations (a) and variations of the Earth's surface temperature (b). Time span: year 1000 to year 2100. The projections on the right sides are based on scenarios of the Intergovernmental Panel on Climate Change (IPCC) [4]. Reproduced by permission of Cambridge University Press

As far as can be seen today, such reduction goals may – in a socially acceptable way – only be realised if renewable energy technologies are applied worldwide on a really large scale. For electricity production, this means above all the use of photovoltaics and to a lesser (but important) extent wind energy, biomass conversion and solar thermal power plants. Thus, the principal ecological dimension of photovoltaics is extremely high. The question arises of course whether we can activate this potential in due time. With respect to this, at least two sub-problems have to be addressed: (1) how fast can the industry produce the required large-area PV energy conversion systems and (2) is it possible to establish a strong long-lasting market-driving mechanism that conforms with today's ideas of a competitive market.

During the last few years, annual market growth rates and thus the increase in industrial PV production have been in the order of 15 to 30% (Figure 2.2). The main drivers behind this impressive growth are several governments and consumers who see an urgent need for a transformation of today's energy systems towards sustainability [5–7]. Financial-support mechanisms have been developed that include clear components of competition inside well-defined areas of energy supply technologies. The financial support is justified by the high potential of PV electricity and its ecologically benign character. On the other hand, such schemes have to be limited in time, which is especially important if the promoted markets evolve exponentially. Thus, the question arises whether grid-coupled PV electricity will become cost-effective within reasonable time frames. Figure 2.5 shows a cost projection of base-load, peak-load and photovoltaic electricity.

The assessment is based on an extrapolation of the prize experience curve given in Figure 2.3, a PV-market growth rate of 20%/annum and an increase of conventional electricity costs by 2% per year. Under these assumptions, a break even between peak load and

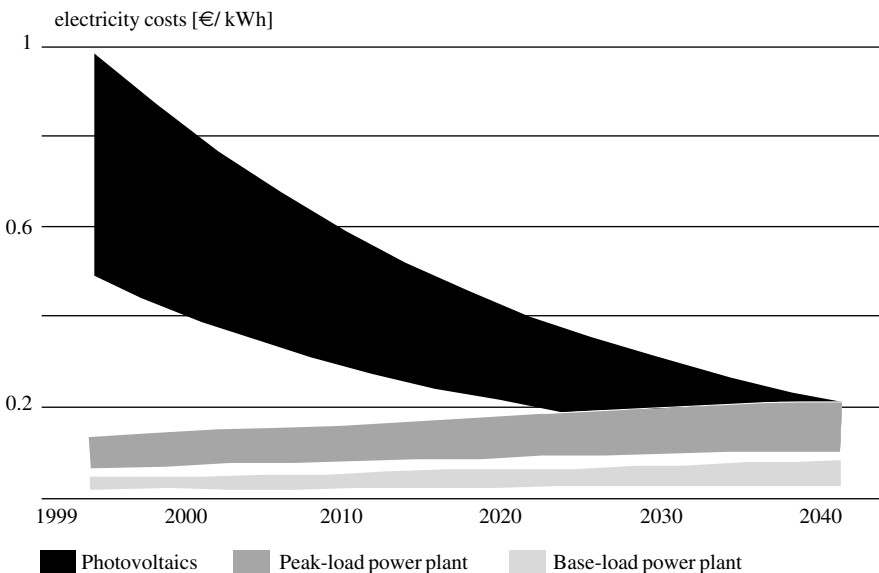


Figure 2.5 Cost projections for photovoltaic electricity. The upper boundary of photovoltaic costs reflects the meteorological situation of Germany, the lower boundary that of Southern Europe [8]

solar electricity is found around 2025; a break even with costs from conventional base-load power plants is not reached in the first half of this century.

The extrapolation of a prize experience curve over several decades bears, of course, a considerable risk. On the other hand, there are good technological arguments that the price-experience curve will continue to decrease in a similar way as in the past for a considerable time span; a strong reduction in the slope of the curve most probably will not be encountered before a further price reduction by a factor of 3 to 5 is reached. It is important (and essential) to mention that most probably this statement is also valid for the balance of system components such as power electronics and so on.

Many conclusions may be drawn from a graph such as that given in Figure 2.5 (based partly on an arbitrary set of parameters). If one aims, for example, at an efficient transformation of today's electricity supply system, one may propose an energy tax on environmentally and socially non-benign energy sources in order to establish competitive market situations at a significantly earlier time. This tax could be based on the internalisation of external costs of the different competing energy supply technologies. In order to allow for a smooth evolution towards sustainability, such a tax should be introduced gradually. If one assumes, for example, a continuous additional tax-induced cost increase of electricity from conventional peak- and base-load power plants of 2% per year, the break even in Figure 2.5 for peak load would occur around 2015 and that for base load around 2030. The public income from such an energy tax could be invested in research and development in the field of renewable energies and in energy efficiency measures. This would support, for example, the continuity of cost reduction of photovoltaics (Figure 2.3) as well as the reduction of the gross energy demand and thus of the energy-related financial burdens.

From an industrial point of view, a strong evolution of PV electricity generation could produce an interesting global market. A long-term price-experience factor $f = 0.82$ (see caption to Figure 2.3) and a market growth rate of 20% per year would generate, for example, the following global markets for PV-modules: 2010 2×10^9 €, 2020 9×10^9 € and 2030 30×10^9 € [8]. The additional market for system components and integration will probably be of the same order. The prospects of such substantial markets are the motivation of today's considerable industrial investments in PV production capacities.

It has been shown so far that if it is possible to maintain a price-experience evolution as shown in Figure 2.3 and if governments adopt a serious energy tax strategy, electricity from photovoltaics may become cost-effective between approximately 2015 (peak power) and 2030 (bulk power). Attractive high-technology markets could develop in the near future. One question still to be answered is 'when will photovoltaics contribute considerably to the global electricity generation?'

In a speculative way, this question may be addressed by stipulating conceivable long-term growth rates for PV electricity generation (Figure 2.6). Rates of 26%/annum results in a growth factor of 10 over one decade. Starting at present-days low level it will – even under these conditions – take at least three to four decades for photovoltaics to contribute in a substantial way to the global electricity demand (for rural electrification see Section 2.3). After this starting period, photovoltaics can become one main supplier of electric energy in the future energy mix. Growth rates of 15% per year on the other hand produce just a growth factor of four over one decade; under such conditions, photovoltaics

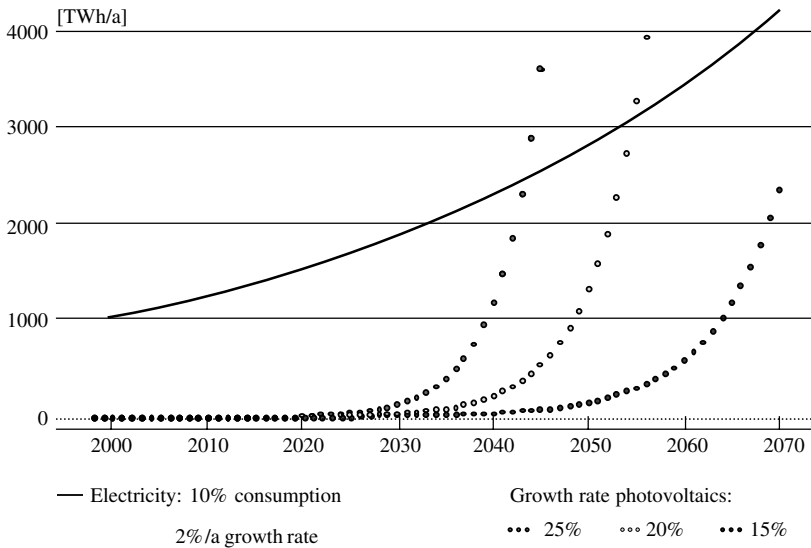


Figure 2.6 Scenarios of global photovoltaic electricity production under the assumption of constant growth rates of 25%/annum, 20%/annum and 15%/annum. The solid curve represents 10% of the global electricity demand assuming a constant growth rate of 2%/annum. A linear scale is used for the energy axis. Thus, although growing exponentially, the energy production by means of photovoltaics is not visible on the scale used until the year 2020

may become a major player only in the second half of our century. Since the man-made climatic problems call for a fast and forceful solution that is both environmentally benign and socially acceptable, high and continuously high growth rates for photovoltaics are extremely advisable.

The liberalisation of the energy market has led to new and innovative concepts, especially in the electricity sector. One of these is the distributed generation scheme – kilowatt to several megawatt installations instead of central units in the gigawatt range. Its main advantages are dispersed on-site heat and power cogeneration, electrical stabilisation of grids especially at the low voltage level, distributed reserves in the case of supply problems and partly favourable investment situations. PV electricity generation is well adapted to the distributed generation scheme (Figure 2.7). This is especially the case if peak-load conditions in the grids are considered that are strongly correlated with solar insolation: cooling and climatisation units. Also, the extreme modularity of photovoltaics turns out to be advantageous for distributed generation. Distributed peak power production will be most probably the first energy market application for optical concentrator PV power stations.

If performed on a continental or even intercontinental level, the highly dispersed application of photovoltaics will also lead to a strong levelling out of its stochastic local power generation characteristics. The remaining slowly varying time pattern of the lumped electricity production (diurnal, seasonal variations) can be compensated (of course, at extra costs) by the control of complementary electricity sources or in the long run by means of storage technologies.



Figure 2.7 Distributed power generation by means of photovoltaics. The roof-integrated photovoltaic system has a peak power of 5 kW

Another area that should be highlighted separately is façade- and roof-integrated grid-coupled photovoltaics. If done in an aesthetically promising way, PV claddings may substitute prestigious building elements. These applications may become the first mass market for homogeneous-looking thin-film PV modules. Even if the area-related investment costs of a PV building element is higher than the cost of conventional high-end elements, the electricity generated and the benefit of architectural double uses (Figure 2.8) may compensate for this difference within a reasonable time.



Figure 2.8 Photovoltaic integration into the glazing of a shed roof. In this case, photovoltaic cells serve also as optical shading elements for the space below, preventing overheating under summer conditions

2.2.1 In Summary

The technical potential of PV electricity is high enough to contribute considerably to the abatement of the man-made global CO₂ problem. With the help of medium-term financial supports and long-term energy taxes (motivated by external costs), the technical potential may be exploited economically. Under grid-coupled operation, photovoltaics will most probably become cost-effective for distributed peak power production and for applications in the building sector (as cladding element). Solar electricity generation has to grow by three orders of magnitude before it encounters a (extrapolated) 10% level of the global electricity demand. Assuming ambitious growth rates, this process of transformation will take three to four decades.

2.3 A TECHNOLOGICAL BASIS FOR OFF-GRID ELECTRICITY SUPPLY – THE DEVELOPMENT DIMENSION OF PHOTOVOLTAICS

Two billion people worldwide have no access to commercial electricity. When possible, they cover their needs for electricity-based services by means of primary batteries, rechargeable batteries (car batteries) or small fossil fuel-driven generator sets. In many (if not in most) cases these supply schemes are very costly, uncomfortable, unreliable and ecologically questionable. This results in the fact that for a large fraction of the global population, services such as electric light, radio, television, telecommunication, health services, clean water, cooling, electromechanical energy and so on are not at all available or are available only at a very low level. It must be stressed that these electricity-based benefits are amongst others crucial for education, business and small commercial activities (handicrafts, agriculture, food processing etc.). Thus the lack of a stable and affordable electricity supply hinders the development of many rural and remote areas. This is ethically not acceptable; it may lead to a destabilisation of regions and foster the growth of megacities, just to name three important reasons why this situation cannot be regarded as socially sustainable.

Beyond the low power level of primary batteries, there are mainly three worldwide applicable technology groups that are able to contribute in a professional way to the electricity supply of remote areas: grid extension, diesel generator sets and renewable energies. The most prominent amongst the renewables are small hydro, wind and photovoltaics. All technologies mentioned will eventually contribute to the electricity supply of rural and remote areas.

At first sight, grid extensions seem to be the most natural and technologically elegant way to overcome shortages in the electricity supply. It turns out, however, that the initial investments for such a strategy are prohibitively high if the consumers are scattered over large areas and if the average electricity demand, that is, the energy transported over the lines, is relatively small. Under these situations it is mostly impossible to recover the investments by selling electricity to the dispersed consumers or to raise it through subsidies from governmental organisations.

The alternatives to grid extension are renewables and diesel electric systems. In the following text, the benefits and characteristics of photovoltaics will be discussed.

Off-grid PV energy supply characteristics

- ❑ High reliability
 - ❑ High lifetime
 - ❑ Low maintenance
 - ❑ No fuel required
 - ❑ Favourable extensibility (modularity)
- ❑ Easy to transport (modularity)
 - ❑ Suitable for harsh environmental conditions
 - ❑ Suitable for mobile energy supply
 - ❑ Environmentally benign (no waste, noise, fuel transports)

Figure 2.9 Characteristics of off-grid photovoltaic energy supply systems

Figure 2.9 summarises some of the salient features of photovoltaics for off-grid electricity supply. The main disadvantage of PV systems is the comparatively high initial investments. Diesel systems on the other hand produce relatively low initial investments but high running costs especially due to fuel requirements.

Off-grid electricity supply systems generally need energy storages. In the case of diesels these are the fuel tanks, and in PV systems electrochemical batteries are applied. Especially because of this fact, solar electric systems are not maintenance-free (though their behaviour with respect to maintenance and wear is generally significantly more favourable than it is for diesel systems). For reliable operation, the storage battery has to be exchanged at regular intervals. Figure 2.10 indicates clearly that at present it is not the PV module but the system electronics (including installation) and the storage devices that constitute the main lifetime cost factors. Thus research and development in the fields of system technology and solar batteries would be highly supportive for an accelerated introduction of PV off-grid systems worldwide.

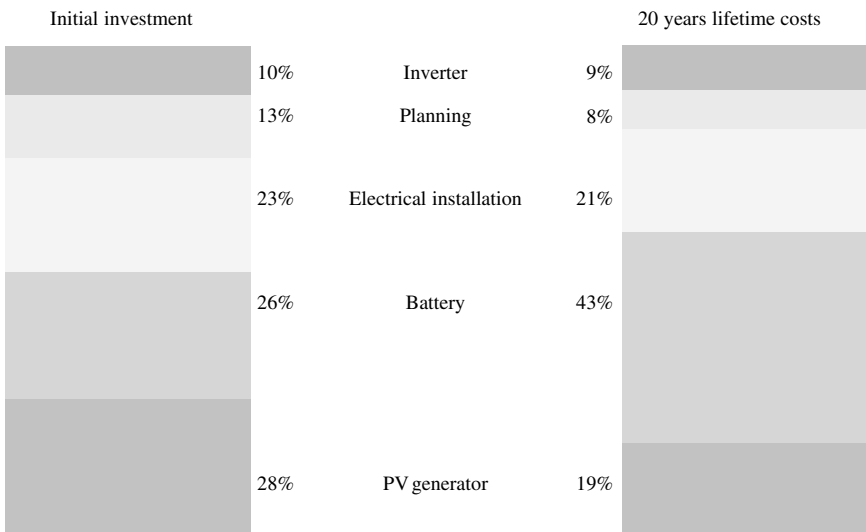


Figure 2.10 Initial versus lifetime costs of small professional autonomous photovoltaic systems – a typical example. System data: PV 1.3 kW_p, battery 35 kWh, battery lifetime 5.4 a, loss of load probability 0.1%, system site Mexico

At present, the main applications of photovoltaics in rural and remote areas are (1) photovoltaic (car-) battery-charging stations where the charged battery is transported to the electricity consumer, (2) photovoltaic solar home systems for the energy supply of electric lights, radios and simple television sets and (3) photovoltaic powered pumping stations for water supply for human requirements and agricultural irrigation.

In particular, the solar home systems have to be highlighted. As might have become clear from the above discussion, they present today in many cases the technical and economic optimal solution for a basic electrification in the areas under discussion. The market volume is in the order of 400 000 systems a year. System prices show increasingly favourable values (Figure 2.11).

The main barriers to a further accelerated introduction of these technologies into practice are non-technological in character. Appropriate financing schemes, social integration, training of engineers and trade and industry structures have to be developed and efficiently integrated into the societies. Photovoltaics may then become one of the main pillars of rural electrification. A market volume of 15 to 30 GW per year is expected in 10 to 20 years [8].

It has already been mentioned that modularity is one of the important characteristics of photovoltaics. In principle, solar home systems may be upgraded step by step. In suitable cases it will be possible to interconnect the individual systems to form PV village power supplies. Besides the social management of such structures, a prerequisite for their widespread applications is the development and industrial production of appropriate power electronics, load management devices and information schemes. For larger installations, hybrid systems (e.g. diesel/photovoltaic) may dominate the market in the near future. It is also conceivable that village power systems may be interconnected by transmission lines or even connected to the main (possibly weak) grids. All these measures increase the complexity and most probably also the cost of such systems. On the other hand, because of technical redundancies and load levelling effects, the performance of such advanced PV-based electricity supply systems could increase considerably.

	Price (US \$)	Price (%)	Lifetime (years)
PV-module (53 W) and support	200	47	>20
Battery (70 Ah)	40	9	4
Battery charge controller	35	8	10
Lamps, wiring, switches	35	8	5
Delivery, installation, retail margins	75	18	-
Duties and taxes	40	10	-
Total	425	100	

Figure 2.11 Cost break down of a typical solar home system

Off-grid PV electricity supply is by no means restricted to the rural areas of developing countries. Mountain lodges, remotely situated farms, holiday houses and so on represent a considerable market for PV energy supply also in industrialised countries. Such installations may be connected to the central grid as well. In these cases photovoltaics serves as a back-up electricity supply in case of line failure or unreliable electricity supply from the utility side.

2.3.1 In Summary

Photovoltaics is an excellently suitable solution for low power electricity supply in rural and remote areas in developing countries. Photovoltaics have a similar but smaller market in industrialised countries as well. In total, one-third of today's world population could benefit from off-grid PV installations. System electronics and storage batteries have to be further developed in order to address the market in an optimal way. Financial engineering, social integration of the new technology, training and the installation of an appropriate trade and industrial infrastructure are the most important prerequisites for a successful worldwide implementation of off-grid PV electricity supplies.

2.4 POWER SUPPLY FOR INDUSTRIAL SYSTEMS AND PRODUCTS – THE PROFESSIONAL LOW POWER DIMENSION

This segment of PV application comprises the electricity supply of consumer products, professional industrial systems and remote low power systems. In this area, photovoltaics substitutes or complements the traditional power supply via batteries or small fossil fuel motor generator sets. The average power demand, especially in the area of consumer products and professional systems, lies generally in the power range of several milliwatts to 100 W. On the other hand, a mass market of billions of units may be envisaged gaining market volumes in the 10-GW range in several decades [8]. The drivers of these markets are strong technological innovations in the field of telecommunication, dispersed electronic intelligence and remote sensors/actuators and so on (Figures 2.12. and 2.13).

Such equipments need small amounts of electric energy for operation and standby. Even if the electric grid is ready-to-hand, wireless and maintenance-free systems are generally preferred by the users. Maintenance-free here means that costly primary batteries with limited energy content can be avoided. In many cases photovoltaics may enter this field of energy supply (1) if the devices are at least temporarily under illumination and (2) if suitable storage devices are applicable. Thus the availability of small and efficient storages (rechargeable batteries, capacitors) is a prerequisite for a widespread application of PV cells in this area.

In this market segment there is a wide range of specific requirements for PV cells. Communication equipment like mobile phones being characterised by low surface area and relatively high energy demand call for high efficiency (e.g. 20%) solar cells; wrist watches on the other hand can be powered by PV cells having only some percentage of efficiency. PV car roofs need aesthetically optimised precision products, while powering a last mile repeater for telecommunication links may be done with small standard PV

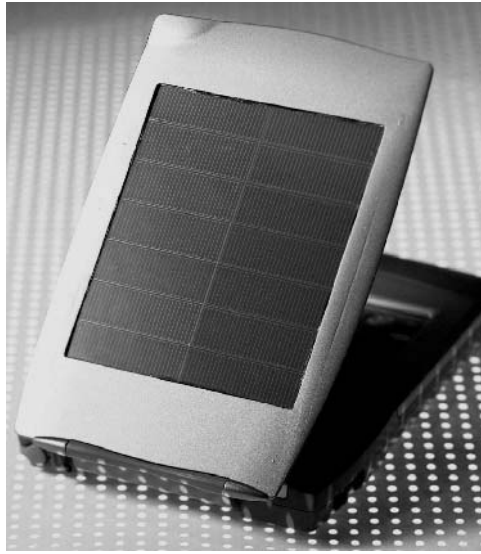


Figure 2.12 Personal digital assistant powered by high efficient silicon solar cells. Module efficiency at one sun $>20\%$; efficiency at $1/100$ sun, 17%



Figure 2.13 Autonomous emergency phone and information system using photovoltaic power supply

modules. The optimal integration of PV cells into the surface of electronic devices may ask for flexible, geometrically tailored or even coloured components.

Especially for indoor applications it is essential to have light-energy converters with high conversion efficiencies at low illumination levels.

These diverse and partly conflicting requirements will result in the development of different types of PV converters, well suited to the individual applications. Dye or organic solar cells may find their first application in such market segments.

2.5 POWER FOR SPACECRAFT AND SATELLITES – THE EXTRATERRESTRIAL DIMENSION OF PHOTOVOLTAICS

The power supply of satellites has been the first professional application of photovoltaics (Vanguard I, 1958). While at the beginning military activities have been in the foreground of space power supply, today commercial activities play an important role as well: powering satellites for telecommunication, remote sensing, navigation and so on.

In these obviously off-grid applications, PV power supplies are more or less without technological competitors. Thus, solar electric systems of this kind would have been

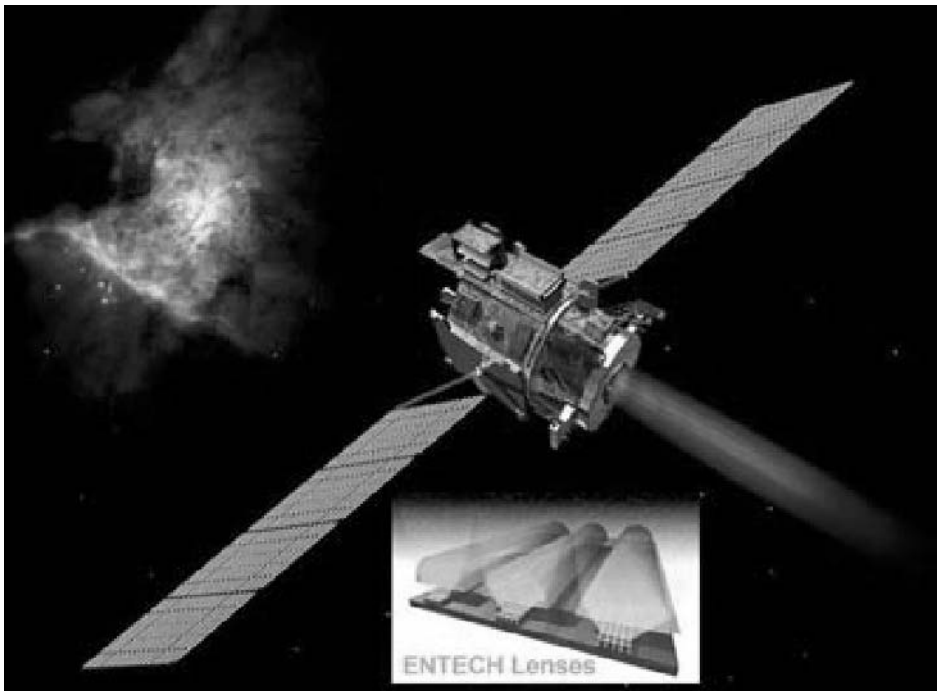


Figure 2.14 Artists view of the “Scarlet Deep Space One Satellite”. The satellite is equipped with triple-junction GaInP/GaAs/Ge photovoltaic cells. For the first time, optical concentration was applied with III/V space cells. Courtesy of NASA/JPL/Caltech

successfully developed even without the terrestrial market addressed above. On the other hand, the parallel (but partly deferred) evolution of space and terrestrial photovoltaics has led to many fruitful and essential cross-stimulations.

Solar modules for space applications (Figure 2.14) have to meet other and mostly more stringent requirements than terrestrial devices such as lowest weight and highest efficiency, extremely high reliability, high resistivity against extraterrestrial particle radiation (high lifetime) and spectral sensitivity that is well matched to the extraterrestrial solar spectrum.

Photovoltaic modules meeting corresponding standards have been realised in a relatively short time span. This success was based on many ingenious inventions and on the fact that cost reduction has not been the most important issue in the first decade of satellite technology. Thus, space photovoltaics became, at least initially, the technological breeder for today's silicon-wafer-based terrestrial solar cell technology.

A similar technology fertilisation might occur again: About one-half of today's space solar cells are already made from GaAs and related compound semiconductors (Figure 2.14). Such solar cells exhibit considerable higher efficiencies and lifetimes than Silicon cells. There is a realistic chance that these space-proven technologies become the basis for a new class of solar cells having light conversion efficiencies in the range of 40 or even 50%. Besides advanced flat-plate solar modules such solar cells, in conjunction with optical concentrators, constitute a strong technological option for future terrestrial large-scale electricity generation.

REFERENCES

1. United Nations Development Programme (UNDP) World Energy Assessment, ISBN 92-1-126126-0, New York (2000).
2. Data Source: Projektgesellschaft Solare Energiesysteme (PSE GmbH), Freiburg, Germany (2002).
3. Scenario for the derivation of CO₂-reduction targets and implementation strategies. Statement of the Germany Advisory Council on Global Change (WBGU) on the occasion of the COP-1 of the UNFCCC in Berlin 1995. Internet: http://www.wbgu.de/wbgu_sn1995_engl.html and IPCC – Intergovernmental Panel on Climate Change, Climate Change 2001: The Scientific Basis. Contribution of Working Group I to the Third Assessment Report of the IPCC, Cambridge University Press, Cambridge, New York (2001).
4. IPCC – Intergovernmental Panel on Climate Change, Climate Change 2001–Synthesis Report. Contribution of Working Groups I, II and III to the Third Assessment Report of the Intergovernmental Panel on Climate Change, Cambridge University Press, Cambridge, New York (2001).
5. Saitoh T, “Restructuring of photovoltaic R&D programs in Japan”, in Sopori B, Ed, *Proc. 11th Workshop on Crystalline Silicon Solar Cell Materials and Processes*, NREL, Estes Park, CO (2001).
6. German Government, *Sol. Energy* **70**, 489–504 (2001).
7. Photovoltaics – Energy for the New Millennium, The National 2000–2004 Photovoltaic Program Plan, DOE/GO-10099-940.
8. Hoffmann W, “PV solar electricity: one among the new millennium industries”, *Proceedings of the 17th European Photovoltaic Solar Energy Conference*, Munich, Germany (2001).

3

The Physics of the Solar Cell

Jeffery L. Gray

Purdue University, West Lafayette, Indiana, USA

3.1 INTRODUCTION

Semiconductor solar cells are fundamentally quite simple devices. Semiconductors have the capacity to absorb light and to deliver a portion of the energy of the absorbed photons to carriers of electrical current – electrons and holes. A semiconductor diode separates and collects the carriers and conducts the generated electrical current preferentially in a specific direction. Thus, a solar cell is simply a semiconductor diode that has been carefully designed and constructed to efficiently absorb and convert light energy from the sun into electrical energy. A simple conventional solar cell structure is depicted in Figure 3.1. Sunlight is incident from the top on the front of the solar cell. A metallic grid forms one of the electrical contacts of the diode and allows light to fall on the semiconductor between the grid lines and thus be absorbed and converted into electrical energy. An antireflective layer between the grid lines increases the amount of light transmitted to the semiconductor. The semiconductor diode is fashioned when an *n*-type semiconductor and a *p*-type semiconductor are brought together to form a metallurgical junction. This is typically achieved through diffusion or implantation of specific impurities (dopants) or via a deposition process. The diode's other electrical contact is formed by a metallic layer on the back of the solar cell.

All electromagnetic radiation, including sunlight, is composed of particles called photons, which carry specific amounts of energy determined by the spectral properties of their source. Photons also exhibit a wavelike character with the wavelength, λ , being related to the photon energy, E_λ , by

$$E_\lambda = \frac{hc}{\lambda} \quad (3.1)$$

where h is Planck's constant and c is the speed of light. Only photons with sufficient energy to create an electron–hole pair, that is, those with energy greater than the semiconductor

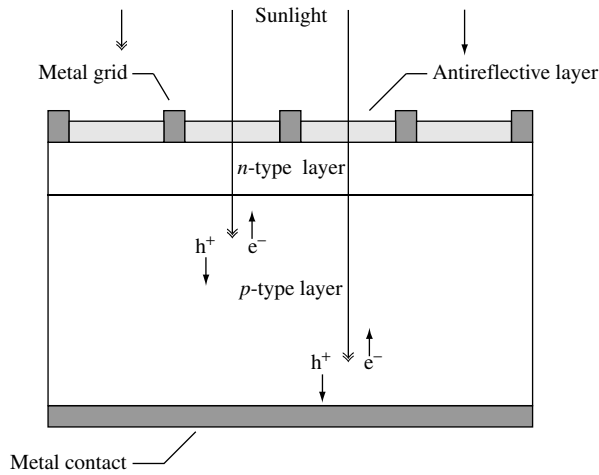


Figure 3.1 A schematic of a simple conventional solar cell. Creation of electron–hole pairs, e^- and h^+ , respectively, is depicted

band gap (E_G), will contribute to the energy conversion process. Thus, the spectral nature of sunlight is an important consideration in the design of efficient solar cells.

The sun has a surface temperature of 5762 K and its radiation spectrum can be approximated by a black-body radiator at that temperature. Emission of radiation from the sun, as with all black-body radiators, is isotropic. However, the Earth's great distance from the sun (approximately 93 million miles) means that only those photons emitted directly in the direction of the Earth contribute to the solar spectrum as observed from Earth. Therefore, for practical purposes, the light falling on the Earth can be thought of as parallel streams of photons. Just above the Earth's atmosphere, the radiation intensity, or Solar Constant, is about 1.353 kW/m^2 [1] and the spectral distribution is referred to as an *air mass zero* (AM0) radiation spectrum. The Air Mass is a measure of how absorption in the atmosphere affects the spectral content and intensity of the solar radiation reaching the Earth's surface. The Air Mass number is given by

$$\text{Air Mass} = \frac{1}{\cos \theta} \quad (3.2)$$

where θ is the angle of incidence ($\theta = 0$ when the sun is directly overhead). The Air Mass number is always greater than or equal to one at the Earth's surface. An easy way to estimate the Air Mass has been given by Green [1] as

$$\text{Air Mass} = \sqrt{1 + (S/H)^2} \quad (3.3)$$

where S is the length of a shadow cast by an object of height H . A widely used standard for comparing solar cell performance is the AM1.5 spectrum normalized to a total power density of 1 kW/m^2 . The spectral content of sunlight at the Earth's surface also has a diffuse (indirect) component owing to scattering and reflection in the atmosphere and surrounding landscape and can account for up to 20% of the light incident on a solar

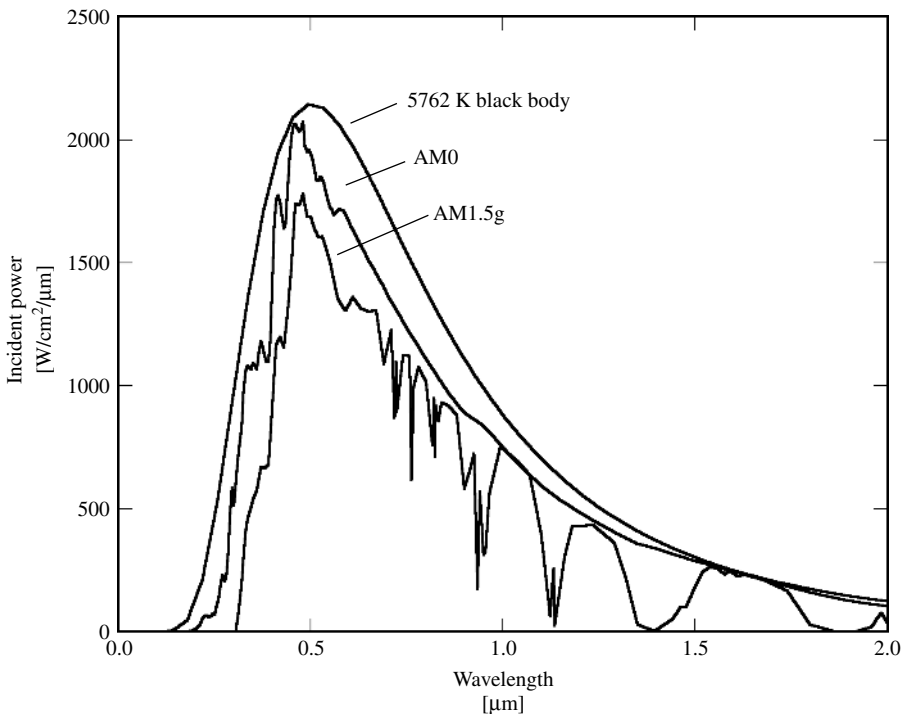


Figure 3.2 The radiation spectrum for a black body at 5762 K, an AM0 spectrum, and an AM1.5 global spectrum

cell. The Air Mass number is therefore further defined by whether or not the measured spectrum includes the diffuse component. An AM1.5g (global) spectrum includes the diffuse component, while an AM1.5d (direct) does not. Black body ($T = 5762$ K), AM0, and AM1.5g radiation spectra are shown in Figure 3.2. The Air Mass and solar radiation are described in more detail in Chapters 16 and 20.

The physical principles underlying the operation of solar cells are the subject of this chapter. First, a brief review of the fundamental properties of semiconductors is given that includes an overview of semiconductor band structure and carrier generation, recombination, and transport. Next, the electrostatic properties of the pn -junction diode are reviewed, followed by a description of the basic operating characteristics of the solar cell, including the derivation (based on the solution of the minority-carrier diffusion equation) of an expression for the current–voltage characteristic of an idealized solar cell. This is used to define the basic solar cell figures of merit, namely, the open-circuit voltage, V_{OC} ; the short-circuit current, I_{SC} ; the fill factor, FF ; the conversion efficiency, η ; and the collection efficiency, η_C . Much of the discussion here centers on how carrier recombination is the primary factor controlling solar cell performance. Finally, some additional topics relevant to solar cell operation, design, and analysis are presented. These include the relationship between band gap and efficiency, the solar cell spectral response, parasitic resistive effects, temperature effects, a brief introduction to some modern cell design concepts, and a short overview of detailed numerical modeling of solar cells.

3.2 FUNDAMENTAL PROPERTIES OF SEMICONDUCTORS

An understanding of the operation of semiconductor solar cells requires familiarity with some basic concepts of solid-state physics. Here, an introduction is provided to the essential concepts needed to examine the physics of solar cells. More complete and rigorous treatments are available from a number of sources [2–6].

Solar cells can be fabricated from a number of semiconductor materials, most commonly silicon (Si) – crystalline, polycrystalline, and amorphous. Solar cells are also fabricated from GaAs, GaInP, Cu(InGa)Se₂, and CdTe, to name but a few. Solar cell materials are chosen largely on the basis of how well their absorption characteristics match the solar spectrum and their cost of fabrication. Silicon has been a common choice due to the fact that its absorption characteristics are a fairly good match to the solar spectrum, and silicon fabrication technology is well developed as a result of its pervasiveness in the semiconductor electronics industry.

3.2.1 Crystal Structure

Electronic grade semiconductors are very pure crystalline materials. Their crystalline nature means that their atoms are aligned in a regular periodic array. This periodicity, coupled with the atomic properties of the component elements, is what gives semiconductors their very useful electronic properties. An abbreviated periodic table of the elements is given in Table 3.1.

Note that silicon is in column IV, meaning that it has four valence electrons, that is, four electrons that can be shared with neighboring atoms to form covalent bonds with those neighbors. In crystalline silicon, the atoms are arranged in a *diamond lattice* (carbon is also a column IV element) with tetrahedral bonding – four bonds from each atom where the angle between any two bonds is 109.5°. Perhaps surprisingly, this arrangement can be represented by two interpenetrating face-centered cubic (*fcc*) unit cells where the second *fcc* unit cell is shifted one-fourth of the distance along the body diagonal of the first *fcc* unit cell. The lattice constant, ℓ , is the length of the edges of the cubic unit cell. The entire lattice can be constructed by stacking these unit cells. A similar arrangement, the *zincblende* lattice, occurs in many binary III–V and II–VI semiconductors such as GaAs (a III–V compound) and CdTe (a II–VI compound). For example, in GaAs, one interpenetrating *fcc* unit cell is composed entirely of Ga atoms and the other entirely of As atoms. Note that the average valency is four for each compound, so that there are four bonds to and from each atom with each covalent bond involving two valence electrons. Some properties of semiconductors are dependent on the orientation of the crystal

Table 3.1 Abbreviated periodic table of the elements

I	II	III	IV	V	VI
		B	C	N	O
		Al	Si	P	S
Cu	Zn	Ga	Ge	As	Se
Ag	Cd	In	Sn	Sb	Te

lattice, and casting the crystal structure in terms of a cubic unit cell makes identifying the orientation easier using Miller indices.

3.2.2 Energy Band Structure

Of more consequence to the physics of solar cells, however, is how the periodic crystalline structure of the semiconductor establishes its electronic properties. An electron moving in a semiconductor material is analogous to a particle confined to a three-dimensional box that has a complex interior structure due primarily to the potential fields surrounding the component atom's nucleus and tightly bound core electrons. The dynamic behavior of the electron can be established from the electron wave function, ψ , which is obtained by solving the time-independent Schrödinger equation

$$\nabla^2\psi + \frac{2m}{\hbar^2}[E - U(\vec{r})]\psi = 0 \quad (3.4)$$

where m is electron mass, \hbar is the reduced Planck constant, E is the energy of the electron, and $U(\vec{r})$ is the periodic potential energy inside the semiconductor. Solving this quantum-mechanical equation is beyond the scope of this work, but suffice it to say that the solution defines the band structure (the allowed electron energies and the relationship between the electron's energy and momentum) of the semiconductor and, amazingly, tells us that the quantum mechanically computed motion of the electron in the crystal is, to a good approximation, like that of an electron in free space if its mass, m , is replaced by an effective mass, m^* , in Newton's law of motion from classical mechanics

$$F = m^*a \quad (3.5)$$

where F is the applied force and a is the acceleration of the electron. A simplified energy band structure is illustrated in Figure 3.3. The allowed electron energies are plotted against the crystal momentum, $p = \hbar k$, where k is the wave vector (represented here as a scalar for simplicity) corresponding to the wave function solutions of the Schrödinger equation. Only the energy bands of immediate interest are shown – energy bands below the valence band are presumed to be fully occupied by electrons and those above the conduction band are presumed to be empty. The electron effective mass is thus defined as

$$m^* \equiv \left[\frac{d^2E}{dp^2} \right]^{-1} = \left[\frac{1}{\hbar^2} \frac{d^2E}{dk^2} \right]^{-1} \quad (3.6)$$

Notice that the effective mass is not constant within each band. In addition, near the top of the valence band, the effective mass is actually negative. Electrons (*) fill the states from bottom to top and the states near the top of the valence band are empty (o) due to some electrons being thermally excited into the conduction band. These empty states can conveniently be regarded as positively charged carriers of current called *holes* with a positive effective mass. It is conceptually much easier to deal with a relatively few number of holes that have a positive effective mass since they will behave like classical positively charged particles. The top of the valence band and the bottom of the conduction band are approximately parabolic in shape and therefore the electron effective mass (m_n^*)

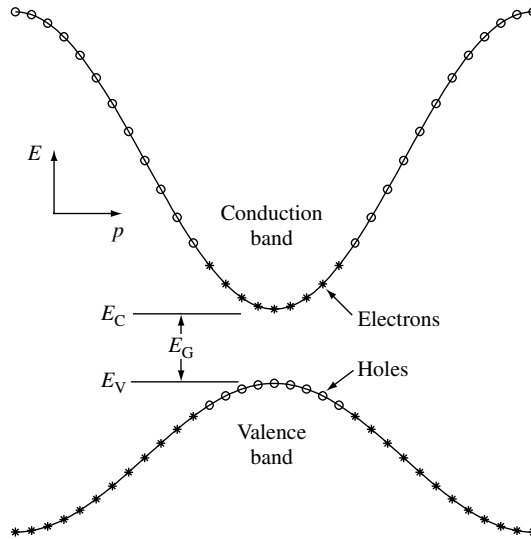


Figure 3.3 A simplified energy band diagram at $T > 0$ K for a direct band gap (E_G) semiconductor. Electrons near the maxima in valence band have been thermally excited to the empty states near the conduction-band minima, leaving behind holes. The excited electrons and remaining holes are the negative and positive mobile charges that give semiconductors their unique transport properties

near the bottom of the conduction band is a constant, as is the hole effective mass (m_p^*) near the top of the valence band. This is a very practical assumption that greatly simplifies the analysis of semiconductors.

When the minimum of the conduction band occurs at the same value of the crystal momentum as the maximum of the valence band, as it does in Figure 3.3, the semiconductor is a *direct band gap* semiconductor. When they do not align, the semiconductor is said to be an *indirect band gap* semiconductor. This is especially important when the absorption of light by a semiconductor is considered later in this chapter.

Even amorphous materials exhibit a similar band structure. Over short distances, the atoms are arranged in a periodic manner and an electron wave function can be defined. The wave functions from these small regions overlap in such a way that a *mobility gap* can be defined with electrons above the mobility gap defining the conduction band and holes below the gap defining the valence band. Unlike crystalline materials, however, there are a large number of localized energy states within the mobility gap (band tails and dangling bonds) that complicate the analysis of devices fabricated from these materials. Amorphous silicon (a-Si) solar cells are discussed in Chapter 12.

3.2.3 Conduction-band and Valence-band Densities of State

Now that the dynamics of the electron motion in a semiconductor has been approximated by a negatively charged particle with mass m_n^* in the conduction band and by a positively charged particle with mass m_p^* in the valence band, it is possible to calculate the density

of states in each band. This again involves solving the time-independent Schrödinger equation for the wave function of a particle in a box, but in this case the box is empty. All the complexities of the periodic potentials of the component atoms have been incorporated into the effective mass. The density of states in the conduction band is given by

$$g_C(E) = \frac{m_n^* \sqrt{2m_n^*(E - E_C)}}{\pi^2 \hbar^3} \text{cm}^{-3} \text{eV}^{-1} \quad (3.7)$$

while the density of states in the valence band is given by

$$g_V(E) = \frac{m_p^* \sqrt{2m_p^*(E_V - E)}}{\pi^2 \hbar^3} \text{cm}^{-3} \text{eV}^{-1} \quad (3.8)$$

3.2.4 Equilibrium Carrier Concentrations

When the semiconductor is in thermal equilibrium (i.e. at a constant temperature with no external injection or generation of carriers), the Fermi function determines the ratio of filled states to available states at each energy and is given by

$$f(E) = \frac{1}{1 + e^{(E - E_F)/kT}} \quad (3.9)$$

where E_F is the Fermi energy, k is Boltzmann's constant, and T is the Kelvin temperature. As seen in Figure 3.4, the Fermi function is a strong function of temperature. At absolute zero, it is a step function and all the states below E_F are filled with electrons and all those above E_F are completely empty. As the temperature increases, thermal excitation will leave some states below E_F empty, and the corresponding number of states above E_F will be filled with the excited electrons.

The equilibrium electron and hole concentrations ($\#/\text{cm}^3$) are therefore

$$n_o = \int_{E_C}^{\infty} g_C(E) f(E) dE = \frac{2N_C}{\sqrt{\pi}} F_{1/2}((E_F - E_C)/kT) \quad (3.10)$$

$$p_o = \int_{-\infty}^{E_V} g_V(E) [1 - f(E)] dE = \frac{2N_V}{\sqrt{\pi}} F_{1/2}((E_V - E_F)/kT) \quad (3.11)$$

where $F_{1/2}(\xi)$ is the Fermi–Dirac integral of order 1/2,

$$F_{1/2}(\xi) = \int_0^{\infty} \frac{\sqrt{\xi'} d\xi'}{1 + e^{\xi' - \xi}} \quad (3.12)$$

The conduction-band and valence-band effective densities of state ($\#/\text{cm}^3$), N_C and N_V , respectively, are given by

$$N_C = 2 \left(\frac{2\pi m_n^* kT}{h^2} \right)^{3/2} \quad (3.13)$$

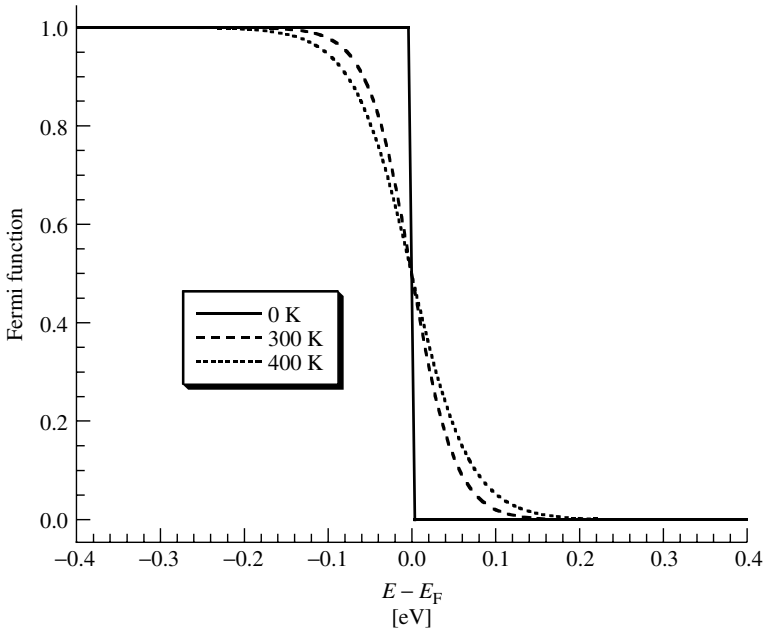


Figure 3.4 The Fermi function at various temperatures

and

$$N_V = 2 \left(\frac{2\pi m_p^* kT}{h^2} \right)^{3/2}. \quad (3.14)$$

When the Fermi energy, E_F , is sufficiently far ($>3kT$) from either bandedge, the carrier concentrations can be approximated (to within 2%) as [7]

$$n_o = N_C e^{(E_F - E_C)/kT} \quad (3.15)$$

and

$$p_o = N_V e^{(E_V - E_F)/kT} \quad (3.16)$$

and the semiconductor is said to be *nondegenerate*. In nondegenerate semiconductors, the product of the equilibrium electron and hole concentrations is independent of the location of the Fermi energy and is just

$$p_o n_o = n_i^2 = N_C N_V e^{(E_V - E_C)/kT} = N_C N_V e^{-E_G/kT}. \quad (3.17)$$

In an undoped (intrinsic) semiconductor in thermal equilibrium, the number of electrons in the conduction band and the number of holes in the valence band are equal; $n_o = p_o = n_i$, where n_i is the intrinsic carrier concentration. The intrinsic carrier concentration can be computed from (3.17), giving

$$n_i = \sqrt{N_C N_V} e^{(E_V - E_C)/2kT} = \sqrt{N_C N_V} e^{-E_G/2kT}. \quad (3.18)$$

The Fermi energy in an intrinsic semiconductor, $E_i = E_F$, is given by

$$E_i = \frac{E_V + E_C}{2} + \frac{kT}{2} \ln \left(\frac{N_V}{N_C} \right) \quad (3.19)$$

which is typically very close to the middle of the band gap. The intrinsic carrier concentration is typically very small compared to the densities of states and typical doping densities ($n_i \approx 10^{10} \text{ cm}^{-3}$ in Si) and intrinsic semiconductors behave very much like insulators; that is, they are not very useful as conductors of electricity.

The number of electrons and holes in their respective bands, and hence the conductivity of the semiconductor, can be controlled through the introduction of specific impurities, or dopants, called *donors* and *acceptors*. For example, when semiconductor silicon is doped with phosphorous, one electron is donated to the conduction band for each atom of phosphorous introduced. From Table 3.1, it can be seen that phosphorous is in column V of the periodic table of elements and thus has five valence electrons. Four of these are used to satisfy the four covalent bonds of the silicon lattice and the fifth is available to fill an empty state in the conduction band. If silicon is doped with boron (valency of three, since it is in column III), each boron atom accepts an electron from the valence band, leaving behind a hole. All impurities introduce additional localized electronic states into the band structure, often within the forbidden band between E_C and E_V , as illustrated in Figure 3.5. If the energy of the state, E_D , introduced by a donor atom is sufficiently close to the conduction bandedge (within a few kT), there will be sufficient thermal energy to allow the extra electron to occupy a state in the conduction band. The donor state will then be positively charged (ionized) and must be considered when analyzing the electrostatics of the situation. Similarly, an acceptor atom will introduce a negatively charged (ionized) state at energy E_A . The controlled introduction of donor and acceptor impurities into a semiconductor allows the creation of the n -type (electrons are the primary source of electrical conduction) and p -type (holes are the primary source of electrical conduction) semiconductors, respectively. This is the basis for the construction of all semiconductor devices, including solar cells. The number of ionized donors and acceptors are given by [7]

$$N_D^+ = \frac{N_D}{1 + g_D e^{(E_F - E_D)/kT}} = \frac{N_D}{1 + e^{(E_F - E'_D)/kT}} \quad (3.20)$$

and

$$N_A^- = \frac{N_A}{1 + g_A e^{(E_A - E_F)/kT}} = \frac{N_A}{1 + e^{(E'_A - E_F)/kT}} \quad (3.21)$$

where g_D and g_A are the donor and acceptor site degeneracy factors. Typically, $g_D = 2$ and $g_A = 4$. These factors are normally combined into the donor and the acceptor energies so that $E'_D = E_D - kT \ln g_D$ and $E'_A = E_A + kT \ln g_A$. Often, the donors and acceptors are assumed to be completely ionized so that $n_o \simeq N_D$ in n -type material and $p_o = N_A$ in p -type material. The Fermi energy can then be written as

$$E_F = E_i + kT \ln \frac{N_D}{n_i} \quad (3.22)$$

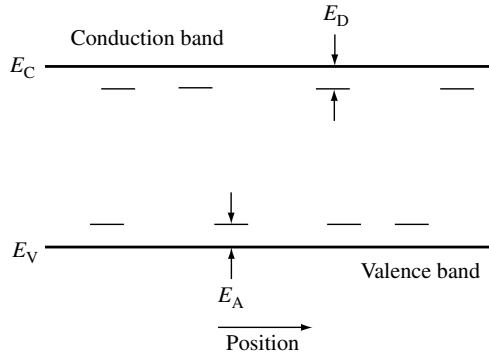


Figure 3.5 Donor and acceptor levels in a semiconductor. The nonuniform spatial distribution of these states reinforces the concept that these are localized states

in n -type material and as

$$E_F = E_i - kT \ln \frac{N_A}{n_i} \quad (3.23)$$

in p -type material.

When a very large concentration of dopants is introduced into the semiconductor, the dopants can no longer be thought of as a minor perturbation to the system. Their effect on the band structure must be considered. Typically, this so-called heavy doping effect manifests itself as a reduction in the band gap, E_G , and thus an increase in the intrinsic carrier concentration, as can be seen from equation (3.18). This band gap narrowing (BGN) [8] is detrimental to solar cell performance and solar cells are typically designed to avoid this effect, though it may be a factor in the heavily doped regions near the solar cell contacts.

3.2.5 Light Absorption

The creation of electron–hole pairs via the absorption of sunlight is fundamental to the operation of solar cells. The excitation of an electron directly from the valence band (which leaves a hole behind) to the conduction band is called *fundamental absorption*. Both the total energy and momentum of all particles involved in the absorption process must be conserved. Since the photon momentum, $p_\lambda = h/\lambda$, is very small compared to the range of the crystal momentum, $p = h/\ell$, the photon absorption process must, for practical purposes, conserve the momentum of the electron.¹ The absorption coefficient for a given photon energy, $h\nu$, is proportional to the probability, P_{12} , of the transition of an electron from the initial state E_1 to the final state E_2 , the density of electrons in the initial state, $g_V(E_1)$, and the density of available final states, and is then summed over

¹ The wavelength of sunlight, λ , is on the order of a micron (10^{-4} cm), while the lattice constant is a few angstroms (10^{-8} cm). Thus, the crystal momentum is several orders of magnitude larger than the photon momentum.

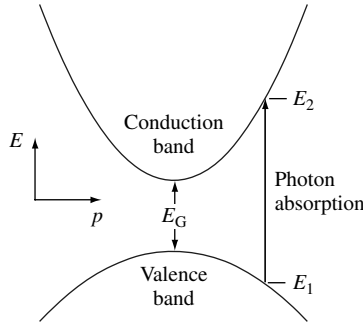


Figure 3.6 Photon absorption in a direct band gap semiconductor for an incident photon with energy $h\nu = E_2 - E_1 > E_G$

all possible transitions between states where $E_2 - E_1 = h\nu$ [9],

$$\alpha(h\nu) \propto \sum P_{12} g_v(E_1) g_c(E_2), \quad (3.24)$$

assuming that all the valence-band states are full and all the conduction-band states are empty. Absorption results in creation of an electron-hole pair since a free electron is excited to the conduction band leaving a free hole in the valence band.

In direct band gap semiconductors, such as GaAs, GaInP, CdTe, and Cu(InGa)Se₂, the basic photon absorption process is illustrated in Figure 3.6. Both energy and momentum must be conserved in the transition. Every initial electron state with energy E_1 and crystal momentum p_1 in the valence band is associated with a final state in the conduction band at energy E_2 and crystal momentum p_2 . Since the electron momentum is conserved, the crystal momentum of the final state is the same as the initial state, $p_1 \approx p_2 = p$.

Conservation of energy dictates that the energy of the absorbed photon is

$$h\nu = E_2 - E_1 \quad (3.25)$$

Since we have assumed parabolic bands,

$$E_V - E_1 = \frac{p^2}{2m_p^*} \quad (3.26)$$

and

$$E_2 - E_C = \frac{p^2}{2m_n^*} \quad (3.27)$$

Combining equations (3.25), (3.26), and (3.27) yields

$$h\nu - E_G = \frac{p^2}{2} \left(\frac{1}{m_n^*} + \frac{1}{m_p^*} \right) \quad (3.28)$$

and the absorption coefficient for direct transitions is [9]

$$\alpha(h\nu) \approx A^*(h\nu - E_G)^{1/2}, \quad (3.29)$$

where A^* is a constant. In some semiconductor materials, quantum selection rules do not allow transitions at $p = 0$ but allow them for $p \neq 0$. In such cases [9]

$$\alpha(h\nu) \approx \frac{B^*}{h\nu}(h\nu - E_G)^{3/2}, \quad (3.30)$$

where B^* is a constant.

In indirect band gap semiconductors like Si and Ge, where the valence-band maximum occurs at a different crystal momentum than the conduction-band minimum, conservation of electron momentum necessitates that the photon absorption process involve an additional particle. Phonons, the particle representation of lattice vibrations in the semiconductor, are suited to this process because they are low-energy particles with relatively high momentum. This is illustrated in Figure 3.7. Notice that light absorption is facilitated by either phonon absorption or phonon emission. The absorption coefficient, when there is phonon absorption, is given by

$$\alpha_a(h\nu) = \frac{A(h\nu - E_G + E_{ph})^2}{e^{E_{ph}/kT} - 1} \quad (3.31)$$

and by

$$\alpha_e(h\nu) = \frac{A(h\nu - E_G - E_{ph})^2}{1 - e^{-E_{ph}/kT}} \quad (3.32)$$

when a phonon is emitted [9]. Because both processes are possible,

$$\alpha(h\nu) = \alpha_a(h\nu) + \alpha_e(h\nu). \quad (3.33)$$

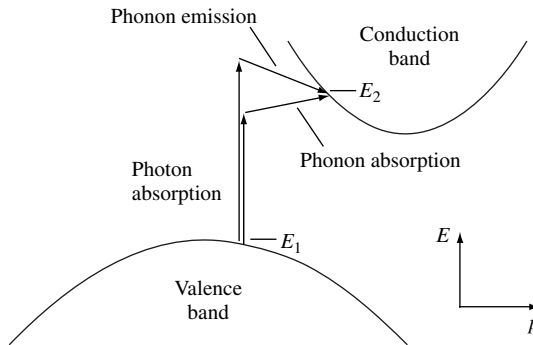


Figure 3.7 Photon absorption in an indirect band gap semiconductor for a photon with energy $h\nu < E_2 - E_1$ and a photon with energy $h\nu > E_2 - E_1$. Energy and momentum in each case are conserved by the absorption and emission of a phonon, respectively

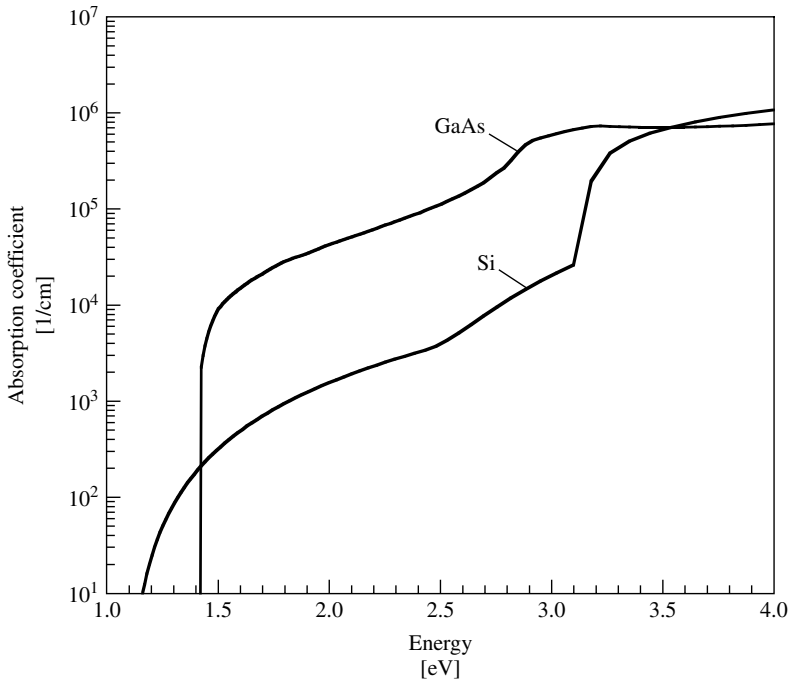


Figure 3.8 Absorption coefficient as a function of photon energy for Si (indirect band gap) and GaAs (direct band gap) at 300 K. Their band gaps are 1.12 and 1.4 eV, respectively

Since both a phonon and an electron are needed to make the indirect gap absorption process possible, the absorption coefficient depends not only on the density of full initial electron states and empty final electron states but also on the availability of phonons (both emitted and absorbed) with the required momentum. Thus, compared to direct transitions, the absorption coefficient for indirect transitions is relatively small. As a result, light penetrates more deeply into indirect band gap semiconductors than direct band gap semiconductors. This is illustrated in Figure 3.8 for Si, an indirect band gap semiconductor, and GaAs, a direct band gap semiconductor. Similar spectra are shown for other semiconductors elsewhere in this handbook.

In both direct band gap and indirect band gap materials, a number of photon absorption processes are involved, though the mechanisms described above are the dominant ones. A direct transition, without phonon assistance, is possible in indirect band gap materials if the photon energy is high enough (as seen in Figure 3.8 for Si at about 3.3 eV). Conversely, in direct band gap materials, phonon-assisted absorption is also a possibility. Other mechanisms may also play a role in defining the absorption process in semiconductors. These include absorption in the presence of an electric field (the Franz–Keldysh effect), absorption aided by localized states in the forbidden gap, and degeneracy effects when a significant number of states in the conduction band are not empty and/or when a significant number of state in the valence band are not full, as can happen in heavily doped materials (BGN) and under high-level injection (the Burstein–Moss shift). The net absorption coefficient is then the sum of the absorption coefficients due to all absorption

processes or

$$\alpha(h\nu) = \sum_i \alpha_i(h\nu). \quad (3.34)$$

In practice, measured absorption coefficients or empirical expressions for the absorption coefficient are used in analysis and modeling. The rate of creation of electron–hole pairs (# of electron–hole pairs per cm^3 per second) as a function of position within a solar cell is

$$G(x) = (1 - s) \int_{\lambda} (1 - r(\lambda)) f(\lambda) \alpha(\lambda) e^{-\alpha x} d\lambda \quad (3.35)$$

where s is the grid-shadowing factor, $r(\lambda)$ is the reflectance, $\alpha(\lambda)$ is the absorption coefficient, $f(\lambda)$ is the incident photon flux (number of photons incident per unit area per second per wavelength), and the sunlight is assumed to be incident at $x = 0$. Here, the absorption coefficient has been cast in terms of the light's wavelength through the relationship $h\nu = hc/\lambda$. The photon flux, $f(\lambda)$, is obtained by dividing the incident power density at each wavelength by the photon energy.

Free-carrier absorption, in which electrons in the conduction band absorb the energy of a photon and move to an empty state higher in the conduction band (correspondingly for holes in the valence band), is typically only significant for photons with $E < E_G$ since the free-carrier absorption coefficient increases with increasing wavelength,

$$\alpha_{fc} \propto \lambda^\gamma \quad (3.36)$$

where $1.5 < \gamma < 3.5$ [9]. Thus, in single-junction solar cells, it does not affect the creation of electron–hole pairs and can be ignored (although free-carrier absorption can be exploited to probe the excess carrier concentrations in solar cells for the purpose of determining recombination parameters [10]). However, free-carrier absorption is a consideration in tandem solar cell systems in which a wide band gap (E_{G1}) solar cell is stacked on top of a solar cell of smaller band gap ($E_{G2} < E_{G1}$). Photons with energy too low to be absorbed in the top cell ($h\nu < E_{G1}$) will be transmitted to the bottom cell and be absorbed there (if $h\nu > E_{G2}$). Of course, more solar cells can be stacked as long as $E_{G1} > E_{G2} > E_{G3} \dots$, and so on. The number of photons transmitted to the next cell in the stack will be reduced by whatever amount of free-carrier absorption occurs. Tandem cells are discussed more completely in Chapters 9 and 12.

3.2.6 Recombination

When a semiconductor is taken out of thermal equilibrium, for instance by illumination and/or injection of current, the concentrations of electrons (n) and holes (p) tend to relax back toward their equilibrium values through a process called *recombination* in which an electron falls from the conduction band to the valence band, thereby eliminating a valence-band hole. There are several recombination mechanisms important to the operation of solar cells – recombination through traps (defects) in the forbidden gap, radiative (band-to-band) recombination, and Auger recombination – that will be discussed here. These three processes are illustrated in Figure 3.9.

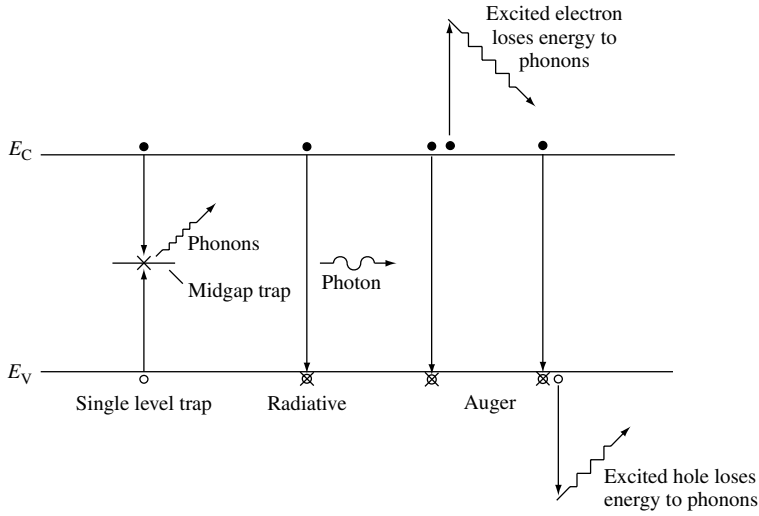


Figure 3.9 Recombination processes in semiconductors

The net recombination rate per unit volume per second through a single level trap (SLT) located at energy $E = E_T$ within the forbidden gap, also commonly referred to as *Shockley–Read–Hall recombination*, is given by [11]

$$R_{SLT} = \frac{pn - n_i^2}{\tau_{SLT,n}(p + n_1 e^{(E_i - E_T)/kT}) + \tau_{SLT,p}(n + n_1 e^{(E_T - E_i)/kT})} \quad (3.37)$$

where the carrier lifetimes are given by

$$\tau_{SLT} = \frac{1}{\sigma v_{th} N_T} \quad (3.38)$$

where σ is the capture cross section, v_{th} is the thermal velocity of the carriers, and N_T is the concentration of traps. The capture cross section can be thought of as the size of the target present to a carrier traveling through the semiconductor at velocity v_{th} . Small lifetimes correspond to high rates of recombination. If a trap presents a large target to the carrier, the recombination rate will be high (low carrier lifetime). When the velocity of the carrier is high, it has more opportunity within a given time period to encounter a trap and the carrier lifetime is low. Finally, the probability of interaction with a trap increases as the concentration of traps increases and the carrier lifetime is therefore inversely proportional to the trap concentration.

Some reasonable assumptions allow equation (3.37) to be simplified. If the material is p -type ($p \approx p_o \gg n_o$), in low injection ($n_o \leq n \ll p_o$), and the trap energy is near the middle of the forbidden gap ($E_T \approx E_i$), the recombination rate can be written as

$$R_{SLT} \approx \frac{n - n_o}{\tau_{SLT,n}} \quad (3.39)$$

Notice that the recombination rate is solely dependent on the minority carrier (also called the limiting carrier). This is reasonable since there are far fewer minority carriers than majority carriers and one of each is necessary for there to be recombination.

If high-injection conditions prevail ($p \approx n \gg p_o, n_o$),

$$R_{\text{SLT}} \approx \frac{n}{\tau_{\text{SLT},p} + \tau_{\text{SLT},n}} \approx \frac{p}{\tau_{\text{SLT},p} + \tau_{\text{SLT},n}}. \quad (3.40)$$

In this case, the effective recombination lifetime is the sum of the two carrier lifetimes. While the recombination rate is high due to the large number of excess holes and electrons, the carrier lifetime is actually longer than in the case of low injection. This can be of significance in the base region of solar cells, especially concentrator cells (solar cells illuminated with concentrated sunlight), since the base is the least doped layer.

Radiative (band-to-band) recombination is simply the inverse of the optical generation process and is much more efficient in direct band gap semiconductors than in indirect band gap semiconductors. When radiative recombination occurs, the energy of the electron is given to an emitted photon – this is how semiconductor lasers and light emitting diodes (LEDs) operate. In an indirect band gap material, some of that energy is shared with a phonon. The net recombination rate due to radiative processes is given as

$$R_\lambda = B(pn - n_i^2). \quad (3.41)$$

If we have an n -type ($n \approx n_o \gg p_o$) semiconductor in low injection ($p_o \leq p \ll n_o$), the net radiative recombination rate can be written in terms of an effective lifetime, $\tau_{\lambda,p}$,

$$R_\lambda \approx \frac{p - p_o}{\tau_{\lambda,p}} \quad (3.42)$$

where

$$\tau_{\lambda,p} = \frac{1}{n_o B}. \quad (3.43)$$

A similar expression can be written for p -type semiconductors.

Auger recombination is somewhat similar to radiative recombination, except that the energy of transition is given to another carrier (in either the conduction band or the valence band), as shown in Figure 3.9. This electron (or hole) then relaxes thermally (releasing its excess energy and momentum to phonons). Just as radiative recombination is the inverse process to optical absorption, Auger recombination is the inverse process to *impact ionization*, where an energetic electron collides with a crystal atom, breaking the bond and creating an electron–hole pair. The net recombination rate due to Auger processes is

$$R_{\text{Auger}} = (\Lambda_n n + \Lambda_p p)(pn - n_i^2) \quad (3.44)$$

In an n -type material in low injection (and assuming Λ_n and Λ_p are of comparable magnitudes), the net Auger recombination rate becomes

$$R_{\text{Auger}} \approx \frac{p - p_o}{\tau_{\text{Auger},p}} \quad (3.45)$$

with

$$\tau_{\text{Auger},p} = \frac{1}{\Lambda_n n_o^2}. \quad (3.46)$$

A similar expression can be derived for minority electron lifetime in p -type material.

Each of these recombination processes occurs in parallel and there can be multiple and/or distributed traps² in the forbidden gap; thus the total recombination rate is the sum of rates due to each process

$$R = \left[\sum_{\text{traps } i} R_{\text{SLT},i} \right] + R_\lambda + R_{\text{Auger}}. \quad (3.47)$$

An effective minority-carrier lifetime for a doped material in low-level injection is given as

$$\frac{1}{\tau} = \left[\sum_{\text{traps } i} \frac{1}{\tau_{\text{SLT},i}} \right] + \frac{1}{\tau_\lambda} + \frac{1}{\tau_{\text{Auger}}}. \quad (3.48)$$

The distribution of traps in the energy gap for specific materials is given in other chapters.

Interfaces between two dissimilar materials, such as, those that occur at the front surface of a solar cell, have a high concentration defect due to the abrupt termination of the crystal lattice. These manifest themselves as a continuum of traps within the forbidden gap at the surface; electrons and holes can recombine through them just as with bulk traps. This is illustrated in Figure 3.10. Rather than giving a recombination rate per unit volume per second, surface traps give a recombination rate per unit area per second. A general expression for surface recombination is [11]

$$R_S = \int_{E_V}^{E_C} \frac{pn - n_i^2}{(p + n_i e^{(E_i - E_i)/kT})/s_n + (n + n_i e^{(E_i - E_i)/kT})/s_p} D_\Pi(E_t) dE_t \quad (3.49)$$

where E_t is the trap energy, $D_\Pi(E_t)$ is the surface state concentration (the concentration of traps is probably dependent on the trap energy), and s_n and s_p are surface recombination velocities, analogous to the carrier lifetimes for bulk traps. The surface recombination rate is generally written, for simplicity, as [11]

$$R_S = S_p(p - p_o) \quad (3.50)$$

in n -type material and as

$$R_S = S_n(n - n_o) \quad (3.51)$$

in p -type material. S_p and S_n are effective surface recombination velocities. It should be mentioned that these effective recombination velocities are not necessarily constants, though they are usually treated as such.

² It is unlikely that more than one trap will be involved in a single recombination event since the traps are spatially separated.

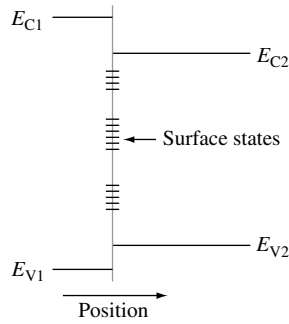


Figure 3.10 Illustration of surface states at a semiconductor surface or interface between dissimilar materials such as two different semiconductors (heterojunction) or a metal and a semiconductor (Schottky contact)

3.2.7 Carrier Transport

As has already been established, electrons and holes in a semiconductor behave much like a free particle of the same electronic charge with effective masses of m_n^* and m_p^* , respectively. Thus, they are subject to the classical processes of drift and diffusion. Drift is a charged particle's response to an applied electric field. When an electric field is applied across a uniformly doped semiconductor, the bands bend upward in the direction of the applied electric field. Electrons in the conduction band, being negatively charged, move in the opposite direction of the applied field and holes in the valence band, being positively charged, move in the same direction of the applied field (Figure 3.11) – in other words, electrons *sink* and holes *float*. This is a useful conceptual tool for analyzing the motion of holes and electrons in semiconductor devices. With nothing to impede their motion, the holes and electrons would continue to accelerate without bound. However, the semiconductor crystal is full of objects with which the carriers collide and are scattered. These objects include the component atoms of the crystal, dopant ions, crystal defects, and even other electrons and holes. On a microscopic scale, their motion is much like that of a ball in pinball machine, the carriers are constantly bouncing (scattering) off objects in the crystal, but generally moving in the direction prescribed by the applied electric field, $\vec{E} = -\nabla\phi$, where ϕ is the electrostatic potential. The net effect is that the carriers appear to move, on a macroscopic scale, at a constant velocity, v_d , the drift velocity. The drift velocity is directly proportional to the electric field

$$|\vec{v}_d| = |\mu\vec{E}| = |\mu\nabla\phi| \quad (3.52)$$

where μ is the carrier mobility. The carrier mobility is generally independent of the electric field strength unless the field is very strong, a situation not typically encountered in solar cells. The drift current densities for holes and electrons can be written as

$$\vec{J}_p^{\text{drift}} = qp\vec{v}_{d,p} = q\mu_p p\vec{E} = -q\mu_p p\nabla\phi \quad (3.53)$$

and

$$\vec{J}_n^{\text{drift}} = -qn\vec{v}_{d,n} = q\mu_n n\vec{E} = -q\mu_n n\nabla\phi. \quad (3.54)$$

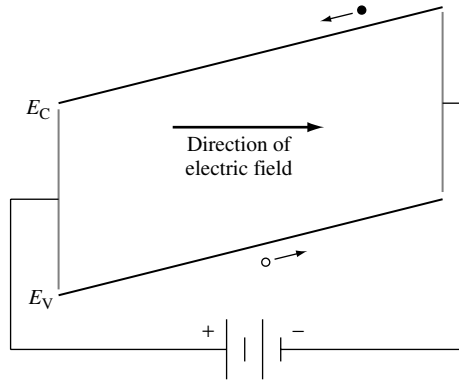


Figure 3.11 Illustration of the concept of drift in a semiconductor. Note that electrons and holes move in opposite directions. The electric field can be created by the internal built-in potential of the junction or by an externally applied bias voltage

The most significant scattering mechanisms in solar cells are lattice (phonon) and ionized impurity scattering. These component mobilities can be written as

$$\mu_L = C_L T^{-3/2} \quad (3.55)$$

for lattice scattering and as

$$\mu_I = \frac{C_I T^{3/2}}{N_D^+ + N_A^-} \quad (3.56)$$

for ionized impurity scattering. These can then be combined using Mathiessen's rule to give the carrier mobility [12]

$$\frac{1}{\mu} = \frac{1}{\mu_L} + \frac{1}{\mu_I}. \quad (3.57)$$

This is a first-order approximation that neglects the velocity dependencies of the scattering mechanisms. These two types of mobility can be distinguished experimentally by their different dependencies on temperature and doping. A better approximation is [12]

$$\mu = \mu_L \left[1 + \left(\frac{6\mu_L}{\mu_I} \right) \left(\text{Ci} \left(\frac{6\mu_L}{\mu_I} \right) \cos \left(\frac{6\mu_L}{\mu_I} \right) + \left[\text{Si} \left(\frac{6\mu_L}{\mu_I} \right) - \frac{\pi}{2} \right] \sin \left(\frac{6\mu_L}{\mu_I} \right) \right) \right], \quad (3.58)$$

where Ci and Si (not to be confused with the abbreviation for silicon) are the cosine and sine integrals, respectively.

When modeling solar cells, it is more convenient to use measured data or empirical formulas. Carrier mobilities in Si at 300 K are well approximated by [12]

$$\mu_n = 92 + \frac{1268}{1 + \left(\frac{N_D^+ + N_A^-}{1.3 \times 10^{17}} \right)^{0.91}} \text{cm}^2/\text{V}\cdot\text{s} \quad (3.59)$$

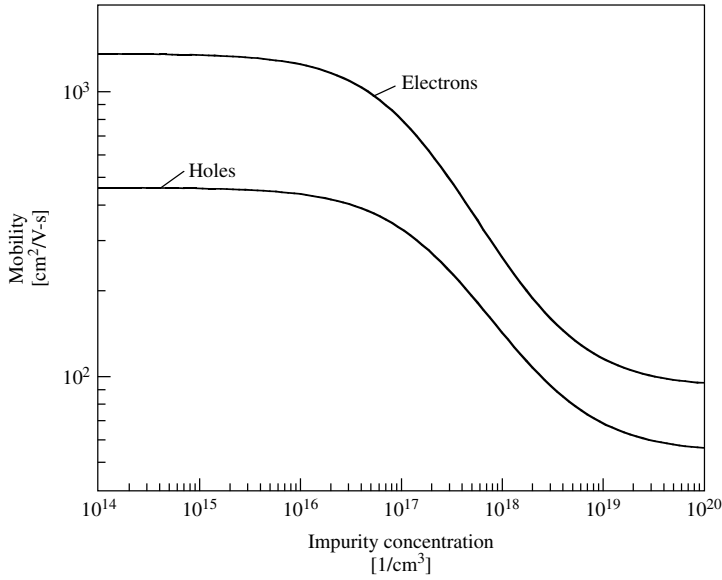


Figure 3.12 Electron and hole mobilities in silicon for $T = 300$ K

$$\mu_p = 54.3 + \frac{406.9}{1 + \left(\frac{N_D^+ + N_A^-}{2.35 \times 10^{17}} \right)^{0.88}} \text{cm}^2/\text{V-s} \quad (3.60)$$

and are plotted in Figure 3.12. At low impurity levels, the mobility is governed by intrinsic lattice scattering, while at high levels the mobility is governed by ionized impurity scattering.

Electrons and holes in semiconductors tend, as a result of their random thermal motion, to move (diffuse) from regions of high concentration to regions of low concentration. Much like how the air in a balloon is distributed evenly within the volume of the balloon, carriers, in the absence of any external forces, will also tend to distribute themselves evenly. This process is called *diffusion* and the diffusion current densities are given by

$$\vec{J}_p^{\text{diff}} = -q D_p \nabla p \quad (3.61)$$

$$\vec{J}_n^{\text{diff}} = q D_n \nabla n \quad (3.62)$$

where D_p and D_n are the hole and electron diffusion coefficients, respectively. Note that they are driven by the gradient of the carrier densities.

In thermal equilibrium, there can be no net hole current and no net electron current – in other words, the drift and diffusion currents must exactly balance. In nondegenerate materials, this leads to the Einstein relationship

$$\frac{D}{\mu} = \frac{kT}{q} \quad (3.63)$$

and allows the diffusion coefficient to be directly computed from the mobility. Generalized forms of the Einstein relationship, valid for degenerate materials, are

$$\frac{D_n}{\mu_n} = \frac{1}{q} n \left[\frac{dn}{dE_F} \right]^{-1} \quad (3.64)$$

and

$$\frac{D_p}{\mu_p} = \frac{-1}{q} p \left[\frac{dp}{dE_F} \right]^{-1}. \quad (3.65)$$

The diffusion coefficient actually increases when degeneracy effects come into play.

The total hole and electron currents (vector quantities) are the sum of their drift and diffusion components

$$\vec{J}_p = \vec{J}_p^{\text{drift}} + \vec{J}_p^{\text{diff}} = q\mu_p p \vec{E} - qD_p \nabla p = -q\mu_p p \nabla \phi - qD_p \nabla p \quad (3.66)$$

$$\vec{J}_n = \vec{J}_n^{\text{drift}} + \vec{J}_n^{\text{diff}} = q\mu_n n \vec{E} + qD_n \nabla n = -q\mu_n n \nabla \phi + qD_n \nabla n \quad (3.67)$$

The total current is then

$$\vec{J} = \vec{J}_p + \vec{J}_n + \vec{J}_{\text{disp}} \quad (3.68)$$

where \vec{J}_{disp} is the *displacement current* given by

$$\vec{J}_{\text{disp}} = \frac{\partial \vec{D}}{\partial t}. \quad (3.69)$$

$\vec{D} = \varepsilon \vec{E}$ is the dielectric displacement field, where ε is the electric permittivity of the semiconductor. The displacement current is typically neglected in solar cells since they are static (dc) devices.

3.2.8 Semiconductor Equations

The operation of most semiconductor devices, including solar cells, can be described by the so-called semiconductor device equations, first derived by Van Roosbroeck in 1950 [13]. A generalized form of these equations is given here.

$$\nabla \cdot \varepsilon \vec{E} = q(p - n + N) \quad (3.70)$$

This is a form of Poisson's equation, where N is the net charge due to dopants and other trapped charges. The hole and electron continuity equations are

$$\nabla \cdot \vec{J}_p = q \left(G - R_p - \frac{\partial p}{\partial t} \right) \quad (3.71)$$

$$\nabla \cdot \vec{J}_n = q \left(R_n - G + \frac{\partial n}{\partial t} \right) \quad (3.72)$$

where G is the optical generation rate of electron–hole pairs. Thermal generation is included in R_p and R_n . The hole and electron current densities are given by

$$\vec{J}_p = -q\mu_p p \nabla(\phi - \phi_p) - kT\mu_p \nabla p \quad (3.73)$$

and

$$\vec{J}_n = -q\mu_n n \nabla(\phi + \phi_n) + kT\mu_n \nabla n. \quad (3.74)$$

Two new terms, ϕ_p and ϕ_n , have been introduced here. These are the so-called band parameters that account for degeneracy and a spatially varying band gap and electron affinity [14]. These terms were ignored in the preceding discussion and can usually be ignored in nondegenerate homostructure solar cells.

The intent here is to derive an analytic expression for the current–voltage characteristic of a simple solar cell, and so some simplifications are in order. It should be noted, however, that a complete description of the operation of solar cells can be obtained by solving the complete set of coupled partial differential equations, equations (3.70) through (3.74). The numerical solution of these equations is addressed later in this chapter.

3.2.9 Minority-carrier Diffusion Equation

In a uniformly doped semiconductor, the band gap and electric permittivity are independent of position. Since the doping is uniform, the carrier mobilities and diffusion coefficients are also independent of position. As we are mainly interested in the steady state operation of the solar cell, the semiconductor equations reduce to

$$\frac{d\vec{E}}{dx} = \frac{q}{\varepsilon}(p - n + N_D - N_A) \quad (3.75)$$

$$q\mu_p \frac{d}{dx}(p\vec{E}) - qD_p \frac{d^2 p}{dx^2} = q(G - R) \quad (3.76)$$

and

$$q\mu_n \frac{d}{dx}(n\vec{E}) + qD_n \frac{d^2 n}{dx^2} = q(R - G) \quad (3.77)$$

In regions sufficiently far from the pn -junction of the solar cell (quasi-neutral regions), the electric field is very small. When considering the minority carrier (holes in the n -type material and electrons in the p -type material) and low-level injection ($\Delta p = \Delta n \ll N_D, N_A$), the drift current can be neglected with respect to the diffusion current. Under low-level injection, R simplifies to

$$R = \frac{n_p - n_{p0}}{\tau_n} = \frac{\Delta n_p}{\tau_n} \quad (3.78)$$

in the p -type region and to

$$R = \frac{p_n - p_{n0}}{\tau_p} = \frac{\Delta p_n}{\tau_p} \quad (3.79)$$

in the n -type region. Δp_N and Δn_P are the excess minority-carrier concentrations. The minority-carrier lifetimes, τ_n and τ_p , are given by equation (3.48). For clarity, the capitalized subscripts, “ P ” and “ N ”, are used to indicate quantities in p -type and n -type regions, respectively, when it may not be otherwise apparent. Lower-case subscripts, “ p ” and “ n ”, refer to quantities associated with minority holes and electrons, respectively. Equations (3.76) and (3.77) thus each reduce to what is commonly referred to as the *minority-carrier diffusion equation*. It can be written as

$$D_p \frac{d^2 \Delta p_N}{dx^2} - \frac{\Delta p_N}{\tau_p} = -G(x) \quad (3.80)$$

in n -type material and as

$$D_n \frac{d^2 \Delta n_P}{dx^2} - \frac{\Delta n_P}{\tau_n} = -G(x) \quad (3.81)$$

in p -type material. For example, Δn_P is the minority electron concentration in the p -type material. The minority-carrier diffusion equation is often used to analyze the operation of semiconductor devices, including solar cells.

3.3 PN-JUNCTION DIODE ELECTROSTATICS

Where an n -type semiconductor comes into contact with a p -type semiconductor, a pn -junction is formed. In thermal equilibrium there is no net current flow and by definition the Fermi energy must be independent of position. Since there is a concentration difference of holes and electrons between the two types of semiconductors, holes diffuse from the p -type region into the n -type region and, similarly, electrons from the n -type material diffuse into the p -type region. As the carriers diffuse, the charged impurities (ionized acceptors in the p -type material and ionized donors in the n -type material) are uncovered – that is, no longer screened by the majority carrier. As these impurity charges are uncovered, an electric field (or electrostatic potential difference) is produced, which limits the diffusion of the holes and electrons. In thermal equilibrium, the diffusion and drift currents for each carrier type exactly balance, so there is no net current flow. The transition region between the n -type and the p -type semiconductors is called the *space-charge region*. It is also often called the *depletion region*, since it is effectively depleted of both holes and electrons. Assuming that the p -type and the n -type regions are sufficiently thick, the regions on either side of the depletion region are essentially charge-neutral (often termed *quasi-neutral*). The electrostatic potential difference resulting from the junction formation is called the *built-in voltage*, V_{bi} . It arises from the electric field created by the exposure of the positive and the negative space charge in the depletion region.

The electrostatics of this situation (assuming a single acceptor and a single donor level) are governed by Poisson’s equation

$$\nabla^2 \phi = \frac{q}{\epsilon} (n_o - p_o + N_A^- - N_D^+) \quad (3.82)$$

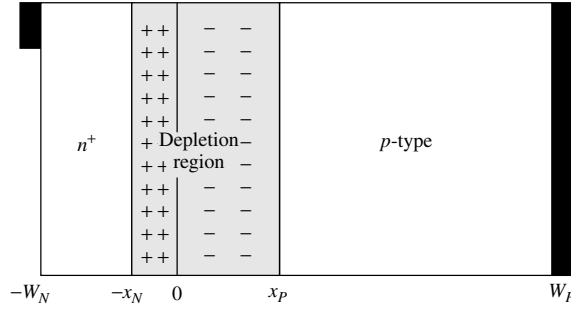


Figure 3.13 Simple solar cell structure used to analyze the operation of a solar cell. Free carriers have diffused across the junction ($x = 0$) leaving a space-charge or depletion region practically devoid of any free or mobile charges. The fixed charges in the depletion region are due to ionized donors on the n -side and ionized acceptors on the p -side

where ϕ is the electrostatic potential, q is magnitude of the electron charge, ε is the electric permittivity of the semiconductor, p_o is the equilibrium hole concentration, n_o is the equilibrium electron concentration, N_A^- is the ionized acceptor concentration, and N_D^+ is the ionized donor concentration. Equation 3.82 is a restatement of equation 3.70 for the given conditions.

This equation is easily solved numerically; however, an approximate analytic solution for an abrupt pn -junction can be obtained that lends physical insight into the formation of the space-charge region. Figure 3.13 depicts a simple one-dimensional (1D) pn -junction solar cell (diode), with the metallurgical junction at $x = 0$, which is uniformly doped N_D on the n -type side and N_A on the p -type side. For simplicity, it is assumed that the each side is nondegenerately doped and that the dopants are fully ionized.

Within the depletion region, defined by $-x_N < x < x_P$, it can be assumed that p_o and n_o are both negligible compared to $|N_A - N_D|$ so that equation (3.82) can be simplified to

$$\begin{aligned}\nabla^2\phi &= -\frac{q}{\varepsilon}N_D, & \text{for } -x_N < x < 0 & \text{ and} \\ \nabla^2\phi &= \frac{q}{\varepsilon}N_A, & \text{for } 0 < x < x_P\end{aligned}\quad (3.83)$$

Outside the depletion region, charge neutrality is assumed and

$$\nabla^2\phi = 0 \quad \text{for } x \leq -x_N \quad \text{and} \quad x \geq x_P. \quad (3.84)$$

This is commonly referred to as the *depletion approximation*. The regions on either side of the depletion regions are the quasi-neutral regions.

The electrostatic potential difference across the junction is the built-in voltage, V_{bi} , and can be obtained by integrating the electric field, $\vec{E} = -\nabla\phi$.

$$\int_{-x_N}^{x_P} \vec{E} dx = - \int_{-x_N}^{x_P} \frac{d\phi}{dx} dx = - \int_{V(-x_N)}^{V(x_P)} d\phi = \phi(-x_N) - \phi(x_P) = V_{bi} \quad (3.85)$$

Solving equations (3.83) and (3.84) and defining $\phi(x_p) = 0$, gives

$$\phi(x) = \begin{cases} V_{bi}, & x \leq -x_N \\ V_{bi} - \frac{qN_D}{2\epsilon}(x + x_N)^2, & -x_N < x \leq 0 \\ \frac{qN_A}{2\epsilon}(x - x_P)^2, & 0 \leq x < x_P \\ 0, & x \geq x_P \end{cases} \quad (3.86)$$

The electrostatic potential must be continuous at $x = 0$. Therefore, from equation (3.86),

$$V_{bi} - \frac{qN_D}{2\epsilon}x_N^2 = \frac{qN_A}{2\epsilon}x_P^2 \quad (3.87)$$

In the absence of any interface charge at the metallurgical junction, the electric field is also continuous at this point (really, it is the displacement field, $\vec{D} = \epsilon\vec{E}$, but in this example, ϵ is independent of position), and

$$x_N N_D = x_P N_A \quad (3.88)$$

This is simply a statement that the total charge in either side of the depletion region exactly balance each other and therefore the depletion region extends furthest into the more lightly doped side.

Solving equations (3.87) and (3.88) for the depletion width, W_D , gives³

$$W_D = x_N + x_P = \sqrt{\frac{2\epsilon}{q} \left(\frac{N_A + N_D}{N_A N_D} \right)} V_{bi}. \quad (3.89)$$

Under nonequilibrium conditions, the electrostatic potential difference across the junction is modified by the applied voltage, V , which is zero in thermal equilibrium. As a consequence, the depletion width is dependent on the applied voltage,

$$W_D(V) = x_N + x_P = \sqrt{\frac{2\epsilon}{q} \left(\frac{N_A + N_D}{N_A N_D} \right)} (V_{bi} - V). \quad (3.90)$$

As previously stated, the built-in voltage, V_{bi} , can be calculated by noting that under thermal equilibrium the net hole and electron currents are zero. The hole current density is

$$\vec{J}_p = q\mu_p p_o \vec{E} - qD_p \nabla p = 0. \quad (3.91)$$

³ A somewhat more rigorous treatment of equation 3.89 would yield a factor of $2kT/q$ which is ~ 50 mV at 300 K, or

$$W_D = \sqrt{\frac{2\epsilon}{q} \left(\frac{N_A + N_D}{N_A N_D} \right)} (V_{bi} - 2kT/q) \quad [3].$$

Thus, in 1D, utilizing the Einstein relationship, the electric field can be written as

$$\vec{E} = \frac{kT}{q} \frac{1}{p_o} \frac{dp_o}{dx} \quad (3.92)$$

Rewriting equation (3.85) and substituting equation (3.92) yields

$$V_{bi} = \int_{-x_N}^{x_P} \vec{E} dx = \int_{-x_N}^{x_P} \frac{kT}{q} \frac{1}{p_o} \frac{dp_o}{dx} dx = \frac{kT}{q} \int_{p_o(-x_N)}^{p_o(x_P)} \frac{dp_o}{p_o} = \frac{kT}{q} \ln \left[\frac{p_o(x_P)}{p_o(-x_N)} \right] \quad (3.93)$$

Since we have assumed nondegeneracy, $p_o(x_P) = N_A$ and $p_o(-x_N) = n_i^2/N_D$. Therefore,

$$V_{bi} = \frac{kT}{q} \ln \left[\frac{N_D N_A}{n_i^2} \right]. \quad (3.94)$$

Figure 3.14 shows the equilibrium energy band diagram, electric field, and charge density for a simple abrupt pn -junction silicon diode in the vicinity of the depletion region. The conduction bandedge is given by $E_C(x) = E_0 - q\phi(x) - \chi$, the valence bandedge

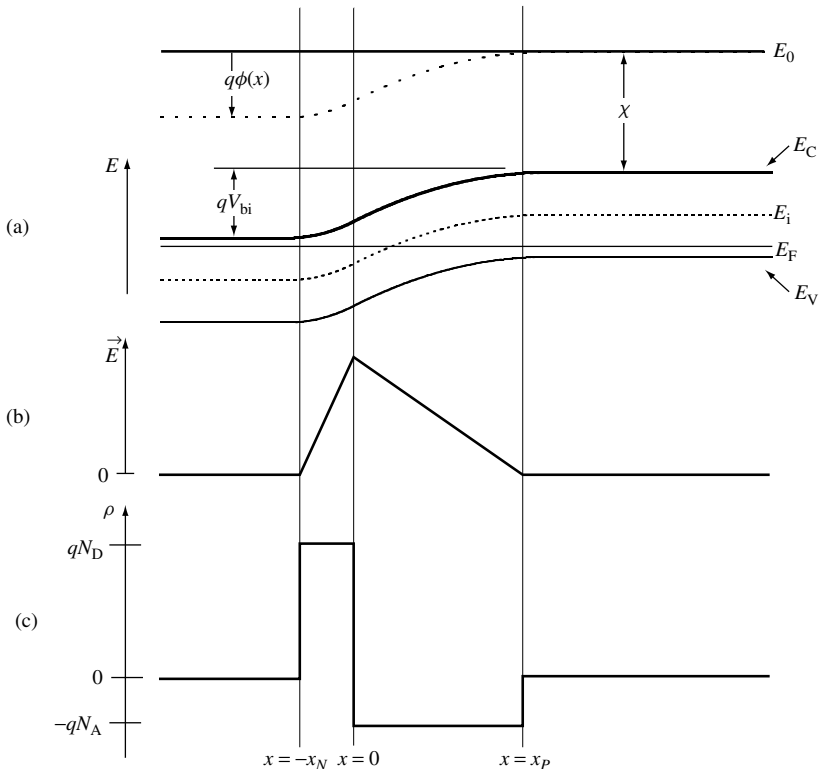


Figure 3.14 Equilibrium conditions in a solar cell: (a) energy bands; (b) electric field; and (c) charge density

by $E_V(x) = E_C(x) - E_G$, and the intrinsic energy by equation (3.19). E_0 , defined as the vacuum energy, serves as a convenient reference point and is universally constant with position. An electron at the vacuum energy is, by definition, completely free of influence from all external forces. The electron affinity, χ , is the minimum energy needed to free an electron from the bottom of the conduction band and take it to the vacuum level. The electric field is a result of the uncovered ionized donors and acceptors and opposes the diffusion of electrons and holes in the quasi-neutral regions. The charge density plot illustrates the balance of charge between the two sides of the depletion region. In heterojunctions, both the band gap and the electron affinity are position-dependent – making the calculation of the junction electrostatics and energy band diagram more involved.

The basic solar cell structure has now been established (Figure 3.13). It is simply a *pn*-junction diode consisting of two quasi-neutral regions on either side of a depletion region with an electrical contact made to each quasi-neutral region. Typically, the more heavily doped quasi-neutral region is called the *emitter* (the *n*-type region in Figure 3.13) and the more lightly doped region is called the *base* (the *p*-type region in Figure 3.13). The base region is also often referred to as the *absorber region* since the emitter region is usually very thin and most of the light absorption occurs in the base. This basic structure will serve as the basis for deriving the fundamental operating characteristics of the solar cell.

3.4 SOLAR CELL FUNDAMENTALS

The basic current–voltage characteristic of the solar cell can be derived by solving the minority-carrier diffusion equation with appropriate boundary conditions.

3.4.1 Solar Cell Boundary Conditions

At $x = -W_N$, the usual assumption is that the front contact can be treated as an ideal ohmic contact. Hence,

$$\Delta p(-W_N) = 0. \quad (3.95)$$

However, since the front contact is usually a grid with metal contacting the semiconductor on only a small percentage of the front surface, modeling the front surface with an effective surface recombination velocity is more realistic. This effective recombination velocity models the combined effects of the ohmic contact and the antireflective passivation layer (SiO_2 in silicon solar cells). In this case, the boundary condition at $x = -W_N$ is

$$\frac{d\Delta p}{dx} = \frac{S_{F,\text{eff}}}{D_p} \Delta p(-W_N) \quad (3.96)$$

where $S_{F,\text{eff}}$ is the effective front surface recombination velocity. As $S_{F,\text{eff}} \rightarrow \infty$, $\Delta p \rightarrow 0$, and the boundary condition given by equation (3.96) reduces to that of an ideal ohmic contact (equation 3.95). In reality, $S_{F,\text{eff}}$ depends upon a number of parameters and is bias-dependent. This will be discussed in more detail later.

The back contact could also be treated as an ideal ohmic contact, so that

$$\Delta n(W_P) = 0. \quad (3.97)$$

However, solar cells are often fabricated with a *back-surface field* (BSF), a thin more heavily doped region at the back of the base region. The BSF keeps minority carriers away from the back ohmic contact and increases their chances of being collected and it can be modeled by an effective, and relatively low, surface recombination velocity. This boundary condition is then

$$\left. \frac{d\Delta n}{dx} \right|_{x=W_P} = -\frac{S_{\text{BSF}}}{D_n} \Delta n(W_P), \quad (3.98)$$

where S_{BSF} is the effective surface recombination velocity at the BSF.

All that remains now is to determine suitable boundary conditions at $x = -x_N$ and $x = x_P$. These boundary conditions are commonly referred to as the *law of the junction*.

Under equilibrium conditions, zero applied voltage and no illumination, the Fermi energy, E_F , is constant with position. When a bias voltage is applied, it is convenient to introduce the concept of quasi-Fermi energies. It was shown earlier that the equilibrium carrier concentrations could be related to the Fermi energy (equations 3.15 and 3.16). Under nonequilibrium conditions, similar relationships hold. Assuming the semiconductor is nondegenerate,

$$p = n_i e^{(E_i - F_p)/kT} \quad (3.99)$$

and

$$n = n_i e^{(F_n - E_i)/kT} \quad (3.100)$$

It is evident that under equilibrium conditions $F_p = F_n = E_F$. Under nonequilibrium conditions, assuming that the majority carrier concentrations at the contacts retain their equilibrium values, the applied voltage can be written as

$$qV = F_n(-W_N) - F_p(W_P) \quad (3.101)$$

Since, in low-level injection, the majority carrier concentrations are constant throughout the quasi-neutral regions, that is, $p_p(x_P \leq x \leq W_P) = N_A$ and $n_n(-W_N \leq x \leq -x_N) = N_D$, $F_n(-W_N) = F_n(-x_N)$ and $F_p(W_P) = F_p(x_P)$. Then, assuming that both the quasi-Fermi energies remain constant inside the depletion region,

$$qV = F_n(x) - F_p(x) \quad (3.102)$$

for $-x_N \leq x \leq x_P$, that is, everywhere inside the depletion region. Using equations (3.99) and (3.100), this leads directly to the *law of the junction*, the boundary conditions used at the edges of the depletion region,

$$p_n(-x_N) = \frac{n_i^2}{N_D} e^{qV/kT} \quad (3.103)$$

and

$$n_P(x_P) = \frac{n_i^2}{N_A} e^{qV/kT}. \quad (3.104)$$

3.4.2 Generation Rate

For light incident at the front of the solar cell, $x = -W_N$, the optical generation rate takes the form (see equation 3.35)

$$G(x) = (1 - s) \int_{\lambda} (1 - r(\lambda)) f(\lambda) \alpha(\lambda) e^{-\alpha(x+W_N)} d\lambda. \quad (3.105)$$

Only photons with $\lambda \leq hc/E_G$ contribute to the generation rate.

3.4.3 Solution of the Minority-carrier Diffusion Equation

Using the boundary conditions defined by equations (3.96), (3.98), (3.103), and (3.104) and the generation rate given by equation (3.105), the solution to the minority-carrier diffusion equation, equation (3.80), is easily shown to be

$$\Delta p_N(x) = A_N \sinh[(x + x_N)/L_p] + B_N \cosh[(x + x_N)/L_p] + \Delta p'_N(x) \quad (3.106)$$

in the n -type region and

$$\Delta n_P(x) = A_P \sinh[(x - x_P)/L_n] + B_P \cosh[(x - x_P)/L_n] + \Delta n'_P(x) \quad (3.107)$$

in the p -type region. The particular solutions due to $G(x)$, $\Delta p'_N(x)$, and $\Delta n'_P(x)$ are given by

$$\Delta p'_N(x) = -(1 - s) \int_{\lambda} \frac{\tau_p}{(L_p^2 \alpha^2 - 1)} [1 - r(\lambda)] f(\lambda) \alpha(\lambda) e^{-\alpha(x+W_N)} d\lambda \quad (3.108)$$

and

$$\Delta n'_P(x) = -(1 - s) \int_{\lambda} \frac{\tau_n}{(L_n^2 \alpha^2 - 1)} [1 - r(\lambda)] f(\lambda) \alpha(\lambda) e^{-\alpha(x+W_N)} d\lambda. \quad (3.109)$$

Using the boundary conditions set above, A_N , B_N , A_P , and B_P are easily obtained.

3.4.4 Terminal Characteristics

The minority-carrier current densities in the quasi-neutral regions are just the diffusion currents, since the electric field is negligible. Using the active sign convention for the current (since a solar cell is typically thought of as a battery) gives

$$\vec{J}_{p,N}(x) = -qD_p \frac{d\Delta p_N}{dx} \quad (3.110)$$

and

$$\vec{J}_{n,p}(x) = qD_n \frac{d\Delta n_p}{dx} \quad (3.111)$$

The total current is given by

$$I = A[J_p(x) + J_n(x)] \quad (3.112)$$

and is true everywhere within the solar cell (A is the area of the solar cell). Equations (3.110) and (3.111) give only the hole current in the n -type region and the electron current in the p -type region, not both at the same point. However, integrating equation (3.72), the electron continuity equation, over the depletion region, gives

$$\int_{-x_N}^{x_P} \frac{d\vec{J}_n dx}{dx} = \vec{J}_n(x_P) - \vec{J}_n(-x_N) = q \int_{-x_N}^{x_P} [R(x) - G(x)] dx \quad (3.113)$$

$G(x)$ is easily integrated and the integral of the recombination rate can be approximated by assuming that the recombination rate is constant within the depletion region and is $R(x_m)$ where x_m is the point at which $p_D(x_m) = n_D(x_m)$ and corresponds to the maximum recombination rate in the depletion region. If recombination via a midgap single level trap is assumed, then, from equations (3.37), (3.99), (3.100), and (3.102), the recombination rate in the depletion region is

$$R_D = \frac{p_D n_D - n_i^2}{\tau_n(p_D + n_i) + \tau_p(n_D + n_i)} = \frac{n_D^2 - n_i^2}{(\tau_n + \tau_p)(n_D + n_i)} = \frac{n_D - n_i}{(\tau_n + \tau_p)} = \frac{n_i(e^{qV/2kT} - 1)}{\tau_D} \quad (3.114)$$

where τ_D is the effective lifetime in the depletion region. From equation (3.113), $\vec{J}_n(-x_N)$, the majority carrier current at $x = -x_N$, can now be written as

$$\begin{aligned} \vec{J}_n(-x_N) &= \vec{J}_n(x_P) + q \int_{-x_N}^{x_P} G(x) dx - q \int_{-x_N}^{x_P} R_D dx \\ &= \vec{J}_n(x_P) + q(1-s) \int_{\lambda} [1-r(\lambda)] f(\lambda) [e^{-\alpha(W_N-x_N)} - e^{-\alpha(W_N+x_P)}] d\lambda \\ &\quad - q \frac{W_D n_i}{\tau_D} (e^{qV/2kT} - 1) \end{aligned} \quad (3.115)$$

where $W_D = x_P + x_N$. Substituting into equation (3.112), the total current is now

$$I = A \left[J_p(-x_N) + J_n(x_P) + J_D - q \frac{W_D n_i}{\tau_D} (e^{qV/2kT} - 1) \right] \quad (3.116)$$

where

$$J_D = q(1-s) \int_{\lambda} [1-r(\lambda)] f(\lambda) (e^{-\alpha(W_N-x_N)} - e^{-\alpha(W_N+x_P)}) d\lambda \quad (3.117)$$

is the generation current from the depletion region and A is the area of the solar cell. The last term of equation (3.116) represents recombination in the space-charge region.

The solutions to the minority-carrier diffusion equation, equations (3.106) and (3.107), can be used to evaluate the minority-carrier current densities, equations (3.110) and (3.111). These can then be substituted into equation (3.116), which, with some algebraic manipulation, yields

$$I = I_{SC} - I_{o1}(e^{qV/kT} - 1) - I_{o2}(e^{qV/2kT} - 1) \quad (3.118)$$

where I_{SC} is the short-circuit current and is the sum of the contributions from each of the three regions: the n -type region (I_{SCN}), the depletion region ($I_{SCD} = AJ_D$), and the p -type region (I_{SCP})

$$I_{SC} = I_{SCN} + I_{SCD} + I_{SCP} \quad (3.119)$$

where

$$I_{SCN} = qAD_p \left[\frac{\Delta p'(-x_N)T_{p1} - S_{F,eff}\Delta p'(-W_N) + D_p \left. \frac{d\Delta p'}{dx} \right|_{x=-W_N}}{L_p T_{p2}} - \left. \frac{d\Delta p'}{dx} \right|_{x=-x_N} \right] \quad (3.120)$$

with

$$T_{p1} = D_p/L_p \sinh[(W_N - x_N)/L_p] + S_{F,eff} \cosh[(W_N - x_N)/L_p] \quad (3.121)$$

$$T_{p2} = D_p/L_p \cosh[(W_N - x_N)/L_p] + S_{F,eff} \sinh[(W_N - x_N)/L_p] \quad (3.122)$$

and

$$I_{SCP} = qAD_n \left[\frac{\Delta n'(x_p)T_{n1} - S_{BSF}\Delta n'(W_p) + D_n \left. \frac{d\Delta n'}{dx} \right|_{x=W_p}}{L_n T_{n2}} + \left. \frac{d\Delta n'}{dx} \right|_{x=x_p} \right] \quad (3.123)$$

with

$$T_{n1} = D_n/L_n \sinh[(W_p - x_p)/L_n] + S_{BSF} \cosh[(W_p - x_p)/L_n] \quad (3.124)$$

$$T_{n2} = D_n/L_n \cosh[(W_p - x_p)/L_n] + S_{BSF} \sinh[(W_p - x_p)/L_n] \quad (3.125)$$

I_{o1} is the dark saturation current due to recombination in the quasi-neutral regions,

$$I_{o1} = I_{o1,p} + I_{o1,n} \quad (3.126)$$

with

$$I_{o1,p} = qA \frac{n_i^2}{N_D} \frac{D_p}{L_p} \left\{ \frac{D_p/L_p \sinh[(W_N - x_N)/L_p] + S_{F,eff} \cosh[(W_N - x_N)/L_p]}{D_p/L_p \cosh[(W_N - x_N)/L_p] + S_{F,eff} \sinh[(W_N - x_N)/L_p]} \right\} \quad (3.127)$$

and

$$I_{o1,n} = qA \frac{n_i^2 D_n}{N_A L_n} \times \left\{ \frac{D_n/L_n \sinh[(W_P - x_P)/L_n] + S_{BSF} \cosh[(W_P - x_P)/L_n]}{D_n/L_n \cosh[(W_P - x_P)/L_n] + S_{BSF} \sinh[(W_P - x_P)/L_n]} \right\} \quad (3.128)$$

These are very general expressions for the dark saturation current and reduce to more familiar forms when appropriate assumptions are made, as will be seen later.

I_{o2} is the dark saturation current due to recombination in the space-charge region,

$$I_{o2} = qA \frac{W_D n_i}{\tau_D} \quad (3.129)$$

and is bias-dependent since the depletion width, W_D , is a function of the applied voltage (equation 3.89).

3.4.5 Solar Cell $I-V$ Characteristics

Equation (3.118), repeated here, is a general expression for the current produced by a solar cell.

$$I = I_{SC} - I_{o1}(e^{qV/kT} - 1) - I_{o2}(e^{qV/2kT} - 1) \quad (3.130)$$

The short-circuit current and dark saturation currents are given by rather complex expressions (equations 3.119, 3.128, and 3.129) that depend on the solar cell structure, material properties, and the operating conditions. A full understanding of solar cell operation requires detailed examination of these terms. However, much can be learned about solar cell operation by examining the basic form of equation (3.130). From a circuit perspective, it is apparent that a solar cell can be modeled by an ideal current source (I_{SC}) in parallel with two diodes – one with an ideality factor of “1” and the other with an ideality factor of “2”, as shown in Figure 3.15. Note that the direction of the current source is opposed to the current flow of the diodes – that is, it serves to forward-bias the diodes.

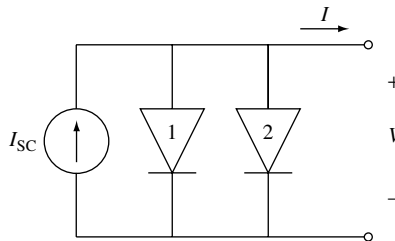


Figure 3.15 Simple solar cell circuit model. Diode 1 represents the recombination current in the quasi-neutral regions ($\propto e^{qV/kT}$), while diode 2 represents recombination in the depletion region ($\propto e^{qV/2kT}$)

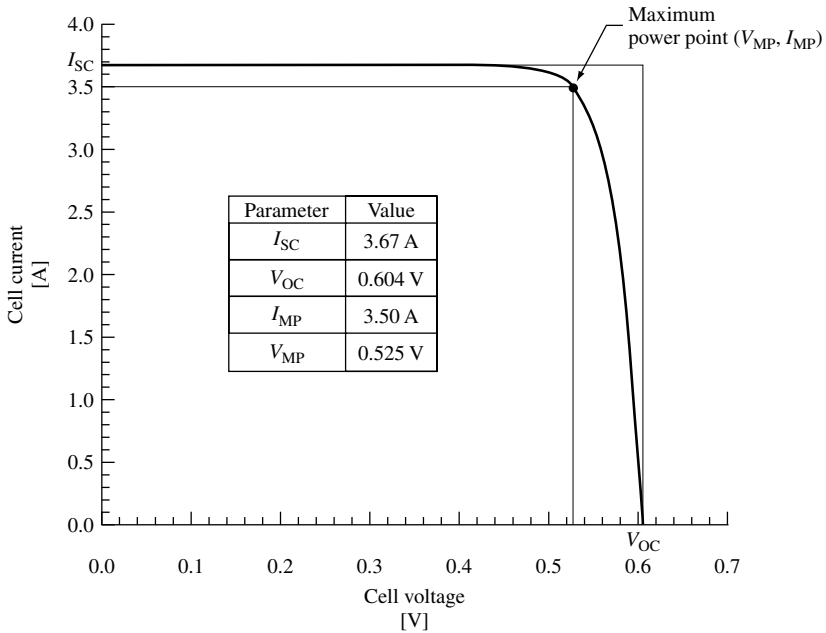


Figure 3.16 Current–voltage characteristic of the silicon solar cell defined by Table 3.2

The current–voltage (I – V) characteristic of a typical silicon solar cell is plotted in Figure 3.16 for the parameter values given in Table 3.2. For simplicity, the dark current due to the depletion region (diode 2) has been ignored (a reasonable and common assumption for a good silicon solar cell, especially at larger forward biases). It illustrates several important figures of merit for solar cells – the short-circuit current, the open-circuit voltage, and the fill factor. At small applied voltages, the diode current is negligible and the current is just the short-circuit current, I_{SC} , as can be seen when V is set to zero in equation (3.130). When the applied voltage is high enough so that the diode current (recombination current) becomes significant, the solar cell current drops quickly.

Table 3.2 shows the huge asymmetry between the n -emitter and the p -base in a typical solar cell. The emitter is ~ 1000 times thinner, 10 000 times more heavily doped, and its diffusion length is ~ 100 times shorter than the corresponding quantities in the base.

At open circuit ($I = 0$), all the light-generated current, I_{SC} , is flowing through diode 1, so the open-circuit voltage can be written as

$$V_{OC} = \frac{kT}{q} \ln \frac{I_{SC} + I_{o1}}{I_{o1}} \approx \frac{kT}{q} \ln \frac{I_{SC}}{I_{o1}}, \quad (3.131)$$

where $I_{SC} \gg I_{o1}$.

Of particular interest is the point on the I – V curve where the power produced is at a maximum. This is referred to as the *maximum power point* with $V = V_{MP}$ and $I = I_{MP}$. As seen in Figure 3.18, this point defines a rectangle whose area, given by $P_{MP} = V_{MP}I_{MP}$, is the largest rectangle for any point on the I – V curve. The maximum

Table 3.2 Si solar cell model parameters

Parameter	Value
A	100 cm ²
W_N	0.35 μm
N_D	1 × 10 ²⁰ cm ⁻³
D_p	1.5 cm ² /V-s
$S_{F,eff}$	3 × 10 ⁴ cm/s
τ_p	1 μs
L_p	12 μm
W_P	300 μm
N_A	1 × 10 ¹⁵ cm ⁻³
D_n	35 cm ² /V-s
S_{BSF}	100 cm/s
τ_n	350 μs
L_n	1100 μm

power point is found by solving

$$\left. \frac{\partial P}{\partial V} \right|_{V=V_{MP}} = \left. \frac{\partial (IV)}{\partial V} \right|_{V=V_{MP}} = \left[I + V \frac{\partial I}{\partial V} \right] \Big|_{V=V_{MP}} = 0 \quad (3.132)$$

for $V = V_{MP}$. The current at the maximum power point, I_{MP} , is then found by evaluating equation (3.130) at $V = V_{MP}$.

The rectangle-defined V_{OC} and I_{SC} provides a convenient means for characterizing the maximum power point. The fill factor, FF , is a measure of the *squareness* of the $I-V$ characteristic and is always less than one. It is the ratio of the areas of the two rectangles shown in Figure 3.16 or

$$FF = \frac{P_{MP}}{V_{OC} I_{SC}} = \frac{V_{MP} I_{MP}}{V_{OC} I_{SC}} \quad (3.133)$$

An empirical expression for the fill factor is [15]

$$FF = \frac{V_{OC} - \frac{kT}{q} \ln[qV_{OC}/kT + 0.72]}{V_{OC} + kT/q}. \quad (3.134)$$

Arguably, the most important figure of merit for a solar cell is its power conversion efficiency, η , which is defined as

$$\eta = \frac{P_{MP}}{P_{in}} = \frac{FF V_{OC} I_{SC}}{P_{in}} \quad (3.135)$$

The incident power, P_{in} , is determined by the properties of the light spectrum incident upon the solar cell. Further information regarding experimental determination of these parameters appears in Chapter 16.

Another important figure of merit is the collection efficiency, which can be defined relative to both optical and recombination losses as an *external* collection efficiency

$$\eta_C^{\text{ext}} = \frac{I_{\text{SC}}}{I_{\text{ph}}} \quad (3.136)$$

where

$$I_{\text{ph}} = qA \int_{\lambda < \lambda_G} f(\lambda) d\lambda \quad (3.137)$$

is the maximum possible photocurrent that would result if all photons with $E > E_G$ ($\lambda < \lambda_G = hc/E_G$) created electron–hole pairs that were collected. The collection efficiency can also be defined with respect to recombination losses as the internal collection efficiency

$$\eta_C^{\text{int}} = \frac{I_{\text{SC}}}{I_{\text{gen}}} \quad (3.138)$$

where

$$I_{\text{gen}} = qA(1 - s) \int_{\lambda < \lambda_G} [1 - r(\lambda)]f(\lambda)(1 - e^{-\alpha(W_N + W_P)}) d\lambda \quad (3.139)$$

is the light-generated current. This represents what the short-circuit current would be if every photon that is absorbed is collected and contributes to the short-circuit current. $I_{\text{gen}} = I_{\text{inc}}$ when there is no grid shadowing, no reflective losses, and the solar cell has infinite optical thickness.

3.4.6 Properties of Efficient Solar Cells

Using these figures of merit, the properties of a good (efficient) solar cell can be ascertained. From equation (3.135), it is clear that an efficient solar cell will have a high short-circuit current, I_{SC} , a high open-circuit voltage, V_{OC} , and a fill factor, FF , as close as possible to 1.

$I_{\text{SC}} = \eta_C^{\text{int}} I_{\text{gen}}$ is directly proportional to both the internal collection efficiency and the light-generated current, I_{gen} . The internal collection efficiency is solely dependent on the recombination in the solar cell and will approach 1 as $\tau \rightarrow \infty$ and $S \rightarrow 0$. To maximize I_{gen} (i.e. $I_{\text{gen}} \rightarrow I_{\text{inc}}$), the solar cell should be designed with a minimum amount of grid shadowing (s), minimum reflectance ($r(\lambda)$), and be optically thick enough such that nearly all the photons with $E > E_G$ are absorbed.

The open-circuit voltage

$$V_{\text{OC}} \approx \frac{kT}{q} \ln \frac{I_{\text{SC}}}{I_{o1}} \quad (3.140)$$

is logarithmically proportional to the short-circuit current and to the reciprocal of the reverse saturation current, I_{o1} (the same is true for I_{o2}). Therefore, reducing the saturation

current will increase the open-circuit voltage. From equations (3.127) and (3.128), it is obvious that $I_{o1} \rightarrow 0$ as $\tau \rightarrow \infty$ and $S \rightarrow 0$.

From equation (3.134) it is clear that increasing V_{OC} will increase the fill factor, FF . Thus, the design and the operation of an efficient solar cell has two basic goals:

- 1) Minimization of recombination rates throughout the device.
- 2) Maximization of the absorption of photons with $E > E_G$.

It is evident that, despite the apparent complexity of the expressions describing the operation of solar cells, the basic operating principles are easy to understand. Electron–hole pairs are created inside the solar cell as a result of absorption of the photons incident on the solar cell from the sun. The objective is to collect the minority carriers before they are lost to recombination.

3.4.7 Lifetime and Surface Recombination Effects

The solar cell characteristics previously derived (equations 3.118 through 3.128) allow examination of the dependence of the solar cell performance on specific sources of recombination. Figure 3.17 shows how the base minority-carrier lifetime affects V_{OC} , I_{SC} , and the FF . Unless otherwise stated, the parameters of Table 3.2 are used to compute the solar cell performance. Short lifetimes mean that the diffusion length in the base is much less than the base thickness and carriers created deeper than about one diffusion length in the base are unlikely to be collected. When this is true ($L_n \ll W_p$), the contribution to the dark saturation current in the base (equation 3.128) becomes

$$I_{o1,n} = qA \frac{n_i^2}{N_A} \frac{D_n}{L_n} \quad (3.141)$$

and is commonly referred to as the *long-base approximation*. In this case, the BSF has no effect on the dark saturation current. On the other hand, when the base minority-carrier lifetime is long ($L_n \gg W_p$), the carriers readily come in contact with the BSF and the dark saturation current is a strong function of S_{BSF}

$$I_{o1,n} = qA \frac{n_i^2}{N_A} \frac{D_n}{(W_p - x_p)} \frac{S_{BSF}}{S_{BSF} + D_n/(W_p - x_p)} \quad (3.142)$$

When S_{BSF} is very large (i.e. no BSF), this reduces to the more familiar short-base approximation

$$I_{o1,n} = qA \frac{n_i^2}{N_A} \frac{D_n}{(W_p - x_p)}. \quad (3.143)$$

Figure 3.18 shows how S_{BSF} affects V_{OC} , I_{SC} , and the FF . Notice that the break point in the curves occurs when $S_{BSF} \approx D_n/W_p = 1000$ cm/s, as can be inferred from equation (3.142).

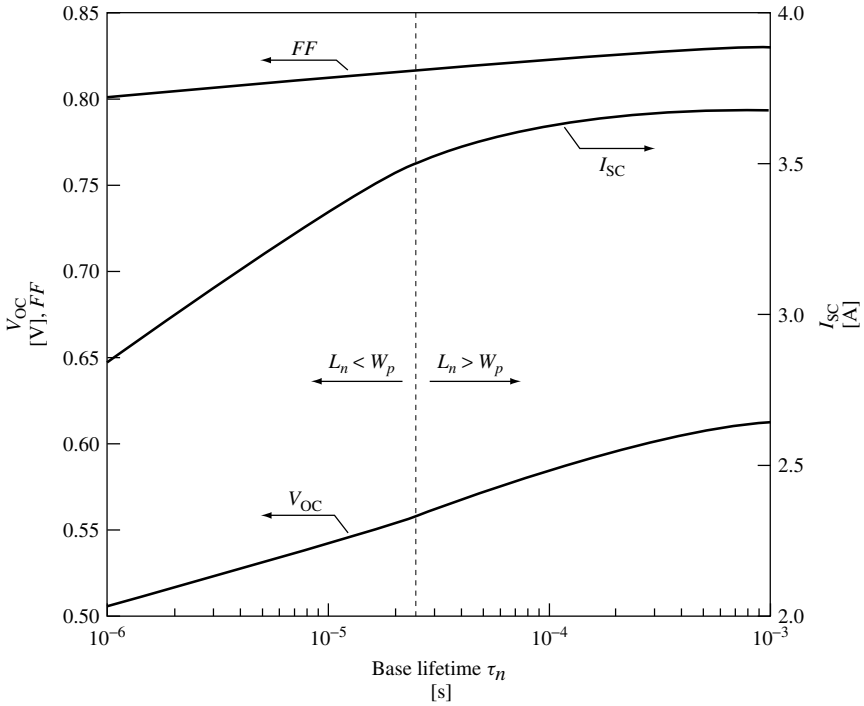


Figure 3.17 Effect of base lifetime on solar cell performance for the solar cell parameters in Table 3.2. The minority-carrier diffusion length ($L_n = \sqrt{D_n \tau_n}$) is equal to the base thickness (W_p) when $\tau_n = 25.7 \mu\text{s}$

Front surface recombination for solar cells with contact grids on the front of the device is really an average over the front surface area of the relatively low surface recombination velocity between the grid lines and the very high surface recombination velocity of the ohmic contact. An expression for the effective front surface recombination velocity is given by [16]

$$S_{F,\text{eff}} = \frac{(1-s)S_F \bar{G}_N \tau_p \left(\cosh \frac{W_N}{L_p} - 1 \right) + p_o (e^{qV/A_o kT} - 1) \left[s \frac{D_p}{L_p} \frac{\cosh \frac{W_N}{L_p}}{\sinh \frac{W_N}{L_p}} + S_F \right]}{(1-s) \left[p_o (e^{qV/A_o kT} - 1) + \bar{G}_N \tau_p \left(\cosh \frac{W_N}{L_p} - 1 \right) \right]} \quad (3.144)$$

where S_F is the surface recombination velocity between the grid lines and \bar{G} is the average generation rate in the emitter region. It is obvious that $S_{F,\text{eff}}$ is dependent upon the solar cell operation point. This is better seen in Table 3.3 where some special cases are illustrated (assuming $L_p \gg W_N$).

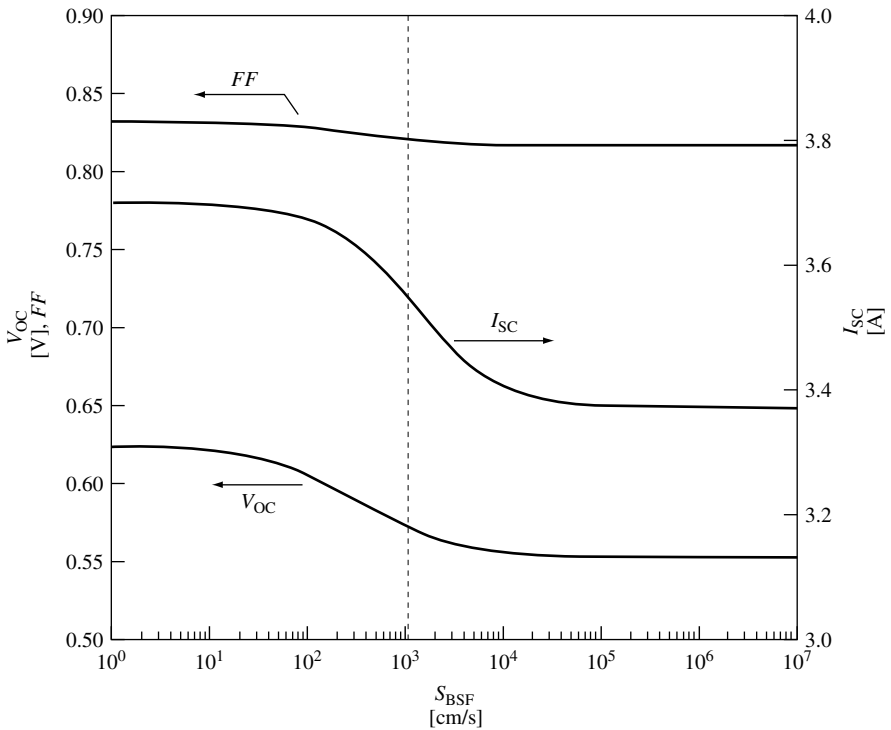


Figure 3.18 Effect of the back-surface field recombination velocity on solar cell performance. All other parameters are from Table 3.2

Table 3.3 Special cases of $S_{F,\text{eff}}$

No grid ($s = 0$)	$S_{F,\text{eff}} = S_F$
Full grid ($s = 1$)	$S_{F,\text{eff}} \rightarrow \infty$
Dark ($\bar{G} = 0$)	$S_{F,\text{eff}} = \frac{S_F + sD_p/W_N}{1 - s}$
Short circuit ($V = 0$)	$S_{F,\text{eff}} = S_F$
V large ($\approx V_{OC}$)	$S_{F,\text{eff}} = \frac{S_F + sD_p/W_N}{1 - s}$

3.4.8 An Analogy for Understanding Solar Cell Operation: A Partial Summary

The following analogy illustrates the importance of minimizing all sources of recombination in the solar cell.⁴ Imagine a funnel that has a variety of holes of different shapes and sizes in it. It also has a stopcock at the bottom for controlling the flow of liquid

⁴ This analogy was developed on the basis of discussions with Professor Richard J. Schwartz of Purdue University, West Lafayette, Indiana.

through the bottom of the funnel. Water, representing the incident sunlight, is poured into the top of the funnel. Water flowing out of the funnel through the stopcock represents the current delivered by the solar cell. Since the funnel is full of holes, some of the water leaks out instead of flowing through the stopcock. This leakage represents the recombination of minority carriers in the solar cell. The different-shaped holes represent different sources of recombination. For instance, square holes might represent recombination in the base region, round holes might be recombination in the space-charge region, triangular holes might be surface recombination at the back contact, and so on. The rate at which water pours in is proportional to the light intensity. At steady state, the water will find a height such that the flow of water in, I_{gen} , is equal to the flow through the stopcock (I) plus the water that leaks through the holes (I_{recomb}). This height represents the solar cell voltage (V).

When the stopcock is fully open, the water flows out through the stopcock at its maximum rate (I_{SC}), although some water will leak out through the holes so that $I_{\text{SC}} < I_{\text{gen}}$. This is analogous to the collection efficiency, η_{C} , of a solar cell – the objective being to minimize the amount of leakage (recombination) so that η_{C} is as close to unity as possible. Smaller holes means less recombination and $I_{\text{SC}} \rightarrow I_{\text{gen}}$.

As the stopcock is slowly closed, the level of liquid in the funnel rises – just as the solar cell voltage increases as the current decreases. When the stopcock is completely closed, the height of the water is representative of the open-circuit voltage (V_{OC}). At open circuit all the minority carriers must recombine just as all the water must leak out of the funnel in this analogy. If the holes are all big, the height of the water will be low. This is equivalent to short minority-carrier lifetimes and large surface recombination velocities that result in a low V_{OC} . By reducing the size of the holes (i.e. increasing the minority-carrier lifetimes and reducing the surface recombination velocities), the height of the water in the funnel (i.e. V_{OC}) is increased. Reducing the size of only the square holes (by increasing the minority-carrier lifetime in the base) will not increase the height of the water as much as might be expected since the round holes (recombination in the depletion region) are still large. All leaks (recombination sources) must be plugged (recombination rates minimized) before the height of the water (V_{OC}) increases substantially.

3.5 ADDITIONAL TOPICS

3.5.1 Efficiency and Band gap

Since only photons with $h\nu > E_{\text{G}}$ can create electron – hole pairs and contribute to the output of the solar cell, it is obvious that the band gap determines how well the solar cell is coupled to the solar spectrum. A simple analysis can be performed to predict the maximum solar cell efficiency. More complete analyses of the theoretical limits of solar cells are given elsewhere [17–19] and are also discussed in Chapter 4 of this handbook. Assuming the maximum energy that can be extracted from an absorbed photon is E_{G} , the maximum efficiency can be expressed as

$$\eta_{\text{max}}(E_{\text{G}}) = \frac{\frac{1}{q} E_{\text{G}} I_{\text{inc}}}{P_{\text{in}}} = \frac{E_{\text{G}}}{(P_{\text{in}}/A)} \int_{\lambda < \lambda_{\text{G}}} f(\lambda) d\lambda. \quad (3.145)$$

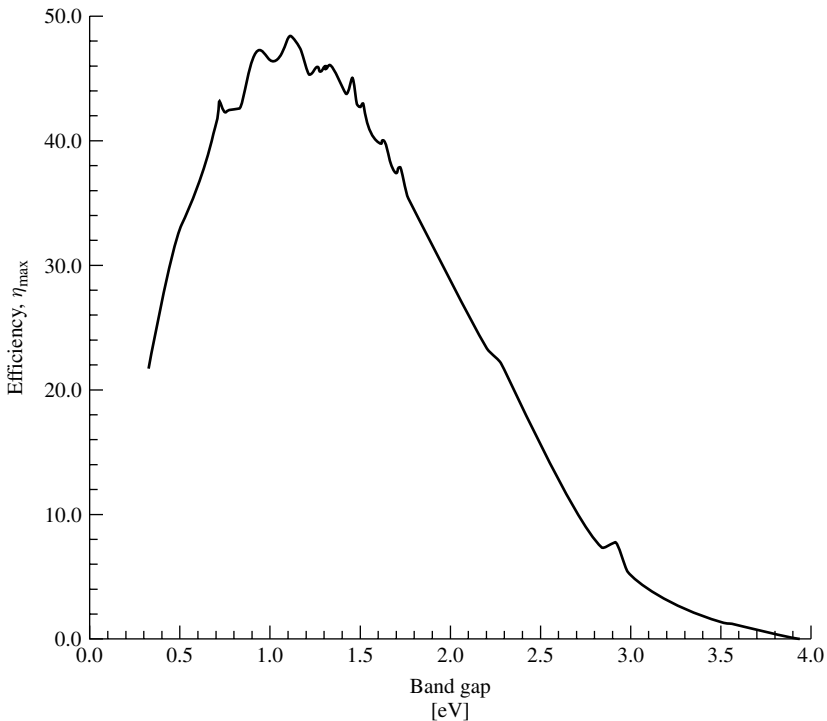


Figure 3.19 Theoretical maximum efficiency as a function of semiconductor band gap for an AM1.5 global spectrum

This is plotted in Figure 3.19 for an AM1.5 global spectrum and shows a maximum efficiency of 48% at about $E_G = 1.1$ eV, close to the band gap of silicon. Of course, this is only a simple estimate and assumes that $V_{OC} = 1/qE_G$ and $FF = 1$, which are obvious exaggerations. Perfect light trapping was also assumed so that $I_{SC} = I_{inc}$, but that is a more realistic prospect. Under nonconcentrated solar illumination, the actual maximum theoretical efficiency for a silicon solar cell is approximately 30%. However, this simple approach does serve to demonstrate the important role the semiconductor band gap plays in determining solar cell performance and shows that band gaps between 1.0 and 1.6 eV have nearly equivalent maximum theoretical efficiencies.

3.5.2 Spectral Response

The spectral response, $SR(\lambda)$, of a solar cell permits an examination of how photons of different wavelengths (energy) contribute to the short-circuit current. Just as the collection efficiency can be measured as either an external or an internal collection efficiency, so can the spectral response. The spectral response is defined as the *short-circuit current*, $I_{SC}(\lambda)$, resulting from a single wavelength of light normalized by the maximum possible current. The external spectral response is defined as

$$SR_{\text{ext}} = \frac{I_{SC}(\lambda)}{qAf(\lambda)} \quad (3.146)$$

and the internal spectral response as

$$SR_{\text{int}} = \frac{I_{\text{SC}}(\lambda)}{qA(1-s)(1-r(\lambda))f(\lambda)(e^{-\alpha(\lambda)W_{\text{opt}}} - 1)}, \quad (3.147)$$

where W_{opt} is the optical thickness of the solar cell (technically, also a function of wavelength). Experimentally, the external spectral response is measured. The internal spectral response is determined from it along with the knowledge of the grid shadowing, reflectance, and optical thickness. W_{opt} can be greater than the cell thickness if light-trapping methods are used. Such methods include textured surfaces [20] and back-surface reflectors [21] and are discussed in Chapter 8. The short-circuit current can be written in terms of the external spectral response as

$$I_{\text{SC}} = \int_{\lambda} SR_{\text{ext}}(\lambda) f(\lambda) d\lambda. \quad (3.148)$$

The internal spectral response gives an indication of which sources of recombination are affecting the cell performance. This is demonstrated in Figure 3.20 where the internal spectral response of the silicon solar cell described by the parameters of Table 3.2 is shown. Also shown is the spectral response when $S_{\text{F,eff}} = 100 \text{ cm/s}$ (a passivated front surface) and the spectral response when $S_{\text{BSF}} = 1 \times 10^7 \text{ cm/s}$ (in effect, no BSF). The short wavelength response improves dramatically when the front surface is passivated

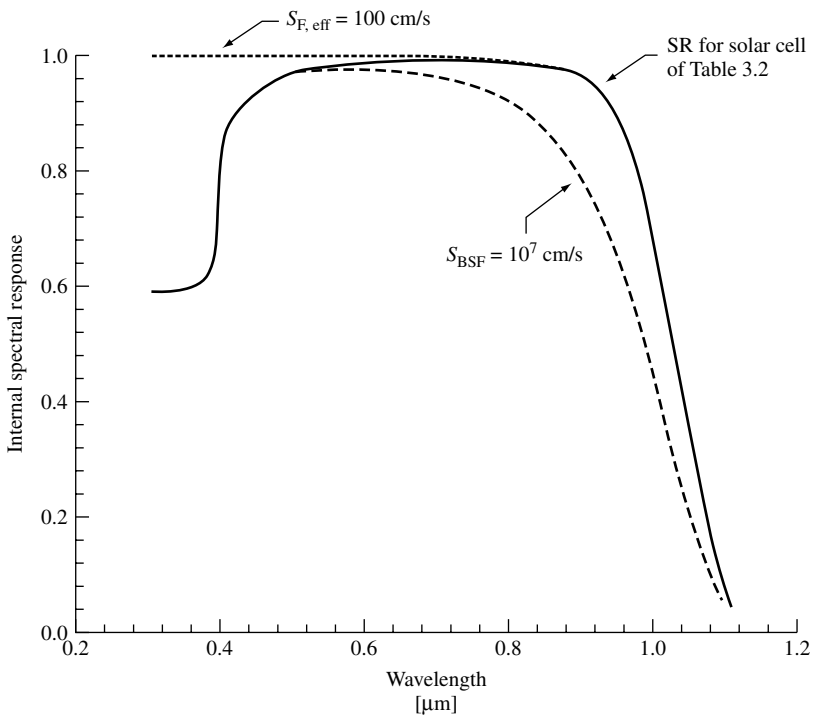


Figure 3.20 Internal spectral response of the silicon solar cell defined in Table 3.2

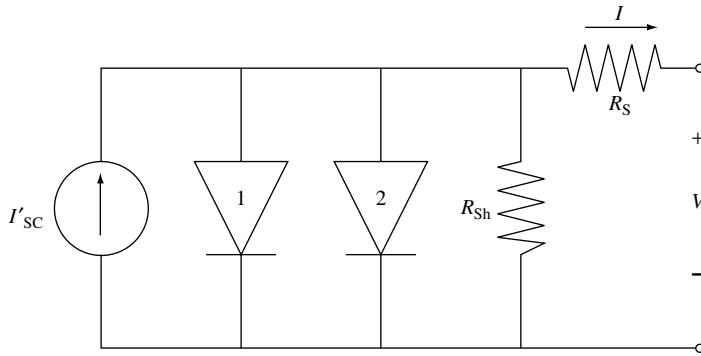


Figure 3.21 Solar cell circuit model including the parasitic series and shunt resistances

since the absorption coefficient is highest for short wavelength (high energy) photons. Conversely, removing the BSF makes it more likely that electrons created deep within the base region of the solar cell (those created by the long wavelength, low-energy photons) will recombine at the back contact and therefore, the long wavelength response is dramatically reduced.

3.5.3 Parasitic Resistance Effects

Equation (3.130) neglects the parasitic series and shunt resistances typically associated with real solar cells. Incorporating these resistances into the circuit model of Figure 3.15, as shown in Figure 3.21, yields

$$I = I'_{SC} - I_{o1}(e^{q(V+IR_S)/kT} - 1) - I_{o2}(e^{q(V+IR_S)/2kT} - 1) - \frac{(V + IR_S)}{R_{Sh}} \quad (3.149)$$

where I'_{SC} is the short-circuit current when there are no parasitic resistances. The effect of these parasitic resistances on the $I-V$ characteristic is shown in Figures 3.22 and 3.23. As can also be seen in equation (3.149), the shunt resistance, R_{Sh} , has no effect on the short-circuit current, but reduces the open-circuit voltage. Conversely, the series resistance, R_S , has no effect on the open-circuit voltage, but reduces the short-circuit current. Sources of series resistance include the metal contacts, particularly the front grid, and the transverse flow of current in the solar cell emitter to the front grid.

It is often more convenient to rewrite equation (3.149) as

$$I = I'_{SC} - I_o(e^{q(V+IR_S)/A_o kT} - 1) - \frac{(V + IR_S)}{R_{Sh}} \quad (3.150)$$

where A_o is the diode ideality (quality) factor and typically has a value between 1 and 2, with $A_o \approx 1$ for diode dominated by recombination in the quasi-neutral regions and $A_o \rightarrow 2$ when recombination in the depletion region dominates. In solar cells where the

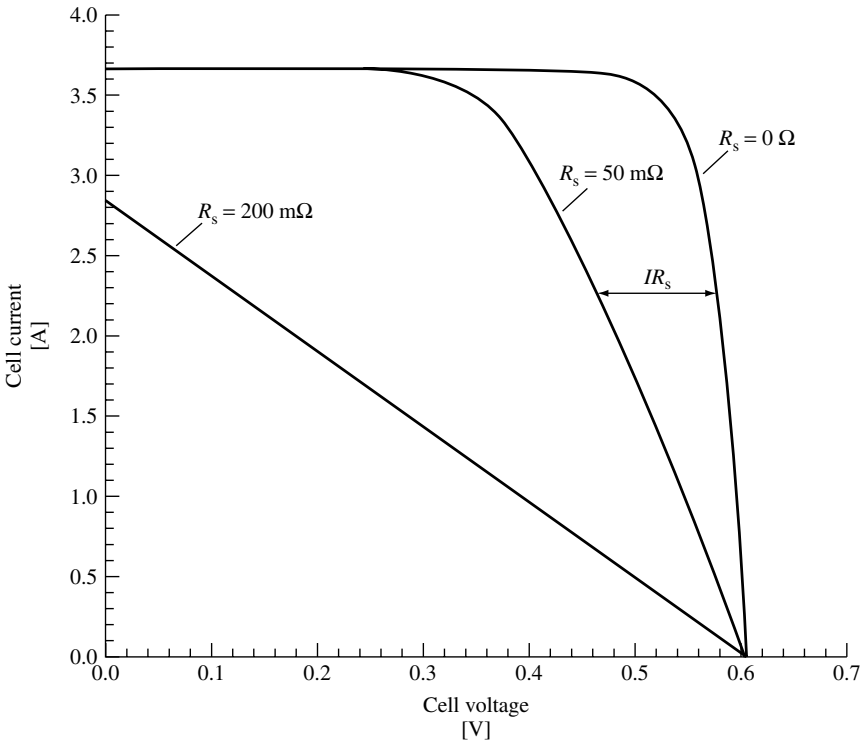


Figure 3.22 Effect of series resistance on the current–voltage characteristic of a solar cell ($R_{Sh} \rightarrow \infty$)

recombination in each region is comparable, A_o is somewhere in-between. At short circuit, equation (3.150) becomes

$$I_{SC} = I'_{SC} - I_o(e^{qI_{SC}R_s/A_o kT} - 1) - I_{SC}R_s/R_{Sh} \tag{3.151}$$

and at open circuit, it becomes

$$0 = I'_{SC} - I_o(e^{V_{OC}/A_o kT} - 1) - V_{OC}/R_{Sh}. \tag{3.152}$$

When $\log(I_{SC})$ is plotted versus V_{OC} (where I_{SC} and V_{OC} are obtained over a range of illumination intensities), there is typically a regime where neither the series nor shunt resistances are important, as illustrated in Figure 3.24. The slope of this line will yield the diode ideality factor A_o , while the y-intercept will give I_o . In the regime where only series resistance is important, equations (3.151) and (3.152) can be combined to give

$$I_{SC}R_s = \frac{A_o kT}{q} \ln \left[\frac{I_o e^{qV_{OC}/A_o kT} - I_{SC}}{I_o} \right] \tag{3.153}$$

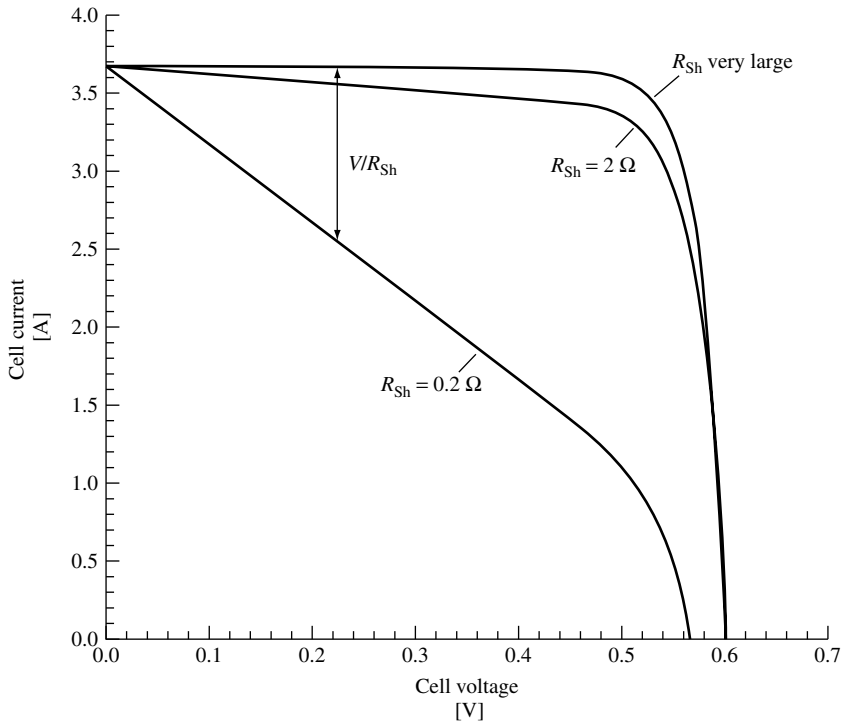


Figure 3.23 Effect of shunt resistance on the current–voltage characteristic of a solar cell ($R_S = 0$)

and a plot of I_{SC} versus $\log[I_o e^{qV_{OC}/A_o kT} - I_{SC}]$ will then permit R_S to be extracted from the slope of this line. Similarly, in the regime where only R_{Sh} is important, equations (3.151) and (3.152) can be combined to give

$$\frac{V_{OC}}{R_{Sh}} = I_{SC} - I_o e^{qV_{OC}/A_o kT} \quad (3.154)$$

and R_{Sh} can be determined from the slope of the line given by plotting V_{OC} versus $[I_{SC} - I_o e^{qV_{OC}/A_o kT}]$. If the series and shunt resistances are such that there is no regime where they can be neglected, the parameters can, with patience, be extracted through the process of trial and error.

3.5.4 Temperature Effects

From equations (3.127) and (3.128), it is apparent that

$$I_{o1,n}, I_{o1,p} \propto n_i^2 \quad (3.155)$$

and from equation (3.129) that

$$I_{o2} \propto n_i. \quad (3.156)$$

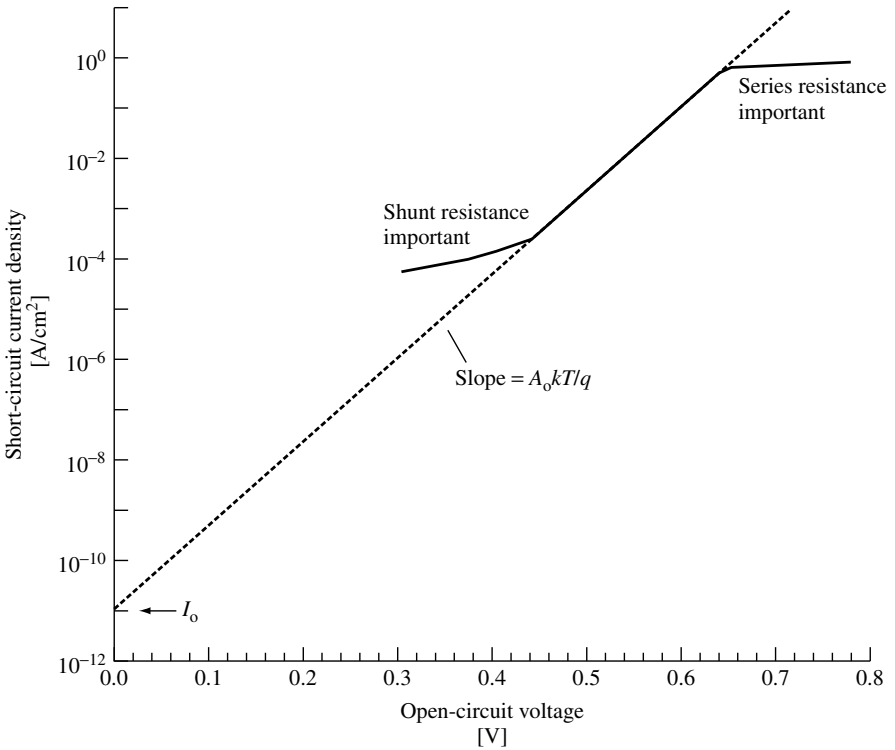


Figure 3.24 Short-circuit current versus open-circuit voltage plot illustrating parameter extraction

An increase in the intrinsic carrier concentration increases the dark saturation (recombination) current and results in a decrease in the open-circuit voltage, as can be seen from equation (3.140). The dark saturation current contains other temperature-dependent terms (D , τ , and S), but the temperature dependence of the intrinsic carrier concentration dominates. The intrinsic carrier concentration is given by equation (3.18), which when combined with equations (3.13) and (3.14) yields

$$n_i = 2(m_n^* m_p^*)^{3/4} \left(\frac{2\pi kT}{h^2} \right)^{3/2} e^{-E_G/2kT}. \tag{3.157}$$

The effective masses are generally taken to be weak functions of temperature. The band gap decreases with temperature and its temperature dependence is well modeled by

$$E_G(T) = E_G(0) - \frac{\alpha T^2}{T + \beta}. \tag{3.158}$$

where α and β are constants specific to each semiconductor. It is clear that as the temperature increases, n_i increases, and thus recombination increases, and cell performance is impaired. Band gap narrowing, referred to earlier, is a reduction in band gap due to high doping and also serves to increase n_i and impair solar cell performance.

The open-circuit current expression, equation (3.140), can be rearranged and the temperature dependence explicitly included to give

$$I_{SC} \approx I_{01} e^{qV_{OC}/kT} \approx BT^\zeta e^{-E_G(0)/kT} e^{qV_{OC}/kT} \quad (3.159)$$

where B is a temperature-independent constant and $T^\zeta e^{-E_G(0)/kT}$ accounts for the temperature dependence of the saturation current. The short-circuit current is relatively unaffected by temperature under typical operating conditions, so by differentiating with respect to T , the temperature dependence of the open-circuit voltage can be expressed as [15]

$$\frac{dV_{OC}}{dT} = -\frac{\frac{1}{q}E_G(0) - V_{OC} + \zeta \frac{kT}{q}}{T} \quad (3.160)$$

which for silicon at 300 K corresponds to about $-2.3 \text{ mV}/^\circ\text{C}$. Equation (3.159) can be rearranged as follows:

$$V_{OC}(T) = \frac{1}{q}E_G(0) - \frac{kT}{q} \ln \left(\frac{BT^\zeta}{I_{SC}} \right). \quad (3.161)$$

V_{OC} varies roughly linearly and inversely with temperature and an extrapolation of V_{OC} to $T = 0$ is approximately the band gap since $\lim_{T \rightarrow 0} [T \ln T] = 0$.

3.5.5 Concentrator Solar Cells

Operating solar cells under concentrated illumination offers two main advantages. The first is that since fewer solar cells are required to collect the sunlight falling on a given area, their cost of manufacture can be higher than that for cells designed for nonconcentrated illumination, and they are therefore presumably of higher quality (efficiency). The second is that operation under concentrated illumination offers an advantage in the solar cell efficiency. If sunlight is concentrated by a factor of X (X sun illumination), the short circuit at that concentration is

$$I_{SC}^{X\text{suns}} = XI_{SC}^{1\text{sun}}. \quad (3.162)$$

This is assuming that the semiconductor parameters are unaffected by the illumination level and that the cell temperature is the same at both levels of illumination – not necessarily valid assumptions especially at very large X , that is, $X > 100$. However, these assumptions will allow the demonstration of the potential efficiency of concentrator solar cells. Substituting equation (3.162) into equation (3.135) gives

$$\eta = \frac{FF^{X\text{suns}} V_{OC}^{X\text{suns}} I_{SC}^{X\text{suns}}}{P_{in}^{X\text{suns}}} = \frac{FF^{X\text{suns}} V_{OC}^{X\text{suns}} X I_{SC}^{1\text{sun}}}{X P_{in}^{1\text{sun}}} = \frac{FF^{X\text{suns}} V_{OC}^{X\text{suns}} I_{SC}^{1\text{sun}}}{P_{in}^{1\text{sun}}} \quad (3.163)$$

From equation (3.131),

$$V_{OC}^{X\text{suns}} = V_{OC}^{1\text{sun}} + \frac{kT}{q} \ln X. \quad (3.164)$$

The FF is a function of V_{OC} (equation 3.134), so

$$\eta^{X\text{suns}} = \eta^{1\text{sun}} \left(\frac{FF^{X\text{suns}}}{FF^{1\text{sun}}} \right) \left(1 + \frac{\frac{kT}{q} \ln X}{V_{OC}^{1\text{sun}}} \right). \quad (3.165)$$

Both factors multiplying the 1 sun efficiency increase as the illumination concentration increases. Therefore, the efficiency of concentrator cells increases as the illumination concentration increases, as shown in Figure 3.25.

Of course, there are many obstacles to achieving this. Concentrator cells must be cooled, since an increase in operating temperature reduces V_{OC} , and hence the cell efficiency. The $FF^{X\text{suns}}$ eventually decreases with increasing X and current due to the parasitic series resistance. Concentrator solar cells are discussed in more detail in Chapter 11.

3.5.6 High-level Injection

In high-level injection, the excess carrier concentrations greatly exceed the doping in the base region, so $\Delta p \approx \Delta n \approx n \approx p$ if the carriers are moving generally in the same direction. This occurs with back-contact solar cells, such as the silicon point-contact solar

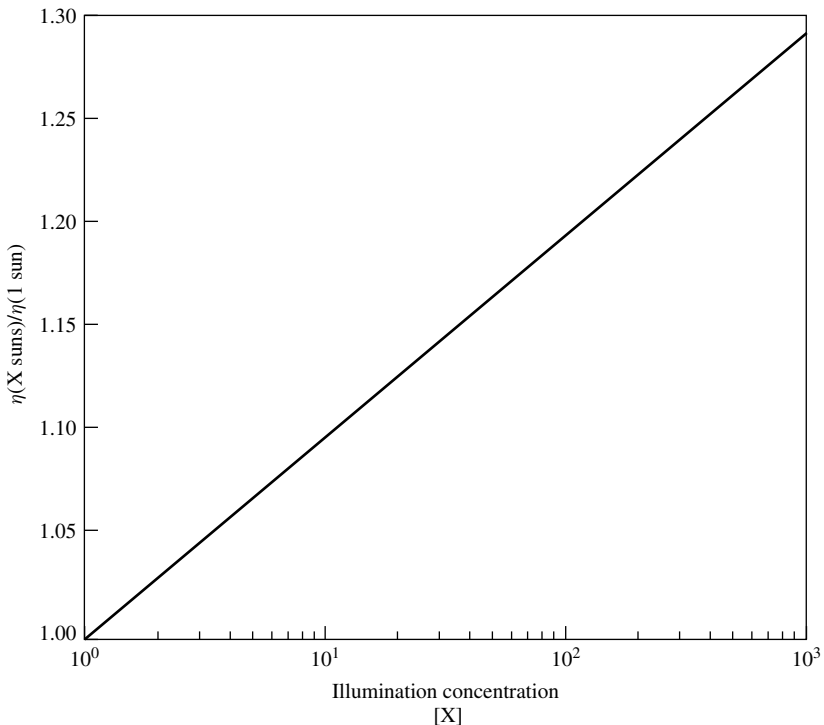


Figure 3.25 Relative efficiency as a function of illumination concentration

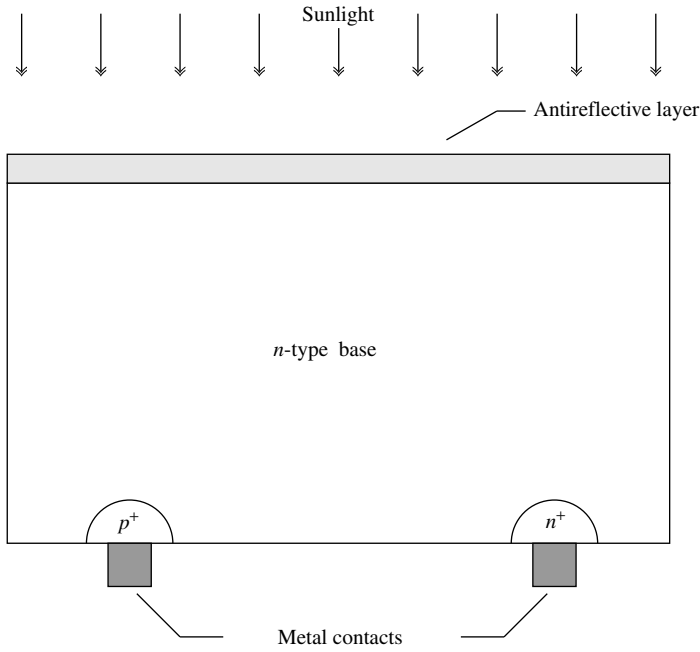


Figure 3.26 Schematic of a back-contact solar cell

cell [22], as illustrated in Figure 3.26. Since both electrical contacts are on the back, there is no grid shadowing. These cells are typically used in concentrator application and high-level injection conditions pervade. Assuming high-level injection, a simple analysis is possible.

Returning to equations (3.76) and (3.77), it can be seen that in high-level injection, the electric field can be eliminated (it is not necessarily zero), resulting in the ambipolar diffusion equation

$$D_a \frac{d^2 p}{dx^2} - \frac{p}{\tau_n + \tau_p} = -G(x), \quad (3.166)$$

where the ambipolar diffusion coefficient is given by

$$D_a = \frac{2D_n D_p}{D_n + D_p}. \quad (3.167)$$

The ambipolar diffusion coefficient is always less than the larger diffusion coefficient and greater than the smaller one.

In silicon, where $D_n/D_p \approx 3$ over a wide range of doping, the ambipolar diffusion coefficient is $D_a \approx 3/2D_p \approx 1/2D_n$ and, if we also assume $\tau_p \approx \tau_n$, the ambipolar diffusion length is

$$L_a \approx \sqrt{3}L_p \approx L_n. \quad (3.168)$$

Thus, the increased high-injection lifetime (see equation 3.40) offsets the reduced ambipolar diffusion coefficient.

It is crucial that the front surface of a back-contacted cell be well passivated, so we will assume that $S_F = 0$. We will further assume that optical generation is uniform throughout the base region. At open circuit, with these assumptions, $d^2 p/dx^2 = 0$ and therefore

$$V_{OC} = \frac{2kT}{q} \ln \left[\frac{G(\tau_n + \tau_p)}{n_i} \right]. \quad (3.169)$$

The short-circuit current (with $p \simeq 0$ at the back of the cell) is

$$I_{SC} = qAL_aG \sinh(W_B/L_a) \quad (3.170)$$

which, when $L_a \gg W_B$, becomes

$$I_{SC} = qAW_BG. \quad (3.171)$$

3.5.7 *p-i-n* Solar Cells

The *p-i-n* solar cell takes advantage of the fact that in many semiconductor materials, especially direct band gap semiconductors (i.e. large absorption coefficient), most of the electron–hole pairs are created very near the surface. If an intrinsic (undoped) layer is placed between the (very thin) *n* and *p* regions, the depletion region thickness is the most significant fraction of the total solar cell thickness, as illustrated in Figure 3.27. Carrier collection is now aided by the electric field in the depletion region, which helps offset the low lifetimes in some materials, such as amorphous silicon (see Chapter 12). The *I*–*V* characteristic of a *p-i-n* solar cell can be described with minor modifications to the previously derived expressions. The most significant modification is to equation (3.129) where the depletion width is now written as

$$W_D = \chi_N + W_I + \chi_P \quad (3.172)$$

where W_I is the thickness of the intrinsic layer. Since χ_N and χ_P are very thin, short-base approximations are in order for equations (3.127) and (3.128). Also, there is no BSF ($S_{BSF} \rightarrow \infty$).

3.5.8 Detailed Numerical Modeling

While analytic solutions such as those discussed thus far in this chapter provide an intuitive understanding of solar cell performance and are therefore very important, they are limited in their accuracy due to the many simplifying assumptions that must be made in order to obtain them. It is rather straightforward to solve the semiconductor equations numerically without the need to make so many simplifications. Several computer codes have been written that solve the semiconductor equations for the explicit purpose of modeling solar cells – PC-1D [23], AMPS [24], ADEPT [25], and its predecessors [16, 26, 27], for example. The basic design of these computer programs is very similar. The semiconductor

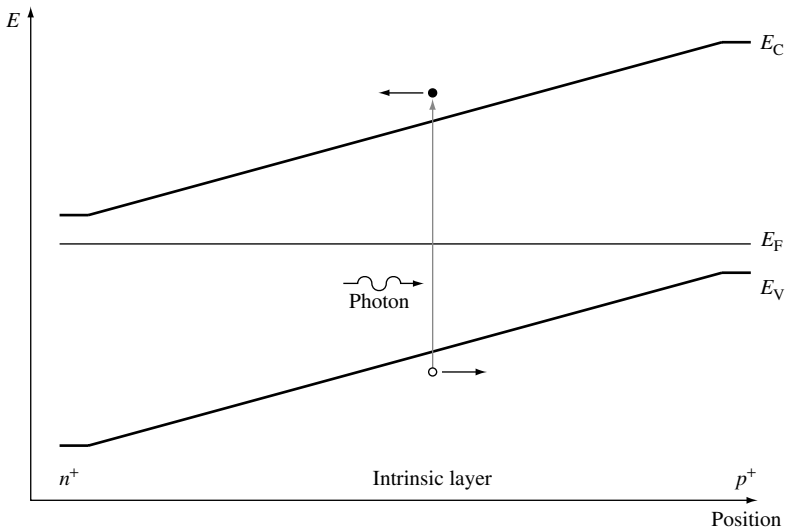


Figure 3.27 Band diagram of a p - i - n solar cell illustrating field-enhanced collection

equations (three coupled nonlinear partial differential equations) are cast in a normalized form [28] to simplify the calculations. Finite difference or finite element methods are then used to discretize the equations on a mesh (grid), resulting in a set of three coupled nonlinear difference equations. Using appropriately discretized boundary conditions, these equations are solved iteratively using a generalized Newton method to obtain the carrier concentrations and electric potential at each mesh point. Each Newton iteration involves the solution of a very large matrix equation of order $3N$, where N is the number of mesh points. One-dimensional simulations typically utilize on the order of 1000 mesh points, so the matrix is 3000×3000 . In 2D, the minimum mesh is typically at least 100×100 , so $N = 10^4$ and the matrix is of order 3×10^4 and contains 9×10^8 elements. Fortunately, the matrices are sparse and can be solved using considerably less computer memory than one would expect at first glance.

Numerical simulation allows analysis of solar cell designs and operating conditions for which simple analytic expressions are inadequate. The necessity of ignoring the spatial variation of parameters is eliminated and more accurate representations of the solar cell are possible. In particular, nonuniform doping, heterojunction solar cells (band gap varies spatially), amorphous silicon solar cells (complex trapping/recombination mechanisms, field-assisted collection), and concentrator solar cells (high-level injection, 2D/3D effects) can all be modeled with more precision.

3.6 SUMMARY

It has been the objective of this chapter to give the reader a basic understanding of the physical principles that underlie the operation of solar cells. Toward that end, the fundamental physical characteristics of solar cell materials that permit the conversion of light into electricity have been reviewed. These characteristics include the ability of

semiconductors to absorb photons by conferring that energy to carriers of electrical current and the ability of semiconductor materials to conduct electricity.

The basic operating principles of the solar cell (a carefully designed *pn*-junction diode) were derived from the (simplified) equations describing the dynamics of holes and electrons in semiconductors. This led to the definition of the solar cell figures of merit – the open-circuit voltage (V_{OC}), the short-circuit current (I_{SC}), the fill factor (FF), and the cell efficiency (η). The two key factors determining solar cell efficiency – electron–hole pair generation and recombination – were identified and discussed. In particular, the need to minimize all sources of recombination in the solar cells was demonstrated through examples and by way of a simple analogy.

The importance of matching the band gap of the solar cell material to the solar spectrum was also discussed and it was shown that silicon, with a band gap of 1.12 eV, is an excellent match to the solar spectrum. The effects of parasitic resistances and temperature on solar cell performance were examined and, finally, some advanced cell concepts were briefly introduced. Many of these topics will be expanded upon in the following chapters of this handbook.

REFERENCES

1. Green M, *Solar Cells: Operating Principles, Technology, and System Applications*, Chap. 1, Prentice Hall, Englewood Cliffs, NJ, 1–12 (1982).
2. Pierret R, in Pierret R, Neudeck G (Eds), *Modular Series on Solid State Devices, Volume VI: Advanced Semiconductor Fundamentals*, Addison-Wesley, Reading, MA (1987).
3. Sze S, *Physics of Semiconductor Devices*, 2nd Edition, John Wiley & Sons, New York, NY (1981).
4. Böer K, *Survey of Semiconductor Physics: Electrons and Other Particles in Bulk Semiconductors*, Van Nostrand Reinhold, New York, NY (1990).
5. Shur M, *Physics of Semiconductor Devices*, Prentice Hall, Englewood Cliffs, NJ (1990).
6. Singh J, *Physics of Semiconductors and Their Heterostructures*, McGraw-Hill, New York, NY (1993).
7. Pierret R, *Semiconductor Device Fundamentals*, Chap. 2, Addison-Wesley, Reading, MA, 23–74 (1996).
8. Slotboom J, De Graff H, *Solid-State Electron.* **19**, 857–862 (1976).
9. Pankove J, *Optical Processes in Semiconductors*, Chap. 3, Dover Publications, New York, NY, 34–81 (1971).
10. Sanii F, Giles F, Schwartz R, Gray J, *Solid-State Electron.* **35**, 311–317 (1992).
11. Pierret R, in Pierret R, Neudeck G (Eds), *Modular Series on Solid State Devices, Volume VI: Advanced Semiconductor Fundamentals*, Chap. 5, Addison-Wesley, Reading, MA, 139–179 (1987).
12. Pierret R, in Pierret R, Neudeck G (Eds), *Modular Series on Solid State Devices, Volume VI: Advanced Semiconductor Fundamentals*, Chap. 6, Addison-Wesley, Reading, MA (1987).
13. Van Roosbroeck W, *Bell Syst. Tech. J.* **29**, 560–607 (1950).
14. Lundstrom M, Schulke R, *IEEE Trans. Electron Devices* **30**, 1151–1159 (1983).
15. Green M, *Solar Cells: Operating Principles, Technology, and System Applications*, Chap. 5, Prentice Hall, Englewood Cliffs, NJ, 85–102 (1982).
16. Gray J, *Two-Dimensional Modeling of Silicon Solar Cells*, Ph.D. thesis, Purdue University, West Lafayette, IN (1982).
17. Gray J, Schwartz R, *Proc. 18th IEEE Photovoltaic Specialist Conf.*, 568–572 (1985).

18. Mathers C, *J. Appl. Phys.* **48**, 3181, 3182 (1977).
19. Shockley W, Queisser H, *J. Appl. Phys.* **32**, 510 (1961).
20. Baraona C, Brandhorst Jr. H, *Proc. 11th IEEE Photovoltaic Specialist Conf.*, 44–48 (1975).
21. Chai A, *Proc. 14th IEEE Photovoltaic Specialist Conf.*, 156–160 (1980).
22. Sinton R, Kwark Y, Swanson R, *Proc. 18th IEEE Photovoltaic Specialist Conf.*, 61–64 (1984).
23. Rover D, Basore P, Thorson G, *Proc. 18th IEEE Photovoltaic Specialist Conf.*, 703–709 (1984).
24. Rubinelli F *et al.*, *Proc. 22nd IEEE Photovoltaic Specialist Conf.*, 1405–1408 (1991).
25. Gray J, *Proc. 22nd IEEE Photovoltaic Specialist Conf.*, 436–438 (1991).
26. Lundstrom M, *Numerical Analysis of Silicon Solar Cells*, Ph.D. thesis, Purdue University, West Lafayette, IN (1980).
27. Gray J, *IEEE Trans. Electron Devices* **36**, 906–912 (1989).
28. Snowden C, *Introduction to Semiconductor Device Modeling*, Chap. 2, World Scientific, Singapore, 14–36 (1986).

4

Theoretical Limits of Photovoltaic Conversion

Antonio Luque and Antonio Martí

Instituto de Energía Solar, UPM, Spain

4.1 INTRODUCTION

Efficiency is an important matter in the photovoltaic (PV) conversion of solar energy because the sun is a source of power whose density is not very low, so it gives some expectations on the feasibility of its generalised cost-effective use in electric power production. However, this density is not so high as to render this task easy. After a quarter of a century of attempting it, cost still does not allow a generalised use of this conversion technology.

Efficiency forecasts have been carried out from the very beginning of PV conversion to guide the research activity. In solar cells the efficiency is strongly related to the generation of electron–hole pairs caused by the light, and their recombination before being delivered to the external circuit at a certain voltage. This recombination is due to a large variety of mechanisms and cannot be easily linked to the material used to make the cell. Nevertheless, already in 1975 Lofersky [1] had established an empirical link that allowed him to predict which materials were most promising for solar cell fabrication.

In 1960, Shockley and Queisser [2] pointed out that the ultimate recombination mechanisms – impossible to avoid – was just the detailed balance counterpart of the generation mechanisms. This allowed them to determine the maximum efficiency to be expected from a solar cell. This efficiency limit (40.7% for the photon spectrum approximated by a black body at 6000 K) is not too high because solar cells make rather ineffective use of the sun's photons. Many of them are not absorbed, and the energy of many of the absorbed ones is only poorly exploited.

Revisiting the topic of efficiency limits is pertinent because today there are renewed attempts to invent and develop novel concepts in solar cells – sometimes known as

third-generation cells [3] – aimed towards obtaining a higher efficiency. The oldest of them, and well established today, is the use of multijunction solar cells, to be studied in detail in Chapter 9 of this book. However, novel attempts are favoured by the general advancement of science and technology that puts new tools in the inventor’s hands, such as nanotechnology, not available just a decade ago.

Conventional solar cells are semiconductor devices in which an interaction between electrons and holes is produced by absorption of light photons in order to produce electric work. Unlike solar thermal converters, they can operate at room temperature.¹ In this chapter we shall start by presenting some of the irreversible thermodynamic background regarding the photon–electron interaction. Special attention is paid to the conditions for complying with the second law of the thermodynamics as a guide for new device inventors.

This thermodynamic approach will give us the efficiency that a certain solar converter can obtain under certain ideal conditions. This will be applied not only to the present solar cells but also to a number of proposed new converters, some of them actually tried experimentally and some not.

The solar converter theory developed in this chapter looks very different from the one presented in Chapter 3 and is complementary to it. There the solar cell will be analysed in a solid-state physics context, on the basis of electric carrier transport and recombination, taking into account the subtleties that a given material may impose. In this chapter all materials will be considered ideal, entropy-producing mechanisms will be reduced to those inherent to the concept being studied and all other mechanisms will be ignored. In this way, the efficiencies given in this chapter are to be considered as upper bounds of the solar cells studied both in Chapter 3 and the remaining chapters of this book. The lower values found there are not necessarily due to poor technology. They may be fundamental when linked to the actual materials and processes used to manufacture real solar cells. However, they are not fundamental in the sense that other materials and processes could, in principle, be found where different materials or process limitations will apply, which perhaps might be less restrictive.

4.2 THERMODYNAMIC BACKGROUND

4.2.1 Basic Relationships

Thermodynamics defines a state function for a system in equilibrium. This function can be the entropy, the internal energy, the canonical grand potential, the enthalpy and so on, all of them mutually equivalent, containing the same information of the system and related to each other through the Legendre’s transformation [4]. The variables used to describe the macroscopic state of a system are divided into *extensive* (volume U , number of particles N , entropy S , internal energy E , etc.) and *intensive* (pressure P , electrochemical potential μ , temperature T , etc.) variables. A number of relationships may be written with them. For instance,

$$dE = T dS - P dU + \mu dN \quad (4.1)$$

¹ Solar cells usually operate at some 40 to 60°C, but there is nothing theoretical against improving cooling to reach a cell temperature as close to the ambient one as desired.

For our purposes it is convenient to choose the grand potential Ω as our preferred state function. It is the state function that describes the state of a system when the electrochemical potential, the volume and the temperature are chosen as independent variables. It is also the Legendre transform of the energy with respect to the temperature and the electrochemical potential:

$$\Omega \doteq E - TS - \mu N = -PU \quad (4.2)$$

Its definition is given by the equal-by-definition sign (\doteq). The right-hand equality represents a property proven with generality [5].

Other thermodynamic variables that characterise the system in equilibrium can be obtained from the grand potential as derivatives. Hence, the number of particles, entropy and pressure of the system under consideration can be obtained as

$$N = - \left. \frac{\partial \Omega}{\partial \mu} \right|_{U,T}; \quad S = - \left. \frac{\partial \Omega}{\partial T} \right|_{U,\mu}; \quad P = - \left. \frac{\partial \Omega}{\partial U} \right|_{\mu,T} \quad (4.3)$$

For describing systems in non-equilibrium, the system under study is assumed to be subdivided into small subsystems each one comprising an elementary volume in the space-of-phases² (x, y, z, v_x, v_y, v_z) and having a size sufficient to allow the definition of thermodynamic magnitudes in it. Within such volumes, the subsystems are assumed to be in equilibrium. Thus, thermodynamic magnitudes are dependent on the position $\mathbf{r} \doteq (x, y, z)$ of the elementary volume and the velocity of motion $\mathbf{v} \doteq (v_x, v_y, v_z)$ of the elementary bodies or particles in it.

For describing the system in non-equilibrium, it is necessary to introduce the concept of *thermodynamic current densities* [6], \mathbf{j}_x . They are related to the extensive variables X and are defined for those elementary bodies with velocity \mathbf{v} at the point \mathbf{r} as follows:

$$\mathbf{j}_x(\mathbf{r}, \mathbf{v}) = x(\mathbf{r}, \mathbf{v}) \mathbf{v} \quad (4.4)$$

where $x = X/U$ is the contribution to the extensive variable X , per unit of volume U at the point \mathbf{r} of the elementary bodies with velocity \mathbf{v} .

Equation (4.2) can be applied to the thermodynamic current densities allowing us to write

$$\mathbf{j}_\omega = \mathbf{j}_e - T(\mathbf{r}, \mathbf{v})\mathbf{j}_s - \mu(\mathbf{r}, \mathbf{v})\mathbf{j}_n = -P(\mathbf{r}, \mathbf{v}) \mathbf{v} \quad (4.5)$$

For the thermodynamic current densities, we can write the following continuity equations [7]:

$$g \doteq \frac{\partial n}{\partial t} + \nabla \cdot \mathbf{j}_n \quad (4.6)$$

$$v \doteq \frac{\partial e}{\partial t} + \nabla \cdot \mathbf{j}_e \quad (4.7)$$

$$\sigma \doteq \frac{\partial s}{\partial t} + \nabla \cdot \mathbf{j}_s \quad (4.8)$$

² x, y and z are the spatial co-ordinates giving the position of the particle and v_x, v_y and v_z are the co-ordinates of its velocity.

where g , ν and σ are formally defined as the number of particles, energy and entropy generation rates per unity of volume. The symbol “ $\nabla \cdot$ ” is the divergence operator.³

4.2.2 The Two Laws of Thermodynamics

Equations (4.7) and (4.8) have close links with the laws of thermodynamics. A certain elementary subsystem or body can draw energy from or release energy to another body close to it, but the first law of thermodynamics states that the sum of the energies generated at all the i elementary bodies at a given position \mathbf{r} must be zero, that is,

$$\sum_i \nu(\mathbf{r}, \mathbf{v}_i) = 0 \quad (4.9)$$

In the same way, the entropy generated by an elementary body can possibly be negative, but the second law of thermodynamics, as stated by Prigogine [7], determines that the sum of all the entropy generated by all the bodies, σ_{irr} , must be non-negative everywhere.

$$\sum_i \sigma(\mathbf{r}, \mathbf{v}_i) = \sigma_{\text{irr}}(\mathbf{r}) \geq 0 \quad (4.10)$$

4.2.3 Local Entropy Production

It is illustrative to have a look at the sources for entropy production. Using equation (4.2) in the basic thermodynamic relationship of equation (4.1), we obtain an interesting relationship between thermodynamic variables per unity of volume:

$$ds = \frac{1}{T} de - \frac{\mu}{T} dn \quad (4.11)$$

If this relationship and equation (4.5) are substituted in equation (4.8), we find that

$$\sigma = \frac{1}{T} \frac{\partial e}{\partial t} - \frac{\mu}{T} \frac{\partial n}{\partial t} + \nabla \cdot \left(\frac{1}{T} \mathbf{j}_e - \frac{1}{T} \mathbf{j}_w - \frac{\mu}{T} \mathbf{j}_n \right) \quad (4.12)$$

Introducing equations (4.6) and (4.7) in (4.12) and after some mathematical handling we obtain that [8]

$$\sigma = \frac{1}{T} \nu + \mathbf{j}_e \nabla \frac{1}{T} - \frac{\mu}{T} g - \mathbf{j}_n \nabla \frac{\mu}{T} + \nabla \cdot \left(-\frac{1}{T} \mathbf{j}_w \right) \quad (4.13)$$

where “ ∇ ” is the gradient operator.⁴ This is an important equation allowing us to identify the possible sources of entropy generation in a given subsystem. It contains terms involving energy generation (from another subsystem: ν) and transfer (from the surroundings:

³ The linear unbounded operator “ $\nabla \cdot$ ” applied to the vector $\mathbf{A} \doteq (A_x, A_y, A_z)$ is defined as $\nabla \cdot \mathbf{A} = \frac{\partial A_x}{\partial x} + \frac{\partial A_y}{\partial y} + \frac{\partial A_z}{\partial z}$.

⁴ The gradient operator, “ ∇ ,” (without being followed by a dot) is a linear unbounded operator whose actuation on a scalar field $f(x, y, z)$ is defined as $\nabla f = \frac{\partial f}{\partial x} \mathbf{e}_1 + \frac{\partial f}{\partial y} \mathbf{e}_2 + \frac{\partial f}{\partial z} \mathbf{e}_3$ where $\mathbf{e}_1, \mathbf{e}_2, \mathbf{e}_3$ are the orthonormal basis vectors of the Cartesian framework being used as reference.

$\mathbf{j}_e \nabla 1/T$), free energy (μg) generation, Joule effect ($\mathbf{j}_n \nabla \mu$) and expansion of the volume that contains the particles ($\nabla \mathbf{j}_\omega/T$). This equation is very important and will be used to prove the thermodynamic consistence of solar cells.

4.2.4 An Integral View

Fluxes, \dot{X} , of the thermodynamic currents, \mathbf{j}_x , will be frequently used in this paper. In this text, they will be also called *thermodynamic variable rates*. By definition, the following relationship exists:

$$\dot{X} \doteq \int_A \sum_i \mathbf{j}_x \, dA \quad (4.14)$$

where the sum refers to the different subsystems with different velocities to be found at a given position. A is the surface through which the flux is calculated. Actually, $\mathbf{j}_x \, dA$ represents the scalar product of the current density vector \mathbf{j}_x and the oriented surface element dA (orientation is arbitrary and if a relevant volume exists the orientation selected leads to the definition of *escaping* or *entering* rates).

4.2.5 Thermodynamic Functions of Radiation

The number of photons in a given mode of radiation is given [9] by the well-known Bose–Einstein factor $f_{\text{BE}} = \{\exp[(\varepsilon - \mu)/kT] - 1\}^{-1}$, which through equation (4.3) is related to the grand canonical potential $\Omega = kT \ln\{\exp[(\mu - \varepsilon)/kT] - 1\}$. In these equations, most of the symbols have been defined earlier: ε is the photon energy in the mode and k is the Boltzman constant. The corresponding thermodynamic current densities for these photons are

$$\mathbf{j}_n = f_{\text{BE}} \mathbf{c}/(Un_r); \quad \mathbf{j}_e = \varepsilon \mathbf{j}_n f_{\text{BE}} \mathbf{c}/(Un_r); \quad \mathbf{j}_\omega = \Omega \mathbf{c}/(Un_r) \quad (4.15)$$

where \mathbf{c} is the light velocity (a vector since it includes its direction) in the vacuum and n_r is the index of refraction of the medium in which the photons propagate, which is assumed to be independent of the direction of propagation. Thus, \mathbf{c}/n_r is the velocity of the photons in the medium.

The number of photon modes with energy between ε and $\varepsilon + d\varepsilon$ is $8\pi Un_r^3 \varepsilon^2 / (h^3 \mathbf{c}^2) d\varepsilon$. When the modes with energies $\varepsilon_m < \varepsilon < \varepsilon_M$ are taken into account, the total grand canonical potential of the photons, Ω_{ph} , associated with these modes is the sum of the contributions from each mode and can be written as

$$\Omega_{\text{ph}}(U, T, \mu) = \frac{8\pi Un_r^3}{h^3 \mathbf{c}^3} \int_{\varepsilon_m}^{\varepsilon_M} \varepsilon^2 kT \ln(1 - e^{(\mu - \varepsilon)/kT}) d\varepsilon \quad (4.16)$$

where h is the Planck's constant.

Photons do not interact among themselves, such that temperatures and chemical potentials can be different for each mode. This means that they can be a function of the energy and of the direction of propagation. In the non-equilibrium case they can also be a

function of the position. If we only take into account the photons' propagation in a small solid angle $d\varpi$, the grand potential in equation (4.16) must be multiplied by $d\varpi/4\pi$. The same coefficient affects other thermodynamic variables of the radiation.

The flux of a thermodynamic variable X of the radiation through a surface A with a solid angle ϖ is then given by

$$\dot{X} = \int_A \sum_i j_x dA = \int_{A,\varpi} \frac{1}{4\pi} \frac{X}{U} \frac{c}{n_r} \cos \theta d\varpi dA = \int_H \frac{1}{4\pi} \frac{X}{U} \frac{c}{n_r^3} dH \quad (4.17)$$

where the angle θ is defined in Figure 4.1. In this case, the sum of equation (4.14) has been substituted by the integration on solid angles. In many cases the integration will be extended to a restricted domain of solid angles. It is, in particular, the case of the photons when they come from a remote source such as the sun.

The differential variable $dH = n_r^2 \cos \theta d\varpi dA$, or its integral on a certain domain (at each position of A it must include the solid angle ϖ containing photons), is the so-called multilinear Lagrange invariant [10]. It is invariant for any optical system [11]. For instance, at the entry aperture of a solar concentrator (think of a simple lens), the bundle of rays has a narrow angular dispersion at its entry since all the rays come from the sun within a narrow cone. Then, they are collected across the whole entry aperture. The invariance for H indicates that it must take the same value at the entry aperture and at the receiver, or even at any intermediate surface that the bundle may cross. If no ray is turned back, all the rays will be present at the receiver. However, if this receiver is smaller than the entry aperture, the angular spread with which the rays illuminate the receiver has to be bigger than the angular spread that they have at the entry. In this way, H becomes a sort of measure of a bundle of rays, similar to its four-dimensional area with two spatial dimensions (in dA) and two angular dimensions (in $d\varpi$). Thus, we may talk of the H_{sr} of a certain bundle of rays linking the sun with a certain receiver.

Besides *Lagrange invariant*, this invariant receives other names. In treatises of thermal transfer it is called *vision* or *view factor*, but Welford and Winston [12] have recovered for this invariant the old name given by Poincaré that in our opinion accurately reflects its properties. He refers to it as *étendue* (extension) of a bundle of rays. We shall adopt in this chapter this name as a shortened denomination for this *multilinear Lagrange invariant*.

When the solid angle of illumination consists of the total hemisphere, $H = n_r^2 \pi A$, where A is the area of the surface traversed by the photons. However, in the absence of optical elements, the photons from the sun reach the converter located on the Earth within

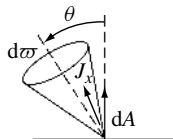


Figure 4.1 Drawing used to show the flux of a thermodynamic variable across a surface element dA

Table 4.1 Several thermodynamic fluxes for photons with energies between ε_m and ε_M distributed according to a black body law determined by a temperature T and chemical potential μ . The last line involves the calculations for a full-energy spectrum ($\varepsilon_m = 0$ and $\varepsilon_M = \infty$). One of the results (the one containing T^4) constitutes the Stefan–Boltzman law

$$\dot{\Omega}(T, \mu, \varepsilon_m, \varepsilon_M, H) = kT \frac{2H}{h^3 c^2} \int_{\varepsilon_m}^{\varepsilon_M} \ln(1 - e^{(\mu-\varepsilon)/kT}) \varepsilon^2 d\varepsilon = \int_{\varepsilon_m}^{\varepsilon_M} \dot{\omega}(T, \mu, \varepsilon, H) d\varepsilon \quad (\text{I-1})$$

$$\dot{N}(T, \mu, \varepsilon_m, \varepsilon_M, H) = \frac{2H}{h^3 c^2} \int_{\varepsilon_m}^{\varepsilon_M} \frac{\varepsilon^2 d\varepsilon}{e^{(\varepsilon-\mu)/kT}} - 1 = \int_{\varepsilon_m}^{\varepsilon_M} \dot{n}(T, \mu, \varepsilon, H) d\varepsilon \quad (\text{I-2})$$

$$\dot{E}(T, \mu, \varepsilon_m, \varepsilon_M, H) = \frac{2H}{h^3 c^2} \int_{\varepsilon_m}^{\varepsilon_M} \frac{\varepsilon^3 d\varepsilon}{e^{(\varepsilon-\mu)/kT}} - 1 = \int_{\varepsilon_m}^{\varepsilon_M} \dot{e}(T, \mu, \varepsilon, H) d\varepsilon \quad (\text{I-3})$$

$$\dot{S} = \frac{\dot{E} - \mu \dot{N} - \dot{\Omega}}{T}; \quad \dot{F} \doteq \dot{E} - T \dot{S} = \mu \dot{N} + \dot{\Omega} \quad (\text{I-4})$$

$$\begin{aligned} \dot{E}(T, 0, 0, \infty, H) &= (H/\pi) \sigma_{\text{SB}} T^4; \quad \dot{S}(T, 0, 0, \infty, H) = (4H/3\pi) \sigma_{\text{SB}} T^3; \\ \sigma_{\text{SB}} &= 5.67 \times 10^{-8} \text{ W m}^{-2} \text{ K}^{-4} \end{aligned} \quad (\text{I-5})$$

a narrow cone of rays. In this case, $H = \pi A \sin^2 \theta_s$, where θ_s is the sun's semi-angle of vision (taking into account the sun's radius and its distance to Earth), which is equal [13] to 0.267° . No index of refraction is used in this case because the photons come from the vacuum.

Fluxes of some thermodynamic variables and some formulas of interest, which can be obtained from the above principles, are collected in Table 4.1.

4.2.6 Thermodynamic Functions of Electrons

For electrons, the number of particles in a quantum state with energy ε is given by the Fermi–Dirac function $f_{\text{FD}} = \{\exp[(\varepsilon - \varepsilon_F)/kT] + 1\}^{-1}$ where the electrochemical potential (the chemical potential including the potential energy due to electric fields) of the electrons is usually called *Fermi level*, ε_F . Unlike photons, electrons are in continuous interaction among themselves, so that finding different temperatures for electrons is rather difficult. In fact, once a monochromatic light pulse is shined on the semiconductor, the electrons or holes thermalise to an internal electron temperature in less than 100 fs. Cooling to the network temperature will take approximately 10 to 20 ps [14]. However, electrons in semiconductors are found in two bands separated by a large energy gap in which electron states cannot be found. The consequence of this is that, in non-equilibrium, different electrochemical potentials, ε_{F_c} and ε_{F_v} (also called *quasi-Fermi levels*), can exist for the electrons in the conduction band (CB) and the valence band (VB), respectively. Sometimes we prefer to refer to the electrochemical potential of the holes (empty states at the VB), which is then equal to $-\varepsilon_{F_v}$. Once the excitation is suppressed, it can even take milliseconds before the two quasi-Fermi levels become a single one, as it is in the case of silicon.

4.3 PHOTOVOLTAIC CONVERTERS

4.3.1 The Balance Equation of a PV Converter

In 1960, Shockley and Queisser (SQ) published an important paper [2] in which the efficiency upper limit of a solar cell was presented. In this article it was pointed out, for the first time in solar cells, that the generation due to light absorption has a detailed balance counterpart, which is the radiative recombination. This SQ efficiency limit, detailed below, occurs in ideal solar cells that are the archetype of the current solar cells. Such cells (Figure 4.2) are made up of a semiconductor with a VB and a CB, more energetic and separated from the VB by the band gap, ε_g . Each band is able to develop separate quasi-Fermi levels, ε_{F_c} for the CB and ε_{F_v} for the VB, to describe the carrier concentration in the respective bands. In the ideal SQ cell the mobility of the carriers is infinite, and since the electron and hole currents are proportional to the quasi-Fermi level gradients, it follows that the quasi-Fermi levels are constant. Contact to the CB is made by depositing a metal on an n^+ -doped semiconductor. The carriers going through this contact are mainly electrons due to the small hole density. The few holes passing through this contact are accounted for as surface recombination, assumed zero in the ideal case. Similarly, contact with the VB is made with a metal deposited on a p -doped semiconductor. The metal Fermi levels ε_{F_+} and ε_{F_-} are levelled, respectively, to the hole and the electron quasi-Fermi levels ε_{F_v} and ε_{F_c} at each interface. In equilibrium, the two quasi-Fermi levels become just one.

The voltage V appearing between the two electrodes is given by the splitting of the quasi-Fermi levels, or, more precisely, by the difference in the quasi-Fermi levels of majority carriers at the ohmic contact interfaces. With constant quasi-Fermi levels and ideal contacts, the split is simply

$$qV = \varepsilon_{F_c} - \varepsilon_{F_v} \quad (4.18)$$

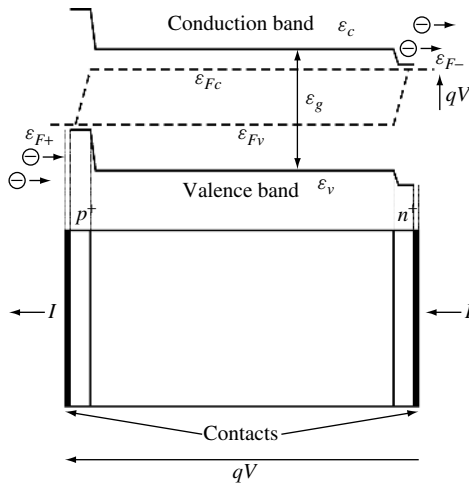


Figure 4.2 Band diagram of a solar cell with its contacts

Photons are absorbed by pumping electrons from the VB to the CB through the process known as electron–hole pair generation. However, as required by the detailed balance, the opposite mechanism is also produced so that a CB electron can decay to the VB and emit a photon, leading to what is called a *radiative recombination process*, responsible for luminescent light emission. In fact, many of such luminescent photons whose energy is slightly above the band gap are reabsorbed, leading to new electron–hole pair generations and balancing out the recombinations. Only the recombination processes leading to the effective emission of a photon out of the semiconductor produce a net recombination. Taking into account that the luminescent photons are emitted isotropically, only those photons emitted near the cell faces, at distances in the range of or smaller than the inverse of the absorption coefficient, and directed towards the cell faces with small angles (those reaching the surface with angles higher than the limit angle will be reflected back) have chances to actually leave the semiconductor, and thus to contribute to the net radiative recombination. The rare device analyses that account for this re-absorption – not yet very common as they are rather involved and the radiative recombination is small in silicon and in many thin-film cells – are said to include photon recycling [15].

In the ideal SQ cell any non-radiative recombination mechanism, which is an entropy-producing mechanism, is assumed to be absent.

The difference between the electrons pumped to the CB by external photon absorption and those falling again into the VB and effectively emitting a luminescent photon equals the current extracted from the cell. This can be presented in an equation form as

$$I/q = \dot{N}_s - \dot{N}_r = \int_{\varepsilon_g}^{\infty} (\dot{n}_s - \dot{n}_r) d\varepsilon \quad (4.19)$$

where $\varepsilon_g = \varepsilon_c - \varepsilon_v$ is the semiconductor band gap and \dot{N}_s and \dot{N}_r are the photon fluxes entering or leaving the solar cell, respectively, through any surface. When the cell is properly contacted, this current is constituted by the electrons that leave the CB through the highly doped *n*-contact. In a similar balance, in the VB, I/q are also the electrons that enter the VB through the highly doped *p*-contact. Note that the sign of the current is the opposite to that of the flow of the electrons.

Using the nomenclature in Table 4.1, the terms in equation (4.19) for unit-area cells are $\dot{N}_s = a\dot{N}(T_s, 0, \varepsilon_g, \infty, \pi \sin^2 \theta_s)$ for the cell facing the sun directly or $\dot{N}_s = a\dot{N}(T_s, 0, \varepsilon_g, \infty, \pi)$ for the cell under full concentration and $\dot{N}_r = \xi\dot{N}(T_a, qV, \varepsilon_g, \infty, \pi)$ where a and ξ are the absorptivity and emissivity of the cell. T_s is the sun temperature and T_a is the room temperature. Full concentration means using a concentrator without losses that is able to provide isotropic illumination; this is the highest illuminating power flux from a given source. The conservation of the étendue requires this concentrator to have a concentration C fulfilling the equation $C\pi \sin^2 \theta_s = \pi n_r^2$, that is, $C = 46050n_r^2$. This concentration is indeed unrealistic, but it does lead to the highest efficiency. Furthermore, it can be proven [16] that when the quasi-Fermi level split is uniform in the semiconductor bulk, then $a = \xi$. We shall assume – from now on in this chapter – that the solar cell is thick enough and perfectly coated with antireflection layers so as to fully absorb any photon with energy above the band gap energy so that $a = \xi = 1$ for these photons.

The assumption $\dot{N}_r = \dot{N}(T_a, qV, \varepsilon_g, \infty, \pi)$ states that the temperature associated with the emitted photons is the room temperature T_a . This is natural because the cell is at this temperature. However, it also states that the chemical potential of the radiation emitted, μ_{ph} , is not zero but

$$\mu_{\text{ph}} = \varepsilon_{Fc} - \varepsilon_{Fv} = qV \quad (4.20)$$

This is so because the radiation is due to the recombination of electron–hole pairs, each one with a different electrochemical potential or quasi-Fermi level. A plausibility argument for admitting $\mu_{\text{ph}} = \varepsilon_{Fc} - \varepsilon_{Fv}$ is to consider that photons and electron–hole pairs are produced through the reversible (i.e. not producing entropy) equation electron + hole \leftrightarrow photon. Equation (4.20) would then result as a consequence of equalling the chemical potentials before and after the reaction. Equation (4.20) can be also proven by solving the continuity equation for photons within the cell bulk [16, 17].

When the exponential of the Bose–Einstein function is much higher than one, the recombination term in equation (4.19) for full concentration can be written as

$$\begin{aligned} \dot{N}_r &= \frac{2\pi}{h^3 c^2} \int_{\varepsilon_g}^{\infty} \varepsilon^2 \exp\left(\frac{\varepsilon - qV}{kT_a}\right) d\varepsilon \\ &= \frac{2\pi kT}{h^3 c^2} [4(kT)^2 + 2\varepsilon_g kT + \varepsilon_g^2] \exp\left(\frac{qV - \varepsilon_g}{kT_a}\right) \end{aligned} \quad (4.21)$$

This equation is therefore valid for $\varepsilon_g - qV \gg kT_a$. Within this approximation, the current–voltage characteristic of the solar cell takes its conventional *single* exponential appearance. In fact, this equation, with the appropriate factor $\sin^2 \theta_s$, is accurate in all the ranges of interest of the current–voltage characteristic of ideal cells under unconcentrated sunlight.

The SQ solar cell can reach an efficiency limit given by

$$\eta = \frac{\{qV[\dot{N}_s - \dot{N}_r(qV)]\}_{\max}}{\sigma_{\text{SB}} T_s^4} \quad (4.22)$$

where the maximum is calculated by optimising V . This efficiency limit was first obtained by Shockley and Queisser [2] (for unconcentrated light) and is plotted in Figure 4.3 for several illumination spectra as a function of the band gap.

Outside the atmosphere the sun is seen quite accurately as a black body whose spectrum corresponds to a temperature of 5758 K [19]. To stress the idealistic approach of this chapter, we do not take this value in most of our calculations but rather 6000 K for the sun temperature and 300 K for the room temperature.

It must be pointed out that the limiting efficiency obtained for full concentration can be obtained also at lower concentrations if the étendue of the escaping photons is made equal to that of the incoming photons [16]. This can be achieved by locating the cell in a cavity [20] that limits the angle of the escaping photons.

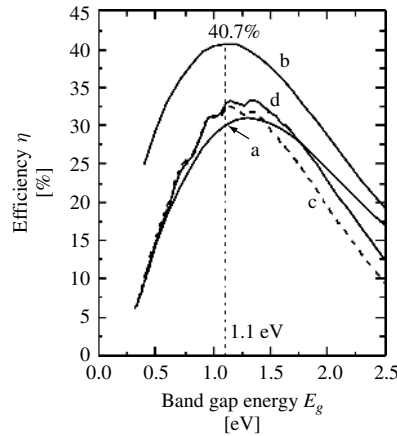


Figure 4.3 SQ efficiency limit for an ideal solar cell versus band gap energy for unconcentrated black body illumination, for full concentrated illumination and for illumination under the terrestrial sun spectrum: (a) unconcentrated 6000 K black body radiation (1595.9 Wm^{-2}); (b) full concentrated 6000 K black body radiation ($7349.0 \times 10^4 \text{ Wm}^{-2}$); (c) unconcentrated AM1.5-Direct [18] (767.2 Wm^{-2}) and (d) AM1.5 Global [18] (962.5 Wm^{-2})

It is interesting to note that the SQ analysis limit does not make any reference to semiconductor *pn* junctions. William Shockley, who first devised the *pn*-junction operation [21], was also the first in implicitly recognising [2] its secondary role in solar cells. In fact, a *pn* junction is not a fundamental constituent of a solar cell. What seems to be fundamental in a solar cell is the existence of two gases of electrons with different quasi-Fermi levels (electrochemical potentials) and the existence of selective contacts [22] that are traversed by each one of these two gases. The importance of the role of the existence of these selective contacts has not been sufficiently recognised. This is achieved today with *n*- and *p*-doped semiconductor regions, not necessarily forming layers, as in the point contact solar cell [23], but in the future it might be achieved otherwise, maybe leading to substantial advancements in PV technology. The role of the semiconductor, of which the cell is made, is to provide the two gases of electrons that may have different quasi-Fermi levels owing to the gap energy separation that makes the recombination difficult.

So far, for non-concentrated light, the most efficient single-junction solar cell, made of GaAs, has achieved an efficiency of 25.1% [24] of AM1.5G spectrum. This is only 23% below the highest theoretical efficiency of 32.8% for the GaAs band gap, of 1.42 eV, for this spectrum [25]. The theoretical maximum almost corresponds to the GaAs band gap. However, most cells are manufactured so that the radiation is also emitted towards the cell substrate located in the rear face of the cell, and little radiation, if any, turns back to the active cell. The consequence of this is that the étendue of the emitted radiation, which is π for a single face radiating to the air, is enlarged. The étendue is then $\pi + \pi n_r^2$. The term πn_r^2 proceeds from the emission of photons towards the substrate of the cell, which has a refraction index n_r . This reduces the limiting efficiency of the GaAs solar cell from 32.8 to 30.7%. Taking this into account, the efficiency of this best experimental cell is only 18.2% below the achievable efficiency of this cell, only on the basis of radiative recombination. Some substantial increase in efficiency might then be achieved by putting a reflector at the rear side of the active layers

of the cells [26] (not behind the substrate!). This would require the use of thin GaAs solar cells [27] or the fabrication of Bragg reflectors [28] (a stack of thin semiconductor layers of alternating refraction indices) underneath the active layers. Bragg reflectors have been investigated for enhancing the absorption of the incoming light in very thin cells, but the reduction of the luminescent emission towards the substrate might be an additional motivation.

4.3.2 The Monochromatic Cell

It is very instructive to consider an ideal cell under monochromatic illumination. When speaking of monochromatic illumination, we mean that, in fact, the cell is illuminated by photons within a narrow interval of energy $\Delta\varepsilon$ around the central energy ε . The monochromatic cell must also prevent the luminescent radiation of energy outside the range $\Delta\varepsilon$ from escaping from the converter.

For building this device an ideal concentrator [29] can be used that collects the rays from the solar disc, with an angular acceptance of just θ_s , with a filter on the entry aperture, letting the aforementioned monochromatic illumination to pass through. This concentrator is able to produce isotropic illumination at the receiver. By a reversal of the ray directions, the rays issuing from the cell in any direction are to be found also at the entry aperture with directions within the cone of semi-angle θ_s . Those with the proper energy will escape and be emitted towards the sun. The rest will be reflected back into the cell where they will be recycled. Thus, under ideal conditions no photon will escape with energy outside the filter energy and, furthermore, the photons escaping will be sent directly back to the sun with the same étendue of the incoming bundle H_{sr} .

The current in the monochromatic cell, ΔI , will then be given by

$$\begin{aligned} \Delta I/q &\equiv i(\varepsilon, V)\Delta\varepsilon/q = (\dot{n}_s - \dot{n}_r)\Delta\varepsilon \\ &= \frac{2H_{sr}}{h^3c^2} \left[\frac{\varepsilon^2\Delta\varepsilon}{\exp\left(\frac{\varepsilon}{kT_s}\right) - 1} - \frac{\varepsilon^2\Delta\varepsilon}{\exp\left(\frac{\varepsilon - qV}{kT_a}\right) - 1} \right] \end{aligned} \quad (4.23)$$

This equation allows for defining an equivalent cell temperature T_r ,

$$\frac{\varepsilon}{kT_r} = \frac{\varepsilon - qV}{kT_a} \Rightarrow qV = \varepsilon \left(1 - \frac{T_a}{T_r}\right) \quad (4.24)$$

so that the power produced by this cell, $\Delta\dot{W}$, is

$$\begin{aligned} \Delta\dot{W} &= \frac{2H_{sr}}{h^3c^2} \left[\frac{\varepsilon^3\Delta\varepsilon}{\exp\left(\frac{\varepsilon}{kT_s}\right) - 1} - \frac{\varepsilon^3\Delta\varepsilon}{\exp\left(\frac{\varepsilon}{kT_r}\right) - 1} \right] \left(1 - \frac{T_a}{T_r}\right) \\ &= (\dot{\varepsilon}_s - \dot{\varepsilon}_r)\Delta\varepsilon \left(1 - \frac{T_a}{T_r}\right) \end{aligned} \quad (4.25)$$

We realise that the work extracted from the monochromatic cell is the same as that extracted from a Carnot engine fed with a heat rate from the hot reservoir $\Delta\dot{q} = (\dot{e}_s - \dot{e}_r)\Delta\varepsilon$. However, this similarity does not hold under a non-monochromatic illumination because, for a given voltage, the cell equivalent temperature would depend on the photon energy ε being unable to define a single equivalent temperature for the whole spectrum. Note that the equivalent cell temperatures corresponding to short-circuit and open-circuit conditions are T_a and T_s , respectively.

To calculate the efficiency, $\Delta\dot{W}$ in equation (4.25) must be divided by the appropriate denominator. We could divide by the black body incident energy $\sigma_{\text{SB}}T_s^4$, but this would be unfair because the unused energy that is reflected by the entry aperture could be deflected with an optical device and used in other solar converters. We can divide by $\dot{e}_s\Delta\varepsilon$, the rate of power received at the cell, thus obtaining the *monochromatic* efficiency, η_{mc} , given by

$$\eta_{\text{mc}} = \left. \frac{q(\dot{n}_s - \dot{n}_r)V}{\dot{e}_s} \right|_{\text{max}} = \left(1 - \frac{\dot{e}_r}{\dot{e}_s} \right) \left(1 - \frac{T_a}{T_r} \right) \Big|_{\text{max}} \quad (4.26)$$

that is represented in Figure 4.4 as a function of the energy ε .

Alternatively, we could have used the standard definition of efficiency used in thermodynamics [30, 31] to compute the efficiency of the monochromatic cell. In this context, we put in the denominator the energy really wasted in the conversion process, that is, $(\dot{e}_s - \dot{e}_r)\Delta\varepsilon$. Actually, the energy $\dot{e}_r\Delta\varepsilon$ is returned to the sun, perhaps for later use (slowing down, for example, the sun's energy loss process!). This leads to the *thermodynamic* efficiency:

$$\eta_{\text{th}} = \left(1 - \frac{T_a}{T_r} \right) \quad (4.27)$$

This efficiency is the same as the Carnot efficiency obtained by a reversible engine operating between an absorber at temperature T_r and the ambient temperature and suggests that an ideal solar cell may work reversibly, without entropy generation. Its maximum,

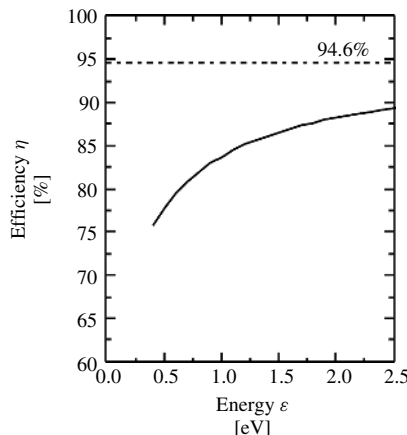


Figure 4.4 Monochromatic cell efficiency versus photon energy

for $\Delta\dot{w} \geq 0$, is obtained for $T_r = T_s$, although unfortunately it occurs when $\Delta\dot{w} = 0$, that is, when negligible (actually, none) work is done by the cell. However, this is a general characteristic of reversible engines, which yield the Carnot efficiency only at the expense of producing negligible power.

4.3.3 Thermodynamic Consistence of the Shockley–Queisser Photovoltaic Cell

Electrons and photons are the main particles interacting in a solar cell [8]. However, other interactions occur as well. In general, looking at equation (4.13), the generation of entropy for each kind of particle (electrons, photons and others) is written as

$$\sigma = \sum_i \left[\frac{1}{T} v + \mathbf{j}_e \cdot \nabla \frac{1}{T} - \frac{\mu}{T} g - \mathbf{j}_n \cdot \nabla \frac{\mu}{T} + \nabla \cdot \left(-\frac{1}{T} \mathbf{j}_\omega \right) \right] \quad (4.28)$$

where the summation extends to the different states of the particle.

First we analyse the generation of entropy by electrons, σ_{ele} . Except for the case of ballistic electrons, the pressure – appearing inside \mathbf{j}_ω as shown in equation (4.5) – is very quickly equilibrated; it is the same for $+\mathbf{v}$ and for $-\mathbf{v}$ as a result of the frequent elastic collisions. Thus, the term in \mathbf{j}_ω for electrons disappears when the sum is extended to all the states in each energy. These collisions also cause the temperature and the free energy to become the same for all the directions, at least for a given energy. Furthermore, in conventional solar cells, the temperature of the electrons is the same for any energy and is equal to the lattice temperature T_a . Also, the electrochemical potential is the same for all the electrons within the same band at a given \mathbf{r} .

In a real cell, the energy flow \mathbf{j}_e goes from the high-temperature regions towards the low-temperature ones [$\nabla(1/T) \geq 0$] so that the term in (4.28) involving \mathbf{j}_e produces positive entropy. The electron flow, \mathbf{j}_n , opposes the gradient of electrochemical potential, thus also producing positive entropy for constant temperature. However, in the ideal cell, the lattice temperature, which is also that of the electrons, is constant and the term involving $\nabla(1/T)$ disappears. Furthermore, in the SQ [2] ideal cell, mobility is infinite and, therefore, its conduction and valence band electrochemical potentials or quasi-Fermi levels (ε_{F_c} , ε_{F_v}) are constant throughout the whole solar cell and their gradients are also zero. Therefore, all the gradients in equation (4.28) disappear and the electron contribution to entropy generation, σ_{ele} , is given by

$$\sigma_{\text{ele}} = \sum_{i-\text{ele}} \left[\frac{1}{T_a} v_{i-\text{ele}} - \frac{\varepsilon_{F_c(v)}}{T_a} g_{i-\text{ele}} \right] \quad (4.29)$$

The quasi-Fermi level to be used in this case is ε_{F_c} or ε_{F_v} depending on the band to which the electronic state i -ele belongs. This is represented by $\varepsilon_{F_c(v)}$.

Other interactions may occur in the cell involving other particles besides the electrons and the photons. We shall assume that in these interactions the bodies involved (labelled as *others*) also have a direction-independent pressure and that they are also at

the lattice temperature. Furthermore, if these particles exist, they are assumed to have zero chemical potential (as it is the case, for example, of the phonons). Using these assumptions, the contribution to the irreversible entropy generation rate from these *other* particles becomes

$$\sigma_{\text{others}} = \sum_{i-\text{others}} \left[\frac{1}{T_a} v_{i-\text{others}} \right] \quad (4.30)$$

For the case of the photons, the situation is rather different. As said before, photons do not interact with each other and, therefore, they are essentially ballistic. Their thermodynamic intensive variables may experience variations with the photon energy and also with their direction of propagation. In fact, they come from the sun in a few directions only, and only in these directions do they exert a pressure. The direct consequence is that a non-vanishing current of grand potential exists for the photons. (It vanishes in gases of photons that are confined and in thermal equilibrium with the confining walls. Using this condition for photon beams from the sun is not correct.)

N_{ph} being the number of photons in a mode corresponding to a certain ray moving inside the semiconductor, their evolution along a given ray path corresponding to a radiation mode is given by [17]

$$N_{\text{ph}}(\zeta) = f_{\text{BE}}(T, qV)[1 - e^{-\alpha\zeta}] + N_{\text{ph}}(0)e^{-\alpha\zeta} \quad (4.31)$$

where ζ is the length of the ray, f_{BE} is the Bose–Einstein factor for luminescent photons whose chemical potential is the separation between the conduction and the valence band electron quasi-Fermi levels – in this case equalling the cell voltage V (times q) – and α is the absorption coefficient. Equation (4.31) shows a non-homogeneous profile for N_{ph} contributed to by luminescent photons that increase with ζ (first term on the right-hand side) and externally fed photons that decrease when the ray proceeds across the semiconductor (second term), and these photons are absorbed. $N_{\text{ph}}(0) = f_{\text{BE}}(T_s, 0)$ is usually taken in solar cells that correspond to illumination by free (i.e. with zero chemical potential) radiation at the sun temperature T_s .

In general, the photons in a mode of energy ε are considered as a macroscopic body [9] for which temperature and chemical potential can be defined. However, thermodynamically, they can be arbitrarily characterised by a chemical potential μ and a temperature T as long as $(\varepsilon - \mu)/T$ takes the same value. For example, the incident solar photons may be considered at the solar temperature T_s with zero chemical potential or, alternatively, at room temperature T_a with an energy variable chemical potential $\mu_s = \varepsilon(1 - T_a/T_s)$. This property has already been used in the study of the monochromatic cell.

Indeed, this arbitrary choice of T and μ does not affect the entropy production. This becomes evident if we rewrite equation (4.28) in the case of photons as

$$\sigma_{\text{ph}} = \sum_{i-\text{ph}} \left[\frac{\varepsilon - \mu}{T} g + \mathbf{j}_n \cdot \nabla \left(\frac{\varepsilon - \mu}{T} \right) + \nabla \cdot \left(-\frac{1}{T} \mathbf{j}_\omega \right) \right] \quad (4.32)$$

where we have made use of equation (4.15) and of the fact that $v = \varepsilon g$. This equation depends explicitly only on $(\varepsilon - \mu)/T$. This is less evident in the term in \mathbf{j}_ω/T , but as

discussed in the context of equation (4.15), \mathbf{j}_ω is proportional to T and thus \mathbf{j}_ω/T only depends on $(\varepsilon - \mu)/T$. Note, however, that \mathbf{j}_ω is affected by the specific choice of T .

For simplicity, we shall consider the photons at room temperature and we shall calculate their chemical potential, μ_{ph} , from setting the equality

$$N_{\text{ph}}(\zeta, \varepsilon) = \frac{\varepsilon^2}{\exp\left[\frac{\varepsilon - \mu_{\text{ph}}(\zeta, \varepsilon)}{kT_a}\right] - 1} \quad (4.33)$$

However, we might have chosen to leave $\mu_{\text{ph}} = 0$, and then the effect of the absorption of light when passing through the semiconductor could have been described as a cooling down of the photons (if N_{ph} actually decreases with ζ).

With the room-temperature luminescent photon description, the production of entropy by photons is given by

$$\sigma_{\text{ph}} = \sum_{i-\text{ph}} \left[\frac{v_{i-\text{ph}}}{T_a} - \frac{\mu_{i-\text{ph}} g_{i-\text{ph}}}{T_a} - \frac{\mathbf{j}_{n,i-\text{ph}} \nabla \mu_{i-\text{ph}}}{T_a} - \frac{\nabla \mathbf{j}_{\omega,i-\text{ph}}}{T_a} \right] \quad (4.34)$$

However, using equations (4.15) and (4.3),

$$\nabla \mathbf{j}_\omega = \frac{c}{Un_r} \frac{d\Omega}{d\mu} \nabla \mu = -\frac{c}{Un_r} f_{\text{BE}} \nabla \mu = -\mathbf{j}_n \nabla \mu \quad (4.35)$$

and

$$\sigma_{\text{ph}} = \sum_{i-\text{ph}} \left[-\frac{v_{i-\text{ph}}}{T_a} + \frac{\mu_{i-\text{ph}} g_{i-\text{ph}}}{T_a} \right] \quad (4.36)$$

where

$$g = (c/Un_r) \alpha f_{\text{BE}}(T_a, qV) e^{-\alpha \zeta} - (c/Un_r) \alpha f_{\text{BE}}(T_s, 0) e^{-\alpha \zeta}; \quad v = \varepsilon g \quad (4.37)$$

The total irreversible entropy production is obtained by adding equations (4.29), (4.30) and (4.36), taking into account equation (4.37). Now, the terms in energy generation, all at the same temperature, must balance out by the first principle of thermodynamics. The net absorption of photons corresponds to an electron transfer (positive and negative generations) between states gaining an electrochemical potential qV , so the terms $\mu g/T$ corresponding to electrons and photons subtract each other. No additional generations are assumed to take place. Thus the total irreversible entropy generation rate can be written as

$$\sigma_{\text{irr}} = \frac{c\alpha}{Un_r} \sum_{i-\text{ph}} \frac{(\mu_{i-\text{ph}} - qV)[f_{\text{BE}}(T_s, 0) e^{-\alpha \zeta} - f_{\text{BE}}(T_a, qV) e^{-\alpha \zeta}]}{T_a} \quad (4.38)$$

For a given mode the second factor balances out when $f_{\text{BE}}(T_s, 0) = f_{\text{BE}}(T_a, qV)$, and so does the irreversible entropy generation. In this case, $N_{\text{ph}} = f_{\text{BE}}(T_a, qV)$ is constant along the ray and $\mu_{i-\text{ph}} = qV$ is constant at all points. The irreversible entropy generation rate is

then zero everywhere. If $f(T_s, 0) > f(T_a, qV)$, then $N_{\text{ph}} > f(T_a, qV)$ and $\mu_{i-\text{ph}} > qV$, so that both factors are positive and so is the product. If $f(T_s, 0) < f(T_a, qV)$, then $N_{\text{ph}} < f(T_a, qV)$ and $\mu_{i-\text{ph}} < qV$. In this case both factors are negative and the product is positive.

Thus, we have proven that every mode contributes non-negatively to the entropy. We can then state that the SQ cell produces non-negative entropy and, in this sense, it complies with the second law of thermodynamics.

For less idealised cases, as we have mentioned above, the existence of quasi-Fermi levels or temperature gradients generally produces additional positive entropy. Non-radiative net recombination of electrons from the conduction to the valence band also produces positive entropy. However, net generation would contribute to the production of negative entropy and, therefore, it may incur in violation of the second law of thermodynamics, if no other mechanism contributing to the creation of positive entropy exists. So the inclusion of imaginative carrier generation rates in novel device proposals, without counterparts, must be considered with some caution.

4.3.4 Entropy Production in the Whole Shockley–Queisser Solar Cell

The preceding approach is applicable to regions in which the physical properties of the system are continuous and differentiable, but not to abrupt interfaces. For testing the compliance with the second law, the continuity equations must be integrated in such cases by choosing volumes surrounding the suspected interfaces. This integral approach can also be extended to the whole converter to check for any violation of the second law and also to calculate the whole entropy production of a device. However, the integral approach, if not complemented with the local approach, is valid for proving thermodynamic inconsistency, but not for proving consistency that has to be proven at every point. An example of the use of such an integral approach is given here.

In the integral analysis we follow steps similar to those used in the local analysis. In particular, the first law of thermodynamics is applied by integrating equation (4.7) and using the first law expressed by equation (4.9). Then, we obtain, for the stationary case

$$0 = \int_A \sum_i \mathbf{j}_{e,i} \cdot d\mathbf{A} = +\dot{E}_r - \dot{E}_s + \dot{E}_{mo} - \dot{E}_{mi} + \dot{E}_{\text{others}} \quad (4.39)$$

where \dot{E}_s and \dot{E}_r are the radiation energies entering or escaping from the converter, \dot{E}_{mi} and \dot{E}_{mo} are the energies of the electrons entering the VB and leaving the CB, respectively, and \dot{E}_{others} is the net flow of energy leaving the semiconductor as a result of other mechanisms.

Taking equation (4.5) into account, the fact that no chemical potential is associated with *other* particles and processes, and the annihilation of the grand canonical potential current density, the term corresponding to the other elements is more conventionally written as

$$\dot{E}_{\text{others}} = T_a \dot{S}_{\text{others}} \doteq \dot{Q} \quad (4.40)$$

where \dot{Q} is defined as the rate of heat leaving the converter.

The second law of thermodynamics, expressed by equations (4.8) and (4.10), integrated into the whole volume of the converter can be written, for the stationary case, as

$$\dot{S}_{\text{irr}} = \int_U \sigma_{\text{irr}} dU = \int_A \sum_i \mathbf{j}_{s,i} dA = \dot{S}_r - \dot{S}_s + \dot{S}_{mo} - \dot{S}_{mi} + \dot{S}_{\text{others}} \quad (4.41)$$

The irreversible rate of entropy production is obtained by the elimination of the terms with subscript *others* by multiplying equation (4.41) by T_a , subtracting equation (4.39) from the result and taking into account (4.40). In this way we obtain

$$T_a \dot{S}_{\text{irr}} = (\dot{E}_s - T_a \dot{S}_s) - (\dot{E}_r - T_a \dot{S}_r) + (\dot{E}_{mi} - T_a \dot{S}_{mi}) - (\dot{E}_{mo} - T_a \dot{S}_{mo}) \quad (4.42)$$

From equation I-4 (Table 4.1) and considering the annihilation of the grand canonical potential flow for electrons, $(\dot{E}_{mi} - T_a \dot{S}_{mi}) = \varepsilon_{Fv} \dot{N}_{mi}$ and $(\dot{E}_{mo} - T_a \dot{S}_{mo}) = \varepsilon_{Fc} \dot{N}_{mo}$, so that we can write

$$T_a \dot{S}_{\text{irr}} = \varepsilon_{Fv} \dot{N}_{mi} - \varepsilon_{Fc} \dot{N}_{mo} + (\dot{E}_s - T_a \dot{S}_s) - (\dot{E}_r - T_a \dot{S}_r) \quad (4.43)$$

Taking into account that $\dot{N}_{mi} = \dot{N}_{mo} = I/q$ and $\varepsilon_{Fc} - \varepsilon_{Fv} = qV$, equation (4.43) is now rewritten as

$$T_a \dot{S}_{\text{irr}} = -\dot{W} + (\dot{E}_s - T_a \dot{S}_s) - (\dot{E}_r - T_a \dot{S}_r) \quad (4.44)$$

Here, this equation has been derived from the *local* model. However, it can also be obtained with more generality from a classical formulation of the second law of thermodynamics [32]. It is valid for ideal as well as for non-ideal devices. The values of the thermodynamic variables to be used in equation (4.44) are given in Table 4.1. Power – which in other cases will be that of the converter under study – corresponds in this case to the power of an SQ ideal solar cell and is given by the product of equations (4.18) and (4.19).

We have already discussed the basic ambiguity for the thermodynamic description of any radiation concerning the choice of the temperature and the chemical potential. A useful corollary is derived from this fact [32]. If the power rate produced by a radiation converter depends on the radiation only through its rate of incident energy or number of photons, then any radiation received or emitted by the converter can be changed into a luminescent radiation at room temperature, T_a , and with chemical potential, μ_x , without affecting the rate of power and of irreversible entropy produced. The chemical potential μ_x of this equivalent luminescent radiation is linked to the thermodynamic parameters of the original radiation, T_{rad} and μ_{rad} , through the equation

$$\frac{\varepsilon - \mu_{\text{rad}}}{kT_{\text{rad}}} = \frac{\varepsilon - \mu_x}{kT_a} \Rightarrow \mu_x = \varepsilon \left(1 - \frac{T_a}{T_{\text{rad}}} \right) + \mu_{\text{rad}} \frac{T_a}{T_{\text{rad}}} \quad (4.45)$$

Note that, in general, μ_x is a function of the photon energy, ε , as it may also be T_{rad} and μ_{rad} .

The proof of the theorem is rather simple and is brought in here because it uses relationships of instrumental value. It is straightforward to see that

$$\dot{n}_x = \dot{n}_{\text{rad}}; \quad \dot{e}_x = \varepsilon \dot{n}_x = \dot{e}_{\text{rad}}; \quad \dot{\omega}_x/T_a = \dot{\omega}_{\text{rad}}/T_{\text{rad}}; \quad \dot{e}_{\text{rad}} - T \dot{s}_{\text{rad}} = \mu_x \dot{n}_x + \dot{\omega}_x \quad (4.46)$$

where, again, the suffix *rad* labels the thermodynamic variables of the original radiation.

The equality of the energy and the number of photons of the original and equivalent radiation proves that the power production is unchanged. Furthermore, the last relationship can be introduced in equation (4.44) to prove that the calculation of the entropy production rate also remains unchanged.

Taking all this into account, the application of equation (4.44) to the SQ solar cell is rather simple. Using the SQ cell model for the power and using the room-temperature equivalent radiation (of chemical potential μ_s) of the solar radiation, we obtain

$$\begin{aligned} T_a \dot{S}_{\text{irr}} &= - \int_{\varepsilon_g}^{\infty} qV [\dot{n}(T_a, \mu_s) - \dot{n}(T_a, qV)] d\varepsilon + \int_{\varepsilon_g}^{\infty} [\mu_s \dot{n}(T_a, \mu_s) + \dot{\omega}(T_a, \mu_s)] d\varepsilon \\ &\quad - \int_{\varepsilon_g}^{\infty} [qV \dot{n}(T_a, qV) + \dot{\omega}(T_a, qV)] d\varepsilon \\ &= \int_{\varepsilon_g}^{\infty} [\dot{\omega}(T_a, \mu_s) - \dot{\omega}(T_a, qV)] d\varepsilon + \int_{\varepsilon_g}^{\infty} [(\mu_s - qV) \dot{n}(T_a, \mu_s)] d\varepsilon \end{aligned} \quad (4.47)$$

The integrand is zero for $qV = \mu_s$, but as μ_s varies with ε it is not zero simultaneously for all ε . To prove that it is positive, we differentiate with respect to qV . Using $d\dot{\omega}/d\mu = -\dot{n}$,

$$\frac{d(T_a \dot{S}_{\text{irr}})}{dqV} = - \int_{\varepsilon_g}^{\infty} [\dot{n}(T_a, \mu_s) - \dot{n}(T_a, qV)] d\varepsilon = I/q \quad (4.48)$$

Thus, for each energy, the minimum of the integrand also appears for $qV = \mu_s(\varepsilon)$. Since this minimum is zero, the integrand is non-negative for any ε and so is the integral, proving also the thermodynamic consistence of this cell from the integral perspective. Furthermore, the minimum of the entropy, which for the non-monochromatic cell is not zero, occurs for open-circuit conditions. However, the ideal monochromatic cell reaches zero entropy production, and therefore reversible operation, under open-circuit conditions, and this is why this cell may reach the Carnot efficiency, as discussed in a preceding section.

4.4 THE TECHNICAL EFFICIENCY LIMIT FOR SOLAR CONVERTERS

We have seen that with the technical definition of efficiency – in whose denominator the radiation returned to the sun is not considered – the Carnot efficiency cannot be reached with a PV converter. What then is the technical efficiency upper limit for solar converters?

We can consider that this limit would be achieved if we could build a converter producing zero entropy [33]. In this case, the power that this converter can produce,

\dot{W}_{lim} , can be obtained from equation (4.44) by setting the irreversible entropy-generation term to zero. Substituting the terms involving emitted radiation by their room-temperature luminescent equivalent, equation (4.44) becomes

$$\dot{W}_{\text{lim}} = \int_{\varepsilon_g}^{\infty} \{[\dot{e}_s - T_a \dot{s}_s] - [\mu_x(\varepsilon) \dot{n}_x + \dot{\omega}_x]\} d\varepsilon = \int_{\varepsilon_g}^{\infty} \dot{w}_{\text{lim}}(\varepsilon, \mu_x) d\varepsilon \quad (4.49)$$

The integrand should now be maximised [32] with respect to μ_x . For this, we calculate the derivative

$$\frac{d\dot{w}_{\text{lim}}}{d\mu_x} = -\dot{n}_x - \frac{d\dot{\omega}_x}{d\mu_x} - \mu_x \frac{d\dot{n}_x}{d\mu_x} = -\mu_x \frac{d\dot{n}_x}{d\mu_x} \quad (4.50)$$

where we have used that the derivative of the grand potential with respect to the chemical potential is the number of particles with a change of sign. This equation shows that the maximum is achieved if $\mu_x = 0$ for any ε , or, in other words, if the radiation emitted is a room-temperature thermal radiation. This is the radiation emitted by all the bodies in thermal equilibrium with the ambient. However, the same result will be also achieved if the emitted radiation is any radiation whose room-temperature luminescent equivalent is a room-temperature thermal radiation.

Now, we can determine this efficiency, according to Landsberg [33], as

$$\begin{aligned} \eta &= \frac{\left(\frac{H_{sr}}{\pi}\right) \left[\left(\sigma T_s^4 - \frac{4}{3}\sigma T_a T_s^3\right) - \left(\sigma T_a^4 - \frac{4}{3}\sigma T_a^4\right) \right]}{(H_{sr}/\pi)\sigma T_s^4} \\ &= 1 - \frac{4}{3} \left(\frac{T_a}{T_s}\right) + \frac{1}{3} \left(\frac{T_a}{T_s}\right)^4 \end{aligned} \quad (4.51)$$

which for $T_s = 6000$ K and $T = 300$ K gives 93.33% instead of 95% of the Carnot efficiency.

No ideal device is known that is able to reach this efficiency. Ideal solar thermal converters, not considered in this chapter, have a limiting efficiency of 85.4% [34, 35] and therefore do not reach this limit. Other high-efficiency ideal devices considered in this chapter do not reach it either. We do not know whether the Landsberg efficiency is out of reach. At least it is certainly an upper limit of the technical efficiency of any solar converter.

4.5 VERY HIGH EFFICIENCY CONCEPTS

4.5.1 Multijunction Solar Cells

A conceptually straightforward way of overcoming the fundamental limitation of the SQ cell, already pointed out by SQ, is the use of several solar cells of different band gaps to convert photons of different energies. A simple configuration to achieve it is by just stacking the cells so that the upper cell has the highest band gap and lets the photons pass through towards the inner cells (Figure 4.5). The last cell in the stack is the one with the narrowest band gap. Between cells we put low-energy pass filters so that the

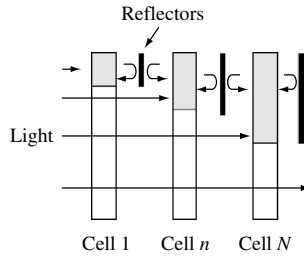


Figure 4.5 Stack of solar cells ordered from left to right in decreasing band gap ($E_{g1} > E_{g2} > E_{g3}$). (Reprinted from *Solar Energy Materials and Solar Cells* V. 43, N. 2, Martí A. and Araújo G. L., *Limiting Efficiencies for Photovoltaic Energy Conversion in Multigap Systems*, 203–222, © 1996 with permission from Elsevier Science)

reflection threshold of each filter is the band gap of the cell situated above. This prevents the luminescent photons from being emitted for energies different to those with which the photons from the sun are received in each cell. In this configuration, every cell has its own load circuit, and therefore, is biased at a different voltage. It has been shown [31] that a configuration without back reflectors leads to a lower efficiency if the number of cells is finite. For the case of a stack with an infinite number of cells, the limiting efficiency is found to be independent of whether reflectors are placed or not.

For example, for the case of a stack with two cells, the power generated is

$$W = qV_l[\dot{N}(T_s, 0, \varepsilon_{gl}, \varepsilon_{gh}, H_s) - \dot{N}(T_a, qV_l, \varepsilon_{gl}, \varepsilon_{gh}, H_r)] + qV_h[\dot{N}(T_s, 0, \varepsilon_{gh}, \infty, H_s) - \dot{N}(T_a, qV_h, \varepsilon_{gh}, \infty, H_r)] \quad (4.52)$$

where the suffixes l and h (low and high) refer to the band gap and the voltage of the two cells involved. The maximum power is obtained by optimising this function with respect to the variables V_l , V_h , ε_{gl} and ε_{gh} . We present in Figure 4.6 the efficiency of

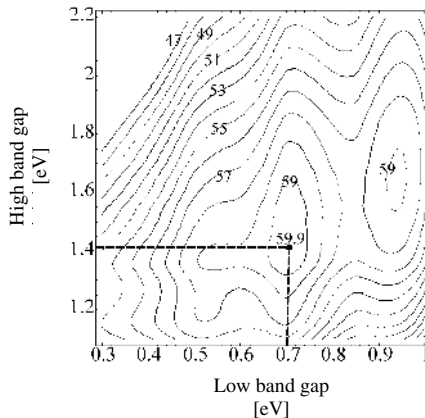


Figure 4.6 Efficiency of a tandem of two ideal cells under AM1.5D illumination as a function of the two cells' band gap ε_l and ε_h

two ideal cells as a function of the two cells' band gaps, which is optimised only with respect to V_l and V_h . The generation term is in this case not the one in equation (4.52) but the one corresponding to a standard spectrum AM1.5D [18]. Power is converted into efficiency by dividing by 767.2 Wm^{-2} , which is the power flux carried by the photons in this spectrum. In the figure, we can observe that the efficiency maximum is very broad, allowing for a wide combination of materials.

A lot of experimental work has been done on this subject. To our knowledge, the highest efficiency so far achieved, 34% (AM1.5 Global), has been obtained by Spectrolab [24, 36], in 2001, using a monolithic (made on the same chip) two-terminal tandem InGaP/GaAs stuck on a Ge cell and operating at a concentration factor of 210, that is, at 21 Wcm^{-2} .

The maximum efficiency is obtained with an infinite number of solar cells, each one biased at its own voltage $V(\varepsilon)$ and illuminated with monochromatic radiation. The efficiency of this cell is given by

$$\eta = \frac{\int_0^\infty \eta_{mc}(\varepsilon) \dot{e}_s \, d\varepsilon}{\int_0^\infty \dot{e}_s \, d\varepsilon} = \frac{1}{\sigma_{SB} T_s^4} \int_0^\infty \eta_{mc}(\varepsilon) \dot{e}_s \, d\varepsilon = \frac{1}{\sigma_{SB} T_s^4} \int_0^\infty i(\varepsilon, V) V |_{\max} \, d\varepsilon \quad (4.53)$$

where $\eta_{mc}(\varepsilon)$ is the monochromatic cell efficiency given by equation (4.26) and $i(\varepsilon, V)$ was defined in equation (4.23). For $T_s = 6000 \text{ K}$ and $T_a = 300 \text{ K}$, the sun and ambient temperature, respectively, this efficiency is [34] 86.8%. This is the highest efficiency limit of known ideal converter.

Tandem cells emit room-temperature luminescent radiation. This radiation presents, however, a variable chemical potential $\mu(\varepsilon) = qV(\varepsilon)$ and therefore it is not a radiation with zero chemical potential (free radiation). In addition, the entropy produced by this array is positive since the entropy produced by each one of the monochromatic cells forming the stack is positive. None of the conditions for reaching the Landsberg efficiency (zero entropy generation rate and emission of free radiation at room temperature) is then fulfilled and, therefore, tandem cells do not reach this upper bound.

It is highly desirable to obtain monolithic stacks of solar cells, that is, on the same chip. In this case, the series connection of all the cells in the stack is the most compact solution. Chapter 9 will deal with this case extensively. If the cells are series-connected, a limitation appears that the same current must go through all the cells. For the case of two cells studied above, this limitation is expressed by the equation

$$\begin{aligned} I &= q[\dot{N}(T_s, 0, \varepsilon_{gl}, \varepsilon_{gh}, H_s) - \dot{N}(T_a, qV_l, \varepsilon_{gl}, \varepsilon_{gh}, H_r)] \\ &= q[\dot{N}(T_s, 0, \varepsilon_{gh}, \infty, H_s) - \dot{N}(T_a, qV_h, \varepsilon_{gh}, \infty, H_r)] \end{aligned} \quad (4.54)$$

This equation establishes a link between V_l and V_h (for each couple $\varepsilon_l, \varepsilon_h$), which reduces the value of the maximum achievable efficiency. The total voltage obtained from the stack is $V = V_l + V_h$.

Our interest now is to determine the top efficiency achievable in this case when the number of cells is increased to infinity. Surprisingly enough, it is found [37, 38] that

the solution is also given by equation (4.53) and therefore, the limiting efficiency of a set of cells that is series-connected is also 86.8%.

4.5.2 Thermophotovoltaic Converters

Thermophotovoltaic (TPV) converters are devices in which a solar cell converts the radiation emitted by a heated body into electricity. This emitter may be heated, for example, by the ignition of a fuel. However, in our context, we are more interested in solar TPV converters in which the sun is the source of energy that heats an absorber at temperature T_r , which then emits radiation towards the PV converter. Figure 4.7 draws the ideal converter for this situation.

An interesting feature of the TPV converter is that the radiation emitted by the solar cells is sent back to the absorber assisting in keeping it hot. To make the cell area different from the radiator area (so far cells in this chapter have all been considered to be of area unity), the absorber in Figure 4.7 radiates into a reflecting cavity containing the cell. The reflective surfaces in the cavity and the mirrors in the concentrator are assumed to be free of light absorption.

In the ideal case [39], the radiator emits two bundles of rays, one of étendue H_{rc} (emitted by the right side of the absorber in the Figure 4.7a), which is sent to the cell after reflections in the cavity walls, with energy E'_r without losses, and another (unavoidable) one H_{rs} , with energy E_r , which is sent back to the sun (by the left face of the absorber) after suffering reflections in the left-side concentrator. Ideally, the radiator illuminates no other absorbing element or dark part of the sky: all the light emitted by the radiator's left side is sent back to the sun by the concentrator. Rays emitted by the radiator into the cavity may return to the radiator again without touching the cell, but since no energy is transferred, such rays are not taken into account.

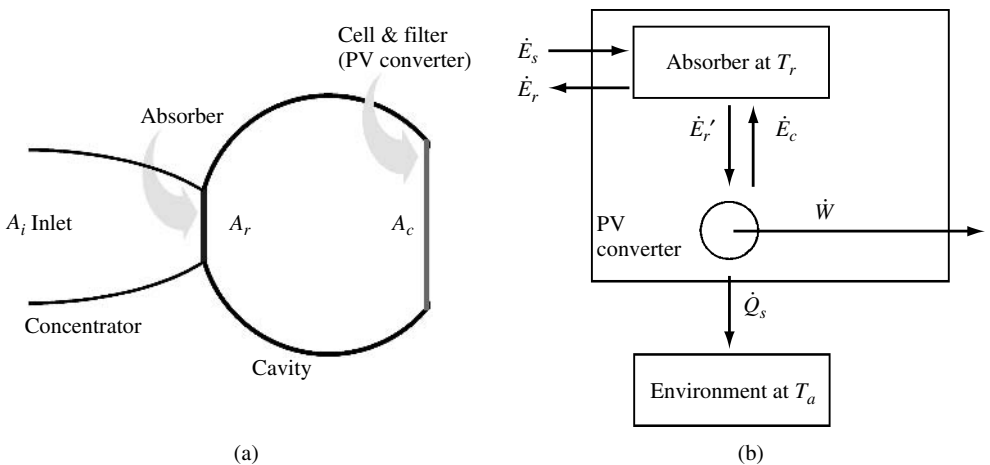


Figure 4.7 (a) Schematic of an ideal TPV converter with the elements inserted in loss-free reflecting cavities and (b) illustration of the thermodynamic fluxes involved. In the monochromatic case, $\dot{E}_s \equiv \dot{E}(T_s, 0, 0, \infty, H_{rs})$, $\dot{E}_r \equiv \dot{E}(T_r, 0, 0, \infty, H_{rs})$, $\dot{E}'_r \equiv \dot{e}(\varepsilon, T_r, 0, H_{rc})\Delta\varepsilon$, $\dot{E}_c \equiv \dot{e}(\varepsilon, T_a, qV, H_{rc})\Delta\varepsilon$

On the other hand, the radiator is illuminated by a bundle of rays, coming from the sun, of étendue $H_{sr} = H_{rs}$ and by the radiation emitted by the cell itself, of étendue $H_{cr} = H_{rc}$. Also, the cell may emit some radiation into the cavity, which returns to the cell again. This radiation is therefore not accounted for as an energy loss in the cell. In addition, we shall assume that the cell is coated with an ideal filter that allows only photons with energy ε and within a bandwidth $\Delta\varepsilon$ to pass through, while the others are totally reflected. In this situation the energy balance in the radiator becomes

$$\dot{E}(T_s, 0, 0, \infty, H_{rs}) + \dot{e}(\varepsilon, T_a, qV, H_{rc})\Delta\varepsilon = \dot{e}(\varepsilon, T_r, 0, H_{rc})\Delta\varepsilon + \dot{E}(T_r, 0, 0, \infty, H_{rs}) \quad (4.55)$$

where the first equation member is the net rate of energy received by the radiator and the second member is the energy emitted.

Using $\dot{e}(\varepsilon, T_r, 0, H_{rc})\Delta\varepsilon - \dot{e}(\varepsilon, T_a, qV, H_{rc})\Delta\varepsilon = \varepsilon\Delta i/q = \varepsilon\Delta\dot{w}/(qV)$, where Δi is the current extracted from the monochromatic cell and $\Delta\dot{w}$ is the electric power delivered, it is obtained that

$$\frac{\varepsilon\Delta\dot{w}}{qV} = \frac{H_{rs}\sigma_{SB}}{\pi}(T_s^4 - T_r^4) \Leftrightarrow \frac{\varepsilon^2\Delta i}{qH_{rc}\Delta\varepsilon} = \frac{H_{rs}\varepsilon}{H_{rc}\Delta\varepsilon} \frac{\sigma_{SB}}{\pi}(T_s^4 - T_r^4) \quad (4.56)$$

This equation can be used to determine the operation temperature of the radiator, T_r , as a function of the voltage V , the sun temperature T_s , the energy ε and the dimensionless parameter $H_{rc}\Delta\varepsilon/H_{rs}\varepsilon$. Notice that the left-hand side of equation (4.56) is independent of the cell étendue and of the filter bandwidth (notice that $\Delta i \propto H_{rc}\Delta\varepsilon$).

Dividing by $H_{rs}\sigma_{SB}T_s^4/\pi$, the solar input power, allows expressing the efficiency of the TPV converter as

$$\eta = \left(1 - \frac{T_r^4}{T_s^4}\right) \left(\frac{qV}{\varepsilon}\right) = \left(1 - \frac{T_r^4}{T_s^4}\right) \left(1 - \frac{T_a}{T_c}\right) \quad (4.57)$$

where T_c is the equivalent cell temperature as defined by equation (4.24). As presented in Figure 4.8, this efficiency is a monotonically increasing function of $H_{rc}\Delta\varepsilon/H_{rs}\varepsilon$. For $(H_{rc}\Delta\varepsilon/H_{rs}\varepsilon) \rightarrow \infty$, $\Delta i \rightarrow 0$ and $T_r \rightarrow T_c$. In this case an optimal efficiency [40] for $T_s = 6000$ K and $T_a = 300$ K is found to be 85.4% and is obtained for a temperature $T_c = T_r = 2544$ K. This is exactly the same as the optimum temperature of an ideal solar thermal converter feeding a Carnot engine. In reality, the ideal monochromatic solar cell is a way of constructing the Carnot engine. This efficiency is below the Landsberg efficiency (93.33%) and slightly below the one of an infinite stack of solar cells (86.8%).

It is worth noting that the condition $(H_{rc}\Delta\varepsilon/H_{rs}\varepsilon) \rightarrow \infty$ requires that $H_{rc} \gg H_{rs}$, and for this condition to be achieved, the cell area must be very large compared to the radiator area. This compensates the narrow energy range in which the cell absorbs. This is why a mirrored cavity must be used in this case.

4.5.3 Thermophotonic Converters

A recent concept for solar conversion has been proposed [3] with the name of thermophotonic (TPH) converter. In this concept, a solar cell converts the luminescent radiation

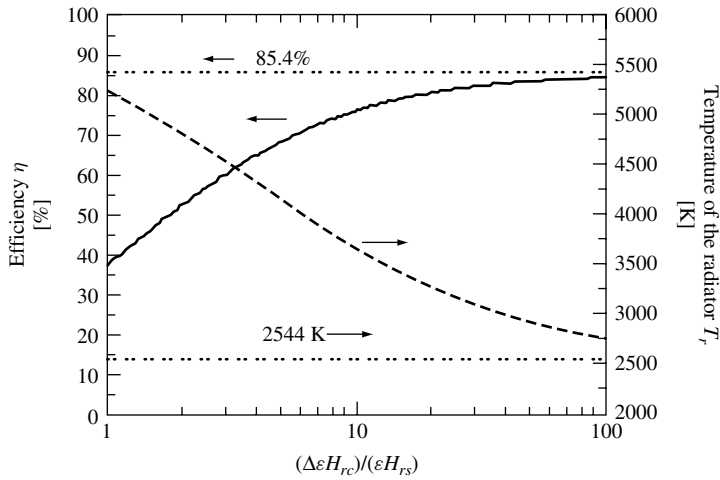


Figure 4.8 TPV ideal converter efficiency versus $H_{rc} \Delta \varepsilon / H_{rs} \varepsilon$. The energy ε and the cell voltage V are optimised

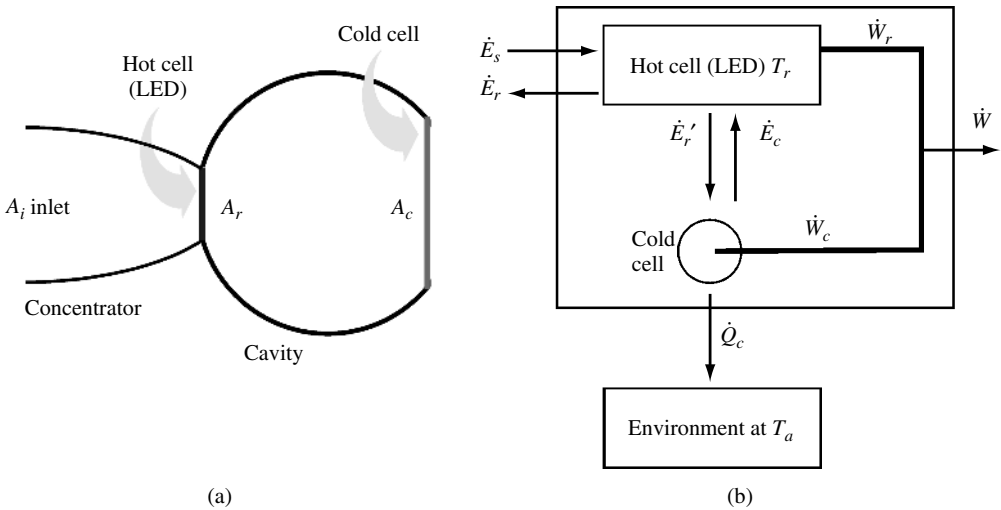


Figure 4.9 Diagram of the TPH converter with cavity. In (b), the energy fluxes are given by $\dot{E}_s \equiv E(T_s, 0, 0, \infty, H_{rs})$, $\dot{E}_r \equiv E(T_r, qV_r, 0, \infty, H_{rs})$, $\dot{Q}_c = \dot{E}_s - \dot{E}_r$, $\dot{E}_r' \equiv E(T_r, qV_r, 0, \infty, H_{rc})$, $\dot{E}_c \equiv E(T_a, qV_c, \varepsilon_g, \infty, H_{rc})$

emitted by a heated light emitting diode (LED) into electricity. A diagram of this device is found in Figure 4.9. As in the TPV device, the LED can be heated with a fuel, but in our context it is heated as well with radiation absorbed from the sun. To emit luminescent radiation, the LED absorbs electric power, \dot{W}_r , in addition to the power delivered from the photons that illuminate the absorber. This power is to be subtracted from the electric power converted by the solar cell \dot{W}_c .

As a matter of fact, this converter is a generalisation of the TPV converter. If the LED is in short circuit, the TPH converter is exactly the same as the TPV converter. The application of a voltage to the LED changes the converter properties.

Ideal LEDs are like solar cells. Thus, to describe the ideal TPH converter, we shall refer to the LED as the hot cell, as opposed to the electric power generator, which is the cold cell. When they are considered as ideal devices, the current–voltage characteristics of both, the LED and the solar cell, are the same. This causes the current passing by the cold cell to be faithfully replicated (with the sign changed) by the hot cell, owing to the reciprocal illumination of both devices, as expressed by the two following equations:

$$I_c/q = \dot{N}(T_r, qV_r, \varepsilon_g, \infty, H_{rc}) - \dot{N}(T_a, qV_c, \varepsilon_g, \infty, H_{rc}) \quad (4.58)$$

$$I_r/q = \dot{N}(T_a, qV_c, \varepsilon_g, \infty, H_{rc}) - \dot{N}(T_r, qV_r, \varepsilon_g, \infty, H_{rc}) \quad (4.59)$$

We shall use the subindex c for the cold solar cell current and voltage and r for the hot solar cell. The power generated by each cell is $\dot{W}_c = I_c V_c$ and $\dot{W}_r = I_r V_r$. In a normal operation, I_r is negative and the power generated by the hot cell is negative.

The application of the first law of thermodynamics to the cold and the hot cell, respectively, leads to

$$\dot{E}(T_r, qV_r, \varepsilon_g, \infty, H_{rc}) = \dot{E}(T_c, qV_c, \varepsilon_g, \infty, H_{rc}) + \dot{W}_c + \dot{Q}_c \quad (4.60)$$

$$\dot{Q}_r + \dot{E}(T_c, qV_c, \varepsilon_g, \infty, H_{rc}) = \dot{E}(T_r, qV_r, \varepsilon_g, \infty, H_{rc}) + \dot{W}_r \quad (4.61)$$

where \dot{Q}_c is the heat rate delivered by the cold cell in the heat sink, while

$$\dot{Q}_r = \dot{E}(T_s, 0, 0, \infty, H_{rs}) - \dot{E}(T_r, 0, 0, \infty, H_{rs}) = \frac{H_{sr}\sigma_{SB}}{\pi}(T_s^4 - T_r^4) \quad (4.62)$$

is the heat injected by the sun into the hot cell. The sum of equations (4.60) and (4.61) leads to

$$\dot{Q}_r - \dot{Q}_c = \dot{W}_r + \dot{W}_c = I_r(V_r - V_c) = I_c(V_c - V_r) = \dot{W} \quad (4.63)$$

where \dot{W} is the algebraic sum of the powers produced by both cells (usually the hot cell will be absorbing, not producing, power).

In the case of monochromatic cell and LED operation, a proper filter of bandwidth $\Delta\varepsilon$ and centred at the energy ε is to be located somewhere in the optical system to allow for an interchange of photons only within the filter bandwidth. The preceding equations can be easily particularised in this case. An interesting relationship holding in this case, $\dot{e}\Delta\varepsilon = \varepsilon\dot{n}\Delta\varepsilon \equiv \dot{E}$, allows for a simple expression of the heat rate in both cells,

$$\dot{Q}_r = (V_r - \varepsilon/q)I_r \quad (4.64)$$

$$\dot{Q}_c = (\varepsilon/q - V_c)I_c \quad (4.65)$$

and this allows for writing the efficiency, using the equations (4.63) to (4.65) as

$$\eta = \frac{\dot{Q}_r}{H_{sr}\sigma_{SB}T_s^4/\pi} \frac{\dot{W}}{\dot{Q}_r} = \left(1 - \frac{T_r^4}{T_s^4}\right) \left(1 - \frac{\dot{Q}_c}{\dot{Q}_r}\right) = \left(1 - \frac{T_r^4}{T_s^4}\right) \left(\frac{qV_c/\varepsilon - qV_r/\varepsilon}{1 - qV_r/\varepsilon}\right) \quad (4.66)$$

As said before, the TPH converter has an extra degree of freedom in the design, as compared to the TPV. It is the hot cell voltage V_r . The hot cell temperature in the monochromatic case depends on the same parameter $H_{rc}\Delta\varepsilon/H_{rs}\varepsilon$ as in the TPV case. When this parameter tends to infinity, the cold cell tends to be in open circuit, V_{coc} , given by

$$\frac{(\varepsilon - qV_{coc})}{kT_a} = \frac{(\varepsilon - qV_r)}{kT_r} \Rightarrow qV_{coc} = \varepsilon \left(1 - \frac{T_a}{T_r}\right) + qV_r \frac{T_a}{T_r} \quad (4.67)$$

Using this equation in equation (4.66), we obtain the same limit equation for the efficiency as the one for the TPV converter (equation 4.57):

$$\eta = \left(1 - \frac{T_r^4}{T_s^4}\right) \left(1 - \frac{T_a}{T_r}\right) \quad (4.68)$$

An interesting feature of this formula is that it holds for any value of V_r . Thus the TPH converter has the same upper limit as the TPV one. Furthermore, T_r is the same as in the TPV.

To our knowledge, this novel concept has not yet been fully explored. However, we present in Figure 4.10 the efficiency versus the cold cell voltage V_c (usually, in other contexts, we call efficiency to the maximum of this curve) for V_r in forward bias, zero bias (TPV mode) and reverse bias. In Figure 4.11, we present the hot cell temperature. We can

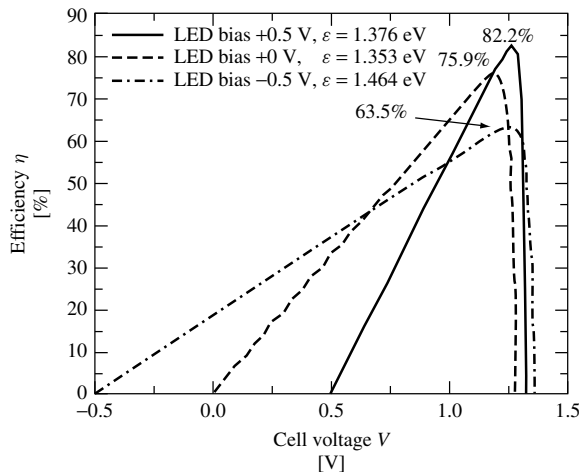


Figure 4.10 TPH efficiency versus V_c for three values of V_r for $H_{rc}\Delta\varepsilon/H_{rs}\varepsilon = 10/\pi$. The energy ε has been optimised

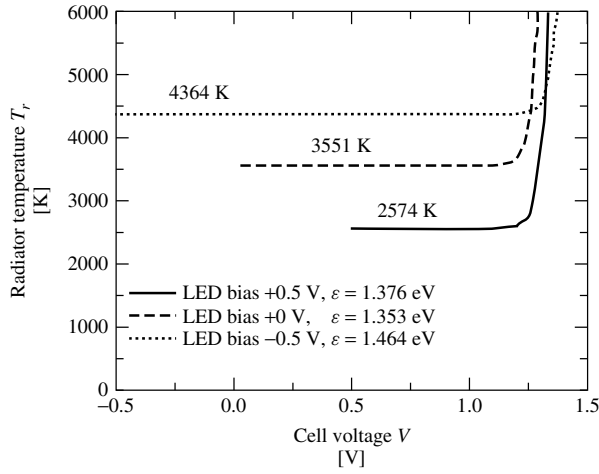


Figure 4.11 Hot cell temperature as a function of the cold cell voltage for several biasing voltages of the hot cell (LED) and for the energy that leads to maximum efficiency ($H_{rc} \Delta \varepsilon / H_{rs} \varepsilon = 10/\pi$). The energy ε has been optimised

see that higher efficiencies at lower temperatures can be obtained using the TPH concept under direct bias. This is not in contradiction to the fact that the limiting efficiency and the temperature for it is the same in both cases.

4.5.4 Higher-than-one Quantum Efficiency Solar Cells

One of the drawbacks that limit the efficiency of single-junction solar cells is the energy wasted from each photon that is absorbed because it is not converted into electrical power. Werner, Kolodinski, Brendel and Queisser [41, 42] have proposed a cell in which each photon may generate more than one electron–hole pair, thus leading to higher-than-one quantum efficiency solar cells. Without discussing which physical mechanisms may allow for this behaviour, let us examine its implications. Admitting that every photon may create $m(\varepsilon)$ electron–hole pairs, the current extracted from the device would be given by

$$I/q = \int_{\varepsilon_g}^{\infty} [m(\varepsilon)\dot{n}_s - m(\varepsilon)\dot{n}_r(T, \mu)] d\varepsilon \quad (4.69)$$

In this equation, ε_g is the energy threshold for photon absorption and the factor m in the generation term is our initial assumption. The same term must appear in the recombination term to reach the detailed balance: if the sun temperature is brought to the ambient temperature, the current will be zero when $\mu = 0$, only if the factor m also appears in the recombination term. For the moment we are saying nothing about the chemical potential μ of the photons emitted.

The power delivered, \dot{W} , is given by

$$\dot{W} = \int_{\varepsilon_g}^{\infty} qV [m\dot{n}_s - m\dot{n}_r(T, \mu)] d\varepsilon \quad (4.70)$$

Let us consider a monochromatic cell and calculate the irreversible entropy generation rate \dot{S}_{irr} in the whole device. With the aid of the general equation (4.44) and equation I-4 in Table 4.1, it is given by

$$T_a \dot{S}_{\text{irr}} / \Delta \varepsilon = (\mu_x \dot{n}_x + \dot{\omega}_x) - (\mu \dot{n}_r + \dot{\omega}_r) - qV(m\dot{n}_x - m\dot{n}_r) \quad (4.71)$$

where the source of photons has been substituted by its equivalent room-temperature luminescent radiation characterised by the chemical potential μ_x and the ambient temperature T_a . The open-circuit conditions are achieved when $\mu_{\text{OC}} = \mu_x$. For this value the entropy rate is zero since then $\dot{n}_x = \dot{n}_r$ and $\dot{\omega}_x = \dot{\omega}_r$.

Let us calculate the derivative of the irreversible entropy generation rate (equation 4.71) with respect to μ and particularise it for the open-circuit value of μ . Considering what follows V as only an unknown function of μ and independent of the way of obtaining the excitation (which is the case for infinite mobility) and using the fundamental relationship $\partial \dot{\omega}_r / \partial \mu = -\dot{n}_r$, the result is

$$\left[\frac{d(T_a \dot{S}_{\text{irr}} / \Delta \varepsilon)}{d\mu} \right]_{\mu_{\text{OC}}} = (qmV_{\text{OC}} - \mu_{\text{OC}}) \left[\frac{d\dot{n}_r}{d\mu} \right]_{\mu_{\text{OC}}} \quad (4.72)$$

This derivative is only zero if $qmV_{\text{OC}} = \mu_{\text{OC}}$. Since $\mu_{\text{OC}} = \mu_x$ can take any value by changing the source adequately, we obtain the result $qmV = \mu$. Any other value would produce a negative rate of entropy generation in the vicinity of the open circuit, against the second law of thermodynamics. This is a demonstration, based on the second law of thermodynamics, of the relationship between the chemical potential of the photons and the voltage (or electron and hole quasi-Fermi level split).

If we could choose m freely, the maximum power is achieved if we can maximise the integrand of equation (4.70) for each value of the energy [43, 44]. Once this is done, the reduction in ε_g so that it tends towards zero increases the power output. For the limit of $\varepsilon_g \rightarrow 0$, the maximum efficiency is the same as in equation (4.53), where a stack of an infinite number of cells was studied. Here $qVm(\varepsilon)$ is the variable that plays the same role as $qV(\varepsilon)$ earlier, although here V is the same for all the terms. In consequence, the upper efficiency is the same as for the tandem cell stack, 86.8%.

The higher-than-one quantum efficiency behaviour has been actually found [45, 46], although very close to one, for visible photons of high-energy and UV photons. The effect is attributed to impact ionisation, a mechanism in which the electron or the hole created by the high-energy photon, instead of thermalising by scattering with phonons, by means of impact processes transfers its high energy to a valence-band electron that gets pumped into the conduction band. This mechanism has a detailed balance counterpart that is the Auger recombination, in which the energy recovered in the recombination is transferred to an electron or a hole, which thus acquires a high kinetic energy.

4.5.5 Hot Electron Solar Cells

Wurfel [47] has studied the impact ionisation cells from another perspective and has shown that they become identical to the hot carrier solar cells proposed by Ross and Nozik [48]

pointing out also in this respect the necessity of providing the cell with special contacts as will be explained below.

In the hot carrier solar cell, the electron gas (semiconductor properties exhibiting a band gap does not seem to be essential for its operation) is in equilibrium at the lattice temperature T_a despite the absence of phonon interaction. This equilibrium is reached through other interactions as, for example, the interaction with thermal photons. Out of the equilibrium, electrons are thermalised by elastic scattering between them that allows a set of energy-dependent chemical potentials, one for the electrons of each energy. Furthermore, transference of energy between electrons exists through mechanisms that include impact ionisation and Auger recombination (this terminology is used in the context of semiconductors, which, as mentioned, we think is not necessary for this cell) according to reactions like $e_1^- + e_2^- \leftrightarrow e_3^- + e_4^-$. Actually in this equation transference of energy between electrons is produced by couples so that $\hat{\varepsilon}_1 + \hat{\varepsilon}_2 = \hat{\varepsilon}_3 + \hat{\varepsilon}_4$ where $\hat{\varepsilon}$ is electron (not photon) energy. However, the equilibrium of the reaction also establishes that the electrochemical potentials of the electrons (that we still call ε_F) are related by $\varepsilon_F(\hat{\varepsilon}_1) + \varepsilon_F(\hat{\varepsilon}_2) = \varepsilon_F(\hat{\varepsilon}_3) + \varepsilon_F(\hat{\varepsilon}_4)$. Therefore, the electrochemical potential of the electrons is a linear function of the energy in the form

$$\varepsilon_F(\hat{\varepsilon}) = \beta\hat{\varepsilon} + \varepsilon_{F0} \quad (4.73)$$

where the Fermi energy reference ε_{F0} becomes the same for both electrons and holes.

Since the Fermi function for electrons is written as

$$\frac{1}{\exp\left[\frac{\hat{\varepsilon} - \beta\hat{\varepsilon} - \varepsilon_{F0}}{kT_a}\right] + 1} = \frac{1}{\exp\left[\frac{\hat{\varepsilon} - \varepsilon_{F0}/(1 - \beta)}{kT_a/(1 - \beta)}\right] + 1} \quad (4.74)$$

the electron distribution can be regarded equivalently as a distribution at the lattice temperature T_a but characterised by a varying electrochemical potential given by equation (4.73) or as a hot carrier distribution with a constant electrochemical potential given by $\mu_{hc} = \varepsilon_{F0}/(1 - \beta)$ and a *hot carrier* temperature $T_{hc} = T_a/(1 - \beta)$.

If the interaction with phonons is introduced, through the reaction $e_1^- + \text{phonon} \leftrightarrow e_2^-$, where $e_{1(2)}^-$ represents an electron with energy $\hat{\varepsilon}_{1(2)}$, the fact that the phonon chemical potential is zero leads to $\varepsilon_F(\hat{\varepsilon}_1) = \varepsilon_F(\hat{\varepsilon}_2)$. However, $\hat{\varepsilon}_1 \neq \hat{\varepsilon}_2$ but $\hat{\varepsilon}_2 = \hat{\varepsilon}_1 + \varepsilon$, where ε is the phonon energy and, therefore, $\varepsilon_F(\hat{\varepsilon}_1) = \varepsilon_F(\hat{\varepsilon}_2)$ is only fulfilled if $\beta = 0$ and consequently all the electrons have the same electrochemical potential ε_{F0} and are at the lattice temperature. Phonon interaction is not considered to occur in what follows.

If the interaction with photons is considered now, $e_1^- + \text{photon} \leftrightarrow e_2^-$, the equilibrium of the reaction is represented by $\varepsilon_F(\hat{\varepsilon}_1) + \mu_{\text{ph}} = \varepsilon_F(\hat{\varepsilon}_2)$ where μ_{ph} is the photon chemical potential. Taking into account equation (4.73), it is obtained that $\mu_{\text{ph}} = \beta(\hat{\varepsilon}_1 - \hat{\varepsilon}_2) = \beta\varepsilon$ where ε is the energy of the photon involved. The result is that we have an energy-dependent photon chemical potential μ_{ph} . The Bose function that describes the occupation probability of the photon energy level ε becomes

$$\frac{1}{\exp\left[\frac{\varepsilon - \beta\varepsilon}{kT_a}\right] - 1} = \frac{1}{\exp\left[\frac{\varepsilon}{kT_a/(1 - \beta)}\right] - 1} \quad (4.75)$$

which can be seen as free radiation (zero chemical potential) at the hot carrier temperature.

Würfel also points out that, provided we can find a material in which a weak phonon coupling is produced in order to manufacture a solar cell, we still should be careful with the contacts because they do not allow for the maintenance of hot carriers inside the absorbing material. These special contacts must be able to cool the electrons from the hot temperature T_{hc} to the contact temperature T_a reversibly by changing their electrochemical potential from ε_{F0} to the electron electrochemical potential at the contacts (Fermi level at the metals) ε_{F+} and ε_{F-} . In Würfel's Reference [47], these special contacts are devised as selective membranes (Figure 4.12) that only allow electrons with energy centred around ε_e (left contact) and ε_h (right contact) to pass through. The reversible change in temperature and electrochemical potential of the electrons at the membranes is obtained by setting

$$\begin{aligned} \frac{\hat{\varepsilon}_e - \mu_{hc}}{kT_{hc}} = \frac{\hat{\varepsilon}_e - \varepsilon_{F-}}{kT_a} &\Leftrightarrow \varepsilon_{F-} = \hat{\varepsilon}_e \left(1 - \frac{T_a}{T_{hc}}\right) + \mu_{hc} \frac{T_a}{T_{hc}} \\ \frac{\hat{\varepsilon}_h - \mu_{hc}}{kT_{hc}} = \frac{\hat{\varepsilon}_h - \varepsilon_{F+}}{kT_a} &\Leftrightarrow \varepsilon_{F+} = \hat{\varepsilon}_h \left(1 - \frac{T_a}{T_{hc}}\right) + \mu_{hc} \frac{T_a}{T_{hc}} \end{aligned} \tag{4.76}$$

where $T_{hc} = T_a / (1 - \beta)$. The cell voltage will therefore be given by

$$qV = \varepsilon_{F-} - \varepsilon_{F+} = (\hat{\varepsilon}_e - \hat{\varepsilon}_h) \left(1 - \frac{T_a}{T_{hc}}\right) \tag{4.77}$$

The current extracted from the cell is determined by the rate at which electron-hole pairs of energy $\hat{\varepsilon}_e - \hat{\varepsilon}_h$ can be withdrawn from the cell. Since no energy is lost as heat, the energy balance equation (first principle) leads to

$$I(\hat{\varepsilon}_e - \hat{\varepsilon}_h)/q = \dot{E}(T_s, 0, \varepsilon_g, \infty, H_s) - \dot{E}(T_{hc}, 0, \varepsilon_g, \infty, H_r) \tag{4.78}$$

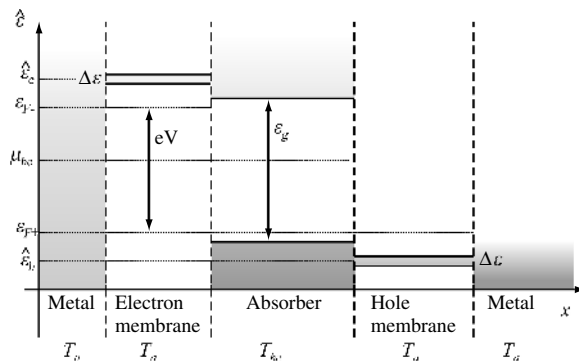


Figure 4.12 Band structure of a hot electron solar cell showing contacting scheme by means of selective membranes. (Reprinted from Solar Energy Materials and Solar Cells V. 46, N. 1, Würfel P., *Solar Energy Conversion with Hot Electrons from Impact Ionisation*, 43–52, © 1997 with permission from Elsevier Science)

and the power extracted from the cell can be finally computed as

$$\dot{W} = IV = [\dot{E}(T_s, 0, \varepsilon_g, \infty, H_s) - \dot{E}(T_{hc}, 0, \varepsilon_g, \infty, H_r)] \left(1 - \frac{T_a}{T_{hc}}\right) \quad (4.79)$$

which is independent of the carrier-extracting energies of the contacts. In other words, a large separation of the extracting energies leads to high voltage and low current and *vice versa*. Note that T_{hc} is a parameter for equation (4.79) and for equation (4.77). By elimination, we obtain the $W(V)$ and from it the derived IV curve. The cell efficiency is obtained from the maximum of $W(V)$ or $W(T_{hc})$.

For $\varepsilon_g \rightarrow 0$ the limit efficiency becomes

$$\eta = \left(1 - \frac{T_{hc}^4}{T_s^4}\right) \left(1 - \frac{T_a}{T_{hc}}\right) \quad (4.80)$$

just as in the TPV converters, leading to a limiting efficiency of 85.4%.

The monoenergetic membrane for electron and hole transfer to the contacting metals might perhaps be an insulator with an impurity band, but the nature of the phonon-insulated absorber is totally unknown. Ross and Nozik [48, 49] who have developed concepts close to those expressed here are investigating the poorer coupling of the electrons with the photons in materials with quantum dots with the idea of favouring this hot electron type of cell or the impact ionisation one that we have described in the preceding section.

4.5.6 Intermediate Band Solar Cell

One of the causes of efficiency reduction in single-junction solar cells is the transparency of the semiconductor to sub-band gap photons [50]. The inclusion of an intermediate band (IB) may greatly increase the efficiency. We show in Figure 4.13 a band diagram of the photon absorption and emission in this intermediate band material. Photons are absorbed not only by pumping electrons from the VB to the CB as in a traditional solar cell (photons with energy $h\nu_3$) but also by transitions from the VB to the IB (photons with energy $h\nu_2$) and from the IB to the CB (photons with energy $h\nu_1$). In total, two low-energy photons are used to pump an electron from the valence band to the conduction band, passing through the intermediate band. This certainly increases the cell current.

The three absorption mechanisms detailed above are effective if the IB is a band partially filled with electrons. In this way, there are empty states in it to accommodate the electrons from the VB and there are electrons to sustain a strong pumping to the CB. The detailed balance imposes photon emissions that are opposite to each one of the three absorption mechanisms.

The cell is contacted as shown in Figure 4.14. The electrons are extracted from the VB and returned to the CB using two layers of *n* and *p* ordinary semiconductors. A high voltage is produced as the sum of the two semiconductor junction voltages occurring at both sides of the IB material.

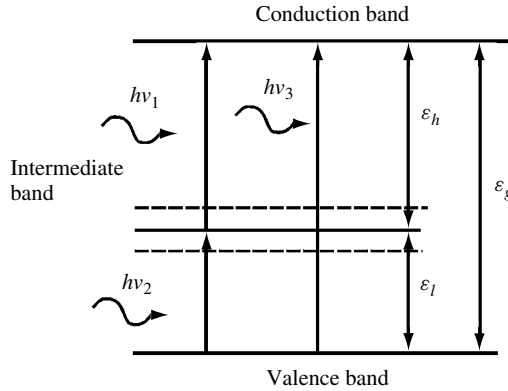


Figure 4.13 The band diagram of an intermediate band solar cell

In this IB material we admit that there are three quasi-Fermi levels, one for each band. The cell voltage is q times the splitting of the CB and VB quasi-Fermi levels.

In general, there is an energy threshold for each one of the absorption mechanisms described earlier. However, the ideal structure is the one in which the upper energy (lintel) of a photon that can be absorbed in certain mechanisms – involving, for example, transitions from the VB to the IB – is the threshold of the next one – for example, transitions from the IB to the CB. More specifically, calling ε_g the energy interval between the conduction and the valence band, ε_l the interval between the Fermi level in the intermediate band and the valence band and $\varepsilon_h = \varepsilon_g - \varepsilon_l$, and assuming that $\varepsilon_l < \varepsilon_h$, we consider that all the photons in the interval $(\varepsilon_l, \varepsilon_h)$ are absorbed by transitions from the VB to the IB, all the photons in the interval $(\varepsilon_h, \varepsilon_g)$ are absorbed by transitions from the IB to the CB and all the photons in the interval (ε_g, ∞) are absorbed by transitions from the VB to the CB.

Under such conditions the equations that rule the current–voltage characteristic of the cell are

$$I/q = [\dot{N}(T_s, 0, \varepsilon_g, \infty, \pi) - \dot{N}(T, \mu_{CV}, \varepsilon_g, \infty, \pi)] + [\dot{N}(T_s, 0, \varepsilon_h, \varepsilon_g, \pi) - \dot{N}(T, \mu_{CI}, \varepsilon_h, \varepsilon_g, \pi)] \quad (4.81)$$

$$\dot{N}(T_s, 0, \varepsilon_l, \varepsilon_h, \pi) - \dot{N}(T, \mu_{IV}, \varepsilon_l, \varepsilon_h, \pi) = \dot{N}(T_s, 0, \varepsilon_h, \varepsilon_g, \pi) - \dot{N}(T, \mu_{CI}, \varepsilon_h, \varepsilon_g, \pi) \quad (4.82)$$

with μ_{XY} being the photon chemical potentials equal to the separation of quasi-Fermi levels between band X and band Y . Equation (4.81) states the balance of electrons in the CB (addition of those that are pumped from the IB and the VB by means of the absorption of the corresponding photon less those that radiatively recombine). Equation (4.82) states a similar balance equation for the electrons in the IB and takes into account that no current is extracted from the IB. In addition,

$$qV = \mu_{CV} = \mu_{CI} + \mu_{IV} \quad (4.83)$$

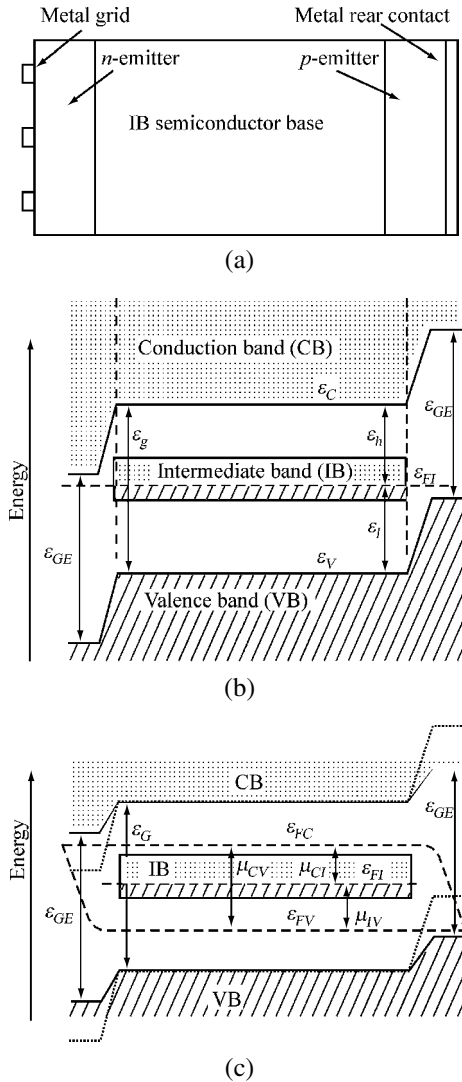


Figure 4.14 (a) Structure of the IB solar cell; (b) band diagram in equilibrium and (c) band diagram of forward bias conditions. (Reproduced from *A Metallic Intermediate Band High Efficiency Solar Cell*, Luque A. and Martí A., by permission of John Wiley & Sons Limited © 2001)

By eliminating μ_{CI} and μ_{IV} from the last three equations, we obtain the current–voltage characteristic of the cell. Efficiencies for different values of ε_l and ε_g are plotted in Figure 4.15.

The maximum efficiency of 63.2% is achieved for a cell of gap 1.95 eV with the IB Fermi level located at 0.71 eV from one of the bands. This efficiency is higher than the one corresponding to two series-connected ideal cells in tandem, of 54.5% (for band gaps of 0.8 and 1.54 eV). A detailed analysis of this cell operation can be found in the References [50–52]. The generalisation of the concept to more than two intermediate

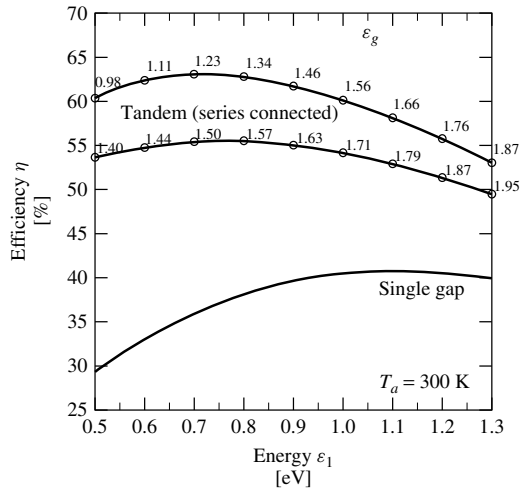


Figure 4.15 Limiting efficiency for the IB solar cell under maximum concentrated sunlight. For comparison, the limiting efficiency of single-gap solar cells (in this case, $\epsilon_l \equiv \epsilon_g$) and a tandem of two cells that are series-connected are also shown (in this case, ϵ_l labels the lowest band gap of the cells and the figures on the curve correspond to the highest of the band gaps). (Reproduced from *Increasing the Efficiency of Ideal Solar Cells by Photon Induced Transitions at Intermediate Levels*, Luque A. and Martí A., Physical Review Letters V. 78 N. 34, 5014–5017, by permission of American Physical Society © 1997)

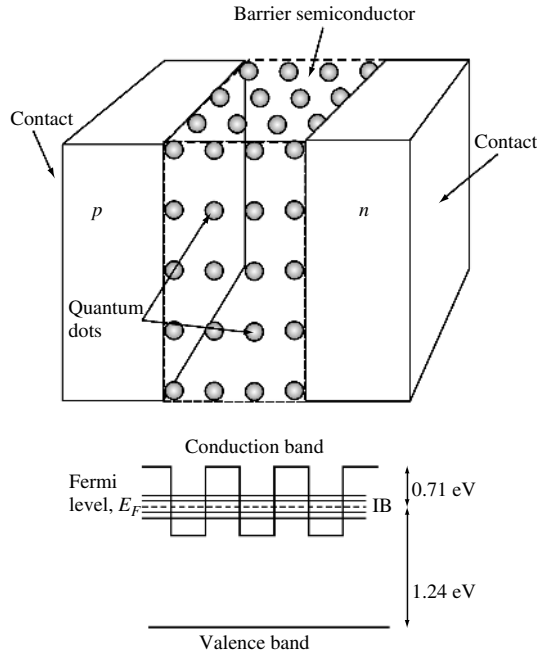


Figure 4.16 IB formation in QD arrays

band gaps (multiband solar cells) has been studied in [53, 54]. Some related concepts are that of an impurity band, in which the IB is made up of impurities [55], and the use of intermediate band materials as up- and down-converters [56, 57].

Suitable materials for a metallic IB are not very common. Accurate theoretical calculations establish that some alloys of the type III₃-V₄-IVb (with four electrons in the outer shell) present the required band [58]. No experiment has been carried out so far for implementing these materials, and therefore it is not certain whether the required metallic IB is actually formed or if the corresponding alloys are thermodynamically stable or separate into phases.

Another proposal [59] for forming the required IB is the use of nanotechnology. In particular, closely spaced quantum dot arrays might produce the desired band Figure 4.16. In_{0.58}Ga_{0.42}As dots (of band gap 0.87 eV) of a radius of 39 nm in a barrier material of Al_{0.4}Ga_{0.6}As of band gap 1.95 eV could produce an IB centred at 0.71 eV from the CB (if strain effects could be avoided and the offset in the VB could be suppressed [60]). The half filling of the IB can be achieved by barrier material doping [61, 62]. Experiments to prove the principle of operation of this type of cell have not yet been carried out.

4.6 CONCLUSIONS

In this chapter we have provided a thermodynamic basis that allows evaluating the thermodynamic consistency of classical and newly proposed solar cells. Also, we have assessed the efficiency limit of several PV concepts.

As deduced by Shockley and Queisser, the upper limit reachable with a single-junction solar cell is 40.7% for the cell illuminated by a black body source of photons at 6000 K and assuming the cell temperature at 300 K. This value is rather low if we take into account that the Carnot limiting efficiency for a reversible engine operating between hot and cold heat reservoirs at 6000 K and 300 K, respectively, is 95%. High-efficiency devices that can ideally surpass the Shockley–Queisser efficiency have been called *third generation PV converters*. Thus, the following question arises: could we invent a solar converter that exhibits this Carnot efficiency?

The answer is negative and the reason for it lies in the definition of efficiency. In the definition of the Carnot efficiency, the term entering in the denominator is the power *consumed*, that is, the power *arriving* at the converter less the power *leaving* the converter owing to the radiation that is emitted. In the conventional definition of the efficiency for solar converters, the term entering in the denominator is the power *arriving* at the converter and because it is higher than the *consumed* power this leads to a lower efficiency. With this definition, the higher achievable efficiency is the Landsberg efficiency of 93.33%. However, this efficiency, if reachable, cannot be reached with any known ideal solar converter.

A very high efficiency of 85.4% can ideally be reached with several devices such as the TPV converter, constituted by one ideal solar cell and one absorber and the TPH converter, conceived with one ideal solar cell and one LED that also plays the role of an absorber, or even a hot carrier solar cell. To reach this efficiency they all must emit radiation with zero chemical potential (free radiation) at 2544 K. This efficiency is also the limit for solar thermal devices.

However, this is not the highest efficiency that can be reached in solar converters. Efficiencies of up to 86.8% can be achieved using an array of solar cells of different band gap, either series-connected or independently connected.

Except for the TPH case, all solar cells operate at ambient temperature. This is a highly desirable feature. The TPH concept, which allows for higher efficiencies at lower temperatures than the TPV concept, may bring some advances. However, such devices to be practical require an almost ideal external quantum efficiency of the LED and the ability of working at high temperatures, both requirements being very difficult to acquire.

Experimental work on IB solar cells – whose upper limit efficiency is 63.2% – is now starting. It is conceivable that IBs may substitute two junction materials with perhaps less complexity. They may also be combined in tandem with more ordinary or IB cells.

Finally, it seems unlikely to us that a semiconductor can be found where the electrons are uncoupled enough from the phonons as to allow effective impact ionisation cells. However, a multilevel organic dye may be found or an array of quantum dots may be engineered where this coupling is reduced. In any case, the operation principles of this cell, and not only that of the usual solar cells, should be taken into account by those trying to bring other technologies into the manufacture of PV converters.

From the preceding statements it is clear that very high efficiencies are possible in a device operating in the PV mode. But what is possible in practice? This is a very difficult question. Certainly, stimulated by space research, there is a trend towards the development of multijunction cells. We stress again here that efficiencies of 34% (Global AM1.5) with a monolithic tandem of InGaP/GaAs, stuck on a Ge cell operating at 212 suns have been achieved. It can be asked whether such solutions are not too expensive for terrestrial use. However, we disagree. The use of very high concentration elements, in the range of 1000 or more, may make very expensive cells [63] usable. Wide acceptance angle concentrators with this concentration factor have already been developed that seem very suitable for mounting in low-cost tracking structures [64].

REFERENCES

1. Lofersky J, *Postepy-Fizyki* **26**, 535–560 (1975).
2. Shockley W, Queisser H, *J. Appl. Phys.* **32**, 510–519 (1961).
3. Green M, *Prog. Photovolt.* **9**, 123–135 (2001).
4. Callen H, *Thermodynamics*, John Wiley & Sons, New York (1981).
5. Landau L, Lifchitz E, *Physique Statistique*, Chap. I §24, Mir, Moscou (1967).
6. Badescu R, *Equilibrium and Nonequilibrium Statistical Mechanics*, Wiley, New York (1975).
7. Kondepudi D, Prigogine I, *Modern Thermodynamics*, Wiley, Chichester (1999).
8. Luque A, Martí A, Cuadra L, *IEEE Trans. Elec. Dev.* **48**, N. 9, 2118–2124 (2001).
9. Landau L, Lifchitz E, *Physique Statistique*, Chap. V §52, Mir, Moscou (1967).
10. Welford W, Winston R, *The Optics of Nonimaging Concentrators*, Appendix I, Academic Press, New York, NY (1978).
11. Landau L, y Lifchitz E, *Mécanique*, Chap. VII §46 La Paix, Moscou, (year not shown: prior to 1965).
12. Welford W, Winston R, *The Optics of Non-imaging Concentrators*, Chapter 2, §2.7. Academic Press, New York (1978).
13. Campbell P, Green A, *IEEE Trans. Elec. Dev.* **33**, 234–239 (1986).

14. Nozik A, *Annu. Rev. Phys. Chem.* **52**, 193–231 (2001).
15. Martí A, Balenzategui J, Reyna R, *J. Appl. Phys.* **82**, 4067–4075 (1997).
16. Araújo G, Martí A, *Sol. Energy Mater. Sol. Cells*, **31**, 213–240 (1994).
17. Luque A, Martí A, *Phys. Rev. Lett.* **78**, 5014–5017 (1997).
18. Hulstrom R, Bird R, Riordan C, *Sol. Cells* **15**, 365–391 (1985).
19. De Vos A, *Endoreversible Thermodynamics of Solar Energy Conversion*, Chap. 2 §2.1, Oxford University, Oxford (1992).
20. Miñano J, “*Optical Confinement in Photovoltaics*”, in Luque A, Araújo G, Eds, *Physical Limitations to Photovoltaic Energy Conversion*, 50–83, Adam Hilger, Bristol (1990).
21. Shockley W, *Bell Syst. Tech.* **28**, 435–489 (1949).
22. Würfel P, *Physica E* **14**, 18–26 (2002).
23. Sinton R, Kwark Y, Gan J, Swanson R, *IEEE Electron. Dev. Lett.* **EDL7**, 567–569 (1986).
24. Green M, *Prog. Photovolt.* **9**, 137–144 (2001).
25. Araújo G, “*Limits to Efficiency of Single and Multiple Bandgap Solar Cells*”, in Luque A, Araújo G, Eds, *Physical Limitations to Photovoltaic Energy Conversion*, 119–133, Adam Hilger, Bristol (1990).
26. Araújo G, Martí A, *IEEE Trans. Elec. Dev.* **37**, 1402–1405 (1998).
27. Gale R, King B, Fan J, *Proc. 19th IEEE PSC*, 293–295, IEEE, New York (1987).
28. Tobin S, Vernon S, Sanfacon M, Mastrovito A, *Proc. 22th IEEE PSC*, 147–152, IEEE, New York (1991).
29. Miñano J, *J. Opt. Soc. Am. A* **3**, 1345–1353 (1986).
30. Parrot J, in Luque A, Araújo G, Eds, *Physical Limitations to Photovoltaic Energy Conversion*, Adam Hilger, Bristol (1990).
31. Martí A, Araújo G, *Sol. Energy Mater. Sol. Cells* **43**, 203–222 (1996).
32. Luque A, Martí A, *Phys. Rev. B* **55**, 6994–6999 (1997).
33. Landsberg P, Tonge G, *J. Appl. Phys.* **51**, R1–20 (1980).
34. De Vos A, Pauwels H, *Appl. Phys.* **25**, 119–125 (1981).
35. Luque A, Martí A, *Sol. Energy Mater. Sol. Cells* **58**, 147–165 (1999).
36. Karam N *et al.*, *Sol. Energy Mater. Sol. Cells* **66**, 453–466 (2001).
37. Brown A, Green M, *Prog. in Photovolt.: Res. Appl.* **10**, 299–307 (2002).
38. Tobias I, Luque A, *Prog. in Photovolt.: Res. Appl.* **10**, 323–329 (2002).
39. Luque A, “*Coupling Light to Solar Cells*”, in Prince M, Ed, *Advances in Solar Energy*, Vol. 8, ASES, Boulder, CO (1993).
40. Castañs M, *Revista Geofísica* **35**, 227–239 (1976).
41. Werner J, Kolodinski S, Queisser H, *Phys. Rev. Lett.* **72**, 3851–3854 (1994).
42. Werner J, Brendel R, Queisser H, *Appl. Phys. Lett.* **67**, 1028–3014 (1995).
43. De Vos A, Desoete B, *Sol. Energy Mater. Sol. Cells* **51**, 413–424 (1998).
44. Spirkel W, Ries H, *Phys. Rev. B* **V. 52 N. 15**, 319–325 (1995).
45. Kolodinski S, Werner J, Queisser H, *Appl. Phys. Lett.* **63**, 2405–2407 (1993).
46. Kolodinski S, Werner J, Queisser H, *Sol. Energy Mater. Sol. Cells* **33**, 275–285 (1994).
47. Würfel P, *Sol. Energy Mater. Sol. Cells* **46**, 43–52 (1997).
48. Ross R, Nozik A, *J. Appl. Phys.* **53**, 3813–3818 (1982).
49. Nozik A, *Photovoltaics for the 21st Century*, *Proceedings of the International Symposium in McConnel R, Kapur V, Eds*, 61–68, The Electrochemical Society, Pennington, NJ (2001).
50. Luque A, Martí A, *Phys. Rev. Lett.* **78**, 5014–5017 (1997).
51. Luque A, Martí A, *Prog. Photovolt.: Res. Appl.* **9**, 73–86 (2001).
52. Luque A, Martí A, Cuadra L, *Proc. of the 16th European Photovoltaic Solar Energy Conference*, 59–61, James & James Ltd, London (2000).
53. Green M, *Prog. Photovolt.: Res. Appl.* **9**, 137–144 (2001).
54. Brown A, Green M, “*Limiting Efficiency for a Multi-Solar Cell Containing Three and Four Bands*” International Workshop on Photovoltaics in nanostructures, Dresden, Germany, Proc. to be published in *Physica E* (Private Communication) (2001).

55. Beaucarne G, Brown A, Keevers M, Corkish R, Green M, *Prog. in Photovolt.: Res. Appl.* **10**, 345–353 (2002).
56. Trupke T, Green M, Würfel P, *J. of Appl. Phys.* **52**, 1668–1674 (2002).
57. Trupke T, Green M, Würfel P, *J. of Appl. Phys.* **92**, 4117–4122 (2002).
58. Wahnón P, Tablero C, *Physical Review B* **65**, 165115, 1–10 (2002).
59. Martí A, Cuadra L, Luque A, *Proc. of 28th IEEE Photovoltaic Specialist Conf.*, 940–943, IEEE, New York (2000).
60. Cuadra L *et al.*, *Proc. of the 17th European Photovoltaic Solar Energy Conference*, 98–101, James&James (Munich, Germany, 2001).
61. Martí A *et al.*, *Photovoltaics for the 21st Century, Proc. de la 199th Electrochemical Society Meeting*, 46–60, The Electrochemical Society, Pennington, NJ (2001).
62. Martí A, Cuadra L, Luque A, *IEEE Trans. Elec. Dev.* **48**, 2394–2399 (2001).
63. Yamaguchi M, Luque A, *IEEE Trans. Electron. Dev.* **46**, 2139–2144 (1999).
64. Miñano J, González J, Benítez P, *Appl. Opt.* **34**, 7850–7856 (1995).

This Page Intentionally Left Blank

5

Solar Grade Silicon Feedstock

Bruno Ceccaroli¹ and Otto Lohne²

¹*Silicon Technologies AS, Kristiansand, Norway,* ²*Norwegian University of Science and Technology (NTNU), Trondheim, Norway*

5.1 INTRODUCTION

The Photovoltaic (PV) industry is still in its infancy and at the moment it is very difficult to predict which technical, economical and social patterns its deployment will follow before reaching maturity. However, if photovoltaics are to become a major energy source in the future, it is appropriate to question which materials and which natural elements are critical to secure the long-term sustainability of this energy source. This is particularly valid for the semiconductor materials whose band gap has to perform the efficient conversion of sunlight to electricity. The recent history of photovoltaics (from the 1950s) reveals an intense activity of research and development embracing a broad range of disciplines and leading to a healthy multitude of innovations. Organic versus inorganic semiconductors, intrinsic versus extrinsic semiconductors, homojunctions versus heterojunctions and amorphous versus crystalline structures are a few dilemma that new research achievements steadily bring to the scientific and industrial community. It will take years, perhaps decades, before mankind is able to solve the challenge and answer the questions addressed above. (These aspects are also described in Chapters 6 to 16 of this handbook.)

Up to now, the dominant semiconductor material used in photovoltaics is silicon, particularly crystalline silicon. The most recent market surveys issued by commercial consultants, (trans)governmental organisations and agencies clearly state this fact.¹ Analysing annual growth by means of technology and material from these quoted sources, multicrystalline silicon takes the lion's share of the growth. In the first half of the 1990s,

¹ For PV News edited by Maycock (2001), commercial shipments to terrestrial and indoor applications of cells or modules based on non-silicon technologies accounted in 2000 for just 1.2 MW of a total 288 MW, that is, 4.2 per thousand. Amorphous silicon was credited in the same period 27 MW shipment or 9.4% and crystalline

multicrystalline sawn wafers accounted for just half of the single-crystal shipments. In 1998 both technologies were equivalent in size. Two years later, multicrystalline technology surpassed single-crystal technology by 55%.

The consensus is that crystalline silicon is and will remain for at least a long decade the workhorse of this growing market. Long-term visionary forecasts predict that by 2050, 30 000 TWh PV electricity will be generated annually worldwide. This will require an installed PV output capacity totalling approximately 15 million metric tons (MT) of solar grade silicon feedstock, assuming that silicon remains dominant and that cell efficiency and material yields have steadily improved. To build up such a capacity over fifty years will represent an annual production of 300 000 MT solar grade silicon feedstock. The annual present consumption of pure silicon for photovoltaics is approximately a hundredth part of that (i.e. 4000 MT), whereas production of metallurgical grade silicon for all purposes in 2000 was approximately one million metric tons. This clearly poses the question of material feasibility and availability. The present chapter is therefore dedicated to silicon, its extraction, purification and availability by current and future practice.

5.2 SILICON

Silicon (Si) is the second member in the Group IVA in the periodic system of elements. It never occurs free in nature, but in combination with oxygen forming oxides and silicates. Most of the Earth's crust is made up of silica and miscellaneous silicates associated with aluminium, magnesium and other elements. Silicon constitutes about 26% of the Earth's crust and is the second most abundant element in weight, oxygen being the largest.

5.2.1 Physical Properties of Silicon Relevant to Photovoltaics

Silicon is a semiconductor with a band gap E_g of 1.12 eV at 25°C. At atmospheric pressure, silicon crystallises into a diamond cubic structure, which converts into a body-centred lattice when subjected to ca 15 GPa. Under some circumstances, slow-growing

silicon the balance, that is, close to 90% of which 49% (141 MW) are cells made of multicrystalline sawn wafers, 31% (90 MW) of single-crystal wafers and 10% (28 MW) are cells based on various crystalline silicon technologies, for example, ribbon (15 MW or 5.1%), amorphous silicon on single-crystal silicon slices (12 MW or 4.2%) and others (approx. 1 MW or 3.5 per thousand).

Solar Modules Shipment by Technology (Source: PV News 2001)

Technologies	Shipped output in 2000
Amorphous silicon	27 MW (9%)
Single crystal silicon wafers	90 MW (31%)
Multicrystalline sawn silicon wafers	141 MW (49%)
Various crystalline silicon technologies (i.e. ribbon, films, amorphous on single crystal)	28 MW (10%)

Other sources available in May–November 2001 at the time of writing this chapter, such as the German magazine Photon International March 2001 published congruent data for the same period. Statistics from non-commercial entities as those edited by the International Energy Agency (IEA-PVPS programme) covering 21 industrialised countries, members of the OECD-organisation, show over years the same trends [1–4].

faces of silicon are (111) but in epitaxial films and polysilicon deposition (111) is the fastest growth direction. Vapour deposition below 500°C results in amorphous silicon. If reheated above this temperature, crystallisation will occur.

Unlike most of the compounds and elements, silicon contracts when melting or expands when solidifying.

Impurities incorporated in the silicon lattice during the crystal growth or during the post-treatment (diffusion, implantation etc.) ionise at low temperatures, thus providing either free electrons or holes. Impurities from the Group IIIA replace a Si atom in the atomic lattice to supply electrons and are called *n*-dopants or donors, whereas elements from the Group VA substitute for a Si atom to supply holes and are called *p*-dopants or acceptors (see Section 5.6.3). Phosphorus and boron represent these groups and are used in PV processing to control the semiconductor properties (doping levels) of silicon. Impurity concentrations are expressed in atoms of impurity per cubic centimeter of the host material (silicon). In silicon semiconductor devices, these vary from 10^{14} to 10^{20} atoms per cm^3 and can be directly measured by analytical instruments. An indirect measure of impurity concentration is the minority-carrier lifetime. This is the time that elapses before a free electron in the lattice recombines with a hole. The transition metals, Fe, Cr, Ni, degrade the minority-carrier lifetime and the solar cell performance. High-purity silicon crystals with metal content less than 10 ppb(w) have minority-carrier lifetime values as high as 10 000 μs . Semiconductor wafers with phosphorus and boron dopants have values from 50 to 300 μs . Solar cells require minority-carrier lifetime value of at least 25 μs .

The relatively high refractive index limits the optical applications of silicon. The absorption/transmission properties in the 0.4 to 1.5 μm wavelength spectra are important in the performance of PV cells and photoconductive devices. In PV applications antireflective layers applied to silicon are commonly used.

Silicon even when alloyed with small quantities of impurities is brittle. Shaping silicon for PV applications requires sawing and grinding. Microelectronic applications require polishing. These mechanical operations are very similar to those applied to glasses.

Various thermal and mechanical properties are reported in Table 5.1.

For more details the reader is invited to consult the References [5–8].

Table 5.1 Thermal and mechanical properties of silicon

Property	Value
Atomic weight	28.085
Atomic density (atoms/ cm^3)	5.0×10^{22}
Melting point ($^{\circ}\text{C}$)	1410
Boiling point ($^{\circ}\text{C}$)	2355
Density (g/cm^3 at 25 $^{\circ}\text{C}$)	2.329
Heat of fusion (kJ/g)	1.8
Heat of vaporisation at MP (kJ/g)	16
Volume of contraction on melting (%)	9.5

5.2.2 Chemical Properties Relevant to Photovoltaics

Silicon is stable in the tetravalent state and has a strong affinity for oxygen, forming stable oxides and silicates, the only natural occurrences known for silicon. Artificially isolated elemental silicon immediately oxidises, forming a thin protective film of silica of less than 100 Å, which prevents further oxidation. Oxygen plays an important role in silicon-semiconductor devices, for instance, in manufacturing metal oxide semiconductor (MOS) transistors.

Silicon and carbon (Group IVA) form a strong Si–C bond and stable products. Silicon carbide is artificially synthesised in several allomorphic structures, finding various applications in photovoltaics and electronics. Primary uses are the abrasive properties of SiC for wafering silicon crystals and the emerging applications of SiC semiconductors. The strong Si–C bond is also the origin of the rich organosilicon chemistry encompassing numerous polysiloxanes (commonly named *silicones*) and organosilanes in which organic radicals are attached to silicon atoms through a covalent Si–C bond.

The tetravalence and the similarity of silicon and carbon are illustrated in the ability of silicon to form bonds with itself, Si–Si, and to form polymers, for example, $-(\text{SiH}_2)_p-$, $-(\text{SiF}_2)_p-$, comparable to hydrocarbons and fluorocarbons, although the length of the chains remains modest in the case of the silanes.

Silicon forms hydrides; Monosilane (SiH_4) is a key chemical compound for the production of amorphous silicon and the purification of silicon to semiconductor grade (see later in this chapter).

The chemical reactivity of silicon with chlorine is also extremely important. Alkyl- and arylchlorosilanes are the necessary intermediates to build the polysiloxane chains (silicones). Trichlorosilane and tetrachlorosilane, because they are volatile at low temperature and can be decomposed to elemental silicon at high temperature, are both the intermediates and the by-products of the purification processes upgrading metallurgical grade silicon to semiconductor purity (see later in this chapter). Other chlorosilanes or halogenosilanes are also used in chemical vapour deposition applications. The halogen atom is easily substituted by a hydroxyl group, $-\text{OH}$, through hydrolysis. Such a hydroxyl group tends to react with other functional groups by exchanging the hydrogen atom. This is the basis of a rich surface chemistry.

Silicon and germanium (Group IVA) are isomorphous and mutually soluble in all proportions.

Tin and lead, also elements of Group IVA, do not react with silicon and are not miscible in silicon, which is mentioned as a remarkable curiosity.

For more details on the chemical properties the reader is invited to consult the References [8–11].

5.2.3 Health Factors

The surface of elemental silicon is oxidised and is relatively inert and is considered as non-toxic. Hazard risks with elemental silicon are high when silicon occurs as a fine

powder in the presence of an ignition source. Damaging and fatal explosions have been reported by the silicon industry. The raw material, from which silicon is made, quartz or quartzite, is one of the sources of silicosis. Most of the hazards are related when quartz/quartzite is quarried, exposure taking place during drilling, crushing, loading and bulk handling. Several protection methods must be applied to the quarries and to the metallurgical plants to prevent silicon dust explosion and silicosis. Volatile silanes such as monosilane and chlorosilanes are extremely reactive in the presence of oxygen, water or moisture. They are also classified as hazardous chemical substances whose handling requires special care. Saturated long chain silanes, polysiloxanes as well as amorphous silica are known to be chemically inert and not toxic. Because of that they are widely used in pharmacy, food industry and cosmetics.

The production of metallurgical silicon and electronic grade silicon has an environmental impact through energy consumption, associated with climatic and polluting gases principally CO_2 , NO_x and SO_2 . However, it must be noticed that the corresponding nuisances and energy consumption involved in manufacturing and installing PV systems are “paid back” by the same system in the form of emission-free “green” electricity only after about four to five years of an average existence of more than 25 years. More quantified examples about environmental and energy “payback” are reported from Europe, Japan and Australia and commented in [12].

5.2.4 History and Applications of Silicon

Since antiquity, silicon has been of great importance to humanity. However, the first applications were based on naturally occurring forms of silicon, for instance, flint (silex-silicis in Latin), a variety of quartz used from the Stone Age to the Neolithic Era to make tools, weapons and later potteries. Glass made of silicate dated back to 12000 B.C. Elemental silicon was prepared for the first time in 1824 by Berzelius, passing silicon tetrachloride over heated potassium. Silicon tetrachloride could be prepared by chlorinating silicate/silica. The first crystalline silicon was made accidentally in 1854 by Sainte-Claire Deville working on aluminium electrolysis. The first preparation of silicon/silicon rich alloys in an electric arc furnace was performed by Moisan in 1895 and the industrial production was by Bozel and Rathenau independently from 1897 to 1898. Acheson also discovered accidentally in this period silicon carbide while trying to make artificial diamond. Silicon alloys, particularly ferroalloys, have from the end of the nineteenth (XIX) century played an important role in the production of steel. Silicon metal (silicon content higher than 96% according to definitions outlined by trade organisations) was not current until the Second World War. Three major applications have since greatly stimulated the production and purification of silicon, that is, aluminium, silicones and solid-state electronics. Silicon carbide has also found a broad range of applications taking advantage of its hardness and chemical noble character. More recently SiC has found applications in electronics because of its excellent semiconductor properties and tends to become a strategic material for cutting silicon and boules into thin wafers.

At the beginning of the new 2000 millennium, approximately one million metric tons of metallurgical grade silicon, also called *silicon metal* in the industry because of its appearance and not because of its physical properties, are produced and sold in the world

Table 5.2 Chemical characteristics of commercial metallurgical grade silicon

Element	O	Fe	Al	Ca	C	Mg	Ti	Mn	V	B	P
Low (ppm)	100	300	300	20	50	5	100	10	1	5	5
High (ppm)	5000	25 000	5000	2000	1500	200	1000	300	300	70	100
Element	Cu	Cr	Ni	Zr	Mo						
Low (ppm)	5	5	10	5	1						
High (ppm)	100	150	100	300	10						

market. This is a relatively small amount compared to the multimillion metric ton markets of crude iron, steel, aluminium or ferroalloys. Industrial location to produce silicon metal has been guided by the vicinity of rich and pure quartz deposits and/or the availability of abundant electrical power. Leading producing countries are PR China, the United States, Brazil, Norway and France. In spite of some recent mergers, the industry remains fragmented. One may find three dozens of companies producing and marketing silicon metal, most of the plants having an annual output of 20 000 to 60 000 MT (see production of silicon metal later in this chapter). The chemical characteristics of commercial metallurgical grade silicon are indicated in Table 5.2.

The silicon metal market is traditionally divided into two main subgroups, that is, the aluminium and the chemical segments each consuming approximately half of the worldwide output. There are, however, some differences in the characteristics requested by each.

5.2.4.1 Applications in aluminium

In the aluminium industry, silicon is added to molten aluminium in which it is dissolved. A simple eutectic composition occurs at 12.6% silicon in aluminium. This has important consequences for industrial applications in the aluminium industry. Silicon is used in order to improve the viscosity, the fluidity of liquid aluminium and the mechanical properties of commercial alloys. The iron, calcium and phosphorus content in silicon are particularly critical for such applications.

There are two important groups of aluminium alloys in which silicon is one of the main alloying elements.

5.2.4.1.1 Casting alloys

By adding silicon to the melt, the fluidity is improved. Aluminium alloys near the eutectic composition are therefore used in thin-walled castings. Typical concentrations are 7 to 12%. If a few tenths of a percent of magnesium is added, the alloys may be age-hardened and thereby nearly double their yield strength.

To counteract the formation of large needle-shaped particles, the alloys are normally modified with sodium, strontium or phosphorus.

The alloys present good corrosion properties.

5.2.4.1.2 Wrought alloys

AlMgSi alloys (6xxx series) are widely used as medium-strength structural alloys. Typical silicon content is 0.5 to 1.0%.

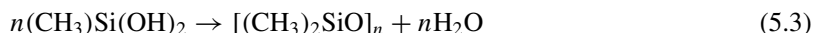
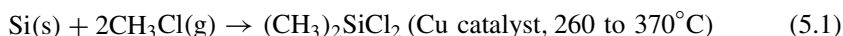
The alloys of the 6xxx series have good hot-working properties and are age-hardening. These alloys are therefore well suited for extrusion of profiles, which by heating at 150 to 200°C are given their final strength.

The alloys present good corrosion and weldable properties. Typical markets are building and transport industries.

5.2.4.2 Applications in chemistry

5.2.4.2.1 Silicones

Since the discovery of the direct synthesis (reaction 5.1) of dimethyldichlorosilane, during the Second World War independently by Rochow and Müller, the silicones industry has developed to become a strong and growing chemical business consuming (year 2000) about 400 000 MT of silicon [8–11].



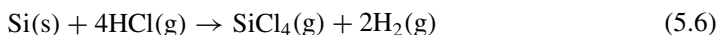
The direct synthesis (5.1) is industrially performed in a fluidised bed reactor requesting small particles or powder of silicon (20–300 μm). The reaction is exothermic and needs to be activated with copper catalysts as well as promoters Zn, Sn, P and others. Whereas Fe does not seem to play an important role, Ca and Al have shown to take an active part in the overall reaction.

5.2.4.2.2 Synthetic silica

Varieties of synthetic silica such as pyrogenic silica (also called *fumed silica*) or silica ingots as feedstock to optical fibres are industrially prepared by burning silicon tetrachloride:



Silicon tetrachloride may be prepared by chlorination of natural silica. However, industrially, silicon tetrachloride is produced by reacting chlorine with metallurgical grade silicon in a direct synthesis performed either in a fluidised bed or a fixed bed reactor:

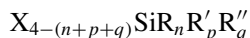


The present fumed silica market is about 100 000 to 120 000 MT, which in turn consumes around 50 000 to 60 000 MT of metallurgical silicon. It is noted that the main market for

fumed silica is as additives in silicone rubbers used to increase the mechanical strength and the elasticity of these elastomers.

5.2.4.2.3 Functional silanes

This generic term covers a broad range of products built on silane molecules, in which an atom of hydrogen or of chlorine is substituted with an organic radical bearing a functional group, for example, amine, acid, ester, alcohol and so on.

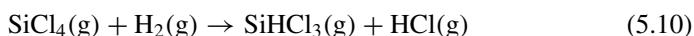
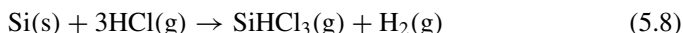


represents a general formula of functional silanes, in which R, R', R'' are organic radicals and X is Cl or OH. There exist a multitude of functional silanes. One of their major applications is as coupling agent between inorganic and organic compounds, for example, inorganic fillers (glass, silica, clays etc.) in organic matrices (epoxy, polyester etc.)

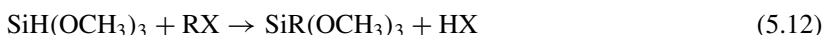
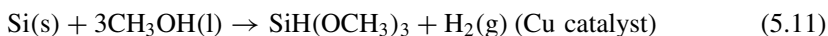
Several routes may be imagined to generate such molecules. The current industrial praxis dictated by economical efficiency is the functionalisation of trichlorosilane according to



whereas trichlorosilane is produced by a direct synthesis in a fluidised or fixed bed reactor:



A variant recently developed for some classes of functional silanes is the direct synthesis involving silicon and methanol:



Orthoethylsilicate or tetraethoxysilane, $\text{Si}(\text{OC}_2\text{H}_5)_4$, is an important chemical molecule for glass, ceramic, foundry and painting. It is produced industrially by substitution of Cl in SiCl_4 or by direct reaction of ethanol with silicon in the presence of a catalyst following the same pattern as (5.7) and (5.12).

The total consumption of silicon metal to functional silanes and orthosilicates may be estimated at 10 000 to 20 000 MT per year.

5.2.4.3 Semiconductor silicon

Silicon is by far the most important and popular semiconductor material since the emergence of solid-state electronics in the late fifties and the early sixties. Ultra-pure

silicon (commercially called *polysilicon*) with the adequate semiconductor properties is industrially prepared through the distillation and the thermal decomposition of volatile silicon compounds, for example, trichlorosilane, SiHCl_3 , and monosilane, SiH_4 . These operations are performed in large chemical plants, which for synergy reasons are sometimes incorporated in plants producing other silicon-based compounds as those described above. Although the ultimate application in the case of polysilicon is in the semiconductor industry, this particular process is, from a silicon raw material perspective, counted among the chemical applications of silicon.

The current production of polysilicon in 2000 was approximately 20 000 MT, whereas the installed worldwide capacity was estimated around 25 000 MT. Compared to the other applications of silicon, the use of semiconductor silicon in terms of volume is very modest. However, it is a high-value product. For example, the silicon value is multiplied by a factor of 30 to 50 through upgrading metallurgical grade silicon to polysilicon. This is also the fastest-growing application of silicon with an annual growth rate of approximately 10%, whereas silicones grows at a 5 to 7% rate, aluminium at 2 to 3% and silicon metal overall at 4%.

The present raw material for all silicon solar cells originates from this route. Therefore, a more detailed description of these processes will be given later in the present chapter.

5.2.4.4 Other applications

There are a few other applications of silicon in various fields such as explosives (silicon powder), refractories and advanced ceramics (silicon nitride and carbide). These applications presently do not account for more than 1% of the worldwide silicon metal output.

Because of their anticipated excellent mechanical and chemical resistant properties, alloys rich in silicon have a bright future. They may be prepared by powder metallurgy, mixing and sintering silicon powder with metallic powders (e.g. Cu, Al, Ti, Co, V etc.) [7].

The present chapter does not review the applications of silicon, such as glasses, ferroalloys and silicon carbide, in which silicon is usually added to the production process as natural silicate, quartz, quartzite or other silicon alloys.

5.3 PRODUCTION OF METALLURGICAL GRADE SILICON

5.3.1 The Carbothermic Reduction of Silica

Metallurgical grade silicon, also called *silicon metal*, with a typical purity of 98.5% Si is produced in submerged electric arc furnaces. In principle, this process is much the same as it was at the beginning of the twentieth (XX) century when it was first developed for ferrosilicon and other alloys. However, practical execution has greatly improved with larger furnaces, more efficient material handling and improved control of the operations. This has led to a continuous decrease of the specific energy consumption concomitant to higher degrees of raw material utilisation.

The furnace consists essentially of a crucible filled with quartz and carbon materials. Silicon is freed by the carbothermic reduction of silica according to the overall reaction:



Contrary to what is often claimed in popular articles or reviews, silica sand is currently not used for this purpose. Lumpy quartz (e.g. 10–100 mm) with appropriate purity and thermal resistance is preferred. Carbon raw material generally consists of metallurgical grade coal as well as woodchips and/or charcoal and coke. The metallurgical coal is co-produced with coal used for crude steel production. As a rule this coal needs to be washed in order to remove most of the ash containing unsuitable impurities. Raw materials, both quartz and carbon, are selected in order to achieve high product quality (silicon and silica fumes), to maximise furnace performances and to minimize the environmental damages (i.e. SO_2 and NO_x emissions). The raw material reactivity and the consistency of the mix of raw materials in the charge, for instance its porosity, are extremely important factors in achieving good furnace performance in terms of high material yield, lower power consumption and good product quality.

The raw material mix or charge is heated by means of an intense electric arc sustained between the tip of three submerged electrodes and the electrical ground of the furnace. Although important exceptions exist, the current practice is to run this process in a three-phase current, open and rotating furnace at a working electrical load normally between 10 and 30 MW, depending on the size of the furnace. The tendency is to increase the furnace size and the electrical load in order to achieve higher output and productivity.

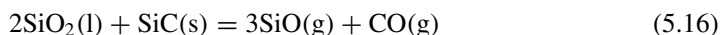
Electrodes are also made of carbon. Originally, expensive graphite electrodes were used. They were displaced by pre-baked electrodes, which in turn tend to be replaced by more cost-efficient self-baking electrodes. The electrode technology is an important aspect to the present development of this industry: half a dozen electrode types ranging from pre-baked to self-baking electrodes of Söderberg type are currently used or are in the process of development.

Liquid silicon metal is tapped from the bottom of the furnace, and the thoroughly mixed raw materials are charged on the top. The reaction co-product, carbon monoxide $\text{CO}(\text{g})$, is further oxidised to carbon dioxide $\text{CO}_2(\text{g})$ in open furnaces and released into the atmosphere. In open furnaces, side-reactions leading to the formation of silica fumes play an important role for the overall economics of the process:



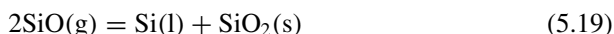
The silica fumes, which consist mainly of very fine particles of amorphous silica less than 1 μm , are passed through filter cloths installed in large bag-house systems adjacent to the furnaces. The collected amorphous finely divided silica finds valuable applications as additives in concrete and refractory. Depending on the quality of the raw materials used and the operational strategy and skills, the silicon yield as metallurgical silicon ranges from 80 to 90%, the balance resulting in silica fume.

Reactions (5.13) to (5.15) are a simplification of the complex system. Several main principles can be understood from a more detailed description of the chemistry. There are two important intermediate compounds: the gaseous silicon monoxide $\text{SiO}(\text{g})$ as already mentioned in reaction (5.14) and the solid silicon carbide $\text{SiC}(\text{s})$. To interpret the chemistry occurring in the furnace, it is convenient to conceptually split the furnace reaction inner space into an inner hot zone and an outer cooler zone. Liquid silicon is produced in the inner zone, where the dominant chemistry is described by the reactions



The temperature in the inner zone is in the range of 1900 to 2100°C, allowing a high proportion of $\text{SiO}(\text{g})$ in this zone, which is absolutely indispensable for further reduction according to reaction (5.17).

In the outer zone, where temperature is below 1900°C, $\text{SiO}(\text{g})$ and $\text{CO}(\text{g})$ convected away from the inner zone meet and react with free carbon. Consequently, silicon carbide $\text{SiC}(\text{s})$ and condensation products of $\text{Si}(\text{l})$ in a matrix of $\text{SiO}_2(\text{s,l})$ are formed as the partial pressure of $\text{SiO}(\text{g})$ drops:



A schematic description of the furnace is given in Figure 5.1.

The high-temperature nature of this process implies operation as continuous as possible. Raw materials are therefore fed in small batches with frequent intervals and are judiciously distributed on the top of the charge. Liquid silicon is continuously, or at frequent intervals, drained out from the bottom of the furnace, whereas gas exhaust and fumes are constantly passing through the filter to clean the fumes and recapture the silica.

Liquid crude silicon contains 1 to 3% impurities depending on the raw materials and the type of electrodes. The main impurities are

Fe: 0.2–1%

Al: 0.4–0.7%

Ca: 0.2–0.6%

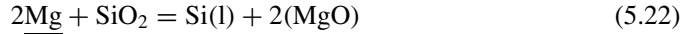
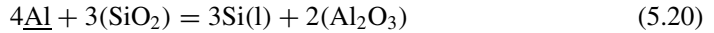
Ti: 0.1–0.02%

C: 0.1–0.15%

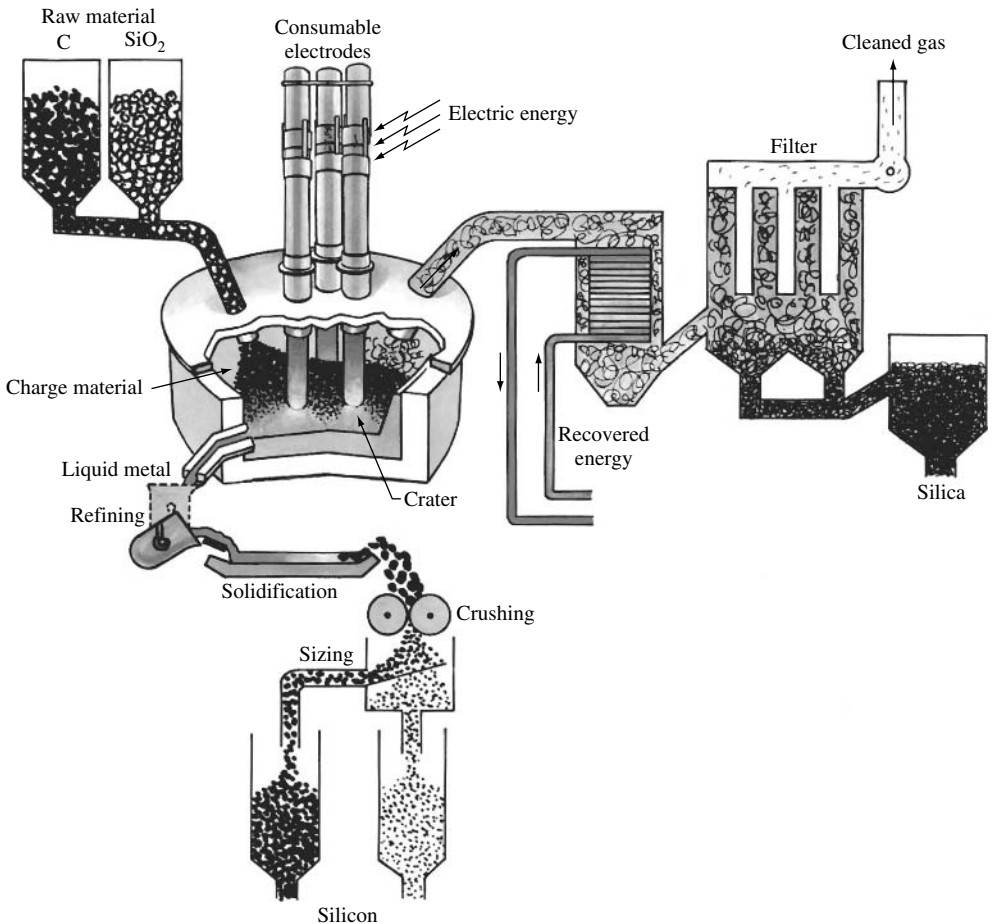
5.3.2 Refining

Most of the applications of silicon as described above request further refining. The crude silicon is therefore tapped as liquid in large ladles (containing up to 10 MT of silicon) and treated when still liquid with oxidative gas and slag-forming additives, mainly silica sand (SiO_2) and lime/limestone (CaO/CaCO_3). Other chemicals such as dolomite ($\text{CaO}-\text{MgO}$), calcium fluoride (CaF_2) and others are used depending on plant practice and customer requirements. Elements less noble than silicon such as Al, Ca and Mg are oxidised and

the degree of refining is determined by distribution equilibria (5.20) to (5.23), where the (parentheses) refer to components dissolved in a slag phase and the underscored symbols refer to dissolved elements in liquid silicon:



Theoretically it is possible to remove Al and Ca to very low levels, but in practice this is prevented by the large heat losses occurring during this operation. Temperature drops to 1700 to 1500°C, and to avoid freezing of the melt, some of the silica needed for slag



(a)

Figure 5.1 (a) and (b) Schematic representation of a furnace for production of metallurgical grade silicon. Reproduced from Schei A, Tuset J, Tveit H, *Production of High Silicon Alloys*, Tapir forlag, Trondheim (1998) with permission by Halvard Tveit

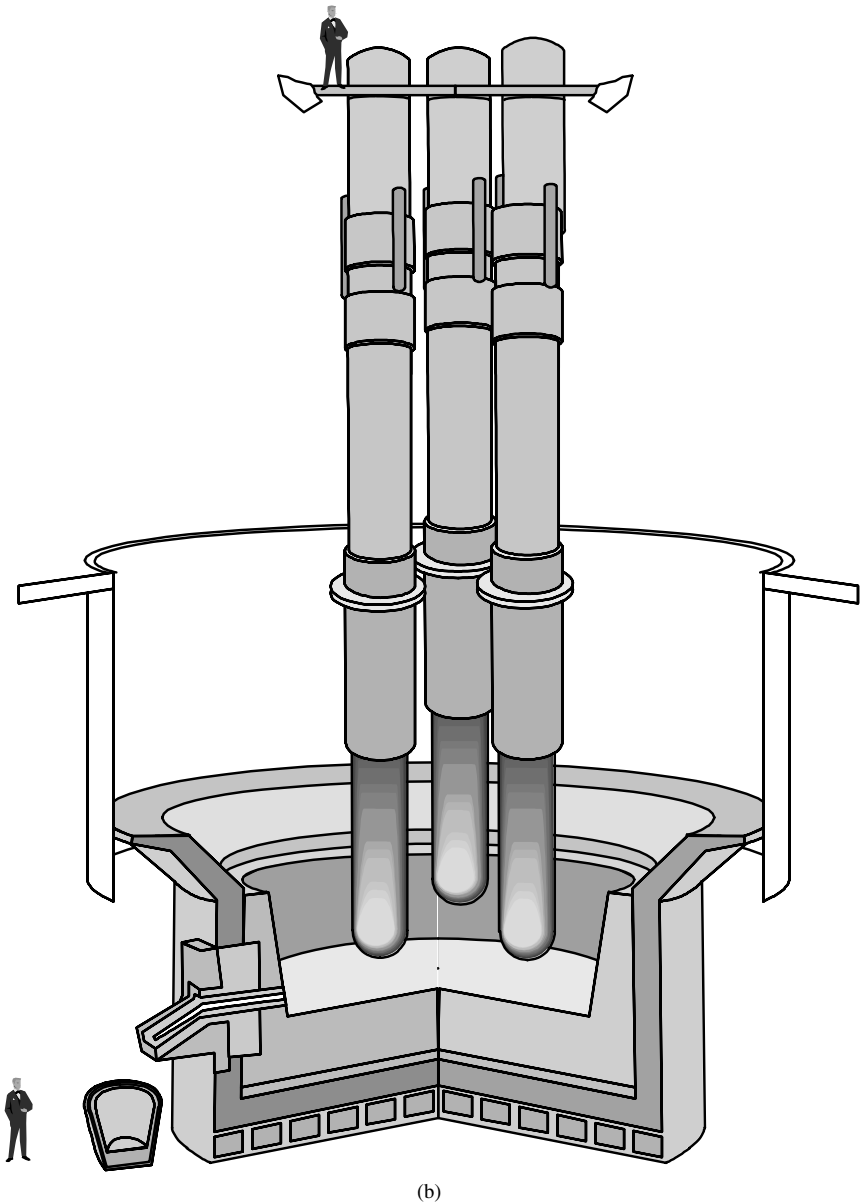


Figure 5.1 (continued)

formation is provided by direct oxidation of Si(l) with added oxygen (oxygen is added to heat silicon to keep it liquid). A disadvantage of this operation is also a partial oxidation of silicon resulting in expensive material losses.

After completion of oxidative refining in the ladle, the slag, which contains part of the impurities, is removed mechanically or by gravity and liquid silicon is poured into a casting mold. The slag-forming additives influence the slag density and viscosity, hence

the practical separation of slag and the ultimate purity of the poured silicon. For instance, a high CaO content will lead to a low viscosity slag, which will sink to the bottom of the ladle, while CaF will increase the viscosity. Sufficiently different properties in density and viscosity of both the slag and the molten silicon are required to achieve a good separation. Many studies and practical on-site developments have been devoted to this step of the process [13].

Carbon is present in crude liquid silicon mainly as dissolved C and suspended SiC particles. The fraction of SiC increases as the temperature is lowered; SiC particles are then efficiently captured by the slag phase and thus are removed from liquid silicon during the ladle treatment and the subsequent pouring. SiC is removed simply by mechanical separation, precipitated particles sticking to the walls of the ladle and the other devices containing the liquid silicon [14]. Dissolved carbon in the range of 80 to 100 ppm(w) in best cases will finally remain in the purified alloy of metallurgical silicon.

The use of these refining principles to prepare solar grade silicon will be further discussed later in the present chapter.

5.3.3 Casting and Crushing

The refined melt is poured from the ladle into a cast iron mold or onto a bed of silicon fines. The casting should preferably be removed from the mold while bleeding, that is, not fully solidified. After solidification in standard industrial conditions, metallurgical grade silicon is multicrystalline. The individual Si grains vary in size typically from 1 mm close to the iron mold wall to up to more than 100 mm in the centre section if cast on a bed of silicon fines [10]. The impurities are generally located at the Si grain boundaries as silicides and intermetallic compounds, but may also be incorporated in the Si grains if solidification has been sufficiently rapid [15]. Oxides and carbides are found as inclusions located at the grain boundaries and to a lesser degree inside the Si grains.

To be used in customers' processes, solidified silicon needs to be further crushed down to small lumps up to 100 mm. This is performed in jaw crushers and roll crushers, since at room temperature metallurgical grade silicon is hard and brittle. This operation generally generates significant amount of fines, which are undesirable because they may be contaminated by impurities and are difficult to handle during further transport and handling. Therefore, fines are removed after the primary crushing. The dominant fracture mode was found by Forwald *et al.* [7, 16] to be transgranular. For chemical applications, silicon lumps need to be further reduced to small powder particles of a few tens to a few hundreds of micrometers. This is carried out in industrial equipment such as ball mills.

Alternative methods based on rapid cooling have recently been developed to increase the homogeneity of the solidified structure of silicon through an even distribution of the impurities and intermetallic phases. Granulation in water, resulting in small granules of a few millimeters and thus avoiding casting and subsequent coarse crushing, has become a standard practice for several producers [17–19]. In an earlier attempt to avoid casting, crushing and milling, gas atomisation was tested by producers and users, but was not further industrialised for economical reasons [20, 21].

5.3.4 Economics

The carbothermic reduction of quartz in the submerged arc furnace consumes large amounts of energy and material. Best industrial performances are 10 to 11 MWh per metric ton (MT) of silicon metal and 90% silicon yield. Both availability and price of electrical power and raw material such as quartz and coal are therefore extremely sensitive to the silicon metal economics. Boardwine *et al.* [22] have presented the average structure for direct cost for Western producers as follows:

Reduction materials (as coal)	20%
Quartz	9%
Electrodes	12%
Electric power	21%
Supplies and equipment	16%
Labour	17%
Transport (to customers)	5%

In spite of dramatic changes and improvement for the individual producers, particularly with the development of new electrode technologies, the above figures are probably still valid for a large group of plants.

Most of the silicon plants are 20 years or more old. New capacity has been added during the past 10 years mainly by converting ferrosilicon furnaces to silicon. High capital expenditure is a barrier to new expansion. Investment of one million US dollars per one thousand MT of silicon is proposed as an indicating information for new furnaces.

A general and detailed source of information on production of metallurgical grade silicon is found in the recent book *Production of High Silicon Alloys* by Schei *et al.* [23].

5.4 PRODUCTION OF SEMICONDUCTOR GRADE SILICON (POLYSILICON)

Impurities in the ppb(a)–ppt(a) range are required for polysilicon supplied to the semiconductor industry. The ultra-high purity is needed to ensure exacting semiconductor properties in the grown silicon crystals. This is achieved first by the preparation of a volatile silicon hydride and its purification generally using fractional distillation. This is followed by the decomposition of this hydride to hyperpure elemental silicon by reductive pyrolysis or chemical vapour deposition. The preparation of the volatile Si compound involves external reactants and its decomposition generates by-products, which need to be recycled. The various polysilicon routes therefore must control four successive steps. All have a strong impact on the overall feasibility and economics of the suitable polysilicon products:

1. preparation/synthesis of the volatile silicon hydride
2. purification

3. decomposition to elemental silicon
4. recycling of by-products.

Many processes to produce polysilicon have been tested, patented and a few operated for many years. Only three large commercial processes are currently active:

1. The most popular process is based on the thermal decomposition of trichlorosilane at 1100°C on a heated silicon rod placed inside a deposition chamber. This process, which was developed in the late fifties, is commonly referred to as the Siemens process with reference to the company that carried out its early development.



In 2001 this process still accounted for at least 60% of the worldwide production of polysilicon.

2. In a more recent process developed by Union Carbide Chemicals in the United States of America, the trichlorosilane has been replaced by monosilane SiH_4 , but the principle of decomposition on a heated silicon rod inside a closed deposition chamber is maintained.



This process, presently run by the company *Advanced Silicon Materials, LLC*, has gained during the past 15 years a significant market acceptance.

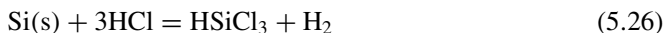
3. Finally, in the third process, also making use of monosilane SiH_4 , the heated silicon rod in the closed reaction chamber has been replaced by a fluidised bed of heated silicon particles. The particles act as seeds on which SiH_4 is continuously decomposed to larger granules of hyper-pure silicon. Unlike (1) and (2) this process is a continuous one. This process is known as the Ethyl Corporation process, after the name of the US chemical company that developed it. This process is presently run by the US corporation MEMC in Pasadena, Texas.

The respective features, advantages and disadvantages of these different routes are described in the following sections.

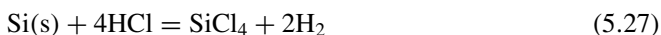
5.4.1 The Siemens Process

A schematic overview of the process is given in Figure 5.2.

Trichlorosilane HSiCl_3 is prepared by hydrochlorination of metallurgical grade silicon in a fluidised bed reactor:



This reaction occurs at 350°C normally without a catalyst. A competing reaction is



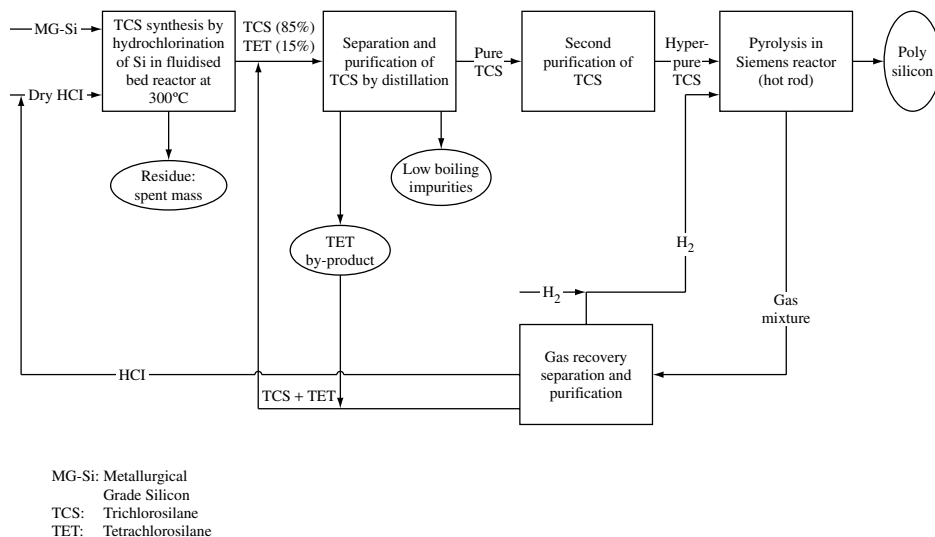


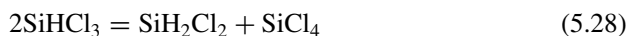
Figure 5.2 Schematic representation of the Siemens process

contributing to the formation of unsuitable tetrachlorosilane in molar proportion of 10 to 20%.

Trichlorosilane is chosen because of its high deposition rate, its low boiling point (31.8°C) and its comparatively high volatility and hence the ease of purification with respect to boron and phosphorus down to the ppb level. The boiling point of other silanes frequently found with trichlorosilane are as follows: SiH_4 (-112°C), SiH_2Cl_2 (8.6°C) and SiCl_4 (57.6°C). The suitable trichlorosilane undergoes a double purification through fractional distillation, the first step removing the heaviest components resulting from the direct synthesis and the second step eliminating the components lighter than trichlorosilane, also called *volatiles*.

High-purity SiHCl_3 is then vaporised, diluted with high-purity hydrogen and introduced into the deposition reactors. The gas is decomposed onto the surface of heated silicon seed rods, electrically heated to about 1100°C , growing large rods of hyper-pure silicon.

The main reactions are:



The stream of reaction by-products, which leaves the reactor, contains H_2 , HCl , HSiCl_3 , SiCl_4 and H_2SiCl_2 .

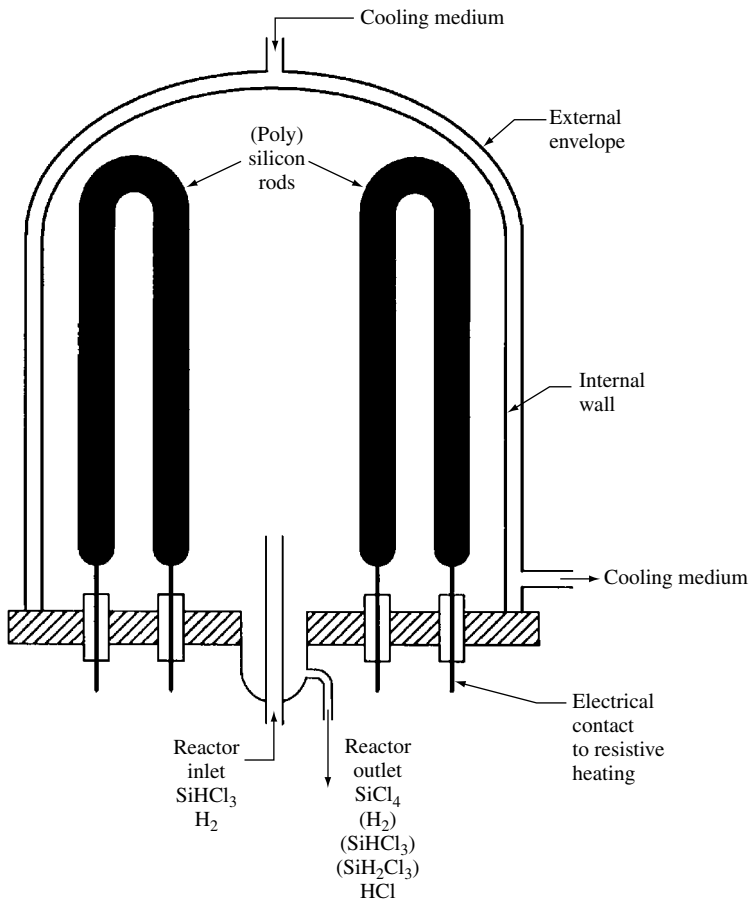


Figure 5.3 Schematic representation of the traditional Siemens reactor

A schematic representation of the Siemens reactor is given in Figure 5.3.

The Siemens process is highly energy consuming, a major part of the energy being dispersed and lost. To avoid deposition on the inner surfaces of the reaction chamber, this has to be cooled. Originally, the decomposition chamber consisted of a quartz bell jar containing one single inverted U-shaped silicon seed rod. A major advancement in polysilicon production was the utilisation of metal bell jars in place of the quartz bell jars. Quartz bell jars could not be produced in large diameters and were susceptible to breakage. The development of steel bell jars made it possible to accommodate 30 or more inverted U-rods in each reactor. This dramatically increased the productivity while decreasing the energy consumption per kilogram of produced polysilicon.

As reactions and equilibria (5.28) to (5.31) show, the deposition process generates by-products. Unfortunately, for each mole of Si converted to polysilicon, 3 to 4 moles are converted to SiCl_4 , binding large amounts of chlorine and valuable silicon. The main industrial application of tetrachlorosilane is as a source material to produce pyrogenic (also called *fumed*) silica as described above in this chapter. The present market of fumed

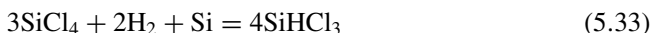
silica is about 60 000 MT measured in terms of silicon unit. This presently corresponds to three times the output of polysilicon in 2000. Moreover, a significant portion of fumed silica is also produced by burning derivated by-products from the silicones industry. In the early stages of the polysilicon industry, the fumed silica business could absorb the excess of silicon tetrachloride generated by the Siemens process. This explains the arrangements between polysilicon and fumed silica producers all around the world. With polysilicon production growing much faster than silicones and fumed silica, the question was whether to eliminate or recycle the tetrachlorosilane. This became an environmental and economical necessity. The concept of recycling on site the by-product back to the valuable starting material to form a closed-loop production process is generally an ideal preferred solution today. There are two basic chemical processes applicable to reconvert SiCl_4 to SiHCl_3 :

1. The high temperature reduction of silicon tetrachloride with hydrogen.



At about 1000°C , a 1:1 molar mixture of SiCl_4 and H_2 produces approximately 20 to 25% molar SiHCl_3 in the gaseous mixture. This process requires a fair amount of electrical energy but has a distinct advantage that the trichlorosilane produced is of very high quality because both reactants, silicon tetrachloride and hydrogen, are basically electronic grade when produced by equations (5.28) and (5.31).

2. The hydrogenation of silicon tetrachloride in a mass bed of metallurgical silicon.



This hydrogenation reaction produces approximately 20% trichlorosilane at 500°C , 35 atm with a 1:1 ratio of SiCl_4 to H_2 in one pass through a mass bed of metallurgical grade silicon in a fluidised bed reactor.

In spite of its widespread and dominant position in the industry, the Siemens process as described above suffers from the following disadvantages:

- High energy consumption, over 90% of the input power is lost to the cold walls of the reactor.
- Two power supplies and preheating of the seed rods are normally required because the high-resistivity ($\sim 230\,000$ ohm cm) seed rods require very high power supplies and high initial power rates to heat the rods. Therefore, a separate power supply for quartz lamps or graphite rod induction heating is used to preheat seed rods to about 400°C (~ 0.1 ohm cm). Lower power electrical supplies can then be used to provide continued heating and control.
- Electrical contacts to seed rods are made of graphite, which is a source of contamination.
- Power failure (especially when starting the process) causes run abortion.
- Hot spot formation and filament burn out may occur.
- Problems arise owing to gas inclusions and to non-uniform deposition at the joints.
- Gas flows and electrical power have to be adjusted during the process to obtain optimal deposition rate.

- The process is operated batchwise.
- Large amount of by-products need to be handled or recycled.

More recent developed processes have attempted to overcome some of these disadvantages.

5.4.2 The Union Carbide Process

Research on this process was initiated in 1976 after the international oil crisis. The US Government funded several projects with the objective of finding a route to inexpensive solar grade polysilicon. The Union Carbide process for silane production, with fluidised bed production of polysilicon, was selected for further funding. When the funding was not provided for political reasons, Union Carbide decided to use the silane technology for the production of semiconductor grade polysilicon. Silane deposition technology for polysilicon rods was licensed from Komatsu Electronic Metals, Japan. In 1990, the business was sold to Komatsu, which became Advanced Silicon Materials (ASiMI). By 1998, two large industrial plants were constructed in the United States with the nominal capacity of 5500 MT polysilicon, thus ranking ASiMI as number two or three worldwide among the polysilicon producers. A schematic overview of the process is given in Figure 5.4.

The main process steps are as follows:

The hydrogenation of tetrachlorosilane through a mass bed of silicon metal is carried out in a fluidised bed reactor as already described by equation (5.33).

The trichlorosilane is separated by distillation while the unreacted tetrachlorosilane is recycled back to the hydrogenation reactor.

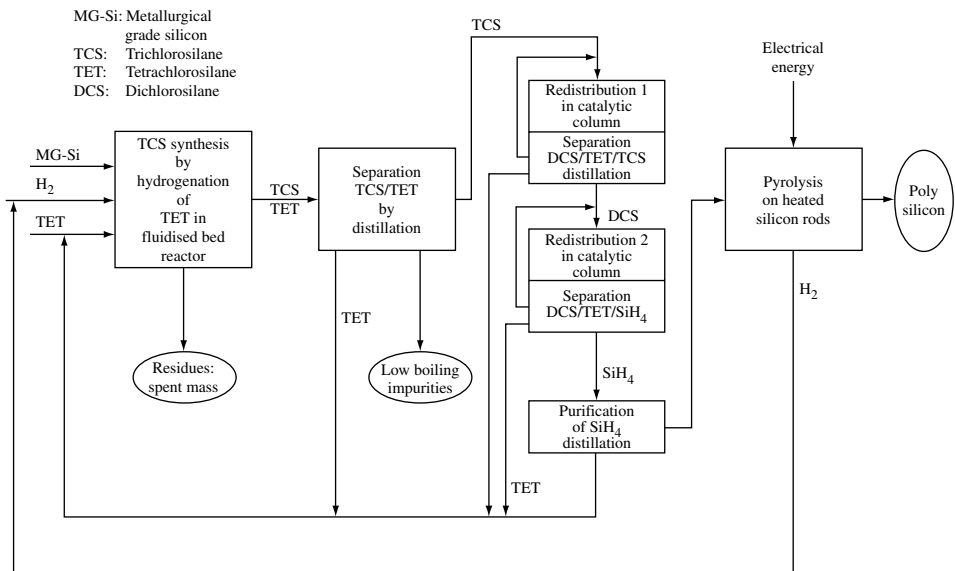
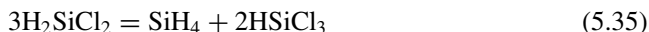
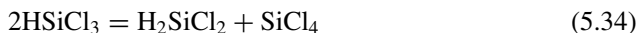


Figure 5.4 A schematic representation of the Union Carbide Polysilicon process

The purified trichlorosilane is then redistributed in two separate steps through fixed bed columns filled with quarternary ammonium ion exchange resins acting as catalyst to both redistribution equations (5.34) and (5.35):



Products of (5.34) and (5.35) are separated by distillation. Tetrachlorosilane and trichlorosilane are recycled to the hydrogenation (5.33) reactor and the first redistribution step (5.34), respectively. Silane is further purified by distillation and then pyrolysed to produce polysilicon onto heated silicon seed rods mounted in a metal bell-jar reactor:



With hydrogen and chlorine recycled, the only raw material requirement is of metallurgical grade silicon in granular form designed for fluidisation. Because equations (5.33) to (5.35) yield low portions of suitable products and because distillation has to take place after each of them, the intermediates tri- and tetrachlorosilane are recycled and purified many times before conversion to silane. This results in extremely high purity for the silane and the subsequent polysilicon. This is operated as a closed-loop process, not as a batch process.

Other advantages of using SiH_4 are that the pyrolysis may be operated at significantly lower temperature, the decomposition is complete, conversion efficiency is higher and no corrosive compounds are formed. Uniform, large-diameter, long, dense, void-free cylindrical rods of polysilicon produced this way are particularly suitable for single-crystal manufacturing by the floating zone (FZ) method.

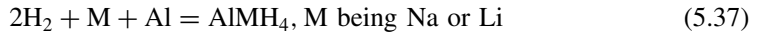
The disadvantage of the monosilane-based process is the higher cost of the volatile molecule, since additional steps are requested to convert trichlorosilane to monosilane. Moreover, the recycling of unsuitable chlorosilanes is compulsory when choosing this option because the redistribution equations yield only a small percentage of the suitable silane.

5.4.3 The Ethyl Corporation Process

This process was developed by the US company Ethyl Corporation at the same time, in similar conditions and political context as the above-described Union Carbide process. Although managed differently, the outcome of both projects was similar in the sense that both shifted their focus from solar grade polysilicon and ended up as new commercial polysilicon processes serving the electronic industry. The Ethyl Corporation process is, by comparison with the Siemens and the Union Carbide processes, revolutionary in all aspects except the concept of purifying and decomposing a volatile silicon compound by pyrolysis.

The first radical change was the choice not to use metallurgical grade silicon as the primary raw material for silane. The idea was to make use of silicon fluoride, which is a waste by-product of the huge fertiliser industry. Tens of thousands of tonnes of silicon fluoride every year are available. This is potentially a very low-cost starting

material. Silicon fluoride is hydrogenated to monosilane by metal hydrides such as lithium aluminium hydride or sodium aluminium hydride.



AlMF_4 is believed to find application in the aluminium industry, making it a valuable saleable product.

After distillation, monosilane SiH_4 is thermally decomposed to polysilicon as described by (5.36). However, to realise this process, Ethyl Corporation introduced a second radical change, not using static silicon seed rods in a bell-jar reactor but dynamic silicon seed spheres in a fluidised bed sustained by a gas stream of silane and hydrogen. A schematic representation of a fluidised bed reactor is given in Figure 5.5.

The fluidised bed reactor offers some significant advantages compared to the bell-jar reactor. Most of the shortcomings identified for the Siemens process are then eliminated. The energy losses and hence the energy consumption are considerably reduced because the decomposition operates at a lower temperature and because the same requirement to cool the bell jar is not there. Another advantage is that large reactors may be constructed and operated continuously, reducing further the capital and operating costs.

The end products are small granules of polysilicon that may present some advantages (e.g. when continuous feeding in customer process is requested) or disadvantages (e.g. not usable for direct float zone crystallisation).

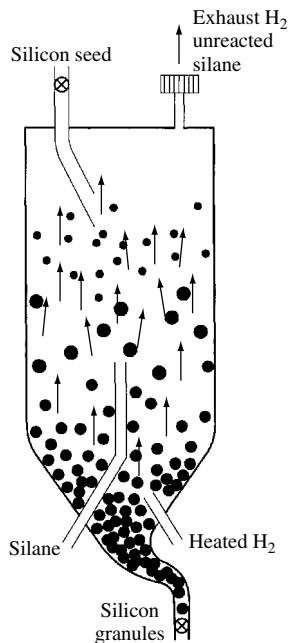


Figure 5.5 A schematic representation of a fluidised bed reactor for polysilicon production

A disadvantage of the process is the generation of powder due to homogeneous decomposition of SiH_4 in the free reactor space and the hydrogen absorption into the polysilicon deposition layer.

5.4.4 Economics and Business

The polysilicon business is completely dedicated to the semiconductor industry and therefore is a high-technology, fast-growing (annual growth approximately 10% on average) and cyclical business. With an average price of 50 US\$ per kg and a sale of 20 000 MT, it is a global business of one billion US\$ supporting a multibillion US\$ semiconductor market. Physical volumes are small but added value is high. This may be judged by taking into consideration that metallurgical grade silicon at 1 US\$ per kg is the only raw material necessary. Small amounts of hydrogen and chlorine or tetrachlorosilane are purchased as make-up to compensate losses occurring in the closed-loop process.

The industry is extremely capital-intensive. Plants have capacities ranging from 1000 to 5000 MT. One unit of 1000 MT may require a capital expenditure of 100 million US\$.

The second characteristic is that the decomposition process requires large amounts of energy. In the early stages of the industry, consumption of 350 kWh per kg polysilicon was not unusual. Efficiencies improved to 150 to 160 kWh per kg, and advanced processes are now about 100 kWh per kg. The fluidised bed process is even more efficient.

The industry is concentrated in the United States (five plants, four producers), the European Union (two plants, two producers) and Japan (three plants, two producers). Small plants are also operating in PR China and the Commonwealth of Independent States (CIS).

Polysilicon is then melted and solidified into a single crystal either by the Czochralski (CZ) or by the floating zone method (FZ). Large single crystal ingots or boules are then sliced into wafers onto which semiconductor devices are built. About 15% of polysilicon production is used to make single- and multicrystalline silicon wafers for solar cell applications.

As it is an important aspect of the PV industry and sciences, crystallisation technologies are covered in Chapter 6 of this handbook and some basic principles are given in the next section of the present chapter.

5.5 CURRENT SILICON FEEDSTOCK TO SOLAR CELLS

Elemental silicon is used in photovoltaics as the main semiconductor material converting light to electricity. Two main classes of silicon must be distinguished: amorphous and crystalline. Crystalline cells are either single- or multicrystalline. Within each group of technology several variants may be distinguished. The elaboration of the cells by different silicon-based technologies and their characteristics are described in Chapter 7. According to recent market surveys [1–3], crystalline silicon is strengthening its dominant position, particularly multicrystalline silicon (including ribbon) with new capacities steadily coming on stream. (See Table 5.3 and References [1–3].)

Table 5.3 Solar modules shipment by technology Source: PV News 2001, Reference [1]

Technology	1998 [MW]	1998 [%]	2000 [MW]	2000 [%]
Single-crystalline silicon wafers	61.5	39.7	89.7	31.2
Multicrystalline silicon wafers	67.0	43.3	140.6	48.9
Ribbon/multicrystalline silicon film	6.0	3.8	16.7	5.8
Amorphous silicon/single-crystalline silicon	–	–	12.0	4.2
Amorphous silicon	19.0	12.3	27.0	9.4
Others	1.4	0.9	1.7	0.6
Total terrestrial PV shipments	154.9	100	287.7	100

(i) *Amorphous silicon.* Monosilane (SiH_4) is the source of silicon required for the deposition of silicon amorphous thin film in a glow discharge or low temperature plasma. Silane is mass-produced by the Union Carbide (ASiMI) and Ethyl Corporation (MEMC) methods, which are described above. The global annual output capacity is approximately 7000 MT including minor volumes produced in Japan. The major part of it is used to produce polysilicon on site (United States), the balance being sold through distributors, for example industrial gas companies, to a vast group of customers. The worldwide silane market for silicon films in the semiconductor, PV, glass and ceramic industries is about 500 MT. Applications include passivating and semiconducting layers for integrated circuits, epitaxial films, architectural glass coatings, special ceramics, surface treatment and amorphous silicon. Silane is available in quantities and purity exceeding the need of the PV market. Quantity and cost of silicon is of less importance for amorphous silicon since the specific consumption per watt output is 50 to 100 times less than that for crystalline silicon cells, that is, 100 to 400 mg/W versus 10 to 20 g/W.

(ii) *Crystalline silicon.* Regardless of the technology, significant quantities of silicon are required to produce multicrystalline silicon solar cells. In the present stage of the technology, 15 to 17 g/W (estimated average value) are consumed. In 2000 this had represented a quantity of approximately 4000 MT. It is expected that this specific consumption per watt will decrease with technology improvement. Firstly, up to 60% of the purchased silicon feedstock is presently wasted during the manufacturing process. Secondly, the thickness of the silicon wafer is unnecessarily high with respect to light conversion. It is presently a mechanical requirement for the further handling of the wafers and the cells. Assuming continuous growth at the same level as during the last decade, several market forecasts predict that the requirement for silicon feedstock will in 2010 reach at least 12 000 MT. If the growth is accelerated as the more recent trends seem to show, the volume demand may be as high as 30 000 MT.

Commercial silicon bulk material is of two types:

- The metallurgical grade, global annual output: 1 million MT, price 0.8 to 1.5 US\$/kg.
- The semiconductor grade, global annual output: 20 000 to 25 000 MT, price 35 to 55 US\$/kg.

Chemical purity of typical metallurgical grade is given in Table 5.2. For some price premium, silicon producers could upgrade it to higher purity by metallurgical treatment

Table 5.4 Metallurgical silicon expected characteristics if upgraded with best currently known metallurgical technology

Impurity	Target concentration [ppm(w)]	Target price [US\$/kg]
Fe	50	5–7
Al	50	
Ca	50	
Ti	5	
C	50	
B	7	
P	7	
O	200	
Other impurities	Less than 5	

Table 5.5 Specification of chemical impurities in lowest-grade silicon currently purchased to produce multicrystalline silicon wafers

Impurity	Specification
Fe, Al, Ca, Ti, metallic impurities	Less than 0.1 ppm(w) each
C	Less than 4 ppm(w)
O	Less than 5 ppm(w)
B	Less than 0.3 ppm(w)
P	Less than 0.1 ppm(w)

Table 5.6 Electrical specification of lowest-grade silicon currently purchased to produce multicrystalline silicon wafers

Property	Specification
Resistivity	Higher than 1 ohm cm, <i>p</i> -type
Minority-carrier lifetime	Higher than 25 μ s

as tentatively indicated in Table 5.4. However, impurity contents, particularly boron and phosphorus, prevent the use of such material in solar cells. The current minimum purity requested for growing multicrystalline silicon ingots for wafering is given in Tables 5.5 and 5.6.

For semiconductor grade silicon, impurity levels are at least at the ppb level and resistivity within 1000 to 30 000 ohm cm. Although purity requirements for solar cells are not as stringent as for semiconductors, the industry has up to now been forced to select its silicon raw material from the semiconductor silicon source. Silicon is one of the main, if not the largest, cost drivers of the installed PV system. It accounts for approximately 25% of the wafer cost and 15% of the cell cost. Taking into account the dominant share of silicon crystalline technology, the industry is very sensitive to the silicon

price. To reduce price, the industry has therefore selected its silicon raw material from various second-grade classifications of semiconductor silicon, being less expensive than prime-grade polysilicon. We may assume that this feedstock has cost the PV industry, on average, one-third of what prime-grade polysilicon would have cost. The present silicon feedstock for crystalline cells consists of the following factors.

1. *Rejects from crystal growth*: Crystal growth, particularly by the CZ method, generates significant amounts of unusable silicon as follows:

- The head (or top) as well as the bottom (or tail) of the single crystal (also called *ingot* or *boule*). These sections are rejected because of size, defects in the crystalline structure and higher impurity levels.
- Ingots from aborted runs, for example, because of electrical power failure during crystal pulling.
- Ingots or ingot sections that fail to meet the specifications of crystal structure, electrical characteristics or carbon (C) and oxygen (O) content.
- Crucible leavings or pot scrap.

As late as ten years ago, almost half of the polysilicon purchased for crystal growth was rejected for the above reasons. Crystal growth yields have improved and processing techniques have been developed to recycle the higher purity reject material into test or so-called *dummy* wafers. These improvements have reduced the quantity of feedstock available to the PV industry. Rejects from crystal growth, except for the pot scrap, *n*-type, and heavily doped *p*-type material, have been the ideal silicon feedstock for crystalline solar cells. Acceptable quality was available at reasonable prices. We estimate this source at 5 to 6% of all polysilicon shipped, that is, in 2000 approximately 1000 MT. Pot scrap is the remainder of the silicon melt in the quartz crucible after the CZ crystal growth is completed. After solidification, the crucible cracks and pieces of it adhere to the solidified silicon residue. Driven by the need to find new cost-effective sources, the PV industry has found ways to clean mechanically (sand blasting) and chemically (treatment by hydrofluoric acid) selected crucible residues. This has resulted in added quantities to the PV silicon feedstock. We estimated this source at 500 to 700 MT in 2000.

2. *Rejects from polysilicon*: Four to five percent of polysilicon produced is also rejected for quality reasons. These are

- chunks and rods from aborted runs (failure under operation);
- broken or imperfect seed rods;
- “carbon ends,” parts of the rod close to the electrical graphite contacts;
- fines and small chips generated during processing of rods into chunk form;
- “popcorn” or excessive dendritic growth with unacceptable surface texture that may occur under certain operative conditions;
- small granules from the fluidised bed process;
- rod sections that have been sawn or fabricated, so have unacceptable purity.

At 5% of polysilicon produced this amounts to another 1000 MT in 2000.

Rejects from crystal growth and from polysilicon plants in 2000 account in total for 2500 to 3000 MT at most, whereas the consumption has been at least 3500 MT and most probably 4000 MT. The balance has necessarily been covered by standard semiconductor grade polysilicon, either prime grade or a grade produced on purpose for PV customers by some polysilicon producers. As pointed out the present polysilicon capacity exceeds the actual demand by some 5000 MT. It may therefore be attractive for some producers to offer a solar grade in order to optimise their overall costs by operating their plants at higher capacity. This option will be valid for a few years (2–4) as long as installed polysilicon capacity exceeds the semiconductor demand.

Driven by the semiconductor business, polysilicon capacity will not grow as fast as the solar cell market demand. As the semiconductor market matures, the historical growth rates of 15 to 20% appear difficult to sustain; more conservative annual growth rates of 7 to 10% have been projected. Having gone through several high growth/negative growth cycles, the polysilicon producers are now adding capacity only on demand from the semiconductor industry, with guaranteed supply contracts. The producers attempt to avoid large oversupply and inventories, thereby reducing the quantity of polysilicon feedstock available to the PV industry. An annual growth of 20% is predicted as an average or “business as usual” growth rate for the solar market. The polysilicon feedstock shortage for PV can therefore only become worse. The challenge is to develop an alternative source of silicon feedstock competitive in quality and price. The fast-growing solar cell market needs to have a feedstock supply independent of the semiconductor market cycles and growth limitations.

This source must emerge as soon as possible and no later than 2004 to 2005, when polysilicon capacity has been planned to be fully booked again by semiconductor demand. This source should be readily scalable to provide more than 10 000 MT by 2010 at a price less than half the price of semiconductor grade polysilicon.

5.6 REQUIREMENTS OF SILICON FOR CRYSTALLINE SOLAR CELLS

Before exploring the potential routes to solar grade silicon, it is worth looking at the structural and chemical limitations imposed on silicon to reach optimal performances for crystalline and particularly for multicrystalline solar cells. After a short description of the valid principles of crystallisation, we will examine the effect of various impurities and the effect of structural imperfections.

5.6.1 Solidification

When silicon solidifies, a homogeneous melt will normally not result in a homogeneous solid. Concentration gradients will appear as shown in the Figures 5.6 and 5.7.

A schematic phase diagram of the silicon corner is shown in Figure 5.6. When cooling a melt of composition X_0 , it starts to solidify at a temperature T_0 . At a lower temperature, T_1 , a fraction has solidified. At equilibrium the fractional compositions of

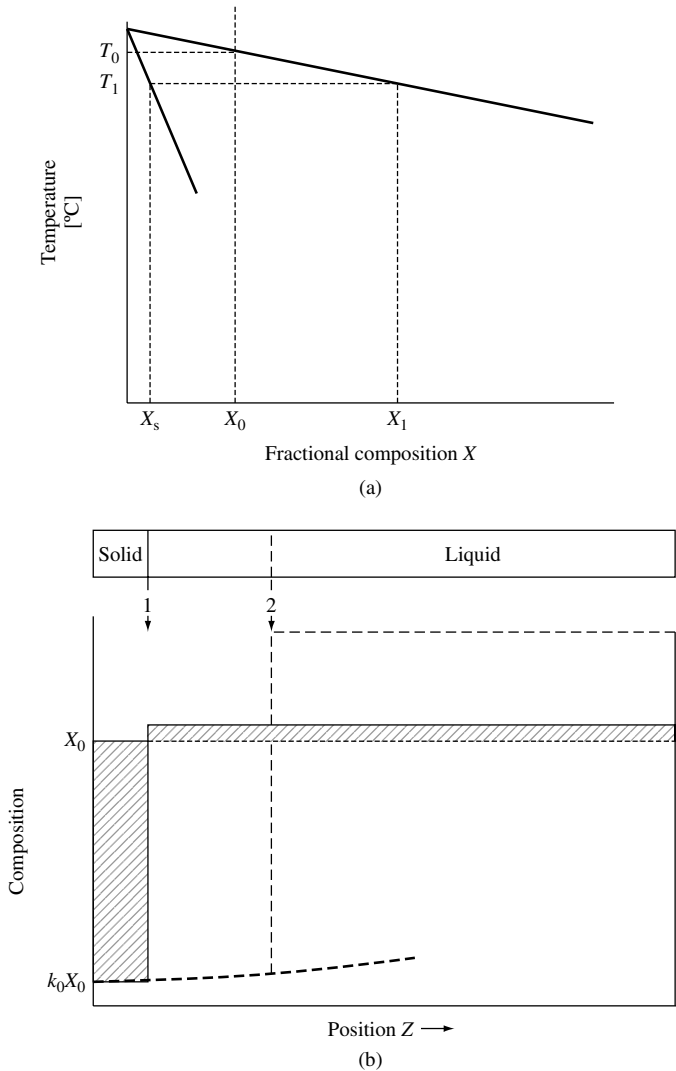


Figure 5.6 (a) Left side of a phase diagram with $k_0 < 1$ and (b) composition development in solid and liquid along a rod solidified from the left end under “normal freezing”

the solid and liquid are X_s and X_1 , respectively. The equilibrium distribution coefficient k_0 at T_1 is defined as the ratio of the equilibrium solid and liquid compositions:

$$k_0 = X_s / X_1$$

(at *equilibrium* both the solid and the liquid have homogeneous compositions X_s and X_1 , respectively).

During normal freezing the solid and the liquid are not in equilibrium. This principle can be used to purify the material. If (1) the solid–liquid interface is flat, (2) the

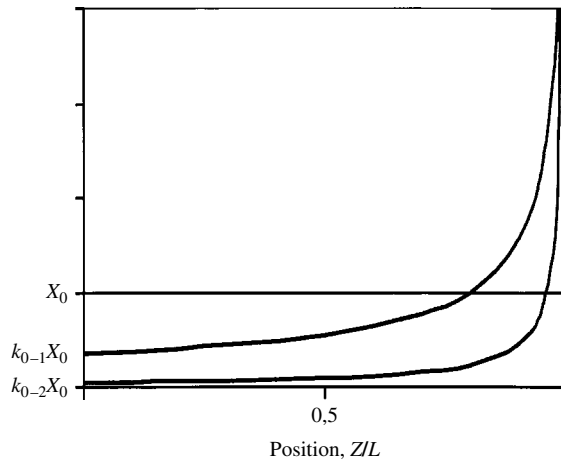


Figure 5.7 Composition profile after the entire rod of Figure 5.6 has solidified, illustrating normal solidification at two different values of k_0 , $k_{0-1} = 0.35$ (upper curve) and $k_{0-2} = 0.05$

melt has a uniform composition and (3) negligible diffusion takes place in the solid, a composition profile like the one in Figure 5.6 is obtained when equilibrium prevails at the interface.

A horizontal cylinder of liquid alloy of initially uniform composition X_0 is cooled at the left end (see Figure 5.6b). Let a small amount of solid form so that the solid–liquid interface is located at position 1. When a small volume has solidified, the composition in that volume has dropped from X_0 to k_0X_0 . A mass of solute proportional to the cross-hatched area to the left of position 1 has been removed from the solid and rejected into the remaining liquid. This will increase the liquid composition to a level above X_0 . If we consider that local equilibrium prevails at the solid–liquid interface during solidification, the liquid and solid compositions at the interface are tied together by the equation $X_s = k_0X_l$. So when the composition of the liquid is raised, the solid composition must also rise as solidification proceeds. When the solid–liquid interface has moved to position 2, the solid composition will have gradually increased, as shown in Figure 5.6(b).

It is shown in Figure 5.7 that k_0 will have a marked effect on the distribution of impurities in solid silicon. Values of k_0 for different elements are given in Table 5.7 [24, 25]. For impurities having a low value of k_0 , for example, $k_{0, \text{Fe}} = 8 \times 10^{-6}$, the solidification process has a large purifying effect: only one Fe atom out of about 100 000 in the melt will enter the solid when solidification starts. For elements in which k_0 is near to 1, no marked change in the concentration of impurities will appear between the melt and the solid silicon.

During the solidification process, the impurity concentration at the interface varies with the fraction of melt solidified and k_0 . If the solute rejected into the boundary region is not transported immediately into the melt in front of the interface, solute will build up at the boundary. As the solute builds up, however, its concentration gradient across the boundary layer becomes steeper and the rate of transport through the boundary layer by diffusion increases until a balance is obtained between the solute being rejected into and

Table 5.7 Distribution coefficients, k_0 , for some elements in silicon at the melting point [24, 25]

Element	k_0	Element	k_0
B	0.8	Ti	3.6×10^{-4}
Al	0.002	Cr	1.1×10^{-5}
Ga	0.008	Mn	1×10^{-5}
N	7×10^{-4}	Fe	8×10^{-6}
P	0.35	Co	8×10^{-6}
As	0.3	Ni	8×10^{-6}
C	0.07	Cu	4×10^{-4}
O	0.25–1.25	Zn	1×10^{-5}

out of the boundary layer. At this point the ratio $(X_1)_{\text{interface}}/(X_1)_{\text{bulk}}$ becomes constant. The effective distribution function k_{eff} is defined as

$$k_{\text{eff}} = X_{s, \text{interface}}/X_{1, \text{bulk}}$$

and tells a great deal about liquid mixing in front of the interface. Poor mixing in the melt results in $k_{\text{eff}} = 1$. Good mixing (no build-up) means $k_{\text{eff}} = k_0$.

Burton *et al.* [26] have derived an expression for k_{eff} when a rotating crystal is pulled from the melt at a velocity v :

$$k_{\text{eff}} = k_0/[k_0 + (1 - k_0)\exp^{-\Delta}]$$

where

$$\Delta = v\delta/D_1 \text{ and } \delta = 1.6 D_1^{1/3} \cdot v^{1/6} \omega^{-1/2}$$

where δ is the distance from the growing interface to where the concentration in the melt is uniformly equal to $X_{1, \text{bulk}}$, D_1 is the diffusion coefficient of the solute, v is the viscosity and ω the crystal rotation rate.

Kodera [27] has applied this to obtain δ/D_1 and D_1 values for melts doped with various impurities at different rotating rates, as shown in Table 5.8. For CZ-grown silicon where v is around 1 mm/min, Δ is small and k_{eff} is close to k_0 [24].

The ability to purify molten feedstock by solidification will therefore vary for the different impurities and with solidification velocity. The validity of the assumption of no diffusion in the solid will not be met at a slow solidification rate and some “back” diffusion will take place. In addition, impurities diffuse from the crucible into the solid, the rate depending on temperature and time. Selection of the optimal casting process parameters is complicated and improvements will depend on the ability to model the total solidification process.

5.6.2 Effect of Crystal Imperfections

Silicon has a diamond lattice atomic structure being cubic with atoms joined to four nearest neighbours by covalent bonds at tetrahedral angles. If the atoms are represented

Table 5.8 Values of δ/D_1 and D_1 for some elements [27]

Impurity element	Rotation rate [rpm]	$\frac{\delta}{D_1}$ [s/cm]	Diffusion coefficient, D_1 [cm ² /s]
B	10	170 ± 19	$(2.4 \pm 0.7) \times 10^{-4}$
	60	84 ± 37	$(2.4 \pm 0.7) \times 10^{-4}$
Al	10	86 ± 34	$(7.0 \pm 3.1) \times 10^{-4}$
	60	40 ± 17	$(7.0 \pm 3.1) \times 10^{-4}$
P	5	127 ± 36	$(5.1 \pm 1.7) \times 10^{-4}$
	55	60 ± 19	$(5.1 \pm 1.7) \times 10^{-4}$
As	5	190 ± 53	$(3.3 \pm 0.9) \times 10^{-4}$
	55	79 ± 16	$(3.3 \pm 0.9) \times 10^{-4}$

as hard spheres, the diamond structure fills 0.34 of the available space, compared to 0.74 for a close-packed structure such as aluminium. The formation of defects in the silicon lattice creates local electronic disturbances because of the nature of the atomic bonding.

The following description follows standard textbook presentations in physical metallurgy and concentrates on some lattice defects appearing in silicon, which are important when discussing the effect of impurities on the electronic properties.

It is common practice to divide the lattice defects into the following categories:

Plane defects

Stacking faults

Twin boundaries

Grain boundaries

Line defects

Dislocations

Point defects

Vacancies

Self-interstitials

Substitutional impurities

Interstitial impurities

Volume defects

Precipitates

Single-crystal material consists of one grain of a continuous crystal structure. Multicrystalline (mc-)/polycrystalline (pc-) material consists of many separate grains with inclined crystal planes that meet at *grain boundaries*. Depending upon the misorientation between adjoining grains, the interfaces are termed *subgrain* boundaries (0–5°) and *grain* boundaries. *Twin* boundaries arise where one crystal grain is a mirror image of its neighbour. Grain boundaries may have a more open and less well organised atomic structure. Atomic diffusion is therefore easier along grain boundaries than in the bulk crystal. Because of the lack of crystal order, some of the covalent bonds are broken and the grain boundaries may therefore carry electric charge. The electrical properties of the grain boundaries vary with the amount of atomic disregister.

The concept of a linear lattice imperfection called a *dislocation* arose primarily from the study of plastic deformation of crystalline materials. The dislocations are borderlines where the atomic planes are out of register. At dislocations some of the covalent bonds in silicon are broken. The dislocations may therefore carry electric charge.

Because of the disregister, the dislocations are surrounded by stress fields and may attract impurity atoms.

In *n*-type silicon, donor impurities can provide electrons to fill the missing charge from a missing bond at the dislocation. As a result of the acquisition of electrons, the dislocation becomes negatively charged, which again may attract the positively charged donor impurities. This situation may lead to a space charge region in the form of a cylinder in which positively charged donor ions surround a negatively charged dislocation.

In *p*-type material, the dopant atoms may accept electrons from a dislocation. In this case the cylinder-shaped space charge region has a positively charged dislocation surrounded by negatively charged acceptor ions.

The category of *point defects* include vacancies, interstitials and impurities either present as intentionally dopant atoms added to control the properties of silicon or unintentionally incorporated as contaminants from the raw materials, processing or crystal growth.

A *vacancy* is a missing atom at a silicon site. The result of the removal of a silicon atom is the formation of four dangling atomic bonds with unpaired electrons and some lattice relaxation. Vacancies thus tend to exhibit acceptor-like behaviour. The concentration of vacancies, n/N_0 , in silicon at a given temperature can be determined from the following expression:

$$n = N_0 \exp(-E_v/kT)$$

where n = number of vacancies/volume, N_0 = number of atoms/volume, k = Boltzmann's constant and T = temperature in K. E_v is the formation energy, which is the energy required to take an atom from a lattice site inside the crystal to a lattice site on the surface. In silicon, $E_v \approx 2.3$ eV.

A *self-interstitial* can be formed by inserting a silicon atom into one of the holes in the structure. The energy of formation of interstitials, E_i , in the loosely packed diamond structure is lower than the formation energy of vacancies, $E_i \approx 1.1$ eV.

An interstitial has four valence electrons that are not involved in covalent bonding with the adjoining atoms. These electrons may be lost to the conduction band and the interstitial may behave as a donor.

At low concentrations the impurities exist as single atoms in the matrix – so-called *solid solutions*. Atoms in the solid solution are incorporated in the matrix in two ways. They can substitute for an atom of the host crystal and maintain the regular atomic structure of the crystal. In this case they are known as *substitutional impurities*. Alternatively, the impurity atoms can occupy positions squeezed in between the atoms of the host crystal. Then they are known as *interstitial impurities*.

The energy levels associated with point defects in silicon are fairly deep. They serve as centres for minority-carrier recombination and therefore reduce the carrier lifetime. The lifetime is inversely proportional to the concentration of point defects.

The diffusion of atoms in a crystal proceeds by thermally activated jumps from sites to sites. The diffusivity is expressed by the diffusion coefficient, D , with units cm^2/s :

$$D = D_0 \exp(-E_D/kT)$$

where D_0 is a constant and E_D is the activation energy for the jumping process.

At higher concentrations the impurities may agglomerate. The ability to be in solid solution increases with temperature (see Section 5.6.3). The impurities in a material at a certain purity level may thus be in solid solution at elevated temperatures and form *pairs* with other atoms or *precipitate* at dislocations, at grain boundaries or with other impurities at lower temperatures. The sequence of precipitation is characterised by *nucleation*, *growth* in which excess atoms diffuse to precipitates and Ostwald *ripening* in which a growth competition exists where large precipitates grow at the expense of small ones.

Minority carriers (being electrons on the p -side and holes on the n -side of the solar cells) flow more readily within a grain than across grain boundaries. Minority carriers may recombine with majority carriers at recombination centres like impurities, precipitates, dislocations and grain boundaries. The average distance that a minority carrier will travel within silicon depends upon the density of recombination centres and their recombination ability. The longer the distance between recombination centres, the better the efficiency of the cell. Precipitation of impurities reduces the number of atoms in solid solution and may therefore change the minority-carrier diffusion length. The density of precipitates is governed by the cooling rate, the ramping sequences and the diffusivity of the impurity elements.

At the surface there are many recombination sites. In the final cell production sequence, gettering and passivation will change the conditions near/at the surface.

Measurements of the local electronic properties in individual grains and near grain boundaries show that the properties may vary from grain to grain. It is hoped that the results of such measurements may stimulate further theoretical and experimental work to clarify the relations between grain structure and the electronic properties in multicrystalline silicon.

The density of dislocations influences the lifetime of the minority carriers. Experiments show good correlation between areas having a high dislocation density and a short effective lifetime. To control the dislocation density has therefore become an important task. The dislocation movements and multiplication and their interaction with impurity atoms being in solid solution or existing as complexes during the production processing steps challenges our ability to model complex relationships. However, it is being claimed that numerical simulation is used as a valuable tool to optimise the crystallisation and cooling processes at plants. This is the kind of work that certainly will develop during the coming years.

5.6.3 Effect of Various Impurities

It is well known that impurity atoms have a strong effect on the efficiency of silicon as a photovoltaic material. It is also known that the effect of impurities can be changed by heat treatments and by exposing the material to gettering atmospheres in which selected elements diffuse into silicon and combine with the impurities (a semantic parallel to getter pumps in which oxygen is adsorbed by certain elements).

The impurity atoms may appear as solid solutions, as pairs with other elements, for example FeB, or as larger aggregates/precipitates with silicon and/or other elements, for example Fe₂Si. This depends upon the temperature, the concentration and the density of the imperfections (dislocations, grain boundaries). If the temperature or the (chemical) surroundings are altered, it will take some time before a new equilibrium is established. The time to reach equilibrium may depend on parameters such as temperature, cooling/heating rate, and chemical composition, grain size, dislocation density and others. When comparing results from literature values in which the specifications of relevant parameters are not defined, it is likely that differences may appear.

Most of the impurities in silicon used for PV cells exist at very low concentrations. Since measurements of trace quantities are difficult, much of the progress has occurred when new and better instrumentation has become available. Over the years many review articles and books dealing with the effect of impurities in crystalline silicon have been published. The interested reader is therefore encouraged to look up some of the references for a wider treatment of the subject [25, 28–33]. The following will therefore be an attempt to briefly summarise and update the general knowledge of the subject.

The maximum solid solubilities, $X_s(\text{max})$, of impurities in silicon are related to the distribution coefficients at the melting point according to an empirical relation found by Fischler [34]:

$$X_s(\text{max}) = 0.1k_0$$

or in units of atoms/cm³:

$$C(\text{max}) = 5.2 \times 10^{21} k_0$$

Although deviations have been found for nitrogen, carbon and oxygen [35], the relation may be useful.

5.6.3.1 Atoms from Groups IIIA (B, Al, Ga...) or VA (N, P, As, Sb...)

These atoms act as substitutional impurities in silicon. At a site where a Group VA impurity (e.g. phosphorus) has replaced a silicon atom, four *d*-electrons are bound to the Si neighbours, while the fifth electron is weakly tied to the Group VA atom. The fifth electron is not completely free to move, but it is easily activated to the conduction band. Group VA atoms are therefore *donor* atoms.

In an analogous way, Group IIIA atoms (e.g. boron) do not have enough valence electrons to satisfy the four covalent neighbour bonds. This gives rise to holes weakly tied to the Group IIIA atoms. These impurities therefore create energy levels for electrons in the forbidden gap just above the valence band edge. Group IIIA atoms are called *acceptors*.

To be able to control the level of doping, the concentration of unwanted elements from the Groups IIIA and VA must be well below the concentration of the doping element.

Our theoretical understanding of the properties of impurities in silicon other than those from the Groups IIIA and VA is less well developed. However, as new instrumentation has become available, a lot of experimental results of high scientific standard have been published.

5.6.3.2 Carbon

Carbon is a common substitutional impurity. Like silicon it has four valence electrons and is therefore electrically neutral. The carbon atom is smaller than the silicon atom and may therefore be involved in precipitation of species expanding the lattice like silicon oxide.

The solid solubility limit is $C_S = 3.5 \times 10^{17}$ atom/cm³ at the melting point or $C_S(T) = 4 \times 10^{24} \exp(-2.3 \text{ eV}/kT)$ atoms/cm³, where k is the Boltzmann's constant [89, 91].

In metallurgical grade (MG) silicon, carbon is present at levels above the solid solubility limit and SiC precipitates are commonly present. In electronic grade (EG) the concentration of carbon is low. But in contact with the crucible and the carbon-rich atmosphere (graphite), it is difficult to avoid contamination of the melt.

As a substitutional element, carbon diffuses rather fast [$D = 1.9 \exp(-3 \text{ eV}/kT)$ cm²/s], but much slower than interstitial impurities.

5.6.3.3 Oxygen

The subject of oxygen atoms in silicon has been studied for many years. Since results from experiments performed under different thermal histories have varied, the discussion goes on.

Oxygen atoms in solid solution are electrically inactive and predominantly enter interstitial sites. The equilibrium value of the solid solubility at the melting point is generally accepted to be 1×10^{18} atom/cm³. However, the results from measurements of solid solubility as a function of temperature differ markedly. The value of k_0 will therefore vary (see Table 5.7).

In a work by Itoh and Nozaki [32] an important point was made that the concentration of oxygen at equilibrium at a given temperature was determined by the type of oxide that was stable at that temperature. So if the type of oxide varied, it would be expected that bends in solid solubility curves at temperatures at which the silicon oxides change would be observed. However, up to 1200°C, SiO₂ is the stable chemical form and the solubility $L = \exp(\Delta S/R) \exp(-\Delta H/kT)$ will have constant values of ΔS and ΔH .

On cooling, super saturation is easily obtained and oxygen precipitates at a rate that depends on oxygen content, temperature, and time at temperature and nucleation sites. Carbon is also found to influence the precipitation of silicon oxides, possibly because the carbon atoms reduce the expansion of the lattice when silicon oxide is growing.

Oxygen has a high diffusion coefficient, $D = 0.13 \exp(-2.53/kT)$ [36]. By heat treatments, the distribution of oxide particles may change since particles may get dissolved when heated and grow when cooled. Oxygen atoms are found to change the effect of other impurities, a process known as internal gettering.

One important oxygen source is the crucible. Silicon is normally melted in high-purity-fused quartz (SiO_2) crucibles (single crystals) or quartz crucibles coated with high-purity Si_3N_4 (multicrystalline ingots). If holes appear in the coating, quartz will easily dissolve in the melt and raise the level of oxygen in the solid.

The variety of effects observed with oxygen in silicon will truly stimulate further research for a long time.

5.6.3.4 Transition metals

Properties of transition-metal impurities in silicon have been reported in a large number of articles, reviews and books [28–30, 33]. The transition metals are presented by the symbols 3d, 4d and 5d, which specify the outer electron configuration of a neutral atom. Most of the metals forming deep energy levels (“midway” between the conduction band and the valence band) in silicon belong to this group and have therefore a large influence on the electronic properties of silicon.

The main impurities found in silicon belong to the 3d transition metals (Sc, Ti, V, Cr, Mn, Fe, Co, Ni, Cu). In general, these are present as interstitial impurities.

The diffusivity increases with increasing atomic number in the 3d row (see Figure 5.8), with Ni and Cu having the largest diffusion coefficients known in silicon.

The concentration of vacancies is very low in silicon. The high diffusion coefficients of 3d elements can therefore only be explained by interstitial diffusion mechanisms independent of vacancies.

The 3d transition metals have a steep temperature-dependent solid solution limit that make them easily supersaturated during cooling (see Figures 5.9 and 5.10). They therefore frequently form complexes/precipitates at dislocations, grain boundaries or other lattice defects.

The solubility at room temperature is very low, of the order of 1 atom/cm^3 . However, some 3d impurities are mobile even at room temperature. So the atoms with the highest mobility (Co, Ni, Cu) will be out of the solid solution during or just after the cooling. The 3d metal atoms with a low diffusivity may remain in the solid solution at interstitial sites for a much longer time after cooling. This may depend upon crystal perfection, which determines the diffusion length to reach sinks such as dislocations, grain boundaries and precipitates.

The solid solubility of the 3d transition metals in silicon is shown in Figure 5.10.

A severe deterioration of the electrical properties is expected from solid solution impurities capturing the minority carriers (being electrons on the *p*-side of a *p-n*

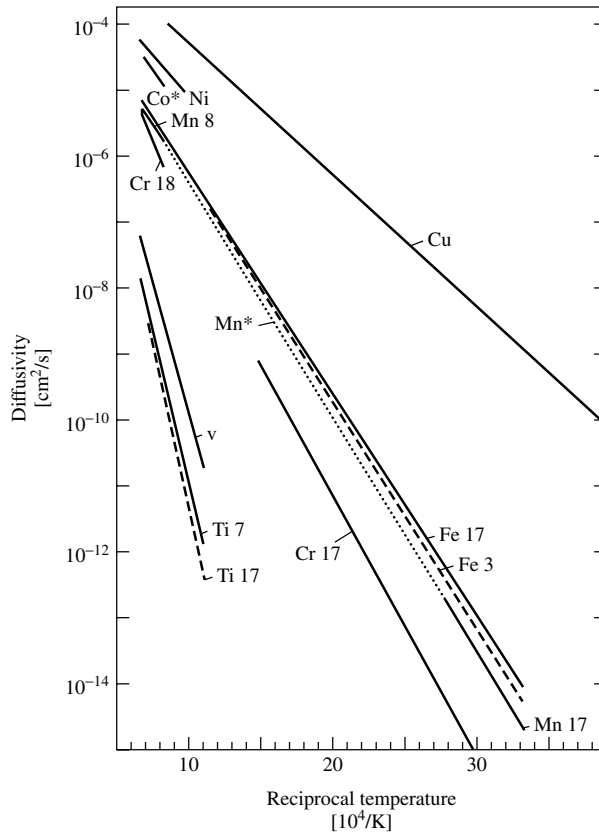


Figure 5.8 Diffusivities of 3d transition elements. Reproduced from *Metal Impurities in Silicon-Device Fabrication*, Graff K, 29, 2000, © Springer-Verlag GmbH & Co. KG

junction). The low-injection-level minority-carriers lifetime, τ_0 , is inversely proportional to the impurity concentration, $N(1/\text{cm}^3)$ [28]:

$$\tau_0 = (\sigma v N)^{-1}$$

where v is the thermal velocity, which is the average speed of the electrons as they randomly collide with atoms, impurities or other defects, and σ , having the units of cm^2 , represents the impurity atoms effective cross-section for the capture of a minority carrier.

Here the carrier capture cross-section for electrons, σ_e (cm^2), must be inserted for p -type silicon and σ_h for holes in n -type silicon. The thermal diffusion velocity v of electrons at room temperature is 2×10^7 cm/s.

The capture cross-sections for different transition metals can differ by several orders of magnitude. As a consequence, the carrier lifetime of a silicon sample can even be determined by an impurity of minor concentration if this is a “lifetime killer” with a high

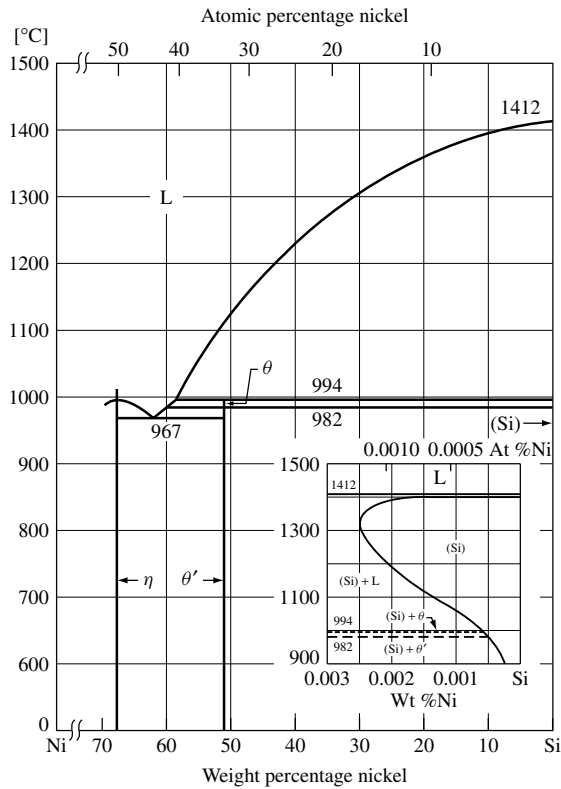


Figure 5.9 The Ni-Si phase diagram. The shape of the solidus line on the Si side is shown in the inserted window. It is seen that the solid solubility of Ni in Si is low, that it increases at temperatures above the peritectic point (at 994°C) (retrograde solubility) and reaches a maximum at about 1300°C. Redrawn from ASM Handbook, Vol. 8, *Metallography, Structures and Phase Diagrams* 8th Edition, ASM International, Materials Park, Ni-Si Phase Diagram, p. 325

minority-carrier capture cross-section. Therefore, the tolerable impurity concentration for acceptable lifetime values depends upon the chemical nature of the respective impurity, and its carrier capture cross-section for electrons in *p*-type silicon and for holes in *n*-type silicon. Both parameters can differ by orders of magnitude and consequently the acceptable concentration for a defined impurity can be quite different in *p*- and *n*-type silicon (Figures 5.11 and 5.12; [30]).

Copper and nickel have high diffusivities and low capture cross-sections. These elements will rapidly enter a low solid solution level after cooling to room temperature and may therefore be expected to have less effect on lifetime than elements with lower diffusivities (Fe, Ti) and high capture cross-sections.

5.6.3.5 Precipitates

Except for copper, which forms Cu_3Si particles when cooled, the other 3d metals form MeSi_2 precipitates. Investigations of crystallographic structure, morphology and

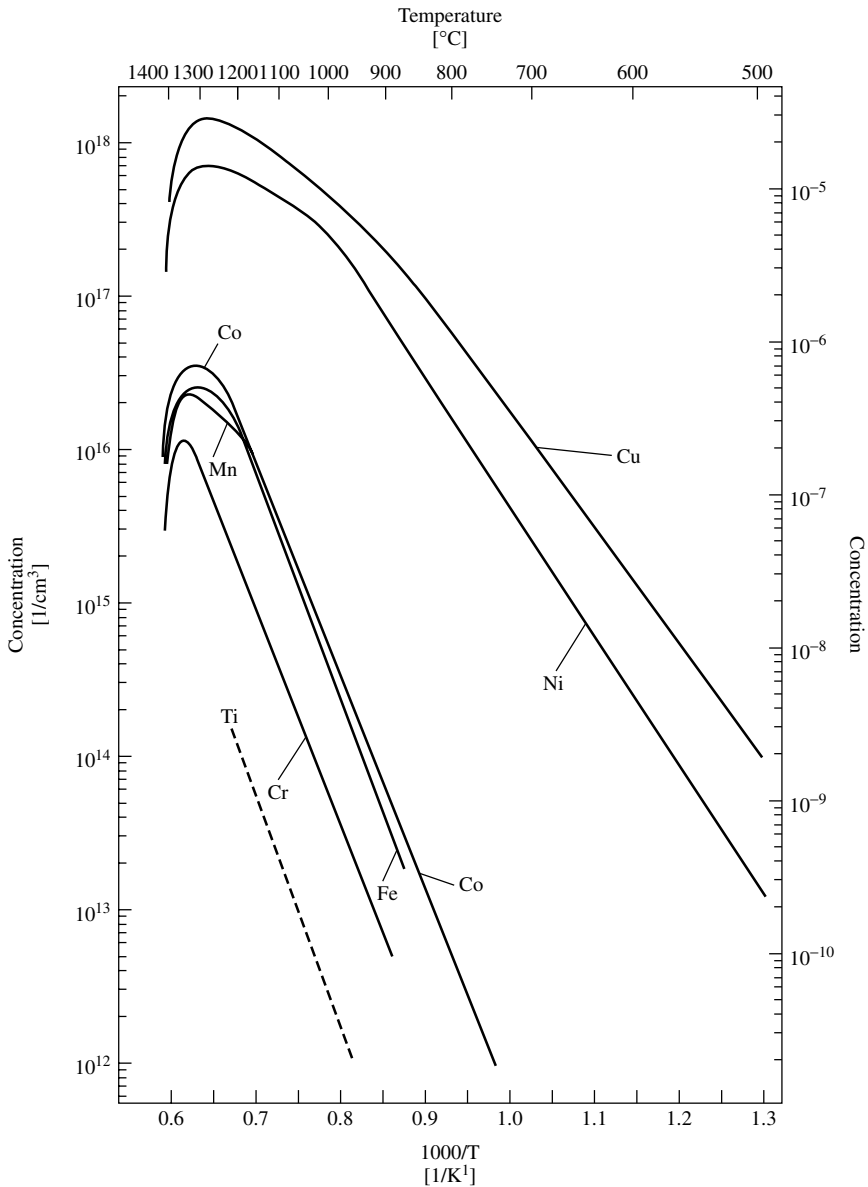


Figure 5.10 Solid solubility of 3d transition elements in silicon. Sc is still missing, but is assumed to be a little below the values of Ti. Adapted from *J. Appl. Phys.* Weber E, **A30**, 1–22 1983, © Springer-Verlag GmbH & Co. KG. The values for Ti are taken from [37]

composition of several transition-metal precipitates in silicon identify crystalline silicides, FeSi_2 , CoSi_2 , NiSi_2 , as compounds that influence the minority-carrier diffusion length. The morphology and density depend upon temperature and time at temperature. Elements having a high diffusivity like Ni and Cu precipitate easily. This reduces the number of atoms in solid solution and may therefore change the electric properties. Kittler and

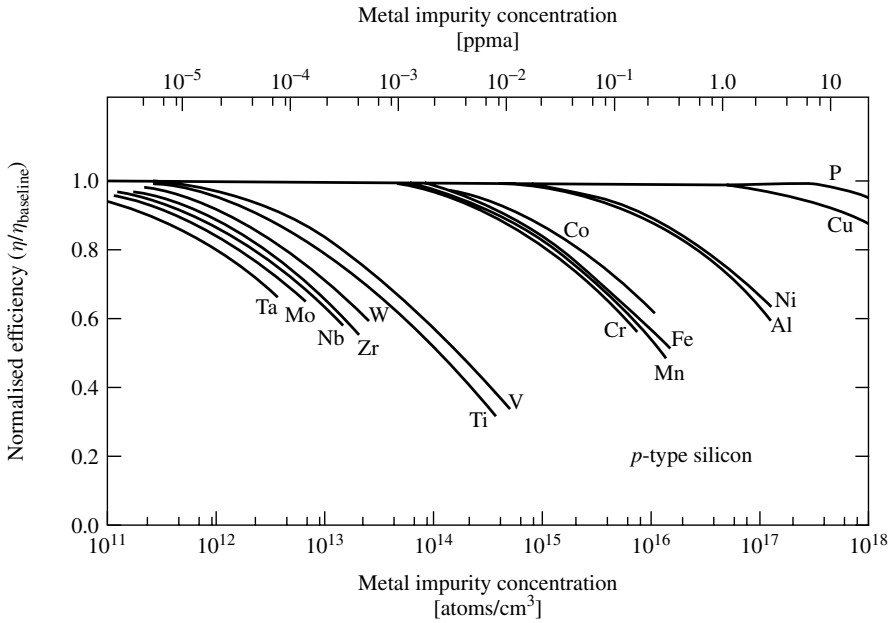


Figure 5.11 Solar cell efficiency versus impurity concentration for 4 ohm cm p-base devices [30]. Reproduced from Davis Jr. J *et al.*, *IEEE Trans. Electron Devices* © 1980 IEEE

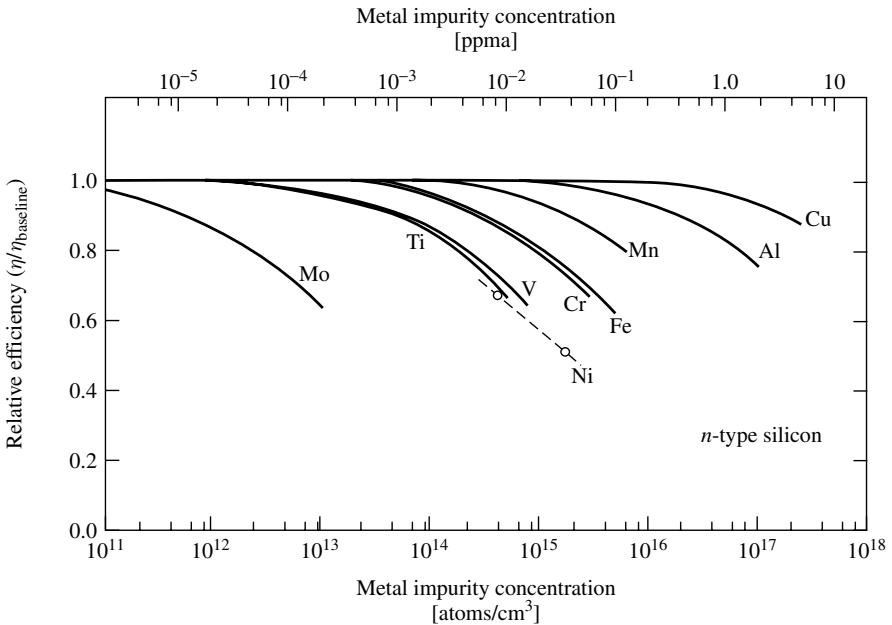


Figure 5.12 Solar cell efficiency versus impurity concentration for 1.5 ohm cm n-base devices [30]. Reproduced from Davis Jr. J *et al.*, *IEEE Trans. Electron Devices* © 1980 IEEE

co-workers [31] studied the precipitation and coarsening of NiSi_2 and the effect of precipitates upon the minority-carrier diffusion length in n -Si single crystals (FZ material). Scanning electron microscopy (SEM) using the method of electron beam-induced current (EBIC) revealed that NiSi_2 precipitates were efficient recombination centres and that the minority-carrier diffusion length, L_D , was related to the precipitate density, N_p , by

$$L_D = 0.7 \cdot N_p^{-1/3}$$

This relationship revealed that the diffusion length depends only on the density of precipitates and not on the concentration of impurities. Therefore, a suitable temperature process can increase the diffusion length, L_D . This occurs if during this process large precipitates grow at the expense of the smaller ones, increasing the free distance between the precipitates. This ripening process of precipitates is observed repeatedly during heat treatments.

5.7 ROUTES TO SOLAR GRADE SILICON

To design a specific route to solar grade silicon between the two existing commercial grades, that is, metallurgical and semiconductor (polysilicon), is not a new challenge. It was first seriously and massively addressed in the mid-seventies after the first international oil crisis. Considerable R&D efforts were made in the years 1975 to 1985 particularly in the United States under the guidance of the Department of Energy (DoE). During and at the end of this productive period, numerous specific articles, exhaustive review-studies and symposium proceedings devoted to these topics were published [38–40]. The following gives a summary and an update of these efforts. All approaches investigated are classified within four subgroups.

1. Crystallisation is generally an effective purification technique. Crystallisation is also a necessary step to produce the silicon device. The question is whether the crystallisation steps in the manufacturing chain to the solar cell can advantageously be combined with the purification.
2. Upgrading the purity of metallurgical silicon is a technique with the potential to produce millions of tonnes of silicon as we have demonstrated earlier in this chapter. The goal of and the challenge for this alternative are to achieve adequate purity at acceptable cost. A guiding number for this option has been and should remain less than 10 US\$/kg.
3. The polysilicon process involving the synthesis, the purification and the decomposition to elemental silicon of volatile silicon hydrides is proven technology. This is presently the sole reliable source of silicon for solar cells. Simplifying it, exploring or revisiting related routes seems therefore an attractive alternative. The challenge in this particular case is to achieve sufficient output at acceptable cost.
4. Electrolysis, electrolytic methods, metallic reduction of silicon and so on are summarised in a fourth category of methods.

5.7.1 Crystallisation

The efficiency of the crystallisation processes may be predicted by the segregation or the distribution coefficient of each impurity element (see Section 5.6.1) between the solid and

the liquid silicon phases. Published data (see Table 5.7) clearly show that the elements belonging to the Group IIIA (B, Al, Ga) and the Group VA (P, As, Sb) have a coefficient close to 1, making it difficult to separate them from the silicon. These elements are the electronic dopants for silicon and their concentration must be closely controlled during all steps of the manufacturing process. Their chemical and physical behaviour in interaction with silicon are two aspects of their close neighbourhood to this element. Crystallisation as such cannot be satisfactory without prior treatments, specifically to remove these elements, particularly P and B.

- *Crystallisation from a silicon-melt*: Various methods have been claimed to be useful for refining silicon by directional solidification resulting in large oriented crystals. All these various crystallisation methods are also used in manufacturing the silicon photovoltaic devices, and they are described in Chapter 6 of this handbook. Other valuable references are to be found in [39, 40].
- *Crystallisation from an aluminium melt*: Silicon forms a unique eutectic phase at the concentration of 12.6%(w) in aluminium. Several companies (Union Carbide, Alcoa and Wacker) have tried to take advantage of this property in order to purify silicon. By cooling a hypereutectic composition, pure silicon phases crystallise and precipitate from the aluminium melt. After solidification of the hypereutectic alloy, the aluminium matrix can be dissolved by leaching, releasing the pure silicon crystals [39, 41–44]. Published data indicated that the aluminium content in the resulting silicon was as high as 300 ppm(w). The segregation coefficient of aluminium in silicon limits further separation. A further reduction of aluminium, by directional solidification of the silicon thus obtained, would add unacceptable cost just for this element. Other metallurgical routes to eliminate Al at 1 ppm(w) level or less need to go through silicon melting and subsequent extraction with the double risk of recontamination and heavy material losses.

5.7.2 Upgrading Purity of the Metallurgical Silicon Route

The processes used in the elaboration of metallurgical grade silicon for the aluminium and the chemical industries proves that most of the metallic impurities could by repetition and combination of methods be decreased to a rather low level, for example 100 ppm(w) (see Table 5.9). Since metals could be further decreased by a post-directional solidification, it was rational to explore the full potential of this expected low-cost route.

5.7.2.1 Use of pure raw materials and pure lining

The use of pure linings in the furnaces and the intermediate vessels containing the liquid silicon was a first approach. It was investigated by several companies and research

Table 5.9 Typical best results achieved with the carbothermic reduction using high-purity raw materials

Impurity	B	P	Al	Fe	Ti
Minimum content ppm(w)	2	1	100	100	10
Maximum content ppm(w)	4	3	300	200	20

consortiums such as Dow-Corning, Elkem/Exxon, Siemens, NEDO, to mention the most accomplished [45–52]. Quartz or silica sand selected for their original purity were chemically treated by leaching or precipitated from water glass solutions. Purified carbon black was used as the reduction material in most of these approaches. The morphology of sand or precipitated silica and carbon black are quite different from, respectively, lumpy crystalline quartz and bulk carbon, charcoal or woodchips currently used in the carbothermic reduction. New technologies, in particular, to agglomerate the powder-like raw materials had to be developed. Pellets consolidated by means of organic non-contaminating binders (e.g. sucrose) or rice hulls perceived as potential high-volume, low-cost raw materials since they contained both silica and carbon are worth mentioning. Extruded pellets of cocked rice hulls, with sucrose, as a binder appeared to be reactive in the submerged arc furnace technology. Using these special raw materials, boron and phosphorus were found in the range of 1 to 4 ppm(w). In standard metallurgical grade, B and P range between 7 and 50 ppm(w), typical average values being around 25 ppm. The boron level achieved with rice hulls could be as low as 1 ppm(w). However, phosphorus was as high as 40 ppm(w) and would request an additional and specific treatment to make use of this source of silicon in solar cells.

5.7.2.2 *Post-treatment by chemical leaching*

Metallic impurities segregate at the grain boundaries, forming intermetallic phases with silicon, basically made of silicides and silicates. Hydrometallurgical upgrading of silicon by acid treatment and leaching has a long history. The *Silgrain* © process, a trademark of Elkem ASA, is currently producing 30 000 MT metallurgical grade silicon by refining ferrosilicon (90% Si) in an acid liquor of ferric chloride. The process is particularly efficient in removing iron and transition elements because these have very low segregation coefficients in silicon. The dissolution of iron and the transition elements in the leaching liquor is eased and enhanced by the formation of stable intermetallic phases with Al, Ca or isostructural elements, for example, Sr, Ba, Ga or a lanthanide. The process has been further developed during the past 15 to 20 years with solar grade silicon as an objective [53–56].

Surface treatment or leaching by hydrofluoric acid or by HCl/HF mixtures is also well known to wash out residual impurities present as oxides and silicates. Grinding silicon prior to leaching to increase the surface exposure is a way to enhance the purification [57, 58]. Acid leaching has therefore been envisaged by several groups and companies, for example Wacker and Elkem, as a post-treatment purification after the carbothermic reduction [53–58].

However, it must be emphasised that this method cannot in practice refine silicon below the dissolution limit characteristic of each element at the solidification composition. For the major impurities Fe, Ca and Al present in metallurgical grade silicon the limit of dissolution as obtained from classical refining in a ladle exceeds by far the ppm level. Effective post-treatment leaching of metallurgical grade silicon has made it possible to achieve less than 10 ppm(w) for these major elements and less than 1 ppm(w) for minor transition elements. One pass of directional solidification was then envisaged as sufficient to achieve the requested purity for solar cells.

The acid treatment or leaching methods is not effective in removing interstitial and substitution impurities such as boron, carbon and oxygen. Adding Ca to the silicon alloy prior to acid treatment, however, proves that P could be reduced by a factor of 5 down to a concentration less than 5 ppm(w), probably because P is dissolved in calciumsilicide [55, 56]. Adding barium also proves some effect on boron dissolution.

5.7.2.3 Post-treatment by extraction metallurgy in ladle

Post-treatments of liquid silicon are common practices in refining metallurgical grade silicon for applications in aluminium and chemical industry. The objective is then to adjust Al, Ca and possibly C to a suitable concentration of some hundreds or thousands of ppm(w). To that respect the reader may with great benefit consult Schei's *et al.* comprehensive handbook [13, 23]. As described above, crystallisation and leaching are efficient means of removing chemical elements with high ability to segregate from liquid to solid silicon, that is, Fe, and most of the metallic transition elements. Extraction metallurgy from a liquid phase of silicon, either liquid-liquid, liquid-solid or liquid-gas, has received considerable attention in order to remove the critical elements P, B and C. When silicon is kept liquid, it is possible to displace the equilibrium between both phases present and gradually remove the unsuitable impurity, by continuously extracting it.

Impurity(liquid silicon) = Impurity(liquid slag)	<i>K_{sl}/l_s</i>
Impurity(liquid silicon) = Impurity(solid slag)	<i>K_{sl}/s_s</i>
Impurity(liquid silicon) = Impurity(gas)	<i>K_{sl}/g</i>

Particular attention has been paid to boron and phosphorus because these elements are the major *p*- and *n*-type dopants of silicon and because they coexist in metallurgical grade silicon in concentration of one or two orders of magnitude too high for solar cell applications.

Boron has nearly the same affinity towards oxygen as silicon. Boron forms gaseous suboxides BO being analogous to SiO, and its stable oxide B₂O₃ behaves similar to SiO₂ in the presence of alkaline earths at slag-forming temperatures. Therefore, there are good reasons to expect the removal of boron as an oxide constituent of the extracting slag or as a gaseous suboxide at elevated temperature. Both theoretical possibilities have been experimentally verified.

Since the work published by Theuerer in 1956 [59], it has been known that liquid silicon becomes purified with respect to boron when brought in contact with a gas mixture of Ar-H₂-H₂O. The sole role of H₂ and H₂O assisting the extraction has been emphasised by several authors such as Khattak *et al.* [60-63], whereas Amouroux, Morvan *et al.* of the University of Paris [64-67] and the Japanese group of Kawasaki Steel/NEDO [68-72] have underlined the benefit of using an oxidative plasma in the presence of moisture and hydrogen. Amouroux, Morvan *et al.* have also shown that boron elimination was enhanced when fluoride, for instance in form of CaF₂, was injected into the plasma gas.

Experiments in removing B by slag extraction have been done by several companies and groups including Kema Nord, Wacker, Elkem and NEDO/Kawasaki. Schei [73] has

described a counter-flow solid–liquid reactor to remove boron by fractional extraction in a semi-continuous process in a patent assigned to Elkem ASA of Norway.

It has been demonstrated that phosphorus could be evaporated from a silicon melt under vacuum conditions [74, 75]. Miki *et al.* [76] have explained the thermodynamics of this process by reactions involving mono- and diatomic phosphorus in the gas phase:



Underscored symbols refer to dissolved element in liquid silicon as already defined in Section 5.3.2.

Silicon produced by carbothermic reduction is so to speak supersaturated in SiC when tapped from the furnace and may contain as much as 1000 to 1500 ppm(w) C. As this silicon is cooled down to the solidification temperature, the majority of this carbon precipitates out as SiC particles leaving around 50 to 60 ppm(w) in liquid silicon. Carbon removal from liquid silicon is therefore a two-step operation:

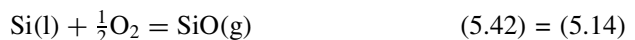
1. the removal of precipitated SiC as close to the solidification temperature as possible
2. the removal of dissolved $\underline{\text{C}}$ by oxidation to CO(g).

As already mentioned, SiC particles become effectively captured by the slag phase during oxidative refining in which the main objective may be to remove Al and Ca as industrially practised today or in a similar operation with the purpose of removing B or P. Depending on the temperature and the degree of slag/molten silicon intermixing, this treatment may give a product with 80 to 100 ppm(w) C. Other methods, which have been applied and proved effective at a temperature closer to the solidification temperature, are filtration, centrifugation or settling combined with slow cooling. Several studies have provided valuable contributions suggesting several methods, for example, settling in combination with directional solidification [77], filtration combined with oxidation [78], oxidative plasma [70–72] and decarburisation by inert gas purging or under vacuum [14, 78]. Klevan [14] has developed a mathematical model, which describes the kinetics of decarburisation when inert purging is applied. Mechanical removal is, however, not efficient enough to affect the substitution carbon. Stronger methods able to displace the equilibria, such as oxidative plasma and vacuum vaporisation, are believed to be more powerful techniques.

It is worth noting that these types of operation can all be carried out in carbon-lined ladles. The several steps dealing with the removal of dissolved carbon $\underline{\text{C}}$ from liquid silicon Si(l), however, has to be carried out in the absence of C and at a highest possible temperature in order to optimise the equilibrium and the kinetic conditions for the reaction:



A parallel reaction, which affects the silicon yield, unfortunately, also takes place:



The value of solid solubility of carbon in silicon is approximately 10 ppm(a), corresponding to the homogeneous distribution of substituted carbon atoms on silicon lattice sites. This type of carbon impurity is detected by infrared spectroscopy. Higher concentrations of carbon result in SiC precipitates of different size and morphology. This type of carbon is detected and analysed by combustion methods or secondary ion mass spectroscopy (SIMS).

5.7.2.4 Challenges and achievements

The improved carbothermic reduction of silica, followed by leaching and directional solidification, has the capability to produce silicon with sub-ppm concentration of all metallic impurities. Controlling the non-metallic elements, particularly B, P, C and O, at the level required for solar cell applications remains the major challenge for the metallurgical route. Unfortunately, there is no universal method for reducing simultaneously these critical elements. As a consequence, several refining steps are necessary, with the risk of reducing the silicon yield. Another risk is the recontamination by impurities from the reactants and the lining during handling and treatment of liquid silicon. Extensive studies were done on this route in the early eighties, but efforts since then have been considerably reduced. The Japanese program headed by NEDO is to our knowledge the most accomplished project representing this route (Table 5.10; [71]). On the basis of this project's results, Kawasaki has built a 60-MT pilot plant, but the economical feasibility of the route remains uncertain. In the NEDO process, metallurgical grade silicon is purified through

1. melting of silicon by electron beam and evaporation under vacuum
2. first directional solidification
3. remelting of silicon and gas treatment ($O_2 + H_2O$) assisted by a plasma torch
4. second directional solidification.

Table 5.10 Solar grade as obtained through upgrading metallurgical grade silicon by the NEDO method according to [71]

B [ppm(w)]	P [ppm(w)]	Al [ppm(w)]	Fe [ppm(w)]	Ti [ppm(w)]	O [ppm(w)]	C [ppm(w)]	Resistivity [ohm cm]	Lifetime [μ s]
0.04–0.10	0.03–0.14	<0.01	<0.05	<0.01	<6	<5	0.8–1.2	>7.7

5.7.3 Simplification of the Polysilicon Process

The Union Carbide and Ethyl Corporation polysilicon processes (Sections 5.4.2 and 5.4.3) resulted from attempts to make the Siemens process more economical. Project goals were to meet a price target of 10 US\$/kg set in 1975 by the US Department of Energy (DoE). The Siemens process was fully developed around 1960, but polysilicon for electronic devices and other purposes had been produced since the forties. The Siemens process was the first design of a rational industrial process, which gained international recognition through rapid and broad licensing. At least a dozen processes had been developed prior to the Siemens process and coexisted with the Siemens process until the beginning of the seventies. Purity and high production rates based on semiconductor industry

demand were the primary criteria for the process design. Capital expenditure and energy consumption were considered secondary criteria. While large production quantities of ultra-pure polysilicon were available at acceptable prices for semiconductors, this price was too expensive for the development of low-cost solar systems. For solar cells, a process with reduced costs, reduced energy consumption and increased production rates, with purity levels not as important, is needed. Since several processes had been developed in the past, a review and re-evaluation of the silicon chemistry of these processes was suggested (see Tables 5.11 and 5.12).

Table 5.11 Historical processes to manufacture polysilicon (according to Strategies Unlimited [79])

Companies	Volatile silicon source	Reduction agent	Reactor type
Dupont	SiCl ₄	Zinc	Inside-quartz tube
Bell lab.	SiCl ₄	Hydrogen	Ta-filament
Union Carbide	SiHCl ₃	Hydrogen	Inside-quartz tube
Int'l Telephone	SiCl ₄	Sodium hydride NaH	Ta-filament
Mallinckrodt	SiI ₄	Hydrogen	Inside-quartz tube
Transitron	SiH ₄	Decomposition	Inside-quartz tube
Texas Instruments	SiCl ₄	Hydrogen	Outside-quartz tube
Foot Mineral	SiI ₄	Decomposition	Si-filament
Chisso	SiCl ₄	Hydrogen	Inside-quartz tube
Siemens	SiHCl ₃	Hydrogen	Si-filament
Komatsu	SiH ₄ SiHCl ₃	Decomposition	Si-filament
Motorola	SiHCl ₃	Hydrogen	W-filament
Phoenix Materials	SiCl ₄	Hydrogen	Si-filament
Texas Instruments	SiHCl ₃	Hydrogen	Fluidised bed spheres

Table 5.12 Polysilicon research projects stimulated by the objectives of low-cost solar cells programs after 1975

Companies/groups	Volatile silicon source	Reduction agent	Reactor type
Aerochem Res. Lab.	SiCl ₄	Sodium	Free space
Eagle Picher/General Atomic/Allied	SiH ₄	Decomposition	Fluidised bed
Battelle	SiCl ₄	Zinc	Fluidised bed
Hemlock	SiH ₂ Cl ₂	Hydrogen	Si-filament/rod
Union Carbide	SiH ₄	Decomposition	Free space
Union Carbide	SiH ₄	Decomposition	Fluidised bed
Ethyl Corp	SiH ₄	Decomposition	Fluidised bed
Motorola	Si _n F _{2n+2}	Decomposition	
NEDO	SiHCl ₃	Hydrogen	Fluidised bed
Rhône-Poulenc	SiH ₄	Decomposition	
Schumacher	SiHBr ₃	Hydrogen	Fluidised bed
SRI International	SiF ₄	Sodium	Solid separation
Westinghouse	SiCl ₄	Sodium	Free space
Bayer	SiCl ₄	Aluminium	Melt
Bayer	SiH ₄	Decomposition	Fluidised bed
Wacker	SiHCl ₃	Hydrogen	Fluidised bed

To make the process cost effective, the economics of both the production of the volatile silicon compound and its decomposition or reduction to elemental silicon had to be reviewed. Compared to the historical processes, the research projects did not discover radically new silicon compounds. Silicon halides $\text{SiX}_{4-n}\text{H}_n$ could apparently not be avoided. However, innovative methods were discovered to produce these silicon compounds. Metallurgical grade silicon remained in most cases the starting point, but silicon fluoride, obtained as co-products from phosphates leaching (fertilisers) and direct chlorination of natural silica to produce tetrachlorosilane, were envisaged as serious challenges. The research abandoned completely the concept of heated filament or seed rod that was clearly perceived as too expensive. Texas Instruments had demonstrated the benefit of the fluidised bed technology, that is,

- larger throughput
- lower energy consumption
- continuous operation
- lower capital expenditure.

Although the quality was not acceptable for making microelectronics devices, this was not a drawback for the development of the solar cell market.

In addition to the fluidised bed, free space reactor implying spontaneous seedless formation of solid silicon particles through homogeneous decomposition of silane has also been envisaged among others by Union Carbide [38].

None of these projects have resulted yet in establishing a new polysilicon route devoted to solar cells and decoupled from the electronic feedstock. The research has to a large extent developed and strengthened the classical polysilicon business by developing new products and processes to produce semiconductor grade silicon (Union Carbide, Ethyl Corporation). However, it is believed that for quality reasons, a significant portion of the Ethyl Corporation process production is still to find outlet in the solar market, making this product to some extent a prime solar grade polysilicon.

The other polysilicon producers have declared that by relaxing the production procedures and quality control they could, when excess capacity is available, produce specifically a solar grade polysilicon at reduced cost. It seems reasonable to expect a price reduction of approximately 35%. The same producers have underlined that specific investments to produce solar grade silicon by this route should not be expected because of too low profitability [80, 81].

At the time of writing, three projects aimed at developing a solar polysilicon route were in the process of being developed:

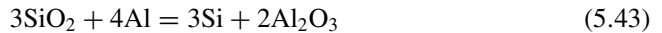
1. The German chemical company Bayer AG has for several years re-explored the decomposition of silane in fluidised bed reactor. The method combines the cost-effective synthesis of silane as in the Union Carbide process and the fluidised bed reactor as in the Ethyl Corporation process. The company has published the results of its basic assumption and made positive announcements [82–84]. Meantime, Bayer AG has withdrawn from the solar wafer business, which was the main driver for this feedstock development. To date it is therefore uncertain what the future of this project will be.

2. Another German company Wacker Chemie, which is one of the leading suppliers of electronic grade polysilicon and a great contributor to the development of materials to photovoltaics in the past, has decided to build a pilot plant to develop solar grade polysilicon by the reduction of trichlorosilane in a fluidised bed reactor. Under industrial conditions, each fluidised bed reactor should produce more than 500 MT/year and should be economical enough to meet the cost target of the solar cell industry.
3. The Japanese company Tokuyama Corporation, also a leading polysilicon manufacturer, has announced at a recent symposium its intention to develop a new deposition process using trichlorosilane in order to specifically produce solar grade silicon [85]. More technical details had not been presented at the time of writing this chapter. The reader is invited to consult later publications.

5.7.4 Other Methods

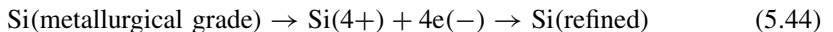
Besides the large avenues described above, one finds some other routes. The following processes are worth noting.

1. The aluminothermic reduction of silica



explored by Wacker [39].

2. The electrolytic transfer of silicon from an anode made partly of metallurgical grade silicon alloyed with Cu in (Cu₃Si-Si) to a graphite cathode through a liquid electrolyte made of KF:LiF:SiK₂F₆ as described by Olson *et al.* [86–88].



Although revisited by several R&D groups, these methods do not seem to have been the subject of extensive new programmes since the eighties.

5.8 CONCLUSIONS

At the time this handbook was written, silicon is the dominant PV material with more than 98% of cells and modules based on it. Crystalline technologies account for nearly 90%. We do not see new materials displacing silicon in the foreseeable future. The crystalline technologies require significant consumption of pure silicon. Purity requirements have not been exactly defined with the industry selecting silicon raw materials among the residuals from single-crystal pulling and second-grade polysilicon. At present, these sources are not sufficient to cover the rapidly growing demand from the solar industry. Polysilicon produced specifically for solar applications and prime-grade polysilicon are extensively used. This has the negative consequence of increasing the cost of solar cells and hence of slowing the market deployment of solar electrical energy. Research on a new dedicated route to solar grade silicon decoupled from the semiconductor business cycles has been going on for almost 30 years. Two directions still retain most of the attention of scientists and technologists: the further development of pyrometallurgical treatments of liquid silicon

and the simplification of the polysilicon processes. The crystallisation processes applied to silicon to produce the PV devices play a role in purifying and shaping silicon and should affect to a larger extent the development and the final definition of solar grade silicon. Quality and cost requirements have imposed strict limits to solar grade silicon. Capital cost is perceived as a significant part of the overall cost and adds to the barriers that need to be overcome.

REFERENCES

1. Maycock P (Ed), PV Energy Systems, *PV NEWS* **20**(3), 2 (2001).
2. Ikki O (Ed), Resources Total System Co, *PV Activities Japan* **7**(3), 1–6 (2001).
3. Schmela M, *PHOTON Int.* **3**, 32–35 (2001).
4. Knight J, *Trends in Photovoltaic Applications in Selected IEA Countries Between 1992 and 1999*, Report IEA-PVPS T1-08 (2000).
5. Murphy G, Brown R, *Silicon in Bulletin 675 Mineral Facts and Problems*, Bureau of Mines, US Department of Interior, Washington DC (1985).
6. Kerkhove D, *Silicon Production Technology*, Technische Universiteit Delft, Delft, Netherlands (1994).
7. Forwald K, *Dissertation NTNU*, Norway, MI-47 (1997).
8. Dosaj V, *Kirk-Othmer Encyclopedia of Chemical Technology*, 4th Edition, Vol. 21, 1104–1122, Wiley, New York (1997).
9. Moretto H, Schulze M, Wagner G, *Ullmann's Encyclopaedia Ind. Chem.* **A24**, 57–93 (1993).
10. Rong H, *Dissertation NTNU*, Norway, IUK-67 (1992).
11. Sørheim H, *Dissertation NTNU*, Norway, IUK-74 (1994).
12. Watt M, *Added Values of Photovoltaic Power Systems*, Report IEA-PVPS T1-09 (2001).
13. Schei A, Tuset J, Tveit H, *Production of High Silicon Alloys*, Chap. 12, Tapir forlag, Trondheim (1998).
14. Klevan O, *Dissertation NTNU*, Norway, MI-167 (1997).
15. Anglezio J, Servant C, *J. Mater. Res.* **5**, 1894–1899 (1990).
16. Forwald K, Schüssler G, *Proc. Silicon for the Chemical Industry I*, 39–46 (Norway, 1992).
17. Nygaard L, Brekken H, *Proc. Silicon for the Chemical Industry II*, 61–67 (Norway, 1994).
18. Brekken H, Nygaard L, Andresen B, *Proc. Silicon for Chemical Industry III*, 33–45 (Norway, 1996).
19. Pachaly B, *Proc. Silicon for Chemical Industry II*, 55–60 (Norway, 1994).
20. Forwald K, Soerli Oe, Schüssler G, EP 0 372 918 B1 (1989).
21. Schulze M, Licht E, *Proc. Silicon for the Chemical Industry I*, 131 (Norway, 1992).
22. Boardwine C *et al.*, Progress in Organic Chemistry, *Proc. of Int. Symp. on Organosilicon Chemistry X (1993)*, 555–569, Gordon & Breach Science Publishers, Amsterdam (1995).
23. Schei A, Tuset J, Tveit H, *Production of High Silicon Alloys*, Tapir forlag, Trondheim (1998).
24. Kobayashi S, in Hull R (Ed), *Properties of Crystalline Silicon*, 6–22, University of Virginia, USA (1999).
25. Trumbore F, *Bell Syst. Tech. J. (USA)* **39**, 205 (1960).
26. Burton J, Kolb E, Slichter W, Struthers J, *J. Chem. Phys.* **21**, 1991–1996 (1953).
27. Koderia H, *Japan J. Appl. Phys.* **2**, 212–219 (1963)
28. Graff K, *Metal Impurities in Silicon-Device Fabrication*, 29, Springer, Berlin (2000).
29. Istratov A, Hieslmair H, Weber E, *Appl. Phys.* **A70**, 489–534 (2000).
30. Davis Jr. J *et al.*, *IEEE Trans. Electron Devices* **Ed-27**, 677–687 (1980).
31. Kittler M, Lärz J, Seifert W, *Appl. Phys. Lett.* **58**, 911–913 (1991).
32. Itoh Y, Nozaki T, *Japan J. Appl. Phys.* **24**, 279–284 (1985).
33. Weber E, *J. Appl. Phys.* **A30**, 1–22 (1983).

34. Fischler S, *J. Appl. Phys.* **33**, 1615 (1962).
35. Jaccodine R, Pearce C, in Bullis W, Kimerling L (Eds), *Defects in Silicon*, 115–119, The Electrochemical Society, Pennington, NJ (1983).
36. Mikkelsen Jr. J, *Mater. Res. Soc. Symp. Proc. (USA)* **59**, 19 (1998).
37. Hocine S, Mathiot D, *Mater. Sci. Forum* **38-41**, 725 (1989).
38. Lutwack G, *Proc. of the Flat-Plate Solar Array Project Workshop on Low-Cost Polysilicon for Terrestrial Photovoltaic Solar-Cell Applications*, Contract DOE/JPL-1012-122, JPL Publication 86-11 (1986).
39. Dietl J, *Silicon for Photovoltaics*, Vol. 2, 285–352, North Holland, Amsterdam (1987).
40. Lanier F, Ang T, *Photovoltaic Engineering Handbook*, 3–17, Adam Hilger, Bristol (1990).
41. Dawless R, US Patent 4,246,249 (1981).
42. Smith F, Dawless R, *Electrochem. Soc.* **81-2**, 1147 (1981).
43. Kotval P, Strock H, US Patent 4,195,067 (1980).
44. Hanoka J, Strock H, Kotval P, *J. Appl. Phys.* **52**, 5829–5832 (1981).
45. Hunt L, Dosaj V, Final Report, Contract DOE/JPL 954 559-78/7 (1979).
46. Hunt L, Dismukes J, Amick J, *Proc. Symp. Materials and Processing Technologies for Photovoltaics*, 106, The Electrochemical Society, Pennington, NJ (1983).
47. Amick J *et al.*, *Proc. Symp. Materials and Processing Technologies for Photovoltaics*, 67, The Electrochemical Society, Pennington, NJ (1983).
48. Amick J *et al.*, *Proc. 5th EC Photovoltaic Solar Energy Conf.*, 336, Kovouri, Athens (1983).
49. Aulich H, Eisenrith K, Urbach H, Grabmaier J, *Proc. 3rd Symp. Materials and Processing Technologies for Photovoltaics*, 177 The Electrochemical Society. Pennington, NJ (1982).
50. Aulich H *et al.*, *Proc. 4th EC Photovoltaic Solar Energy Conf.*, 868 (Stresa, 1982).
51. Aulich H, *Proc. 5th EC Photovoltaic Solar Energy Conf.*, 936 Kovouri, Athens (1983).
52. Yoshiyagawa M *et al.*, “Production of SOG-Si by Carbothermic Reduction of High Purity Silica”, Presented at *Silicon for Solar Cells Workshop* (Schliersee, 1981).
53. Aas H, Kolflaath J, US Patent 3,809,548 (1974).
54. Aas H, *The Met. Soc. AIME, TMS Paper Selection* **A71-47**, 651–667 (1971).
55. Halvorsen G, US Patent 4 539 194 (1985).
56. Ceccaroli B, Friestad K, Norwegian Patent Application WO 01/42 136 (2000).
57. Pizzini S, *Sol. Energy Mater.* **6**, 253 (1982).
58. Dietl J, *Sol. Cells* **10**, 145 (1983).
59. Theuerer H, *J. Met.* **8**, 1316 (1956).
60. Khattak C, Schmid F, Hunt L, *Proc. of the Symp. on Electronic Properties of Polycrystalline or Impure Semiconductors and Novel Silicon Growth Methods*, 223–232, Saint Louis, MO, The Electrochemical Society, Pennington, NJ (1980).
61. Khattak C, Schmid F, *Proc. Symp. Materials and Processing Technologies for Photovoltaics*, 478–489, The Electrochemical Society. Pennington, NJ (1983).
62. Khattak C, Schmid F, *Silicon Processing for Photovoltaics II*, 153–183, Elsevier Science Publishers B.V., Amsterdam (1987).
63. Schmid F, Khattak C, US Patent 5,972,107 (1999).
64. Amouroux J, Morvan D, *High Temp. Chem. Processes* **1**, 537–560 (1992).
65. Cazard-Juvernat I, Bartagnon O, Erin J, *High Temp. Chem. Processes* **3**, 459–466 (1994).
66. Combes R, Morvan D, Picard G, Amouroux J, *J. Phys. III France* **3**, 921–943 (1993).
67. Erin J, Morvan D, Amouroux J, *J. Phys. III France* **5**, 585–604 (1995).
68. Suzuki K, Sakaguchi K, Takano K, Sano N, *J. Jpn. Met.* **54**, 168–172 (1990).
69. Suzuki K, Kumagai T, Sano N, *ISJN Int.* **32**, 630–634 (1992).
70. Baba H *et al.*, *Proc. 13th Euro. Conf. Photovoltaic Solar Energy Conversion*, 390–394 (Nice, 1995)
71. Nakamura N *et al.*, *Proc. 2nd World Conf. on Photovoltaic Solar Energy Conversion* (Vienna, 1998).
72. Nakamura N *et al.*, EP Patent 0 855 367 A1 (1998).

73. Schei A, US Patent 5,788,945 (1998).
74. Suzuki K, Sakaguchi K, Nakagiri T, Sano N, *J. Jpn. Inst. Met.* **54**, 61 (1990).
75. Ikeda T, Maeda M, *ISIJ Int.* **32**, 635–642 (1992).
76. Miki T, Morita K, Sano N, *Met. Mater. Trans.* **27B** 937–941 (1996).
77. Aulich H, Schulze F, Urbach H, Lerchenberger A, *Proc. of the Flat-Plate Solar Array Project Workshop on Low-Cost Polysilicon for Terrestrial Photovoltaic Solar-Cell Applications*, Contract DOE/JPL-1012-122, JPL Publication 86-11, 267–278 (1986).
78. Sakaguchi K, Maeda M, *Met. Trans. B* **23B**, 423–427.
79. *Silicon Industry Vol. 2 – Technology Assessment*, Strategies Unlimited, Mountain View, CA 94040, USA (1983)
80. Ossenbrink H, Bishop J, Aulich H (Eds), *Dependable and Economic Silicon Materials Supply for Solar Cell Production*, Report on Workshop, JRC Ispra (VA) Italy, 7th December 1998 Special Publication No. I.99.56 (1999).
81. Maurits J, *Proc. of the 8th Workshop on Crystalline-Silicon Solar Cell Materials and Processes*, 10–17 (1998).
82. Block H, Wagner G, *Proc. of the 16th EPSEC*, 1059–1063 (Glasgow, 2000).
83. Block H, Wagner G, *Proc. of Silicon for the Chemical Industry V*, 271–280 (Norway, 2000).
84. Tilg A, Mleczko L, *Proc. of Silicon for the Chemical Industry V*, 281–295 (Norway, 2000).
85. EPIA Round Table on Solar Grade Silicon Feedstock: The Global Perspective, 17th *European Solar Energy Conf. and Exhib.* (Munich, Germany, 2001).
86. Olson J, Carleton K, Kibbler A, *Proc. 16th IEEE Photovoltaic Specialists Conf.*, 123–127 (1982).
87. Olson J, Carleton K, *J. Electrochem. Soc.* **128**, 2698 (1981).
88. Carleton K, Olson J, Kibbler A, *J. Electrochem. Soc.* **130**, 782–786 (1983).
89. Nozaki T, Yatsurgui Y, Akiyama N, Endo Y, Makida Y, Behaviour of Light Impurity Elements in the Production of Semiconductor Silicon, *J. Radioanal. Chem.* **19**, 109–128 (1974).
90. ASM Handbook, Vol. 8, *Metallography, Structures and Phase Diagrams* 8th Edition, ASM International, Metals Park, Ni-Si Phase Diagram, p. 325.
91. Bean A, Newmon R, *J. Phys. Chem. Solids* **32**, 1211–1219 (1971).

6

Bulk Crystal Growth and Wafering for PV

**W. Koch¹, A. L. Endrös², D. Franke³, C. Häbeler¹,
J. P. Kalejs⁴ and H. J. Möller⁵**

¹Bayer AG, Krefeld, Germany, ²Siemens and Shell Solar GmbH, Munich, Germany, ³Access e.V., Aachen, Germany, ⁴RWE Schott Solar, Massachusetts, USA, ⁵TU Bergakademie Freiberg, Freiberg, Germany

6.1 INTRODUCTION

The workhorse of the photovoltaics industry is silicon. More than four out of five amperes of solar-module produced current come from crystalline silicon modules. Of this amount, over 50% is produced by a steadily increasing share from multicrystalline silicon material.

Silicon solar cells first were made about 50 years ago from Czochralski (Cz)-pulled monocrystals with technology adapted from the microelectronics industry. Subsequently, world-record cell efficiencies have been achieved at a very high cost on a laboratory scale with Float Zone (FZ) monocrystals.

Cost pressures have forced the development of multicrystalline material solidification processes for production of very large silicon ingots (blocks), which have reached typical sizes of 250 kg in 2000. A good theoretical understanding of growth processes, together with numerical simulations of the entire process down to a microstructural defect level in the crystal today has resulted in the economical production of high-quality material. Sawing of silicon crystal into the thin wafers required for the best performance in solar cells wastes about 50% of expensive, pure silicon feedstock and is very costly. This has led to the development of several crystalline silicon foil, that is, ribbon production processes, and these are now in various stages of R&D and commercialization.

6.2 BULK MONOCRYSTALLINE MATERIAL

The dominant issue of the photovoltaic industry is to fabricate solar cells in large volumes that are both highly efficient and cost-effective. An overall industrial goal is to significantly lower the costs per watt. The dominant absorber material used today for the majority of the commercially produced solar cells is the Czochralski-grown crystalline silicon (c-Si) in monocrystalline and block-cast material in multicrystalline form (mc-Si). Up to now, a lot of effort has been undertaken to increase the electrical efficiency of solar cells reproducibly towards and even above 20% [1], whereas much higher efficiencies were indeed claimed [2] but were most probably never reached [3]. Unfortunately, efficiency improvements are often reached only with the help of cost-intensive process steps so that most steps cannot be directly implemented into industrial products but have to be reengineered for low-enough cost. Hence, there still remains a significant efficiency gap between monocrystalline laboratory cells with efficiencies up to 24% and cost-effective, commercial Cz solar cells that are presently produced and sold in high volume at approximately 14 to 17% efficiency.

While some years ago the cost of a module was driven almost equally by the cost of the wafer (33%), the cell process (33%) and the module making (33%), this well-known ratio has changed significantly – both for C-Si and mc-Si. Today, in most products the wafer attributes to sometimes more than 50% (!) of the module cost, whereas the cell process and the module process attribute to the rest with similar portions of ~25%. The main reason for this is on one hand a steady cost reduction in the cell and module processes and on the other hand a significant increase in feedstock price together with an almost unchanged wafer thickness of 250 to 350 μm in production.

One way to meet today's demand of lower wafer cost is to (1) reduce the cost of crystal growth by improvement of productivity and material consumption at constant wafer quality, (2) reduce the cost of the wire-sawing process and (3) cut thinner wafers. While commercial Si solar cells still have a present wafer thickness of 250 to 350 μm for reasons of mechanical stability, a thickness of only 60 to 100 μm has been calculated to be the physical optimum thickness for silicon solar cells [4]. In this thickness regime the maximum theoretical efficiency for c-Si solar cells can be reached. In this optimum thickness regime, however, monocrystalline silicon becomes very fragile so that not only the electronic but also the mechanical properties of the wafer as well as the handling and processing techniques become of utmost importance for a good overall fabrication yield. Besides the mere mechanical wafer stability, manufacturing processes have to be adapted, redesigned or newly developed to avoid bending and breaking of ultra-thin wafers. With reduced wafer thickness, the necessity for surface passivation has to be taken into account. Since this cannot be done without adding to the cost, any added process step has to add adequate efficiency to remain cost-effective. Other important issues to get as much efficiency as possible out of the "valuable" wafer are improvements in anti-reflection (AR) coating, grid shadowing, "blue" response of the emitter and both surface and volume passivation.

The demand for high-quality polysilicon feedstock in the world market grew quickly not only in the microelectronic but also in the photovoltaic industry. In 1980 the worldwide production of single-crystal silicon amounted to approximately 2000 metric tons per year. This number was equivalent to ~100 000 silicon crystals every year

by either the Czochralski technique (80%) or the floating-zone technique (20%). The PV industry used both the high-quality tops and tails of the microelectronic crystals for less than 5\$/kg to fit the feedstock demand and the depreciated Cz pullers of the “big brother” microelectronic industry. Since the microelectronic industry was and is still driven by continuously increasing ingot diameters, the “small” Cz machines became available for the PV-industry at interesting prices. During the last expansion phase of the microelectronic industry (1993–99), the PV industry had to struggle with a severe shortage of affordable feedstock. To reach the production volume, even pot scrap Si material had to be used. New and demanding techniques were developed in a hurry to separate the Si from the quartz crucible parts and to pre-select and pre-clean this material. Also, fine grain material had to be made usable. However, the annual world requirement for solar quality silicon in 2010 is estimated at 8000 to 10000 metric tons for PV use, that is, the silicon demand will be roughly as high in volume as today’s world production for microelectronics. A dedicated Si feedstock supply only for PV is therefore a necessity.

It can no longer be denied that the growing of silicon crystals has matured from an art into a scientific business. In today’s PV-business, some of the bigger companies convert more than ~ 1 to 2 tons of silicon per day into solar grade Cz crystals and solar cells. Since PV has different main requirements for crystal growing from the microelectronic industry, the focus of machine and process development differ.

6.2.1 Cz Growth of Single-crystal Silicon

Solar cells made out of Czochralski (Cz)-grown crystals and wafers play – together with multicrystalline cells – a dominant part in today’s PV industry. This is due to the following advantages.

Cz crystals can be grown from a wide variety of differently shaped and doped feedstock material. This enables the PV industry to buy cost-effective feedstock Si with sufficient quality even on spot markets. Since the feedstock is molten in a crucible, the shape, the grain size and the resistivity of the different feedstock materials can be mixed for the required specifications, although a given feedstock alone would fail. However, special care must be taken to avoid any macroscopic particles (SiO_2 , SiC) that would not be dissolved in the melt especially when pot scrap material is used.

The Cz process acts as a purification step with respect to lifetime-limiting elements. The effective distribution coefficients of the most dominant lifetime-limiting metals (Fe, Ni, Au, Ti, Pt, Cr) are in the range of 10^{-5} or below. Together with appropriate gettering steps during cell processing, highly efficient commercial solar cells can even be made out of ingots grown from low-grade pot scrap material. The targeted iron equivalent concentration in the finished cell must be $<10^{12}$ atoms/cm³ to achieve a minority carrier diffusion length well above ~ 150 μm .

The Cz process itself acts as a quality control step since proper crystallisation, that is, dislocation-free growth of an ingot, can only take place in a well-defined process window. The homogeneity of a well-grown solar grade Cz ingot for PV application is excellent with respect to the bandwidth of electronic and structural properties, whereas mc-Si block casting produces specifications with higher variances in most parameters. Cell

processes with Cz-Si can therefore use high-efficiency processes with smaller process windows that require well-defined starting material.

Cz technology is mature and cost-effective. Equipment and processes for semi-automated growing of crystals are commercially available so that several Cz pullers can be run by a single operator. Owing to the robust making of the machines, many Cz growers more than 20 years age are still in production.

The ingot can be pulled in a defined $\langle 100 \rangle$ orientation. This is a big economic advantage since the solar cell process can use this crystallographic property to homogeneously texture solar cells with a very cost-effective wet chemical etching step. By anisotropic etching, a surface structure with random pyramids is built that couples the incoming light very effectively into the solar cell. This effect together with the usually higher diffusion length of Cz crystals gives rise to the increased efficiency of Cz-Si solar cells compared to similarly processed mc-Si cells.

There exists a high potential for increasing the net pulling speed, that is, the productivity of a puller by a clever design of the hot zone, by sophisticated recharging concepts of Si in the hot crucible and by tuning the growth recipe to the optimum pull speed. Here the PV industry is in the novel position that it can neglect most specifications that are required in the microelectronic industry.

This is possible since the PV specifications are strongly reduced in the number of required parameters in contrast to microelectronic material. A PV specification “simply” focuses on the maximum productivity, a minority-carrier diffusion length of the material that should be exceeding the cell thickness and a shallow p -type doping that leads to a specific resistivity between 0.3 and 10 Ωcm , depending on the fabricated solar cell type.

One of the main disadvantages of Cz crystallisation of silicon is the fact that square cells are best suited to build a highly efficient solar module, whereas Cz ingots have a round cross section. In order to use both the crystal and the module area in the best manner, the ingots are usually cut into a pseudosquare cross section before they are cut into wafers. Additionally, the tops and tails of the ingots cannot be used for wafer production. The cropped and slapped materials, that is, tops and tails and so on, are then fed back into the growth process again.

The equipment and the basic principle for Cz pulling is shown in Figure 6.1. The Cz equipment consists of a vacuum chamber in which feedstock material, that is, polycrystalline silicon pieces or residues from single crystals, is melted in a crucible and a seed crystal is first dipped into the melt. Then the seed is slowly withdrawn vertically to the melt surface whereby the liquid crystallises at the seed. High vacuum conditions can be used as long as the melt weight is small ($<1\text{--}2$ kg), but with larger melts (often more than 30 kg) only pulling under argon inert gas stream is practicable. Owing to the reduced argon consumption, the argon pressure is set in the 5 to 50 mbar regime in the PV industry, whereas in the microelectronic industry, atmospheric pressure is also used.

After the silicon is completely molten, the temperature of the melt is stabilised to achieve the required temperature to lower the seed into the melt. The temperature must be chosen so that the seed is not growing in diameter (melt too cold) or decreasing in diameter (melt too hot). In PV the seed is usually $\langle 100 \rangle$ -oriented, is monocrystalline and



Figure 6.1 Cz pullers in a PV-production environment (a) and growing Cz crystal (b) in a quartz crucible

is pulled upwards to grow a “crystal neck”. Since dislocations propagate on (111) planes that are oblique in an $\langle 100 \rangle$ -oriented crystal, the dislocations grow out of the crystal neck after a couple of centimetres so that the rest of the crystal grows dislocation-free even if the growth was started from a dislocated seed. The dislocation-free state of the grown crystal manifests itself in the development of “ridges” on the crystal surface. If this state is achieved, the diameter of the crystal can be enlarged by slower pulling until it reaches the desired value. The transition region from the seed node to the cylindrical part of the crystal has more or less the shape of a cone and is therefore called the “seed cone”. This cone can be pulled differently, either flat or steep.

Shortly before the desired diameter is reached, the pulling velocity is raised to the specific value at which the crystal grows with the required diameter. Owing to the seed rotation, the crystal cross section is mostly circular. In general, the pulling velocity during the growth of the cylindrical part is not kept constant, but is reduced towards the bottom end of the crystal. This is mainly caused by the increasing heat radiation from the crucible wall as the melt level sinks. The heat removal of the crystallisation thus becomes more difficult and more time is needed to grow a certain length of the crystal. Standard pull speeds in the body range from 0.5 to 1.2 mm/min. The diameter of the crystal in PV is often chosen between 100 and 150 mm. This is due to the short-circuit current of big solar cells where values of 6 A per cell are exceeded. It is difficult to provide a proper contacting scheme in screen print technology that can handle such high currents in the front contacts without high series-resistance losses. With even larger cell sizes, this effect becomes more problematic.

To complete the crystal growth free of dislocations, the crystal diameter has to be reduced gradually to a small size, whereby an end cone develops. For this purpose, the pulling speed is raised and the crystal diameter is decreased. If the diameter is small enough, the crystal can be separated from the melt without a dislocation forming in the cylindrical part of the crystal. The withdrawal of the crystal from the residual melt can be done with a rather high velocity, but not too fast, because thermal shock would cause plastic deformation called “slip” in the lower part of the crystal. The final crystal length is dependent on the crucible charge and varies between 40 and 150 cm.

Nowadays, the seed crystals used for Cz crystal growth are usually dislocation-free. However, each time the seed crystal is dipped into the melt, dislocations are generated by the temperature shock and by surface tension effects between the melt and the crystal. Normally these dislocations are propagated, or move into the growing crystal, particularly if the crystals have large diameters. The movement of dislocations is affected by cooling strain and faulty crystal growth.

The strain that occurs as a result of different cooling rates between the inner and the outer parts of the crystal is probably the main reason for the dislocation movement in the case of large crystals. At the usual $\langle 100 \rangle$ -crystal orientation, no (111) lattice plane, that is, no main glide plane, extends parallel to the crystal axis. All (111) glide planes are oblique to the crystal axis and as a result all dislocations that move only on one glide plane are conducted out of the crystal at some time. For movement in the pulling direction, the dislocations have to move downwards in a zigzag motion using at least two of the four different (111) glide planes. Dislocation-free crystal growth is relatively stable even for large crystal diameters, in spite of the higher cooling strain. This is so because it is difficult for a perfect crystal to generate a first dislocation. However, if a first dislocation has been formed, it can multiply and move into the crystal. In this way, numerous dislocations are generated and spread out into the crystal until the strain becomes too low for further movement of dislocations. Therefore, if a dislocation-free growing crystal is disturbed at one point, the whole cross section and a considerable part of the already-grown good crystal are inundated with backward-moving slip dislocations. The length of the slip-dislocated area is approximately equal to the diameter. Wafers and cells that show these types of dislocations can easily be hydrogen-passivated.

After losing the dislocation-free state, the crystal continues to grow with a high density of dislocations that usually are irregularly arranged. They are partly grown-in into the crystal and partly generated later by strain-induced processes. At high temperatures, climb processes take place that distort the dislocation array even more. This further increases the irregular shape and the distribution of the dislocations. In contrast to simple “slip” dislocations, these “grown-in” dislocations cannot be passivated well by a hydrogen-passivation step later in the solar cell processing. With crystal diameters above 30 mm, the monocrystalline but dislocated growth is not stable and in most cases changes to polycrystalline growth because of the tendency of a Si crystal to form twins in the presence of strain and dislocations. These twins also multiply and form higher-order twins and thus rapidly form a polycrystal. This fine-grained poly-Si material is not usable for solar cell production. Known causes for the generation of the critical first dislocation are either solid particles in the melt that move to the solidification front, gas bubbles that are trapped at the solidification front, impurities that exceed the solubility limit in the melt, vibrations of crystals and melt, thermal shocks or a too high cooling strain.

The growth of the seed cone is the most critical stage in the pulling of the Cz crystal. For productivity reasons very flat seed cones are preferable since the time for the making of the cone is not productive. However, the probability of introducing dislocations in the seed cone is lowest for tapered cones, although this means an increase in the pulling time by 15 to 25% for the same body length and additional loss in usable material. The loss of time and material gets worse for larger ingot diameters.

Owing to the reaction between the liquid Si and the quartz crucible, the crucible is of considerable importance to the growth. The silica of the crucible supplies considerable amounts of oxygen to the melt and, owing to the high purity of the silica, only small amounts of other impurities. However, the crucible tends to dissolve after a long-standing time so that the risk for particles in the melt from the crucible is increased with increased pulling time. The oxygen of the melt adds up to 10^{18} oxygen atoms/cm³ to the growing crystal, whereas carbon is usually $<10^{17}$ /cm³ and has only little impact on the solar cell performance. Oxygen effects like thermal donors and precipitates can be well controlled in Cz cell processing.

6.2.2 Tri-crystalline Silicon

The mechanical properties of tri-crystalline silicon (tri-Si) allow slicing of ultra-thin wafers with higher mechanical yield than monocrystalline silicon (see [5, 6]). Tri-Si is a crystal compound consisting of three mutually tilted monocrystalline silicon grains [5, 6]. The crystal compound has a (110) surface orientation in all grains in contrast to the standard (100) orientation of wafers for today's solar cell production. While two of the grain boundaries in a tri-crystal are $\Sigma 3$ classified, that is, first-order twins, the third grain boundary is a $\Sigma 9$ structure, that is, a second-order twin. All boundaries are perpendicular to the (110) wafer plane and meet at the ingot centre forming a characteristic tri-star. Tri-Si growth is fully compatible with standard Cz monocrystalline growth, but it is faster. Using a tri-crystal seed that contains the complete generic information, tri-Si ingots of 100 to 150 mm diameter and up to 700 mm length are grown in standard commercial crystal pullers using optimised growth parameters for neck, crown and body (see Figure 6.2).

As the pulling axis is parallel to the common $<110>$ orientation of all three grains, the dislocations often cannot be completely eliminated during necking, resulting in ingots that are not dislocation-free. The maximum local dislocation densities are about $105/\text{cm}^2$ in the ingot top and about $107/\text{cm}^2$ in the ingot bottom. The dislocations are often arranged

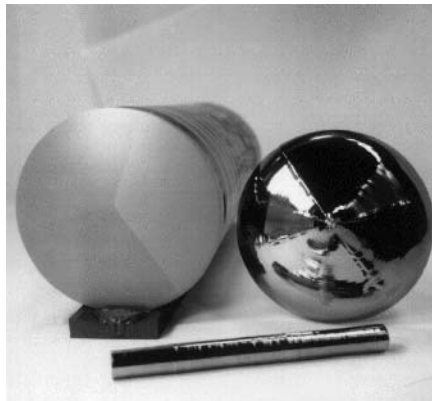


Figure 6.2 Tri-crystal seed (front), tri-crystal with cropped crown (left) and tri-crystal crown (right) with typical facets

in a streetlike geometry, while the dislocation density is significantly reduced in between the streets. However, despite the presence of dislocation from the very beginning (!), ingots of up to 700-mm length can be Cz-grown with multiple recharges at increased pull speed (see Figure 6.3). This is in fundamental contrast to the traditional c-Si growth with (100) orientation where dislocations must be completely avoided because otherwise the crystalline structure is totally lost after only a few centimetres of dislocated growth due to rapid dislocation multiplication. This peculiar structural stability of tri-Si, studied in detail through a geometrical stress model, is attributed to a reduction of cross slip in the tri-Si structure [7, 8].

Regarding electrical properties, ELYMAT mappings [9] show that there is a good spatial correlation between dislocation density and minority-carrier diffusion length: areas of high dislocation density show low diffusion length values. For dislocation lean ingots with 4- to 10- Ωcm resistivity, diffusion length values of more than 1000 μm (see Figure 6.4) can be obtained before light-induced degradation (LID).

The LID of the diffusion length of Cz-Si has recently been investigated extensively by several groups [1, 10, 11]. Although the identification of the defect structure is yet

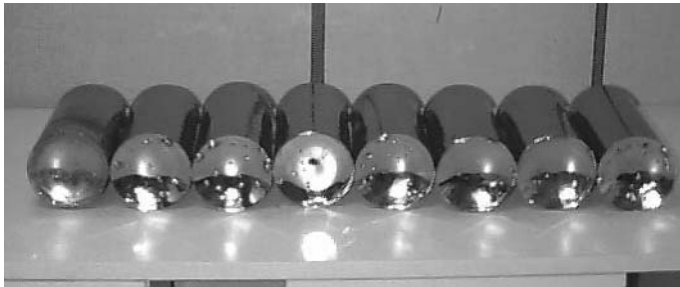


Figure 6.3 Tri-Si ingots ($\text{\O}140$ mm) from quasi-continuous pulling

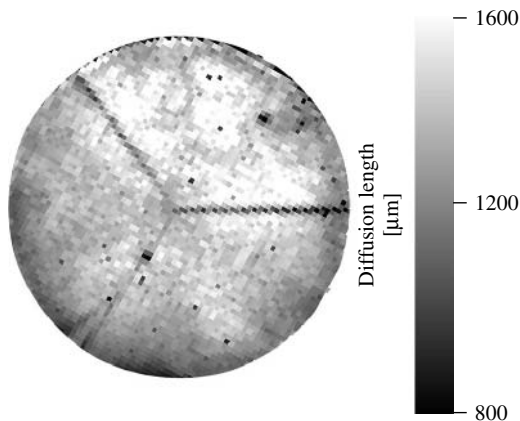


Figure 6.4 Diffusion length map of a 10- Ωcm as-grown wafer cut from the top of a dislocation lean tri-Si ingot. Lateral average diffusion length is 1300 μm

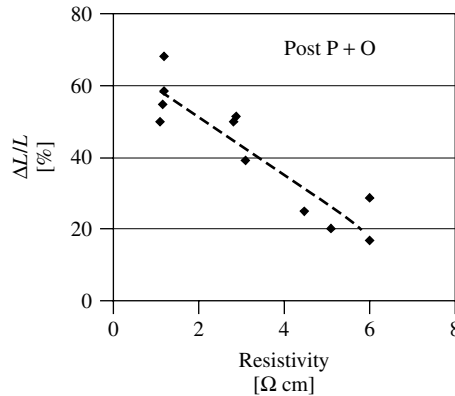


Figure 6.5 Relative degradation of diffusion length versus base resistivity for tri-crystalline silicon, measured after a standard P-diffusion and oxidation process

to be accomplished, a strong correlation of the effect with boron and oxygen is well established. Because tri-Si is grown with boron doping using standard Cz technology, an impact of LID on electrical quality is also present. Figure 6.5 shows a plot of the relative degradation as a function of base resistivity after a standard P-diffusion and oxidation process. Relative degradation values of less than 30% can be reached with 4- to 6- Ω cm material.

Tests on Si crystals fabricated from virgin poly-feedstock material with gallium, indium or aluminium as doping material have been performed to study LID. Best results have been obtained for Indium-doped material, for which the LID effect is reduced to almost below 3% of the diffusion length, which is within the accuracy limit of the ELYMAT measurements. With this material, light stable diffusion length values above 1 mm (!) can be achieved. This material is therefore best suited for high-efficiency cell processes.

In order to test the tri-Si material with standard solar cell processes, test cells are manufactured with a modified “Siemens Solar Boron Back Surface Field” (BSF) process with screen-printed contacts, as described in [12]. The final cell thickness was between 120 and 250 μ m. A boron-BSF process was chosen since the BSF is crucial for high efficiency at reduced wafer thickness and beneficial for material with high diffusion length. SiN deposited with a commercial low pressure chemical vapour deposition (LP-CVD) method was applied as an AR coating, that is, no volume passivation can be expected since no molecular hydrogen was present during SiN deposition. In this case no complicated passivation or activation effects of hydrogen in Si must be taken into account [13–16]. In order to eliminate the effect of the different surface orientations and in order to focus on the pure material response, the wafers were *not* textured.

Table 6.1 shows that the efficiencies reach 15.5% in a lab-scale average. This efficiency compares well and slightly exceeds the results of corresponding solar cells from *solar-grade* <100> mono-material that was grown in standard production. The champion tri-Si cell efficiency without surface texturing was 15.9% using this cost-effective process.

Table 6.1 AM1.5 cell efficiencies for non-textured BSF cells on tri-Si and mono-Si substrates. Cell area is $103 \times 103 \text{ mm}^2$ pseudo square

Material (non-textured)	Thickness average [μm]	Average efficiency [%]	V_{OC} [mV]	I_{SC} [mA/cm ²]	FF [%]	Rho [ohm cm]
Tri-Si	140	15.5	615	33.4	75.5	4
Mono-Si	200	15.2	612	32.7	76	1

6.3 BULK MULTICRYSTALLINE SILICON

Multicrystalline silicon besides monocrystalline silicon represents the basis of today's photovoltaic technology. Multicrystalline silicon offers advantages over monocrystalline silicon with respect to manufacturing costs and feedstock tolerance at, however, slightly reduced efficiencies. Another inherent advantage of multicrystalline silicon is the rectangular or square wafer shape yielding a better utilisation of the module area in comparison to the mostly round or pseudosquare monocrystalline wafers. The efficiencies of multicrystalline silicon solar cells are affected by recombination-active impurity atoms and extended defects such as grain boundaries and dislocations. A key issue in achieving high solar cell efficiencies is a perfect temperature profile of both ingot fabrication and solar cell processing in order to control the number and the electrical activity of extended defects. Moreover, the implementation of hydrogen-passivation steps in solar cell processing turned out to be of particular importance for multicrystalline silicon. With the introduction of modern hydrogen-passivation steps by Si_3N_4 layer deposition, the efficiencies of industrial multicrystalline silicon solar cells were boosted to the 14 to 15% efficiency range and consequently market shares were continuously shifted towards multicrystalline silicon as the standard material of photovoltaics.

6.3.1 Ingot Fabrication

Two different fabrication technologies for multicrystalline silicon, the Bridgman and the block-casting process (see illustrations in Figures 6.6 and 6.7) are employed. In both processes the solidification of high-quality multicrystalline silicon ingots with weights of 250 to 300 kg, dimensions of up to $70 \times 70 \text{ cm}^2$ and heights of more than 30 cm have been successfully realised. While the Bridgman technology is a quite commonly used technique, the only two companies mainly employing the casting technology are Kyocera (Japan) and Deutsche Solar GmbH (Germany) [17, 18].

The main difference between both the techniques is that for the melting and crystallisation process only one crucible (Bridgman) is used, whereas for the crystallisation process a second crucible (block casting) is used.

In the case of the Bridgman process, a silicon nitride (Si_3N_4)-coated quartz crucible is usually employed for melting of the silicon raw material and subsequent solidification of the multicrystalline ingot. The Si_3N_4 coating thereby serves as an anti-sticking layer preventing the adhesion of the silicon ingot to the quartz crucible walls that owing to the volume expansion during crystallisation of the silicon material would inevitably lead to a destruction of both the silicon ingot and the crucible. Concerning the block-casting

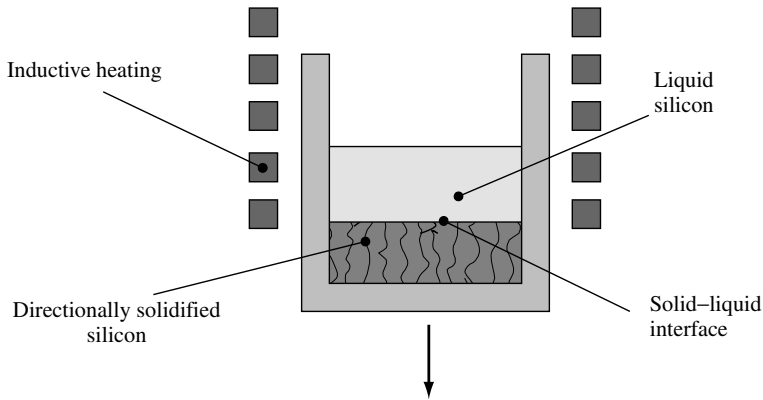


Figure 6.6 Conventional Bridgman technique that still is mainly used for the fabrication of multicrystalline ingots. Both melting and crystallisation of the silicon is performed in a Si_3N_4 -coated quartz crucible. Crystallisation is realised by slowly moving downward the liquid silicon-containing crucible out of the inductively heated hot zone of the process chamber

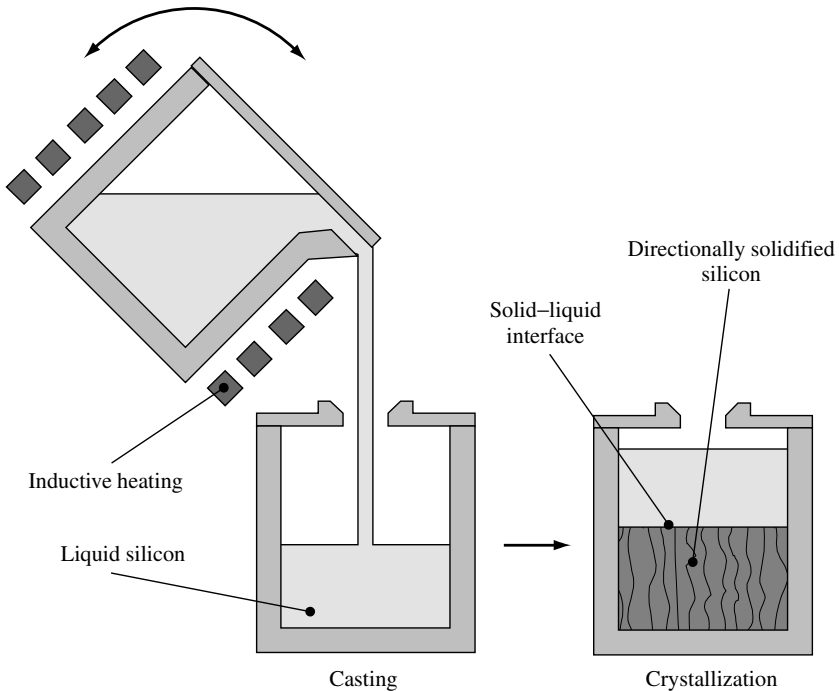


Figure 6.7 Block-casting process for the fabrication of multicrystalline silicon. After melting the silicon in a quartz pot, the silicon is poured into a second quartz crucible with a Si_3N_4 coating. The heating elements of the crystallisation crucible are not shown in the figure. In comparison with the Bridgman technique (see Figure 6.6), shorter crystallisation and cooling times can be realised by employing a more variable heater system

process, the melting is performed in a quartz crucible without a coating, whereas – after pouring the molten silicon into a second crucible – for the crystallisation also a Si_3N_4 -coated one is used.

Usually, in both production technologies, crystallisation starts at the bottom of the crucible by lowering the temperature below the melting temperature (1410°C) of silicon. Within the Bridgman process the temperature reduction is achieved by simply descending the liquid silicon-containing crucible out of the hot area of the crystallisation furnace. Contrarily, the temperature control during the block-casting process is achieved by a corresponding adjustment of the heaters, whereas the crucible itself is not moved during solidification.

After solidification starts in the bottom region, the crystallisation front, that is, the liquid–solid interphase, moves in a vertical direction upwards through the crystallisation crucible. This so-called directional solidification results in a columnar crystal growth and consequently adjacent wafers fabricated out of the ingots show nearly identical defect structures (grain boundaries and dislocations).

Common crystallisation speeds used for the Bridgman technology are in a range of about 1 cm/h (corresponding to a weight of approximately 10 kg/h for large ingots). With regard to the increase in crystallisation speed, that is, productivity, mainly cooling of the already crystallised fraction of the ingot has to be taken into account. Too high process speeds cause large thermal gradients within the solidified silicon that may result in cracks or even destruction of the ingot. For the block-casting technology, however, owing to the more versatile and sophisticated heater system, considerably higher crystallisation speeds can be achieved [18].

6.3.2 Doping

Standard multicrystalline silicon is a boron-doped *p*-type material with a specific electrical resistivity of about $1\ \Omega\text{cm}$, which corresponds to a boron concentration of about $2 \times 10^{16}/\text{cm}^3$. The specific resistivity is adjusted in a way such that optimal solar cell performance is guaranteed. Naturally, the boron concentration can be varied according to the requirements of specific solar cell processes. Specific resistivities in a range of 0.1 to $5\ \Omega\text{cm}$ have been used for solar cell fabrication so far. The boron concentration is normally adjusted by adding the equivalent amount of B_2O_3 to the silicon raw material prior to melting of the silicon. Considering alternative doping elements like gallium (*p*-type) or phosphorous (*n*-type) first, the segregation coefficient governing the resistivity decrease with increasing block height has to be considered. With a segregation coefficient of 0.8, boron nearly always is the optimal doping element giving only a small resistivity change over the silicon ingot (see Figure 6.8), whereas gallium and phosphorous with segregation coefficients of 0.008 and 0.35, respectively, are less favourable.

For phosphorous as an *n*-type dopant, additionally the disadvantage of a lower minority charge carrier (i.e. holes) mobility and a more complicated solar cell process using, for example, higher process temperatures for boron instead of phosphorous diffusion is encountered. However, recent results indicate that the activity of extended defects in *n*-type multicrystalline silicon is unexpectedly low, which could render *n*-type material nevertheless an attractive new feedstock source for photovoltaics.

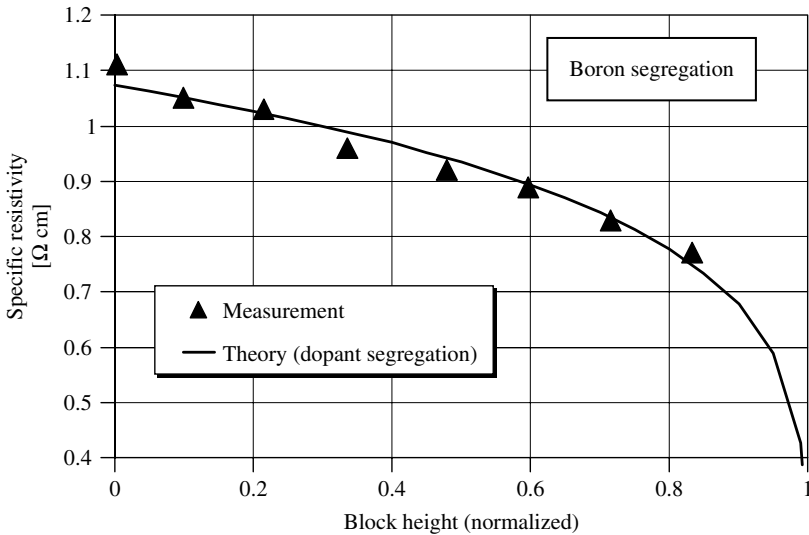


Figure 6.8 Decrease in the specific resistivity of *p*-type multicrystalline silicon due to segregation of the doping element boron

6.3.3 Crystal Defects

The main crystal defects in multicrystalline silicon are grain boundaries and dislocations. Concerning the attainable efficiencies of solar cells, not only the concentration of these defects but also their electrical activity is considered as crucial.

With respect to the grain boundaries and the grain size, basically smaller grains are observed at the beginning of the crystallisation process in the ingot bottom part. With increasing block height, individual grains prevail at the expense of surrounding grains and thus give rise to an increase in the mean grain size. This increase of grain size, however, depends on the crystallisation speed (see Figure 6.9). A higher crystallisation speed also means higher temperature gradients and thus an increased probability for the formation of crystal seeds in the melt that in turn lead to a limitation of the grain size. This is also the reason for faster crystallised block-cast material usually exhibiting smaller grains than conventional Bridgman-type multicrystalline silicon.

On the other hand, the grain sizes achieved with modern block-cast material are still large enough to not degrade solar cell efficiencies provided that the electrical activity of the grain boundaries is low enough. Grain boundaries and dislocations, if electrically charged, effectively attract minority charge carriers and consequently represent highly active recombination centres for photo-generated charge carriers. The electrical activity of grain boundaries and dislocations is determined by their impurity decoration (specifically by transition metals) and strongly increases with higher impurity concentrations.

Moreover, it was discovered that the shape of the crystallisation front during solidification also has considerable influence on the grain boundary activity [19]. Preserving a strictly planar solidification front clearly leads to a reduced grain boundary activity.

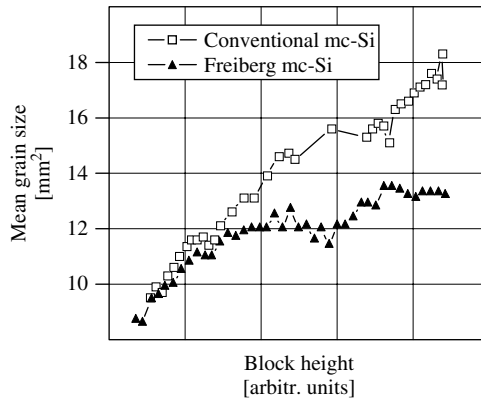


Figure 6.9 Mean grain size as a function of the block height for conventional Bridgman-type multicrystalline silicon (mc-Si) and the faster crystallised block-cast material from the Freiberg production facility of Deutsche Solar GmbH. Reduced crystallisation times lead to slightly lower grain sizes of the Freiberg mc-Si

Because also in modern high-throughput production processes a nearly perfectly planar solidification front is kept throughout the crystallisation process, grain boundaries show only weak electrical activities and therefore are generally considered as less important for solar cell efficiencies.

Crystal dislocations, however, turned out to be the most efficiency-relevant defects in multicrystalline silicon for solar cells. The dislocation density that is experimentally accessible by counting micrometer-small etch pits after appropriate chemical etching steps nearly shows a perfect correlation to the wafer lifetime and diffusion length (Figure 6.10) that are closely linked to solar cell performance. Dislocations are induced and multiplied

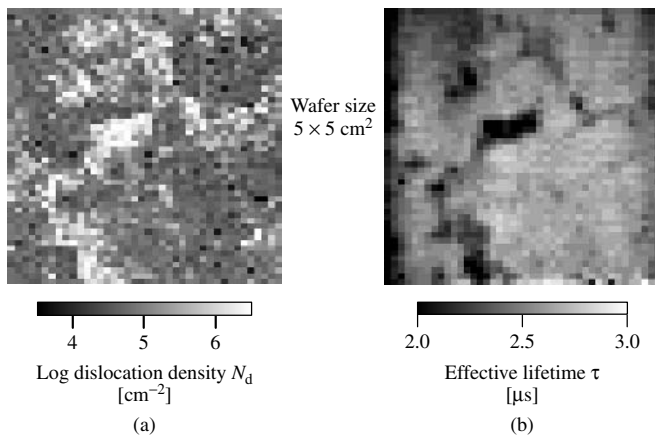


Figure 6.10 Topographies of the dislocation density N_d (a) and the effective lifetime τ_{eff} (b) of a typical multicrystalline silicon wafer showing the excellent correlation of both parameters. The effective lifetime measurements were conducted out without any surface passivation and thus are limited to less than approximately $3 \mu\text{s}$ by surface recombination processes

by thermal stress that is originated from temperature non-homogeneities during crystallisation and cooling of the ingot. The reduction of these temperature variations while keeping high process speed is therefore considered one of the most important issues for the further improvement of multicrystalline silicon.

An optimal process scenario for the production of multicrystalline silicon from both the crystal defect and the productivity point of view starts with a small crystallisation speed and minimal temperature gradients in order to secure a low-defect density bottom region of the ingot. After that, crystallisation speed should be largely increased for productivity reasons while keeping the solidification front planar and thermal gradients within the solidified silicon low.

6.3.4 Impurities

Despite boron being the standard dopant and thus an intentionally introduced impurity, even higher impurity concentrations in multicrystalline silicon are observed for both oxygen and carbon.

The interstitial oxygen concentration in multicrystalline silicon is affected by two processes, which are oxygen incorporation via the quartz crucible during melting and oxygen loss through evaporation of SiO, that is, the evaporating gaseous silicon monoxide that is stable at high temperatures only.

Because the segregation coefficient > 1 , the oxygen content decreases with increasing block height. Typical concentrations of the interstitial oxygen content of Bridgman and block-cast material are given in Table 6.2. Obviously, although the silicon melt never stays in direct contact with the quartz crucible, lower oxygen concentrations with Bridgman-type material compared to silicon from the block-casting process are not feasible. We therefore conclude that there also has to exist an oxygen release from the Si₃N₄ coating (containing some percentage of oxygen) into the silicon melt during the Bridgman process. In addition, we observe a much more rapid decrease of the oxygen concentration with increasing block height for block-cast material, which is attributed to the normally employed lower ambient pressure and enhanced gas exchange during this process.

Table 6.2 Typical concentrations of interstitial oxygen [O_i] for block-cast material from the Freiberg production plant of Deutsche Solar GmbH and for typical material coming from a Bridgman process. For the determination of the oxygen concentration by Fourier Transform Infrared Spectroscopy (FTIR), a conversion factor of $2.45 \times 10^{17}/\text{cm}^2$ was used

Ingot position	Interstitial oxygen concentration [O _i] [$10^{17}/\text{cm}^3$]	
	Block-casting process	Bridgman process
Bottom	6.5	6
Middle	0.9	3.5
Top	0.5	2

Although oxygen residing on interstitial lattice sites is not electrically active, recombination-active oxygen complexes such as thermal donors [20–22], new donors [23, 24] and oxygen precipitates may be formed after annealing steps, specifically in the high oxygen concentration bottom part of the ingot (see an example of the donor activity in Figure 6.11).

Specifically, thermal donors turned out to be mainly responsible for a broad low-lifetime region with a width of 4 to 5 cm in the bottom part of Bridgman-type ingots [25]. Owing to the instability of the thermal donors in high-temperature steps during solar cell processing, these low lifetimes, however, does not lead to low efficiencies. It is worth noting that the width of this low-lifetime region in the bottom part of the ingots is largely reduced for material from the block-casting process. The most likely explanation for this is the shorter process times that consequently give less time for the formation of oxygen complexes out of interstitial oxygen atoms.

Similar to metals, oxygen segregation at grain boundaries and dislocations enhances the recombination strength of these extended defects. Oxygen precipitates may also getter metal impurities during crystallisation, which are released afterwards during solar cell processing as highly recombination-active point defects.

Generally, the manifold involvement of oxygen in efficiency-relevant microscopic processes makes the reduction of the oxygen incorporation into multicrystalline silicon one of the most important targets of material improvement efforts.

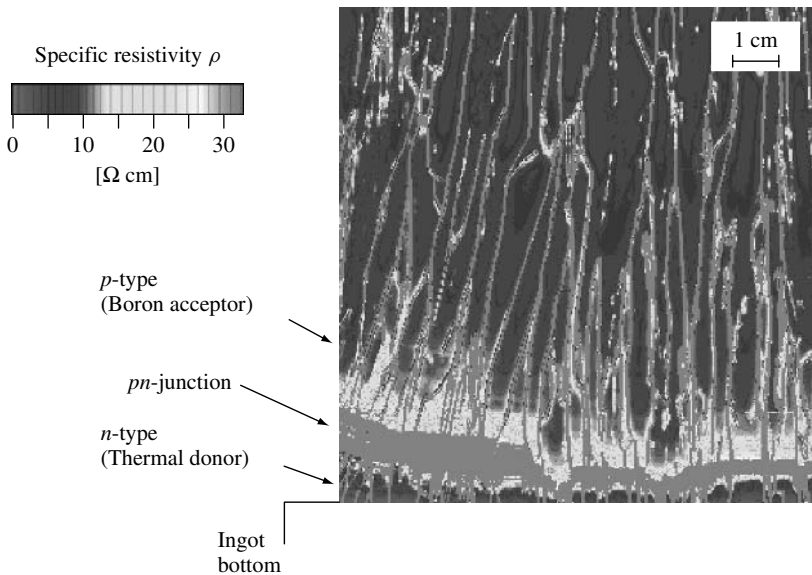


Figure 6.11 High resolution map of the specific resistivity (van-der-Pouw measurement technique) of a vertically cut wafer from a special high resistivity *p*-type multicrystalline silicon test ingot. Owing to the increased oxygen content, the formation of thermal oxygen donors changes the conductivity to *n*-type in the bottom part. The *pn*-junction can be identified by a remarkable increase in the specific resistivity

Like oxygen, carbon in multicrystalline silicon appears in concentrations considerably higher than those of the boron dopant concentrations. Typical concentrations of substitutional carbon are in the range of $2\text{--}6 \times 10^{17}/\text{cm}^3$ generally increasing with increasing block height. The incorporation of carbon into the silicon melt takes place via gaseous CO formation inside the crystallisation chamber by SiO chemically reacting with the graphite heaters. The main problem that is caused by an increased carbon concentration is the formation of needle-shaped SiC crystals (often associated with oxygen and nitrogen, see Figure 6.12) within the silicon material. SiC representing an electrically conductive semiconductor material effectively shorts the solar cell *pn*-junction, thereby leading to drastically reduced efficiencies. The problem of SiC formation, however, usually occurs only in the uppermost region of the ingot that is anyway rejected because of segregation of metallic impurities.

Despite oxygen and carbon being present in much higher concentrations, transition metals like iron or titanium are considered as much more important with regard to solar cell efficiencies with the exception of the outer edges (width 5–10 mm) of an ingot where in-diffusion from the Si₃N₄ coating may occur and the top segregation region metal point defects in high-quality multicrystalline silicon are present in concentration levels below the detection limit of Deep Level Transient Spectroscopy (DLTS) measurements,

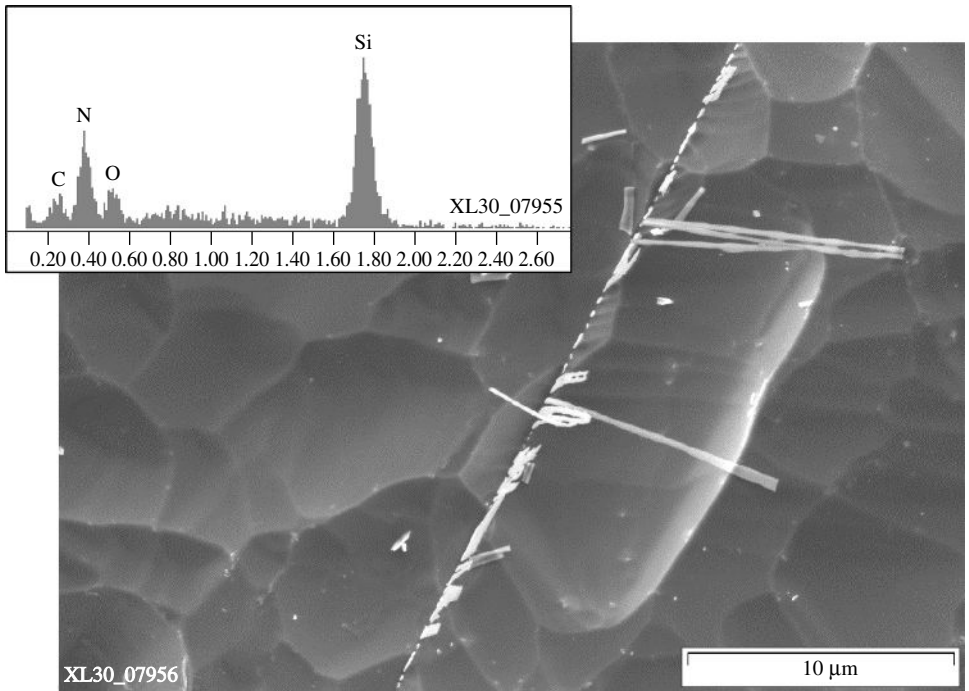


Figure 6.12 SEM (Scanning Electron Microscope) image of a heavily shunted solar cell region. The microscopic investigations reveal needle-shaped structures containing silicon, nitrogen, oxygen and carbon. The shunting mechanism is assumed to be due to electrically conductive SiC that short-circuits the solar cell *pn*-junction

that is, below approximately $10^{12}/\text{cm}^3$. The importance of metal impurities for multicrystalline silicon solar cells is, however, based on metal impurities controlling the activity of extended defects, specifically that of crystal dislocations.

We anticipate that metallic impurities are, for example, responsible for the observed systematic changes of the lifetime of multicrystalline silicon wafers after high-temperature steps in the range of 800 to 1000°C (e.g. the phosphorous diffusion step for fabrication of the solar cell *pn*-junction). The wafer lifetime quite commonly decreases in annealing steps above 900°C, where this decrease is even more significant at enhanced cooling speeds after the anneal. The proposed mechanism behind this lifetime degradation is a release of metal atoms from extended defects like dislocations into the wafer bulk material and a subsequent quenching of the metal atoms as highly recombinative point defects.

Another hint of an extensive interaction between extended defects and metal impurities is given in Figure 6.13 that depicts the theoretical segregation profile of iron in an intentionally contaminated multicrystalline ingot (mean iron concentration: $7.9 \times 10^{17}/\text{cm}^3$) as compared to the experimental one. We clearly can state a reduced experimentally determined segregation effectiveness most probably caused by iron segregation into extended defects competing with the segregation process in the liquid silicon phase during crystallisation.

In order to prevent such defect–metal interaction processes leading to enhanced recombination activity, a very effective segregation of metallic impurities into the ingot top region has to be assured. This segregation effectiveness, however, decreases with both increasing crystallisation speed and increasing concentration of extended defects.

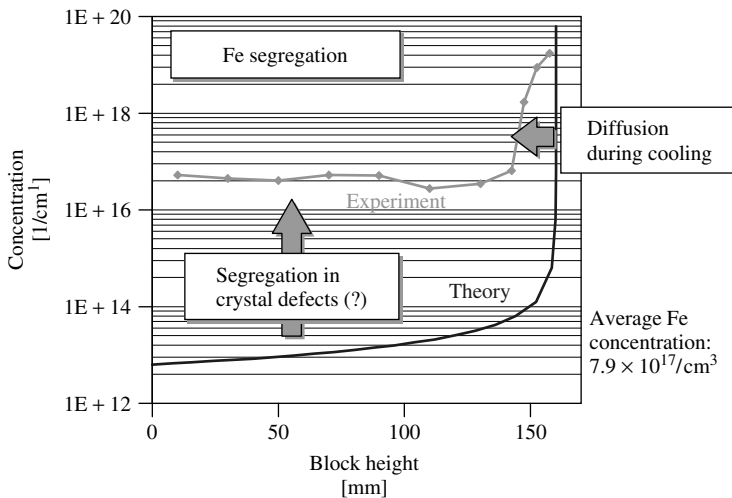


Figure 6.13 Experimentally determined iron concentration of an intentionally contaminated multicrystalline silicon test ingot (mean Fe concentration: $7.9 \times 10^{17}/\text{cm}^3$). The experimental data is given as a function of the block height and in comparison to the theoretically expected profile. The much higher than theoretically predicted concentration in the bottom and middle part of the ingot is attributed to a segregation not only into the silicon melt but also into extended crystal defects during solidification

This in turn verifies the importance of a properly adjusted and controlled crystallisation speed. In order to assure an effective impurity segregation for high-quality multicrystalline silicon, specifically in regions with increased defect densities (e.g. ingot bottom part), solidification at a low crystallisation speed is essential.

6.4 WAFERING

More than 80% of the current solar cell production requires the cutting of large silicon crystals. Multicrystalline ingots grown by the Bridgman or gradient freeze technique now reach cross sections of more than $50 \times 50 \text{ cm}^2$ and weigh over 250 kg; monocrystalline Cz crystals have diameters of up to 20 cm today. While in the last few years the cost of solar cell processing and module fabrication could be reduced considerably, the sawing costs remain high.

Figure 6.14 shows that the sawing costs are a substantial part (29%) of the wafer production cost and thus contribute considerably to the total module cost. Since the sawing of the crystals is connected with high material losses (about 50%), ribbon growth techniques or the thin film technology, which avoid the sawing step, have a high potential for developing cheaper solar cells. However, both technologies still have to overcome serious difficulties and their development will probably take another 5 to 10 years. The present task is therefore to optimise the sawing technique for further cost reduction in mass production.

At the beginning of the PV industry, the available sawing technology of the micro-electronic industry was used. The ingots were mainly cut by inner diameter (ID) saws. This technology is, however, relatively slow and not economical for mass production [26]. It was therefore gradually replaced by the multi-wire slicing technology [27]. The advantages are the higher throughput of about 500 to 700 wafers per day and per machine, a smaller kerf loss of about $180 \mu\text{m}$ and almost no restrictions on the size of the ingots. Currently, wafers between 250 and $350 \mu\text{m}$ are usually cut, but a wafer thickness down to about $100 \mu\text{m}$ can be achieved by the technique. Since the technology is relatively new and still under development, most wafer manufacturers have to optimise the sawing process by their own experience. The sawing process depends on several variable parameters as will be described next, which makes it difficult to optimise the process in view of throughput, material losses, reduction of supply materials and wafer quality.

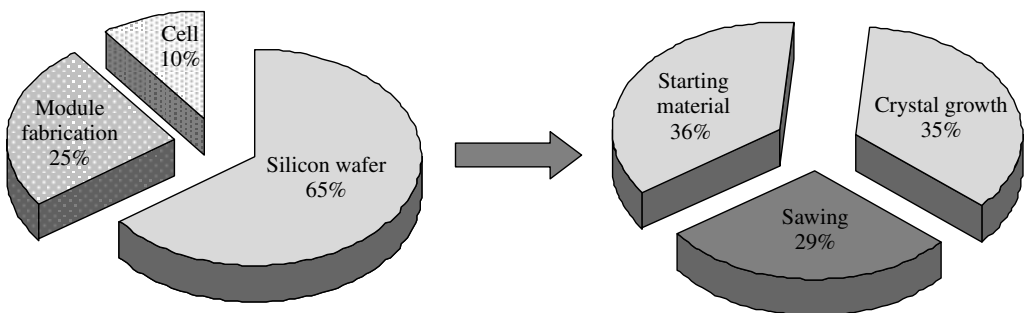


Figure 6.14 Cost distribution for modules and silicon wafers

Basic knowledge about the microscopic details of the sawing process is required in order to slice crystals in a controlled way. In the following section, the principles of the sawing process will be described as far as they are understood today.

6.4.1 Multi-wire Wafering Technique

After crystal growth the silicon ingots are cut in a first step by band saws into columns with a cross section that is determined by the final wafer size. Standard sizes are about $10 \times 10 \text{ cm}^2$, but larger wafers sizes up to $15 \times 15 \text{ cm}^2$ are increasingly used in the solar cell technology. The columns are glued to a substrate holder and placed in a multi-wire saw that slices them into the final wafers. The principle of the multi-wire technology is depicted in Figure 6.15. A single wire is fed from a supply spool through a pulley and tension control unit to the four wire guides that are grooved with a constant pitch. Multiple strands of a wire net (known as a web) are formed by winding the wire on the wire guides through the 500 to 700 parallel grooves. A take-up spool collects the used wire. The wire is pulled by the torque exerted by the main drive and slave as shown in the figure. The tension on the wire is maintained by the feedback control unit at a prescribed value. The silicon column on the holder is pushed against the moving wire web and sliced into hundreds of wafers at the same time. The wire either moves in one direction or oscillates back and forth. Solar cell wafers are mainly cut by a wire that is moving in one direction, whereas wafers for the microelectronic industry are cut by oscillating wires. Cutting in one direction allows higher wire speeds between 5 and 20 m/s, but yields less planar surfaces. Smoother and more even surfaces are obtained by oscillating sawing. Depending on the pulling speed, the wires have a length between 150 and 500 km in order to cut a single column in one run. The wire material is usually stainless steel.

Cutting is achieved by an abrasive slurry, which is supplied through nozzles over the wire web and carried by the wire into the sawing channel. The slurry consists of a

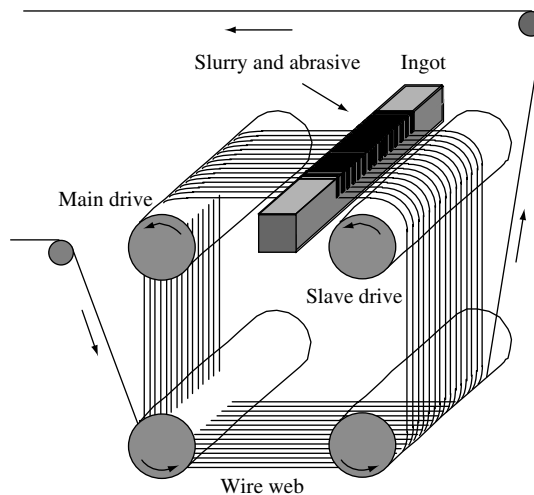


Figure 6.15 Schematic diagram depicting the principle of the multi-wire sawing technique

suspension of hard grinding particles. Today, SiC and diamond are the most commonly used abrasives. Both materials are very expensive and account for 25 to 35% of the total slicing cost. The volume fraction of solid SiC particles can vary between 20 and 60% and the mean grain size between 5 and 30 μm . For polishing smaller grain sizes below 1 μm are used. The main purpose of the slurry is to transport the abrasive particles to the sawing channels and to the crystal surface. It also has to keep the particles apart and must prevent their agglomeration. The entry of the slurry is a result of the interaction between the wire and the highly viscous slurry. Normally, only a small amount of slurry enters the cutting zone. The factors that are important here are the viscosity and the wire speed, but to understand the fluid mechanical problems that are involved a complex physical modelling is required. First attempts of a description have been reported recently [28–31].

Most of the commercial slurries are based on oil, but water-based or water-washable slurries based on ethylene glycol have been tested as well. Oil slurries have several drawbacks. The wafers can stick together and are difficult to separate after sawing. This problem will become even more severe when the wafer thickness will be reduced in the future. The removal of oil from the wafer surfaces requires comprehensive cleaning procedures. Since large quantities of slurry and SiC are used during sawing and recycling is not possible at present, the disposal of these materials has to be considered as well. The disposal causes, however, environmental hazards and is therefore complicated and expensive. On the contrary, water-based slurries or slurries that are very hygroscopic have the problem that hydrogen gas is generated from the interaction of water and silicon, which can cause the hazard of explosion. From the environmental point of view, water-washable slurries may be the choice of the future.

Material is continuously removed through the interaction of the SiC particles below the moving wire and the silicon surface. The abrasive action of the SiC depends on many factors such as wire speed, force between wire and crystal, the solid fraction of SiC in the suspension, the viscosity of the suspension, the size distribution and the shape of the SiC particles. The viscosity of the slurry depends on the temperature and the solid fraction of particles. Since the temperature rises as a result of the cutting process, the suspension has to be cooled and the temperature controlled during sawing. The viscosity of the slurry also changes because of the continuous abrasion of silicon and iron from the wire. This gradually deteriorates the abrasive action and the slurry has to be replaced or mixed with new slurry after some time.

The kerf loss and surface quality are determined by the diameter of the wire, the size distribution of the SiC particles and the transverse vibrations of the wire. The amplitude of vibration is mainly sensitive to the tension of the wire, but it also depends on the damping effect of the slurry. Increasing the tension will reduce the amplitude of vibration, hence the kerf loss [32]. Typical wire diameters are around 180 μm and the mean size of active particles can vary between 5 and 30 μm . This yields kerf losses around 200 to 250 μm per wafer.

The objective of efficient sawing is to slice with a high throughput, with a minimum loss of slurry and silicon and with a high quality of the resulting wafers. Since many parameters can be changed, the optimisation of sawing becomes a difficult task and today it is mainly done by the wafer manufacturers. They are mostly guided by experience. In

the following section, the main results of investigations are summarised, which describe the current understanding of the microscopic details of the wire sawing and yield some guidelines to optimise the process.

6.4.2 Microscopic Process of Wafering

Figure 6.16 shows schematically a cross section of the wire in the cutting zone. The space between the wire and the crystal surface is filled with slurry and SiC particles. The pressure of the wire on the particles varies along the contact area. The forces are maximal directly below the wire and decrease towards the side faces. Because of the transverse vibrations, the wire also exerts forces sideward, which determines the surface quality of the sliced wafers. The interaction between the abrasive SiC particles and the silicon crystal yields a distinct damage pattern on the surface that can be analysed by microscopic techniques. A typical surface structure as seen under an optical microscope is shown in Figure 6.17. Similar structures are obtained along the entire contact zone, which shows that the abrasive process is the same in all directions.

The surface structure consists of local indentations with a mean diameter of a few micrometers. Such a uniform structure can be explained by the interaction of loose, rolling particles that are randomly indented into the crystal surface until small silicon pieces are chipped away. Since SiC particles are faceted and contain sharp edges and

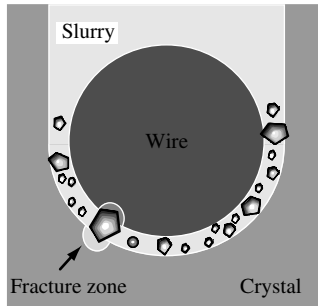


Figure 6.16 Cross section of wire, slurry with abrasive and crystal in the cutting zone

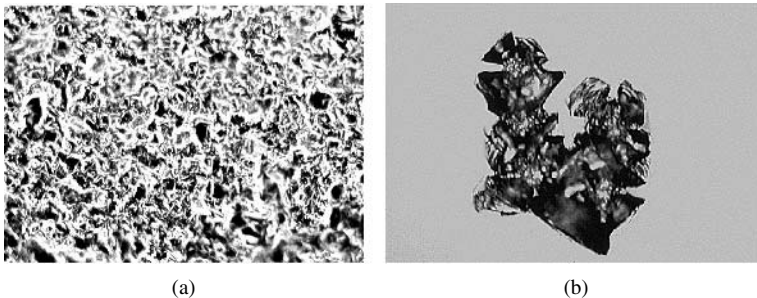


Figure 6.17 Optical micrograph of the surface of an as-cut silicon wafer (a) and several micro-indentations on a polished silicon surface (b)

tips, they can exert very high local pressures on the surface. This “rolling grain” model forms the physical basis of the wire sawing process. Similar surface structures also form after lapping semiconductor surfaces with loose abrasive particles.

The individual process of the interaction of a single particle with sharp edges and the surface of a brittle material can be studied by micro-indentation experiments. This is shown in Figure 6.17(b) for a silicon surface. The damage structure of several overlapping micro-indentations with a Vickers diamond indenter resembles the structure of an as-cut wafer. Numerous micro-indentation experiments on monocrystalline silicon have been carried out in the past to investigate the damage structure quantitatively (e.g. [33–37]). The main results are summarised schematically in Figure 6.18 for a “sharp” Vickers indenter with pyramid geometry. Loading by sharp indenters first leads to the generation of a remnant plastic impression in the surface known as the elastic–plastic zone. Recent Raman investigations of this region have shown that under high pressures the silicon lattice transforms into other crystal structures. Several phase changes have been observed directly under the indenter, in particular a metallic high-pressure phase [38, 39]. Under loading at 11.8 GPa an endothermic transformation to metallic silicon (Si II) occurs ($\Delta G = 38$ kJ/mol), which partly transforms back to another high-pressure phase (Si III at 9 GPa, $\Delta G = -8.3$ kJ/mol). In the metallic state the silicon can plastically deform and

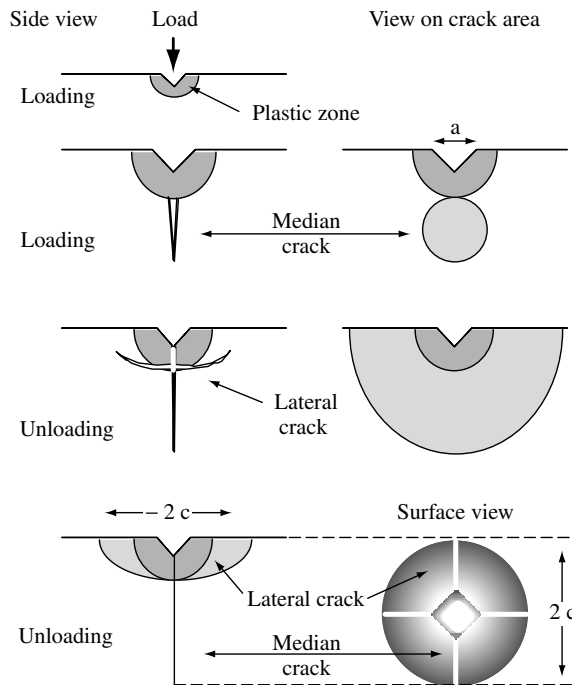


Figure 6.18 Schematic diagram of the development of the crack system below a sharp indenter upon loading and unloading. Dark gray areas indicate the plastic zone below the indenter. The dotted areas are the crack planes of the halfpenny-shaped median crack system. They are viewed from end-on (left side) or perpendicular to the plane (right side). In case radial cracks also occur, they may coalesce with the median crack and form a similar crack pattern

the material can be removed by processes known for ductile metals. This is, however, a slow but moderate process.

With increasing pressure the material begins to break and cracks are generated parallel to the load axis emanating from the plastic zone. Median cracks are generated beneath the plastic zone, where the tensile stresses are maximal, in the form of full or truncated circles. At a critical size they become unstable and extend towards the surface. In addition, shallow radial cracks may be generated at the edges of the plastic zone. Both radial and median cracks may coalesce to form halfpenny-shaped cracks that are visible at the surface (as shown in Figure 6.19). Upon unloading, residual stresses from the elastic–plastic zone can lead to lateral cracks parallel to the surface. When these lateral cracks reach the surface, material is chipped away. This is the main process for material removal during sawing. Chipping requires a certain minimum load to occur (chipping threshold). Above the limit when material is removed only the median and radial cracks remain. They are finally part of the saw damage.

A quantitative model based on the rolling grain interaction described above has been developed. Results have been compared with experimental investigations of the sawing process on commercial multi-wire saws, allowing for the extraction of useful conclusions. Details can be found in Reference [40].

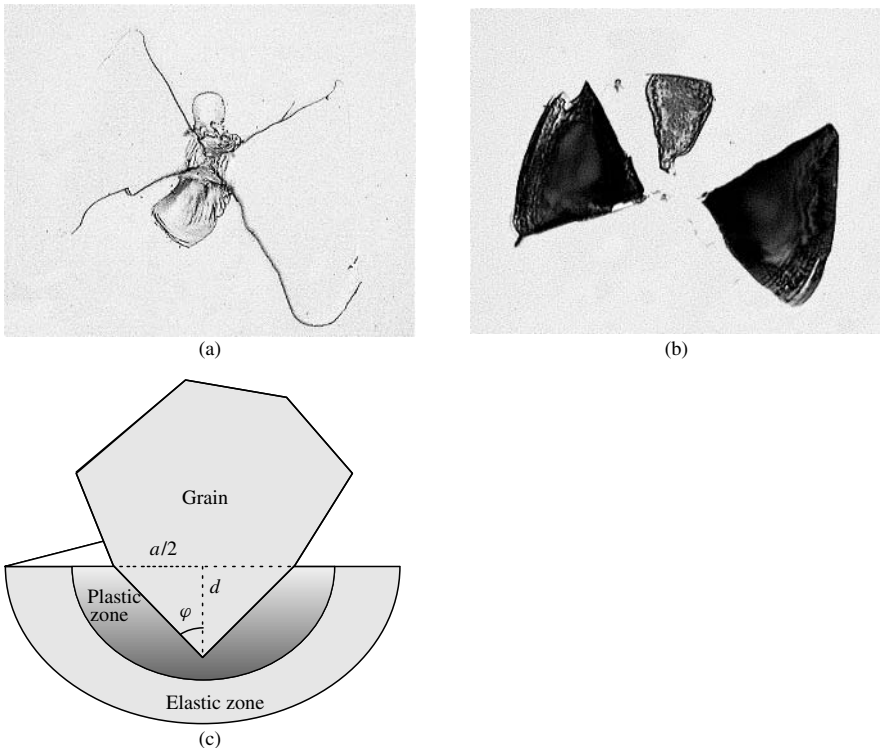


Figure 6.19 (a) Optical micrograph of median and (b) lateral cracks (below the surface) at a Vickers indentation. (c) Schematic representation of the impression of a sharp grain into a surface

6.4.3 Wafer Quality and Saw Damage

Several factors are currently considered to determine the quality of the wafers: fracture behaviour, crack density, thickness variations, surface roughness and cleanness. After sawing the surface of the wafer is damaged from the fracture processes and contaminated with organic and inorganic remnants from the slurry. Therefore, the wafers have to be cleaned and the saw damage removed by etching before a solar cell can be fabricated. In addition, the thickness and surface roughness of the wafer may vary, which may be detrimental for some of the further processing steps. All factors are related to the sawing process. Figure 6.20 shows an example of the topology of an as-cut surface. It consists of thickness variations on different length scales. On the scale of millimetres, one can observe grooves parallel to the direction of the wire. They occur particularly under higher loads and can be caused by a deficit of slurry, mechanical vibrations or inhomogeneities of the material. Mostly a large number of parallel wafers are then affected. Grooves on wafers cannot be removed by etching and thus reduce the quality of a wafer.

On a length scale of about $100\ \mu\text{m}$, the surface may have a wavy topology that is not detrimental unless sharp steps occur. On the micrometer-length scale the surface shows a certain roughness, which is directly related to the microscopic sawing process as described before. The extent of saw damage, which has to be etched away before solar cell processing, lies typically in the range of 5 to $10\ \mu\text{m}$.

Saw damage also occurs in the abrasive grains and the wire itself. Although the fracture strength of the SiC particles is higher than that of silicon, the grains eventually lose their sharpness owing to breakage that reduces their sawing performance. To reduce the abrasion of the grains, sawing should be done in a stress range where the load on the individual grains lies above the fracture strength of silicon but below that of SiC.

Typically, the wires have diameters between 150 and $180\ \mu\text{m}$ and a length of about 150 to $500\ \text{km}$. They are made of stainless steel and coated with a brass layer.

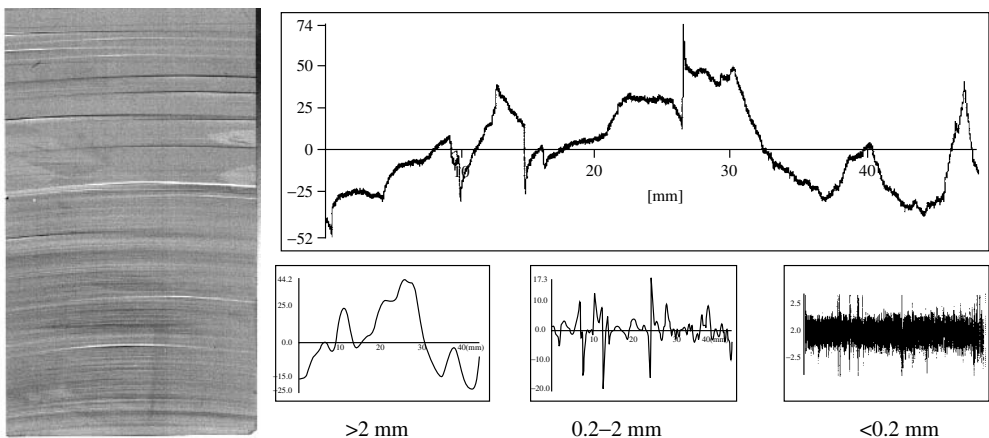


Figure 6.20 Surface structure of a wafer with grooves resulting from uneven cutting. It also shows the bowing of the wire under load during sawing. The surface profile measured by a laser scanner profiler is depicted on the right. Different wavelengths filtered from the profile are shown below

It is important that the thickness is very uniform over the entire length, because sudden changes in the diameter can lead to fracture of the wire or damage to the wafer surface. The abrasion of the steel wires is also due to the interactions with the grains. Excessive wear can lead to breakage, which is undesirable during sawing because it is very time consuming to build up the wire web inside the machine. Some manufacturers are beginning to develop *in situ* detection systems to control the sawing process and thus prevent the wire breakage.

6.4.4 Cost and Size Considerations

The investigations of the microscopic processes of wire sawing have laid the basis for the selection of the best range of parameters and for further modifications. It allows one to increase the sawing performance, to reduce the consumption of slurry, SiC powder, wire material and etchant, and hence directly the costs of slicing. Furthermore, the quality of the wafers such as roughness, flatness and saw damage of the surfaces can be improved. This is important in view of the development of thinner wafers for solar cells, which will reduce the consumption of expensive silicon. The current sawing technique in production allows the sawing of wafers with thickness down to about 200 μm . The goal is to further reduce the thickness to about 100 to 150 μm in production. Sawing of thinner wafers is possible but at present still at the expense of more breakage. The problem becomes even more severe when the wafer size increases at the same time to $15 \times 15 \text{ cm}^2$ or more. In mass production such a development will only become possible by a careful selection of the parameter range and an *in situ* control of all the factors that determine the slicing process.

6.5 SILICON RIBBON AND FOIL PRODUCTION

Research and development on crystal growth technologies for production of crystalline silicon ribbon have been under way for three decades. Interest in methods of crystalline silicon wafer production was initiated during the oil crises of the mid-1970s. Out of this period arose the first large-scale efforts in R&D to develop low-cost methods of producing substrates for solar cell manufacture. A seminal program was conducted in the US, which was led between 1975 and 1985 by the Jet Propulsion Laboratory (JPL) Flat Plate Array Project [41]. It was the activity in this project in this time period, combined with larger investments from the private sector both in the US and internationally, that developed the seeds of the technology of crystalline silicon ribbon and foil production methods being commercialised today.

The past decade of R&D on crystalline silicon materials has culminated in the expansion of wafer manufacturing at an unprecedented pace. While established methods of production based on Cz growth, directional solidification and ingot casting have flourished, a new generation of ribbon technologies has moved past the R&D stage into large-scale manufacturing and is in competition with these conventional approaches. Ribbon technologies, some of which had entered R&D already in the early 1970s, and have now reached maturity with the start up of manufacturing on a megawatt (MW) scale, include Edge-defined Film-fed Growth (EFG), String Ribbon (STR) and Silicon FilmTM (SF).

Dendritic Web (WEB) production and the Ribbon Growth on Substrate (RGS) technique are moving to pilot demonstration phases. A summary of the changes in the status of leading ribbon/foil technologies over the past decade and projections for manufacturing capacities are given in Table 6.3. It is anticipated that the ribbon production will contribute in excess of 30 MW of wafers to world solar energy markets by the end of 2001.

Development has not been continuous for most of the methods listed above. The R&D has been interrupted and then restarted in several cases when the technological status changed to generate new opportunities for cost-effective production. EFG development has the longest continuous history. After initial technology development on EFG started at Tyco Laboratories in 1971, it was subsequently augmented with funding from Mobil Oil, starting in 1974. In the time span from 1971 to the present, pilot lines using five different variations of the EFG process have been evaluated, starting with single ribbons in 1971 to the octagonal crystal tube now being commercialised. Ownership transferred to ASE Americas in 1994, at which time the transition to manufacturing was initiated. After periods of decreased activity, WEB, STR and RGS have all been strengthened with R&D in the past several years subsequent to being revitalised by new owners. WEB development was initiated with funding from Westinghouse in the 1970s, but now is being carried out by EBARA Solar. STR technology underwent an R&D phase in the early 1980s under the name of Edge-Stabilised Ribbon (ESR) and Edge-Supported Pulling (ESP) at the National Renewable Energy Laboratory and at Arthur D. Little, respectively, before being taken up in 1994 by Evergreen Solar. RGS development was initiated at Bayer, but is currently continuing with ECN of the Netherlands. If successful, a future commercialisation is anticipated by Deutsche Solar in Germany and Sunergy in the Netherlands.

Ribbon and foil technologies must meet the challenges of the photovoltaic marketplace and overcome a number of existing technical barriers if they are to continue to expand manufacturing and to position themselves to remain competitive in the next decade. Challenges to be met are productivity increases on a per furnace basis to drive down labour and overhead (capital) costs, improved mechanical and electronic quality of ribbon wafers together with the development of low-cost solar cell designs that will raise efficiencies to 18 to 20% and reduction of wafer thickness while maintaining high yields in order to reduce demand on silicon feedstock. Achievement of these goals in the next decade can lead to cost decreases, which will drive additional volume expansion for

Table 6.3 Historic record on R&D and manufacturing status of leading ribbon/foil technologies of the past decade

Wafer process/ year started		1990 status level	2000	2001	Schematic
WEB/1967	R&D	<0.1 MW	R&D <0.2 MW	Pilot –0–1 MW	Figure 6.20
EFG/1971 (Ribbon); 1988 (Octagon)	Pilot	1.5 MW	Production –12 MW	Production –20 MW	Figure 6.21
ESP (STR)/1980	R&D	–	Pilot <0.5 MW	Production <5 MW	Figure 6.23
SF/1983	–	–	Pilot –1–2 MW	Production >5 MW	–
RGS/1983	R&D	–	R&D	Pilot <1 MW	Figure 6.24

ribbon and foils and allow these new-generation technologies to become market leaders in silicon wafer production. Technology description, the status of each of the growth approaches and the barriers for each of the technologies to overcome in order to remain competitive are the topics of the following sections.

6.5.1 Process Description

The ribbon technologies that have been proposed over the past three decades and that have survived till the commercial manufacturing and R&D phases (Table 6.3) may be grouped into two basic approaches: “vertical” and “horizontal” growth (pulling) methods. The latter category is further subdivided into methods in which either a substrate is used to assist in the formation of the crystal or foil or those that do not use any substrate material. The horizontal methods refer not so much to the geometrical aspects related to the ribbon-pulling direction as to the disposition of the temperature gradients, which act at the interface and influence growth characteristics. The EFG, WEB and STR methods are examples of the vertical method category, while both the RGS foil and the SF methods grow crystals in a horizontal-pulling configuration with the aid of a substrate. The term “foil” is used interchangeably with wafer, but here we use it to refer more specifically to the RGS wafer to distinguish a unique aspect: the wafer is crystallised upon contact with a substrate, and is then detached and the substrate material recycled.

Ribbon/foil growth techniques have historically been evaluated in a number of variants and modifications of the techniques listed in Table 6.3. Successes and failures in many of these variants often spawned new processes or led to evolution and modifications in old variants. A bibliography and descriptions of the techniques and a detailed historical perspective of the many variant ribbon technologies that have been pursued can be found in the endnote [42] and in References [43, 44].

Fundamental differences exist in the heat transfer and the interface temperature gradients during growth for these two general categories of ribbon and foil production methods. These lead to very different process limits in several important areas: the capacity, or throughput potential in a single furnace configuration, crystallite or grain nucleation characteristics and the pulling speed. The speed is constrained as a consequence of the thermoelastic stress acting on the crystal during growth. The pull speed and stress affect the defect density and electronic quality. For example, for the vertical techniques – WEB, EFG and STR – the crystal growth direction and dominant heat transfer of latent heat from the interface are both parallel to the pulling axis of the ribbon and essentially perpendicular to the growth interface. The latent heat conducted along the ribbon is radiated to the environment. The pulling speed and the interface growth velocity are the same. For RGS and SF, crystals nucleate on the substrate and grow nearly perpendicular to the substrate-pulling direction, while the growth interface tends to be angled towards the pulling axis of the substrate. Thermal conduction of latent heat from the growth interface is augmented in the direction perpendicular to the pulling axis, that is, through the thickness of the ribbon, because of conduction into the substrate. This augmented heat removal allows very high ribbon production rates, whereby low interface growth rates, v_I , are realised with high pull rates, v_P , that is,

$$v_P = v_I / \cos(\theta)$$

where θ is the angle between the normal to the interface and the pull direction and is close to 90° . The low interface growth rate, in turn, reduces the need for the high interface temperature gradients required to maintain growth stability in vertical ribbon growth. The gradients in the vertical methods are the cause of high thermoelastic stresses and set practical productivity limits when low defect densities and flat ribbon are required. Details on the process limits affecting the horizontal growth techniques may be found in other publications [45, 46]. We next give a description of each of the techniques listed in Table 6.3.

WEB. WEB is grown directly from melted silicon in a crucible with no shaping device (Figure 6.21) [47]. A dendritic seed or button is lowered into a supercooled melt. The seed spreads laterally to form a button. When the seed is withdrawn, two secondary dendrites propagate from the ends of the button into the melt, forming a frame to support the freezing ribbon. The dendrites grow into the melt that has been supercooled by several degrees. Very accurate melt temperature control is required in order to maintain the supercooled interface condition and prevent “pull-out”, whereby the growth terminates by voiding of the meniscus. The width of the ribbon is controlled by the position of the two dendrites that support the liquid film. The growth velocity is determined by the rate of removal of the latent heat into the ribbon and of the heat conducted through the melt through the meniscus. Typical growth rates are from 1 to 3 cm/min.

In vertical ribbon growth, the meniscus contains the suspended melt volume that connects the bulk melt to the growth interface and crystal. Its shape and the heat conduction taking place within it critically affect impurity segregation and the crystallisation

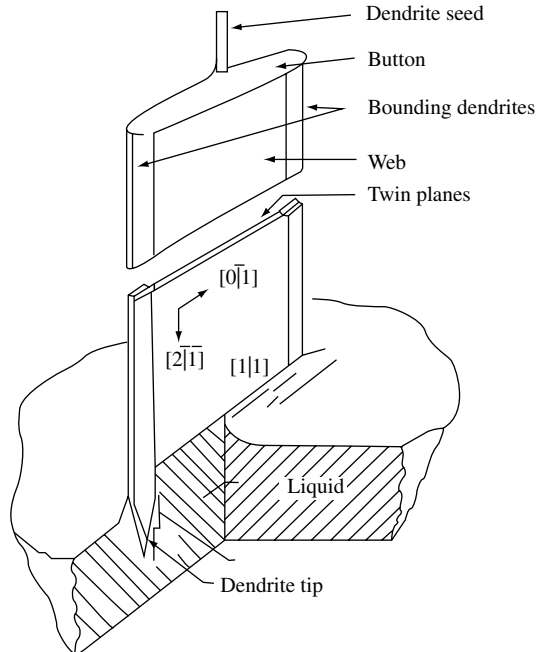


Figure 6.21 Schematic of Dendritic Web (WEB) growth process for ribbon

conditions and shape of the crystal. The meniscus height, h , away from the influence of the dendrites, is fixed by the surface tension, liquid-silicon contact angle and liquid density. This can be calculated from the solution of the Young–Laplace equation requiring a contact angle of $\Theta = 11^\circ$ at the liquid–solid interface that gives

$$h = a[1 - \sin(\Theta)] \quad \text{where} \quad a = (2\sigma/\rho g)^{1/2}$$

where $\sigma = 720$ dyne/cm is the surface tension, $\rho = 2.53$ g/cm³ is the density of liquid silicon and g is the gravitational acceleration. Because thermal radiation dominates the heat flow from the ribbon, the geometry of the heat shields and the susceptor lid controls the isotherms in the melt and the ribbon.

Accurate temperature control, within a few tenths of one degree, is necessary to ensure a uniform ribbon width and thickness. The temperature of the melt surface must be constant over the width of the growing web to prevent the dendrites from growing in or out. The dominant impurity in the WEB in production today is oxygen since a quartz crucible is used. Typical WEB thicknesses range from 100 to 150 μm and widths up to 8 cm have been grown. Growth lengths between seedings in pilot production extend to many tens of meters.

EFG. In this technique, the geometry of the ribbon is controlled by a slotted graphite die through which silicon is fed via capillary action (Figure 6.22) [48]. A seed crystal is

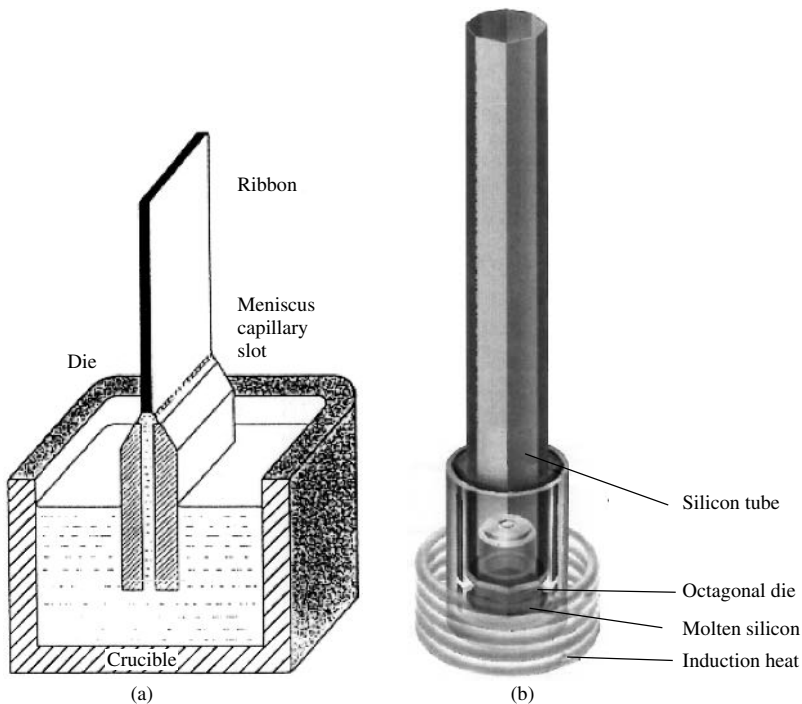


Figure 6.22 Schematics of Edge-defined Film-fed Growth (EFG) growth process: (a) ribbon die and crucible configuration and (b) octagonal configuration

lowered until it contacts the liquid in the capillary. The liquid spreads out over the top of the die to the edges where it is pinned by surface tension. The seed is withdrawn, pulling the liquid up while more liquid flows upward through the capillary. As the ribbon is withdrawn, the liquid freezes on the solid crystal. The die and the crucible are integral, that is, made of the same piece of graphite. The thickness of the sheet material is fixed by the width of the die top, distance between the die tip and melt level, meniscus shape, heat loss from the sheet and the pull rate. The shape of the liquid–gas interface, or meniscus, which connects the die to the solidifying ribbon, is described by the Young–Laplace or the capillary equation. As with WEB, the growth rate is controlled by how fast heat can be conducted away from the interface and lost by radiation or convection from the solid crystal. Growth is self-stabilising because the meniscus height increases with an increase in pull rate. The curvature of the meniscus causes the thickness of the crystal to decrease. This increases the rate of heat removal per unit area of the interface, thus increasing the growth rate until it is again equal to the pull rate.

The dominant impurity in EFG ribbon is carbon, which is in supersaturation. Temperature control of a few degrees along the interface is sufficient to prevent ribbon pull-out or freezing of a growing ribbon to the die top. Over time, the die becomes eroded affecting ribbon properties and leading to a non-uniform ribbon thickness and growth difficulties.

Ribbons with thicknesses from 400 μm to as little as 100 μm have been grown. Rather than a single flat ribbon, hollow EFG polygons are grown to enhance the rate of throughput. The favoured geometries for commercial development today are octagons with 10-cm- or 12.5-cm-wide faces, equivalent to growth of up to a 100-cm-wide ribbon from a single furnace. Various closed geometries, including nonagons with 5-cm faces, and large-diameter cylinders have been grown. Growth velocities for the EFG octagon are 1.7 cm/min. The relationships between the EFG process parameters and the silicon ribbon characteristics, including thermal stress and the influence of impurities and defects on the quality of the material, have been extensively examined and are reviewed in Reference [49].

An extension of the EFG process to growth of 50-cm-diameter cylinders has recently been demonstrated [50]. An example of such a cylinder 1.2 m in length is shown in Figure 6.23. The cylindrical geometry offers some relief from the large thermoelastic stresses generated in plane ribbon. This allows consideration of higher productivity furnaces from a combination of larger perimeters and potentially higher growth speeds. Growth of EFG cylinders with average wall thickness down to 100 μ has been demonstrated, and solar cells have been made on this material [51].

STR. In this technique, ribbon growth takes place directly from a pool of melted silicon without a die (Figure 6.24) in a process mirroring the WEB geometrically. Rather than dendrites, as with WEB, the position of the ribbon edges in STR is maintained by two strings fed through holes in the bottom of the crucible. The strings are drawn upward out of the melt to support the meniscus and the ribbon, and their pull rate determines the growth speed of the ribbon. The thickness of the ribbon is controlled by surface tension, heat loss from the sheet and pull rate. An important difference of the STR process from WEB growth is that the constraints of maintaining propagating dendrites and a supercooled melt are eliminated, and this relaxes the high degree of temperature control required in the WEB furnace. The high meniscus, 7 mm (see Equation 2), allows simple control of



Figure 6.23 Experimental 50-cm-diameter EFG cylinder exiting from furnace

the growth process and maximises its stability to mechanical and thermal fluctuations. Depending upon the wetting qualities of the strings and their diameter, the meniscus height at the strings near the edges differs from that at the centre, and it is usually much lower at the edges [52, 53].

For comparable thicknesses, the growth velocities of STR are similar to EFG and WEB. Careful adjustment of the growth parameters can allow very thin ribbon, down to $5\ \mu\text{m}$, to be grown [54]. Generally passive after heaters are used, but some work on an active after heater has been carried out to allow low-stress, $100\text{-}\mu\text{m}$ -thick ribbon to be grown. This material was sufficiently flat to be made into solar cells. Because of the concave downward meniscus curvature at the string, any grains nucleated at the strings can propagate into the ribbon.

RGS. In this growth technique, the silicon melt reservoir and die are placed in close proximity to the top surface of a substrate, on which the ribbon/foil grows. The substrate may be graphite or ceramic (Figure 6.25) [55]. The principle is to have a large wedge-shaped crystallisation front. The die contains the melt and acts to fix the width

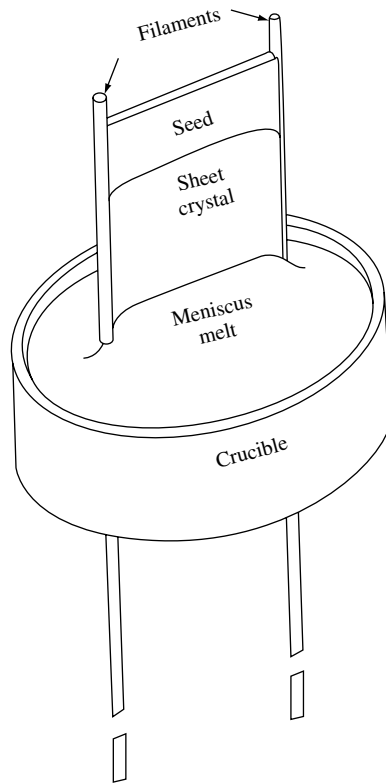


Figure 6.24 Schematic of String Ribbon (STR) growth system

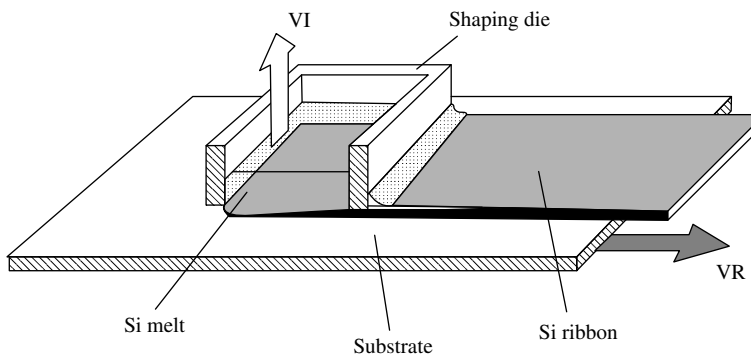


Figure 6.25 Schematic of Ribbon Growth on a Substrate (RGS) configuration

of the foil. The thickness of the foil is controlled by the heat-removal capacity of the substrate, pull rate and surface tension. The direction of crystallisation and growth are nearly perpendicular. The area of the growth interface now can be very large compared to the foil thickness. The latent heat is extracted by conduction into the substrate. The thermal gradients near the interface are small, thus reducing thermally induced stress in

the wafer. Growth rates from 4 to 9 m/min have been demonstrated. One example was an 8.6-cm-wide foil, 300- μm thick, grown at 6.5 m/min.

An important goal in the R&D phase of RGS has been to make a substrate that can be reused. After cooling, the silicon foil may be separated from the substrate by stresses arising from differences in thermal expansion between substrate and silicon. Experimentation with coated foils is in progress and offers the most promise in providing a cost-effective reusable substrate. Thicknesses between 100 and 500 μm have been grown. By working with the lower thermal gradients in the foil thickness direction, but still large enough for rapid growth, fluctuations in the pulling speed and gradient only affect the foil thickness slightly [55].

SF. The details of the SF process are proprietary. The silicon crystal is grown in a thin layer directly upon either an insulating or a conducting substrate, with a barrier layer that promotes nucleation [56]. In the case of an insulating substrate, the barrier layer must also act as a conductor to collect the current generated in the cell. In the case of a conducting substrate, the substrate can also act as an electrical conductor if *vias*, or holes, are provided to connect the thin silicon crystal layer and the substrate. The SF thin film and barrier layer do not separate from the substrate on cooling as in RGS, but become the active part of the solar cell. The grown polycrystalline silicon layer is made very thin ($\ll 100 \mu\text{m}$), thus reducing the amount of silicon required. Currently, layers of 20- μm thickness are under development. A variety of substrate materials have been used including steel, ceramics and graphite cloth [56, 57]. It is necessary that the barrier layer prevent the transport of impurities from the substrate into the silicon. The barrier layer allows wetting and nucleation during growth. It should also act to electrically passivate the back surface and have a high optical reflectivity.

An insulating barrier layer has been reported that promotes growth of large columnar grains (greater than 1 mm) through the thickness of the grown SF silicon film [56]. As-grown films on coated ceramic substrates exhibit very low diffusion lengths of less than 10 μm . The new barrier layer and the substrate result in longer diffusion lengths, 20 to 40 μm , and the silicon has an improved response to phosphorous gettering.

6.5.2 Productivity Comparisons

Ribbon crystal growth technology for production of silicon wafers has been historically faced with the evaluation of the trade-off between bulk electronic quality and throughput (productivity per furnace). The choice of crystal growth conditions is made on the basis of wafer cost parameters and the premium imposed by the marketplace on solar cell efficiency. Material quality that can translate into high solar cell efficiencies has always been a primary market driver guiding ribbon growth process development. Ribbon wafers have inherently lower wafer production costs than those obtained from directionally solidified and cast ingots, or Cz boules, because ribbon growth avoids the large material losses due to sawing, which exceed 50% of the starting feedstock. The ribbon geometry has an additional cost advantage in that high levels of radiative cooling allow very rapid pulling rates. On the other hand, the higher wafer cost for the cast ingot or Cz boule production methods demand that these products maintain an advantage in bulk electronic quality, and higher solar cell and module efficiencies, in order to stay competitive with respect

Table 6.4 Single-furnace performance metrics for ribbon technologies under development and in commercialisation

Method/ parameter	Pull speed [cm/min]	Width [cm]	Throughput [cm ² /min]	Furnaces per 100 MW ^a
WEB	1–2	5–8	5–16	2000
EFG Octagon	1.65	8 × 12.5	165	100
STR	1–2	5–8	5–16	1175
SF	^b	15–30	^b	^b
RGS	600–1000	12.5	7500–12 500	2–3

^aFurnace data are taken from Reference [58], where throughput is normalised for comparison purposes to an overall yield of 90% and cell efficiency of 15% for all processes

^bPulling rate parameters for the SF process are not available

to ribbon technology. Superior electronic quality is generally achieved at the expense of throughput in bulk crystal growth from the melt.

A summary of performance metrics for ribbon technologies currently under development is given in Table 6.4. A critical driving parameter in technology development of ribbon methods for large-scale manufacture and commercialisation is the productivity per furnace. Productivity governs the capital cost of installed capacity and direct labour costs, which constitute significant barriers to ongoing commercialisation on a large scale for all ribbon technologies.

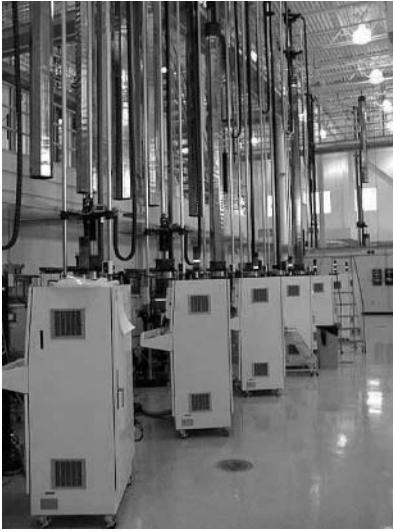
6.5.3 Manufacturing Technology

Table 6.4 shows that development of ribbon technologies is proceeding along two distinct paths. WEB and STR rely on low furnace cost to remain competitive in wafer costs. Development of SF and RGS technologies is focused on achieving superior throughput per furnace.

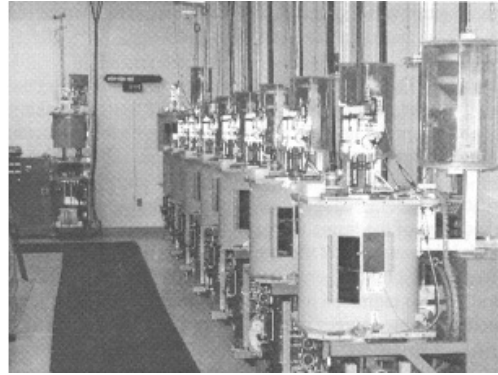
Scaling of ribbon factories significantly beyond the manufacturing levels practised now, for example, 100 MW, poses different challenges for technology development in these two cases. The low throughput ribbon furnace (WEB, STR) requires a simple and low-cost furnace design, a high level of automation and low infrastructure costs. In contrast, high reliability and uptime of furnaces and the growth process are most critical for the high throughput technologies SF and RGS. EFG technology development is moving in a direction that is trending towards the middle of these two extremes.

Examples of commercial installations and equipment now in manufacturing for EFG and STR technologies are shown in Figure 6.26. Figure 6.26(a) pictures a group of furnaces in the EFG octagon manufacturing line, with a high bay area to accommodate the 5.4-m octagon growth lengths. EFG wafers of 10-cm width and of 10- or 15-cm lengths are standard products and are cut from the octagon tubes using high-speed lasers (not shown). More detail on this technology is given in Reference [59].

Single ribbon furnaces for the growth of 8-cm-wide ribbon of the STR manufacturing line are shown in Figure 6.26(b). Ribbon sections up to a meter long are scribed



(a)



(b)

Figure 6.26 Manufacturing crystal growth equipment in commercialisation for (a) EFG and (b) STR technology

from the ribbon while it is growing, and then further cut into wafers of 10-cm length prior to processing.

WEB, SF and RGS ribbon technologies all are in various stages of R&D and pilot demonstrations leading to commercialisation. SF is perhaps the closest to successfully scaling up the technology, as a wider (20 cm) and higher throughput furnace is reaching the final demonstration phase. WEB is basing its expansion to a 1- to 2-MW pilot operation on a single ribbon furnace for producing 5-cm-wide wafers. RGS is moving towards the use of 12.5-cm-wide ribbon in which high sustained throughput technology and consistent high material quality needs to be demonstrated.

6.5.4 Ribbon Material Properties and Solar Cells

Except for WEB, all the growth processes produce multicrystalline ribbon. WEB ribbon grows with (111) crystallographic faces (see Figure 6.21). It typically does not have any grain boundaries, but has a single multiple-twin boundary located about mid-way through the ribbon thickness. Each (111) surface is made up of a single grain, and the dislocation density is the lowest of any ribbon, 10^3 to $10^4/\text{cm}^2$.

For the other two vertical ribbon growth cases, EFG and STR, extraneous crystals are generated most often at the sides of the ribbon (i.e. octagon tube corners) and propagate along the growth axis of the ribbon. These crystals form elongated grains often many centimetres in length along the growth axis, and which extend through the ribbon thickness. In EFG, the grains are interspersed with numerous twin boundary arrays. The grains at the ribbon edge in STR are generally smaller than in the centre. Because the meniscus near each string is concave downward, the grains nucleated at the string can

propagate into the ribbon centre. In both EFG and STR, the grain dimensions typically are large compared to the ribbon thickness and the as-grown diffusion length, and the charge collection and solar cell efficiency are minimally influenced by grain boundary recombination.

For SF and RGS, the substrates provide the dominant nucleation sites for crystals. The grains usually are columnar and extend through the ribbon thickness with dimensions that can be made large compared to the diffusion length with proper adjustments of the pulling speed and interface inclination.

Fast movement of the solid–liquid interphase reduces the ability of the freezing process to segregate impurities to the melt. This is represented in Table 6.5 together with the crystalline aspect and the dislocation density of the different technologies.

Stresses produced by thermal gradients during growth generate most of the intra-granular dislocations in ribbon material. In the best quality EFG material, it has been shown that the loss in background current is highly correlated with the dislocation density and not grain boundaries [60]. It is not clear if the intrinsic qualities of the dislocations act as recombination centres or if the associated impurity cloud is responsible. Dislocations decorated with SiO_x precipitates have been reported to limit the lifetime in WEB [61] and RGS material [62]. Recent photoluminescence studies suggest similar causes for dislocation recombination activity in EFG material [63].

A critical parameter for solar cell efficiency is the ribbon thickness. As shown by Bowler and Wolf [64], an optimum thickness for peak efficiency occurs. This thickness is dependent on the fabrication technique and material properties, including front and back surface recombination velocities, minority-carrier lifetime and base resistivity among other parameters. For a “typical” $n^+ pp^+$ structure with a 200- μm diffusion length, L_d , a back surface field and a single layer anti-reflection coating, the optimum thickness region consists of a broad peak near 80 μm (Figure 6.27) as calculated using PC-1D [65]. For a 100- μm L_d the optimum thickness peaks at about 50 μm and for a 400- μm L_d it is near 120 μm . A front surface recombination velocity of 10^5 cm/s is assumed.

Table 6.5 Comparison of silicon ribbon material characteristics. In all cases the columnar grains extend through the thickness of the ribbon. An equilibrium segregation coefficient of $k_0 \sim 10^{-5}$ is typical of the most detrimental impurities for ribbon bulk lifetime

Material	Crystallinity	Dislocation density [1/cm ²]	Effective segregation	Thickness [μm]
EFG	Columnar grains in growth direction	$10^5 - 10^6$	$k_0 < k_{\text{eff}} < 10^{-3}$	250–350
WEB	Single (111) face central twin planes	$10^4 - 10^5$	$k_0 < k_{\text{eff}} < 10^{-3}$	75–150
STR	Columnar grains in growth direction	5×10^5	$k_0 < k_{\text{eff}} < 10^{-3}$	100–300
SF	Columnar grains through thickness	10^4 to 10^5	$k_{\text{eff}} < 1$	50–100
RGS	Columnar grains through thickness	$10^5 - 10^7$	$k_{\text{eff}} < 1$	300–400

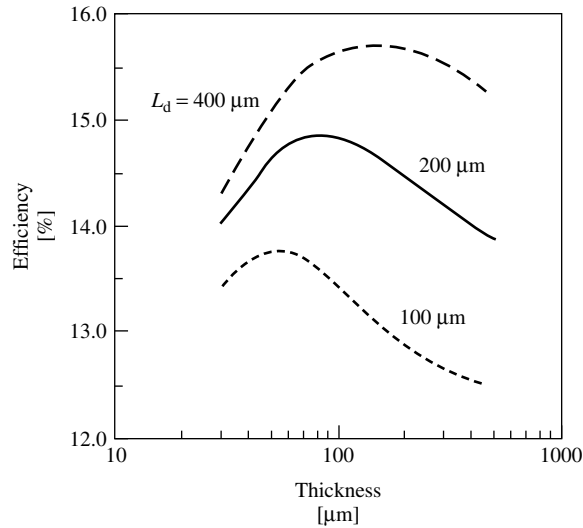


Figure 6.27 Solar cell efficiency versus thickness. (See the text for a description of the solar cell parameters)

The thickness of WEB and SF is closer to the optimum than the other three ribbon growth techniques. Light trapping will move the optimum to a thinner base, but such optical structures on multicrystalline ribbon are not yet practical. For growth on a substrate, it is possible to texture the substrate to trap light. This has been shown on SF wafers [57].

Solar cell fabrication processes used for conventional Cz and cast material wafers are commonly applied to silicon ribbon. If the ribbon is doped *p*-type with boron, the *n*-type emitter typically is formed by phosphorus diffusion either from POCl_3 , PH_3 or a spin-on source. Front contacts are usually screen-printed or evaporated with diffused or alloyed aluminium as back contact to produce a back surface field. A double or single layer anti-reflection coating may be used. For SF grown on an insulating substrate, contact with the back surface requires etching holes to allow contact with the conducting barrier layer. Table 6.6 summarises material characteristics and solar cell performance potential of the various forms of ribbon material. Boron dopes the ribbon *p*-type. Antimony can be used to produce *n*-type material as reported for WEB.

Table 6.6 Some “best” solar cell efficiency levels for various ribbon technologies

Material	Resistivity [Ω cm]	Carbon [$1/\text{cm}^3$]	Oxygen [$1/\text{cm}^3$]	Efficiency [%]
EFG (Reference [66])	2–4, <i>p</i> -type	10^{18}	$<5 \times 10^{16}$	15–16
WEB	5–30, <i>n</i> -type	Not detected	10^{18}	17.3
STR	1–3, <i>p</i> -type	4×10^{17}	$<5 \times 10^{16}$	15–16
SF (Reference [67])	1–3, <i>p</i> -type	5×10^{17}	5×10^{17}	16.6
RGS (Reference [68])	2, <i>p</i> -type	10^{18}	2×10^{18}	12.0

Ribbon cell processing, nevertheless, needs to recognise the unique growth constraints of all of the techniques. As noted above, a common material characteristic for ribbon materials historically has been the compromised as-grown bulk electronic quality, dictated by the development of desired high-throughput growth configurations. This strategy has its base in a commercial demand for very low cost wafers that must compete at relatively low volumes with already established dominant products based on single-crystal Cz wafers or directionally solidified and cast ingots. As-grown ribbon diffusion lengths most often are less than 100 μm . To obtain the maximum cell efficiency on this ribbon, with higher dislocation densities and contaminating impurities than in competitor wafers, a solar cell processing strategy was devised early in the history of ribbon technology development that incorporates special bulk lifetime upgrading steps. For example, bulk lifetime upgrading via aluminium alloying and hydrogen is particularly effective for EFG material [69, 70]. Another approach is to use plasma-enhanced chemical vapour deposition (PECVD) of silicon nitride to generate hydrogen for passivating the silicon bulk [71].

6.5.5 Ribbon/Foil Technology – Future Directions

Ribbon/foil wafer production is poised to move on to face a new round of challenges in the construction of large (50–100 MW) manufacturing facilities for crystalline silicon ribbon wafers. The RGS foil technology, with the greatest potential of all ribbon methods for cost reduction on the basis of a high throughput per furnace, is entering a pilot demonstration phase. This process faces challenges in process and equipment development before it can enter high-volume manufacturing of wafers. In the next pilot phase, we may expect that RGS will demonstrate a consistent material quality sufficient for improving cell efficiency to greater than 12% from the current 10 to 11%; process control capable of reproducibly producing a low stress, regular structure, with a shaped 12.5-cm-wide wafer suitable for high-yield cell processing at about a 300- μ thickness and a reliable prototype furnace with melt replenishment to enable continuous production, which will gain full benefit from the high throughput growth concept.

The future focus of WEB and STR ribbon development is on process automation and capital cost reduction for furnaces and infrastructure based on a concept of a low throughput (per furnace) process. Production will probably grow to between 1 and 10 MW for each of these approaches over the next several years. Process parameters that will be practised in this next round of manufacturing equipment expansion for both of them are narrowed down to a single ribbon per furnace concept with similar throughput parameters – a ribbon width of about 8 cm and a pull speed in the 1 to 2 cm/min range. The WEB ribbon technology is embarking on its pilot expansion with a unique process for the growth and manufacturing of solar cells at a 100- μm wafer thickness. STR is expanding its manufacturing with a 300- μm -thick wafer. Although wafer bulk quality is demonstrated on an R&D level to be capable of achieving 15 to 16% cell efficiencies for STR, and over 17% for WEB, quality and cell efficiency levels on a multi-megawatt scale are yet to be established. Both approaches will attempt to demonstrate the cost-effectiveness of operating on a multi-MW level in the next few years. R&D directions, which would appear to have the most potential for the reduction of wafer material costs for these techniques, are growth of wider ribbons and more ribbons per furnace.

EFG and SF ribbon technology have successfully completed their initial scale up of wafer production to the multi-megawatt level. Process control and equipment reliability improvements, which can drive throughput and yield higher, become increasingly more dominant in determining the manufacturing cost. As throughput per furnace increases, capital cost impact on variable manufacturing costs from the growth furnace decreases. There is pressure on all ribbon technologies to concentrate on reducing the capital cost of the wafer production equipment if the transition to large-scale wafer manufacturing of 50- to 100-MW annual capacity factories is to be sustained.

Process variable ranges are firmly established for the EFG process. Octagon tube length, throughput and wafer thickness parameters will remain within the ranges given in Table 6.4 for the next generation of equipment, while octagon face width, and hence the EFG wafer dimension, will increase from 10 to 12.5 cm. The major thrust in R&D on the EFG process in this phase will be on process control and process and equipment automation.

The benefits of the savings in silicon feedstock and potential gains in cell efficiency with a reduction of the ribbon/foil thickness are well understood for all these technologies. However, the pressure to carry out R&D in this direction for the case of wafers made from ribbons is not as acute as for conventional crystalline silicon wafer manufacturing methods because of the large benefit in feedstock savings already realised for ribbons on account of their favourable geometry. The R&D for the next generation of vertical ribbon technology beyond about five years will target the demonstration of production methods for very thin wafers. A strong motivator driving thickness reduction will be the pressure to increase the cell efficiency, which is seen to be capped in the 16 to 17% range (see Table 6.6) for current cell designs and wafer bulk quality. Low-cost cell designs, which can break this barrier and achieve desired targets of 18 to 20% for ribbon, are most easily found for thinner wafers, but this also requires improvements in bulk electronic quality to be achieved concurrently.

The major problem in this development for all vertical growth techniques will be to find methods to reduce the effects of thermal stress. At present, the only means by which this can be done is to reduce the pull speed. The cylinder geometry has the potential to offer some relief to the EFG process at the expense of having to work with thin curved wafers in cell and module processing. Although thermal stress is not a problem with substrate-assisted growth techniques, there probably will be a trade-off between good bulk quality with large grains and throughput.

6.6 NUMERICAL SIMULATIONS OF CRYSTAL GROWTH TECHNIQUES

Commercial finite element simulation tools for structural analysis in computer-aided engineering started to develop at the beginning of the seventies. Today, simulation tools are an essential part in various industry productions; see crash test simulation for automobile development or airflow simulations in the aerospace industry. As an advanced application the descriptions of whole production processes are the goal of the strategies for simulations. If these strategies are successful, computer modelling opens the opportunity to shorten development time for production facilities, to reduce the costs for the

engineering and to speed up process optimisation. In this chapter we will report on those simulation tools, various thermal models and examples of numerical simulations of silicon crystallisation processes.

6.6.1 Simulation Tools

Numerical simulation tools can be distinguished in universal and special-purpose programs. Examples of commercial universal-purpose programs are ABAQUS [72], ANSYS [73] and MARC [74] with a wide range of applications in structural analysis, thermal and fluid-flow simulations or electromagnetic field simulations. The number of special-purpose programs cannot be estimated seriously. Many universities and companies are working with specially developed software tools to obtain solutions of their specific problems. Recently, the large commercial programs both compromise and enable the user to add their specific subroutines to a program run.

The main structure of most of the simulation tools is similar: A pre-processing is designed to define the initial and boundary conditions of a simulation run and includes the generation of the simulation domain (finite element mesh) as well as a set of physical data that describes the material properties. The main-processing is normally not interactive and contains the solver of the mathematical formulations. The post-processing visualises the simulation results.

The demand for simulation tools depends on the complexity of the physical problem or on the technical process that the user wants to simulate. In general, the description of all physical relationships is reachable only in relatively simple and well-known problems. The full description of an industrial production facility by numerical simulations is not possible today, and neither is it reachable in the near future because too many details are too complex to be described by the numerical models. Therefore, the development of useful simplifications is one of the important keys to a successful simulation. This demand requires an integrated teamwork between the user of a simulation tool and the operators at the production facility and other process specialists.

Not the another important requirement is the validation of simulation results by experimental data. At least two experiments are necessary to validate simulation results concerning the process behaviour of a production facility. This means that the simulation model should be validated by measurements during a standard process and in a worst-case scenario to ensure the correctness of the results in an enlarged area of validity. Normally, these experiments are expensive and difficult to realise during a running production, but otherwise, running a non-optimised production would be quite more expensive. Anyhow, the validation of simulation results is necessary to ensure the success of the simulation method.

6.6.2 Thermal Modelling of Silicon Crystallisation Techniques

The wafer material for crystalline silicon solar cells can be divided into those from ribbon and bulk crystals. For most of wafer production processes, numerical simulations are in use to describe the thermal conditions during the crystallisation. In the case of ribbon crystals, only the EFG [75, 76] and the STR process [77] have reached a market

production. The RGS process [78] is now in preparation for a commercial production. The Cz crystal-pulling technique is the standard process for microelectronic single-crystal wafers and covers an essential part of the PV market share [79, 80]. The TriSi crystal is a new variation of this process, especially for photovoltaic applications [81]. The characteristics of ingot crystallisation can be explained by the shape of their liquid–solid interface. Anyhow, today’s ingot crystallisation goes more and more towards a mostly planar solidification. For the use of numerical simulations of the Cold Wall process, see [82, 83]; for the Heat Exchange Method (HEM), see [84] and for the Solidification by Planar Interface (SOPLIN) processes, see [85, 86].

To simulate the temperature history during crystallisation, various thermal effects must be taken into account. In Figure 6.28 the scheme of thermal conditions for the ribbon growth and ingot crystallisation is presented. The biggest difference between the two is the strong variation of the cooled surface to volume relation (SV) during crystal growth. This relationship can be used to qualify the cooling behaviour of the different crystals in an equivalent surrounding. For ribbon growth SV is given as $2/\text{ribbon thickness}$ and for ingots as $1/\text{ingot height}$. The high number for ribbon growth (e.g. $SV = 66/\text{cm}$) means that the surface affects the crystallisation, while the low number for an ingot geometry (e.g. $SV = 0.033/\text{cm}$) shows that volume effects are more important for crystallisation. By this, the SV parameter characterises the requirements for the modelling of different crystallisation techniques. In the case of bulk crystallisation, the latent heat at the liquid–solid interface must be lead away by a heat sink at the bottom of the ingot. By this, the crystallisation is propagated by a conductive heat flow through the solid ingot volume and the temperature gradients inside the volume have to be simulated with high attention. In the case of ribbon growth, heat flow by convection and radiation at the silicon surface is the dominant heat-transport mechanism to lead away latent heat and propagate the solidification. Therefore, simulation results are very sensitive to heat-transition coefficients and the emission behaviour at the ribbon surface.

Furthermore, both techniques can be distinguished into quasi-steady state and moving boundary processes. Assuming a constant pulling speed, the ribbon growth is

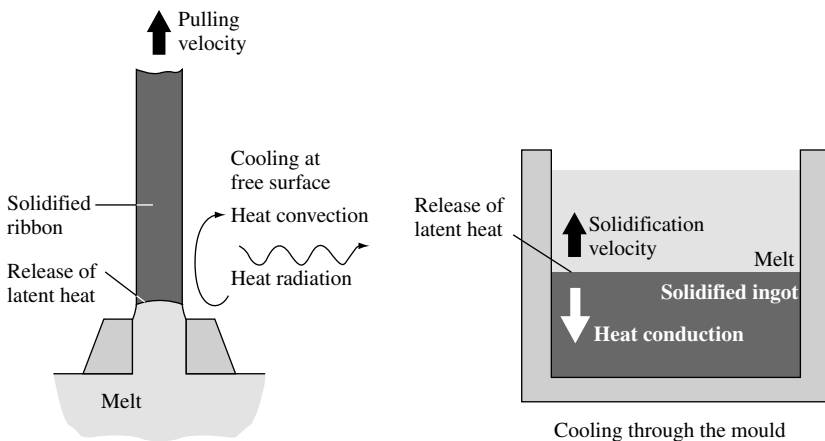


Figure 6.28 Scheme of thermal effects during ribbon growth and ingot crystallisation

characterised by a steady-state temperature field and the liquid–solid phase boundary can be modelled by a fixed-temperature boundary condition, as the silicon melting temperature of 1410°C. In the case of the ingot casting, the phase boundary moves through the crystal and the release of latent heat can be modelled by an enthalpy formulation. By this, the release of the latent heat of finite elements can be taken into account directly after their total solidification, or the fraction of latent heat must be considered for partly solidified elements [87, 88]. The importance of an accurate modelling of the release of latent heat may become more clear by estimating the crystallised volume rate in typical ingot processes to be around 9000 cm³ per hour, which means a latent heat source of more than 8 kW at the location of the phase boundary. Pulling one 10-cm-wide ribbon, the crystallised volume rate is about 30 cm³ per hour with a latent heat release of 0.03 kW.

The Czochralski and TriSi crystal-pulling techniques can be classified between ribbon and ingot crystallisation. The temperature profile can be assumed to be stationary and the SV parameter, given as 1/crystal diameter, lies, for example, in the range of 0.066/cm.

In general, the heat flow in silicon during crystallisation can be described by the heat-transport equation [89–91]:

$$\rho c_p \frac{\partial T}{\partial t} = \lambda \nabla^2 T + L \frac{\partial f_c}{\partial t}$$

with the silicon data:

density of solid silicon	$\rho_{(1410^\circ\text{C})} = 2.30$ [g/cm ³]
density of liquid silicon	$\rho_{(1411^\circ\text{C})} = 2.53$ [g/cm ³]
heat capacity	$c_{p(20^\circ\text{C})} = 0.83$ [J/g K]
	$c_{p(1410^\circ\text{C})} = 1.03$ [J/g K]
heat conductivity	$\lambda_{(20^\circ\text{C})} = 1.68$ [W/cm K]
	$\lambda_{(1410^\circ\text{C})} = 0.31$ [W/cm K]
latent heat of phase change	$L = 3300$ [J/cm ³]

The time t and the temperature T are variable and result from the simulation. For the moving boundary case the solid fraction f_c becomes important. This parameter depends on the finite element temperature and varies between zero for a completely liquid finite element and one for a solid element.

Additionally to these material properties and the heat flow mechanisms in the silicon material, the description of the internal furnace construction must be taken into account to perform simulations of crystallisation facilities. This includes the geometrical description and material properties of the internal set-up as well as the radiative heat exchange with heaters and cooling facilities.

6.6.3 Simulation of Bulk Silicon Crystallisation

As an example of the temperature simulation of silicon ingot crystallisation, the SOPLIN casting technique is selected. To simulate this process, a finite element mesh of about 230 000 elements was built to describe the furnace geometry. This mesh includes the silicon ingot, the mould, all insulation materials and active heating and cooling facilities,

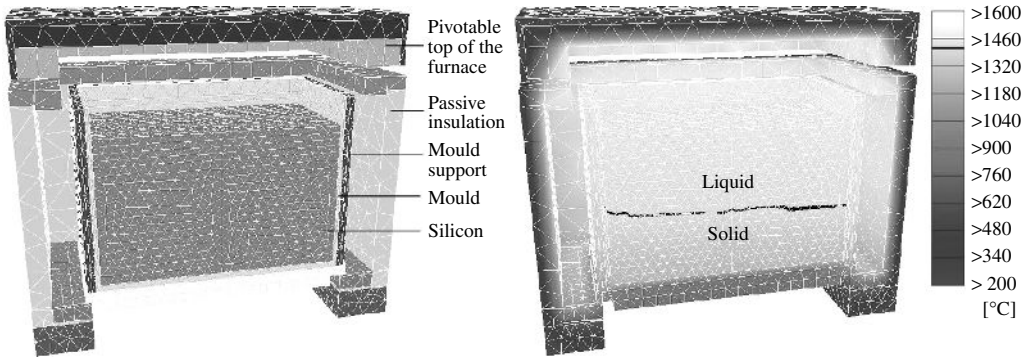


Figure 6.29 Finite element geometry of an ingot casting furnace and simulated temperature distribution during a reference process. The liquid–solid interface is marked by the black line

as shown in Figure 6.29. Because of confidentiality agreements with the industry, the heating and cooling systems are not shown in detail in this figure. All heat conductance and capacity effects as well as the non-stationary release of latent heat are taken into account. All material contact regions between silicon, mould or insulation materials are modelled by heat flow–resistance parameters. To describe the heat flux by radiation inside the furnace, a view-factor model is included in the software. All material data are treated in their temperature dependency and all the internal control systems of the furnace are added to the simulation software.

To start one simulation run, only the cooling water temperature and the time-dependent process control information are necessary as input data, as they are entered in the crystallisation furnace. Output from one calculation is the three-dimensional temperature history in the furnace, beginning after pouring the melt and ending with a homogeneous temperature of about 300°C inside the ingot. This calculation needs less than 6 h on a common one-processor workstation.

In Figure 6.29, an example of the temperature distribution during a reference process is shown in the middle, cut through the furnace. The liquid–solid interface is marked by the melting temperature isotherm. The solidification front is mostly flat, and a slight non-symmetry is caused by the specific construction of the heating system. These simulation results are verified in an experimental crystallisation furnace with good agreement to the measurement in the ingot volume during crystallisation.

In general, the shape of the solidification front is controlled by the lateral heat flux, while the vertical heating and cooling conditions control the solidification velocity. To investigate these general reflections for the described furnace, variations of the process control were simulated. In Figure 6.30, two variations are presented. By a 30% raise of heating power at the side walls of the ingot, the shape of the solidification front becomes more convex. Otherwise, a reduction of heating power by about 20% turns the solidification front to a more concave shape. Additionally, to this more or less predictable effect, simulation results show an increase in the solidification time for the convex crystallisation of 44% and a 30% reduced processing time for the concave solidification. Both effects are due to the total varying power input in the furnace. These simulation results enable

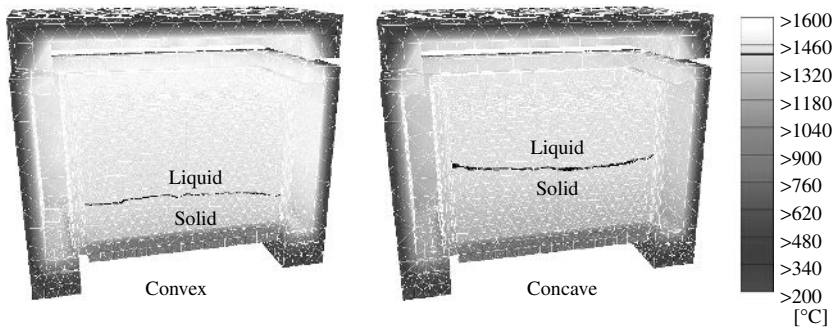


Figure 6.30 Examples of convex and concave liquid–solid interfaces due to the variation of side wall heating power. Both pictures are taken at the same process time

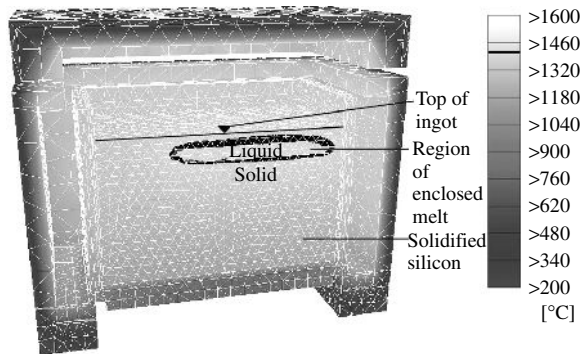


Figure 6.31 Simulation result representing a remarkable decrease of heating power at the top region of the ingot. By this, the solidification time is reduced to half, but solidification ends with an inclusion of silicon melt

the furnace operator to find the balance between material quality, which is known to be high in the case of planar solidification, and process economy.

In Figure 6.31, simulation results are shown, representing a noticeable reduction of heating power at the ingot top. By this, the solidification velocity can be speeded up and the time for solidification is reduced to half. However, in the simulated case study, the solidification ends with an encapsulation of the melt by solidified silicon. Because of the 10% higher density of liquid silicon with respect to the solid phase, this process scenario causes a burst out of melt from ingots volume. This can lead to a crack in the mould and to a damage of the furnace. These case-study simulations can find worst-case process conditions that must be avoided in production. For more simulation results of the SOPLIN process, see [92–94].

6.6.4 Simulation of Silicon Ribbon Growth

As a second example of silicon crystallisation processes, the RGS is taken. The basic idea of this process is the de-coupling of the pulling direction of substrates on which silicon

solidifies and the solidification direction of the silicon itself, as shown in Figure 6.32. By this, a very high production rate of one wafer per second is realisable. For this process numerical simulations were performed describing the crystallisation of the silicon ribbon in further detail. This simulation is realised by a phase-field approach [95]. In Figure 6.33 two nucleation states of the silicon on the substrate are compared by their temperature field in two-dimensional simulations. In the first case a supercooled region in front of the tip of the growing crystal leads to a more dendritic growth mode of the crystal, because the liquid–solid interface is morphologically non-stable. In the second crystallisation mode,

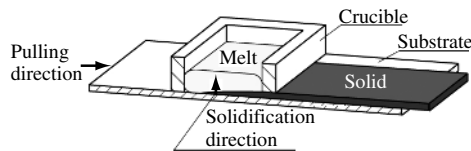


Figure 6.32 Scheme of the RGS process. The latent heat is removed through the substrate. By this, solidification is propagated vertical to the substrate and is de-coupled from substrates' pulling direction

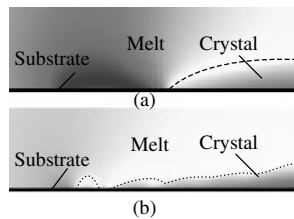


Figure 6.33 Simulated temperature profile on the RGS substrate. Light grey scales indicate high temperatures. The liquid–solid interface is marked with the dotted line. Unstable crystal growth into a supercooled melt at the tip of the ribbon. Nucleation of new grains limits the supercooling and leads to a stable columnar grain growth

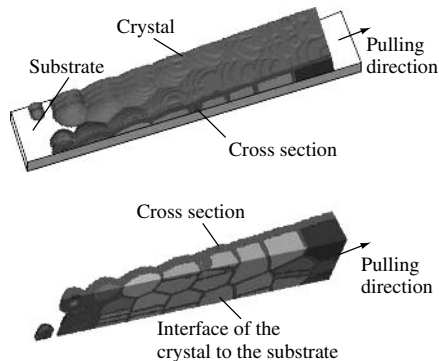


Figure 6.34 Simulation results of the growth of silicon grains on the RGS substrate during solidification. Different grains are marked by different grey scales. The liquid–solid interface is marked by a darker grey scale and envelops the grains. For a better visibility, the melt is not shown in this figure

the supercooling decreases owing to a nucleation of new grains on the substrate surface, which leads to a more columnar growth of the silicon sheet. Both crystallisation modes depend on the surface of the substrate and on the heating power controlled temperatures of the substrate and the melt. Numerical simulations allow investigating this crystal-growth tendency as well as the temperature field at the contact region of the ribbon on the substrate. In Figure 6.34 an example of the simulation of single silicon grain growth on the substrate is given [96]. In this way, numerical simulations can study the grain growth under various temperature conditions and grain-selection mechanisms of silicon crystals.

6.7 CONCLUSIONS

At the present time, the PV industry relies on solar cells made on crystalline silicon wafers, which provide around 90% of the total PV power installed. It is expected that monocrystalline and multicrystalline solar cells will continue dominating the industry for the next 10 years.

With rejects from the microelectronic industry as feedstock, the PV industry grows monocrystalline ingots by the Czochralski technique. Owing to more relaxed specifications than in microelectronics, the throughput of PV Cz pullers can be increased and still produce high-quality silicon, allowing the achievement of 15 to 17% efficient solar cells.

Tri-crystalline silicon (tri-Si) can be grown in standard production Cz growers using a quasi-continuous pulling with multiple recharging with high productivity and feedstock usage. Tri-Si allows slicing of ultra-thin wafers with higher mechanical yield than monocrystalline Si and obtaining solar cells of similar performance.

Multicrystalline Si can be manufactured at a lower cost than monocrystalline Si, but produces less efficient cells, mainly owing to the presence of dislocations and other crystal defects. With the introduction of new technologies, the gap between multicrystalline and monocrystalline solar cells is reducing.

Si ingots are sliced into thin wafers with multi-wire saws, with throughputs of about 500 to 700 wafers per day and per machine. Sawing is responsible for high material losses, and amounts to a substantial part of the wafer production cost. Understanding the microscopic processes of wire sawing allows optimising the technique and improving the sawing performance.

Silicon ribbon wafer/foil technologies have matured in the past decade to where they are serious contenders for competing on a scale equal to that of conventional silicon wafers. Several ribbon technologies have already demonstrated robust and reproducible processes, which have been scaled up to megawatt levels. The next round of expansion will probably reach the 50 to 100 MW factory size for individual technologies within 5 years. Factories of this scale will require considerable development of automated equipment and infrastructure in addition to continuous improvement on the basic process control and material quality. EFG and SF ribbon technologies are most notably in a position today to manufacture wafers on this scale and lead the anticipated growth of the photovoltaic industry.

During the last decade, computer power has been increasing strongly and there is a high progress in the modelling of physical phenomena and in the development of

simulation tools. By this, computer simulations become a powerful tool in science and industrial applications. The simulation results of industrial crystallisation processes that are shown and the detailed study of the crystallisation mode by numerical simulations are some examples of the possibilities today. These numerical simulations offer a wide range of possibilities to increase the knowledge about the basic physics of crystallisation and technical processes. One insistent demand on computer simulations is to close the gap between science and engineering to get a closer picture of reality.

6.8 ACKNOWLEDGEMENTS

This chapter has been coordinated by W. Koch. Section 6.2 has been prepared by A.L. Endrös, Section 6.3 by C. Häßler, Section 6.4 has been prepared by H. J. Möller, Section 6.5 by J. P. Kalejs and Section 6.6 by D. Franke. The editor also wants to recognise the work of C. del Cañizo, senior researcher at his institute (IES-UPM), who greatly reduced the original text to keep it under the budgeted extension without losing readability and homogeneity.

REFERENCES

1. Knobloch J *et al.*, *Proc. 13th Euro. Conf. Photovoltaic Solar Energy Conversion*, 9 (1995).
2. Li J *et al.*, *Appl. Phys. Lett.* **60**, 2240 (1992).
3. Zundel M, Csaszar W, Endrös A, *Appl. Phys. Lett.* **67**, 3945 (1995).
4. Güttler G, Queisser H, *Energy Conversion* **10**, 51 (1970).
5. Martinelli G, Kibizov R, *Appl. Phys. Lett.* **62**, 3262 (1993).
6. Endrös A, Einzinger R, Martinelli G, *Proc. 14th Euro. Conf. Photovoltaic Solar Energy Conversion*, 112 (1997).
7. Palm J *et al.*, *Proc. 16th Euro. Conf. Photovoltaic Solar Energy Conversion*, 1222–1225 (2000).
8. Palm J *et al.*, *Proc. 28th IEEE Photovoltaic Specialist Conf.*, 40–45 (2000).
9. Carstensen J, Lippik W, Föll H, “Mapping of Defect Related Silicon Bulk and Surface Properties with the ELYMAT Technique”, in Huff H, Bergholz W, Sumino K, Eds, *Semiconductor Silicon 94*, 1105–1116, The Electrochemical Society, Pennington, NJ (1994).
10. Schmidt J, Aberle A, Hezel R, *Proc. 26th IEEE Photovoltaic Specialist Conf.*, 13 (1997).
11. Glunz S *et al.*, *Proc. 2nd World Conf. Photovoltaic Solar Energy Conversion*, 1343 (1998).
12. Münzer A *et al.*, to be published.
13. Endrös A, *Phys. Rev. Lett.* **63**, 70 (1989).
14. Endrös A, *Solid State Phenomena* **32–33**, 143 (1993).
15. Csaszar W, Endrös A, *Phys. Rev. Lett.* **73**, 2 (1994).
16. Csaszar W, Endrös A, *Mater. Sci. Eng.* **B36**, 112 (1996).
17. Koch W *et al.*, *Solid State Phenomena* **401**, 57–58 (1997).
18. Häßler C *et al.*, *Proc. 2nd World Conf. Photovoltaic Solar Energy Conversion*, 1886 (1998).
19. Koch W, Krumbe W, Schwirtlich I, *Proc. 11th EU Photovoltaic Specialist Conf.*, 518 (1992).
20. Fuller C, Logan R, *J. Appl. Phys.* **28**, 1427 (1957).
21. Kaiser W, Frisch H, Reiss H, *Phys. Rev.* **112**, 1546 (1958).
22. Wagner P, Hage J, *Appl. Phys. A: Solids Surf.* **49**, 123 (1989).
23. Cazcarra V, Zunino P, *J. Appl. Phys.* **51**, 4206 (1980).
24. Pensl G *et al.*, *J. Appl. Phys. A* **48**, 49 (1989).
25. Häßler C *et al.*, *Proc. 14th Euro. Conf. Photovoltaic Solar Energy Conversion*, 720 (1997).
26. Chonan S, Jiang Z, Yuki Y, *J. Vib. Acoustics* **115**, 529 (1993).
27. Wells R, *Solid State Technol.* **30**, 63 (1987).

28. Sahoo R *et al.*, in Subramania K, Ed, *ASME – IMECE Manufacturing Science and Engineering*, 131, ASME press, New York (1996).
29. Li J, Kao I, Prasad V, *ASME – IMECE Manufacturing Science and Engineering*, 439, ASME press, New York (1997).
30. Yang F, Kao J, *J. Electron. Packaging* **121**, 191 (1999).
31. Bhagavat M, Kao I, Prasad V, *ASME J. Tribology* (2001) in press.
32. Kao I, Wie S, Chiang P, *Proc. of NSF Design & Manufacturing Grantees Conf.* 239 (1997).
33. Chen C, Leipold M, *J. Am. Ceram. Soc.* **59**, 469 (1980).
34. Lawn B, Marshall D, *J. Am. Ceram. Soc.* **62**, 347 (1979).
35. Anstis G, Chantikul P, Lawn B, Marshall D, *J. Am. Ceram. Soc.* **64**, 533 (1981).
36. Evans A, Charles E, *J. Am. Ceram. Soc.* **59**, 371 (1976).
37. Lawn B, Evans A, *J. Mater. Sci.* **12**, 2195 (1977).
38. Gogots Y, Baek C, Kirscht F, *Semicond. Sci. Technol.* **14**, 936 (1999).
39. Weppelmann E, Field J, Swain M, *J. Mater. Res.* **8**, 246 (1993).
40. Borst C, Möller H, German BMBF VEDRAS Report, 23 (1999).
41. “Electricity from Solar Cells” *Flat Plate Array Project*, 10 Years of Progress, JPL Publication 400–279 10/85 (Oct. 1985).
42. For comprehensive reviews see bibliographies in *J. Cryst. Growth*, **50** (1980); *J. Cryst. Growth*, **82** (1987); *J. Cryst. Growth*, **104** (1990).
43. Ciszek T, *J. Cryst. Growth* **66**, 655 (1984).
44. Bell R, Kalejs J, *J. Mat. Res.* **13**, 2732 (1998).
45. Chalmers B, *J. Cryst. Growth* **70**, 3 (1984).
46. Thomas P, Brown R, *J. Cryst. Growth* **82**, 1 (1987).
47. Hopkins R *et al.*, *J. Cryst. Growth* **82**, 142 (1987).
48. Ravi K, *J. Cryst. Growth* **39**, 1 (1977).
49. Kalejs J, in Khattak C, Ravi K, Eds, *Silicon Processing for Photovoltaics II*, 185–254, North Holland, Amsterdam (1987).
50. Garcia D *et al.*, *J. Cryst. Growth* **225**, 566 (2001).
51. Mackintosh B *et al.*, *Proc. 28th IEEE Photovoltaic Specialist Conf.*, 46 (2000).
52. Sachs E, in *Proc. of the Flat-Plate Solar Array Project Research Forum on the High-Speed Growth and Characterisation of Crystals for Solar Cells*, JPL, 279 (1984).
53. Sachs E, Ely D, Serdy J, *J. Cryst. Growth* **82**, 117 (1987).
54. Wallace R *et al.*, Sixth Workshop on the Role of Impurities and Defects in Silicon Device Processing – Extended Abstracts and Papers, NREL/SP-413-21550, 203 (1996).
55. Lange H, Schwirtlich I, *J. Cryst. Growth* **104**, 108 (1990).
56. Cotter J *et al.*, *Proc. 13th Euro. Conf. Photovoltaic Solar Energy Conversion*, 1732 (1995).
57. Barnett A *et al.*, *Proc. 18th IEEE Photovoltaic Specialist Conf.*, 1094 (1985).
58. Ruby D, Ciszek T, Soporì B, *NCPV Program Review Meeting*, April, 16–19, Denver, CO, unpublished.
59. Schmidt W, Woesten B, Kalejs J, *Proc. 16th EPVSEC*, 1082–1086 (2000).
60. Sawyer W, Bell R, Schoenecker A, *Solid State Phenomena* **37–38**, 3 (1994).
61. Meier D, Hopkins R, Campbell R, *J. Propulsion Power* **4**, 586 (1988).
62. Koch W *et al.*, *Proc. of 2nd World Conf.* 1254 (1998).
63. Koshka Y *et al.*, *Appl. Phys. Lett.* **74**, 1555 (1999).
64. Bowler D, Wolf M, *IEEE Trans. Components, Hybrids Manufacturing Technology* **3**, 464 (1980).
65. Basore P, Clugston D, PC1D Version 4.2 for Windows, Copyright by University of New South Wales.
66. Bathey B *et al.*, *Proc. 28th IEEE Photovoltaic Specialist Conf.*, 194 (2000).
67. Sims P *et al.*, *Annual Report on DOE/NREL Subcontract No. DE-AC36-98-GO20337*, Publication No. NREL/SR-520-28547 (2000).
68. Hahn G *et al.*, *Proc. 16th EPVSEC*, **1095** (2000).

69. Sana P, Rohatgi A, Kalejs J, Bell R, *Appl. Phys. Lett.* **64**, 97 (1994).
70. Bailey J, Kalejs J, Keaveny C, *Proc. 24th IEEE Photovoltaic Specialist Conf.*, **1356** (1994).
71. The earliest work is reported in the 3rd *Jpn. Photovoltaic Solar Energy Conversion* by Morita H *et al.*, *Jpn. J. Appl. Phys.* **21** 47 (1982); U.S. patent No. 4,640,001 (1987) and Australian patent No. 609424 (1991); a comprehensive review of recent developments is given by Szlufcik J *et al.*, *Proc. E-MRS Spring Meeting*, E-VI.1 (2001).
72. See: www.abaqus.com.
73. See: www.ansys.com.
74. See: www.marc.com.
75. Lambropoulos J *et al.*, *J. Cryst. Growth* **65**, 324–330 (1983).
76. Kalejs J, Schmidt W, *Proc. 2nd World Conf. Photovoltaic Solar Energy Conversion*, 1822–1825 (1998).
77. Wallace R, Janoch R, Hanoka J, *Proc. 2nd World Conf. Photovoltaic Solar Energy Conversion*, 1818–1821 (1998).
78. Koch W, Höfs H, Häßler C, Thurm S, *Proc. 2nd World Conf. Photovoltaic Solar Energy Conversion*, 1254–1259 (1998).
79. Chang C, Brown R, *J. Cryst. Growth* **63**, 343–352 (1983).
80. Zulehner W, Huber D, *Crystals*, Vol. 8, 3–143, Springer Verlag, Berlin, Heidelberg, New York (1982).
81. Palm J *et al.*, *Proc. 16th Euro. Conf. Photovoltaic Solar Energy Conversion*, 1222–1225 (2000).
82. Helmreich D, “*The Wacker Ingot Casting Process*”, in Khattak C, Ravi K, Eds, *Silicon Processing for Photovoltaics*, Vol. II, 97–115, North-Holland, Amsterdam (1987).
83. Schätzle P *et al.*, *Proc. 11th Euro. Conf. Photovoltaic Solar Energy Conversion*, 465–468 (1992).
84. Khattak C, Schmid F, *Proc. 25th IEEE Photovoltaic Solar Energy Conversion*, 597–600 (1996).
85. Koch W *et al.*, *Proc. 12th Euro. Conf. Photovoltaic Solar Energy Conversion*, 797–798 (1994).
86. Häßler C *et al.*, *Proc. 2nd World Conf. Photovoltaic Solar Energy Conversion*, 1886–1889 (1998).
87. Zabarás N, Ruan Y, Richmond O, *Computer Methods in Applied Mechanics and Engineering*, Vol. 8, 333–364, Elsevier Science Publisher B.V., Amsterdam (1990).
88. Diemer M, Franke D, “*Modelling of Thermal Stress Near the Liquid-Solid Phase Boundary*”, in Thomas B, Beckermann C, Eds, *Modelling of Casting, Welding and Advanced Solidification*, Vol. 8, 907–914, TMS (1998).
89. Zienkiewicz O, Taylor R, *The Finite Element Method*, McGraw-Hill, London (1989).
90. Bathe K, *Finite Element Procedures in Engineering Analysis*, München Verlag, Wien (1984).
91. Kurz W, Fischer D, *Fundamentals of Solidification*, Trans Tech Publications, Zürich (1998).
92. Franke D *et al.*, *Proc. 25th IEEE Photovoltaic Specialist Conf.*, 545–548 (1996).
93. Häßler C *et al.*, *Solid State Phenomena* **67–68**, 447–452 (1999).
94. Franke D, Apel M, Häßler C, Koch W, *Proc. 16th Euro. Conf. Photovoltaic Solar Energy Conversion*, 1317–1320 (2000).
95. Steinbach I *et al.*, *Physica D* **94**, 135–147 (1996).
96. Steinbach I, Höfs H, *Proc. 26th IEEE Photovoltaic Solar Energy Conversion*, 91–93 (1997).

7

Crystalline Silicon Solar Cells and Modules

Ignacio Tobías¹, Carlos del Cañizo¹ and Jesús Alonso²

¹*Universidad Politécnica de Madrid, Madrid, Spain,* ²*Isofotón S.A., Málaga, Spain*

7.1 INTRODUCTION

Crystalline silicon solar cells and modules have dominated photovoltaic (PV) technology from the beginning. They constitute more than 85% of the PV market today, and although their decline in favor of other technologies has been announced a number of times, they presumably will retain their leading role for a time, at least for the next decade.

One of the reasons for crystalline silicon to be dominant in photovoltaics is the fact that microelectronics has developed silicon technology greatly. On the one hand, not only has the PV community benefited from the accumulated knowledge but also silicon feedstock and second-hand equipment have been acquired at reasonable prices. On the other hand, Microelectronics has taken advantage of some innovations and developments proposed in Photovoltaics.

For several decades, the terrestrial PV market has been dominated by *p*-type Czochralski silicon substrates. Continuous improvements in performance, yields and reliability have allowed an important cost reduction and the subsequent expansion of the PV market. Because of the lower cost of mc-Si wafers, multicrystalline (MC) silicon cells emerged in the 1980s as an alternative to single-crystal ones. However, their lower quality precluded the achievement of similar efficiencies to those of Cz, so that the figure of merit $\$ W^{-1}$ has been quite similar for both technologies over a long time (see Table 7.1).

Deeper understanding of the physics and optics of the mc-Si material led to improved device design, which allowed a wider spread of the technology. A combination

Table 7.1 Breakdown of costs of fabrication of single-crystalline (SX) and multicrystalline (MC) solar cells (corresponding to year 1990) [1]

Item	SX	MC
Pure Si	38	38
Ingot formation	115	35
Sawing	77	77
Wafer cost	230	150
Cell fabrication	80	80
Total components	310	230
Yield	0.95	0.9
Cell cost	326	256
Module assembling	75	75
Lamination	75	75
Module cost (Euro m⁻²)	476	406
Efficiency	0.14	0.12
Module cost (Euro Wp⁻¹)	3.40	3.38

Table 7.2 Market share of monocrystalline and multicrystalline solar cells [2]

Year	Cz-Si solar cells		MC-Si solar cells	
	Output [MW]	Market share [%]	Output [MW]	Market share [%]
1996	48.7	55	28.4	32
2000	92.0	32	146.7	51

of improved material quality and material processing has allowed higher efficiencies at a still lower cost, increasing the share of MC in the PV market, well ahead of monocrystalline. Recent evolution of the market can be seen in Table 7.2 [2].

This chapter offers an overview of silicon solar cell and module technology. First, Si properties justifying its use as photovoltaic material are presented. Then, design of Si solar cells is reviewed, highlighting the benefits and limits of different approaches. Manufacturing processes are described, paying special attention to technologies that are currently implemented at the industrial level, mostly based on screen-printing metallization technology. Considerations of ways of improving solar cell technology are also specified. Peculiarities of multicrystalline material are explained in Section 7.6, while other approaches that are already in industrial production are also described briefly. Next, crystalline Si modules are reviewed, pertaining to electrical performance, fabrication sequence and reliability concerns.

7.2 CRYSTALLINE SILICON AS A PHOTOVOLTAIC MATERIAL

7.2.1 Bulk Properties

Crystalline silicon has a fundamental indirect band gap $E_G = 1.17$ eV and a direct gap above 3 eV [3] at ambient temperature. These characteristics determine the variation of optical properties of Si with wavelength, including the low absorption coefficient for carrier generation for near band gap photons [4]. At short ultraviolet (UV) wavelengths in the solar spectrum, the generation of two electron–hole pairs by one photon seems possible, though quantitatively this is a small effect [5]; at the other extreme of the spectrum parasitic free-carrier absorption competes with band-to-band generation [6]. The intrinsic concentration is another important parameter related to the band structure; it links carrier disequilibrium with voltage [7].

At high carrier densities, doping- or excitation-induced, the band structure is altered leading to an increase in the effective intrinsic concentration: this is one of the so-called heavy doping effects that degrade the PV quality of highly doped regions [8].

Recombination in Si is usually dominated by recombination at defects, described with Shockley–Read–Hall (SRH) lifetimes. The associated lifetime τ (which can also be described in terms of diffusion length L) increases for good quality materials. Auger recombination, on the contrary, is a fundamental process that becomes important at high-carrier concentration [9]. The Auger coefficients are reported to be higher at moderate carrier densities due to excitonic effects [10]. Band-to-band direct recombination is also a fundamental process but quantitatively negligible (it is instructive, however, to notice that record-efficiency solar cells have such extraordinarily low SRH recombination levels that they perform as 1%-efficient light-emitting diodes, that is, radiative recombination is significant [11]).

At low and moderate doping, electrons present mobilities about three times higher than holes, both limited by phonon scattering. Impurity scattering dominates for higher doping densities [12, 13]. Carrier–carrier scattering affects transport properties in highly injected material [14].

7.2.2 Surfaces

7.2.2.1 Contacts

Contacts are structures built on a semiconductor surface that allow charge carriers to flow between the semiconductor and the external circuit. In solar cells, contacts are required to extract the photogenerated carriers from the absorbing semiconductor substrate. They should be selective, that is, should allow one type of carrier to flow from Si to metal without energy loss while blocking the transport of carriers of the opposite type.

Direct Si-metal contacts, in general, do not behave this way. As an exception, good hole contacts to highly doped p -Si substrates with aluminum are possible. But the

most used approach is to create heavily doped regions under the metal, p -type for hole extraction and n -type for electron extraction. Majority carriers in this region can flow through the contact with low voltage loss. The transport of minority carriers is described by a surface recombination velocity (SRV), S . Although the SRV is high, limited only by thermal diffusion so that $S \cong 10^6 \text{ cm}\cdot\text{s}^{-1}$ [15], the concentration of minority carriers, for a given pn product, is suppressed by the high doping and the flow is reduced.

As will be seen later on, the contact for the minority carriers is usually placed at the front (illuminated) face of the substrate, and the corresponding heavily doped layer is usually called *emitter*. The doped region under the majority carrier contact at the back is called a *Back Surface Field* (BSF).

Recombination at these heavily doped regions is described by the saturation current density J_0 that includes volume and true contact recombination. Their thickness w should be much higher than the minority-carrier diffusion length L so that few excess carriers reach the contact, and the doping level must be very high to decrease contact resistance and the minority-carrier concentration, although heavy doping effects may limit the doping level advisable for such regions. The recombination activity of BSF layers is often described in terms of an effective SRV instead of the saturation current density.

Typical 10^{-13} to $10^{-12} \text{ A}\cdot\text{cm}^{-2}J_0$ values are achieved [16, 17]. Diffused phosphorus is used for n -contacts. Aluminum alloying has the advantages over boron for p -contacts that very thick p^+ layers can be formed in a short time at moderate temperatures and that gettering action is achieved [18]. As a shortcoming, the p^+ layer is nonhomogeneous and can even be locally absent; the obtained J_0 is larger than expected for a uniform layer. In comparison to aluminum, boron offers higher doping levels because of a larger solubility [19] and transparency to light so that it can also be used at illuminated surfaces.

Other structures have been tested to obtain selective contacts: metal-insulator-semiconductor (MIS) contacts [20], polysilicon contacts [21] and heterojunction to a-Si or other wide band gap material [22].

7.2.2.2 Noncontacted surfaces

Because of the severe alteration of the bonding of Si atoms, a large number of band gap states exist at a bare Si surface which, acting as SRH recombination centers, make the SRV very large, around $10^5 \text{ cm}\cdot\text{s}^{-1}$ [23, 24]. In order to reduce surface recombination, two main approaches are followed [25].

In the first one, the density of electron surface states in the gap is decreased. This is accomplished by depositing or growing a layer of an appropriate material that partially restores the bonding environment of surface Si atoms. This material must be an insulator.

Thermal SiO_x is grown in an oxygen-rich atmosphere at the expense of substrate Si atoms at high temperatures around 1000°C . SiN_x is deposited by plasma-enhanced chemical vapor deposition (PECVD) [26] at low temperatures between 300 and 400°C range. The quality of both techniques is very sensitive to subsequent treatments, with hydrogen playing a major role in obtaining low SRV values below $100 \text{ cm}\cdot\text{s}^{-1}$.

As a general rule, S increases with the doping of the substrate [23, 24]. It also depends on the injection level and doping type, because the interfaces contain positive

charges that affect the number of carriers at the surface, and because the capture probability for electrons and holes is different [27]. *N*-type or intrinsic surfaces are usually better than *p*-type ones. Stability under UV exposure is another fundamental concern.

In the second approach, the excess carrier density at the interface is decreased relative to the bulk. This effect has already been commented upon with respect to contacts and results in a reduced effective SRV at the bulk edge of the corresponding space charge region. It can be produced by charges in the surface layer, by the electrostatics associated to a MOS structure [28] or by doping.

The surface layer can be accumulated or inverted, or, correspondingly, doped with the same or the opposite type of the substrate. Its recombination activity is better described by a constant saturation current density, J_0 , whose minimization follows the same rules as mentioned for the contacts if S at the surface is high. On the contrary, if S is low when compared to D/L for minority carriers (with D the diffusion constant and L the diffusion length in the substrate) in the surface layer, it is better for it to be thin or “transparent” to minority-carrier flow ($w < L$). The optimum doping level is a compromise between reduction of the excess carriers, and heavy doping effects and the increase of the SRV with doping. Moderate doping levels are favored in this case. Under passivated surfaces, J_0 values around 10^{-14} A·cm⁻² are achievable, with phosphorus-doped substrates giving better results than boron-doped ones [16, 17].

In conclusion, recombination at a noncontacted surface can be made much smaller than at a metallized one, and this has a deep influence in the evolution of Si solar cell design.

7.3 CRYSTALLINE SILICON SOLAR CELLS

7.3.1 Cell Structure

Several studies have been carried out to find the limiting efficiency and the optimum structure of a-Si solar cell [29–31]. All avoidable losses are assumed to be suppressed:

1. no reflection losses and maximum absorption as achieved by ideal light-trapping techniques,
2. minimum recombination: SRH and surface recombination are assumed avoidable and only Auger recombination remains,
3. the contacts are ideal: neither shading nor series resistance losses,
4. no transport losses in the substrate: the carrier profiles in the substrate are flat so that recombination is the minimum possible for a given voltage.

The optimum cell should use intrinsic material, to minimize Auger recombination and free-carrier absorption, and should be around 80- μ m thick, the result of the trade-off between absorption and recombination. It could attain nearly 29% efficiency at one sun AM1.5 Global, 25°C [30].

This ideal case does not tell us where to put the contacts. To realize Condition 4 mentioned above, the contacts should be located at the illuminated or the front face, closest to photogeneration (Figure 7.1a). Because of metal shading losses this threatens

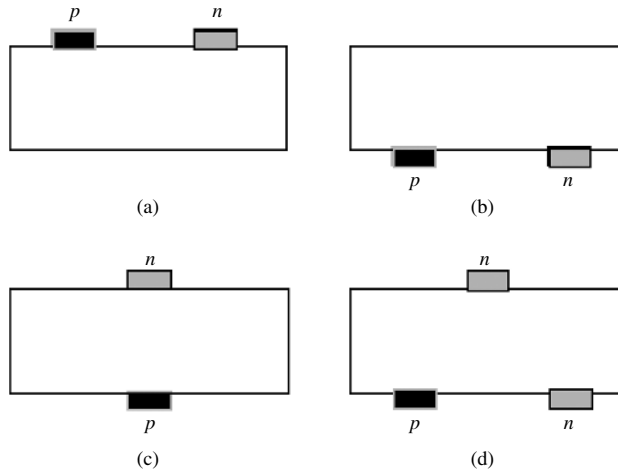


Figure 7.1 Contacting structures: (a) both contacts at the front; and (b) at the back; (c) both faces contacted; and (d) one carrier extracted at both faces. The structures with interchanged n - and p -types are also possible

Condition 3 mentioned above. This solution is being considered for concentration [32]. Putting both contacts at the back works the other way round (Figure 7.1b). Back-contacted cells exhibit record efficiencies under concentration and demonstrate very high values near 23% at one sun [33].

In most cells, each contact is placed on a different face, which is technologically simpler (Figure 7.1c). Minority carriers in the substrate are usually collected at the front since their extraction is more problematic because of their low density. The diffusion length describes the maximum distance from where they can be collected. Majority carriers can drift to the back contact with low loss. Several designs extract minority carriers both at the front and at the back (Figure 7.1d) [34], thus increasing the volume of profitable photogeneration.

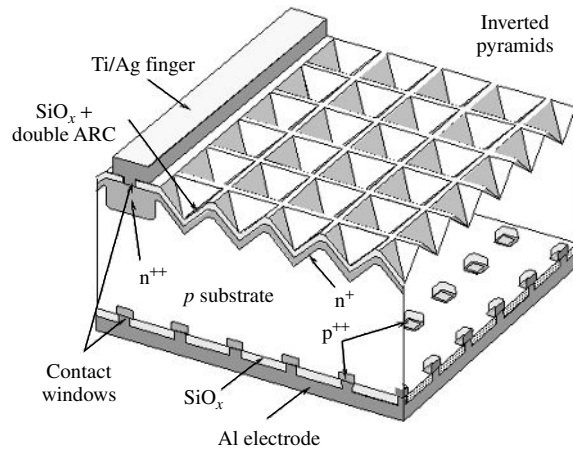
Bifacial cells are designed to collect light incident at both faces, which allows a boost in output power if there is a significant albedo component. They can be implemented with any structure in Figure 7.1 on the condition that both surfaces allow light through [35].

Both 24.7% record-efficiency laboratory solar cells [36] (Figure 7.2a) and mass-produced industrial devices (Figure 7.2b), typically 15% efficient, display the contacting structure in Figure 7.1(c). They will be described in the paragraphs that follow with the aim of illustrating the amplitude and the reasons for the performance gaps between the ideal and the best Si cell, and between this cell and industrial cells.

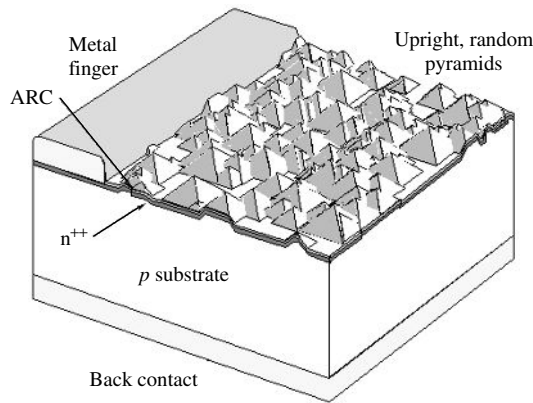
7.3.2 Substrate

7.3.2.1 Materials and processing

Highest efficiencies are achieved with monocrystalline float zone (FZ-Si) material, which in addition to extreme crystalline perfection shows the lowest contamination levels of both



(a)



(b)

Figure 7.2 (a) Passivated emitter and rear locally diffused (PERC) cell; and (b) industrial cell with screen-printed contacts. (Not to scale)

metallic and light (O, C, N) impurities. This translates into the longest post-processing SRH lifetimes in the millisecond range, but still shorter than the Auger limit. Magnetic Czochralski (MCz) material contains much less oxygen than conventional Czochralski and also allows very high efficiencies to be obtained [36].

Industrial cells use Czochralski (Cz-Si) wafers because of their availability. Cz wafers are also perfect crystals but they contain a high concentration of oxygen that affects lifetime in several ways [37]. Some commercial devices are made on multicrystalline (mc-Si) substrates grown in blocks or ribbons with procedures specially developed for photovoltaics. In addition to crystal defects, such as grain boundaries and dislocations, the potential content of metallics is higher because of lower segregation to the melt during the faster solidification process. As a result, the lifetime of mc-Si is lower.

But lifetime is important at the end of solar cell fabrication during which it can undergo strong variations. This issue is handled in different ways in a laboratory and a factory environment. In the laboratory, measures are taken to maintain long initial lifetimes by avoiding contamination during high-temperature steps: furnace cleaning, ultra pure chemicals and so on. In a rough, industrial environment and with defect-containing (Cz- and mc-Si) materials, the problem is more complex: in addition to contamination from the surroundings, impurities and defects in the substrate move, interact and transform at high temperature. The solution is to integrate gettering steps [38] in the fabrication flow that reduce the impact of contamination, and to tailor the thermal treatments to the peculiarities of the material. Final substrate lifetimes of industrial cells range from 1 to 10 μ s.

Gettering techniques eliminate or reduce contaminant impurities in a wafer, and so neutralize the effect of lifetime reduction. Although gettering processes are not always well understood, it is admitted, in general, that in a gettering process a sink region is formed, which is able to accommodate the lifetime-killing impurities in such a way that they are not harmful to the device being manufactured, or at least they are where they can be easily removed.

In solar cell fabrication, we take advantage of the fact that phosphorus and aluminum diffusions, appropriate candidates for emitter and BSF layers, respectively, produce gettering in certain conditions [39]. Other techniques have been explored [40, 41], but their integration in a solar cell process is not so straightforward.

P gettering effect has been proved for a wide variety of P diffusion techniques (spin-on, POCl_3 , PH_3 etc), provided diffusion is done in supersaturation conditions (i.e. over its solid solubility in silicon). Unfortunately, this leaves a “dead layer” of electrically inactive phosphorus near the surface, which reduces UV response of the cells in case it is not etched away [42]. Another phenomenon related to this supersaturated P is the injection of silicon self-interstitials to the bulk of the material, which is responsible for an enhancement of the gettering effect [43].

When Al is deposited on Silicon (by different techniques such as sputtering, vacuum evaporation or screen printing) and annealed over the eutectic temperature (577°C), a liquid Al-Si layer is formed, where impurities tend to segregate because of their enhanced solubility [44]. They will remain in this gettering layer while cooling, so that bulk lifetime will improve after the process.

Another approach to improve material quality is “bulk passivation”, a treatment with hydrogen, for example, during SiN_x deposition, to which some defected materials respond very well [45].

7.3.2.2 Doping level and type

Both laboratory record-efficiency and industrial cells use boron-doped substrates. Rather than fundamental advantages [46], there are practical (properties of P diffusion, easiness of Al alloying) and historical reasons for this preference [47]. However, the situation may change once the role of boron in the degradation of Cz-Si cells under illumination has been established [48].

The optimum substrate doping depends on the cell structure and dominant recombination mechanism. Though intrinsic substrates present the advantage of highest Auger-limiting lifetimes, higher doping is favored when SRH recombination is present, since recombination is proportional to the excess density that decreases, for a given voltage, as doping increases [29]. This is balanced with a reduction of the lifetime itself.

A high doping also helps in minimizing the series resistance losses associated to the transport of carriers to the back face in thick cells with the majority carrier contact at the back.

Doping levels in the 10^{16} cm^{-3} range are found in the substrate of industrial cells. Very high efficiencies have been obtained with both low ($1 \Omega\cdot\text{cm}$ for PERL cells) and high substrate resistivities, as in the point-contact cells [33].

7.3.2.3 Thickness

From the point of view of electrical performance, the choice of the optimum substrate thickness also depends on the structure and the quality of the materials and involves several considerations. In cells with diffusion lengths longer than the thickness, the most important issue is surface recombination: if S at the back is higher than D/L for the minority carriers in the substrate (around $250 \text{ cm}\cdot\text{s}^{-1}$ for the best cells), thinning the cell increases recombination at a given voltage, and vice versa. Thinner cells always absorb less light as well, which is attenuated by light-trapping techniques. Passivated emitter and rear locally diffused (PERL) cells were reported to improve when going from 280- to 400- μm thickness because of a (relatively) high rear surface recombination and nonideal light-trapping [49].

The losses associated with the transport of carriers extracted at the nonilluminated face decrease with thinning: in conventional structure cells; this leads to decreased series resistance. In back-contacted cells, both types of carriers benefit from thinning and the trade-off in absorption leads to lower w values, around 150 to 200 μm .

The diffusion length of industrial cells (around 100 μm) is generally lower than thickness. These cells are rather insensitive to thinning because they collect only the generation near the contact and are not affected by rear surface recombination. The driving criteria are cost and fabricability. A thickness in the 200- to 300- μm range is usually employed but there is a clear trend toward thinner wafers for saving expensive silicon material [47], and advanced wafering techniques and procedures to process very thin, large-area substrates without breaking are being developed: light-trapping and back recombination will become increasingly important.

7.3.3 The Front Surface

7.3.3.1 Metallization techniques

Metal grids are used at the front face to collect the distributedly photogenerated carriers. The compromise between transparency and series resistance requires metallization technologies able to produce very narrow but thick and highly conductive metal lines with

a low contact resistance to Si. Laboratory cells use photolithography and evaporation to form 10- to 15- μm metal fingers. Ti/Pd/Ag structures combine low contact resistance to n -Si and high bulk conductivity. These processes are not well suited to mass production that relies on thick-film technologies. Ag pastes are screen printed, resulting in over 100- μm wide lines with higher bulk and contact resistance. Laser-grooved buried-grid (LGBG) industrial cells implement a finer metallization technology [50], which will be presented in Section 7.7.3.

Coarser metallization techniques imply higher shading and resistance losses, and restrict the efficiency enhancement that could be achieved by internal cell design.

7.3.3.2 Homogeneous emitters

Under the metal lines, the substrate must be heavily doped to make the contact selective. Usually the doped region, the emitter, extends all across the front surface, acting as a “transparent electrode” by offering minority carriers in the substrate a low resistance path to the metal lines.

When the exposed surface is not passivated (Figure 7.3a), the emitter should be as thin as possible, because the high SRV makes the light absorbed in this region poorly collected, and also highly doped to decrease recombination. On the other hand, a sufficient low-sheet resistance is to be achieved. The solution is to make very thin and highly doped emitters.

If the surface is passivated (Figure 7.3b), the collection efficiency of the emitter can be raised by lowering the doping level thus avoiding heavy doping and other detrimental

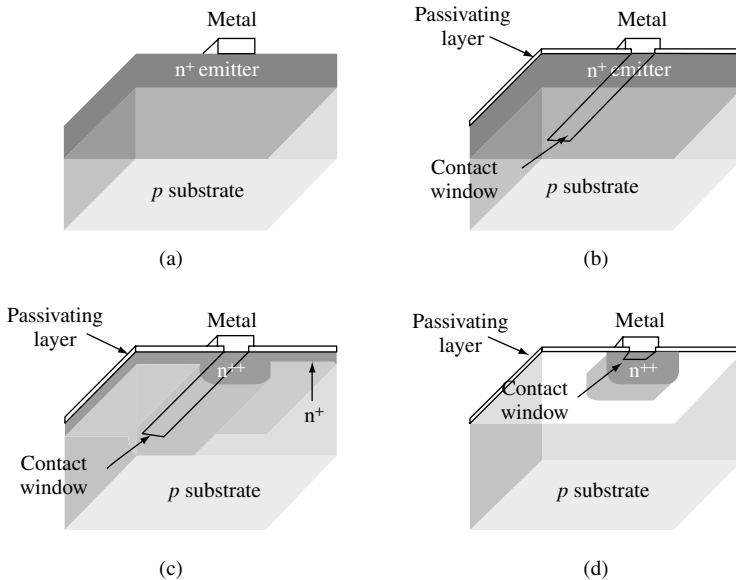


Figure 7.3 Different emitter structures: (a) homogenous emitter without surface passivation; (b) homogenous emitter with surface passivation; (c) selective emitter; and (d) localized emitter

effects. This must be balanced with contact resistance. Etching off of the passivating layer before metallization is usually needed (not in screen-printed cells). To maintain low sheet resistance and diminish recombination at the metallized fraction, the emitter is deep (around 1 μm). Note that the collection of carriers near the surface implies that the emitter is thin in terms of the minority-carrier diffusion length ($w < L$) and so it is very sensitive to surface recombination. Recombination is further reduced, by making the contact window narrower than the finger width, as illustrated in Figure 7.3 [51].

Control of both the surface concentration and the depth of the emitter, is achieved by depositing, in a thermal step, the desired amount of phosphorus or boron (predeposition) and then diffusing it into the substrate (drive-in) during subsequent furnace steps. The MIS solar cell, on the contrary, uses no diffusion for the n region, which is electrostatically induced by charges on top of the surface [20].

The J_0 of the emitter is the average, weighted by the contacted area, of the J_0 of contacted and noncontacted portions.

7.3.3.3 *Selective and point emitters*

A further improvement involves making separate diffusions for the different regions since the requirements are so different (Figure 7.3c) [52]: a heavily doped and thick region under the contacts, a thin and lowly doped region under the passivating layer. These structures, known as “selective emitters”, come at the expense of more complicated processing usually involving photolithographic delineation and alignment of the diffusions (not in LGBG cells to be seen later).

If a very low SRV is possible, it would be best to have no emitter at all since doping always degrades bulk lifetime (Figure 7.3d). Examples are the back point-contact solar cell and the point-emitter design with bifacial contact [53], originally designed for concentration but capable of very high one-sun efficiency as well.

With localized contacts, surface recombination decreases with the penalty of an increase in transport losses in the substrate: deeper gradients for minority carriers, or increased series resistance for majority carriers, because of current crowding near the contacts. The trading is more favorably solved as the contact size shrinks [54]. Light and/or localized diffusions also have the drawback of decreased gettering action.

7.3.3.4 *Industrial cells*

Screen printing drastically affects the design of the emitter: it must be very highly doped to decrease the high-contact resistance and not very shallow so that it is not perforated during paste firing, which would short-circuit the junction [55]. Besides, the wide metal lines must be placed well apart; and in order to keep shading losses moderate, the emitter lateral conductance must be high, which also advises deep and highly doped regions. These characteristics are good to decrease recombination at the contacts, but are far from optimum at the exposed surface.

Industrial phosphorus emitters, typically, feature surface concentrations over 10^{20} cm^{-3} and 0.4- μm depth, and result in a sheet resistance around 40 Ω . As already

mentioned, the very highly doped region exhibits almost no photovoltaic activity due to the presence of precipitates (“dead layer”). As a result, the collection of short-wavelength light is very poor and the J_0 large, irrespective of a hypothetical surface passivation is therefore not implemented. The advantage is that heavy phosphorus diffusions produce very effective gettering. Some ways of incorporating selective emitters to screen-printed cells are being considered, SiN_x appearing very well suited for surface passivation [55]. This, however, must be accompanied by a decrease in the finger width so that lower sheet resistances are tolerated.

7.3.4 The Back Surface

The majority carrier, back p -contact of industrial solar cells is usually made by printing, and subsequently, firing an aluminum-containing Ag-conducting paste.

The p^+ layer would be useful in decreasing contact recombination, as explained, but this is immaterial to the electrically thick ($w > L$) present industrial cells and it is not optimized for this purpose.

For high-efficiency cells, contact passivation is essential. A BSF is a first step (Figure 7.4a). Localized contacts, as shown in Figure 7.4(b), further reduce recombination. This structure is presented by some of the bifacial cells [56].

If the surface passivation is good, the BSF is restricted to point contacts, some microns in size, as in PERL and similar cells (Figure 7.4c) [57]. The back face of bifacial cells passivated with SiN_x is shown in Figure 7.4(d).

A shallow and light diffusion helps in decreasing surface recombination (Figure 7.4e). The diffusion can be the same type of the substrate, or the opposite one: so-called PERT (Passivated emitter rear totally diffused) [36] and PERF (Passivated emitted rear floating junction) [58] cells demonstrate these concepts. The latter structure benefits from the lower J_0 values of n^+ layers, and it is essential that no electron flow is injected from the n region to the p contact: the junction must be in open-circuit (a “floating” junction). Note that this structure has nothing to do with structures sometimes found at the back of industrial cells (Figure 7.4f) where a coarse metal mesh is fired through the parasitic n^+ layer formed during front diffusion. A mesh is preferred to a continuous layer for mechanical reasons. The junction is shorted and presents to the substrate a high SRV.

7.3.5 Size Effects

Substrate edges are highly recombining surfaces that adversely affect cell performance, especially for small size, large diffusion length devices. For laboratory cells, efficiency is defined on the basis of a design area. The emitter is limited to it by planar masking or mesa etching. The true edge is thus placed far away from the cell limit, and then recombination is reduced. For real applications, on the contrary, only the substrate area counts, and edge optimization is more complex. Advanced passivation schemes such as edge diffusions are being considered [59, 60]. In large industrial cells, this recombination is much less important.

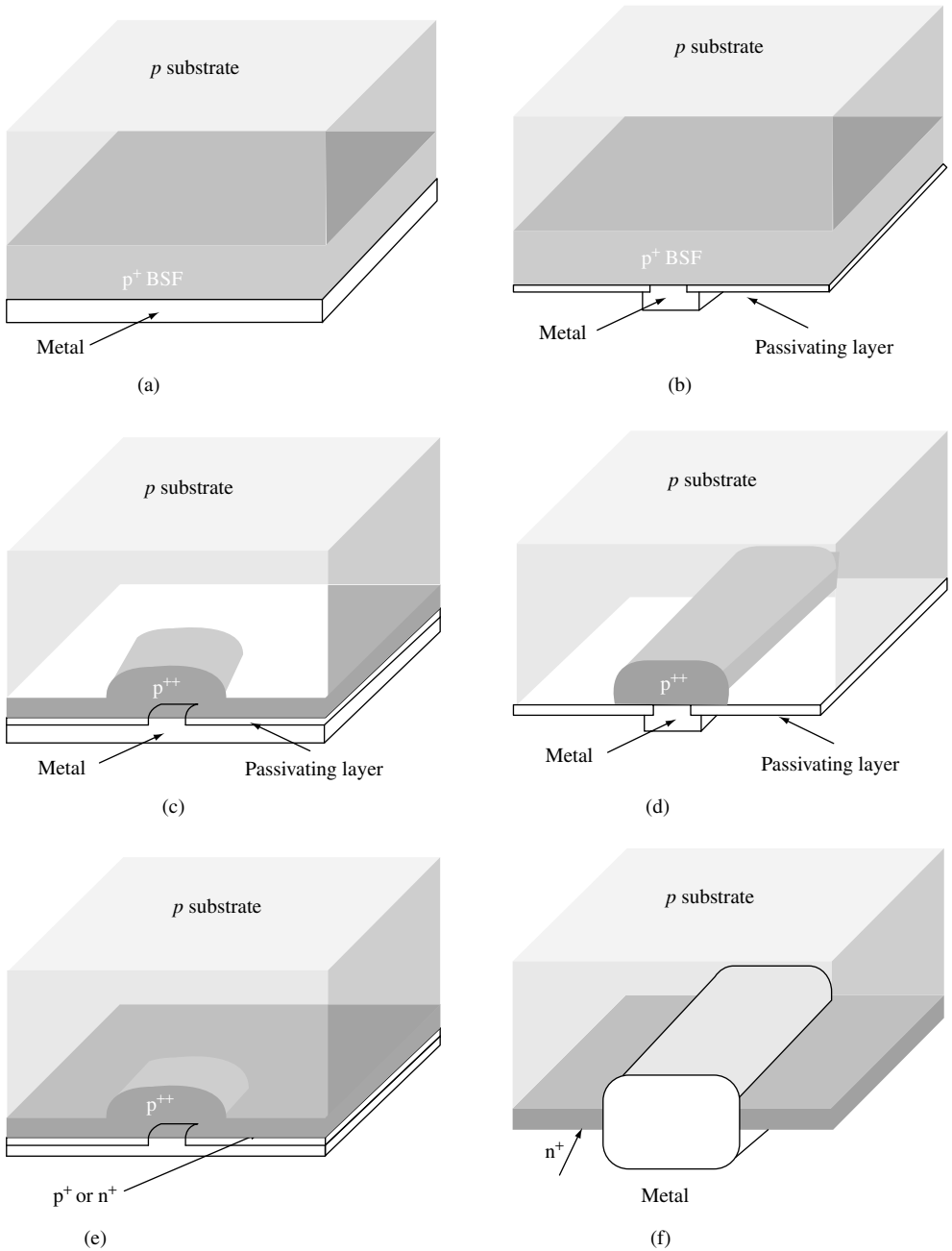


Figure 7.4 Rear contact structures: (a) continuous BSF; (b) bifacial cell; (c) local BSF; (d) local BSF, bifacial cell; (e) selective emitter or floating junction passivation; and (f) shorted junction at the back face of industrial cells

Large cell sizes are preferred by the industry, $10 \times 10 \text{ cm}^2$ or $12.5 \times 12.5 \text{ cm}^2$ being standard. Apart from fabricability concerns, a bigger cell means that more current must be collected at the terminals, making Joule losses grow: the longitudinal resistance of the metal lines increases quadratically with their length. This problem, more severe for coarser metallization techniques, decreases efficiency with increasing size. To alleviate series resistance at the price of increased shading, terminals are soldered to metal bus bars inside the cell's active area, thus decreasing the distance from where current must be collected along the fingers.

7.3.6 Cell Optics

Flat plate solar cells in operation are illuminated from a large portion of the sky, not only because of the isotropic components of radiation, but also because of the sun's apparent motion over the day and the year. So, with regard to angular distribution, these cells must accept light from the whole hemisphere. The spectral distribution also varies with time, weather conditions, and so on. For calibration purposes, a standard spectral distribution AM1.5 Global is adopted as a representative condition, usually specified at $0.1 \text{ W}\cdot\text{cm}^{-2}$.

A solar cell should absorb all useful light. For nonencapsulated cells, the first optical loss is the shading by the metal grid at the illuminated face, if any. This loss can amount to more than 10% for industrial cells while for laboratory cells using fine metallization it is much lower. Though several techniques have been proposed to decrease the effective shading, such as shaped fingers, prismatic covers, or cavities [61], their efficacy depends upon the direction of light and so they are not suited to isotropic illumination.

7.3.6.1 Antireflection coatings

Next, loss comes from the reflectance at the Si interface, more than 30% for bare Si in air due to its high refraction index. A layer of nonabsorbing material with a lower refraction index (n_{ARC}) on top of the Si substrate decreases reflectance: this is a step toward the zero-reflection case of a smoothly varying refraction index. If the layer is thick in terms of the coherence length of the illumination, around $1 \mu\text{m}$ for sunlight, there are no interference effects inside it. The encapsulation (glass plus lamination) belongs to this category.

Antireflection coating (ARC) means an optically thin dielectric layer designed to suppress reflection by interference effects. Reflection is at a minimum when the layer thickness is (an odd multiple of) $n_{\text{ARC}}\lambda_0/4$, with λ_0 the free space wavelength, since in this case reflected components interfere destructively. At other wavelengths reflection increases, but is always below the value with no ARC or, at most, equal [62]. The ARC is usually designed to present the minimum at around 600 nm, where the flux of photons is a maximum in the solar spectrum. For reflection to become zero at the minimum, the coating index should be the geometric average of those of air and silicon, that is, 2.4 at 600 nm for nonencapsulated cells.

The industry uses TiO_x deposited by chemical vapor deposition (CVD). PECVD SiN_x is very interesting since it also serves as a passivating layer, as explained earlier.

By using double layer coatings with $\lambda/4$ design, with growing indices from air to silicon, the minimum in reflection is broader in wavelength. Evaporated SZn and MgF_2

are used in laboratory high-efficiency cells. The low index of passivating SiO_x in contact with Si degrades the performance of the ARC. The SiO_x layer is then made as thin as is compatible with efficient passivation [63].

7.3.6.2 Texturing

Alkaline (KOH or NaOH-based) solutions etch anisotropically a-Si crystal exposing $\{1\ 1\ 1\}$ planes on which the etching rate is lowest. On $[1\ 0\ 0]$ -oriented wafers, randomly distributed, square-base pyramids are formed, whose size is adjusted to a few microns by controlling etching time and temperature. In a textured face, a ray can be reflected toward a neighboring pyramid (Figure 7.5a) and hence absorption is enhanced. Though calculation of reflection requires ray tracing, a rough estimate of near-normal incidence can be derived, by assuming that each ray strikes twice the Si surface so that reflection is the square of the untextured case.

Texturing is incorporated into both industrial and laboratory Si solar cells, and, in combination with antireflection (AR) coating, reduces reflection losses to a few percent. In the latter case, in order to better control the pyramid geometry and to allow delineation of fine features on the surface, photolithographic techniques are used to define inverted or upright pyramids at the desired positions. It has to be noted that in this case the reflectivity is similar to that of a random texture [64].

Light entering the substrate at a textured surface is tilted with respect to the cell normal. This means that photogeneration takes place closer to the collection junction, which is very beneficial for low-diffusion length cells, by enhancing the collection efficiency of medium- to long wavelengths (Figure 7.5a). The effect is equivalent to an increase of the absorption coefficient. As a drawback, textured surfaces present higher SRVs.

7.3.6.3 Light-trapping

Long-wavelength photons are weakly absorbed in silicon, and, unless internal reflectances are high, they will escape the substrate without contributing to photogeneration. The aim of light-trapping or light confinement techniques is to achieve high internal reflectances.

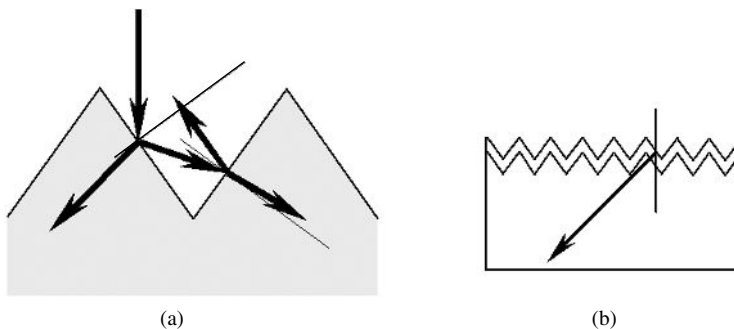


Figure 7.5 Effects of surface texturing: (a) decreased reflection; and (b) increased photogeneration in the base

Practical back mirrors that are fully compatible with the cell electrical design, can be implemented, such as those schematized in Figure 7.4. A metal can make a good reflector, but Al, especially after heat treatment, gives low reflectance. The Si-oxide-metal structure in Figure 7.4(c) can present a high reflectance by capitalizing on interference effects [65].

At the front, the metal mirror is not applicable because the ray paths must be kept open for the entering light. Still, high front reflectance can be achieved because of total internal reflection [61]. Rays striking the surface at angles larger than the critical air-Si one are totally reflected. Texturing one or both surfaces with macroscopic or microscopic features serves this purpose by tilting the rays. Even in the case of geometric texturing with well-defined surface orientations, after a few internal reflections, the direction of rays inside the wafer is randomly distributed: this is the lambertian case, useful analytic approximation to light-trapping. Bifacial structures in Figure 7.4 can, for the same reason, be very efficient at confining the light [66].

Light-trapping increases the effective thickness of the wafer for absorption. In the geometrical optics regime, it has been shown that for one-side isotropic illumination the maximum enhancement factor (though perhaps not realizable) is $4(n_{\text{Si}}/n_{\text{air}})^2$, that is, each ray traverses 50 times the cell thickness before escaping [67]. The corresponding enhancement in photogeneration will be lower because of the competition of the absorption by free carriers at long wavelength.

Light-trapping is essential for thin cells. Even in the thick PERL design it can suppose around $1 \text{ mA}\cdot\text{cm}^{-2}$ enhancement in short-circuit current with respect to the case where the internal reflectances were zero.

7.3.7 Performance Comparison

For illustration purposes, Table 7.3 collects relevant parameters of the Auger-limited ideal Si solar cell [30], the best one-sun PERL cell [36] and a typical screen-printed, industrial cell on Cz-Si. The different concepts behind each set of data must be accounted for when comparing the figures. For instance, the ideal cell is assumed as being isotropically illuminated, while measurements are made for near-normal incidence.

Table 7.3 Cell performance (25°C, AM1.5 Global 0.1 W·cm⁻²)

Cell type	Ideal (calculated)	PERL (measured)	Industrial (typical)
Size (cm ²)	–	4	100
Thickness (μm)	80	450	300
Substrate resistivity (Ω·cm)	Intrinsic	0.5	1
Short-circuit current density, J_{SC} (A·cm ⁻²)	0.0425	0.0422	0.034
Open-circuit voltage, V_{OC} (V)	0.765	0.702	0.600
Fill factor, FF	0.890	0.828	0.740
Efficiency, η (%)	28.8	24.7	15.0

The most striking difference between the best and the ideal solar cell is the difference in design: thick and low injection *versus* thin and high injection. The PERL cell is surely the best design for the currently achievable levels of surface recombination, which limit open-circuit voltage and shift the optimum thickness to high values. The low resistivity follows then from transport considerations for the chosen structure. The very high fill factor of the ideal cell is characteristic of high injection, Auger-limited operation.

Reduction of surface recombination in the best laboratory cells relies on surface passivation and the restriction of very heavily doped regions to a minimum. In the end, this is possible because of the possibility of defining and aligning very small features on the surfaces.

The very heavily doped emitter, along with lower substrate lifetimes, is responsible for the reduced short-circuit current and open-circuit voltage in the industrial cell. The fill factor is affected by the large device area in conjunction with the limitations of the metallization technique, which further reduces the current because of shading.

Continuous improvement in material quality and cost-driven thinning of the substrates will increase the need for industrial cells to implement surface passivation schemes. This will require the refinement of the metallization technique; another issue is that substrate lifetimes in an industrial environment depend on the gettering action of very heavy diffusions, which are not compatible with optimum surface performance. The PERL approach – high-temperature processes and delineation of fine features – is the most successful path to high efficiency, but it is not the only one that can inspire the forthcoming developments in industrial cells. It is worth noting, in this respect, that heterojunction with intrinsic thin-layer (HIT) solar cells have entered the exclusive club of more than 20% efficiency with a different approach (see Section 7.7.2).

7.4 MANUFACTURING PROCESS

7.4.1 Process Flow

Figure 7.6 shows the main steps of a simple process for solar cell fabrication based on screen printing. With more or less minor modifications, this process is currently used by many manufacturers. The main virtues of this 30-year-old PV technology are easy automation, reliability, good usage of materials and high yield. The drawback, as explained in preceding sections, is the efficiency penalty derived from the coarse and aggressive metallization technique. Some specific treatments worked out for mc-Si will be explained in Section 7.6.

Each step is briefly described in the following text with illustrative purposes: values of temperature, time and so on will only be indicative.

1. *Starting material*: The industry uses so-called solar grade Cz-Si wafers, round in origin but very often trimmed to a pseudo-square shape, or multicrystalline square wafers. Wafer dimensions are between 10- and 15-cm side and between 200- and 350- μm thickness. Doping is *p*-type (boron) to a resistivity of around 1 $\Omega\cdot\text{cm}$.
2. *Saw damage removal*: The sawing operation leaves the surfaces of “as cut” wafers with a high degree of damage. This presents two problems: the surface region is of

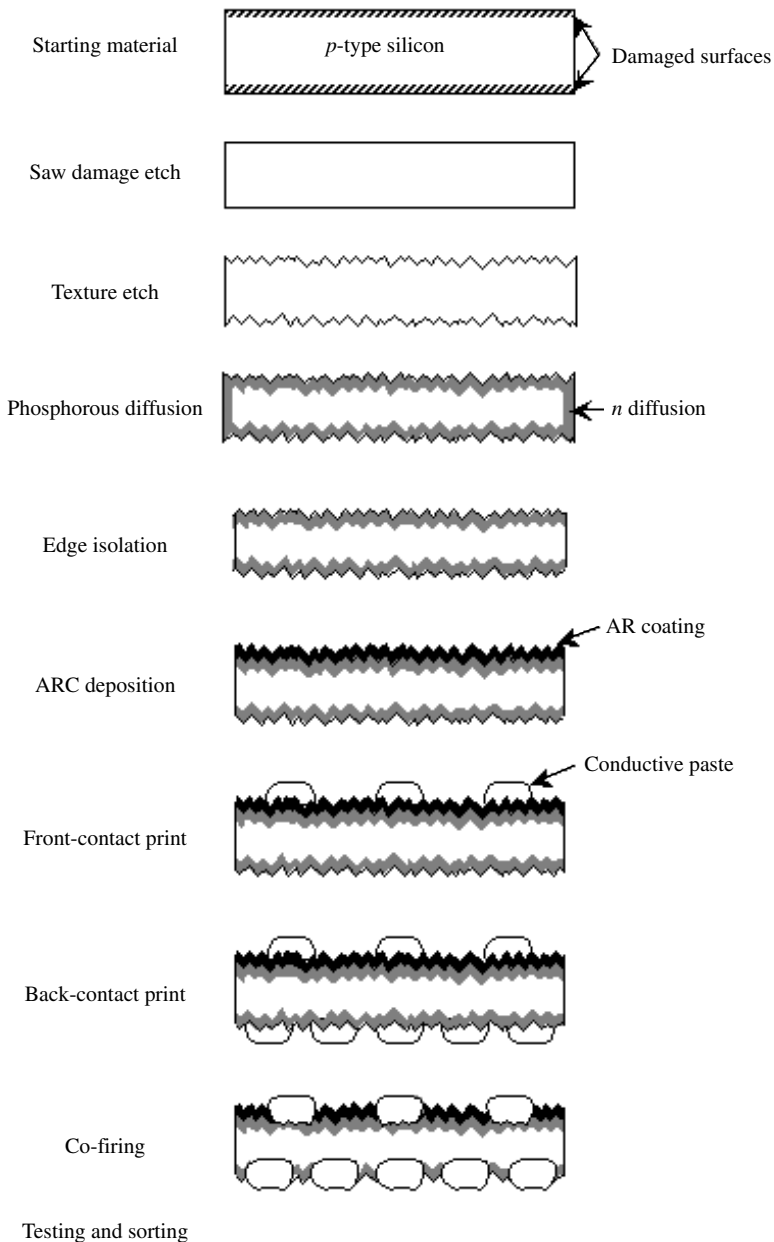


Figure 7.6 A typical processing sequence with schematic illustrations of the resulting structures

a very bad quality and the defects can lead to wafer fracture during processing [68]. For this reason, about ten microns are etched off from each face in alkaline or acid solutions. The wafers, in Teflon cassettes, are immersed in tanks containing the solution under temperature and composition control. Alkaline etches are preferred to acid solutions due to considerations of waste disposal.

3. *Texturization*: NaOH etching leading to microscopic pyramids is commonly employed. Their size must be optimized, since very small pyramids lead to high reflection, while very large ones can hinder the formation of the contacts. To ensure complete texturing coverage and adequate pyramid size, the concentration, the temperature and the agitation of the solution and the duration of the bath must be controlled (in fact NaOH at a higher concentration and at a higher temperature is commonly used as an isotropic etch for saw damage removal). Alcohol is added to improve homogeneity through an enhancement of the wettability of the silicon surface. Typical parameters are 5% NaOH concentration, 80°C and 15 min [69].

Texturing alternatives for multicrystalline material are presented in Section 7.6.

4. *Phosphorus diffusion*: Phosphorus is universally used as the n -type dopant for silicon in solar cells. Since solid-state diffusion demands high temperature, it is very important that the surfaces are contamination-free before processing. To this end, after the texturing the wafers are subjected to acid etch to neutralize alkaline remains and eliminate adsorbed metallic impurities.

The industry uses a number of procedures to perform the phosphorus diffusion. The following classification is based on the type of furnace in which the high-temperature step takes place:

Quartz furnaces: The cells to be diffused, loaded in quartz boats, are placed in a quartz tube with resistance heating and held at the processing temperature (Figure 7.7a). The cells enter and exit the furnace through one end, while gases are fed through the opposite one. Phosphorus itself can be supplied in this way, typically by bubbling nitrogen through liquid POCl_3 before injection into the furnace. Solid dopant sources are also compatible with furnace processing. Five to fifteen minutes at temperatures in the range from 900 to 950°C can be considered representative. As suggested in Figure 7.6, both surfaces and the edges of the wafer will be diffused.

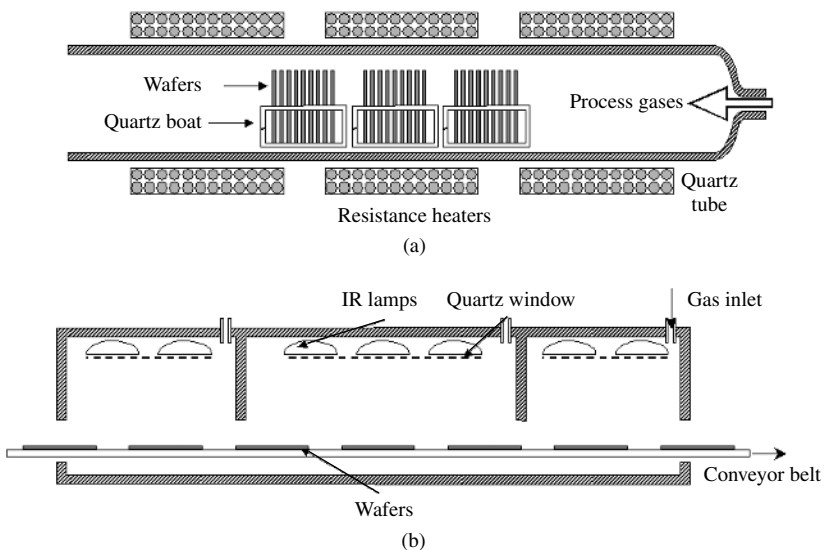


Figure 7.7 (a) A quartz furnace; and (b) a belt furnace for the diffusion of phosphorus

Belt furnaces: In this case, solid phosphorus sources are used: screen printed, spun-on or CVD pastes containing phosphorus compounds are applied on one wafer face and, after drying, placed in a conveyor belt passing through the furnace (Figure 7.7b). The temperature inside it can be adjusted in several zones and, though the furnace is open, gases can be supplied. The temperature cycle undergone by the wafer will mimic the temperature profile along the furnace with the time scale set by the advancing speed of the belt. A cycle begins with several minutes at around 600°C with clean air to burn off the organic materials of the paste, followed by the diffusion step in nitrogen at 950°C for 15 min. Only one face of the wafer is diffused, but the parasitic junction formed at the edges is also present in this technique due to diffusion from the gas phase. Resistance or infrared heating can be employed, the latter offering the possibility of faster heating–cooling rates of the wafer.

The main benefit of the quartz furnace is cleanliness, since no metallic elements are hot and no air flows into the tube. Though this is a batch step, high throughput can be achieved since many wafers can be simultaneously diffused in each tube, commercial furnaces consisting of stacks of four tubes. In a belt furnace, the ambient air can get into the furnace and the hot conveyor belt is a source of metallic impurities. The assets of belt furnaces are found in automation and in-line production, throughput and the ability to implement temperature profiles. New designs try to reconcile the advantages of both types of equipment [70].

After diffusion, an amorphous glass of phospho-silicates remains at the surface that is usually etched off in diluted HF because it can hinder subsequent processing steps.

5. *Junction isolation:* The *n*-type region at the wafer edges would interconnect the front and back contacts: the junction would be shunted by this path translating into a very low shunt resistance. To remove this region, dry etching, low temperature procedures are used.

For the widely employed etch with plasma, the cells are coin-stacked and placed into barrel-type reactors. In this way, the surfaces are protected and only the edges remain exposed to the plasma. This is obtained by exciting with an RF field a fluorine compound (CF₄, SF₆), which produces highly reactive species, ions and electrons that quickly etch the exposed silicon surface [71]. Though this is a batch step, a large number of wafers can simultaneously be processed allowing high throughput. Laser cutting of the wafer edges is an alternative in industrial use.

6. *ARC deposition:* Titanium dioxide (TiO₂) is often used for creating the antireflecting coating due to its near-optimum refraction index for encapsulated cells. A popular technique is atmospheric pressure chemical vapor deposition (APCVD) from titanium organic compounds and water: the mixture is sprayed from a nozzle on the wafer held at around 200°C and the compound is hydrolyzed on the surface [72]. This process is easily automated in a conveyor-belt reactor. Other possibilities include to spin-on or screen print appropriate pastes.

Silicon nitride is also used as AR coating material with unique properties that will be described in Section 7.6.

7. *Front contact print and dry:* The requirements for the front metallization are low contact resistance to silicon, low bulk resistivity, low line width with high aspect ratio, good mechanical adhesion, solderability and compatibility with the encapsulating

materials. Resistivity, price and availability considerations make silver the ideal choice as the contact metal. Copper offers similar advantages, but it does not qualify for screen printing because subsequent heat treatments are needed during which its high diffusivity will produce contamination of the silicon wafer.

Screen printing compares very unfavorably with vacuum evaporation in the first three requirements. It has been already commented how this affects the cell design and leads to a significant efficiency gap between laboratory and commercial cells. But throughput and cost compensate for it.

Screen printing will be described in more depth in the following section. It is used to stick a paste containing silver powder to the front face of the wafer in the comblike (fingers plus bus bars) pattern. Automatic screen printers are available that are capable of in-line, continuous operation with high throughput. These machines accept wafers from packs, cassettes or a belt line, place them with sufficient accuracy under the screen and deliver the printed wafers to the belt line. The paste is a viscous liquid due to the solvents it contains; these are evaporated in an in-line furnace at 100 to 200°C. The dried paste is apt for subsequent processing.

8. *Back contact print and dry*: The same operations are performed on the backside of the cell, except that the paste contains both silver and aluminum and the printed pattern is different.

Aluminum is required because silver does not form ohmic contacts to p -Si, but cannot be used alone because it cannot be soldered. The low eutectic temperature of the Al-Si system means that some silicon will be dissolved and then recrystallize upon cooling in a p -type layer.

Though in principle a continuous contact will give better electrical performance (lower resistance), most commercial wafers feature a back contact with a mesh structure: apart from paste-saving considerations, this is preferred to a continuous layer because the different expansion coefficients would produce warp of the cell during the subsequent thermal step.

9. *Cofiring of metal contacts*: A high-temperature step is still needed: organic components of the paste must be burnt off, the metallic grains must sinter together to form a good conductor, and they must form an intimate electric contact to the underlying silicon. As Figure 7.6 shows, the front paste is deposited on an insulating layer (the AR coating) and the back contact on the parasitic n -type rear layer.

Upon firing, the active component of the front paste must penetrate the ARC coating to contact the n -emitter without shorting it: too mild a heat treatment will render high contact resistance, but too high a firing temperature will motivate the silver to reach through the emitter and contact the base. In extreme situations, this renders the cell useless by short-circuiting it. In more benign cases, small shunts appear as a low shunt resistance or dark current components with a high ideality factor that reduces the fill factor and the open-circuit voltage.

The back paste, in its turn, must completely perforate the parasitic back emitter to reach the base during the firing.

In order to comply with these stringent requirements, the composition of the pastes and the thermal profile of this critical step must be adjusted very carefully.

10. *Testing and sorting*: The illuminated $I-V$ curve of finished cells is measured under an artificial light source with a spectral content similar to sunlight (a sun simulator)

at a controlled temperature of 25°C. Defective devices are then rejected, and the rest are classified according to their output. The manufacturer establishes a number of classes attending, typically, to the cell current at a fixed voltage near the maximum power point. Modules will subsequently be built with cells of the same class, thus guaranteeing minimal mismatch losses. If, for instance, cell currents within a class must be equal within 5%, the accuracy and stability of the system must be better than that. Automatic testing systems that meet the very demanding requirements of high throughput processing are available.

7.4.2 Screen-printing Technology

Screen printing is a thick-film technology, a terminology that opposes it to the usual microelectronic procedures of evaporation of thin films. It consists in translating a layer of a material in a desired pattern to the surface of the wafer. Though it can be employed for virtually any step in solar cell manufacturing, contact formation constitutes the most demanding, frequent and conspicuous application of screen printing. Screens and pastes are the essential elements of this technology [68].

1. *Screens*: Screens are tight fabrics of synthetic or stainless steel wires stretched on an aluminum frame, as sketched in Figure 7.8. The screen is covered with a photosensitive emulsion, which is treated with photographic techniques in such a way that it is removed from the regions where printing is desired.

For printing fine and thick layers, as is needed for the front contact of a solar cell, the wires must be very thin and closely spaced [73]. On the other hand, the opening of the reticule must be several times larger than the largest particle contained in the paste to be printed. Screens for solar cell production typically feature 200 wires per inch, wire diameter around 10 μm , mesh opening around 30 μm , corresponding to

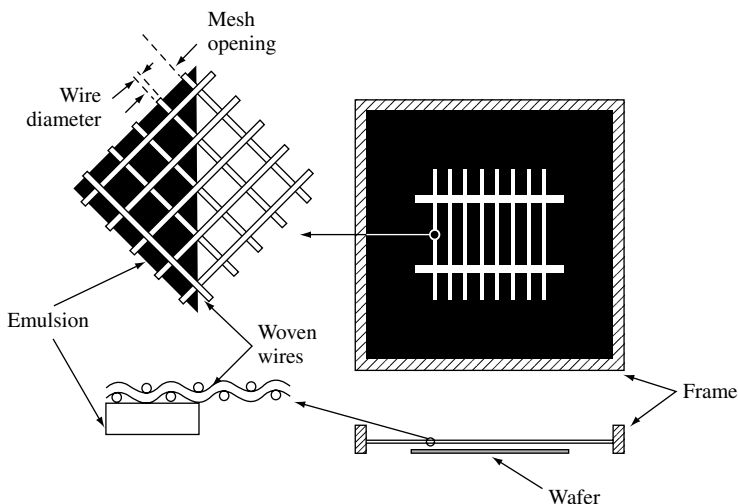


Figure 7.8 A screen for transferring the top contact pattern to a solar cell

nearly 50% open surface, that is, not intercepted by wires and a total thickness (woven wires plus emulsion) of around 100 μm .

2. *Pastes*: The pastes are the vehicles that carry the active material to the wafer surface. Their composition is formulated to optimize the behavior during printing. A paste for the metallic contacts of the solar cell is composed of the following:

Organic solvents that provide the paste with the fluidity required for printing

Organic binders that hold together the active powder before its thermal activation

Conducting material, which is a powder of silver composed of crystallites of a size of tenths of microns; for the *p*-contact, aluminum is also present. This amounts to 60 to 80% in weight of the paste

Glass frit, 5 to 10% in weight, a powder of different oxides (lead, bismuth, silicon etc.) with a low melting point and high reactivity at the process temperature, that enables movement of the silver grains and etches the silicon surface to allow intimate contact.

The paste composition is extremely important for the success of the metallization and is critically linked to the heat treatment.

3. *Printing*: Figure 7.9 illustrates the process of printing a paste through the patterned emulsion on a screen. The screen and the wafer are not in contact, but a distance apart called the *snap-off*. After dispensing the paste, pressure is applied to the squeegee, which can be made of metal or rubber: this puts the screen in contact with the wafer. The squeegee is then moved from one side of the screen to the opposite one, dragging and pressing the paste in front of it. When an opening is reached, the paste fills it and sticks to the wafer, remaining there after the squeegee has passed and the screen has elastically retired.

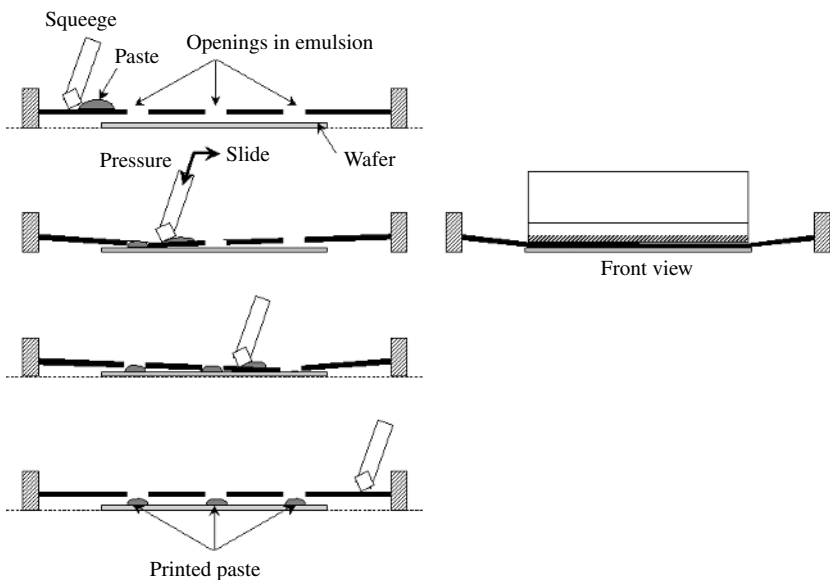


Figure 7.9 Illustration of a printing sequence

The amount of printed paste depends on the thickness of the screen material and the emulsion and the open area of the fabric. It also depends on the printed line width.

The viscous properties are of utmost relevance: when printing, the paste must be fluid enough to fill without voids all the volume allowed by the fabric and the emulsion, but after being printed it must not spread over the surface.

Critical parameters of this process are the pressure applied on the screen, the snap-off distance and the velocity of the squeegee.

4. *Drying*: Solvents are evaporated at 100 to 200°C right after printing so that the wafer can be manipulated without the printed pattern being damaged.
5. *Firing*: Firing of the pastes is usually done as a three-step process in an IR belt furnace. In the first step, when heating up, the organic compounds that bind the powder together are burnt in air. In the next step, the highest temperature between 600 and 800°C is reached and maintained for a few minutes. Higher temperatures are needed if an AR coating must be penetrated; crystal orientation and paste composition must be considered too. In the last step, the wafer is cooled down.

The phenomena that take place during firing are very complex and not completely understood. The oxides forming the glass frit melt, enabling silver grains to sinter and form a continuous conductor so that the layer can present low sheet resistance. Neither the silver melting point nor the silicon–silver eutectic temperature is reached, sintering consisting of the intimate contact of solid silver crystallites. At the same time, the reactive molten glass etches some silicon and silver grains are allowed to form intimate contact with the substrate. The amount of etched silicon is on the order of 100 nm. When a layer of TiO₂ or SiN is present, the glass frit is able to etch through it. In fact, the quality of the contact improves because of a better homogeneity.

The picture of the contact after cooling down shows two zones [74]. In the inner one, crystallites of silver are plugged into silicon forming crystalline interfaces and presumably very good electrical contact in a sort of “point contact”. These grains are embedded in a compact amorphous glass. The outer zone is more porous and contains silver grains and glass frit: this porosity explains why the resistivity of silver paste is much higher than that of pure silver.

Besides, the contact resistance of printed contacts is much higher than that of an evaporated contact to *n*-Si of the same doping. It seems that, although enough silver grains make good contact with silicon, not all them are connected to the grains in the outer layer; many remain isolated by the glass.

When the paste, in the case of the back metallization, contains aluminum as well as silver, the Al-Si eutectic formed and recrystallized ensures a good contact. With dielectric layers the contact appears to be localized as well, and some beneficial role is attributed to the metal atoms in the frit [75].

6. *Limitations and trends in screen printing of contacts*: As explained in former sections, the high contact resistance and the etching action of the glass frit require the front emitters to be highly doped and not very thin if screen printing is used. Only improved paste formulation and processing can overcome this limitation.

Narrow but thick fingers with good sheet conductance are also needed. Well-defined lines must be much wider than the pitch of the woven fabric; 60-μm lines seem achievable, with 100-μm ones being standard (see Figure 7.10). Incrementing the amount of transferred paste implies increasing the thickness of the emulsion or the

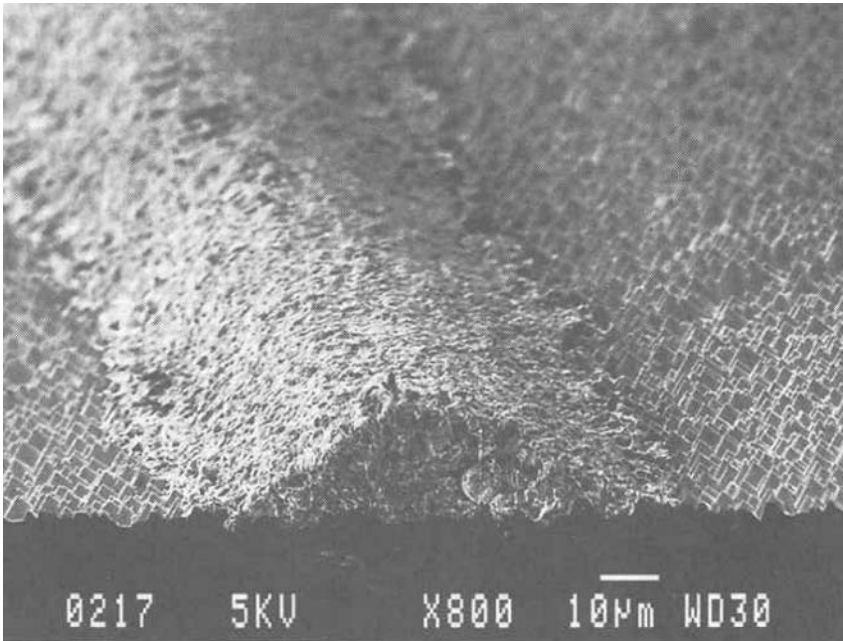


Figure 7.10 Screen-printed contact finger; texture pyramids are also visible. (Reprinted from *Solar Energy Materials and Solar Cells*, **41/42**, Nijs J, Demesmaecker E, Szulfcik J, Poortmans J, Frisson L, De Clerq K, Ghannam M, Mertens R, Van Overstraeten R, “Recent improvements in the screen-printing technology and comparison with the buried contact technology by 2D-simulation”, 101–107, (1997), with permission from Elsevier Science)

pitch-to-diameter ratio of the wires, which are both limited. Besides, screens become deformed with usage and a continuous deterioration of printed patterns is observed.

Metal stencils [76] can outperform screens: they produce finer lines with better aspect ratio, endure more printing operations without degradation and need less cleaning and maintenance.

In screen printing, the wafer is subjected to considerable pressure. This can pose a problem with very thin or irregular wafers, such as those obtained by sheet growth of silicon, which can break down. Metallization alternatives have been developed, some of which are used in industries. They will be presented in Section 7.7.

7.4.3 Throughput and Yield

Because of the rapidly growing demand, photovoltaic factories are quickly expanding their production volumes so that there is a strong driving force to increase the throughput of processes and equipment. Automation is being extensively applied to the fabrication of solar cells and in-line, continuous processing tends to displace batch steps: in the process outlined above, only chemical etches, tube diffusion and edge isolation are batch steps. Automation and large-scale production lead to reduced costs [77].

Most processes described above have been borrowed from the electronic industry: diffusion, plasma etching, and so on are standard in microelectronics, while screen printing

was extensively used by thick-film technology in hybrid circuits. The character of the industries being different, their requirements for equipment differ, and it is to be expected that substantial improvements of photovoltaics will take place, now that the business volume makes it attractive for equipment manufacturers to get involved in.

A modern fabrication line is capable of processing around 1000 wafers h^{-1} , that is, an operation in a cell takes 2 to 3 s. Of course, the slowest operation along the flow line will limit the overall throughput. In order to get an estimate of how this translates into yearly production, let us consider $10 \times 10 \text{ cm}^2$ cells with 15% efficiency (1.5 Wp power per cell). If the line operates without interruption and all wafers are successfully processed, during one year it will produce

$$1.5 \text{ Wp/cell} \times 1000 \text{ cells/h} \times 24 \text{ h/day} \times 365 \text{ days/year} \cong 13 \text{ MWp/year}$$

This number has to be decreased by (1) the downtime of the equipment due to maintenance, repair, and so on and (2) the yield, that is, the percentage of defective or broken wafers. Allowing for both would give a throughput in the range of 5 to 10 MWp/year per production line with available, commercial equipment.

Yield is a most important parameter for cell production: it can be defined as the ratio of successful finished cells to starting wafers. Since PV technology is material-intensive, yield has a strong influence on cost. Breakage and poor electrical performance are the causes of low yield, which is, generally speaking, benefited by automation. In this respect, in-line quality control acquires a great relevance to quickly detect and amend problems affecting yield.

For a given time per operation per cell, the throughput increases if the power of the cell increases. This is achieved by increasing the cell's area and the efficiency, which also helps in decreasing the cost. The standard wafer size is shifting from $10 \times 10 \text{ cm}^2$ to $12.5 \times 12.5 \text{ cm}^2$ and $15 \times 15 \text{ cm}^2$. Series resistance and the uniformity of the obtained layers (emitter, AR coating), that may compromise the electrical performance, become important issues. Besides, larger cells are more difficult to handle without breaking and the yield may be affected.

There is a lot of room for efficiency improvement of industrial solar cells and the processes to realize it are proved in the laboratory. The question is how to implement them in an industrial environment so that they are cost-effective.

7.5 VARIATIONS TO THE BASIC PROCESS

This section introduces some variations to the basic process described above that aims at improving the efficiency, the throughput or the cost. While some modifications are already in production, most of these improvements are still being developed at the laboratory.

7.5.1 Thin Wafers

Wafering and sheet-growth techniques improve and produce thinner substrates, with wafer thickness below $200 \mu\text{m}$ being envisaged for the near term [78]. When processing these thin cells, several relevant issues appear.

The probability of fracture of the wafer during handling increases, especially in conjunction with a larger size. Adequate handling tools must be designed. Some steps appear to be critical: for instance, in chemical baths convection can exert significant torque on the wafers. This issue is fostering the study of the mechanical properties of silicon [79, 80] and even the development of new crystallization procedures.

The behavior during heat treatments is modified due to a decreased thermal mass. On the other hand, wafers can more easily become bent. Processes need to be specifically optimized for thin cells [81].

Thin cells largely depend on surface passivation and optical confinement. If attained to reasonable degrees, efficiency improvement comes as a bonus for thin cells, but otherwise the performance is degraded. New optimal structures must be developed.

7.5.2 Back Surface Passivation

The enhancement of material quality and the decrease of wafer thickness will make it necessary to passivate the back surface. Several approaches are feasible to be incorporated to the basic screen-printing process [55, 82]:

- *Aluminum back surface field*: With the benefit of gettering action, a highly doped *p*-type region at the back can easily be formed by screen-printing aluminum paste on the entire surface followed by high-temperature alloying. Several manufacturers implement aluminum BSF in their production lines. It can be integrated in the process flow (1) before metallization, possibly at the same time as phosphorus diffusion, and (2) by printing the aluminum paste after the front contact print so that the alloy forms during paste firing, though in this case lower temperatures are possible leading to worse properties.

In either case, a back, silver-based contact is still needed for solderability. Bending of the wafers is an issue for thin cells.

- *Boron back surface field*: Like phosphorus, boron can be diffused from solid sources, so that it can easily be integrated into the basic process. Though it would be very attractive to diffuse both phosphorus and boron during the same thermal step, it appears that the obtained profiles are far from optimum and that a two-step diffusion seems necessary.
- *Silicon nitride passivation*: The surface and bulk passivation properties of silicon nitride are explained below. This replaces AR coating deposition and does not alter the basic process, though the parasitic junction must not be allowed to form in this case. This structure, as well as boron BSF, is compatible with the bifacial operation of the solar cell.

7.5.3 Improvements to the Front Emitter

Quantitative improvements in both recombination currents and spectral response will be derived from front surface passivation only when better paste formulations and finer line prints allow more resistive emitters – thinner and/or less doped – to be used [83]. In that case, tube oxidation and silicon nitride deposition appear as good candidates for industrial use.

Selective emitters are being developed at the laboratory level for screen-printed solar cells. A number of techniques have been proposed [84] that are compatible with the screen-printing process; none of them is at present implemented in production lines:

- Two separate diffusions for metallized and unmetallized regions, the heavy diffusion being restricted to the regions to be metallized by a screen-printed mask.
- A homogeneous and thick emitter is diffused by conventional means; a screen-printed mask is applied to protect the regions to be metallized from the plasma etch that follows. In this way, in the unprotected regions the emitter is thinner and less doped.
- Self-aligned selective emitter by diffusion from a patterned solid dopant source: under the dopant source a highly doped emitter is formed, while a much lighter diffusion from the gas phase takes place at the uncovered regions.
- First a high sheet resistance emitter is formed to which self-doping pastes containing phosphorus as well as silver are applied. Firing is performed above the silver–silicon eutectic temperature, thus leading to the formation of an alloyed layer heavily doped with phosphorus [85].

Except the last one, all the techniques require some kind of pattern aligning to print the front contact fingers on the heavily doped regions. Automatic screen printers feature enough accuracy to perform this task.

Obviously, the unmetallized part of these emitters is sensitive to surface passivation, which must thus be implemented by oxidation or nitride deposition.

7.5.4 Rapid Thermal Processes

In conventional furnaces of the closed-tube or conveyor-belt types, not only are the wafers heated to the process temperature but also the equipment itself: chambers, substrates or boats and so on. This brings about (1) long heating–cooling times, due to the large thermal masses involved, (2) a high potential for contamination, since a lot of parts, some of them metallic, are held at a high temperature and (3) high-energy consumption.

On the other hand, the microelectronic industry has developed in the last years, so-called *rapid thermal processes* (RTP), whereby only the wafers, and not their environment, are heated up to high temperature. Selective heating is accomplished by intense UV illumination of the semiconductor. The interest of RTP for solar cell fabrication comes from very short thermal cycles down to a few minutes including heating and cooling, so that throughput can be boosted. Besides, the absence of hot parts in the equipment diminishes potential contamination and energy consumption.

At the laboratory scale rapid thermal diffusion of very thin emitters (which is beneficial from the electrical point of view) has been demonstrated. Rapid thermal firing of screen-printed contacts and aluminum alloying have also been successfully implemented, along with other promising techniques such as rapid thermal nitridation and oxidation of the surfaces for passivation purposes [86, 87]. It can be said that every thermal step in the solar cell process can be made by RTP.

A possible drawback of the technique is a degradation of substrate lifetime as compared to conventional processing of some materials, due to the formation and quenching-in

of defects because of the very fast heating and cooling cycles and possibly also due to precluded gettering action [88].

A hurdle to industrial deployment of RTP is the lack of suitable equipment, since Microelectronics uses one-wafer reactors while Photovoltaics would need large capacity batch reactors or, better, in-line continuous equipment. It seems possible to furnish conveyor-belt furnaces with UV lamps to obtain these industrial RTP reactors, but some problems such as temperature uniformity must be solved [89].

7.6 MULTICRYSTALLINE CELLS

It has already been pointed out that the peculiarities of mc cells may prevent, in some cases, the use of standard processing technologies. Some of the proposed alternatives are not yet so cost-effective as to be incorporated in an industrial production line, but others are finding their way. Two main differences with single-crystalline silicon can be highlighted:

- Mc-material quality is poorer because of crystalline defects (such as grain boundaries, dislocations, etc) and metallic impurities (dissolved or precipitated), giving lower bulk lifetimes and hence lower cell efficiencies. To address this problem, two main strategies are followed: implementation of gettering steps and defect passivation with hydrogen.
- Texturing is more difficult because of different exposed crystallographic planes, so that standard alkaline solutions are not appropriate. To improve light-trapping and absorption, other techniques have to be implemented.

7.6.1 Gettering in mc Solar Cells

As already explained, gettering processes are also used in monocrystalline Si processing, but in the case of mc-Si they are even more important to improve material quality. P and Al gettering steps are routinely integrated in mc solar cell processing. Gettering conditions (temperature, process duration etc) differ from those of single crystal, because of the interaction among metal impurities, crystalline defects and other impurities present in mc-materials (mainly O and C).

It has been realized that gettering efficiency is strongly material dependent [90, 91]. This is explained by the fact that different techniques to grow mc-Si ingots produce wafers with different number and distribution of defects. Differences are even found in regions of the same ingot [92].

Additionally, a single mc wafer may exhibit nonuniform properties, both areal and in-depth, so that response to a gettering process can be inhomogeneous, affecting the final electrical performance of the solar cell [93, 94].

7.6.2 Passivation with Hydrogen

Silicon nitride is widely used as masking film in microelectronics [95]. For solar cells, it presents the advantage of performing as an effective antireflection coating. Films can

be deposited by several techniques, but the most commonly used process is chemical vapor deposition (CVD), involving the reaction of silane gas and ammonia. Plasma-Enhanced Chemical Vapor Deposition (PECVD) is preferred to other CVD technologies (atmospheric pressure CVD or low pressure CVD) because it is a low temperature process ($T < 500^\circ\text{C}$), and this means reducing complexity and preventing lifetime degradation.

But the most outstanding property of PECVD for mc-material is that it produces hydrogenation, and its benefits for silicon are well known [96, 97]. Atomic H interacts with impurities and defects in the bulk of Si, neutralizing their recombination properties to a certain extent, a phenomenon that is usually expressed as “bulk passivation”. In the case of PECVD, amorphous silicon nitride films are produced with up to 40 atomic % of hydrogen (i.e. although these films are usually referred to as SiN_x they are really a- $\text{SiN}_x\text{:H}$). A subsequent thermal step is needed to activate hydrogenation, and in an industrial process the metal firing step fulfills this objective [98].

Additionally, surface passivation due to SiN_x deposition by PECVD has also been reported [99]. Achievable surface recombination velocity on a phosphorus-doped emitter is similar to that of a high-quality oxide passivated one, and a value as low as 4 cm s^{-1} has been obtained on a polished $1.5 \ \Omega\cdot\text{cm}$ FZ *p*-type silicon wafer [100].

These three different properties (AR coating, bulk passivation and surface passivation) cannot be varied independently, an optimization of processing parameters (temperature, plasma excitation power and frequency, gas flow rate) is necessary, and a compromise should be reached [101, 102]. Furthermore, there are different PECVD techniques giving different results.

The state of the art of the industrial PECVD equipments today is the “direct” PECVD, schematized in Figure 7.11(a). The processing gasses are excited by means of an electromagnetic field, and the wafers are located within the plasma. Bulk is effectively passivated, but surface damage is sustained due to direct exposure of wafers to plasma, precluding the achievement of good surface passivation. Furthermore, surface passivation degrades with exposition to UV light.

There is a high frequency direct PECVD (13.56 MHz) and a low frequency one (in the range of 10–500 kHz), the former being better in terms of surface passivation and UV stability. On the other hand, it is more difficult to obtain uniform layers.

A different approach is the “remote” PECVD, where wafers are located outside the region in which the plasma is formed. Surface damage is avoided in this way, so that

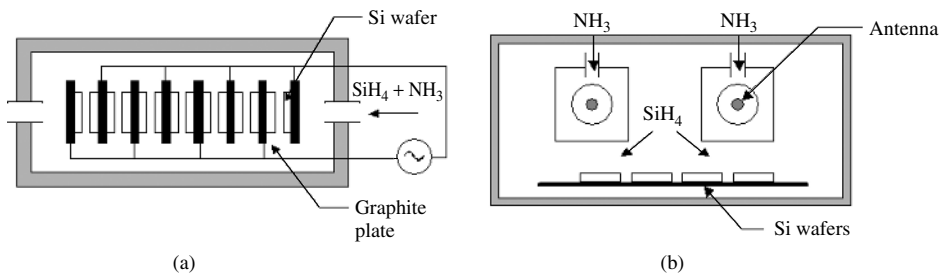


Figure 7.11 Industrial PECVD reactors: (a) direct-plasma reactor; and (b) remote-plasma system

better surface passivation is achieved. On the other hand, bulk passivation is reduced. This technique has been developed at the laboratory level in the last decade, and is currently being introduced into the industry. Figure 7.11(b) shows a sketch of an industrial remote PECVD. It implements a continuous feed of wafers, an advantage that should be compared to the batch-type direct PECVD.

7.6.3 Optical Confinement

Anisotropic texture with alkaline solutions (NaOH or KOH), standard in single crystal solar cells, is also applied to multicrystalline wafers, but with much poorer results, which is one of the reasons for their reduced performance. Reflectance of the textured wafers is relatively high because for randomly oriented grains the etch rate is not the same as that of (100) crystals. Another drawback is the existence of steps between grains, which may cause interruption in the screen-printed metal contacts.

That is why new alternatives are being considered. Their evaluation should take into account not only gains in reflectivity, but also surface damage and compatibility with metallization. In any case, the potential of some of these have been proved, and they are now being developed for industrial applications. Others need more research. The surface features produced by some of these are comparable in size or smaller than the wavelength, and geometrical optics is no longer applicable. They act as diffraction gratings, as scattering media or, in the limit of very small feature size, as graded index layers.

7.6.3.1 Chemical texturing

Several chemical techniques have been proposed. Some of them result in an inverted pyramid structure, but need photolithography patterning, which is a serious drawback for compatibility with the industry [103]. The result of nearly 20% for a mc-Si solar cell relies on an oxide-forced acidic texturing scheme [104]. A simpler approach is based on isotropic etching with an acidic solution containing nitric acid, hydrofluoric acid and some additives. The resulting etch pits of 1–10 μm in diameter are uniformly distributed, giving a homogeneous reflectance over the surface of the wafer and the absence of steps between grains (see Figure 7.12). An increase of short-circuit current of about $1 \text{ mA}\cdot\text{cm}^{-2}$ is reported for solar cells processed on isotropic textured wafers when compared to cells processed on anisotropic textured wafers [105]. Some technical difficulties, such as depletion of the solution and exothermic effects, can be encountered to come to an industrially compatible processing step. An automatic wet-bench, with temperature control of the etching solution and automatic replenishment of chemicals, has been designed recently.

Reduction in reflection, by forming porous silicon, is also being developed [106]. A detailed analysis taking into account the sum of reflectance and absorption within the porous Si layer shows an optimum of about 5 to 6% total optical loss. Besides its potential, the compatibility of the porous Si formation with screen-printed contacts still needs to be addressed.

7.6.3.2 Mechanical texturing

V-grooves about 50- μm deep can be formed in Si wafers by mechanical abrasion using conventional dicing saws and beveled blades, followed by an alkaline etching to reduce

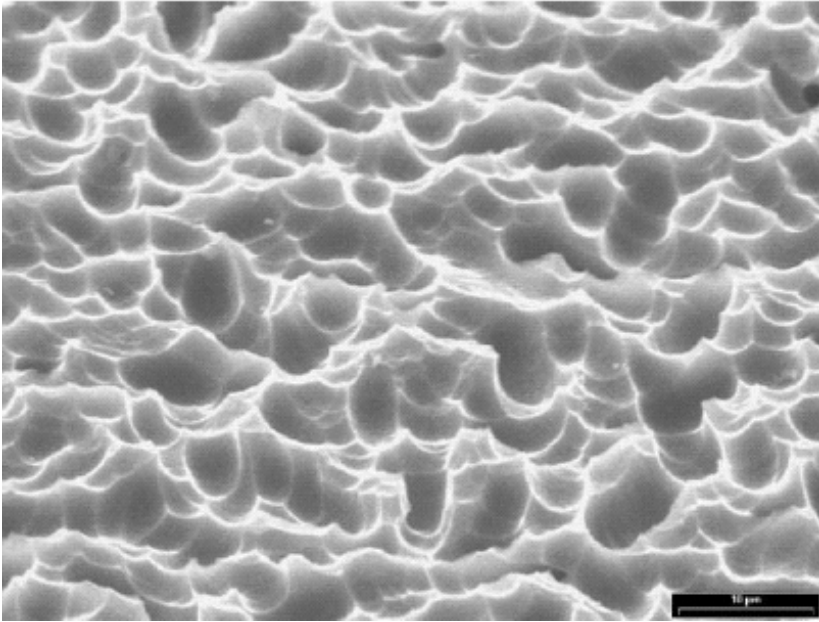


Figure 7.12 Mc-Si surface after acid etching. (Reprinted from *Solar Energy Materials and Solar Cells*, 74, Szulfcik J, Duerinckx F, Horzel J, Van Kerschaver E, Dekkers H, De Wolf S, Choulat P, Allebe C and Nijs J, “High-efficiency low-cost integral screen-printing multicrystalline silicon solar cells”, 155–164, (2002), with permission from Elsevier Science)

surface damage. With this technique, efficiency gains of 5% (relative) after encapsulation have been reached [107]. Contact fingers should be screen printed parallel to the grooves, on plateaus left untextured to ensure easy printing, so that some kind of alignment is maintained. Other contacting alternatives can be implemented, such as roller printing [108] or buried contact [109]. Currently, automated systems are being developed to check industrial feasibility.

Another approach is scribing grooves by laser [110]. Upright pyramids of 7- μm height can be created by two orthogonal sets of parallel grooves, followed by a chemical etch to remove the silicon residues. Combined with a single layer ARC, laser texturing can reduce weighted reflectivity to 4%, half of that given by anisotropic etching and the same AR coating. Adjustments have been made to obtain smoother and smaller grooves, in order to adapt the technique to a screen-printed process.

7.6.3.3 Reactive ion etching (RIE)

Reactive ion etching (RIE) texturization of silicon in chlorine plasma is a dry isotropic etching process that creates a surface with a high density of steep etching pits, with typical dimensions below 1 μm (see Figure 7.13) [111]. Increases of up to 1.4 $\text{mA}\cdot\text{cm}^{-2}$ in short-circuit current compared to anisotropic texture have been reported with a maskless technique [112]. RIE can also be performed in conjunction with a masking layer to produce more regular features [113]. The main obstacle in industrial implementation is too

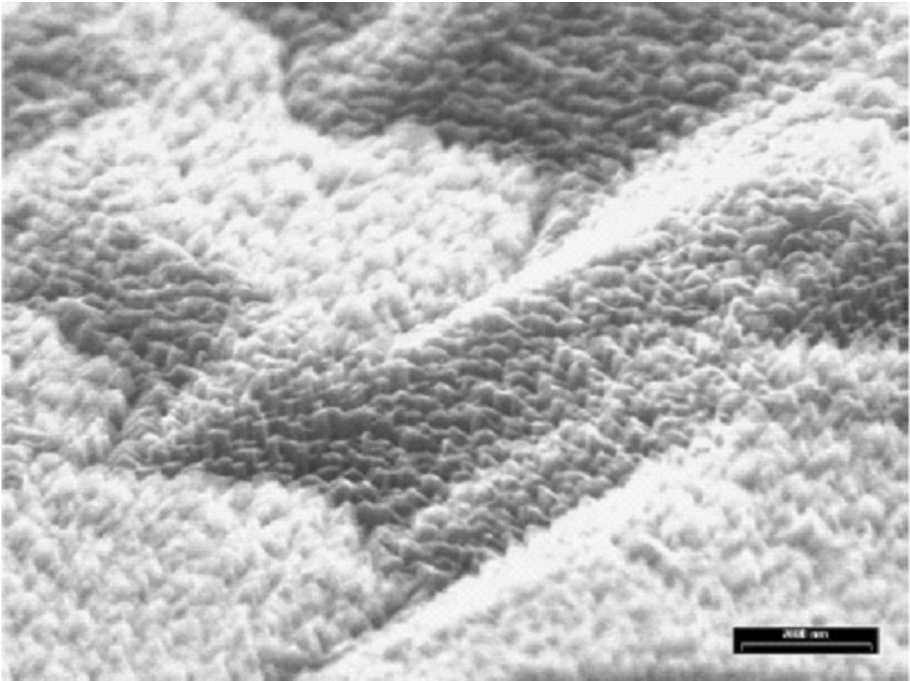


Figure 7.13 Mc-Si surface after RIE. (Reprinted from *Solar Energy Materials and Solar Cells*, 74, Szulfcik J, Duerinckx F, Horzel J, Van Kerschaver E, Dekkers H, De Wolf S, Choulat P, Allebe C and Nijs J, “High-efficiency low-cost integral screen-printing multicrystalline silicon solar cells”, 155–164, (2002), with permission from Elsevier Science)

low process throughput. Alternatives to the use of toxic and corrosive Cl_2 are also being investigated [114].

7.6.3.4 AR coating and encapsulation

It has to be taken into account that cell reflection properties differ from those of texturing because it is usually complemented by AR coating (typically, by atmospheric pressure CVD deposition of TiO_2 or $\text{TiO}_2/\text{SnO}_2$ or by PECVD of SiN_x), and cell encapsulation, so that the relative difference between several texturing methods normally reduces, as can be noticed in Table 7.4.

Table 7.4 Comparison of weighted AM1.5 reflectivities for mc-Si wafers with several surface treatments [115]

Reflectivity [%]	Alkaline textured	Acidic textured	Maskless RIE
Bare	34.4	27.6	11.0
With SiN AR coating	9.0	8.0	3.9
SiN & encapsulated	12.9	9.2	7.6

7.7 OTHER INDUSTRIAL APPROACHES

Other commercially available technologies will be described in this section. They all look for a decrease in the $\$ W^{-1}$ figure of merit, following different approaches:

- using ribbons, presented in Chapter 6, as substrates;
- implementing techniques that do not need high-temperature processes: HIT, based on a-Si/*x*-Si heterojunction emitter;
- substituting screen-printing metallization by a more efficient technique: LGBG, based on the buried contact concept;

These only cover a small fraction of the PV market today, but they all have big expansion plans for the next few years.

7.7.1 Silicon Ribbons

Ribbon technologies offer a cost advantage over crystalline silicon, thanks to the elimination of the slicing process. They cover at the moment around 5% of the PV market, Edge-defined-Film-fed Growth (EFG) being the most mature of them, while string ribbon (STR) and dendritic web (WEB) are also into industrial production.

A specific solar cell process is needed for ribbon substrates, to account for the high density of defects (dislocations, grain boundaries, impurities, etc). Al paste is usually printed to create a deep BSF and to benefit from gettering, and silicon nitride is deposited by PECVD for bulk defect passivation and anti-reflection coating.

For EFG solar cells, the uneven surface of the sheets precludes the use of screen-printing metallization, and back and front contact formation is done by pad-printing and direct writing (extrusion) of silver pastes and inks. Efficiencies exceeding 14% on an average have been produced in the manufacturing line, achieving more than 14.7% in some cases [116]. Further reduction of production costs is expected by the growth of large-diameter EFG cylinders, which reduce thermoelastic stresses and can result in thinner and more uniform wafers. Thin curved wafers will require new technology for solar cell processing.

In the case of STR, 14.7% efficiencies have been reported for a process including screen-printed contacts fired with RTP [117], and 50 and 100 W modules are commercially available [118]. Regarding dendritic web, an $n^+ np^+$ structure (phosphorus front diffusion and rear Al alloyed emitter) is implemented on a high-resistivity antimony-doped substrate. Because of the low substrate thickness (100 μm), it can benefit from the location of the p - n junction at the back, performing an effective front surface field, enabling a high diffusion length and immunity to light-induced degradation. Using only production-worthy, high-throughput processes, dendritic web cells have been fabricated with efficiencies of up to 14.2% [119].

7.7.2 Heterojunction with Intrinsic Thin Layer

A new structure called HIT has been developed recently, which makes use of the cheaper amorphous silicon (a-Si) technology, depositing a-Si layers on crystalline silicon by

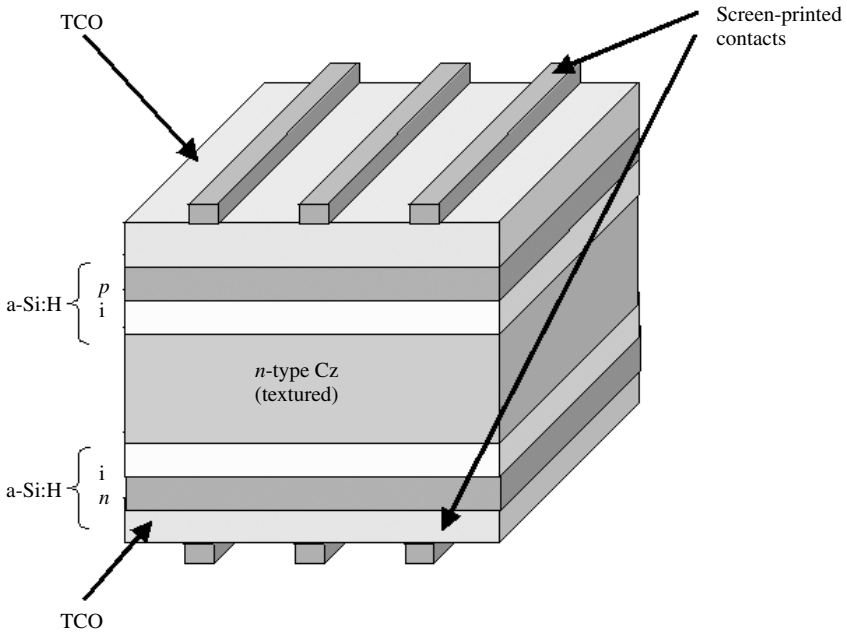


Figure 7.14 Structure of the HIT cell

PECVD [120]. It provides an excellent surface passivation with very low temperature processes (below 200°C), avoiding lifetime degradation of the bulk material. Figure 7.14 shows the structure of the HIT cell. A textured n -type Cz-Si substrate is used. The emitter and BSF are made of p -type and n -type a-Si layers, respectively. Very thin intrinsic a-Si layers are inserted between a-Si and the crystalline substrate, to improve the characteristics of the a-Si/c-Si interface. Thickness of these amorphous layers is on the order of 10 to 20 nm. On both doped layers, transparent conductive oxide (TCO) layers are formed, by sputtering, and metal fingers are screen printed. Back metallization is also combllike to reduce thermal and mechanical stresses, making the cell symmetrical and enabling it to perform as a bifacial cell.

In 1994, 20% efficiency was achieved with a similar HIT structure on a 1 cm^2 cell. Mass production of HIT cells started in 1997, with conversion efficiencies of 17.3% on 100 cm^2 substrates. 180 W modules are fabricated, and special modules exist for roof-tile and bifacial applications.

7.7.3 Buried Contact Technology

The buried contact solar cell process was developed at the University of New South Wales [50]. It is based on forming grooves in the silicon surface, where the metal is deposited by electroless plating, so that high aspect ratios and low metal shading losses are achieved. Several techniques have been proposed for groove formation, laser scribing being the most attractive for large-scale production. A metallized groove, typically $40\text{-}\mu\text{m}$ deep and $20\text{-}\mu\text{m}$ wide, is presented in Figure 7.15. Additionally, other high-efficiency

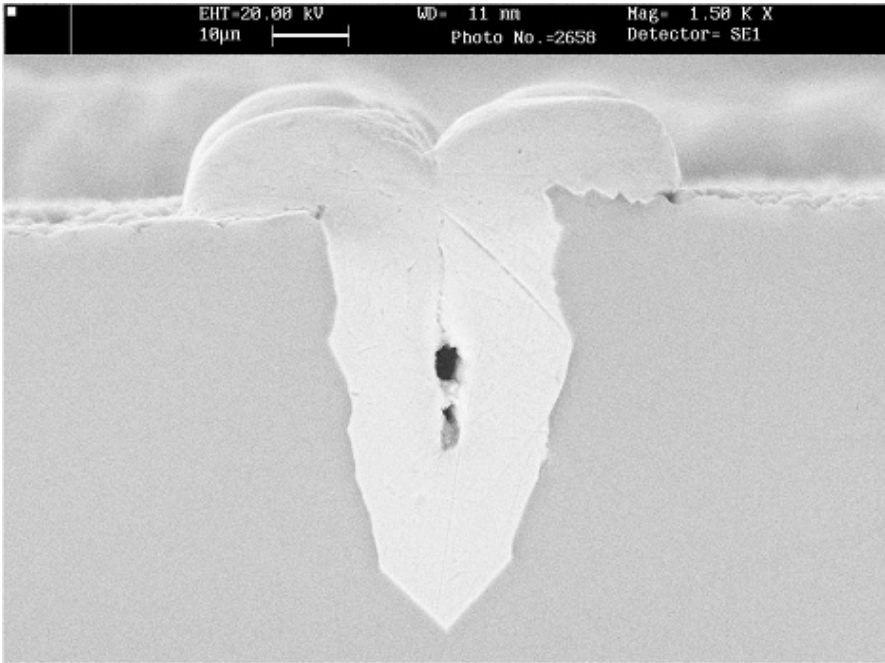


Figure 7.15 Cross-section of a buried contact. (Reprinted with permission from BP Solar)

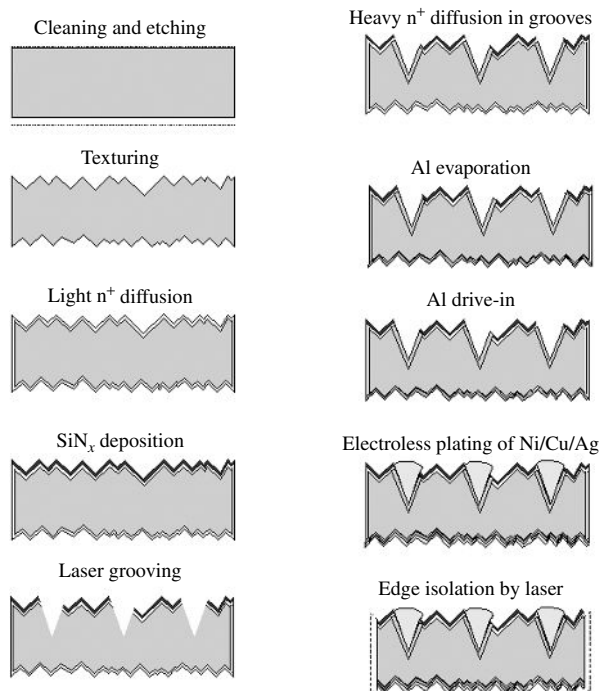


Figure 7.16 Laser-grooved buried-grid solar cell process

features are implemented, such as a selective emitter (highly doped under the metal fingers and low-doped and surface-passivated in the active area) and a Back Surface Field by Al evaporation and alloying, which also produces gettering effect.

The buried contact solar cell has been licensed to many manufacturers, but for the moment only one of them has implemented it at the industrial level, commercializing it as the LGBG solar cell. The LGBG process is sketched in Figure 7.16. Three high-temperature steps are needed, and a number of wet steps must be performed. A key element is the silicon nitride layer, which serves as a masking layer for heavy phosphorus diffusion and plating, and also performs as an antireflection coating and surface passivator. Efficiencies of 17% are routinely achieved with Cz-Si [121], and improvements are being researched and implemented to further increase cell efficiency [122].

The buried contact approach relies on compensating the increase in process complexity as compared to screen-printed technology with an increase in cell efficiency. A midway is proposed with a simplified buried contact solar cell process, with only one high-temperature step, TiO₂ antireflection coating and screen-printed Al BSF [123].

7.8 CRYSTALLINE SILICON PHOTOVOLTAIC MODULES

The power of a single solar cell being small, several of them must be electrically associated to make a practical generator. The module is the building unit for generators that can be purchased in the market, that is, it is the real PV product. Performance and lifetime of PV systems depend on the protection that module construction offers to the active photovoltaic devices.

The basic module fabrication procedure used by most manufacturers was developed three decades ago and is described below briefly. Modules for special applications (building integration, marine operation, etc) require slight modifications of the process and the materials.

7.8.1 Cell Matrix

In a module, the cells are usually arranged in series. After cell finishing, tinned copper ribbons (tabs) are soldered to the bus bars at the front (Figure 7.17a). It has to be noted that tabs must overlap a long distance along bus bar length since the conductance of the printed bus bars is too low. Conductive epoxies can replace conventional solder alloys and illumination used instead of iron heating.

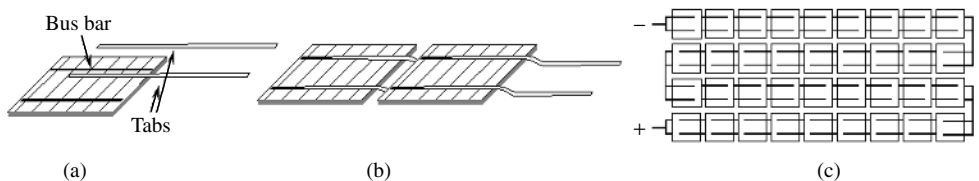


Figure 7.17 (a) Cell interconnection with tabs; (b) two cells in series; and (c) layout of 36 series-connected cells

Two tabs per cell are employed thus providing redundancy that allows current to flow in case electrical continuity is broken because of some failure [124]. Besides, the effective length of grid fingers is one-fourth the cell side and series resistance is alleviated. Tabs provide a nonrigid link between cells that allow thermal expansions to be accommodated.

Series interconnection of strings by soldering the tabs to the rear side of another cell follows (Figure 7.17b). The strings are interconnected with auxiliary tabs to form the cell matrix. This can consist of a single series string or several strings (Figure 7.17c). If the strings are not internally paralleled, their terminals are brought outside the module to permit flexible circuit configuration.

A common module configuration uses 36 series-connected cells, which, under operating conditions, would produce around 15 V at maximum power, appropriate for 12 V battery charging [125]. As building-integrated, grid-connected applications grow, modules with different electrical configurations enter the market.

A few years ago these operations were performed manually, but current factories use sophisticated equipment that performs most of the operations automatically. Both throughput and yield benefit from automation since the connected cells are very fragile and difficult to handle.

7.8.2 The Layers of the Module

The array of cells must be properly encapsulated for reliable outdoor operation for more than 20 years, paying attention to factors like rigidity to withstand mechanical loads, protection from weather agents and humidity, protection from impacts, electrical isolation for the safety of people and so on.

The different layers that the module is made up of are then stacked. A common structure is sketched in Figure 7.18.

A 2- to 3-mm thick soda lime glass is used as a superstrate that provides mechanical rigidity and protection to the module while allowing light through. It must have low iron content or otherwise the light transmission will be low. Modern modules use glass with cerium that absorbs UV radiation to enhance reliability [126]. Tempered glass must be employed to increase the resistance to impacts.

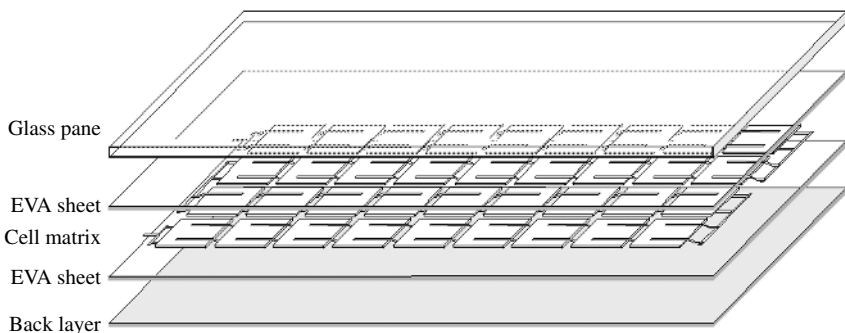


Figure 7.18 Stack of materials to be laminated

The cell matrix is sandwiched between two layers of the encapsulant or pottant material. The most popular encapsulant is the copolymer ethylene-vinyl-acetate (EVA), a plastic composed of long molecules with a backbone of carbon atoms with single covalent bonding. EVA is a thermoplastic, that is, shape changes made under heating are reversible. It is sold in rolls of extruded film around 0.5-mm thick. Along with the polymer, the film contains (1) curing agents and (2) stabilizers whose role will be described later.

The outer layer at the nonilluminated module side is usually a composite plastic sheet acting as a barrier for humidity and corroding species. Some manufacturers use another glass, which increases protection.

7.8.3 Lamination and Curing

These steps are carried out in a laminator, a table that can be heated and furnished with a cover that closes the edges tightly. The cover has an internal chamber and a diaphragm that separates this from the chamber containing the module. Both chambers can be independently evacuated: this configuration allows the module to be kept in a vacuum while mechanical pressure is exerted on it.

In the lamination stage, both chambers are evacuated while temperature is raised above the EVA melting point at around 120°C. Vacuum is important to extract air – to prevent voids from forming – and moisture and other gases. The EVA flows and embeds the cells. After a few minutes, with the module chamber still in vacuum, the upper chamber is filled with air so that the diaphragm presses the laminate. The temperature is increased to 150°C and the curing stage begins: the curing agents induce cross-linking of the EVA chains, that is, chemical bonds are formed transversely among the long molecules that before curing are only weakly linked to one another. The plastic then acquires elastomeric, rubberlike properties and indeed the curing step is analogous to the vulcanization of rubber. This stage takes up to 60 min for standard cure EVA [127]. After cooling down, the laminates are unloaded from the laminator.

Lamination used to be a bottleneck in the module fabrication process. To improve throughput several solutions have been followed by the industry: (1) commercial fast-curing EVA formulations allow drastic reductions of curing time to less than 10 min [128], (2) performing the curing step in a separate oven decreases the residence time in the laminator and (3) a large lamination area – up to several square meters – enables simultaneous process of several modules or very large ones.

Another polymeric material, poly vinyl butyral (PVB), was used in early times of module fabrication. It is processed in a similar way to EVA and can present some advantages over EVA [129] but it requires low temperature storing. For modules using two glass panes, resin fill-in is an alternative to EVA with reliability advantages. A sealed cavity is formed between the glass panes with the cells in-between and the liquid resin is poured into it. Care must be taken to ensure that no bubbles form [125]. Resins do not require heating to cure. Silicone resins are expensive but very stable and some modules for building integration use them. Yet curing can be inhibited by the module sealant so that they are difficult to handle. Acrylic resins with UV curing are being investigated.

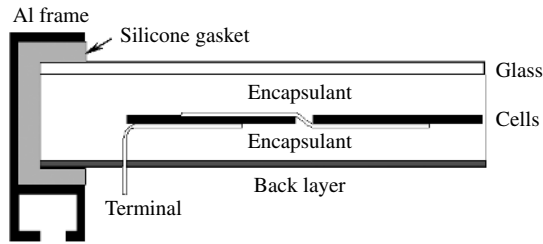


Figure 7.19 Cross-section of a standard module

7.8.4 Postlamination Steps

These include (1) trimming the edges of the laminate to remove spread-out encapsulant, (2) sealing them with silicone rubber to close this potential path of moisture penetration in the module, (3) sticking the plastic junction box at the back of the laminate and performing the connections and (4) when required, installing the anodized aluminum frame (Figure 7.19). The frame must be electrically insulated from the active cell circuit so that high-voltage differences can be sustained between the electrical terminals and the frame without current flow.

Besides, among other final tests, the $I-V$ curve of all modules under standard conditions is measured in a solar simulator to check if they fulfill specifications. Flash simulators are commonly utilized to save energy, with the electronic equipment able to record a complete $I-V$ curve in a fraction of a second. They must have a spectral content matched to the AM1.5 standard, or else, they must be calibrated with a calibrated cell of the same technology.

7.8.5 Special Modules

7.8.5.1 BIPV products

Building integration of PV modules (BIPV) has emerged as one of the most important – by volume – applications of Photovoltaics. Modules perform two tasks: as constructive materials as well as power generators. Modules can be incorporated to a building in a number of ways and special products are being developed so that the typical framed module is no longer the only PV product. Very large modules with special fixing for roof or façade integration, roof tiles with cells and semitransparent modules allowing light through are available. Visual appearance is enhanced by module shape, encapsulation and cell color [130]. Besides, these products must comply with building normative such as fire resistance.

7.8.5.2 Bifacial modules

Several cell structures have been presented that can operate with bifacial illumination. By encapsulation between two glass panes, bifacial modules offering increased power output per unit cell area can be produced without technology changes. In spite of their potential, their presence in the market is very small at the moment.

7.8.5.3 Modules with back contact cells

Several cell structures have been proposed that bring both contacts to the back face, which is usually accomplished by implementing phosphorus diffusions at both faces that are internally connected through processing. They fit the scheme in Figure 7.1(d) [131]. Back contact cells are interconnected without tabs by soldering them to a layer with the connection paths printed, similar to PCB practice in electronic circuits. These experimental designs offer simplified module fabrication and enhanced visual appeal.

7.9 ELECTRICAL AND OPTICAL PERFORMANCE OF MODULES

7.9.1 Electrical and Thermal Characteristics

The voltage of the module is, in principle, the number of series-connected cells times the voltage of the single cell, and the module current the number of paralleled cells times the single cell current. Whatever the combination, the module power equals the power of a single cell times the number of them. Mass-produced modules offered in the catalogues of manufacturers show power ratings that typically range from 50 to 200 Wp, delivered at current levels between 3 and 8 A and at voltages between 20 and 40 V. Lower and higher values are possible for special applications.

The manufacturer usually provides values of representative points (short-circuit, open-circuit and maximum power) of the module $I-V$ curve measured at standard cell conditions (STC), that is, $1 \text{ kW}\cdot\text{m}^{-2}$ irradiance ($=0.1 \text{ W}\cdot\text{cm}^{-2}$), AM1.5 spectral distribution and 25°C cell temperature. The maximum power of the module under STC is called the peak power and given in watts-peak (Wp). While efficiency has the greatest importance for a solar cell, for a module it has the less relevant meaning since part of the area is not occupied by the expensive solar cells.

The conditions in real operation are not the standard ones; instead, they vary strongly and influence the electrical performance of the cell, causing an efficiency loss with respect to the STC nominal value. This loss can be divided into four main categories [132]:

1. *Angular distribution of light*: Because of the movement of the sun and the diffuse components of the radiation, light does not fall perpendicular to the module, as is the case when measurements are done and the nominal efficiency is determined.
2. *Spectral content of light*: For the same power content, different spectra produce different cell photocurrents according to the spectral response. And the solar spectrum varies with the sun's position, weather and pollution and so on, and never exactly matches the AM1.5 standard.
3. *Irradiance level*: For a constant cell temperature, the efficiency of the module decreases with diminished irradiance levels. For irradiances near one sun, this is primarily due to the logarithmic dependence of open-circuit voltage on photocurrent; at very low illumination the efficiency loss is faster and less predictable.
4. *Cell temperature*: The ambient temperature changes and, because of the thermal insulation provided by the encapsulation, light makes cells in the module heat over it;

higher temperature means reduced performance. This is usually the most important performance loss.

But, prediction of the module response under different conditions is required to correctly assess the yearly production of a PV system in the field. The physical mechanisms of influence of temperature and irradiance on cell performance are well known, so that, in principle, prediction of module output could be rooted in physical models. This is however unpractical and would be a different approach if followed by PV system engineers.

Instead, very simple methods are used for translating the $I-V$ performance to different operating conditions and standardized procedures have been developed for PV modules of industrial technologies [133]. These methods are applicable within a limited range of temperature and irradiance conditions that are not very far from those met when testing the module and which require a small number of easily measurable parameters. The module datasheets from the manufacturers used to include some of these, allowing simplest estimates to be made, such as:

1. The steady-state power balance determines cell temperature: the input is the absorbed luminous power, which is partially converted into useful electrical output and the rest is dissipated into the surroundings. Convection is the main mechanism for heat dissipation in terrestrial, flat plate applications, and radiation is the second nonnegligible mechanism of heat dissipation. A common simplifying assumption is made that the cell-ambient temperature drop increases linearly with irradiance. The coefficient depends on module installation, wind speed, ambient humidity and so on, though a single value is used to characterize a module type. This information is contained in the Nominal Operating Cell Temperature (*NOCT*), which is defined as the cell temperature when the ambient temperature is 20°C , irradiance is $0.8 \text{ kW}\cdot\text{m}^{-2}$ and wind speed is $1 \text{ m}\cdot\text{s}^{-1}$. *NOCT* values around 45°C are typical. For different irradiance values G , this will be obtained by

$$T_{\text{cell}} = T_{\text{ambient}} + G \times \frac{\text{NOCT} - 20^{\circ}\text{C}}{0.8 \text{ kW}\cdot\text{m}^{-2}}$$

2. The module short-circuit current is assumed strictly proportional to irradiance. It slightly increases with cell temperature (this stems from a decrease in band gap and an improvement of minority-carrier lifetimes). The coefficient α gives the relative current increment per degree centigrade. By combining both assumptions, the short-circuit current for arbitrary irradiance and cell temperature is calculated as

$$I_{\text{SC}}(T_{\text{cell}}, G) = I_{\text{SC}}(\text{STC}) \times \frac{G}{1 \text{ kW}\cdot\text{m}^{-2}} \times [1 + \alpha(T_{\text{cell}} - 25^{\circ}\text{C})]$$

For crystalline Si, α is around 0.4% per degree centigrade.

3. The open-circuit voltage strongly depends on temperature (the main influence is that of the intrinsic concentration), decreasing linearly with it. Knowledge of the coefficient, called β , allows the open-circuit voltage to be predicted by

$$V_{\text{OC}}(T_{\text{cell}}, G) = V_{\text{OC}}(\text{STC}) - \beta(T_{\text{cell}} - 25^{\circ}\text{C})$$

The irradiance dependence is buried in T_{cell} . For crystalline Si, β is around $2 \text{ mV}/^{\circ}\text{C}$ per series-connected cell.

4. A lot of factors affect the variation of the maximum power (or, equivalently, the efficiency) with irradiance and temperature. The parameter γ is defined as the relative decrease in module efficiency per degree centigrade of cell temperature increase

$$\eta(T_{\text{cell}}, G) = \eta(\text{STC}) \times [1 - \gamma(T_{\text{cell}} - 25^{\circ}\text{C})]$$

Usual γ values are near 0.5% per degree centigrade.

7.9.2 Fabrication Spread and Mismatch Losses

So-called mismatch losses arise when cells with different $I-V$ characteristics are interconnected because of the fewer degrees of freedom left to bias the devices, so that the array output is less than the sum of the powers that the individual cells could deliver. The differences come from the unavoidable fabrication spread or from nonuniform irradiance or working temperature within the array.

To minimize mismatch losses, finished cells are measured and sorted in the factory. For series connection, the important parameter is the current at the maximum power point (mpp). It is the common practice to measure the current before encapsulation at a fixed voltage close to the mpp and to classify the cells accordingly, though other classification criteria are possible [134]. Within each class all devices present similar currents within the specified tolerance that ensures that, when connected in series to form the module, the mismatch loss will be below the desired limit [135]. Depending on the class being processed, the power rating of the resulting module will vary and this explains why manufacturers offer different module families though they are built in exactly the same way.

7.9.3 Local Shading and Hot Spot Formation

Because of local shading or failure, one or several solar cells can present a much smaller short-circuit current than the rest of devices in the series string. If the defected cells are forced to pass a current higher than their generation capabilities, they become reverse-biased, even enter the breakdown regime, and sink power instead of sourcing it.

Figure 7.20 illustrates this behavior for an 18-cell string with one cell shaded so that its short-circuit current is half that of the remaining devices. String short-circuit is marked with a horizontal line, showing that in this condition the shaded cell is strongly reverse-biased and dissipates the power produced by the unshaded cells. This effect of course severely degrades the efficiency of the module, but more important is the fact that it can get damaged.

Avalanche breakdown is characterized by a nonuniform distribution of current across the junction, breakdown occurring preferentially at localized regions, possibly correlated to damage during processing. Intense local heating can produce very high temperatures (a hot spot). If a temperature of around 150°C is reached, the lamination material becomes degraded and the module irreversibly deteriorated [136, 137]. Because of the localized nature of the process solar cells show large scattering in their reverse characteristics so that the module behavior under partial shading is not accurately predictable.

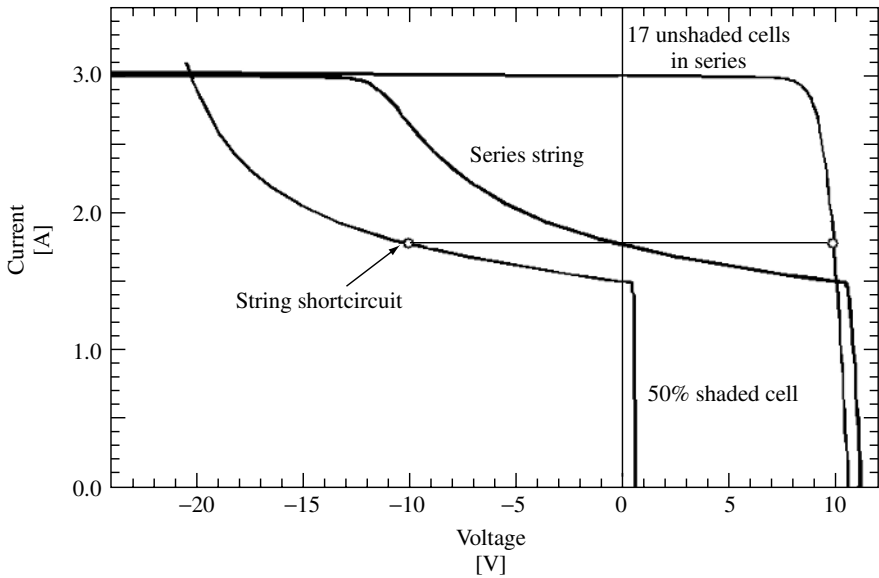


Figure 7.20 Computer simulation of the I - V curves of a 50% shaded cell, showing the typical “soft” reverse breakdown, and of 17 identical cells, unshaded, in series. When series-connected with the shaded cell, the curve labeled “series string” is obtained

In order to devise the means of preventing hot spot failure from occurring, the worst case is considered. This occurs when the N -cell series string is short-circuited and a shaded solar cell is reverse-biased with the voltage of the remaining $N - 1$ good devices, as shown in Figure 7.20. The minimum N that will lead to hot spot formation (i.e. the maximum N for safe operation) depends on rather uncontrollable factors, as explained. For Si solar cells of standard technology, it is around 15 to 20.

Since larger series strings are generally used, the approach followed is to put a diode (bypass diode) in parallel, but in opposite polarity, with a group cells. The number of cells in the group is chosen so that hot spots cannot be formed. When one or several cells are shaded, they are reverse-biased only to the point where the diode across the group starts forward conduction. The diode carries away the necessary current to keep the group near short-circuit.

Figure 7.21 illustrates the operation of the bypass diodes. When the current forced through the shaded substring is such that the reverse bias equals the diode threshold voltage, the bypass diode sinks all necessary current to keep the string at this biasing point thus preventing the power dissipated in the shaded cell to increase. It is also apparent that the bypass diode leads to a significant increase of output power allowing the module to keep delivering the power generated by the unaffected groups.

It is clear then that the smaller the number of cells per bypass diode, the lower the efficiency loss for a shading condition, but this means a higher cost and more complex fabrication. It has been proposed to integrate a bypass diode in each cell so that these effects will be minimized at the expense of more complicated cell processing [138].

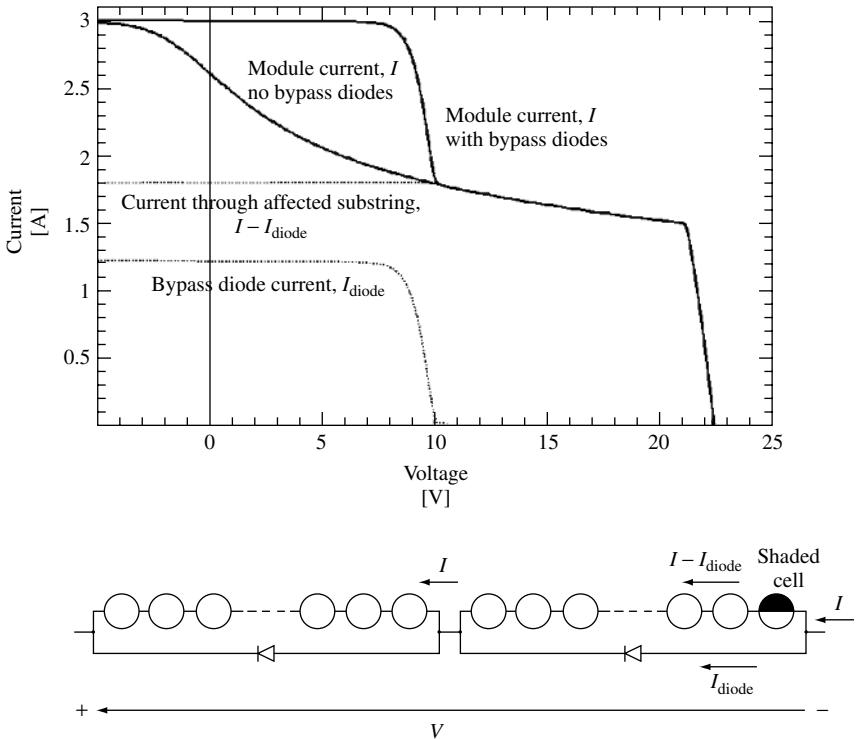


Figure 7.21 Computer simulation of the $I-V$ curves of a 36-cell series string without and with two bypass diodes, connected as shown in the bottom of the figure, when one cell is 50% shaded. The currents through the shaded substring and its bypass diode are also shown

The practice is to take electrical terminals outside the encapsulation not only for the extremes of the series string, but also for intermediate points as well, so that bypass diodes are connected in the junction box 12 or 18 cells each (Figure 7.22). Endurance to shading is a standard test for module qualification.

The influence of local shading on the module output depends on the details of the $I-V$ curve of the cells as well. Under certain circumstances of partial shading, it is beneficial that the cells show some shunt resistance. However, tight control of leakage currents by processing is not easy.

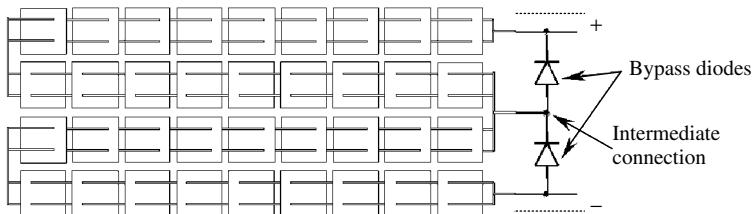


Figure 7.22 Two bypass diodes in a 36-cell module. The connections are done in the junction box

7.9.4 Optical Properties

The encapsulation affects the optical properties of the cells in several ways. The optical properties of the cells must be optimized attending to cost and performance after encapsulation.

Some effects of encapsulation are [139] as follows:

- The refraction index of glass and EVA is similar, around 1.5, between those of air and Si. Encapsulation acts, then, as a thick AR. For well textured Si solar cells, this antireflection action is enough and sometimes no thin ARC is used.
- The design of the ARC coating must account for the fact that the cell is illuminated from a medium with this index. The optimum ARC refractive index is larger than in air.
- Glass and EVA absorb some light in the short-wavelength range.
- Typically, 4% reflection occurs at the air–glass interface [Figure 7.23 (1)]. ARC coatings and texturing can be applied to decrease this loss.
- The light reflected by the metal fingers and the cell surface, if the reflected rays are tilted with respect to the normal to the glass surface, can be partly recovered by total internal reflection at the glass–glass interface [Figure 7.23 (2)]. This effect could be enhanced by texturing the cell surface with tilted pyramids, instead of the upright pyramids obtained by alkaline etching of (1 0 0) surfaces [140].
- Though the trapping capabilities of the cell, due to the lower difference in refractive index, appear to worsen with encapsulation, the escaped rays are trapped in the glass so that the absorption enhancement in the ideal case is not affected.
- For cells without a back metal mirror, the transmitted light can be recovered by putting a reflector, detached from the cell, at the back of the module [Figure 7.23 (3)]. The back plastic layer, if white, serves this purpose.
- The same white layer, since it reflects diffusively, allows some of the light incident between the cells to be collected [Figure 7.23 (4)].

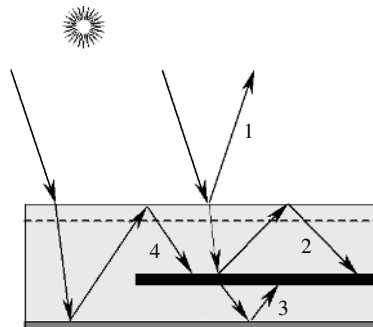


Figure 7.23 Optical effects of encapsulation: (1) glass reflection; (2) trapping of cell reflectance; (3) trapping of cell transmittance; (4) collection of peripheral light

7.10 FIELD PERFORMANCE OF MODULES

7.10.1 Lifetime

Long lifetime is claimed as one of the main virtues of PV and some manufacturers currently offer warranty for more than 20 years, with 30-year lifetime being the objective for short-term development. This should mean that for this period of time the module will keep working, that is, producing electrical power with an efficiency similar to the starting efficiency and without deterioration that compromises the safety or the visual appearance. Two factors determine lifetime: reliability, that refers to premature failure of the product, and durability, that attends to slow degradation that eventually decreases production to unacceptable levels. Cost effectiveness, energy payback balance and public acceptance of photovoltaic energy strongly rely on the reliability and the long lifetime of modules.

PV systems worldwide have been working for more than 20 years, and this allows us to gather information concerning degradation mechanisms. Modules in the field are subjected to static and dynamic mechanical loads, thermal cycling, radiation exposure, ambient humidity, hail impact, dirt accumulation, partial shading and so on. Common failure modes [124, 141] are related to the action of weather agents in combination with deficiencies in fabrication.

Location-dependent steady degradation of module output is also observed, with short-circuit current and fill factor being the most affected parameters. In many cases, this has been proved to correlate with degradation of EVA encapsulation [127]. EVA, like most polymers, is known to undergo photothermal degradation: UV radiation breaks molecular chains. Diffusion of chemical species is also relatively easy through it, so that moisture and corroding agents can enter while absorbers and stabilizers can out-diffuse.

Yellowing or browning of EVA reduces its optical transmission affecting module current. For this reason, EVA incorporates UV absorbers in its formulation. Cerium-containing glasses alleviate this problem. Degradation also decreases the strength of the encapsulant, leading to loss of adhesion to the cells and even detachment of the layer (delamination). This is promoted by the shear stress that accompanies different expansion coefficients upon diurnal thermal cycles. Delamination brings about optical and thermal degradation. Besides, the degraded encapsulant can be penetrated more easily by moisture and chemicals. Among these, sodium from the glass and phosphorus from the cell emitter are known to precipitate at the cell surface, corroding solder joints and increasing series resistance [141]. Encapsulant formulations are being continuously improved to address these problems.

7.10.2 Qualification

Several organisms, such as the International Electrotechnical Commission (IEC), the Institute of Electrical and Electronic Engineers (IEEE) and so on, have designed tests aimed at guaranteeing the quality of PV products [142]. Test procedures have been defined that, if successfully passed by a product, should guarantee the reliability of the PV module.

Manufacturers voluntarily submit their products for qualification tests in an accredited laboratory. These include verification of the module performance claimed in the datasheets as well as reliability tests. The certifications obtained are intended as a quality assurance for the customer.

Qualification tests consist in verifying the module integrity by visual inspection, measurement of the electrical performance at STC and of the electrical isolation before and after treatments that simulate, in an accelerated manner, real operation conditions. For instance, the IEC Standard 61 215 [143] specifies the following:

- Ultraviolet exposure using xenon lamps.
- Thermal cycling (-40°C to 50°C , 50 cycles) in climatization chamber.
- Humidity freeze cycling (thermal cycling with 85% relative humidity).
- Damp heat (1000 h at 85°C and 90% relative humidity).
- Twist test for testing resistance to torques.
- Pressure is applied to the module to test resistance to static mechanical loads.
- Hail impact test, where the module is stricken by 25 mm diameter ice balls at 23 m seg^{-1} .
- Outdoor exposure.
- Hot spot tests, where the module is selectively shaded.

Different test combinations are applied to a sample of a few modules. The modules will qualify if no major failures are found and the visual inspection reveals no damage, the electrical power is within 90% of specifications, and isolation is maintained.

7.11 CONCLUSIONS

This chapter has reviewed current state of crystalline silicon solar cells and modules. The main lines defining the structure of the described situation can be summarized as follows:

- *Changing scale*: The current booming of the markets enables and fosters technological and processing improvements.
- *Laboratory-industry gap*: There is a mature technology at the laboratory that has led to impressive performance levels, on the one hand, and a reliable, fast, 30-year-old industrial process producing modest efficiency, on the other hand. Closing this gap is the key to a lower $\$ \text{Wp}^{-1}$ figure of merit.
- *Novel silicon materials*: Market growth and the threat of silicon shortage stimulates new materials and very thin substrates that demand new technological solutions.
- *Technology diversification*: These two challenges are to be faced by solar cell production technology in the coming years. Intensive preindustrial research is being conducted and solutions are being developed along several different lines.
- *Quality*: Product reliability and durability and environmental and aesthetical friendliness are as important as cost for the growth of PV industry and this also influences technology.
- *Long-term scenario*: Alternatives to crystalline silicon technology are being researched thoroughly and presumably some of them will succeed in reducing photovoltaic costs to competitive ones. Nevertheless, for these so-called “leapfrogs” to take place, a mature PV market should consolidate, for which silicon technology is essential at least for the next decade.

REFERENCES

1. Luque A, *Solar Power*, Notes of the Cycle d'études de Postgrade en Energie, 5–12, EPFL (2001–2003).
2. Maycock P, *Photovolt. News* **20** (2), 1 (2001).
3. Turton R, “Band Structure of Si: Overview”, in Hull R (Ed), *Properties of Crystalline Silicon*, INSPEC, Stevenage, UK (1999).
4. Green M, Keevers M, *Prog Photovolt.* **3**, 189–192 (1995).
5. Kolodinski S, Werner J, Wittchen T, Queisser H, *Appl. Phys. Lett.* **63**, 2405–2407 (1993).
6. Clugston D, Basore P, *Prog. Photovolt.* **5**, 229–236 (1997).
7. Sproul A, Green M, *J. Appl. Phys.* **70**, 846–854 (1991).
8. Altermatt P *et al.*, *Proc. 16th Euro. Conf. Photovoltaic Solar Energy Conversion*, 102–105 (2000).
9. Dzewior J, Schmid W, *Appl. Phys. Lett.* **31**, 346–351 (1977).
10. Altermatt P *et al.*, *Proc. 16th Euro. Conf. Photovoltaic Solar Energy Conversion*, 243–246 (2000).
11. Green M *et al.*, *Nature* **412**, 805–808 (2001).
12. Thurber W, Mattis R, Liu Y, Filliben J, *J. Electrochem. Soc.* **127**, 1807–1812 (1980).
13. Thurber W, Mattis R, Liu Y, Filliben J, *J. Electrochem. Soc.* **127**, 2291–2294 (1980).
14. Kane D, Swanson R, *Proc. 20th IEEE Photovoltaic Specialist Conf.*, 512–517 (1988).
15. Sze S, *Physics of Semiconductor Devices*, Chap. 5, John Wiley & Sons, New York (1981).
16. King R, Sinton R, Swanson R, *IEEE Trans. Electron Devices* **37**, 1399–1409 (1990).
17. King R, Swanson R, *IEEE Trans. Electron Devices* **38**, 365–371 (1991).
18. Narasimha S, Rohatgi A, Weeber A, *IEEE Trans. Electron Devices* **46**, 1363–1370 (1999).
19. Honsberg C *et al.*, *Proc. 16th Euro. Conf. Photovoltaic Solar Energy Conversion*, 1655–1658 (2000).
20. Grauvogl M, Hezel R, *Prog. Photovolt.* **6**, 15–24 (1998).
21. Gan J, Swanson R, *Proc. 21st IEEE Photovoltaic Specialist Conf.*, 245–250 (1990).
22. Taguchi M *et al.*, *Prog. Photovolt.* **8**, 503–514 (2000).
23. Cuevas A, Basore P, Giroult-Matlakowski G, Dubois C, *Proc. 13th Euro. Conf. Photovoltaic Solar Energy Conversion*, 337–342 (1995).
24. Cuevas A, Stuckings M, Lay J, Petravic M, *Proc. 14th Euro. Conf. Photovoltaic Solar Energy Conversion*, 2416–2419 (1997).
25. Aberle A, *Prog. Photovolt.* **8**, 473–488 (2000).
26. Aberle A, Hezel R, *Prog. Photovolt.* **5**, 29–50 (1997).
27. Eades W, Swanson R, *J. Appl. Phys.* **58**, 4267–4276 (1985).
28. Aberle A, Glunz S, Warta W, *Sol. Energy Mater. Sol. Cells* **29**, 175–182 (1993).
29. Luque A, “The Requirements of High Efficiency Solar Cells”, in Luque A, Araújo G (Eds), *Physical Limitations to Photovoltaic Energy Conversion*, 1–42, Adam Hilger Ltd, Bristol (1990).
30. Green M, *Silicon Solar cells. Advanced Principles and Practice*, Chap. 7, Centre for Photovoltaic Devices and Systems, University of New South Wales, Sydney (1995).
31. Tiedje T, Yablonovitch E, Cody G, Brooks B, *IEEE Trans. Electron Devices* **31**, 711–716 (1984).
32. 5th Framework Programme EC Project ERK5-1999-00002 “High efficiency silicon solar cells concentrator (HISICON)”.
33. Verlinden P *et al.*, *Proc. 14th Euro. Conf. Photovoltaic Solar Energy Conversion*, 96–100 (1997).
34. Ohtsuka H, Sakamoto M, Tsutsui K, Yazawa Y, *Prog. Photovolt.* **8**, 385–390 (2000).
35. Luque A, Ruiz J, Cuevas A, Agost M, *Proc. 1st Euro. Conf. Photovoltaic Solar Energy Conversion*, 269–277 (1977).
36. Zhao J, Wang A, Green M, *Prog. Photovolt.* **7** 471–474 (1999).
37. Saitoh T, Hashigami H, Rein S, Glunz S, *Prog. Photovolt.* **8** 535–547 (2000).
38. Myers S, Seibt M, Schröter W, *J. Appl. Phys.* **88** 3795–3819 (2000).

39. McHugo S, Hieslmair H, Weber E, *Appl. Phys. A* **64**, 127–137 (1997).
40. Ohe N, Tsutsui K, Warabisako T, Saitoh T, *Sol. Energy Mater. Sol. Cells* **48**, 145–150 (1997).
41. Martinuzzi S *et al.*, *Mater. Sci. Eng., B* **71**, 229–232 (2000).
42. Wenham S, Green M, *Prog. Photovolt.* **4**, 3–33 (1996).
43. Schröter W, Kühnpafel R, *Appl. Phys. Lett.* **56**, 2207–2209 (1990).
44. Joshi S, Gösele U, Tan T, *J. Appl. Phys.* **77**, 3858–3863 (1995).
45. Soporì B *et al.*, *Sol. Energy Mater. Sol. Cells* **41/42** 159–169 (1996).
46. Waver P, Schmidt A, Wagemann H, *Proc. 14th Euro. Conf. Photovoltaic Solar Energy Conversion*, 2450–2453 (1997).
47. Green M, *Prog. Photovolt.* **8**, 443–450 (2000).
48. Schmidt J, Hezel R, *12th Workshop on Crystalline Si Solar Cell Materials and Processes*, National Renewable Energy Laboratory NREL/BK-520-32717, 64–71 (2002).
49. Zhao J, Wang A, Green M, *Prog. Photovolt.* **2**, 227–230 (1994).
50. Wenham S, *Prog. Photovolt.* **1**, 3–10 (1993).
51. Cuevas A, Russell D, *Prog. Photovolt.* **8**, 603–616 (2000).
52. Green M, *Silicon Solar Cells. Advanced Principles and Practice*, Chap. 10, Centre for Photovoltaic Devices and Systems, University of New South Wales, Sydney (1995).
53. Cuevas A, Sinton R, Swanson R, *Proc. 21st IEEE Photovoltaic Specialist Conf.*, 327–332 (1990).
54. Luque A, *Solar Cells and Optics for Photovoltaic Concentration*, Chap. 6, Adam Hilger Ltd, Bristol (1989).
55. Nijs J *et al.*, *IEEE Trans. Electron Devices* **46**, 1948–1969 (1999).
56. Moehlecke A, Zanesco I, Luque A, *Proc. 1st World CPEC* 1663–1666 (1994).
57. Glunz S, Knobloch J, Biro D, Wettling W, *Proc. 14th Euro. Conf. Photovoltaic Solar Energy Conversion*, 392–395 (1997).
58. Wenham S *et al.*, *Proc. 1st World CPEC*, 1278–1282 (1994).
59. Mulligan W *et al.*, *Proc. 28th IEEE Photovoltaic Specialist Conf.*, 158–163 (2000).
60. Zhao J, Wang A, Altermatt P, Zhang G, *Prog. Photovolt.* **8** 201–210 (2000).
61. Luque A, “Coupling Light to Solar Cells”, in Prince M (Ed), *Advances in Solar Energy* Vol. 8, 151–230, American Solar Energy Society, Boulder (1993).
62. Born M, Wolf E, *Principles of Optics*, 7th Edition, Chap. 1, Cambridge University Press, Cambridge, UK (1999).
63. Zhao J, Green M, *IEEE Trans. Electron Devices* **38**, 1925–1934 (1991).
64. Rodríguez J, Tobías I, Luque A, *Sol. Energy Mater. Sol. Cells* **45**, 241–253 (1997).
65. Green M, *Silicon Solar Cells. Advanced Principles and Practice*, Chap. 6, Centre for Photovoltaic Devices and Systems, University of New South Wales, Sydney (1995).
66. Moehlecke A, *Conceptos avanzados de tecnología para células solares con emisores p⁺ dopados con boro*, Chap. 5, Ph.D. thesis, Universidad Politécnica de Madrid, Madrid (1996).
67. Mi nano J, “Optical Confinement in Photovoltaics”, in Luque A, Araújo G (Eds), *Physical Limitations to Photovoltaic Energy Conversion*, 50–83, Adam Hilger Ltd, Bristol (1990).
68. Van Overstraeten R, Mertens R, *Physics, Technology and Use of Photovoltaics*, Chap. 4, Adam Hilger Ltd, Bristol (1986).
69. Hylton J *et al.*, *Prog. Photovolt.* **4**, 435–438 (1996).
70. Horzel J *et al.*, *Proc. 17th Euro. Conf. Photovoltaic Solar Energy Conversion*, 1367–1370 (2001).
71. Gandhi S, *VLSI Fabrication Principles*, Chap. 9, John Wiley & Sons, New York (1994).
72. Richards B, Cotter J, Honsberg C, Wenham S, *Proc. 28th IEEE Photovoltaic Specialist Conf.*, 375–378 (2000).
73. Nijs J *et al.*, *Proc. 1st World CPEC*, 1242–1249 (1994).
74. Ballif C, Huljić F, Hessler-Wyser A, Willeke G, “Nature of the Ag-Si Interface in Screen-Printed Contacts: A Detailed Transmission Electron Microscopy Study of Cross-Sectional Structures”, *Proc. 29th IEEE Photovoltaic Specialist Conf.* (New Orleans, 2002); in press.

75. Lenkeit B *et al.*, *Proc. 16th Euro. Conf. Photovoltaic Solar Energy Conversion*, 1332–1335 (2000).
76. Hoornstra J, de Moor H, Weeber A, Wyers P, *Proc. of the 16th Euro. Conf. Photovoltaic Solar Energy Conversion*, 1416–1419 (2000).
77. Bruton T *et al.*, *Proc. 14th EC Photovoltaic Specialist Conf.*, 11–19 (1997).
78. Tool C *et al.*, *Prog. Photovolt.* **10**, 279–291 (2002).
79. Martinelli G *et al.*, *Proc. 14th European Photovoltaic Solar Energy Conversion*, 778, 779 (1997).
80. Münzer K, Holdermann K, Schlosser R, Sterk S, *IEEE Trans. Electron Devices* **46**, 2055–2061 (1999).
81. Finck von Finckenstein B *et al.*, *Proc. 28th IEEE Photovoltaic Specialist Conf.*, 198–200 (2000).
82. King R, Mitchell K, Gee J, *Proc. 1st World CPEC*, 1291–1294 (1994).
83. Moschner J *et al.*, *Proc. of the 2nd World CPEC*, 1426–1429 (1998).
84. Nijs J *et al.*, *IEEE Trans. Electron Devices* **46**, 1948–1969 (1999).
85. Hilali M *et al.*, “Optimization of Self-Soping Ag Paste Firing to Achieve High Fill Factors on Screen-Printed Silicon Solar Cells with a 100 Ω /sq. Emitter” *Proc. of the 29th IEEE Photovoltaic Specialist Conf.*, (New Orleans, 2002); in press.
86. Sivothythaman S *et al.*, *Proc. 14th Euro. Conf. Photovoltaic Solar Energy Conversion*, 400–403 (1997).
87. Doshi P *et al.*, *Proc. 25th IEEE Photovoltaic Specialist Conf.*, 421–424 (1996).
88. Doshi P *et al.*, *Sol. Energy Mater. Sol. Cells* **41/42**, 31–39 (1996).
89. Biro D *et al.*, *Sol. Energy Mater. Sol. Cells* **74**, 35–41 (2002).
90. Périchaud I, Floret F, Martinuzzi S, *Proc. 23rd IEEE Photovoltaic Specialist Conf.*, 243–247 (1993).
91. Narasimha S, Rohatgi A, *IEEE Trans. Electron Devices* **45**, 1776–1782 (1998).
92. Macdonald D, Cuevas A, Ferraza F, *Solid-State Electron.* **43**, 575–581 (1999).
93. Gee J, Sopori B, *Proc. 26th IEEE Photovoltaic Specialist Conf.*, 155–158 (1997).
94. del Cañizo C, Tobías I, Lago R, Luque A, *J. Electrochem. Soc.* **149**, 522–525 (2002).
95. Gandhi S, *VLSI Fabrication Principles*, Chap. 8, John Wiley & Sons, New York (1994).
96. Johnson J, Hanoka J, Gregory J, *Proc. 18th Photovoltaic Specialist Conf.*, 1112–1115 (1985).
97. Sopori B, Deng X, Narayanan S, Roncin S, *Proc. 11th Euro. Conf. Photovoltaic Solar Energy Conversion*, 246–249 (1992).
98. Szulfcik J *et al.*, *Proc. 12th EC Photovoltaic Specialist Conf.*, 1018–1021 (1994).
99. Leguijt C *et al.*, *Sol. Energy Mater. Sol. Cells* **40**, 297–345 (1996).
100. Aberle A, Hezel R, *Prog. Photovolt.* **5**, 29–50 (1997).
101. Soppe W *et al.*, “On Combining Surface and Bulk Passivation of SiN_x:H Layers for mc-Si Solar Cells”, *Proc. 29th IEEE Photovoltaic Specialist Conf.* (New Orleans, 2002); in press.
102. Ruby D, Wilbanks W, Fieddermann C, *IEEE 1st WPEC* 1335–1338 (1994).
103. Shirasawa K *et al.*, *Proc. 21st IEEE Photovoltaic Specialist Conf.*, 668–673 (1990).
104. Zhao J, Wang A, Campbell P, Green M, *IEEE Trans. Electron Devices* **46**, 1978–1983 (1999).
105. De Wolf S *et al.*, *Proc. 16th Euro. Conf. Photovoltaic Solar Energy Conversion*, 1521–1523 (2000).
106. Bilyalov R, Stalmans L, Schirone L, Lévy-Clement C, *IEEE Trans. Electron Devices* **46**, 2035–2040 (1999).
107. Spiegel M *et al.*, *Sol. Energy Mater. Solar Cells* **74**, 175–182 (2002).
108. Huster F *et al.*, *Proc. 28th IEEE Photovoltaic Specialist Conf.*, 1004–1007 (2000).
109. Joos W *et al.*, *Proc. 16th Euro. Conf. Photovoltaic Solar Energy Conversion*, 1169–1172 (2000).
110. Pirozzi L *et al.*, *Proc. 12th Euro. Conf. Photovoltaic Solar Energy Conversion*, 1025–1028 (1994).
111. Ruby D *et al.*, *Proc. of the 2nd World CPEC*, 39–42 (1998).

112. Inomata Y, Fukui K, Shirasawa K, *Sol. Energy Mater. Sol. Cells* **48**, 237–242 (1997).
113. Winderbaum S, Reinhold O, Yun F, *Sol. Energy Mater. Sol. Cells* **46**, 239–248 (1997).
114. Lüdemann R, Damiani B, Rohatgi A, Willeke G, *Proc. 17th Euro. Conf. Photovoltaic Solar Energy Conversion*, 1327–1330 (2001).
115. Macdonald D *et al.*, “Texturing Industrial Multicrystalline Silicon Solar Cells”, *ISES Solar World Congress* (2001).
116. Schmidt W, Woesten B, Kalejs J, *Prog. Photovolt.* **10**, 129–140 (2002).
117. Yelundur V, Rohatgi A, Jeong J, Hanoka J, *IEEE Trans. Electron Devices* **49**, 1405–1410 (2002).
118. Janoch R *et al.*, *Proc. IEEE 28th Photovoltaic Specialist Conf.*, 1403–1406 (2000).
119. Meier D *et al.*, *Sol. Energy Mater. Sol. Cells* **65**, 621–627 (2000).
120. Taguchi M *et al.*, *Prog. Photovolt.* **8**, 503–513 (2000).
121. Jordan D, Nagle J, *Prog. Photovolt.* **2**, 171–176 (1994).
122. Bruton T *et al.*, *Proc. 17th Euro. Conf. Photovoltaic Solar Energy Conversion*, 1282–1286 (2001).
123. Honsberg C *et al.*, *Proc. 14th Euro. Conf. Photovoltaic Solar Energy Conversion*, 146–149 (1997).
124. Wenham S, Green M, Watt M, *Applied Photovoltaics*, Chap. 5, Centre for Photovoltaic Devices and Systems, University of New South Wales, Sydney (1995).
125. Van Overstraeten R, Mertens R, *Physics, Technology and Use of Photovoltaics*, Chap. 8, Adam Hilger Ltd, Bristol (1986).
126. King D *et al.*, *Prog. Photovolt.* **8**, 241–256 (2000).
127. Czanderna A, Pern J, *Sol. Energy Mater. Sol. Cells* **43**, 101–181 (1996).
128. Galica J, Sherman N, *Proc. 28th IEEE Photovoltaic Specialist Conf.*, 30–35 (2000).
129. Schmidhuber H, Krannich K, *Proc. 17th Euro. Conf. Photovoltaic Solar Energy Conversion*, 662–663 (2001).
130. Ishikawa N *et al.*, *Proc. 2nd World CPEC*, 2501–2506 (1998).
131. Smith D, Gee J, *Proc. 16th Euro. Conf. Photovoltaic Solar Energy Conversion*, 1104–1107 (2000).
132. Parreta A, Sarno A, Schloppo R, Zingarelli M, *Proc. of the 14th EC Photovoltaic Specialist Conf.*, 242–246 (1997).
133. Herrmann W, Becker H, Wiesner W, *Proc. 14th Euro. Conf. Photovoltaic Solar Energy Conversion*, 224–228 (1997).
134. Appelbaum J, Segalov T, *Prog. Photovolt.* **7**, 113–128 (1999).
135. Zilles R, Lorenzo E, *Int. J. Sol. Energy* **13**, 121–133 (1993).
136. Herrmann W, Wiesner W, Vaaßen W, *Proc. 26th IEEE Photovoltaic Specialist Conf.*, 1129–1132 (1997).
137. Herrmann W, Adrian M, Wiesner W, *Proc. 2nd World CPEC*, 2357–2359 (1998).
138. Roche D, Outhred H, Kaye R, *Prog. Photovolt.* **3**, 115–127 (1995).
139. Hauselaer P, van den Bossche J, Frisson L, Poortmans J, *Proc. 17th Euro. Conf. Photovoltaic Solar Energy Conversion*, 642–645 (2001).
140. Green M, “Surface Texturing and Patterning in Solar Cells”, in Prince M (Ed), *Advances in Solar Energy*, Vol 8, 231–269, American Solar Energy Society, Boulder (1993).
141. Quintana M, King D, McMahon T, Osterwald C “Commonly Observed Degradation in Field-Aged Photovoltaic Modules”, *Proc. 29th IEEE Photovoltaic Specialist Conf.* (New Orleans, 2002); in press.
142. Wilshaw A, Bates J, Oldach R, *Proc. 16th Euro. Conf. Photovoltaic Solar Energy Conversion*, 795–797 (2000).
143. IEC Standard 61215, *Crystalline Silicon Terrestrial PV Modules – Design Qualification and Type Approval* (1993).

8

Thin-film Silicon Solar Cells

Bhushan Sopori

National Renewable Energy Laboratory, Golden, CO, USA

8.1 INTRODUCTION

Because silicon (Si) is an indirect band gap material, it is generally perceived that the thickness of Si required to absorb usable sunlight should be larger than $(\alpha_{\text{bandedge}})^{-1}$, where α_{bandedge} is the absorption coefficient for wavelength (λ) of light corresponding to the near-bandedge. Using this simple rule of thumb, on the basis of absorption due to a single pass of light, and using the mid-point of the bandedge ($\lambda = 1.05 \mu\text{m}$), one gets $\alpha^{-1} \sim 700 \mu\text{m}$. This implies that the wafer thickness for sufficient absorption of the solar spectrum is $>700 \mu\text{m}$. This is quite a large thickness for a Si wafer and is not desirable for commercial production of solar cells for two reasons: the wafer cost can be very high and its effectiveness for collection of photogenerated carriers will be small because it is difficult to have a minority-carrier diffusion length (MCDL) comparable to such a large wafer thickness. Thus, for practical reasons, wafer thickness must be less than this value. Furthermore, detailed models that take into account surface characteristics and the multiple reflections within the wafer show that absorption can be greatly enhanced; thus, the need for such a thick wafer is diminished. Later in this chapter, we will show that by employing an appropriate structure, a very thin layer of Si can offer a high degree of absorption of the solar spectrum – nearly as much as a thick wafer. The physics and modeling capabilities for analyses of solar cell structures have taken two decades to develop and have been responsible for the majority of the improvements in Si solar cell efficiency.

As an introduction, it is necessary to have a general understanding of the requirements for a thin-film Si solar cell and the problems that emerge when the thickness of a Si solar cell is reduced. Clearly just reducing the cell thickness will result in reduced absorption, and thus, a reduced photocurrent. To get a quantitative feel of such a reduction in the photocurrent, consider a planar solar cell. Figure 8.1 is a plot of maximum achievable current density (MACD) generated by a planar solar cell, with an optimum antireflection (AR) coating, for different values of the cell thickness. These calculations are

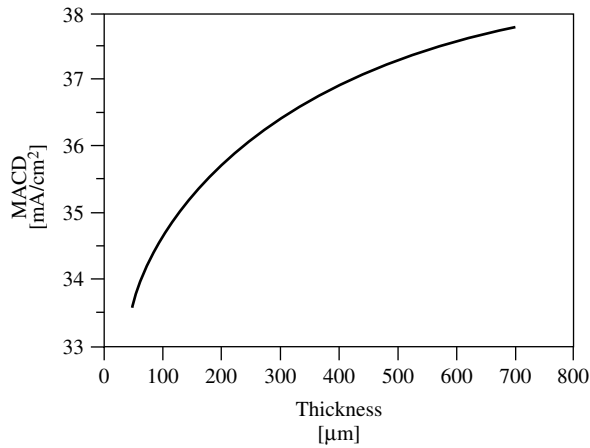


Figure 8.1 Maximum achievable current density (MACD) from a planar, AR-coated Si solar cell as a function of cell thickness. These calculations assume an optimized AR coating and AM1.5 incident spectrum. These results are obtained with *PV Optics*

performed using *photovoltaic (PV) Optics* software, which assumes the generation of one electron-hole pair per photon and a collection efficiency of unity. These assumptions are tantamount to a zero surface-recombination velocity and absence of other electronic loss mechanisms. Thus, the photocurrent in Figure 8.1 corresponds to a maximum achievable current density for the AM1.5 solar spectrum. Figure 8.1 shows that the photocurrent increases with an increase in thickness and saturates at a thickness of about 700 μm . At a thickness of ~ 300 μm , the current density is within 5% of the saturation value, which implies that a thickness of 300 μm is suitable for fabricating high-efficiency solar cells on planar substrates. This is fortunate because a similar demand on wafer thickness comes from requirements for maintaining a high yield in handling and processing other semiconductor devices.

The PV industry has traditionally borrowed technological know-how of device handling and processing from the semiconductor industry, which traditionally uses thick wafers to prevent breakage through mechanical handling or generation of thermal stresses by high-temperature processing. Concomitantly, the PV community found it compelling to use wafers of similar thickness for Si solar cells. The choice of thick wafers permitted the PV community to focus on the material and device-processing issues, which helped develop the science and technology of Si solar cells to the current level.

Recently, however, there have been many advances in wafer handling and in the development of gentler processing methods to accommodate high throughput. These advances have sparked interest in using thinner substrates for two reasons: (1) To reduce the amount of Si for each watt of PV energy generation. Because the PV industry has gone through periods of Si shortage, an efficient use of Si can minimize such hardships; and (2) To improve the efficiency of solar cells fabricated on low-cost substrates using improved cell designs.

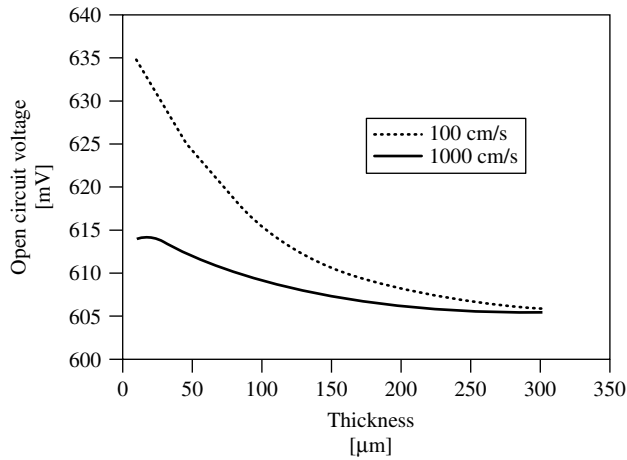


Figure 8.2 V_{OC} of a Si solar cell as a function of thickness for high and low surface-recombination velocities. These calculations were performed with PC1D

One approach to simultaneously accomplish these demands is to use thinner wafers. Thinner wafers conserve material and also offer a performance advantage by decreasing the bulk-carrier recombination within the solar cell. Hence, for a given material quality of the substrate, a reduction in the cell thickness can result in improving the open-circuit voltage (V_{OC}) and the fill factor (FF) of the solar cell. However, as the cell thickness is reduced, the surface recombination becomes an increasingly important component of the total recombination. In particular, surface recombination can severely degrade V_{OC} . This can be seen in Figure 8.2, which shows V_{OC} as a function of thickness (for a rather simple solar cell) for two different values of surface-recombination velocity, $S = 100$ cm/s and $S = 1000$ cm/s. In the calculations for Figure 8.2, we have used a front-textured cell with $S_f = S_b$, where S_f and S_b are the recombination velocities at the front and back surfaces, respectively. The important conclusion is that although a reduction in thickness can lead to an increase in V_{OC} , it can have the opposite effect if surface recombination is not reduced simultaneously. Clearly, the full advantage of reducing the volume recombination by thinner wafers can be achieved only if the device has built-in features to generate and reflect minority carriers away from interfaces using electronic reflectors (such as high–low fields), and optical reflectors. These are important considerations for thin solar cells.

Thus, thinner cells can yield higher voltages and higher fill factors if the surface recombination demands are met. However, they may suffer a loss in the photocurrent unless the optical losses associated with thickness reduction are compensated through superior light-trapping design. If these conditions are met, thinner cells can be more efficient than their thicker counterparts. Thin-film cells can also offer a direct cost advantage associated with the use of less Si and by employing thin-film technologies that (in principle) are deemed to be low-cost methods. It is clear that thinner cells can offer significant reduction in the PV energy cost. The photovoltaic industry is planning to reduce the wafer thickness incrementally from its current value of about 350 μm to less than 100 μm within

the next ten years, staying within the realm of the existing technologies at each major step of thickness. However, the arguments above provide motivation for a major reduction in thickness – to a new generation of Si solar cells using Si films less than 10 μm thick. Such a thin-film Si (TF-Si) solar cell offers many advantages that can lower the cost of generating solar electricity. A TF-Si cell offers (1) reduced bulk recombination leading to lower dark current, higher V_{OC} and higher FF of the device. Compared to a thick cell, a thin cell of the same material quality can yield higher device performance. Likewise, for a comparable performance, TF-Si solar cell requires lower material quality than a thick cell. It also offers (2) potential for low-cost cells/modules, (3) potential for lightweight photovoltaics, (4) lower energy consumption for device fabrication, and (5) potential for flexible solar cells.

These advantages of TF-Si solar cells, in concurrence with the performance advantage, make them very attractive for the future. Practical realization of solar cells with the above advantages poses many challenges in both the design and device fabrication. These challenges include an efficient method for light-trapping to compensate for reduced thickness, and a low-cost substrate to support the thin film. Low-cost substrates generally imply materials that may not be compatible with the high temperatures required for formation and processing of Si film. This incompatibility can arise because of impurities in the substrate that can diffuse into the Si film, softening of the substrate, thermal mismatch, and less desirable electronic properties of the interface leading to high S_b .

This chapter will discuss current efforts to develop a new technology (or set of technologies) that can achieve the potential performance of very thin Si solar cells. In the last few years, a number of R&D groups around the world have embarked on the design and fabrication of TF-Si solar cells. These efforts have already led to some exciting results. However, the design and fabrication of high-efficiency TF-Si solar cells continue to present a host of challenges. We review the salient aspects of the current research on TF-Si cells, and we present a systematic approach to the analysis, design, and fabrication of such devices.

8.2 A REVIEW OF CURRENT THIN-FILM SI CELLS

Many basic concepts of thin-film Si solar cells were suggested decades ago [1, 2]. It was apparent then that thinner cells would require a means of enhancing optical absorption. As early as 1975, it was proposed that enhanced optical absorption accompanying light-trapping can help lower the cell thickness required for efficient generation of photocurrent to a few microns. The proposed approach used a prismatic configuration to deflect light into a thin film at oblique incidence, so that the light would be total internally multireflected within the thin cell. This approach is similar to launching guided waves in integrated optics. Although this approach did not flourish because of evident drawbacks, other cell configurations that would support the use of very thin Si films for solar cell applications were later suggested [3, 4]. Some simple (approximate) calculations showed that cell efficiencies approaching 10% could be obtained with polycrystalline Si films of 10- μm thickness with 1- μm grain size [3]. These calculations only considered bulk recombination arising from grain boundaries (GBs) in polycrystalline Si and planar cell structures. Although the possibility of the thin-film Si solar cell was envisioned long ago, a practical realization has begun only recently. The path to TF-Si cells has

awaited some understanding of how to improve optical losses through enhanced absorption and the recognition and mitigation of electronic losses because of carrier recombination at interfaces.

Initial theoretical analysis based on thermodynamic considerations [5] suggested that rough surfaces and an asymmetric cell structure would effectively enhance optical absorption in the cell. Surface texturing, which was initially introduced to reduce surface reflectance for broadband illumination, also resulted in an increase in the optical path of light transmitted into a Si wafer [6–10]. Following the initial success, texture etching became a standard process step for fabricating Si solar cells, both in the laboratory and commercially. Figure 8.3 shows calculated short-circuit current density (J_{SC}) values as a function of thickness for different texture structures including planar, standard chemical texture, pyramids, inverted pyramids, and perpendicular slats. The surface structures are illustrated in Figure 8.4. However, only the laboratory cells, fabricated on high-quality wafers and with high-reflectance back contacts, realized the advantage of light-trapping. Although commercial cells also use texturing, its usefulness was perhaps largely limited to lowering the surface reflectance, rather than enhancing light-trapping. This is because the typical commercial solar cells use an Al-alloyed back contact that develops a rough interface, which has very low reflectance and allows most of the light to be transmitted into the metal where it is absorbed. The light absorbed in the metal constitutes an optical loss.

Surface texture has been successfully produced by anisotropic chemical etching in solutions of KOH or NaOH. It is known that texturing involves exposition of (111) crystallographic planes, which yield pyramids on (100) wafers. However, good texturing requires tedious process steps of developing a chemical composition containing silicates [11]. It was fortunate that texture etching could be combined with saw-damage removal for a low cost process. Recently, other texturing techniques have been developed that include reactive-ion etching, mechanical scribing of grooves, and acid etching [12–14]. However, none of these methods are suitable for thin-film solar cells because they produce deep

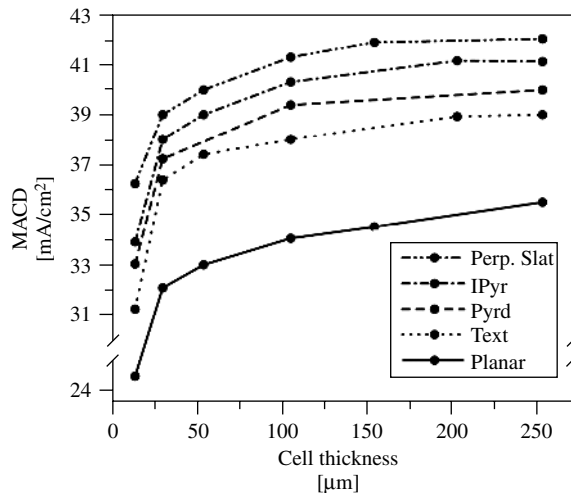


Figure 8.3 Calculated MACD for Si solar cells with different texture shapes: perpendicular slats, inverted pyramids, uniformly textured pyramids, chemically textured random pyramids and planar

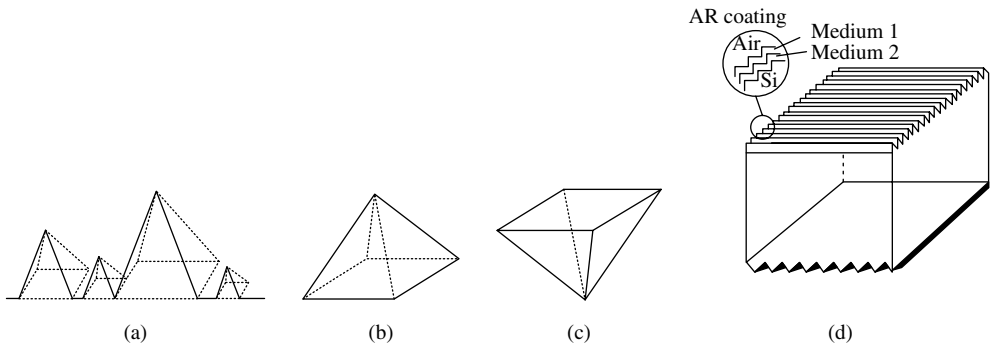


Figure 8.4 Sketches of various surface structures used in calculations shown in Figure. 8.3: (a) chemically textured random pyramids; (b) uniformly textured pyramids; (c) inverted pyramids; and (d) perpendicular slats

texture. A suitable approach for producing texture in TF-Si may be intrinsic to the use of polycrystalline material. This method has worked well for transparent conducting oxides used in thin-film a-Si.

Surface texturing naturally occurs in polycrystalline films deposited from a Si-bearing gas phase, as well as in thin and thick films grown at or near the melting point. Although exact mechanisms are not well established, texturing appears to be a grain-boundary effect. In a gas-phase growth, the high-energy grain-boundary sites allow migration of Si atoms away from the grain-boundary regions into the main grains, leading to a loss of material (thickness of the Si film) in the vicinity of the grain boundary [15, 16]. In a melt regime, such as in the growth of Si ribbons, there are local variations in the solidification temperature between the intragrain and grain-boundary regions. Because the surface tension of liquid Si or Si at high temperatures is quite high, it has the tendency to ball up at the free surfaces. This process results in grooving at the grain boundaries [17, 18]. Texturing is also observed in Si thin films crystallized by metal-induced crystallization [19]. A natural formation of texture in a Si film can play an important role in cost-effectiveness of TF-Si solar cells by obviating the need for a separate layer to enhance light-trapping. Because texturing is related to the growth or deposition process, it is important to note that texture shape and depth can change with a change in grain size. Brief discussions of the effects of texture height and texture angle are given in the next section. One of the drawbacks of texturing is that it greatly increases the surface area, thereby increasing dark current and reducing V_{OC} .

As pointed out in the previous section, interfaces (surfaces) attain a particularly significant role in a TF-Si solar cell because, for a given solar spectrum, a thinner cell has higher-generated carrier density near the surface due to enhanced light trapping. A simple way to envision increased sensitivity to surface recombination is to examine the distribution of absorbed photon flux in a thick wafer and a thin film. Figures 8.5(a) and 8.5(b) compare the distribution of absorbed photon flux in a 300- μm wafer and a 10- μm thin film of Si, respectively. Both cells have front and back texture, with an Al back-reflector. The texture heights for thick and thin cells are 3 μm and 0.6 μm , respectively. It is seen that the thin cell has an absorbed photon flux density about 3

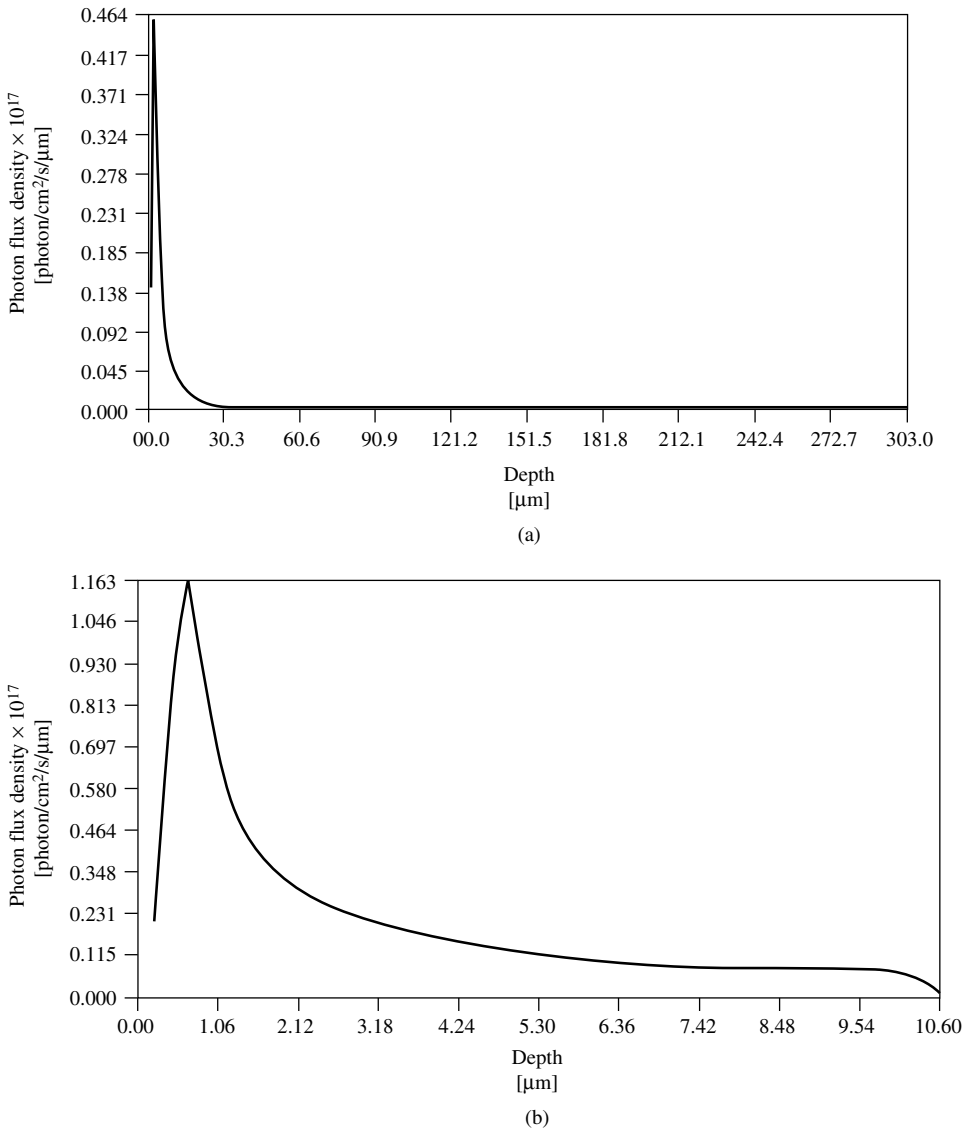


Figure 8.5 Calculated photon flux absorbed within the thickness of a (a) 300- μm wafer; and (b) 10- μm thin film. Both structures have double-sided texture and an Al back-reflector

times higher at each interface; implying that carrier generation at the interfaces of the thinner cell is about three times higher. Consequently, for the same surface-recombination velocity, the carrier recombination for the thinner cell will be 3 times higher. Therefore, it is imperative that an efficient TF-Si cell design will minimize contributions from all components of surface-related recombination.

It is important to recognize that there can be several contributions to the surface recombination in a solar cell (in addition to that from the cell-air interface). These

contributions include Si-metal (Si-M) interface(s) and edge leakage (e.g. from the mesa edge). Many approaches are used to minimize the effective surface recombination at each surface. A prudent approach to minimize the Si-M contact area (both at the front and back) is through appropriate grid design. This consideration has led to the design of point-contact and buried-contact cells [20, 21]. This feature will also minimize the shadow loss for the incident light (except for back-contact cells). Another means of reducing the effect of Si-M interaction on the carrier loss is to employ a minority-carrier reflector consisting of a high–low field (such as n^+/n or p^+/p) under the metal. Several schemes have been developed for forming the back contact of wafer-based cells that include either a partial or total diffusion of the back surface. For a TF-Si cell fabricated by deposition, these features can be accomplished by tailoring the dopant profile during deposition.

Surface passivation of unmetallized regions can be further improved by oxidation. It has been shown that such passivation can reduce the surface-recombination velocity to about 100 cm/s [22, 23] – values that are essential for high-efficiency TF-Si cells. In wafer-based cells, passivation schemes are embodied in various configurations called *passivated emitter rear locally diffused (PERL)* and *passivated emitter rear totally-diffused (PERT)* as described in Chapter 7. Application of wafer-based passivation methods to TF-Si solar cells may not be straightforward. For example, oxide growth at conventional temperatures ($>1000^\circ\text{C}$) is not feasible for cells deposited on low-cost substrates like glass. However, it has been shown that low-temperature oxides grown by rapid thermal processing (RTP)-like processes can have excellent passivation properties [24]. Another approach to produce effective surface passivation can be the use of low-temperature plasma-enhanced chemical vapor deposition (PECVD) nitride. It is now well known that SiN (or oxy nitrides) produces a positive charge at the Si interface that results in excellent passivation characteristics for *p*-type Si [25, 26].

It is fruitful to briefly review some preliminary work that was instrumental in establishing the advantages of TF-Si solar cell structures and promoting further research. The capability of a thin cell to yield high performance with effective incorporation of light-trapping and surface passivation was demonstrated by a number of researchers. Table 8.1 compares the cell parameters of three devices of different thickness. One of them is a typical high-efficiency thick cell with light-trapping and surface passivation; the other two are thin cells fabricated by different processes. These cells include light-trapping, as well as oxide passivation. Figure 8.6 illustrates the structure of the devices.

The first device is a 44- μm -thick cell with n^+pp^+ structure [27]. Its surfaces are not well passivated, but include a good light-trapping design. The second device is a PERL cell fabricated on a 47- μm single-crystal, float-zone (FZ), wafer. The wafer was chemically thinned, and NF_3 was used during the oxidation step to reduce wafer-bending

Table 8.1 Parameters of two types of thin cells and comparison with a thick cell

Structure	Thickness [μm]	V_{OC} [mV]	J_{SC} [mA/cm ²]	Fill Factor [%]	Efficiency [%]
n^+pp^+	44	643	35.3	75.8	17.2
PERL	47	698	37.9	81.1	21.5
PERL	400	702	41.2	81.2	23.5

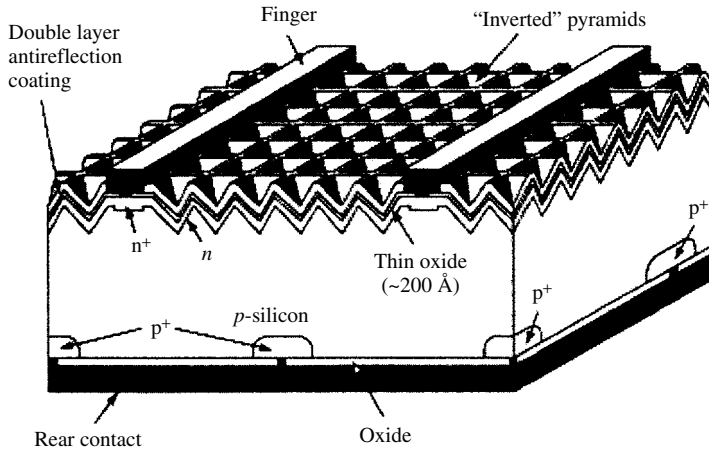


Figure 8.6 Structure of the test cells whose parameters are given in Table 8.1

due to oxide stress. The third device is also a PERL cell, but was fabricated on a 400- μm FZ wafer, and its device structure is similar to the 47- μm device. Figure 8.6 shows the structure of these devices. They include excellent passivation and light-trapping using the PERL process and inverted pyramids, respectively. The performance of the 44- μm n^+pp^+ cell is considerably lower than that of the other two cells, primarily due to inadequate passivation. Chapter 7 further discusses Si wafer-based solar cell technology. The results shown in Table 8.1 clearly demonstrate the potential of thin Si cells.

The table shows that light-trapping in the 47- μm cell can yield a J_{SC} that is only 3.3 mA/cm^2 lower than that of the 400- μm cell. Comparing the two PERL cells shows that it is possible to reduce the thickness by a factor of 10, and yet reduce the efficiency only by 10% (23.5% vs. 21.5%). It is interesting to note that the J_{SC} values of these cells are very close to the theoretical values, indicating very efficient light-trapping and carrier collection. From Figure 8.3, it is seen that inverted pyramids can produce J_{SC} values of 38 and 39 mA/cm^2 for cells having thicknesses of 44 and 47 μm , respectively. It is also seen that beyond a 250 μm cell thickness, the J_{SC} saturates at about 42 mA/cm^2 .

Another cell that illustrates the high performance capability of thin cells was fabricated on a crystalline Si film made by zone-melting recrystallization (ZMR) [28]. Figure 8.7 illustrates the structure and processing sequence for ZMR cells. To minimize substrate issues, a single-crystalline Si wafer was used as a support. A thin layer of SiO_2 was deposited on the Si substrate as a stopping layer for impurity diffusion, and then a 60- μm -thick layer of poly-Si was deposited by a chemical vapor deposition (CVD) technique. The sample was then heated in vacuum by a line-shaped carbon strip, located just above the sample, to about 1200°C to recrystallize the poly-Si layer. A (100)-dominated surface was obtained with a growth speed of 0.2 mm/s, and grain sizes of millimeter to centimeter were reached. They achieved a high conversion efficiency of more than 14% for a 10 \times 10-cm cell with $V_{OC} = 608$ mV, $J_{SC} = 30$ mA/cm^2 , and $FF = 78.1\%$, and 16% for a 2 \times 2-cm² cell with $V_{OC} = 608$ mV, $J_{SC} = 35.1$ mA/cm^2 , and $FF = 77.1\%$. These results are quite impressive for solar cells fabricated on the poly-Si thin film obtained by ZMR technology.

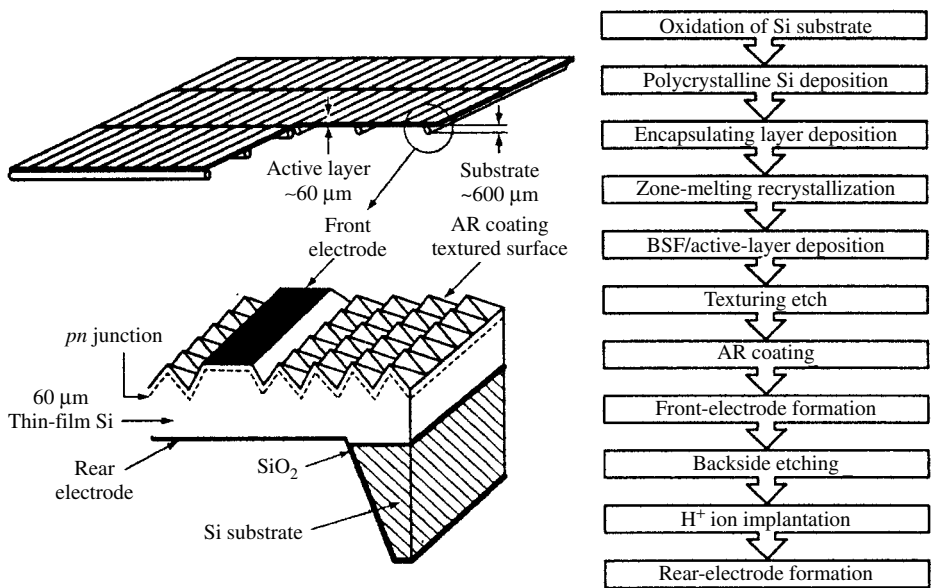


Figure 8.7 A schematic of the structure of the ZMR solar cell with a 60- μm poly-Si active thickness, and an illustration of the process steps involved in cell fabrication

Following the success of researchers who fabricated thin cells using conventional technology of wafer thinning and device processing, several laboratories began investigating alternate methods to produce thin films of Si in which production of Si film and cell processing are compatible. Some of the considerations that went into the qualitative cell design are identified below.

Efficient carrier generation. Thin Si films have an inherent drawback of being weakly absorbing in a significant region of the solar spectrum. A well-known solution to this issue is to incorporate light-trapping by creating surface roughness or texture. The initial attempts at fabricating TF-Si cells relied heavily on this approach. In most cases, back reflections were expected to come from refractive-index discontinuity at the backside of the film and the film support. Some of the approaches resemble those used in a-Si technology. But there are many issues that still remain unresolved about the light trapping in thin films. Some of the details of light-trapping and its applications to thin cells are discussed in the next section.

Efficient carrier collection. Although TF-Si cells are expected to perform well with poor material quality, the minority-carrier diffusion length must still be longer than the film thickness. An approach that can circumvent this restriction is to use a pin structure or multiple junctions, in a manner similar to that in a-Si solar cells.

Mechanical support. A thin Si film, less than 10 μm thick, is not a self-standing structure; it needs a support. Typically, two approaches may be used for supporting thin-film solar cells: (1) the cell is fabricated on a temporary substrate that has suitable properties to participate in the device processing, and it is then transferred or lifted off to a permanent support. In this case, the cell fabrication itself can be done using conventional processes,

and the permanent support can be a rather inexpensive material. The temporary support can be a Si wafer, which is reusable for growing other Si films. A liftoff CLEFT (cleavage of lateral epitaxial films for transfer) technique was originally developed for Ge- and GaAs-based cells using zone-melting recrystallization [29–32]. This technique is very successful, but is not warranted for a low-cost device. (2) A thin film of Si is deposited on a permanent substrate and is then processed into a solar cell. To use conventional processes, such a substrate must withstand high-temperature processing. For example, several laboratories have investigated development of high-temperature glass, thermally matched to Si [33, 34]. Alternately, newer processing methods must be developed that are compatible with low-cost substrates.

The current techniques for TF-Si solar cell fabrication are diverse and use single-crystalline, large-grain multicrystalline, or fine-grain microcrystalline Si films. Although this distinction appears to be related to grain size, in reality, it separates the technologies related to the growth of the film itself. The single- and multicrystalline Si films require high temperature $>800^{\circ}\text{C}$, use of a Si substrate, some type of epitaxial growth, and/or separation from the substrate. The fine-grain films (μ -crystalline) are deposited on a low-cost substrate typically at $<600^{\circ}\text{C}$. Thus, the approaches currently used in thin-film Si solar cell fabrication can be categorized on the basis of processing temperature and substrates used for depositing the thin film. These approaches include using a single-crystalline wafer for deposition of a thin-Si layer, which is subsequently separated from it (or removing a thin layer from a single-crystal wafer and transferring it to another substrate), depositing thin films on a multicrystalline Si wafer, and using a non-Si substrate. Table 8.2 summarizes various substrate types, processing approaches, and the cell efficiencies obtained in the laboratory. Recently, a number of papers have reviewed approaches for TF-Si solar cells [35–37]. Here, we have selected some approaches for further discussion and to illustrate general requirements for design and processing of thin-film Si solar cells.

8.2.1 Single-crystal Films Using Single-crystal Si Substrates

This approach involves separating a single-crystal thin film from a single-crystal substrate. Three techniques are currently being followed. One approach consists of generating a porous-Si layer on a single-crystal substrate, which is then followed by epitaxial growth of a thin film. The thin film is then separated from the substrate by chemically etching the porous-Si interface. Figure 8.8 illustrates various process steps used for this approach [38, 39]. The best efficiency attained by such cells is about 12.5%. The parameters for the best cell (4 cm^2) are $V_{\text{OC}} = 623\text{ mV}$, $J_{\text{SC}} = 25.5\text{ mA/cm}^2$, and $FF = 79\%$.

The second approach that has been suggested is similar to the “smart cut” method used in the microelectronics field for wafer-bonding [40, 41]. It involves implanting a Si wafer with hydrogen and creating a defect interface below the surface, followed by a separation of the surface layer. This technique has been used successfully to separate thin ($<1\text{ }\mu\text{m}$) layers of Si, but may not be cost-effective for making the $10\text{-}\mu\text{m}$ -thick, separable layers needed for solar cells. For the hydrogen atoms to penetrate such a thick layer required for PV applications, requires a very high-energy implant. No single-junction cells have been made using this approach. Recently, however, this approach has been used for making stacked multijunction solar cells that use GaAs-based and Si-based devices.

Table 8.2 A summary of various TF-Si solar cells [35–37]

Technique	Institution	Temperature [°C]	Substrate	Processing	Efficiency	Remarks
ZMR	Mitsubishi Electric Co.	>1300	SiO ₂ on MG-Si	LPCVD 50–60 micron active layer, alkaline wet etching, P in diffusion, H passivation by ion implantation, DARC, backside etching for rear electrode	4.2%, 100 cm ² (1993) 16.4%, 4 cm ²	Recrystallization speed = 1 mm/s
	FhG-ISE	>1300	Perforated SiO ₂ on Si	No seeding, no texture, no defect passivation, interdigitated grid, 30 micron by thermal CVD	6.1%, 4 cm ² (1996)	9.3% by Large-Area Recrystallisation (LAR)
		>1300	Graphite	Interdigitated grid, reactive ion etching	11.0%, 4 cm ² (1997)	9.3% on ceramic, >17% expected for screen printing
SPC	Sanyo Electric Co.	600	Metal	PECVD <i>p</i> -type a-Si:H (SiH ₄), ITO sputtering, evaporation of Ag finger contacts	9.2%, 1 cm ² (1994)	10-um a-Si, 10–600 min annealing
LPE	Astropower Inc.	~1000	Graphite cloth	Gas phase P in diffusion, PECVD H passivation, photolithographic contacts, DARC	13.4%, 1 cm ² (1994)	Si directly deposited on substrate, active layer = 80 μm
			n/r	POCl ₃ , Al gettering, H passivation, PECVD SiO ₂ as ARC	14.6%, 1 cm ² (1996)	Film thickness unknown
			n/r	n/r	16.6%, 1 cm ² (1997)	Record thin-film Si on foreign substrate, no vacuum process

CVD	Univ. de Neuchatel	200	Textured TCO/glass	3.6- μm , $\mu\text{c-Si}$ by PECVD at 100 MHz (SiH_4), doping by PH_3 and B_2H_6 , ZnO/Ag back contact	8.5%, 1 cm^2 (1999) 13.1% a-Si:H/ $\mu\text{c-Si}$ 10.7% (1999)	Deposition rate <2 A/s, unstabilized, stabilized (other substrates possible)
	IMEC	>1000	p^+ SILSO	20- μm film by thermal CVD, DARC, no texture, SiN passivation, evaporated contacts	13.7%, 4 cm^2 (1997)	No H passivation 11.6%, 7.6% on SSP, 10.3% on RGS, 13.2% on EFG
	FhG-ISE	>1000	Silicon Sheets from Powder (SSP)	First deposition BSF, 30 micron by thermal CVD, no texture, no H passivation, SiN coating	8.00%, 4 cm^2 (1997)	Dep. Rate >10 $\mu\text{m}/\text{min.}$, 11.1% on SiLSO, 17.4% on FZ (inverted pyramids, local emitter, thermal oxide)
	Ecole Polytechnique	150	Textured TCO/glass	Polymorphous standard <i>p-i-n</i> , 0.4–0.8 micron <i>i</i> -layer.	9.30%, 0. 1 cm^2	Mixed a-Si:H/ $\mu\text{c-Si}$ matrix
	Canon Co	200–400	n/r	Standard <i>n-i-p</i> structures, Ag/ZnO back contact, >1 micron thick <i>i</i> -layer, VHF PECVD.	7.4%, 0.25 cm^2 (1999) 11.5% a-Si:H/ $\mu\text{c-Si}$	Stabilized results
Excimer laser crystallization	Kaneka Co.	<550	Glass	Laser crystallization of 100-nm a-Si by PECVD ($\text{B}_2\text{H}_6/\text{SiH}_4$), followed by <i>n</i> - and <i>p</i> -type $\mu\text{c-Si}$ and 6 micron intrinsic poly-Si (all PECVD), ITO front contact and Ag fingers.	10.1% 0.25 cm^2 (1997) 12.8% a-Si:H/ $\mu\text{c-Si}$ (1997)	Efficiency >14% expected

Note: n/r = not reported (proprietary reasons); BSF: back surface field; LPCVD: low pressure CVD; TCO: transparent conducting oxide; RGS: ribbon grown on substrate; EFG: edge-defined film-fed growth; ARC: antireflection coating; DARC: double layer ARC; SPC: solid phase crystallization; LPE: liquid-phase epitaxy

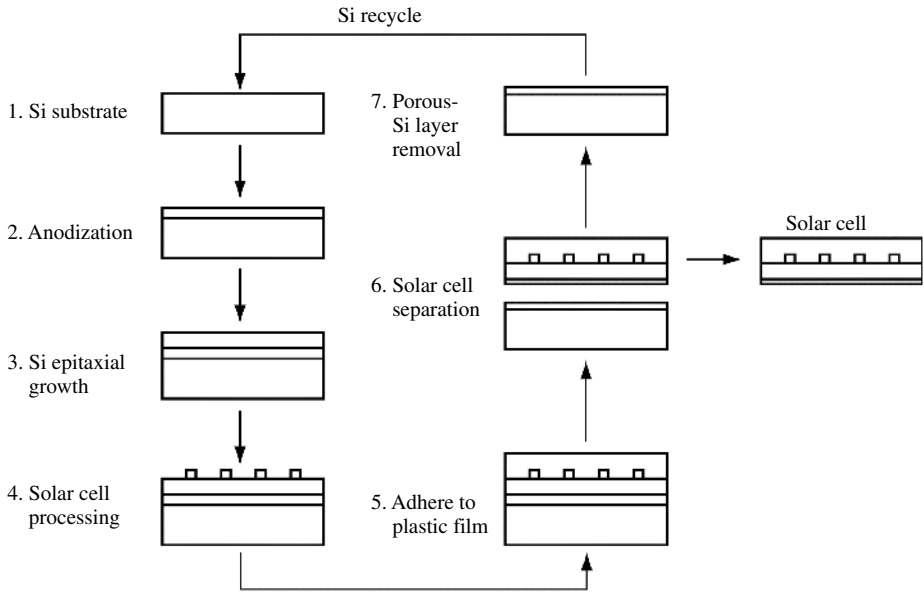


Figure 8.8 A schematic of various process steps involved in the use of porous Si as a separation layer

The third technique, called *epilift*, consists of depositing an epilayer on a patterned single-crystal wafer through a mask with openings along $\langle 110 \rangle$ directions [42]. The masking layer is exposed in a mesh pattern; the lines are 2 to 20 μm wide and spaced 50 to 100 μm apart. The growth faces have an (111) orientation, and the layer has a diamond cross-section giving it an antireflection texture. Figure 8.9 is a schematic of the cell configuration. Although this approach appears to have been commercialized, to date no cell performance has been reported.

8.2.2 Multicrystalline-Si Substrates

Thin Si films can be deposited on a multicrystalline Si (mc-Si) substrate by an epitaxial process. The general objective is to use a low-cost, large-grain, cast-Si wafer, such as a metallurgical grade feedstock, as the substrate and to deposit a high-quality thin layer on it. The epitaxially grown layer would be low in impurity content, as well as in crystallographic defects [43, 44]. There is interest in the use of liquid-phase epitaxy, as well as other vapor-phase deposition techniques for high-growth-rate. Some of the issues in this method include impurity contamination from the low-cost substrate, different growth rates of different grains, and prevention of substrate defects from propagating into the film.

One of the major problems in this method is that the solar cell is not amenable to efficient light-trapping designs because the backside becomes a Si-Si interface with little or no discontinuity in the refractive index for high reflectance from this interface.

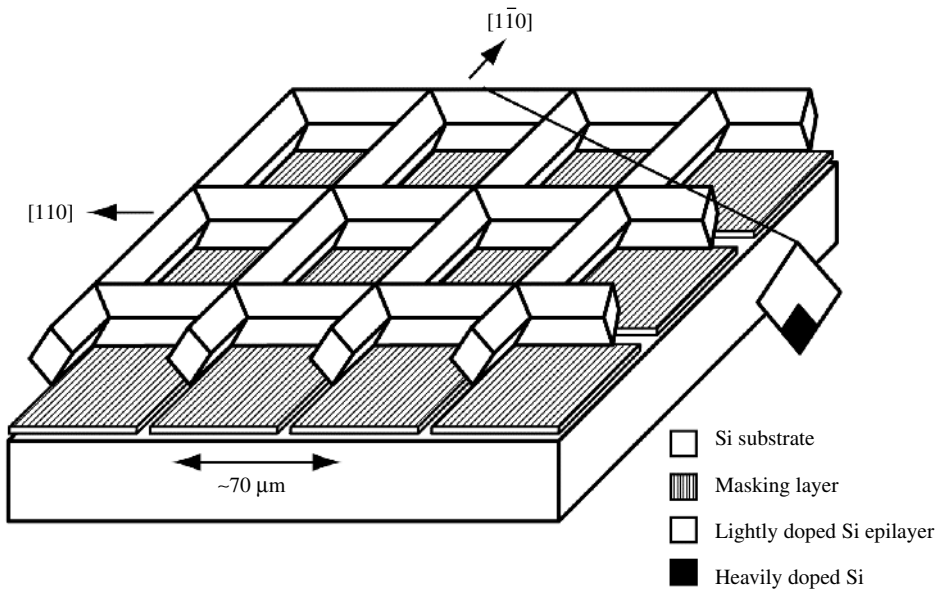


Figure 8.9 A schematic of the epilift process. Masking layer – Si_3N_4 ; epi layer is grown by LPE process. Typical epi thickness = $20 \mu\text{m}$

8.2.3 Non-Si Substrates

The cost advantages of thin-film Si are likely to be realized if the support for the thin film consists of a low-cost substrate. Clearly, in this case, it is not possible to directly deposit a crystalline or mc-Si film. Use of a non-Si substrate has gained some prominence because of the recent success in depositing $\mu\text{c-Si}$ on glass substrates at reasonably low temperatures. However, there are a number of challenges in making such a device. These challenges are related to both the design and the fabrication process(es) of the device. A major issue in the device design is identifying method(s) for efficient light-trapping that are compatible with a low-cost cell design. Theoretical calculations show that film thicknesses of about $10 \mu\text{m}$ are sufficient to yield photocurrent densities of 35 mA/cm^2 in fairly simple thin film device structures [19]. Other issues of device design are related to the carrier-collection approaches, such as the nature of junction(s), electrode geometry, and electronic and optical reflectors. Finally, all of these aspects must be achieved compatible with low-cost methods of cell fabrication.

A recent advance in Si-based thin-film technology has led to a new realm of thin-film $\mu\text{c-Si}$ solar cells. The Kaneka group has developed a cell configuration called *Surface Texture and enhanced Absorption with a back Reflector* (STAR) [45, 46]. Figure 8.10 shows a sketch of the STAR cell. It consists of a glass substrate with a back-reflector on which an n -type $\mu\text{c-Si}$ film is deposited by the plasma CVD process. Next, an i -type poly-Si film (typically 2 to $4 \mu\text{m}$ thick) is deposited at substrate temperature $<550^\circ\text{C}$; this layer has no intentional doping, but is slightly p -type and has a carrier concentration

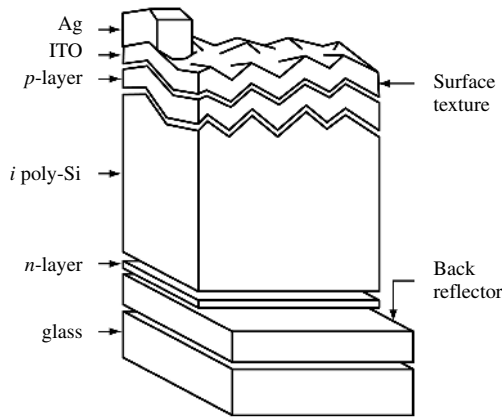


Figure 8.10 Illustration of the structure of a STAR cell. The $\mu\text{c-Si}$ I-layer is typically 2 to 3 μm in thickness

Table 8.3 Measured $I-V$ parameters of STAR cells of different film thickness. The efficiencies are measured as the *Aperture efficiency*, which includes metallization, and *inside efficiency*, which excludes metallization area

Cell thickness	J_{SC} [mA/cm ²]	V_{OC} [mV]	FF [%]	Total area efficiency [%]	Active area efficiency [%]
1.5	22.9	526	77.2	9.3	–
2.5	24.39	510	75.5	9.4	9.8
3.5	26.12	480	74.8	9.4	9.8

of about 10^{15} to $10^{16}/\text{cm}^3$. This layer is followed by depositions of a p -type Si film, a layer of ITO and an Ag-grid electrode. Some of the results obtained on the STAR devices are given in Table 8.3. This approach has shown astounding progress, manifested in a cell of about 10.4% efficiency, in a very short time. Initial theoretical calculations indicate that 16 to 18% cell efficiencies are possible with moderate grain size and some novel cell designs. It is important to note that the main part of the device uses an intrinsic material based on an nip structure. As pointed out earlier, the drift field within the i -layer can greatly increase the effective minority-carrier lifetime. However, because GBs exist within this region, the structure is prone to shunting effects that can limit the V_{OC} and FF . It is interesting to note that although the J_{SC} values increase with thickness, the V_{OC} values of the STAR cells decrease with increasing thickness. This behavior was explained in the previous section in Figures 8.1 and 8.2.

A novel approach for obtaining high V_{OC} could be to use thin-film material consisting of a mixture of a-Si and $\mu\text{c-Si}$. Although the physics of the $\mu\text{c-Si}$ phase within an a-Si matrix is only beginning to be studied, it is likely that properties of such a composite phase can be tailored to exhibit behavior of either species. Thus, an a-Si-rich phase in the I-region can display higher V_{OC} , whereas a $\mu\text{c-Si}$ -rich phase can yield higher J_{SC} . Indeed, there appears to be some evidence of this behavior. Researchers from Institut fur

Photovoltaic have fabricated TF-Si solar cells with a $V_{OC} = 600$ mV and an efficiency of 10.2%, using a two-phase material with a ratio of a-Si: μ c-Si of 4:6 [47, 48].

Recently, a new structure has been proposed at the National Renewable Energy Laboratory (NREL) that integrates several processing advantages in the cell design and overcomes many of the substrate problems [49–51]. Figure 8.11 is a sketch of the cell, which consists of a *p*-type Si film, about 10 μ m thick, deposited on a metal-coated glass substrate. An *n*-type junction can be made by any conventional method, followed by an AR coating and front metallization. As illustrated in the figure, the cell has texture on both the back (Si-metal) interface and the front surface. Some other important features of the cell are: (1) the thickness of the Si film is about 10 μ m, with a preferred grain size in the range of 10 to 50 μ m; (2) it is double-side textured with an AR coating on the front side, and the texture height is about 1 μ m; and (3) the substrate material is low-cost glass, which is isolated by a metal layer from the Si layer. The back metal (at the Si-glass interface) has multiple functions – it serves as an optically reflecting back-electrode, a gettering medium, and an interface layer to relieve the stress resulting from thermal mismatch between the glass and Si.

Many cell designs use textured interface(s) and a reflecting back-electrode that is directly located on the thin cell. A disadvantage of the reflecting metallic or conducting oxide back-electrode is that it can lead to significant losses due to optical absorption. However, this loss decreases with an increase in the film thickness. The mechanism of metallic loss is discussed in detail later in Section 8.3.

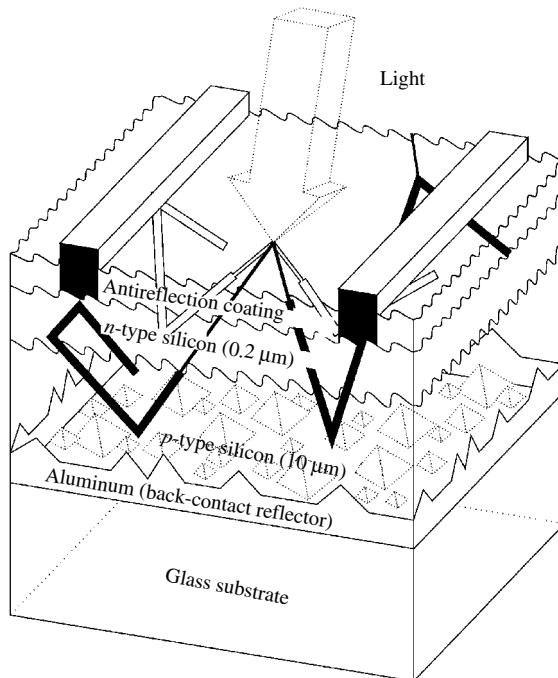


Figure 8.11 A schematic of the proposed thin silicon solar cell

The primary aim of exploiting a thin cell is to lower the bulk recombination losses that can lead to higher FF and V_{OC} . However, this must be done in a way that promotes good carrier generation and collection. Carrier collection can be a particularly difficult problem in a $\mu\text{-c-Si}$ cell because of carrier recombination at the GBs and the small grain size. The University of New South Wales (UNSW) has developed a multijunction cell approach to overcome this problem. The multijunction approach, reminiscent of a-Si cell designs, can circumvent the effect of poor material quality (i.e. short minority-carrier diffusion length) by providing closely spaced collecting junctions. Although the details of the cell material are not known, it is expected that the semiconductor film will consist of hydrogenated microcrystalline silicon. Such a film consists of polycrystalline Si with grain size typically $<1\ \mu\text{m}$, hydrogenated grain boundaries, and material that contains a significant amount of amorphous tissue in the film. Recently, UNSW group reported 7.2% efficiency using this approach. Details of the device structure and processing methods were not disclosed. However, it is believed that a PECVD technique is used for Si deposition [52]. This type of material, deposited by plasma-assisted deposition, has been used by the Neuchatel group in Switzerland [53], which has reported an efficiency of 12%.

8.3 DESIGN CONCEPTS OF TF-SI SOLAR CELLS

Like any other emerging technology, the fabrication of TF-Si solar cells has, to date, followed empirical optical and electronic designs. The optical design aims at a high degree of light-trapping, such that the effective optical thickness of the absorber is similar to that of a much thicker wafer-based cell. It is generally known that one or more interfaces must be rough or textured to produce effective light-trapping. The electronic design of a TF-Si cell, particularly one using small-grain Si, is very difficult because such a structure has three-dimensional nonuniformity. Later in this chapter, we will illustrate some preliminary calculations using a software package that is currently being developed. However, qualitative designs can be derived using lumped material parameters such as effective minority-carrier lifetime, effective surface-recombination velocity, and absence of local shunting.

The material quality of a TF-Si cell should be such that the volume recombination is significantly lower than its thick-cell counterpart. In a thin-Si cell, the carrier recombination is expected to arise primarily from impurities, grain boundaries, and interfaces. Impurity effects can be minimized by the use of Al gettering, whereas a large ratio of grain size/Si thickness can minimize shunting effects of grain boundaries. A more difficult task is that of interface passivation, particularly if the Si film is in contact with a substrate material that may be conducting.

Unfortunately, cell design and processing are intimately connected. We will, however, attempt to consider a representative cell structure (that has nearly all the elements of any TF-Si cell) and illustrate optical and electronic design concepts. The emphasis will be on the physics and methods of designs. The cell structure we consider is illustrated in Figure 8.12. It consists of a glass substrate coated with a layer of a metal such as Al. A thin layer of p -type amorphous or fine-grained $\mu\text{-c-Si}$ film is deposited on the Al-coated substrate. The deposited film may be grain-enhanced by using one of the techniques described in the next section describing deposition techniques. In particular, it must employ a technique that allows the substrate temperature to remain below its softening point. The grain-enhanced film forms the base region of the cell. The method of

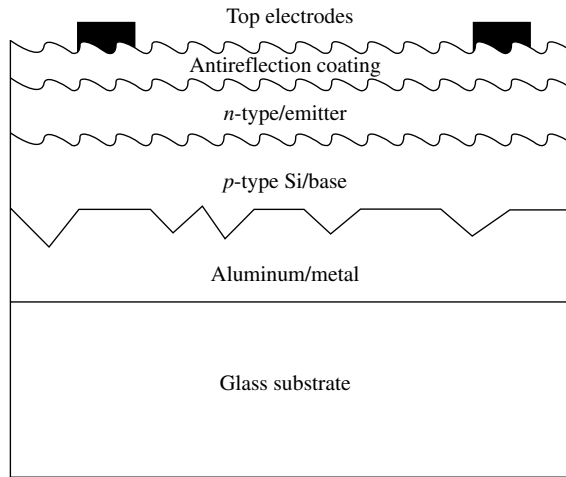


Figure 8.12 A sketch of the generic device structure used for cell design discussion

deposition for amorphous or μc -film is not critical to the grain-enhancement process, and can be done by any technique that can produce high throughput and good material quality. Thus, a variety of film-deposition techniques such as sputtering, PECVD, hot-wire CVD, and photo-CVD can be used for Si deposition. The junction is expected to be fabricated by a low-temperature process, such as the deposition of an n -type, μc -Si layer. Use of low-temperature deposition technologies is a major difference between TF-Si and the conventional wafer-based Si solar cells. In addition to maintaining the integrity of the substrate and rear metal layer, a low-temperature process can minimize the diffusion of dopant along grain boundaries. Other techniques that can exploit defect-engineering concepts also have the potential of forming an n/p junction at low temperatures. An important feature of the device configuration of Figure 8.12 is the interfacial Al film. This layer functions as a multipurpose buffer layer. It participates in grain enhancement, acts as an ohmic back contact, serves as an impurity-gettering layer, and provides back reflection for effective light-trapping.

Qualitatively, one can identify various built-in features of the cell structure that potentially can make it a high-efficiency design. These include the following:

1. An interfacial texture to promote light-trapping. Some details on the nature of the texture, such as shape, height, and location(s) of the texture, are determined in the next section.
2. The use of a backside optical reflector to enhance light-trapping.
3. A large grain-size-to-film-thickness ratio compatible with high V_{OC} and FF . Large grain size is obtained by solid-phase grain growth using photo-excitation (e.g. IR (infrared) lamps, lasers, RTA).
4. A built-in impurity-gettering mechanism that can improve the material quality of the deposited Si. It is common for thick Si wafer-based solar cell processing to require advanced techniques, such as impurity gettering and hydrogen passivation. The proposed structure offers a simple means of using Al gettering. As discussed in

the next section, phosphorous diffusion and Al alloying are very effective impurity-gettering methods.

8.3.1 Light-trapping in Thin Si Solar Cells

As pointed out earlier, a thin-film Si solar cell requires highly efficient light-trapping designs to absorb a significant fraction of the incident sunlight and to minimize reflection. Light-confinement approaches have been discussed in detail for wafer-based cells [54]. Here, we will concentrate only on thin cells. A true optical confinement (or light-trapping) implies that once the light is transmitted into a wafer, the structure sustains the light without transmission from the surfaces. In electromagnetic devices, this is referred to as a *guided wave*. In thin dielectric films used as waveguides in integrated optics, the guided waves use total internal reflection and some specific coherent features to achieve this condition. In a solar cell structure, such modes are not possible. The modes of the structure are radiation modes. Thus, light-trapping as used in solar cells is a misnomer. However, it is supposed to imply relative enhancement of optical absorption over the planar configuration. This necessitates two features of the structure: (1) capability of increasing the optical path of the light transmitted into the cell, and (2) making the structure asymmetrical, such that reflectance at two surfaces is different. An additional requirement in a solar cell is to minimize the reflectance of the illuminating sunlight.

Antireflection (AR) coatings and front-side texturing can be used to fulfill this goal. Choosing appropriate materials for AR coatings and designing the configuration of the front-side texture are among the tasks for optical design of solar cells [55]. The only way to enhance light-trapping in a terrestrial (completely illuminated) solar cell is to use rough surfaces/interfaces instead of planar structures. An analysis of light-trapping concepts using thermodynamic equilibrium conditions suggested that a semiconductor slab with rough surfaces can produce an effective increase in the optical path by a factor of $2n^2$, where n is the refractive index of the semiconductor [5]. The shape of the surface/interface of the device will play a critical role in the light-trapping process. Finding the most appropriate surface configuration that can maximize light-trapping is one of the major goals of optical design of the solar cell. Depending on its morphology, a rough surface can be either Lambertian reflective (a random roughness that causes scattering to follow a $(\cos\theta)^2$ distribution) or geometric reflective (textured surface having a feature size larger than the wavelength of light). Only the surface/interface structure that is geometric reflective will be investigated in this chapter. A number of software packages are available for calculating absorption in a solar cell. These include Sun Rays, Texture, and PV Optics [56–58]. Of these, *PV Optics* is the most general and allows investigation of many features as will be shown later.

One of the important issues in a thin-film solar cell that is seldom considered for thick cells is the metallic absorption loss. All solar cells need contacts, and in many cases, contacts may be expected to serve as optical reflectors. For example, a-Si solar cells use Al or Ag as part of the back-reflector. Unfortunately, a metal surface is not totally reflective. Typical reflectance at an air–metal interface may be quite high, $\sim 90\%$ for Al and 95% for Ag. However, when such a metal is used in a solar cell, the metal loss is enhanced. The reflectance at the semiconductor metal interface is lower than that at the air–metal interface; the light that is transmitted into the metal is absorbed there,

contributing to the enhanced loss. Furthermore, if the interface is rough or textured, the area of the metal is increased contributing to a higher loss. In a good light-trapping cell design, the light at the weaker end of the spectrum can encounter many reflections within the cell. At each reflection, a part of the light incident on the metal will be absorbed instead of being reflected back to the semiconductor. The photon loss due to metal will become a severe problem when the thickness of the cell decreases and the number of passes increases. Minimization of the metal loss is also an important task in the design of the solar cell.

In this chapter, the optical-modeling software, *PV Optics*, is used to discuss the optical design of TF-Si cells. We use the example of a single-junction thin-film solar cell illustrated in Figure 8.12. The results of a series of calculations will be presented to provide information on the influence of various features of the cell configuration on the optical properties of the device, which can help select the best configuration for single-junction Si thin-film solar cells. It should be emphasized again that the optical design of the cells is only an optimization process of the cell structure which was itself determined by other design criteria. The results of the optical design can be very different for different structures.

8.3.2 Description of PV Optics

PV Optics is an optical-modeling software developed by Sopori *et al.* at NREL [59]. This software can calculate a variety of optical parameters for multilayer devices operating in air or within an encapsulated module. These parameters include reflectance, transmittance, distribution of absorbed photons in each layer, and integrated absorbance weighted with an AM1.5 spectrum to determine the MACD for each layer. The method is the numerical equivalent to shining a beam of light on the sample that has an arbitrary surface morphology. This beam is split into a large number of beamlets that impinge on a small region of the surface. Each beamlet is permitted to propagate within the sample, and we keep track of its entire path while it undergoes reflection, transmission, and absorption. In this manner, each beamlet bounces back and forth within the sample. The net energy absorbed at each plane within the sample is determined. This procedure is continued for each beamlet until the energy in the beam is reduced to nearly zero. This process yields the net reflection, transmission, and absorption in the device structure. *PV Optics* uses a combination of ray and wave optics to suitably address thin and thick media, and metal optics.

In our calculations, MACD is used to evaluate the ability of the device to absorb photons in the semiconductor layers. It is defined as the current density that could be generated if every photon (in AM1.5 spectrum) absorbed in the semiconductor layer would generate an electron-hole pair and this pair would contribute to current that is collected by the external circuit. Another parameter, metal loss, is used to estimate the amount of photons lost at the semiconductor/metal interface. Metal loss is defined as the current density that could be generated if every photon (in AM1.5 spectrum) lost at the semiconductor/metal interface would generate an electron-hole pair and this pair would result in a current that is collected by the external circuit. Thus, better devices have higher MACD and lower metal loss.

It should be pointed out that a metallic back-reflector requires a careful design, because such a reflector is accompanied by a loss of photon flux caused by free-carrier

absorption. The amount of the absorption loss depends on the texture parameters, the thickness of the film, and on the metal itself. The approach for minimizing the reflector loss in thin amorphous-silicon solar cells is discussed in several papers [60, 61]. Here we use a similar approach to optimize parameters for the cell structure shown in Figure 8.12.

Figure 8.13(a–d) shows the calculated optical properties of the cells with the basic structures shown in the inserts of these figures. The MACD and metal loss under different conditions are also denoted in these figures. In this calculation, the thickness of the cell considered is 10 μm and the back-contact metal is Al. The texture height is 1.0 micron. From this figure, it can be seen that as long as either surface is textured, the MACD of the device will be higher than that of double-side planar cells, even if metal loss is higher in some cases. Another observation that can be made from these figures is that the MACD will be improved more (about 30%) in double-sided textured or front-side textured/backside planar cells. Double-sided textured cells will yield the highest MACD. This conclusion suggests that double-sided textured or front-side textured structures should be used in the design of solar cells. The important point is that it is more effective to

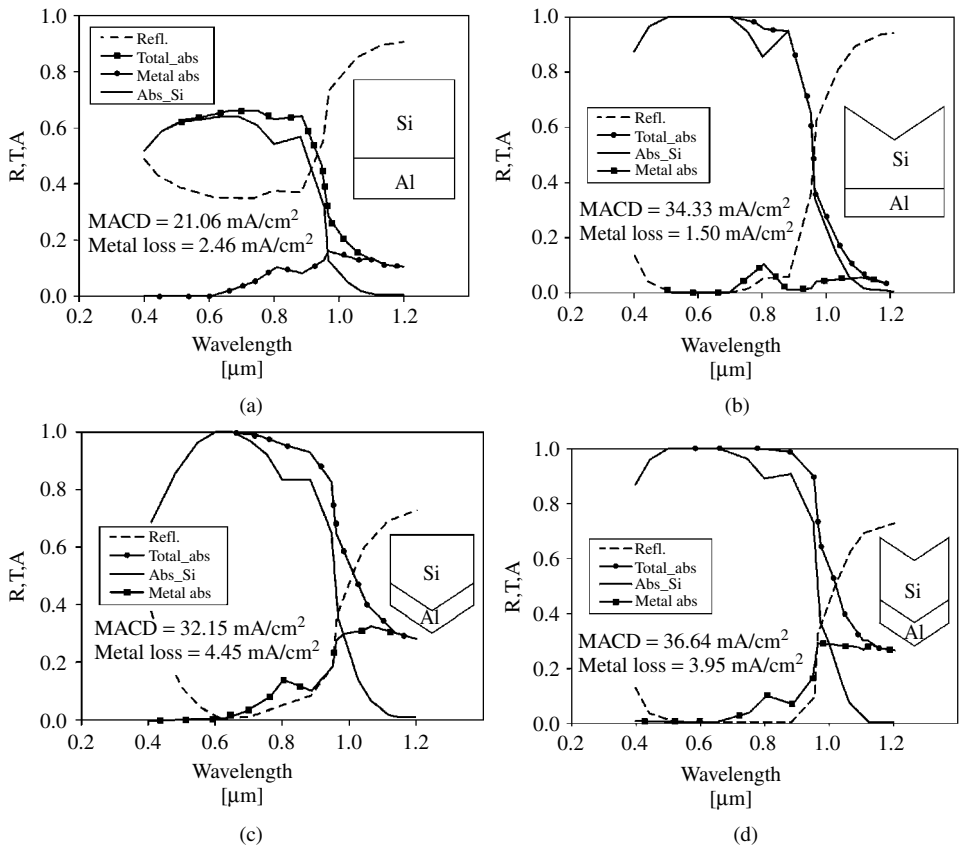


Figure 8.13(a–d) Calculated reflectance (R), transmittance (T), and absorbance (A) of a single-junction cell under different surface configurations. The cell structures are shown in the inset of the figures. Absorber thickness = 10 μm . (a) Planar, (b) FTBP, (c) FPBT, and (d) DT

scatter light entering the cell than at the back-reflection. The same conclusion has been reached by other a-Si solar cell researchers [62, 63]. Another key observation is that any textured surface, front or back, drastically reduces the reflection losses (note how high they are in Figure 8.13(a) between 400 and 1000 nm).

Figure 8.14 shows calculated metallic loss (as mA/cm²) arising because of the Al back-reflector as a function of the film thickness for three cases of the texture: (1) front-polished and back-textured (FPBT), (2) front-textured and back-polished (FTBP), and (3) double-sided textured (DT). These calculations assume an AR coating consisting of 710 Å Si₃N₄ and 100 Å of SiO₂. It is seen that the metallic absorption is lowest for back-polished configuration for all film thicknesses, and that all losses decrease as the Si thickness increases because less light reaches the back contact.

To further understand the effect of thickness on various optical losses, Figure 8.15 shows the calculated values of reflectance, the Si absorbance, and the metallic loss as a function of wavelength for two different values of the cell thickness. The cell structure, depicted in the inset, consists of front-polished and back-textured surfaces; the cell thicknesses are 5 μm and 15 μm. From this figure, we can conclude that an increased absorbance in the thicker Si film results not only from increased single-path absorption but also because of a reduction in the metal loss associated with reduced energy impinging at the back semiconductor/metal interface.

The details of light-trapping presented in Figures 8.13 to 8.15 provide insight into various mechanisms that control dependence of J_{SC} on the absorber thickness, and the losses arising from metal contacts, for different texture configurations. We can now examine the influence of thickness of a single-junction Si cell on the MACD for different texture configurations. Figure 8.16 shows the calculated MACD as a function of the Si-film thickness for three surface configurations: FTBP, FPBT, and DT. The texture height used in these calculations is 1 μm. It is seen that in all cases the MACD nearly saturates after

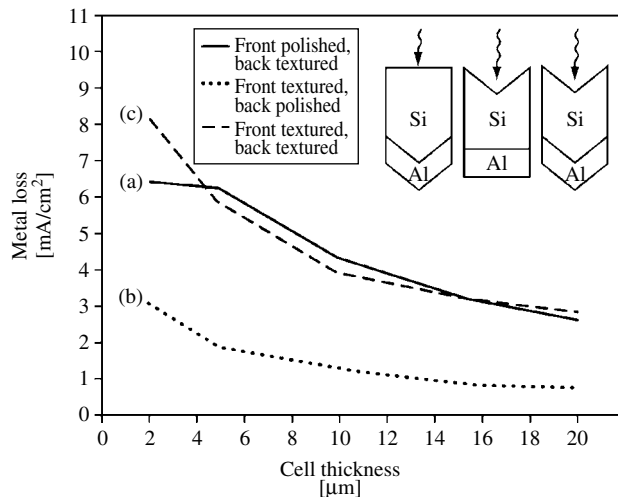


Figure 8.14 Metal loss due to absorption by an Al back-reflector as a function of thickness for three different cell structures. Texture height was 1.0 μm

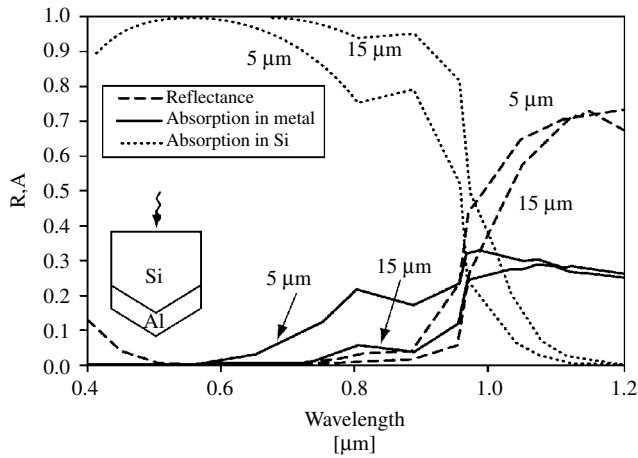


Figure 8.15 Calculated values of reflectance, Si absorbance, and metal absorbance for two cells, 5 μm and 15 μm thick, showing mechanisms of the enhanced absorption. The cells have front-polished and back-textured configuration. Texture height was 1.0 μm

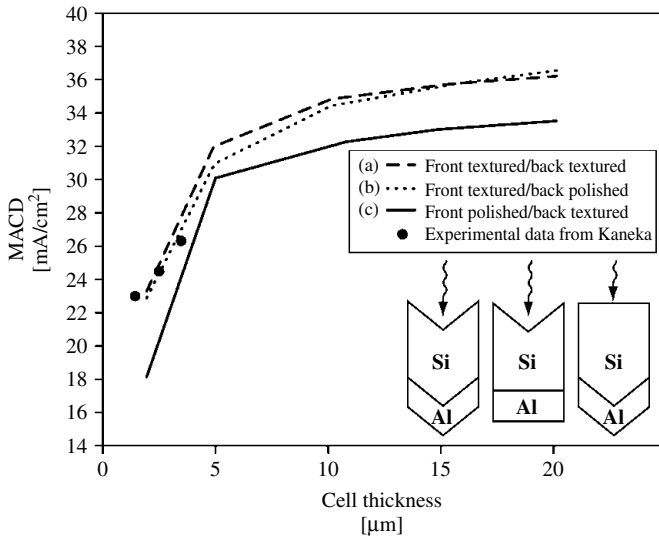


Figure 8.16 Calculated maximum photocurrent generated in a cell with light-trapping involving a metal reflector

the film thickness has reached about 10 μm. Furthermore, texturing at both interfaces appears to be the most suitable cell configuration. Figure 8.16 includes experimental data from Kaneka [45, 46]; the solid points show excellent agreement with calculated results. One can deduce the effect of light-trapping by comparing J_{SC} values in Figures 8.1 and 8.3 for the same thickness of the cell. In Figure 8.1, the thickness required to generate a J_{SC} of 34 mA/cm² is 80 μm. However, the structures of Figure 8.16 can produce the same values of J_{SC} for a thickness of about 10 μm – a factor of 8 thinner.

Figure 8.16 shows that the MACDs in FTBP and DT cells are much higher than that of FPBT cells, although the metal loss of DT cells is not too different from those of FPBT cells. It can be seen that, with proper optical design, the MACD tends to saturate when the cell is in excess of $10 \sim 15 \mu\text{m}$. Thus, from the view of the optical designer, the thickness of thin-film solar cells should be around $10 \sim 20 \mu\text{m}$ to obtain maximum benefit. Indeed, it is expected that $10 \sim 20\text{-}\mu\text{m}$ -thick cells with proper light-trapping will generate the same J_{SC} as $300\text{-}\mu\text{m}$ -thick cells.

Several processing techniques that can produce texturing in the silicon solar cells were mentioned earlier. They can produce texture with vastly different shapes. We will now briefly discuss the influence of different texture shapes on the properties of thin-film solar cells. For the pyramid-shaped texture pits, three parameters will control the properties of the texture structure: the depth, the bottom angle, and the density of the texture pits. A set of calculations is performed on the cell structure shown in Figure 8.13 using different texture configurations. The terminology used in the text is as follows: the pyramid-shaped pits on the textured surface are simply called *texture pits*. The geometry parameters of the texture pits, such as the depth and the bottom angle, are illustrated in Figure 8.17. When the density of the texture pits is investigated, the ratio between the area of the textured part and the whole area is called area ratio (in which the “area” of a region is actually the length of the corresponding region).

8.3.2.1 Influence of the texture height on MACD

As pointed out earlier in this chapter, texture is typically generated by exposure of (111) crystallographic planes that subtend an angle of 70.4° with each other. To investigate the effect of the texture height on the photocurrent generation, we will assume that pits, having a texture angle of 70.4° , cover the whole surface of the cell. Calculated MACD for a solar cell having a $10\text{-}\mu\text{m}$ -thick Si absorber is about 31 mA/cm^2 . This value is nearly independent of the texture height (between 0.1 and $2 \mu\text{m}$), when the bottom angle remains unchanged. This indicates that very shallow texture pits can be used in the device without degrading performance. This conclusion is important to the thin-film cell structure, which will not accommodate deep pits.

8.3.2.2 Influence of the bottom angle of the texture pits on MACD

In a previous section, we mentioned that texturing produced by chemical etching will result in a fixed texture angle. Many other ways of texturing have been developed recently for

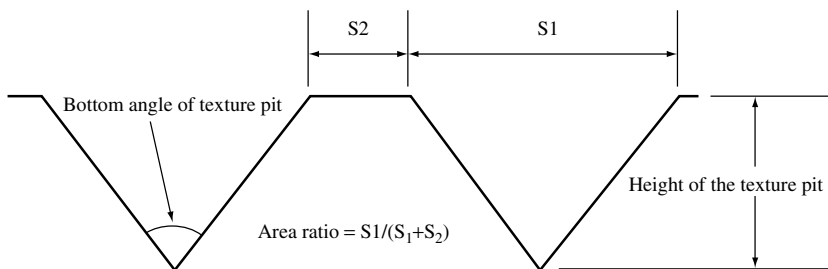


Figure 8.17 The geometry and the terminology used in the texture shape study [19]

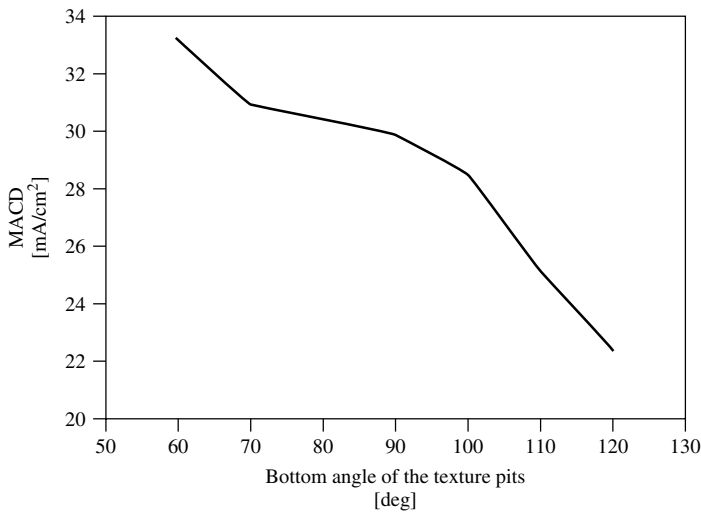


Figure 8.18 The calculated MACD as a function of the bottom angle of texture pits. Si thickness = 10 μm

wafer-based solar cells that use mechanical grooving and surface-shaping techniques. We have also indicated that in deposited films, the texture angle can be related to the grain size. It is useful to investigate the influence of the texture angle of the pits on the cell performance. Here, we show results of calculations performed with *PV Optics* to study the influence of texture angle on the cell current. We assume a 10- μm -thick absorber layer, having a texture pit 1 μm deep on the front side while the backside is planar, and we change the bottom angle from 60 to 120 degrees. Figure 8.18 shows the calculated MACD as a function of the bottom angle of the texture pits. From these results, it can be seen that MACD will drop by about 30% when the bottom angle changes from 60 to 120 degrees. It is important to point out that the dominant effect of changing the bottom angle is to change the reflectance. Analysis of the reflectance spectra shows that the reflectance increases with an increase in the texture angle (i.e. as the surface becomes smoother) in the wavelength range of 0.4 μm to 0.9 μm . In this wavelength range, the reflectance is primarily from the front surface. Therefore, to get better performance, “sharper” texture pits should be used in the cell design. In wafer-based Si solar cell processing, sharp texture is produced by reactive-ion etching (RIE). In the past, RIE texturing has resulted in cells with lower V_{OC} due to shunting. Such shunting results from breakage of the peaks and (or) penetration of metal through the junction during processing. However, this technology is now used commercially by some solar cell manufacturers.

8.3.2.3 Influence of density of the pits

In some processing techniques, the texture pits cannot cover the surface totally. This example will investigate the relation between the optical properties of the cells and the density of the pits.

Figure 8.19 evaluates the influence of pit density on MACD and metal loss. The MACD increases as the fraction of texture pit area increases.

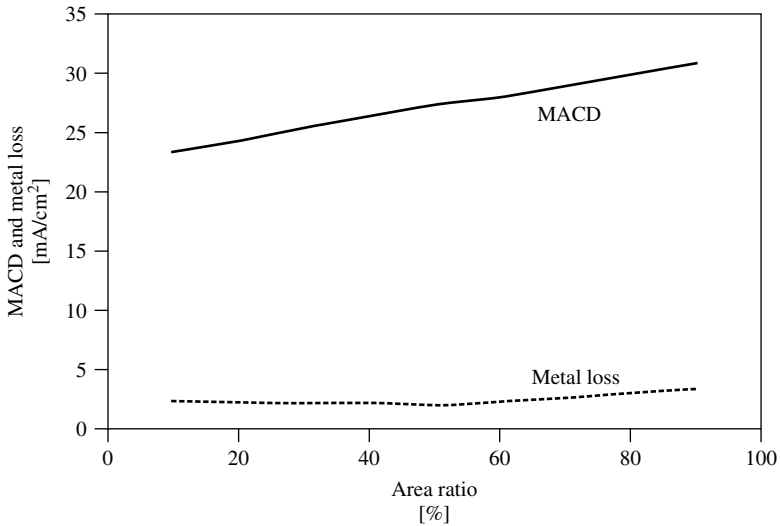


Figure 8.19 Calculated MACD and metal loss as functions of area ratio for a Si cell with 10- μm -thick absorber

8.3.2.4 Summary from optical modeling

From the analysis performed in the preceding sections, we can make some conclusions about the structure of the thin-film solar cells:

1. The thickness of the cell should be 10 to 20 μm in order to get satisfactory J_{SC} .
2. The best structure will be front-surface-textured/backside-polished or front-surface textured/backside-textured.
3. The texture pits should be as sharp as possible, and should occupy the entire surface of the cells.

8.3.3 Electronic Modeling

A generalized electronic model of a TF-Si solar cell should address features such as nonuniformities arising from grain boundaries (GBs) and intragrain defects, as well as detailed optical generation resulting from light-trapping, as illustrated in the previous section. Clearly, this requires a 3-D modeling capability. 3-D modeling is also needed to include metal contacts appropriately. Unfortunately, no modeling package suitable for this purpose is available at this time.

There are two major problems in building an appropriate modeling software for a polycrystalline Si device. First, it is difficult to model electrical fields, recombination, and boundary conditions at GBs and other crystal defects (later we will show one approach to handle fields associated with defects). Second, it is difficult to assign values to parameters associated with defects and GBs. This is because the grain-boundary parameters depend strongly on the interactions of these defects with impurities. For example, clean GBs have been found to have very little electron beam-induced current (EBIC) contrast

which implies very little recombination. The contrast increases with increased impurity segregation.

A good deal of preliminary understanding of the design of a TF-Si solar cell can be acquired through modeling a single-crystalline TF-Si cell. Such a cell may be considered to have uniform material properties, but inclusion of metallization can introduce large spatial nonuniformities (because shadowing effects can be more pronounced in a thinner cell). However, for a first approximation, 1-D analysis can yield reasonably accurate results. In the beginning of the chapter, we used *PV Optics* and PC1D to show dependence of J_{SC} on the cell thickness and V_{OC} on the thickness and the surface-recombination velocity, respectively [64, 65]. Another electronic modeling package, used by most a-Si cell designers, is AMPS (analysis of microelectronic and photonic structures) [66]. To date, PC1D is only a 1-D package and is valid for uniform, homogeneous material without GBs or intragrain defects. Because PC1D does not include detailed light-trapping, a good 1-D modeling would still require a combination of an optical model like *PV Optics* and PC1D.

Accurate modeling of a polycrystalline TF-Si solar cell is complicated not only because of GB issues but also because of a recently observed phenomenon known as *defect-clustering*. It is observed that polycrystalline Si exhibits segregation of intragrain defects into grains of some specific orientations. Thus, one is able to find grains of zero-defect density adjacent to very heavily defected grains (defect clusters). The formation of defect clusters in polycrystalline Si is attributed to relief of thermal stress (produced during crystal growth or deposition) through dislocation generation by grains having certain preferred orientations. These orientations have the lowest-yield stress for the growth or deposition conditions [67]. When the defects are clustered, it is expected that the potentials introduced by different defects may couple with each other if they are close enough spatially, so that some second-order extra energy levels, or even an energy-band-like structure, will be generated. But, unfortunately, there is so far no study on this subject. As a result, modeling of TF-Si cells must include laterally nonuniform material.

A first-order approximate (but simple to handle) model for a polycrystalline TF-Si solar cell is to regard cell performance as being controlled by the spatial variations arising from changes in the grain-to-grain properties such as dislocation density. Each grain can be assumed to be uniform. In this approximation, one can embed GB effects into lumped series resistance that interconnects various grains through a network model. This model was developed at NREL to predict the effects of spatial nonuniformities in a large-area solar cell [68, 69]. Here, the total cell consists of a parallel combination of a large number of smaller cells (in this case, each cell corresponding to a different grain). The characteristics of each cell are determined by the local properties of that grain.

Figure 8.20 illustrates the network model. The solar cell is divided into an array of diodes, where each diode is small enough to assume a uniform distribution of defects. Each node in the matrix depicts a local cell, connected to other cells by a resistor representing the series resistance. The series resistance arises from a number of sources that include the sheet resistivity of the emitter in an n/p device.

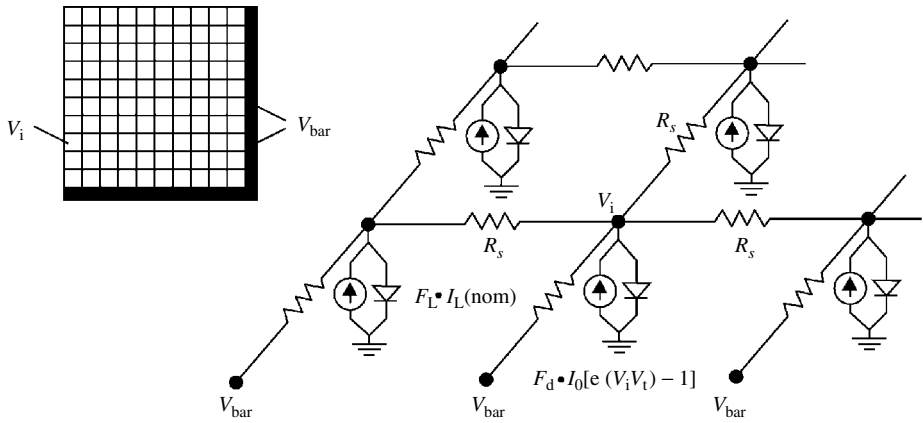


Figure 8.20 A network model of a solar cell showing voltage and current sources corresponding to dark (indicated by subscript d) and illuminated (indicated by subscript L) conditions, and the resistive components due to the sheet resistivity of the emitter

Current–voltage (I – V) curves of a cell are synthesized using diode equations for individual cells. For each cell, we can write the total current density, J , as

$$J = J_{ph} - J_{dark}(V)$$

where J_{ph} and $J_{dark}(V)$ are the photogenerated and the dark-current densities, respectively. The dark current of each local region of a known defect density, is described by

$$J_{dark} = J_{01}\{\exp(eV/kT - 1)\} + J_{02}\{\exp(eV/2kT - 1)\} + J_{03}\{\exp(\beta V - 1)\} \quad (8.1)$$

The first two terms in the above equation are well-known expressions for representing band-to-band and midgap defect recombination respectively in a p – n junction (see Chapter 3). The last term is added to include tunneling currents (as a generalized expression) that occur in heavily defected regions. These tunneling currents arise because of a carrier-hopping mechanism, which is independent of temperature; here β is a constant needed to fit the specific voltage dependence. Hence, a local cell element (i, j) in the matrix is represented by a current source comprising J_{01ij} , J_{02ij} , J_{03ij} , and a corresponding light-induced current density $J_{ph,ij}$. For room temperature operation, the tunneling current can be neglected. One can represent all current components of cell elements in terms of nominal currents of defect-free devices. Accordingly,

$$\begin{aligned} J_{01ij} &= J_{01} \cdot A_{ij} \cdot \exp(eV/kT - 1) \text{ and} \\ J_{02ij} &= J_{02} \cdot B_{ij} \cdot \exp(eV/2kT - 1) \end{aligned} \quad (8.2)$$

where J_{01} and J_{02} represent dark-saturation current densities in the nominal “defect-free” device element. A_{ij} and B_{ij} are the factors representing the ratio of dark current

normalized by the nominal “defect-free” current for each component device. A finite-element computer code, written in Microsoft Excel, is used to analyze the network.

$$V_{ij} = \frac{F_{\text{ph}ij} I_{\text{ph}nom} - [A_{ij} I_{01nom} (e^{V_{ij}/akT} - 1) + B_{ij} I_{02nom} (e^{V_{ij}/bkT} - 1)] + (V_{\text{neighbors}}) / R_s}{N / R_s} \quad (8.3)$$

where

- V_{ij} : Voltage at a node ij
- $F_{\text{ph}ij}$: Fraction of short-circuit current at the node compared to nominal defect-free short circuit (< 1)
- I_{01nom}, I_{02nom} : Nominal short-circuit current per node
- A_{ij}, B_{ij} : Fraction of dark currents at the node (> 1)
- $V_{\text{neighbors}}$: Voltage of the nearest-neighbor cells
- N : Number of nearest-neighbor cells
- R_s : Electrical resistance between cells.

This above network model allows the synthesis of the I - V characteristics of the total cell. Here we will use this model to illustrate the influence of crystal defects on the cell performance. We first consider a spatially uniform, defect-free solar cell; the cell performance is limited by the material properties such as impurity content and the minority-carrier lifetime. The values of various current components are assumed to be: $J_{\text{ph}} = 35 \text{ mA/cm}^2$, $J_{01} = 3.6 \times 10^{-6} \text{ mA/cm}^2$, $J_{02} = 4.5 \times 10^{-10} \text{ mA/cm}^2$. Because this cell is uniform, all device elements in the network model of this cell are identical. Figure 8.21 shows the I - V curve (dotted line) of the total cell. The parameters of the total cell are $V_{\text{OC}} = 650 \text{ mV}$, $J_{\text{SC}} = 34.5 \text{ mA/cm}^2$, $FF = 81\%$, and Efficiency = 18.4%. Now, we consider another cell with same material properties but having 20% of the area covered by heavily dislocated regions. The network model of this cell consists of two kinds of device elements. One similar to those of the defect-free cell, and the other representing defected regions. The parameters for the defected device elements are determined from

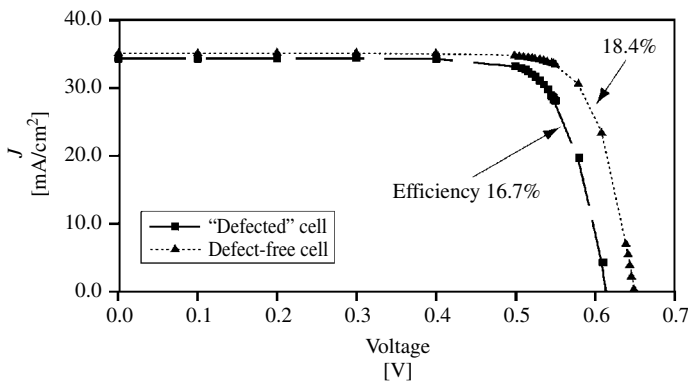


Figure 8.21 Calculated I - V curves of defect-free and defected cells (20% area with defects) showing degradation due to defected regions

experimental measurements, as $J_{ph} = 24.5 \text{ mA/cm}^2$, $J_{01} = 3.6 \times 10^{-5} \text{ mA/cm}^2$, $J_{02} = 4.5 \times 10^{-8} \text{ mA/cm}^2$ [..]. These low-performing devices, constituting 20% of the total device elements, are now randomly distributed in our network model. The resultant I - V curve for the total cell is also shown in Figure 8.21 (solid line). The parameters of the total cell with defects are $V_{OC} = 620 \text{ mV}$, $J_{SC} = 32.7 \text{ mA/cm}^2$, $FF = 75.8\%$, and Efficiency = 16.7%.

It is seen that all the parameters of the “defected” cell are lower than that of the “defect-free” cell. However, the major reduction is in the V_{OC} and the FF . The reduction in V_{OC} is 30 mV whereas J_{SC} is reduced by 1.45 mA/cm^2 . It should be pointed out that in a “defect-free” cell, a reduction of 30 mV in V_{OC} would require a large reduction in J_{SC} (in accordance with the cell equation). This disproportionate reduction in the voltage is caused by increased recombination, which manifests as shunting, due to defected regions. Such shunts represent sources of internal power dissipation within the cell. The network model is directly applicable to multigrain solar cells, if the distribution of defects in various grains is known.

The extent of influence of a GB on the photovoltaic properties of the grains constituting the GB depends on several parameters of the grains themselves. These parameters include density of defects, barrier height, and the carrier density of the grains. In a small-grain material, the grain size can be of the same order as the size of “influence” of a GB. Thus, grains and GBs are modeled as regions with different properties. It is important to note that each region (whether a grain or a GB) is characterized by defects. All grains and the boundaries between adjacent grains can be modeled using categorization developed by Chen [19]. This categorization of various grains (or regions) is based on the properties of defects, summarized below.

Type I: These regions have very low defect densities and may be considered as standard regions where the recombination of the majority carriers can be neglected, and the density of extra charges introduced by defect levels is negligibly small.

Type II: The recombination of majority carriers can be neglected, but the extra charges introduced by defect levels in these regions cannot be.

Type III: These are heavily defected, effectively “dead” regions in which almost all the carriers (both majority and minority carriers) will recombine. In the modeling, the details of carrier distribution inside this type of region are ignored because these regions do not contribute any free carriers to the system. This type of region can include GBs or other defect-rich regions such as heavily diffused emitters.

Type IV: A highly defected region in which a significant fraction of the majority carriers recombine. As a result, the Fermi levels in this region will be different from the Type I regions with the same doping concentrations. Because of the high density of defect levels, it is likely that these regions also have extra charges.

In Type I regions, the electric field $E(x, y)$ is 0. But in the regions of Type II or Type III, which have extra charges, these charges will induce internal electric fields; hence, $E(x, y)$ will not be 0.

An important feature of the characterization of regions into four types is that it includes defect-free regions, defected regions, as well as GBs. In particular, one can appropriately define GB in terms of the properties of adjacent grains (see a later part of this Section 8.3.3.1).

Here, we will present some preliminary results of this model to illustrate the influence of material parameters, such as grain-size and grain-boundary recombination, on cell performance. This model can also be used to study effects of material parameters on the minority-carrier lifetime and carrier transport. We consider a sample with a columnar (two-dimensional) grain structure, which may have many regions of different lifetimes due to different defect distributions, separated by GBs. The sample is illuminated with light to generate photocarriers. The procedure for solving the 2-D continuity equation, subjected to appropriate boundary conditions, is discussed in References [19, 70, 71]. However, some physical insight can be gained by addressing the boundary conditions involving different region types.

8.3.3.1 Boundary/interface conditions

Because we are dealing with multiregion samples, there are two different boundaries: the surfaces of the entire sample and the boundaries between adjacent regions (grains) in the sample. These will be referred to as *boundary condition* and *interface condition*, respectively.

At the surface of the sample, the boundary condition is

$$D \frac{\partial n}{\partial \vec{n}} = Sn, \quad (8.4)$$

where S is the surface-recombination velocity, \vec{n} is a unit vector, n is the concentration of electrons, and D is the diffusion coefficient.

At the interfaces between different regions, the boundary conditions depend on the types of the regions. The GBs between Type I or II regions can be treated as a surface with specific recombination velocities. At the interfaces, the following interface condition applies

$$n_1 = n_2 \quad (8.5)$$

$$D_1 \frac{\partial n_1}{\partial \vec{n}} - D_2 \frac{\partial n_2}{\partial \vec{n}} = Sn_{1or2} \quad (8.6)$$

Here, S is the “effective” surface-recombination velocity. However, if one of the grains is heavily defected, Type III, its boundary will have a finite width due to the field extending into the adjacent grain. This condition is illustrated in Figure 8.22. If the lifetimes of electrons and holes are τ_e and τ_h , respectively, in the Type III region, we can extend the algorithm of Fossum and Lindholm to the bulk region to express the electron current (in p -type samples) at the edge of the interface space-charge region [72].

The interface between a Type IV and a Type I (or Type II) region can be treated as a high–low junction because of their Fermi levels.

Because a solar cell involves an n/p junction for carrier collection, we must also consider how the junction is influenced in different region types. The fabrication of such a junction will influence the nature of the depletion regions, but all the equations developed earlier, including boundary conditions, still apply in the quasi-neutral region (QNR) of

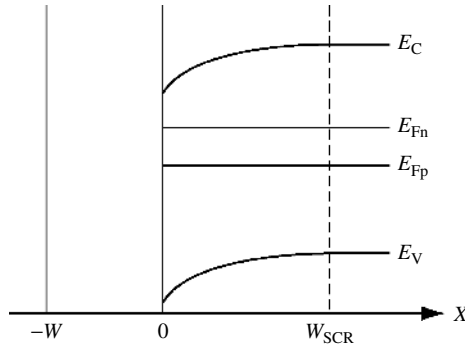


Figure 8.22 The energy band model used for boundary-condition analysis around a Type III region

the n/p junction. However, the depletion space charge region (SCR) region in different types of material need to be treated differently: SCR inside Type I regions should have the same behavior as the SCR in a normal $n-p$ junction. In Type II or Type III regions, because there are extra charges (other than the dopant ions) and they are opposite to the charges of dopant ions, the net total charge should be less than that in the region without extra charges. The most apparent effect of the charges trapped in the $p-n$ junctions may be the change of the width of the depletion region. This change can be easily determined by the Shockley model

$$W_{SCR} = \sqrt{\frac{2\epsilon_{si}(N_A + N_D - 2N_x)(V_{bi} - V)}{e(N_A - N_x)(N_D - N_x)}} \tag{8.7}$$

where N_x is the extra charge density trapped in the Si. This value is the same for n -type and p -type regions, because we assume that the density of defect-related energy levels is the same in these two regions.

The calculation of the recombination current inside the space-charge region due to the Type IV can also be done following the Fossum and Lindholm algorithm.

The resultant band configurations used for device analysis are illustrated in Figure 8.23. The finite element method is used in this model. To limit the number of variables in this calculation, we assume that all the grains are similar. This assumption also brings other benefits to the calculation – since all the grains are similar, no net carrier flow will exist between grains at steady state. Therefore, the current collected by the device is just the summation of the current collected by each grain in the sample.

First, we will examine dependence of cell parameters, V_{OC} and J_{SC} , on the grain size of μc -Si thin-film solar cells. Figures 8.24(a) and 8.24(b), show the calculated values of J_{SC} and V_{OC} for two values of the GB interface recombination velocity, 100 cm/s and 1000 cm/s. The S-value of 100 cm/s corresponds to “clean” GBs. In practice, such a low value of S is hard to achieve. The μc -Si for PV applications is likely to contain impurities, which segregate at the GBs resulting in higher S-values. Thus, $S = 1000$ cm/s represents a more realistic μc -Si. The other parameters used in these calculations are given in Table 8.4. Here, G is the generation rate due to incident light and α is the

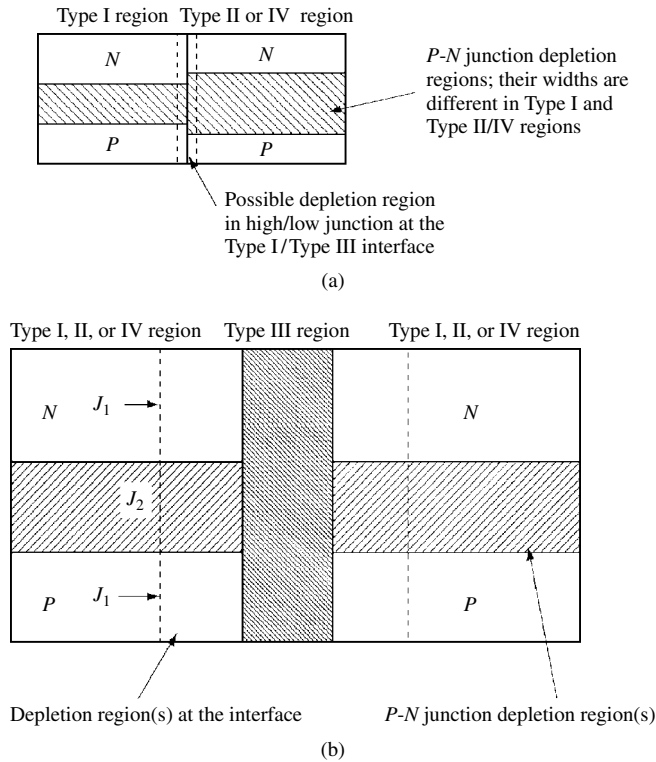


Figure 8.23 The proposed model of different regions in an $n-p$ junction built on imperfect material. (a) The model of Type I, II, and IV regions, and the relationship among them inside a device. (b) The junction at the interface of Type I, II, IV region, and Type III region. J_1 and J_2 are current flows discussed in Reference [19]. The distribution of carriers inside the Type III region is not considered

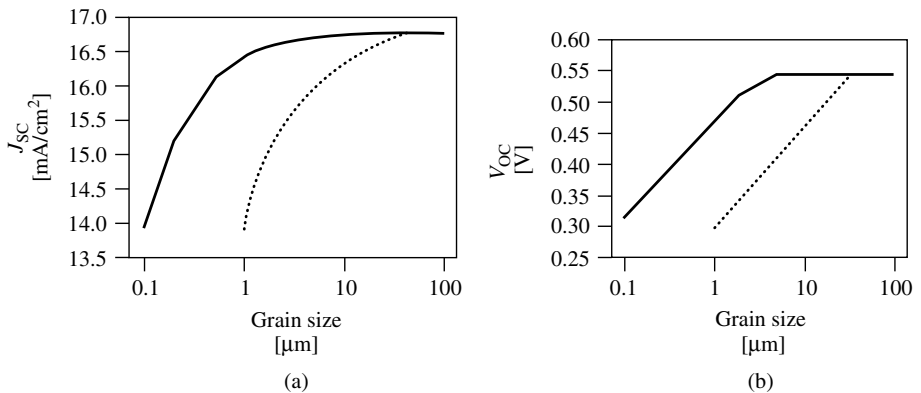


Figure 8.24 Calculated dependence of (a) J_{SC} ; and (b) V_{OC} on the grain size of the 10- μm -thick cell for two values of interface recombination velocity, 100 cm/s (solid lines) and 1000 cm/s (dotted lines)

Table 8.4 The parameters used in calculating the solar cell characteristics

G [s^{-1}]	α [cm^{-1}]	D [$cm \cdot s$]	Junction depth	n -doping	p -doping
10^{18}	100	50	0.5 μm	10^{18}	10^{17}

absorption coefficient. $G = \alpha \times$ number of photons incident at the surface (photons/unit area-second).

Calculated J - V curves, depicting the influence of grain-boundary recombination, are shown in Figure 8.25. Figure 8.25(a) is for a 5- μm -grain-size sample, and Figure 8.25(b) is for a 0.5- μm -grain-size sample. It can be seen that, for larger grain size, the recombination at the GBs will mainly degrade V_{OC} , and not J_{SC} . From Figures 8.24 and 8.25, it can be seen that the larger the grain size, the better the performance of the device. However, the interface recombination has a strong influence on each parameter. For low interface recombination velocity, when grain size is large ($\sim 1 \mu m$), a decrease in the grain size will primarily degrade V_{OC} and not J_{SC} . However, for small grain size ($< 0.5 \mu m$), J_{SC} will also decrease rapidly with a decrease in grain size. Because interface recombination has a very strong influence on the device performance, passivation of the GBs is very important for μc -Si thin-film solar cells. Furthermore, it can also be concluded that, to get a device with satisfactory J_{SC} and V_{OC} , the grain size of a μc -Si thin solar cell should be several microns.

8.3.4 Methods of Making Thin-Si Films for Solar Cells

The deposition techniques for Si films run the gamut from single-crystal deposition using crystalline substrates to microcrystalline Si thin films on glass or steel foil. A variety of techniques are now used for the deposition of thin films for solar cells [73, 74]. These include RF and DC glow-discharge techniques such as plasma-enhanced CVD (PECVD), hot-wire CVD (HWCVD), the electron cyclotron resonance CVD (ECRCVD), and other microwave- and plasma-beam deposition methods. Of these, the PECVD system is well suited to large-area depositions. Some of the newer techniques, such as ECRCVD, remote plasma-assisted CVD, and HWCVD have produced materials with interesting properties such as lower defect density, greater minority-carrier diffusion length, and lower hydrogen concentration. Some of these techniques may hold promise for the future.

Today, commercial a-Si:H solar cells are mostly deposited in multichamber reactors. Hydrogen incorporation is an important issue in the deposition of a-Si:H cells. A Si-bearing gas, typically silane, is used as the process gas in a DC or an RF (13.56–200 MHz) plasma in a pressure range of 0.1 to 1 torr. Typically, the deposition rates are 1–5 $\text{\AA}/s$. A material with good electronic quality requires a dense and a homogeneous network of amorphous Si with minimum void density. These conditions dictate low deposition rates. Hydrogen dilution appears to have a strong influence on the properties of a-Si. However, a high hydrogen dilution rate is accompanied by a reduction in the deposition rate. Typically, VHF plasma excitation involves a source in the vicinity of 50 MHz. Operation

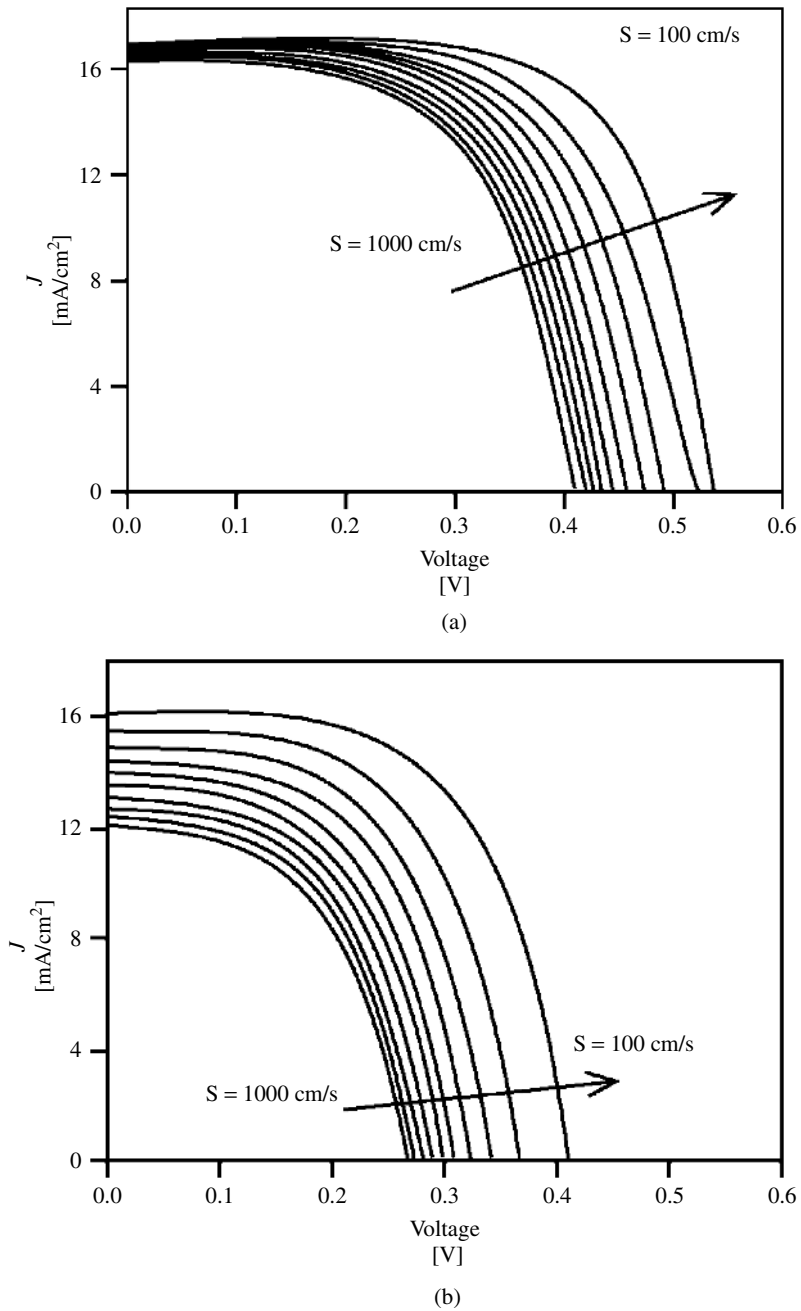


Figure 8.25 The calculated J - V curves for different grain boundary interface recombination velocities (S). In the figures, S changes from 1000 cm/s to 100 cm/s in steps of 100 cm/s . Other parameters are given in Table 8.4. The grain sizes used in the calculations are: (a) $5 \mu\text{m}$; (b) $0.5 \mu\text{m}$ [19]

Table 8.5 Grain-enhancement methods for already-deposited amorphous or fine-grain Si films. Temperature $>600^{\circ}\text{C}$ cannot be applied to low-cost glass substrates

Method	Processing temp. [$^{\circ}\text{C}$]	Processing time	Metal contamination
CVD growth	1000	>10 h	No
Annealing	500	20–40 h	No
ZMR	1200	Quick	No
MIC	<500	Quick	Severe
LIC	>1000	Quick	No

LIC – laser induced crystallization; MIC – metal induced crystallization

in such a frequency range leads to higher deposition rates. See Chapter 12 for a more complete discussion of a-Si materials and deposition techniques.

It is known that typical, low-temperature ($<400^{\circ}\text{C}$) CVD methods generally yield fine-grain ($<0.1\ \mu\text{m}$) Si films. The solar cells fabricated on such films exhibit shunting, low V_{OC} , and poor carrier collection. Thus, it is imperative that a fine-grain (or amorphous) Si film on a glass or some other low-cost substrate be grain-enhanced by a low-temperature process. Table 8.5 gives a summary of the grain-enhancement techniques currently used in thin-film $\mu\text{c-Si}$ formation. The grain enhancement involves the movement of GBs in an attempt to minimize the overall energy. A simple approach for accomplishing this is to perform a high-temperature anneal. However, high temperature ($>600^{\circ}\text{C}$) processing is not compatible with low cost substrates like glass. The processing temperature can, however, be significantly lowered by a suitable choice of film properties and processing conditions.

8.3.5 Methods of Grain Enhancement of a-Si/ $\mu\text{c-Si}$ Thin Films

The grain-growth phenomenon in a crystal is caused by the material's effort to minimize its excess Gibbs free energy from the presence of GBs by minimizing the total grain-boundary area. GBs are a higher energy, nonequilibrium condition compared to a single-crystal structure. Thus, any technique that applies sufficient energy to mobilize GBs will cause grain enhancement.

(a) Annealing

When an a-Si film deposited on glass substrate is subjected to a thermal anneal for an extended period of time, crystallization of the film occurs leading to an increase in the grain size. The thin film remains in the solid phase during the whole process, which is why this kind of process is also called *solid-phase crystallization*. The grain enhancement in this process results from a movement of GBs activated by the heating. An increase in the time or temperature, or both, can further promote the grain growth. The major drawback of the thermal annealing process is that it requires a long time. A typical annealing process will take 20 to 40 h [75]. The annealing time can be reduced somewhat if a surface-textured substrate or doped a-Si layers are used. These methods accelerate the

velocity of grain enhancement, either by introducing some kind of seeds or by activating the grain-boundary movement.

(b) Metal-induced crystallization (MIC)

MIC of a-Si can be used to produce $\mu\text{c-Si}$ with grains larger than those achievable either by thermal annealing of a-Si or by direct deposition of $\mu\text{c-Si}$ by plasma or HW processes. If a-Si is deposited at low temperatures on substrates coated with certain metals, and then heated to a temperature $>300^\circ\text{C}$, the a-Si film can be converted to $\mu\text{c-Si}$. Alternatively, if the deposition of a-Si can be carried out at such higher temperatures on these metals, one can obtain large-grain $\mu\text{c-Si}$ films directly. Here the metal acts as a catalyst to induce crystallization. The effects of several kinds of metals, such as Sb, Au, Al, and In (which form eutectics with Si), and those of Pd, Ti, and Ni (which form silicides with Si), have been studied. Al is a particularly interesting metal for solar cell because it can offer other advantages, as described in this chapter. Earlier studies on very thin ($<1\ \mu\text{m}$) a-Si films found that Al-induced crystallization of a-Si could occur as low as 167°C [76]. However, the grain size of the crystallized films was very small and the annealing time required was between 10 and 60 min. This led to a conclusion that MIC involves intermixing of metal with Si and the formation of a high concentration of metal alloy in the amorphous/crystalline interface. Furthermore, it was found that the growth of the crystalline phase would stop when no more metal is available.

Although the mechanism(s) involved in MIC are not well understood, it is generally believed that nucleation requires a strong interaction between metal and Si [77–79]. These interactions may involve a solid-phase diffusion or formation of an alloy or eutectic. For solar cell applications, each of these mechanisms must be highly controlled. Incorporation of high metal concentrations into the crystallized Si film poses a major limitation on MIC technique. Typically, MIC-formed Si films have very low minority-carrier lifetime. Solar cells fabricated on them can have severe shunting effects because some of the metal segregates at the GBs. Two approaches have been attempted to overcome these drawbacks in MIC films. One, use of metal-induced lateral crystallization (MILC), in which crystallization is started from a metallized region and then extended laterally into a metal-free area. Typically, Pd and Ni, have been used for MILC which yielded films with a grain size up to several microns [80]. However, it is found that crystallized regions away from the initial metal also have large concentration of metal.

The second approach is to use optical excitation instead of furnace annealing to crystallize an a-Si film deposited on a metallic layer. Because the absorption of optical energy within a Si film is not uniform, optical excitation can be tailored to produce an absorption profile favorable for MIC. In particular, infrared excitation of an a-Si film, deposited on an Al layer, will result in a peak in the energy dissipation near the a-Si-metal interface. Thus, optical processing can initiate nucleation at the interface followed by a grain-enhancement process. Initial work comparing thermal processing and optical processing to achieve MIC of a thin layer of a-Si [81] showed that crystallization by optical excitation occurs very rapidly and at temperatures as low as 200°C – features important for TF-Si solar cell fabrication. Optical excitation can initiate nucleation at the interface and the crystallization propagates into the a-Si film. This process is also accompanied by injection of point defects that promotes grain enhancement. Thus, optical processing is a two-step process – a higher-temperature alloying to produce nucleation,

followed by a lower-temperature vacancy injection to enhance the grain size and continue conversion of amorphous to crystalline phase. Optical processing of the TF-Si samples is done in a quartz furnace, with tungsten-halogen lamps fitted on one side. The sample is illuminated from the a-Si side. The intensity of the light is controlled to provide a predetermined intensity versus time profile including a slow ramp-up and ramp-down of temperature.

Figure 8.26(a) is an XRD (x-ray diffraction) spectrum of a 3- μm film, deposited by HWCVD at $<100^\circ\text{C}$ on a Al/Cr-coated 7059 glass substrate, showing absence of crystalline structure in the Si film. Only Al peaks are seen in the spectrum [82]. It may be pointed out that it is necessary to deposit a thin layer of Cr on glass prior to deposition of Al to improve the adhesion of Al. Figure 8.26(b) is the XRD spectrum of this sample after optical processing at $\sim 480^\circ\text{C}$ for 3 min. An important feature of Figure 8.26(b) is the presence of two preferred orientations – (220) and (111). One can also notice the existence of a large Al peak due to unused Al. The initial Al thickness was 2 μm . Longer times can also help increase grain size, however, because optical processing is a transient process, its advantages diminish (approaching a thermal process), if the process times are too long. This indicates that the crystallization of a-Si can happen very rapidly with optical excitation processing technique.

If the deposition of a-Si on Al/Cr-coated substrates is carried out at temperatures in excess of 300°C , some crystallization and some (or total) consumption of Al can occur during the deposition itself. Figure 8.27(a) is an XRD spectrum of a 2- μm , Si film deposited by HWCVD at 500°C showing the crystallization was strongly textured in (220) direction. However, optical processing can further enhance crystallization. Figure 8.27(b) shows an XRD spectrum of the same sample after optical processing at 480°C for 3 min. The intensity of the (111) peak becomes much stronger, and the intensity of (220) peak increases more than 200%. The increase in (111) and (220) peaks could result from formation of new grains of the preferred orientations, and/or (more likely) by enlargement of the original grains during processing.

Additional results show that an increase in process time and/or temperature leads to enhancement of grain size, while crystallization spreads over the entire thickness of the a-Si film with two preferred orientations. However, there appears to be an “incubation temperature” at which the grain enhancement begins. We have carried out studies to investigate crystallization at different temperatures. The samples were optically processed to change the maximum light intensity while keeping the process time constant. Figures 8.28(a) and 8.28(b) show the intensity of XRD peaks for (111) and (220) orientations as a function of process temperature. These results are shown for three (3 μm , 6 μm , and 10 μm) thicknesses of a-Si films deposited by HWCVD. The deposition temperatures for these films are as follows: 3 μm at $<100^\circ\text{C}$, 6 μm at $<250^\circ\text{C}$, and 10 μm at $\sim 500^\circ\text{C}$. Each of the XRD measurements was made after calibrating the system with standard reference samples. Hence, the intensities of the XRD peaks are representative of the extent of crystallization in those specific orientations. From these plots, one may also infer that thinner films can be crystallized more readily than thicker ones. Despite the fact that the 6 and 10 μm films had some crystallization occurring during the deposition itself, the incubation temperature is lower for thinner films. This conclusion is also supported by TEM (transmission electron microscope) results, which show that the initial part of the optical process leads to a nucleation occurring over the entire interface. Then a

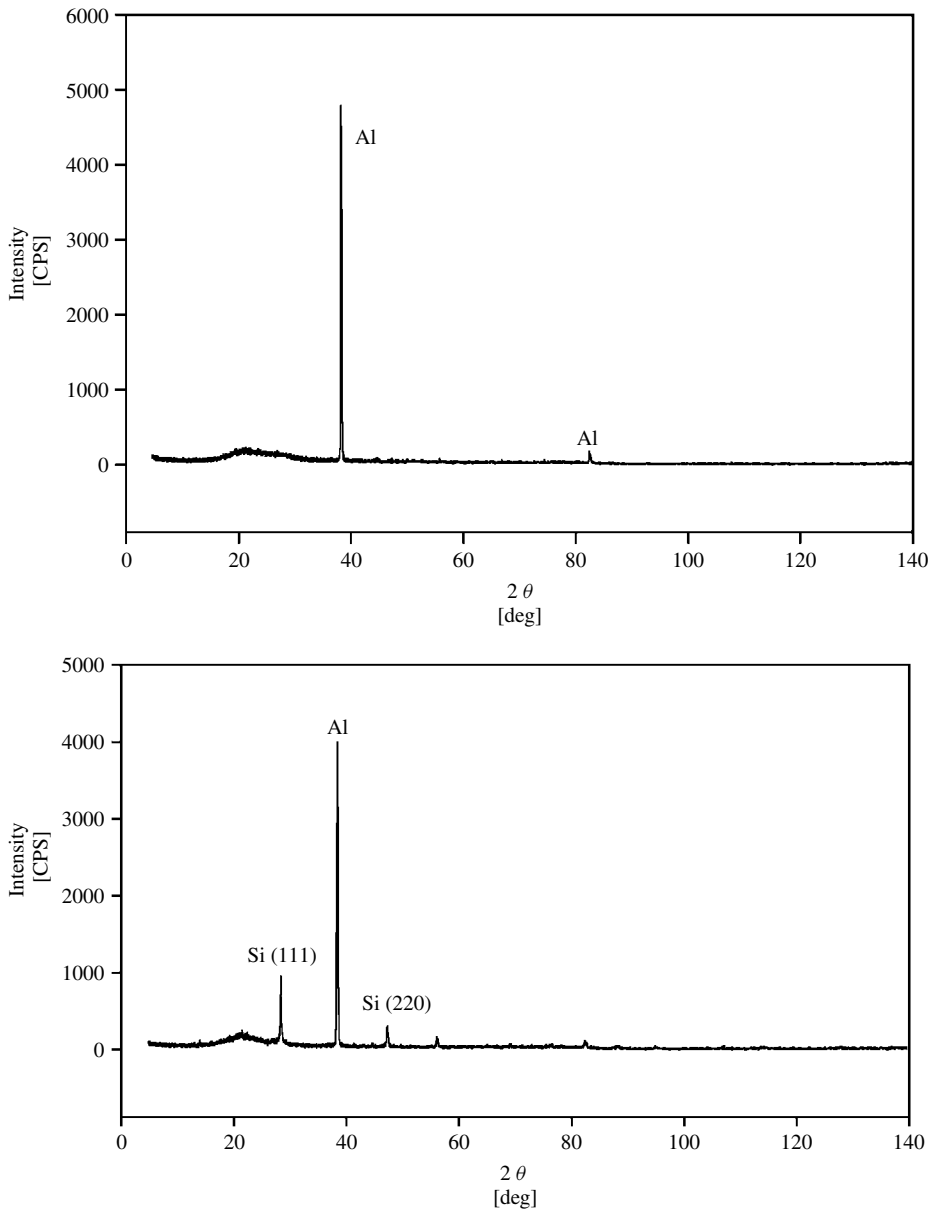


Figure 8.26 XRD spectrum of a 3- μm -thick HWCVD a-Si film, deposited on Al/Cr/glass at about 100°C (a) before optical processing; and (b) after optical processing at $\sim 480^\circ\text{C}$ for 3 min

crystallization front propagates away from the interface converting a-Si into crystalline Si. These features can be seen in Figure 8.29(a), which is a TEM cross-section of a partially crystallized Si film on a glass substrate. The film, 6 μm thick, was deposited at 250°C and processed for 3 min at 460°C . The various regions of the structure are identified in the figure. The largest grain size near the Al interface is about 0.1 μm and decreases

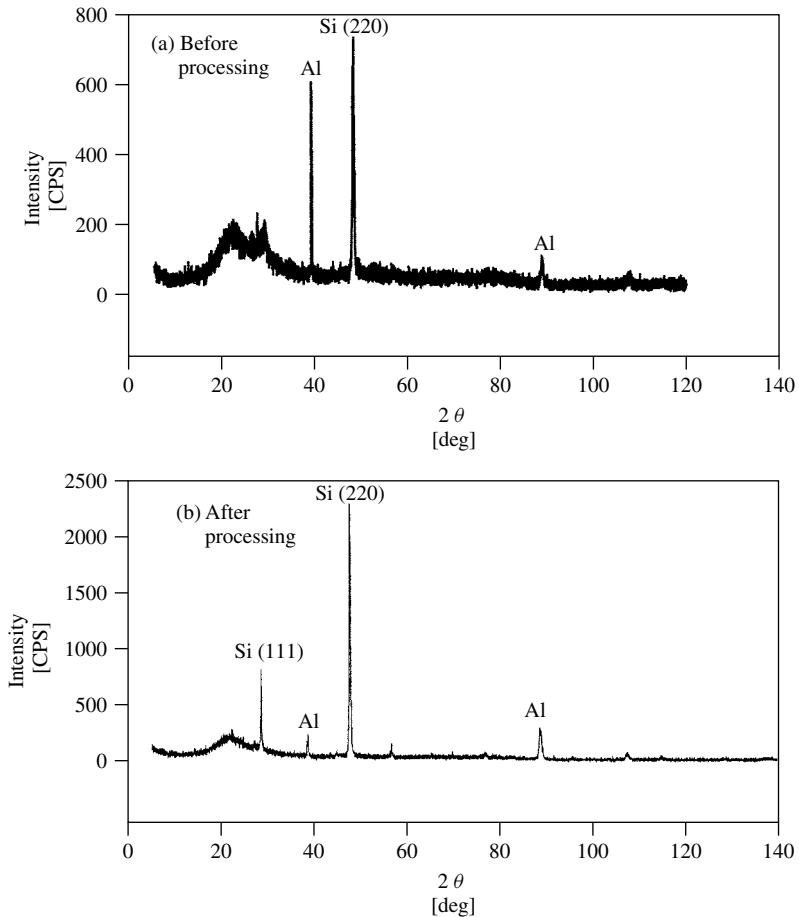


Figure 8.27 XRD spectrum of a 2- μm -thick HWCVD Si film, deposited on Al/Cr/glass at about 500°C (a) before optical processing; and (b) after optical processing at $\sim 480^\circ\text{C}$ for 3 min. A significant increase in Si (220) compared to Si (111) orientation can be seen in (b)

toward a-Si. From this figure, it is clear that 3 min of optical processing time was not sufficient to crystallize the entire film at 460°C. Figure 8.29(b) is a TEM plan view of the film showing distribution of grain sizes near the Si–Al interface.

Detailed profiling of Al across the crystallized films, done by SIMS (secondary ion mass spectroscopy) and micro-X-ray, showed that in optically crystallized films the Al concentration dropped by several orders of magnitude within about 1 μm from the Al–Si interface [81, 83]. These results indicate that Al is required only for the initiation of crystallization. After the nucleation, the crystallization front propagates into a-Si while grain enhancement occurs in the crystallized film. It is believed that vacancy injection from Al–Si interface is responsible for grain enhancement.

Investigation of the possibility of applying optically assisted MIC showed that crystallization of a-Si can start at about 200°C in less than 3 min. This crystallization

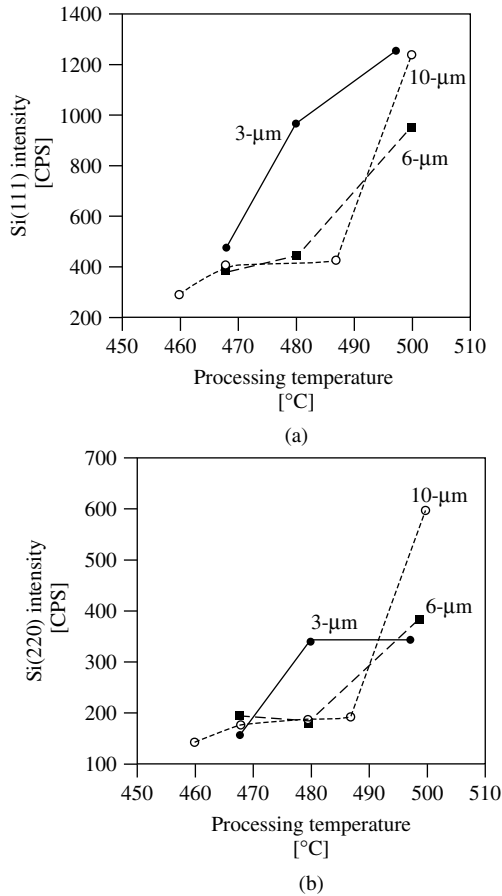


Figure 8.28 Intensity of (a) Si (111) and (b) Si (220) peaks in the XRD spectra of processed samples as functions of processing temperature. A “jump” of peak intensity around 490°C can be observed for the 10- μm -thick sample

becomes much stronger at temperatures close to 450°C. By controlling the process conditions, it is possible to confine Al to the vicinity of the Si–Al interface, leaving the crystallized film (away from the interface) with a low Al concentration. In contrast, thermally crystallized films have nearly uniform and high concentration of Al. Some films, thermally processed at higher temperatures, may exhibit lateral nonuniformities because of segregation into Si-rich and Al-rich phases.

The proposed explanation of the optically assisted, Al-induced crystallization and grain enhancement of thick samples is as follows:

- Optical processing generates a nonuniform temperature distribution within the film structure, especially at the Al–Si interface where energy can be locally absorbed, producing a higher temperature spike.
- In high-temperature (>450°C) optical processing, although the monitored film surface temperature is lower than the eutectic point of an Al–Si system, melting in the local

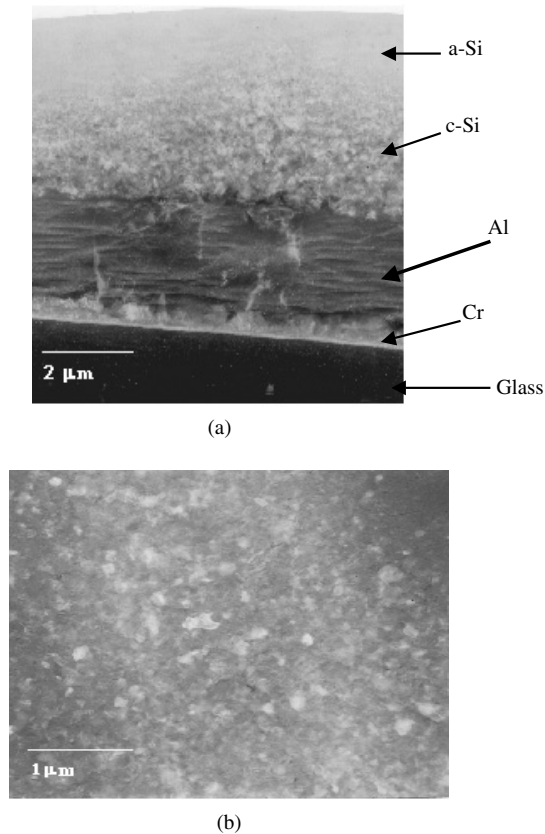


Figure 8.29 TEM photos of a partially crystallized Si film showing (a) start of nucleation and grain growth from the Al interface in cross-section; and (b) grain size distribution near the Si–Al interface in plan view

regions around the Al/Si interface may still occur. This local melting will induce crystallization at the interface area, and this crystallization can be much stronger than the crystallization caused by Al-Si intermixing at a solid phase.

- For thick samples, once the initial crystallization has occurred, it is possible to continue crystallization and grain enhancement via injection of defects. It is believed that in this process vacancies are injected into Si, especially when temperature is below 450°C, which can promote grain growth. This could suggest that following a high-temperature dwell, the optical power could be reduced to stimulate grain enhancement.

One may think that a preferred approach for crystallization would be to deposit the a-Si film at a higher temperature and then use optical processing. However, results to date seem to indicate that the effect of optical processing is somewhat diminished, if the film is deposited at higher temperatures. Thus, contrary to intuition, low-temperature deposition appears to favor crystallization during optical processing. One may explain this behavior by assuming that the formation of thick Al-rich alloyed layer retards vacancy injection. More research needs to be done to understand behavior of point-defect injection.

(c) Zone-melting recrystallization (ZMR)

In zone-melting recrystallization, a narrow zone on the surface of the sample is melted with heating. The film is recrystallized by moving this melted zone around the surface. A range of energy sources, including strip heaters, electron beams, and radio-frequency (RF) heaters, have been used. Because the thin film is heated to the temperature around the melting point of silicon ($\sim 1200^\circ\text{C}$), this method is not suitable for the crystallization of an a-Si film on a normal glass substrate. For the other kinds of low-cost substrate (such as metallurgical Si and carbon), preventing the impurity diffusion from the substrate to the film is also a major issue. Ishihara *et al.* reported impressive results for solar cells fabricated on poly-Si thin films obtained by ZMR technology [84].

(d) Laser-induced recrystallization

XeCl excimer laser recrystallization (ELR) and annealing (ELA) of a-Si has been studied extensively in recent years. Although most works are concentrated on the use of this method for thin-film transistor (TFT), it is also used for solar cells. The focused short-pulsed laser beam is scanned over the a-Si or $\mu\text{c-Si}$ thin film to heat the sample. In laser recrystallization, depending on the power of the incident light, the part of the thin film under illumination can be either in liquid phase (melted totally) or in liquid + solid phase (partly melted), which will result in different grain sizes. It is interesting that the grain size does not increase even though the temperature in the thin film is around the melting point of Si. Because short-pulse laser is used, the temperature of the substrate can be much lower than that of the film; this is a major difference between ZMR and ELR. By placing a thin oxide and/or nitride layer between the substrate and a-Si, both heat transfer from the thin film to the substrate and impurity diffusion from the substrate to the thin film can be dramatically reduced. Other alternatives such as using prepatterned a-Si and multiple-step laser processing can improve the quality of the film. TFTs fabricated on ELR films have yielded excellent overall performance [85]. At present, solar cells fabricated on laser-crystallized Si have achieved conversion efficiencies close to 9%.

Solid-phase crystallization processing using ELA combined with RTP is also reported [86]. The ELA treatment can be at a temperature of 550°C . Poly-Si thin films with a grain size as large as several microns have been obtained.

8.3.6 Processing Considerations for TF-Si Solar Cell Fabrication

The performance of crystalline Si solar cells is strongly controlled by impurities and defects in the material [87]. Although the quality of the starting material used for wafer-based commercial Si solar cells is quite poor, the PV industry has developed solar cell fabrication methods that improve the material quality during the cell fabrication. As explained in the previous sections, one of the advantages of the TF-Si solar cell is its partial immunity to the quality of the material. However, high-efficiency device fabrication does require material quality and processing procedures that may not be compatible with low cell costs unless careful consideration is given to minimizing impurities and defects. It is prudent to include a brief discussion of the processing approaches used to ameliorate deleterious effects of impurities and defects in the design and processing of TF-Si cells.

Thus, it may be important to include impurity gettering and hydrogen passivation in TF-Si solar cell fabrication [88–92].

The impurities of most interest in PV-Si are the transition metals (TM), particularly Fe, Cr, and Ni. They are typically present in concentrations as high as $10^{14}/\text{cm}^3$ in the as-grown substrates. In the dissolved state, these impurities are highly mobile with diffusivities close to $10^{-6} \text{ cm}^2/\text{s}$ at typical process temperatures [93]. They produce deep level electronic states within the bandgap which act as efficient recombination sites. For example, at room temperature, the interstitial iron (Fe_i) introduces a donor level at $E_T \approx E_V + (0.375 \pm 0.015) \text{ eV}$. The hole capture cross section of interstitial iron can be written as (in cm^{-2})

$$\sigma_p(\text{Fe}_i) = (3.9 \pm 0.5) \times 10^{-16} \times \exp\left(-\frac{0.045 \pm 0.005 \text{ eV}}{k_B T}\right), \quad (8.8)$$

where k_B stands for the Boltzman constant and T is the temperature. The electron-capture cross-section of Fe at room temperature was measured as $\sigma_n = 4 \times 10^{-14}/\text{cm}^2$. Because of near-mid gap energy and a large-capture cross-section, it is expected that Fe will produce high-recombination or low minority-carrier lifetime.

TMs in Si also have the ability to form complexes with each other. For example, B can form Fe–B and B–O pairs. B–Fe forms a donor level at $E_V + 0.1 \text{ eV}$ ($\sigma_n = 4 \times 10^{-13}/\text{cm}^2$ at the room temperature) and an acceptor level at $E_C - 0.29 \text{ eV}$. At low injection levels, the recombination rate caused by the Fe–B pair is lower than that of interstitial Fe. Recent studies have also shown that B–O pair formation occurs in some solar cells. This effect is manifested as a decrease in the minority-carrier diffusion length (MCDL) of the cell under sunlight. This mechanism has a pronounced effect of reducing the efficiency of a Si solar cell.

Impurity gettering is used in microelectronic device fabrication to trap impurities away from the active region of the device by oxygen precipitates. This leaves a very clean, denuded surface region, while the impurities are driven into the bulk. For this reason, it is often referred to as *internal gettering*. Because microelectronic devices use only the near-surface region of the wafer, internal gettering works well for them. Solar cells, being minority-carrier devices, use nearly the entire thickness for the device. Hence, it is necessary to apply external gettering techniques to clean up the bulk of the material. In external gettering, a surface region serves as a sink for impurities. Fortunately, phosphorous diffusion and Al alloying are some of the processes that have worked well for efficient gettering in solar cells. Because these processes are extensively used in solar cell fabrication for junction and contact formation, all Si solar cells experience a certain degree of gettering. In a typical junction formation or Al alloying process, the Fe concentration can be reduced by two orders of magnitude. Theoretical and experimental details of P and Al gettering are reviewed in several papers [94, 95]. For a typical multicrystalline Si wafer, P diffusion for formation of an n^+p solar cell can lead to an improvement in the average MCDL from a value of about $50 \mu\text{m}$ to $75 \mu\text{m}$. This increase in the MCDL is caused by removal of fast-diffusing transitional metal impurities from the bulk of the substrate into the P diffused region. Similar results are obtained with the Al-alloying used for formation of the backside p^+ region and back metallization.

Impurity gettering can also play an important role in fabrication of high-efficiency TF-Si solar cells. The Si as deposited for TF-Si cells also contains high concentrations of impurities. Although it is possible to deposit high-purity a-Si or poly-Si for laboratory purposes, it is difficult to maintain “cleanliness” in a high-throughput deposition system. In addition, low-cost substrates such as glass or ceramics will release impurities through desorption or diffusion, which can contaminate the deposition system and the Si film. Because of the small thickness of the Si film, gettering times can be short and/or process temperatures can be low. A unique way to provide for impurity gettering in a TF-Si solar cell is to include a layer of Al in the device structure (see Figure 8.12). Another approach for low-temperature gettering may be to inject vacancies. Because the impurities that kill minority-carrier lifetime are typically interstitial transition metals, a region of vacancy injection can be a “sink” for the impurities. Sources of interstitial sinks can also be interfaces (such as heterointerfaces), GBs, and other crystal defects. However, it has been observed that such sites can lead to precipitation of metallic impurities. Because it is very difficult to getter precipitated impurities, it is desirable to maintain impurity concentrations below the saturation levels. Precipitated impurities form local shunts which can severely degrade V_{OC} and FF of the device.

Similar to impurities, defects are sites for high-carrier recombination, causing degradation in solar cell performance. In a polycrystalline TF-Si solar cell, the dominant defects are GBs and intragrain dislocations. In both mc-Si and poly-Si, one often finds that intragrain defects segregate in certain preferred grains. Most solar cell processing does not change the nature or density of crystal defects because these defects are generally tangled, which prevents them from gliding. Like impurities, defects introduce energy levels in the band gap. The nature of the levels in a real material is quite complex, because the defects represent a host of defect configurations. Crystal defects always appear to have detrimental effects on material quality.

Typical solar-cell processes do not fully remove impurities from Si. Even the impurities that are readily gettered remain in the solar cell in significant levels and produce strong harmful effects on solar cell performance. In addition to residual impurities, many crystallographic defects are stable at the processing temperatures used. It is often observed that defect concentrations remain essentially unaltered by solar cell processing. Therefore, it is important to identify methods of dealing with the residual impurities and defects. Fortunately, hydrogen passivation has proven to be a very valuable process to deal with residual impurities and defects.

H is known to be electronically very active in Si, and it interacts with nearly all impurities and defects. H saturates dangling bonds at interfaces, and at point and extended defects, thereby reducing the carrier recombination and improving device characteristics. H can also interact with impurities in Si. The nature of such interactions depends on the type of impurities. For example, it can deactivate shallow dopants, both acceptor and donor types, leading to changes in the resistivity of the wafer. Although this effect is an undesirable feature for most cases, it can be used to reversibly alter dopant activity and to form erasable p/n junctions in some future applications. Atomic H can interact with metallic impurities such as Fe, Cr, Ni, Cu, and Au to reduce their effectiveness for carrier recombination in Si. H interactions with O exhibit a very interesting behavior – it appears that H diffusivity is lowered by the O, whereas the diffusivity of oxygen donors is greatly enhanced.

Introduction of H after impurity gettering can help improve solar cell efficiency by as much as 3 to 4 absolute points. Generally, such a passivation results in a significant decrease in the dark current and an improvement in the illuminated cell parameters. However, the degree of improvement can vary significantly over the wafer in a manner very similar to impurity gettering [96–98]. It has been determined that better-performing regions improve more than the poorer regions. This behavior can be explained by the dependence of H diffusion on the structure of defects, such as defect clusters and impurity precipitation. The defects and impurities act as trapping centers for atomic H, reducing its effective diffusivity [99–102].

Several methods have been used for incorporating H in solar cells. These include ion implantation, plasma processing, and, more recently, a process in which hydrogenation is combined with deposition of a Si_3N_4 layer by a PECVD process. The nitride layer is used as an AR coating. Another advantage of the nitride coating is that the front metal can be fired through the nitride using an RTP-like process, typically 800 to 850°C for about 10 s.

In a wafer-based cell, passivation of impurities and defects requires a deep diffusion of H into the bulk of the solar cell. In addition, it is important that H interacts with only those impurities that degrade device performance. For example, H should not deactivate dopants because that would lead to a change in the resistivity of the device. These considerations dictate a careful design of a hydrogenation process. A deep diffusion of H may appear to be quite trivial because a high value of diffusivity of H in Si is often assumed. However, the effective diffusion of H in Si is primarily controlled by its defects and impurities. H can associate with impurities and defects to form complexes, leading to “trapping” of H during its diffusion into Si – causing a greatly reduced diffusivity of H at low temperatures (e.g. <400°C typically used for hydrogenation by plasma or ion implantation). To minimize the effects of trapping, it is necessary to use a high-temperature process step. At higher temperatures, the complexes begin to dissociate, causing the H to diffuse with intrinsic lattice diffusivity.

Trapping of H is also expected in poly TF-Si solar cells because of the abundance of GBs. However, by incorporating suitable process design, the trapped H can be released for impurity-defect passivation. This feature may be valuable for TF-Si solar cells because many a-Si or poly-Si deposition techniques result in copious amounts of H in the thin film.

8.4 CONCLUSION

The thin-film Si solar cell was envisaged during the infancy of solar-cell technology as a potential candidate to reduce the amount of Si needed for an efficient solar cell. Although it was recognized that the quality of the material needed for a TF-Si solar cell does not have to be very high, experimental work on cell fabrication had to await technologies in two different areas – a lift-off type of technology for making single-crystal cells, and low-temperature processing of large-grain polycrystalline deposition to make thin films on low-cost substrates. Clearly, this is just the beginning of thin-film Si solar-cell technology, but there has been astounding progress in a very short time frame. In addition to vigorous research, there is also interest in commercial production of such

devices. Like any other technology, many methods for TF-Si solar cell production will emerge. The lift-off approaches for potentially high-efficiency single-crystal cells are very attractive. However, there are questions about the reliability of a technique that involves mechanical transfer from one substrate to the other. Likewise, reuse of the single crystal substrate is another issue.

The use of $\mu\text{c-Si}$ seems to have a large potential because of being a true thin-film technology that can use some established thin-film processes. Furthermore, it can also derive benefits from ongoing R&D within the a-Si community. Because $\mu\text{c-Si}$ is now used in traditional a-Si cells for junction formation, there is considerable added interest in studying deposition kinetics, phase transformation, and electronic and optical properties of $\mu\text{c-Si}$. To date, the performance of $\mu\text{c-Si}$ is clearly limited by the grain size (controlling V_{OC} and FF). The highest efficiencies are obtained by using nip structure, which offers the advantage in achieving high currents. Higher voltages have been obtained using a mixture of a-Si and $\mu\text{c-Si}$ phases. Because of the similarities in a-Si cells and $\mu\text{c-Si}$ TF cells, there may be common features in module technology, too.

TF-Si solar cell technology will eventually compete with other thin-film technologies based on polycrystalline thin films of CdTe or CIGS ($\text{Cu}(\text{UnGa})\text{Se}_2$). It may be argued that Si is a simpler material system and that its processing can be low cost compared to compound semiconductors. On the flip side, it is believed that GBs in poly thin films are "benign," making these material systems easy to process. Clearly, there is much more work to be done before such arguments can be resolved.

The TF-Si solar cell is an excellent solution to reduction in the use of Si and achievement of high efficiency at low cost. Many problems need to be solved before this technology can compete with existing solar cells, but the future looks very bright for TF-Si solar cells.

REFERENCES

1. Redfield D, *Appl. Phys. Lett.* **25**, 647 (1974).
2. Esher J, Redfield D, *Appl. Phys. Lett.* **25**, 702 (1974).
3. Gosh K, Fishman C, Feng T, *J. Appl. Phys.* **51**, 446–454 (1980).
4. Green M, *Silicon Solar Cells*, University of New South Wales, Sydney, Australia (1995).
5. Yablonovitch E, Cody G, *IEEE ED-29*, 300 (1982).
6. Arndt A, Allison J, Haynos J, Muelenberg A, *Proc. 11th IEEE Photovoltaic Specialists Conf.*, 40 (1976).
7. Spitzer M, Schewchunn J, Vera E, Loferski J, *Proc. 14th IEEE Photovoltaic Specialists Conf.*, 375 (1980).
8. Barona C, Brandhorst N, *Proc. 11th IEEE Photovoltaic Specialists Conf.*, 44 (1975).
9. Haynos J, Allison J, Arndt R, Muelenberg M, *Intl. Conf. on Photovoltaic Power Generation*, 487 (Hamburg, 1974).
10. Campbell P, Wenham S, Green M, *Proc. 20th IEEE Photovoltaic Specialists Conf.*, 713 (1988).
11. Coleman M *et al.*, *Proc. 12th IEEE Photovoltaic Specialists Conf.*, 313 (1976).
12. Sopori B, *Appl. Opt.* **27**, 25 (1988).
13. Craighead H, Howard R, Tennant D, *Appl. Phys. Lett.* **37**, 653 (1980).
14. Hansen T, Johnson C, U.S. Patent 4,229,233 (Oct. 1980).
15. Mataré H, *Defect Electronics in Semiconductors*, Wiley-Interscience, New York (1971).
16. McLean D, *Grain Boundaries in Metals*, Oxford University Press, New York (1957).

17. Kamins T, Ed, *Polycrystalline Silicon for Integrated Circuit Applications*, Kluwer Academic Press, Boston, MA (1988).
18. Strunk H, Werner J, Fortin B, Bonnaud O, *Polycrystalline Semiconductors III – Physics and Technology*, Scitec Publications, Switzerland (1994).
19. Chen W, Ph.D. thesis, New Jersey Institute of Technology, NJ (2000).
20. Swanson R *et al.*, *IEEE Trans. Electron Dev.* **ED-31**, 661 (1984).
21. Chong C, Wenham S, Green M, *Appl. Phys. Lett.* **52**, 107 (1988).
22. Godfrey R, Green M, *Appl. Phys. Lett.* **34**, 790 (1979).
23. Gruenbaum P, Gan G, King R, Swanson R, *Proc. 21st IEEE Photovoltaic Specialists Conf.*, 317 (1990).
24. Sopori B, Application of Optical Processing for Growth of Silicon Dioxide, US Patent No 5,639,520 (1997).
25. Yasutake K, Chen Z, Pang S, Rohatgi A, *J. Appl. Phys.* **75**, 2048 (1994).
26. Lauinger T, Moschner J, Aberle A, Hezel R, *Proc. 25th IEEE Photovoltaic Specialists Conf.*, 417 (1996).
27. Zhao J, Wang A, Wenham S, Green M, *Prog. Photovolt.:* **4**, 55 (1996).
28. Ishihara T, Arimoto S, Kumabe H, Murotani T, *Prog. Photovolt.:* **3**, 105 (1996).
29. Fan J, Zeiger, H, *Appl. Phys. Lett.* **36**, 158 (1980).
30. McClelland R, Boyler C, Fan J, *Appl. Phys. Lett.* **37**, 560 (1980).
31. Lush G *et al.*, *Proc. 23rd IEEE Photovoltaic Specialists Conf.*, 1343 (Louisville, KY, 1993).
32. Gale R, King B, Fan JC, *Proc. 19th IEEE Photovoltaic Specialists Conf.*, 293 (New Orleans, LA, 1987).
33. Pinckney L, *J. Non-Cryst. Solids* **255**, 171 (1999).
34. Mahhailovich K, *Novel Glass-Ceramic Substrates for Polycrystalline Thin Film Electronics*, Ph.D. thesis, Cornell University (May 2002).
35. McCann M, Catchpole K, Weber K, Blakers A, *Sol. Energy Mater. Sol. Cells* **68**, 135 (2001).
36. Catchpole K, McCann M, Weber K, Blakers A, *Sol. Energy Mater. Sol. Cells* **68**, 173 (2001).
37. Bergmann R, *Appl. Phys. A* **69**, 187 (1999).
38. Tayanaka H, Yamauchi K, Matsushita T, *Proc. 2nd World Conf. on Photovoltaic Solar Energy Conversion*, 1272 (1998).
39. Bergmann R, Rinke T, Wagner T, Werner J, *Photovoltaic Science and Engineering Conference-11* (1999).
40. DeJule R, *Semiconductor International* (Nov. 1998).
41. Auberton-Herve A *et al.*, *Proc. 2nd International Symposium on Advanced Science and Technology of Silicon Materials*, 214 (Kona, Hawaii, Nov. 1996).
42. Weber K, Catchpole K, Stocks M, Blakers A, *Proc. 26th Photovoltaic Solar Conference*, 107 (1997).
43. Wang T, Ciszek T, *J. Cryst. Growth* **174**, 176 (1997).
44. Wang T, Ciszek T, *J. Electrochem. Soc.* **147**, 1945 (2000).
45. Yamamoto K, Suzuki T, Yoshimi M, Nakaijima A, *Jpn. J. Appl. Phys.* **36**, L569 (1997).
46. Yamamoto K *et al.*, *Proc. 26th IEEE Photovoltaic Specialists Conf.*, 575 (Anaheim, CA, 1997).
47. Klein S *et al.*, *2nd International Conf. On Cat-CVD (Hot-Wire CVD) Process*, to be published in *Thin Solid Films* (2003).
48. Koval R *et al.*, *Proc. 29th IEEE Photovoltaic Specialists Conf.*, 1090 (2002).
49. Sopori B, Chen W, Madjdpour J, Symko M, *MRS* **485**, 101 (1997).
50. Chen W, Sopori B, *Electrochem. Soc. Proc.* **99-11**, 145 (1999).
51. Sopori B, U.S. Patents 5,897,331 (1999) and 6,201,261 (2001).
52. Basore P, *Proc. 29th IEEE Photovoltaic Specialists Conf.*, 49 (2002).
53. Shah A *et al.*, *Proc. 26th IEEE Photovoltaic Specialist Conference*, 569 (1997).
54. Campbell P, Green M, *J. Appl. Phys.* **62**, 243 (1987).
55. Sopori B, Pryor R, *Sol. Cells* **8**, 249 (1983).

56. Sunrays is developed by Rolf Brendel, Max-Planck-Institut and is distributed by Garching Innovations GmbH.
57. Rohatgi A, Smith A, *Texture* is available from Georgia Institute of Technology, Atlanta, GA.
58. Sopori B, *PV Optics* is available from National Renewable Energy Laboratory, Golden, CO.
59. Sopori B, *Laser Focus World*, 159 (Feb. 1998).
60. Sopori B *et al.*, *MRS Proc.* **467**, 777 (1997).
61. Hegedus S, Sopori B, Paulson P, *Proc. 29th IEEE-Photovoltaic Specialist Conf.*, 1122 (May 2002).
62. Guha S, *Proc. 25th IEEE Photovoltaic Specialists Conf.*, 1017 (1996).
63. Hegedus S, Deng X, *Proc. 25th IEEE Photovoltaic Specialists Conf.*, 1061 (1996).
64. Basore P, *IEEE Trans. Electron Devices* **ED-37**, p. 337 (1990).
65. PCID is available from University of New South Wales.
66. AMPS is a software developed by Penn State University and is available through Prof. S. Fonash.
67. Sopori B, in Davies G, Nazare M, Eds, *Proc. ICDS-19*, 527–534, Trans. Tech. Publ., Aveiro, Portugal (1997).
68. Sopori B, Murphy R, *Proc. 12th European Photovoltaic Solar Energy Conference*, 1797 (1994).
69. Murphy R, Sopori B, Rose D, *Mat. Res. Soc. Symp. Proc.* **378**, 749–754 (1995).
70. Liou J, *Advanced Semiconductor Device Physics and Modeling*, Artech House, Boston, MA (1994).
71. Sopori B, Chen W, Symko M, in Gupta D, Batcher F, Hughes W, Eds, *Silicon Recombination Lifetime Characterization Methods*, ASTMSTP1340, 328, American Society for Testing and Materials, West Conshohocken, Pennsylvania US (1998).
72. Fossom J, Lindholm F, *IEEE Trans.* **ED-27**, 692 (1980).
73. Bergmann R *et al.*, *Semicond. Sci. Technol.* **12**, 224 (1997).
74. Schropp R, Zeman M, *Amorphous and Microcrystalline Silicon Solar Cells: Modeling, Materials and Device Technology*, Kluwer Academic Publications, Boston/Dordrecht (1988).
75. Baba T *et al.*, *MRS Proc.* **Fall** 1994, 895 (1995).
76. Haque M, Naseem H, Brown W, *J. Appl. Phys.* **75**, 3928 (1994).
77. Tu K, *Appl. Phys. Lett.* **27**, 221 (1975).
78. Ashtikar M, Sharma G, *J. Appl. Phys.* **78**, 913 (1995).
79. Masaki Y, Ogata T, Ogawa H, Jones D, *J. Appl. Phys.* **76**, 5225 (1994).
80. Sok-Woon Lee *et al.*, *IEEE Electron Device Lett.* **17**(8), 407 (1996).
81. Sopori B *et al.*, *Mat. Res. Soc. Symp. Proc.* **470**, 419 (1997).
82. Cullity B, *Elements of X-Ray Diffraction*, Addison-Wesley, Reading, MA (1956).
83. Chen W *et al.*, *MRS Meeting*, (April 2001).
84. Ishihara T *et al.*, *Mat. Res. Soc. Symp. Proc.* **485**, 3 (1997).
85. Cao M *et al.*, *IEEE Trans. Electron Devices* **ED-43**, 561 (1996).
86. Efremov M *et al.*, *Proc. SPIE* **2801**, 263 (1996).
87. Sopori B, *J. Electron. Mater.* **31**, 972 (2002).
88. Narayanan S, Wenham S, Green M, *IEEE Trans.* **ED-37**, 382 (1990).
89. Joshi S, Gosele U, Tan T, *J. Appl. Phys.* **77**, 3858 (1995).
90. Gilles D, Weber E, Hahn S, *Phys. Rev. Lett.* **64**, 196 (1990).
91. Sana P, Rohatgi A, Kalejs J, Bell R, *Appl. Phys. Lett.* **64**, 97 (1994).
92. Sopori B, Jastrzebski L, Tan T, Narayanan S, *Proc. 12th Photovoltaic Science and Engineering Conf.*, 1003 (1994).
93. Istratov A, Hieslmair H, Weber E, *Appl. Phys.* **A69**, 13 (1999).
94. Perichaud I, Martinuizi S, *Proc. 22nd IEEE Photovoltaic Specialists conf.*, 877 (1991).
95. Sopori B, Chen W, Tan T, Plekhanov P, *AIP Conf. /Proc.* **462**, 341 (1998).
96. Sopori B, Zhang Y, N Ravindra, *J. Electron. Mater.* **30**, 1616 (2001).
97. Sopori B *et al.*, *Sol. Energy Mater. Sol. Cells* **41/42**, 159 (1996).

-
98. Symko M, Sopori B, Reedy R, Jones K, in Davies G, Nazare M, Eds, *Proc. ICDS-19*, 527, Tran. Tech. Publ. Aveiro, Portugal (1997).
 99. Sopori B, *Appl. Phys. Lett.* **52**, 1718 (1988).
 100. Sopori B, *J. Appl. Phys.* **64**, 5264 (1988).
 101. Estreicher S, Hastings J, Fedders P, *Phys. Rev. B* **57**, 12663 (1998).
 102. Zhang Y, *Modeling Hydrogen Diffusion for Solar Cell Passivation and Process Optimization*, Ph.D. thesis, New Jersey Institute of Technology, NJ (2002).

This Page Intentionally Left Blank

9

High-Efficiency III-V Multijunction Solar Cells

J. M. Olson, D. J. Friedman and Sarah Kurtz

National Renewable Energy Laboratory, Golden, CO

9.1 INTRODUCTION

The large-scale use of photovoltaics is slowly becoming a reality. Small scale (~ 10 – 20 kW) power systems using Si solar cells now compete with fossil-fueled electric generators for remote applications, where “remote” in the United States means less than one kilometer from the electrical grid. The total worldwide solar cell production in the year 2000 was 0.3 GW, mostly in the form of flat-plate Si solar cells. Compared to the PV production capacity 20 years ago, this represents remarkable progress. Silicon solar cells have reached efficiencies exceeding 20%, and the cost has been reduced to under \$10/W. However, in the context of world energy consumption, 0.3 GW is a miniscule number. The problem is related to the diffuse nature of solar radiation. For example, to generate 1 GW of electrical power using Si solar cells requires an aperture area on the order of 10^7 m². The main problem is not the land area, but the daunting task of producing 10^7 m² of what has been termed *solar-grade silicon*, which in reality is virtually indistinguishable from semiconductor-grade silicon. One solution to this problem is to use “concentrator technology.” Here, lenses or mirrors focus the sunlight (usually the direct portion) on a smaller solar cell. The concentration ratio can be as large as 200X to 300X for Si and 1000X to 2000X for a GaAs solar cell. At these concentration ratios, the cost of the cell becomes less important than its efficiency. For example, a GaInP/GaAs/Ge tandem cell with an efficiency of 34% at 1000X and a cost of \$10/cm² may be more cost-effective than a Si concentrator cell with an efficiency of 28% at 200X and a cost of \$0.50/cm². The trade-offs are complex and currently not well quantified, but it seems clear that concentrator photovoltaics must be a dominant player if photovoltaics have to supply a significant fraction of the world’s energy needs.

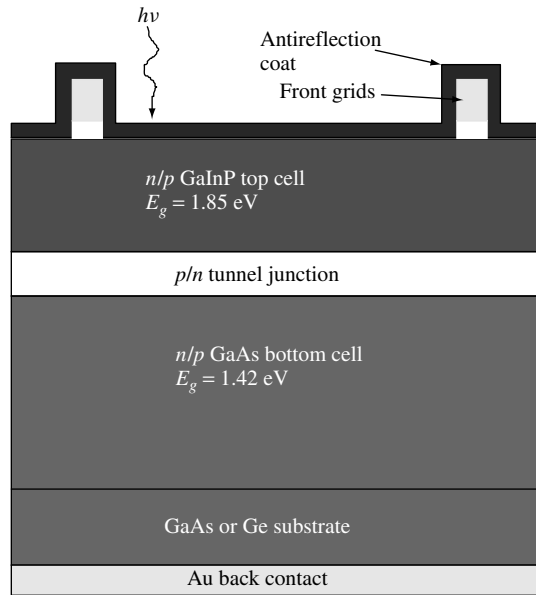


Figure 9.1 Schematic of GaInP/GaAs multijunction solar cell. When grown on a Ge substrate, there is an option for introducing a third junction in the Ge substrate, thus boosting the voltage and efficiency of the overall device. Dimensions are not to scale

It was in this context that researchers at the National Renewable Energy Laboratory (NREL) conceived and began work on the GaInP/GaAs tandem solar cell more than a decade ago [1]. A schematic of the cell is shown in Figure 9.1. The cell consists of a $\text{Ga}_x\text{In}_{1-x}\text{P}$ top cell (with a band gap of 1.8–1.9 eV) grown monolithically on a lattice-matched interconnecting tunnel junction and a GaAs bottom cell. As shown in Figure 9.2, for $x \approx 0.5$, $\text{Ga}_x\text{In}_{1-x}\text{P}$ has the same lattice constant as GaAs with a band gap energy between 1.8 and 1.9 eV. Prior to this, several groups were working on tandem device designs that theoretically should achieve efficiencies approaching 36 to 40% [2]. These included mechanical stacks of a high band gap top cell on a Si bottom cell and monolithic combinations of AlGaAs, GaAs, and GaInAs or GaAsP on Si. However, the mechanical stacks were viewed as too costly and cumbersome (perhaps prematurely). The defects generated by the lattice mismatch between top and bottom cells in some of the monolithic structures (i.e. GaAs and GaInAs or GaAsP and Si) were a problem that could not be solved easily. The AlGaAs/GaAs tandem cell is lattice matched with a theoretical efficiency of 36% [2]. However, the sensitivity of AlGaAs to trace levels of oxygen in all growth systems and source materials made it difficult to produce high yield and, thus, limited its use in a production environment. The novel NREL idea was to trade manufacturability (i.e. lattice-matched top and bottom cells and oxygen-tolerant device materials) for a slightly lower theoretical efficiency of 34%.

By most standards, progress was rapid (see Figure 9.3). Despite initial problems with the growth of GaInP due to metalorganic chemical vapor deposition (MOCVD) and complications associated with an anomalous red shift of the band gap energy, by 1988 reasonably good GaInP top cells could be fabricated [3–5]. In 1990, efficiencies greater

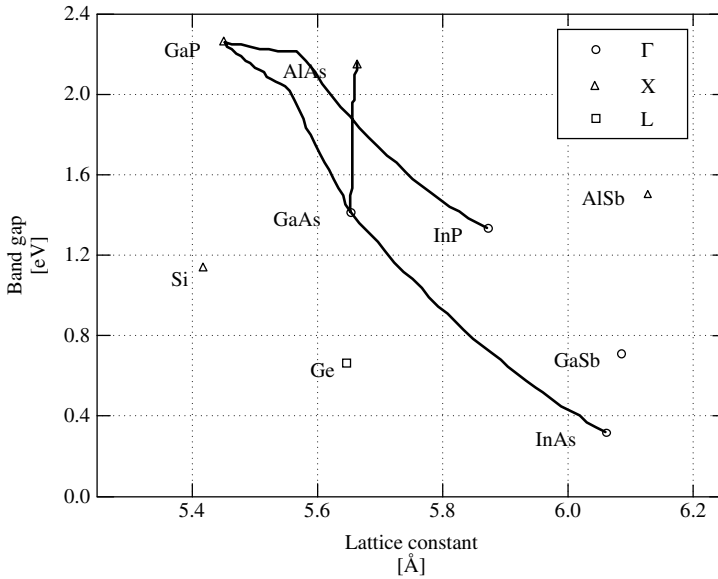


Figure 9.2 Estimated band gap as a function of lattice constant for Si, Ge, III-V binaries and their alloys

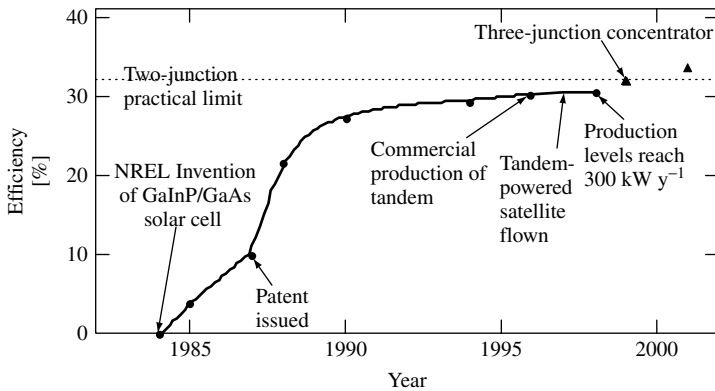


Figure 9.3 These GaInP/GaAs cell efficiencies were measured at one sun with the AM1.5 global spectrum. The triangles were measured under concentrated sunlight for three-junction GaInP/GaAs/Ge cells

than 27% one-sun air mass 1.5 global (AM1.5G) were achieved by changing the top-cell thickness to achieve current matching [6, 7]. This tuning of the top-cell thickness can also be used to achieve current matching under different solar spectra, for example, AM0 and AM1.5direct (AM1.5D). Using this feature of the GaInP/GaAs tandem solar cell, NREL, over the next three years, set records at AM1.5G with an efficiency $\eta = 29.5\%$ [8], at 160-suns AM1.5D with $\eta = 30.2\%$, [9] and at one-sun AM0 with $\eta = 25.7\%$ [10]. Soon, numerous laboratories around the world were studying this device, and the 29.5% record was eventually eclipsed by researchers at the Japan Energy Corporation with an efficiency

Table 9.1 Record solar cell efficiencies. Unless otherwise specified, the cells were fabricated from single crystal materials and the measurements were two-terminal [12]

Cell	Efficiency [%]	Area [cm ²]	Intensity [suns]	Spectrum	Description
GaAs	25.1 ± 0.8	3.9	1	Global	Kopin, AlGaAs window
GaAs (thin film)	23.3 ± 0.7	4.0	1	Global	Kopin, 5-mm
GaAs(poly)	18.2 ± 0.5	4.0	1	Global	Res. Triangle Inst. (RTI) Ge substrate
InP	21.9 ± 0.7	4.0	1	Global	Spire, epitaxial
GaInP/GaAs	30.3	4.0	1	Global	Japan Energy
GaInP/GaAs/Ge	28.7 ± 1.4	29.93	1	Global	Spectrolab
Si	24.7 ± 0.5	4.0	1	Global	UNSW, PERL
GaAs	27.6 ± 1.0	0.13	255	Direct	Spire
GaInAsP	27.5 ± 1.4	0.08	171	Direct	NREL, ENTECH cover
InP	24.3 ± 1.2	0.08	99	Direct	NREL, ENTECH cover
GaInP/GaAs/Ge	32.4 ± 2.0	0.1025	414	Direct	Spectrolab
GaAs/GaSb	32.6 ± 1.7	0.053	100	Direct	Boeing, four-terminal mechanical stack
InP/GaInAs	31.8 ± 1.6	0.063	50	Direct	NREL, three-terminal, monolithic
GaInP/GaAs	30.2 ± 1.4	0.103	180	Direct	NREL, monolithic
Si	26.8 ± 0.8	1.6	96	Direct	Sunpower, back contact

of 30.3% [11]. The current record solar cell efficiencies for this device, along with the record efficiencies of other multijunction devices, are given in Table 9.1.

In 1994, it was discovered that the GaInP/GaAs tandem cells had very good radiation tolerance for operating in space. Kurtz and coworkers published results for a GaInP/GaAs cell with $\eta = 19.6\%$ (AM0) after irradiation with 1-MeV electrons at a fluence of $10^{15}/\text{cm}^2$, [10] a standard radiation dose used to compare various solar cells. This efficiency was higher than the beginning-of-life efficiency of an unirradiated Si solar cell. These attributes soon attracted the attention of the commercial sector. Production of GaInP/GaAs solar cells (on Ge substrates) began in 1996, and the first GaInP-/GaAs-powered satellite was launched in 1997. Today, the production capacity for these tandem cells is about 0.5 MW/year.

This chapter discusses the principles and operation of multijunction solar cells fabricated from III-V semiconductor compounds and alloys, with a particular emphasis on the GaInP/GaAs tandem cell. III-V semiconductors have several characteristics that make them especially suitable for solar cells. A wide selection of these materials is available with direct band gaps, and therefore, high absorption coefficients, in the ~ 1 - to 2-eV range of interest for solar cells; GaAs, with a band gap of 1.42 eV, and Ga_{0.5}In_{0.5}P, with a band gap of 1.85 eV, are especially important examples. Both *n*- and *p*-type doping of these materials are generally straightforward, and complex structures made from these materials can be grown with extremely high crystalline and optoelectronic quality by high-volume growth techniques. As a result, III-V cells have achieved the highest single-junction efficiencies. Although these *single-junction* efficiencies are only slightly higher than the impressive efficiencies achieved by the best silicon cells, the ease of fabricating

complex III-V structures (including layers with different band gaps) makes possible the creation of III-V *multijunction* cells with efficiencies in excess of 30%, exceeding that of any single-junction device.

9.2 APPLICATIONS

9.2.1 Space Solar Cells

The higher efficiencies and radiation resistance of III-V cells have made them attractive as replacements for silicon cells on many satellites and space vehicles. Over the years, GaAs cells have replaced silicon cells on new satellite launches. The GaInP/GaAs/Ge cells are integrated into modules very much like single-junction GaAs solar cells and have the added advantage of operating at high voltage and low current, as well as having excellent radiation resistance. They also have a smaller temperature coefficient than silicon cells, which implies better performance under the operating conditions encountered in space applications. Space applications of GaInP/GaAs/Ge and other III-V solar cells are discussed in detail in Chapter 10.

9.2.2 Terrestrial Energy Production

The PV industry currently services a wide range of terrestrial applications, from power for small consumer products to larger grid-connected systems. III-V solar cells are currently too expensive for most one-sun applications. While satellites represent an example of an application for which the extra cost is acceptable, for bulk electricity generation, a concentration of 400 suns or greater may be needed to achieve an acceptable cost. Concentrator cells and systems are discussed in detail in Chapter 11.

The use of GaInP/GaAs/Ge cells in high-concentration (e.g. 1000X) systems has the potential of generating electricity at 7 cents/kWh [13]. The current space-cell production capacity of ~ 0.5 MW/year translates into a 1000X concentrator cell production capacity of ~ 0.5 GW/year. These solar cells have achieved a record efficiency of 34%, measured at 210X under the AM1.5 global spectrum [14]. An outdoor module efficiency for a linear (low X) concentrator has been reported in the range of 25.5 to 29% [15]. The high efficiency, the projected low cost, and the ease with which production of concentrator cells could be initiated with existing production equipment make terrestrial applications attractive for these cells. Nevertheless, considerable industry investment will be required to develop a product that is reliable. The specific issues associated with the development of concentrator solar cells are discussed below.

9.3 PHYSICS OF III-V MULTIJUNCTION AND SINGLE-JUNCTION SOLAR CELLS

9.3.1 Wavelength Dependence of Photon Conversion Efficiency

As a prelude to the detailed examination of the design and performance of multijunction cells, it is useful to review briefly the fundamental factors that limit the efficiency of

single-junction cells. Consider an ideal single-junction cell with characteristic band gap E_g . A photon incident on this cell with photon energy $h\nu > E_g$ will be absorbed and converted to electrical energy, but the excess energy $h\nu - E_g$ will be lost as heat. The greater $h\nu$ is in excess of E_g , the lower is the fraction of that photon's energy that will be converted to electrical energy. On the other hand, a photon of energy $h\nu < E_g$ will not be absorbed and converted to electrical energy at all. Thus, the efficiency of photon conversion is a maximum efficiency at $h\nu = E_g$. Note that this maximum efficiency is less than 100%; the maximum work per absorbed photon is calculated by Henry [16].

Since the solar spectrum is broad, containing photons with energies in the range of about 0 to 4 eV, single-junction solar cell efficiencies are thus inherently limited to significantly less than the efficiency with which monochromatic light can be converted. The solution to this problem is (in principle) simple: rather than trying to convert all the photon energies with one cell with one band gap, divide the spectrum into several spectral regions and convert each with a cell whose band gap is tuned for that region. For instance, suppose the spectrum is divided into three regions $h\nu_1 - h\nu_2$, $h\nu_2 - h\nu_3$, and $h\nu_3 - \infty$, where $h\nu_1 < h\nu_2 < h\nu_3$. The light from these spectral regions would be converted by cells with band gaps $E_{g1} = h\nu_1$, $E_{g2} = h\nu_2$, and $E_{g3} = h\nu_3$, respectively. The greater the number of spectral regions allowed, the higher the potential overall efficiency.

9.3.2 Theoretical Limits to Multijunction Efficiencies

Henry has calculated the limiting terrestrial one-sun efficiencies for conversion with 1, 2, 3, and 36 band gaps; the respective efficiencies are 37, 50, 56, and 72% [16]. The improvement in efficiency on going from one to two band gaps is considerable, but the returns diminish as more band gaps are added. This is fortunate since the practicality of a device with more than four or five junctions is doubtful. Note that the promise of the multijunction efficiency improvements will not be realized unless the band gaps of the multiple junctions are correctly chosen; this choice will be discussed below in detail. Theoretical efficiency limits for multijunction devices based on thermodynamic fundamentals are presented in Chapter 4.

9.3.3 Spectrum Splitting

The multijunction approach requires that incident photons be directed onto the junction that is tuned to the photon's energy. Perhaps the conceptually simplest approach would be to use an optically dispersive element such as a prism to spatially distribute photons with different energies to different locations, where the appropriate cells would be placed to collect these photons. This approach is illustrated in Figure 9.4(a). Although conceptually simple, in practice the mechanical and optical complexities of this scheme make it undesirable in most circumstances. A generally preferable approach is to arrange the cells in a stacked configuration, as illustrated in Figure 9.4(b), arranged so that the sunlight strikes the highest band gap first, and then goes to the progressively lower band gap junctions. This arrangement makes use of the fact that junctions act as low-pass photon energy filters, transmitting only the sub-band gap light. Thus, in Figure 9.4(b), photons with $h\nu > E_{g3}$ get absorbed by that junction, photons with $E_{g2} < h\nu < E_{g3}$ get absorbed by the E_{g2} junction, and so on; in other words, the junctions themselves act as optical elements to

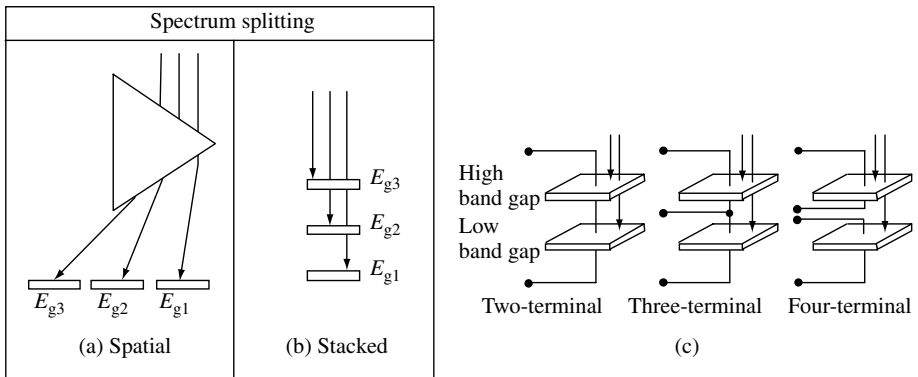


Figure 9.4 Schematic comparison of (a) spatial-configuration approaches and (b) stacked-configuration approaches to distributing light to subcells of different band gaps. (c) Illustration of two-, three-, and four-terminal connection to a two-junction cell. The figure shows the subcells as mechanically separate, but the two- and three-terminal devices can be monolithic

distribute the spectrum to the appropriate junctions for multijunction photoconversion. The band gaps *must* decrease from top to bottom of the stack. The stacked arrangement avoids the necessity for a separate optical element such as a prism to distribute the spectrum. Also, even if the junctions are physically separate from each other, they can be mechanically brought together into a relatively compact package, called a *mechanical stack*. The stacked configuration requires, of course, that all the junctions in the stack except the bottom one be transparent to light below their band gaps, which, in practice, can set challenging constraints on the substrates and the back-contact metallizations of these junctions through which sub-band gap light must pass. An elegant approach to this problem, which has several other advantages as well, is to fabricate all the junctions, each one atop the last, monolithically on a single substrate. This monolithic-stack approach will be the emphasis of this chapter.

9.4 CELL CONFIGURATION

9.4.1 Four-terminal

There are several ways to connect power leads to the junctions comprising a multijunction stack. These configurations, which provide for varying degrees of electrical isolation of the subcells, are illustrated in Figure 9.4(c) for a two-junction stack. In the four-terminal configuration, each subcell has its own two terminals and is electrically isolated from the other subcells. This configuration has the advantage that it sets no constraints on the polarities (p/n vs. n/p) of the subcells, or on their currents or voltages. However, the terminals and the electrical isolation between subcells in the four-terminal configuration would be very difficult to accomplish monolithically, because it requires a complicated cell structure and processing. Generally, a four-terminal device is, of necessity, a mechanical stack, whose complexities of fabrication and assembly make it a significantly less desirable structure than the monolithic device.

9.4.2 Three-terminal Voltage-matched Interconnections

In contrast, in the three-terminal configuration the subcells are not electrically isolated; the bottom of each cell is electrically connected to the top of the cell beneath it. The fabrication of a monolithic three-terminal device is relatively straightforward, although more complex than the fabrication of a two-terminal device. The semiconductor structure must be designed to provide a layer for contact to the intermediate terminal, and to accommodate the processing steps necessary to put the intermediate terminal in place. With this intermediate terminal, the different subcells in the stack do not have to have the same photocurrents. Furthermore, in this three-terminal configuration, the different subcells in the stack may have different polarities, for example, p/n for the top cell and n/p for the bottom cell. Module-level interconnection of four- and three-terminal devices is discussed in detail by Gee [17].

9.4.3 Two-terminal Series-connected (Current Matched)

The two-terminal series-connected configuration provides the most restrictions for interconnection of the devices. This configuration requires that the subcells be of the same polarity and that the photocurrents of the subcells be closely matched, since in this series connection the subcell with the least photocurrent limits the current generated by the entire device. This current-matching constraint, about which more will be said shortly, puts relatively tight constraints on the selection of band gaps for the various junctions in this structure. Against these disadvantages, however, are critical advantages. The existence of high-quality monolithic tunnel-junction subcell interconnects means that these stacks can be made as monolithic two-junction structures with metallization at the very top and bottom of the stack only. This, in turn, means that such devices can be integrated into modules with the same simplicity afforded by single-junction devices. The two-terminal, series-connected configuration will be the focus of the following sections, in which we analyze in detail the dependence of the cell performance on the cell design parameters.

9.5 COMPUTATION OF SERIES-CONNECTED DEVICE PERFORMANCE

9.5.1 Overview

This section discusses the quantitative modeling of the performance of series-connected, two-terminal, two-junction devices. This analysis will provide the basis for a qualitative understanding of the general trends in series-connected multijunction devices, as well as the quantitative design of these devices. Emphasis is placed on selecting band gap pairs and predicting the efficiency of the resulting structures. This modeling also lays the groundwork for the analysis of the dependence of the device performance on the spectrum, the concentration, and the temperature. Although the emphasis is on two-junction devices, we will occasionally extend the discussion to the analysis of a three-junction device, GaInP/GaAs/Ge, which is of special interest due to its technical and commercial success in space applications. Following the treatments of References [7, 18], we make

simplifying assumptions, which include (1) transparent zero-resistance tunnel-junction interconnects, (2) no reflection losses, (3) no series-resistance losses, and (4) junctions that collect every absorbed photon, and whose current–voltage ($J-V$) curves are described by the ideal ($n = 1$) diode equation. Later, we relax assumption (2) to analyze the effect of antireflection coatings; the relaxation of the other assumptions is straightforward, as well. It should be noted that high-quality III-V cells have achieved 90% of these predicted efficiencies.

9.5.2 Top and Bottom Subcell QE and J_{SC}

The short-circuit current density (J_{SC}) of each subcell is determined by the quantum efficiency of the subcell, $QE(\lambda)$, and by the spectrum of light incident on that cell $\Phi_{inc}(\lambda)$ in the usual way:

$$J_{SC} = e \int_0^{\infty} QE(\lambda) \Phi_{inc}(\lambda) d\lambda \quad (9.1)$$

The QE for an ideal cell of finite base thickness x_b , emitter thickness x_e , and depletion width W (for a total thickness $x = x_e + W + x_b$), is given by the standard equations [19]

$$QE = QE_{emitter} + QE_{depl} + \exp[-\alpha(x_e + W)]QE_{base} \quad (9.2)$$

where

$$QE_{emitter} = f_{\alpha}(L_e) \left(\frac{\ell_e + \alpha L_e - \exp(-\alpha x_e) \times [\ell_e \cosh(x_e/L_e) + \sinh(x_e/L_e)]}{\ell_e \sinh(x_e/L_e) + \cosh(x_e/L_e)} - \alpha L_e \exp(-\alpha x_e) \right) \quad (9.3)$$

$$QE_{depl} = \exp(-\alpha x_e)[1 - \exp(-\alpha W)] \quad (9.4)$$

$$QE_{base} = f_{\alpha}(L_b) \left(\alpha L_b - \frac{\ell_b \cosh(x_b/L_b) + \sinh(x_b/L_b) + (\alpha L_b - \ell_b) \exp(-\alpha x_b)}{\ell_b \sinh(x_b/L_b) + \cosh(x_b/L_b)} \right) \quad (9.5)$$

$$\ell_b = S_b L_b / D_b, \ell_e = S_e L_e / D_e, D_b = kT \mu_b / e, D_e = kT \mu_e / e \quad (9.6)$$

$$f_{\alpha}(L) = \frac{\alpha L}{(\alpha L)^2 - 1} \quad (9.7)$$

The photon wavelength dependence is not explicit in these equations, but enters through the wavelength dependence of the absorption coefficient $\alpha(\lambda)$. The quantities $\mu_{b(e)}$, $L_{b(e)}$, and $S_{b(e)}$ are, respectively, the mobility, diffusion length, and surface recombination velocity for the minority carriers in the base (emitter); T is the absolute temperature. Later in this chapter, we will illustrate the use of these equations in the analysis of real-world III-V cells. However, in this section, we shall make the simplifying assumption that each absorbed photon is converted to photocurrent, a remarkably good first approximation

for high-quality III-V junctions. In this case, the QE depends very simply on the total thickness of the device, $x = x_e + W + x_b$, as

$$QE(\lambda) = 1 - \exp[-\alpha(\lambda)x] \quad (9.8)$$

because a fraction $\exp[-\alpha(\lambda)x]$ of the incident light is transmitted through the cell instead of being absorbed. [Although this last equation is self-evident, it can also be deduced from equations (9.2)–(9.5) by setting $S = 0$, $L \gg x$, and $L \gg 1/\alpha$.]

For sub-band gap photons, $\alpha(\lambda) = 0$, and thus $\exp[-\alpha(\lambda)x] = 1$. The light Φ_{inc} incident on the top cell is simply the solar spectrum, Φ_S . In contrast, the light hitting the bottom cell is filtered by the top cell, so that the bottom cell sees an incident spectrum $\Phi_S \exp[-\alpha_t(\lambda)x_t]$, where x_t and $\alpha_t(\lambda)$ are the top-cell thickness and absorption coefficient, respectively. Assuming that the bottom cell is thick enough to absorb essentially all of the above band gap photons incident on it, we conclude that the short-circuit current densities of the top cell, J_{SCt} , and the bottom cell, J_{SCb} , are given by

$$J_{\text{SCt}} = e \int_0^{\lambda_t} (1 - \exp[-\alpha_t(\lambda)x_t]) \Phi_S(\lambda) d\lambda, \quad J_{\text{SCb}} = e \int_0^{\lambda_b} \exp[-\alpha_t(\lambda)x_t] \Phi_S(\lambda) d\lambda \quad (9.9)$$

where $\lambda_b = hc/E_{\text{gb}}$ and $\lambda_t = hc/E_{\text{gt}}$ are the wavelengths corresponding to the band gaps of the bottom and top cells, respectively. The lower limit on the J_{SCb} integral is 0, not λ_t , because unless the top cell is infinitely thick, it will transmit some short-wavelength photons to the bottom cell. Because the bottom subcell is filtered by the top subcell, J_{SCb} depends on both E_{gb} and E_{gt} , whereas J_{SCt} depends only on E_{gt} . Equation (9.10) shows this dependence with special clarity in the case of an infinitely thick top cell. In this case, $\exp[-\alpha_t(\lambda)x_t] = 0$ for all photon energies above E_{gt} , so that the J_{SC} equations become

$$J_{\text{SCt}} = e \int_0^{\lambda_t} \Phi_S(\lambda) d\lambda, \quad J_{\text{SCb}} = e \int_{\lambda_t}^{\lambda_b} \Phi_S(\lambda) d\lambda \quad (9.10)$$

9.5.3 Multijunction J – V Curves

For any set of m series-connected subcells (or, indeed, any sort of two-terminal element or device) whose individual current–voltage (J – V) curves are described by $V_i(J)$ for the i th device, the J – V curve for the series-connected set is simply

$$V(J) = \sum_{i=1}^m V_i(J) \quad (9.11)$$

that is, the voltage at a given current is equal to the sum of the subcell voltages at that current. Each individual subcell will have its own maximum-power point $\{V_{\text{mp}_i}, J_{\text{mp}_i}\}$, which maximizes $J \times V_i(J)$. However, in the series-connected multijunction connection of these subcells, the currents through each of the subcells are constrained to have the same value, and therefore *each subcell will be able to operate at its maximum-power point only if J_{mp_i} is the same for all the subcells*, that is, $J_{\text{mp}_1} = J_{\text{mp}_2} = \dots = J_{\text{mp}_m}$. If this is the case, then the maximum power output of the combined multijunction device is

the sum of the maximum power outputs $V_{mp_i} J_{mp_i}$ of the subcells. On the other hand, if the subcells do not all have the same value for J_{mp_i} , then in their series-connected multijunction combination, some of the subcells must necessarily operate away from their maximum-power points.

The consequences of this last point are especially important when, as is the case for high-quality III-V junctions, the subcells do not leak or quickly break down in reverse bias. The adding of series $J-V$ curves in this case is illustrated graphically in Figure 9.5, which shows $J-V$ curves for a GaInP top subcell, a GaAs bottom subcell, and the two-junction series-connected combination of these two subcells. In this example, the bottom subcell has a higher J_{SC} than the top subcell; the top subcell is slightly shunted, to make the illustration of its behavior at the tandem J_{SC} easier to see. For any given value of current, the tandem voltage satisfies $V_{tandem} = V_{top} + V_{bottom}$, as can be verified by the inspection of the figure. The region of current near the tandem cell $J_{SC} = -14 \text{ mA/cm}^2$, shown in expanded scale in the bottom panel of the figure, is of special interest. At $J = -13.5 \text{ mA/cm}^2$, both subcells are in forward bias, with voltages only slightly less than their respective open-circuit voltages (V_{OC} s). As the magnitude of the current density is further increased to -14 mA/cm^2 and beyond, the bottom subcell remains in forward bias near its V_{OC} . At the same time, in contrast, the top subcell voltage becomes rapidly more negative, so that at $J = -14 \text{ mA/cm}^2$, it has reached a negative bias of about -1 V , equal in magnitude but opposite in sign to the top subcell's forward bias of $+1 \text{ V}$. At this

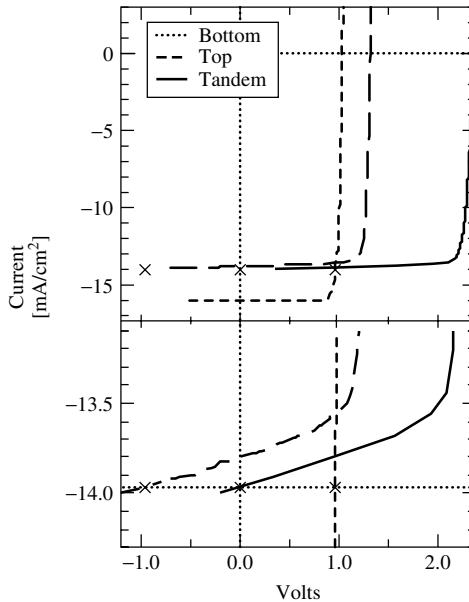


Figure 9.5 Illustration of the addition of $J-V$ curves for two series-connected subcells. The lower panel is an expanded view of the current range in the vicinity of the current-limiting top subcell J_{SC} , showing how the tandem J_{SC} is limited to the lesser of the subcell currents. The $J-V$ of the top subcell in this example is slightly leaky, which makes the addition of the subcell $J-V$ curves near J_{SC} easier to see. The X's mark voltage of the top, bottom, and tandem when the tandem is at short circuit of 14 mA/cm^2

value of current, the tandem cell is at zero bias; hence J_{SC} . This behavior illustrates the general principle that for subcells without significant leakage or reverse-bias breakdown, *the tandem J_{SC} is constrained to be, to a very good approximation, the lesser of the J_{SC} s of the subcells.* (Note that this current-limiting characteristic makes series-connected multijunction cells of the type considered here much *worse* than single-junction cells for conversion of narrowband spectra such as the light from a laser! The reader should try to make sure to understand why this is the case.)

To model multijunction devices quantitatively, we need expressions for the subcell J - V curves, $V_i(J)$. To proceed, we use the classical ideal-photodiode J - V equations (neglecting the depletion region), [19]

$$J = J_0[\exp(eV/kT) - 1] - J_{SC} \quad (9.12)$$

where e is the electric charge, and we have assumed that the diode ideality factor is 1. An important special case of this is

$$V_{OC} \approx (kT/e) \ln(J_{SC}/J_0) \quad (9.13)$$

because, in practice, $J_{SC}/J_0 \gg 1$. The dark current density J_0 is given by

$$J_0 = J_{0,\text{base}} + J_{0,\text{emitter}} \quad (9.14)$$

where

$$J_{0,\text{base}} = e \left(\frac{D_b}{L_b} \right) \left(\frac{n_i^2}{N_b} \right) \left(\frac{(S_b L_b / D_b) + \tanh(x_b / L_b)}{(S_b L_b / D_b) \tanh(x_b / L_b) + 1} \right) \quad (9.15)$$

and a similar equation describes $J_{0,\text{emitter}}$. The intrinsic carrier concentration n_i is given by

$$n_i^2 = 4M_c M_v (2\pi kT / h^2)^3 (m_e^* m_h^*)^{3/2} \exp(-E_g / kT) \quad (9.16)$$

where m_e^* and m_h^* are the electron and hole effective masses, and M_c and M_v are the number of equivalent minima in the conduction and valence bands, respectively. $N_{b(e)}$ is the base (emitter) ionized-impurity density.

Each junction in a multijunction structure is described by eqs. (9.12)–(9.16); the i th junction will have dark current $J_{0,i}$ short-circuit $J_{SC,i}$ etc, with a corresponding J - V characteristic $V_i(J)$. Adding these $V_i(J)$ curves for the individual junctions gives the full multijunction $V(J)$ curve of eq. (9.11). The maximum-power point $\{J_{mp}, V_{mp}\}$ can be calculated numerically as the point on the $V(J)$ curve that maximizes $J \times V(J)$. The various solar cell performance parameters of interest can be extracted from the J - V curve in the usual way; for example, $V_{OC} = V(0)$, $FF = J_{mp} V_{mp} / (V_{OC} J_{SC})$.

9.5.4 Efficiency versus Band Gap

To obtain concrete, numerical values for the cell performance, we need to choose numbers for the material properties of the junctions. Reference [7] provides a reasonable model of a two-junction n/p cell, in which the bottom junction has the properties of GaAs, except

that the band gap is allowed to vary. The absorption coefficient is shifted rigidly with the band gap so that it correctly goes to zero as the photon energy decreases below the band gap energy. Likewise, for the top subcell, the model uses the material properties of GaInP, again allowing the band gap to vary. The diffusion lengths at 300 K for the GaAs cell are $L_b = 17 \mu\text{m}$ and $L_e = 0.8 \mu\text{m}$; for the GaInP cell, $L_b = 3.7 \mu\text{m}$ and $L_e = 0.6 \mu\text{m}$. For simplicity, and to give results representing the maximum possible performance, all surface recombination is taken as zero. The emitters for both subcells have thickness $x_e = 0.1 \mu\text{m}$ and ionized dopant concentration $N_e = 2 \times 10^{18}/\text{cm}^3$, and the bases for both subcells have $N_b = 10^{17}/\text{cm}^3$. These values are comparable to those used in actual GaInP/GaAs multijunction cells, which provide an optimal combination of high quantum efficiency, low dark current, and low series resistance. Using this model, Figure 9.6(a) plots contours of cell efficiency for a two-junction series-connected cell with infinitely thick subcells, calculated for the one-sun standard AM1.5 global spectrum. Similar contours are shown for a variety of spectra and concentrations by Nell and Barnett [20] and by Wanlass *et al.* [18]. At the optimal band gap combination of $\{E_{\text{gt}} = 1.75 \text{ eV}, E_{\text{gb}} = 1.13 \text{ eV}\}$ an efficiency of almost 38% is predicted, well in excess of the 29% efficiency that the model would predict for the best single-junction device.

Even at a bandgap combination of $\{E_{\text{gt}} = 1.95 \text{ eV}, E_{\text{gb}} = 1.42 \text{ eV}\}$, though well away from the optimal bandgap combination, the efficiency is still much higher than the best single-junction efficiency. This band gap pair was chosen for consideration because the bottom-subcell band gap is the band gap of GaAs, while the top-subcell band gap is only slightly higher than the 1.85 eV band gap obtained under typical growth conditions for GaInP. But as E_{gt} decreases from 1.95 eV to the GaInP band gap of 1.85 eV (with E_{gb} held at the GaAs band gap of 1.42 eV) the efficiency falls very rapidly, from 35 to 30%. This drop-off is due to the dependence of the top- and bottom-subcell photocurrents

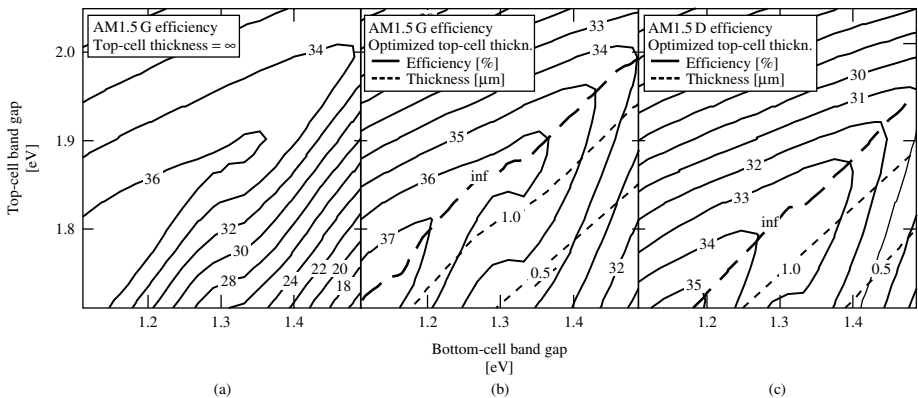


Figure 9.6 Contour plots of efficiency versus subcell band gaps for a series-connected two-terminal two-junction tandem cell. Adapted from Kurtz S, Faine P and Olson J, *J. Appl. Phys.* **68**, 1890 (1980) [7]. Panel (a) is calculated for the AM1.5 global spectrum, with an infinitely thick top subcell. Panel (b) is calculated for the same spectrum, but for the top subcell thickness that optimizes the tandem-cell efficiency at each combination of top- and bottom-cell band gap; the dashed contours show this optimal thickness. In the region of the graph above the thickness = ∞ contour, the tandem current is limited by the top cell. Panel (c) shows efficiencies and optimal top-cell thicknesses calculated as in (b) but for the AM1.5 direct spectrum

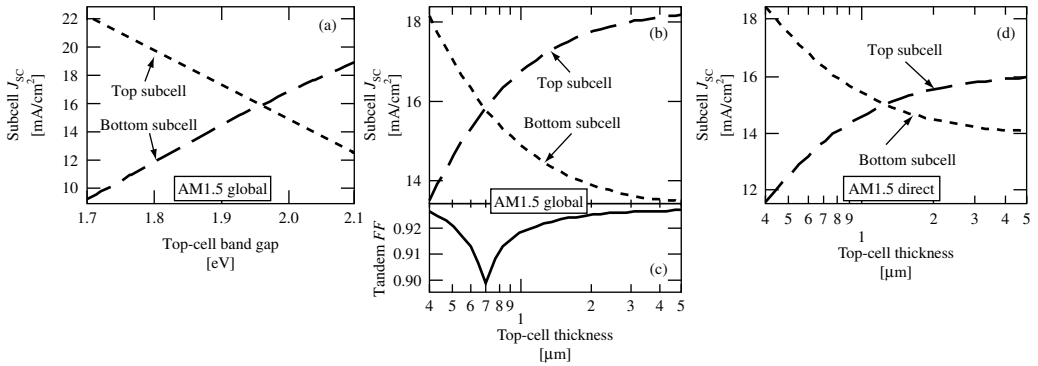


Figure 9.7 (a) J_{SCt} and J_{SCb} for an infinitely thick top subcell as a function of top-subcell band gap E_{gt} for a bottom-subcell band gap $E_{gb} = 1.42$ eV. (b) J_{SCt} and J_{SCb} as a function of top-subcell thickness for the AM1.5 global spectrum, with $E_{gb} = 1.42$ eV and $E_{gt} = 1.85$ eV. The subcells are current matched at a base thickness of $0.7 \mu\text{m}$. (c) The corresponding tandem-cell fill factor. (d) J_{SCt} and J_{SCb} as a function of top-subcell thickness as in (b) but for the AM1.5 direct spectrum. The current-matching thickness is significantly greater than that for the global spectrum

on the top-subcell band gap. As noted above, lowering the top-subcell band gap while holding the bottom-subcell band gap constant increases the top-subcell J_{SC} at the expense of the bottom-subcell J_{SC} . Figure 9.7(a) illustrates this for the case at hand by showing J_{SCt} and J_{SCb} as a function of E_{gt} for $E_{gb} = 1.42$ eV. The J_{SC} for the series-connected combination of these two cells will be the lesser of J_{SCt} and J_{SCb} . The figure shows that this quantity is a maximum at the current-matched band gap $E_{gt} = 1.95$ eV, and falls off rapidly as E_{gt} decreases below 1.95 eV. This falloff in J_{SC} due to the bottom subcell limiting the photocurrent at low E_{gt} is responsible for the corresponding drop-off in the tandem-cell efficiency shown in Figure 9.6(a). This dependence of tandem J_{SC} and efficiency on E_{gt} would suggest that a GaInP/GaAs cell would not have a useful high efficiency. Fortunately, as will be discussed in the next section, this rapid drop-off of efficiency can be greatly alleviated by thinning the top subcell.

9.5.5 Top-cell Thinning

Because the absorption coefficient $\alpha(h\nu)$ for solar cell materials is not infinite, a cell of finite thickness will not absorb all the incident above band gap light. Some light will be transmitted (especially at photon energies near the band gap where α is small); the thinner the cell, the greater the transmission. Therefore, for a two-junction cell, thinning the top subcell will reappportion the light between the two subcells, increasing the bottom-subcell current at the expense of the top-subcell current. If, before thinning, $J_{SCb} < J_{SCt}$, then the top subcell can be thinned to make $J_{SCb} = J_{SCt}$. Because the series-multijunction cell current J_{SC} is limited to the lesser of J_{SCb} and J_{SCt} , J_{SC} and hence the cell efficiency will be maximized when the top subcell is thinned to achieve this current matching. Figure 9.7(b) illustrates this current matching for the tandem device under discussion, for the case that $E_{gt} = 1.85$ eV (GaInP) and $E_{gb} = 1.42$ eV (GaAs). The tandem current $J_{SC} \approx \min(J_{SCt}, J_{SCb})$ is maximized at a top-subcell thickness of $0.7 \mu\text{m}$, for which the subcells are current matched. At this thickness, $J_{SC} = J_{SCt} = 15.8 \text{ mA/cm}^2$, or about 85%

of what J_{SCt} would be for an infinite-thickness top subcell. The ability of such a thin cell to absorb such a high fraction of the incident light is due to the large absorption coefficient of this direct gap material.

By comparison with the thinned top-subcell case, for an infinitely thick top subcell the multijunction J_{SC} would be determined by the bottom subcell at a current $J_{SCb} = 13.4 \text{ mA/cm}^2$. This improvement in J_{SC} on thinning the top cell results in a corresponding improvement in the cell efficiency, from 30% to approximately $15.8/13.4 * 30\% \approx 35\%$. This estimate is only approximate because, as will be discussed below, top-cell thinning affects the fill factor and V_{OC} , as well as J_{SC} . However, these are second-order effects, and the approximation of scaling efficiency with J_{SC} alone is quite good. We can see this in Figure 9.6(b), which shows contours of cell efficiency vs. top- and bottom-subcell band gap, for optimal top-subcell thickness. The figure confirms that the cell efficiency at $\{E_{gt} = 1.85 \text{ eV } E_{gb} = 1.42 \text{ eV}\}$ is about 35%. The figure also shows contours of the optimal top-subcell thickness. The optimal thickness decreases with increasing E_{gb} or decreasing E_{gt} , as required, to maintain current matching. The thick dashed line is the contour of infinite top-subcell thickness; above this contour, the tandem-cell current is always limited by the top subcell, whereas below this contour, thinning the top subcell improves the tandem-cell efficiency. Comparing the optimized efficiencies to the infinite-thickness efficiencies of Figure 9.6(a), we see that the top-subcell thinning greatly reduces the sensitivity of the tandem efficiency on subcell band gap, in effect widening the range of band gaps that can be selected.

9.5.6 Current-matching Effect on Fill Factor and V_{OC}

The fill factor (FF) of the tandem cell depends on the top- and bottom-subcell photocurrents. Figure 9.7(c) shows the fill factor as a function of top-cell thickness, and thus effectively as a function of J_{SCt}/J_{SCb} , for the device of Figure 9.7(b). The fill factor is a minimum at the current-matched condition, an effect that holds in general for reasonably ideal (nonleaky) subcells. This effect slightly undermines the efficiency gains that accrue from the increase in J_{SC} at the current-matched condition; however, the decrease in fill factor at current matching is roughly half the increase in J_{SC} . This dependence of fill factor on the ratio of the subcell currents is important, because it implies that correctly measuring the fill factor of an actual device requires correctly light-biasing the subcells. This subject is discussed further in the chapter on measurements (see Chapter 16).

As equations (9.13–9.15) show, V_{OC} also depends on cell thickness. Figure 9.8 shows how finite base thickness x_b and base surface recombination velocity S_b affect the V_{OC} of a GaInP cell. These curves were calculated using equations (9.13–9.15), assuming a bulk recombination velocity $D_b/L_b = 2.8 \times 10^4 \text{ cm/s}$, a typical value for a GaInP cell. The figure shows that for a cell with a well-passivated base, that is, S_b small enough that $S_b \ll D_b/L_b$, thinning the cell results in a meaningful increase in V_{OC} . On the other hand, for a cell whose base is so poorly passivated that $S_b > D_b/L_b$, thinning the cell lowers V_{OC} . For the GaInP/GaAs tandem structure, with the thin top subcell required for current matching, the passivation of the base of the top subcell is thus an important consideration for the overall device efficiency. The passivation of GaInP surfaces will be discussed later in this chapter.

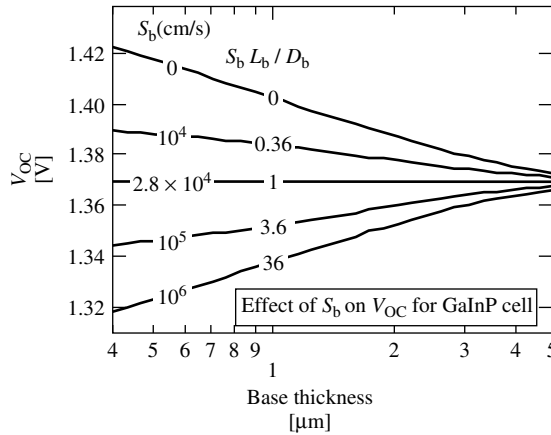


Figure 9.8 Effect of base thickness x_b and surface-recombination velocity S_b on V_{OC} for a GaInP top cell with $J_{SC} = 14 \text{ mA/cm}^2$. The base is characterized by a *bulk* recombination velocity $D_b/L_b = 2.8 \times 10^4 \text{ cm/s}$. Note that when the bulk and surface recombination velocities are equal, V_{OC} is independent of base thickness

9.5.7 Spectral Effects

The amount of light distributed to each subcell, and thus, the photocurrents generated by each subcell, is determined by the spectrum of the incident light. (See Chapters 3 and 16 for a more complete discussion of spectra and absorption.) Therefore, the optimal band gaps and the optimal top-subcell thinning depend on the incident spectrum. Figure 9.6(c) shows the efficiency versus top- and bottom-subcell band gap for the standard AM1.5 direct spectrum for the same two-junction device as was modeled for the global spectrum in Figure 9.6(b). For a given bottom-subcell band gap, the optimal top-subcell band gap E_{gt} is lower for the direct spectrum than for the global spectrum. This difference arises because the direct spectrum has less blue light than the global spectrum, resulting in a diminished J_{SCt}/J_{SCb} ; lowering E_{gt} compensates for this by directing more light to the top cell. Likewise, for a given E_{gt} and E_{gb} , the optimal top-subcell thickness is greater for the direct spectrum than for the global spectrum. Figure 9.7(d) shows J_{SCt} and J_{SCb} for the {1.85, 1.42} eV band gap pairing as a function of top-subcell thickness as in Figure 9.7(a), but calculated for the direct spectrum instead of the global spectrum. The thickness required for current matching is roughly $1.2 \mu\text{m}$, significantly greater than the $0.7\text{-}\mu\text{m}$ current-matching thickness for the global spectrum. For comparison, the AM0 spectrum is even more blue-rich than the AM1.5 global spectrum, and the top subcell would correspondingly be thinner, about $0.5 \mu\text{m}$ in thickness.

9.5.7.1 Spectral fluctuations

While the analysis above shows how to choose a top-cell thickness for a given spectrum, no one spectrum precisely represents the actual spectrum seen by a terrestrial solar cell. Fluctuations in the spectrum with time due to the changing position of the sun in the sky, and the changing atmospheric conditions, can be quite significant. The detailed

implications for tandem-cell design are complicated [21]. In general, it is found that series tandem cells are quite sensitive to fluctuations in air mass in particular. Fortunately, efficiency at high air mass is relatively unimportant because the net power output is small under these conditions. Overall, a well-designed multijunction cell is expected to outperform a single-junction cell by a comfortable margin even when spectral fluctuations are taken into account. (It is interesting to note that spectral fluctuations are less of a concern for voltage-matched devices than for current-matched devices, because a change in a subcell current is reflected only logarithmically in the corresponding change in voltage.)

9.5.7.2 Chromatic aberration

A related issue of concern for series-connected multijunction cells is the chromatic aberration of the spectrum that can be caused by the concentrating optics in concentrator modules, especially the Fresnel lenses used by some concentrator configurations. Such aberration will not only change the spectrum from the incident solar spectrum, but may also result in a position-dependent variation in the spectrum across the receiver. It is found that the detrimental effect of such spatial variations may be mitigated by making the emitters of the bottom subcells highly conductive [22]. This aids current matching by lateral conduction between adjacent areas of a cell.

9.5.8 AR Coating Effects

9.5.8.1 Introduction

Our discussion has so far assumed for simplicity that there is no reflection of the incident light from the front surface of the cell. However, without an antireflective (AR) coating, III-V cells typically have large reflectances on the order of 30% in the spectral region of importance for converting the solar spectrum. AR coats can reduce this reflectance to ~1%, but only over a limited spectral range; this limitation has important implications for tandem-cell current matching. An examination of AR coating issues is therefore especially important for III-V multijunction cells.

9.5.8.2 Calculation

For analyzing the effect of AR coating parameters on multijunction performance, it is useful to have a realistic numerical model for the reflectance. Here, we use the relatively simple model of Lockhart and King [23]. This model calculates the normal-incidence reflection of a three-layer coating. Each layer is assumed to be lossless so that the index of refraction n_j of the j th layer, along with its thickness d_j , fully characterizes the optical properties of the layer. The layers are numbered $j = 1$ to 4, with $j = 4$ being the top layer and $j = 1$ being the substrate. For example, for a two-layer MgF_2/ZnS coat on a GaInP cell with an AlInP window layer, layers 4/3/2/1 are $\text{MgF}_2/\text{ZnS}/\text{AlInP}/\text{GaInP}$, respectively. The reflection R as a function of wavelength λ is given by

$$R = |(X - 1)/(X + 1)|^2 \quad (9.17a)$$

where

$$X = [n_2(n_3n_4 - n_2n_4t_2t_3 - n_2n_3t_2t_4 - n_3^2t_3t_4) + i n_1(n_3n_4t_2 + n_2n_4t_3 + n_2n_3t_4 - n_3^2t_2t_3t_4)]/[n_1n_4(n_2n_3 - n_3^2t_2t_3 - n_3n_4t_2t_4 - n_2n_4t_3t_4) + i n_2n_4(n_2n_3t_2 + n_3^2t_3 + n_3n_4t_4 - n_2n_4t_2t_3t_4)] \quad (9.17b)$$

and

$$t_j = \tan(2\pi n_j d_j/\lambda) \quad (9.17c)$$

Although this approach incorrectly assumes that there is no absorption from the layers of the top subcell, and completely neglects all the deeper layers in the cell stack, in practice, it gives results that agree reasonably well with more rigorous approaches [24], and it has the virtue of simplicity. The AR coating calculations that illustrate the following discussion were done using equations (9.17). Note, however, that more complex problems such as the calculation of backside AR coats needed for mechanical stacks require the more rigorous formalism.

9.5.8.3 Current matching

Figure 9.9(a) shows the modeled reflectance for a GaInP cell with a MgF₂/ZnS AR coating, for several different combinations of the layer coating thicknesses [25], using optical constants from the literature [26, 27]. The dependence of the reflectance on the layer thicknesses can, roughly, be broken down into two parts, that is, the ratio of the two thicknesses and the total thickness of each layer. Proper choice of the ratio, as for the layer thicknesses in Figure 9.9(a), yields a reflectance with a flat, low, notch-shaped minimum. With this ratio held constant, the total thickness of the coating determines the position of the minimum, with increasing thickness shifting the notch position to lower photon energy. The width of the notch is less than the solar spectral range, so regardless of the position of the notch, the photocurrents of the subcells will be less than what they would be for the ideal case of zero reflectance. Shifting the notch to higher photon energy will send more light to the top subcell at the expense of the bottom subcell, and vice versa; the AR coating thus affects the current matching in the cell. Figure 9.9(b) shows the photocurrent of a GaInP(1.85 eV)/GaAs(1.42 eV) tandem cell as a function of ZnS/MgF₂ AR coating layer thicknesses, for the AM1.5 direct spectrum. As the top-subcell thickness increases, the optimal AR coating thickness increases, to compensate by directing more of the light to the bottom subcell.

9.5.9 Concentration

Terrestrial application of high-efficiency multijunction solar cells is generally in concentrator systems, given the high solar cell costs. These types of cells are well suited for concentrator operation, not only because of their high one-sun efficiencies, but also because these high efficiencies can be maintained up to concentration levels exceeding 1000 suns. This section discusses the adaptations needed for the one-sun devices to be made suitable for concentrator operation, and describes the resulting concentrator

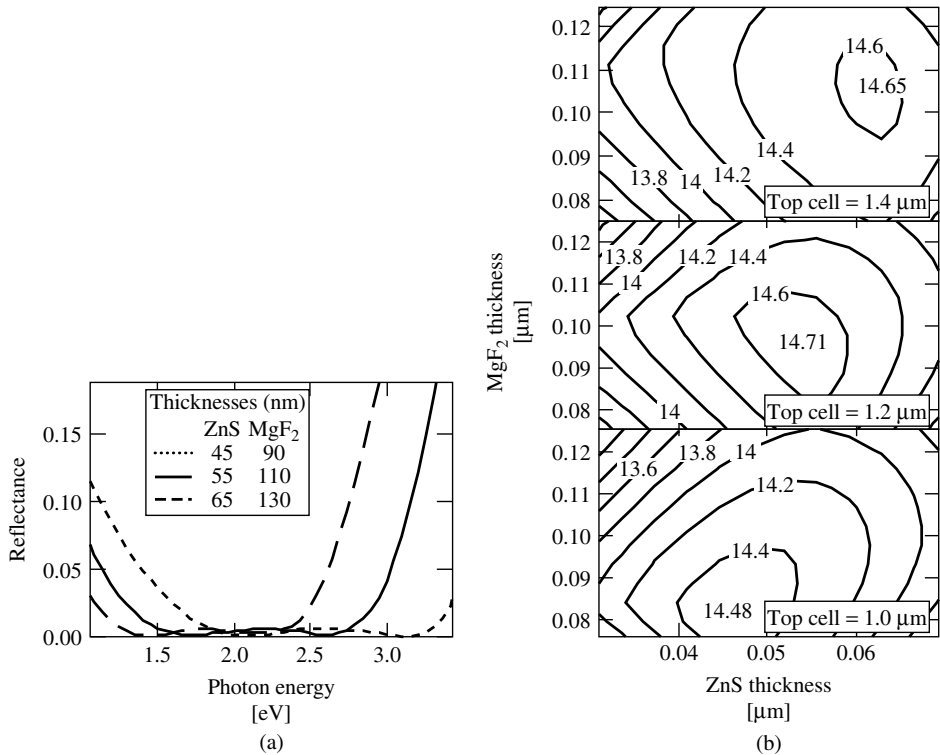


Figure 9.9 (a) Calculated reflectance for a GaInP cell with a MgF₂/ZnS AR coating, for several different combinations of the layer coating thicknesses. (b) Calculated photocurrent (in mA/cm²) of a GaInP/GaAs two-terminal tandem cell under the AM1.5 direct spectrum as a function of ZnS/MgF₂ AR coating layer thicknesses, for several different top-subcell thicknesses

performance to be expected from these devices. A detailed discussion of general issues in concentrator PV is given in Chapter 11 (see also Reference [28]).

9.5.9.1 Spectrum

Cells in a terrestrial concentrator module will be exposed to a spectrum containing significantly less high-energy light than the AM0 spectrum to which multijunction devices are exposed in space applications. This difference calls for the thickness of the terrestrial concentrator top subcell to be greater than that of a space cell, to satisfy current-matching requirements. As noted above, current-matching top-subcell thicknesses for GaInP/GaAs tandem cells are on the order of 0.5 μm for the AM0 spectrum and 1 μm for the AM1.5 direct spectrum. In practice, the situation is not so simple, because the spectrum that a terrestrial cell sees will vary as a function of time, and in most typical operating situations will rarely be as blue-poor as the ASTM (formerly American Soc. for Testing and Materials) standard AM1.5 direct spectrum. The cell design also depends on cell temperature, which will depend on the details of the module (and which, of course, will also vary with time). Further discussion of these issues for multijunction concentrators is given in Reference [29].

9.5.9.2 Concentration dependence of efficiency

Equation (9.13) shows that, for each decade of increase in J_{SC} due to a corresponding increase in the incident light flux, V_{OC} will increase by $(kT/e) \ln(10) = 60$ mV for an ideal $n = 1$ junction at 300 K. For a series-connected multijunction device, each junction will contribute this amount to the net increase in V_{OC} with concentration. This increase in V_{OC} gives a significant boost to cell efficiency with concentration, a boost that is relatively greater for low band gap junctions. For instance, a two-junction GaInP/GaAs cell with a one-sun V_{OC} of 2.4 V will go to $V_{OC} = 2.76$ V at 1000 suns for an increase of 15%, whereas a three-junction GaInP/GaAs/Ge cell with a one-sun V_{OC} of 2.6 V will go to $V_{OC} = 3.14$ V at 1000 suns for an increase of 21%. For a cell with negligible series resistance, the fill factor will also increase with concentration, although not in as numerically simple a fashion as does V_{OC} . The increase with concentration is proportionally much less than that for V_{OC} ; the fill factor typically increases on the order of 1 to 2% as the concentration is raised from 1 to 1000 suns, for the ideal case of no series resistance.

It is interesting to note that while series-connected multijunction devices maintain their current matching with increasing light intensity (assuming that the spectrum does not change), the increase in junction voltage with concentration means that voltage-matched devices are voltage-matched only for a fixed concentration ratio.

9.5.9.3 Series resistance and metallization

In practice, of course, series resistance is unavoidable. The resulting J^2R power loss scales as the square of the current, and thus eventually becomes a dominant factor for the cell efficiency with increasing current. This series resistance will manifest itself as a loss in the fill factor (and, at very high currents or for very high resistance, in J_{SC} as well). Series-connected multijunction cells, which distribute the spectrum into several subcells and are thus inherently lower-current devices than single-junction cells, therefore have a great advantage in minimizing J^2R losses at high concentrations. For example, the GaInP/GaAs tandem operates at half the current of a single-junction GaAs cell, and thus suffers only one quarter the J^2R loss for a given resistance and concentration.

Even with this low-current advantage of multijunction cells, in adapting a cell from one sun to concentrator operation it may be well worth reducing series resistance. One of the most vital adaptations of a cell design for concentrator operation is the front-contact metallization. The series resistance of the cell depends on the density of front-contact grid fingers [30]; a grid design optimized for 1000 suns will have a much higher density of grid fingers than a one-sun grid. Grid-finger spacings of 200 μm or less are not unusual at 1000 suns. Naturally, decreasing the grid-finger spacing increases the device shadowing and so decreases the current; thus, concentrator grid design involves careful trade-offs of the shadowing versus the series resistance. Fortunately, with the sophisticated photolithography/evaporation/liftoff metallization processing used for high-efficiency devices, grid-finger widths on the order of 3 μm , with height/width aspect ratios of two or more, can be achieved. Such finger dimensions allow a very dense packing of high-conductivity grids, while maintaining a reasonably low shadow loss.

An additional approach to decreasing the series resistance is to raise the emitter conductivity in the top subcell (for monolithic two-terminal devices, there is no lateral

conduction in the emitters of the other subcells, so only the top-cell emitter conductivity is important). This may be accomplished by raising the emitter doping and/or the thickness. Because doing so may decrease the quantum efficiency of the top subcell, increasing the conductivity is a trade-off that must be made carefully. Achieving a sufficiently high emitter conductivity is easier for n/p than for p/n devices, because of the higher *majority*-carrier mobility in n -type material than in otherwise comparable p -type material.

At least as important to the concentrator operation of monolithic two-terminal multijunction devices is the necessity for tunnel-junction interconnects (TJICs) with low series resistance, high peak tunneling currents, and low absorption losses. These considerations are discussed in more detail later in this chapter.

9.5.9.4 Measured performance of GaInP/GaAs/Ge concentrator cell

The considerations of device performance versus concentration that we have just described are well illustrated by the plot of efficiency versus concentration for the GaInP/GaAs/Ge three-junction concentrator device, as shown in Figure 9.10. For concentrator operation, this device incorporated adaptations to the top-subcell emitter conductivity, the grid-finger spacing, and the top-subcell current-matching thickness. The V_{OC} of the resulting device increases with concentration at a rate quite near the ideal 60 mV/junction/decade. Because of the low one-sun current and the low series resistance, the fill factor remains virtually unaffected by series-resistance losses until several hundred suns concentration. At higher concentration, the increasingly dominant series resistance causes the efficiency to roll off. Note, however, that at 1000 suns, the efficiency is still well in excess of 30%.

9.5.9.5 Linearity

In measuring the concentration dependence of device performance, it is usually assumed that J_{SC} is linear with concentration, so that J_{SC} can be used as the measure of the concentration level. The assumption of linearity is generally considered to be quite good

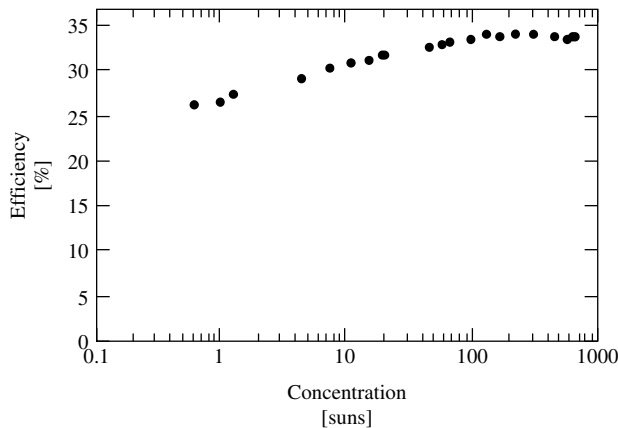


Figure 9.10 Efficiency versus concentration of a state-of-the-art GaInP/GaAs/Ge cell under the AM1.5 global spectrum [14]

for III-V devices. Although a detailed discussion of linearity is outside the scope of this chapter, it is worth mentioning because different degrees of nonlinearity for different subcells in the device could lead to a crossover between top-cell-limited and bottom-cell-limited performance as a function of concentration.

9.5.10 Temperature Dependence

To predict device performance at realistic operating temperatures, and to be able to interpret measured device characteristics at these temperatures, it is useful to analyze the temperature coefficients of these devices using the basic cell equations (9.1–9.16) [31]. We shall see that the current-matching constraint for series-connected multijunction cells leads to effects in the temperature coefficients that are not seen for single-junction devices.

9.5.10.1 V_{OC}

Because the series-connected multijunction V_{OC} is simply the sum of the subcell V_{OC} s, the temperature coefficient dV_{OC}/dT of the multijunction V_{OC} is likewise the sum of the dV_{OC}/dT values for the subcells. Taking the GaInP/GaAs tandem cell as an example, both the GaInP and GaAs subcells have $dV_{OC}/dT \approx -2 \text{ mV}/^\circ\text{C}$. The tandem therefore has $dV_{OC}/dT \approx -4 \text{ mV}/^\circ\text{C}$ [31]. Table 9.2 compares these temperature coefficients for several types of cells. The GaInP/GaAs/Ge three-junction cell is seen to have a more negative $1/V_{OC} dV_{OC}/dT$ value than the GaInP/GaAs two-junction cell, due to the contribution of the low band gap Ge junction. However, going to high concentrations reduced the magnitude of $1/V_{OC} dV_{OC}/dT$, due to the increase in V_{OC} with concentration.

9.5.10.2 J_{SC}

Although the V_{OC} temperature coefficients for the subcells of a series-connected multijunction cell are independent and additive, the multijunction J_{SC} temperature coefficient

Table 9.2 V_{OC} temperature coefficients at 300 K for multijunction cells and their single-junction component subcells, assuming junction ideality factors $n = 1$. One-sun illumination is assumed except as noted. Values are guidelines for comparison with actual cells, but precise agreement should not be expected, especially for junctions whose ideality factor deviates significantly from $n = 1$. For comparison, data are also shown for a passivated emitter rear locally diffused (PERL) Si cell, which has a significantly lower temperature coefficient than that of standard Si cells [32]

Cell	V_{OC} [mV]	dV_{OC}/dT [mV/K]	$1/V_{OC} dV_{OC}/dT$ [%/K]
Ge	200	-1.8	-0.90
GaAs	1050	-2.0	-0.19
GaInP	1350	-2.2	-0.16
GaInP/GaAs	2400	-4.2	-0.17
GaInP/GaAs/Ge	2600	-6.0	-0.23
GaInP/GaAs/Ge (500 suns)	3080	-6.0	-0.19
PERL Si	711	-1.7	-0.24

is more complex. Again taking the GaInP/GaAs tandem as an example, recall that GaAs subcell J_{SC} depends not only on the GaAs band gap but also on the GaInP band gap, because the GaInP subcell filters the light to the GaAs subcell. When the tandem-cell temperature is raised, the bottom-subcell band gap decreases, tending to increase its J_{SC} ; at the same time, however, the top-subcell band gap also decreases, which decreases the amount of light going to the bottom cell and thus minimizes the increase in the bottom-subcell J_{SC} with temperature.

The tandem J_{SC} is limited by the least of the subcell J_{SC} s. In general, these subcell J_{SC} s will not have identical temperature coefficients. For a tandem cell that is nearly current matched, there will, therefore be a crossover temperature below which the tandem J_{SC} is limited by one subcell and above which the tandem J_{SC} is limited by the other subcell. Figure 9.11 illustrates this crossover for a modeled GaInP/GaAs tandem

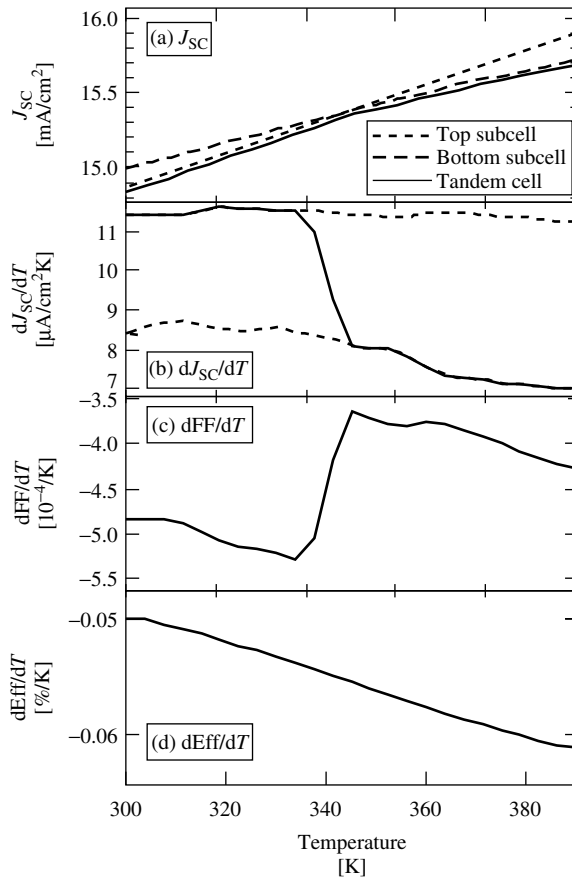


Figure 9.11 (a) Subcell and corresponding tandem-cell J_{SC} s as a function of temperature for a GaInP/GaAs tandem cell that is slightly top-subcell current limited at 300 K. (b) The corresponding temperature derivatives dJ_{SC}/dT . As the cell temperature is raised above ~ 340 K, the cell crosses over from top limited to bottom limited, and dJ_{SC}/dT changes correspondingly. (c) Tandem-cell fill factor temperature derivative dFF/dT . (d) Efficiency temperature coefficient $dEff/dT$

cell that is slightly top-subcell limited at 300 K. The top-subcell J_{SC} increases faster with temperature than does the bottom-subcell J_{SC} , leading to a crossover from top- to bottom-subcell limited as the temperature is raised above 350 K. The tandem dJ_{SC}/dT likewise crosses over from dJ_{SCt}/dT to dJ_{SCb}/dT .

9.5.10.3 Fill factor

Because the tandem-cell fill factor is determined more by the current-limiting subcell than by the other subcell(s), the current-matching crossover has similar implications for dFF/dT as for dJ_{SC}/dT . For the cell of Figure 9.11, the crossover from top- to bottom-subcell limited causes dFF/dT to change, as shown in Panel (c).

9.5.10.4 Efficiency

Because the efficiency is proportional to $V_{OC} \times J_{SC} \times FF$, and dJ_{SC}/dT and dFF/dT change in opposite directions as the temperature goes through the current-matched temperature, $dEff/dT$ is a relatively smooth function of temperature.

9.6 MATERIALS ISSUES RELATED TO GaInP/GaAs/Ge SOLAR CELLS

9.6.1 Overview

In the previous section, we discussed the basic elements of a monolithic, multijunction solar cell, such as that shown in Figure 9.1, including subcell band gaps and thicknesses, metallization, and AR coating effects. We also assumed unity collection efficiency for all photogenerated carriers, implying that component semiconductor materials, interfaces, and junctions are virtually perfect. In practice, however, numerous intrinsic and extrinsic factors tend to limit the quality and performance of multijunction solar cells. In this section, we review various aspects of real materials and devices, including issues associated with their growth.

9.6.2 MOCVD

The GaInP/GaAs/Ge dual- and triple-junction solar cells are produced commercially in relatively large volumes by several companies in the United States. These cells are fabricated in large MOCVD reactors made by Emcore Corporation in the United States and Aixtron in Germany. Although these devices can be grown by other techniques such as molecular beam epitaxy (MBE) [33], the predominant growth technique is MOCVD and is, therefore, the focus of this section. A description of the basic MOCVD reactors used at NREL can be found elsewhere [34]. Briefly, most of the results presented here are from layers and devices grown by MOCVD using trimethylgallium (TMG), trimethylindium (TMI), arsine, and phosphine in a Pd-purified H_2 carrier gas. The dopants sources included H_2Se , Si_2H_6 , diethylzinc (DEZ), and CCl_4 .

9.6.3 GaInP Solar Cells

9.6.3.1 Lattice matching

One of the major advantages of the monolithic GaInP/GaAs/Ge solar cell is that it is composed of semiconductors that are all closely lattice matched. The fabrication of such a monolithic structure is achieved by the generic process of heteroepitaxy, the specific process being MOCVD. Close lattice matching makes the job of heteroepitaxy much easier, especially for chemically similar materials such as AlGaAs on GaAs. The heteroepitaxy of lattice-mismatched materials is generally more difficult. The lattice mismatch is accommodated by nucleation and by propagation of dislocations in concentrations that depend on the amount of mismatch and the thickness of the individual layers. These dislocations are often centers for nonradiative recombination, in effect limiting the minority-carrier lifetime or diffusion length, and ultimately the efficiency of the device.

The lattice constant of the semiconductor alloy $\text{Ga}_x\text{In}_{1-x}\text{P}$ is linearly related to the composition x by

$$a_{\text{Ga}_x\text{In}_{1-x}\text{P}} = xa_{\text{GaP}} + (1 - x)a_{\text{InP}} \tag{9.18}$$

where $a_{\text{GaP}} = 0.54512$ nm and $a_{\text{InP}} = 0.58686$ nm are the lattice constants of GaP and InP, respectively (see Table 9.3). An epitaxial layer of $\text{Ga}_x\text{In}_{1-x}\text{P}$ on GaAs with $a_{\text{GaAs}} = 0.565318$ nm will be lattice matched to GaAs at 25°C for $x = 0.516 = x_{\text{LM}}$. The quality of a thin, epitaxial $\text{Ga}_x\text{In}_{1-x}\text{P}$ layer is relatively good for small variations of x around x_{LM} . This case is shown in Figure 9.12, in which a broad-spectrum photocurrent from an electrolyte/ $\text{Ga}_x\text{In}_{1-x}\text{P}$ junction is plotted as a function of $\Delta\theta$ (see Section 9.7.1). The quantity $\Delta\theta$ is measured by double-crystal X-ray rocking-curve diffraction and is a measure of x [35]. If the thickness of the $\text{Ga}_x\text{In}_{1-x}\text{P}$ layer is less than the x -dependent critical thickness, then

$$\Delta\theta = \tan\theta_B \left(\frac{xa_{\text{GaP}} + (1 - x)a_{\text{InP}} - a_{\text{GaAs}}}{a_{\text{GaAs}}} \right) \left(\frac{1 + [\nu_{\text{GaP}}x + \nu_{\text{InP}}(1 - x)]}{1 - [\nu_{\text{GaP}}x + \nu_{\text{InP}}(1 - x)]} \right) \tag{9.19}$$

Table 9.3 Lattice constants, force constants, and Poisson ratios for selected III-V binary compounds. Values from Reference [37]

Material	Lattice constant [nm]	C_{11} [10^{10} N/m 2]	C_{12} [10^{10} N/m 2]	Poisson ratio, ν
AIP	0.546354			
GaP	0.54512	14.12	6.25	0.307
InP	0.58686	14.05	6.203	0.306
InP		10.22	5.76	0.360
InP		10.11	5.61	0.357
$\text{Ga}_x\text{In}_{1-x}\text{P}$ [$x = 0.516$]				0.333
GaAs	0.565318	11.81	5.32	0.311
		11.91	5.951	0.333
InAs	0.60583	8.329	4.526	0.352
Ge	0.5657906	12.89	4.83	0.273
		12.40	4.13	0.250

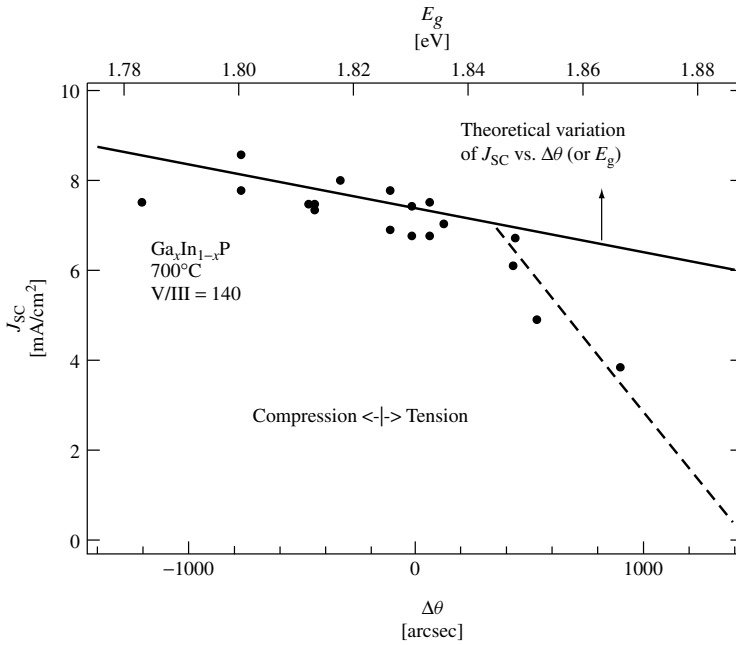
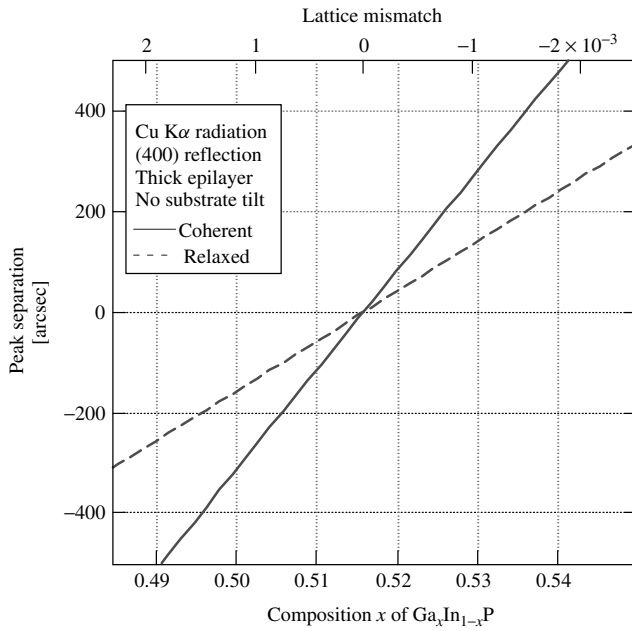


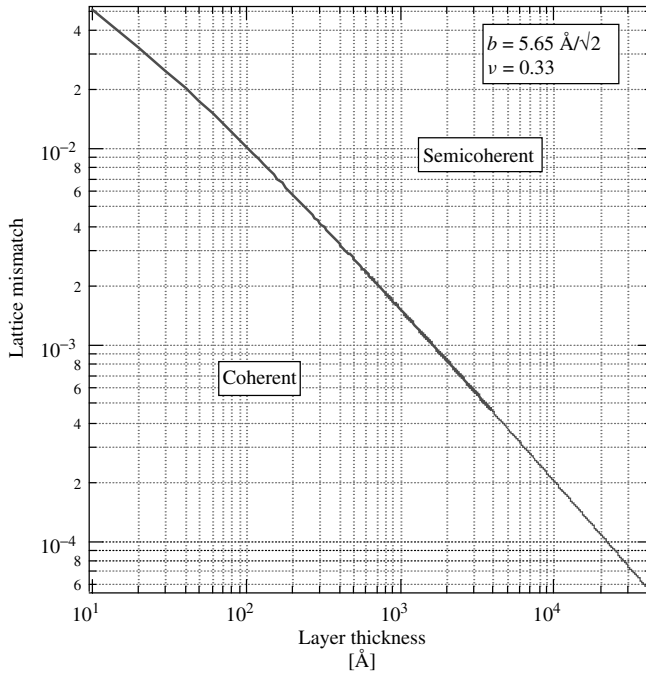
Figure 9.12 Saturated photoelectrochemical current density of $\text{Ga}_x\text{In}_{1-x}\text{P}$ as a function of the lattice mismatch as measured by X-ray rocking-curve peak separation in units of arc seconds, or equivalently as a function of the resulting E_g [35]. The growth temperature is 700°C and V/III ratio ($\text{PH}_3/(\text{TMGa} + \text{TMIIn})$) is 140. The dashed line is included to guide the eye

where θ_B is the Bragg angle and $\nu_{\text{GaP}}x + \nu_{\text{InP}}(1 - x)$ is the Poisson ratio for $\text{Ga}_x\text{In}_{1-x}\text{P}$ obtained from Poisson ratios for GaP and InP (see Table 9.3). (The Poisson ratio is defined as the negative of the ratio of the lateral to the longitudinal strains under uniaxial stress.) If the epilayer is fully relaxed, the last multiplicative term of equation (9.19) goes to one. A plot of $\Delta\theta$ versus x for $\text{Ga}_x\text{In}_{1-x}\text{P}$ on GaAs for these two extremes is shown in Figure 9.13(a). The critical layer thickness is simply the balance between the coherent energy created by strain, the relief of this strain energy by the introduction of dislocations, and the self-energy of dislocations. Below the critical layer thickness, the lowest-energy state of the system is an epilayer with a lattice constant, in the plane of the interface between the epilayer and the substrate, equal to the lattice constant of the substrate. Above the critical epilayer thickness, the lowest-energy state is one composed of some epilayer strain and some strain-relieving dislocations. The problem was first solved by Matthews and Blakeslee [36]. The relationship between lattice mismatch and layer thickness is shown in Figure 9.13(b).

Referring to Figure 9.12, for $\Delta\theta = 0$, the critical layer thickness is infinite and J_{SC} is a measure of the intrinsic minority-carrier transport quality of the epilayer in the absence of misfit dislocations. The solid line with negative slope is the theoretical variation of J_{SC} with $\Delta\theta$. For $\Delta\theta < 0$, the epilayer is In-rich ($x < x_{LM}$), and its band gap is lower than that of lattice-matched $\text{Ga}_x\text{In}_{1-x}\text{P}$. Hence, J_{SC} increases with decreasing $\Delta\theta$. For $\Delta\theta > 0$, the epilayer is Ga-rich ($x > x_{LM}$). At first, J_{SC} decreases with increasing $\Delta\theta$ in line with the In-rich portion of the curve, but then falls off rapidly with increasing $\Delta\theta$. The critical



(a)



(b)

Figure 9.13 (a) A plot of $\Delta\theta$ versus x for $\text{Ga}_x\text{In}_{1-x}\text{P}$ on GaAs; (b) Critical misfit versus layer thickness

$\Delta\theta$ at which this occurs is a function of kinetic factors including the layer thickness, growth temperature, and growth rate. Experimentally, the critical $\Delta\theta$ also depends on the sign of $\Delta\theta$ as can be seen in Figure 9.12. Indium-rich material is under compression. It is generally more difficult (and takes longer) to generate misfit and threading dislocations in compressively strained material compared to material under tension; hence, the difference in strain-relaxation behavior. Intuitively, the critical layer thickness for compressively strained material will generally approach that of tensively strained material as the growth temperature is increased and/or the growth rate is decreased. This behavior is relatively common. Note that this is contrary to the theoretical calculation shown in Figure 9.13(b). This calculation considers only the equilibrium state of the epilayer; the sign of the strain is, therefore, immaterial.

The thickness of the $\text{Ga}_x\text{In}_{1-x}\text{P}$ top cell for most conditions will be on the order of $1\ \mu\text{m}$ or less. From Figure 9.13(b) this would imply that the critical lattice mismatch should be less than 2×10^{-4} or $|\Delta\theta| \leq 50$ arcsecond. There are several factors that tend to increase or decrease this tolerance limit such as the following:

- Material lattice matched at room temperature is lattice mismatched at growth temperature. This is due to a difference in the thermal expansion coefficients between $\text{Ga}_x\text{In}_{1-x}\text{P}$ and GaAs (see Table 9.4). For kinetic reasons, it is probably more important that the layers are lattice matched at growth temperature. A layer that is lattice matched at a growth temperature of 625°C will exhibit a lattice mismatch of $\Delta\theta \sim -200$ arcsecond at room temperature [38], or alternatively, a layer that is lattice matched at room temperature, would exhibit a $\Delta\theta = 200$ arcsecond at 625°C . Because it is easier to introduce misfit dislocations at high temperatures, it is probably better to grow the layer lattice matched at the growth temperature. Hence, a ± 50 arcsecond tolerance at growth temperature would yield a room temperature tolerance of $-250 < \Delta\theta < -150$ arcsecond.

Table 9.4 Important properties of Ge, GaAs, and GaInP at 298 K

	Ge	GaAs	$\text{Ga}_x\text{In}_{1-x}\text{P}$	$\text{Al}_x\text{In}_{1-x}\text{P}$
Atoms/cm ³	4.42×10^{22}	4.44×10^{22}		
Lattice constant [\AA]	5.657906 [37]	5.65318 [37]	$= a_{\text{GaAs}}$ for $x = 0.516$	$= a_{\text{GaAs}}$ for $x = 0.532$
Energy gap [eV]	Indirect 0.662 Direct 0.803 [37]	1.424 [37]	Disordered 1.91 [41]	Indirect 2.34 Direct 2.53 [37]
Density of states				
Conduction band N_c [cm ⁻³]	1.04×10^{19}	4.7×10^{17}		
Valence band N_v [cm ⁻³]	6.0×10^{18}	7.0×10^{18}		
Intrinsic carrier concentration [cm ⁻³]	2.33×10^{13}	2.1×10^6		
Linear coefficient of thermal expansion [K ⁻¹]	7.0×10^{-6} [37]	6.0×10^{-6} [37]	5.3×10^{-6} [38]	6.63×10^{-6} [38]

- As mentioned above, material grown under compression is usually more stable to relaxation than material under tension, allowing one to err more toward negative values of $\Delta\theta$.
- Because of dynamical scattering effects, the measured $\Delta\theta$ for a thin ($\leq 0.1 \mu\text{m}$) epilayer will be less than that of a thicker layer with the same composition and lattice mismatch [39].
- The value of $\Delta\theta$ for epilayers grown on nonsingular (100) substrates is not unique, but depends on the orientation of the substrate with respect to the X-ray beam. The effective $\Delta\theta$ is the average of two measurements of $\Delta\theta$. The first measurement is made in the conventional manner; the second measurement is made with the sample rotated by 180° [40]. For vicinal substrates close to (100), this effect is small, usually $\sim 10\%$ at misorientation of 6° ; however, for {511} substrates, the effect is closer to 50%.

9.6.3.2 Optical properties of GaInP

9.6.3.2.1 Ordering in GaInP

Prior to 1986, it was generally assumed that the band gap of a III-V ternary alloy semiconductor such as $\text{Ga}_x\text{In}_{1-x}\text{P}$ was a unique function of the composition, and most publications showed $\text{Ga}_x\text{In}_{1-x}\text{P}$, lattice matched to GaAs, as having a band gap of 1.9 eV. However, in 1986 Gomyo *et al.* [42] reported that the band gap of $\text{Ga}_x\text{In}_{1-x}\text{P}$ grown by MOCVD was usually less than 1.9 eV and depended on the growth conditions. In a subsequent paper [43], they showed that the band gap shift was correlated with the ordering of Ga and In on the Group III sublattice. The ordered structure is CuPt-like, with alternating {111} planes of $\text{Ga}_{0.5+\eta/2}\text{In}_{0.5-\eta/2}\text{P}$ and $\text{Ga}_{0.5-\eta/2}\text{In}_{0.5+\eta/2}\text{P}$, where η is the long-range order parameter. Perfectly ordered GaInP ($\eta = 1$) would be composed of alternating {111} planes of GaP and InP. The first theoretical treatments of ordering in $\text{Ga}_x\text{In}_{1-x}\text{P}$ were put forward by Kondow and coworkers [44] using the tight binding theory, and by Kurimoto and Hamada [45] using the “first-principles” Linearized Augmented Plane Wave (LAPW) theory.

The functional relationship between the band gap’s change, ΔE_g , and the order parameter for GaInP was first published by Capaz and Koiller [46]:

$$\Delta E_g = -130\eta^2 + 30\eta^4 \quad (\text{in meV}) \quad (9.20)$$

A more recent result [47] suggests that

$$\Delta E_g = -484.5\eta^2 + 435.4\eta^4 - 174.4\eta^6 \quad (\text{in meV}) \quad (9.21)$$

The effects of various growth parameters on the ordering and the band gap of $\text{Ga}_x\text{In}_{1-x}\text{P}$ have been studied extensively. The band gap of $\text{Ga}_x\text{In}_{1-x}\text{P}$ is a function not only of the growth temperature, T_g , but also of the growth rate, R_g , the phosphine partial pressure, P_{PH_3} , substrate misorientation from (100), and the doping level. Some of these effects are illustrated in Figure 9.14. Although the behavior is very complicated, there are a few characteristics that stand out. For example, for substrates that are closely oriented to within a few degrees of (100), the band gap of GaInP, using typical values for T_g , R_g , and

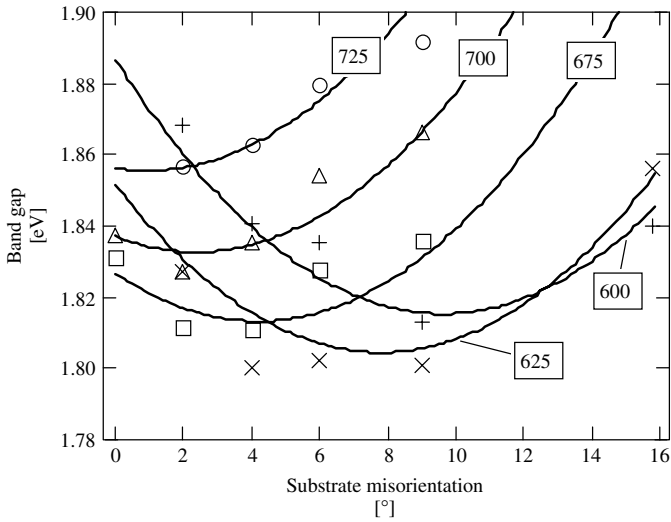


Figure 9.14 Band gap of $\text{Ga}_x\text{In}_{1-x}\text{P}$ versus T_g (from 600 to 725°C) and substrate misorientation

P_{PH_3} , is closer to 1.8 eV than 1.9 eV. One can obtain band gaps closer to 1.9 eV using extreme values for T_g , R_g or P_{PH_3} , but the material typically suffers in some other way, for example, minority-carrier diffusion length, composition, or morphology. The most straightforward way to obtain higher band gaps is by using substrates that are strongly misoriented from (100) toward {111}. The {111} surface in the zinc blende system is the Group III terminated surface and is often referred to as (111)A. Substrates misoriented towards (111)B generally enhance the degree of ordering. When growing on Ge there is no distinction between A and B misoriented substrates, and it is typically very difficult to control the A/B character of the III-V (GaAs or GaInP) epilayer. Hence, the easiest way to obtain high band gap GaInP on Ge is to use misorientation angles larger than about 15°, coupled with high R_g , moderate T_g , and low P_{PH_3} .

There are other material properties that are affected by ordering, including optical anisotropy [48–51], transport anisotropy [52, 53], and surface morphology [54, 55].

9.6.3.2.2 Absorption coefficient

For modeling and characterization of GaInP epilayers and solar cells, accurate models for the optical properties of GaInP are required. The optical constants of GaInP have been measured by using spectroscopic ellipsometry and modeled by several groups [56, 57] and by using transmission measurements by Kurtz *et al.* [10]. These results are summarized in Figure 9.15. For the most part, there is no single model that adequately describes the broadband optical properties of lattice-matched GaInP with some arbitrary degree of ordering. The model of Kato [57] appears adequate for short wavelengths but fails for near-gap optical properties. The models of Schubert and Kurtz only account for near band gap transitions. The model of Kurtz *et al.* for the absorption coefficient is given by:

$$\alpha = 5.5\sqrt{E - E_g} + 1.5\sqrt{E - (E_g + \Delta_{\text{so}})} [\mu\text{m}^{-1}] \quad (9.22)$$

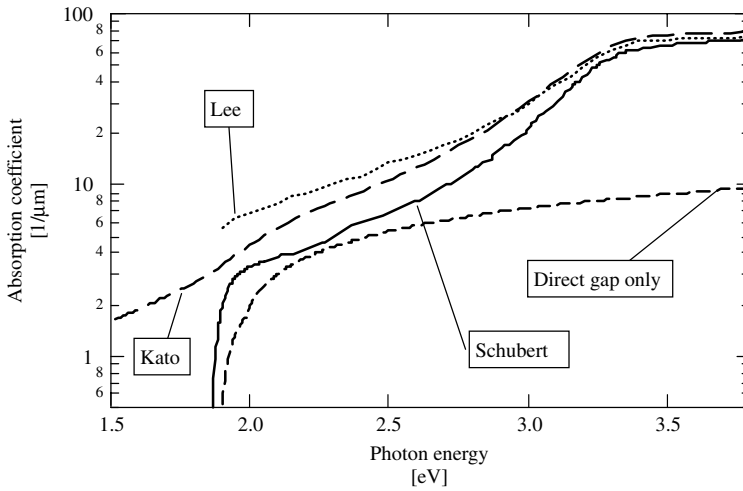


Figure 9.15 Comparison of absorption coefficients of $\text{Ga}_x\text{In}_{1-x}\text{P}$ published in the literature. The data of Lee *et al.* [59] and Schubert *et al.* [56] are ellipsometric data. The model of Kato *et al.* [57] is a reasonably good fit at high energies, but is a poor fit for sub-band gap photon energies. The curve marked “direct gap only” is a plot of equation (9.22)

where the photon energy E , the band gap energy E_g , and the spin orbit energy Δ_{so} are in units of eV. The value of E_g , of course, varies with the degree of order, η , and the value of Δ_{so} is typically set to 0.1 eV, independent of η . This model reasonably accounts for the absorption associated with the two near-band transitions at E_g and $E_g + \Delta_{\text{so}}$ and is useful for deducing the minority-carrier diffusion length from near-gap photoresponse measurements [58]. It is not a good model for adsorption at higher photon energies.

9.6.3.3 Doping characteristics

9.6.3.3.1 *n*-type dopants

Selenium

The element Se is a commonly used *n*-type dopant in III-V materials and is usually obtained from the decomposition of H_2Se . The doping behavior of H_2Se has been studied by a number of investigators [60–65]. Under most growth conditions, the electron concentration increases with H_2Se flux or partial pressure and then saturates at about $2 \times 10^{19}/\text{cm}^3$, depending on T_g . The incorporation of Se also depends on the partial pressure of PH_3 (for GaInP) or AsH_3 (for GaAs). These data best fit an equation of the form

$$n^{-1} = (1 + \alpha P_V)(\beta P_{\text{Se}})^{-1} + k^{-1} \quad (9.23)$$

where n is the electron concentration and P_V and P_{Se} are Group V and Se partial pressures, respectively. The coefficients α and β depend on T_g and carrier flow rate (residence time) and, therefore, must be determined for each reactor system. This doping behavior can be derived from a modified Langmuir adsorption model that accounts for the competitive absorption of Se and the Group V species on a fixed number of sites, k , which will depend,

for example, on the density of steps and kinks, that is, the substrate misorientation. This model is a much better fit than the *ad hoc* form $n \propto P_{\text{Se}}^x P_{\text{V}}^y$ most often published in the literature.

For electron concentrations greater than about $2 \times 10^{18}/\text{cm}^3$, the band gap energy of GaInP increases, the ordering decreases, and the morphology of the growth surface becomes very smooth [63]. At sufficiently high fluxes of Se, the surface again begins to roughen. At the same time, the electron concentration begins to decrease [60] and Se precipitates are observed in Transmission Electron Microscopy (TEM) [1]. Selenium has been linked to DX-like centers in $(\text{Al}_x\text{Ga}_{1-x})_{0.5}\text{In}_{0.5}\text{P}$ with Al concentrations greater than about $x = 0.4$ [66].

Silicon

Silicon is another widely used dopant in III-V materials and devices and the most popular source is Si_2H_6 . The first report of using Si_2H_6 to dope GaInP was by Hotta and coworkers [67]. They found that for $T_g < 640^\circ\text{C}$, n decreased with decreasing T_g presumably due to a decrease in Si_2H_6 pyrolysis rate. For $T_g > 640^\circ\text{C}$, n saturates at about $n = 5 \times 10^{18}/\text{cm}^3$ with Si_2H_6 , presumably due to the formation of nonionized complexes, such as $(\text{Si}_{\text{III}}^+ - \text{Si}_{\text{V}}^-)$ or $(\text{Si}_{\text{III}}^+ - \text{V}_{\text{III}}^-)$. The results [67] for Si-doped GaAs were quantitatively similar. Scheffer and coworkers [68] saw no evidence of saturation for electron concentrations up to $8 \times 10^{18}/\text{cm}^3$ using Si_2H_6 , whereas Minagawa and coworkers [69] found that the electron concentration saturated at about $1 \times 10^{19}/\text{cm}^3$, essentially independent of substrate orientation and growth temperature.

It has been shown that Si delta doping (where the doping is confined to a single layer or series of layers) in GaInP increases the maximum electron concentration and increases the electron mobility relative to that of uniformly doped layers [70, 71]. The conclusion from these studies is that Si delta doping yields fewer Si shallow acceptor defects. Silicon apparently does not introduce any deep states in GaInP, but does so in $(\text{Al}_x\text{Ga}_{1-x})_{0.5}\text{In}_{0.5}\text{P}$ for $x > 0.3$ [72]. As with Se, Si concentrations above some critical level tend to disorder $\text{Ga}_x\text{In}_{1-x}\text{P}$, causing the band gap to increase. However, the details can be quite varied. Gomyo and coworkers [62] reported that a lower concentration of Si than that for Se was required to disorder GaInP. However, Minagawa and coworkers [69] found that Si concentrations closer to $1 \times 10^{19}/\text{cm}^3$, depending on T_g , were required to dissolve the ordering in $\text{Ga}_x\text{In}_{1-x}\text{P}$.

9.6.3.3.2 *p*-type dopants

Zinc

The most common *p*-type dopant in GaInP is Zn. The typical sources are dimethylzinc (DMZ) and diethylzinc (DEZ). The Zn doping characteristics have been studied by a number of investigators [35, 60, 61, 73]. The incorporation efficiency is typically sublinear with the input flow, and increases with lower growth temperature and higher growth rate R_g . A model that accounts for some of these effects has been proposed by Kurtz *et al.* [73].

High Zn concentrations cause several problems in GaInP. Carrier concentrations in the neighborhood of $1 \times 10^{18}/\text{cm}^3$ destroy the ordering in $\text{Ga}_x\text{In}_{1-x}\text{P}$ and increase the

band gap [74]. And high Zn concentrations (or more accurately, high DEZ flows) cause a loss of In from both GaInP [35] and AlGaInP [75]. The problem is probably associated with some parasitic gas-phase reaction involving DEZ, TMI_n, and PH₃. The effect can be large enough to measurably change the growth rate and the Ga/In ratio in the material. The Ga/In ratio can be so far from lattice-matched conditions as to affect the morphology. High DEZ flows also inhibit the incorporation of Ga, but to a lesser extent.

Diffusion of zinc during epilayer growth can cause degradation of the performance of solar cells [76]. The zinc dopant in the substrate, back-surface field (BSF), or tunnel-junction layers can serve as a reservoir for zinc diffusion into the base region of an *n-on-p* cell. The diffusion is largely driven by point defects that are injected during the growth of the *n*-type layers. The diffusion can be reduced by reducing the doping levels of any of the layers (including the *n*-type layers), by adding diffusion barriers, and/or by using Se instead of Si doping of the *n*-type layers [76]. A side effect of the Zn diffusion is a disordering of any of the ordered structures [77].

The effect of changing the cap or overlying layer and cooling atmosphere on the hole concentration in Zn-doped (Ga_{1-x}Al_x)_{0.5}In_{0.5}P, $x = 0.7$, has been studied by Minagawa and coworkers [78]. Cooling in a H₂ atmosphere containing AsH₃ or PH₃ reduces the hole concentration. Hydrogen radicals from the decomposition of Group V hydrides easily diffuse into the epilayers and passivate the Zn acceptors. Cap layers of *n*- or *p*-GaAs help impede the indiffusion of H, and underlying layers can enhance the indiffusion of H, a special problem with *p-on-n* cells [76].

Magnesium

Magnesium doping (with cyclopentadienyl magnesium) in AlGaInP has been studied by a number of investigators [74, 79–82]. It is useful for achieving higher hole concentrations in AlGaInP and AlInP layers. However, the Mg incorporation efficiency decreases with decreasing temperature. Therefore, higher growth temperatures are favored, which is an advantage for AlGaInP. However, since dopant diffusion rates increase rapidly with temperature, this is a disadvantage for the fabrication of stable tunnel junctions and stable GaAs/Ge interfaces. For GaInP, it has no obvious advantages over Zn, and suffers from rather severe memory effects [80]. Also, relatively good-quality Zn-doped AlInP can be obtained by paying careful attention to source material and system purity [83].

Carbon

The use of C (from CCl₄ or CBr₄) has not been studied extensively. The halide tends to etch GaInP [84], indium more so than gallium. Also, C-doped GaInP exhibits poor minority-carrier transport properties [84, 85].

9.6.3.4 Window layers and back-surface fields

9.6.3.4.1 AlInP window layers

The function of an emitter window layer is to passivate the surface states associated with the emitter surface. These states are minority-carrier traps. Their effect is characterized by a quantity called the surface (or interface) recombination velocity, *S*. The value of *S*

can range from 10^7 cm/s for an unpassivated GaInP emitter to less than 10^3 cm/s for a high-quality AlInP/GaInP interface. A high interface recombination velocity will reduce the photoresponse of the GaInP solar cell, most strongly in the blue portion of the spectral response. To be an effective window layer for an n -on- p cell, the material should have a

- lattice constant close to that of GaInP,
- E_g much larger than that of the emitter,
- large valence-band offset with respect to the emitter to provide a potential barrier for minority holes,
- relatively high electron concentration (on the order of $n \geq 18/\text{cm}^3$), and
- material quality sufficient to produce low-interface recombination velocity.

The semiconductor AlInP has most of the required characteristics. $\text{Al}_x\text{In}_{1-x}\text{P}$ is lattice matched to GaAs for $x = 0.532$. The indirect band edge of AlInP is 2.34 eV, 0.4 to 0.5 eV larger than that of GaInP. The $\text{Al}_x\text{In}_{1-x}\text{P}/\text{GaInP}$ band alignment appears to be Type 1 with $\Delta E_c \sim 0.75\Delta E_g$ and $\Delta E_v \sim 0.25\Delta E_g$ [86]. This implies that it should provide reasonable confinement of the holes in the emitter of an n -on- p device. It is easily doped n -type with either Si or Se. The internal quantum efficiency of a GaInP cell with a good $\text{Al}_x\text{In}_{1-x}\text{P}$ window layer is greater than about 40% at a photon energy of 3.5 eV. However, there is a strong affinity between the Al in $\text{Al}_x\text{In}_{1-x}\text{P}$ and oxygen, and oxygen is a deep donor in $\text{Al}_x\text{In}_{1-x}\text{P}$. Hence, if the reactor chamber or the source materials are contaminated with water vapor or other oxygenated compounds, the quality of the $\text{Al}_x\text{In}_{1-x}\text{P}$ will suffer. Poor-quality $\text{Al}_x\text{In}_{1-x}\text{P}$ will degrade the blue response of a GaInP cell and degrade the fill factor (via contact resistance) [8].

9.6.3.4.2 Back-surface barrier

The function of the top-cell back-surface barrier is to passivate the interface between the top-cell base and the tunnel-junction interconnect (TJIC). Also, in some cases, it may help reduce outdiffusion of dopants from the TJIC [87]. The high recombination velocity at this interface will affect both the photoresponse (in particular, the red photoresponse) and the V_{OC} . The V_{OC} effect is shown in Figure 9.8. Note that the magnitude of the effect can be quite large and is also affected by the base minority-carrier diffusion length and thickness. The requirements of a good back-surface barrier layer are similar to those of a front-surface window layer. For an n -on- p cell, it should have a

- lattice constant close to that of GaInP,
- E_g larger than E_g of GaInP,
- large conduction-band offset with respect to GaInP,
- relatively high hole concentration (on the order of $p = 1 \times 10^{18}/\text{cm}^3$),
- relatively good minority-carrier transport properties, and
- high transparency to photons destined for the underlying GaAs cell.

For back-surface fields, initial results from Friedman *et al.* [88] implied that disordered or high- E_g GaInP was the best BSF for a low- E_g GaInP top cell compared to an AlGaInP BSF. This was probably due to oxygen contamination in the AlGaInP layer.

As a deep donor, oxygen is a bigger problem in p -type AlGaInP. Other researchers found that strained, Ga-rich $\text{Ga}_x\text{In}_{1-x}\text{P}$ was superior to either disordered lattice-matched GaInP or AlGaAs [89]. Recently, however, the best commercial tandem solar cells use AlGaInP [90] or AlInP [91] BSFs. The growth of high-quality Zn-doped AlInGaP and the techniques for assessing the quality thereof have been published by several others [81, 83, 92].

9.6.3.5 Characteristics of state-of-the-art GaInP cells

Because the band gap of GaInP can change so dramatically with growth conditions, it is not meaningful to talk of “state-of-the-art” GaInP cells using only efficiency as the measure of quality. As the band gap increases, V_{OC} should increase, but J_{SC} and efficiency should decrease. (Note, however, that the efficiency of a current-matched GaInP/GaAs tandem cell should increase slightly with increasing GaInP band gap as discussed in Section 9.5.4 above.) Also, in any optimized multijunction solar cell the thickness of the GaInP cell is likely to be optically thin, that is, it will absorb fewer photons and hence *may* be lower in efficiency than an optically thick cell. So thickness and band gap are two important parameters that must be considered when comparing single-junction efficiencies. In general, relative measures of quality, for example, V_{OC}/E_g , are more useful.

9.6.4 GaAs Cells

9.6.4.1 Quality of GaAs on Ge(100) substrates

Despite the close lattice matching between GaAs and Ge substrates, the quality of GaAs grown on Ge can be quite variable. (See Section 9.6.5.3 for a discussion on the heteroepitaxy of GaAs on Ge.) The primary criterion for good-quality heteroepitaxial GaAs is, of course, the efficiency of overlying GaAs and GaInP solar cells. Generally, a good indicator of quality is a specular episurface with little or no haze (often caused by antiphase domains or APDs) and few extended defect features such as pits, hillocks, or slip lines. For a specular, epitaxial GaAs layer, one should observe a faint “crosshatch” pattern. This “crosshatch” is a replica or shadow of the misfit dislocation array located in the GaAs/Ge interface plane. Sometimes, the absence of this “crosshatch” pattern is an indicator that the misfit is being relaxed by threading dislocations. The density of these threading dislocations can become high enough to affect the minority-carrier transport properties of the GaAs and GaInP solar cells, and should, therefore, be avoided.

The morphology of $\text{Ga}_x\text{In}_{1-x}\text{P}$ grown on GaAs is an even more sensitive indicator of the quality of the original GaAs surface. Morphologically faint defects in or on the GaAs will be “decorated” by the growth of $\text{Ga}_x\text{In}_{1-x}\text{P}$. This is probably caused by differences in the attachment of Ga and In to the different surface orientations offered by the defect.

GaAs grown on Ge can be “lattice matched” to the Ge substrate by the addition of about 1% indium. This eliminates the “crosshatch” in good heteroepitaxy, but does not appear to make the task of heteroepitaxy any easier. Under the best conditions, a $\text{Ga}_{0.99}\text{In}_{0.01}\text{As}$ solar cell will be slightly better than a GaAs cell on Ge [93].

9.6.4.2 Optical properties

The optical parameters of GaAs are tabulated in the work of Aspnes and coworkers [94] and a model for the optical dielectric function of GaAs (and $\text{Al}_x\text{Ga}_{1-x}\text{As}$) has been proposed [95].

9.6.4.3 Window layers and back-surface fields

$\text{Ga}_x\text{In}_{1-x}\text{P}$ and $\text{Al}_x\text{In}_{1-x}\text{P}$ should both make excellent window layers and back-surface field layers for GaAs solar cells [96, 97]. Both have Type 1 band alignment with GaAs, with reasonably adequate conduction- and valence-band offsets [86, 98]. Ideally, $\text{Al}_x\text{In}_{1-x}\text{P}$ would make a better window layer than $\text{Ga}_x\text{In}_{1-x}\text{P}$ because of its larger band gap energy. However, because of its sensitivity to oxygen contamination, $\text{Al}_x\text{In}_{1-x}\text{P}$ will probably never produce as good an interface with GaAs as does $\text{Ga}_x\text{In}_{1-x}\text{P}$. (This is the main problem with the AlGaAs/GaAs interface used widely for single-junction GaAs solar cells [19].) The undoped $\text{Ga}_x\text{In}_{1-x}\text{P}$ /GaAs interface has one of the lowest interface recombination velocities ($S < 1.5$ cm/s) of any heterostructure ever measured, including the SiO_2/Si interface [96]. In addition, it is difficult to dope $\text{Al}_x\text{In}_{1-x}\text{P}$ p -type at a level of $p > 1 \times 10^{18}/\text{cm}^3$. For these reasons, $\text{Ga}_x\text{In}_{1-x}\text{P}$ is usually the preferred window layer and BSF layer for GaAs solar cells in GaInP/GaAs tandem-cell structures.

9.6.5 Ge Cells

9.6.5.1 Optical properties of Ge

The optical and electronic properties of Ge are well documented (see Reference [37]). Germanium has a lattice constant close to that of GaAs and has a diamond structure. It is also mechanically stronger than GaAs and, hence, has long been viewed as an excellent substitute for GaAs substrates. With a band gap of 0.67 eV, it is current matched to a thin GaAs top cell [7] and is also a good bottom-cell candidate in a four-junction stack [99]. However, in both these cases, it has several properties that put it at a disadvantage:

- The V_{OC} is limited by its indirect band gap to about 300 mV and is relatively more sensitive to temperature [100].
- It is relatively expensive, hence, it cannot be viewed as a one-sun solar cell material (with the exception of its use in space).
- Germanium is an n -type dopant in GaAs and GaInP. In GaInP, it also exhibits amphoteric behavior with a compensation ratio $N_a/N_d = 0.4$ [101] and has been associated with a deep acceptor state [102].
- Gallium, As, In, and P are all shallow dopants in Ge. Hence, the control of the junction-formation process becomes complicated when it is combined with the III-V heteroepitaxy process (*vide infra*).

9.6.5.2 Junction formation

Diffusion of a Group V or a Group III dopant into a Ge substrate is the most common junction-formation process for Ge subcells. Indeed, because of the proximity of III-V

epilayers and the high temperatures involved in heteroepitaxial process, diffusion of both Group III and Group V atoms into the Ge substrate is unavoidable. The challenge is to control the process so as to obtain a Ge subcell with good photovoltaic properties and simultaneously form a defect-free heteroepitaxial layer of GaAs with the appropriate conductivity type and level. A detailed description of the optimum process is beyond the scope of the review, but a few critical factors that have to be considered are listed below:

- Diffusion coefficients are thermally activated. So, in general, dopants and junctions are less mobile and more stable at lower growth temperatures.
- As noted by Tobin *et al.* [103], the diffusion coefficient of As in Ge at 700°C is higher than that of Ga, but the solid solubility of Ga is larger than that of As.
- For three-junction GaInP/GaAs/Ge devices with a reasonably good-quality Ge subcell, the only Ge device parameter that is of consequence is the V_{OC} , because the J_{SC} of the Ge subcell is potentially much greater than that of the GaInP (or GaAs) subcell.
- The highest V_{OC} of a Ge solar cell reported to date is 0.239 [100]. This V_{OC} is a sensitive function of process conditions and is most sensitive to the quality of the III-V/Ge interface and its fabrication [100].
- AsH₃ etches Ge. The etch rate increases with temperature and AsH₃ partial pressure. Heavily etched, singular and vicinal Ge(100) surfaces are microscopically rough [104]. Hence, prolonged AsH₃ exposures should be avoided.
- The etch rate for PH₃ is much lower, and there appears to be much less roughening of the surface from PH₃ exposure [104]. The diffusion coefficient of P at 600°C is about two orders of magnitude lower than that of As [37]. Hence, PH₃ may be a better Group V, *n*-type dopant than AsH₃.

9.6.5.3 III-V heteroepitaxy

Although there are a number of “recipes” for the growth of GaAs on Ge(100) with specular morphologies or low antiphase domain (APD) or low stacking-fault densities, many present contradictory results. For example, Pelosi *et al.* [105] found that the GaAs surface morphology is best for very low V/III ratio (on the order of 1), using a moderate growth rate ($R_g \sim 3.5 \mu\text{m/h}$) and a low growth temperature ($T_g = 600^\circ\text{C}$). On the other hand, Li *et al.* [106] found that the lowest APD density occurs for high V/III, low R_g , and high T_g . Chen *et al.* [107] showed that “good” morphology could only be obtained for growth temperatures in the range of 600°C to 630°C.

The cause for this striking difference is not known with certainty. It may be due to differences in reactor design or purity. It may be related to the quality of the Ge substrates. Other researches [104] would suggest that it is related to the prenucleation conditions or the state of the Ge surface immediately prior to the GaAs nucleation step.

A lot has been published about the structure of Ge(100), but most of it is with regard to surfaces prepared in ultrahigh-vacuum (UHV) or MBE environments. It has been shown, however, that under most conditions, AsH₃-treated surfaces in an MOCVD reactor are quite different as explained below [104, 108, 109]. Arsenic on a Ge(100) terrace forms rows of dimers, similar to As on GaAs(100) [108, 109]. This reduces the (1×1) symmetry of the unreconstructed Ge surface to a surface that now has a (2×1)

or a (1×2) surface symmetry. For the (2×1) reconstruction, the dimer bonds are parallel and rows of dimers run perpendicular to the step edges. Adjacent terraces on an (100) As-terminated Ge surface can be composed of orthogonal reconstructions; adjacent terraces on a (100) GaAs are always of the same type. An As-terminated Ge surface prepared in a UHV or MBE environment usually exhibits a single-domain, (1×2) symmetry. An MOCVD-prepared surface will initially be (1×2) , but tends toward (2×1) symmetry with a transition time that ranges from one minute to tens of minutes and that depends on temperature, AsH_3 partial pressure, and substrate temperature. Intermediate states, of course, are composed of a mixture of (1×2) and (2×1) domains, a condition that is conducive to the formation of APDs in a GaAs heterolayer. Also, as mentioned above, AsH_3 etches Ge. This etching causes significant step bunching or faceting and microscopically rough surfaces.

9.6.6 Tunnel-junction Interconnects

The purpose of the tunnel-junction interconnect between the GaInP and GaAs subcells is to provide a low-resistance connection between the p -type BSF of the GaInP cell and the n -type window layer of the GaAs bottom cell. Without the TJIC, this p - n junction has a polarity or forward turn-on voltage that is in opposition to that of the top or bottom cells and, when illuminated, would produce a photovoltage that could roughly negate the photovoltage generated by the top cell. A tunnel junction is simply a $p^{++} n^{++}$ junction where p^{++} and n^{++} represent heavily or degenerately doped material. The space charge region for a $p^{++} n^{++}$ junction should be very narrow, ~ 10 nm. In forward bias, the normal thermal current characteristic of a p - n junction is “shorted” by tunneling through the narrow space charge region. Hence, the forward IV characteristic of a tunnel junction behaves much like a resistor for current densities less than some critical value, called the peak tunneling current, J_p . The functional form of J_p is dominated by an exponential term of the form:

$$J_p \propto \exp\left(-\frac{E_g^{3/2}}{\sqrt{N^*}}\right) \quad (9.24)$$

where E_g is the band gap and $N^* = N_A N_D / (N_A + N_D)$ is the effective doping concentration [110]. The value of J_p must be larger than the photocurrent of the tandem cell. For a concentrator cell operating at 1000 suns, $J_{SC} \sim 14$ A/cm². If $J_p < J_{SC}$, the behavior of the tunnel junction current switches to that dominated by the usual thermionic emission and the voltage drop across the tunnel junction increases to that of a typical p - n junction.

The best tunnel junctions for very high efficiency solar cells are relatively defect-free. Lifetime limiting, midgap defects usually only add to the excess current. There is no evidence in the literature that point or extended defects add to J_p or increase the conductivity in the tunneling portion of the I - V curve. High excess currents can mask a low J_p , but usually the junction conductivity is also unacceptably low. On the other hand, it is possible that high concentrations of point or extended defects can compensate donors or acceptors in the junction leading to increased depletion width and lower tunneling currents. In addition, defects can reduce the thermal stability of the tunnel junction and the quality of the overlying layers. Therefore, in general, it is usually best to grow the TJICs free of point or extended defects.

The first high-efficiency GaInP/GaAs dual-junction solar cells were fabricated using an optically thin GaAs TJIC. The best tunnel junctions were doped with C and Se. Hence, they were reasonably stable under the thermal conditions required to grow the top cell and were capable of operating at more than 1000 suns, that is, $J_p > 14 \text{ A/cm}^2$. They were also less than 30 nm thick and obscured less than 3% of the light destined for the lower cell. With optically thick, unannealed devices, peak tunneling currents were greater than 300 A/cm^2 with excess current densities close to zero [8].

9.6.6.1 AlGaAs/GaInP TJIC

Despite the higher band gap and its concomitant penalty, the p^{++} -AlGaAs/ n^{++} -GaInP heterojunction tunnel diode proposed by Jung and coworkers is the preferred TJIC for one-sun operations and may be suitable for concentration [111]. It takes advantage of the innate propensity for AlGaAs to incorporate C and for GaInP to incorporate Se, so that high values of N^* are easily achieved. Hence, peak tunneling currents as high as 80 A/cm^2 were reported. The devices are also thermally stable; J_p is reduced to about 70 A/cm^2 for 30-min anneal at 650°C and to about 30 A/cm^2 for a 30-min anneal at 750°C . This TJIC is more optically transparent than a thin GaAs TJIC and therefore should yield a higher tandem-cell photocurrent.

9.6.7 Chemical Etchants

The processing of epitaxial products into finished devices is beyond the scope of this chapter. Most of the processes used by the industry are proprietary, and there are numerous laboratory processes, such as evaporation of metals and optical coatings, that are suitable for research. One very useful area that is common to both industrial and laboratory processes is the use of selective and nonselective etchants for the various materials used in GaInP/GaAs multijunction solar cells. A list of these etchants is given below (etch rates are at room temperature). Note that solutions containing H_2O_2 typically exhibit an etch rate that depends on the age of the solution [112].

- Mixtures of ammonia, hydrogen peroxide, and water etch GaAs, but do not etch GaInP and AlInP. A common formulation is 2 parts NH_4OH , 1 part 30% H_2O_2 , and 10 parts H_2O (2:1:10). Also, a solution of H_3PO_4 , H_2O_2 , and H_2O combined in a ratio of 3:4:1 etches GaAs and not GaInP.
- Concentrated HCl rapidly etches GaInP, but the surface is easily passivated by dilute HCl and HCl vapor. HCl does not etch GaAs.
- Dilute HCl: H_2O etches AlInP [113].
- Au metallization is impervious to both 2:1:10 and concentrated HCl.
- A 1:20 solution of HCl and CH_3COOH (acetic acid) etches GaInP at a rate of 70 nm/min and GaAs at a rate of $<5 \text{ }\mu\text{m/min}$ [112].
- $5\text{H}_2\text{SO}_4:1\text{H}_2\text{O}_2:1\text{H}_2\text{O}$ at room temperature etches GaInP at a rate of about 25 nm/min . It etches GaAs much more rapidly ($>1 \text{ }\mu\text{m/min}$).
- Mixtures of HCl: H_3PO_4 : H_2O etch GaInP [114]. For high HCl compositions, the etch rate is $\sim 1 \text{ }\mu\text{m/min}$.

9.6.8 Materials Availability

A question of interest for all solar cell technologies is the availability of the component materials required for very large scale, long-term production of the cell. Predicting the long-term availability of such natural resources as gallium, indium and germanium is very difficult. This issue has been studied periodically over the years, including a recent thorough work by Andersson [115]. It appears that the material whose availability constrains production for the GaInP/GaAs/Ge structure may prove to be germanium. If so, one approach would be to forfeit the relatively small additional contribution of the Ge third junction by using the two-junction GaInP/GaAs structure grown on GaAs. Also, reuse of the substrate by liftoff of the active junctions may prove practical. In any case, high-concentration operation of these cells makes the best use of their constituent materials.

9.7 TROUBLESHOOTING

The standard procedures for measuring light and dark I - V curves and QE curves are described in Chapter 16. Here, we describe additional techniques for characterizing materials and devices. The symptoms of common problems are tabulated in Table 9.5.

9.7.1 Characterization of Epilayers

When working with alloys like GaInP, rocking-mode X-ray diffraction is very helpful toward confirming that the desired lattice constant (alloy composition) was realized (see above).

A modified Polaron profiler (available from Bio Rad) can measure the carrier concentration, band gap, and minority-carrier diffusion length of an epilayer [58, 116]. The sample is mounted in a special holder that allows the formation of front and back contacts in a fraction of the time that is required by a typical solid-state device. An ohmic contact is made to the back of the wafer by passing a surge of current (something like a spot weld). A junction is formed between the epilayer and an aqueous electrolyte (e.g. 0.1 M HCl). The capacitance-voltage (C - V) characteristics of this junction provide a measure of the carrier concentration as a function of depth. In a finished device, the carrier concentrations of the individual layers can be checked by profiling (etching) through the structure in the electrochemical cell, or by using selective etches to uncover the layer(s) of interest. C - V measurements on a processed single-junction device (rather than on an aqueous-semiconductor junction) tend to give lower dissipation factors because of lower series resistance, but only give information about the lightly doped side of the junction. Thus, it can be difficult to ascertain whether the emitter is underdoped by a C - V profile on the solid-state device. Although a Polaron profiler is designed to measure the doping level of each layer as a multilayered stack is etched, etch profiles of a multijunction solar cell require considerable skill and some luck. Nonuniform etching can distort the results, especially if the material has some defects. Also, some layers may be completely depleted. Often, a Polaron profiler gives the best information when the etching is partly done by the profiler and partly by applying selective etches *ex situ*. (See Section 9.6.7.) A (dilute) mixture of ammonia and hydrogen peroxide etches GaAs, but stops at GaInP and AlInP,

Table 9.5 Troubleshooting for *n-on-p* cells

Problem	Symptom	Confirmation
Window too thick	Poor blue response	Model <i>QE</i>
High front-surface recombination	Poor blue response (lower V_{OC})	Model <i>QE</i>
$L_{emitter} <$ emitter thickness	Poor blue response (lower V_{OC})	Model <i>QE</i>
Emitter doping too high	Poor blue response (low V_{OC} , low emitter sheet res.)	Measure doping of emitter
Emitter doping too low	Low V_{OC} ; higher emitter sheet resistance	Depleted emitter
Base doping too low	Low V_{OC}	Measure doping of base
Base doping too high	Low V_{OC} ; reduced red response	Dark <i>I-V</i> likely to have $n = 1$
$L_{base} <$ base thickness	Low V_{OC} ; reduced red response	Dark <i>I-V</i> likely to have $n = 1$
High back-surface recombination	Low V_{OC} (reduced red response)	Dark <i>I-V</i> likely to have $n = 1$
Threading dislocations	Low V_{OC} (low FF and J_{SC})	High dark current, probably with $n = 2$
Thin metallization	Low FF – series resistance	Measure grid-line resistance
Bad tunnel junction	Low FF – series resistance and/or low V_{OC}	Measure tunnel junction by itself
Extra junction	Low FF – (nonohmic?) series resistance	Shape of <i>I-V</i> may depend on spectrum
Metallization does not make good contact	Low FF – (nonohmic?) series resistance	Use transmission line on front; two pads on back
Resistive window layer	Low FF – series resistance	Use transmission line to measure resistance to emitter
Particulate	Low FF – shunt	Light emitted in forward bias may be correlated with morphological defects
Incomplete mesa isolation	Low FF – shunt, sometimes with unphysically high J_{SC}	Etch mesas deeper or cleave edges
Front metal touches lower layer	Low FF – shunt	Examine under microscope
Severe chromatic aberrations	Low FF for cell measured under concentration	Shape of <i>I-V</i> is unusual [22]

whereas concentrated HCl etches GaInP and AlInP, but not GaAs. GaInP does not always etch in concentrated HCl, especially if the surface is wet, the HCl is not full strength, and/or if the GaInP surface has previously been in contact with a dilute HCl solution.

A window is provided in the Polaron cell for shining light on the aqueous semiconductor junction. The photocurrent (*QE*) from the junction can fit the form

$$QE = \alpha(h\nu)^*L/[1 + \alpha(h\nu)^*L] \quad (9.25)$$

where $h\nu$ is the photon energy, and it is assumed that L is much longer than the depletion width but less than the layer thickness.

The fit value for L will reflect the minority-carrier diffusion length when L is greater than the depletion width, but less than the thickness of the layer. For small $\alpha(h\nu)^*L$, the QE is proportional to $\alpha(h\nu)$, allowing an easy fit to determine E_g from $\alpha(h\nu) = A^*(h\nu - E_g)^{0.5}$.

Photoluminescence (PL) intensity is commonly used to test the quality of a material, but the intensity strongly depends on carrier concentration and surface recombination. Time-resolved PL measurements on double heterostructures (passivated layers) of different thicknesses can quantify both the minority-carrier lifetime and the interface recombination velocity [117, 118].

9.7.2 Transmission Line Measurements

Once a device is made, in addition to the I - V and QE measurements, characterization of the device contacts using a transmission line measurement is useful toward diagnosing problems. Transmission lines [119] allow determination of the contact resistance (ρ_c) and the sheet resistance (R_s). The resistance, R , between any two pads as a function of x , the distance between the pads, is estimated by:

$$R = 2\rho_c/(w^2) + R_s/w^*x \quad (9.26)$$

where w is the width of the transmission line and the dimension of the square pads. ρ_c and R_s are calculated from the intercept and slope of the line [119]. If the sheet resistance is large compared with the contact resistance, then the current across the semiconductor/pad interface is not uniform, and the estimated ρ_c can be refined to a more accurate value of the contact resistance, ρ'_c , using the equation:

$$\rho'_c = \rho_c^2/(w^2 R_s)^* \tanh^2\{w^2 R_s/[\rho_c^* \tanh(w^2 R_s/\rho_c)]\} \quad (9.27)$$

9.7.3 I - V Measurements of Multijunction Cells

The chapter on measurements (Chapter 16) describes how to measure the light I - V curve for a standard reference spectrum and for systematically varied spectra. Complete diagnosis of a multijunction cell requires characterization (an I - V curve) of each of the active junctions to quantify their photocurrents and shunting. It would also be useful to establish the photovoltages and series resistances of each junction, but these are difficult or impossible for a two-terminal, series-connected cell. We describe here some alternative approaches for characterizing the individual junctions.

In some situations, it is possible to apply a contact between the series-connected junctions. The three-terminal configuration allows measurement of each junction of a two-junction cell. For a three-junction cell, a three-terminal measurement allows independent measurement of the top or bottom cells, but measurement of the middle cell by itself may require four connections. A primary advantage of the three-terminal approach is that it allows measurement of the photovoltage of each junction. The measured photocurrents should be adjusted for the change in junction area that occurred when the third connection

was applied. Also, the increased perimeter area of the top cell sometimes affects the dark current.

Underlying junctions may be investigated by first chemically removing the upper junctions. In this case, the underlying junction will respond to a wider spectral range.

It is also useful to be able to characterize two-terminal multijunction cells. The shape of the I - V curve of a series-connected multijunction cell is dominated by the characteristics of the junction that generates the smallest photocurrent. (This concept can be understood by reviewing Figure 9.5 above.) The I - V curve for each junction can be measured by adjusting the spectrum so that that junction has the smallest photocurrent. Using these measurements, the estimated individual junction I - V curves can be derived mathematically, as described in Reference [120]. An example is given below. From the individual I - V curves, one can calculate the I - V curve for the multijunction cell under an arbitrary spectrum. For some samples, the J_{SC} values may be measured by reverse biasing the cell beyond the breakdown points of the junctions [121].

9.7.4 Evaluation of Morphological Defects

Careful examination of the devices with a microscope can identify many problems, especially when the device is forward biased so that it emits light, or when an optical beam-induced current (OBIC) image is available. GaInP junctions emit red light that is usually visible to the naked eye. GaAs emission may be observed with an infrared (IR) imaging device. If the emission shows dark or bright spots, these can usually be correlated with a morphological defect, giving an explanation to the problem. Also, metal (e.g. a contact pad) that extends to the very edge of the pad may touch a layer that is nearby and short the device. This failure mode can sometimes be detected by microscopic examination.

9.7.5 Device Diagnosis

In general, a low J_{SC} may be evaluated from the energy dependence of the photocurrent loss. It is useful to measure and model the internal QE . The external QE measurements are described in Chapter 16. The internal QE is modeled according to equations (9.2–9.8) (Figure 9.16) and is determined experimentally from

$$QE_{\text{Internal}} = QE_{\text{external}} / (1 - \text{Reflectivity}) \quad (9.28)$$

Accurate knowledge of the absorption coefficient is essential to successfully model the QE . The absorption coefficients of GaAs and GaInP were discussed above.

Figure 9.17(a) compares the QE of a typical GaInP cell QE (solid line) with what would be expected if there were no loss in the AlInP window (top curve) or a poor collection in the emitter (bottom curves). Although window absorption losses can easily be distinguished from emitter losses, the similarity of the two lower curves demonstrate the difficulty of distinguishing poor front-surface recombination from poor emitter material quality. However, it is somewhat easier to differentiate poor base material quality from poor rear passivation using a series of devices with variable base thickness. A cell with a

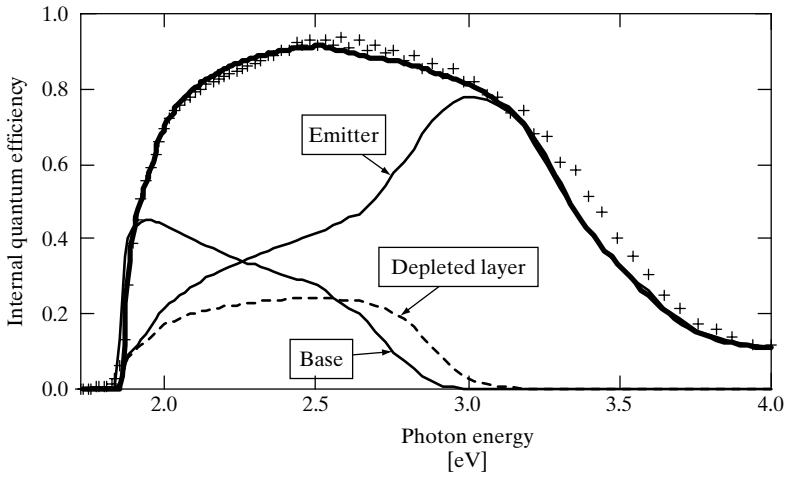


Figure 9.16 Measured (crosses) and modeled (lines) quantum efficiency of a GaInP solar cell. The contributions from the different layers of the solar cell are labeled and demonstrate how the emitter dominates the blue response, whereas the base dominates the red response

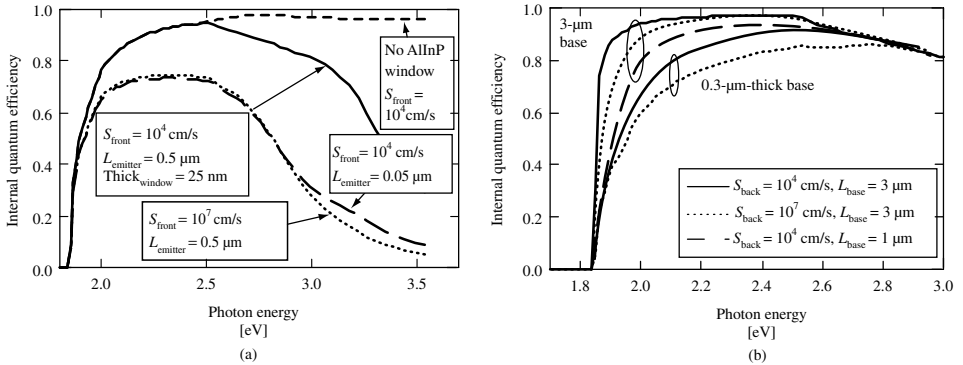


Figure 9.17 Modeled QE of GaInP cell. (a) The solid line, relative to the “no AlInP window” line, shows the effect of absorption of 25 nm of AlInP. The two lower curves show the degradation from an increased front-surface recombination velocity (S_{front}) or from a decreased emitter diffusion length (L_{emitter}). (b) Compares a thin and a thick GaInP cell

thick base layer is more sensitive to the diffusion length in the base, whereas a cell with a thin base layer is relatively more sensitive to the quality of the back-surface field (see Figure 9.17(b)).

There are numerous reasons why the V_{OC} or FF may be degraded. Table 9.5 enumerates many of these, and Figure 9.18(a) illustrates one example.

Extra junctions are more likely to be problems when working with Ge because III-V elements dope Ge and Ge dopes the III-V materials. The back of the Ge wafer must be etched before processing to avoid an extra junction at the back [100]. Accidental junctions in Ge are often highly shunted, with nearly ohmic I - V characteristics. In this case, these

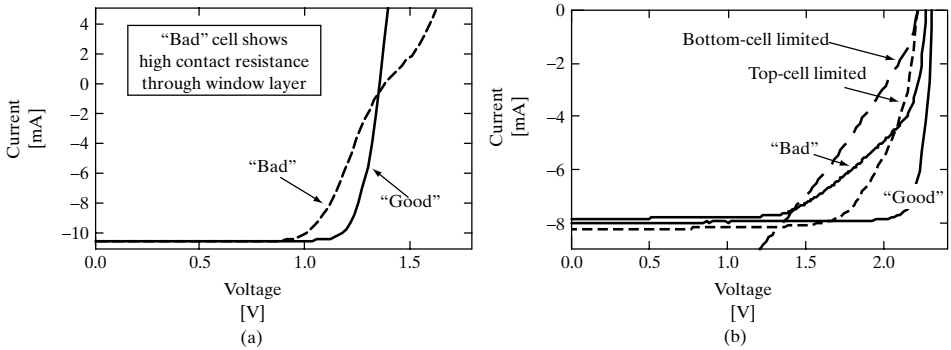


Figure 9.18 (a) Comparison of I - V curves for a “good” GaInP cell and a GaInP cell with an extra junction caused by the AlInP window. Transmission line measurements showed that the contact resistance was high through the window layer. (b) I - V curves for good and bad GaInP/GaAs tandem cells. The “bad” curve shows a shunt; measurements of the same cell under bottom-cell limited and top-cell limited conditions show that the shunt is in the bottom junction

are easiest to observe at high concentration because the V_{OC} of the Ge junction increases faster with the photocurrent than that of the intended junction. Spurious junctions in the Ge may add, subtract, or do both (in the case of back-to-back junctions) to the V_{OC} .

When a two-junction cell shows evidence of shunting, it is useful to determine which of the two junctions is shunted. This can be determined by measuring the light I - V curve under two different spectra, one of which reduces the photocurrent of the top junction, and the other which reduces the photocurrent of the bottom junction [120]. The example in Figure 9.18(b) shows a case in which the bottom cell is shunted. This sort of problem is often related to defects originating from particulate or poor wafer quality. Particulate exposure before or during growth is often a bigger problem for GaInP/GaAs cells than for single-junction cells.

9.8 FUTURE-GENERATION SOLAR CELLS

The GaInP/GaAs/Ge cell is close to maturity for space applications, but the efficiencies being reported by the manufacturers are continuing to increase, with champion cells measuring near 30% AM0 efficiency [122]. The efficiency reported by Spectrolab for a terrestrial concentrator version of the GaInP/GaAs/Ge solar cell [14, 123] is likely to improve. The theoretical efficiency is 45% at 500 suns under the AM1.5 global spectrum. Historically, III-V based multijunction cells have achieved 80% to 90% of their theoretical efficiencies [99].

9.8.1 Refinements to the GaInP/GaAs/Ge Cell

An improvement in the AM0 efficiency of the GaInP/GaAs/Ge cell is predicted when the GaInP band gap is increased. However, addition of aluminum to the GaInP cell has been shown to increase the band gap, but not the efficiency, of the top cell because the J_{SC} was reduced by more than 10% while the V_{OC} increased only slightly, if at all,

presumably because of the adverse effect of Al (and the associated oxygen contamination) on minority-carrier properties [122].

The Ge junction collects about twice as much photocurrent as the other two junctions in the GaInP/GaAs/Ge cell. The three-junction cell efficiency will increase, theoretically, if the GaAs band gap is lowered, the Ge band gap is increased, or a fourth junction is added between the GaAs and Ge junctions.

The most common approach is to add indium to the GaAs layer and perhaps to the GaInP layer. A small amount of indium improves the lattice matching to Ge and improves the efficiency of the cell even without the use of any buffer layer [124]. Addition of larger quantities of indium (e.g. 12%) is being widely investigated in the hope of increasing the efficiency by $\sim 2\%$ absolute [125]. Higher efficiencies require the growth of a buffer layer that successfully relieves the strain without allowing threading (and other) dislocations to propagate into the active layers of the solar cell. Results are promising, but the efficiencies, so far, have been similar to those for lattice-matched cells [125–128]. Researchers at Varian studied a two-step approach allowing the mismatched layers to be grown on the back of the wafer, whereas the “sunny-side” layers were grown lattice matched [129, 130]. The effects of lattice mismatch on the manufacturability and lifetime of solar cells are not known.

Considerable effort has also been invested toward the addition of a fourth, 1-eV junction (to be added between the GaAs and Ge junctions). Such a four-junction structure has a theoretical efficiency of $>50\%$ [99], translating to a practical efficiency of 40% if appropriate materials could be identified. Unfortunately, identifying an appropriate (high quality and lattice matched to GaAs) 1-eV material has proven difficult. The most promising candidate for this junction is currently the alloy GaInAsN. Other materials have been investigated, but do not show as much promise. ZnGeAs₂ is somewhat difficult to grow (especially at low pressures) and can cause cross contamination (e.g. Zn contamination of subsequent growth) [131]. Ga_{0.5}Tl_{0.5}P was reported to be lattice matched to GaAs with a band gap of about 0.9 eV [132], but a number of laboratories have been unable to duplicate the original report [133, 134]. The band gap of BGaInAs lattice matched to GaAs has been pushed down to 1.35 eV, but so far, not to 1.0 eV [135]. BGaInAs also exhibits inferior material quality [136], resulting in devices with decreased photovoltages and currents.

Ga_{1-x}In_xAs_{1-y}N_y can be grown lattice matched ($x = 3y$) to GaAs with a band gap of about 1 eV [137], but the minority-carrier diffusion length is small [138–140]. GaAsN is unusual because the band gap decreases from 1.4 eV to about 1 eV with the addition of about 3% nitrogen. The alloy scattering is expected to be larger than in a conventional alloy, partially explaining the reduced majority-carrier mobility. However, the more serious problem is the low minority-carrier lifetimes, which have not yet been adequately explained. C and H contamination of MOCVD-grown GaInAsN is reported to be higher than that for MBE-grown GaInAsN [141], but the MBE material has not been evaluated for solar cells.

9.8.2 Mechanical Stacks

A high-efficiency result may also be obtained by a mechanical stack, relaxing the need to consider lattice matching. The most probable candidates for this are GaInP/GaAs stacked

over either GaInAsP (1 eV)/GaInAs (0.75 eV) or GaSb [142, 143]. The difficulties in implementing these stacks are associated with making the upper cell very transparent to the sub-band gap light (use of a transparent GaAs substrate, nonconventional approach for the back contact, and a good AR coating on the back, as well as the front, of the upper cell) and with finding a way to mount both cells with simultaneous heat sinking and electrical isolation, a much greater problem at 500 to 1000X than at 10 to 50X. An advantage of this approach is the decoupling of the photocurrents of the two pieces (assuming that four-terminal measurements are made), allowing for greater flexibility in the choice of materials and higher efficiency when the spectrum is changed [99].

The efficiency of a solar cell depends on the operating conditions, complicating the prediction of outdoor performance of solar cells. This is especially complicated for series-connected, multijunction solar cells under variable spectra. The losses expected for two-terminal operation of three- and four-junction cells, compared with six- or eight-terminal operation of the same cells are significant, but may not be much more than the loss that a silicon cell experiences by operating at elevated temperature [29]. For two-terminal operation, the mechanical stack may most easily be accomplished by bonding the two semiconductor materials directly. Because wafer bonding is now routinely used for integrating many devices, techniques are available, and the wafer bond avoids the need to use a transparent substrate, avoids reflection losses, and removes the difficulty of heat sinking and electrically isolating the stacked cells. If a method for reusing the substrate can be made economical, wafer bonding also has the potential to reduce the substrate cost.

There are many more approaches to making a multijunction cell than can be discussed in this chapter. All approaches are variations on the structures shown in Figure 9.4. Wafer bonding of III-V multijunction cells to silicon would provide a lighter substrate (an advantage for space cells) and could reduce the cost if the original substrate could be reused. A method for making a GaAs-Si bond with ohmic character between a GaAs cell and a silicon wafer has been reported [144]. Wafer bonding has not yet been developed for high-yield manufacturing of solar cells, but large-area wafer bonding is a possibility given that eight-inch wafer-bonded silicon-on-insulator substrates are commercially available. The cost of these wafers is currently high (comparable to the cost of four-inch Ge wafers), but may be reduced in the future.

9.8.3 Growth on Other Substrates

A silicon-III-V stack may also be made by growing III-V epitaxial layers directly on silicon. Growth of GaAs on Si has always been problematic because of the large lattice mismatch between the two materials. However, growth of a lattice-matched III-V alloy on silicon might be more similar to the growth of GaAs on Ge. Tu and coworkers have reported the growth of AlGaNP alloys with lattice constants similar to silicon, but having band gaps in the range of 1.4 to 1.95 eV [145]. The use of Si as the 1-eV material in a multijunction higher-efficiency stack is compromised by the poor red *QE* of most Si cells, but the lower cost and weight of the silicon substrate might make it attractive even if higher efficiencies are not achieved.

High efficiencies have been achieved with two-junction (InP/GaInAs) structures on InP [18]. A three- or four-junction structure based on InP could, potentially, achieve

higher efficiencies. This approach is limited by the availability of high band gap materials that are lattice matched to InP and by the weight and current cost of the InP substrates.

9.8.4 Spectrum Splitting

Over the years, a number of groups have proposed to separate the light, shining each portion on a solar cell optimized for that wavelength range. If four or five single-junction solar cells are used, the theoretical efficiency is quite high. However, the balance-of-system issues imply that this approach only makes sense for space missions for which high efficiency is essential, and the economics allow for the added cost of multiple substrates without requiring a high concentration ratio.

9.9 IMPLEMENTATION INTO TERRESTRIAL SYSTEMS

The implementation of multijunction III-V cells into terrestrial concentrator systems will require appropriate design of the optics, optical coupling between the optics and cells, avoidance of chromatic aberration problems, heat sinking of the cells, electrical connections/isolation, and large-scale production to reduce the cost to an acceptable range.

9.9.1 Economic Issues

The current economics imply that the cells should be implemented in a system with a concentration of about 400X or higher. The cell cost is estimated to be in the range of \$3 to 10/cm² [146]. Swanson estimates that the cost of electricity from a medium-sized dish-concentrator PV plant in Albuquerque, New Mexico, would be 7 to 15 cents/kWh [13]. He assumed that the cell cost would be \$3 to 10/cm², with an efficiency of 28.5 to 33.25% and a concentration ratio of 1000 [13].

9.9.2 Concentrator Systems

Several point-focus designs are available or are being developed. Amonix is installing Si-based concentrators using Fresnel lenses and concentration near 250X [147]. Solar Systems is installing reflective dishes using Si solar cell receivers [148]. Spectrolab and Concentrating Technologies are designing a III-V multijunction solar cell receiver for a dish [149]. With the dishes, a key issue is uniformity of the illumination. The solar cells must be connected in series to boost the voltage, but the current that comes out will be determined by the cell illuminated by the smallest amount of sunlight. SunPower is developing a high-concentration, thin (flat-plate-like) concentrator [150]. ENTECH is redesigning their terrestrial concentrator for use with III-V multijunction cells. The Ioffe and Fraunhofer Institutes have joined to design a 130X glass-Fresnel concentrator using III-V cells [151]. A more complete description of concentrator systems is included in Chapter 11. A number of designs for using multijunction cells under low concentration for space applications are reviewed in Chapter 10.

9.9.3 Terrestrial Spectrum

The GaInP/GaAs/Ge cells that are currently produced in high volume for space applications require only minor modifications for terrestrial use. Specifically, under concentrated sunlight, the series resistance must be reduced (as discussed above). And because the direct terrestrial spectrum includes less blue light than the AM0 spectrum, the GaInP cell should be thicker so that it generates a photocurrent that approximately equals that generated by the GaAs junction. There is evidence that the AM1.5 direct reference spectrum is seldom observed in locations that are well suited for concentrators [152]. The AM1.5 global reference spectrum is sometimes observed, but more frequently the spectra lie between these two.

The direct spectrum observed at solar noon is usually richer in short-wavelength light, especially when compared with the AM1.5 direct reference spectrum. Therefore, optimization of the performance at solar noon is slightly different than the optimization for annual electricity production. The Module Energy Rating (MER) Procedure (Chapter 16) addresses this question by defining hourly data for different types of days. The highest performance over a day depends on the location, but may be found when cells are optimized for a spectrum between the AM1.5 global and AM1.5 direct spectra [153]. If the performance early and late in the day is the most important, then thicker top cells are better. However, the increased performance late in the day will reduce the power generated at the times when the most power is available; so this is a trade-off that must be evaluated relative to the application.

The sensitivity of the multijunction structures to variable spectrum has been studied theoretically [21, 29], but not yet experimentally. Modeling of the system performance for concentrators using multijunction cells will be more difficult than modeling Si-based modules because of the spectral sensitivity, but the temperature sensitivity is reduced.

Fundamentally, there should be no difficulty with the lifetime of the cells, but in practice, the need for encapsulation and the complexity of the device structure (tunnel junctions and/or use of Ge substrate, which can cause a higher defect density) could lead to challenges in achieving reliable, manufacturable modules.

REFERENCES

1. Olson J, Gessert T, Al-Jassim M, *Proc. 18th IEEE Photovoltaic Specialists Conference*, 552–555 (1985).
2. Fan J, Tsaur B, Palm B, *Proc. 16th IEEE Photovoltaic Specialist Conf.*, 692 (1982).
3. Olson J, Kurtz S, Kibbler A, *Proc. 18th IEEE Photovoltaic Specialists Conference*, 777 (1988).
4. Kurtz S, Olson J, Kibbler A, *Sol. Cells* **24**, 307 (1988).
5. Kurtz S, Olson J, Kibbler A, *Appl. Phys. Lett.* **57**, 1922–1924 (1990).
6. Olson J, Kurtz S, Kibbler A, Faine P, *Appl. Phys. Lett.* **56**, 623–625 (1990).
7. Kurtz S, Faine P, Olson J, *J. Appl. Phys.* **68**, 1890 (1990).
8. Bertness K *et al.*, *Appl. Phys. Lett.* **65**, 989–991 (1994).
9. Friedman D *et al.*, *Prog. Photovolt.: Res. Appl.* **3**, 47–50 (1995).
10. Kurtz S *et al.*, *Proc. 1st World Conference on PV Energy Conversion*, 2108 (1994).
11. Yamaguchi M, Wakamatsu S, *Proc. 25th IEEE Photovoltaic Specialists Conference*, 9–11 (1996).

12. Green M *et al.*, *Prog. PV* **9**, 49–56 (2001).
13. Swanson R, *Prog. Photovolt.: Res. Appl.* **8**, 93–111 (2000).
14. King R *et al.*, *Proc. 29th IEEE Photovoltaic Specialists Conference*, 776–779 (2002).
15. O'Neill M *et al.*, *Proc. 28th IEEE Photovoltaic Specialists Conference*, 1161 (2000).
16. Henry C, *J. Appl. Phys.* **51**, 4494–4500 (1980).
17. Gee J, *Sol. Cells* **24**, 147–155 (1988).
18. Wanlass M *et al.*, *Proc. 22nd IEEE Photovoltaic Specialists Conference*, 38–45 (1991).
19. Hovel H, *Solar Cells*, Vol. 11, Academic Press, New York (1975).
20. Nell M, Barnett A, *IEEE Trans. Electron Devices* **ED-34**, 257–266 (1987).
21. Faine P, Kurtz S, Riordan C, Olson J, *Sol. Cells* **31**, 259 (1991).
22. Kurtz S, O'Neill M, *Proc. 25th IEEE Photovoltaic Specialists Conference*, 361–364 (1996).
23. Lockhart L, King P, *J. Opt. Soc. Am.* **37**, 689 (1947).
24. Bader G, Ashrit P, Girouard F, Truong V, *Appl. Opt.* **34**, 1684–1691 (1995).
25. Friedman D *et al.*, *Proc. 12th NREL Photovoltaic Program Review*, Vol. AIP 306, 521 (1993).
26. Palik E, Addamiano A, in Palik E, Ed, *Handbook of Optical Constants of Solids*, Vol. I, 597–619, Academic Press, San Diego, CA (1998).
27. Cotter T, Thomas M, Tropsch W, in Palik E, Ed, *Handbook of Optical Constants of Solids*, Vol. II, 899–918, Academic Press, San Diego, CA (1998).
28. Andreev V, Grilikhes V, Rumyantsev V, *Photovoltaic Conversion of Concentrated Sunlight*, John Wiley & Sons, Chichester, Sussex (1997).
29. Kurtz S, Olson J, Faine P, *Sol. Cells* **30**, 501 (1991).
30. Gessert T, Coutts T, *J. Vac. Sci. Technol., A* **10**, 2013–2024 (1992).
31. Friedman D, *Proc. 25th IEEE Photovoltaic Specialists Conference*, 89–92 (1996).
32. Zhao J, Wang A, Robinson S, Green M, *Prog. Photovolt.* **2**, 221–225 (1994).
33. Lammasniemi J *et al.*, *Proc. Second World Conference and Exhibition on Photovoltaic Energy Conversion*, 1177 (1998).
34. Bertness K *et al.*, *Proc. 12th NREL Photovoltaic Program Review Meeting*, Vol. AIP 306, 100 (1993).
35. Olson J, Kibbler A, Kurtz S, *Proc. 19th IEEE Photovoltaic Specialists Conference*, 285 (1987).
36. Matthews J, Blakeslee A, *J. Cryst. Growth* **27**, 118 (1974).
37. Madelung O (Ed), *Semiconductors: Group IV Elements and III-V Compounds*, Springer-Verlag, Berlin, Germany (1991).
38. Kudman I, Paff R, *J. Appl. Phys.* **43**, 3760–3762 (1972).
39. Wie C, *J. Appl. Phys.* **66**, 985 (1989).
40. Tanner B, Miles S, Peterson G, Sacks R, *Mater. Lett.* **7**, 239 (1988).
41. Delong M *et al.*, *Appl. Phys. Lett.* **66**, 3185–3187 (1995).
42. Gomyo A *et al.*, *J. Cryst. Growth* **77**, 367–373 (1986).
43. Gomyo A *et al.*, *Appl. Phys. Lett.* **50**, 673 (1987).
44. Kondow M *et al.*, *J. Cryst. Growth* **93**, 412 (1988).
45. Kurimoto T, Hamada N, *Phys. Rev. B* **40**, 3889 (1989).
46. Capaz R, Koiller B, *Phys. Rev. B* **47**, 4044–4047 (1993).
47. Zhang Y, Mascarenhas A, Wang L, *Phys. Rev. Lett.* **63**, 201312 (2000).
48. Mascarenhas A, Olson J, *Phys. Rev. B* **41**, 9947 (1990).
49. Mascarenhas A, Kurtz S, Kibbler A, Olson J, *Phys. Rev. Lett.* **63**, 2108 (1989).
50. Luo J *et al.*, *J. Vac. Sci. Technol. B* **12**, 2552–2557 (1994).
51. Luo J *et al.*, *Phys. Rev. B* **51**, 7603–7612 (1995).
52. Friedman D *et al.*, *Proc. Material Res. Soc. Symp.*, Vol. 280, 493 (1993).
53. Chernyak L *et al.*, *Appl. Phys. Lett.* **70**, 2425–2427 (1997).
54. Friedman D *et al.*, *Appl. Phys. Lett.* **63**, 1774–1776 (1993).
55. Friedman D *et al.*, *Appl. Phys. Lett.* **65**, 878–880 (1994).
56. Schubert M *et al.*, *J. Appl. Phys.* **77**, 3416–3419 (1995).
57. Kato H, Adachi S, Nakanishi H, Ohtsuka K, *Jpn. J. Appl. Phys.* **33**, 186–192 (1994).

58. Kurtz S, Olson J, *Proc. 19th IEEE Photovoltaic Specialists Conference*, 823–826 (1987).
59. Lee H, Klein M, Olson J, Hsieh K, *Phys. Rev. B* **53**, 4015–4022 (1996).
60. Iwamoto T, Mori K, Mizuta M, Kukimoto H, *J. Cryst. Growth* **68**, 27 (1984).
61. Ikeda M, Kaneko K, *J. Appl. Phys.* **66**, 5285 (1989).
62. Gomyo A *et al.*, *Jpn. J. Appl. Phys.* **28**, L1330–L1333 (1989).
63. Kurtz S *et al.*, *J. Electron. Mater.* **19**, 825–828 (1990).
64. Goral J, Kurtz S, Olson J, Kibbler A, *J. Electron. Mater.* **19**, 95 (1990).
65. Kurtz S *et al.*, *J. Electron. Mater.* **23**, 431–435 (1994).
66. Watanabe M, Ohba Y, *J. Appl. Phys.* **60**, 1032 (1986).
67. Hotta H, Hino I, Suzuki T, *J. Cryst. Growth* **93**, 618–623 (1988).
68. Scheffer F *et al.*, *J. Cryst. Growth* **124**, 475–482 (1992).
69. Minagawa S, Ishitani Y, Tanaka T, Kawanaka S, *J. Cryst. Growth* **152**, 251–255 (1995).
70. Wang C *et al.*, *Jpn. J. Appl. Phys.* **34**, L1107–L1109 (1995).
71. Malacky L *et al.*, *Appl. Phys. Lett.* **69**, 1731–1733 (1996).
72. Suzuki M *et al.*, *J. Cryst. Growth* **115**, 498–503 (1991).
73. Kurtz S, Olson J, Kibbler A, Asher S, *Proc. of the InP and Related Materials Conf.* (1992).
74. Suzuki T *et al.*, *Jpn. J. Appl. Phys.* **27**, L1549–L1552 (1988).
75. Nishikawa Y, Ishikawa M, Tsuburai Y, Kokubun Y, *J. Cryst. Growth* **100**, 63–67 (1990).
76. Kurtz S *et al.*, *Proc. 25th IEEE Photovoltaic Specialists Conference*, 37–42 (1996).
77. Dabkowski F *et al.*, *Appl. Phys. Lett.* **52**, 2142–2144 (1988).
78. Minagawa S, Kondow M, Yanagisawa H, Tanaka T, *J. Cryst. Growth* **118**, 425–429 (1992).
79. Hino I *et al.*, *Inst. Phys. Conf. Ser. No. 79* **79**, 151–156 (1985).
80. Kondo M, Anayama C, Sekiguchi H, Tanahashi T, *J. Cryst. Growth* **141**, 1–10 (1994).
81. Bauhuis G, Hageman P, Larsen P, *J. Cryst. Growth* **191**, 313–318 (1998).
82. Stockman S *et al.*, *J. Electron. Mater.* **28**, 916–925 (1999).
83. Bertness K, Kurtz S, Asher S, Reedy R, *J. Cryst. Growth* **196**, 13–22 (1999).
84. Kibbler A, Kurtz S, Olson J, *J. Cryst. Growth* **109**, 258 (1991).
85. Friedman D, Kibbler A, Reedy R, *Appl. Phys. Lett.* **71**, 1095–1097 (1997).
86. Ishitani Y *et al.*, *J. Appl. Phys.* **80**, 4592–4598 (1996).
87. Sugaira H, Amano C, Yamamoto A, Yamaguchi M, *Jpn. J. Appl. Phys. Pt. 1* **27**, 269 (1988).
88. Friedman D, Kurtz S, Kibbler A, Olson J, *Proc. 22nd IEEE Photovoltaic Specialists Conference*, 358–360 (1991).
89. Rafat N *et al.*, *Proc. First World Conference on Photovoltaic Energy Conversion*, 1906–1909 (1994).
90. Karam N *et al.*, *Sol. Energy Mater. Sol. Cells* **66**, 453–466 (2001).
91. Chiang P *et al.*, *Proc. 28th IEEE Photovoltaic Specialists Conference*, 1002 (2000).
92. Kadoiwa K *et al.*, *J. Cryst. Growth* **145**, 147–152 (1994).
93. Takamoto T, Agui E, Ikeda E, Kurita H, *Proc. 28th IEEE Photovoltaic Specialists Conference*, 976 (2000).
94. Aspnes D, Studna A, *Phys. Rev. B* **27**, 985–1009 (1983).
95. Kim C, Garland J, Raccach P, *Phys. Rev. B* **47**, 1876–1888 (1993).
96. Olson J *et al.*, *Appl. Phys. Lett.* **55**, 1208 (1989).
97. Kurtz S, Olson J, Kibbler A, *Proc. Twenty First IEEE Photovoltaic Specialists Conference*, 138–140 (1990).
98. Oshea J *et al.*, *Appl. Phys. Lett.* **69**, 3022–3024 (1996).
99. Kurtz S, Myers D, Olson J, *Proc. 26th IEEE Photovoltaic Specialists Conference*, 875–878 (1997).
100. Friedman D *et al.*, *Proc. 28th IEEE Photovoltaic Specialists Conference*, 965 (2000).
101. Lee J, Kim I, Kwon H, Choe B, *Appl. Phys. Lett.* **62**, 1620–1622 (1993).
102. Yoon I, Han S, Park H, Kim T, *J. Phys. Chem. Solids* **62**, 607–611 (2001).
103. Tobin S *et al.*, *Proc. 20th IEEE Photovoltaic Specialist Conf.*, 405–410 (1988).
104. Olson J, McMahon W, *Proc. 2nd World Conf. on Photovoltaic Energy Conversion* (1998).

105. Pelosi C *et al.*, *J. Electron. Mater.* **24**, 1723–1730 (1995).
106. Li Y *et al.*, *J. Cryst. Growth* **163**, 195–202 (1996).
107. Chen J, Ristow M, Cabbage J, Werthen J, *J. Electron. Mater.* **21**, 347–353 (1992).
108. McMahon W, Olson J, *Phys. Rev. B: Condens. Matter* **60**, 2480–2487 (1999).
109. McMahon W, Olson J, *Phys. Rev. B: Condens. Matter* **60**, 15999–16005 (1999).
110. Sze S, *Physics of Semiconductor Devices*, Wiley, New York, NY (1969).
111. Jung D, Parker C, Ramdani J, Bedair S, *J. Appl. Phys.* **74**, 2090–2093 (1993).
112. Flemish J, Jones K, *J. Electrochem. Soc.* **140**, 844–847 (1993).
113. Lothian J *et al.*, *J. Vac. Sci. Technol. B* **10**, 1061–1065 (1992).
114. Lothian J, Kuo J, Ren F, Pearton S, *J. Electron. Mater.* **21**, 441–445 (1992).
115. Andersson B, *Prog. Photovolt.* **8**, 61–76 (2000).
116. Blood P, *Semicond. Sci. Technol.* **1**, 7–27 (1986).
117. Ahrenkiel R, *Solid State Electron.* **35**, 239–250 (1992).
118. Ahrenkiel R, in Ahrenkiel R, Lundstrom M, Eds, *Minority Carriers in III – V Semiconductors: Physics and Applications*, Vol. 39, 39–150, Academic Press, San Diego, CA (1993).
119. Berger H, *J. Electrochem. Soc.* **119**, 507–514 (1972).
120. Kurtz S, Emery K, Olson J, *Proc. First World Conference on Photovoltaic Energy Conversion*, 1733–1737 (1994).
121. King D, Hansen B, Moore J, Aiken D, *Proc. 21st IEEE Photovoltaic Specialists Conference*, 1197 (2000).
122. King R *et al.*, *Proc. 28th IEEE Photovoltaic Specialists Conference*, 998 (2000).
123. Cotal H *et al.*, *Proc. 28th IEEE Photovoltaic Specialists Conference*, 955 (2000).
124. Takamoto T, Agui T, Ikeda E, Kurita H, *Sol. Energy Mater. Sol. Cells* **66**, 511–516 (2001).
125. King R *et al.*, *Proc. 28th IEEE Photovoltaic Specialists Conference*, 982 (2000).
126. Bett A *et al.*, *Proc. 28th IEEE Photovoltaic Specialists Conference*, 961 (2000).
127. Dimroth F, Lanyi P, Schubert U, Bett A, *J. Electron. Mater.* **29**, 42–46 (2000).
128. Sinharoy S *et al.*, *Proc. 28th IEEE Photovoltaic Specialists Conference*, 1285 (2000).
129. Partain L *et al.*, *21st IEEE Photovoltaic Specialists Conference* 184–189 (1990).
130. Schultz J *et al.*, *J. Electron. Mater.* **22**, 755–761 (1993).
131. Timmons M, private communication.
132. Asahi H *et al.*, *J. Cryst. Growth* **175**, 1195–1199 (1997).
133. Friedman D, Kurtz S, Kibbler A, *Proc. NREL/SNL PV Program Review Meeting*, 401–405 (1998).
134. Antonell M *et al.*, *Proc. InP and Related Materials Conf.* 444–447 (1997).
135. Geisz J *et al.*, *Appl. Phys. Lett.* **76**, 1443–1445 (2000).
136. Geisz J, Friedman D, Kurtz S, *Proc. 28th IEEE Photovoltaic Specialists Conference*, 990 (2000).
137. Kondow M *et al.*, *Jpn. J. Appl. Phys.* **35**, 1273–1275 (1996).
138. Geisz J *et al.*, *J. Cryst. Growth* **195**, 401–408 (1998).
139. Kurtz S, Allerman A, Jones E, Gee J, Banas J, Hammons B, *Appl. Phys. Lett.* **74**, 729–731 (1999).
140. Friedman D, Geisz J, Kurtz S, Olson J, *J. Cryst. Growth* **195**, 409–415 (1998).
141. Miyamoto T *et al.*, *J. Cryst. Growth* **209**, 339–344 (2000).
142. Moto A, Tanaka S, Tanabe T, Takagishi S, *Sol. Energy Mater. Sol. Cells* **66**, 585–592 (2001).
143. Fraas L *et al.*, *Proc. 28th IEEE Photovoltaic Specialists Conference*, 1150 (2000).
144. Arokiaraj J *et al.*, *Sol. Energy Mater. Sol. Cells* **66**, 607–614 (2001).
145. Hong Y, Tu C, Photovoltaic for the 21st Century, *Proc. 199th Meeting Electrochemical Soc.* Vol. 2001-10, 415–422 (2001).
146. Kroll W *et al.*, *Proc. 2nd World Conference on PV Energy Conversion*, 3753 (1998).
147. Garboushian V, Roubideaux D, Yoon S, Gunn J, *Proc. 25th IEEE Photovoltaic Specialists Conference*, 1373–1376 (1996).

-
148. Lasich J *et al.*, *Proc. First World Conference on Photovoltaic Energy Conversion*, 1938–1941 (1994).
 149. Kurtz S, McConnell R, *Compound Semicond.* **7**, 82, 83 (2001).
 150. Terao A *et al.*, *Proc. 28th IEEE Photovoltaic Specialists Conference*, 1416 (2000).
 151. Rummyantsev V *et al.*, *Proc. 28th IEEE Photovoltaic Specialists Conference*, 1169 (2000).
 152. Myers D *et al.*, *Proc. 28th IEEE Photovoltaic Specialists Conference*, 1202 (2000).
 153. McMahon W, Kurtz S, Emery K, Young M, *Proc. 29th IEEE Photovoltaic Specialists Conference* 931–934 (2002).

This Page Intentionally Left Blank

10

Space Solar Cells and Arrays

Sheila Bailey¹ and Ryne Raffaele²

¹NASA Glenn Research Center, Cleveland, OH, USA, ²Department of Physics, Rochester Institute of Technology, Rochester, NY, USA

10.1 THE HISTORY OF SPACE SOLAR CELLS

10.1.1 Vanguard I to Deep Space I

In the mid 1950s, the development of single-crystal photovoltaic (PV) solar cells based on Si, as well as GaAs, had reached solar conversion efficiencies as high as 6% [1, 2]. By 1958, small-area silicon solar cells had reached an efficiency of 14% under terrestrial sunlight. These accomplishments opened the door to the possibility of utilizing solar power on board a spacecraft. On March 17, 1958 the world's first solar-powered satellite was launched, Vanguard I [3]. It carried two separate radio transmitters to transmit scientific and engineering data concerning, among other things, performance and lifetime of the 48 p/n silicon solar cells on its exterior. The battery powered transmitter operated for only 20 days, but the solar cell powered transmitter operated until 1964, at which time it is believed that the transmitter circuitry failed. Setting a record for satellite longevity, Vanguard I proved the merit of space solar cell power. The solar cells used on Vanguard I were fabricated by Hoffman Electronics for the US Army Signal Research and Development Laboratory at Fort Monmouth. In 1961, many of the staff from the silicon cell program at Fort Monmouth transferred to the National Aeronautics and Space Administration (NASA), Lewis Research Center (now Glenn Research Center) in Cleveland, Ohio. From that time to the present, the Photovoltaic Branch at Glenn has served as the research and development base for NASA's solar power needs. Impressed by the light weight and the reliability of photovoltaics, almost all communication satellites, military satellites, and scientific space probes have been solar-powered. It should be noted that the history presented here focuses on the United States space program. NASA was created in 1958; the Institute of Space and Astronautical Sciences (ISAS) and the National Space Development Agency (NASDA) in Japan were created in 1965 and 1969, respectively;

the European Space Agency (ESA) was created in 1975 by the merger of the European Organization for the Development and Construction of Space Vehicle Launchers (ELDO) and the European Space Research Organization (ESRO), which had begun in the early sixties. There are notable achievements in photovoltaics from these multiple agencies.

As the first PV devices were being created, there were corresponding theoretical predictions emerging that cited $\sim 20\%$ as the potential efficiency of Si and 26% for an optimum band gap material (~ 1.5 eV) under terrestrial illumination [4]. In addition, it was not long before the concept of a tandem cell was proposed to enhance the overall efficiency. An optimized three-cell stack was soon to follow with a theoretical optimum efficiency of 37% [5]. Early solar cell research was focused on understanding and mitigating the factors that limited cell efficiency (e.g. minority carrier lifetime, surface recombination velocity, series resistance, reflection of incident light, and nonideal diode behavior).

The first satellites needed only a few watts to several hundred watts. They required power sources to be reliable and ideally to have a high specific power (W/kg), since early launch costs were $\sim \$10\,000/\text{kg}$ or more. The cost of the power system for these satellites was not of paramount importance since it was a small fraction of the satellite and the launch cost. The size of the array, and therefore the power, was limited for many early satellites owing to the body-mounted array design. Thus, there were multiple reasons to focus on higher-efficiency solar cells. Explorer I launched in 1958 discovered the van Allen radiation belts, adding a new concern for space solar cells (i.e. electron and proton irradiation damage). The launch of Telstar in 1962 also ushered in a new era for space photovoltaics (i.e. terrestrial communications) [6]. Telstar's beginning of life (BOL) power was 14 W but high radiation caused by the "Starfish" high-altitude nuclear weapon test reduced the power output [7]. This test caused a number of spacecraft to cease transmission. The lessons learnt from Explorer I and Telstar prompted a surge of activity in radiation protection of space solar cells and prompted the use of *n-on-p* silicon semiconductor type (rather than *p-on-n*) for superior radiation resistance. Radiation damage studies at the Naval Research Laboratories in the 1960s provided much in the way of guidance to spacecraft designers in accounting for cell degradation [8].

As communication satellites evolved throughout the 1960s, so did their power requirements and thus the size and mass of the solar arrays. There were some early attempts to address the issue of mass by developing thin-film cells such as CdS on CuS_2 heterojunction devices [9]. Unfortunately, their use was prohibited by severe degradation over time. CdTe cells were developed reaching efficiencies of $\sim 7\%$ [10]. However, the higher efficiency and stability of the silicon solar cells assured their preeminence in satellite power for the next three decades. Research on thin-film cells for space applications, because of their higher specific power and projected lower costs, is still an area of intense research today.

In 1973, the largest solar array ever deployed up to that time was placed in low-Earth orbit (LEO) of Skylab 1 [11]. Skylab was powered by the Orbital Workshop array and the Apollo Telescope Mount array. The orbital Workshop array had 2 deployable wings, each with 73 920 ($2\text{ cm} \times 4\text{ cm}$) *n-on-p* Si cells that provided over 6 kW of power. Unfortunately, one of these wings was lost during launch. The Apollo Telescope Mount array had 4 wings with 123 120 ($2\text{ cm} \times 4\text{ cm}$) cells and 41 040 ($2\text{ cm} \times 6\text{ cm}$)

cells providing over 10 kW of power. The 1970s also saw the first use of shallow junction silicon cells for increased blue response and current output, the use of the back surface field, the low–high junction theory for increased silicon cell voltage output, and the development of wraparound contacts for high efficiency silicon (HES) cells to enable automated array assembly and to reduce costs.

In the 1980s, the gap between theoretical efficiencies and experimental efficiencies for silicon, gallium arsenide, and indium phosphide became almost nonexistent (see Figure 10.1) [12]. New thin-film cells of amorphous silicon and CuInGaSe_2 brought the possibility of higher thin-film efficiencies and flexible, lightweight substrates that excited the space community. However, silicon still provided the majority of the power for space and eventually the solar arrays for the International Space Station (ISS) (see Figure 10.2).

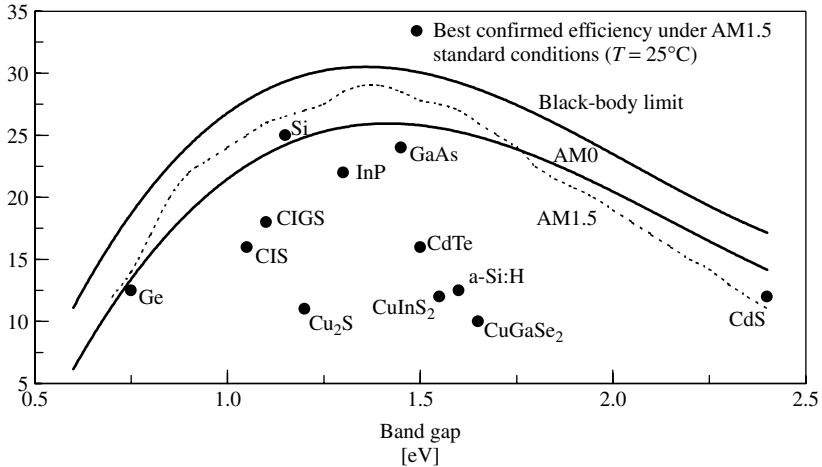


Figure 10.1 Comparison of measured cell efficiencies to the theoretical limits as a function of band gap [12]

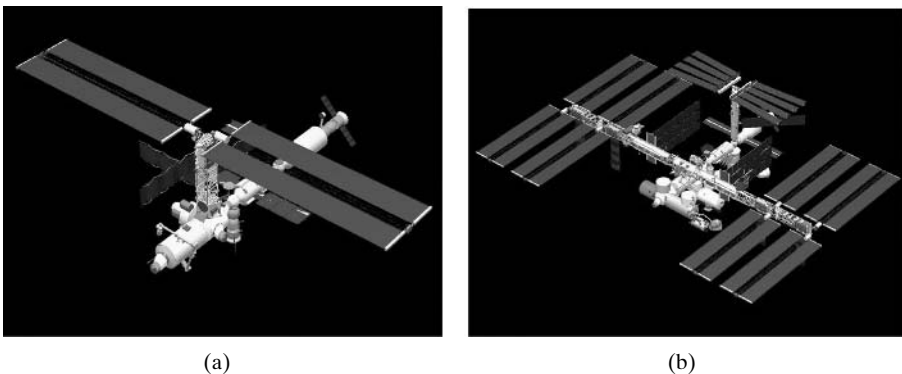


Figure 10.2 (a) Current status of International Space Station (ISS) and (b) planned configuration of ISS by 2004. (Pictures courtesy of NASA)

Table 10.1 Summary of existing space solar cell performance [15] obtained at AM0

Parameter	Silicon	High-efficiency silicon	Single-junction GaAs	Dual-junction III-V	Triple-junction III-V
Status	Obsolete	SOA	Obsolete	Nearly obsolete	SOA
Efficiency (%)	12.7–14.8	16.6	19	22	26.8
Operating voltage (V)	0.5	0.53	0.90	2.06	2.26
Cell weight (kg/m ²)	0.13–0.50	0.13–0.50	0.80–1.0	0.80–1.0	0.80–1.0
Normalized efficiency temperature coefficient at 28°C	–0.55%/C	–0.35%/C	–0.21%/C	–0.25%/C	–0.19%/C
Cell thickness (μm)	50–200	76	140–175	140–175	140–175
Radiation tolerance	0.66–0.77	0.79	0.75	0.80	0.84
Absorptance (ratio of absorbed radiant flux to the incident AM0 flux)	0.75	0.85	0.89	0.91	0.92

The ISS will have the largest PV power system ever present in space. It will be powered by 262 400 (8 cm × 8 cm) silicon solar cells with an average efficiency of 14.2% on 8 US solar arrays (each ~34 m × 12 m) [13]. This will generate about 110 kW of average power, which after battery charging, life support, and distribution, will supply 46 kW of continuous power for research experiments. The Russians also supply an additional 20 kW of solar power to ISS.

Space solar cell research in the 1990s focused on the III-V and multijunction (MJ) solar cells that had higher efficiencies and were more tolerant of the radiation environment. Satellites continued to grow in both size and power requirements and structures were designed to deploy large solar arrays. The mass and fuel penalty for attitude control of these large arrays continued to drive the space photovoltaics community to develop more efficient cells. Costs for satellite power systems remained at about a \$1000/W.

The Deep Space 1 spacecraft, launched in October 1998, was the first spacecraft to rely upon SCARLET concentrator arrays to provide power for its ion propulsion engines [14]. Concentrator arrays use either refractive or reflective optics to direct concentrated sunlight onto a smaller active area of solar cells. Deep Space 1 had two such arrays and each was capable of producing 2.5 kW at 100 V (DC). The SCARLET arrays were developed by AEC-ABLE Engineering, Inc., under a program sponsored by the Ballistic Missile Defence Organization (BMDO). These arrays performed flawlessly under this inaugural demonstration.

The state-of-the-art (SOA) space solar cells available today are triple-junction III-V semiconductor cells. However, high-efficiency Si cells are still utilized in a number of space applications. Table 10.1 summarizes the SOA in space solar cells [15].

10.2 THE CHALLENGE FOR SPACE SOLAR CELLS

A team from NASA, Department of Energy (DOE), and the Airforce Research Laboratory (AFRL) engineers recently reviewed the power technology needs of mid- and

long-term proposed space science missions and assessed the adequacy of SOA solar cell and array technologies [16]. At present, while low-cost thin-film cells are just beginning to present a viable space power option [$\sim 10\%$ air mass zero (AM0) efficiency for small-area cells], the best space solar cells are triple-junction III-V cells with an AM0 efficiency around 27%, and conventional arrays have reached a specific power of around 70 W/kg. These arrays meet the needs of many near-Earth missions but fail to meet some critical NASA Office of Space Science (OSS) mission needs in three ways. These are (1) missions that utilize solar electric propulsion (SEP) and require much higher specific power (150–200 W/kg), (2) missions that involve harsh environments [low solar intensity/low temperature, high solar intensities (HIHT), high-radiation exposure, and Mars environments], and (3) Sun–Earth connection missions that require electrostatically clean arrays that do not allow the array voltage to contact and thereby distort the plasma environment of the array. The entire surface of an electrostatically clean array is maintained at approximately the same potential as the spacecraft structure.

Work is in progress at several U.S. National Labs, universities, and solar cell companies to develop four-junction III-V cells with 30 to 35% efficiency and/or low-cost thin-film cells with large-scale efficiencies greater than 12%. This work is supported mainly by NASA, AFRL, and DOE [National Renewable Energy Lab (NREL)]. Unfortunately, no significant programs are presently under way to develop solar cells that can function efficiently in harsh environments. The majority of the ongoing work on advanced arrays is focused on developing flexible thin-film arrays. A limited amount of work is in progress on the development of concentrator arrays and electrostatically clean arrays. Table 10.2 compares space solar power (SSP) drivers and current SOA technology.

10.2.1 The Space Environment

All solar cells that are developed for use in space must take into consideration the unique aspects of the space environment. The spectral illumination that is available in space is not filtered by our atmosphere and thus is different from what is experienced on Earth. Space solar cells are designed and tested under an Air Mass Zero (AM0) spectrum (see Figure 16.1). A more complete discussion of air mass (AM) can be found in Chapters 16 and 20.

In the terrestrial PV world, cost is still the driver in PV development, and this has generated interest in several thin-film material systems (i.e. amorphous silicon, CuInGaSe₂, CdTe). The smaller material costs and higher production potential for thin-film arrays may well drive PV modules below current costs. The current National Photovoltaics Goal is the development of a 20% thin-film cell. The problem is more complicated for space applications since these cells must also be developed on a lightweight flexible substrate that can withstand the rigors of the space environment. This suggests that a minimum of 15% AM0 efficiency will be needed to be competitive with current satellite power systems. The current benchmark for the space PV world are commercially available multijunction III-V cells of GaInP/GaAs/Ge described further in Chapter 9. Table 10.3 lists the current status of cell efficiencies measured under standard conditions (AM1.5 global) as well as extraterrestrial (AM0) spectra.

The major types of radiation damage in solar cells that are of interest to designers are ionization and atomic displacement due to high-energy electrons and protons

Table 10.2 Comparison of technology requirements with state-of-the-art space solar cells [16]

Technology	Driving missions	Mission application	State of the art
High-power arrays for solar electric propulsion (SEP)	Comet nucleus sample return, outer planet missions, Venus surface sample return, Mars sample return	>150 W/kg specific power Operate to 5 AU	50–100 W/kg Unknown LILT effect
Electrostatically clean arrays	Sun Earth connection missions	<120% of the cost of a conventional array	~300% of the cost of a conventional array
Mars arrays	Mars smart lander, Mars sample return, scout missions	26% efficiency >180 sols @ 90% of full power	24% 90 sols @ 80% of full power
High-temperature solar arrays	Solar probe, sentinels	≥350°C operation (higher temperatures reduce risk and enhance missions)	130°C steady state; 260°C for short periods
High-efficiency cells	All missions	30+%	27%
Low intensity low temperature (LILT), resistant arrays	Outer planet missions, SEP missions	No insidious reduction of power under LILT conditions	Uncertain behavior of MJ cells under LILT conditions
High-radiation missions	Europa and Jupiter missions	Radiation resistance with minimal weight and risk penalty	Thick cover glass

Table 10.3 Measured global AM1.5 and measured or ^aestimated AM0 efficiencies for small-area cells

Cells	Efficiency [%] Global AM1.5	Efficiency [%] AM0	Area [cm ²]	Manufacturer
c-Si	22.3	21.1	21.45	Sunpower [17]
Poly-Si	18.6	17.1 ^a	1.0	Georgia Tech/HEM [18]
c-Si film	16.6	14.8 ^a	0.98	Astropower [19]
GaAs	25.1	22.1 ^a	3.91	Kopin [19]
InP	21.9	19.3 ^a	4.02	Spire [19]
GaInP (1.88 eV)	14.7	13.5	1.0	ISE [18]
GaInP/GaAs/Ge	31.0	29.3	0.25	Spectrolab [20]
Cu(Ga,In)Se ₂	18.8	16.4 ^a	1.04	NREL [19]
CdTe	16.4	14.7 ^a	1.131	NREL [19]
a-Si/a-Si/a-SiGe	13.5	12.0	0.27	USSC [19]
Dye-sensitized	10.6	9.8 ^a	0.25	EPFL [19]

^aEstimated AM0 efficiencies based on cells measured under standard conditions. The calculated efficiency used the ASTM E490-2000 reference spectrum and assumes that the fill factor does not change for the increased photocurrent. Quantum efficiencies corresponding to the table entries were used in the calculations

(although, low-energy protons can cause problems in the unshielded gap areas on the front of solar cells and on the unshielded back). Ionization effects can reduce the transmittance of the solar cell cover glasses through the development of color centers. Ionized electrons caused by the radiation become trapped by impurity atoms in the oxide to form

stable defect complexes. Ionizing radiation is also a large detriment to the other materials associated with space solar arrays. It causes trapped charges to be created in silicon dioxide passivating layers that can lead to increased leakage currents. Ionizing radiation, including ultraviolet photons, is particularly bad for organic materials such as polymers used in array development as it can produce ions, free electrons, and free radicals that can dramatically change the optical, electrical, and mechanical properties of these materials.

The loss of energy of the high-energy protons and electrons due to interactions with electrons in a material accounts for a large fraction of the dissipated energy. In fact, these collisions are used to determine the penetration range for the electrons and protons in the 0.1 to 10 MeV range. However, it is the atomic displacements created by irradiation that are the major cause of degradation in space solar cells.

The displacement of an atom from a lattice site requires energy similar to that necessary to sublime an atom or to create a vacancy. The energy of sublimation for Si is 4.9 eV and for vacancy formation is 2.3 eV. The displacement of an atom requires the formation of a vacancy, an interstitial, and usually the creation of some phonons. Therefore, to create a displacement will require energy several times larger than that to create a vacancy.

The main importance of displacement defects due to irradiation is their effect on minority carrier lifetime. The lifetime in the bulk *p*-type material of a Si solar cell is the major radiation-sensitive parameter. This was the basis for the switch from *p*-on-*n* to *n*-on-*p* Si solar cells in the 1960s [21]. The minority carrier lifetime or diffusion length in an irradiated solar cell may be a function of excess or nonequilibrium minority carriers. This behavior is referred to as injection level dependence. This is usually associated with damage due to high-energy protons.

The primary radiation defects in Si are highly mobile. The radiation damage effects in Si are primarily due to the interaction of primary defects with themselves and with impurities in the material. Radiation damage in these cells can be mitigated to a certain extent by removing some of the damage before it becomes consolidated. Radiation-resistant Si cells use intrinsic gettering to remove a part of the radiation damage while it is still mobile. These cells contain a relatively pure region near the surface or “denuded zone” with a gettering zone rich in oxygen deeper in the wafer away from the junction. Although this approach decreases the beginning-of-life (BOL) output, it increases the end-of-life (EOL) output. The cells are much more radiation-resistant, which can dramatically extend the mission lifetime.

Annealing of irradiated solar cells can be used to remove some of the damage, although not at temperatures that would be considered practical for space applications. Temperatures of nearly 400°C are required for significant improvement in Si cells. However, there is some amount of ambient annealing of radiation damage that can occur. In space the damage and annealing process are occurring simultaneously and are thus hard to quantify. However, in the lab, ambient annealing improvement of as much as 20% in the short-circuit current has been observed after 22 months.

The main method for mitigating radiation damage in space solar cells is to prevent damage by employing a cover glass. The cover glass not only stops the low-energy protons but also slows down the high-energy particles. It can also serve to stop micrometeors,

act as an antireflection coating, provide resistance to charging, and even provide added thermal control to the spacecraft. In the 1970s, manufacturers began adding a nominal 5% cerium oxide to the cover glasses. This was shown to significantly improve the resistance of the glass to darkening from radiation or ultraviolet light [22]. The protection offered by the cerium also will improve the lifetime of the adhesives that are used to bond the cover glasses. The SOA cover glass is a drawn cerium-doped borosilicate glass. Research today is focused on improving the transmission of the glasses over a wider spectral range to accommodate the development of new MJ devices.

Current methods for calculating damage to solar cells are well documented in the GaAs Solar Cell Radiation Handbook (JPL 96-9). Recently the displacement damage dose (Dd) method has been developed to model radiation degradation. This method is currently being implemented in the SAVANT radiation degradation modeling computer program [23].

The bombardment of cells by charged particles can also lead to dangerously high voltages being established across solar arrays. These large voltages can lead to catastrophic electrostatic discharging events. This is especially true in the case of large arrays and pose significant problems for future utilization of large-area arrays on polymeric substrates. Much work has been done on the grounding and shielding of arrays to mitigate the effects of array charging [24]. Progress in addressing these effects has been made through the development of plasma contactors that ground the arrays to the space plasma.

Solar cell performance is also diminished over time due to neutral particle or micrometeor bombardment. These events account for approximately a 1% decrease in EOL space solar cells performance [25]. These events may also have a correlation to the initiation of discharging events discussed above. Space solar cells and arrays must also be equipped to contend with the plasma environment (radiation and charging). Removed from much of the shielding effects of the Earth's magnetic field, solar cells in space are continually bombarded with high-energy electrons and protons. The radiation damage caused by these particles will degrade solar cell performance and can dramatically limit spacecraft life. This is especially true for mid-Earth orbits (MEO, defined as ~2000 to 12 000 km) in which cells must pass through the Van Allen radiation belts and thus get a much higher dose of radiation than would be experienced in low-Earth orbits (LEO, defined as <1000 km) or geosynchronous Earth orbits (GEO, defined as 35 780 km). LEO orbits vary in their radiation dose depending on their orientation, with, for example, polar orbits yielding a higher radiation dose than equatorial orbits. Figure 10.3 shows a comparison of equivalent fluence on a silicon solar cell in a variety of orbits. Figure 10.4 shows the dramatic decline in EOL power of cells in MEO orbit [26]. The degradation of cells in space due to radiation damage can be mitigated through the use of cover glasses at the expense of added mass to the spacecraft. Figure 10.5 shows the decline in power density as a function of time over 10 years in an 1853-km, 103° sun-synchronous orbit.

10.2.2 Thermal Environment

There is a considerable range of temperatures and intensities that may be encountered for the space use of photovoltaics. The temperature of a solar cell in space is largely determined by the intensity and duration of its illumination [32]. In a typical LEO, such as the orbit of the ISS, the operating temperature of the silicon solar cells is 55°C when

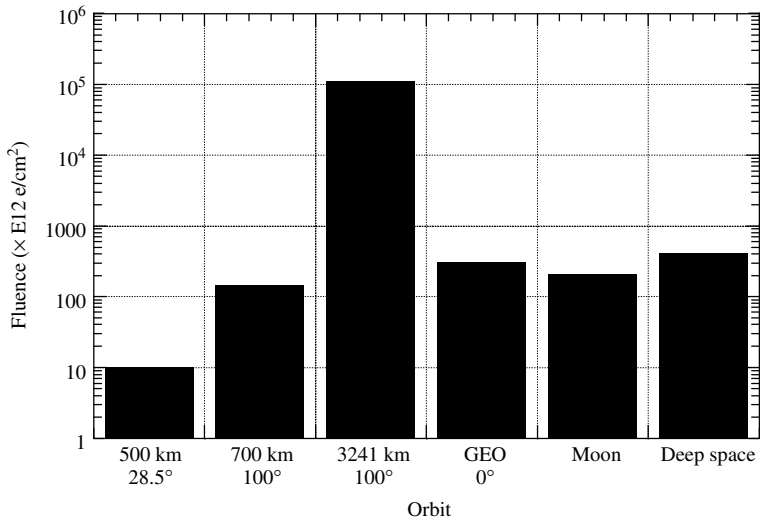


Figure 10.3 Equivalent 1-MeV electron fluence for a silicon solar cell in a variety of orbits (altitude in kilometer) and inclinations (°)

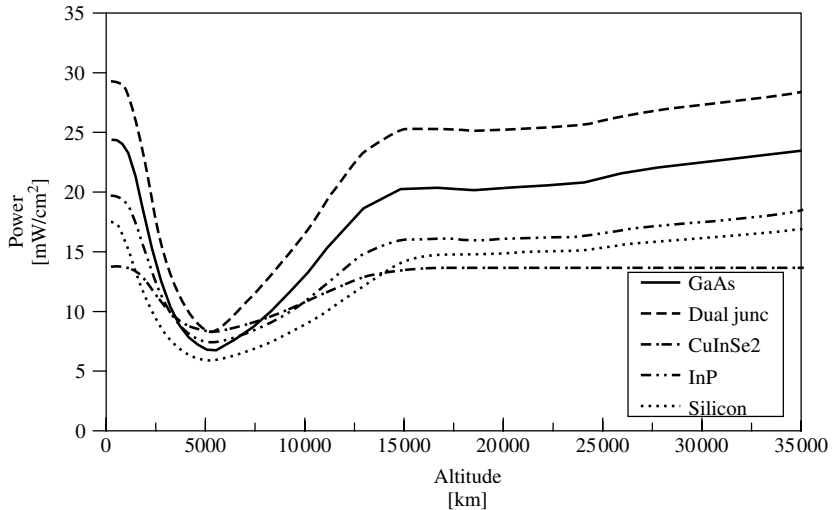


Figure 10.4 Solar cell power density as a function of altitude after 10 years in a 60° orbit with a cover glass thickness of 300 μm (GaAs: BOL 24.4 (mW/cm²) [27]; Dual Junc – GaInP/GaAs/Ge [28]: BOL 29.3 (mW/cm²); CuInSe2: BOL 14.4 (mW/cm²) [29]; InP: BOL 19.7 (mW/cm²) [30]; Si: BOL 17.5 (mW/cm²) [31]). (Graph courtesy of Tom Morton, Ohio Aerospace Institute)

sun tracking and -80°C when in the longest eclipse. The average illuminated temperature at the orbit of Jupiter is -125°C , whereas at the average orbit of Mercury the temperature is 140°C . Similarly, the average intensity at the orbit of Jupiter is only 3% of the solar intensity at the Earth's radius, whereas the average intensity at Mercury is nearly double

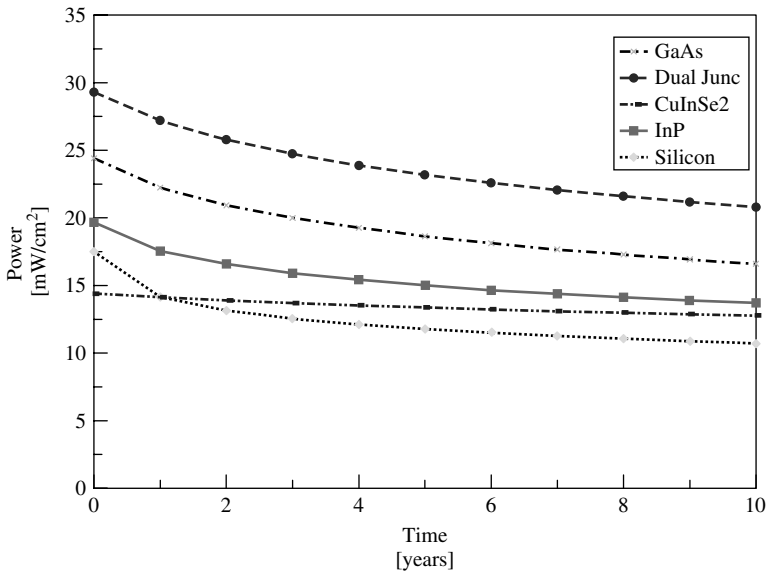


Figure 10.5 Solar cell power density as a function of time in a 1853-km altitude, 103° sun-synchronous orbit for the same cells as in Figure 10.6. (Graph courtesy of Tom Morton, Ohio Aerospace Institute)

that at Earth. The solar intensity in the orbit around the Earth will vary seasonally because of the ellipticity of the Earth's orbit around the sun. Orbital characteristics are also a major source of thermal variation. Most spacecraft experience some amount of eclipse that will vary as the orbit precesses. This can result in very large and rapid temperature changes as shown above for the space station cell. The temperature of a solar cell in space is also affected by the fraction of incident solar radiation returned from a planet or albedo. The average albedo from the Earth is 0.34, but can range anywhere from 0.03 (over forests) to 0.8 (over clouds) [7]. Typically, the range of temperatures experienced by solar cells in orbit about the Earth is from about 20°C to as high as 85°C.

An increase in solar cell temperature will cause a slight increase in the short-circuit current but a significant decrease in the open-circuit voltage (see Figure 10.6). Therefore, the overall effect is a reduction in power of a solar cell with an increase in temperature. It is typically less than 0.1%/°C, but can vary dramatically depending on cell type. This change coupled with rapid changes in temperature associated with eclipses can result in power surges that may be problematic.

The degradation of solar cell performance as a function of temperature is expressed in terms of temperature coefficients. There are several different temperature coefficients used to describe the thermal behavior of solar cells. These coefficients are generally expressed as the difference in a device parameter (i.e. I_{SC} , V_{OC} , I_{mp} , V_{mp} , or η) measured at a desired temperature and at a reference temperature [traditionally 28°C, although the new International Space Organization (ISO) standard is 25°C] divided by the difference in the two temperatures. Solar cell response to temperature is fairly linear for most cells over the range of -100 to 100°C. Unfortunately, for cells of amorphous silicon or low

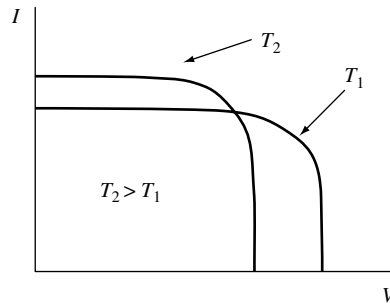


Figure 10.6 Effect of increasing temperature on solar cell $I-V$ photoresponse

Table 10.4 Theoretical normalized efficiency temperature coefficients [33]

Cell type	Temperature [°C]	η (28°C)	$(1/\eta)(d\eta/dT)$ [$\times 10^{-3}/^{\circ}\text{C}$]
Si (calc.)	27	0.247	-3.27
Ge (calc.)	27	0.106	-9.53
GaAs (calc.)	27	0.277	-2.4

Table 10.5 Measured temperature coefficients for various types of solar cells used in space [26]

Cell type	Temp [°C]	η (28°C)	$(1/\eta)(d\eta/dT)$ [$\times 10^{-3}/^{\circ}\text{C}$]
Si	28-60	0.148	-4.60
Ge	20-80	0.090	-10.1
GaAs/Ge	20-120	0.174	-1.60
2-j GaAs/Ge	35-100	0.194	-2.85
InP	0-150	0.195	-1.59
a-Si	0-40	0.066	-1.11 (nonlinear)
CuInSe ₂	-40-80	0.087	-6.52

band gap cells such as InGaAs, the response is only linear with temperature for small temperature differences. Another frequently used definition for the temperature coefficient is the normalized temperature coefficient. In the case of the efficiency it is defined as

$$\beta = \frac{1}{\eta} \frac{d\eta}{dT} \quad (10.1)$$

or the fractional change in efficiency with temperature. Theoretical values for the normalized efficiency temperature coefficients for Si, Ge, and GaAs are given in Table 10.4. Representative temperature coefficients for the various types of cells used in space are given in Table 10.5. In general, the temperature coefficient decreases in magnitude with the increasing band gap but is always negative except in the case of a-Si, which can have a positive coefficient.

10.2.3 Solar Cell Calibration and Measurement

Calibration of solar cells for space is extremely important for satellite power system design. Accurate prediction of solar cell performance is critical to solar array sizing, often required to be within 1%. Calibration standards as a function of band gap are required to perform simulated AM0 efficiency measurements on earth. The calibration standards are produced by evaluating various cell types in space via the Shuttle or in the near future aboard the ISS. A less-costly means of developing standards is through the use of high-altitude aircraft or balloon flights. NASA Glenn Research Center solar cell calibration airplane facility has been in operation since 1963 with 531 flights to date [34]. The calibration includes real data to AM0.2 and uses the Langley plot method plus an ozone correction factor to extrapolate to AM0. Comparison of the AM0 calibration data indicates that there is good correlation with Balloon and Shuttle flown solar cells.

Solar intensity is a function of the thickness of the atmosphere that the sunlight must pass through (AM). Plotting the logarithm of solar cell short-circuit current, proportional to solar intensity, as a function of AM permits extrapolation to an unmeasured AM and AM0 (Langley Plot Method). Early ground-based measurements were based on the change in atmosphere that the sun would pass through as it moves across the sky (i.e. more atmosphere at dawn and dusk and a minimum at solar noon). This is the same basic method that is used with an airplane, changing altitude to vary the AM.

Data analysis from early flights between 1963 and 1967 showed that the AM0 extrapolation was slightly lower than what was expected from radiometer data. This was found to be due to ozone absorption of sunlight in the upper atmosphere. A change in the data linearity was also noticed when the plane flew below the tropopause. This was later correlated with Mie scattering from particulate matter in the atmosphere and with absorption by moisture. These effects are primarily manifested in the higher-energy region of the solar spectrum. Calibration flights currently are performed above the troposphere and a correction for ozone absorption is used. Today calibration runs are performed with a Lear 25A jet housed at the NASA Glenn Research Center (see Figure 10.7). It has flown 324 flights since 1984. The plane can fly up to ~15 km and gets above AM0.2 at 45°N latitude. The data is now gathered using a continuous descent rather than remaining level over a range of altitudes.

The current Lear test setup has a 5:1 collimating tube in place of one of the original aircraft windows. This tube illuminates a 10.4-cm-diameter temperature-controlled plate. The tube angle can be adjusted to the sun angle. During descent IV curves for up to 6 cells, a pressure transducer, a thermopile, and a temperature sensor are all measured. The cells are held at a constant temperature of $\pm 1^\circ\text{C}$. A fiber optic connected to the test-plate is also connected to a spectroradiometer that can measure the solar spectrum from 250 to 2500 nm with 6-nm resolution, and a second spectrometer is used to measure the spectrum from 200 to 800 nm with 1-nm resolution. Both of these spectrometers are used to check for any spectral anomalies and to provide information on the ozone absorption.

There are currently several commercially available steady-state and pulse solar simulators that can simulate the sun's light in a variety of conditions (i.e. AM1.5, AM0). The NASA Glenn Research Center uses a Spectrolab X-25 Mark II xenon arc-lamp solar simulator. Steady-state solar simulators are generally used in laboratory or production environments for precision testing of PV devices. Solar simulators are also used on



Figure 10.7 The NASA Glenn Research solar cell calibration aircraft. (Photo courtesy of NASA)

terrestrial, aerospace, and satellite products as a long-term simulated sunlight exposure system to test optical coatings, thermal control coatings, paints, and so on. Pulse simulators make it possible to test large solar cell assemblies and solar array blankets.

NASA Glenn uses a Spectrolab Spectrosun Large Area Pulsed Solar Simulator. It has a xenon arc lamp that is flashed to produce approximately 1-sun illumination with a nearly AM0 spectrum. The flash lasts approximately 2 ms, during which time the voltage across the cell is ramped and the resulting current is measured. At the same time the short-circuit current from a standard solar cell of a similar type is used to adjust the measured test sample current for the slightly changing illumination during the flash.

The standards for space solar cell calibration fall under the auspices of the ISO technical committee 20: Aircraft and Space Vehicle, sub committee 14: Space Systems and Operation. The working draft ISO 15387 addresses the requirements for reference solar cells, the extraterrestrial solar spectral irradiance, and the testing conditions. Round robin testing procedures, which rotate the cell measurements from agency to agency, involving NASA, CAST, and ESA for space solar cell calibration are currently under way.

10.3 SILICON SOLAR CELLS

Silicon solar cells are the most mature of all space solar cell technologies and have been used on practically every near-Earth spacecraft since the beginning of the US space program. In the early 1960s, silicon solar cells were $\sim 11\%$ efficient, relatively inexpensive, and well suited for the low-power (100 s of watts) and short mission duration (3–5 years). The conversion efficiency of current “standard-technology” silicon ranges from around 12 to 15% under standard AM0 test conditions [19]. The lower efficiency cells are generally more resistant to radiation.

Cell efficiencies for any application should be adjusted for the array packing factor, radiation damage, ultraviolet degradation, assembly losses, and for corrections due to variations in intensity and temperature from standard conditions. At operating temperature, a silicon solar cell will degrade about 25% over 10 years in GEO orbit owing to charged

particle irradiation damage [35]. The performance of these cells degrades significantly (often exceeding a 50% loss) in very high-radiation environments such as experienced near Jupiter or in MEO. The relatively large temperature coefficient of silicon cells also results in large reductions in efficiency at high temperatures [26].

There have been many enhancements to silicon cells over the years to improve their efficiency and make them more suitable to space utilization. Textured front surfaces for better light absorption, extremely thin cells with back surface reflectors for internal light trapping, and passivated cell surfaces to reduce losses due to recombination effects are just a few examples and are discussed in more detail in Chapters 7 and 8. Currently, high-efficiency Si (HES) cells approaching 17% AM0 efficiency in production lots are available from several producers. The advantage of the HES cell to that of a III-V lies in their relatively lower cost and lower material density. However, silicon solar cells are less tolerant of the radiation environment of space.

10.4 III-V SOLAR CELLS

The efficiency of space solar cells achieved dramatic improvements as the focus shifted from Si toward GaAs and III-V semiconductor systems. The 1.43 eV direct band gap is nearly ideal for solar conversion (see Figure 10.1). By 1980 several types of III-V cells had been tested in space, with a 16% GaAs solar cell being developed by 1984 and a 18.5% efficient GaAs/Ge solar cell developed by 1989. It was also found that the GaAs cells had significantly better radiation resistance than Si cells. GaAs cells with efficiencies in excess of 80% of their theoretical maximum were routinely available commercially by 1998. Single-junction GaAs on Ge cells are currently commercially available with an AM0 efficiency of 19% and V_{OC} of 0.9 V. III-V solar cells for space applications are currently grown on Ge wafers because of the lower cost and higher mechanical strength over GaAs wafers.

Investigations on further efficiency improvement toward the end of the 20th century turned toward the development of multiple-junction cells and concentrator cells. Much of the development of “multijunction” GaAs-based photovoltaics was supported by a cooperative program funded by the Air Force Manufacturing Technology (ManTech) program and Space Vehicles Directorate, the Space Missile Center, and NASA [36]. This work resulted in the development of a “dual-junction” cell that incorporates a high band gap GaInP cell grown on a GaAs low band gap cell. The 1.85-eV GaInP converts short wavelength photons and the GaAs converts the lower energy photons. Commercially available dual-junction GaInP/GaAs cells have an AM0 efficiency of 22% with a V_{OC} of 2.06 V. See Chapter 9 for a complete discussion of this type of solar cell.

The highest-efficiency solar cells currently available for space use are triple-junction cells consisting of GaInP, GaAs, and Ge. They are grown in series of connected layers and have been produced with a 26.9% efficiency with a V_{OC} of 2.26 V in production lots, with laboratory cells of 29% (see Figure 10.8). Emcore, Inc., Tecstar, Inc., and SpectroLab, Inc., currently produce cells that are commercially available in the 25 to 27% range. Hughes Space and Communications Company’s HS601 and HS702 spacecraft currently use MJ technology as do most other contractors for their high-performance spacecraft.

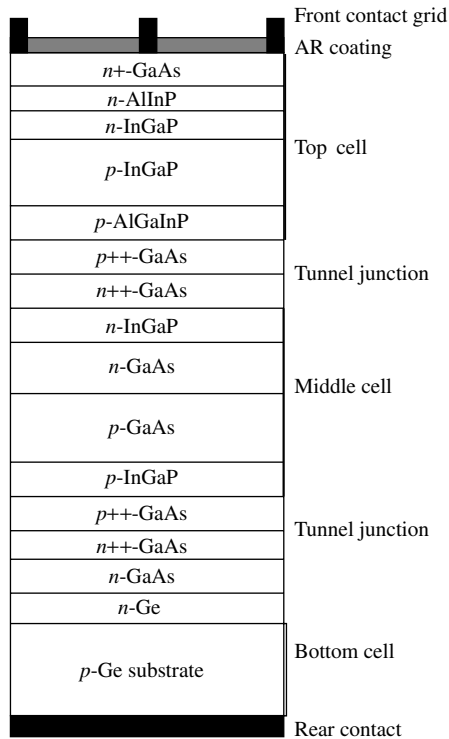


Figure 10.8 Commercially available 26.9% GaInP/GaAs/Ge triple-junction cell

Spectrolab, supplier of more than half of the world's spacecraft solar cells, has reached a milestone of 25 000 triple-junction GaInP/GaAs/Ge solar cells, with a maximum efficiency of 27.1% and an average conversion efficiency of 24.5%. They are currently providing 1 MW of cells to global spacecraft manufacturers (e.g. Hughes Space and Communication Company, Ball Aerospace & Technologies Group, Lockheed Martin, and Boeing). Their high-efficiency cells retain 86% of their original power after 15 years of operation. There is currently more than 50 kW of Spectrolab dual-junction solar cells in orbit.

The new multijunction III-V cells have allowed a reduction in solar array size and mass over the previously used Si cells while maintaining comparable power levels. The alternative way to view the efficiency increase offered by the III-V cells is that they have increased available payload power over using a comparably sized Si array. Scientists expect the majority of the 800 commercial and military spacecraft launched in the next five years to use multijunction III-V technology. This should result in the lower costs for telecommunications, Internet, television, and other wireless services. The AFRL recently initiated a 35% efficient four-junction solar cell program.

Multijunction III-V cells are relatively expensive to produce. The development of large-area arrays using these cells can become cost-prohibitive. One option to reduce the overall cost is to use the cells in solar concentrators, where a lens or mirror is used to decrease the required cell area. The previously mentioned SCARLET concentrator

arrays used on Deep Space 1 used GaInP/GaAs high-efficiency dual-junction cells. A more advanced SCARLET-II array will build on the SCARLET technology with lower cost, easier fabrication, and simplified assembly and testing [14].

10.4.1 Thin-film Solar Cells

One of the first thin-film cells, $\text{Cu}_2\text{S}/\text{CdS}$, was developed for space applications. Reliability issues eliminated work on this particular cell type for both space and terrestrial considerations even though AM1.5 efficiencies in excess of 10% were achieved. Thin-film cells require substantially less material and thus lower mass and promise the advantage of large-area, low-cost manufacturing. Until recently, the focus in space cells has been on efficiency rather than cost. In a several billion dollar spacecraft the solar cell cost is relatively small at even a thousand dollars per watt, which is approximately the current array cost. This has primarily been true for spacecraft with power needs from a few hundred watts to tens of kilowatts. However, deployment of a large Earth-orbiting space power system or some of the proposed SEP missions will require major advances in the PV array weight, stability in the space environment, efficiency, and ultimately the cost of production and deployment of such arrays. The development of viable thin-film arrays has become a necessity for a host of space missions [37]. Mission examples include ultra-long duration balloons (e.g. Olympus), deep space SEP “tug” array, Mars surface power outpost, and Mars SEP Array (see Figure 10.9). Solar electric propulsion missions are those in which the solar array is used to provide power for an electric propulsion system such as a Hall thruster or an ion thruster. These missions require large, lightweight, low-cost power systems. Studies have shown that the specific power or power per mass that will be required (i.e. 1 kW/kg) cannot be achieved with single-crystal technology [30]. The specific power required is almost 40 times what is presently available in commercial arrays. While high-efficiency ultralightweight arrays are not likely to become commercially available anytime soon, advances in thin-film photovoltaics may still impact other space technologies (i.e. thin-film integrated power supplies) and thus support a broad range of future missions.

Lighter power generation will allow more mass to be allocated to the balance-of-spacecraft (i.e. more payload). In addition, less expensive power generation will allow

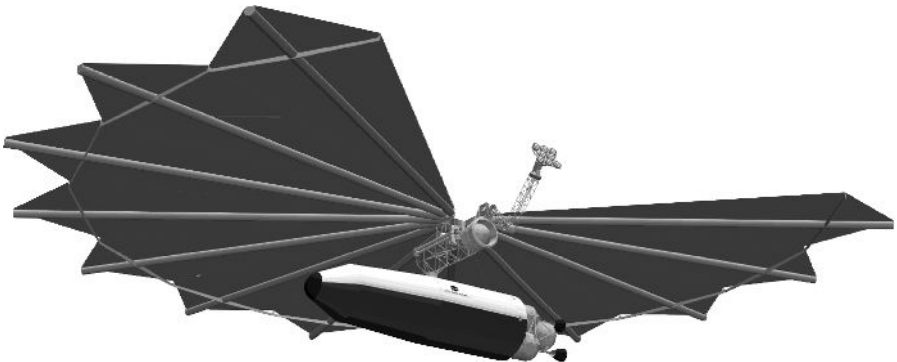


Figure 10.9 Proposed Mars solar electric propulsion vehicle. (Picture courtesy of NASA)

missions with smaller budgets and/or the allocation of funds to the balance-of-spacecraft. This is an essential attribute in enabling such missions as the Mars Outpost SEP Tug. An example of the benefits of thin-film PV arrays for the now-canceled ST4/Champlion indicates a \$50 million launch cost savings and 30% mass margin increase when thin-film solar array power generation was combined with advanced electric propulsion. A parametric assessment showed similar advantages for other solar system missions (e.g. main belt asteroid tour, Mars SEP vehicle, Jupiter orbiter, Venus orbiter, Lunar surface power system) [30].

Much of the original development of thin-film PV arrays was performed with the terrestrial marketplace in mind. This has been a tremendous benefit to researchers hoping to develop such arrays for space. Features such as cell efficiency, material stability and compatibility, and low-cost and scalable manufacturing techniques are important to both environments. However, many key array aspects necessary for space utilization are not important for terrestrial use and thus have not experienced a similar progress. Features such as radiation tolerance, air mass zero (AM0) performance, use of lightweight flexible substrates, stowed volume and lightweight space deployment mechanisms must be developed before a viable space array can become a reality. Unfortunately, the costs associated with developing these features along with the subsequent space qualification studies mitigate the savings of using a thin-film array for space, and thus have inhibited their application.

On-going efforts by NASA and the U.S. Air Force are now addressing these issues associated with the development of thin-film arrays for space. Copper indium gallium diselenide (CIGS), cadmium telluride (CdTe), and amorphous silicon (a-Si) thin-film materials appear to have a good chance of meeting several proposed space power requirements [38]. Reasonably efficient ($\sim 8\%$ AM1.5) large area flexible blankets using a-Si triple junction technology are already being manufactured.

Table 10.6 summarizes the thin-film solar cell technologies that are currently available. Further details on a-Si, CIGS, and CdTe solar cells can be found in Chapters 12–14, respectively. Several device structures offer specific power exceeding 1000 W/kg, but these values only include the device and substrate not the entire module and array. This table shows the importance of lighter or thinner substrates in achieving higher specific power. Note that multijunction cells (like the a-Si triple cells) whose thicknesses and bandgaps have been optimized for the terrestrial AM1.5 spectra should be re-optimized for AM0 since the distribution of photons between top, middle and bottom cells will be different. This changes the current matching. Reoptimization is not required for single junction thin-film devices. References 39 and 40 showed no substrate dependence for a-Si devices; that is, the same efficiency resulted between deposition on thin (10–25 μm) or thick (125 μm) stainless steel or between stainless steel or Kapton. This is good news for obtaining lighter thin film modules with higher specific power. In contrast, efficiency of Cu(InGa)S devices decreased from 10.4% to 4.1% as the stainless steel substrate decreased in thickness from 128 μm to 20 μm [44]. An 11% efficiency for CdTe on 10 μm polyimide was reported but is unpublished [45].

Development of other wide bandgap thin-film materials to be used in conjunction with CIGS to produce a dual-junction device is underway. As has already been demonstrated in III-V cells for space use, a substantial increase over a single-junction device

Table 10.6 Small area thin-film solar cell efficiency and specific power. AM0 and AM1.5 given when available. Results for a-Si devices in initial state before stabilization. AM0 results for a-Si triple junctions of a-Si/a-SiGe/a-SiGe [42] are higher than AM1.5 because they were optimized for AM0 spectrum, all other cells optimized for AM1.5. Substrate thickness estimated in some cases. Specific power calculated by authors with some assumptions. (n/a means not available)

Cell type	Cell + substrate thickness	AM1.5 efficiency [%]	AM0 efficiency [%]	Specific power [W/kg] @AM1.5	Reference for cell results
a-Si triple junction	Stainless steel, 128 μm	11.9	12.7	108	[39]
a-Si triple junction	Stainless steel, 7 μm	6.5	n/a	1080	[40]
a-Si triple junction	Kapton, 52 μm	~ 12 (est.)	12.7	~ 1200	[39]
a-Si double junction	Glass, ~ 1.5 mm	11.7	n/a	31	[41]
Cu(InGa)Se ₂	Glass, ~ 1.5 mm	18.8	n/a	50	[42]
Cu(InGa)Se ₂	Stainless steel 128 μm	17.4	n/a	156	[42]
Cu(InGa)Se ₂	Polyimide 54 μm	12.1	n/a	1260	[43]
Cu(InGa)S ₂	Stainless steel 128 μm	10.4	8.8	93	[44]
CdTe	Polyimide 10 μm	8.6	n/a	n/a	[45]
CdTe	Glass, ~ 1.5 mm	15	n/a	40	[46]

efficiency is possible with a dual-junction device. NASA and NREL have both initiated dual-junction CIS-based thin-film device programs. The use of Ga to widen the bandgap of CIGS and thus improve the efficiency is well established [42]. The substitution of S for Se also appears to be attractive as a top cell material. In particular, AM0 cell efficiencies 8.8% have been measured for $\text{CuIn}_{0.7}\text{Ga}_{0.3}\text{S}_2$ (E_g 1.55 eV) thin-film devices on flexible stainless steel substrates [44]. Other wide bandgap top cell possibilities under investigation include adding CdZnTe absorbers as discussed at the end of Chapter 14 .

The majority of thin-film devices developed for terrestrial applications have been on heavy substrates such as glass. However, progress is being made in reducing substrate mass through the use of thin metal foils and lightweight flexible polyimide or plastic substrates [47]. The use of such plastic substrates as Upilex or Kapton puts a slight restriction on the processing temperatures. This of course can be obviated by the use of metal foil if one is willing to accept the mass penalty.

In addition to cost and weight savings for spacecraft, thin-film solar cells have potential for improved radiation resistance relative to single-crystal cells, possibly extending mission lifetimes. For example, after a dose of 10^{16} 1 MeV *electrons/cm²*, the maximum power generated by a GaAs cell can decrease to less than half of its BOL value. By contrast, after a dose of $10^{13}/\text{cm}^2$ 10 MeV *protons* (which would degrade GaAs cell power performance to less than 50% of BOL), the power generated by CIS cells has been shown to retain more than 85% of its BOL value [48].

In addition to thin-film cell development, there is the problem of making thin-film arrays for space. The flexibility of a thin-film cell on a polymeric substrate is a great advantage when it comes to stowability and deployment; however, it must be rigidly

supported after deployment. Work must be done to determine how best to deploy and maintain thin-film arrays. The same issues concerning stability in the space environment that were addressed for arrays with crystalline cells must now be addressed for thin-film arrays. As outlined in US Government Military Standard 1540C, the array must pass a number of qualification tests, including those for integrity and performance after exposure to elevated temperatures, radiation (particularly electrons and protons), thermal cycling, vibration and mechanical stress, and atomic oxygen.

The Air Force is leading a large, multidisciplinary team under the auspices of the Air Force Dual-Use Science and Technology program to develop a functional thin-film array for space within three years [49]. This program has the specific goals of demonstrating

1. a stabilized 10 to 15% AM0 efficient thin-film submodule;
2. submodule and module electrical architectures including bypass and blocking diode technology;
3. submodule and module mechanical interface architectures, module strength, and structural support requirements;
4. array support structure design for an array with a wide range of power levels;
5. space environment and thermal control protection/qualification standards for thin-film arrays.

This effort will culminate in the design of a-1 kW LEO and 20-kW GEO thin-film solar array.

10.5 SPACE SOLAR ARRAYS

Solar array designs have undergone a steady evolution since the Vanguard 1 satellite. Early satellites used silicon solar cells on honeycomb panels that were body-mounted to the spacecraft. Early space solar arrays only produced a few hundred watts of power. However, satellites today require low-mass solar arrays that produce several kilowatts of power. Several new solar array structures have been developed over the past 40 years to improve the array specific power and reduce the stowed volume during launch.

The most important characteristics of solar arrays required for space applications are

- high specific power (W/kg)
- low stowed volume (W/m³)
- low cost (\$/W)
- high reliability.

In addition, several proposed space missions have put other constraints on the solar arrays. Several proposed Earth-orbiting missions designed to study the sun require “electrostatically clean” arrays. Inner planetary missions and mission to study the sun within a few solar radii require solar arrays capable of withstanding temperatures above 450°C and functioning at high solar intensities (HIHT). Outer planetary missions require solar arrays that can function at low solar intensities and low temperatures (LILT). In addition to the near-sun missions, missions to Jupiter and its moons also require solar arrays that can withstand high-radiation levels.

The EOL power generated by an array is impacted in a variety of ways. Radiation damage will result in an 8% loss of BOL power/m² after 5×10^{14} 1 MeV electrons (i.e. typical EOL fluence in geosynchronous orbit). The temperature correction due to the operation of the solar cell at 75°C rather than at the 25°C test conditions will reduce the power/m² by ~9%. Degradation due to UV exposure is around 1.7%. Loss in power over time due to micrometeors and ordinary surface contamination are each around 1% [24].

The solar arrays presently in use can be classified into six categories:

- Body-mounted arrays
- Rigid panel planar arrays
- Flexible panel array
- Flexible roll-out arrays
- Concentrator arrays
- High-temperature/intensity arrays
- Electrostatically clean arrays.

A summary of the important typical characteristics of these arrays are given in Table 10.7.

10.5.1 Body-mounted Arrays

Body-mounted arrays are preferred for small satellites that only need a few hundred watts. Early spherical satellites and spin-stabilized cylindrical satellites used body-mounted arrays of silicon solar cells on the honeycomb panels. This type of array is simple and has proven to be extremely reliable. One of the limitations of this type of array is that it puts a constraint on the direction the spacecraft must point. This type of array is still used on smaller spacecraft and spin-stabilized spacecraft. The recently deployed Mars Pathfinder Sojourner Rover also used body-mounted solar arrays (see Figure 10.10).

10.5.2 Rigid Panel Planar Arrays

Rigid panel arrays have been used on many spacecraft requiring several hundred watts to many tens of kilowatts of power. They consist of rigid honeycomb core panels that

Table 10.7 Space solar array characteristics [16]

Technology	Specific power [W/kg] (BOL) @ cell efficiency	Cost [\$K/W]	Area per power [m ² /kW]
High-efficiency silicon (HES) rigid panel	58.5 @ 19%	0.5–1.5	4.45
HES flexible array	114 @ 19%	1.0–2.0	5.12
Triple junction (TJ) GaAs rigid	70 @ 26.8%	0.5–1.5	3.12
TJ GaAs ultraflex	115 @ 26.8%	1.0–2.0	3.62
CIGS thin film ^a	275 @ 11%	0.1–0.3	7.37
Amorphous-Si MJ/thin film ^a	353 @ 14%	0.05–0.3	5.73

^aRepresents projected values. These arrays are unavailable commercially

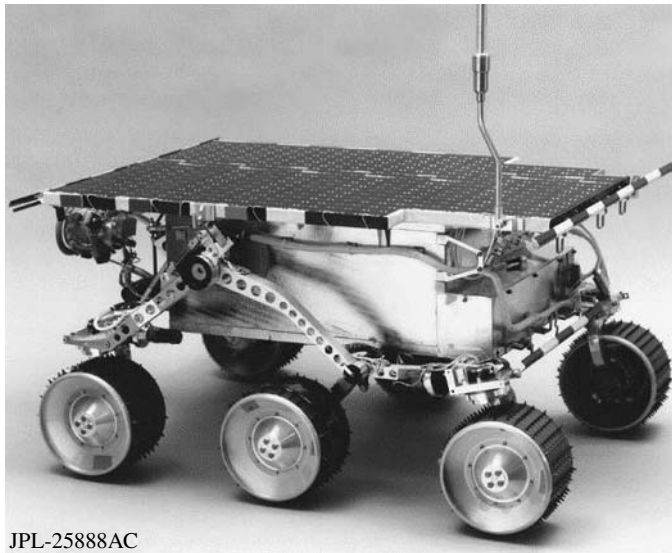


Figure 10.10 Body-mounted array on the Mars sojourner rover. (Picture courtesy of NASA JPL)

are hinged such that they can be folded against the side of the spacecraft during launch (see Figure 10.11). Each panel is rigid and quite strong, but can add considerably to the overall weight of the array. There has been much development recently on panels of materials other than aluminum (i.e. graphite/epoxy sheets and ribbons). Hybrid panels with aluminum honeycombs and epoxy/glass face sheets have also been developed. The folded arrays are deployed by means of pyrotechnic, paraffin, or knife blade actuators and damper-controlled springs.

The BOL power density of the rigid panel array is extremely dependent on the type of solar cell used. BOL power densities range from 35 to 65 W/kg for silicon cells and 45 to 75 W/kg for GaAs/Ge cells. The panel assembly of a rigid array accounts for 75 to 80% of the total mass, with the stowed and deployment structure making up the balance [16]. The Tropical Rainfall Measuring Mission (TRMM) and Rossi X-Ray Timing Explorer (XTE) both employ rigid panel arrays. Available power supplied by typical rigid panel arrays range from very small to in excess of 100 kW.

10.5.3 Flexible Fold-out Arrays

Flexible fold-out arrays are attractive for missions that require several kilowatts of power because of their high specific power, high packaging efficiency (low stowed volume), and simple deployment system. These arrays are generally designed in two basic configurations:

1. Flexible flat panel array with linear deployment as shown in Figure 10.12.
2. Flexible round panel array with circular deployment as shown in Figure 10.13.

These arrays have flexible or semiflexible panels that are stowed for launch with accordion folds between each panel. On reaching an appropriate orbit, these are unfurled



Figure 10.11 Rigid panel GaAs solar array (Picture courtesy of NASA). (The PV array is the two rectangular panels of five modules each)

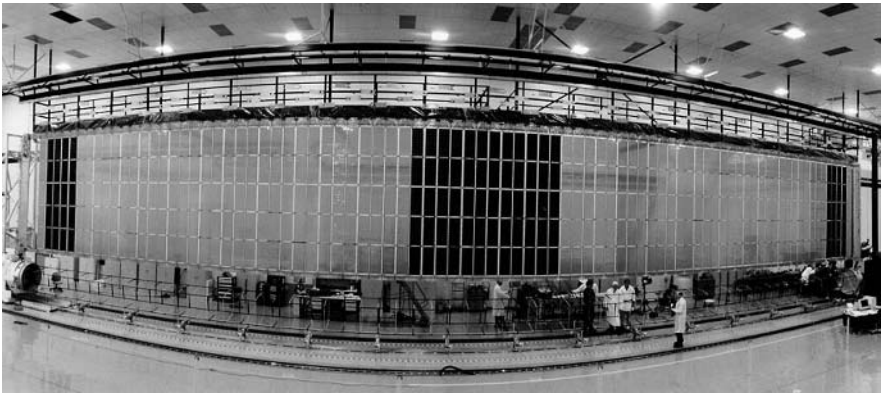


Figure 10.12 ISS array with linear deployment. (Figure courtesy of NASA)

by means of an Astromast™, an Ablemast™, or some other similar device. The specific power of these types of arrays varies from 40 to 100 W/kg, depending on the cell type, power, mission-reliability requirements, spacecraft orientation and maneuverability capabilities, and safety requirements. Initially, they were marketed as a significant improvement in power produced per unit mass. However, even though flexible arrays have an excellent figure-of-merit in this regard, the best rigid honeycomb panels have thus far matched their specific power performance. Very large flexible blanket solar arrays present complex structural and spacecraft design issues. This type of array is used on the MIL-STAR series of spacecraft, on the TERRA spacecraft, and on the ISS (see Figure 10.2).

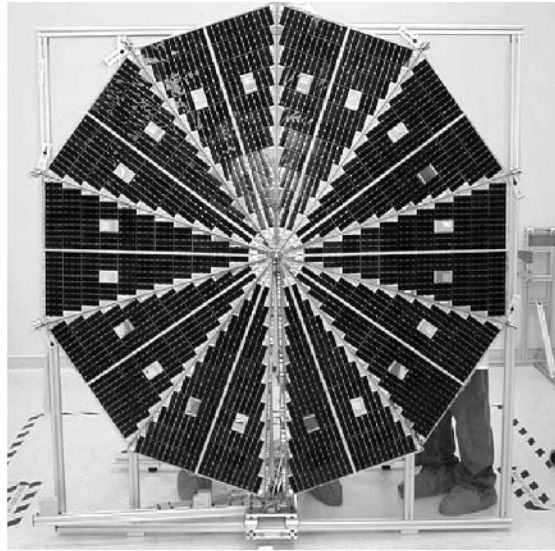


Figure 10.13 Flexible round panel array with circular deployment. (Picture courtesy of AEC-ABLE)

TRW, Inc., developed a flexible flat panel/rectangular array in the late 1980s, known as the Advanced Photovoltaic Solar Array (APSA), under a contract with NASA/JPL [50]. A similar array development was performed with DOD support. These arrays were based on the same fundamental concept of using polyimide panels stretched between lightweight hinges that could be deployed by an extendible mast. Silicon cells with an average AM0 efficiency of 14% were used for the arrays. The structure (mast, release motor, containment box) accounted for $\sim 51\%$ of the array mass with the panel assembly (polyimide substrate, solar cells, cover glass, and interconnect tabs, hinges, wiring harness) making up the balance.

The original APSA design was for 130 W/kg at 5.3 kW BOL in GEO. However, the specific power of this type of array does not scale linearly. The low-power arrays of this design had a specific power on the order of 40 to 60 W/kg. Projected BOL and EOL specific power of the APSA array for both Si and GaAs cells available in the early 1990s are given in Figure 10.14.

The Terra satellite uses an APSA-type array. The specific power of this array is only ~ 40 W/kg. This was due to the necessity of reinforcing the stowage box because the box could not be stiffened by the spacecraft structure as APSA had assumed. Also, a stronger and heavier substrate than that APSA had assumed would be possible was used. The ISS Array also had a BOL specific energy of 40 W/kg owing to additional maneuverability and safety and reliability requirements put on the arrays [13].

10.5.4 Thin-film or Flexible Roll-out Arrays

The flexible roll-out array is similar to the accordion-folded array mentioned earlier, except the fact that the semiflexible or flexible substrate is rolled onto cylinder for launch.

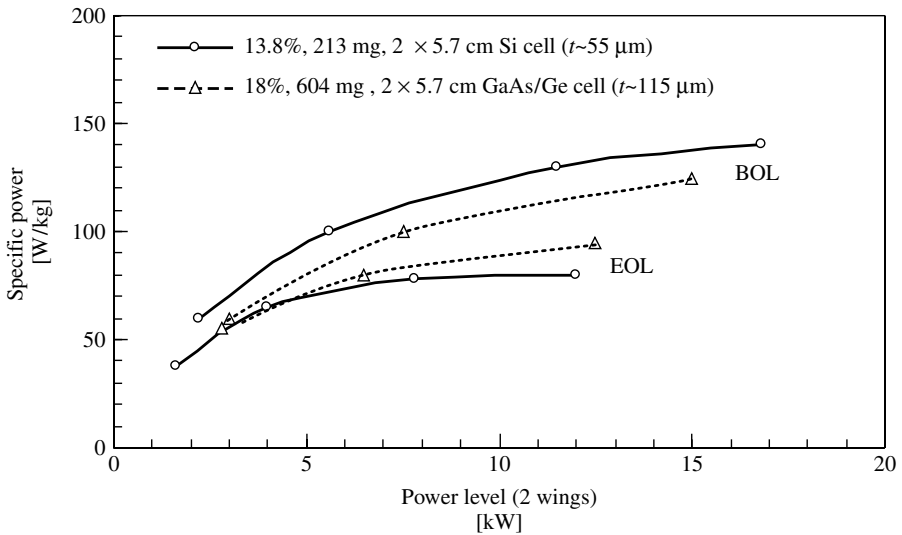


Figure 10.14 Projected specific power of the APSA array with various cell technologies [13]

The Hubble Space Telescope used such a roll-out array (see Figure 10.15). It contained a polyimide blanket in a roll-up stowed configuration. The array was deployed by a tubular, extendable boom (Bi-STEM) deployment system. The flexible roll-out array design was developed for the US Air Force.

After eight years in orbit, the solar arrays on Hubble were replaced on orbit owing to degradation [51]. During the repair mission, delamination of the solar array bus bars was observed and it was also noticed that two of the hinge pins had started to creep out. One of the arrays was returned to Earth to be studied, while the other array was jettisoned into space. The returned solar array was shipped to ESA for further study. These roll-out arrays were replaced with rigid panels that were thought to be more reliable.

AFRL has begun a \$6 M, three-year program with two prime contractors (Boeing and Lockheed Martin) to investigate and design complete arrays uniquely tailored to thin-film solar cells. The SquareRigger™ solar array being developed by AEC-ABLE is a flexible blanket system composed of modular “bays.” This array is attempting to combine an ultra-high-power capability (>30 kW) with a high stowed packaging efficiency. The SquareRigger™ solar array system is projected to achieve a specific power between 180 to 260 W/kg BOL, depending on the type of cells used. A SquareRigger™ system using thin-film cells is projected to offer an order-of-magnitude reduction in cost over conventional rigid panel systems.

10.5.5 Concentrating Arrays

Photovoltaic concentrating arrays have been proposed for missions to outer planetary missions, solar electric propulsion missions, and missions that operate in high-radiation environments. These arrays are attractive for these missions because they have the potential to provide a high specific power, higher radiation tolerance, and improved performance in

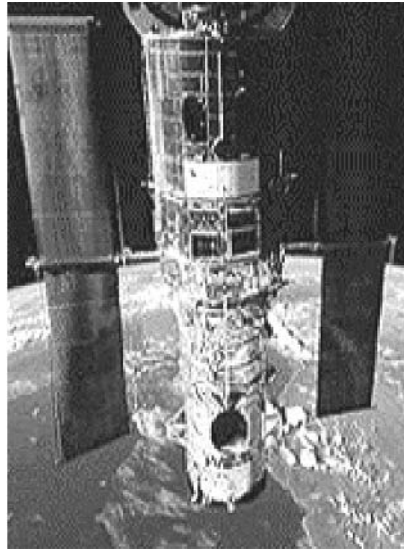


Figure 10.15 Roll-out arrays used on the Hubble space telescope. (Photo courtesy of NASA)

LILT environments. The technical issues in using concentrating arrays are precision pointing, thermal dissipation, nonuniform illumination, optical contamination, environmental interactions, and complexity of deployment. They can also decrease overall spacecraft reliability because a loss of pointing may cause significant power loss to the spacecraft.

Reflective systems can have concentration ratios from 1.6X to over 1000X, with a practical limit of around 100X. Refractive designs are generally limited to the range of about 5X to 100X, with a practical limit of around 20X. Solar energy may be focused on a plane, line, or point depending on the geometry of the concentrator design. These concentrators may be small and numerous if used in a distributed focus design or they may be a single large concentrator as in a centralized focus design.

AstroEdge™ array on the NRO STEX spacecraft, launched in October 1998, was the first spacecraft to use a concentrator as its main power source. This system used a reflective trough design with a nominal 1.5X concentration. The arrays were successfully deployed and cell currents were slightly higher than predicted. Thermal problems did occur on some of the panels owing to the higher concentrator operating temperature.

The Deep Space 1 spacecraft launched in October 1998 used SCARLET concentrator arrays to provide power to its ion propulsion engines (see Figure 10.16) [14]. Its two arrays were capable of producing 2.5 kW at 100VDC. The Scarlet array was developed by AEC-ABLE under a program sponsored by BMDO.

The SCARLET array has a refractive linear distributed focus with a 7.5X concentration ratio. The array has 720 lenses to focus sunlight onto 3600 solar cells. Deep Space 1 has two SCARLET solar array wing assemblies. Each assembly is made up of a composite yoke standoff structure, four composite honeycomb panel assemblies, and four lens frame assemblies. High-efficiency triple-junction GaInP₂/GaAs/Ge cells were used in this array.

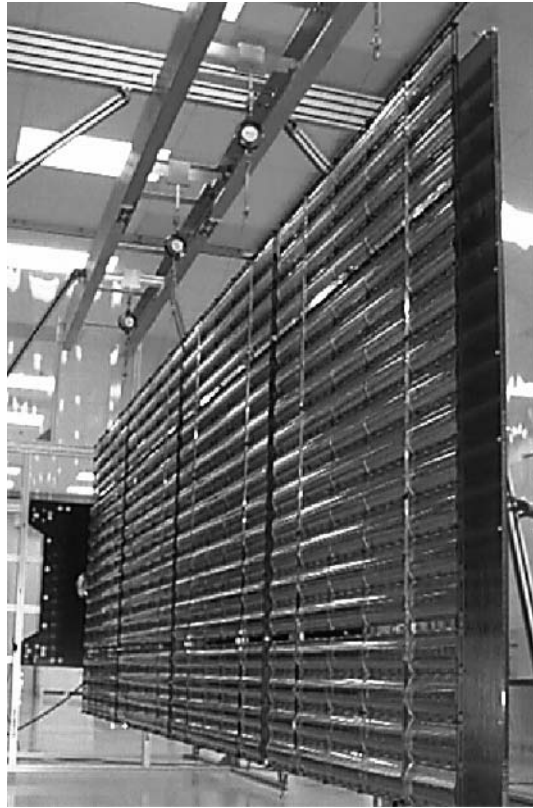


Figure 10.16 The SCARLET array used on Deep Space 1

The first commercial concentrator array developed for space was the Boeing 702. It was used on the Galaxy XI spacecraft and was deployed on January 12, 2000. It has a reflective planar centralized focus concentrator design in which the sun's rays are reflected onto a single rectangular plane of solar cells. It used thin-film reflectors and had a 1.7X concentration. It was designed for power levels of 7 to 17 kW over a 16+ year design life. The array deployed as expected and its initial power output was within the expected range. However, its concentrator surfaces degraded very quickly while in orbit. The specific power of this array was ~ 60 W/kg using 24% efficient MJ solar cells. The similar Boeing 601 bus, which uses an ordinary planar solar array, is limited to about 15 kW of power owing to the array stowed volume limitations.

10.5.6 High-temperature/Intensity Arrays

Missions to Mercury and other missions with close encounters to the sun (i.e. solar probe) have generated the need for cells and arrays that are capable of operating in high-light intensity, high-radiation, and high-temperature environments. Two missions that had to contend with such an environment have already flown. Helios A, which reached

0.31 Astronomical Units (AU) – the average Earth to sun distance – was launched on December 10, 1974 and Helios B, which reached 0.29 AU, was launched on January 15, 1976. These spacecraft used ordinary silicon cells that were modified for high-intensity use and had second surface mirrors to cool the array. The remainder of their technology was very similar to what is used on standard arrays. In addition to these missions, the upcoming MESSENGER Discovery mission is planned for travel to 0.31 AU. Its solar array design is already under development.

The current solar array technology can meet the needs of MESSENGER or other spacecraft that approach the sun to about 0.3 AU, but with reduced performance and increased risk compared to other applications. Further progress is required in both cell and array development for closer encounters to the sun. The common feature to the high-temperature and high-intensity solar arrays that have operated thus far is the replacement of a significant fraction of the solar cells by optical solar reflectors (OSRs). These are mirrors that help control the array temperature near the sun at the cost of reduced power at larger distances.

The MESSENGER design also off-points the array as the spacecraft nears the sun to keep the array below 130°C. The array is designed to tolerate pointing at the sun for a maximum of 1 h (probably much longer). However, it will be unable to function under this extreme condition (i.e. 260°C).

The US Air Force and BMDO also developed some high-temperature arrays in the late 1980s. The Survivable CONcentrating Photovoltaic Array (SCOPA) and SURvivable POWER System (SUPER) were designed to be capable of surviving laser attack. These were concentrator arrays that directed the incident laser light away from the solar cells. Although the laser light would not impinge directly, the arrays' temperature would increase dramatically and thus the arrays needed to withstand several hundred degrees Celsius.

The high-temperature survivability of SCOPA and SUPER was achieved through changes to the contact metallization and through the use of diffusion barriers in the GaAs cells used. Both Tecstar and Spectrolab developed the cells in conjunction with this effort. Other smaller companies such as Astropower, Kopin, and Spire have also worked on developing high-temperature cells. GaAs cells reaching an AM0 efficiency of 18% were produced that degraded less than 10% under one-sun after annealing in vacuum for 15 min at 550°C. Concentrator cells were produced that survived repeated 7-min excursions to 600°C. These same cells exhibited only 10% loss with exposure to 700°C. NASA is also currently funding an effort to develop wide band gap solar cells for high-temperature/high-intensity environments. Cells using materials such as SiC, GaN, and AlGaInP are being developed [52]. These cells may also benefit from high-emissivity selective coatings that will limit the unusable IR entering the solar cells and reduce their steady-state temperature.

10.5.7 Electrostatically Clean Arrays

There is an entire class of proposed missions designed to study the Sun–Earth Connection (SEC). These spacecraft typically measure the fields and particles associated with the solar wind. This requires that arrays be developed that do not distort the local environment

or be electrostatically “clean.” These arrays must have their voltage separated from the space plasma and the array must be maintained at the same potential as the spacecraft. This is usually accomplished by coating the cell cover glass and arrays between the cells with a conductor. Since the coating for the cover glass must be transparent, a transparent conducting oxide (TCO) such as indium tin oxide is used. The coatings between the cells must not short them out, so an insulating coating must first be applied to all of the interconnects before the conductive coating or “v” clips. All of this must be done within a thickness of ~ 0.08 mm and within a width of about 0.8 mm.

Fabricating an electrostatically clean array presently costs three to six times as much as a typical array. This is due in large part to the hand labor involved in developing such arrays. These arrays are also less reliable due to the lack of robustness of the conductive coatings used to maintain the equipotential. In addition, these arrays are also generally body-mounted, which cuts down on the available power to the spacecraft (i.e. pointing issues, etc.). The power is also limited due to the thicker cover glass that is employed owing to the high-radiation environment associated with SEC missions. Unfortunately, there is not a wide knowledge base on how to develop electrostatically clean arrays. This was demonstrated in the cost of developing the Fast Auroral Snapshot (FAST) solar array. The electrostatically clean body-mounted solar panels for FAST cost in excess of \$7400 per test condition watt.

The use of monolithic diodes on the latest generation of MJ solar cells could prove to be a tremendous advantage in developing electrostatically clean arrays. The presence of antennas, booms and outcroppings from a body-mounted array, requires that solar cells have bypass diodes to reduce the shadowing losses and potential damage to the arrays. The new built-in diodes will obviate the need and the expense involved in adding the diodes to the array circuitry. The NASA Goddard Space Flight Center (NASA-GSFC) recently funded Composites Optics Incorporated (COI) to study electrostatically clean arrays through the Solar Terrestrial Probe (STP) Program’s Magnetospheric Multiscale (MMS) and Geospace Electrodynamics Connection (GEC) projects. COI will be supplying the electrostatically clean solar panels for the Communication/Navigation Outage Forecast System (CNOFS).

10.5.8 Mars Solar Arrays

Mars orbiters have used PV arrays that are quite similar to those used in Earth orbit with good results. However, Mars surface missions, in which the solar spectrum is depleted at short wavelengths, causes the efficiency of the cells to be lower than that if the cells were operated above the atmosphere of Mars. The cell efficiency is reduced by about 8% (relative %). In addition, the effect of dust accumulating on arrays was observed on the Mars Pathfinder mission by monitoring the J_{SC} of cells exposed to the environment whose short-circuit current could be monitored on a routine basis. One cell indicated an increase in obscuration of about 0.3%/sol for the first 20 sols (note that a “sol” is a Martian day of 24.6 h). The other cell indicated that over a longer period of ~ 80 sols, the obscuration flattened out and seemed to be approaching an asymptote of around 20% obscuration [53]. Cells that are “tuned” to the Martian solar spectrum and methods for mitigating dust obscuration will be necessary to produce efficient arrays for Mars surface power.

10.5.9 Power Management and Distribution (PMAD)

There are a number of different devices involved in efficiently connecting a space solar array to its intended loads. A system for managing and distributing the power consists of regulators, converters, charge controllers, blocking diodes, and wiring harness [54]. This system must condition the power to maintain the appropriate current and voltage levels to the power subsystems under varying illumination, temperature, and with cell degradation over the mission lifetime. The electrical bus for this system must also be able to isolate individual panel faults in such a way that the entire spacecraft will not lose total power in the case of a panel failure. The entire Power Management and Distribution (PMAD) typically will account for 20 to 30% of the entire power system mass in the case of a conventional array. This can be reduced if an unregulated system is used.

Very often solar power generation is combined with a battery storage element that can be used in eclipse. In order to provide the appropriate charging conditions for the batteries and to avoid overcharging and heating, peak-power tracking (PPT) or direct energy transfer (DET) are used. PPT controls the arrays, so they only produce the power levels required by means of a DC-DC converter in series with the array. Peak-power tracking is typical on missions that need less power at EOL. A PPT system uses about 5% of the power produced by the array. Systems using DET operate using the fixed voltage of the array and shunt the excess power through shunt resistors. The fixed voltage of the array is chosen to be close to the EOL maximum power point voltage. These systems generally have a higher EOL efficiency and therefore are used on longer missions.

On an unregulated bus with a battery storage component, the loads will experience whatever voltage is currently on the batteries. This can lead to a large swing in voltage (i.e. 20%) to the load depending on the battery chemistry and the depth of discharge. In a quasi-regulated system that employs a simple battery charger, the loads will be maintained at a voltage that is higher than the voltage on the batteries during charging. However, the loads will track the decrease in battery voltage as they are discharged (i.e. during eclipse). A fully regulated system that uses a regulator will maintain a constant load voltage independent of the charging or the discharging cycle. A fully regulated system requires more elements and thus increases the PMAD complexity and mass. There will also be a decrease in system efficiency due to the power loss from overall bus resistance. However, it does provide more reliability and increases battery life. The resistive power losses can be minimized by using a higher bus voltage. The maximum voltage limits on an array is set by the voltage that the exposed parts of the power system can hold off without discharging through the space plasma (i.e. ~ 50 V for LEO).

10.6 FUTURE CELL AND ARRAY POSSIBILITIES

10.6.1 Low Intensity Low Temperature (LILT) Cells

The term LILT is used to refer to solar arrays operating under conditions encountered at distances greater than 1 AU from the sun. Typical Earth-orbiting solar arrays have steady-state illuminated temperatures of approximately 40 to 70°C. The efficiency of most cells increases down to about -50°C . This temperature would correspond to around

3 AU. Currently available solar cells have uncertain performance under LILT conditions. NASA Glenn Research Center has initiated a program to evaluate solar cells under LILT conditions and to look for ways of enhancing their performance.

10.6.2 Quantum Dot Solar Cells

A recent approach to increasing the efficiency of thin-film PV solar cells involve the incorporation of quantum dots [55]. Semiconductor quantum dots are currently a subject of great interest mainly due to their size-dependent electronic structures, in particular the increased band gap and therefore tunable optoelectronic properties. To date these nanostructures have been primarily limited to sensors, lasers, LEDs, and other optoelectronic devices. However, the unique properties of the size-dependent increase in oscillator strength due to the strong confinement exhibited in quantum dots and the blue shift in the band gap energy of quantum dots are properties that can be exploited for developing PV devices that offer advantages over conventional photovoltaics. Theoretical studies predict a potential efficiency of 63.2%, for a single size quantum dot, which is approximately a factor of 2 better than any SOA device available today. For the most general case, a system with an infinite number of sizes of quantum dots has the same theoretical efficiency as an infinite number of band gaps or 86.5%. See Chapter 4 for a more complete discussion of quantum dots and theoretical efficiencies.

A collection of different size quantum dots can be regarded as an array of semiconductors that are individually size-tuned for optimal absorption at their band gaps throughout the solar energy emission spectrum. This is in contrast with a bulk material in which all photons with $E > E_g$ are absorbed at the same energy, that is, the band gap. Their excess energy $E - E_g$ is wasted. In addition, bulk materials used in solar energy cells suffer from reflective losses at energies about the band gap, whereas for individual quantum dots reflective losses are minimized. Some recent work has shown that quantum dots may offer some additional radiation resistance and favorable temperature coefficients [56].

10.6.3 Integrated Power Systems

NASA has also been working to develop lightweight, integrated space power systems on small-area flexible substrates [57]. These systems generally consist of a high-efficiency thin-film solar cell, a high-energy density solid-state Li-ion battery, and the associated control electronics in a single monolithic package. These devices can be directly integrated into microelectronic or micro-electromechanical systems (MEMS) devices and are ideal for distributed power systems on satellites or even for the main power supply on a nanosatellite. These systems have the ability to produce constant power output throughout a varying or intermittent illumination schedule as would be experienced by a rotating satellite or “spinner” and by satellites in a LEO by combining both generation and storage.

An integrated thin-film power system has the potential to provide a low-mass and low-cost alternative to the current SOA power systems for small spacecraft. Integrated thin-film power supplies simplify spacecraft bus design and reduce losses incurred through energy transfer to and from conversion and storage devices. It is hoped that this simplification will also result in improved reliability.

The NASA Glenn Research Center has recently developed a microelectronic power supply for a space flight experiment in conjunction with the Project Starshine atmospheric research satellite (<http://www.azinet.com/starshine/>).

This device integrates a seven-junction small-area GaAs monolithically integrated photovoltaic module (MIM) with an all-polymer $\text{LiNi}_{0.8}\text{Co}_{0.2}\text{O}_2$ lithium-ion thin-film battery. The array output is matched to provide the necessary 4.2 V charging voltage, which minimizes the associated control electronic components. The use of the matched MIM and thin-film Li-ion battery storage maximizes the specific power and minimizes the necessary area and thickness of this microelectronic device. This power supply was designed to be surface-mounted to the Starshine 3 satellite, which was ejected into a LEO with a fixed rotational velocity of 5° per second. The supply is designed to provide continuous power even with the intermittent illumination due to the satellite rotation and LEO [58].

10.6.4 High Specific Power Arrays

To achieve an array specific power of 1 kW/kg, a much higher cell specific power will be necessary. Similarly, the blanket specific power (i.e. interconnects, diodes, and wiring harnesses) must be over 1 kW/kg as well. The APSA assessment determined that the mass of the deployment mechanism and structure is essentially equal to the blanket mass for a lightweight system [21]. Therefore, a blanket specific power of approximately 2000 W/kg would be necessary to achieve a 1-kW/kg array. NASA is currently sponsoring an effort by AEC-ABLE Engineering to develop lightweight thin-film array deployment systems.

Gains in array specific power may be made by an increase in the operating voltage. Higher array operating voltages can be used to reduce the conductor mass. The APSA was designed for 28 V operation at several kilowatts output, with the wiring harness comprising $\sim 10\%$ of the total array mass, yielding a specific mass of ~ 0.7 kg/kW. If this array was designed for 300-V operation, it could easily allow a reduction of the harness specific mass by at least 50%. This alone would increase the APSA specific power by 5% or more without any other modification.

The extremely high specific power arrays that need to be developed for SEP and SSP applications will require lightweight solar arrays that are capable of high-voltage operation in the space plasma environment. SEP missions alone will require 1000 to 1500 V to directly power electric propulsion spacecraft (i.e. no voltage step-up is required to operate the thrusters). NASA has proposed a thin-film stand-alone array specific power that is 15 times the SOA III-V arrays, an area power density that is 1.5 times that of the SOA III-V arrays, and specific costs that are 15 times lower than the SOA III-V arrays [59].

10.6.5 High-radiation Environment Solar Arrays

There are several approaches to mitigating the effects of a high radiation on a solar array. The simplest is to employ thick cover glass (assuming that a commercial source could be developed). Thick cover glasses protect the cell from the highly damaging low-energy protons, but will cause a significant decrease in the specific power of the array. However, this can be reduced if one adopts a concentrator design, assuming of

course that the additional elements associated with the concentrator can withstand the high-radiation environment as well. A different approach is to try and develop cells that are more radiation-resistant. Several of the materials that are being investigated for high-temperature/high-intensity missions have also shown good radiation resistance. However, these will not be suited to the high-radiation missions involving LILT. Many of the high-radiation NASA missions being considered occur at distances much greater than 1 AU. Thin films may offer a possibility since they have demonstrated some advantages with regard to radiation tolerance as previously mentioned, provided the problem of their low efficiencies are solved.

10.7 POWER SYSTEM FIGURES OF MERIT

There are many figures of merit that must be considered in developing an SSP system (i.e. specific mass, specific power, cost per watt, temperature coefficients, and anticipated radiation degradation of the solar cells used).

The radiation hardness and the temperature coefficients for the III-V multijunction cells are significantly better than Si cells, as previously discussed. This leads to significantly higher EOL power level for a multijunction cell as compared to a Si cell. This is shown in Table 10.8, where the BOL cell efficiencies at room temperature and the typical EOL cell efficiencies for LEO and GEO operating temperatures and radiation environments are presented.

The difference in radiation degradation can have a huge impact on power system design. For example, if the area for a typical rigid panel is approximately 8 m^2 and the area of a typical solar cell is 24 cm^2 , using a panel packing factor of 0.90 will allow the panel to have 3000 cells. Under GEO conditions, this panel populated with high-efficiency Si cells will produce 1.2 kW of EOL power. The EOL power could almost be doubled to 2.2 kW if it were populated with SOA triple-junction cells.

Table 10.8 A comparison of relative radiation degradation of 75- μm multijunction cells and high-efficiency Si under GEO and LEO operation [52]

Solar cell technology	BOL efficiency @ 28°C [%]	EOL efficiency on orbit [%]
<i>GEO conditions (60°C) – 1-MeV, 5E14 e/cm²</i>		
HE Si	14.1	12.5
2J III-V	20.9	20.0
3J III-V	23.9	22.6
<i>LEO conditions (80°C) – 1-MeV, 1E15 e/cm²</i>		
HE Si	13.4	10.6
2J III-V	19.7	18.1
3J III-V	22.6	20.3

Alternatively, the solar arrays populated with high-efficiency Si cells would need to be 77% larger than arrays using triple-junction cells in order to deliver the equivalent amount of EOL power in GEO and 92% larger in LEO.

The large difference in size between solar arrays populated with Si and MJ cells is very significant in terms of stowage, deployment, and spacecraft attitudinal control. This is especially true for very high-powered GEO communication satellites in which Si solar array area can exceed 100 m². The comparable array with triple-junction cells, although by no means small, would have an area of ~59 m². The array size will impact the spacecraft's weight, volume (array stowage), and system requirements on spacecraft attitude control systems (additional chemical fuel).

Three important figures of merit used in power system optimization are EOL area power density (W/m²), specific weight (W/Kg), and cost (\$/W). Representative values for the various SOA cell technologies are listed in Table 10.9.

The EOL power per unit area for a MJ cell is significantly better than a Si cell. However, the EOL specific weight for Si is almost a factor of two greater than a MJ cell. This results in a slightly smaller EOL cost per watt for a high-efficiency Si. This demonstrates the dramatic reduction in cost of MJ cells over the past few years.

If one considers the mass of the necessary array components (i.e. panel substrate, face sheet, adhesive, hinges, insulators, wiring, etc.) along with equivalent power per area for the different cell types, and also the cost involved in having the cells interconnected and covered (CIC) and laid on rigid panels, then the cost for developing an array using MJ cells is slightly less than that for HES cells. The EOL specific weight values at the CIC (with 100- μ m ceria-doped microsheet cover glass) and the panel levels for these cells and the normalized cost per watt for the panels is shown in Table 10.10. A similar comparison with somewhat less expensive 100- μ m high-efficiency Si cells (at the panel level) shows a slightly smaller cost advantage for the multijunction cells. The 100- μ m Si

Table 10.9 EOL area power density (W/m²), specific weight (W/Kg), and normalized (to HE Si) cost (\$/W) for high-efficiency Si, dual-junction (2J), and triple-junction (3J) bare solar cells [52]

Solar cell technology	[W/m ²]	[W/Kg]	Normalized (to HE Si) cell cost [\$/W]
<i>GEO conditions (60°C) – 1-MeV, 5E14 e/cm²</i>			
75 μ m HE Si	169	676	1.00
2J III-V	271	319	1.38
3J III-V	306	360	1.22
<i>LEO conditions (80°C) – 1-MeV, 1E15 e/cm²</i>			
75 μ m HE Si	143	574	1.00
2J III-V	245	288	1.29
3J III-V	275	323	1.15

Table 10.10 EOL specific weight (W/Kg) at the CIC and panel levels for three-mil high-efficiency Si, dual-junction (2J), and triple-junction (3J) cells [52]

Solar cell technology	CIC specific power [W/kg]	Panel specific power [W/kg]	Normalized (to HE Si) panel cost [\$/W]
<i>GEO conditions (60°C) – 1-MeV, 5E14 e/cm²</i>			
75 μm H.E. Si	261	75	1.00
2J III-V	219	95	0.9
3J III-V	248	108	0.8
<i>LEO conditions (80°C) – 1-MeV, 1E15 e/cm²</i>			
75 μm H.E. Si	221	63	1.00
2J III-V	199	86	0.84
3J III-V	223	97	0.75

cells are less radiation-hard and have lower specific power (W/Kg) than 75-μm Si cells, but they cost about 35% less.

Currently conventional space Si cells are less expensive than MJ cells at the panel level. However, their EOL power is much lower than either the high-efficiency Si cells or the MJ cells. The increased mass and area that their usage entails would have to be considered against the cost savings and other mission considerations in any comparative study.

Engineers have worked on ways to improve space solar cells and arrays in terms of all the important figures of merit since the early days of our space program. Numerous mission studies have shown that even extremely high array costs can be worth the investment when they result in lower array mass. In general, mass saving in the power system can often be used by payload. If the revenue generated by this payload (i.e. more transmitters on a communications satellite) is greater than the cost of higher-efficiency solar cells, the choice is rather an easy one to make. However, often more instrument capabilities will require more support from the spacecraft (e.g. command and data handling, structure, attitude control, etc.) as well as more power. These additions can negate any apparent advantage to the overall spacecraft.

REFERENCES

1. Chapin D, Fuller C, Pearson G, *J. Appl. Phys.* **25**, 676–681 (1954).
2. Jenny D, Loeferski J, Rappaport P, *Phys. Rev.* **101**, 1208–1212 (1956).
3. Easton R, Votaw M, *Rev. Sci. Instrum.* **30**, 70–75 (1959).
4. Loeferski J, *J. Appl. Phys.* **27**, 777–785 (1956).
5. Jackson E, *Trans. of the Conf. on the Use of Solar Energy*, Vol. 5, 122–128 (Tucson, AZ, 1955).
6. *Bell Syst. Tech. J.* **42** (1963).
7. Solar Cell Array Design Handbook, *JPL SP43-38*, Vol. 1, 1.1–2 (1976).

8. Statler R, Curtin D, *Proc. International Conf. on the Sun in the Service of Mankind*, 361–367 (1973).
9. Reynolds D, Leies G, Antes L, Marburger R, *Phys. Rev.* **96**, 533 (1954).
10. Lebrun J, *Proc. 8th IEEE Photovoltaic Specialist Conf.*, 33–37 (1970).
11. North N, Baker D, *Proc. 9th IEEE Photovoltaic Specialist Conf.*, 263–270 (1972).
12. Bailey S, Raffaele R, Emery K, *Proc. 17th Space Research and Technology Conf.* (2001).
13. Hague L *et al.*, *Proc. 31st Intersociety Energy Conversion Engineering Conf.*, 154–159 (1996).
14. Stella P *et al.*, *Proc. 34th Intersociety Energy Conversion Engineering Conf.* (1999).
15. Bailey S, Landis G, Raffaele R, to be published in *The Proc. 6th European Space Power Conf.* (2002).
16. Bailey S *et al.*, “Solar Cell and Array Technology for Future Space Science Missions”, Internal NASA report to Code S (2002).
17. Bücher K, Kunzelmann S, *Proc. 2nd World Conference and Exhibition on Photovoltaic Solar Energy Conversion*, 2329–2333 (1998).
18. Green M *et al.*, *Prog. Photovolt.* **6**, 35–42 (1998).
19. Green M *et al.*, *Prog. Photovolt.* **9**, 287–293 (2001).
20. King R *et al.*, *Proc. 28th IEEE Photovoltaic Specialist Conf.*, 982–985 (2000).
21. Reynard D, Peterson D, *Proc. 9th IEEE Photovoltaic Specialist Conf.*, 303 (1972).
22. Crabb R, *Proc. 9th IEEE Photovoltaic Specialist Conf.*, 185–190 (1972).
23. Bailey S *et al.*, *Proc. 2nd World Conf. Photovoltaic Solar Energy Conversion*, 3650–3653 (1998).
24. Ferguson D, *Interactions between Spacecraft and their Environments*, AIAA Paper #93-0705, NASA TM 106115 (1993).
25. Landis G, Bailey S, *AIAA Space Sciences Meeting*, AIAA-2002-0718 (Reno, NV, 2002).
26. Flood D, *Proc. NHTC'00, 34th National Heat Transfer Conf.* (2000).
27. Anspaugh B, *GaAs Solar Cell Radiation Handbook*, 6–54, NASA JPL Publication 96-9 (1996).
28. Marvin D, Nocerino J, “Degradation Predictions for Multijunction Solar Cells on Earth-Orbiting Spacecraft”, Aerospace Report No. TOR-2000(1210)-2, 9 (2000).
29. Walters R *et al.*, *Technical Digest of the International PVSEC-11*, 813–814 (1999).
30. Walters R, *Proc. 15th SPRAT*, 30–34 (1997).
31. Tada H, Carter J, Anspaugh B, Downing R, *Solar Cell Radiation Handbook*, 3–82, JPL Publication 82-69 (1982).
32. Fahrenbruch A, Bube R, *Fundamentals of Solar Cells*, Chap. 2, Academic Press, Boston (1983).
33. Landis G, *Proc. 13th SPRAT*, 385–399 (1994).
34. Scheiman D *et al.*, *Proc. 17th SPRAT Conference* (Cleveland, OH, Sept. 11–13, 2001).
35. Bailey S, Flood D, *Prog. Photovolt.* **6**, 1–14 (1998).
36. Keener D *et al.*, *Proc. 26th IEEE Photovoltaic Specialist Conf.*, 787–281 (1997).
37. Hoffman D *et al.*, *Proc. 35th IECEC*, AIAA-2000-2919 (2000).
38. Bailey S, Hepp A, Raffaele R, *Proc. 36th Intersociety Energy Conversion Engineering Conference*, 235–238 (2001).
39. Guha S *et al.*, *Proc. 2nd World Conf. PV Solar Energy Conversion*, 3609–3612 (1998).
40. Deng X, Povolny H, Han S, Agarwal P, *Proc. 28th IEEE Photovoltaic Specialist Conf.*, 1050–1053 (2000).
41. Arya R *et al.*, *Proc. 1st World Conf. Photovoltaic Solar Energy Conversion*, 394–400 (1994).
42. Contrera M *et al.*, *Prog. Photovoltaics* **7**, 311–316 (1999).
43. Hanket G *et al.*, *Proc. 29th IEEE Photovoltaic Specialist Conf.*, 567–570 (1988).
44. Dhere N, Ghongadi S, Pandit M, Jahagirdar A, Scheiman D, *Prog. Photovoltaics* **10**, 407–416 (2002).
45. Romeo A, Blatzner D, Zogg H, Tiwari A, *Mat. Res. Soc. Symp. Proc.* Vol. 668, H3.3.1–3.6 (2001); results with 11% AM1.5 efficiency on polyimide have been submitted for publication.
46. Ferekides C *et al.*, *Thin Solid Films* 361–362, 520–526 (2000).
47. Marshall C *et al.*, *IECEC*, 1999-01-2550 (1999).

48. Messenger S *et al.*, *Proc. 16th European Photovoltaic Energy Conference*, 974–977 (2000).
49. Tringe J, Merrill J, Reinhardt K, *Proc. 28th IEEE Photovoltaic Specialist Conf.*, 1242–1245 (2000).
50. Stella P, West J, *Proc. 21st IEEE Photovoltaic Specialist Conf.*, 1362–1366 (1990).
51. Gerlach L, Fournier-Sirce A, Fromberg A, Kroehnert S, *Proc. 21st IEEE Photovoltaic Specialist Conf.*, 1308–1312 (1990).
52. Scheiman D, Landis G, Weizer V, *AIP Conf. Proc.* **458**, 1–6 (1999).
53. Landis G, *Acta Astronautica* **38**, 1 (1996).
54. Larson W, Pranke L, Eds, *Human Spaceflight Mission Analysis and Design*, McGraw Hill, New York (1999).
55. Luque A, Marti A, *Phys. Rev. Lett.* **78**, 5014 (1997).
56. Leon R *et al.*, *Appl. Phys. Lett.* **76**, 2071 (2000).
57. Hoffman D, Raffaele R, Landis G, Hepp A, *Proc. 36th IECEC*, IECEC-2001-AT-21 (2001).
58. Raffaele R *et al.*, *Proc. 36th IECEC*, IECEC2001-AT-66 (2001).
59. Bailey S *et al.*, *Proc. 17th Euro. Photovoltaic Solar Energy Conference*, 2137–2143 (2001).

11

Photovoltaic Concentrators

Richard M. Swanson

SunPower Corporation, Sunnyvale, California

11.1 INTRODUCTION

Photovoltaic (PV) concentrators use lenses or mirrors to concentrate sunlight onto PV cells. This allows for a reduction in the cell area required for producing a given amount of power. The goal is to significantly reduce the cost of electricity generated by replacing expensive PV converter area with less expensive optical material. This approach also provides the opportunity to use higher performance PV cells that would be prohibitively expensive without concentration. As a result, concentrator modules can easily exceed 20% energy conversion efficiency. In the future, the use of multijunction cells is expected to increase this to over 30%. While the concept is simple, and has been examined since the time of the earliest interest in terrestrial photovoltaics, the practice has proven to be deceptively difficult. Concentrator research has focused much effort on the PV cells themselves, which are now largely developed and available commercially. The main remaining technical barriers, however, are due to the difficult cell packaging requirements stemming from the high heat flux and electrical current density, plus the need for more cost-effective and reliable tracking systems and module designs.

The main market barriers have been due to the fact that concentrating systems, which in most cases must track the sun, are not well suited to the existing PV market that serves small remote loads and, more recently, are building integrated applications. Concentrators were conceived of as a vehicle to generate large amounts of nonpolluting renewable energy. As yet, costs are still too high to compete with fossil fuel-fired generation, or even the most direct renewable competitor – wind power. The cost gap is narrowing, however, and there appears a strong likelihood that in the future concentrator systems will find cost-effective niche applications that will continue to expand as natural gas prices rise and concern over power-plant emissions increases. This chapter discusses the current state of the art in concentrating PV cells and systems and outlines issues remaining before full commercialization is possible.

This chapter is written for researchers and interested developers to be an instructive guide to the original literature in order to aid them in further development. It is not intended to be a stand-alone document. Most of the literature can be found in the various *Proceedings of the IEEE Photovoltaic Specialists Conferences* and the *European Photovoltaic Solar Energy Conferences*, along with a number of important books. Some of the material is less easily accessible in the form of various publications and reports of the US Department of Energy (DOE) and the Electric Power Research Institute (now called EPRI). Use of this latter type of material will be minimized.

The reader will be amazed at the variety of concentrator systems that have been explored. The concentration ratio (ratio of module aperture area to cell area) varies from 2 to 4 in static concentrator designs that require no sun tracking to over 1000 times in some two-axis tracking systems. The means of optical concentration includes a variety of two-axis and one-axis reflective and refractive approaches, as well as many novel means such as luminescent and holographic concentrators. While this wide variety gives support to the notion that a cost-effective approach will surely emerge, it nevertheless reminds the author of the early stage of many technology developments (such as airplanes) prior to the eventual emergence of the dominant concept (single wings with trailing rudder and elevator in the case of airplanes). In the same way as aircraft, the development of concentrators has been aided and impacted by the parallel development of materials and other technologies. For example, the once cumbersome aspect of finding and tracking the sun is now made relatively straightforward by the emergence of very low-cost computing technology, the Global Positioning System, and the like. On another path, developments in the global semiconductor industry often have direct application to concentrator cells. Examples include larger wafers, improved processing equipment, the emergence of organo-metallic chemical vapor deposition (OMCVD) for fabricating multijunction III-V cells, and improved packaging materials with superior thermal properties (e.g. AlN). Many of the technical issues facing further concentrator development can be thought of as material issues. These include the development of polymer reflectors with improved weatherability, lower cost molding methods for Fresnel lenses, and such. In other words, concentrator development takes place in the larger technology arena. New material and technology developments can come from any direction and make possible what was only a dream previously. Unfortunately, tracking the sun is still effected by the distinctly nineteenth-century technology of gears and motors. The necessity for tracking remains concentrating PV's Achilles heel.

11.1.1 The Concentrator Dilemma

In the 1970s, concentrators were originally conceived of as a technology for large power plants that provide wholesale electricity in competition with, or as replacement for, fossil fuel-generated power, that is, as a vehicle for reducing green house gasses, pollution, and for providing a renewable energy source as fossil fuels were depleted. PV markets, however, have evolved since the 1970s in a somewhat unexpected manner. Flat-plate (nonconcentrating) PV has emerged as an important and viable power source for small remote loads. In parallel, a subsidized, but vital and fast-growing, grid-connected market has emerged in many developed countries. Concentrators are not particularly suitable for these markets and have never gained a foothold in them. The issues of reliability and suitability for remote markets have plagued them from the start, and the new grid-connected

markets most often use building-integrated or roof-mounted panels, for which concentrators have been found generally unsuitable. Meanwhile, fossil fuel prices have remained low in the face of abundant supply, and the international inability to seriously confront global warming and the external costs associated with pollution have limited the market for large PV power plants.

Several additional interesting factors have compounded the hurdle facing concentrators. First, semiconductor silicon material costs have declined in inflation-adjusted dollars to a level that is only 50% more than the long-term DOE goal for “solar grade silicon” set in 1975. Second, wire sawing has evolved as a far more cost-effective wafering solution than imagined at the onset. Third, nonconcentrating cell efficiencies are higher than envisioned because of the development of cost-effective back-surface fields, screen-printed grids, and the like. Standard modules have evolved as a more competitive power source than it was thought possible. In short, the incumbent technology, wafered silicon flat-plate modules, has been enjoying the benefits usually associated with an incumbent technology.¹ Continued improvements can be expected as manufacturing experience grows ever more rapidly. Finally, electric power markets have evolved in a manner that supports small amounts of nonpolluting distributed generation as opposed to large central plants, be they fossil-fueled or PV.

Today, developers of concentrators face a dilemma – what market to target. There are two possibilities: develop highly reliable systems for smaller applications or continue with the quest for large systems that displace significant power. Several major difficulties face the small remote market. One is that the module cost is only a fraction of the total installed system cost. Having a dollar per watt less module cost, as a concentrator module might offer, results in perhaps only a 10 to 20% overall reduction in total installed system cost. Second, the requirement for tracking structures restricts installation options and applications (for instance, it limits rooftop applications that are the biggest market for grid-connected systems), and begs the need for periodic maintenance. Another is the need for the manufacturer or installer to maintain a service network that can provide periodic maintenance. The prospects do not look too good for small concentrator installations, unless cost-effective low concentration static concentrators are developed, which eliminates the need for tracking. For large installations, the issue is more closely *cost*. Here installations compete with standard generation technologies (which have established low cost, but are vulnerable to fossil fuel depletion, cost escalation, and perhaps pollution concerns) and other renewables such as biomass and wind. Wind clearly has the lead with energy costs less than 5 cents/kWh at good sites. PV can easily coexist alongside the other options owing to its unique capabilities, competitive cost, and widespread applicability and scalability. Against wind, however, PV must look more to its particular advantages. These are easier siting close to the load, more distributed resource availability, less visual impact, and the like. Can concentrating PV get costs close enough to wind to compete, given its other advantages? This is a technology and market issue that is yet to be sorted out.

It is the author’s opinion that concentrator developers can beneficially focus efforts on two approaches. The first is to continue to explore for cost-effective static concentrators

¹ In fairness, it should be noted that the other major alternative to wafered silicon, namely, thin film modules, has suffered from the same force.

that can compete in the standard flat-plate market and that use existing silicon solar-cell manufacturing infrastructure. The second is to focus on large installations and relentlessly seek lower cost through high-concentration, high-performance cells and designs that benefit from the economy of scale of large systems through artifices such as on-site assembly, automated installation, and the like. The goal must be to get large system costs below \$2.00/W. Attaining this goal is necessary, but not sufficient. Other market requirements are capturing some measure of social costs into the value stream, supportive utility transmission environment that enables renewable generators to effectively provide service, and eventually the development of new storage technologies and energy transport vectors such as hydrogen or global superconducting grids. Seen in this light, concentrators are not an immediate solution, but rather a long-range option of vital importance to the energy security of the world. Cost analyses indicate that it certainly has the possibility of becoming the low-cost PV approach in large installations. It is likely to find attractive niches initially in sun-resource-rich areas with little wind. Considerable risk investment will be needed to make it a reality. How the energy and investment climate evolves over the next few years, in the face of pollution concerns, global warming, and eventual fossil fuel depletion, is likely to dictate whether such capital will actually become available. It is hoped that this chapter helps guide researchers, policy makers, and investors to make it a reality.

This chapter begins by presenting an overview of the various types of concentrators. Then the history of concentrators is covered, followed by a section on the optical theory of concentrators, and finally a section on current concentrator research. Concentrator cells themselves operate by the same principles as nonconcentrating cells. Because of this, as well as space limitations, the design of concentrator cells is not covered in this chapter. The reader interested in the details of cell design specifically for concentrator applications is referred to the relevant literature [1, 2]. The methodology of concentrator cost projections is also not covered, although some results of this type of analysis are quoted. Further information on costs can be found in [3], as well as in many of the cited references.

11.2 BASIC TYPES OF CONCENTRATORS

Concentrators may be divided into different classes, depending on the optical means used to concentrate the light, the number of axes about which they move to track the sun, the mechanical mechanism that effects the tracking, and so forth. The major types are discussed below to acquaint the reader with the terminology. Detailed analysis of the operation of these devices can be found in Section 11.4.

11.2.1 Types of Optics

Most concentrators use either refractive lenses or reflective dishes and troughs. Lenses of any size over 5 cm in diameter will be too thick and costly to be practical; therefore, Fresnel lenses are usually chosen. A Fresnel lens may be thought of as a standard plano-convex lens that has been collapsed at a number of locations into a thinner profile. The facets may be either flat, if they are small and numerous enough, or actual sections of a curved lens surface. Fresnel lenses may be made either point-focus, in which case they

have circular symmetry about their axis, or linear focus, in which the lens has a constant cross section along a transverse axis. Such lenses focus the light into a line. Point-focus lenses usually use one cell behind each lens, whereas line-focus lenses have a linear array of cells. A particularly successful linear configuration is the domed Fresnel lens. As will be seen in the section on concentrator optics, this minimizes the image dispersion coming from chromatic aberration and flexural distortion. It also provides the lens with greater rigidity. Domed point-focus lenses have also been developed. These variations are illustrated in Figure 11.1.

The material of choice for the lens is usually Acrylic plastic (polymethyl methacrylate or PMM), which molds well and has shown good weatherability. Nevertheless, there remain some long-term durability concerns for PMMA, and so attempts to make the lens from glass, or to mold the lens material to the underside of a glass substrate, have been made. So far, these ideas have remained in the laboratory.

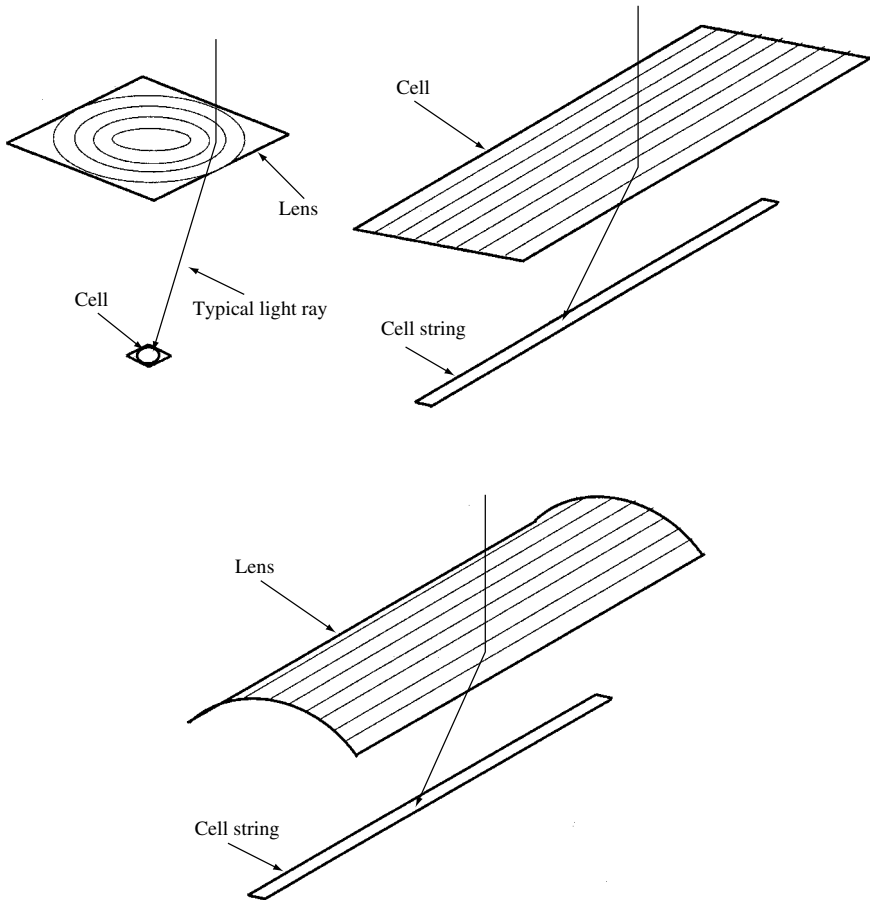


Figure 11.1 Fresnel lens configurations. (a) Point focus Fresnel lens showing a typical ray hitting the circular active area of the solar cell. (b) Linear, or one-axis, Fresnel lens focusing on a line of solar cells in a string. (c) Domed linear Fresnel Lens

Fresnel lenses are usually incorporated into modules that contain a lens, or multiple lenses in parquet, a housing to protect the backside of the lens, which is difficult to clean due to the sharp facets, and the cells. The cell may incorporate a secondary optical element (SOE) whose purpose is to further concentrate the light or to make the image more uniform. A typical Fresnel lens module is shown in Figure 11.9.

An alternative to refractive lenses is to use reflective lenses or mirrors. As is well known, a reflective surface with the shape of a parabola will focus all light parallel to the parabola's axis to a point located at the parabola's focus. Like lenses, parabolas come in a point-focus configuration (which is formed by rotating the parabola around its axis and creating a paraboloid) and line-focus configuration (which is formed by translating the parabola perpendicular to its axis). These configurations are illustrated in Figure 11.2.

Another approach is the compound parabolic concentrator (CPC) shown in Figure 11.24. Here the sides of the concentrator are parabolas; however, the focus for each side is at the opposite side of the cell and the axis of parabola a is along the direction of maximum acceptance angle, θ_{\max} . The CPC is interesting in that it is a class of concentrator called "ideal," in that it provides the maximum possible concentration given the region of the sky it sees, or alternatively for a given maximum acceptance angle. It is also termed a "nonimaging" concentrator in that output bears no relation to the image of the sun. For high concentration, a CPC is rather tall and thin, and thus its use

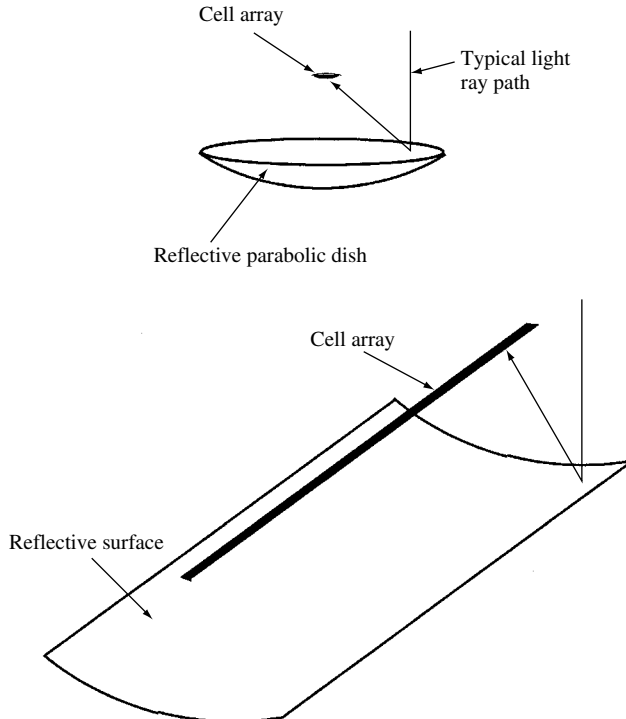


Figure 11.2 Reflective concentrator configurations. (a) Reflective paraboloid, or dish, focusing on a cell array. (b) Linear parabolic trough focusing on a line of cells

is restricted to either low concentration applications or as a secondary optical element. Nonimaging concentrators will be discussed more fully in Section 11.4.

11.2.2 Concentration Ratio

There are several definitions of concentration ratio in use. The most common is “geometric concentration ratio.” This is defined as the area of the primary lens or mirror divided by the active cell area. The active cell area is the region of the cell that is designed to be illuminated. Unlike in most nonconcentrating systems, the entire cell need not be illuminated by the primary lens. The nonilluminated edge of the cell is often provided with buss bars for electrical connection, and this need not result in an efficiency loss as would be the case in a flat-plate module. Another measure of concentration is intensity concentration, or “suns.” Since standard peak solar irradiance is often set at 0.1 W/cm^2 , the “suns” concentration is defined as the ratio of the average intensity of the focused light on the cell active area divided by 0.1 W/cm^2 . For example, if 10 W were focused onto a cell of 2-cm^2 active area, the intensity concentration would be 50 suns. If all the insolation from the direction of the sun (the so-called direct beam insolation), or more accurately from the region of the sky that is focused on the cell, had an intensity of 0.1 W/cm^2 and if the lens had 100% transmission, the geometric and intensity concentration would be the same. In actuality, whereas the global insolation is often close to 0.1 W/cm^2 , the direct beam insolation is typically less. The difference is the diffuse insolation, the radiation that is scattered by the atmosphere or clouds, and comes from directions other than the sun. Typically, the direct beam radiation is around 0.085 W/cm^2 on a clear day, so many concentrator systems are rated at this level. If the lens has a transmission of 85%, then the intensity concentration will be $0.85 \times 0.85 = 0.72$ of the geometric concentration. In the above example the cell will be illuminated at 36 suns.

The reader will note that the reduction cell area through concentration, and hence cost for a given power, is not by a factor of one over the geometric concentration, but rather even less than the intensity concentration. First, the active area of the cell is often less than the actual cell area. A typical $1 \text{ cm} \times 1 \text{ cm}$ cell will have an active area of around $0.8 \text{ cm} \times 0.8 \text{ cm} = 0.64 \text{ cm}^2$. When it is also recognized that most concentrator cells are cut from a round wafer, much of the edge of the wafer cannot be used.² A 10-cm wafer will produce 52 cells of $1 \text{ cm} \times 1 \text{ cm}$ (assuming 100% yield). Suppose this cell is operated at 100X geometric concentration. This means the primary lens is $8 \text{ cm} \times 8 \text{ cm} = 64 \text{ cm}^2$. The total power on the cells from this wafer is then, assuming an 85% lens transmission, $0.85 \times 0.085 \times 64 \times 52 = 240 \text{ W}$. If the wafer had been made into a flat-plate cell, it would have an area of 78 cm^2 and would receive a power of 7.8 W . Thus, the effect of the concentration is to increase the potential output by a ratio of 240 to 7.8, or 31. Our 100X concentrator is really only giving us a 31 times reduction in wafer usage.³ This could still be very useful; however, sometimes, simplistic economic analyses of concentrators overlook this difference.

² Also in single crystal one-sun cells, silicon ingots are round (cylindrical) and they are rendered almost square (prismatic) by cutting off lateral silicon chips.

³ This assumes equal cell efficiency in both cases. In actuality, it will be seen below that most concentrator cells have a higher efficiency than flat-plate cells. Weighed against this advantage is the fact that, except in the sunniest of regions, concentrating systems have lower annual capacity factor (ratio of annual output to rated power times the length of a year).

11.2.3 Types of Tracking

Point-focus optics generally require that the concentrator track about two axes so that it is always pointed at the sun, and the focused light falls on the cell. From a mechanical standpoint, two-axis tracking is more complex than one-axis tracking; however, point-focus systems are also capable of higher concentration ratio and hence lower cell cost. Line-focus reflective troughs need only track along one axis such that the image falls along the focus line. Linear Fresnel concentrators suffer severe optical aberrations when the sun is not perpendicular to the lens' translation axis. (Basically the focal length decreases as the sun's angle moves from normal to the lens.) This generally limits linear Fresnel systems to two-axis tracking. Modest geometric concentration ratios of around 10 are possible, however, if the lens tracks on a polar axis, which limits the sun's angle off normal to 23° maximum [4].

There are three common types of two-axis trackers as shown in Figure 11.3. The pedestal form uses a central pedestal supporting a flat tracking array structure. Tracking is usually effected by a gearbox, which tracks the array along a vertical axis (the azimuth rotation) and along a horizontal axis (the elevation rotation). An advantage of this configuration is the simplicity of installation (basically drilling a single hole, inserting the pedestal into the hole, back-filling with concrete, and placing the array and gear drive on the pedestal). A disadvantage is that wind loads are translated to the central gear drive in the form of very large torque, necessitating large capacity gears. Another form of two-axis tracking is the roll-tilt structure of Figure 11.3(b). Here wind loads on drive components are considerably reduced; however, there are now more rotating bearings and linkages required. Obtaining the required stiffness along the roll axis can necessitate a rather large-section horizontal support member. The structure also requires multiple foundations that must be aligned, complicating installation. The roll axis is most usually placed in a north–south direction, as this minimizes shadowing by adjacent modules along the roll axis. Another roll-tilt configuration uses a box frame with the Fresnel modules pivoted between the upper and the lower frame. This is shown in Figure 11.3(c). The final common configuration is the turntable of Figure 11.3(d). This structure provides for the lowest profile and lowest wind loading, and can use rather small drive components and support members. On the other hand, it presents the most complex installation scenario.

One-axis trackers are generally configured with either a horizontal axis of rotation or a polar axis of rotation as shown in Figure 11.4. A horizontal axis provides for lower profile and larger area per tracking structure, as compared to the polar-axis approach. Horizontal-axis trackers usually use reflective troughs. It can be seen that the sun can be at a fairly large angle to the array, especially in the winter with a north–south axis or early and late in the day with an east–west axis. This causes the image to move a distance down the focus axis and can result in significant end losses and image broadening. The polar-axis configuration, on the other hand, gives higher intercepted annual energy and limits the incoming sun angle to a maximum of 23° from the plane of the concentrator. The simplicity and low profile of the horizontal-axis configuration makes it the more common choice over the polar-axis approach.

11.2.4 Static Concentrators

In principle, it is possible to provide some concentration without any tracking at all. The reasons for this are severalfold. First, the sun appears in only a restricted portion of the

sky. For example, it will never be due north at zero-degree elevation to the horizon. This means that the ability of a flat-plate module to receive light from every direction is somewhat wasted. It can be seen in the section on concentrator optics that the maximum attainable concentration is related to the angular regions where the system can accept light in such a manner that if it can accept a fraction f of the diffuse light falling on it from all directions, then the maximum possible concentration is $1/f$. This relation is further enhanced by a factor of n^2 if the cell is immersed in a dielectric of index of refraction n . Since it is possible to build cells that can receive light from both sides, so-called bifacial cells, another factor of 2 is available by using bifacial cells. The sum result of these

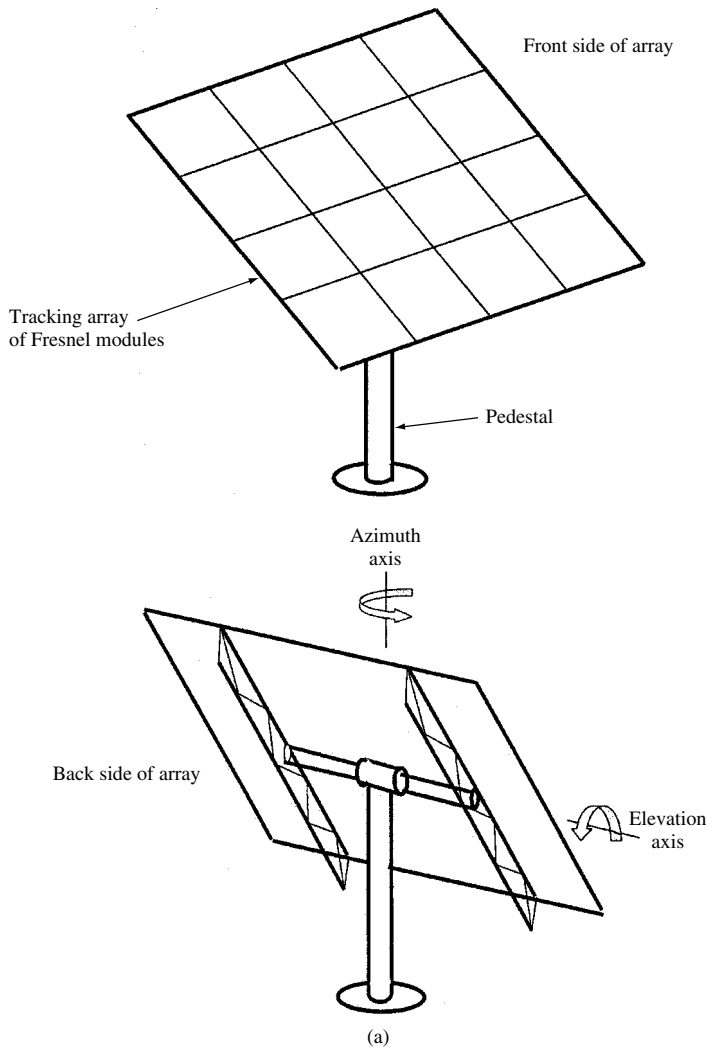


Figure 11.3 Two-axis tracking configurations. (a) Two-axis tracker with elevation and azimuth tracking mounted on a pedestal. (b) Roll-tilt tracking arrangement using central torque tube. (c) Roll-tilt tracking arrangement using box frame. (d) Turntable two-axis tracker

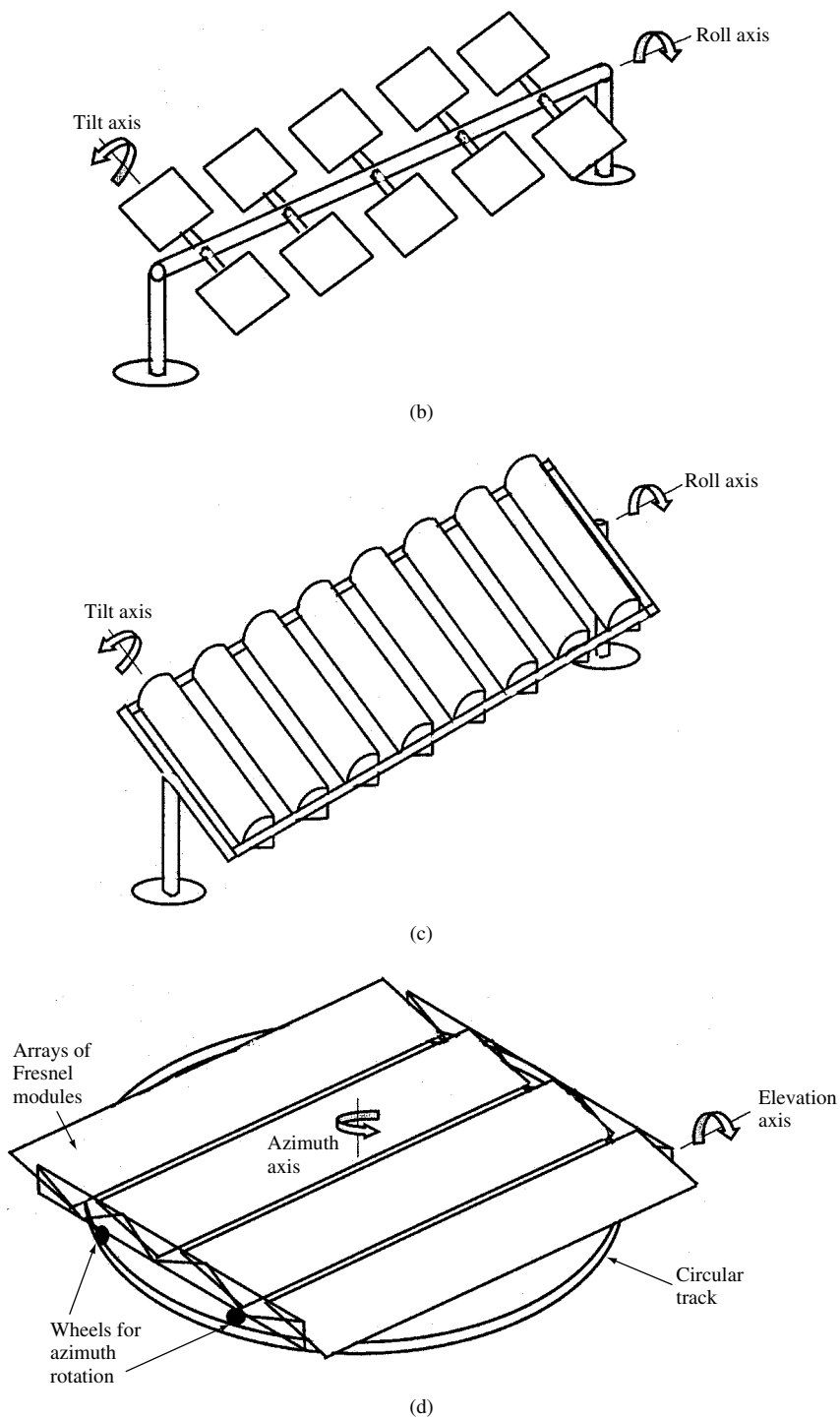


Figure 11.3 (continued)

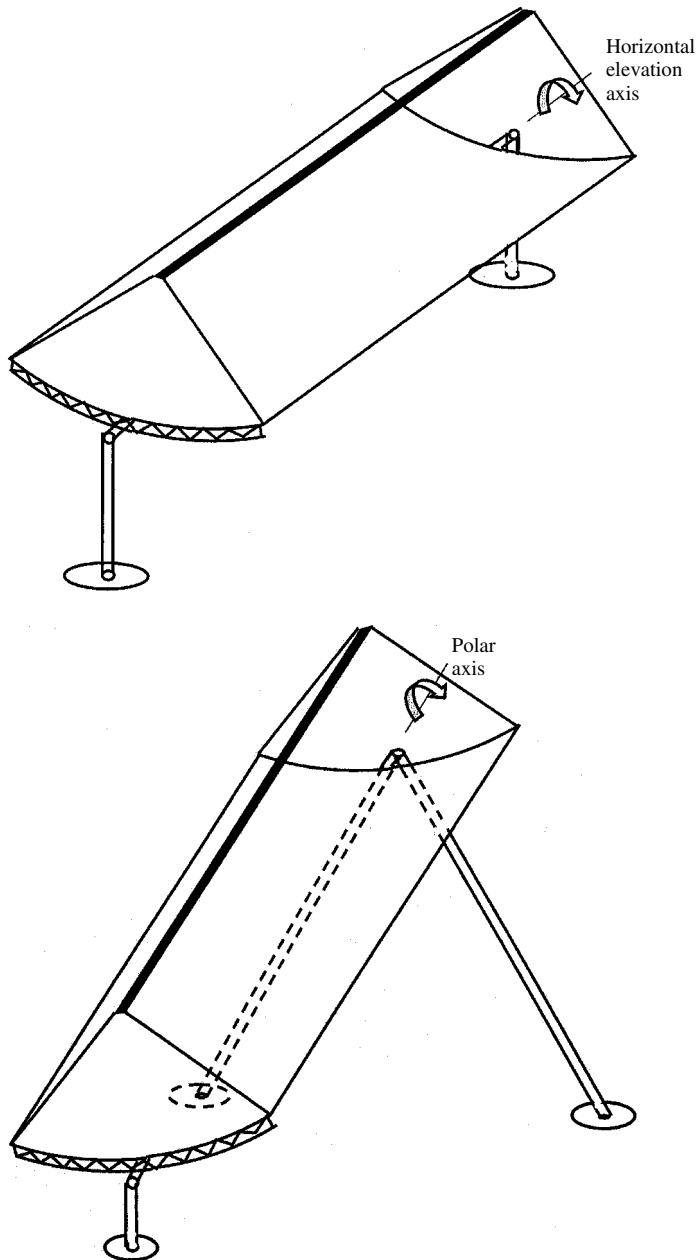


Figure 11.4 One-axis tracking configurations. (a) One-axis horizontal tracker with reflective trough. (b) One-axis polar axis tracker with reflective trough

effects is that static concentrator design with concentration ratios in the range of 2 to 12 have been proposed and researched. Usually they employ nonimaging optics such as the compound parabolic concentrator (CPC) shown in Figure 11.5 or total internal reflecting concentrators that will be discussed in Section 11.4.

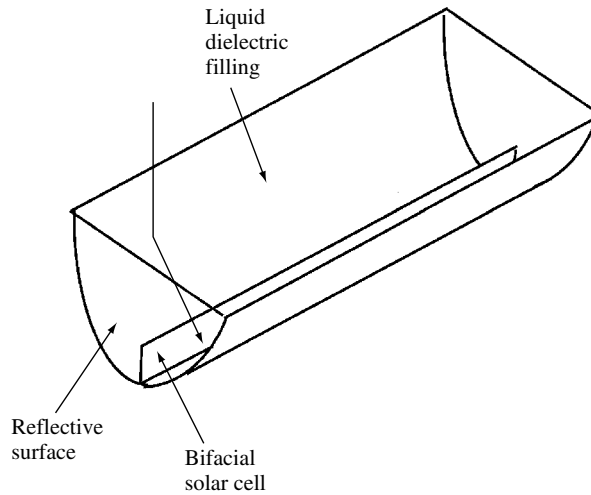


Figure 11.5 One of many static concentrator configurations. In this case a bifacial cell, which is sensitive to light from both surfaces, is mounted in a reflective CPC-like trough that is filled with liquid dielectric. The dielectric forms the dual role of cooling the cell and providing additional concentration

The allure of static concentrators is indeed great because of the elimination of the tracking requirement and, hence, the opening of the general PV marketplace to their use. Unfortunately, no static concentrator design has yet been found where the decrease in cell cost through concentration is sufficiently more than the added cost of the concentrator to warrant widespread commercialization. The discovery and development of a practical, cost-effective static concentrator would be a significant contribution to photovoltaics.

11.3 HISTORICAL OVERVIEW

This section reviews the early efforts to develop concentrators in order to put into context the issues facing current development efforts. The concept and practice of concentrators were well known to early workers in photovoltaics because many of the early solar thermal electric systems used concentrators to generate the high temperatures needed for efficient conversion. These systems generally relied on reflective concentrators that could benefit from the relatively mature technology of glass mirrors. Shuman's oft-mentioned solar electric system built in Egypt in 1913 used reflective troughs, and reportedly attained a conversion efficiency of 3 to 4% from sunlight to electricity [5]. It would be another 40 years before solar cells attained such performance.⁴

Bell Laboratories demonstrated the silicon solar cell in 1952 and developed it into a practical device of 10% conversion efficiency by 1955 [6]. The high cost of the cell precluded its use as a primary source of terrestrial energy, except in small, remote applications. Work on concentrating PV systems as a means to reduce cost began shortly

⁴ Indeed, as discussed later, photovoltaic concentrators based on reflective troughs were able to achieve only 5% conversion efficiency in 1980.

thereafter. In the early 1960s, the Wisconsin Solar Energy Center researched the performance of solar cells under concentrated sunlight. They showed that cells could operate at intensities of several hundred times normal sunlight [7]. The critical issues proved to be (1) reducing series resistance to enable efficient handling of the large currents involved and (2) maintaining low-enough cell temperature. Much of the improvement in concentrating systems since these early days has come from reducing the negative impact of these two factors. The Wisconsin group went on to design a working 50-W system using a parabolic dish concentrator, thereby demonstrating the feasibility of the concept [8].

In 1965, Eugene Ralph, then with the Heliotek Division of Textron (later Spectrolab), proposed several approaches to concentrating systems, from low-concentration reflective cones to high-concentration heliostat fields. He clearly articulated the vision that concentrating PV systems might one day supply large amounts of terrestrial power [9]. At a time when flat-plate systems cost hundreds of dollars per watt, Ralph projected that megawatt-sized systems could be built in the future for less than \$1.00/W. Interestingly, this is \$5.40/W in current dollars, which is about what current concentrator systems would cost in megawatt production quantities.⁵

Despite these early efforts, not much happened in the development of practical concentrating systems until the energy crisis of 1973 renewed concerns about the availability and depletion of fossil fuels.

11.3.1 The Sandia National Laboratories Concentrator Program (1976 to 1993)

One of the US Government's responses to the issues raised by the 1973 oil crisis was to upgrade the status and funding of energy research, first, through the National Science Foundation's Research Applied to National Needs program, then through the Energy Research and Development Administration (a renamed and remissioned Atomic Energy Commission), and finally through the DOE, which was created in 1977. From the beginning, concentrators played a significant role in the mission to develop cost-effective PV power. Sponsored research began in 1976 and included university research at Arizona State University headed by Professor Charles Bacus, plus a variety of industrial laboratories. Sandia National Laboratories in Albuquerque, New Mexico, became the lead agency for managing the concentrator program. The first Project Integration Meeting was held in 1978 [10]. Already 19 subcontractors were under contract to develop cells and systems, and they reported their plans and progress. DOE established a goal of having commercial systems available in 1981 at \$2.00/W. This proved wildly optimistic, but was in a grand tradition with other wildly optimistic projections about PV cost reductions. In fact, in constant dollars, this goal was achieved about 20 years later.⁶

⁵ Unfortunately, this is only marginally less than the cost of today's flat-plate systems, and is still too expensive for large-scale power production. Another factor of three-cost reduction is needed. In later sections, this chapter discusses possible avenues for realizing this cost reduction; however, the reader should keep in mind that concentrator manufacturers are able to achieve these prices at rather small, almost prototype production volumes, whereas flat-plate modules are now produced in automated factories producing up to 100 MW/year.

⁶ \$2.00/W is \$5.60/W in 2001 dollars, about what today's concentrators and flat-plate systems cost in large installations.

Almost every type of concentrating technology was explored during this period, including reflective dishes (Boeing), reflective troughs (Acurex, GE), point-focus Fresnel lenses (RCA, Varian, Motorola, Martin Marietta), linear Fresnel lenses (E-Systems), luminescent concentrators (Owens-Illinois), compound parabolic concentrators (Sun Trac, University of Chicago), and small heliostat fields with a central receiver (AAI). Silicon cell research was conducted at Purdue University, Arizona State University, RCA, GE, Applied Solar Energy Corporation, Spectrolab, and Motorola. Gallium arsenide cells were also researched at Varian, Hughes, The Research Triangle Institute, and Rockwell International. In addition to these outside contractors, Sandia conducted in-house research on cells, lenses, and systems. A dynamic research program was created that was coordinated and documented through annual review meetings.

In 1978, DOE initiated a program to test concentrator concepts called the *Photovoltaic Concentrator Applications Experiments*. Seventeen projects ranging in size from 20 to 500 kW were awarded Phase I contracts to do feasibility studies. These projects to a large extent covered the gamut of possible system options. Eight concepts were awarded continuing funding to build prototype systems. By 1980, system efficiencies for these prototypes ranged from 5% for the reflective trough systems to 10% for point-focus Fresnel systems, and 12% for linear Fresnel systems [11].

Early experience indicated that reflective approaches were much more problematic and difficult compared with Fresnel lenses, mainly due to flux uniformity issues [12]. This, along with funding constraints, led Sandia to focus on Fresnel lens systems for continued development. Flux uniformity remains a critical factor to be considered in all concentrator system designs.⁷

Two system approaches survived the cut and were deployed in large (for the time) demonstration projects. These were the point-focus Fresnel modules of Martin Marietta (later Intersol) and the line-focus Fresnel approach of Entech.

11.3.2 The Martin Marietta Point-focus Fresnel System

Martin Marietta participated throughout the Sandia program developing a series of point-focus Fresnel modules and systems.⁸ First-generation units had four lenses per housing. The housing was made of injection molded plastic and each lens was 30 cm × 30 cm. The cells were round and of approximately 6-cm diameter (having been made from 2.25-inch diameter wafers), resulting in a concentration ratio of 33X, rather low for a point-focus system. These modules demonstrated efficiencies in the 9 to 10% range, placing the concept at the upper end of efficiencies at that time (1978). Figure 11.6 shows the overall design concept. The large extruded aluminum heat sink doubled as the structural mounting support. First-generation modules were deployed in two significant demonstration projects as discussed in the section describing the Sandia National Laboratories Concentrator Program.

⁷ The reader will note that in a line-focus system in which the cells are connected in series along the focus, the source current will be limited by that of the cell receiving the least illumination. Minor flux nonuniformities thus have a serious impact on overall efficiency.

⁸ In 1984, this work was “spun out” of Martin Marietta to a start-up dedicated to commercializing the technology by the name of Intersol.

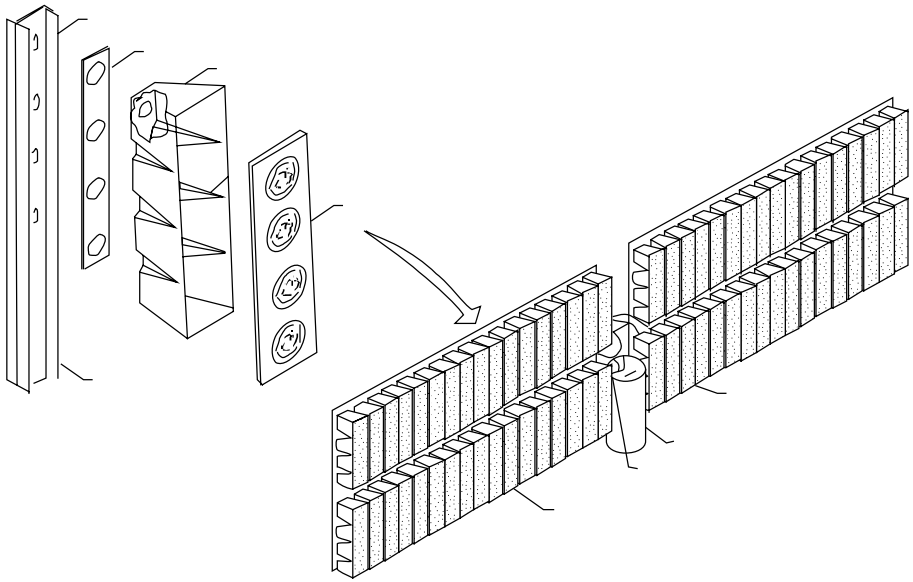


Figure 11.6 First-generation Martin Marietta point-focus design concept [13]. Reproduced with permission by Sandia National Laboratories

Martin Marietta and Intersol continued developing concentrator modules with support from Sandia. It was determined that the large lens and cell sizes resulted in a difficult situation regarding cell mounting and cooling. Therefore, the lens size was reduced to $23\text{ cm} \times 23\text{ cm}$ and the concentration ratio increased to 70X. Reflective secondary concentrators were eventually incorporated to improve tolerance to tracking errors. There were now 14 lenses per parquet in a 2×7 arrangement and still mounted with a plastic housing. Now each cell was mounted on individual aluminum heat sinks. Figure 11.7 shows the second-generation unit introduced in 1983 [14].

Intersol improved the module performance to over 15% by 1984 [15], which clearly demonstrated the feasibility and promise of point-focus Fresnel concentrators. Despite this, no further large deployments were made using this technology, and Intersol ceased operations around 1986.

11.3.3 The Entech Linear-focus Fresnel System

Sandia also supported the continued development of a linear-focus Fresnel concentrator at Entech.⁹ The heart of the Entech concept is an innovative domed Fresnel lens. Figure 11.8 shows a cutaway section of the Entech module. The principle of lens operation is similar to the SEA Corporation extruded lens shown in Figure 11.10. This lens has larger facets and so the operation is easier to see from a drawing. As illustrated, the domed shape allows the rays to have equal angles to the Fresnel surface at both incidence and exit. This has

⁹ This concept was initially proposed by E-Systems in Dallas, Texas, and later spun out to a start-up company, Entech.

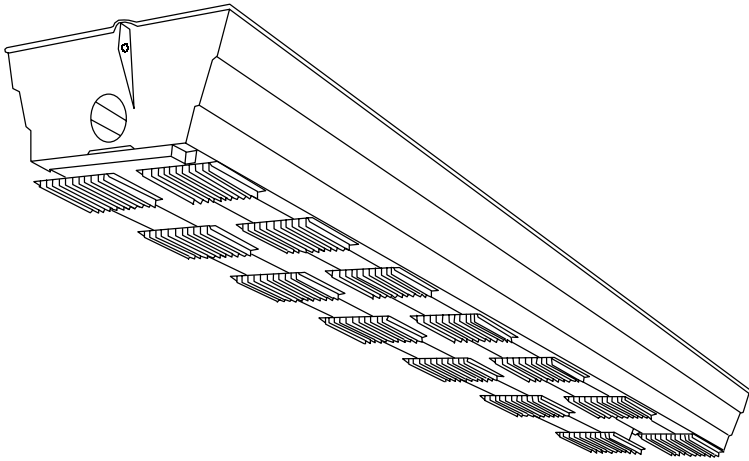


Figure 11.7 Drawing of Intersol second-generation module [14]. Reproduced with permission by Sandia National Laboratories

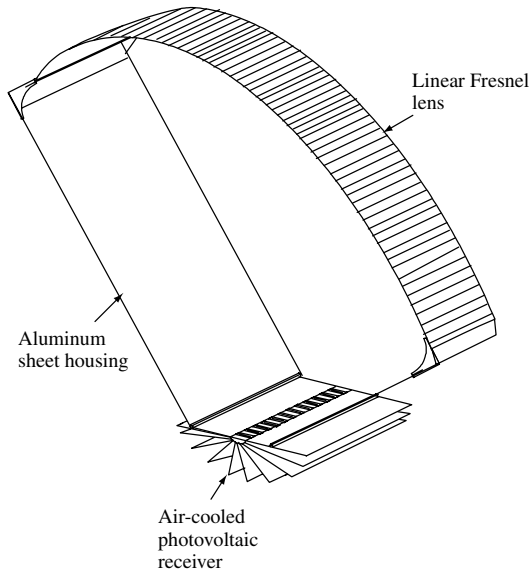


Figure 11.8 Cutaway view of the Entech domed Fresnel module [17]. Reproduced with permission by Sandia National Laboratories

four beneficial effects. First, it minimizes chromatic aberration caused by the index of refraction variation throughout the solar spectrum. Second, the angle of deflection of the ray is independent to the first order of the orientation of the prism. This minimizes the required tolerances in lens shape and minimizes the impact of lens deformation. Third, it minimizes the overall loss in transmission due to reflection. Finally, the nonplanar domed shape makes for a more rigid, self-supporting lens structure. 3M developed a roll forming process for the manufacture of Fresnel lenses that provided for a high speed, low-cost

production method. Entech worked closely with 3M to develop Lensfilm™ versions of their lens. This proved to be an excellent combination, and early lenses exhibited transmissions of over 90% with reasonable manufacturing cost. Early versions of the Entech module had an efficiency of over 15% at standard test conditions (STC) [16], and this continued to improve throughout the program. Entech built four significant demonstration projects, as described below.

11.3.4 Other Sandia Projects

Throughout the 1980s, Sandia maintained a research program that included both in-house research and research sponsored at companies and universities. In-house activities included solar cell modeling and device research, module development, lens design and testing, cell packaging, and system testing and evaluation. Along with the large programs at Intersol and Entech, sponsored research included cell development at ASEC, Boeing, Varian, and university research at Purdue, Stanford, and the UNSW in Australia. This work was generally reviewed in periodic presentations at the IEEE Photovoltaic Specialists Conference. An illustrative discussion of this work toward the end of the program can be found in the 1988 review by Boes [18]. Rather than detail this work here, it will be covered in the relevant sections below.

Sandia developed a laboratory test module that demonstrated 20% conversion efficiency (STC), which pointed the way to eventual 20% commercial modules [19]. The Sandia module development culminated the Sandia Baseline III module [20]. This was intended as a concept design to be adopted and modified as needed by interested companies. Efficiency at STC was around 16 to 17%, placing it among the highest demonstrated performance for a manufacturable design at that time. Figure 11.9 shows the concept. Most commercial attempts at high-concentration modules have great similarities to this design.

11.3.5 The Concentrator Initiative

Despite over 15 years of sponsored research, no viable concentrator industry had emerged by 1990. Therefore, the DOE decided to create the Concentrator Initiative. This was

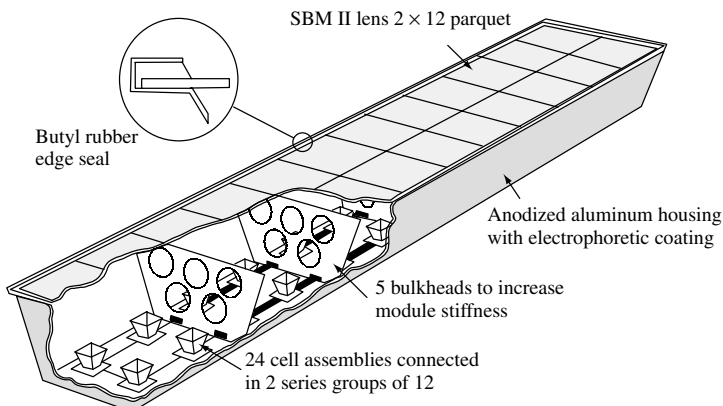


Figure 11.9 The Sandia Baseline III point-focus Fresnel module design. Reproduced with permission by Sandia National Laboratories

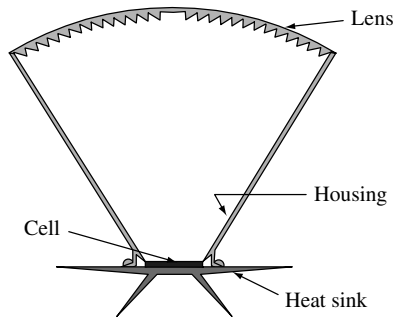


Figure 11.10 Cross-section of the SEA Corporation extruded lens linear Fresnel module. Reproduced from Kaminar N, Curchod D, “SEA 10X Module Development”, Presented at 1990 DOE/Sandia Crystalline Photovoltaic Technology Project Review Meeting (1990) with permission by Sandia National Laboratories

envisioned as a final push to jump-start a concentrator industry. Eight research contracts were let, four in cell development and four in collector development. The program was split between two low-concentration, linear-focus approaches and two high-concentration approaches. The low-concentration approaches were pursued by Entech, further refining the previous work they had done, and by SEA Corporation (later Photovoltaics International). SEA Corporation had developed an innovative extruded Fresnel lens, shown in Figure 11.10, which promised further cost reductions [21]. This lens is domed similarly to the Entech lens, and has therefore similar benefits.

The two high-concentration point-focus modules were developed by Alpha Solarco of Cincinnati, Ohio, and Solar Kinetics of Dallas, Texas. Both used modules similar to the Sandia Baseline 3 module, shown in Figure 11.9.

The high-concentration cell contracts were to Applied Solar Energy Corporation (ASEC), Spectrolab, and SunPower Corporation. SunPower was a new company created to commercialize concentrators based on the point-contact cell developed under EPRI funding described below. ASEC and Spectrolab adapted for concentration use the passivated emitter rear contact (PERC) cell developed by the University of New South Wales. Solarex worked on adapting the buried contact cell process from the UNSW to low concentration use. This program was reviewed by Maish in 1993 [22]. Despite excellent technical progress, funding shortfalls forced the termination of the program in 1993, and no long-lasting commercial effort resulted.¹⁰

11.3.6 Early Demonstration Projects

First-generation Martin Marietta modules were deployed in two significant demonstration projects. The first was the 350-kW SOLERAS system in Saudi Arabia and the second was a 225-kW system at the Phoenix Sky Harbor Airport. The SOLERAS system, which operated from 1981 to 1998, is shown in Figure 11.11. These systems demonstrated the

¹⁰SEA Corporation (later Photovoltaics International) continued under reduced funding for a period and deployed several demonstration projects prior to exiting the business in 2000. In addition, SunPower Corporation continues to market high concentration solar cells and Entech is working on space concentrator systems.



Figure 11.11 Photograph of the Martin Marietta 350-kW SOLERAS system in Saudi Arabia

viability of the concentrator concept, and despite being first-generation demonstration units, had a remarkably reliable operating history [23].

Entech built four significant demonstration plants. The first was a 27-kW combined heat and electricity unit at the Dallas Fort Worth Airport and the second was a 300-kW unit on the roof of a 3M parking structure in Austin, Texas. In 1991 they installed a 20-kW test system at PVUSA, a test facility operated at that time by PG&E. This system demonstrated an overall efficiency of 11% at PVUSA Test Conditions (PTC), making it the most efficient system tested at PVUSA [24]. Similar results were obtained for a 100-kW system installed at the Central and Southwest Services (CSW) site in Fort Davis, Texas. This is shown in Figure 11.12. Another 100-kW system was installed at the TU Electric Power Park in Dallas, Texas. Entech predicted an installed price of under \$3.00/W for their systems when produced at over 20 MW/year production rate [25]. Entech continued to participate in sponsored R&D through the Concentrator Initiative (discussed below) and PVMaT.

11.3.7 The EPRI High-concentration Program

The Electric Power Research Institute (EPRI) was formed in 1974 in response to the first energy crisis. It is sponsored by a consortium of member utility companies. EPRI was conceived to fill the void in utility-related R&D that existed because utilities traditionally had very limited R&D budgets. After reviewing the field, EPRI selected high-concentration systems as the centerpiece of its PV activity. These appeared most suited for achieving the low costs needed for large PV solar farms, which was the market application envisioned at the time. (Later, the EPRI program was expanded to include amorphous silicon and ribbon silicon.) EPRI began sponsoring research on high-efficiency cells at Stanford

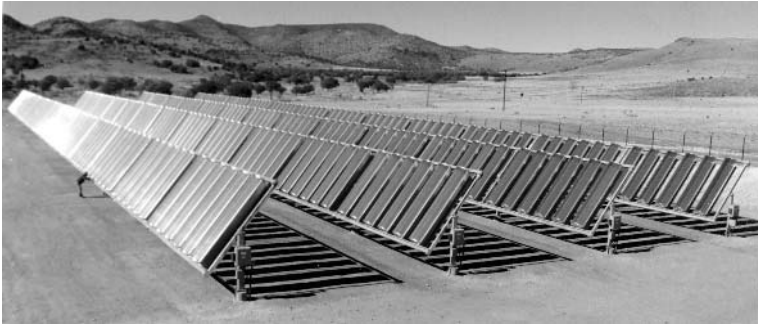


Figure 11.12 Entech 100-kW line-focus concentrator system in Fort Davis, Texas. Reproduced with permission by Entech, Inc.

University in 1975. At first this was targeted toward ThermoPhotoVoltaic (TPV) conversion [26]. The concept was to use highly concentrated sunlight to heat a radiating surface to incandescence, and to use the resulting thermal radiation to produce electric power with a PV device. This was shown in principle to permit very high efficiencies, perhaps over 50%. The laboratory conversion of radiant energy to electric energy reached a high of 26% [27].

The concept in TPV conversion is to have the solar cell absorb light only for photon energies near the semiconductor band gap. The remainder of the spectrum is reflected back to the radiator. This creates the concept of “photon recycling” whereby photons with energies less than optimum for conversion are sent back to the radiator for recycling until they come back at the proper energy.¹¹ This recycling can be effected by several means, such as having a selective filter between the cell and the radiator or by having a reflector behind the cell and making the cell as transparent as possible to below-bandgap photons. In the EPRI/Stanford program, the latter approach was taken. Experiments showed that major losses in below band gap reflectance came from free carrier absorption in the doped junction regions as well as from absorption in the metal-semiconductor contact area. It was found that when the metal back contact was separated from the silicon by a thin, one-fourth-wavelength silicon oxide layer, the reflectance was very high. This led to the concept of the “point-contact cell” shown in Figure 11.13. The doping has been removed from the base, that is, very high resistivity silicon is used for the starting material and the diffused, highly doped junction regions are made as small as possible to reduce free carrier absorption to a minimum.

It was found that the point-contact cell structure had many unanticipated advantages, the understanding of which emerged over the following years. It was ideal for promoting light trapping in the silicon because of the reflective back contact, and contact-area recombination is reduced by restricting the contact coverage fraction. In addition, the

¹¹ The reader can see the reason for the requirement for a radiator in between the sun and the cell. If this was not present, nonoptimal photons would be reflected back to outer space. Interestingly, if the cell was at the focus of an optimal concentrator (Section 11.4), the reflected photons would be returned to the sun. This would be a reasonable proposition if we were paying to fuel the sun, but of course we are not. It can also be seen that the radiator and cell area must be large compared to the entrance aperture for concentrated light so that energy lost through the entrance will be small.

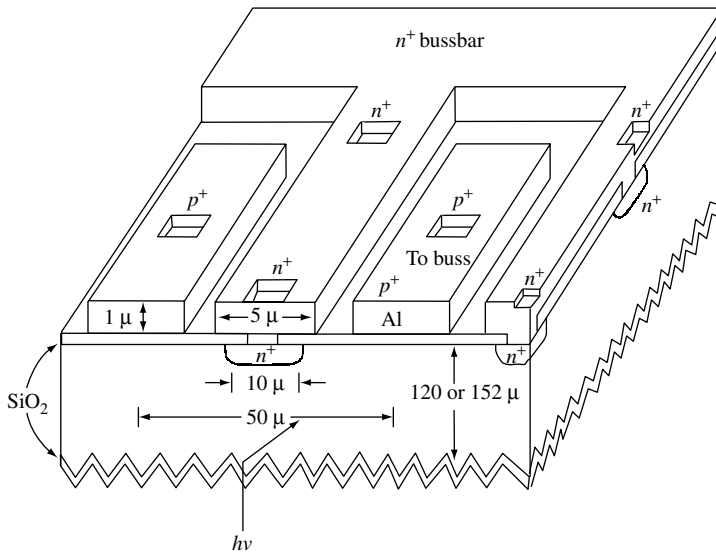


Figure 11.13 The point-contact cell design. Reproduced from Sinton R, Swanson R, “An Optimization Study of Si Point-Contact Solar Cells”, Presented at *Nineteenth IEEE Photovoltaic Specialists Conference* (New Orleans, LA, 1987) with permission by © 1987 IEEE

oxide layer was found to produce very good surface passivation, which further reduced recombination. Many high-efficiency cell concepts such as the UNSW PERL (Passivated Emitter Rear Localized) cell [28] adopted these concepts to attain their performance. Solar TPV was found to have serious practical drawbacks, however. These included (1) ancillary absorption problems such as from radiator support mounts, (2) the difficulty of the very high concentration required (over 10 000X), and (3) material problems from the very high radiator temperatures of over 2000°C. The resulting high performance of point-contact TPV cells in normal sunlight was very compelling, however, and so in 1980 EPRI elected to abandon solar TPV and began developing normal high-concentration systems in which the sunlight impinges directly on the cell. The point-contact cell was further developed and reconfigured with all contacts on the back. These cells eventually reached a conversion efficiency of 28% [29]. Having all contacts on the back of the cell provides two main advantages. First, the shadowing of the top surface is eliminated. Second, the metal may be made to cover the entire back, reducing series resistance considerably (a particular advantage in concentrator cells).

EPRI funded the development of systems based on the point-contact cell starting in 1980. The initial system conceptual design work was performed by Black & Veatch. Figure 11.14 shows the resulting design. The design concentration ratio was 500X; geometric and reflective secondaries were used in a Fresnel module consisting of a 6×6 array of Fresnel lenses, each lens being 18 cm on a side [30].

Several large test arrays were built to check the mechanical and thermal performance of the structure. Unfortunately, these were not populated with cells because the point-contact cell was found to be unstable. The problem was traced to the generation of interface recombination centers at the Si–SiO₂ interface by ultraviolet photons. Several

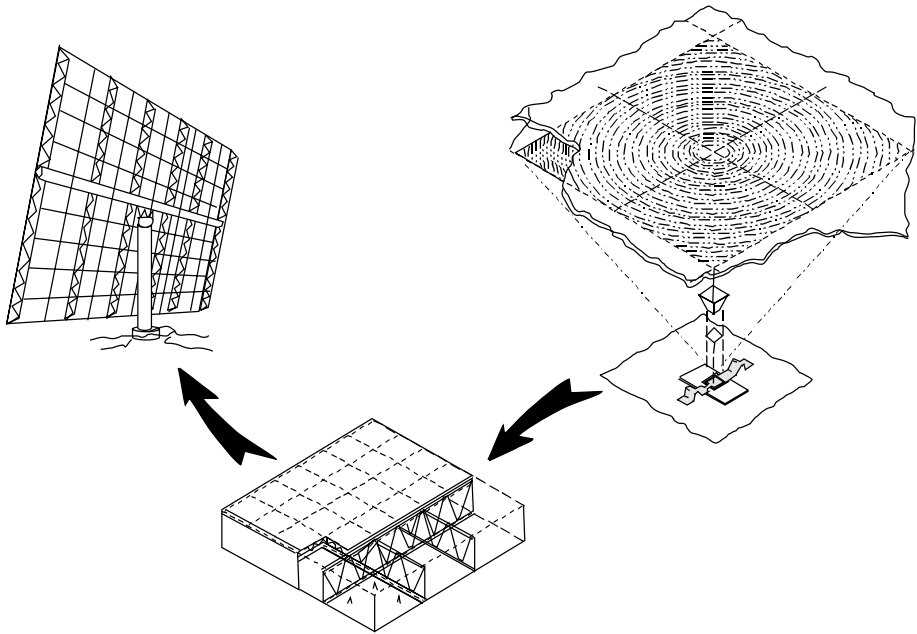


Figure 11.14 The Black & Veatch conceptual design for a high-concentration photovoltaic array. (Copyright © 1984. Electric Power Research Institute. AP-3263. *Conceptual Design for a High-Concentration (500X) Photovoltaic Array*. Reprinted with permission)



Figure 11.15 Static concentrator formed by an oil-filled CPC with bifacial cells

years of research were required to develop a UV-stable interface that had sufficiently low surface recombination velocity [31].

In 1989, EPRI decided to have a contract solicitation to continue commercialization of high-concentration systems. Two companies, SunPower Corporation and MCom/Phi (later spun out into a start-up called Amonix), were awarded contracts. SunPower explored reflective optics using parabolic dishes as well as heliostats [32] and Amonix continued the development of Fresnel modules using a simplified approach, the integrated backplane

array [33]. EPRI terminated funding in 1993. Since then, Amonix and SunPower have continued development using other sources of funds. Both companies have since demonstrated modules with efficiency around 20%, showing the potential of point-contact silicon cells [34, 35]. These companies will be discussed in more detail in Section 11.5.

11.3.8 Other Concentrator Programs

Most PV concentrator activity, until recent times, was centered in the United States, probably because of the large direct normal solar resource located in the desert southwest region of that county. Cloudier regions were less prone to see an advantage in concentrators. Nevertheless, there were significant activities in Spain and small activities scattered elsewhere. The Spanish group at the Polytechnic University of Madrid, headed by Professor A. Luque, developed since 1975 bifacial cells for static concentrators, in order to achieve more concentration in static concentrators of the CPC type in Figure 11.5. Three different cell approaches were investigated with the support of the Spanish funding Agency CAICYT: a vertical multijunction cell, similar to the one developed in the United States by Sater and Brandhorst [36], and two more original structures, one n^+pn^+ interdigitated in the back [37] and another one n^+pp^+ [38], were examined and the latter was retained as the most promising and commercialized by the start-up Isofotón, today the seventh world cells manufacturer.¹²

The retained cell structure was based on the long base lifetime found in lowly doped silicon. Lowly doped silicon was thought at the time to produce low voltages, but as the cell operated in high injection the pp^+ homopolar junction provided additional voltage to the existing level of voltage in ordinary cells [39].

A module of size similar to a flat module was built [40], as shown in Figure 11.15. The optics is a derivation of the Winston's CPC. The concentrator was filled with transparent oil that allowed the concentration to increase and provided convective cooling to the bifacial cells. A geometrical concentration over 4 for a static system that collected the sunbeam for the full year was achieved.

The potential of concentrators based on diffusive reflectors of the sunlight, that is, of surfaces painted on white (or just snowed) were used with bifacial cells. This gave rise to the so-called albedo-collecting modules that consisted of flat modules of bifacial cells that collected the diffusely reflected light of a white background on its rear face. In some optimal cases the extra output due to the albedo was over 50% [39] but in most cases it was limited to around 20 to 30%. Figure 11.16 shows an example of such albedo-collecting fields.

Stimulated by the Sandia program, several groups in Europe developed similar approaches. In particular, three modules were developed by the LAAS of Toulouse, France, the Spanish Group of the Polytechnic University of Madrid, and the Italian company Ansaldo. A later additional effort was made at the Fraunhofer Institute for Solar Energy, Frankfurt, Germany. Both of these groups are active in concentrator systems today. Their activities will be covered in Section 11.5. One noteworthy concept from the

¹² This company, founded in 1981, stopped the production of bifacial cells around 1986, to fabricate the more conventional monofacial cells that they found cheaper to manufacture.

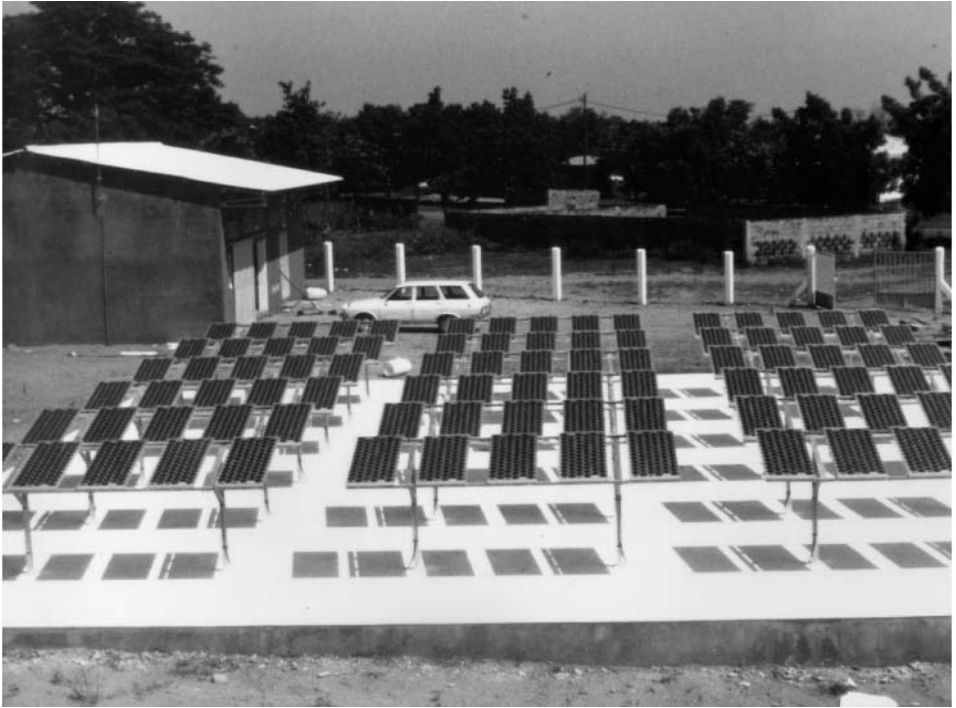


Figure 11.16 Albedo-collecting modules in a 10 kWp installation in the Senegalese village of Noto

Fraunhofer group is a one-axis tracing approach that achieves high concentration through the use of secondary optical elements [41]. The concept is shown in Figure 11.17.

11.3.9 History of Performance Improvements

The performance on concentrator cells and modules has steadily improved over time, as would be expected. Figure 11.18 presents the independently verified efficiency records from 1977 to 2001. Early silicon concentrator cells were basically 1-sun cells redesigned for high current by providing a fine, high metal coverage grid. The efficiency of this approach rapidly achieved 20% by 1982 [12]. The Swanson group at Stanford University introduced the back point-contact cell in 1984 with an efficiency of 22% [42]. The point-contact cell has maintained the efficiency record for silicon concentrator cells to the present. GaAs-based cells have always had superior performance to silicon. Varian introduced a 26% GaAs cell in 1980, and increased this to 29% in 1988. Unfortunately, it was eclipsed in 1988 by the first multijunction cell to set a record – a 31% mechanically stacked GaAs cell on a silicon bottom cell [43]. This result was eclipsed by a mechanically stacked GaAs on GaSb, which set a record that lasted until 2001. In 2000, Spectrolab announced a 32% monolithically stacked GaInP on GaAs cell [44]. They followed this up with a 34% result in 2001 (Spectrolab press release), finally outdoing the 1988 mechanically stacked record with a fully monolithic triple-junction cell.

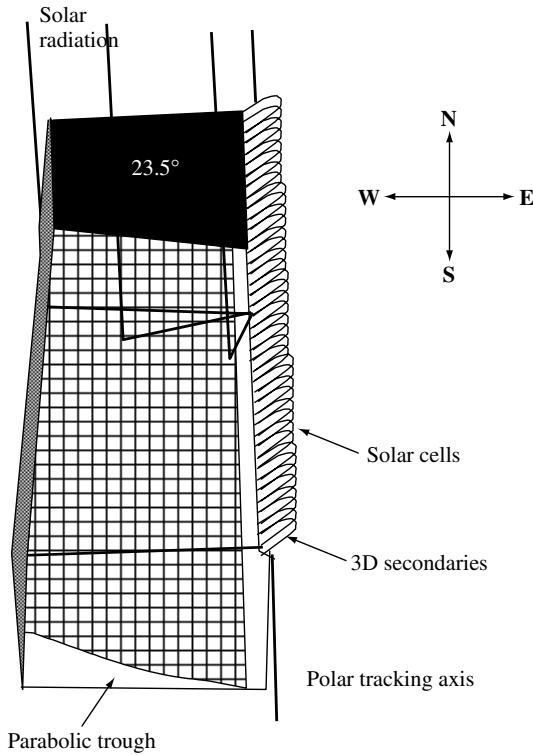


Figure 11.17 A two-stage concentrator permitting 300X concentration with one-axis tracking. Reprinted from *Sol. Energy*, **56**, Brunotte M, Goetzberger A, Blieske U, 285–300, © (2002), with permission from Elsevier Science

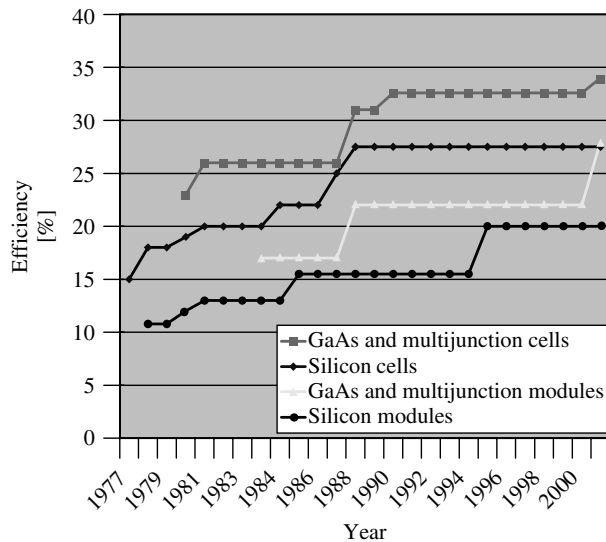


Figure 11.18 Record concentrator cell and module efficiencies

Generally, module improvements have followed the increase in cell efficiencies, with a lag in time to incorporate the cell into suitable packages. Noteworthy recent results are the 20% record held by point-contact silicon-based modules since 1995 [34, 35], and the recent 28% multijunction module based on an Entech domed Fresnel lens [45].

11.4 OPTICS OF CONCENTRATORS

The basic concept of light concentration by reflective or refractive means is conceptually simple and straightforward. Simple lenses are generally imaging devices. Some thought, however, will reveal that in a concentrator system, an image of the sun is not needed, or even desired. What is desired is to gather the light as efficiently as possible onto a receiver that is smaller than the concentrator's entrance aperture. As a further requirement, it is often desirable to have the receiver illuminated as uniformly as possible. Another important consideration is that it is generally desirable to have the concentrator accept light from as large an angular region as possible. This minimizes the accuracy at which the concentrator must be pointed toward the sun and thereby relaxes structural requirements and assembly tolerances. These factors, which are generally different from the ones encountered in traditional optical system design, spurred a whole new discipline called *nonimaging* optics. This field was pioneered by Professor Roland Winston and his group at the University of Chicago [46]. Another center of excellence in nonimaging optics developed at the Polytechnical University of Madrid. It is beyond the scope of this chapter to cover the principles of nonimaging optics, for that is a difficult topic that is well covered in textbooks [2, 47].

11.4.1 Basics

One of the remarkable theorems of nonimaging optics is that there exists a relationship between the maximum angle that is accepted by the concentrator and the maximum possible concentration that is attainable, C_{\max} . Consider the schematic representation of a general concentrator shown in Figure 11.19. Here the light that hits the entrance aperture, of area A_{conc} , at an angle less than $\theta_{\text{max,in}}$ from the normal is transmitted to the exit aperture where the receiver of area A_{rec} is located (PV cells in our case), emerging at an angle less than $\theta_{\text{max,out}}$ to the normal of the receiver. For one-axis, or two-dimensional, concentrators the following relationship holds:

$$C = A_{\text{conc}}/A_{\text{rec}} \leq C_{\max} = \sin(\theta_{\text{max,out}})/\sin(\theta_{\text{max,in}})$$

For two-axis, or three-dimensional, concentrators the corresponding maximum is

$$C = A_{\text{conc}}/A_{\text{rec}} \leq C_{\max} = \sin^2(\theta_{\text{max,out}})/\sin^2(\theta_{\text{max,in}})$$

If the receiver is immersed in a dielectric medium of index of refraction n , then these relationships become

$$C = A_{\text{conc}}/A_{\text{rec}} \leq C_{\max} = n \sin(\theta_{\text{max,out}})/\sin(\theta_{\text{max,in}})$$

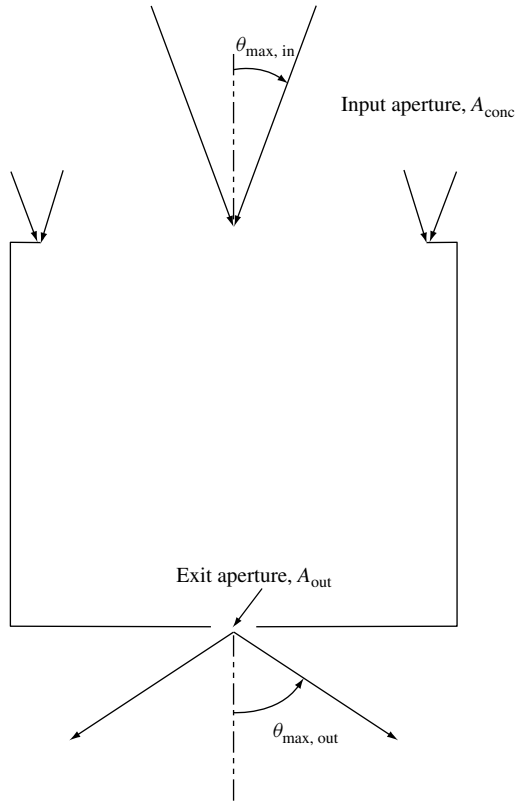


Figure 11.19 Schematic representation of a generalized concentrator

and

$$C = A_{\text{conc}}/A_{\text{rec}} \leq C_{\text{max}} = n^2 \sin^2(\theta_{\text{max,out}})/\sin^2(\theta_{\text{max,in}})$$

respectively. A concentrator that achieves this maximum is called an *ideal* concentrator.

Some observations are in order. First, in order to attain the maximum concentration, it is necessary to have $\theta_{\text{max,out}}$ as large as practical. The maximum it could be is 90° , but even angles approaching this result in many rays striking the receiver at grazing angles. This may prove impractical, as such rays are prone to have high reflectance and can easily miss the target owing to mechanical alignment errors. The above equations are often stated when $\theta_{\text{max,out}} = 90^\circ$, whereby they become

$$C = A_{\text{conc}}/A_{\text{rec}} \leq C_{\text{max}} = n/\sin(\theta_{\text{max,in}})$$

and

$$C = A_{\text{conc}}/A_{\text{rec}} \leq C_{\text{max}} = n^2/\sin^2(\theta_{\text{max,in}})$$

in the two and three-dimensional case, respectively. The designer is cautioned, however, not to persist in designing concentrators with very large exit angles just to gain higher concentration ratio.

If one designs a concentrator that accepts as a maximum input angle the half angle of the sun as seen from the Earth, about $1/4^\circ$, then it could have a maximum concentration of about 200 in the two-dimensional case and 40 000 in the three-dimensional case. Such a concentrator would accept light only directly from the surface of the sun. Regions of the sky outside this area would be rejected by the concentrator; that is, it would not reach the receiver. Interestingly, the concentration of 40 000 restores the radiative power density at the receiver to that at the surface of the sun. This leads to a simple proof of the above equations. Suppose we have a hot spherical radiator, which could be the sun but need not be, that is radiating black-body radiation. A portion of the radiation is intercepted by a concentrator as shown in Figure 11.20.

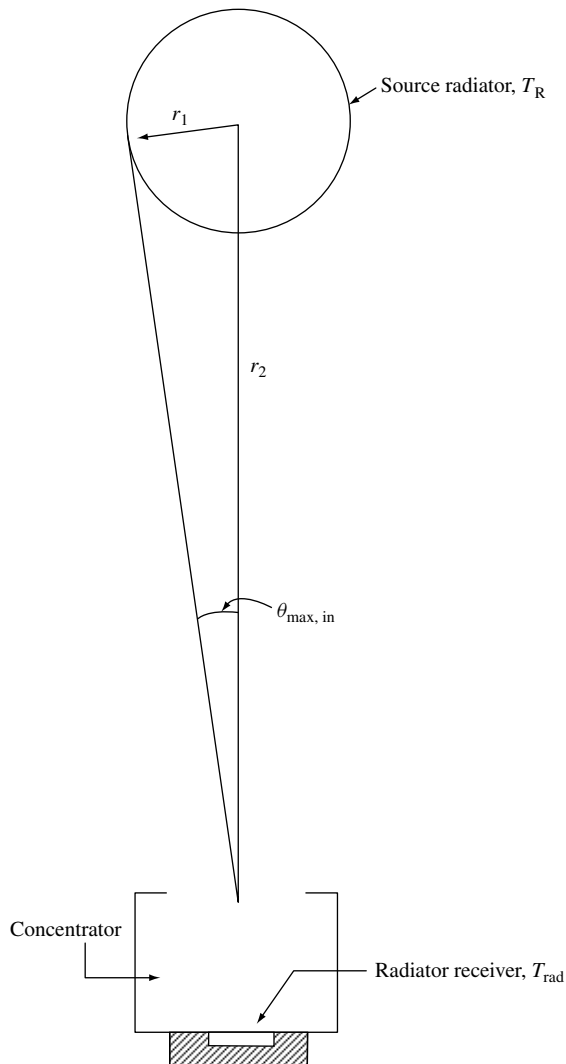


Figure 11.20 Geometry of a spherical radiator and concentrator

If r_1 is the radius of the radiator and r_2 is the distance from the center of the radiator to the concentrator input, then it is clear from Figure 11.20 that $\sin \theta_{\max, \text{in}} = r_1/r_2$. If we assume that the radiator is radiating as a black body, then the total power density at the surface of the radiator is $P_{\text{rad}} = \sigma T_s^4$, where σ is the Stefan Boltzmann constant and T_s is the radiator source temperature. Simple geometry gives the power density at the entrance to the concentrator as $P_{\text{canc}} = (r_1/r_2)^2 P_{\text{rad}} = \sin^2 \theta_{\max, \text{in}} P_{\text{rad}}$. The power density at the receiver is simply that at the concentrator entrance, multiplied by the concentration ratio, so $P_{\text{rec}} = C \sin^2 \theta_{\max, \text{in}} P_{\text{rad}}$. Now, imagine that the receiver is a black body insulated so that its only heat loss is by thermal radiation back from the receiving surface. Then the receiver will heat up until it is losing power by thermal radiation at the same rate it is receiving it. This will occur when the receiver is at a temperature such that $P_{\text{rec}} = \sigma T_r^4$. Equating this to the received power above

$$P_{\text{rec}} = \sigma T_r^4 = C \sin^2 \theta_{\max, \text{in}} P_{\text{rad}} = C \sin^2 \theta_{\max, \text{in}} \sigma T_s^4$$

or

$$C = \frac{T_r^4}{T_s^4} \frac{1}{\sin^2 \theta_{\max, \text{in}}}$$

Now, here is the thermodynamic part. It must be that $T_r \leq T_s$, for otherwise heat would be transferred from the source at a lower temperature to the receiver at a higher temperature without the use of work, in violation of the second law of thermodynamics. In other words, if the receiver was hotter than the source, one could build a perpetual motion machine. Inserting this inequality into the above equation gives

$$C \leq C_{\max} = \frac{1}{\sin^2 \theta_{\max, \text{in}}}$$

The origin of the n^2 in the concentration equation can be seen from the fact that in a dielectric medium, the Stefan Boltzmann law becomes $P = n^2 \sigma T^4$. The factor n^2 comes from the fact that the three-dimensional electromagnetic mode density is increased by n^3 owing to the decrease in wavelength by $1/n$, but the speed of light is decreased by $1/n$. Therefore, in thermal equilibrium, the density of photons is increased by n^3 , but the number of photons crossing a surface per unit time, and hence the power crossing this surface, is increased by only n^2 .

If a concentrator can accept light from anywhere in the upper hemisphere, then $\theta_{\max} = 90^\circ$ and $C_{\max} = 1$, or $C_{\max} = n^2$ if the receiver is immersed in a dielectric. The history of concentrators is replete with proposed concentrators that achieve high concentration without tracking the sun; that is, it will accept light from any point in the sky. In each case the concept is supposed to skirt the maximum concentration theorem by some means. Examples are the use of diffraction (as with holograms), or bent light fibers, or quantum dyes (as in luminescent concentrators¹³). Most derivations of the maximum concentration theorem are based on geometric optics, and so it is conceivable that it could be

¹³ The case of luminescent concentrators requires more care because of the spectral shift. This can be done by incorporating spectral filters into the thermodynamic analysis, but the finding is that they have rather limited concentration and efficiency potential.

violated by diffraction, for example. But the thermodynamic basis of this theorem shows that the search for a nontracking concentrator with high concentration is doomed to fail.

By restricting the acceptance angles to the region of the sky where the sun is actually found, modest concentrations on the order of 2 to 3 are possible. A further factor of 2 is obtained by using bifacial cells that can accept light from both top and bottom. If the cell is immersed in a dielectric of $n = 1.4$, then yet another factor of 2 is possible. This means that it is possible in principle to obtain concentration ratios of up to around 8 to 12 without tracking the sun. The search for practical, cost-effective static concentrators is ongoing and discussed in Section 11.5.

11.4.2 Reflection and Refraction

Most concentrators use reflection, refraction, or a combination of both to effect their concentration, and standard geometric optics is appropriate for their analysis. Some concepts use diffraction gratings or graded index materials, but that is beyond the scope of this discussion. It is assumed that the reader is familiar with elementary optics. The laws governing light rays at reflective and refractive interfaces are well known; the angle of reflection equals the angle of incidence in the case of reflection and Snell's law in the case of refraction. For three-dimensional analysis, a vector formulation is convenient. Figure 11.21 shows the incident and reflected rays at a reflective surface where the unit vector normal to the surface, and pointing in the direction from which the rays are coming, is \mathbf{n} . The following vector equation is easily derived relating the reflected ray to the incident ray and \mathbf{n} :

$$\mathbf{r}_r = \mathbf{r}_i + 2(\mathbf{n} \cdot \mathbf{r}_i)$$

In the case in which a ray is incident at a boundary between two dielectric media, Snell's law applies. This is usually expressed as $n_2 \sin \theta_2 = n_1 \sin \theta_1$, where the coplanarity of the rays is understood. A vector form that expresses this is

$$n_1 \mathbf{r}_1 \times \mathbf{n} = n_2 \mathbf{r}_2 \times \mathbf{n}$$

Simple geometric shapes can be analyzed analytically using these relations, but modern practice is to use one of the many available ray-tracing packages that solve these equations numerically. This allows for incorporating various imperfections such as surface waviness and imperfections, and can give plots of the intensity profile at the receiver, and so on.

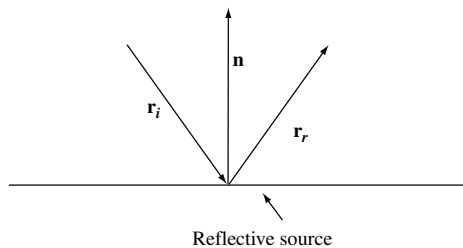


Figure 11.21 Relationship of the incident and the reflected rays to the surface normal

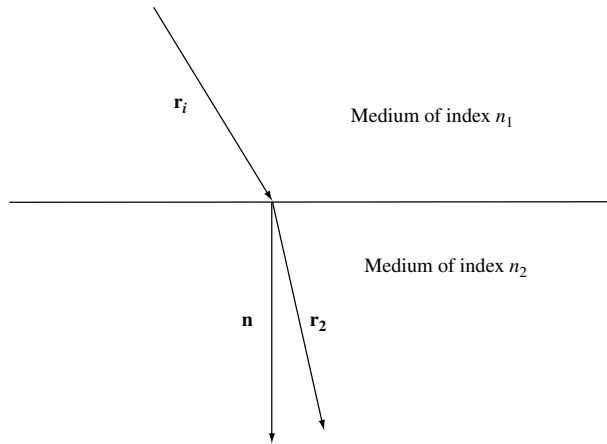


Figure 11.22 Vector relations during refraction

11.4.3 The Parabolic Concentrator

A basic concentrator configuration is the reflective parabolic concentrator shown in Figure 11.23. The two-dimensional cross section is shown, which could represent the cross section of either a two-dimensional linear parabolic trough or the cross section of a three-dimensional paraboloid of revolution.

The equation relating the x and y components of the parabolic surface is $y = 1/4Fx^2$, where F is the focal length of the parabola. It can be shown that all rays coming from straight up (i.e. with no x -component) will pass through the focus. If D is the diameter or width of the parabola, then this can be written in the normalized form

$$\frac{y}{D/2} = \frac{1}{8f} \left(\frac{x}{D/2} \right)^2$$

where $f = F/D$ is called the f -number of the parabola. Note that if $f = 1/4$, then when $x = D/2$, that is, at the rim of the parabola, $y = D/4 = F$. In other words, for an $f = 1/4$ parabola, the rim height is equal to the focal length. Obviously the slope at the rim is then 45° . Another useful relation that relates the distance from the focus to the parabolic surface, r , to the angle that the ray hits the receiver, θ_r , is

$$r = \frac{2F}{1 + \cos \theta_r}$$

and

$$x = r \sin \theta_r = \frac{2F \sin \theta_r}{1 + \cos \theta_r}$$

From this we can see that at the rim, when $x = D/2$ and the angle of rays at the receiver is maximum, we have

$$f = \frac{F}{D} = \frac{1}{4} \frac{1 + \cos \theta_{\max,r}}{\sin \theta_{\max,r}}$$

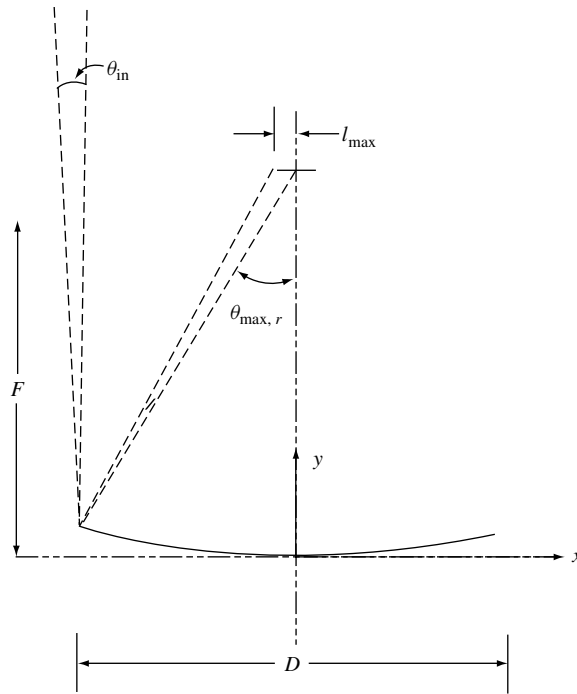


Figure 11.23 Cross section of a parabolic reflective concentrator

Now consider a ray that arrives at a small angle θ_{in} to the normal axis. It can be calculated that it will intercept the receiver at a distance s from the focus given by

$$s = \frac{r \sin \theta_{in}}{\cos \theta_r} = \frac{2F \sin \theta_{in}}{\cos \theta_r (1 + \cos \theta_r)}$$

This shows that s increases as one moves toward the rim, increasing θ_r . Clearly, the rays hitting the rim at $x = D/2$ will have the largest s . Noting that the total receiver size, S , required to capture all rays up to incident angles of $\pm\theta_{max,in}$ is $S = 2s_{max}$, gives

$$S = \frac{4F \sin \theta_{max,in}}{\cos \theta_{max,r} (1 + \cos \theta_{max,r})} = D \frac{\sin \theta_{max,in}}{\cos \theta_{max,r} \sin \theta_{max,r}}$$

For a two-dimensional parabolic trough, the concentration ratio is $C = D/S$, giving

$$C = \cos \theta_{max,r} \frac{\sin \theta_{max,r}}{\sin \theta_{max,in}}$$

It is interesting to note that the maximum concentration for a parabola without a secondary occurs at a rim angle of 45° (which corresponds to an f -number of 0.6) and is

$$C = \frac{1}{2} \frac{1}{\sin \theta_{max,in}}$$

When $\theta_{\max,\text{in}}$ is $1/4^\circ$, as for the sun, this equation gives a maximum concentration ratio of 100. We see that the parabola is not an ideal concentrator, but at a rim angle of 45° it does achieve half of the maximum possible concentration. As the rim angle becomes small, it actually approaches an ideal concentrator because then $\cos \theta_r \approx 1$, but at small rim angles the concentration ratio is also lowered. A parabola can be used in conjunction with various secondary concentrators located at the receiver to boost the concentration toward the ideal. If we have an ideal secondary concentrator that transforms $\theta_{\max,r}$ into $\theta_{\max,\text{out}}$, then it would have a concentration of $C_{\text{secondary}} = \sin \theta_{\max,\text{out}} / \sin \theta_{\max,r}$. The combined concentration of the parabola and secondary is

$$C_{\text{tot}} = C_{\text{secondary}} C_{\text{parabola}} = \cos \theta_{\max,r} \frac{\sin \theta_{\max,\text{out}}}{\sin \theta_{\max,\text{in}}}$$

This differs from an ideal concentrator of maximum output angle and high concentration by the cosine of the rim angle and approaches an ideal for small rim angles. In practice, small rim angles result in a rather unwieldy shape and a compromise is sought. The f -numbers in the range of 0.7 to 1 are usually specified when using a secondary concentrator.

For three-dimensional paraboloidal concentrators, one squares the above ratios to get the concentration. Specifically,

$$C = \cos^2 \theta_{\max,r} \left(\frac{\sin \theta_{\max,r}}{\sin \theta_{\max,\text{in}}} \right)^2$$

and at a rim angle of 45° , we have

$$C = \frac{1}{4} \left(\frac{1}{\sin \theta_{\max,\text{in}}} \right)^2$$

This gives a concentration ratio of 10 000 for a perfect paraboloid with $f = 0.6$.

Parabolic dishes are thus capable of quite high-concentration ratios. In practice, slope errors, or waviness in the reflective surface, degrade the performance. This can be analyzed to first approximation by realizing that a slope error of value θ_s will cause the reflected ray to deviate from the intended path by $2\theta_s$, and this will add to the angle of arrival $\theta_{\text{in,max}}$. A high-quality paraboloid for solar concentration use might have $\theta_s = 1/8^\circ$, thus doubling the divergence of light from the sun from $1/4^\circ$ to $1/2^\circ$. This has the effect of decreasing the concentration by one-fourth, to 2500 for a three-dimensional concentrator, or one-half, to 50, for a two-dimensional trough. Detailed designs should be conducted with actual ray-tracing programs, but this gives an idea of the results that can be achieved.

Parabolic concentrators are more highly developed for solar thermal applications in which high temperature is desired and flux uniformity is not so big an issue as with PV receivers. The successful Luz trough concentrators generate heat for steam turbines and have a combined output of over 300 MW [48]. A comprehensive review of parabolic dishes for solar thermal applications is given in [49].

In practice, reflective dishes can achieve higher concentration than desired for PV receivers. There is no need for SOEs to increase concentration, so the concentration ratio

is usually sacrificed to achieve flux uniformity and pointing tolerance. One method of doing this is the kaleidoscope flux homogenizer. This is simply a box in front of the receiver having internal reflecting walls. When properly designed, the incoming rays are scrambled by reflecting several times and are distributed relatively uniformly over the receiver, independently of where they arrived at the entrance aperture [32, 50].

11.4.4 The Compound Parabolic Concentrator

We have seen that the parabolic concentrator is not an ideal concentrator. The first realization of an ideal concentrator was the compound parabolic concentrator (CPC). As seen in Figure 11.24, this actually comprises two parabolic surfaces; however, the axis of each is tilted by $\pm\theta_{\max,\text{in}}$ and their foci are at opposite edges of the receiver. The parabolas are extended upwards until the surface is vertical, at which point the entrance aperture is as large as possible. When light is incident at the maximum angle, it is clear that all the light hits one parabolic surface and ends up focused at the receiver edge. As the light moves toward the normal, all the rays are directed more downward and continue to hit the receiver. Using the geometry of parabolic surfaces, it is straightforward, if a little tedious, to show that $C = 1/\sin\theta_{\max,\text{in}}$. So the CPC concentrator is ideal. If the CPC is

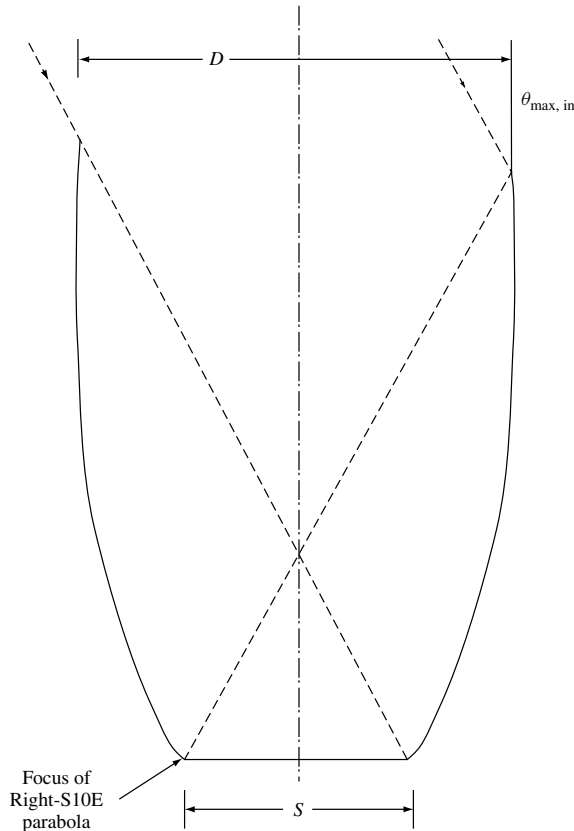


Figure 11.24 Geometry of the compound parabolic concentrator, in this case for $\theta'_{\max,\text{in}} = 30^\circ$

filled with a dielectric of index n , the incoming ray is refracted downward according to Snell's law so that the ray enters the CPC at angle $\theta'_{\max, \text{in}}$, giving $C = 1/\sin \theta'_{\max, \text{in}}$. Now $n \sin \theta'_{\max, \text{in}} = \sin \theta_{\max, \text{in}}$, which gives $C = n/\sin \theta_{\max, \text{in}}$, and so the CPC is still ideal.

Three-dimensional CPC concentrators can be made by revolving the two-dimensional cross section about the central axis. It turns out that, while the three-dimensional CPC has near-ideal concentration, it is not strictly ideal. Some rays (those that come near the edge with a large skew component) are rejected.

A problem with CPC concentrators is that they are rather long and narrow for high concentration. For dielectric-filled CPCs, this problem can be somewhat ameliorated by doming the top surface to get some initial concentration from the resulting lens. Figure 11.25 shows how doming the top affects CPC shape [2] in concentrators operating by total internal reflection (called DTIR for Direct Total Internal Reflection), which are also ideal in two dimensions.

CPCs are often used as secondary concentrators at the focus of a primary concentrator, particularly for Fresnel lens systems, because then they have a rather large acceptance angle and the resulting design is rather compact.

At the time of writing this, there were no known ideal three-dimensional concentrators that image onto a flat surface (unless with graded index of refraction, not treated here). The author knows of only one ideal three-dimensional concentrator, and it is shown in Figure 11.26. This images all rays striking a sphere onto a smaller sphere imbedded in a dielectric. If the radius of the outer sphere is r_1 and the inner sphere is r_2 , where $r_2 = r_1/n$, then the concentration ratio is n^2 , referenced to the surface areas of the spheres. Unfortunately, solar cells are generally not spherical.

11.4.5 The V-trough Concentrator

The CPC, while admittedly ideal, has some drawbacks. One is that the intensity pattern at the exit aperture is quite nonuniform under typical illumination conditions. It can be

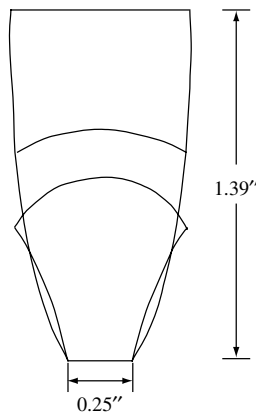


Figure 11.25 A series of dielectric-filled CPCs with flat and domed tops [2], all having the same concentration and a 10° acceptance angle. Adapted from Luque A, *Solar Cells and Optics for Photovoltaic Concentration*, 1989, Adam Hilger, © 2002 with permission by IOP Publishing Limited

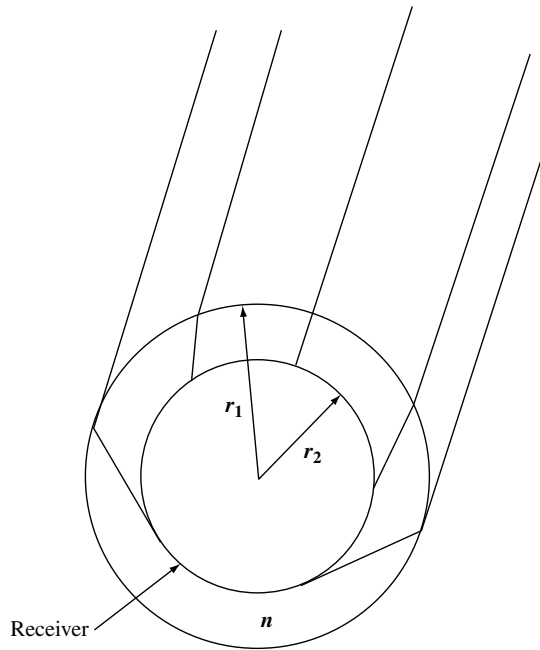


Figure 11.26 The ideal spherical concentrator of concentration ratio n^2

shown that the output intensity is uniform when the illumination is uniform over all directions within the acceptance angle. Such is not the case in practice, however, because the sun provides a localized region of the sky that is much brighter than the surrounding acceptance region (assuming that the acceptance angle is greater than the sun's half angle). A simplified version shown in Figure 11.27 uses planar reflectors and is often called a v-trough. The v-trough concentrator has a maximum intensity concentration of 3, thereby avoiding the hot spots of the CPC.

Referring to the symbols in Figure 11.27, some rather tedious but straightforward calculations indicate that the concentration ratio of the v-trough concentrator is (hint: use the law of signs on the triangle inside the trough)

$$C = 1 + \frac{2 \sin \theta_m \cos(\theta_i + 2\theta_m)}{\sin(\theta_i + \theta_m)}$$

When $\theta_i = 0$, one obtains $C = 1 + 2 \cos(2\theta_m)$, so the concentrator is clearly not ideal. In fact, it reaches a maximum concentration of 3 for small θ_m , that is, steep mirrors.

It should not be thought that the v-trough is necessarily inferior to the CPC concentrator. Besides the reduction in hot spots, it can be easier to manufacture, especially with flat glass mirrors. For wide acceptance angles and reasonable maximum exit angles such as 60° , v-troughs closely approach ideal concentrators. For example, when $\theta_i = 30^\circ$ and $\theta_m = 15^\circ$, then $\theta_{\text{out}} = 60^\circ$ and $C = 1.37$. This is 79% of the ideal concentration.

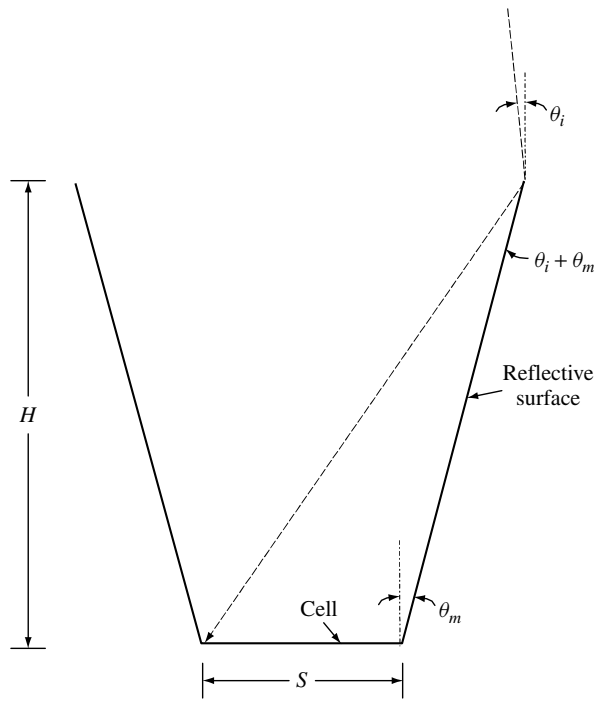


Figure 11.27 Geometry of a v-trough concentrator

Interestingly, if one allows for multiple reflections, then the v-trough approaches an ideal concentrator for small θ_m [51]. This results, however, in a very tall, narrow structure with many reflections. In contrast, the CPC has a maximum of one reflection.

Two-axis v-trough concentrators are made either by rotating the v-trough about its central vertical axis, forming an inverted truncated cone, or by combining two v-troughs at right angles, forming an inverted truncated pyramid. The resulting two-axis concentration approaches the square of the above numbers; however, as in the two-axis CPC, some of the rays within θ_i will not strike the receiver. The rotational version produces some regions of high intensity under certain illumination conditions as the light is focused off the cylindrical surface, whereas the square version does not suffer from this effect. Two-axis v-troughs are often used as secondary concentrators in conjunction with point-focus Fresnel lenses. With proper design, they can also smooth the flux profile over that obtained with the Fresnel alone.

11.4.6 Refractive Lenses

Refractive lenses are a common alternative to reflective lenses. Such a lens is shown in Figure 11.28.

The lens can be analyzed by ray-tracing using Snell's law. In the case we have shown, a plano-convex lens with the flat surface facing upwards, the analysis can be expedited using Fermat's principle, which states that rays at the focus all travel the same

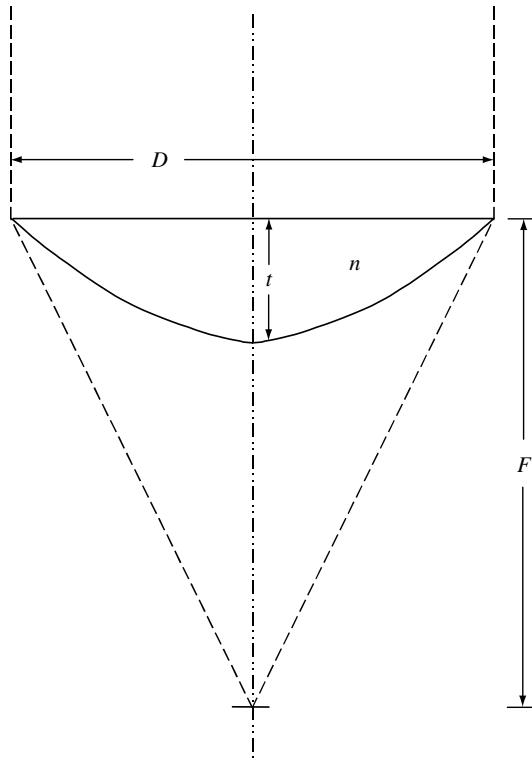


Figure 11.28 Refractive lens geometry

optical path length. (And hence, if they leave the source at the same time, they will arrive at the focus at the same time, regardless of where they strike the lens.) By equating the optical path length of the two rays shown in Figure 11.28, one obtains

$$F + (n - 1)t = \sqrt{(F - y)^2 + x^2} + ny$$

This is the equation of a hyperbola. Such a lens is called *aspheric* to differentiate it from the common spherical lens that is an approximation of the above for large F and small x . The thickness of the lens can be related to the f -number by setting $x = D/2$, the edge of the lens, giving

$$\frac{t}{D} = \frac{\sqrt{F^2/D^2 + 1/4} - F/D}{n - 1}$$

A serious problem with such a lens is that it becomes rather thick for short f -numbers. For example, for $F/D = 1$ and $n = 1.5$, one obtains $t/D = 0.24$. If the lens has a diameter of 10 cm, then the thickness will be 2.4 cm, resulting in a rather heavy, material-intensive structure. For small lenses on the order of several centimeters in diameter, the thickness is quite acceptable. Such “microlenses,” accompanied by small cells at the focus, are an interesting avenue for possible development. This approach was explored by Wattsun [52].

For larger lenses it is usual to collapse the lens back to zero thickness at a number of points, forming the Fresnel lens of Figure 11.29. Because of the need for very high optical quality surfaces on the curved facets, it has proved difficult to manufacture such lenses with high transmission [53] because the mold tool is manufactured using diamond point turning. This leaves microscopic grooves, which are difficult to polish out because of the presence of the vertical region between facets.¹⁴ If the facets are made small compared to the size of the cell, then flat facets can be used with little loss of concentration. In this case, the mold can be manufactured using a flat diamond turning tool, which gives very good optical surfaces.

Fresnel lenses do not transmit all the light they intercept to the focus. Losses come from several sources. First, Fresnel reflection from the optical interfaces causes about 8% loss (more for a short focal length lens because of the steep angle of the exit ray to the facet surface). This can potentially be reduced by the use of antireflection coatings. Second, the vertical regions between facets cannot be completely vertical or the lens cannot be removed from the mold. The angle of this portion is called the draft angle, and is in the neighborhood of 2° . Light striking this wall is deflected out of the focus. Finally, the tips and valleys have nonzero radius. Clearly, the smaller the facets, the more important

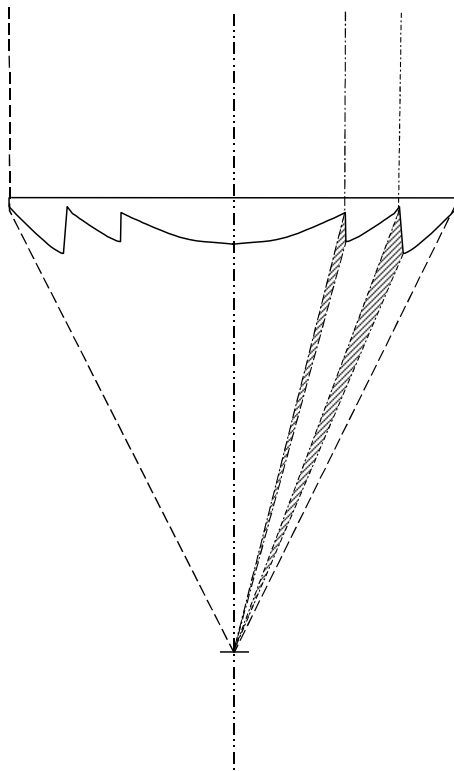


Figure 11.29 Cross section of a Fresnel lens

¹⁴ This work was performed in the 1980s. It is very likely that the modern tool making machines can produce a very high-quality mold.

this loss is. Modern flat-facet, compression-molded lenses have an optical transmission of typically about 85%.

To date, the highest performance point-focus Fresnel lenses have been made only by compression molding. This results in a rather expensive product because of the long cycle times in the molding machine. Attempts at injection molding, which has a much shorter cycle time, have been disappointing. To the author's knowledge, little effort has been expended on Fresnel-lens development using recent plastic molding technology such as compression-injection molding. Significant improvements in performance and cost are likely possibilities with a concerted effort.

Entech has developed an innovative domed linear Fresnel lens illustrated in Figure 11.30. Because of the dome, the light is refracted upon entering the lens, and refracted again upon exiting. Many benefits are obtained by making the angle of the rays to the lens surface approximately the same as they enter and exit the lens. It can be shown that this condition minimizes reflection loss, minimizes chromatic aberration (spreading of the image for different wavelengths due to dispersion in the index of refraction), minimizes the effect of deflection in the lens, and minimizes the size of the focus. In addition, the draft region and tip radius can be outside the ray path, as seen in Figure 11.30. The transmission of a domed Fresnel lens can exceed 90%, close to the loss for a flat acrylic sheet alone [54].

One cost-effective method of producing Fresnel lenses has been 3M, and is called Lensfilm. In his method, a thin acrylic plastic sheet is molded by an embossed roller

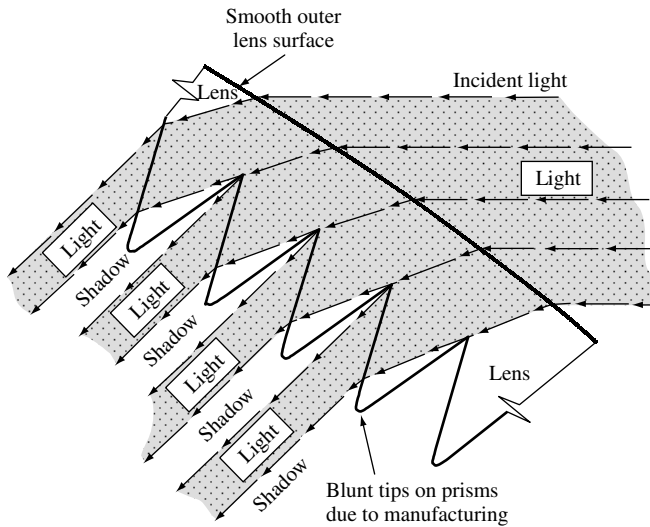


Figure 11.30 Cross section of the Entech domed Fresnel lens showing how the angle of incidence is nearly equal to the angle of exit, as well as how rays are shielded from the draft and the tip radius regions. Reproduced from O'Neill M, "Acrylic Extrusion/Embossing Process Development for the Low-Cost Production of Linear Fresnel Lenses", Presented at *Photovoltaic Concentrator Technology Development Project, Sixth Project Integration Meeting* (Albuquerque, NM, 1980) with permission by Sandia National Laboratories

on a continuous basis. The sheet is later bonded to an acrylic superstrate for mechanical strength. This method yields larger draft angles than compression molding and results in slightly lower transmission for flat, point-focus lenses. In contrast, it is particularly suited to the domed linear Fresnel approach of Entech, because when the lens is warped into the domed shape, the facets are deflected to an angle where the draft is out of the ray path.

The reader interested in the details of Fresnel lens design is referred to textbooks on the subject [2]. Modern design usually involves numerical ray-tracing analysis coupled with electronic design transfer to numerically controlled machining for tool making. Commercial programs, such as those available from James and Associates, are available for implementing this procedure.

11.4.7 Secondary Optics

Secondary optical elements are often used to increase concentration, or alternatively to increase acceptance angle. They are applicable with either reflective or refractive systems; however, they are most often used with point-focus Fresnel lenses in which concentration ratios in the range of 200 to 1000 are typical. Three types of secondaries are common: v-troughs, refractive CPCs, and refractive silos. These are described below.

Figure 11.31 shows the case of a Fresnel lens coupled with a v-trough. This design was for a 500X Fresnel module [30]. In this case the lens was designed with multiple

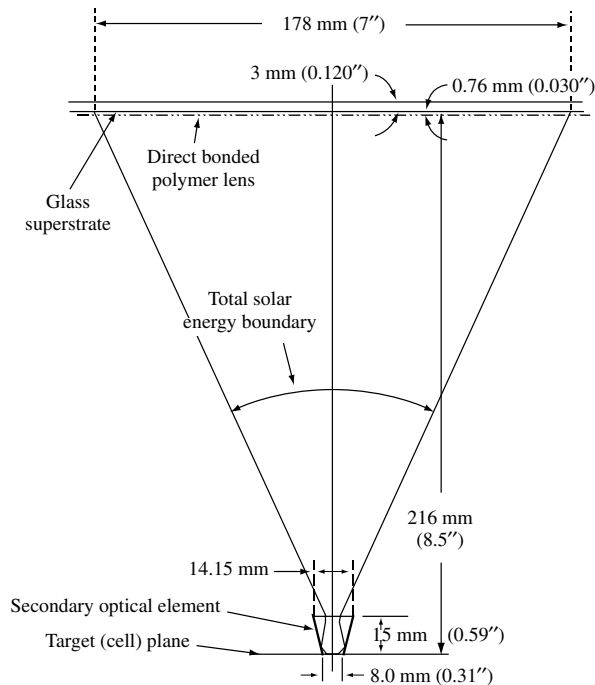


Figure 11.31 Lens cell configuration for a Fresnel lens with v-trough secondary [30]. Copyright © 1984. Electric Power Research Institute. AP-3263. *Conceptual Design for a High-Concentration (500X) Photovoltaic Array*. Reprinted with permission

zones of different focal lengths in order to smooth the flux profile. The secondary provides additional smoothing while providing 3X concentration. Generally, such secondaries are made with reflective aluminum sheet.

Dielectric-filled CPCs have also been used as secondary optical elements. In one case a concentration of 1000X was achieved on GaAs cells with an acceptance angle of $\pm 0.8^\circ$ [55].

As mentioned above, CPCs can have a rather nonuniform output. There is another type of secondary that gives almost uniform illumination intensity. The basic idea is to image the primary lens onto the cell [56]. Thus, if light strikes the primary uniformly, the illumination on the cell will be uniform. The principle is illustrated in Figure 11.32. The top surface of the secondary is an aspheric surface that images the lens on the cell. The definition of this surface can be found by using the same methodology as for the plano-convex lens mentioned above. In practice, however, it is usual to use ray tracing to optimize the shape of the lens in order to minimize the effect of edge ray distortion.

It is seen that the center of the primary lens is imaged on the center of the cell and the edge is imaged on the edge of the cell. If the lens is uniformly bright, then so will be the cell illumination. Some understanding of the operation of a silo secondary can be

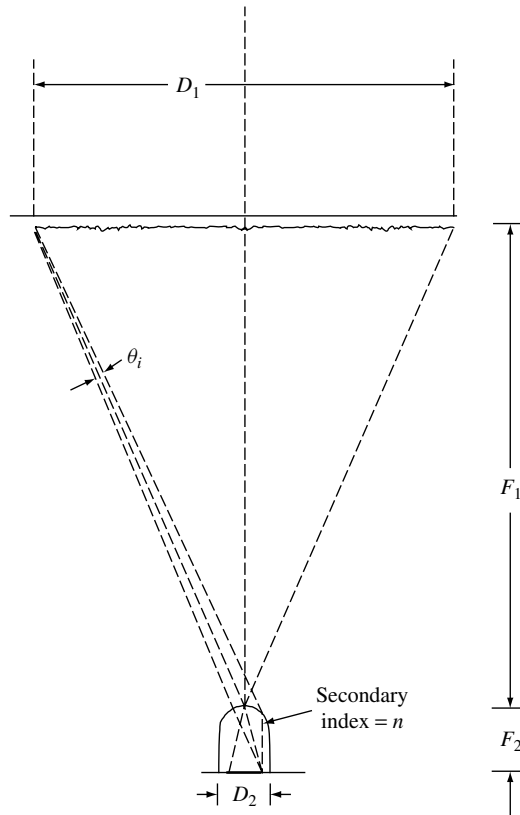


Figure 11.32 Geometry of a silo secondary

gleaned by a simple analysis using the above rays where it is found that for large primary lens f -numbers, the concentration is

$$C = \frac{nF_1}{F_2} = \frac{n}{2(F_2/D_2) \sin \theta_i}$$

For two-axis concentration, this relation is squared. The combination of Fresnel primary and silo secondary is seen to be ideal if the f -number of the secondary is 1/2. Note that it can be shown that a lens with f -number less than 1/2 cannot be realized, preventing the above from violating the maximum concentration law.¹⁵ Nevertheless, concentration ratios of around one-fourth the maximum are readily obtained. Despite the loss of some acceptance angle, the uniform output provides significant advantages to this approach.

11.4.8 Static Concentrators

The necessity of tracking concentrators has long been considered a disadvantage. While there is little doubt that tracking systems can be made cost-effectively when manufactured in very large volumes and installed in large “energy parks” with 50-MW or more capacity [57], the existing markets for PV systems are for smaller installations. This has led to considerable research to find a nontracking or static concentrator. Most of the early work was for solar thermal concentrators in which the basic principles were established [58].

Static concentrators rely on three factors to generate concentration greater than unity. First, the region of the sky where most of the energy falls within a band $\pm 24^\circ$ of a plane normal to the Earth’s axis of rotation. Figure 11.33 shows a typical yearly average distribution of light falling on a plane tilted at the latitude angle, for a latitude of 34° south [59]. This is representative of what is found at most locations, where the bulk of the energy falls in a band of angles around the normal to a plane that is tilted at the latitude angle. An ideal one-axis concentrator with an acceptance angle of 24° has a concentration of 2.5. When the details of such concentrators are examined, it is found that they do not receive all the light early in the morning or late in the evening when the sun is near the solstices, but most of the energy can be harvested if the acceptance angle is opened slightly [2].

The second reason that the concentration can be increased is that the cell can be immersed in a dielectric with index of refraction greater than unity. This can typically provide another factor of 1.5X for one-axis and 2.25X for two-axis concentrators.¹⁶ Unfortunately, such dielectric-filled concentrators are rather heavy and expensive if the cells are large. One possibility is to make very small cells coupled with small dielectric concentrators [60]. The practicality of this “microconcentrator” approach depends on the ability to highly automate the assembly of many small cells into the module. Finally, solar cells can be made bifacial, that is, sensitive to light from both sides. This provides

¹⁵ More correctly, this should be thought of as proof that it is impossible to make a lens shorter than $f/0.5$.

¹⁶ Sometimes it is also overlooked that immersing a cell in a dielectric medium that is not a thin planar surface (such as in a glass module) will increase the escape probability of rays reaching the cell’s top surface from within and, hence, reducing the impact of light trapping. This type of effect also happens in dielectric secondaries, and results in the loss of several percent in current for silicon cells that rely on light trapping.

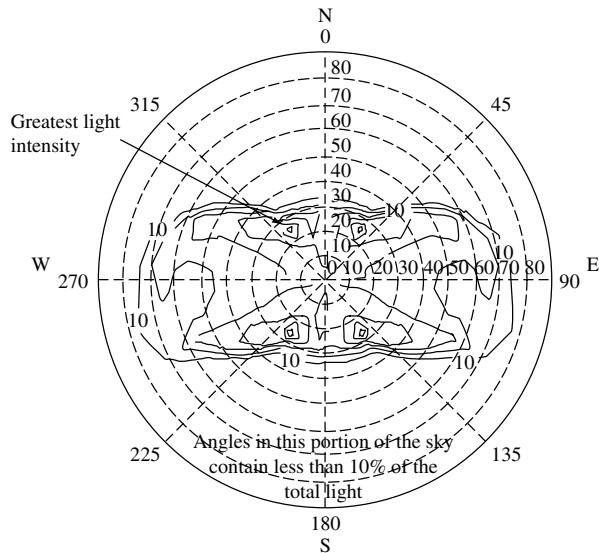


Figure 11.33 Yearly average distribution of incident light as seen by a module with tilt angle equal to the latitude of 34° south. Reproduced from Bowden S, Wenham S, Green M, “High Efficiency Photovoltaic Roof Tiles with Static Concentrators”, *Proc. 12th European Photovoltaic Solar Energy Conference*, 1893–1896 (1994) with permission by WIP

potentially another factor of $2X$ concentration. Bifaciality alone can yield a concentration of $2X$ by providing for cusps that direct light to the cell [61]. Goetzberger reviewed various static concentrator options and proposed a combination of all of the above that attains a concentration of $12X$ [62]. Figure 11.34 illustrates the possibilities.

Another approach to static concentrators is the dielectric prism, which relies on total internal reflection. This concept has been refined by incorporating grooves on the back surface, which improves the light trapping [63]. Concentration ratios of around $4X$ are achieved. Figure 11.35 illustrates the concept.

To date, no firm has succeeded in commercializing static concentrators. Apparently, no concept examined so far appears to offer compelling advantages over a standard flat-plate module. It is a fruitful line of research to see if a cost-effective design can be found. The concentrator must have wide acceptance angle (over 30° in one direction and near 90° in the perpendicular direction) and have reasonable concentration (say, over $2X$). Both of these are clearly possible. In addition, however, the device must not cost more to implement than the cell area replaced, and must not significantly degrade the module performance compared to a flat-plate. Therein lies the challenge. Until it is clear that such a device is impossible, the payoff is sufficient to warrant continued search.

11.4.9 Innovative Concentrators

The methodology of nonimaging optics has been extended to a large variety of new and innovative designs. Many of these are covered in the text *Solar Cells and Optics for Photovoltaic Concentration* [2]. One recent and particularly interesting case is the RXI

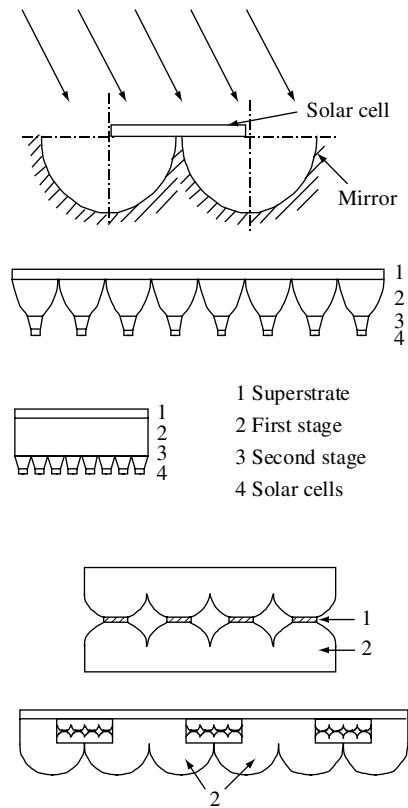


Figure 11.34 A combination of concentrators achieving 12X concentration. (a) 2X trough; (b) dielectric CPC; and (c) the combination. Goetzberger A, *Static Concentration Systems with Enhance Light Concentration*, 20th IEEE Photovoltaic Specialists Conference © 1988 IEEE

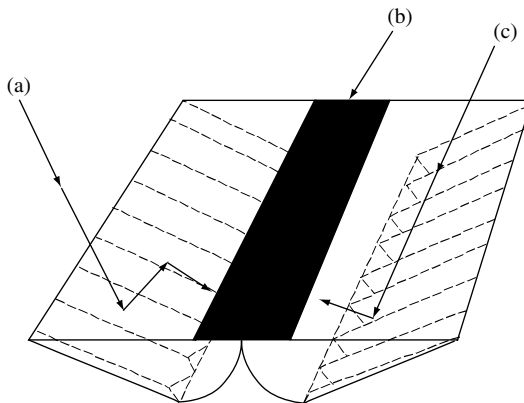


Figure 11.35 Static concentrator using bifacial cells with dielectric prisms. Bowden S, *High Efficiency Photovoltaic Roof Tiles with Static Concentrators*, First World Conference on Photovoltaic Energy Conversion © 1994 IEEE

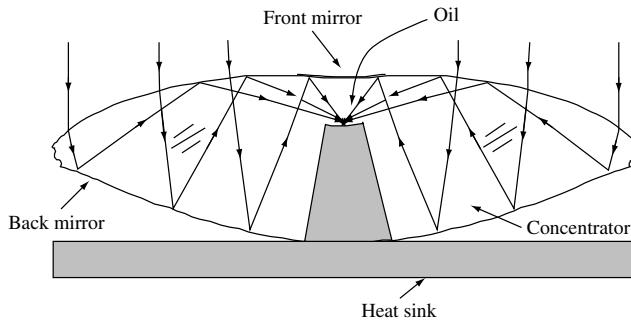


Figure 11.36 The RXI concentrator cross section. This version has an acceptance angle of 2.7° and a concentration of 1000X, and is close to ideal. Minano J, Gonzalez J, Zanesco I, Flat High Concentration Devices, *First World Conference on Photovoltaic Energy Conversion* © 1994 IEEE

concentrator shown in Figure 11.36 [64]. The name RXI comes from the fact that the lens uses refraction, reflection (denoted by X), followed by internal reflection. This device can be thought of as a two-axis version of the prism concentrator that relies on total internal reflection and that has been fine-tuned for optimum performance. The result is a very shallow device using a minimum of dielectric material. It is most suited for small apertures, and hence very small cells, so that the overall thickness and volume of material is minimized.

Other innovative concentrators include the D-SMSTS (Dielectric-Single Mirror Two Stage) trough, which incorporates refractive secondaries into a reflective trough primary lens [65]. This device, whose cross section is shown in Figure 11.37, achieves one-axis concentration of 30X with a high acceptance angle of 2.44° . This is close to an ideal concentrator, which would give 2.87° acceptance angle at 30X and $n = 1.5$.

11.4.10 Issues in Concentrator Optics

The preceding sections discuss the theoretical aspects of designing PV concentrating optics. The designer is also faced with difficult materials and manufacturing issues.

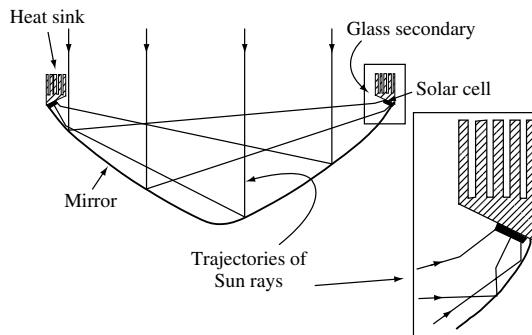


Figure 11.37 Cross section of the D-SMSTS reflective trough concentrator. Reproduced from Mohedano R, Benitez P, Perez F, Minano J, “Design of a Simple Structure for the D-SMSTS Concentrator”, Presented at 16th *European Photovoltaic Solar Energy Conference* (Glasgow, UK, 2000) by permission of WIP [65]

The optical concentrator must withstand at least 20 years of outdoor weathering. It must also be cleanable in order to remove accumulated dust and grime. On top of this, it must meet cost targets and have good optical performance. These are difficult requirements.

For reflective surfaces, the only suitable material found to date is back-surface-silvered, low-iron glass. Glass is very durable and protects the silver surface from corrosion and damage. This has been well proven in the large LUZ solar thermal plants [66]. If the radius of curvature for the surface is less than about 10 m, then the glass must be sagged at high temperature to the desired shape (much as automobile windshields are manufactured), which adds to the cost. Many attempts at making reflectors of polymer film with deposited silver have been tried; however, to date none has had sufficient weatherability for commercial concentrator use. Anodized aluminum sheet is another option, but it has lower reflectance than silvered glass and questionable weatherability. Anodized aluminum can be used in the interior of modules, such as for SOEs, where it is protected from the weather.

The most common material for refractive lenses is acrylic plastic (PMMA).¹⁷ When combined with UV stabilizers, acrylic has shown very good weatherability [67]. It has some disadvantages, however, which must be worked around. Chief among these is its large thermal expansion coefficient, low strength and stiffness, water absorption expansion, and susceptibility to scratches when cleaning with any method other than spray rinsing. Considerable effort has been expended on ways to bond thin acrylic lenses behind glass [68], but the large difference in expansion coefficients has stymied any solution. Another approach to realize the advantage of a glass front surface has involved the lamination of alternative materials to acrylic, particularly those with a low Young's modulus [30]. Recently, the idea of molding silicone rubber to glass has been revived [69]. This may be the ultimate solution for long-lasting Fresnel lenses that can be integrated into practical modules.

For point-focus SOEs, acrylic is unsuitable because the small amount of residual absorption causes the lens to overheat and melt. In this case, optical glass is needed. Quartz has been successfully used, but is expensive. Pyrex is cost-effective, but has too high an absorptance and overheats. Schott BK7 optical glass works well initially, but tends to solarize (turn purple) with exposure to the intense, concentrated light in a secondary [70]. Groups developing glass secondaries must work closely with glass suppliers to select the best glass with the best combination of cost, moldability, and resistance to solarizing.

11.5 CURRENT CONCENTRATOR ACTIVITIES

There are a number of groups working on concentrator PV systems around the world. This section outlines the diversity of this global effort. Only the larger, more well-funded activities are included. There are a number of small-scale, exploratory activities in addition to those discussed. The promise, quality, and vitality of research on concentrators will become apparent when reviewing the diversity and scope of this work.

¹⁷ The only common optical plastics that are sufficiently stable under UV radiation in sunlight are acrylic plastic, Teflon, Tedlar, Tefzel, and silicone. Silicone cannot be used on an exterior surface.

11.5.1 Amonix

Amonix, Inc. and SunPower Corporation are the two companies that licensed the high-efficiency point-contact solar cell from EPRI. This cell was developed at Stanford University under EPRI funding. Amonix has developed a 20-kW point-focus Fresnel lens array intended for the utility market. It has an innovative integral-backplane module design that greatly reduces the number of parts by incorporating the wiring and cell package as a part of the module back [34]. Systems have been installed at PVUSA and the Arizona Public Service's STAR facility. They recently announced that five more systems are under order. Figure 11.38 shows a recent Amonix array.

11.5.2 Australian National University

Australian National University (ANU) is developing a linear trough concentrator system. They are also developing a novel, rather simple silicon concentrator cell, which is expected to have 22 to 23% efficiency with only one nonaligned photolithography step. The cells are designed for operation at 30X concentration. Work is under way on a 2-kW demonstration at Spring Valley, Australia. They expect the system to have a 15% overall efficiency [71].

11.5.3 BP Solar and the Polytechnical University of Madrid

A 480-kW concentrator project (the largest ever) has been built recently in Tenerife, Canary Islands [50]. It is called the Euclides Project and is part of the European Joule program. Euclides is composed of 14 one-axis tracking reflective parabolic troughs, each 84 m long, with specially designed PV receiver modules built by BP Solar using buried contact solar cells operating at 38X geometric concentration. The reflector is a very lightweight and innovative space-frame design developed at the Polytechnical University of Madrid. The system uses passive cooling, accomplished with another innovative concept – heat sinks built of compression-bonded, thin aluminum fins. The system has approximately 13% overall efficiency and is projected to produce power at 23 cents per kWh, half the cost of power from a crystalline flat-plate plant. This cost is projected to



Figure 11.38 Amonix 100-kW high-concentration Fresnel lens array at the Glendale, California Airport

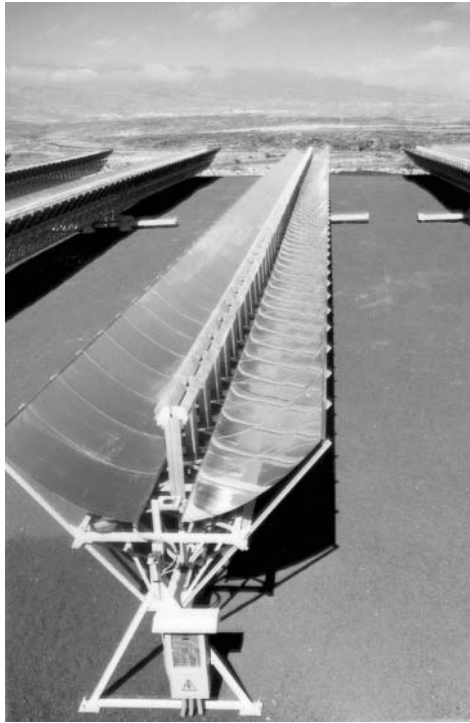


Figure 11.39 Picture of the Euclides linear trough system

drop to 13 cents per kWh at a production volume of 15 MW/year. Figure 11.39 shows a picture of the Euclides system.

11.5.4 Entech

Entech, Inc. has been pursuing line-focus Fresnel concentrators since the start of the Federal PV program. They hold a fundamental patent on curved Fresnel lenses that have very high transmission (90%). These systems have improved over the years through demonstration projects at PVUSA, the 300-kW Austin 3M system, a 100-kW system at the Solar Park in Ft. Davis, Texas, being developed by Central and South West Utilities, and a 100-kW system at the Energy Park near Dallas, Texas, being developed by TU Electric. Entech was also part of the DOE PVMaT program to improve PV manufacturing processes. Entech systems use modified one-sun cells operating at 20X. Their newest, fourth-generation modules have an efficiency of about 15% at standard operating conditions. Entech projects a levelized electricity cost of 7 to 15 cents/kWh at an annual production rate of 30 MW/year [72]. A picture of an Entech system appears in Figure 11.12.

11.5.5 Fraunhofer-Institut für Solare Energiesysteme

The Fraunhofer Institute has been researching both concentrator cells and systems. GaAs cell efficiencies in the 24% range have been demonstrated. Fresnel module efficiencies

of 19% were achieved [73]. Concentrator silicon cells are also being researched. An innovative one-axis reflective tracking concentrator design was demonstrated that achieves 300X concentration through a refractive CPC-type secondary concentrator [41].

11.5.6 Ioffe Physical-Technical Institute

The Ioffe Physical-Technical Institute has a long history with compound semiconductor solar cell development, particularly for concentrator cells. Recently, they have been developing GaSb and AlGaAs cells for multijunction applications. As part of a European consortium, they have developed a unique, all-glass concentrator module that uses GaAs cells and a thin silicone Fresnel lens, molded to the inside of the top glass sheet. This approach appears very promising [69].

11.5.7 National Renewable Energy Laboratory

National Renewable Energy Laboratory (NREL) conducts leading-edge research on high-efficiency, multijunction solar cells. They have achieved a record 30% efficient GaInP/GaAs two-junction monolithic concentrator cell operating at 150X [74], and even higher efficiency in collaboration with Spectrolab, as seen below. Interestingly, the pioneering research on compound semiconductor solar cells conducted at NREL has found widespread application in high-efficiency space solar cells. It is curious to contemplate that when the concentrating PV industry is ready to accept high-efficiency multijunction cells, the lowest cost route to securing their supply could be through the space solar cell industry, which would have had considerable manufacturing experience with multijunction cells by then.

11.5.8 Polytechnical University of Madrid

The Polytechnical University of Madrid has had a long-term program on concentrators, of which the Euclides project mentioned above is only a part. This includes pioneering work in the optics of concentrators, as well as GaAs concentrator cells. Their work, particularly that on static concentrators, is well described in the textbook, *Solar Cells and Optics for Photovoltaic Concentration* [2]. Recently, a new type of concentrator has been invented and researched, called the RXI concentrator discussed in Section 11.4 [64]. It is designed to use small GaAs cells that are only 1 mm on a side and manufactured and packaged similarly to LEDs. Modules built using this approach will resemble flat-plate modules, yet potentially exhibit very high performance and low cost. Additionally, the large acceptance angle reduces the cost of tracking structure. Such modules could be applicable for certain markets currently served by flat-plate modules. A consortium has been formed to further develop the RXI concentrator including the University of Madrid, the Ioffe Physico-Technical Institute (Russia), Energies Nouvelles et Environment (Belgium), Vishay Semiconductors (Germany), and Progressive Technologies (Russia). The system is called Hercules [75]. The team calculates that it could deploy systems that produce electric power at 0.104 euros/kWh using present performance and ultimately 0.033 euros/kWh at a production volume of 1000 MW. This is the lowest cost of energy projection reported

for a PV system, and would be very remarkable if it holds up in practice. SunPower is also working on a similar concept in partnership with the Polytechnical University of Madrid, except that they are using silicon cells [76].

11.5.9 Solar Research Corporation

Solar Research Corporation, Pty. Ltd., is developing reflective dish concentrators and water-cooled close-packed PV arrays for use at the focus [77]. A single close-packed silicon array produced more than 200 W with a reported efficiency (not independently confirmed) of 22% at 239 suns and a GaAs module produced 85 W with an efficiency of 18% at 381 suns. These systems will be deployed first in the Australian outback by an affiliated company, Solar Systems, Pty. The design has progressed to the point where full-sized prototype dishes have been tested and Solar Research Corporation is preparing for a larger system test. Figure 11.40 shows the Solar Systems dish in operation.

11.5.10 Spectrolab

Spectrolab, a major manufacturer of multijunction solar cells for space application, has initiated a concentrator cell and module development effort utilizing their high-efficiency cells. They recently announced a 34% conversion efficiency cell, a remarkable result, especially considering that the high efficiency was obtained at sufficiently high concentration for practical, low-cost module use.¹⁸

11.5.11 SunPower Corporation

SunPower Corporation manufactures a variety of high-efficiency silicon concentrator solar cells. These include cells designed for point-focus Fresnel lens applications as well as cells designed for closely spaced arrays for use with large dishes and central receivers. Design concentration ratios vary from 250X to 400X. Peak efficiency is around 27% at 100X, dropping to 26% at 250X. SunPower has built complete water-cooled dense



Figure 11.40 Solar Systems 24-kW dish concentrator-PV system in operation

¹⁸ Spectrolab press release.

arrays for dish and TPV applications. These cells are supplied to companies developing concentrating systems.

11.5.12 University of Reading

The University of Reading, United Kingdom, is researching a variety of concentrating approaches including point-focus Fresnel modules [78] and novel reflective trough modules [79].

11.5.13 Tokyo A&T University

Tokyo A&T University has been researching two and three-dimensional refractive static concentrators. These are designed to accept most of the diffuse light and, hence, are suitable for cloudy climates [80]. The two-dimensional lens has a concentration of 1.65X and the three-dimensional lens has a concentration of around 2X. While it might be concluded that this modest concentration is hardly worth the effort, it must be remembered that these systems use standard one-sun cells and the cell cost, which dominates module cost, is correspondingly reduced by these factors.

11.5.14 Zentrum fur Sonnenenergie und Wasserstoff Forschung Baden Wurttemberg (ZSW)

Zentrum fur Sonnenenergie und Wasserstoff Forschung Baden Wurttemberg (ZSW), in conjunction with a European consortium consisting of BP Solar, the Instituto de Energias Renovables (Spain) and the University of Crete, is developing a promising low-concentration system based on a 2X v-trough concentrator. The system uses polar-axis tracking that is driven by a passive, thermo-hydraulic system. This results in a simple, maintenance-free system that is projected to offer a 40% cost advantage over fixed, flat-plate modules [81].

REFERENCES

1. Swanson R, Sinton R, "High-Efficiency Silicon Solar Cells", in Boer K, Ed, *Advances in Solar Energy*, Vol. 6, 427–484, Plenum Press, New York (1990).
2. Luque A, *Solar Cells and Optics for Photovoltaic Concentration*, Adam Hilger, Bristol, Philadelphia (1989).
3. Swanson R, *Prog. Photovolt.: Res. Appl.* **8**, 93–111 (2000).
4. Kaminar N *et al.*, "Cost Effective Concentrator Progress", *Twenty Third IEEE Photovoltaic Specialists Conference*, 1213–1215 (1993).
5. Butti K, Perlin J, "The History of Terrestrial Uses of Solar Energy", in Kreider J, Kreith F, Eds, *Solar Energy Handbook*, McGraw-Hill, New York (1981).
6. Chapin D, Fuller C, Pearson G, *J. Appl. Phys.* **25**, 676 (1954).
7. Pfeifer C, Schoffer P, Spars B, Duffie J, *Trans. ASME, J. Eng. Power* **January**, 33–38 (1962).
8. Beckman W, Schoffer P, Hartmann Jr. W, Lof G, *Sol. Energy* **10**, 132–136 (1966).
9. Ralph E, *Sol. Energy* **10**, 67–71 (1966).
10. Sandia, Presented at *First Project Integration Meeting* (Denver, CO, 1978).

11. Boes E, "Photovoltaic Concentrators", *Proc. IEEE Photovoltaic Specialists Conference*, 944–951 (1980).
12. Boes E, "Photovoltaic Concentrator Progress", *Proc. IEEE Photovoltaic Specialists Conference*, 702–712 (1982).
13. Donovan R, "10 kW Photovoltaic Concentrator Array Fabrication", Presented at DOE/Sandia *Photovoltaic Concentrator Technology Development Project, Second Project Integration Meeting* (Albuquerque, NM, 1978).
14. Broadbent S, "Development, Fabrication and Performance Improvement of Current Baseline Concentrating Photovoltaic Converters", Presented at *Tenth Photovoltaic Concentrator Project Integration Meeting* (Albuquerque, NM, 1983).
15. Edenburn M, Boes E, "Photovoltaic Concentrators: Performance and Reliability Data and Future Design Directions", *IEEE Photovoltaic Specialists Conference*, 473–481 (1984).
16. O'Neill M, "A Low-Cost 22.5X Linear Fresnel Lens Photovoltaic Concentrator Module, Which Uses Modified, Mass Produced, One-Sun Silicon Solar Cells", *Proc. IEEE Photovoltaic Specialists Conference* (1885).
17. McDanal A, *Development of a Stand-Alone Linear Fresnel Lens Photovoltaic Collector Array*, Sandia National Laboratories, Albuquerque, NM, SAND84-0556 (1984).
18. Boes E, "A Summary of Recent Photovoltaic Concentrator Technology Developments", *Proc. IEEE Photovoltaic Specialists Conference*, 21–30 (1988).
19. Chiang C, Richards E, "A Twenty-Percent-Efficient Photovoltaic Concentrator Module", Presented at *Twenty-First IEEE Photovoltaic Specialists Conference*, Orlando, FL (1990).
20. Richards E, Chiang C, Quintana M, "Performance Testing and Qualification of Sandia's Third Baseline Photovoltaic Concentrator Module", Presented at *1990 DOE/Sandia Crystalline Photovoltaic Technology Project Review Meeting*, Albuquerque, NM (1990).
21. Kaminar N, Curchod D, "SEA 10X Module Development", Presented at *1990 DOE/Sandia Crystalline Photovoltaic Technology Project Review Meeting* (1990).
22. Maish A, "Progress in the Concentrator Initiative Program", Presented at *Twenty Third IEEE Photovoltaic Specialists Conference* (Louisville, KY, 1993).
23. Salim A, Huraib F, Eugenio N, Lepley T, "Performance Comparison of Two Similar Concentrating PV Systems Operating in the U.S. and Saudi Arabia", *Proc. IEEE Photovoltaic Specialists Conference*, 1351–1357 (1987).
24. Farmer B, *1995 PVUSA Progress Report*, PG&E March 1996.
25. O'Neill M, McDanal A, "The 25 kW SolarRow: A Building Block for Utility-Scale Concentrator Photovoltaic Systems", *Proc. IEEE Photovoltaic Specialists Conference*, 1529–1532 (1996).
26. Swanson R, "Silicon Photovoltaic Cells in TPV Conversion", Presented at *IEEE International Electron Devices Meeting* (Washington, DC, 1978).
27. Swanson R, "Silicon Photovoltaic Cells in TPV Conversion," Electric Power Research Institute EPRI ER-1272, December, 1979.
28. Zhao J, Wang W, Green M, "24% PERL Structure Solar Cells", Presented at *Twenty First IEEE Photovoltaic Specialists Conference* (Kissimmee, FL, 1990).
29. Sinton R, Swanson R, "An Optimization Study of Si Point-Contact Solar Cells", Presented at *Nineteenth IEEE Photovoltaic Specialists Conference* (New Orleans, LA, 1987).
30. Levy S, *Conceptual Design for a High-Concentration (500X) Photovoltaic Array*, Electric Power Research Institute, Palo Alto, CA, AP-3263 (1984).
31. Gruenbaum P, Sinton R, Swanson R, "Stability Problems in Point-Contact Solar Cells", Presented at *Twentieth IEEE Photovoltaic Specialists Conference* (Las Vegas, NV, 1988).
32. Verlinden P, Sinton R, Swanson R, Crane R, "Single-Wafer Integrated 140 W Silicon Concentrator Module", *Proc. IEEE Photovoltaic Specialists Conference*, 739–743 (1991).
33. Gunn J, Dostalek F, "EPRI 25 kW High Concentration Photovoltaic Integrated Array Concept and Associated Economics", Presented at *Twenty Third IEEE Photovoltaic Specialists Conference* (Louisville, KY, 1993).

34. Garboushian V *et al.*, "A Novel High Concentration PV Technology for Cost Competitive Utility Bulk Power Generation", Presented at *First World Conference on Photovoltaic Energy Conversion* (Hawaii, 1994).
35. Verlinden P, Swanson R, Crane R, Wickham K, "A 26.8% Efficient Concentrator Point-Contact Solar Cell", Presented at *Thirteenth EC Photovoltaic Solar Energy Conference* (Nice, France, 1995).
36. Sater B, Brandhorst H, Riley T, Hart R, "The Multiple Junction Edge Illuminated Solar Cell", *Tenth IEEE Photovoltaic Specialists Conference*, 188 (1972).
37. Luque A *et al.*, "Double Sided (D.S.) Solar Cells to Improve Static Concentration", Presented at *Proc. European Photovoltaic Solar Energy Conference* (Luxembourg, 1977).
38. Luque A, Cuevas A, Eguren J, *Solid State Electron.* **21**, 793–794 (1978).
39. Cuevas A, Luque A, Eguren J, Alamo J, *Sol. Energy* **29**, 419–420 (1982).
40. Luque A *et al.*, "Quasi Static Concentrated Array with Double Sided Illuminated Solar Cells", Presented at *Proc. ISES International Meeting* (Atlanta, GA, 1979).
41. Brunotte M, Goetzberger A, Blieske U, *Sol. Energy* **56**, 285–300 (1996).
42. Swanson R, "Point Contact Silicon Solar Cells", Presented at *Seventeenth IEEE Photovoltaic Specialists Conference* (Kissimmee, FL, 1984).
43. Gee J, Virshup G, "A 31%-Efficient GaAs/Silicon Mechanically Stacked Multijunction Concentrator Solar Cell", Presented at *Twentieth IEEE Photovoltaic Specialists Conference* (Las Vegas, NV, 1988).
44. Cotal H *et al.*, "Triple Junction Solar Cell Efficiencies Above 32%: The Promise and Challenges of their Application in High-Concentration-Ratio PV Systems", Presented at *Twenty-Eighth IEEE Photovoltaic Specialists Conference* (Anchorage, AK, 2000).
45. O'Neill M *et al.*, "Development of Terrestrial Concentrator Modules Incorporating High-Efficiency Multi-Junction Cells", Presented at *Twenty-Eighth IEEE Photovoltaic Specialists Conference* (Anchorage, AK, 2000).
46. Winston R, *J. Opt. Soc. Am.* **60**, 245 (1970).
47. Welford W, Winston R, *Optics of Nonimaging Concentrators*, Academic Press, New York (1978).
48. DeMeo E, Steitz P, "The U.S. Electric Utility Industry's Activities in Solar and Wind, Survey and Perspective", in Boer K, Ed, *Advances in Solar Energy*, Vol. 6, 60–64, Plenum Press, New York (1990).
49. Jaffe L, *Sol. Energy* **42**, 173–187 (1989).
50. Tilford C *et al.*, "Development of a 10 kW Reflective Dish PV System", *Proc. IEEE Photovoltaic Specialists Conference*, 1222–1227 (1993).
51. Rabl A, *Sol. Energy* **18**, 93–111 (1976).
52. Erbert V, "Short Focal Length Concentrating Photovoltaic Collector", Presented at *Proc. Twentieth IEEE Photovoltaic Specialists Conference* (1988).
53. Arvisu D, "Photovoltaic Concentrator Module Overview", Presented at *Photovoltaic Concentrator Technology Project, Fourteenth Project Integration Meeting* (Albuquerque, NM, 1986).
54. O'Neill M, "Acrylic Extrusion/Embossing Process Development for the Low-Cost Production of Linear Fresnel Lenses", Presented at *Photovoltaic Concentrator Technology Development Project, Sixth Project Integration Meeting* (Albuquerque, NM, 1980).
55. Kaminar N *et al.*, "A Passive Cooled 1000X GaAs Module with Secondary Optics", *Proc. Sixteenth IEEE Photovoltaic Specialists Conference*, 675–678 (1982).
56. James L, *Using Refractive Secondaries in Photovoltaic Concentrators*, Sandia National Laboratories, Albuquerque, NM, SAND89-7029 (1989).
57. Levy S, Stoddard L, *Integrated Photovoltaic Central Station Conceptual Designs*, Electric Power Research Institute, Palo Alto, CA, AP-3264 (1984).
58. Rabl A, Goodman N, Winston R, *Sol. Energy* **22**, 373–381 (1979).
59. Bowden S, Wenham S, Green M, "High Efficiency Photovoltaic Roof Tiles with Static Concentrators", *Proc. 12th European Photovoltaic Solar Energy Conference*, 1893–1896 (1994).

60. Uematsu T *et al.*, “Static Micro-Concentrator Photovoltaic Module with an Acorn Shape Reflector”, Presented at *Proc. of the 2nd World Conference on Photovoltaic Solar Energy Conversion* (Vienna, Austria 1998).
61. Ortabasi U, “Performance of a 2X Cusp Concentrator PV Module Using Bifacial Solar Cells”, Presented at *Proc. 26th IEEE Photovoltaic Specialists Conference* (Anaheim, CA, 1997).
62. Goetzberger A, “Static Concentration Systems with Enhance Light Concentration”, Presented at *20th IEEE Photovoltaic Specialists Conference* (Las Vegas, 1988).
63. Bowden S, “High Efficiency Photovoltaic Roof Tiles with Static Concentrators”, Presented at *First World Conference on Photovoltaic Energy Conversion* (Hawaii, 1994).
64. Minano J, Gonzalez J, Zanesco I, “Flat High Concentration Devices”, Presented at *First World Conference on Photovoltaic Energy Conversion* (Hawaii, 1994).
65. Mohedano R, Benitez P, Perez F, Minano J, “Design of a Simple Structure for the D-SMTS Concentrator”, Presented at *16th European Photovoltaic Solar Energy Conference* (Glasgow, UK, 2000).
66. Lotkar M, “Barriers to Commercialization of Large-scale Solar Electricity; Lessons Learned from the LUZ Experience,” Sandia National Laboratories SAND91-7014, November 1991.
67. Salim A *et al.*, “Four Year Performance Summary of 350 kW Concentration Photovoltaic Power System”, *Proc. IEEE Photovoltaic Specialists Conference*, 1545–1552 (1985).
68. Hodge R, *Development of a Laminated Fresnel Lens Using Injection Molded Lenses – Phase II*, Sandia National Laboratories, Albuquerque, NM (1982).
69. Rumyantsev V *et al.*, “Concentrator Array Based on Ga As Cells and Fresnel Lens Concentrators”, Presented at *Sixteenth European Photovoltaic Solar Energy Conference* (Glasgow, UK, 2000).
70. Carroll D *et al.*, *Alpha Solarco’s Concentrator Initiative Progress*, Sandia National Laboratories, Albuquerque, NM, SAND92-1454 (1992).
71. Blakers A, Smeltink J, “The ANU PV/Trough Concentrator System”, Presented at *Proc. Second World Conference on Photovoltaic Solar Energy Conversion* (Vienna, Austria, 1998).
72. O’Neill M, Danal A, “Fourth-Generation Concentrator Systems: form the Lab to the Factory to the Field”, Presented at *Proc. First World Conference on Photovoltaic Energy Conversion* (Hawaii, 1994).
73. Blieske U *et al.*, “Optimization of GaAs Solar Cells for Application in Concentrator Modules”, Presented at *Proc. Twelfth European Photovoltaic Solar Energy Conference* (Amsterdam, 1994).
74. Friedman D *et al.*, *Prog. Photovolt.: Res. Appl.* **3**, 47–50 (1995).
75. Algora C *et al.*, *Ultra Compact High Flux GaAs Cell Photovoltaic Concentrator*, 2241–2244 (2000).
76. Mulligan W *et al.*, “A Flat-Plate Concentrator: Micro-Concentrator Design Overview”, Presented at *Twenty Eighth IEEE Photovoltaic Specialists Conference* (Anchorage, AK, 2000).
77. Lasich J *et al.*, “Close-Packed Cell Arrays for Dish Concentrators”, Presented at *First World Conference on Photovoltaic Energy Conversion* (Hawaii, 1994).
78. Hunt A, “Design and Manufacture of Point Focus Fresnel Lens Concentrator for Stand-Alone PV System”, Presented at *Proc. Second World Conference and Exhibition on Photovoltaic Solar Energy Conversion* (Vienna, Austria, 1998).
79. Weatherby C, Bentley R, “Further Development and Field Test Results of Two Low-Materials-Cost Parabolic-Trough Concentrators”, Presented at *Proc. Second World Conference and Exhibition on Photovoltaic Solar Energy Conversion* (Vienna, Austria, 1998).
80. Yoshida K, Suzuki A, Saitoh T, “Evaluation of a Non-Imaging, Two-Dimensional Lens for PV Concentrator by Using an Insolation Model”, Presented at *Proc. Second World Conference and Exhibition on Photovoltaic Solar Energy Conversion* (Vienna, Austria, 1998).
81. Klotz F *et al.*, “European Photovoltaic V-Trough Concentrator System with Gravitational Tracking (Archimedes)”, Presented at *Sixteenth European Photovoltaic Solar Energy Conference* (Glasgow, 2000).

This Page Intentionally Left Blank

12

Amorphous Silicon–based Solar Cells

Xunming Deng¹ and Eric A. Schiff²

¹University of Toledo, Toledo, OH, USA, ²Syracuse University, Syracuse, NY, USA

12.1 OVERVIEW

12.1.1 Amorphous Silicon: The First Bipolar Amorphous Semiconductor

Crystalline semiconductors are very well known, including silicon (the basis of the integrated circuits used in modern electronics), Ge (the material of the first transistor), GaAs and the other III-V compounds (the basis for many light emitters), and CdS (often used as a light sensor). In crystals, the atoms are arranged in near-perfect, regular arrays or *lattices*. Of course, the lattice must be consistent with the underlying chemical bonding properties of the atoms. For example, a silicon atom forms four covalent bonds to neighboring atoms arranged symmetrically about it. This “tetrahedral” configuration is perfectly maintained in the “diamond” lattice of crystal silicon.

There are also many *noncrystalline* semiconductors. In these materials the chemical bonding of atoms is nearly unchanged from that of crystals. Nonetheless, a fairly small, disorderly variation in the angles between bonds eliminates the regular lattice structure. Such noncrystalline semiconductors can have fairly good electronic properties – sufficient for many applications. The first commercially important example was xerography [1, 2], which exploited the *photoconductivity* of noncrystalline selenium. As do all semiconductors, selenium absorbs those photons from an incident light beam that have photon energies exceeding some threshold energy. The photon that is absorbed generates a positively charged “hole” and a negatively charged electron that are separated and swept away by the large electric fields used in xerography.

However, solar cells require that photogenerated electrons and holes be separated by relatively modest electric fields that are “built-in” to the device, and selenium and many other noncrystalline semiconductors proved unsuitable for making efficient cells.

In Dundee, Scotland, Walter Spear and Peter LeComber discovered around 1973 that amorphous silicon prepared using a “glow discharge” in silane (SiH_4) gas had unusually good electronic properties; they were building on earlier work by Chittick, Sterling, and Alexander [3]. Glow discharges are the basis for the familiar “neon” light; under certain conditions, an electric voltage applied across a gas can induce a significant electrical current through the gas, and the molecules of the gas often emit light when excited by the current. Amorphous silicon was deposited as a thin film on substrates inserted into the silane gas discharge.¹ Spear and LeComber reported in 1975 [4] that amorphous silicon’s conductivity could be increased enormously either by mixing some phosphine (PH_3) gas or some diborane (B_2H_6) gas with the silane. Just as for crystal silicon, the phosphorus doping of the amorphous silicon had induced a conductivity associated with mobile electrons (the material was “*n*-type”), and the boron doping had induced a conductivity associated with mobile holes (the material was “*p*-type”).

In 1974, at the Radio Corporation of America (RCA) Research Laboratory in Princeton, David Carlson discovered that he could make fairly efficient solar cells using a silane glow discharge to deposit films. In 1976, he and Christopher Wronski reported a solar cell based on amorphous silicon [5] with a solar conversion efficiency of about 2.4% (for historical discussion see Reference [6, 7]).

Carlson and Wronski’s report of the current density versus output voltage is presented in Figure 12.1 (along with the curve from a far more efficient cell reported in 1997 [8]). As these scientists had discovered, the optoelectronic properties of amorphous silicon made by glow discharge (or “plasma deposition”) are very much superior to the amorphous silicon thin films prepared, for example, by simply evaporating silicon.

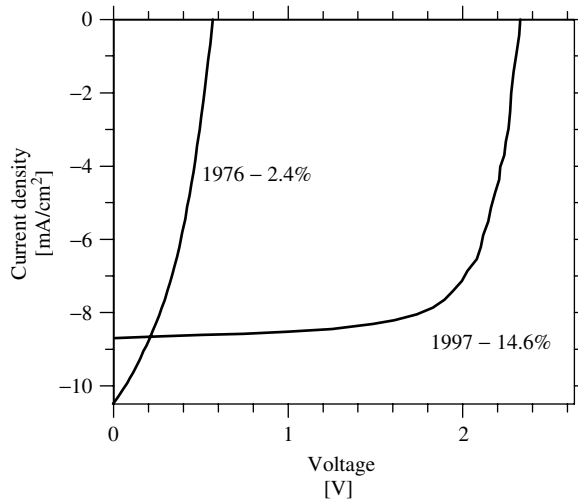


Figure 12.1 Current density versus voltage under solar illumination for a very early single-junction amorphous silicon solar cell (Carlson and Wronski [5]) and from a recent “triple-junction” cell (Yang, Banerjee, and Guha [8]). The stabilized efficiency of the triple-junction cell is 13.0%; the active area is 0.25 cm^2

¹ The term *amorphous* is commonly applied to noncrystalline materials prepared by deposition from gases.

After several years of uncertainty, it emerged that plasma-deposited amorphous silicon contained a significant percentage of hydrogen atoms bonded into the amorphous silicon structure and that these hydrogen atoms were essential to the improvement of the electronic properties of the plasma-deposited material [9]. As a consequence, the improved form of amorphous silicon has generally been known as *hydrogenated amorphous silicon* (or, more briefly, a-Si:H). In recent years, many authors have used the term *amorphous silicon* to refer to the hydrogenated form, which acknowledges that the unhydrogenated forms of amorphous silicon are only infrequently studied today.

Why was there so much excitement about the amorphous silicon solar cells fabricated by Carlson and Wronski? First, the technology involved is relatively simple and inexpensive compared to the technologies for growing crystals. Additionally, the optical properties of amorphous silicon are very promising for collecting solar energy, as we now explain. In Figure 12.2, the upper panel shows the spectrum for the optical absorption coefficients $\alpha(h\nu)$ for amorphous silicon and for crystalline silicon [10].² In the lower panel of the figure, we show the spectrum of the “integrated solar irradiance;” this is the intensity (in W/m^2) of the solar energy carried by photons above an energy threshold $h\nu$ [11].

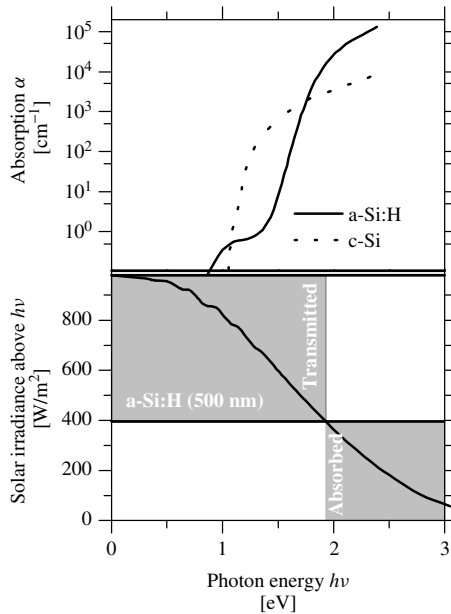


Figure 12.2 (Upper panel) Spectra of the optical absorption coefficient $\alpha(h\nu)$ as a function of photon energy $h\nu$ for crystalline silicon (c-Si) and for hydrogenated amorphous silicon (a-Si:H). (Lower panel) The solid curve indicates the irradiance of photons in the solar spectrum with energies $h\nu$ or larger. An a-Si:H film that is 500 nm thick mostly absorbs photons above 1.9 eV; as indicated by the shaded areas, this corresponds to an absorbed irradiance of about $390 \text{ W}/\text{m}^2$. After Vaněček M *et al.*, *J. Non-Cryst. Solids* **227–230**, 967 (1998) [10]

² We assume familiarity with the concept of a photon energy $h\nu$ and of an optical absorption coefficient α ; see Chapter 3.

We use these spectra to find out how much solar energy is absorbed by layers of varying thickness. The example used in the figure is an a-Si:H layer with a thickness $d = 500$ nm. Such a layer absorbs essentially all photons with energies greater than 1.9 eV (the energy at which $\alpha = 1/d$). We then look up how much solar irradiance lies above 1.9 eV. Assuming that the reflection of sunlight has been minimized, we find that about 420 W/m^2 is absorbed by the layer (the gray area labeled “absorbed”). Through such a layer 580 W/m^2 of energy is transmitted. These energies may be compared to the results for c-Si, for which a 500-nm-thick layer absorbs less than 200 W/m^2 .

To absorb the same energy as the 500-nm a-Si:H layer, a c-Si layer needs to be much thicker. The implication is that much less material is required to make a solar cell from a-Si than from c-Si.³ In the remainder of this section, we first describe how amorphous silicon solar cells are realized in practice, and we then briefly summarize some important aspects of their electrical characteristics.

12.1.2 Designs for Amorphous Silicon Solar Cells: A Guided Tour

Figure 12.1 illustrates the tremendous progress over the last 25 years in improving the efficiency of amorphous silicon-based solar cells. In this section we briefly introduce three basic ideas involved in contemporary, high-efficiency devices: (1) the *pin* photodiode structure, (2) the distinction between “substrate” and “superstrate” optical designs, and (3) multijunction photodiode structures. A good deal of this chapter is devoted to more detailed reviews of the implementation and importance of these concepts.

12.1.2.1 *pin* photodiodes

The fundamental photodiode inside an amorphous silicon-based solar cell has three layers deposited in either the *p-i-n* or the *n-i-p* sequence. The three layers are a very thin (typically 20 nm) *p*-type layer, a much thicker (typically a few hundred nanometer), undoped *intrinsic* (*i*) layer, and a very thin *n*-type layer. As illustrated in Figure 12.3, in this structure excess electrons are actually donated from the *n*-type layer to the *p*-type layer, leaving the layers positively and negatively charged (respectively), and creating a sizable “built-in” electric field (typically more than 10^4 V/cm).

Sunlight enters the photodiode as a stream of photons that pass through the *p*-type layer, which is a nearly transparent “window” layer. The solar photons are mostly absorbed in the much thicker intrinsic layer; each photon that is absorbed will generate one electron and one hole photocarrier [12, 13]. The photocarriers are swept away by the built-in electric field to the *n*-type and *p*-type layers, respectively – thus generating solar electricity!

The use of a *pin* structure for a-Si:H-based solar cells is something of a departure from solar cell designs for other materials, which are often based on simpler *p-n* structures.

³ The very different optical properties of c-Si and a-Si reflect the completely different nature of their electronic states. In solid-state physics textbooks, one learns about the “selection rules” that greatly reduce optical absorption in c-Si, which is an “indirect band gap” semiconductor. Such selection rules do not apply to a-Si. Additionally, the “band gap” of a-Si is considerably larger than that for c-Si.

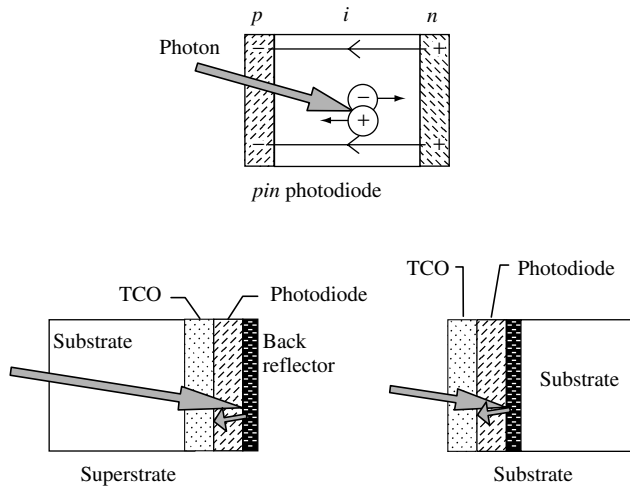


Figure 12.3 In a *pin* photodiode, excess electrons are donated from the *n*-type to the *p*-type layers, leaving the charges and electric fields illustrated. Each photon absorbed in the undoped, intrinsic layer generates an electron and a hole photocarrier. The electric field causes these carriers to drift in the directions shown. *pin* diodes are incorporated into solar cells in either the superstrate or substrate designs. For amorphous silicon-based cells, photons invariably enter through the *p*-type window layer as shown here

For doped a-Si:H, it turns out that minority photocarriers (holes in *n*-type a-Si:H, electrons in *p*-type a-Si:H) do not move very far, and so a *p-n* structure would only collect photocarriers from photons generated in an extremely thin layer of doped a-Si:H. Indeed, in analyzing the performance of a-Si:H-based solar cells, one normally considers any photons absorbed by the doped layers to be “wasted.” The trick of keeping the doping atoms out of the absorber layer enables this layer to be thick enough to capture most of the sunlight.

In Section 12.4 you will find a more detailed description of the device physics of the *pin* solar cell; the description explains why the window layer is the *p*-type one, and also explains the design trade-offs that determine the thickness of the absorber layer.

12.1.2.2 Substrate and superstrate designs

One of the advantages of amorphous silicon-based solar cells is that they absorb sunlight very efficiently: the total thickness of the absorbing layers in amorphous silicon solar cells is less than 1 μm . Consequently, these layers need to be supported on a much thicker substrate. Two totally different designs for amorphous silicon solar cells have evolved corresponding to transparent and opaque substrates. We have illustrated the two designs in Figure 12.3.

In the “superstrate” design, sunlight enters through the transparent substrate, which is usually glass or a transparent plastic. The insulating substrate needs a conducting layer, which is typically a “transparent conductive oxide” (TCO) such as SnO_2 . The amorphous silicon photodiode layers are then deposited onto the TCO, starting with a *p*-type window

layer. Finally, a “back” reflector is deposited onto the photodiode; the back reflector acts as an electrode to the n -type photodiode layer.

In the “substrate” design, sunlight enters the photodiode before it reaches the substrate. Starting with the substrate, the cell is fabricated in the reverse order compared to the superstrate design: first a back reflector, then the photodiode layers (starting with an n -type layer), and finally a TCO layer to act as an electrode to the topmost, window layer of the photodiode.

These two designs permit a very wide range of applications for amorphous silicon solar cells. The superstrate design (light enters through the substrate) is particularly suited to building-integrated solar cells in which a glass substrate can be used as an architectural element. The substrate design has generally been applied to solar cells using flexible, stainless steel (SS) substrates. The detailed construction of a deposition facility of course depends upon whether the substrate is rigid or flexible. Finally, it turns out that there is a profound effect of the substrate upon the properties of the first photodiode layers deposited upon it; this effect has led to fairly different photodiode structures for the superstrate and substrate designs.

12.1.2.3 Multijunction solar cells

The conversion efficiency of the relatively simple, amorphous silicon pin photodiode structure just described can be significantly improved by depositing two or three such photodiodes, one on top of another, to create a “multijunction” device. We illustrate a “tandem” device in Figure 12.4, which shows a combination of two pin diodes.⁴ Note that the “bottom” cell is not based on $a\text{-Si:H}$, but rather upon an amorphous silicon–germanium alloy made by including germane (GeH_4) gas in the plasma-deposition recipe.

The main advantage of the tandem design over the simpler single-junction one is due to “spectrum splitting” of the solar illumination. Since the absorption coefficient of light rises rapidly with the photon energy, the topmost layer of a tandem cell acts

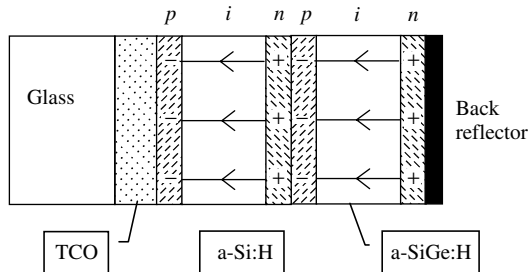


Figure 12.4 A multijunction solar cell consisting of two pin solar cells deposited in series. Double-junction (or “tandem,” as shown) and triple-junction designs can be significantly more efficient than single-junction designs. Substrate texturing, which is important in real devices, is not indicated; see Section 12.4.5

⁴ It is worth noting that the adjoining p -type and n -type layers do *not* form a p - n junction diode, but rather a simple Ohmic contact. We discuss the interesting physics underlying this fact in Section 12.5.3.

as a “low-pass” optical filter. This effect is illustrated in Figure 12.2, which shows that a 0.5- μm layer of a-Si:H absorbs photons with energies larger than 1.9 eV and passes photons with smaller energies. The “wasted” lower energy photons can be efficiently harvested by amorphous silicon-germanium, which has a much larger optical absorption coefficient below 1.9 eV than does a-Si:H, hence a lower threshold energy. Overall, the advantages of the multijunction design are sufficiently compelling that they usually overcome the additional complexity and cost of the deposition facility. Both tandem and triple-junction devices are being manufactured today. We discuss multijunction solar cells in detail in Section 12.5.

12.1.3 Staebler–Wronski Effect

One of the most intriguing and actively researched facets of amorphous silicon solar cells is the significant decline in their efficiency during their first few hundred hours of illumination. Figure 12.5 illustrates this effect for a single-junction cell and for a triple-junction module made at United Solar Systems Corp. [14, 15]. The single-junction cell loses about 30% of its initial efficiency after about 1000 h; the triple-junction module loses about 15% of its initial efficiency.

All amorphous silicon-based solar cells exhibit this type of initial behavior under illumination; the behavior is mostly due to the “Staebler–Wronski” effect [16], which is the light-induced change in hydrogenated amorphous silicon (a-Si:H) and related materials used in the cell. Although we have not illustrated it here, the Staebler–Wronski effect can be annealed away within a few minutes at temperatures of about 160°C (and the initial performance of the solar cell largely restored).

The Staebler–Wronski effect contributes to noticeable seasonal variations in the conversion efficiency of a-Si:H-based modules in the field. In Figure 12.6 we illustrate

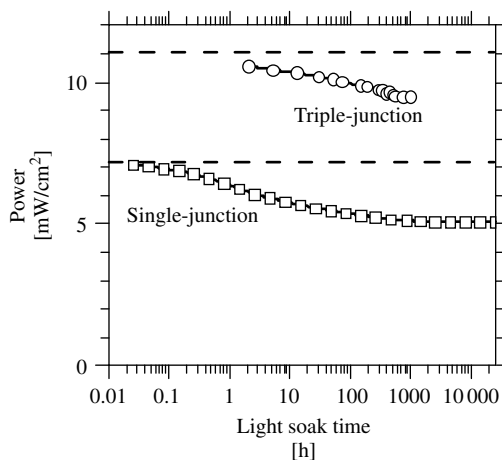


Figure 12.5 The conversion efficiency in a-Si:H-based solar cells declines noticeably upon the first exposure to sunlight. The figure illustrates this decline under a solar simulator (100 mW/cm²) for a single-junction cell (260-nm *i*-layer thickness) and for a triple-junction module made at United Solar Systems Corp. [14, 15]; the dashed lines indicate the initial power measured for each device

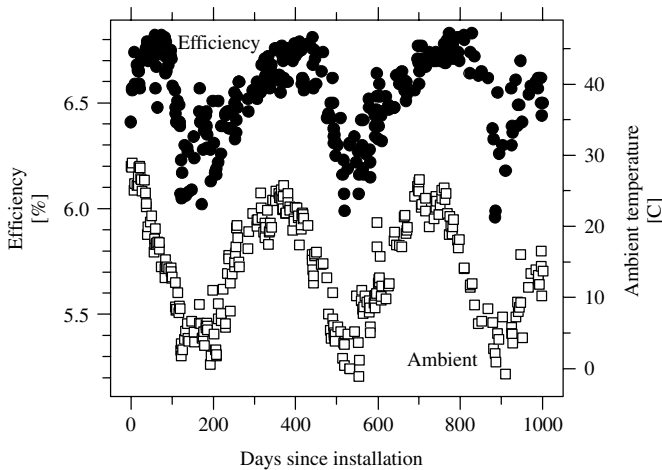


Figure 12.6 Seasonal variations in the average conversion efficiency (solid symbols) of an amorphous silicon triple-junction module [18], along with the daily mean temperature (open symbols)

the daily average conversion efficiency and ambient temperature of a triple-junction module installation in Switzerland. The module performed best in hot weather. Up to 20°C, the relative increase in efficiency with temperature is about $+5 \times 10^{-3}/\text{K}$. It is noteworthy that there was no permanent degradation of this module over the three-year extent of the test. The conclusion that amorphous silicon modules reach a steady state after about 1000 h of steady illumination was also reached in a much larger study of modules manufactured by Advanced Photovoltaics Systems, Inc. [17].

This positive trend of efficiency with temperature is atypical of solar cells made with other materials; for example, the temperature coefficient of crystal silicon solar cells is about $-4 \times 10^{-3}/\text{K}$ [19, 20]. Interestingly, if the temperature dependence of a-Si:H solar cells is measured quickly – so that there is no time for the Staebler–Wronski effect to set in – the temperature coefficient is also negative (about $-1 \times 10^{-3}/\text{K}$) [19]. The behavior of a module in the field may be understood as a competition of the slow annealing of the Staebler–Wronski effect (which yields the positive temperature coefficient) and of a smaller, intrinsic negative coefficient [21, 22]. The effects of temperature on solar cell performance are discussed in more detail in Chapters 3 and 16.

12.1.4 Synopsis of this Chapter

The remainder of this chapter is organized as follows. In Section 12.2 we introduce some of the fundamental physical concepts required to interpret the scientific literature about amorphous silicon and related materials (such as amorphous silicon-based alloys and, to a much lesser degree, microcrystalline silicon). Section 12.3 surveys the principal methods such as plasma deposition that are used to make amorphous silicon-based solar cells. Section 12.4 describes how the simplest, single-junction solar cell “works,” by which we mean how the photoelectric behavior of the cell is related to the fundamental concepts. High-efficiency solar cells based on amorphous silicon technology are multijunction devices, and in Section 12.5 we discuss how these are made and how their

performance can be understood and optimized. Section 12.6 describes some of the issues involved in manufacturing modules. To conclude this chapter, Section 12.7 presents some of the directions that we consider important for future progress in the field.

There have been several excellent monographs and review chapters on amorphous silicon and amorphous silicon-based solar cells in recent years. In the body of the chapter, we direct the reader to these works where we feel that they may be useful for expanded or complementary discussion.

12.2 ATOMIC AND ELECTRONIC STRUCTURE OF HYDROGENATED AMORPHOUS SILICON

12.2.1 Atomic Structure

Silicon atoms in amorphous silicon largely retain the same basic structure as that of crystal silicon: each silicon atom is connected by covalent bonds to four other silicon atoms arranged as a tetrahedron. This understanding emerges from measurements of the scattering (“diffraction”) of X rays by the two materials [23] as well as from theoretical and computational studies of the two materials.

If you build a noncrystalline silicon structure with wooden sticks (to represent covalent bonds) and wooden balls drilled with four small holes for the sticks (to represent the silicon atoms), you will have some trouble in making a noncrystalline structure. To avoid a crystalline structure, you will need to bend the sticks. Quite soon, you will have to give up on the fourth stick on some atom, and you will have created an imperfect noncrystalline structure with a “dangling bond.” Your problem is related to tetrahedral bonding: there are too many constraints on the positions of atoms to keep *all* bond lengths and angles reasonably close to the values demanded by silicon’s chemistry in any noncrystalline structure. The same conclusion is reached by mathematical and computational methods [24, 25]. Alloys such as As_2Se_3 , which easily form noncrystalline glasses by cooling from a liquid, have an average number of bonds per atom of about 2.7 or less.

For hydrogenated amorphous silicon (a-Si:H), silicon–hydrogen bonds resolve this structural problem. Several percent of the silicon atoms make covalent bonds with only three silicon neighbors; the fourth valence electron of the silicon bonds to a hydrogen atom. This crucial hydrogen is essentially invisible to X rays, but is quite evident in nondestructive measurements (proton magnetic resonance [26] and infrared spectroscopy [27]) as well as destructive testing (secondary ion mass spectroscopy [28] and hydrogen evolution during annealing [29]).

There are quite a few distinct atomic configurations for the hydrogen in a-Si:H. The two principal “phases” of hydrogen evidenced by proton magnetic resonance are termed the *dilute* and *clustered* phases [26]. In the dilute phase a particular hydrogen atom is about 1 nm away from any other hydrogen atom; in the clustered phase there are two or more hydrogen atoms in close proximity. A computer calculation of a particular instance of this structure [30] is presented in Figure 12.7(a). The densities of hydrogen in each of the individual phases, as well as the total density of hydrogen, depend upon the conditions under which the material is made.

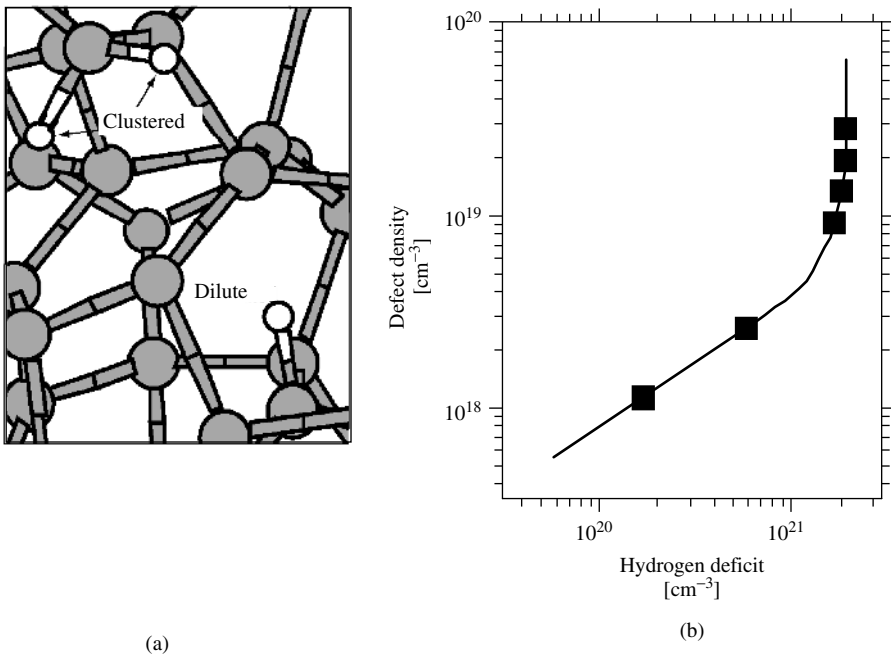


Figure 12.7 (a) Computer model of the chemical bonding of hydrogenated amorphous silicon. The larger, gray spheres indicate Si atoms; the smaller, white spheres indicate hydrogen atoms, which are found in clustered and relatively isolated, dilute-phase configurations as indicated. (b) Correlation of the defect (dangling bond) density in a-Si:H with the density of hydrogen removed from the material by heating (the hydrogen deficit). The data points are derived from deuterium and defect profiles by Jackson *et al.* [31] (350°C deuteration). The curve is a fit to a model proposed by Zafar and Schiff [32]

12.2.2 Defects and Metastability

While the underlying structure illustrated in Figure 12.7 is noncrystalline, it is a chemically ideal structure: each atom forms the normal number of chemical bonds (four for silicon, one for hydrogen). This noncrystalline atomic structure largely determines the overall electronic and optical properties of the material, as we will discuss shortly. However, many electronic properties in a-Si:H are also strongly affected by the gross defects of chemical bonding. The atomic structure of the bonding defects in a-Si:H has been extensively studied using electron spin resonance. A single type of defect, the *D*-center, dominates most measurements in undoped a-Si:H [23]. The *D*-center is generally identified as a silicon dangling bond [33].

A dangling bond may be envisioned using Figure 12.7: just imagine that the hydrogen atom is removed from the dilute-phase site in the lower right-hand corner of the figure, leaving behind a single unbonded electron (the “dangling bond”). This simple picture is consistent with the following observation: the density of dangling bonds increases when hydrogen is removed from a-Si:H by heating. We present a comparison of a model for this relationship together with measurements illustrating the effect in Figure 12.7(b) [31, 32]. Note that the density of dangling bonds is generally much lower than the density of

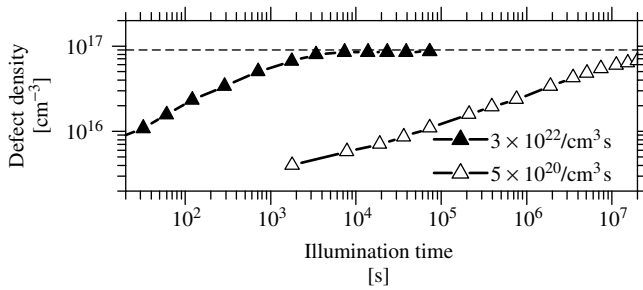


Figure 12.8 Plot of the defect (dangling bond) density during extended illumination of an a-Si:H film as measured by Park, Liu, and Wagner [34]. Data are given for high- and low-intensity illumination; the legend indicates the photocarrier generation rate of each intensity

hydrogen lost from the structure; this effect has been attributed to the evolution of hydrogen from clustered-phase sites, which presumably does not create dangling bonds.

The most intense defect research in a-Si:H has not been focused on the direct hydrogen-defect relation, but rather on the light-soaking effects. We illustrated how light soaking degrades the solar conversion efficiency in Figure 12.5, and in Figure 12.8 we illustrate how it increases the defect density. For the high intensity illumination, the defect density reaches a steady state at about $10^{17}/\text{cm}^3$. For purposes of engineering and commercial applications, it is very important that a-Si:H reaches such a “stabilized” condition after extended light soaking.

Although the defect density is not the only property of a-Si:H modified following light soaking [35], most workers believe that the principal cause of the Staebler–Wronski effect is this increase in dangling bond density after light soaking. The close connection between hydrogen and defects in a-Si:H has led to several efforts to understand the defect creation in terms of metastable configurations of hydrogen atoms [35, 36]. The idea is that illumination provides the energy required to shift hydrogen atoms away from their dilute-phase sites, thus creating dangling bonds. The technological importance of establishing the atomic mechanism underlying the Staebler–Wronski effect lies in the possibility that this effect can be mitigated in a-Si:H by changing its preparation conditions.

An essential feature of the light-soaking effects on a-Si:H cells and films is that most of the effects are “metastable” and can be removed nearly completely by annealing of a light-soaked sample at a temperature above 150°C . More generally, the stabilized condition of a-Si:H cells and films is quite temperature-dependent. For example, Figure 12.6 showed that the module efficiency is substantially affected by the seasons and is highest following the hottest days. The measurement may be understood by considering that the stabilized condition is due to competition between two rates: the creation of metastable defects by light and a thermally activated process that anneals them away.

12.2.3 Electronic Density-of-states

The most important concept used in understanding the optical and electronic properties of semiconductors is the electronic density-of-states, $g(E)$. The idea is a simple approximation: if a single electron is added to a solid, it may be viewed as occupying a well-defined

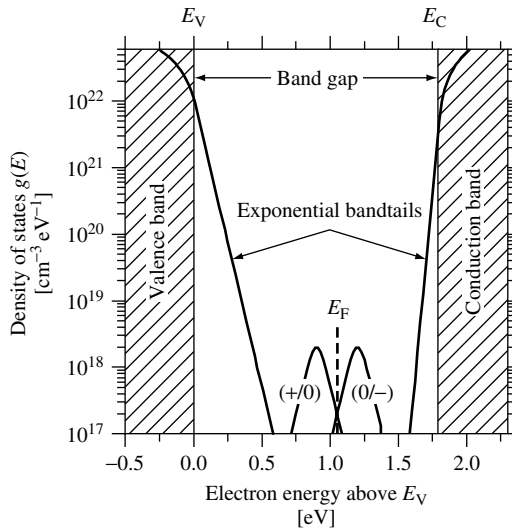


Figure 12.9 Density of electronic states $g(E)$ in hydrogenated amorphous silicon. The shaded areas indicate delocalized states in the bands; these bands themselves have tails of localized states with an exponential distribution. Midway between the bands are levels belonging to gross defects such as dangling Si bonds indicated by the two peaked bands around E_F

state (or molecular “orbital”) at a particular energy level E . In a range of energies ΔE , the number of such states per unit volume of the solid is $g(E)\Delta E$.

In Figure 12.9 we have illustrated the density-of-states for hydrogenated amorphous silicon as it has emerged primarily from measurements of electron photoemission [37, 38], optical absorption [39], and electron and hole drift mobilities [40]. In the dark at low temperatures, the states with energies below the Fermi energy E_F are filled by electrons; above the Fermi energy the states are empty. There are two strong bands of states illustrated: an occupied valence band ($E < E_V$), originating with the Si–Si and Si–H bonding orbitals and an unoccupied conduction band ($E > E_C$), originating with “antibonding” orbitals.

12.2.4 Bandtails, Bandedges, and Band Gaps

Between the conduction and valence bands lies an “energy gap” where the density-of-states is very low. Any functional semiconductor, crystalline or noncrystalline, must have such an energy gap. For perfect crystals, the valence and conduction bandedge energies E_V and E_C are well defined, as is the *band gap* $E_G = E_C - E_V$. Interestingly, in disordered semiconductors there are exponential distributions of bandtail states near these bandedges. For the valence bandtail, we write $g(E) = g_V \exp[-(E - E_V)/\Delta E_V]$. The width ΔE_V of this exponential distribution is important in interpreting optical absorption experiments, in which it is usually identified with the exponential “Urbach” tail of the spectrum apparent in Figure 12.2. For a-Si:H, a typical value $\Delta E_V = 50 \times 10^{-3}$ eV. ΔE_V is also used to account for the very slow drift of holes in an electric field (i.e. the hole *drift mobility*) [40, 41]. The conduction bandtail width ΔE_C is much narrower; for

the best a-Si:H materials, it is about 22×10^{-3} eV, but increases markedly for amorphous silicon-germanium alloys [42].

Given the presence of exponential bandtails, the very existence of bandedge energy can reasonably be questioned. Remarkably, detailed analysis of drift-mobility measurements supports the concept of a well-defined bandedge [40, 43]. Most workers consider the bandedge to be the energy that separates electron orbitals that are localized (i.e. have well-defined locations in space) from orbitals that are delocalized. The bandedges are correspondingly termed the conduction and valence band *mobility edges* [44].

Unfortunately, for noncrystalline semiconductors there is no single, conclusively established procedure for locating the bandedges within the density-of-states. The band gap is thus difficult to determine without some ambiguity. Since amorphous silicon-based materials with varying band gaps are used in solar cells, it is nonetheless very important to establish conventional procedures for comparing band gaps. By far the most common approach is to analyze measurements of the optical absorption coefficient $\alpha(h\nu)$ similar to those in Figure 12.2; one typical analysis yields an “optical” or “Tauc” band gap E_T [45]

$$\alpha(h\nu) = (A/h\nu)(h\nu - E_T)^2 \quad (12.1)$$

The proportionality constant A incorporates several effects and is not usually studied separately.

The band gap obtained using this procedure is typically about 1.75 eV in a-Si:H, but varies substantially with deposition conditions and alloying with germanium or carbon. A simpler procedure than that of Tauc is to define the band gap to be the photon energy corresponding to a particular optical absorption coefficient α ; using $\alpha = 3 \times 10^3/\text{cm}$ yields values (denoted as $E_{3,5}$) similar to the Tauc procedure. Finally, there is undoubtedly a difference between these optical estimates of the band gap and the true, “electrical” band gap $E_G = E_C - E_V$. Internal photoemission measurements [46] indicate that the electrical band gap is 50 to 100 meV larger than the Tauc band gap.

12.2.5 Defects and Gap States

Between the bandtails lie defect levels; in undoped a-Si:H, these levels appear to be due entirely to the dangling bonds (“ D -centers”) measured by electron spin resonance. For example, infrared absorption at photon energies around 1.2 eV is sensitive to the optical processes that detach an electron from a defect and promote it to the conduction band or that transfer an electron from the valence band to a defect. This infrared signal is visible in Figure 12.2; for samples of varying electronic properties, the infrared absorption coefficient is proportional to the D -center density over a range of at least a factor of 100 in the density [47].

The next issue to be resolved is the positions of the corresponding levels, as illustrated in Figure 12.9. The D -center is “amphoteric:” there are three charge states (with $+e$, 0 , and $-e$ charges), leading to two levels (transitions between the $0/+$ and $-/0$ charge states). A *rough* guide to level positions estimated under near-dark conditions is the following. The $(-/0)$ level is about 0.6 eV below E_C in low defect-density, undoped

a-Si:H [48]. The (+/0) level lies about 0.3 eV below the (-/0) levels; the difference between the 2 levels is usually termed the *correlation energy* of the *D*-center [49].

The actual level positions apparently vary between doped and intrinsic a-Si:H [23], between intrinsic samples with varying densities of *D*-centers [48], and possibly between dark and illuminated states [50].

12.2.6 Doping

Doped layers are integral to *pin* solar cells. Doping itself, which is the intentional incorporation of atoms like phosphorus and boron in order to shift the Fermi energy of a material, works very differently in amorphous silicon than in crystals. For example, in crystalline silicon (c-Si), phosphorus (P) atoms substitute for silicon atoms in the crystal lattice. P has five valence electrons, so in the “fourfold coordinated” sites of the Si lattice, four electrons participate in bonding to neighboring silicon atoms. The fifth “free” electron occupies a state just below the bottom of the conduction band, and the dopants raise the Fermi energy to roughly this level.

In a-Si, most phosphorus atoms bond to only three silicon neighbors; they are in “threefold coordinated” sites. This configuration is actually advantageous chemically; phosphorus atoms normally form only three bonds (involving the three valence electrons in “p” atomic orbitals). The final two electrons are paired in “s” atomic orbitals, do not participate in bonding, and remain tightly attached to the P atom. The reason that this more favorable bonding occurs in a-Si, but not in c-Si, is the absence of a rigid lattice. As a thin film of a-Si grows, the network of bonds adjusts to incorporate impurity atoms in a nearly ideal chemical arrangement. In c-Si, it would be necessary to grossly rearrange several Si atoms in the lattice and to leave a number of dangling Si bonds, in order to accommodate the P atom in this configuration. The extra energy for this rearrangement is larger than what would be gained from more ideal bonding of P, and substitutional doping is favored.

Thus, phosphorus doping is a paradox in amorphous silicon. It is, at first, unclear why it occurs at all, since doping involves fourfold coordinated P, and P atoms are generally threefold coordinated in a-Si. This puzzle was first solved in 1982 by Street, who realized that independent formation of both a positively charged, fourfold coordinated P_4^+ and a negatively charged dangling bond D^- can occur occasionally instead of the more ideal threefold coordination [23]. This understanding leads to two important consequences. First, doping is inefficient in a-Si; most dopant atoms do not contribute a “free” electron and do not raise the Fermi energy. Second, for each dopant atom that does contribute an electron, there is a balancing, Si dangling bond to receive it. These defect levels lie well below the conduction band, so the fourfold coordinated phosphorus atoms are less effective in raising the Fermi energy than that in c-Si. Additionally, the negatively charged dangling bonds induced by doping are very effective traps for holes. Since bipolar transport of both electrons and holes is essential to photovoltaic (PV) energy conversion, photons absorbed in doped layers do not contribute to the power generated by solar cells.

12.2.7 Alloying and Optical Properties

The structural and optical properties we have described can be varied substantially by changes in deposition conditions. For example, changing the substrate temperature or the

dilution of silane by hydrogen (in plasma deposition) causes a change in the optical band gap for a-Si:H films over at least the range 1.6 to 1.8 eV [51]; these changes can be ascribed to changes in the hydrogen microstructure of the films. Even larger changes can be effected by alloying with additional elements such as Ge, C, O, and N; alloying is readily accomplished by mixing the silane (SiH_4) source gas with gases such as GeH_4 , CH_4 , O_2 or NO_2 , and NH_3 , respectively. The resulting alloys have very wide ranges of band gaps, as we illustrate for a- $\text{Si}_{1-x}\text{Ge}_x$:H in Figure 12.10. For simplicity, we shall usually refer to these alloys using the abbreviated notation: a-SiGe for a- $\text{Si}_{1-x}\text{Ge}_x$:H, and so on.

Only some of these materials have proven useful in devices. In particular, a-SiGe alloys with optical gaps down to about 1.45 eV are employed as absorber layer in multi-junction *pin* cells; the narrower band gap of a-SiGe compared to a-Si allows for increased absorption of photons with lower energies [52]. Figure 12.10(a) illustrates how the spectrum of the absorption coefficient $\alpha(h\nu)$ changes for a-SiGe alloys with different atomic percentages x ; the different optical band gaps are indicated as labels. Two features of these data should be noted. First, the Urbach slopes remain constant (at about 50 meV) over the entire range of band gaps. Second, the plateau in the absorption coefficient at the lowest photon energies increases steadily as the band gap diminishes, which is indicative of a corresponding increase in defect density.

Figure 12.10(b) is a contour plot showing how the optical band gap of a- $\text{Si}_{1-x}\text{Ge}_x$:H varies with the Ge-ratio x and with atomic fraction h of hydrogen. The figure reflects experimental results for a-Si:H alloys of varying H-fraction [51] and for a-SiGe:H alloys for which both x and h were reported [53].⁵ Note that, for constant fraction h , the band

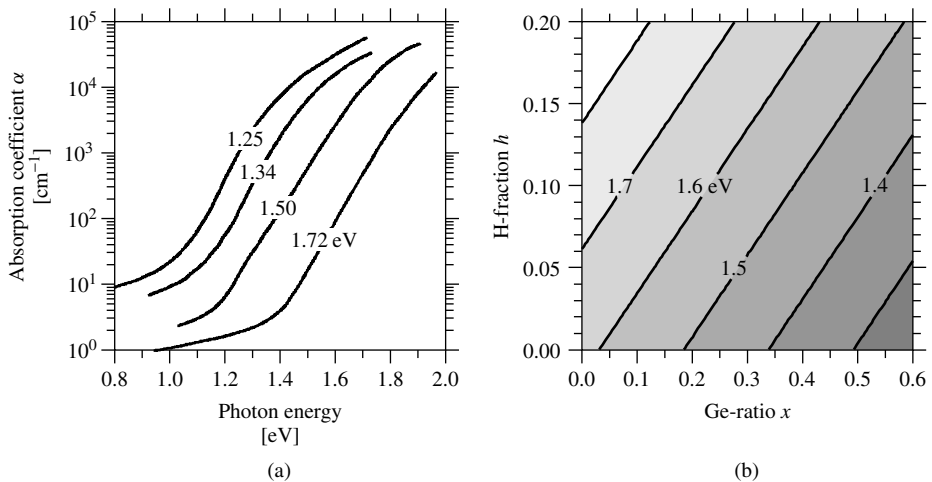


Figure 12.10 (a) Absorption coefficient spectra for a-SiGe alloys; the optical band gaps and corresponding Ge fractions x are 1.25 to 0.58, 1.34 to 0.48, 1.50 to 0.30, 1.72 to 0.0 [52]. (b) Typical optical band gaps for a- $\text{Si}_{1-x}\text{Ge}_x$:H alloys for varying Ge-ratio x and atomic fraction h of hydrogen

⁵ Figure 12.10 is based on the function $E_G = 1.62 + 1.3h - 0.7x$ obtained by fitting to experimental results reported by Hama *et al.* [51] and Middya *et al.* [53].

gap decreases about 0.7 eV as the Ge ratio x increases from 0 to 1. The band gap increases with atomic fraction of hydrogen h . Figure 12.10(b) should be viewed as a useful approximation; in particular, the atomic fraction h is only one aspect of the hydrogen microstructures in a-SiGe alloys, and quantitative deviations from the contour plot are likely. Additionally, only some of the materials represented in the figure are useful as absorber layers. In particular, as the Ge ratio x rises to about 0.5, the optoelectronic properties become so poor that these alloys are no longer useful in solar cells [54]. Similarly, only limited ranges of the atomic fraction of hydrogen h yield useful absorber layers.

It might be thought that a-SiC would be equally useful as a wider band gap absorber; despite some promising research [55], this material is not being used as an absorber layer by manufacturers. B-doped a-SiC is used extensively as a p -type, window layer [56]. a-SiO and a-SiN are used as insulators in thin-film transistors [57], but are not major components in solar cells.

12.3 DEPOSITING AMORPHOUS SILICON

12.3.1 Survey of Deposition Techniques

The first preparations of a-Si:H by Chittick *et al.* [58] and by Spear and LeComber [59] used a silane-based glow discharge induced by radio frequency (RF) voltages; the method is now often termed plasma enhanced chemical vapor deposition (PECVD). Since this pioneering work, many deposition methods have been explored with the intention of improving material quality and deposition rate. Among these methods, PECVD using 13.56-MHz excitation is still the most widely used today in research and manufacturing of a-Si-based materials. However, emerging film deposition methods, mostly toward higher deposition rate or toward making improved microcrystalline silicon films, have been extensively explored in recent years. Table 12.1 summarizes the most extensively studied deposition processes used as well as some of their advantages and disadvantages. Among these, PECVD with very high frequency (VHF) and hot-wire (HW) catalytic deposition

Table 12.1 Various deposition processes used for depositing amorphous silicon-based materials

Processes	Maximum rate ^a [Å/s]	Advantages	Disadvantages	Manufacturers	References
RF PECVD	3	High quality uniform	Slow	Many	[60–62]
DC PECVD	3	High quality uniform	Slow	BP Solar	[63, 64]
VHF PECVD	15	Fast	Poor uniformity	None	[65, 66]
Microwave PECVD	50	Very fast	Film quality not as good	Canon	[67]
Hot-wire	50	Very fast	Poor uniformity	None	[68, 69]
Photo-CVD	1	High quality	Slow	None	[70, 71]
Sputtering	3		Poor quality, slow	None	[72, 73]

^aMaximum deposition rate: The deposition rate beyond which the film quality deteriorates rapidly; these numbers are empirical, not fundamental limits, and represent current results at the time of publication

process will be further discussed in this section because of their potential for use in future high-throughput solar cell manufacturing.

12.3.2 RF Glow Discharge Deposition

Figure 12.11 shows a schematic of a typical RF PECVD chamber and related parts. A silicon-containing gas such as a mixture of SiH_4 and H_2 flows into a vacuum chamber that is evacuated by a pump. Two electrode plates are installed inside, and an RF power is applied between them; one option is to ground one of these electrodes. At a given RF voltage across the plates, there is usually a range of gas pressures for which a plasma will occur. The plasma excites and decomposes the gas and generates radicals and ions in the chamber. Various substrates may be mounted on one or both of the electrodes, and thin hydrogenated silicon films grow on the substrates as these radicals diffuse into them. The substrates are heated to achieve optimum film quality; this effect is attributed to thermally activated surface diffusion of adatoms on the growing film.

A PECVD system usually consists of several major parts: (1) a gas delivery system (gas cylinders, pressure regulators, mass flow controllers, and various gas valves to direct gas flows); (2) a deposition chamber that has electrodes, substrate mounts, substrate heaters, and the RF power feed through; (3) a pumping system that usually has a turbomolecular pump backed with a mechanical pump; (4) a pressure control system that has a capacitance manometer, ionization gauges, thermocouple gauges, and/or throttle valve to monitor and control the chamber pressure; (5) an exhaust system for the process gases (typically either with a chemical scrubber to neutralize the gases or with a “burn box” to pyrolyze them). In multichamber systems there is a transfer system to move substrates inside the vacuum system between various deposition chambers through appropriate gate valves. Many of these elements are connected to an instrument control panel that contains an RF power supply, impedance matching box, and readouts or controllers for the vacuum gauges, mass flow controllers, throttle valves, pneumatic valves, and turbomolecular pumps.

The film growth in a PECVD process consists of several steps: source gas diffusion, electron impact dissociation, gas-phase chemical reaction, radical diffusion, and deposition [60, 61, 74]. To deposit good-quality a-Si films, the deposition conditions need to be

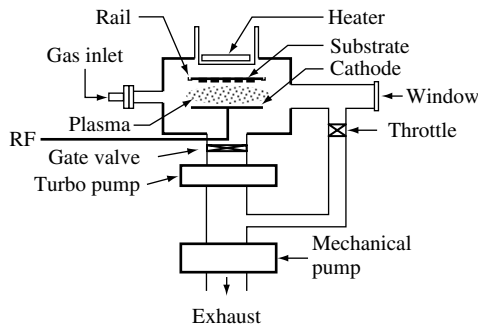


Figure 12.11 Schematic of a typical RF glow discharge deposition chamber

Table 12.2 Ranges of RF-PECVD deposition conditions for a-Si:H films with optimal properties. These numbers are empirical, not fundamental limits, and represent current results at the time of publication

Range	Pressure [Torr]	RF power density [mW/cm ²]	Substrate temperature [C]	Electrode spacing [cm]	Active gas flow ^a [sccm/cm ²]	H ₂ dilution <i>R</i> ^b
Upper	2	100	350	5	0.02	100
Medium	0.5	20	250	3	0.01	10
Lower	0.05	10	150	1	0.002	0

^aFlows of active gases, such as SiH₄, GeH₄, or Si₂H₆, for each unit area of the deposition area (electrode + substrate + chamber walls)

^bHydrogen dilution *R*, defined here as the ratio of hydrogen and active gas flows (e.g. H₂/SiH₄)

controlled within certain ranges desirable for high-quality a-Si growth. Typical ranges of parameters for a-Si are summarized in Table 12.2.

The pressure range is usually between 0.05 and 2 Torr. Lower pressure is desirable for making uniform deposition, and higher pressure is more desirable for preparing microcrystalline silicon films. Most researchers use a pressure between 0.5 and 1 Torr for a-Si deposition. The RF power should be set at around 10 to 100 mW/cm² for a capacitively coupled reactor. Below 10 mW/cm², it is difficult to maintain a plasma. Higher power is desirable for higher deposition rate. However, above 100 mW/cm², the rapid reactions in the gas can create a silicon polyhydride powder that contaminates the growing Si film. This problem can be mitigated by using very low pressure or strong hydrogen dilution.

The substrate temperature is usually set between 150 and 350°C. At lower substrate temperature, more H is incorporated in the film. As expected from Figure 12.10, this increases the band gap of a-Si:H slightly [51, 75]. However, lower substrate temperature (<150°C) exacerbates silicon polyhydride powder formation unless high hydrogen dilution is used. At higher substrate temperature, less hydrogen is incorporated and the band gap is somewhat reduced. These effects are attributed to the thermal enhancement of the surface diffusivity of adatoms during growth; presumably at higher temperatures the silicon network is more ideal and binds less hydrogen. Researchers exploit the substrate temperature effect on the band gap in device making. Wider band gap materials are useful in the top component cell of a triple-junction solar cell [76, 77]. Narrower band gap a-Si is useful as the top cell *i*-layer of an a-Si/a-SiGe tandem cell. However, at temperatures higher than 350°C the quality of the material degrades; this effect is attributed to loss of hydrogen passivation of dangling bonds.

The electrode spacing in an RF glow discharge reactor is usually set between 1 and 5 cm for a-Si deposition. Smaller spacing is more desirable for a uniform deposition, while with a larger spacing it is easier to maintain a plasma. The flow rate that is required is determined by deposition rate and the area of the reactor plates. Some of the silicon atoms in the gases directed into the chamber are deposited onto the substrates or the chamber walls; the remainder gets pumped to the exhaust. Manufacturers may prefer conditions that lead to higher gas utilization (lower gas flows and higher RF power). But this compromises the quality of a-Si films deposited near the downstream area when a linear flow scheme

is used. For an R&D type deposition system with a 200-cm² electrode area and for the deposition of a-Si at the rate of 1 Å/s, a few sccm (cubic centimeters per minute at atmospheric pressure) of SiH₄ flow is typical. As one may easily calculate, for such a chamber with an electrode diameter of 16 cm and an electrode gap of 2.54 cm, 1 sccm of SiH₄ (or 0.005 sccm/cm² for this chamber) for a 1-Å/s deposition rate corresponds to a gas utilization of 11%. For the deposition of high-quality, stable a-Si material, a hydrogen dilution at appropriate level is usually used, as will be discussed in Section 12.3.6.

Another important aspect of the growth of high-quality a-Si films is the reduction of contaminants, such as oxygen, carbon, nitrogen, or metal elements. Fortunately, because of the flexibility of the bonding network in an amorphous solid, the tolerance level for contaminants in a-Si is much higher than that of its crystalline counterpart. For example, for one of the cells (with a 1.84-eV intrinsic layer) whose optoelectronic behavior is shown in Figure 12.23, a secondary ion mass spectroscopy (SIMS) measurement [78] reveals that the intrinsic layer has concentrations of O, C, and N around 1.3×10^{19} , 2.2×10^{18} , and $1.7 \times 10^{17}/\text{cm}^3$. Despite these contamination levels, this cell has a very good efficiency; the contamination levels indicated are typical for a-Si-based *i*-layers. However, when the amount of contaminants are higher than these in the *i*-layers, the device performance, particularly the fill factor, will suffer as a result of the reduced diffusion length of photogenerated carriers.

To understand and monitor the film growth in a PECVD process, various spectroscopic tools, including optical emission spectroscopy [79], optical absorption spectroscopy [80], and residual gas analyzer [81] have often been used to measure the plasma and the concentration of various species inside the reactor. It is believed that the SiH₃ radical is mostly responsible for the growth of high-quality a-Si film [82]. Such spectroscopic tools could be useful in studying and monitoring the active species and contaminants during growth, especially for process control in manufacturing.

RF glow discharge systems may be designed with different geometries based on specific needs and deposition requirements. While in R&D process the substrates and electrode are usually placed horizontally, in manufacturing processes the substrates are often installed vertically for high throughput production.

12.3.3 Glow Discharge Deposition at Different Frequencies

The standard RF frequency for glow discharge deposition is $f = 13.56$ MHz, which is a frequency allotted for industrial processes by federal and international authorities. A much larger frequency range has been explored, including DC ($f = 0$), low frequency ($f \sim$ kHz), very high frequency (VHF) ($f \sim 20$ –150 MHz), and microwave frequency (MW) ($f = 2.45$ GHz). DC glow discharges were used in the early days of amorphous silicon at RCA Laboratories, and they are presently used in manufacturing at BP Solar, Inc. [63, 64]. AC glow discharge, including RF, VHF, and MW PECVD, are more widely used because of the relative ease in maintaining the plasma and because of more efficient ionization. VHF and MW deposition have been intensively studied because of the higher deposition rate both for amorphous and, recently, for microcrystalline and polycrystalline silicon films. In the following, we discuss the use of VHF and MW PECVD for a-Si deposition.

12.3.3.1 VHF glow discharge deposition

The group at Université de Neuchatel [65, 83] has pioneered VHF plasma as a route to higher deposition rates. Figure 12.12 shows a linear increase in the deposition rate of a-Si films as a function of plasma excitation frequency (under constant plasma power). One key to the success of this approach is that higher excitation frequency enables researchers to deposit a-Si films at rates exceeding 10 \AA/s , without making polyhydride powder, as is found when deposition rates are increased by increasing RF power at a lower frequency.

The exact reasons for the high-rate, powder-free deposition of a-Si using a VHF plasma are not well understood. At this moment, it is thought that the beneficial effect is due to an enhancement in the high-energy tails of the electron energy distribution function of the plasma [66, 84].

High-quality films and devices have been obtained using VHF deposition [66, 83, 85]. Table 12.3 compares four single-junction solar cells with intrinsic layers fabricated using low and high frequencies and low and high RF power; otherwise the deposition conditions were identical. While for low-power deposition the cell performances are similar, at high deposition rate, the VHF-produced devices are superior

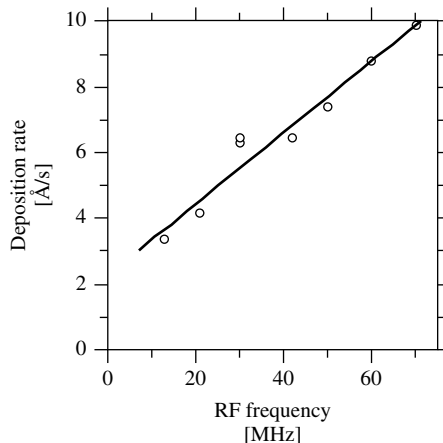


Figure 12.12 Deposition rate for a-Si:H films as a function of RF excitation frequency (at constant power); (After Shah A *et al.*, *Mater. Res. Soc. Symp. Proc.* **258**, 15 (1992) [83])

Table 12.3 Comparison of solar cell properties for cells with *i*-layers deposited using RF and VHF frequencies and different deposition rates. The VHF-deposited devices are superior at high deposition rate [85]

Excitation frequency [MHz]	Deposition rate [\AA/s]	Initial cell power [mW/cm^2]	Degradation [%]
RF (13.56)	0.6	6.6	14
VHF (70)	10	6.5	10
RF (13.56)	16	5.3	36
VHF (70)	25	6.0	22

in both initial efficiency and stability. The ability to make high-quality a-Si material at high rate using VHF could be very important for high-throughput manufacturing.

Although the advantages of using VHF deposition for high-rate growth have been clearly demonstrated, VHF process had not yet been used in large-scale production at the time of publication of this book. There are two principal challenges to applying VHF deposition in manufacturing. (1) Nonuniform deposition on a large, production-scale substrate. RF standing waves may be formed on the electrode when the electrode size is comparable to half the wavelength of the RF wave. (2) VHF coupling. It is fairly difficult to couple VHF power from the generator to large electrodes. Several research groups are working in this area and have made significant progress [86].

12.3.3.2 Microwave glow discharge deposition

Glow discharge deposition at a microwave frequency of 2.45 GHz has also been studied [87, 88]; as expected from Figure 12.12, very high deposition rates are obtained. When the MW plasma is in direct contact with the substrate, the deposited films show poor optoelectronic properties compared with RF-deposited films, and are not suitable as intrinsic layers for high-efficiency solar cells. *Remote* MW excitation has also been studied [89], and high-quality films have been obtained. In remote plasma-deposition processes, substrates are placed outside the plasma region. The MW plasma is used to excite or decompose a carrier gas such as He, Ar, or H₂ that passes through the MW zone toward the substrates. The excited carrier gas then excites SiH₄ or Si₂H₆ directed into the chamber near the substrates. Using such an indirect excitation process, the concentration of SiH₃ radicals can be maintained, while the concentrations of other radicals (SiH₂, SiH, etc.) can be minimized. However, the high deposition rate of the direct plasma deposition is also reduced with remote plasmas. MW plasma deposition has been studied at United Solar [90] and Canon [91, 92], and is used for the deposition of some of the *i*-layers in Canon's 10 MWp triple-junction production line. Generally, the structural and optoelectronic properties of MW-deposited a-Si-based films are poorer than RF-deposited films. However, at a very high deposition rate, for example 50 Å/s, the MW-deposited films will be superior to films made using RF and VHF deposition.

12.3.4 Hot-wire Chemical Vapor Deposition

Several years after Hot-Wire Chemical Vapor Deposition (HWCVD) was introduced [68, 93], Mahan *et al.* [69] improved the deposition process and produced a-Si films with superior material performance. Since then, HWCVD has been studied and used on an experimental scale worldwide for depositing high-quality a-Si- and μ c-Si-based films at high rate. The setup for a HWCVD system is similar to the schematic shown in Figure 12.11 for RF-PECVD except that the RF electrode is replaced with a heated filament. In a HW process, SiH₄ gas or a mixture of SiH₄ and other gases such as H₂ or He is directed into the chamber. The gas is catalytically excited or decomposed into radicals or ions by a metal filament heated to a high temperature (around 1800–2000°C). The silicon radicals then diffuse inside the chamber and deposit onto a substrate placed a few centimeters away and heated to an elevated temperature of 150 to 450°C. Mahan *et al.* demonstrated that HWCVD a-Si materials show relatively lower H

content in the film and improved stability against light-induced degradation compared with RF PECVD films [69]. The improved HWCVD a-Si has been incorporated in an *n-i-p* solar cell as the intrinsic layer and solar cells with $\sim 10\%$ initial efficiency have been demonstrated [94, 95].

HWCVD is considered very promising. Although it has not yet been incorporated into any of today's large-scale manufacturing facilities, the ability to deposit a-Si and a-SiGe films at very high rate (\sim up to 150–300 Å/s) [96, 97] has attracted tremendous interest. Another reason researchers are interested in HW CVD is its effectiveness in making microcrystalline and polycrystalline silicon films.

There are several concerns about incorporating HW processes in manufacturing. First, the uniformity of HW films is still poorer than that of RF PECVD films, although some companies have worked on this and made significant improvement [98]. Second, the filament needs to be improved to reduce the maintenance time in production. Third, HW-deposited solar cells have not yet achieved the same performance as cells prepared using low deposition rate, RF PECVD.

12.3.5 Other Deposition Methods

Beside PECVD and HW deposition methods, other deposition processes have been explored for depositing a-Si films. These include (1) reactive sputter deposition from silicon targets using a mixture of hydrogen and argon [99, 100]; (2) e-beam evaporation, assisted with various hydrogenation methods [101, 102], (3) spontaneous chemical vapor deposition [103], (4) photo-CVD [70, 71] using ultraviolet excitation and mercury sensitization, (5) remote plasma chemical vapor deposition [104], (6) electron cyclotron resonance (ECR) microwave deposition [105, 106], (7) pulsed laser deposition [107, 108], and (8) gas jet deposition [109]. Most of these deposition methods yield poorer a-Si films or solar cells compared with RF PECVD deposited films and devices, and therefore, are not (or not yet) used in large-scale a-Si PV production.

12.3.6 Hydrogen Dilution

Strong hydrogen dilution of the silane gas mixture during a-Si deposition has been found to reduce the density of defect states and improve the stability of the material against light-soaking effects [110–112]. Solar cells with *i*-layers deposited using strong H₂ dilution show improved performance and stability [113, 114]. There are two other important effects of hydrogen dilution. As the dilution is increased, the deposition rate declines. When hydrogen dilution is increased sufficiently, the thin silicon films that are deposited become microcrystalline.

Ferlauto *et al.* [115] have made a careful study of the “phase diagram” for silicon thin films deposited under varying levels of hydrogen dilution of silane. Some of their results, which are based on *in situ* spectroscopic ellipsometry of the growing film, are presented as Figure 12.13; this diagram pertains to a particular RF power level, substrate (c-Si), and substrate temperature. For lower dilutions ($R < 10$), films are invariably amorphous, but there is a transition to a “roughened” surface beyond a critical thickness. This roughening transition is suppressed as dilution is increased. For higher dilutions, the

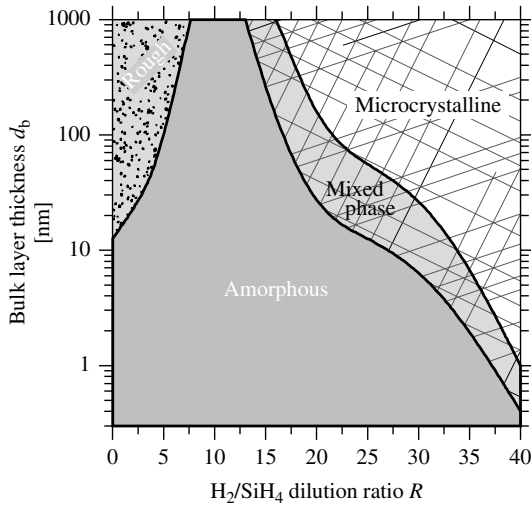


Figure 12.13 Phase diagram for the structure of plasma-deposited silicon thin films for varying dilution ratios R of silane in hydrogen and film thickness d_b ; thin films were deposited onto a single-crystal Si substrate. For lower dilutions ($R < 10$) the films remain amorphous, but undergo a roughening transition in thicker films. For high dilutions, films start out as amorphous, develop and silicon crystallites, and ultimately become entirely microcrystalline. Based upon the phase diagram proposed by Ferlauto *et al.* [115] on the basis of *in situ* spectroscopic ellipsometry measurements

growing thin film first adopts an amorphous structure. As the film thickens, crystallites form in the amorphous matrix (creating a “mixed phase”). Ultimately, the film becomes entirely microcrystalline. The details of the phase diagram do depend upon the details of deposition, in particular upon power and substrate conditions, but the structure of the phase diagram is thought to be universal.

These effects of hydrogen dilution during growth are likely owing to the following effects. (1) Atomic hydrogen “etches” a growing film, removing strained weaker bonds that are in energetically unfavorable locations; (2) a high flux of atomic hydrogen promotes the surface diffusivity of adatoms so that they can move around to more energetically stable positions and form stronger bonds; (3) atomic hydrogen diffuses into the network, restructuring it and promoting a more stable structure. For the same reasons, sufficiently large hydrogen dilution induces the formation of microcrystalline Si. The enhancement of short-range and long-range order through hydrogen dilution has been observed in many deposition techniques, including PECVD (DC, RF, VHF, and MW) and HW CVD; of course, the transitions from amorphous to microcrystalline structures occur at different dilution levels for different deposition techniques. There is evidence that the more stable amorphous silicon is deposited under the conditions that are close to the microcrystalline formation [116].

The hydrogen dilution level for the transition from amorphous to microcrystalline silicon thin films depends on other deposition conditions as well. At higher substrate temperatures (above 300°C), the transition from amorphous to microcrystalline state occurs at a higher H dilution; this effect is likely to be due to the low sticking coefficient

of hydrogen on the surface [117]. At the low temperature side (below 250°C), it again takes a higher hydrogen dilution to reach the transition between amorphous to microcrystalline [117]; this effect is likely due to the low surface diffusivity of hydrogen during growth. When a-Si is deposited at a lower temperature with higher H dilution, more H is incorporated and the material has a wider band gap. By following the edge of the transition curve (but staying on the amorphous side) while reducing the deposition temperature, wide-gap a-Si and single-junction a-Si *n-i-p* cells with 1.053 V open-circuit voltage were deposited [76, 118]. It was also observed that materials deposited near the edge of microcrystalline formation show intermediate-range structural order [119].

12.3.7 Alloys and Doping

As was discussed in Section 12.2.7, a-Si-based alloys can be deposited using a gas mixture of SiH₄ with other gases such as GeH₄, CH₄, O₂ (or NO₂), and NH₃ for obtaining a-SiGe_x, a-SiC_x, a-SiO_x and a-SiN_x, respectively. Among these alloy materials, a-SiGe has been explored extensively for PV applications as the narrow band gap absorber. As we see from Figure 12.10, the band gap E_G decreases with increasing Ge content. When E_G is decreased to below 1.4 eV, the defect density becomes so high that the materials can no longer be used as the intrinsic layer for solar cells. Various approaches have been explored to make a-SiGe or a-Ge with low band gap (below 1.3 eV) and low defect density [61]. Despite tremendous progress, device quality a-SiGe with low band gap (below 1.3 eV) has not been demonstrated.

Another related aspect for a-SiGe deposition is the deposition uniformity. Because of the different dissociation rates of germane (GeH₄) and of silane (SiH₄) in an RF plasma, the film deposited near the gas inlet side of the chamber has higher Ge content than the film near the exhaust. This nonuniformity makes it difficult to implement the process over large areas in manufacturing. By taking advantage of the approximately similar dissociation rate of GeH₄ and disilane (Si₂H₆), many research groups use a mixture of GeH₄ and Si₂H₆ for the fabrication of a-SiGe alloy and successfully obtain uniform film [52].

As discussed in Section 12.2.6, a-Si can be doped *n*-type by mixing phosphine (PH₃) with the gas mixture or doped *p*-type by mixing diborane (B₂H₆), BF₃, or trimethylboron [TMB, B(CH₃)₃] with the gas mixture during deposition. Because of the need for transparency in *p*-layers, which act as the “window” layer for sunlight, most cells have either μ c-Si or a-SiC as the uppermost *p*-layer. Amorphous SiC *p*-layers are usually made using a mixture of SiH₄ and CH₄ strongly diluted in hydrogen [61]. The μ c-Si *p*-layer is generally made in a PECVD process using high H dilution with high RF power at relatively low temperature. There have been suggestions that the optimum *p*-layer for a-Si solar cells is either nanocrystalline or is very close to the transition from amorphous to microcrystalline [120, 121].

12.4 UNDERSTANDING a-Si *pin* CELLS

12.4.1 Electronic Structure of a *pin* Device

Profiles showing electronic levels such as bandedges are an important tool in understanding device physics. Figure 12.14 illustrates the profiles of the bandedge levels E_C and E_V

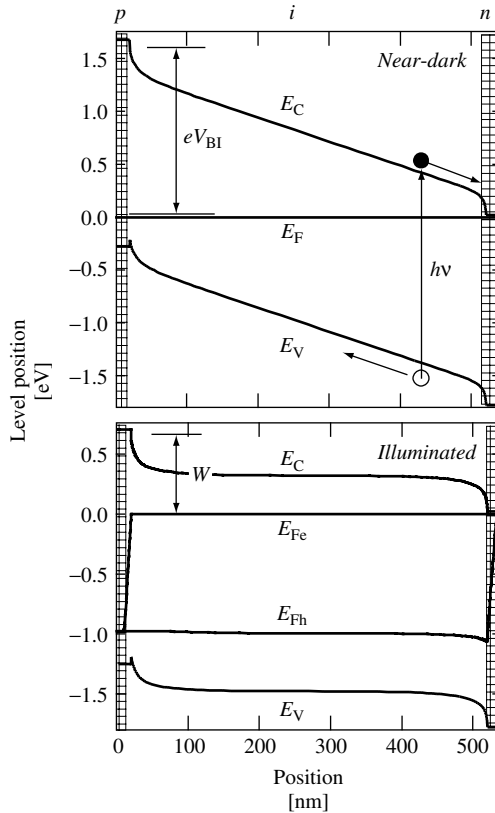


Figure 12.14 Bandedge and Fermi-level profiles in a *pin* solar cell under open-circuit conditions. The open-circuit voltage is precisely the value of E_{Fh} at the left interface ($x = 0$). The built-in potential V_{BI} is illustrated. Note that the *p*-layer has a slightly (0.2 eV) larger band gap than the *i*-layer; the calculation assumes symmetrical offsets of the valence and conduction bands at the *p/i* interface

for an a-Si:H-based *pin* solar cell in the dark and under illumination. The figure is based on calculations using the AMPS-1D[®] computer program [122, 123] and an idealized set of parameters to describe a-Si:H [124].⁶ The electric field $F(x)$ within the device causes all electron level energies such as E_C and E_V to vary in space in the same way; for E_C the expression is $eF(x) = \partial E_C(x)/\partial x$.

Where do these built-in electric fields come from? In isolation, *p*-type and *n*-type materials have very different Fermi energies; in the calculation of Figure 12.14, we assumed that E_F was 1.7 eV below E_C for the *p*-layer and was 0.05 eV below E_C for the *n*-layer. When the *pin* device is assembled, these Fermi energies must be equalized to create thermal equilibrium. Electrons are donated from the *n*-layer to the *p*-layer, which generates a built-in electric field; while the level positions such as E_C and E_V now vary

⁶ Many computer modeling codes have been developed; Schropp and Zeman give a good overview in Section 6.1 of their monograph [123].

across the device, the Fermi energy itself is constant. The original difference in Fermi energies becomes the “built-in potential” eV_{BI} across the device illustrated in the figure.⁷ Electrons and holes that are generated by photon absorption will drift in the built-in electric field in the directions illustrated in Figure 12.14.

The profiles of Figure 12.14 were calculated assuming that the p -layer has an electrical band gap of 2.0 eV and that both the middle, intrinsic layer and the n -layer have band gaps of 1.8 eV. The use of a wider band gap p -layer, which is generally desirable in a-Si:H devices, can both increase V_{BI} and reduce optical absorption in this layer. Because illumination generally enters amorphous silicon cells through the p -layer, this layer is also called the cell’s *window layer*.

12.4.2 Photocurrent Drift in Absorber Layers

The design of amorphous silicon-based solar cells is strongly affected by how rapidly electron and hole photocarriers drift in an electric field. Ideally, electrons and holes should drift across the cell without interacting with each other, with the electrons ultimately being collected in the n -layer and holes in the p -layer. If, however, electrons and holes annihilate each other (in other words, if they “recombine” and generate heat), then there will be a loss of power from the cell. In this section, we illustrate one aspect of this loss process, which is the “collapse” of the internal electric field that occurs when the densities of photogenerated, drifting holes and electrons become sufficiently large.

Figure 12.15 is a double logarithmic plot of the mean displacements $L(t)$ for electrons and for holes as a function of the time since their generation by a photon. The results are presented for an electric field $F = 3 \times 10^4$ V/cm, which is about the right magnitude for a 500-nm intrinsic layer under short-circuit conditions. It is important

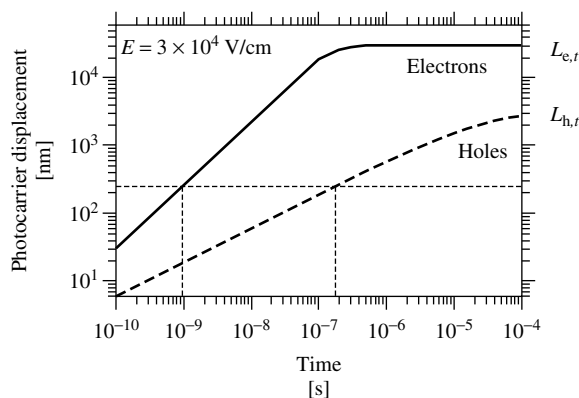


Figure 12.15 Displacements (or drift lengths) of electron and hole photocarriers in a-Si:H as a function of time following generation at room temperature [41]. Note that displacements are proportional to electric field. The saturation in the displacement for longer times (at $L_{e,t}$ and $L_{h,t}$) is due to deep trapping of electrons and holes by defects. Dotted lines illustrate the time required to drift 250 nm

⁷ We neglect interface dipoles.

to note that these displacements are proportional to electric field. They are based on laser-pulse “time-of-flight” measurements [41].

First consider the electron behavior. For the earlier times (10^{-10} to 10^{-7} s), the displacement is simply proportional to the time, so we can just write the displacement as $L(t) = \mu_e Ft$. The parameter μ_e is an electron mobility; it is about $1 \text{ cm}^2/\text{Vs}$, which is much lower than the mobility for electrons in crystal silicon (about $1000 \text{ cm}^2/\text{Vs}$ near room temperature). For longer times the electron displacement saturates at a value $L_{e,t} = 3 \times 10^{-3} \text{ cm}$. This effect is due to the capture of electrons by defects, which is called deep trapping.⁸

Let us briefly consider how these electron parameters affect the functioning of an amorphous silicon cell under short-circuit conditions. The main concern is the possible buildup of electric charge in the cell under solar illumination. If this “space charge density” is too large, then the electric field across the cell will “collapse.” A collapsed field reduces the range over which the cell collects carriers, and reduces the cell’s efficiency.

We start by determining the travel time of an electron under short-circuit conditions. If the absorber (undoped) layer has a thickness $d = 500 \text{ nm}$ and a built-in potential $V_{\text{BI}} = 1.5 \text{ V}$ across it (as for Figure 12.14), then the electric field $E \approx V_{\text{BI}}/d$ in the dark is about $3 \times 10^4 \text{ V/cm}$. Note that Figure 12.15 was prepared using this value for E . An electron that is photogenerated near the middle of the absorber layer needs to travel about 250 nm to reach the n -layer (moving right across Figure 12.14). Inspection of Figure 12.15 shows that an electron’s typical travel time t_{T} across the absorber layer will be about 1 ns .

We can use this travel time of 1 ns to roughly estimate how much the total charge of electrons builds up under solar illumination. We write $\zeta = jt_{\text{T}}/2$, where ζ is the total electron space charge in the absorber layer (per unit area of the cell); the factor of 2 implies that the current is carried equally by electrons and holes. For short-circuit conditions with $J_{\text{SC}} = 10 \text{ mA/cm}^2$, we obtain $\zeta = 5 \times 10^{-12} \text{ C/cm}^2$. To find out whether the built-in electric field is affected by this space charge density, we compare it to the built-in charge density σ_{BI} near the doped layers; σ_{BI} is the charge that actually creates the built-in electric field. Using the standard expression for the charge densities in a parallel plate capacitor, we estimate $\zeta_{\text{BI}} = \varepsilon\varepsilon_0 V_{\text{BI}}/d$ (ε is the dielectric constant and ε_0 is the “permittivity of the vacuum;” their product is about 10^{-10} C/Vm for silicon). We obtain $\zeta_{\text{BI}} \approx 3 \times 10^{-8} \text{ C/cm}^2$. Since ζ_{BI} is about 6000 times larger than the drifting space charge σ of electrons, we conclude that the drifting electrons do not significantly modify the built-in electric field.

We now turn to holes. Two aspects deserve particular attention. First, Figure 12.15 shows that the drift of holes is *much* slower (orders of magnitude slower) than that of electrons. Second, and this also differs significantly from the properties of electrons, the displacement of holes is *not* proportional to time. Instead, the displacement $L(t)$ for holes rises as a peculiar power law with time:

$$L(t) = K(\mu_{\text{h}}/v)(vt)^\alpha E \quad (12.2)$$

⁸ Quantitative study of deep trapping involves normalizing of measured values for the drift length $L_{e,t}$ by the electric field E , which yields the “deep-trapping mobility-lifetime product” $\mu\tau_{e,t} = L_{e,t}/E$. $L_{e,t}$ varies inversely with the density of defects in undoped a-Si:H [23, 48].

where the numerical factor K is about unity [125]. This type of *dispersive transport* [126] is actually rather common in noncrystalline semiconductors. The parameter α in the equation is the “dispersion parameter;” μ_h is the “microscopic mobility of holes,” and ν is the “escape frequency.” Typical parameters for a-Si:H at room temperature are $\alpha = 0.52$, $\mu_h = 0.5 \text{ cm}^2/\text{Vs}$, and $\nu = 8 \times 10^{10}/\text{s}$ [41]. For a-Si:H, the dispersive transport for holes is explained by the “trapping” of holes in localized, exponential bandtail states just above the valence band (see Figure 12.9). The dispersion parameter α is related to the valence bandtail width ΔE_V by the expression $\alpha = (k_B T / \Delta E_V)$, where $k_B T$ is the thermal energy (k_B is Boltzmann’s constant and T is the temperature in kelvins). Electrons in a-Si:H also exhibit dispersive transport, but this is important only below room temperature.

How much does the space charge of holes build up under solar illumination conditions? The simple “travel time” calculation that we used for electrons is not valid for dispersive transport. Instead, we illustrate the effects of hole buildup using a computer simulation. In Figure 12.16, we have presented the electric field profiles $F(x)$ of four widely varying intensities of light; we assume that the light is absorbed uniformly throughout the absorber layer. At low intensities, the electric field is fairly uniform throughout the *i*-layer. As the illumination flux (and short-circuit current density) rises, the density of holes (and positive charge) builds up. At the highest intensity, the electric field “collapses” at the backside of cell (near the *n*-layer). In the next section we show how field collapse influences the power generated by a cell. We have chosen to

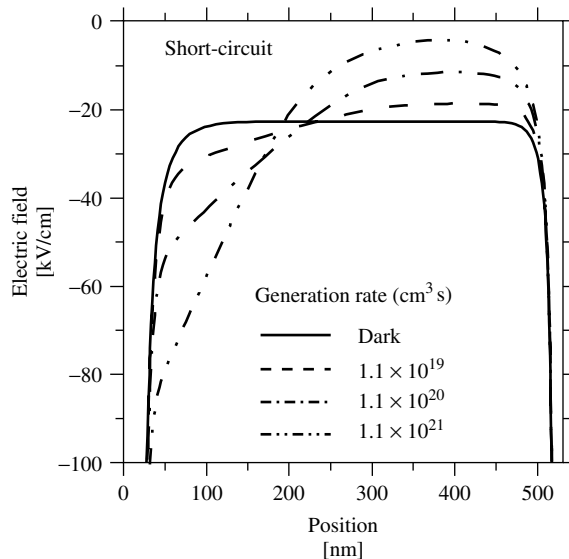


Figure 12.16 Computer calculation (cf. Figure 12.14) of the electric field profile of a *pin* solar cell for several illumination intensities; the cell is under short-circuit conditions. The illumination is uniformly absorbed ($\alpha = 5 \times 10^3/\text{cm}$) throughout the *i*-layer, and the corresponding photogeneration rates are indicated. At low intensities, the electric field is nearly uniform across the intrinsic layer (which starts at a position 20 nm from the origin). As the intensities increase, the electric field collapses nearly to zero close to the *n*-layer, which starts at 520 nm. The field becomes stronger near the *p*-layer. At the highest intensity, the fully collected photocurrent density is $11.5 \text{ mA}/\text{cm}^2$, which is about the same as that for solar illumination

neglect other aspects of power loss in the cell, which apply when field collapse may be neglected [127, 128], in particular for lower intensities.

12.4.3 Absorber Layer Design of a *pin* Solar Cell

In this section we address the issues that determine the absorber (or “intrinsic”) layer thickness. Figure 12.17 illustrates a computer calculation showing how the output power of an a-Si-based *pin* cell varies with intrinsic layer thickness. The differing curves represent results for monochromatic illumination using varying photon energies with the specified absorption coefficients. All the curves were calculated for the same photon flux. Such illumination conditions might be achieved experimentally using a laser whose photon energy could be tuned from 1.8 to 2.3 eV; sunlight, of course, presents a much more complex situation, as we discuss in Section 12.4.6.

We first discuss results for illumination through the *p*-layer (solid symbols in the figure). For intrinsic layers that are sufficiently thin, the power is proportional to the number of photons absorbed (i.e. to the product of the thickness d and the absorption coefficient α). In this limit the fill factors have nearly ideal values around 0.8.

As the thickness of the cell increases, the power saturates. First consider the behavior for strongly absorbed illumination ($\alpha = 100\,000/\text{cm}$ – corresponding to a photon energy of about 2.3 eV in Figure 12.2). Power saturation occurs for thickness greater than 100 nm, which is the typical distance at which the photons are absorbed. Since thicker cells do not absorb much additional light, the power stops increasing past this length.

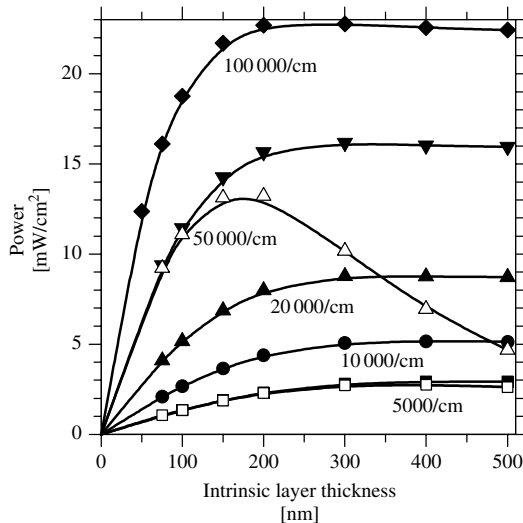


Figure 12.17 Computer calculation of the power output from a *pin* solar cell as a function of intrinsic layer thickness. The differing curves indicate results for monochromatic illumination with absorption coefficients from 5000/cm to 100 000/cm; for typical a-Si:H, this range corresponds to a photon energy range from 1.8 to 2.5 eV (cf. Figure 12.2). Solid symbols indicate illumination through the *p*-layer and open symbols indicate illumination through the *n*-layer. Incident photon flux $2 \times 10^{17}/\text{cm}^2\text{s}$; no back reflector

For weakly absorbed illumination (5000/cm – corresponding to a photon energy of 1.8 eV in Figure 12.2), power saturation occurs when the intrinsic layer is about 300-nm thick. This collection length [128] originates in the region where field collapse had occurred in Figure 12.16. The collapsed electric field is strongest near the p -layer and weaker near the n -layer. It may not be evident, but recombination of electrons and holes occurs predominantly in the weak field regions. This effect can be roughly understood from the following argument. In regions with a field near zero, drift processes driven by electric fields do not determine the densities of photogenerated electrons and holes. Since the electrons and holes are being generated at the same rate, their densities are equal, and they build up under illumination until their rate R of recombination with each other matches the rate G of photogeneration, $G = R$. It is worth noting that these conditions also apply to photoconductivity measurements that are made on isolated films of a particular material.

The asymmetry in the drift of electrons and holes explains why amorphous silicon-based pin solar cells are more efficient when illuminated through their p -layers. In Figure 12.17 we have also shown (as open symbols) calculations for the power produced by cells that are illuminated through their n -layers. Consider first the results with weakly absorbed light (5000/cm). In this case, the photogeneration of carriers is essentially uniform throughout the cells for all the thicknesses shown, and the cells do not “know” which side has been illuminated. Correspondingly, the power generation is essentially the same for illumination through the p -layer and through the n -layer.

Now consider more strongly absorbed light entering through the n -layer (50 000/cm). When the cells are thinner than the absorption length (about 200 nm in this case), the photogeneration is essentially uniform. There is again no difference in the power generated for illumination through the n - and p -layers. However, for thicker cells, there is a pronounced drop in the power from the cell for illumination through the n -layer compared to illumination through the p -layer. The power falls because the holes, on average, must drift noticeably further to reach the p -layer than when they are generated by illumination through the p -layer. The electric charge of the slowly drifting holes builds up and “collapses” the electric field, leading to recombination and loss of power.

12.4.4 The Open-circuit Voltage

In Figure 12.18 we present a summary of the open-circuit voltages (V_{OC}) for a-Si:H-based solar cells from United Solar Systems Corp. as a function of the band gap of the intrinsic absorber layer [129].⁹ The measurements were done under standard solar illumination conditions. This graph is quite important for understanding the efficiencies of a-Si:H solar cells. For each photon absorbed, the solar cell delivers an energy $E = (FF)eV_{OC}$. The relation $V_{OC} = (E_G/e) - 0.80$ shows that most cells deliver a voltage that is 0.80 V below the band gap. We can now roughly estimate the power delivered by a cell. For a 500-nm-thick cell and a 1.75-eV band gap, Figure 12.2 shows that a typical photon absorbed by the cell under solar illumination actually carries nearly $h\nu \approx 2.5$ eV of energy. Since fill factors are necessarily less than 1, the energy actually delivered by the cell can be no

⁹ We have assumed familiarity with the standard solar cell terminology of short-circuit current density J_{SC} , open-circuit voltage V_{OC} , and fill factor FF . See Chapter 3 for definitions of these terms.

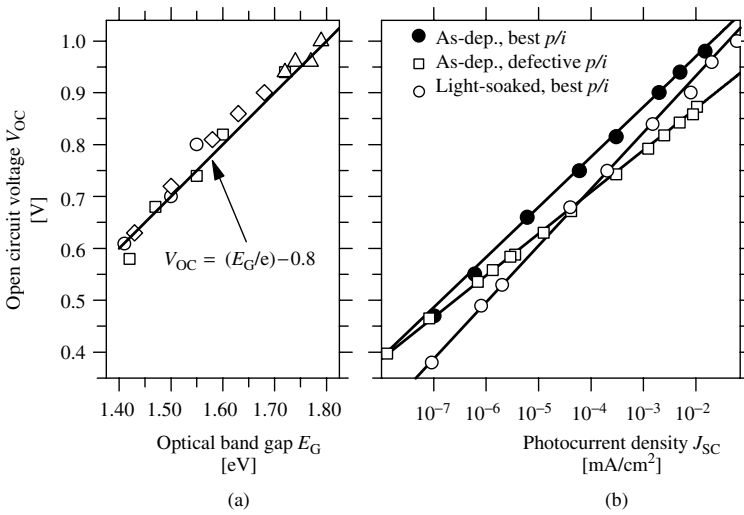


Figure 12.18 (a) Open-circuit voltages for a-Si:H-based solar cells as a function of optical band gap [129]. The band gap variation is mostly due to germanium incorporation. The measurements are from several laboratories; consult the reference for details. (b) Open-circuit voltage V_{OC} versus short-circuit photocurrent density J_{SC} for *nip* solar cells as reported by Pearce *et al.* [130]. The short-circuit current density is proportional to the intensity of the illumination, which had a “white” spectrum similar to solar illumination

larger than 0.95 eV per photon – so over 60% of the absorbed energy must, alas, be lost in such a cell.

The simplicity of the dependence of V_{OC} upon band gap in Figure 12.18 is only possible because open-circuit voltages depend only weakly on (1) the thickness of a-Si:H solar cells and (2) the intensity of illumination. As a result, most details about the cells and measurement conditions are unimportant. For example, in the calculations of Figure 12.17, the open-circuit voltage changed about 10% (from 0.9–1.0 V), while the output power varied from 1 to over 20 mW/cm².

Still another simplification applies to many cells. Most workers think that the very best open-circuit voltages in a-Si:H-based cells have reached their “intrinsic limit.” This means that these best values are not limited by the details of the *p*- and *n*-type electrode layers [130], but are a fundamental property of the intrinsic layer.

We now give a short argument to explain how V_{OC} is related to the energy profile of Figure 12.14 and why V_{OC} depends only weakly on thickness. The lower panel of Figure 12.14 presents calculated open-circuit profiles of the bandedge levels E_C and E_V of a cell with uniformly absorbed illumination. No Fermi energy is shown in this lower panel because the cell is not in thermal equilibrium – it is exposed to light. Instead, electron and hole quasi-Fermi energies E_{Fe} and E_{Fh} are illustrated, which we will define shortly. Notice that these quasi-Fermi energies merge together at the left edge of the *p*-layer and again at the right edge of the *n*-layer; this merging means that an ordinary Fermi energy can be defined at these edges despite the presence of light. The product eV_{OC} is the difference between these two Fermi levels, as illustrated in the figure. The illuminated

solar cell acts somewhat like an ordinary electrical battery, which also maintains different Fermi levels at its two terminals.

We now define the electron and hole quasi-Fermi energies E_{Fe} and E_{Fh} [131, 132]. For the electron quasi-Fermi energy E_{Fe} , we write

$$n \equiv N_C \exp(-(E_C - E_{\text{Fe}})/k_B T) \quad (12.3)$$

where n is the density of mobile electrons in the conduction band (i.e. in the shaded region of the conduction band in Figure 12.9). N_C is the effective density ($1/\text{cm}^3$) of these conduction band states. A similar expression accounts for the density of holes p in terms of a distinct quasi-Fermi energy for holes E_{Fh} and for the effective density N_V of valence band states.

Interestingly, in Figure 12.14 the hole quasi-Fermi level is nearly constant across the cell, showing sizable variation only where it catches up to E_{Fe} in the n -layer. Similarly, the electron quasi-Fermi level is constant except near the p -layer. This constancy means that the quasi-Fermi levels in the middle of the cell largely determine V_{OC} . The panel also shows that, in the middle of the cell, the band-edge potentials are essentially constant and the electric field is very weak. As mentioned earlier, in such field-free regions the electron and hole photocarrier densities are equal and are determined by the condition that the recombination and photogeneration rates are matched. For cells that have attained the intrinsic limit, it is these fundamental processes that determine V_{OC} .

We now turn to the measured dependence of V_{OC} upon the illumination intensity. Some recent measurements are presented in Figure 12.18(b) [130]. The intensity was varied by using “neutral density” filters that attenuate all photon energies to the same extent. The short-circuit current density J_{SC} has been used as a “surrogate” for intensity based on their proportionality. Consider first the uppermost set of measurements (“as-deposited, best p/i interface”). The logarithmic dependence of V_{OC} upon incident photon flux F is typical of photodiodes [124, 133]. For this sample, the slope of this dependence is determined by the defects; a second line in Figure 12.18 (“light-soaked, best p/i ”) indicates how the dependence changed following an extended period of light soaking. Interestingly, the difference in the two V_{OC} versus $\ln(J_{\text{SC}})$ lines is fairly small (about 0.02 V) under full solar illumination (about $10 \text{ mA}/\text{cm}^2$), where the effect of defects upon electron and hole motions is relatively unimportant. This fact partly explains why the dependence of V_{OC} upon band gap can be simple despite the wide variations in defect density for varying materials.

Our previous discussion concerns open-circuit voltages in the intrinsic limit. As might be expected, it is easy to fabricate a-Si:H solar cells with inferior open-circuit voltages. In Figure 12.18, we have also shown the V_{OC} versus $\ln(J_{\text{SC}})$ relation [130] for a cell with a (intentionally) defective p/i interface (open squares). This cell was based on the same intrinsic material as the as-deposited cell with the best p/i interface (solid circles); the slope of the V_{OC} versus $\ln(J_{\text{SC}})$ relation is now noticeably reduced by the interface effect.

What aspect of nonideal p/i interfaces leads to a reduction in V_{OC} ? The physical mechanism through which a poor p/i interface diminishes V_{OC} is the flow of photogenerated holes from the intrinsic layer (where they are generated) to the p/i interface (where

they recombine with electrons) [124]. The flow means that the hole quasi-Fermi level has a gradient [132] near the p/i interface that reduces V_{OC} below its intrinsic limit. You can just barely notice this gradient effect in Figure 12.14.

The reason this hole current flows is to balance an exactly equal current of electrons. The electrons are being thermionically emitted from the intrinsic layer and over the electrostatic barrier at the p/i interface. You can envision this thermionic process using the bottom panel of Figure 12.14, which shows a barrier of $W = 0.6$ eV for electron emission from the quasi-Fermi level E_{Fe} in the intrinsic material into the p -layer.

The best open-circuit voltages in substrate solar cells are achieved using a boron-doped silicon film [134]. This material is generally referred to as microcrystalline, although extensive characterization of the type presented in Figure 12.13 suggests this p -layer may also be dominated by an amorphous phase. The best open-circuit voltages in superstrate solar cells have been achieved using boron-doped amorphous silicon–carbon alloys (a-SiC:H:B). An indication of the subtlety required to achieve high open-circuit voltages is that cells using a-SiC:H:B p -layers also include a thin (<10 nm) “buffer layer” of undoped a-SiC:H between the p -layer and the intrinsic layer of the cell [135–137]. The precise mechanism by which these buffer layers improve V_{OC} is not conclusively established. We would speculate that the buffer layer impedes electron emission into the p -layer, in accordance with the “thermionic emission” model for the p/i interface effects just described.

12.4.5 Optical Design of a-Si:H Solar Cells

In this section we briefly review the use of *back reflectors* and *substrate texturing*, which are optical design principles that are used to improve the power output of amorphous silicon–based solar cells. The interested reader will find a more comprehensive treatment in the recent monograph of Schropp and Zeman [123] and Chapter 8.

Incorporating a back reflector increases the power output of solar cells. In Figure 12.19, an ideal back reflector doubles the power output for weakly absorbed light (5000/cm in the figure); we are neglecting optical interference and “rereflection” of light by the top of the cell, so the light passes through the cell twice, once on its way down to the reflector, and again on its way back out the top. The back reflector has no effect on power output for strongly absorbed light (50 000/cm in the figure), since that light never “sees” the back reflector. The effects of the back reflector are fairly complex when the thickness, absorption length of the illumination, and collection length for the holes are all comparable, which is what occurs for thicknesses in the range of 100 to 300 nm with 50 000/cm illumination.

For weakly absorbed light, a back reflector for the simple planar structures just described increases power collection about twofold. Much larger improvements may be envisaged. The fundamental idea is “light trapping.” An optical beam propagating inside a dielectric structure may be trapped by total internal reflection at the interface with air, which has a lower index of refraction than the dielectric. The principle is the same as that underlying the operation of optical fibers: an optical beam that enters the fiber at one end can travel kilometers without leaving the fiber. For solar cells, the light-trapping idea

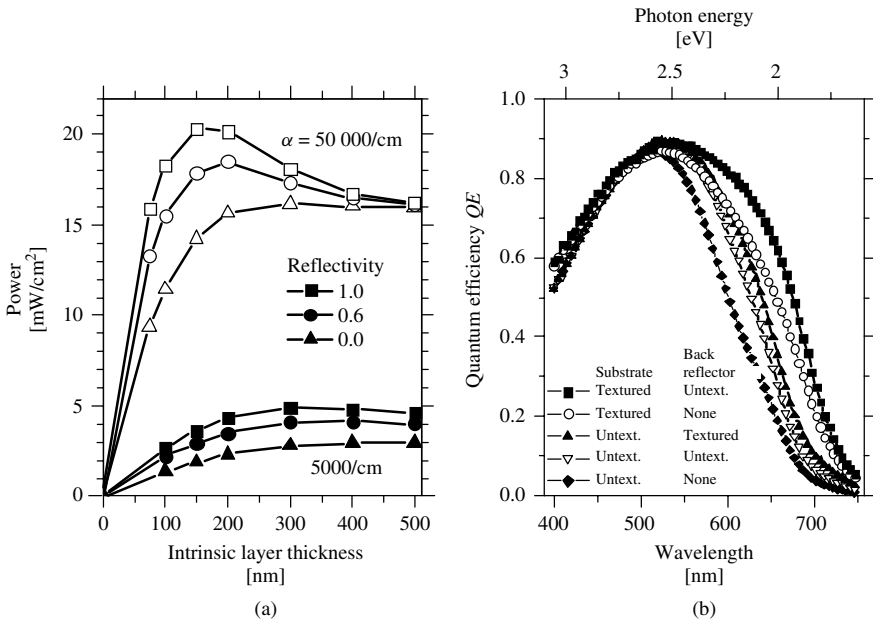


Figure 12.19 (a) Computer calculation of the power output from a *pin* solar cell as a function of intrinsic layer thickness. The two sets of curves indicate results for monochromatic illumination (photon flux $2 \times 10^{17}/\text{cm}^2\text{s}$) with absorption coefficients of 5000/cm (black symbols) and 50 000/cm (gray symbols). Results are shown for varying back reflectance; interference effects are neglected. (b) Quantum efficiency (QE) spectra for *nip* solar cells deposited under identical conditions, but with two differing substrate textures and differing back reflectors [138]. The sequence of layers in the structure was (TCO/*p/i/n*/TCO/glass/Ag). The Ag is the back-reflector material (when present); the TCO on top of the glass was either smooth or textured (14% haze).¹⁰ Measured at -1 V bias

implies that a cell might fully absorb light even when its thickness is much less than the absorption length $1/\alpha$ for the light's wavelength.

Light trapping is realized in amorphous silicon (and other) solar cells by using substrates that are “textured” or rough on the same scales as the principal wavelengths in solar illumination. The idea is that the random reflection/diffraction of light by the irregular, textured topography leads to internal reflection. Yablonovitch [139] showed that the maximum gain for such “statistical light trapping” in a textured film on an ideal reflector is $4n^2$, where n is the index of refraction of the film; Yablonovitch's argument is fundamental and not based on any particular form for texturing. For silicon films, with $n \sim 3.5$, the maximum predicted gain is nearly a factor of 50 (for light that is *very* weakly absorbed).

Experimentally, optical gains up to a factor of ten have been reported from the use of textured substrates and weakly absorbed light [138, 140]. In Figure 12.19 we have presented measurements by Hegedus and Deng [138] of the “quantum efficiency” (QE)

¹⁰ Haze is defined as the percentage of the light incident upon a film that is scattered incoherently. For transparent films, most of the remaining light is transmitted undeviated. Haze depends strongly upon the photon energy. The same value of haze can be obtained from films with quite different morphologies.

for a-Si:H solar cells made with several different textures and back reflectors. The quantum efficiency is defined as the ratio, at a specific photon energy, of the photocurrent density j (A/cm^2) to the incident photon flux f :

$$QE = j/ef \quad (12.4)$$

Consider first the lowest of the curves (smooth substrate, no back reflector shown with black diamonds). In this sample, photons incident on the p -layer are either absorbed in the cell or pass through the cell and leave it through the glass substrate. The rise of QE as the photon energy increases up to about 2.5 eV is due to the increase in absorption. A -1 V bias was applied, and the resulting electric field prevented the loss of photocarriers to recombination. Near 2.5 eV the QE is nearly one: essentially all incident photons are absorbed and nearly all the photocarriers generated are subsequently collected. The result is sensible. Inspection of Figure 12.2 shows that the absorption coefficient is about $10^5/cm$ at this energy, so that photons are absorbed within about 100 nm of the top surface of the a-Si:H. Since this length is much smaller than the sample thickness, essentially all photons are absorbed. Some photons are lost because of reflection from the glass and TCO interfaces, which accounts for most of the remaining losses.

For photon energies greater than 2.5 eV, the absorption coefficient continues to increase, so photons are absorbed within a few tens of nanometer at the top of the p -layer. A significant fraction of these photons is absorbed in the p -layer or the TCO; these photons do not contribute to the photocurrent, and so the QE declines for higher photon energies.

Now consider the data for the cell with an untextured substrate (0% haze) and a smooth Ag back reflector (open triangles). For photon energies that are weakly absorbed (below 2.5 eV), the QE increases about twofold because of the back reflector; for strongly absorbed photons, there is little effect of the back reflector. These effects were just explained for the computer modeling of Figure 12.19(a). Interestingly, the use of a textured back reflector further improves the QE . The textured reflector increases the typical angle between the paths of reflected photons and the axis normal to the substrate; this effect increases the typical path length of the reflected photon in the a-Si:H as well as the chance of reflection when a reflected photon arrives back at the top of the cell. The uppermost two curves, with the highest QE s, correspond to cells with textured substrates. For lower photon energies, the textured substrates further improve the QE , although certainly not to the maximum extent $4n^2$ calculated by Yablonovitch. Note also that substrate texturing also leads to a modest improvement of the QE in the blue spectral region (beyond 2.5 eV) due to a reduction in the front-surface reflectance of the cell.

Roughly, the effect of back reflectors and texturing for lower photon energies shown in Figure 12.19 is to reduce the energy threshold for collection of an incident photon by about 0.2 eV. Using Figure 12.2 one can estimate that this reduction in threshold increases the incident solar power absorbed by a 0.5- μ m cell from 420 to 520 W/m^2 . This estimate is broadly consistent with measurements showing an increase in short-circuit photocurrent under solar illumination of about 25% when textured substrates are used [140–142].

The implementations of texturing and back reflectors, as well as of a front “anti-reflection” coating to reduce the reflection, vary dramatically between superstrate and

substrate cell designs. Superstrate cells usually incorporate a textured, TCO coating on the transparent substrate (usually glass). There are many technologies for producing TCO layers from varying materials (typically SnO_2 or ZnO for a-Si-based cells) and with varying texture and electrical properties. The semiconductor layers are then deposited onto the textured TCO. Plasma deposition of the p -layer onto a textured TCO can lead to difficulties: the oxide layer may be chemically “reduced,” and achieving ideal properties for a thin p -layer could be difficult. Finally, the back reflector deposited on top of the semiconductor layers is often a two-layer structure: a thin TCO layer, followed by the reflective metal (typically Ag – for best reflectivity – or Al – for improved yield in production).

In substrate cells, the semiconductor layers are actually deposited onto the back-reflector, which is again a two-layer structure starting with a textured silver or aluminum metallization and then a textured TCO [143]. Following deposition of the semiconductor layers, a top TCO layer is applied.

12.4.6 Cells under Solar Illumination

In the previous few sections, we have discussed the components of a-Si:H pin solar cell design. For monochromatic light and for a given intrinsic layer thickness, we have described the effects of the absorption length and the intensity, the effects of the slow (and dispersive) hole transport and the relatively rapid electron transport, and the use of back reflectors and texturing to enhance the photocurrents realized from weakly absorbed light. In this section we use essentially the same model for these effects as we have in previous sections, but extend it to a cell’s operation under polychromatic, solar illumination. In addition, when we changed the band gap, we left all other model parameters unchanged. This discussion continues in the following sections on multijunction (and multi-band gap) cells.

In Figure 12.20 we present calculations of the PV parameters J_{SC} , FF , V_{OC} , and solar conversion efficiency for pin solar cells of varying thickness and electrical band gap. First note the increase in short-circuit current J_{SC} as the band gap is reduced (at constant thickness); this effect is due to the increase in optical absorption coefficients in the infrared as the band gap is reduced (cf. Figure 12.10). Also note that the short-circuit current depends only weakly upon thickness beyond the first 100 nm of thickness, which accounts for a substantial fraction of the total absorption. The decline of V_{OC} with band gap of course duplicates the experimental trend of Figure 12.19. Interestingly, V_{OC} remains essentially independent of thickness under solar illumination, despite the “front loading” of the photon absorption. On the other hand, the fill factors under solar illumination are substantially larger than that for uniform illumination. Finally, the differing trends of V_{OC} and of J_{SC} with band gap conspire to determine a maximum efficiency of about 11.3% for a cell with a band gap of 1.45 eV and a thickness greater than about 300 nm. While the neglect of deep levels is too idealized for these calculations to precisely describe the efficiencies, the calculations nonetheless indicate the principal trends of changing the band gap. They also suggest the strategy that has been used to achieve higher efficiencies. In particular, the effects of a decline in V_{OC} with band gap in single-junction cell can be avoided by building multijunction solar cells, as we describe in the next section.

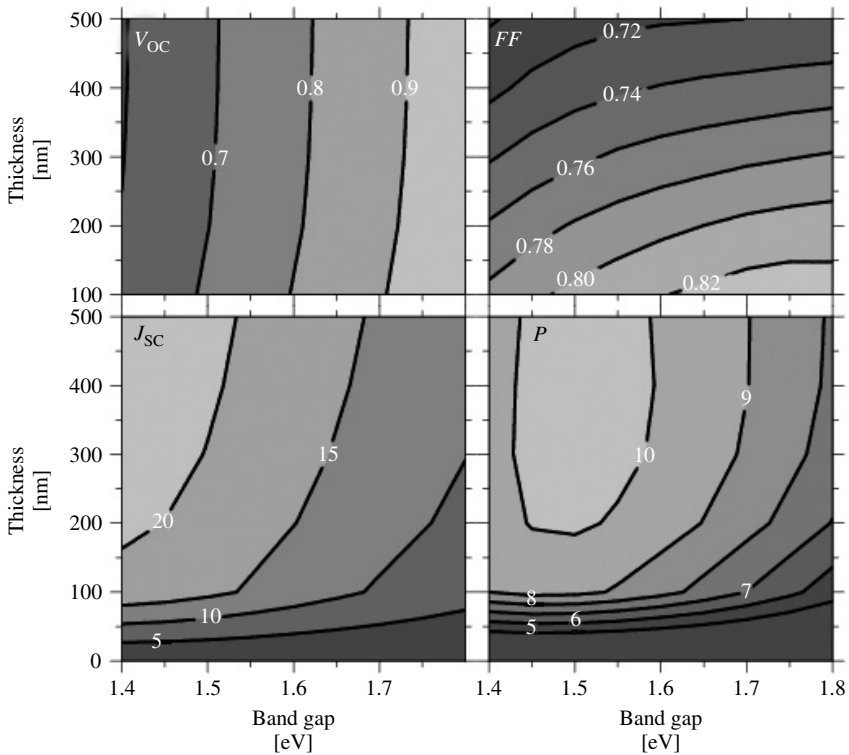


Figure 12.20 Model calculations of the short-circuit current J_{SC} (mA/cm^2), open-circuit Voltage V_{OC} (V), fill factor FF , and power P under AM1.5 illumination for a-Si:H-based *pin* solar cells with varying intrinsic layer band gaps and thicknesses. No back reflector or texturing effects are included

12.4.7 Light-soaking Effects

In Figure 12.21 we illustrate the power output (standard solar illumination) of a series of cells of varying thickness prepared at United Solar Systems Corp. [14]. The cells are “substrate” type cells prepared on stainless steel. Results are shown both for the initial state of the cells and after 30 000 h (degraded state). For the initial state of the cells, the power rises with thickness and saturates for thicknesses greater than about 400 nm, which is more or less consistent with the modeling presented in Figure 12.17. In their degraded state, the cells reach their maximum power for a thickness of around 200 to 300 nm; substantially thicker cells actually lose some power. As we have noted previously, the degradation effect is correlated with the increase in the defect density in a-Si:H as light-soaking proceeds. Although we did not include defects in the modeling presented in this section, one can understand the degradation effect qualitatively as a result of hole trapping by light-induced defects instead of by valence bandtail states. We do not know whether the fact that the power “peaks” in the degraded state for thicknesses greater than about 300 nm is due to back reflection (cf. Figure 12.19) or due to subtleties in the profile of light-induced defects.

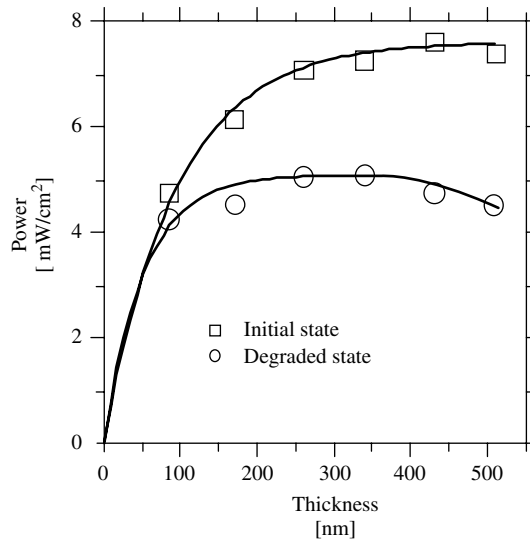


Figure 12.21 Power output (standard solar illumination) for a series of *nip* solar cells with varying intrinsic layer thickness [14]. The degraded state was obtained by 25 000 h of light soaking. The curves are guides only

12.5 MULTIPLE-JUNCTION SOLAR CELLS

12.5.1 Advantages of Multiple-junction Solar Cells

Amorphous silicon solar cells can be fabricated in a stacked structure to form multijunction solar cells. This strategy is particularly successful for amorphous materials, both because there is no need for lattice matching, as is required for crystalline heterojunctions, and also because the band gap is readily adjusted by alloying. Figure 12.4 illustrated the structure of a tandem cell with two junctions (i.e. two *pin* photodiodes) in series. Multijunction, a-Si-based solar cells can be fabricated with higher solar conversion efficiency than single-junction cells and are presently used in most commercial cells.

The fundamental concept underlying multijunction solar cells is “spectrum splitting.” Consider what happens if we deposit a second *pin* junction structure on top of a first one. The second structure “filters” the sunlight: photons absorbed in the top junction are of course removed from the light that reaches the bottom cell. We illustrated this filtering effect in Figure 12.2, which shows that 500 nm of a-Si:H absorbs essentially all incident photons with energies greater than 2 eV, and passes photons with smaller energies. In practice, the thickness of the top *pin* junction is adjusted so that it filters out about half of the photons that would otherwise have been absorbed in the bottom *pin* junction.¹¹ Since the photons that are absorbed in the top junction have relatively large energies, we can use a material with a relatively large band gap as the absorber for this junction, and

¹¹ We discuss only “two-terminal” multijunction cells in this chapter in which a single electrical current flows through the series-connected cells. See Chapter 9 for further discussion of 2, 3 and 4 terminal multijunction cell operation.

we shall obtain a larger open-circuit voltage across the top junction than that across the bottom junction. This is the “spectrum-splitting” effect.

For specificity, consider a tandem cell that bases the bottom junction on material with a 1.55 eV electrical band gap and bases the top junction on material with 1.80 eV electrical band gap material. In the absence of the top, 1.80-eV junction, the 1.55-eV junction might deliver about $J_{SC} = 20 \text{ mA/cm}^2$ at an open-circuit voltage of 0.65 V. Assuming a fill factor (FF) of 0.7, the power output will be 9.1 W/m^2 . When assembled in tandem, the current through each junction is about half this value, but the open-circuit voltage will more than double ($V_{OC} = 0.65 + 0.90 = 1.55 \text{ V}$). The power output rises to 11.2 W/m^2 – for a 19% spectrum-splitting improvement over the single-junction device.

For ideal semiconductors arranged with optimal band gaps, the maximum efficiencies for single, tandem, and triple-junction solar cells under concentrated sunlight are 31%, 50%, and 56%, respectively [144]. Figure 12.22 shows the conversion efficiency contour plot calculated using an a-Si:H-based computer model for two-junction tandem cells; the two axes are the band gaps for the top and bottom component cells [145, 146]. The best efficiency of over 20% occurs with a combination of a 1.8-eV intrinsic layer in the top *pin* junction and a 1.2-eV layer in the bottom. Of course, these model results have not yet been achieved in practice!

We can distinguish three reasons for improved efficiency in a-Si-based multijunction cells over single-junction cells. The first is the spectrum-splitting effect we have just

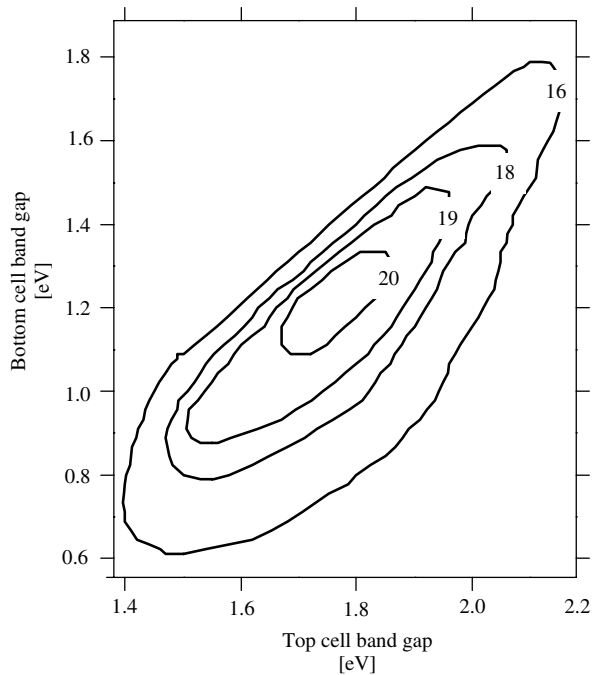


Figure 12.22 Contour plot of constant solar conversion efficiency for a-Si-based tandem solar cells for varying band gaps E_G of the top cell and the bottom cell [145]

described. Second, the *i*-layers in an optimized, multijunction cell are thinner than in single-junction cells [147, 148]; as can be seen in Figure 12.20, this “junction thinning” means that each individual junction will have a somewhat better fill factor than in the optimized single-junction device, and there will be less change from the initial to the stabilized efficiency of the cell. Third, a multijunction cell delivers its power at a higher operating voltage and lower operating current than a single-junction cell; the lower current reduces resistive losses as the current flows away from the junctions and into its load.

On the other hand, it is more challenging to fabricate multiple-junction solar cells than single-junction cells. The performance of a multijunction cell is more sensitive to the spectrum of the incident light due to the spectrum-splitting feature. This makes it even more critical to control the band gaps and thicknesses of the individual layers. In addition, most multijunction cells incorporate a-SiGe alloys. These alloys are made using germane gas as the germanium source. Germane is several times more expensive than silane and is highly toxic. Manufacturers need to implement strict safety procedures to handle these types of gases. Overall, the advantages and benefits of higher stabilized output power for multiple-junction cells do outweigh the difficulties in the fabrication.

12.5.2 Using Alloys for Cells with Different Band Gaps

As was mentioned in Section 12.2.7, when a-Si is alloyed with other elements such as Ge, C, O, and N, amorphous alloy materials with different band gaps can be obtained. This allows the selection of appropriate band gap combinations for high-efficiency solar cell fabrication. Since the band gap of the a-SiGe alloy can be continuously adjusted between 1.7 and 1.1 eV when different amounts of Ge are incorporated in the alloy, it can be used as the low band gap bottom cell absorber layer for a multijunction solar cell. It is desirable to select a band gap near 1.2 eV to achieve the maximum efficiency according to the contour plot in Figure 12.22. Unfortunately, the optoelectronic quality of a-SiGe degrades rapidly when the a-SiGe band gap is reduced below 1.4 eV, and these materials have not proven useful for PV application.

Figure 12.23 shows the J - V characteristics of a series of a-SiGe solar cells with different Ge concentrations in the *i*-layer (of constant thickness, and without a backreflector) [149]; the band gaps are indicated in the legend. As the band gap is reduced by incorporating more Ge in an *i*-layer, V_{OC} goes down and J_{SC} goes up (for a constant thickness), in agreement with trends for the calculations in Figure 12.20. In Figure 12.24, we plot the QE curves of these same a-SiGe cells (along with one curve for a cell with a back reflector, and one curve for a cell with a microcrystalline Si *i*-layer). Consistent with the increase in J_{SC} , the QE is increased for longer wavelengths (smaller photon energies) as the band gap decreases.

The fill factors of the cells also decrease as the band gap decreases. This effect is due to the increased defect density in the alloyed materials. We have not included this important effect in the discussion previously. As the defect density in the *i*-layer increases, a given cell's performance will ultimately be dominated by the trapping of photocarriers on defects instead of by bandtail trapping. Roughly speaking, one can think of defect trapping as reducing the “collection length” that determines the useful thickness of the intrinsic layer (cf. Figure 12.17). Naturally, one is principally interested in these effects for the “light-soaked” state achieved by operating cells.

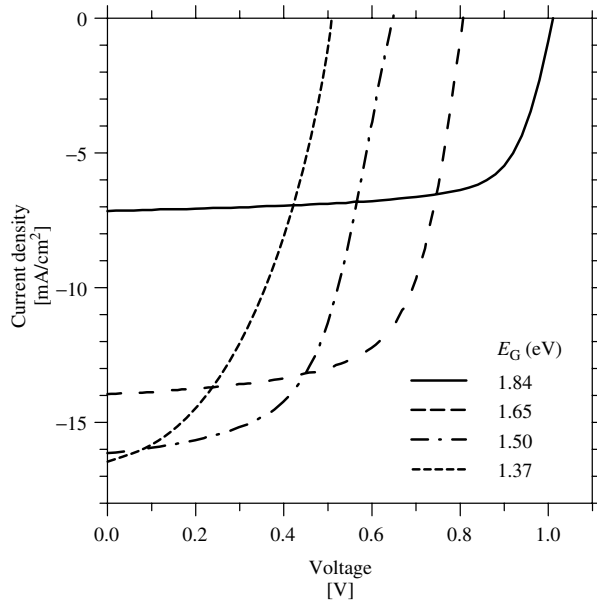


Figure 12.23 Performance of a-Si and a-SiGe *nip* solar cells with different Ge concentrations in the *i*-layer; the *i*-layer band gaps are indicated in the legend. The fill factors for these cells are 0.70, 0.62, 0.55, and 0.43 for the cells with *i*-layer band gaps of 1.84, 1.65, 1.50, and 1.37 eV, respectively [149]

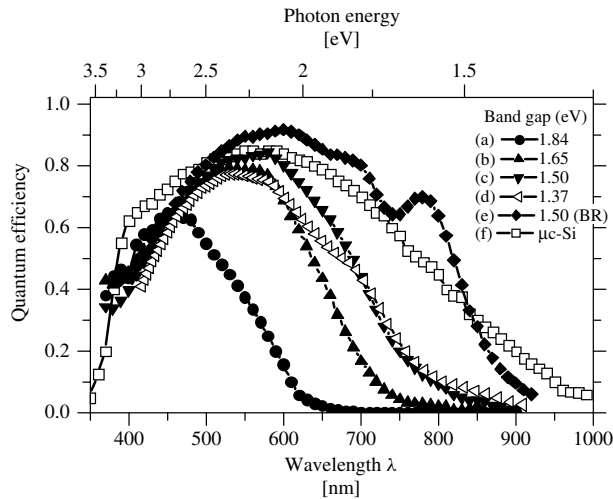


Figure 12.24 Quantum efficiency (*QE*) spectra for a series of a-Si- and a-SiGe-based *pin* single-junction solar cells. Shown in the figure are *QE* curves for single junction solar cells with (a) 1.84 eV a-Si *i*-layer, (b) 1.65 eV a-SiGe *i*-layer, (c) 1.50 eV a-SiGe *i*-layer, (d) 1.37 eV a-SiGe *i*-layer, (e) 1.50 eV a-SiGe *i*-layer, with the device deposited on a back-reflector (BR), (f) μ c-Si *i*-layer. Curve (f) is included here for a later discussion in Section 12.5.4. Curves (a) through (e) are from [149] and curve (f) is from [150]

When the Ge content is increased such that the band gap of a-SiGe is reduced below 1.4 eV (see the J - V curve for the 1.37-eV cell in Figure 12.23), the FF deteriorates rapidly. In this case, the short-circuit current density does not increase compared to the 1.50-eV cell even though more photons are absorbed. This lack of increase in J_{SC} with further decrease in the band gap occurs because the fraction of photocarriers that recombine has become more significant than the increase in the rate of photocarrier generation.

Similar to the deposition of a-Si, a-SiGe films and devices made with high hydrogen dilution show improved quality and light stability [151]. Optoelectronic properties of narrow band gap a-SiGe material are nonetheless inferior to those of a-Si.

12.5.2.1 Band gap grading

To enhance the fill factor of cells made using a-SiGe, band gap *grading* is used to enhance the collection of holes [152, 153]. In such a design, an asymmetric “V”-shaped band gap profile is created by adjusting the Ge content across the i -layer. Wider band gap material lies closest to the n - and p -layers. The plane of narrowest band gap lies closer to the p -layer (through which the photons enter into the device). Such a grading scheme allows more light to be absorbed near the p -layer so that “slower” holes do not have to travel far to get collected (see Figure 12.10). Also, the tilting of the valence band assists holes generated in the middle or near the n -side of the i -layer to move toward the p -layer. With appropriate hydrogen dilution during growth and band gap grading, a-SiGe cells can be made to generate up to 24.4 mA/cm² (27 mA/cm² as the bottom cell in a triple cell) when a light enhancing back reflector is used [154].

12.5.2.2 a-SiC alloys

The band gap of a-SiC can be adjusted between 1.7 and 2.2 eV, depending mainly on the C concentration [155]. After extensive research, most workers decided that a-SiC is not suitable for use as the i -layer of the uppermost cell in a multijunction structure. After light soaking, a-SiC material that has an appreciable band gap increase over a-Si is fairly defective and must be used in very thin layers; these layers do not absorb enough sunlight to be optimal. The wide band gap material presently used in triple-junction cells is a-Si with a relatively higher concentration of H (achieved by using lower substrate temperature and H dilution) [8].

12.5.3 a-Si/a-SiGe Tandem and a-Si/a-SiGe/a-SiGe Triple-junction Solar Cells

Several types of multijunction solar cells have been used in a-Si photovoltaics. Dual-junction a-Si/a-Si (same band gap tandem) solar cells have lower material cost than tandem cells using a-SiGe, but have lower efficiencies than more advanced structures [156]. Dual-junction a-Si/a-SiGe cell and triple-junction a-Si/a-SiGe/a-SiGe cells, which use a spectrum-splitting approach to collect the sunlight, achieve higher conversion efficiencies. Some additional details and references may be found later in Table 12.4. Among these, a-Si(1.8 eV)/a-SiGe(1.6 eV)/a-SiGe(1.4 eV) triple-junction solar cells have been used to obtain the most efficient a-Si-based cells today [8]. Figure 12.25 shows the structure of

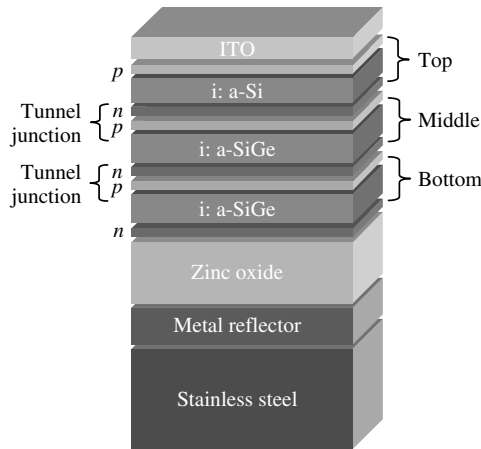


Figure 12.25 Structure of triple-junction *nip* substrate-type solar cells

a triple-junction substrate cell¹² grown on SS foil; a superstrate-type tandem cell (glass substrate) was illustrated previously in Figure 12.4. In both cases, light enters from the *p*-layer so that holes need to travel less distance to get collected than electrons. In the following, we will briefly describe the two designs and typical deposition processes that are most broadly used today.

In *nip* cells deposited on an SS substrate, a reflective metal layer is deposited first on the substrate by sputtering or evaporation, followed by the sputter deposition of a ZnO buffer layer. Usually, silver is used as the reflective layer for research cells because of its high reflectivity, whereas aluminum is used in production because of difficulties with production yield for silver. The metal layer is deposited at high temperature (300–400°C); self-segregation in the metal film forms the texture needed for light trapping. The sample is then moved into a RF PECVD deposition system for the deposition of semiconductor layers. The bottom *nip* with an a-SiGe *i*-layer (1.4–1.5 eV band gap) is deposited first. A second a-SiGe-based middle cell (1.6–1.65 eV *i*-layer band gap) is then added. Finally, the top a-Si-based cell (1.8–1.85 eV *i*-layer band gap) is added; the intrinsic layer is made using high H dilution at relatively low temperature. An indium-tin-oxide (ITO) layer is deposited on top via evaporation or sputtering. This layer is approximately 70-nm thick and serves as both the top electrode and an antireflection coating. Metal grids are evaporated or sputter-deposited on top of ITO to further reduce contact resistance.

In *pin* superstrate cells deposited on glass, the glass substrate is first coated with a textured transparent conducting oxide, usually SnO₂ or ZnO, using one of the several methods such as atmospheric pressure chemical vapor deposition (APCVD) [167, 168]. A *pin* top cell having an a-Si *i*-layer is then deposited, followed by the a-SiGe middle cell, and finally the narrow band gap a-SiGe bottom cell. The vertical structure is finished with the deposition of a ZnO buffer layer and metal reflector in the back.

¹² Substrate and superstrate cells were illustrated in Figure 12.3. The substrate-type cells are also called *nip*-type cells, and superstrate-type cells are also called *pin*-type cells, corresponding to the sequence in which the layers are deposited.

12.5.3.1 Current matching

In a triple-junction cell, the three component cells are stacked monolithically. Since these component cells are connected in series to form a two-terminal device, the cell with minimum current density during operation will limit the total current of the triple-junction stack. Therefore, the current densities of each of the component cells need to be *matched* (made the same) at the maximum power point for each cell in sunlight. The short-circuit currents J_{SC} of the component cells are only a rough guide to this matching. For an a-Si/a-SiGe/a-SiGe triple-junction cell, the bottom a-SiGe cell usually has the lowest FF and the top a-Si cell usually has the highest FF . Therefore, the J_{SC} of the bottom cell needs to be slightly greater than the J_{SC} of the middle cell, which in turn needs to be slightly greater than the J_{SC} of the top cell. For an optimized triple-junction cell, the differences in J_{SC} between the bottom and the middle and between the middle and the top cells are each about 0.5–1 mA/cm². This is referred to as an intentional “mismatch” in the J_{SC} values designed to match the cells at the operating point. To obtain the highest stabilized solar cell efficiency, the triple cell needs to be designed, by adjusting the band gaps and thicknesses of the component cell i -layers, such that the component cell currents are matched at the maximum power point in the light-soaked state.

While adjusting for current matching, one needs to consider that the bottom cell benefits from the light enhancement from the back reflector, as can be seen from Figure 12.24, while the middle and top cells receive little benefit from the back reflector.

12.5.3.2 Tunnel junctions

Another area that needs attention in fabricating a multijunction solar cell are the *tunnel junctions* at the interfaces between adjacent *pin* cells. These interfaces lie between n -type and p -type layers, and one might think that they would have electrical properties like classic pn junction diodes. However, researchers take advantage of one of the special properties of a-Si material that was discussed in Section 12.2.6: dangling bonds are generated when doping is increased. Carriers that are trapped on defects on one side of the interface can move to traps on the other side simply by quantum mechanical tunneling. This process is sufficiently efficient that it “short-circuits” electrical transport involving the conduction band and valence band states [169]. For this reason, the doped layers at the tunnel junction, particularly the sublayers near the interface, are made with very high doping. The large density of dangling bonds permits the efficient recombination¹³ (by tunneling) of holes from the cell below and electrons from the cell above, as illustrated in Figure 12.25. This tunnel junction is reverse-biased under normal operation; it must generate negligible V_{OC} and have negligible resistance and optical absorption [169].

12.5.3.3 I - V measurement

In measuring the I - V performance of a multiple-junction, spectrum-splitting solar cell, researchers need to pay particular attention to the spectrum of the illuminating light

¹³ One can consider this as a neutralization process.

(see Chapter 16 for more detailed discussion). A triple-junction cell for which the *pin* component cells are current-matched under the standard AM1.5 global spectrum may show poor performance under a different light source, for example, a tungsten lamp. The triple-cell J_{SC} is usually close to the J_{SC} of the limiting component cell except when there is a large mismatch and the limiting cell has a very low fill factor. The V_{OC} of the triple cell is the sum of the V_{OC} of the component cells (and reduced by any photovoltages at the tunnel junctions). It should be noted here that the bottom component cell in a triple-stack generates only about one-third of the photocurrent that it would under full sunlight; therefore, its V_{OC} is slightly smaller (usually by ~ 20 mV) than when it is exposed to the full sunlight. The middle cell will have about half the current that it would under the full sunlight. The fill factor of the triple cell depends sensitively on the fill factor of the limiting component cell and on the current mismatch among the component cells. A large mismatch leads to a higher triple-cell FF , while on the other hand it also leads to a lower triple-cell current.

12.5.3.4 Quantum efficiency measurements in multijunction cells

In measuring the QE of a triple-junction solar cell, appropriate light bias and electrical bias need to be applied during the QE measurements ([170, 171] or Chapter 16). A direct QE measurement without these optical and electrical biases, just as one measures a single-junction cell, would yield a “ Λ ”-shaped curve, because a current can flow through the cell only if all of the component cells are illuminated simultaneously. When the QE of a specific component cell needs to be measured, say the middle cell, a DC bias light is illuminated on the cell through a filter that transmits only blue light and red light so that the top and bottom cells are illuminated. Under this condition, the middle cell current is limiting when the light through the monochromator is absorbed by the cell. Therefore, the current through the sample is that of the middle cell, that is, the AC photo current at the monochromatic light that is absorbed in the middle cell. This AC photocurrent is modulated by an optical chopper, and therefore can be easily detected using a lock-in amplifier.

The other two component cells can be measured in the same way except that different optical filters for the bias light need to be used. When the cells are measured without externally applied electrical voltage bias, the component cell being measured is actually under reverse bias, equal to the sum of the V_{OC} of the other two component cells. In this case, the QE curve would indicate the QE of the cell under reverse bias condition, which mostly is close to the QE under short-circuit condition when the component cell FF is high. To measure the QE under short-circuit current condition, electrical voltage needs to be externally applied to cancel out the voltage generated by the other component cells under the optical bias light. Figure 12.26 shows the QE curves of a triple-junction solar cell measured using this method [158]. The short-circuit current of component cells can be calculated by integrating the QE values with the AM1.5 light spectrum. The outer profile in Figure 12.26 is obtained by adding the three component cell QE curves. Comparing the QE curves in Figure 12.26 and Figure 12.24, the middle cell QE is roughly the same as the difference between curves (b) and (a), while the bottom cell QE is roughly the same as the difference between curves (e) and (b). The outer profile is roughly the same as curve (e) in Figure 12.24.

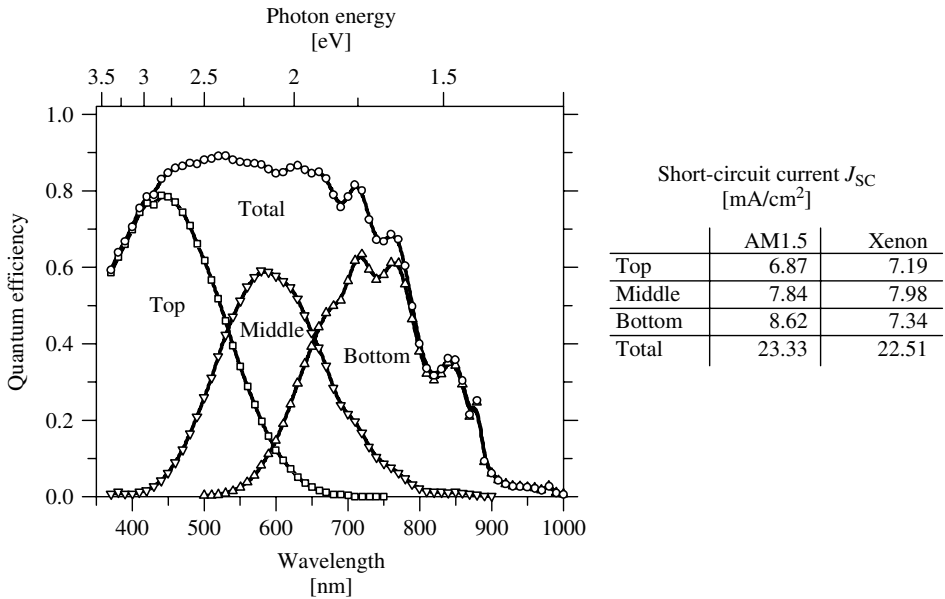


Figure 12.26 Quantum efficiency curves of component cells of a typical triple-junction solar cell. The table indicates the short-circuit current densities J_{SC} for the component cells measured for AM1.5 illumination and with a xenon illuminator [158]

12.5.3.5 Matching component cells in multijunction designs

In matching component cell currents in the triple cell design, researchers usually take the following steps. Take the triple cell in Figure 12.26 as an example. The design is largely dictated by the bottom a-SiGe component cell. If this component cell were fabricated on the back reflector as a stand-alone single-junction cell, it would have a short-circuit current around 23 mA/cm² and a QE curve similar to the one labeled “Total” in Figure 12.26. In order to achieve current matching in the triple cell, a stand-alone, single-junction version of the middle a-SiGe component cell (without a back reflector) needs to generate about two-third of the bottom cell’s current. The band gap and/or the thickness of the a-SiGe middle component cell’s i -layer are then adjusted to accomplish this. Finally, the top component cell’s thickness is adjusted to obtain one-third of the bottom cell’s current (again, without a back reflector). In this way, all three cells would have the same current when they are stacked in series.

In Figure 12.26, the long-wavelength behavior of the QE curves for each of the component cells is determined by the component cell’s i -layer thickness and band gap, and (for the bottom component cell) by the back reflector performance. However, the short-wavelength behaviors for the middle and bottom component cell’s QE curves are largely determined by the thicknesses and band gaps of the top and middle cells, respectively, since these component cells act as filters for the shorter wavelength (higher energy) photons. The short-wavelength behavior of QE for the top cell is sensitive to the absorption of ITO and top cell p -layer as well as the loss of electrons that are diffused back to the p -layer and get trapped.

Table 12.4 Efficiency of small-area solar cells fabricated in different laboratories

Structure	Initial η [%]	Stable η [%]	Organization	References
a-Si/a-SiGe/a-SiGe	15.2	13.0	United Solar	[8]
a-Si/a-SiGe/a-SiGe	11.7	11.0	Fuji	[157]
a-Si/a-SiGe/a-SiGe	12.5	10.7	U. Toledo	[158]
a-Si/a-SiGe/a-SiGe		10.2	Sharp	[159]
a-Si/a-SiGe	11.6	10.6	BP Solar	[160]
a-Si/a-SiGe		10.6	Sanyo	[161]
a-Si/ μ c-Si		12.0	U. Neuchatel	[162]
a-Si/ μ c-Si	13.0	11.5	Canon	[163]
a-Si/poly-Si/poly-Si	12.3	11.5	Kaneka	[164]
a-Si/a-SiGe/ μ c-Si	11.4	10.7	ECD	[165]
a-Si/a-SiGe		12.4	United Solar	[166]

12.5.3.6 High-efficiency multiple-junction solar cells

Table 12.4 above lists some properties of multiple-junction solar cells fabricated in selected laboratories around the world. The degradation of multiple-junction solar cells is usually in the range of 10 to 20%, while the degradation of single-junction solar cells is usually in the range of 20 to 40%. These percentages apply to the cell's properties after 1000 h of light soaking under 1 sun light intensity at 50°C, which is the standard protocol used for gauging light degradation today. The degradation of triple cells is smaller because (1) the *i*-layers are thinner and (2) each *i*-layer absorbs only one-third of the total current, therefore having less photogenerated recombination in the *i*-layer. As one can see from the table, the highest stabilized cell efficiency is 13.0% for a triple-junction device structure made at United Solar Systems Corp. Table 12.4 also includes the best solar cells made using μ c-Si as a component cell. The highest stable efficiency so far using a-Si/ μ c-Si tandem structure is 12% for a cell made at Univ. of Neuchatel using VHF plasma deposition.

12.5.4 Microcrystalline Silicon Solar Cells

Microcrystalline silicon (μ c-Si) has been studied extensively for three decades [172] and has been used for doped layers in a-Si solar cells for over 15 years [134, 173]. Because of the difficulties in passivating the defects located at the grain boundaries, μ c-Si was not actively considered as an intrinsic layer in the *pin* or *nip* type solar cells until 1992, when Faraji *et al.* [174] and Meier *et al.* [150] reported the fabrication of μ c-Si-based *pin* solar cells using VHF PECVD. Since then, μ c-Si and poly-Si solar cells have been fabricated by a number of research groups [163, 175–177].

A *QE* curve for such a μ c-Si-based cell was presented in Figure 12.24. One can see that the μ c-Si has a larger *QE* than the a-Si and a-SiGe cells at longer wavelengths (>850 nm). The total photocurrent generated from a μ c-Si cell has reached 26 mA/cm² [150, 176]. Therefore, such cells are suitable for use as the bottom cell of a multijunction cell with a-Si-based cells as the top cell. The advantages of using μ c-Si as the narrow band gap cell instead of a-SiGe are (1) the higher *QE* in the long-wavelength

region, (2) negligible light induced degradation, (3) reduced materials cost, since $\mu\text{c-Si}$ can be made using SiH_4 , which is a relatively low-cost gas compared to GeH_4 , and (4) $\mu\text{c-Si}$ cells can be made with high FF . On the other hand, the concerns associated with using $\mu\text{c-Si}$ compared to a-SiGe bottom cell are (1) $\mu\text{c-Si}$ cells require much thicker i -layers (several micrometers thick) to absorb the sunlight; this is an effect of the lower interband absorption coefficients in (indirect band gap) crystals compared to amorphous semiconductors, (2) the deposition rate for $\mu\text{c-Si}$ material is generally low, so that a much longer time is needed to complete the deposition of a thick $\mu\text{c-Si}$ layer than what is needed for an a-SiGe layer, and (3) $\mu\text{c-Si}$ solar cells have lower V_{OC} (around 0.53 V) than do a-SiGe cells yielding the same J_{SC} .

Beside VHF technique, $\mu\text{c-Si}$ has also been deposited using other high deposition rate methods such as HW CVD [178], GasJet/MW deposition [179], and high-power/high-pressure RF deposition [180]. A typical deposition rate for an a-SiGe i -layer is 3 Å/s; to complete a $\mu\text{c-Si}$ cell with comparable deposition time, one would need to deposit $\mu\text{c-Si}$ with at least ~ 20 to 30 Å/s deposition rate so that it would not be rate-limiting during production.

12.5.5 Micromorph and Other $\mu\text{c-Si}$ -based Multijunction Cells

Meier *et al.* [181] used an a-Si pin junction as the top component cell and a $\mu\text{c-Si}$ pin as the bottom component cell for a-Si/ $\mu\text{c-Si}$ tandem cells; they named these cells *Micromorph* devices. The 1.7 eV/1.1 eV band gaps for the top/bottom cell provide a nearly ideal band gap pair for tandem cells (see contour diagram in Figure 12.22 above).

In order for an a-Si/ $\mu\text{c-Si}$ tandem cell to have comparable performance as an a-Si/a-SiGe cell, the bottom cell $\mu\text{c-Si}$ must have at least 26 mA/cm² current density. Since $\mu\text{c-Si}$ has an indirect band gap, generating such a high current requires the $\mu\text{c-Si}$ layer to be several micrometers thick. In addition, advanced light enhancement schemes need to be used. In order to maintain current matching in a micromorph cell, the top a-Si component cell must generate 13 mA/cm² (i.e. half the current for a stand-alone $\mu\text{c-Si}$). In addition, this a-Si cell needs to be stable under light so that the tandem cell could be stable.

Two approaches were taken to accomplish this [182, 183]. First, the a-Si i -layer is made at a relatively higher temperature, so that there is a lower H concentration (and a reduced band gap, ~ 1.65 eV). Secondly, a semireflective layer was inserted at the tunnel junction between the top and the bottom cell. This semireflective layer permitted current matching (enhancing the top component cell current at the expense of the bottom cell). With these two approaches, 13 mA/cm² J_{SC} was obtained from the top cell with a 3000 Å thick a-Si layer. Innovative approaches need to be taken to further increase the current beyond the present level. With the micromorph tandem design, solar cells with 11 to 12% stable efficiency have been fabricated [163, 183].

One can also combine a-Si and $\mu\text{c-Si}$ cells to fabricate a-Si/ $\mu\text{c-Si}$ / $\mu\text{c-Si}$ triple cells. Such a design would relax the stringent requirement on the a-Si top cell due to current matching since it now only needs to generate one-third of the bottom cell current. However, the presently low V_{OC} of a $\mu\text{c-Si}$ cell militates against the triple-junction design.

Still another approach to a triple-junction cell design is to combine a 1.8 eV a-Si top cell, a 1.6 eV a-SiGe middle cell, and a 1.1 eV $\mu\text{c-Si}$ bottom cell [165]. Such a cell design would have the advantages of a thinner and more stable top cell than for a micromorph tandem cell, would have better long-wavelength collection, and would reduce consumption of (expensive) GeH_4 gas compared with an all-amorphous, a-Si/a-SiGe/a-SiGe triple-junction cell.

12.6 MODULE MANUFACTURING

Although the stabilized conversion efficiency of a-Si-based solar cells is presently lower than those of several other types of solar cells, a-Si-based PV products are highly attractive for terrestrial applications since they can be produced using low-cost manufacturing methods. The a-Si PV products are environmentally friendly. They are made mostly using silicon, which is abundant on earth. In addition, the a-Si PV products can be made lightweight, flexible, and radiation-resistant. These make them highly desirable for portable power applications as well as for space power applications. Furthermore, the fact that a-Si products have higher stabilized power output at higher temperature makes these products more desirable in warm weather environment.

During the past 10 years, there has been a rapid increase in the worldwide a-Si production. Presently in 2002, the total worldwide a-Si production capacity exceeds 85 MW/year, including about 30 MW at United Solar Systems Corp. (USA), 20 MW at Kaneka Corp. (Japan), 10 MW at BP Solar, Inc. (USA), 10 MW at Canon (Japan), 6 MW at Sanyo (Japan), 3 MW at EPV (USA), 2 MW at Sovlux (Russia), and several 1-MW plants in various companies in different parts of the world.

These production facilities can be roughly divided into two major categories: those with substrate-type a-Si PV products and those with superstrate-type a-Si PV products. To transform small-area R&D developments into any type of large-scale manufacturing, key issues including uniform deposition over large areas, process gas utilization, deposition rate, production throughput, process reproducibility, machine maintainability and serviceability, process automation, and production yield must be addressed.

For a large-scale production line, in-line processes have been used by all major manufacturers. In the following, we use the production process at United Solar as the example for the substrate-type process and that at BP Solar as the example for the superstrate-type process.

12.6.1 Continuous Roll-to-roll Manufacturing on Stainless Steel Substrates

The continuous, “roll-to-roll” a-Si PV manufacturing process was developed by Energy Conversion Devices, Inc. (ECD) and has been used by ECD’s PV joint ventures and partners (United Solar, Sovlux, and Canon) [184–186]. Roll-to-roll refers to the process whereby a “roll” of flexible SS is unrolled and fed into the manufacturing process, and then the SS is again “rolled up” after a manufacturing step has been completed. The production process can be separated into two distinct parts: the front-end coating process and the back-end module assembly process.

The front-end process consists of four continuous, roll-to-roll steps in separate machines: (1) substrate washing, (2) sputter deposition of the back reflector, (3) a-Si semiconductor deposition, and (4) ITO top electrode deposition. Rolls of magnetic SS web, typically 125 μm thick, 0.35 m wide, and 700 m long, are guided through these roll-to-roll machines by magnetic rollers. The roll is unwound from a modular “payoff” chamber on one side and wound up in a modular “take-up” chamber on the other side. Figure 12.27 is a photo of front-end facilities at an ECD designed 2-MW plant, operated by Sovlux, and showing all four roll-to-roll machines.

In the roll-to-roll washing machine, the SS web is guided through ultrasonic detergent cleaning stations with spinning brushes rubbing the surface, multiple deionized water rinse baths, and an infrared drying chamber. An oil-free, particle-free, clean SS roll is then wound up with protective interleaf.

The roll is then unloaded from the take-up chamber of the wash machine and loaded into the payoff chamber of the back-reflector sputter machine. In this machine, the SS web is pulled through several DC magnetron sputter deposition zones with metal targets (Al, Ag, or other alloys) for the reflective layer and ZnO targets for the deposition of ZnO buffer layer. The substrate is maintained at elevated temperature during sputtering so that the metal films develop a texture useful for optical enhancement [185, 187].

The roll is then loaded into the RF PECVD machine for the continuous roll-to-roll deposition of nine layers of semiconductors (*nip/nip/nip*) as well as all of the buffer layers on both sides of a-SiGe absorber layers. The deposition of the different layers occurs sequentially but in a single pass. Innovative “gas-gate” design allows the manufacturer to isolate the feedstock gases in different chambers and to prevent cross-contamination, while at the same time the web passes through the sequence of chambers continuously. The gas gate utilizes laminar gas flow to effectively isolate the gases in adjacent chambers.



Figure 12.27 A photograph of the Energy Conversion Devices, Inc. 2-MW plant showing all four front-end roll-to-roll machines for washing, back reflector sputter deposition, PECVD deposition (right-hand side) and TCO deposition [185]

After the semiconductor deposition, the roll is then loaded into the TCO deposition machine, which uses either reactive evaporation of indium in oxygen ambient or sputtering from an ITO target in an argon atmosphere. The thickness of the ITO is carefully monitored to achieve antireflection properties.

The four roll-to-roll steps are currently not integrated into one machine. This design reflects the different pressure ranges for the four machines: atmospheric pressure for the washing, a few mTorr for back-reflector sputtering, around 1 Torr for PECVD, and a few mTorr for TCO sputtering.

At this point, the SS roll is a giant solar cell, 700 m long, which needs to be converted into many smaller series connected cells to get higher voltage for the modules. The semiautomatic back-end process for cell interconnect and module assembly includes the following steps. The roll of TCO coated a-Si solar cells is first cut into slabs of selected sizes with a slab cutter. Etching paste is then applied to the edge of the slab and activated through a belt furnace to remove ITO around the perimeter of the slab and to define effective solar cell area. Selected small samples (coupons) are collected throughout the run for quality-assurance and quality-control (QA/QC) evaluation. The standard slabs then go through a shunt passivation process in an electrolyte bath to remove and isolate small shunts by converting the TCO at the shunting point into an insulator [188]. The grids, either carbon paste or copper wire coated with carbon paste, are then applied to the slab to complete a strip cell, which is a big cell that generates ~ 2.3 V voltage and ~ 2 A current. Different numbers of strip cells, depending on the module specification, are connected together in series with the grids/bus bar of one strip cell connected to SS substrate (the opposite electrode) of the neighboring strip cell. By-pass diodes are also installed at this step for the strip cell protection. The connected cells are then covered with ethylene vinyl acetate (EVA) and Tefzel, which are transparent encapsulating layers, and cured in an oven for appropriate time for lamination. This is then followed by selected module framing.

Despite the need for relatively labor-intensive module assembly process at the moment, the continuous roll-to-roll production of a-Si solar panels on SS substrate has a number of advantages. The product is lightweight and flexible. The front-end production process requires low maintenance and can be easily scaled up. The coated SS roll may be cut into slabs of various sizes to make different products. For example, small sizes are suitable as battery charger, and large sizes as metal roof shingles (more than 5 m long). A high production yield can be maintained. The disadvantage is the need for labor-intensive cutting, gridding, and interconnecting individual cells to create a module.

In the process at Iowa Thin Films, Inc., a flexible Kapton¹⁴ substrate is used. The cell interconnect is achieved by laser scribing, similar to the process at BP Solar for superstrate-type solar cells, as to be described below.

12.6.2 a-Si Module Production on Glass Superstrate

The manufacturing of a-Si solar panels on glass superstrates is being developed by several companies including BP Solar, Inc. (USA), Energy Photovoltaics, Inc. (USA), and

¹⁴ ® Registered trademark of the Dupont Corporation.

Phototronics Solartechnik GmbH (Germany) [189]. A typical process is that of BP Solar's 10-MW plant (TF1) in Toano, Virginia, (USA) [190].

The process begins with large sheets of "float" glass, 3 mm thick, with a typical size of 1 m by 0.5 m. A textured tin oxide TCO layer is deposited using an APCVD process either at the glass supplier's plant or at the PV plant. The substrate is edge-polished and cleaned before silver frits are applied as bus bars and cured in a belt furnace. This TCO layer is "scribed" by a laser into strips about 9 mm wide. The substrates are then loaded in the PECVD machine for the deposition of the six semiconductor layers for an a-Si/a-SiGe *pin/pin* tandem structure. The semiconductor deposition is followed by the deposition of a ZnO buffer layer. Another laser scribing is done at this point adjacent to the first scribe lines. This second scribing is done at a lower laser power so that, while the ZnO and a-Si layers are scribed, the underlying tin oxide layer remains intact. An aluminum layer is sputter-deposited as the back reflector and back contact. A third scribing of the Al adjacent to the second completes the interconnection of neighboring cells in series, as shown in Figure 12.28. A fourth, high-power laser scribing around the perimeter of the solar panel isolates the active area from the edges. The panel is then finished by bonding a second glass plate onto the cells with EVA. This second piece of glass is needed for encapsulation, which unfortunately adds weight and cost to the module.

12.6.3 Manufacturing Cost, Safety, and Other Issues

An important aspect of any manufacturing process is cost, which generally consists mostly of raw materials, labor, capital depreciation of the machines, and administration. The overall production cost per unit of product is reduced as the production volume goes up. At a high production volume, perhaps 100 peak megawatts/year, 100 MW_p/year, (under illumination yielding peak power production), the cost is expected to be lower than \$1/Wp. Currently, for a-Si modules intended for outdoor use for extended time, the major costs are the module framing, encapsulation, and the substrates (glass or SS). As an example, for the materials cost, the current breakdown at BP Solar's 10-MW plant is 33% for framing and packaging, 38% for TCO/glass, 17% for germane, 7% for encapsulation, and 5% for silane and other feedstocks [63].

Another important aspect with regard to a-Si PV manufacturing is the plant safety. Although there is no toxic material in the final product, the manufacturing processes do involve toxic and pyrophoric gasses such as germane, phosphine, trimethylboron, silane, hydrogen, and so on. Amorphous Si PV manufacturers, who have learned and borrowed

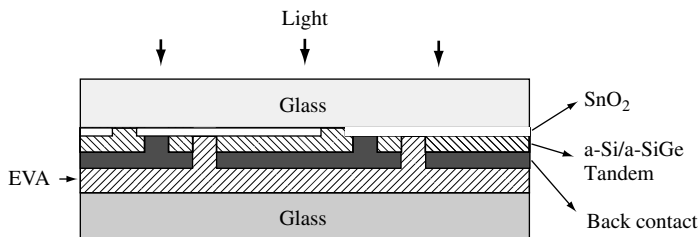


Figure 12.28 Cell interconnection of superstrate-type solar cells, used at BP Solar

heavily from the safety procedures developed by the integrated circuit industry, use a variety of methods to improve the safety of workers. Toxic gases are diluted in hydrogen or silane to 1 to 20%. Gas cylinders are installed outside the building or in fireproof gas cabinets. Toxic gas monitors are installed throughout the plants. Automatic gas isolation and operation shutdowns are implemented. These, among other safety procedures, ensure safe operations in these plants.

The solar conversion efficiency of production modules is generally lower than the efficiency of the research and development (R&D) scale, small-area solar cells since production processes are more restrained by cost reductions. The differences in efficiency are mostly from the TCO performance, semiconductor material quality, deposition uniformity, encapsulation loss, bus bar shadow loss and electrical loss, and small shunts. Rech *et al.* provided a detailed analysis in the efficiency differences between R&D and manufacturing at Phototronics, Germany [191].

12.6.4 Module Performance

Two aspects of PV modules are generally evaluated: maximum solar conversion efficiency and environmental stability. Table 12.5 lists PV modules produced by selected organizations around the world; the table separately lists modules made in R&D type machines (area about 0.1 m²) and large-area modules (area 0.4 m² or greater), mostly produced from production lines. Presently in 2002, large-area modules, with approximately 8% stable efficiency, are manufactured at United Solar and BP Solar and are commercially available in large quantities.

Photovoltaic modules are also evaluated through various environmental tests, as listed in UL, IEC, and IEEE standard testing procedures (see Chapter 16 for more on module testing). These tests generally include thermal cycles between -40 to 90°C ; humidity freeze cycles between -40 to 85°C at 85% humidity; hail impact; wet hi-pot

Table 12.5 Stabilized efficiency of a-Si PV modules manufactured by various companies

Structure	Stable η [%]	Size [m ²]	Company	Reference
<i>R&D modules</i>				
a-Si/a-SiGe/a-SiGe	10.5	0.09	United Solar	[186]
a-Si/a-SiGe	9.1	0.08	BP Solar	[160]
a-Si/a-SiGe	9.5	0.12	Sanyo	[192]
<i>Large-area modules</i>				
a-Si/a-SiGe	9.3	0.52	Sanyo	[193]
a-Si/a-SiGe/a-SiGe	9.0	0.32	Fuji	[160]
a-Si/a-SiGe	8.1	0.36	BP Solar	
a-Si/a-SiGe/a-SiGe	7.9	0.45	United Solar	
a-Si/a-Si/a-SiGe	7.8	0.39	ECD	[185]
a-Si/poly-Si	10.0	0.37	Kaneka	[194]

test and light soaking. PV modules that are sold for commercial use have generally been qualified by these testing programs.

12.7 CONCLUSIONS AND FUTURE PROJECTIONS

12.7.1 Status and Competitiveness of a-Si Photovoltaics

Over the last quarter of a century, significant progress has been made in the understanding of properties and of deposition processes for a-Si-based materials and solar cells. There have been impressive achievements both in increasing the conversion efficiency of solar cells and in reducing the cost of fabrication. In 1997, a-Si-based solar cells with 15.2% initial efficiency and 13% stable efficiency were demonstrated [8]. The manufacturing volume of a-Si solar modules has increased more than tenfold over the past 10 years, and capacity is presently more than 85 MW_p/year. There are now seven a-Si PV manufacturers with production capacity of 2 MW_p/year or more.

In the pipeline for the future, significant progress has been made in the development of rapid deposition processes ($>5 \text{ \AA/s}$) that achieve essentially the same quality as the present slow processes, as discussed in Section 12.3. As rapid deposition and high gas utilization processes are incorporated into production, further cost reduction will be achieved.

Additionally, the use of microcrystalline silicon as the narrow band gap absorber layer in an a-Si-based tandem solar cell has been demonstrated, and cells exceeding 12% conversion efficiency (stabilized) have been produced in different labs. The cells incorporating $\mu\text{-c-Si}$ show superior light stability over extended light soaking.

Amorphous Si-based PV technology is unique compared with other PV technologies. Amorphous Si absorbs sunlight more strongly than c-Si and poly-Si because it is amorphous; the selection rules that weaken absorption in c-Si (an “indirect band gap” semiconductor) do not apply to a-Si. A rather thin layer of a-Si is sufficient to absorb sunlight. Amorphous Si can be made at a low temperature on inexpensive substrates. The product is made through a low-cost process. The energy payback time (the time required for an a-Si module to generate the energy used in its production) was estimated as one to two years in 1989, and has probably shrunk substantially since then [194]. One expects that the cost will continue to decline as the production volume is increased. When deposited on selected substrates, the product can be made lightweight and flexible, which is important for many applications. The output power of a-Si PV products also has a positive temperature coefficient: at higher ambient temperature, for example, in areas with more sunshine, the efficiency is higher.

Compared with other types of thin-film PV technologies, such as CdTe and copper-indium-diselenide (CIS)-based PV technologies that have demonstrated higher efficiency in small-area R&D type cells, a-Si photovoltaics looks attractive because (1) it has been developed for approximately 20 years and the production process is more mature and proven and (2) the product does not contain any hazardous materials such as Cadmium as in CdTe photovoltaics or a large amount of expensive metal such as indium as in CIS-based photovoltaics. The materials in amorphous silicon-based cells originate in raw materials that are abundant on earth.

12.7.2 Critical Issues for Further Enhancement and Future Potential

To increase application of a-Si-based PV significantly beyond today's level, the following issues are critical and must be addressed.

1. Light-induced degradation must be better understood. Approaches for reducing or controlling the degradation need to be further developed. At this moment, there are many engineering compromises in the device design, such as the use of thin *i*-layers to limit the degradation. If the materials can be made more stable under light, these compromises can be relaxed and the device can be made with much higher efficiency.
2. As the gross defects associated with light soaking are minimized, we shall need to explore improvements in the drift mobility of holes.
3. We need to improve a-SiGe so that narrower band gap materials can be incorporated into cells and more of the infrared region of the solar spectrum can be exploited.
4. Faster deposition processes need to be developed that (at least) preserve the conversion efficiencies achieved by present processes. This is critical for low-cost and high-throughput manufacturing. In addition, these high-rate processes must also achieve high gas utilization.
5. Microcrystalline Si-based solar cells need to be fully explored as alternative, narrow band gap component cells in tandem or triple-junction cells. We expect that rather fast, $>20 \text{ \AA/s}$, deposition processes will be required. The device physics of $\mu\text{c-Si}$ -based solar cells, especially the possibilities for improving the open-circuit voltage, need to be better understood.
6. Module design needs to be further improved and the costs associated with framing and encapsulation need to be further reduced. At the same time the durability of modules in standard environmental tests must be preserved or improved.
7. We need to find new applications for a-Si PV products in all of its present markets, including building-integrated PV, space power, and consumer electronics as well as grid-connected, large-scale power generation.

As these critical issues are successfully addressed, we expect that a-Si-based solar cells will become more inexpensive, that there will be explosive increases in the volume of production and widespread expansion in the market. Amorphous silicon-based cells will become an environmentally friendly, inexpensive, and a ubiquitous source of electrical power for our life on Earth!

12.8 ACKNOWLEDGMENTS

This work was supported by the Thin Film Photovoltaics Partnership of the US National Renewable Energy Laboratory. We thank Rana Biswas (Iowa State University), Nerio Cereghetti (LEEE), Gautam Ganguly (BP Solar, Inc.), Subhendu Guha (United Solar Systems Corp.), Scott Jones (Energy Conversion Devices), Stan Ovshinsky (Energy Conversion Devices), Bolko von Roedern (National Renewable Energy Laboratory), Chris Wronski (Pennsylvania State University), and Jeff Yang (United Solar Systems Corp.) for their generous help in writing this article.

REFERENCES

1. Williams E, *The Physics and Technology of Xerographic Processes*, Wiley, New York, NY (1984).
2. Mort J, *The Anatomy of Xerography: Its Invention and Evolution*, McFarland, Jefferson, NC (1989).
3. Chittick R, Sterling H, in Adler D, Fritzsche H, Eds, *Tetrahedrally Bonded Amorphous Semiconductors*, pp. 1–11, Plenum Press, New York, NY (1985).
4. Spear W, LeComber P, *Solid State Commun.* **17**, 1193 (1975).
5. Carlson D, Wronski C, *Appl. Phys. Lett.* **28**, 671 (1976).
6. Perlin J, *Space to Earth: The Story of Solar Electricity*, aatec Publications, Ann Arbor (1999).
7. Wronski C, Carlson D, in Archer M, Hill R, Eds, *Clean Electricity from Photovoltaics*, World Scientific, Singapore (2001).
8. Yang J, Banerjee A, Guha S, *Appl. Phys. Lett.* **70**, 2977 (1997).
9. Fritzsche H, *Mater. Res. Soc. Symp. Proc.* **609**, A17.1.1–12 (2001).
10. Vaněček M, Poruba A, Remeš Z, Beck N, Nesládek M, *J. Non-Cryst. Solids* **227–230**, 967 (1998).
11. The figure was calculated based on the hemispherical irradiance (37° south facing) American Society for Testing and Materials (ASTM) Table G159-98 Standard Tables for References Solar Spectral Irradiance at Air Mass 1.5: Direct Normal and Hemispherical for a 37° Tilted Surface.
12. Near room temperature, a-Si:H has a “quantum efficiency” of essentially 1.00 for generating photocarriers when a photon is absorbed. Carasco F, Spear W, *Philos. Mag. B* **47**, 495 (1983). This ideal value is rather surprising. Many other non-crystalline materials have “geminate recombination” of the electron and hole immediately after their generation, which would of course lead to a loss of conversion efficiency; see ref. 13.
13. Schiff E, *J. Non-Cryst. Solids* **190**, 1 (1995).
14. Guha S, in Street R, Ed, *Technology and Applications of Amorphous Silicon*, 252–305, Springer, Berlin (1999). Figure 6.10 of this paper is a valuable compilation of power measurements for varying cell thicknesses and light-soaking histories.
15. Guha S, Yang J, Banerjee A, Glatfelter T, Hoffman K, Xu X, *Technical Digest – 7th International Photovoltaic Science and Engineering Conference (PVSEC-7)*, 43 (Nagoya, Japan, 1993).
16. Staebler D, Wronski C, *Appl. Phys. Lett.* **31**, 292 (1977).
17. Shugar D, *Proc. 24th Photovoltaic Specialists Conference*, 670, IEEE (1994).
18. Measurements furnished through the courtesy of N. Cereghetti, Laboratory of Energy, Ecology and Economy (LEEE), Scuola Universitaria Professionale della Svizzera Italiana. These data apply to the 0.5 kW array, and are described in more detail by Cereghetti N, Chiamese D, Rezzonico S, Travaglini G, *Proceedings of the 16th European Photovoltaic Solar Energy Conference*, James & James, London (2001).
19. Emery K, Burdick J, Calyem Y, Dunlavy D, Field H, Kroposki B, Moriarty T, Ottoson L, Rummel S, Strand T, Wanlass M, *Proc. 25th Photovoltaic Specialists Conference*, 1275, IEEE (1996).
20. Kameda M, Sakai S, Isomura M, Sayama K, Hishikawa Y, Matsumi S, Haku H, Wakisaka K, Tanaka K, Kiyama S, Tsuda S, Nakano S, *Proc. 25th Photovoltaic Specialists Conference*, 1049, IEEE (1996).
21. del Cueto J, von Roedern B, *Prog. Photovoltaics* **7**, 101 (1999).
22. Carlson D, Lin G, Ganguly G, *Proc. 28th Photovoltaic Specialists Conference*, 707, IEEE (2000).
23. Street R, *Hydrogenated Amorphous Silicon*, Cambridge University Press, Cambridge (1991).
24. Phillips J, *J. Non-Cryst. Solids* **34**, 153 (1979).
25. Boolchand P, Thorpe M, *Phys. Rev. B* **50**, 10366 (1994).

26. Reimer J, Petrich M, in Fritzsche H, Ed, *Amorphous Silicon and Related Materials*, Vol. A, 3–27, World Scientific, Singapore (1989).
27. Zhao Y, Zhang D, Kong G, Pan G, Liao X, *Phys. Rev. Lett.* **74**, 558 (1995).
28. Santos P, Johnson N, Street R, *Phys. Rev. Lett.* **67**, 2686 (1991).
29. Beyer W, Herion J, Wagner H, Zastrow U, *Philos. Mag. B* **63**, 269 (1991).
30. Figure courtesy of R. Biswas; for information on the calculations, see Biswas R, Li Y, *Phys. Rev. Lett.* **82**, 2512 (1999).
31. Jackson W, Tsai C, Thompson R, *Phys. Rev. Lett.* **64**, 56 (1990).
32. Zafar S, Schiff E, *Phys. Rev. Lett.* **66**, 1493 (1991).
33. The assignment of the D-center observed in electron paramagnetic resonance measurements with a dangling bond has been challenged in favor of “floating bonds” (Stathis J, Pantelides S, *Phys. Rev. B* **37**, 6579–6582 (1988)).
34. Park H, Liu J, Wagner S, *Appl. Phys. Lett.* **55**, 2658 (1989).
35. See the review of Fritzsche H, *Annu. Rev. Mater. Res.* **31**, 47 (2001).
36. Branz H, *Phys. Rev. B* **59**, 5498 (1999).
37. Ley L, *J. Non-Cryst. Solids* **114**, 238 (1989).
38. Jackson W, Kelso S, Tsai C, Allen J, Oh S, *Phys. Rev. B* **31**, 5187 (1985).
39. Cody G, Tiedje T, Abeles B, Brooks B, Goldstein Y, *Phys. Rev. Lett.* **47**, 1480 (1981).
40. Tiedje T, in Joannopoulos J, Lucovsky G, Eds, *Hydrogenated Amorphous Silicon II*, 261–300, Springer-Verlag, New York (1984).
41. Gu Q, Wang Q, Schiff E, Li Y, Malone C, *J. Appl. Phys.* **76**, 2310 (1994).
42. Wang Q, Antoniadis H, Schiff E, Guha S, *Phys. Rev. B* **47**, 9435 (1993).
43. Gu Q, Schiff E, Chevrier J, Equer B, *Phys. Rev. B* **52**, 5695 (1995).
44. Mott N, *Conduction in Non-Crystalline Solids*, Oxford University Press, Oxford (1987).
45. Tauc J, in Abeles F, Ed, *Optical Properties of Solids*, 277–313, North Holland, Amsterdam (1972).
46. Chen I, Wronski C, *J. Non-Cryst. Solids* **190**, 58 (1995).
47. Jackson W, Amer N, *Phys. Rev. B* **25**, 5559 (1982).
48. Antoniadis H, Schiff E, *Phys. Rev. B* **46**, 9482–9492 (1992).
49. Lee J, Schiff E, *Phys. Rev. Lett.* **68**, 2972 (1992).
50. Han D, Melcher D, Schiff E, Silver M, *Phys. Rev. B* **48**, 8658 (1993).
51. Hama S, Okamoto H, Hamakawa Y, Matsubara T, *J. Non-Cryst. Solids* **59–60**, 333 (1983).
52. Guha S, Payson J, Agarwal S, Ovshinsky S, *J. Non-Cryst. Solids* **97–98**, 1455 (1987).
53. Middya A, Ray S, Jones S, Williamson D, *J. Appl. Phys.* **78**, 4966 (1995).
54. Stutzmann M, Street R, Tsai C, Boyce J, Ready S, *J. Appl. Phys.* **66**, 569 (1989).
55. Li Y, *Proc. Materials Research Society Symp.*, **297**, 803–814 (1994).
56. Arya R, Catalano A, Oswald R, *Appl. Phys. Lett.* **49**, 1089 (1986).
57. Tsukada T, in Street R, Ed, *Technology and Applications of Amorphous Silicon*, 7–93, Springer, Berlin, Germany (2000).
58. Chittick R, Alexander J, Sterling H, *J. Electrochem. Soc.* **116**, 77–81 (1969).
59. Spear W, LeComber P, *J. Non-Cryst. Solids* **8–10**, 727–738 (1972).
60. Chapman B, *Glow Discharge Processes*, John Wiley & Sons, New York (1980).
61. Luft W, Tsuo Y, *Hydrogenated Amorphous Silicon Alloy Deposition Processes*, Marcel Dekker, New York (1993).
62. Guha S, Yang J, Banerjee A, Glatfelter T, Hoffman K, Ovshinsky S, Izu M, Ovshinsky H, Deng X, *Mater. Res. Soc. Symp. Proc.* **336**, 645 (1994).
63. Arya R, Carlson D, *Prog. Photovoltaics* **10**, 69–76 (2002).
64. Carlson D, US Patent 4,317,844 (1982).
65. Curtins H, Wyrsh N, Shah A, *Electron. Lett.* **23**, 228–230 (1987).
66. Chatham H, Bhat P, Benson A, Matovich C, *J. Non-Cryst. Solids* **115**, 201–203 (1989).
67. Saito K, Sano M, Matsuyama J, Higashikawa M, Ogawa K, Kajita I, *Tech. Digest PVSEC-9*, 579 (1996).

68. Matsumura H, *Jpn. J. Appl. Phys.* **25**, L949–L951 (1986).
69. Mahan A, Carapella J, Nelson B, Crandall R, Balberg I, *J. Appl. Phys.* **69**, 6728–6730 (1991).
70. Konagai M, Kim W, Tasaki H, Hallerdt M, Takahashi K, *AIP Conf. Proc.* **157**, 142–149 (1987).
71. Rocheleau R, Hegedus S, Buchanan W, Jackson S, *Appl. Phys. Lett.* **51**, 133–135 (1987).
72. Paul W, Lewis A, Connel G, Moustakas T, *Solid State Commun.* **20**, 969–972 (1976).
73. Moustakas T, Wronski C, Tiedje T, *Appl. Phys. Lett.* **39**, 721–723 (1981).
74. Knights J, *Mater. Res. Soc. Symp. Proc.* **38**, 372 (1985).
75. Ueda M, Imura T, Osaka Y, *Proc. 10th Symp. on Ion Sources and Ion-Assisted Technology* (1986).
76. Deng X, Narasimhan K, Evans J, Izu M, Ovshinsky S, *Proc. 1st World Conf. on Photovoltaic Energy Conversion*, 678 (1994).
77. Yang J, Xu X, Banerjee A, Guha S, *Proc. 25th Photovoltaic Specialists Conference*, 1041, IEEE (1996).
78. Cherepin V, *Secondary Ion Mass Spectroscopy of Solid Surfaces*, VNW Science Press, Utrecht (1987).
79. Kampas F, *J. Appl. Phys.* **54**, 2276–2280 (1983).
80. Jasinski, J, Whittaker, E, Bjorklunk G, Dreyfus R, Estes R, Walkup R, *Appl. Phys. Lett.* **44**, 1155–1157 (1984).
81. Robertson R, Gallagher A, *J. Chem. Phys.* **85**, 3623–3630 (1986).
82. Gallagher A, *J. Appl. Phys.* **63**, 2406–2413 (1988).
83. Shah A, Dutta J, Wyrsh N, Prasad K, Curtins H, Finger F, Howling A, Hollenstein C, *Mater. Res. Soc. Symp. Proc.* **258**, 15 (1992).
84. Heintze M, Zedlitz R, Bauer G, *Mater. Res. Soc. Symp. Proc.* **297**, 49–54 (1993).
85. Deng X, Jones S, Liu T, Izu M, Ovshinsky S, *Proc. 26th Photovoltaic Specialists Conference*, 591, IEEE (1997).
86. Ito N, Kondo M, Matsuda A, *Proc. 28th Photovoltaic Specialists Conference*, 900 (2000).
87. Kato I, Wakana S, Hara S, Kezuka H, *Jpn. J. Appl. Phys.* **21**, L470 (1982).
88. Huges S, Johncock A, Ovshinsky S, *J. Non-Cryst. Solids* **77–78**, 809 (1985).
89. Watanabe T, Azuma K, Nakatani M, Suzuki K, Sonobe T, Shimada T, *Jpn. J. Appl. Phys.* **25**, 1805 (1986).
90. Guha S, Xu X, Yang J, Banerjee A, *Appl. Phys. Lett.* **66**, 595–597 (1995).
91. Saito K, Sano M, Ogawa K, Kajita I, *J. Non-Cryst. Solids* **164–166**, 689 (1993).
92. Saito K, Sano M, Matsuyama J, Higasaki M, Ogawa K, Kajita I, *Tech. Digest PVSEC-9*, 579 (1996).
93. Wiesmann H, Ghosh A, McMahon T, Strongin M, *J. Appl. Phys.* **50**, 3752 (1979).
94. Wang Q *et al.*, *Proc. 29th Photovoltaic Specialists Conference*, 1222–1225, IEEE (2002).
95. Wang Q, Iwaniczko E, Yang J, Lord K, Guha S, Wang K, Han D, *J. Non-Cryst. Solids* **299–302**, 2–8 (2002).
96. Mahan A, Xu Y, Nelson B, Crandall R, Cohen J, Palinginis K, Gallagher A, *Appl. Phys. Lett.* **78**, 3788 (2001).
97. Povolny H, Deng X, to be published in *Thin Solid Films* (2003).
98. Morrison S, Madan A, *Proc. 28th Photovoltaic Specialists Conference*, 837, IEEE (2000).
99. Moustakas T, Maruska H, Friedman R, *J. Appl. Phys.* **58**, 983–986 (1985).
100. Abelson J, Doyle J, Mandrell L, Maley N, *Mater. Res. Soc. Symp. Proc.* **268**, 83–94 (1992).
101. Miller D, Lutz H, Weismann H, Rock E, Ghosh A, Ramamoorthy S, Strongin M, *J. Appl. Phys.* **49**, 6192, 6193 (1978).
102. Shimizu T, Kumeda M, Morimoto A, Tsujimura Y, *Mater. Res. Soc. Symp. Proc.* **70**, 311–318 (1986).
103. Hanna J, Kamo A, Azuma M, Shibata N, Shirai H, Shimizu I, *Mater. Res. Soc. Symp. Proc.* Vol. 118, 79–84 (1988).
104. Parsons G, Tsu D, Lucovsky G, *J. Vac. Sci. Technol.*, A **6**, 1912–1916 (1988).

105. Sakamoto Y, *Jpn. J. Appl. Phys.* **16**, 1993–1998 (1977).
106. Dalal V, Maxson T, Girvan R, Haroon S, *Mater. Res. Soc. Symp. Proc.* **467**, 813–817 (1997).
107. Hanabusa M, Suzuki M, *Appl. Phys. Lett.* **39**, 431, 432 (1981).
108. Ovshinsky S, Deng X, Young R, US Patent 5,231,047 (1993).
109. Jones S, Crucet R, Deng X, Izu M, *Mater. Res. Soc. Symp. Proc.* **609**, A4.5 (2000).
110. Guha S, Narasimhan K, Pietruszko S, *J. Appl. Phys.* **52**, 859 (1981).
111. Tanaka K, Matsuda A, *Mater. Sci. Rep.* **2**, 139–184 (1987).
112. Yang J, Lord K, Guha S, Ovshinsky S, *Mater. Res. Soc. Symp. Proc.* **609**, A15.4 (2000).
113. Yang J, Xu X, Guha S, *Mater. Res. Soc. Symp. Proc.* **336**, 687–692 (1994).
114. Yang L, Chen L, *Mater. Res. Soc. Symp. Proc.* **336**, 669–674 (1994).
115. Ferlauto A, Koval R, Wronski C, Collins R, *Appl. Phys. Lett.* **80**, 2666 (2002).
116. Yang J, Banerjee A, Lord K, Guha S, *Proc. 28th Photovoltaic Specialists Conference*, 742, IEEE (2000).
117. Deng X, *Record of the NREL-EPRI Amorphous Silicon Guidance Team Review Meeting* (Feb. 25–26, 2002).
118. Deng X, *Development of High, Stable-Efficiency Triple-Junction a-Si Alloy Solar Cells*, Annual Subcontract Report, Submitted to NREL, NREL/TP-411-20687, Feb. 1996.
119. Ovshinsky S, Guha S, Yang C, Deng X, Jones S, US Patent 8,766,219 (1996).
120. Liao X, Wang W, Deng X, *Proc. 29th Photovoltaic Specialists Conference*, 1234–1237, IEEE (2002).
121. Koval R, Chen C, Gerreira G, Ferlauto A, Pearce J, Rovira P, Collins R, Wronski C, *Proc. 29th Photovoltaic Specialists Conference*, 1090–1093 (2002).
122. AMPS-1D is a copyright of Pennsylvania State University. Zhu H, Fonash S, *Symp. Proc.*, Vol. 507, 395–402 (1998).
123. Schropp R, Zeman M, *Amorphous and Microcrystalline Silicon Solar Cells: Modeling Materials, and Device Technology*, Kluwer, Boston, MA (1998).
124. Welcome, expert. The electronic characteristics of a-Si:H used in the modeling in this chapter include only bandtail states – and not defects. The parameters for a-Si:H are published in Jiang L, Rane S, Schiff E, Wang Q, Yuan Q, *Symp. Proc.*, Vol. 609, A18.3.1–A18.3.11 (2001).
125. $K = \{\sin(\alpha\pi)\}/\{\alpha(1 - \alpha)\pi\}$.
126. Scher H, Shlesinger M, Bendler J, *Phys. Today* **44**, 26 (1991).
127. Crandall R, *J. Appl. Phys.* **54**, 7176 (1983).
128. Hegedus S, *Prog. Photovoltaics* **5**, 151 (1997).
129. Crandall R, Schiff E, in Ullal H, Witt C, Eds, *13th NREL Photovoltaics Program Review, Conf. Proc.*, Vol. 353, 101–106, American Institute of Physics, Woodbury (1996).
130. Pearce J, Koval R, Ferlauto A, Collins R, Wronski C, Yang J, Guha S, *Appl. Phys. Lett.* **77**, 19 (2000).
131. Rose A, *Photoconductivity and Allied Phenomena*, Robert E. Krieger, Huntington, NY (1978).
132. Fonash S, *Solar Cell Device Physics*, John Wiley & Sons, New York, NY (1981).
133. Tiedje T, *Appl. Phys. Lett.* **40**, 627 (1982).
134. Guha S, Yang J, Nath P, Hack M, *Appl. Phys. Lett.* **49**, 218 (1986).
135. Arya R, Catalano A, Oswald R, *Appl. Phys. Lett.* **49**, 1089 (1986).
136. Hegedus S, Rocheleau R, Tullman R, Albright D, Saxena N, Buchanan W, Schubert K, and Dozler R, *Conference Record of the 20th IEEE Photovoltaic Specialists Conference*, 129–134, IEEE (1988).
137. Hegedus S, Rocheleau R, Tullman R, Albright D, Saxena N, Buchanan W, Schubert K, Dozler R, *J. Appl. Phys.* **67**, 3494 (1990).
138. Hegedus S, Deng X, *Conference Record of the 25th IEEE Photovoltaic Specialists Conference*, 1061–1064, IEEE (1996).
139. Yablonoitch E, *J. Opt. Soc. Am.* **72**, 899 (1982).
140. Deckman H, Wronski C, Witzke H, Yablonoitch E, *Appl. Phys. Lett.* **42**, 968 (1983).

141. Hegedus S, Buchanan W, Liu X, Gordon R, *Conference Record of the 25th IEEE Photovoltaic Specialists Conference*, 1129–1132, IEEE (1996).
142. Lechner P, Geyer R, Schade H, Rech B, Müller J, *Conference Record of the 28th IEEE Photovoltaic Specialists Conference*, 861–864, IEEE (2000).
143. Banerjee A, Guha S, *J. Appl. Phys.* **69**, 1030 (1991).
144. Sze S, *Physics of Semiconductor Devices*, 798, John Wiley & Sons, New York, NY (1981)
145. Mitchell K, *Tech. Digest 1st International Photovoltaic Solar Energy Conversion*, 691–694 (1984).
146. Kuwano Y *et al.*, *Conference Record of the 16th IEEE Photovoltaic Specialists Conference*, 1338–1343, IEEE (1982).
147. The thickness of i-layers are in the range of 100 nm to 200 nm, while for single junction a-Si solar cells the i-layer needs to be much thicker to get high efficiency.
148. Hack M, Shur M, *J. Appl. Phys.* **59**, 2222 (1986).
149. Agarwal P, Povolny H, Han S, Deng X, *J. Non-Cryst. Solids* **299-302**, 1213–1218 (2002).
150. Meier J, Fluckiger R, Keppner H, Shah A, *Appl. Phys. Lett.* **65**, 860–862 (1994).
151. Yang L, Chen L, Catalano A, *Mater. Res. Soc. Symp. Proc.* **219**, 259–264 (1991).
152. Guha S, Yang J, Pawlikiewicz A, Glatfelter T, Ross R, Ovshinsky S, *Appl. Phys. Lett.* **54**, 2330 (1989).
153. Zimmer J, Stiebig H, Wagner H, *J. Appl. Phys.* **84**, 611–617 (1998).
154. Yang J, Banerjee A, Glatfelter T, Sugiyama S, Guha S, *Conference Record of the 26th IEEE Photovoltaic Specialists Conference*, 563–568, IEEE (1997).
155. Hamakawa Y, Tawada Y, Nishimura K, Tsuge K, Kondo M, Fujimoto K, Nonomura S, Okamoto H, *Conference Record of the 16th IEEE Photovoltaic Specialists Conference*, 679–684, IEEE (1982).
156. Guha S, in Street R, Ed, *Technology and Applications of Amorphous Silicon*, Springer-Verlag, Berlin, Heidelberg, New York (2000). (See Table 6.9 in the reference.)
157. Yoshida T, Tabuchi K, Takano A, Tanda M, Sasaki T, Sato H, Fijikake S, Ichikawa Y, Harashima K, *Conference Record of the 28th IEEE Photovoltaic Specialists Conference*, 762–765 (2000).
158. Wang W, Povolny H, Du W, Liao X, Deng X, *Conference Record of the 29th IEEE Photovoltaic Specialists Conference*, 1082–1085 (2002).
159. Nomoto K, Saitoh H, Chida A, Sannomiya H, Itoh M, Yamamoto Y, *Intl. Tech. Digest PVSEC-7*, 275 (1993).
160. Arya R, Oswald R, Li Y, Maley N, Jansen K, Yang L, Chen L, Willing F, Bennett M, Morris J, Carlson D, *Proc. 1st World Conf. Photovoltaic Solar Energy Conversion*, 394 (1994).
161. Hishikawa Y, Ninomiya K, Maryyama E, Kuroda S, Terakawa A, Sayama K, Tarui H, Sasaki M, Tsuda S, Nakano S, *Proc. 1st World Conf. Photovoltaic Solar Energy Conversion*, 386–393 (1994).
162. Meier J, Keppner H, Dubail S, Droll U, Torres P, Pernet P, Ziegler Y, Selvan J, Cuperus J, Fischer D, Shah A, *Mater. Res. Soc. Symp. Proc.* **507**, 139–144 (1998).
163. Saito K, Sano M, Matuda K, Kondo Takaharu, Nishimoto T, Ogawa K, Kajita I, *Proc. 2nd World Conf. Photovoltaic Solar Energy Conversion*, 351–354 (1998).
164. Yamamoto K, Yoshimi M, Suzuki T, Okamoto Y, Tawada Y, Nakajima A, *Conference Record of the 26th IEEE Photovoltaic Specialists Conference*, 575–580 (1997).
165. Jones S, Cruet R, Capangpangan R, Izu M, Banerjee A, *Mater. Res. Soc. Symp. Proc.* **664**, A15.1 (2001).
166. Yang J, Banerjee A, Lord K, Guha S, *Proc. 2nd World Conf. on Photovoltaic Energy Conversion*, 387–390 (1998).
167. Iida H, Shiba N, Mishuka T, Karasawa H, Ito A, Yamanaka M, Hayashi Y, *IEEE Electron Device Lett.* **EDL-4**, 157–159 (1983).
168. Gordon R, Proscia J, Ellis F, Delahoy A, *Sol. Energy Mater.* **18**, 263–281 (1989).
169. Hegedus S, Kampas F, Xi J, *Appl. Phys. Lett.* **67**, 813 (1995).

170. Burdick J, Glatfelter T, *Sol. Cells* **18**, 310–314 (1986).
171. Mueller R, *Sol. Energy Mater. Sol. Cells* **30**, 37–45 (1993).
172. Veprek S, Marecek V, *Solid-State Electron.* **11**, 683 (1968).
173. Hattori Y, Kruangam D, Toyama T, Okamoto H, Hamakawa Y, *Tech. Digest PVSEC-3*, 171 (1987).
174. Faraji M, Gokhale S, Ghoudhari S, Takwake M, Ghaisas S, *Appl. Phys. Lett.* **60**, 3289–3291 (1992).
175. Meier J, Kroll U, Dubail S, Golay S, Fay S, Dubail J, Shah A, *Conference Record of the 28th IEEE Photovoltaic Specialists Conference*, 746–749 (2000).
176. Yamamoto K, *Mater. Res. Soc. Symp. Proc.* **507**, 131–138 (1998).
177. Repmann T, Appenzeller W, Roschek T, Rech B, Wagner H, *Conference Record of the 28th IEEE Photovoltaic Specialists Conference*, 912–915 (2000).
178. Rath J, Galetto M, van der Werf C, Feenstra K, Meiling H, van Cleef M, Schropp R, *Tech. Dig. 9th Int. PV Sci. and Eng. Conf.*, 227 (1996).
179. Jones S, Crucet R, Deng X, Izu M, *Mater. Res. Soc. Symp. Proc.* **609**, A4.5 (2000).
180. Roschek T, Repmann T, Muller J, Rech B, Wagner H *et al.*, *Conference Record of the 28th IEEE Photovoltaic Specialists Conference-1996*, 150–153 (2000).
181. Meier J, Dubail S, Cuperus J, Kroll U, Platz R, Torres P, AnnaSelvan J, Pernet P, Pellaton N, Fischer D, Keppner H, Shah A, *J. Non-Cryst. Solids* **227–230**, 1250 (1998).
182. Platz R, Pellaton Vaucher N, Fischer D, Meier J, Shah A, *Conference Record of the 26th IEEE Photovoltaic Specialists Conference*, 691–694 (1997).
183. Shah A, Meier J, Vallat-Sauvain E, Droz C, Kroll U, Wyrsh N, Guillet J, Graf U, *Thin Solid Films* **403–404**, 179–187 (2002).
184. Izu M, Ovshinsky S, *Thin Solid Films* **119**, 55 (1984).
185. Izu M, Deng X, Krisko A, Whelan K, Young R, Ovshinsky H, Narasimhan K, Ovshinsky S, *Conference Record of the 23th IEEE Photovoltaic Specialists Conference*, 919 (1993).
186. Banerjee A, Yang J, Guha S, *Mater. Res. Soc. Symp. Proc.* (1999).
187. Deng X, Narasimhan K, *IEEE 1st World Conf. on Photovoltaic Energy Conversion*, 555 (1994).
188. Nath P, Hoffman K, Vogeli C, Ovshinsky S, *Appl. Phys. Lett.* **53**, 986–988 (1988).
189. Frammelsberger W, Lechner P, Rubel H, Schade H, *Proc. 14th European Photovoltaic Solar Energy Conference*, 2006 (1997).
190. Forest H, *Proc. 14th European Photovoltaics Solar Energy Conf.*, 2018–2020 (1997).
191. Rech B *et al.*, *Proc. 2nd World Conf. on Photovoltaic Solar Energy Conversion*, 391–396 (1998).
192. Kinoshita T *et al.*, *Proc. 14th EU Photovoltaic Solar Energy Conversion*, 566 (1997).
193. Okamoto S, Terakawa A, Maruyama E, Shinohara W, Hishikawa Y, Kiyama S, *Conference Record of the 28th IEEE Photovoltaic Specialists Conference*, 736–741 (2000).
194. Hagedorn G, *Proc. 9th European Photovoltaic Solar Energy Conversion*, 542 (Freiburg, 1989).
195. Yamamoto K, Yoshimi M, Suzuki T, Nakata T, Swada T, Nakajima A, Hayashi K, *Conference Record of the 28th IEEE Photovoltaic Specialists Conference*, 1428–1432 (2000).

This Page Intentionally Left Blank

13

Cu(InGa)Se₂ Solar Cells

William N. Shafarman¹ and Lars Stolt²

¹University of Delaware, Newark, DE, USA, ²Uppsala University, Uppsala, Sweden

13.1 INTRODUCTION

Cu(InGa)Se₂-based solar cells have often been touted as being among the most promising of solar cell technologies for cost-effective power generation. This is partly due to the advantages of thin films for low-cost, high-rate semiconductor deposition over large areas using layers only a few microns thick and for fabrication of monolithically interconnected modules. Perhaps more importantly, very high efficiencies have been demonstrated with Cu(InGa)Se₂ at both the cell and the module levels. Currently, the highest solar cell efficiency is 18.8% with 0.5 cm² total area fabricated by the National Renewable Energy Laboratory (NREL) [1]. Furthermore, several companies have demonstrated large area modules with efficiencies >12% including a confirmed 13.4% efficiency on a 3459 cm² module by Showa Shell [2]. Finally, Cu(InGa)Se₂ solar cells and modules have shown excellent long-term stability [3] in outdoor testing. In addition to its potential advantages for large-area terrestrial applications, Cu(InGa)Se₂ solar cells have shown high radiation resistance, compared to crystalline silicon solar cells [4, 5] and can be made very lightweight with flexible substrates, so they are also promising for space applications.

The history of CuInSe₂ solar cells starts with the work done at Bell Laboratories in the early 1970s, even though its synthesis and characterization were first reported by Hahn in 1953 [6] and, along with other ternary chalcopyrite materials, it had been characterized by several groups [7]. The Bell Labs group grew crystals of a wide selection of these materials and characterized their structural, electronic, and optical properties [7–9]. The first CuInSe₂ solar cells were made by evaporating *n*-type CdS onto *p*-type single crystals of CuInSe₂ [10]. These devices were initially recognized for their potential as near-infrared photodetectors since their spectral response was broader and more uniform than Si photodetectors. Optimization for solar cells increased the efficiency to 12% as measured under outdoor illumination “on a clear day in New Jersey” [11].

There has been relatively little effort devoted to devices on single-crystal CuInSe₂ since this early work, in part because of the difficulty in growing high-quality crystals [12]. Instead, nearly all the focus has gone to thin-film solar cells because of their inherent advantages. The first thin-film CuInSe₂/CdS devices were fabricated by Kazmerski *et al.* using films deposited by evaporation of CuInSe₂ powder along with excess Se [13]. However, thin-film CuInSe₂ solar cells began to receive a lot of attention when the first high-efficiency, 9.4%, cells were demonstrated by Boeing [14]. At the same time, interest in Cu₂S/CdS thin-film solar cells waned owing to problems related to electrochemical instabilities and many of these researchers turned their focus to CuInSe₂.

The Boeing devices were fabricated using CuInSe₂ deposited by coevaporation, that is, evaporation from separate elemental sources [15], onto ceramic substrates coated with a Mo back electrode. Devices were completed with evaporated CdS or (CdZn)S deposited in two layers with undoped CdS followed by an In-doped CdS layer that served as the main current-carrying material [15]. Throughout the 1980s, Boeing and ARCO Solar began to address the difficult manufacturing issues related to scale-up, yield, and throughput leading to many advancements in CuInSe₂ solar cell technology. The two groups pursued different approaches to CuInSe₂ deposition, which today remain the most common deposition methods and produce the highest device and module efficiencies. Boeing focused on depositing Cu(InGa)Se₂ by coevaporation, while ARCO Solar focused on a two-stage process of Cu and In deposition at a low temperature followed by a reactive anneal in H₂Se.

The basic solar cell configuration implemented by Boeing provided the basis for a series of improvements that have led to the high-efficiency device technology of today. The most important of these improvements to the technology include the following:

- The absorber-layer band gap was increased from 1.02 eV for CuInSe₂ to 1.1–1.2 eV by the partial substitution of In with Ga, leading to a substantial increase in efficiency [16].
- The 1- to 2- μm -thick doped (CdZn)S layer was replaced with a thin, ≤ 50 nm, undoped CdS and a conductive ZnO current-carrying layer [17]. This increased the cell current by increasing the short wavelength (blue) response.
- Soda lime glass replaced ceramic or borosilicate glass substrates. Initially, this change was made for the lower costs of the soda lime glass and its good thermal expansion match to CuInSe₂. However, it soon became clear that an increase in device performance and processing tolerance resulted primarily from the beneficial indiffusion of sodium from the glass [18].
- Advanced absorber fabrication processes were developed that incorporate band gap gradients that improve the operating voltage and current collection [19, 20].

From its earliest development, CuInSe₂ was considered promising for solar cells because of its favorable electronic and optical properties including its direct band gap with high absorption coefficient and inherent *p*-type conductivity. As science and technology developed, it also became apparent that it is a very forgiving material since (1) high-efficiency devices can be made with a wide tolerance to variations in Cu(InGa)Se₂ composition [21, 22], (2) grain boundaries are inherently passive so even films with grain sizes less than 1 μm can be used, and (3) device behavior is insensitive to defects at the junction caused by a lattice mismatch or impurities between the Cu(InGa)Se₂ and

CdS. The latter enables high-efficiency devices to be processed despite exposure of the Cu(InGa)Se_2 to air prior to junction formation.

High-efficiency CuInSe_2 -based solar cells have been fabricated by at least 10 groups around the world. While these groups employ a variety of processing technologies, all the solar cells have the same basic cell structure built around a $\text{Cu(InGa)Se}_2/\text{CdS}$ junction in a substrate configuration with a Mo back contact. Figure 13.1 shows a cross-sectional schematic of a standard device. This structure utilizes a soda lime glass substrate, coated with a sputtered Mo layer as a back contact. After Cu(InGa)Se_2 deposition, the junction is formed by chemical bath–deposited CdS with thickness ≤ 50 nm. Then a high-resistance (HR) ZnO layer and a doped high-conductivity ZnO layer are deposited, usually by sputtering or chemical vapor deposition. Either a current-collecting grid or monolithic series interconnection completes the device or module, respectively. A TEM micrograph of the same structure, shown in Figure 13.2, clearly demonstrates the polycrystalline nature of these materials and the conformal coverage of the CdS layer.

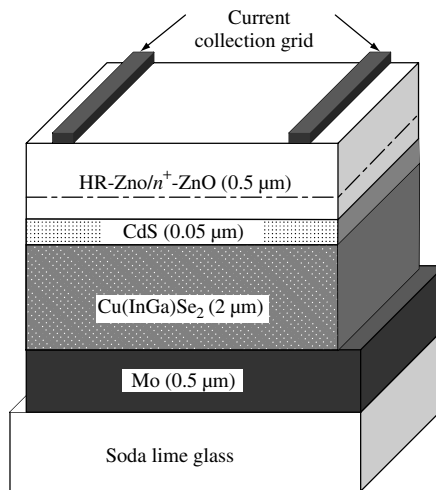


Figure 13.1 Schematic cross section of a typical Cu(InGa)Se_2 solar cell

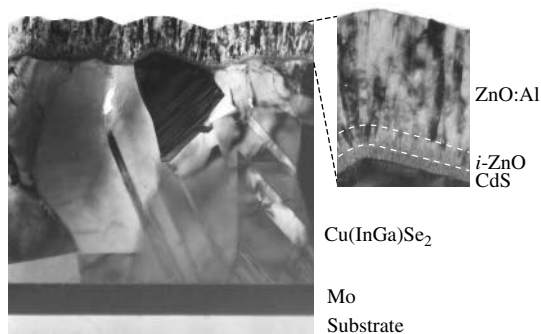


Figure 13.2 TEM cross section of a Cu(InGa)Se_2 solar cell

Several companies worldwide are pursuing the commercial development of Cu(InGa)Se₂-based modules. The most advanced, having demonstrated excellent reproducibility in its module manufacturing using the two-stage selenization process for Cu(InGa)(SeS)₂ deposition [3], is Shell Solar Industries (SSI) in California, which was formerly ARCO Solar and then Siemens Solar. They are now in production with 5-, 10-, 20-, and 40-W modules that are commercially available. In Germany, Würth Solar is in pilot production using an in-line coevaporation process for Cu(InGa)Se₂ deposition and has also reported large area modules with >12% efficiency. In the USA, several companies are in preproduction or pilot production: Energy Photovoltaics, Inc. (EPV) is using its own in-line evaporation process, International Solar Electric Technology (ISET) is developing a particle-based precursor for selenization, and Global Solar Energy (GSE) is pursuing a process for roll-to-roll coevaporation onto a flexible substrate. In Japan, Showa Shell, using a two-stage selenization process, and Matsushita, using coevaporation for Cu(InGa)Se₂ deposition, are also in production development stages.

Despite the level of effort on developing manufacturing processes, there remains a large discrepancy in efficiency between the laboratory-scale solar cells and minimodules, and the best full-scale modules. In part, this is due to the necessity for developing completely new processes and equipment for the large-area, high-throughput deposition needed for manufacturing thin-film photovoltaics. This is compounded by the lack of a comprehensive scientific base for Cu(InGa)Se₂ materials and devices, due partly to the fact that it has not attracted a broader interest for other applications. This lack of a science base has been perhaps the biggest hindrance to the maturation of Cu(InGa)Se₂ solar cell technology as most of the progress has been empirical. Still, in many areas a deeper understanding has emerged in the recent years.

In this chapter we will review the current status and the understanding of thin-film Cu(InGa)Se₂ solar cells from a technology perspective. For deeper scientific discussion of some aspects, we refer to suitable references. In order of presentation, this review covers (Section 13.2) structural, optical, and electrical properties of Cu(InGa)Se₂ including a discussion of the influence of Na and O impurities; (Section 13.3) methods used to deposit Cu(InGa)Se₂ thin films, the most common of which can be divided into two general types, multisource coevaporation and two-stage processes of precursor deposition followed by Se annealing; (Section 13.4) junction and device formation, which typically is done with chemical bath CdS deposition and a ZnO conduction layer; (Section 13.5) device operation with emphasis on the optical, current-collection, and recombination-loss mechanisms; (Section 13.6) module-manufacturing issues, including process and performance issues and a discussion of environmental concerns; and finally, (Section 13.7) a discussion of the outlook for CuInSe₂-based solar cells and critical issues for the future. In places where aspects of Cu(InGa)Se₂ solar cells cannot be covered in full, reference will be made to other review works that serve to complement this chapter.

13.2 MATERIAL PROPERTIES

The understanding of Cu(InGa)Se₂ thin films, as used in photovoltaic (PV) devices, is primarily based on studies of its base material, pure CuInSe₂. Thorough reviews on CuInSe₂ can be found in References [23–25]. However, the material used for making solar cells is Cu(InGa)Se₂ containing significant amounts (of the order of 0.1%) of Na [26].

Even though the behavior of CuInSe_2 provides a good basis for the understanding of device-quality material, there are pronounced differences when Ga and Na are present in the films. More recently, Cu(InGa)Se_2 has been reviewed in the context of solar cells with an emphasis on electronic properties [27].

In this section the structural, optical, and electrical properties of CuInSe_2 are reviewed along with information about the surface and grain boundaries and the effect of the substrate. In each case, as appropriate, the effect of the alloying with CuGaSe_2 to form Cu(InGa)Se_2 and the impact of Na and O on the material properties will be discussed.

13.2.1 Structure and Composition

CuInSe_2 and CuGaSe_2 have the chalcopyrite lattice structure. This is a diamond-like structure similar to the sphalerite structure but with an ordered substitution of the group I (Cu) and group III (In or Ga) elements on the group II (Zn) sites of sphalerite. This gives a tetragonal unit cell depicted in Figure 13.3 with a ratio of the tetragonal lattice parameters c/a close to 2 (see Table 13.1). The deviation from $c/a = 2$ is called the tetragonal distortion and stems from different strengths of the Cu–Se and the In–Se or Ga–Se bonds.

The possible phases in the Cu–In–Se system are indicated in the ternary phase diagram in Figure 13.4. Thin films of Cu–In–Se prepared under an excess supply of Se, that is, normal conditions for thin-film growth of Cu(InGa)Se_2 , have compositions that fall on, or close to, the tie-line between Cu_2Se and In_2Se_3 . Chalcopyrite CuInSe_2 is located on this line as well as a number of phases called ordered defect compounds (ODC), because they have a lattice structure described by the chalcopyrite structure with an ordered insertion of intrinsic defects. A comprehensive study of the Cu–In–Se phase diagram has been completed by Gödecke *et al.* [32]. A detail of the Cu_2Se – In_2Se_3 tie-line near CuInSe_2 is described by the pseudobinary phase diagram reproduced in Figure 13.5 [32]. Here α is the chalcopyrite CuInSe_2 , δ is a high-temperature (HT) phase with the sphalerite structure, and β is an ODC phase. It is interesting to note that the single phase field for CuInSe_2 at low temperatures is relatively narrow as compared to earlier beliefs, and does not contain

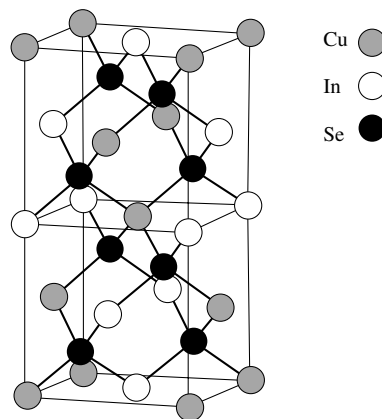
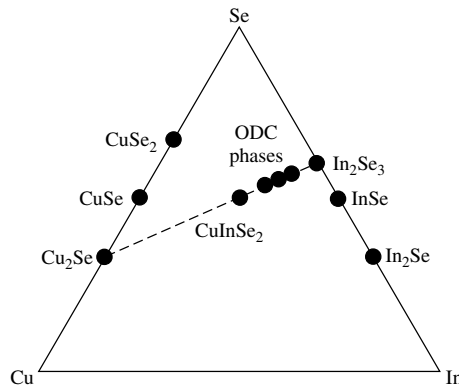


Figure 13.3 The unit cell of the chalcopyrite lattice structure

Table 13.1 Selected properties of CuInSe₂

Property		Value	Units	Reference
Lattice constant	<i>a</i>	5.78	Å	[28]
	<i>c</i>	11.62	Å	
Density		5.75	g/cm ³	[28]
Melting temperature		986	C	[29]
Thermal expansion coefficients at 273 K	(<i>a</i> axis)	8.32×10^{-6}	1/K	[30]
	(<i>c</i> axis)	7.89×10^{-6}	1/K	
Thermal conductivity at 273 K		0.086		[30]
Dielectric constant	Low frequency	13.6 ± 2.4		[31]
	High frequency	8.1 ± 1.4		
	Electrons	0.09		
Effective mass [<i>m_e</i>]	Holes (heavy)	0.71		[30]
	Holes (light)	0.092		[30]
				[30]
Energy gap		1.02	eV	[30]
Energy gap temperature coefficient		-2×10^{-4}	eV/K	[30]

**Figure 13.4** Ternary phase diagram of the Cu–In–Se system. Thin-film composition is usually near the pseudobinary Cu₂Se–In₂Se₃ tie-line

the composition 25% Cu. At higher temperatures, around 500°C, where thin films are grown, the phase field widens toward the In-rich side. Typical average compositions of device-quality films have 22 to 24 at.% Cu, which fall within the single-phase region at growth temperature.

CuInSe₂ can be alloyed in any proportion with CuGaSe₂, thus forming Cu(InGa)Se₂. Similarly, the binary phase In₂Se₃ at the end point of the pseudobinary tie-line can be alloyed to form (InGa)₂Se₃, although it undergoes a structural change at Ga/(In + Ga) = 0.6 [33]. In high-performance devices, Ga/(In + Ga) ratios are typically 0.2 to 0.3.

One of the central characteristics of Cu(InGa)Se₂ is its ability to accommodate large variations in composition without appreciable differences in optoelectronic properties.

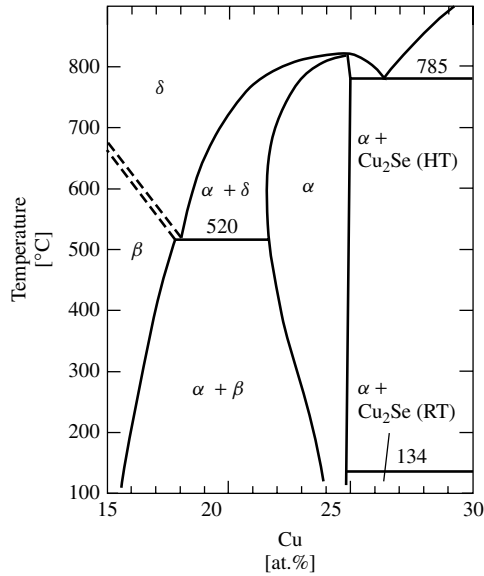


Figure 13.5 Pseudobinary $\text{In}_2\text{Se}_3\text{--Cu}_2\text{Se}$ equilibrium phase diagram for compositions around the CuInSe_2 chalcopyrite phase, denoted α . The δ phase is the high-temperature sphalerite phase, and the β phase is an ordered defect phase (ODC). Cu_2Se exists as a room-temperature (RT) or high-temperature (HT) phase. (After Gödecke T, Haalboom T, Ernst F, *Z. Metallkd.* **91**, 622–634 (2000) [32])

This tolerance is one of the cornerstones of the potential of $\text{Cu}(\text{InGa})\text{Se}_2$ as a material for efficient low-cost PV modules. Solar cells with high performance can be fabricated with $\text{Cu}/(\text{In} + \text{Ga})$ ratios from 0.7 to nearly 1.0. This property can be understood from theoretical calculations that show that the defect complex $2V_{\text{Cu}} + \text{In}_{\text{Cu}}$, that is, two Cu vacancies with an In on Cu antisite defect, has very low formation energy, and also that it is expected to be electrically inactive [34]. Thus, the creation of such defect complexes can compensate for Cu-poor/In-rich compositions of CuInSe_2 without adverse effects on the photovoltaic performance. Furthermore, crystallographic ordering of this defect complex is predicted [34], which explains the observed ODC phases $\text{Cu}_2\text{In}_4\text{Se}_7$, CuIn_3Se_5 , CuIn_5Se_8 , and so on.

The chalcopyrite phase field is increased by the addition of Ga or Na [35]. This can be explained by a reduced tendency to form the ordered defect compounds owing to higher formation energy for Ga_{Cu} (in CuGaSe_2) than for In_{Cu} (in CuInSe_2). This leads to destabilization of the $2V_{\text{Cu}} + \text{In}_{\text{Cu}}$ defect cluster related to the ODC phases [36, 37]. The effect of Na in the CuInSe_2 structure has been calculated by Wei *et al.* [38], with the result that Na replaces In_{Cu} antisite defects, reducing the density of compensating donors. This theoretical result is supported by measurements of epitaxial $\text{Cu}(\text{InGa})\text{Se}_2$ films in which Na is found to strongly reduce the concentration of compensating donors [37]. Together with a tendency for Na to occupy Cu vacancies, the reduced tendency to form antisite defects also suppresses the formation of the ordered defect compounds. The calculated effect of Na is therefore consistent with the experimental observations of increased compositional range in which single-phase chalcopyrite exists and increased conductivity [38, 39].

13.2.2 Optical Properties

The absorption coefficient α for CuInSe₂ is very high, larger than 10⁵/cm for 1.4 eV and higher photon energies [40]. In many studies it was found that the fundamental absorption edge is well described by [30]

$$\alpha = A(E - E_g)^2/E \quad (13.1)$$

as for a typical direct band gap semiconductor. The proportionality constant A depends on the density of states associated with the photon absorption. From this relation, a band gap value of $E_g = 1.02 \pm 0.02$ eV is obtained. The temperature dependence follows

$$E_g(T) = E_g(0) - aT^2/(b + T) \quad (13.2)$$

where a and b are constants that vary between different measurements. In general, dE_g/dT is about -2×10^{-4} eV/K [41].

A rather complete picture of the optical properties of CuInSe₂ and other Cu-ternary chalcopyrites is given in Reference [42]. Ellipsometric measurements of carefully prepared single-crystal samples were carried out and the dielectric functions were obtained together with the complex refractive index for different polarizations. From these measurements a band gap value for CuInSe₂ of 1.04 eV was determined.

A similar study was also made on bulk polycrystalline ingots of Cu(InGa)Se₂ having different compositions from $x \equiv \text{Ga}/(\text{Ga} + \text{In}) = 0$ to 1 [43]. Curves describing the complex refractive index, $n + ik$, for samples with $x = 0$ and 0.2 are reproduced in Figure 13.6. The complex refractive index can be used to calculate other optical parameters like the absorption coefficient

$$\alpha = 4\pi k/\lambda \quad (13.3)$$

In the same work the fundamental transitions for the different compositions were fit to an equation describing the band gap for CuIn_{1-x}Ga_xSe₂ as

$$E_g = 1.010 + 0.626x - 0.167x(1 - x) \quad (13.4)$$

In this equation the so-called bowing coefficient is 0.167. A value of 0.21 was obtained by theoretical calculations as compared to values in the range of 0.11 to 0.26 determined in various experiments [44].

13.2.3 Electrical Properties

CuInSe₂ with an excess of Cu is always p -type but In-rich films can be made p -type or n -type [45]. By annealing in a selenium overpressure, n -type material can be converted to p -type, and conversely, by annealing in a low selenium pressure, p -type material becomes n -type [46]. It is believed that this affects the concentration of Se vacancies, V_{Se} , which act as compensating donors in p -type films. Device-quality Cu(InGa)Se₂ films, grown with the excess Se available, are p -type with a carrier concentration of about 10¹⁶/cm³.

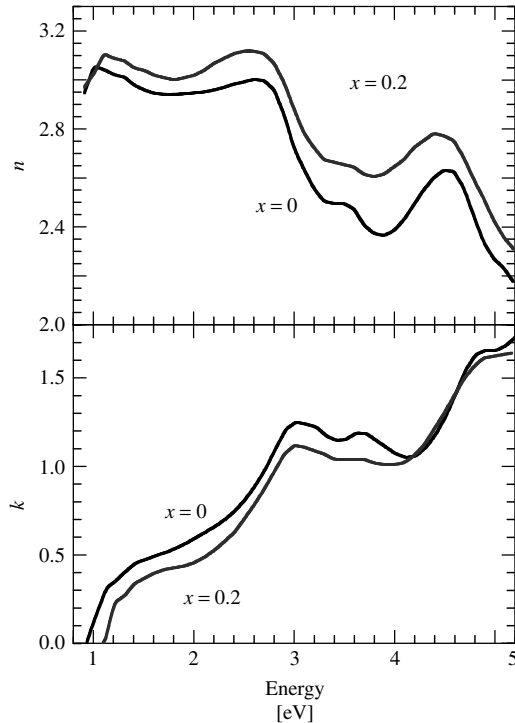


Figure 13.6 Complex refractive index for CuInSe_2 and $\text{CuIn}_{1-x}\text{Ga}_x\text{Se}_2$ with $x = 0.2$ (After Alonso M *et al.*, *Appl. Phys. A* **74**, 659–664 (2002) [43])

There is a large spread in mobility values reported for CuInSe_2 . The highest values of hole mobilities have been obtained for epitaxial films, where $200 \text{ cm}^2/\text{Vs}$ has been measured for $\text{Cu}(\text{InGa})\text{Se}_2$ with about $10^{17}/\text{cm}^3$ in hole concentration [37]. Single crystals have yielded values in the range of 15 to $150 \text{ cm}^2/\text{Vs}$. Electron mobilities determined from single crystals range from 90 to $900 \text{ cm}^2/\text{Vs}$ [46]. Conductivity and Hall effect measurements of thin-film samples are made cross-grain, but for device operation through-the-grain values are more relevant, since individual grains may extend from the back contact to the interface of the junction. The sheet conductivities of polycrystalline p -type films correspond to mobility values of 5 to $50 \text{ cm}^2/\text{Vs}$, but it is quite possible that they are limited by transport across grain boundaries.

A large number of intrinsic defects are possible in the chalcopyrite structure. Accordingly, a number of electronic transitions have been observed by methods such as photoluminescence, photoconductivity, photovoltage, optical absorption, and electrical measurements (see, for example, Reference [31]). However, it is difficult to assign transitions to specific defects on an experimental basis. Instead, theoretical calculations of the transition energies and formation energies provide a basis for identification of the different intrinsic defects that are active in $\text{Cu}(\text{InGa})\text{Se}_2$. Calculations of intrinsic defects in CuInSe_2 and comparison with experimental data can be found in the comprehensive paper by Zhang *et al.* [47]. A summary of their results is schematically shown in Figure 13.7. The defects that are considered most important in device-quality material are presented in Table 13.2.

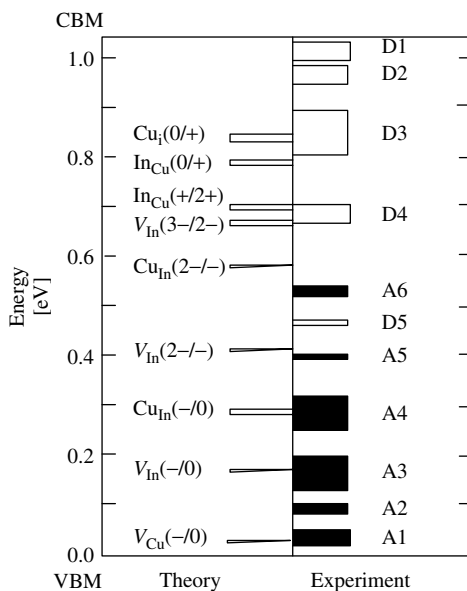


Figure 13.7 Electronic levels of intrinsic defects in CuInSe₂. On the left side the theoretical values are presented and on the right side experimentally reported values are presented. The height of the histogram columns on the right side represents the spread in experimental data. (From Zhang S, Wei S, Zunger A, Katayama-Yoshida H, *Phys. Rev. B* **57**, 9642–9656 (1998) [47])

Table 13.2 The most important intrinsic defects for device-quality CuInSe₂

Defect	Energy position	Type
V_{Cu}	$E_{\text{V}} + 0.03 \text{ eV}$	Shallow acceptor
In_{Cu}	$E_{\text{C}} - 0.25 \text{ eV}$	Compensating donor
V_{Se}		Compensating donor
Cu_{In}	$E_{\text{V}} + 0.29 \text{ eV}$	Recombination center

The effect of Ga on the electronic and defect properties is discussed in Reference [36]. In those calculations, acceptor levels did not differ very much between CuInSe₂ and CuGaSe₂, but the donor levels are deeper in the Ga-containing compound. This is consistent with observations of increased *p*-type conductivity at high Ga-concentrations [48]. At typical device compositions, $\text{Ga}/(\text{Ga} + \text{In}) < 0.3$, any effect of increased Ga content on conductivity has not been verified.

13.2.4 The Surface and Grain Boundaries

The surface morphology and grain structure are most commonly characterized by scanning electron microscopy (SEM), but transmission electron microscopy (TEM) and atomic force microscopy have also proved valuable. A typical SEM image is shown in Figure 13.8 and a TEM cross-sectional image in Figure 13.2. In general, the films used in devices

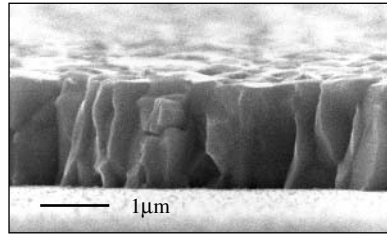


Figure 13.8 Scanning electron microscopy image of a typical Cu(InGa)Se_2 film deposited on a Mo-coated glass substrate by coevaporation

have grain diameters on the order of $1 \mu\text{m}$ but the grain size and morphology can vary greatly depending on fabrication method and conditions. A variety of defects including twins, dislocations, and stacking faults have been observed [49–51].

It has been shown by X-ray photoelectron spectroscopy (XPS) that the free surfaces of CuInSe_2 films with slightly Cu-poor composition have a composition close to CuIn_3Se_5 [52], corresponding to one of the ordered defect phases. Many attempts have been made to identify such a layer on top of the films without success. It merely seems as if the composition gradually changes from the bulk to the surface of the films. It was proposed by Herberholz *et al.* [35] that band bending induced by surface charges drives electromigrating Cu into the bulk leaving the surface depleted of Cu. This depletion is stopped when the composition is that of CuIn_3Se_5 , since further depletion requires a structural change of the material. Electromigration of Cu in CuInSe_2 has been demonstrated and also correlated with type conversion of the chalcopyrite material [53].

The band bending as well as the CuIn_3Se_5 composition of CuInSe_2 surfaces disappears when the material is exposed to atmosphere for some time as oxides form on the surface. The surface oxidation is enhanced by the presence of Na [39]. The surface compounds after oxidation have been identified as In_2O_3 , Ga_2O_3 , SeO_x , and Na_2CO_3 [54]. A review of the surface and the interface properties can be found in Reference [55].

It has been common practice to posttreat Cu(InGa)Se_2 devices in air at typically 200°C . When devices were fabricated using vacuum-evaporated CdS or $(\text{CdZn})\text{S}$ to form the junction, these anneals were often done for several hours to optimize the device performance [14, 56]. The main effect associated with oxygen is explained as passivation of selenium “surface” vacancies on the grains [57]. The V_{Se} at the grain boundaries can act as a recombination center. The positive charge associated with these donor-type defects reduces the effective hole concentration at the same time that the intergrain carrier transport is impeded. When oxygen substitutes for the missing selenium, these negative effects are canceled.

The overall noted beneficial effect of the presence of Na on the PV performance of Cu(InGa)Se_2 thin films lacks a complete explanation. In Reference [58] it is proposed that the catalytic effect of Na on oxidation, by enhanced dissociation of molecular oxygen into atomic oxygen, makes the passivation of V_{Se} on grain surfaces more effective. This model is consistent with the observation that Na and O are predominantly found at the grain boundaries rather than in the bulk of the grains in CuInSe_2 thin films [59].

13.2.5 Substrate Effects

The effects of the substrate on the properties of thin-film polycrystalline Cu(InGa)Se₂ can be classified into three categories: (1) thermal expansion, (2) chemical effects, and (3) surface influence on nucleation.

It can be assumed that after growth, when the substrate and film are still at the growth temperature, the stress in the Cu(InGa)Se₂ film is low. The cooling down from growth temperature imposes a temperature change of about 500°C, and if the thermal expansion of the substrate and Cu(InGa)Se₂ is different stress will be built up in the film. The thermal expansion coefficient for CuInSe₂ is around $9 \times 10^{-6}/\text{K}$ in the temperature interval of interest, which is similar to that of soda lime glass. A CuInSe₂ film deposited on a substrate with a lower thermal expansion coefficient, such as borosilicate glass, will be under increasing tensile stress during cooldown. Typically, such films exhibit voids and microcracks [50]. When the thermal expansion coefficient of the substrate is higher than that of the film material, like for polyimide, it will result in compressive stress in the thin-film material, which may lead to adhesion failures.

The most important effect of the soda lime glass substrate on Cu(InGa)Se₂ film growth is that it supplies sodium to the growing chalcopyrite material. It has been clearly shown that this effect is distinct from the thermal expansion match of soda lime glass [60]. The sodium diffuses through the Mo back contact, which also means that it is important to control the properties of the Mo [61]. The resulting microstructure of Cu(InGa)Se₂ is clearly influenced by the presence of Na with larger grains and a higher degree of preferred orientation, with the (112) axis perpendicular to the substrate. An explanation for this effect when high concentrations of Na are present has been proposed by Wei *et al.* [38].

There is a wide range of preferred orientation between different growth processes, in spite of similar device performance. One reason for this variation is most likely the different properties of the surfaces on which the chalcopyrite material nucleates. A comparison between Cu(InGa)Se₂ grown on normal Mo-coated substrates and directly on soda lime glass shows that a much more pronounced (112) orientation occurs on glass, in spite of no difference in the Na concentration, as measured in the films afterwards [18]. Further, the preferred orientation of the Cu(InGa)Se₂ film has been shown to be correlated to the orientation of the Mo film [62] or an (InGa)₂Se₃ precursor layer [63].

13.3 DEPOSITION METHODS

A wide variety of thin-film deposition methods has been used to deposit Cu(InGa)Se₂ thin films. To determine the most promising technique for the commercial manufacture of modules, the overriding criteria are that the deposition can be completed at low cost while maintaining high deposition or processing rate with high yield and reproducibility. Compositional uniformity over large areas is critical for high yield. Device considerations dictate that the Cu(InGa)Se₂ layer should be at least 1 μm thick and that the relative compositions of the constituents are kept within the bounds determined by the phase diagram, as discussed in Section 13.2.1. For solar cell or module fabrication, the Cu(InGa)Se₂ is most commonly deposited on a molybdenum-coated glass substrate,

though other substrate materials including metal or plastic foils have also been used and may have processing advantages.

The most promising deposition methods for the commercial manufacture of modules can be divided into two general approaches that have both been used to demonstrate high device efficiencies and in pilot scale manufacturing. The first approach is vacuum coevaporation in which all the constituents, Cu, In, Ga, and Se, can be simultaneously delivered to a substrate heated to 400 to 600°C and the Cu(InGa)Se₂ film is formed in a single growth process. This is usually achieved by thermal evaporation from elemental sources at temperatures greater than 1000°C for Cu, In, and Ga. The second approach is a two-step process that separates the delivery of the metals from the reaction to form device-quality films. Typically the Cu, Ga, and In are deposited using low-cost and low-temperature methods that facilitate uniform composition. Then the films are annealed in a Se atmosphere, also at 400 to 600°C. The reaction and anneal step often takes longer time than formation of films by coevaporation due to diffusion kinetics, but is amenable to batch processing. High process rate can be achieved by moving continuously through sequential process steps or with a batch process whereby longer deposition or reaction steps can be implemented by handling many substrates in parallel.

13.3.1 Substrates

Soda lime glass, which is used in conventional windows, is the most common substrate material used for Cu(InGa)Se₂ since it is available in large quantities at low cost and has been used to make the highest efficiency devices. Cu(InGa)Se₂ deposition requires a substrate temperature (T_{SS}) of at least 350°C and the highest efficiency cells have been fabricated using films deposited at the maximum temperature, $T_{SS} \approx 550^\circ\text{C}$, which the glass substrate can withstand without softening too much [64]. The glass is electrically insulating and smooth, which enables monolithic integration into modules.

The soda lime glass has a thermal expansion coefficient of $9 \times 10^{-6}/\text{K}$ [64], which provides a good match to the Cu(InGa)Se₂ films. The glass composition typically includes various oxides such as Na₂O, K₂O, and CaO. These provide sources of alkali impurities that diffuse into the Mo and Cu(InGa)Se₂ films during processing [18], producing the beneficial effects discussed in Section 13.2. However, a process that provides a more controllable supply of Na than diffusion from the glass substrate is preferred. This can be achieved by blocking sodium from the substrate with a diffusion barrier such as SiO_x or Al₂O₃. Then sodium can be directly provided to the Cu(InGa)Se₂ growth process by depositing a sodium-containing precursor layer onto the Mo film [65, 66]. Commercially available soda lime glass may also contain significant structural defects that can adversely impact module production [67]. Borosilicate glass does not contain the alkali impurities and may have fewer structural imperfections but has a lower thermal expansion coefficient, $4.6 \times 10^{-6}/\text{K}$ [64], and is more expensive.

Substrates such as metal or plastic foils have advantages over glass substrates owing to their light weight and flexibility, which will be discussed in Section 13.6. Cu(InGa)Se₂ devices have been demonstrated with different metal and high-temperature polyimide substrates [68, 69].

13.3.2 Back Contact

The Mo back contact, used for all high-efficiency devices, is typically deposited by direct current (dc) sputtering. The thickness is determined by the resistance requirements that depend on the specific cell or module configuration. A film with thickness 1 μm will typically have a sheet resistance of 0.1 to 0.2 Ω/\square , a factor of 2 to 4 higher resistivity than bulk Mo. Sputter deposition of the Mo layer requires careful control of the pressure to control stress in the film [70] and to prevent problems such as poor adhesion that it might cause. During Cu(InGa)Se₂ deposition, a MoSe₂ layer forms at the interface [71]. Its properties are influenced by the Mo film with less MoSe₂ forming on dense Mo, sputter-deposited under low pressures [51]. This interfacial layer does not necessarily degrade device performance. Metals other than Mo have been investigated with limited success [72].

13.3.3 Coevaporation of Cu(InGa)Se₂

The highest efficiency devices have been deposited by thermal coevaporation from elemental sources [73]. An illustration of a laboratory system for Cu(InGa)Se₂ coevaporation is shown in Figure 13.9. The process uses line-of-sight delivery of the Cu, In, Ga, and Se from Knudsen-type effusion cells or open-boat sources to the heated substrate. While the evaporation temperatures for each metal will depend on the specific source design, typical ranges are 1300 to 1400°C for Cu, 1000 to 1100°C for In, 1150 to 1250°C for Ga, and 300 to 350°C for Se evaporation.

The sticking coefficients of Cu, In, and Ga are very high, so the film composition and growth rate are determined simply by the flux distribution and effusion rate from each source. The composition of the final film tends to follow the pseudobinary tie-line between (InGa)₂Se₃ and Cu₂Se (see Figure 13.4) according to the relative concentration of Cu compared to In and Ga. The relative concentrations of In and Ga determine the band gap of the film, according to equation (13.4), and the effusion rates can be varied over the course of a deposition to change the film composition through its thickness. Se has a

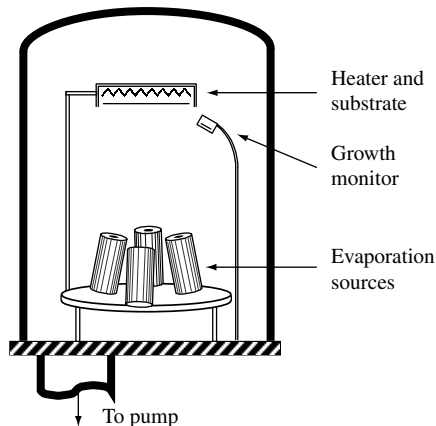


Figure 13.9 Configuration for multisource elemental coevaporation

much higher vapor pressure and lower sticking coefficient, so it is always evaporated in excess of that needed in the final film. Insufficient Se can result in a loss of In and Ga in the form of In_2Se or Ga_2Se [74].

Different deposition variations, using elemental fluxes deliberately varied over time, have been explored using coevaporation. Four different sequences that have been used to fabricate devices with efficiencies greater than 16% are shown in Figure 13.10. In each case, the targeted final composition is Cu-deficient with $\text{Cu}/(\text{In} + \text{Ga}) = 0.8 - 0.9$. The total deposition time may vary from 10 to 90 min, depending on the effusion rates from the sources. So, for a film thickness of 2 μm , typical deposition rates vary from 20 to 200 nm/min.

The first process is the simplest stationary process in which all fluxes are constant throughout the deposition process [75]. In most cases, however, the fluxes are varied using what is referred to as the Boeing process in which the bulk of the film is grown with Cu-rich overall composition so that it contains a Cu_xSe phase in addition to $\text{Cu}(\text{InGa})\text{Se}_2$ [15]. The fluxes are then adjusted to finish the deposition with In- and Ga-rich flux so that the final film composition has the desired Cu-deficient composition. One modification of this is the second process shown in Figure 13.10. This process was first implemented with CuInSe_2 films deposited on non-Na containing substrates at $T_{\text{SS}} = 450^\circ\text{C}$, producing films with increased grain size and improved device performance. The effect of Cu_xSe as a flux for enhanced grain growth at higher T_{SS} was proposed by Klenk *et al.* [76]. However, in devices containing Na and Ga and with $T_{\text{SS}} > 500^\circ\text{C}$, no difference was found in the device performance using films with Cu-rich or uniform growth processes [75].

The third process shown in Figure 13.10 is a sequential process in which the In and Ga are deposited separately from the Cu. This was first proposed by Kessler *et al.* [77] with the deposition of an $(\text{InGa})_x\text{Se}_y$ compound, followed by the deposition of Cu and Se until the growing film reaches the desired composition. The layers interdiffuse to form the $\text{Cu}(\text{InGa})\text{Se}_2$ film. A modification by Gabor *et al.* [78] allows the Cu delivery to continue until the film has an overall Cu-rich composition. Then a third step is added to the process in which In and Ga, again in the presence of excess Se, are evaporated to bring the composition back to Cu-deficient. The metals interdiffuse, forming the ternary chalcopyrite film. This process has been used to produce the highest efficiency devices [1]. The improved device performance has been attributed to a band gap gradient, which results from the Ga concentration decreasing from the Mo back contact to the film's free surface [19], and to improved crystallinity of the films [79].

The last process shown in Figure 13.10 is an in-line process in which the flux distribution results from the substrate moving sequentially over the Cu, Ga, and In sources. This was first simulated in a stationary evaporation system [80] and has subsequently been implemented by several groups in pilot manufacturing systems (see Section 13.6).

A reproducible coevaporation process requires good control of the elemental fluxes from each evaporation source. While the evaporation rates from each source can be controlled simply by the source temperature, this may not give good reproducibility, especially for the Cu source that is at the highest temperature. Open-boat sources in particular will not give reproducible evaporation rates. Consequently, direct *in situ* measurement of the fluxes is often used to control the evaporation sources. Electron impact spectroscopy [15], quadrupole mass spectroscopy [81], and atomic absorption spectroscopy [82] have all

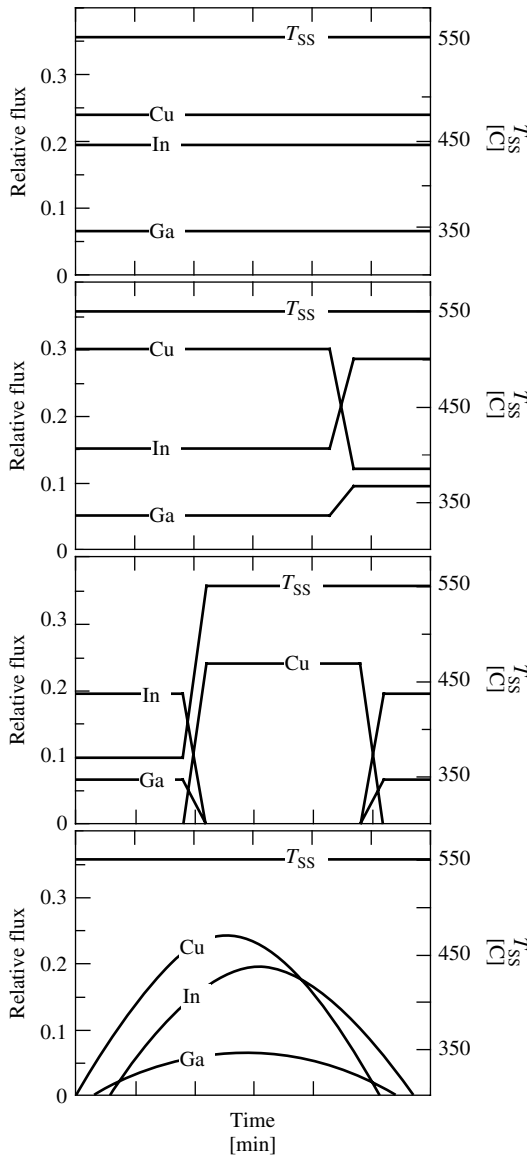


Figure 13.10 Relative metal fluxes and substrate temperature for different coevaporation processes. In all cases, a constant Se flux is also supplied

been successfully implemented. Direct flux measurement may be critical in a manufacturing scale process, particularly if source depletion over long run times causes the relation between source temperature and effusion rate to vary over time. In addition, the process can be monitored by *in situ* film thickness measurement using a quartz crystal monitor, or optical spectroscopy or X-ray fluorescence of the growing film [83]. The latter has also been used to measure composition. When the process includes a transition from Cu-rich to Cu-poor composition near the end of the deposition, it can be monitored by a change

in the temperature resulting from a change in the emissivity of the film [84] or by the infrared transmission [85].

The primary advantage of elemental coevaporation for depositing Cu(InGa)Se_2 films is its considerable flexibility to choose the process specifics and to control film composition and band gap. As proof of this flexibility, high-efficiency devices have been demonstrated using many process variations. The primary disadvantage results from the difficulty in control, particularly of the Cu-evaporation source, and the resulting need for improved deposition, diagnostic, and control technology. A second disadvantage is the lack of commercially available equipment for large-area thermal evaporation.

13.3.4 Two-step Processes

The second common approach to Cu(InGa)Se_2 film formation, usually referred to as two-step processing or selenization, has many variations in both the precursor deposition and the Se reaction steps. This general approach was first demonstrated by Grindle *et al.* [86] who sputtered Cu/In layers and reacted them in hydrogen sulfide to form CuInS_2 . This was first adapted to CuInSe_2 by Chu *et al.* [87]. The highest-efficiency Cu(InGa)Se_2 cell reported using the reaction in H_2Se is 16.2%, on the basis of the active area [88], but there has been less effort at optimizing laboratory-scale cell efficiencies than with coevaporated Cu(InGa)Se_2 . Showa Shell and Shell Solar have successfully scaled up this process to pilot commercial production and have demonstrated large-area module efficiencies as high as 13.4% [2].

The metal precursor is used to determine the final composition of the film and to ensure spatial uniformity. Sputtering is an attractive process because it is easily scalable using commercially available deposition equipment and can provide good uniformity over large areas with high deposition rates. However, other processes may have lower cost. CuInSe_2 has been formed using metal precursor layers deposited by electrodeposition [89], thermal or electron beam evaporation [90], screen printing [91], and application of nanoparticles [92]. Precursors that include Se, such as stacked layers of Cu/In/Se [93] or binary selenides, have also been used as precursor materials in various sequences and combinations [94]. Electrodeposition [95, 96] of Cu, In, Ga, and Se is effectively just another option for precursor deposition since the films similarly require a selenium reaction step.

The precursor films are typically reacted in either H_2Se or Se vapor at 400 to 500°C for 30 to 60 min to form the best device quality material. Poor adhesion [89] and formation of a MoSe_2 layer [97] at the Mo/ CuInSe_2 interface may limit the reaction time and temperature. Reaction in H_2Se has the advantage that it can be done at atmospheric pressure and can be precisely controlled, but the gas is highly toxic and requires special precautions for its use. The precursor films can also be reacted in a Se vapor, which might be obtained by thermal evaporation, to form the CuInSe_2 film [98]. A third reaction approach is rapid thermal processing (RTP) of either elemental layers, including Se, [99, 100] or amorphous evaporated Cu–In–Se layers [101].

The reaction chemistry and kinetics for the conversion of Cu–In precursors to CuInSe_2 has been characterized by X-ray diffraction of time-progressive reactions [102] and by *in situ* differential scanning calorimetry [103]. The results of these experiments

describe CuInSe₂ formation as a sequence of reactions starting with the formation of Cu₁₁In₉ and In liquid, which will contain a small concentration of dissolved Cu. These react with Se to form a series of binary compounds. The formation of CuInSe₂ then follows from



with complete reaction in ~ 15 min at 400°C. The reaction path was shown to be the same for the reaction of Cu/In layers in either H₂Se or elemental Se [104].

The addition of Ga, regardless of the precursor deposition sequence, does not readily give a film with uniformly increased band gap. Instead, all Ga in the reacted film accumulates near the Mo forming a CuInSe₂/CuGaSe₂ structure, so the resulting device behaves like CuInSe₂ [105] and lacks the increased operating voltage and other benefits of a wider band gap discussed in Section 13.5.4. Nevertheless, Ga inclusion provides improved adhesion of the CuInSe₂ film to the Mo back contact and greater device performance, possibly owing to an improved structure with fewer defects [105]. The Ga and In can be effectively interdiffused, converting the films to uniform band gap, by annealing in an inert atmosphere for 1 h at 600°C [106]. This anneal, however, may be impractical for commercial processing, so films in the best devices have the band gap increased by the incorporation of S near the front surface, forming a graded Cu(InGa)(SeS)₂ layer [20, 107] that can give enhanced operating voltage in devices.

The primary advantages of two-step processes for Cu(InGa)Se₂ deposition are the ability to utilize more standard and well-established techniques for the metal deposition and reaction and anneal steps and to compensate for long reaction times with a batch processing mode or RTP of Se-containing precursors. Composition and uniformity are controlled by the precursor deposition and can be measured between the two steps. The biggest drawback to these processes is the limited ability to control composition and increase band gap, which may limit device and module performance. Other difficulties that must be overcome include poor adhesion and the use of hydrogen selenide, which is hazardous and costly to handle.

13.3.5 Other Deposition Approaches

CuInSe₂-based films have been deposited using a wide range of thin-film deposition methods, in addition to those discussed above, which have been proposed as potential low-cost alternatives for manufacturing. These include reactive sputtering [108], hybrid sputtering in which Cu, In, and Ga are sputtered while Se is evaporated [109], closed-space sublimation [110], chemical bath deposition (CBD) [111], laser evaporation [112], and spray pyrolysis [113]. Great effort was made to explore different thin-film deposition techniques before coevaporation and the two-step processes above became dominant. These methods are reviewed in Reference [25].

13.4 JUNCTION AND DEVICE FORMATION

The first experimental device that indicated the potential for CuInSe₂ in high-performance solar cells was a heterojunction between a *p*-type single crystal of CuInSe₂ and a thin film of *n*-type CdS [10, 11]. Consequently, in the early thin-film work the junction was

formed by depositing CdS on the CuInSe₂ films [114]. The device was further developed to contain an undoped layer of CdS, followed by CdS doped with In, both deposited by vacuum evaporation [14]. This defined the device structure (see Figure 13.1), which is basically the same as is commonly used today since the doped CdS is functionally a transparent conductor. A performance gain was achieved by alloying the CdS with ZnS to widen the band gap [15]. Further improvement of the performance was achieved when the doped CdS layer was replaced with doped ZnO [115, 116]. The undoped CdS layer adjacent to the Cu(InGa)Se₂ film was reduced in thickness in order to maximize the optical transmission. Since ZnO has a wider band gap than CdS, more light is transmitted into the active part of the device, resulting in a current gain. A conformal and pinhole-free coating of this thin CdS layer is obtained by using chemical bath deposition to make the CdS buffer layer.

13.4.1 Chemical Bath Deposition

Chemical bath deposition (CBD) of thin-film materials can be viewed as a chemical vapor deposition (CVD) in the liquid phase instead of the gas phase. It is also referred to as solution growth. The method has been used in particular for chalcogenide materials such as PbS [117], CdS [118], and CdSe [119]. A variety of precursor compounds or ions can be used to deposit a specific compound.

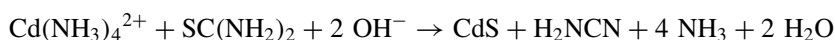
Deposition of CdS buffer layers on Cu(InGa)Se₂ is generally made in an alkaline aqueous solution (pH > 9) of the following three constituents:

1. a cadmium salt; for example, CdSO₄, CdCl₂, CdI₂, Cd(CH₃COO)₂
2. a complexing agent; commonly NH₃ (ammonia)
3. a sulfur precursor; commonly SC(NH₂)₂ (thiourea).

The concentrations of the various components of the solution can be varied over a range and each laboratory tends to use its own specific recipe. One example of a recipe that is being used to fabricate state-of-the-art Cu(InGa)Se₂ solar cells is

1. $1.4 \times 1/10^3$ M CdI₂ or CdSO₄
2. 1 M NH₃
3. 0.14 M SC(NH₂)₂

The Cu(InGa)Se₂ film is immersed in a bath containing the solution and the deposition takes place in a few minutes at a temperature of 60 to 80°C. This can be done either by immersion in a room-temperature bath that subsequently is heated to the desired temperature or by preheating the solution. The reaction proceeds according to the formula



In practice, the chemical bath deposition is typically done in the laboratory with a very simple apparatus consisting of a hot plate with magnetic stirring, a beaker holding the solutions into which the substrate is immersed, and a thermocouple to measure bath

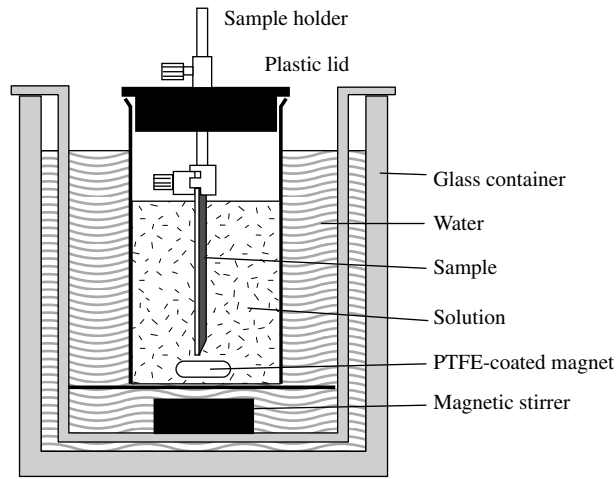


Figure 13.11 Typical laboratory apparatus for chemical bath deposition of CdS

temperature. A typical arrangement, incorporating a water bath for more uniform temperature, is shown in Figure 13.11. Scale-up of the CBD process for manufacturing will be discussed in Section 13.6.1.

The growth of CdS thin films by CBD occurs from ion by ion reaction or by clustering of colloidal particles. Depending on the bath condition, the resulting CdS lattice structure may be cubic, hexagonal, or a mixture [120]. Under typical conditions used for Cu(InGa)Se₂ solar cells, the relatively thin CdS layers grow ion by ion, resulting in dense homogeneous films [121] with mixed cubic/hexagonal or predominantly hexagonal lattice structure [51, 122, 123]. The films consist of crystallites with a grain size of the order of tens of nanometers [122].

Compositional deviation from stoichiometry is commonly observed. In particular, films tend to be sulfur-deficient and contain substantial amounts of oxygen [124, 125]. In addition to oxygen, significant concentrations of hydrogen, carbon, and nitrogen have also been detected in device quality films [126]. The concentration of these impurities has been correlated to a reduction of the optical band gap and the amount of cubic CdS in relation to hexagonal CdS [127].

13.4.2 Interface Effects

The interface between the Cu(InGa)Se₂ and the CdS is characterized by pseudoepitaxial growth of the CdS and intermixing of the chemical species. Electronic band alignment will be discussed in Section 13.5.3. Transmission electron microscopy has shown that chemical bath-deposited CdS layers on Cu(InGa)Se₂ films exhibit an epitaxial relationship at the interface with (112) chalcopyrite Cu(InGa)Se₂ planes parallel to the (111) cubic or (002) hexagonal CdS planes [51, 123]. The lattice mismatch is very small for pure CuInSe₂ with a (112) spacing of 0.334 nm as compared to a spacing of 0.336 nm for (111) cubic and (002) hexagonal CdS. In Cu(InGa)Se₂ the lattice mismatch increases with the Ga content. CuIn_{0.7}Ga_{0.3}Se₂ and CuIn_{0.5}Ga_{0.5}Se₂ have (112) spacing of 0.331 nm

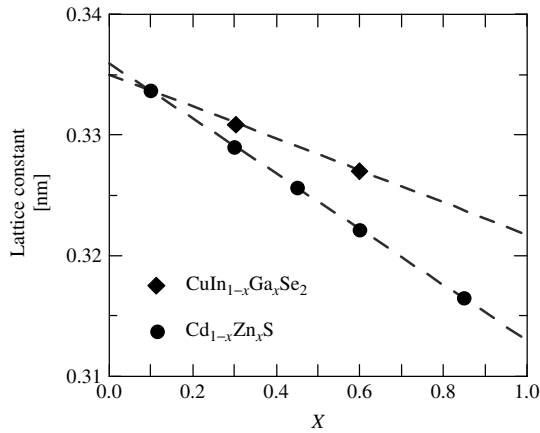


Figure 13.12 The lattice spacing of the (112) planes of $\text{CuIn}_{1-x}\text{Ga}_x\text{Se}_2$ and the (111) cubic or the (002) hexagonal planes of $\text{Cd}_{1-x}\text{Zn}_x\text{S}$. Empirical data from References [128] ((CdZn)S) and [129] (CuInSe_2 , CuGaSe_2 , and $(\text{Cu}(\text{InGa})\text{Se}_2)$) are included

and 0.328 nm, respectively. Figure 13.12 displays the (112) spacing for $\text{Cu}(\text{InGa})\text{Se}_2$ as a function of $\text{Ga}/(\text{In} + \text{Ga})$ ratio together with the (111)/(002) spacing of $\text{CdS}-\text{ZnS}$ alloys.

When $\text{Cu}(\text{InGa})\text{Se}_2$ films are immersed in the chemical bath for deposition of CdS, they are also subjected to chemical etching of the surface. In particular, native oxides are removed by the ammonia [130]. Thus, the CBD process cleans the $\text{Cu}(\text{InGa})\text{Se}_2$ surface and enables the epitaxial growth of the CdS buffer layer.

In early single-crystal work, $p-n$ homojunction diodes were fabricated by indiffusion of Cd or Zn into p -type CuInSe_2 [131, 132] at 200 to 450°C. Investigations of $\text{CuInSe}_2/\text{CdS}$ interfaces did show interdiffusion of S and Se above 150°C and rapid Cd diffusion into CuInSe_2 above 350°C [133]. More recently, intermixing of the constituents of the $\text{Cu}(\text{InGa})\text{Se}_2/\text{CdS}$ heterojunction has been observed even when the relatively low-temperature CBD process is used for growth of the CdS layer [134]. Investigations of the effect of a chemical bath without the thiourea showed an accumulation of Cd on the $\text{Cu}(\text{InGa})\text{Se}_2$ surface, possibly as CdSe [130]. Accumulation of Cd on the $\text{Cu}(\text{InGa})\text{Se}_2$ surface was also observed in the initial stage of CdS growth in the complete chemical bath [135]. The results were not conclusive on whether any interfacial compound is formed, but TEM investigations showed the presence of Cd up to 10 nm into the Cu-deficient surface region of the $\text{Cu}(\text{InGa})\text{Se}_2$ layer [123]. At the same time, a reduction of the Cu concentration was noted. An interpretation in which Cu^+ is replaced with Cd^{2+} is proposed, on the basis of the very close ion radii of these ions, 0.96 and 0.97, respectively. XPS and secondary ion mass spectrometry (SIMS) profiles of $\text{Cu}(\text{InGa})\text{Se}_2$ films and CuInSe_2 single crystals exposed to chemical baths without thiourea also show evidence of indiffusion or electromigration of Cd [136].

13.4.3 Other Deposition Methods

In the early days of $\text{Cu}(\text{InGa})\text{Se}_2$ research, vacuum evaporation of 2 to 3- μm -thick CdS was the standard method to fabricate the junction and 9.4% efficiency was obtained with

pure CuInSe₂ absorbers [14]. With evaporation it is difficult to nucleate and grow very thin continuous CdS layers such as those normally used in current state-of-the-art Cu(InGa)Se₂ devices, and the optical transmission of the window will be limited to energies less than the CdS band gap, 2.4 eV. Substrate temperatures of 150 to 200°C are used to obtain good optical and electrical properties of the evaporated CdS films. This is substantially higher than the substrate temperature used for chemical bath deposition. Improved device performance was achieved by alloying the evaporated CdS with ZnS [15]. Mixed (CdZn)S has a wider band gap, allowing increased optical transmission, and better lattice match to Cu(InGa)Se₂ than CdS.

The main drawback with vacuum evaporation is poor conformal coating resulting in nonuniform and incomplete coverage of the sometimes relatively rough Cu(InGa)Se₂ films. Sputter deposition leads to more conformal coverage. The general success of sputtering for industrial large-area deposition motivated the exploration of sputter-deposited CdS buffer layers. Using optical emission spectroscopy to control the sputtering process, Cu(InGa)Se₂ devices with efficiencies up to 12.1% were fabricated, as compared to 12.9% for reference cells with chemical bath-deposited CdS [137]. Both evaporation and sputtering are vacuum processes, which can be incorporated in-line with other vacuum processing steps and do not create any liquid wastes. Still, CBD remains the preferred process for the CdS layer owing to its advantages in forming thin conformal coatings.

Atomic layer chemical vapor deposition (ALCVD) is a method that also allows accurate control of the growth of thin conformal layers [138]. The method is being industrially used for deposition of another II-VI compound, ZnS. Inorganic precursors for deposition of CdS require the substrate temperature to be excessively high (>300°C) and work with organic precursors has been limited. The strong driving force for replacement of the environmentally nondesirable cadmium has focused the development of ALCVD on materials other than CdS. This is also valid for regular CVD, although some metal organic CVD (MOCVD) work has been reported. The full potential for chemical vapor-deposited CdS has therefore not been explored.

Electrodeposition can be used to deposit CdS films but its use has not been reported in Cu(InGa)Se₂ devices.

13.4.4 Alternative Buffer Layers

The cadmium content in Cu(InGa)Se₂ PV modules with CBD CdS buffer layers is low. Investigations show that the cadmium in Cu(InGa)Se₂ modules can be handled safely, both with respect to environmental concerns and hazards during manufacturing (see Section 13.6.5). In spite of this, it would be preferable to eliminate cadmium in new products. There are in principle two approaches to Cd-free devices: (1) finding a buffer material that replaces CdS and (2) omitting the CdS layer and depositing ZnO directly onto the Cu(InGa)Se₂ film. In practice, the two approaches tend to merge when the chemical bath deposition of CdS is replaced with a surface treatment of the Cu(InGa)Se₂ with no or negligible film deposition before the subsequent deposition of the ZnO.

A number of approaches and materials have been tried. A selection of promising results are presented in Table 13.3.

Table 13.3 Performance of Cu(InGa)Se₂ thin-film solar cells with various buffer layers and junction-formation methods alternative to chemical bath deposition of CdS

Buffer material	Deposition method	Efficiency [%]	V _{OC} [mV]	J _{SC} [mA/cm ²]	FF [%]	Reference
None		10.5 ^a	398	39.0	68	[139]
None		15.0 ^b	604	36.2	69	[1]
ZnO	MOCVD	13.9 ^a	581	34.5	69	[140]
ZnO	ALCVD	11.7	512	32.6	70	[141]
Zn treatment	ZnCl ₂ solution	14.2 ^b	558	36.3	70	[142]
Zn(O,S,OH) _x	Chemical bath	14.2 ^{c,d}	567 ^e	36.6 ^e	68	[143]
ZnS	Chemical bath	16.9 ^{a,b}	647	35.2	74	[144]
Zn treatment + ZnS	Chemical bath + ILGAR ^f	14.2	559	35.9	71	[145]
Zn(Se,OH)	Chemical bath	13.7 ^{b,d}	535	36.1	71	[146]
ZnSe	ALCVD	11.6 ^a	502	35.2	65	[147]
ZnSe	MOCVD	11.6	469	35.8	69	[148]
In _x Se _y	Coevaporation	13.0 ^a	595	30.4	72	[149]
ZnIn _x Se _y	Coevaporation	15.1	652	30.4	76	[150]
In _x (OH,S) _y	Chemical bath	15.7 ^{a,b}	594	35.5	75	[151]
In ₂ S ₃	ALCVD	13.5	604	30.6	73	[152]

^aActive area^bWith antireflection layer^cMinimodule^dConfirmed^eRecalculated to single-cell values^fIon Layer Gas Reaction

When the numbers in Table 13.3 are analyzed, one must keep in mind that the quality of the Cu(InGa)Se₂ layer varies significantly between the experiments. For example, in the early results with direct ZnO [139], the reference cells with chemical bath–deposited CdS showed 12.4% efficiency, whereas the 15% efficiency results [1] are obtained from Cu(InGa)Se₂, which at best yielded an efficiency of 18.8%. On the other hand, an inferior junction-formation method may cause a larger degradation of cell efficiency at higher efficiency levels, since its defects may be relatively more important to the cell performance. In order to evaluate the various Cd-free junction-formation methods from that respect, the efficiency from each experiment is displayed in Figure 13.13 together with its reference, or estimation thereof. In most cases, the Cd-free device is comparable to the CBD–CdS device within typical variations.

Altogether, it appears as if there are several possibilities for obtaining high efficiency without Cd. All the listed methods include one or more of the elements Zn, In, and S. Zn is directly included in most of the buffer materials or indirectly as ZnO transparent contact with In_xSe_y, In(OH,S)_x, and In₂Se₃. Indications that *n*-type doping with Zn occurs similarly to that with Cd have been found by the treatment of Cu(InGa)Se₂ in Cd and Zn solutions [136], and are consistent with junction formation by solid-state diffusion into single crystals [132].

In Figure 13.13 a slight tendency can be noted toward larger difference between Cd-free and CdS reference cells for the direct ZnO approaches. It appears as if a buffer layer between the Cu(InGa)Se₂ and the ZnO is beneficial. Such a layer could passivate the

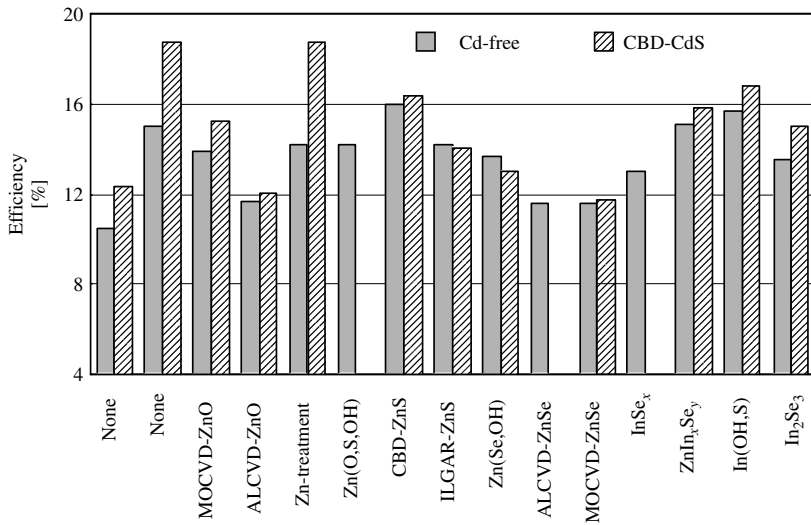


Figure 13.13 The efficiency of Cu(InGa)Se₂ solar cells with a selection of Cd-free junction-formation methods together with corresponding values of Cu(InGa)Se₂ cells with chemical bath-deposited CdS

Cu(InGa)Se₂ surface, which would reduce the recombination in a shallow *n*-type emitter, and possibly also serve to protect the junction and near-surface region during subsequent deposition of the transparent contact materials.

13.4.5 Transparent Contacts

The early Cu(InGa)Se₂ devices used CdS doped with In or Ga as front-contact layers in addition to the CdS buffer layer. Short wavelength light (<520 nm) was absorbed near the surface in the thick CdS layer and did not generate any photocurrent. When chemical bath deposition allowed CdS buffer layers to be thin enough such that it no longer limited the short wavelength collection in the Cu(InGa)Se₂, photocurrent could be gained by increasing the band gap of the contact layer. Since the contact layer must also have high conductivity for lateral current collection, the obvious choice is a transparent conducting oxide (TCO), a class of materials used in such devices as displays and low-emission coatings on window glass panes. There are three main materials in this class: SnO₂, In₂O₃:Sn (ITO), and ZnO. SnO₂ requires relatively high deposition temperatures that restrict the potential in Cu(InGa)Se₂ devices that cannot withstand temperatures greater than 200 to 250°C after CdS is deposited. ITO and ZnO can both be used, but the most common material is ZnO, favored by potentially lower material costs. A good overview of TCO thin-film materials can be found in Reference [153].

The most commonly used low-temperature deposition method for TCO films is sputtering. ITO layers are routinely fabricated on an industrial scale using dc sputtering. Industrial practice is to use ceramic ITO targets and to sputter in an Ar:O₂ mixture. Typical sputter rates range between 0.1 to 10 nm/s, depending on the application [154].

Sputtering of doped ZnO films is not as developed as is sputtering of ITO. Nevertheless, it is the preferred method for depositing the transparent front contact on Cu(InGa)Se₂

devices, with and without CBD–CdS, in the majority of the R&D groups. Typically, ZnO:Al films are deposited by radio frequency (rf) magnetron sputtering from ceramic ZnO:Al₂O₃ targets with 1 or 2 weight% Al₂O₃. In large-scale manufacturing, dc sputtering from ceramic targets is favored since it requires simpler equipment and offers higher deposition rates [155].

Reactive dc sputtering from Al/Zn alloy targets has also been used in the fabrication of Cu(InGa)Se₂/CdS devices with the same performance as with rf sputtered ZnO:Al [156]. The use of Zn/Al alloy targets allows lower costs than ceramic ZnO:Al₂O₃ targets, but reactive sputtering requires very precise process control owing to the so-called hysteresis effect [157] so that optimal optoelectronic properties are achieved only within a very narrow process window. Deposition rates in 4 to 5 nm/s range have been achieved.

Chemical vapor deposition (CVD) provides another deposition option and is used by one commercial manufacturer of Cu(InGa)Se₂ modules to deposit ZnO [158]. The reaction occurs at atmospheric pressure between water vapor and diethylzinc and the films are doped with fluorine or boron.

ALCVD deposition of ZnO has also been tested [159]. The atomic layer by atomic layer growth gives very low deposition rates, but the surface-controlled growth process gives uniform layers within a wide process window concerning reactant flow. This allows large batches to be processed, resulting in a reasonable throughput in spite of the limited growth rate.

As with the Mo back contact, the requirements for sheet resistance of the transparent contact layer will depend on the specific cell or module design. Typically, small area cells use layers with 20–30 Ω/□, while modules may require 5–10 Ω/□. In either case, the sheet resistance is usually controlled by the layer thickness.

13.4.6 Buffer Layers

It is common practice to use a buffer layer of undoped high-resistivity (HR) ZnO before sputter deposition of the TCO layer. Depending on the deposition method and conditions, this layer may have a resistivity of 1–100 Ω cm compared to the transparent contact with 10⁻⁴–10⁻³ Ω cm. Typically, 50 nm of HR ZnO is deposited by rf magnetron sputtering from an oxide target.

The gain in performance by using an HR ZnO buffer layer in ordinary devices with CBD–CdS is related to the CdS thickness [156, 160, 161]. One explanation of the role of a ZnO buffer layer is given by [160] as resulting from locally nonuniform electronic quality of the Cu(InGa)Se₂ layer that can be modeled by a parallel diode with high recombination current. The influence of these regions on the overall performance is reduced by the series resistance of the HR ZnO layer. This series resistance has a negligible effect on the performance of the dominant parts of the device area. A related explanation would attribute the local areas with poor diode characteristics caused by pinholes in the CdS layer, which create parallel diodes with a Cu(InGa)Se₂/ZnO junction. In this case improved diode quality due to the ZnO buffer would improve overall performance. Either case is consistent with the observation that a beneficial effect from the ZnO buffer is not observed when the CBD–CdS layer is thick enough [161].

Another potential reason for using an HR ZnO buffer layer is to add protection of the interface region from sputter damage induced during deposition of the TCO layer which typically requires more harsh conditions. This seems to be particularly important for some alternative Cd-free buffer layers or with dc magnetron-sputtered TCO layers [162].

13.4.7 Device Completion

In order to contact laboratory test cells, a metal contact is deposited onto the TCO layer. It is shaped as a grid with minimum shadow area in order to allow as much light as possible into the device. Solar cell measurement standards recommend a minimum cell area of 1 cm², but many labs routinely use cells in the order of 0.5 cm². The metal grid contact can be made by first depositing some tens of nanometers of Ni to prevent the formation of a high resistance oxide layer, and subsequently depositing a few micrometers of Al. Evaporation through an aperture mask is a suitable deposition method.

After deposition of the metal grid, the total cell area is defined by removing the layers on top of the Mo outside the cell area by mechanical scribing or laser patterning. Alternatively, just the layers on top of the Cu(InGa)Se₂ can be removed, by photolithography and etching, since the lateral resistance of the Cu(InGa)Se₂ prevents collection outside the cell area.

The only significant difference in the device layers between lab cells and modules is the thickness of the TCO. Modules normally do not have any grid that assists in current collection over the cell area, so a substantially thicker TCO layer, that is, higher sheet conductivity, is needed in order to keep resistive losses low. A TCO layer with higher sheet conductivity may also have lower optical transmission in the infrared due to increased free-carrier absorption resulting in a decreased photocurrent.

13.5 DEVICE OPERATION

Cu(InGa)Se₂ solar cells have achieved efficiencies approaching 20%, the highest of any thin-film solar cells, largely by empirical processing improvements and in spite of relatively poor understanding of the underlying mechanisms and electronic defects that control the device behavior. However, a more complete picture of the device operation is emerging to enable both a better understanding of the devices and identification of pathways to further improvements.

The operation of Cu(InGa)Se₂/CdS solar cells is characterized by high quantum efficiency (QE) and short-circuit current. The open-circuit voltage increases with the band gap of the absorber layer and is insensitive to grain boundaries and defects at the Cu(InGa)Se₂/CdS interface. A basic device model can be constructed in which the voltage is limited by recombination through bulk trap states in the space charge region of the Cu(InGa)Se₂ absorber layer. Recombination at the Cu(InGa)Se₂/CdS interface is minimized by proper doping and band alignment or surface treatment to create an effective n -type inversion layer in the near-junction region of the absorber layer.

The device operation can be described by identifying loss mechanisms. These can be divided into three categories. The first are optical losses that limit generation of carriers and therefore the device current. The second are recombination losses that limit

the voltage. Finally, there are parasitic losses, such as series resistance, shunt conductance, and voltage-dependent current collection, which are most evident by their effect on the fill factor but can also reduce J_{SC} and V_{OC} .

13.5.1 Light-generated Current

The highest efficiency Cu(InGa)Se₂ device has $J_{SC} = 35.2 \text{ mA/cm}^2$ [1] out of a possible 42.8 mA/cm^2 available for a band gap of 1.12 eV under AM1.5 global illumination. Quantum efficiency is a valuable tool to characterize the losses responsible for this difference in current. The light-generated current is the integral of the product of the external quantum efficiency (QE_{ext}) and the illumination spectrum. QE_{ext} is controlled by the band gap of the Cu(InGa)Se₂ absorber layer, the CdS and ZnO window layers, and a series of loss mechanisms. These losses are illustrated in Figure 13.14 where typical QE curves at two different voltage biases, 0 V and -1 V , are shown. The QE curve at -1 V is slightly higher at longer wavelengths. The current loss under 100 mW/cm^2 illumination is listed in Table 13.4 for each of these mechanisms. Losses 1 to 5 are optical and 6 is electronic. In practice, the magnitude of each of these losses will depend on the details of the device design and optical properties of the specific layers. The losses include the following:

1. Shading from a collection grid used for most devices. In an interconnected module this will be replaced by the area used for the interconnect, as discussed in Section 13.6.2.
2. Front surface reflection. On the highest-efficiency devices this is minimized with an antireflection layer for which an evaporated MgF₂ layer with thickness $\sim 100 \text{ nm}$ is commonly used. However, this is not practical in a module in which a cover glass is typically required.

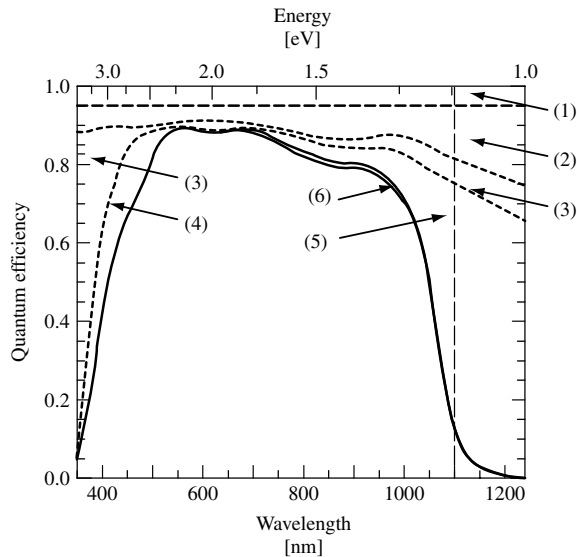


Figure 13.14 Quantum efficiency (solid lines) at 0 V and -1 V and optical losses for a Cu(InGa)Se₂/CdS solar cell in which the Cu(InGa)Se₂ has $E_g = 1.12 \text{ eV}$

Table 13.4 Current loss, ΔJ , for $E > 1.12$ eV due to the optical and collection losses illustrated in Figure 13.14 for a typical Cu(InGa)Se₂/CdS solar cell

Region in Figure 13.14	Optical loss mechanism	ΔJ [mA/cm ²]
(1)	Shading from grid with 4% area coverage	1.7
(2)	Reflection from Cu(InGa)Se ₂ /CdS/ZnO	3.8
(3)	Absorption in ZnO	1.8
(4)	Absorption in CdS	0.8
(5)	Incomplete generation in Cu(InGa)Se ₂	1.9
(6)	Incomplete collection in Cu(InGa)Se ₂	0.4

3. Absorption in the TCO layer. Typically, there is 1 to 3% absorption through the visible wavelengths, which increases in the near IR region, $\lambda > 900$ nm, where free-carrier absorption becomes significant, and for $\lambda < 400$ nm near the ZnO band gap.
4. Absorption in the CdS layer. This becomes appreciable at wavelengths below ~ 520 nm corresponding to the CdS band gap 2.42 eV. The loss in QE for $\lambda < 500$ nm is proportional to the CdS thickness since it is commonly assumed that electron–hole pairs generated in the CdS are not collected. Figure 13.14 shows a device with a ~ 30 nm-thick CdS layer. In practice, the CdS layer is often thicker and the absorption loss greater.
5. Incomplete absorption in the Cu(InGa)Se₂ layer near the Cu(InGa)Se₂ band gap. Band gap gradients, resulting from composition gradients in many Cu(InGa)Se₂ films, also affect the steepness of the long-wavelength part of the QE curve. If the Cu(InGa)Se₂ is made thinner than ~ 1.0 μm , this loss becomes significant [163] because of insufficient absorption at long wavelengths.
6. Incomplete collection of photogenerated carriers in the Cu(InGa)Se₂, discussed below.

QE_{ext} is then given by

$$QE_{\text{ext}}(\lambda, V) = [1 - R(\lambda)][1 - A_{\text{ZnO}}(\lambda)][1 - A_{\text{CdS}}(\lambda)] QE_{\text{int}}(\lambda, V) \quad (13.5)$$

where R is the total reflection, including the grid shading, A_{ZnO} is the absorption in the ZnO layer and A_{CdS} is the absorption in the CdS layer. QE_{int} , the internal quantum efficiency, is the ratio of photogenerated carriers collected to the photon flux that arrives at the absorber layer and can be approximated by [164]

$$QE_{\text{int}}(\lambda, V) \cong 1 - \frac{\exp[-\alpha(\lambda)W(V)]}{\alpha L + 1} \quad (13.6)$$

where α is the Cu(InGa)Se₂ absorption coefficient, W is the space charge width in the Cu(InGa)Se₂, and L is the minority carrier diffusion length. This approximation assumes that all carriers generated in the space charge region are collected without recombination loss. Since W is a function of the applied voltage bias, QE_{int} and total light-generated current are, in general, voltage-dependent, so the latter can be written as $J_L(V)$. Values of W in the range 0.1–0.5 μm have been reported for typical cells at 0 V.

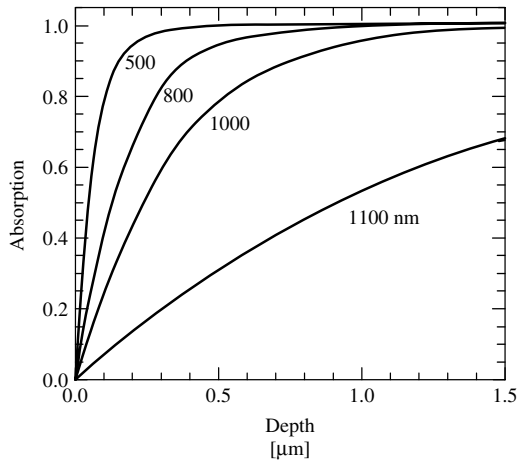


Figure 13.15 Absorption of light with different wavelengths in Cu(InGa)Se₂ with $x = 0.2$

The absorption of light with different wavelengths in Cu(InGa)Se₂ with $x = 0.2$ is shown in Figure 13.15. At thickness d , this is given by $\exp(-\alpha d)$ with α calculated at each wavelength using equation (13.3) and the data in Figure 13.6. If the effective collection length $L + W$ is smaller than 0.5 to 1 μm , a significant fraction of electrons are generated deeper into the Cu(InGa)Se₂ layer, and their incomplete collection can be a significant loss mechanism for Cu(InGa)Se₂ devices [116, 165]. The effect of $J_L(V)$ on current–voltage behavior increases with forward voltage bias and therefore has its largest effect on the fill factor and V_{OC} [166, 167]. The effect of a voltage-dependent collection on J_{SC} is illustrated in Figure 13.14 by the increase in QE measured at -1 V applied voltage bias compared to that measured at 0 V.

13.5.2 Recombination

The current–voltage ($J-V$) behavior of Cu(InGa)Se₂/CdS devices can be described by a general diode equation:

$$J = J_D - J_L = J_O \exp\left[\frac{q}{AkT}(V - R_S J)\right] + GV - J_L \quad (13.7)$$

with the diode current J_O given by:

$$J_O = J_{O0} \exp\left(-\frac{\Phi_b}{AkT}\right) \quad (13.8)$$

The ideality factor A , barrier height Φ_b , and prefactor J_{O0} depend on the specific recombination mechanism that dominates J_O , while the series resistance R_S and shunt conductance G are losses that occur in series or parallel with the primary diode. General expressions for A , Φ_b , and J_{O0} in the cases of recombination through the interface, space charge region, or bulk of the absorber layer can be found in various textbooks (see, for example [168]).

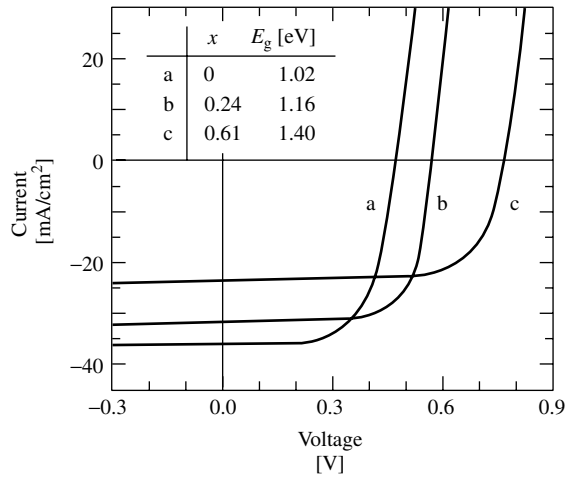


Figure 13.16 Current–voltage curves for Cu(InGa)Se₂/CdS solar cells with different relative Ga content giving (a) $E_g = 1.02$, (b) 1.16, and (c) 1.4 eV

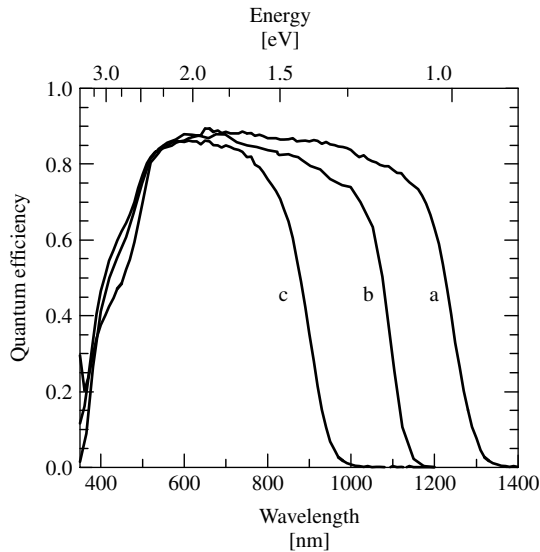


Figure 13.17 Quantum efficiency curves for the devices shown in Figure 13.16

To understand the specific diode behavior of Cu(InGa)Se₂/CdS solar cells, it is instructive to look at the effect of the Cu(InGa)Se₂ band gap, varied by changing $x \equiv \text{Ga}/(\text{In} + \text{Ga})$, and temperature. Figures 13.16 and 13.17 show J – V and QE curves for 3 devices with $x = 0, 0.24$, and 0.61 , corresponding to $E_g = 1.02, 1.16$, and 1.40 eV, respectively. V_{OC} increases and the position of the long-wavelength QE edge shifts to greater energy as E_g increases. Figure 13.18 shows the temperature dependence of V_{OC} for these devices. In each case, as $T \rightarrow 0$, $V_{OC} \rightarrow E_g/q$. Thus, combining equations (13.7)

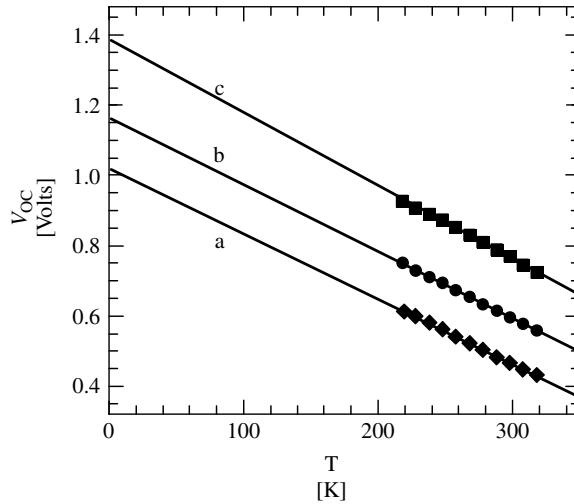


Figure 13.18 Temperature dependence of V_{OC} for the devices shown in Figure 13.16

and (13.8) and assuming $G \ll J_L/V_{OC}$, the open-circuit voltage becomes

$$V_{OC} = \frac{E_g}{q} - \frac{AkT}{q} \ln \left(\frac{J_{OO}}{J_L} \right) \quad (13.9)$$

with the barrier height $\Phi_b = E_g$.

The different recombination paths are effectively connected in parallel so that V_{OC} will be controlled by the single dominant mechanism with the highest current. The values of Φ_b and A can be used to distinguish between recombination in the bulk absorber, in the space charge region of the $\text{Cu}(\text{InGa})\text{Se}_2$, or at the $\text{Cu}(\text{InGa})\text{Se}_2/\text{CdS}$ interface [27, 169]. Each of the curves in Figure 13.16 can be fit to equation (13.7) with $A = 1.5 \pm 0.3$. For a wide range of thin-film solar cells, it has been demonstrated that $V_{OC}(T \rightarrow 0) = QE_g$ and $1 < A < 2$ similar to the data above. Specifically, this has been shown for CuInSe_2 [116, 170] and $\text{Cu}(\text{InGa})(\text{SeS})_2$ [171] devices, independent of the $(\text{CdZn})\text{S}$ buffer-layer band gap [170], and for a variety of different absorber-layer deposition processes [172]. These results for Φ_b and A indicate that $\text{Cu}(\text{InGa})\text{Se}_2/\text{CdS}$ solar cells operate with the diode current controlled by Shockley–Read–Hall type recombination in the $\text{Cu}(\text{InGa})\text{Se}_2$ layer [168]. This recombination is greatest through deep trap states in the space charge region of the $\text{Cu}(\text{InGa})\text{Se}_2$ where there are comparable supplies of electrons and holes available, that is, $p \approx n$. The variation in A between 1 and 2 depends on the energies of the deep defects that act as dominant trap states [173]. As these states move toward the band edges, $A \rightarrow 1$ and the recombination becomes closer to band-to-band bulk recombination.

These observations exclude recombination in the neutral bulk region of the absorber layer, which should give $A = 1$. Interface recombination would give $\Phi_b < E_g[\text{Cu}(\text{InGa})\text{Se}_2]$ with a dependence on the $(\text{CdZn})\text{S}$ band gap, although A might vary from 1 to >2 [174]. Back surface recombination at the $\text{Mo}/\text{Cu}(\text{InGa})\text{Se}_2$ interface will

be negligible so long as the minority-carrier diffusion length is small compared to the total Cu(InGa)Se₂ thickness. If $L + W \approx d$, a back surface field may be implemented, for example, by increasing the Ga content near the Mo to give a band gap gradient.

In real Cu(InGa)Se₂ materials with imperfect structures, trap defects will not exist at discrete energies but form defect bands or tails at the valence and conduction bands. Then the total recombination current can be determined by integrating over the defect spectrum. Recombination through an exponential bandtail was used to explain the temperature dependence in A observed in some devices [175]. Analysis of the temperature dependence of A was further explained by a tunneling enhancement of the recombination current, particularly at reduced temperatures [176]. The same defects in the Cu(InGa)Se₂ space charge region that control recombination were also used to explain observed metastabilities including persistent photoconductivity and open-circuit voltage decay [177]. Admittance spectroscopy has proved to be a useful tool to characterize the distribution of electronic defects in Cu(InGa)Se₂/CdS solar cells [178] and the density of an acceptor state ~ 0.3 eV from the valence band has been correlated to V_{OC} [179]. The minority-carrier lifetime is another valuable parameter to characterize Cu(InGa)Se₂/CdS devices. Transient photocurrent [180] and time-resolved photoluminescence [167] measurements each were used to calculate lifetimes in the range of 10 to 100 ns for high-efficiency devices. Still, a critical problem that remains is to identify which of the calculated or measured defects discussed in Section 13.2 provides for the recombination traps that limit voltage in the devices. A good review of the characterization of electronic defects and their effect on Cu(InGa)Se₂ devices is provided by Rau and Schock [27].

In practice, analysis of $J-V$ data is commonly used to determine the diode parameters J_O , A , and Φ_b . This requires that R_S and G are negligible, or suitable corrections are made to the data, and that J_L is independent of V . Failure to account for $J_L(V)$ can lead to errors in analysis of current–voltage data [166] and in many cases the fundamental diode parameters cannot be reliably determined except from $J-V$ data measured in the dark. In addition, it must be verified that there are no nonohmic effects at any contacts or junctions, which cause the appearance of a second diode for which equation (13.7) does not account. Such nonohmic behavior is often observed at reduced temperatures [170, 172]. Once it has been demonstrated that all these parasitic effects are negligible, or corrections have been made, then J_O can be determined by a linear fit to a semilogarithmic plot of $J + J_L$ versus $V - R_S J$ and A can be determined from the slope of the derivative dV/dJ versus $1/J$ in forward bias [181], or both J_O and A can be obtained by a least squares fit to equation (13.7). Finally, Φ_b can be determined from the temperature dependence of V_{OC} as in Figure 13.18.

It must be noted that most descriptions of transport and recombination ignore the effect of grain boundaries, implicitly assuming that grains are columnar and all transport can proceed without crossing grain boundaries. However, this is rarely, if ever, strictly true, so a comprehensive description of Cu(InGa)Se₂ solar cells must account for the possibility of recombination at grain boundaries reducing current collection or voltage. The effect of grain boundaries can be expressed as an effective diffusion length, leading to the conclusion that grain-boundary recombination is small [27]. This can occur if the grain boundaries are doped more p -type than the bulk grains so that electrons are prevented from reaching and recombining at defects in the grain boundaries [169].

13.5.3 The Cu(InGa)Se₂/CdS Interface

It may seem surprising that recombination at the Cu(InGa)Se₂/CdS interface does not limit V_{OC} since, in processing Cu(InGa)Se₂ solar cells, no special efforts are made to match lattices or reduce interface defects and the devices are typically exposed to air between the Cu(InGa)Se₂ and CdS depositions. This can be explained by type inversion of the near-junction region of the Cu(InGa)Se₂ induced by the band alignment and doping [169, 182–184]. In this case, the Fermi level at the interface is close to the conduction band so that electrons in the near surface region of the Cu(InGa)Se₂ are effectively majority carriers and there is an insufficient supply of holes available for recombination through the interface states. It has alternatively been proposed that doping due to Cd diffusion during the chemical bath deposition of CdS results in the formation of an n -type emitter and a p - n homojunction in the Cu(InGa)Se₂ [136]. This would require the junction to remain very close to the Cu(InGa)Se₂/CdS interface to minimize recombination of carriers generated near the interface, and would therefore be very process-specific.

The Cu(InGa)Se₂/CdS band diagram shown in Figure 13.19 demonstrates that the conduction-band offset ΔE_C between the CdS and the Cu(InGa)Se₂ is critical for creating the type inversion in the Cu(InGa)Se₂. In this diagram, the bulk Cu(InGa)Se₂ layer is p -type with E_g depending on the relative Ga concentration, the CdS layer is n -type with $E_g = 2.4$ eV and is totally depleted, and the bulk ZnO n^+ -layer has $E_g = 3.2$ eV. A thin HR ZnO layer between the n^+ -ZnO layer and the CdS is also assumed to be depleted. Positive ΔE_C indicates a spike in the conduction band, that is, the conduction-band minimum in the CdS is at higher energy than the conduction-band minimum of the Cu(InGa)Se₂. Figure 13.19 shows the case with $\Delta E_C = 0.3$ eV and a -0.3 eV conduction-band offset between the ZnO and the CdS [52]. Models of current transport and recombination have considered the effect of ΔE_C [184–187]. These models show that if ΔE_C is greater than about 0.5 eV, collection of photogenerated electrons in the Cu(InGa)Se₂ is impeded and

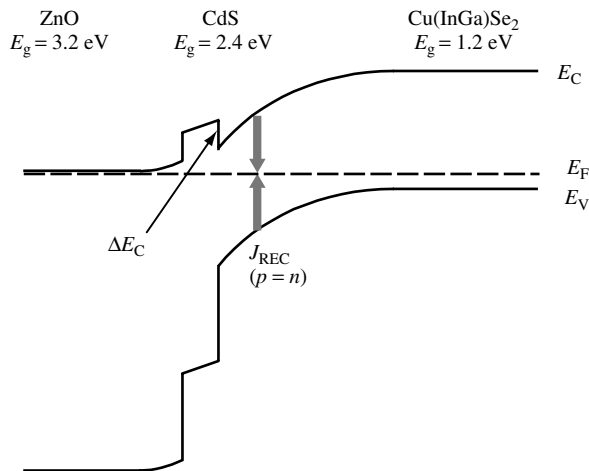


Figure 13.19 Band diagram of a ZnO/CdS/Cu(InGa)Se₂ device at 0 V in the dark. Note that the recombination current J_{REC} is greatest where $p = n$ in the space charge region of the Cu(InGa)Se₂ and not at the interface

J_{SC} or FF is reduced sharply. With a smaller spike, electrons can be transported across the interface assisted by thermionic emission [185]. On the other hand, for sufficiently negative ΔE_C the induced type inversion of the Cu(InGa)Se₂ near the interface is eliminated and interface state recombination will limit V_{OC} . An ODC layer at the surface of the absorber layer increases the band gap and primarily affects the valence band [188], so it may enhance type inversion near the junction. However, there is no convincing evidence that this layer exists in devices, so it is not shown in Figure 13.19.

Owing to its importance in the electronic behavior of Cu(InGa)Se₂/CdS devices, several efforts have been made to calculate or measure ΔE_C with varying results. Band-structure calculations gave $\Delta E_C = 0.3$ eV [189]. XPS and ultraviolet photoelectron spectroscopy (UPS) measurements of the valence band alignment indicate a positive ΔE_C between 0.2 and 0.7 eV [52, 190, 191]. These electron spectroscopy methods require ultrahigh vacuum conditions that necessitates that the CdS is deposited by vacuum evaporation. It is possible that the interface formation is different when CdS is grown by chemical bath deposition, for example, due to chemical interdiffusion, resulting in a different alignment of the conduction bands. Indirect measurements of the junction formed with chemical bath deposited CdS using a surface photovoltage technique gave $\Delta E_C = -0.1$ eV [192]. Finally, inverse photoemission spectroscopy showed that substantial chemical intermixing occurs across the interface resulting in $\Delta E_C = 0$ [193].

13.5.4 Wide and Graded Band Gap Devices

While the highest efficiency devices generally have $Ga/(In + Ga) \approx 0.1-0.3$ giving $E_g \approx 1.1-1.2$ eV, significant effort has been made to develop high-efficiency solar cells based on wider band gap alloys. This is driven primarily by the expectation that wider band gap alloys will yield higher module efficiencies due to reduced losses related to the trade-off between higher voltage and lower current at maximum power. The resulting reduction in power loss, proportional to I^2R , can be used to either (1) increase the module's active area by reducing the spacing between interconnects or (2) decrease the optical absorption in the TCO layers since they can tolerate greater resistance. Wider band gap should give a lower coefficient of temperature for the device or module output power, which will improve performance at the elevated temperatures experienced in most real terrestrial applications. Wide band gap devices could also be used as the top cell in a tandem or multijunction cell structure.

The wider band gap materials that have attracted the most attention for devices are Cu(InGa)Se₂ and CuInS₂. CuGaSe₂ has $E_g = 1.68$ eV, which is well suited for the wide band gap cell in tandem structures. CuInS₂ has $E_g = 1.53$ eV, which could be nearly optimum for a single-junction device. The highest-efficiency devices based on CuInS₂ are deposited with Cu-rich overall composition and then the excess Cu, in the form of a Cu_xS second phase, is etched away before CdS deposition [194]. Cu(InAl)Se₂ solar cells have also been considered [195]. Since CuAlSe₂ has $E_g = 2.7$ eV, the alloy requires smaller changes in relative alloy concentration and lattice parameter from CuInSe₂ than the Ga alloys to achieve comparable band gap. The highest efficiency devices of different alloys are listed in Table 13.5.

The effects of Ga incorporation on device behavior are not fully understood. The addition of a small amount of Ga to CuInSe₂ increased the open-circuit voltage even when

Table 13.5 Highest-efficiency devices for different alloy absorber layers

Material	E_g [eV]	Efficiency [%]	V_{OC} [%]	J_{SC} [mA/cm ²]	FF [%]	Reference
CuInSe ₂	1.02	15.4	515	41.2	72.6	[80]
Cu(InGa)Se ₂	1.12	18.8	678	35.2	78.6	[1]
CuGaSe ₂	1.68	8.3	861	14.2	67.9	[196]
CuInS ₂	1.53	11.4	729	21.8	71.7	[197]
Cu(InAl)Se ₂	1.16	16.9	621	36.0	75.5	[198]

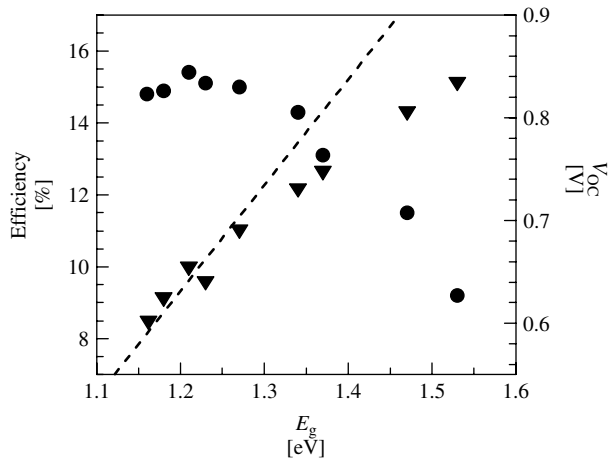


Figure 13.20 Efficiency (▼) and V_{OC} (●) as a function of Cu(InGa)Se₂ band gap, varied by increasing the relative Ga content, (From Shafarman W, Klenk R, McCandless B, *Proc. 25th IEEE Photovoltaic Specialist Conf.*, 763–768 (1996) [199]. The dashed line has slope $\Delta V_{OC}/\Delta E_g = 1$

the Ga was confined to the back of the absorber and did not increase the band gap in the space charge region [105]. The effect of increasing band gap in Cu(InGa)Se₂/CdS solar cells on V_{OC} and efficiency is shown in Figure 13.20. Efficiency is roughly independent of band gap for $E_g < 1.3$ eV or Ga/(In + Ga) < 0.5 [165, 199]. With even wider band gap, V_{OC} increases to greater than 0.8 V, but the efficiency decreases. This indicates poorer electronic properties of the Cu(InGa)Se₂ absorber layer, which has two effects: voltage-dependent current collection [165], which causes the fill factor to decrease, and increased recombination [200], which reduces V_{OC} below that expected from equation (13.9) [27]. The dashed line in Figure 13.20 shows a line with slope $\Delta V_{OC}/\Delta E_g = 1$. Ideally, the increase in V_{OC} would have only a slightly smaller slope due to the dependence on J_L in the second term of equation (13.9). Admittance spectroscopy showed a correlation between the recombination and the density of a defect with an activation energy ~ 0.3 eV, which increases with E_g [200]. Transient photocapacitance measurements showed a defect band centered at 0.8 eV from the valence band, which moves closer to midgap for increasing band gap and therefore becomes more efficient as a recombination trap [201]. As the band gap becomes wider, type inversion of the absorber layer near the interface may no longer occur and interface recombination can become more significant. Analysis of both CuGaSe₂ [202] and CuInS₂ [203] solar cells showed that the low open-circuit voltages

could be caused by either space charge or interface recombination, depending on the device preparation.

Band gap gradients formed by controlled incorporation of Ga or S have been proposed as a means to increase device efficiency by separately reducing recombination and collection losses [19, 204–206]. A gradient in the conduction band from wide at the Cu(InGa)Se₂/Mo interface to narrow near the space charge region has been used to enhance minority-carrier collection [199, 206] and to reduce back surface recombination when the diffusion length is comparable to the film thickness [207]. Alternatively, a gradient from wide at the Cu(InGa)Se₂/CdS interface to narrow at the edge of the space charge region could reduce recombination and increase V_{OC} . In this case, the smaller band gap in the bulk portion of the device can still enable high optical absorption and J_{SC} [19, 206]. The most effective implementation of a surface band gap gradient may be the incorporation of S near the front surface [20] since the main effect is in lowering the valence band, instead of raising the conduction band as with Ga, and there should be less impact on collection of light-generated electrons.

13.6 MANUFACTURING ISSUES

The competitiveness of a PV technology will primarily be governed by its performance, stability, and costs. The best Cu(InGa)Se₂ cells and modules have demonstrated efficiency on a par with commercial crystalline silicon products. Long-term stability appears not to be a significant problem, as shown in field tests of prototype modules, but low-cost production remains to be demonstrated in practice.

It is evident that thin films have the potential to be produced at very low costs. Moisture barriers of aluminum films that are deposited on plastic foils to be used, for example, in potato chip bags cost less than 0.01 \$/m² to produce. This particular example is at the low end of production costs and more advanced functional coatings are in general substantially more expensive to manufacture. Thin film coatings on architectural glass cost on the order of 1 \$/m². Thus PV modules constructed from thin-film materials have the possibility for very low manufacturing costs. Whether Cu(InGa)Se₂ module production will be able to achieve this low-cost potential will depend on how well the process technology fulfills the requirements for material costs, throughput, and yield.

13.6.1 Processes and Equipment

Deposition processes can be either batch-type, in which a number of substrate plates are processed in parallel, or in-line, in which one substrate plate immediately follows the preceding one. In batch processing, a process step is completely finished before the next batch is started, whereas a substrate plate may enter an in-line process step before the previous substrate is finished in order to keep the line continuously running.

One common view on volume production is that in-line continuous processing is a prerequisite for low costs. Fabrication of large-area thin-film products with physical vapor deposition is often made in a continuous or quasi-continuous in-line system. However, the cost of a batch process can be equally low, provided the throughput is large enough. For manufacturing of Cu(InGa)Se₂ modules, this means that the CdS chemical bath deposition

can well fulfill low-cost production criteria even though it is normally a batch process. Similarly, growth of the Cu(InGa)Se_2 layer by batch selenization does not necessarily need to be associated with higher costs than Cu(InGa)Se_2 fabricated by in-line coevaporation, provided the cycle time is short enough or batch size large enough.

The commercial availability of large-area deposition systems depends on the specific process. Sputtering deposition is widely used for fabrication of large-area thin-film coatings of various kinds, for example, in the glass industry. Similar processes are used in the fabrication of most Cu(InGa)Se_2 modules for the Mo back contact and the TCO front contact, so the same type of equipment, available from a number of suppliers, can be used.

Sputtering is also typically used for deposition of the metal precursor films for fabrication of the Cu(InGa)Se_2 layer by a two-step process. The selenization step, however, requires specific custom-made process equipment. This could be selenization furnaces in which batches of plates with the precursor layers are exposed to a selenium-containing atmosphere or an in-line selenization chamber in which the plates are continuously transported through an environment with elemental selenium and substrate temperature control [208].

Elemental coevaporation of the Cu(InGa)Se_2 layer requires custom-made equipment including specially designed evaporation sources for uniform deposition of large-area substrates with accurate control. In-line evaporation using linear sources is a straightforward approach that is being developed at several laboratories and companies. An example of such a piece of equipment is illustrated in Figure 13.21.

The chemical bath deposition of CdS or Cd-free buffer layers is suitable for low-cost batch processing, in that it is a surface-controlled process that requires a limited solution volume. The equipment for dipping batches of Cu(InGa)Se_2 -coated substrate plates is relatively simple and can be custom-made. The dry buffer deposition methods under investigation have not been developed to a stage in which manufacturing is under consideration.

Chemical vapor-deposited doped ZnO as an alternative to sputtering is typically done as a batch process with a relatively small number of substrate plates deposited per

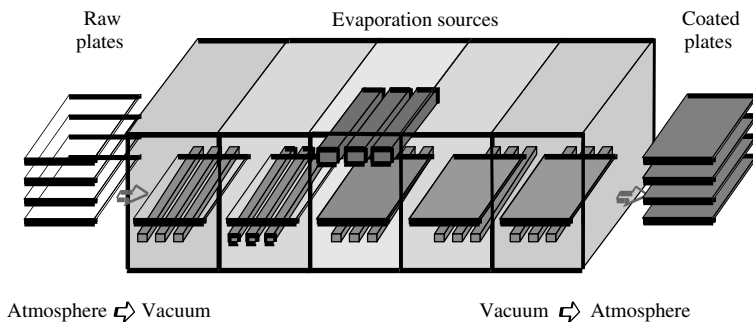


Figure 13.21 In-line coevaporation system for Cu(InGa)Se_2 with linear evaporation sources above the substrate plates and heaters below them [Courtesy of Zentrum für Sonnenenergie- und Wasserstoff-Forschung (ZSW)]. Reproduced by permission of Michael Powalla, ZSW Stuttgart, 2001

run. Throughput will eventually become an issue. However, in-line CVD processes have been developed, for example, in the manufacture of amorphous silicon solar modules.

13.6.2 Module Fabrication

Soda lime float glass is the substrate material that so far has given the best results in terms of both performance and reproducibility. It fulfills criteria on cost (3 \$/m² for 4-mm-thick glass in large volumes), smoothness, and stability, so it is well suited for commercial production. One limitation that needs to be addressed in the development of production processes is that soda lime glass starts to soften above 500°C. At the same time, the best PV properties of Cu(InGa)Se₂ are achieved at growth temperatures above 500°C. Plastic deformation due to glass softening is not acceptable in a module-production process and careful optimization of the time–temperature profile is needed to minimize the deformation.

Flexible substrate materials are attractive both for the possibility to make a lightweight flexible product with advantages for certain applications and for the possibility to deposit the thin-film materials in roll-to-roll processes, which are potentially cost-advantageous. Such roll-to-roll processing of semiconductor thin films was originally demonstrated with evaporation of CdS for solar cells [209]. The substrate materials that have shown promising results are polyimide, titanium, and steel [68, 69]. The drawbacks of polyimide are low-temperature tolerance, since the best polyimide films readily available can only withstand 400 to 450°C, and high thermal expansion. The main drawback of titanium and steel is their conductivity, which means that an electrically isolating layer is needed in order to allow monolithic series-interconnection of the cells. Such an isolation layer is not easy to make without local defects that will cause shunting of the cells. For these flexible substrate materials, sodium has to be supplied separately.

An essential cost advantage with thin-film PV modules as compared to silicon wafer–based PV modules is the possibility of monolithic interconnection. This allows modules to be fabricated directly, instead of first making cells followed by tabbing and stringing to make the series interconnection as required for silicon-wafer solar cells. A typical monolithic interconnection is illustrated schematically in Figure 13.22. The most common way to make the patterning is by using laser ablation for the Mo patterning (P1) and mechanical scribing for the two subsequent patterning steps (P2 and P3).

The final fabrication steps include attachment of electrical wires and buss bars. These are metal stripes that can be soldered, welded, or glued to contact areas near the edges of the substrate plates. Before lamination with a front cover glass, the thin-film layers are removed from the outer rim of the substrate plate in order to improve the adhesion to the lamination material, which is usually ethylene vinyl acetate (EVA). Edge sealing and framing finishes the product, but can be omitted for some applications.

13.6.3 Module Performance

The evolution of record efficiencies as reported from the certified measurement labs is displayed in Figure 13.23. The module efficiencies lag behind the cell efficiencies but follow the same basic trend. There are additional losses associated with making

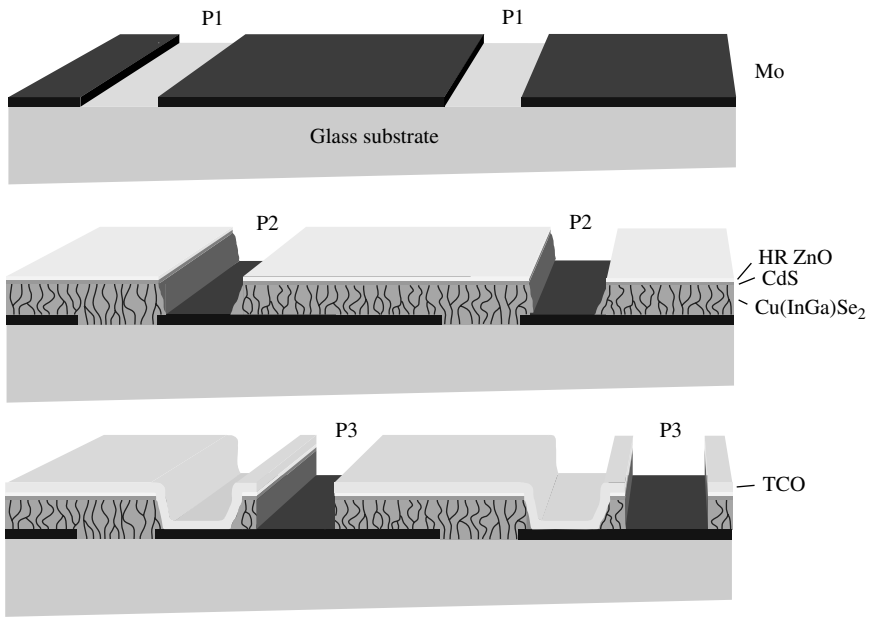


Figure 13.22 Schematic description of the manufacturing steps to make monolithic interconnections for thin-film Cu(InGa)Se_2 PV modules

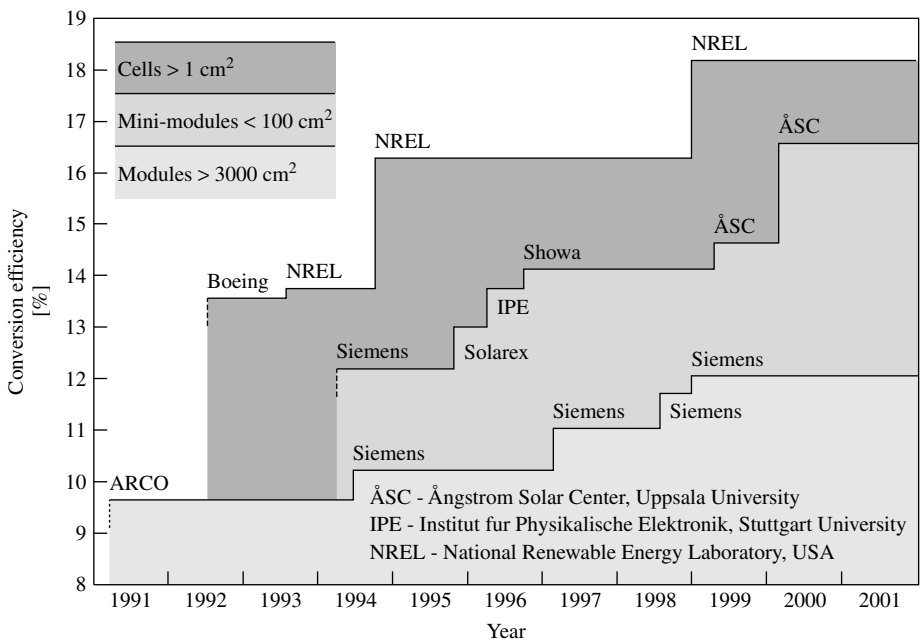


Figure 13.23 Evolution of Cu(InGa)Se_2 device record efficiencies in the past decade. All data are taken from the Solar Cell Efficiency Tables periodically published in *Progress in Photovoltaics*

series-interconnected modules instead of cells, both from series resistance and from inactive device area. In an optimized, conventional thin-film module design, these kinds of losses correspond to about 1% unit of efficiency. With a more advanced design using metal grids for interconnection, interconnect losses can be made nearly negligible [210]. Another kind of difference between modules and record cells is associated with the freedom to use higher process temperatures for cells that are not sensitive to deformed glass. These results are not necessarily relevant to module fabrication but indicate the potential of the materials.

In a product the initial efficiency is of little interest if it deteriorates after some time in operation. Cu(InGa)Se₂ modules fabricated by ARCO Solar and later Siemens Solar have shown stable performance in field tests over more than 12 years [3], as shown in Figure 13.24. On the other hand, severe degradation has been observed after exposure of cells to 85% relative humidity at 85°C for 1000 h [211], the so-called damp heat test, which is one of the certification tests in the IEC 61 646 protocol. While this test is rather severe and may not be relevant to thin-film modules, it shows the need for encapsulation techniques that minimize the exposure of the thin-film materials to moisture.

The outdoor module performance demonstrated in Figure 13.24 shows that Cu(InGa)Se₂ PV modules have the stability and performance to compete in any power application, be it stand-alone or grid-connected. Thin-film modules have a great advantage over silicon-wafer PV for consumer applications in which the power needed often is relatively small. The large substrate plates, which have a power of 40 W_p or more, can easily be cut into smaller pieces, to essentially any power specification. This is much less costly than making small crystalline-silicon modules in which each cell has to be cut into pieces before assembling the modules. Additionally, the patterning structure of the interconnects can be designed to fit a large variety of shape and voltage requirements. Aesthetically, the solid black appearance of Cu(InGa)Se₂ modules may be preferred to the nonuniform bluish appearance of the silicon-wafer modules in some building-integrated applications.

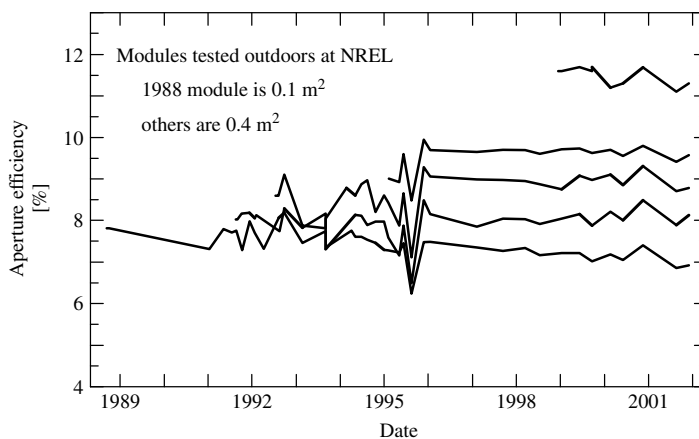


Figure 13.24 Examples of outdoor testing results at NREL of Cu(InGa)Se₂ modules showing stability over 12 years. Fluctuations in years 1992–1996 are due to changes in testing conditions. (Data courtesy of Shell Solar Industries)

Finally, for space applications, Cu(InGa)Se_2 thin-film solar cells offer potential advantages since the radiation tolerance is high as compared to crystalline-silicon solar cells [4, 5]. The potential to use a lightweight plastic substrate could lead to solar cells with very high specific power, that is, power divided by mass, which is critical for some space applications (see Chapter 10 for a more complete discussion). However, Cu(InGa)Se_2 space solar cell technology has not yet reached a commercial stage.

13.6.4 Production Costs

Material costs have direct and indirect components, and depend on the material yield of the deposition processes. The direct material costs, that is, the cost of the feedstock, will not be reduced by an increased volume of the production, depending only on the feedstock market price and how much material is needed in the film. The indirect costs, including preparation of sputtering targets or other source materials, will be reduced when production volumes are sufficiently large. The material yield, or fraction of the source material that ends up in the film, may be less than 50% for various thin-film processes. For sputtering, typically 30% of the target material ends up in the films.

In addition to materials, the other main production cost for thin-film modules is the capital cost of the equipment. To first order, any large-scale automated deposition equipment will have comparable price. Therefore, the throughput or production capacity will be very important for determining the capital cost.

Costs around 20 $\$/\text{m}^2$ for each thin-film deposition or process step may be acceptable in pilot production, but clear pathways toward costs in the range 1 to 5 $\$/\text{m}^2$ for large-volume production need to be identified. Throughput has a direct effect on cost. In an in-line process, this will depend on the substrate width and linear speed, which fundamentally depends on the deposition rate and desired thickness of the layer. If the deposition rate is relatively low, it can be compensated by having a long deposition zone in the system, for example, by having multiple targets in a sputtering system with only a relatively small increase in capital cost.

All cost advantages for thin films are lost if the production is not completed with high yield. The overall manufacturing yield can be broken down into electrical yield and mechanical yield. The electrical yield reflects the module reproducibility since it is the fraction of the modules produced which fulfill minimum performance criteria. The mechanical yield is the fraction of the substrates entering the production line that make it to the end. Mechanical losses result from broken glass substrates or malfunctioning equipment. In general, the overall yield should be well over 80%.

Another manufacturing cost is the energy usage. The energy payback time for Cu(InGa)Se_2 modules is expected to be fairly low; four months has been estimated by Alsema and van Engelenburg [212], compared to three years for crystalline-silicon modules [213].

Production-cost analyses result in a range of projected manufacturing costs. There are predictions of 1.5 to 2 $\$/\text{W}_p$ for first-generation Cu(InGa)Se_2 plants with a few MW_p yearly capacity and projected costs of 0.4 to 0.6 $\$/\text{W}_p$ for large-volume manufacturing [214, 215].

13.6.5 Environmental Concerns

One of the environmental issues related to the materials in Cu(InGa)Se₂ modules is the availability of less common elements. The content of the critical materials in grams per kW_P has been calculated assuming 12% module efficiency and the result is compared with the amount refined annually in Table 13.6 [216]. The fourth column expresses how much module power could be obtained from the amount refined annually and the last column shows a similar calculation based on the reserves of the various elements. Owing to uncertainties in estimates of reserves, or maximum resources, Table 13.6 just gives an indication of where, and at what level, potential problems in material supply may occur. It is clear that In is the potential bottleneck as regards primary material supply.

CuInSe₂ toxicity has been studied by administering it to rats [217]. Even at high doses negligible effects were detected. A lowest observed adverse effect level (LOAEL) of 8.3 μg/kg/day for humans was derived from these studies.

The other substances that constitute Cu(InGa)Se₂ modules are largely nontoxic except for Cd. Many aspects of its use in PV manufacturing have been studied by Fthenakis and Moskowitz [218]. Chemical bath deposition of CdS is the process step that presents the greatest health concerns due to the use of Cd, thiourea, and the generation of waste solutions. In electrodeposition of CdTe, which also is a wet process using Cd precursors, it was found that the greatest health hazards from Cd are from dust generated during feedstock preparation and from fine particles near the baths [218]. Biological monitoring at a process station showed that exposures can be maintained at a level that presents no risk to workers. Thiourea is a toxic and carcinogenic substance that also presents an exposure risk. Rinse water and dilute solutions of acids and Cd-compounds can be treated by a two-stage precipitation/ion exchange process. The Cd can be removed, and recycled, down to 1 to 10 ppb levels [218].

Most Cu(InGa)Se₂ processes use elemental Se, but the forms that are handled are solid shots or pellets that give off very little dust that could be inhaled. Elemental Se is considered to have a relatively low biological activity, but many compounds are very

Table 13.6 Critical materials in Cu(InGa)Se₂ modules with respect to primary supply (After Andersson B, Azar C, Holmberg J, Karlsson S, *Energy* **5**, 407–411 (1998) [216])

Element	Material content [g/kW _P]	Amount refined [kton/y]	Amount refined/content [GW _P /y]	Reserves/content [TW _P]
Mo	42	110	2600	130
Cu	17	9000	529 000	30 000
In	23	0.13	5.7	0.1
Ga	5	0.06	12	2.2
Se	43	2	46	1.9
Cd	1.6	20	12 500	330
Zn	37	7400	200 000	4100

active and highly toxic. In particular, hydrogen selenide, a gas used in some selenization processes, is extremely toxic with an “immediately dangerous to life and health” (IDLH) value of only 2 ppm [218].

There are also environmental concerns for the hazards during the operation of Cu(InGa)Se₂ modules with one potential risk being the leaching of critical materials into rainwater. This only happens if a module is broken or crushed, so the normally well-encapsulated active layers are exposed. An experimental study of the emissions of toxic elements into rainwater from crushed CuInSe₂ modules and into soil exposed to the water concluded that no acute danger to humans or the environment is likely to occur [219]. The main hazard during the active life of the CuInSe₂ modules is related to fire accidents. A study of the potential risks associated with fires in PV power plants shows that they are very limited [220]. A fire in a commercial-size system could result in harmful concentrations up to 300 m downwind of the fire if most of the CuInSe₂ materials are released. With release of 10% of the CuInSe₂ materials, concentrations were not harmful even under worst-possible meteorological conditions. The study concluded that there are no immediate risks to the public from fires in sites with CuInSe₂ modules.

Concerns for disposal of Cu(InGa)Se₂ have also been tested with respect to leachability. Zn, Mo, and Se are eluted in the highest amounts. On the basis of landfill criteria, CuInSe₂ modules will pass requirements in both Germany and the United States [217]. Because of the low volume and leaching rates of critical elements from CuInSe₂ modules, they will not be classified as hazardous waste according to most US regulations [221].

The evolution of environmental regulations, disposal options, and economics makes recycling increasingly important. In large-scale use of Cu(InGa)Se₂ modules, the supply of rare elements, in particular indium, but also selenium and gallium, provides a further motivation for recycling. The cost of recycling may be favorably offset if module materials can be reclaimed. In particular, if the glass sheets can be salvaged and reused, there will be a net gain associated with the recycling procedure. Thus, recycling may be an important consideration in the choice of encapsulation method. Double glass structures are functional and may reduce the release of CuInSe₂ materials during fires, but may increase the costs for recovering metals and reusing glass plates [221].

13.7 THE Cu(InGa)Se₂ OUTLOOK

Clearly, there has been tremendous progress in Cu(InGa)Se₂ solar cells as evidenced by the high module and cell efficiencies fabricated by many groups, the range of deposition and device options that have been developed, and the growing base of science and engineering knowledge of these materials and processes. There is good reason to be optimistic that cell efficiencies greater than 20% will be achieved before long and that module performance and yield will continue to improve. Still, there is a lack of understanding of many of the critical problems associated with semiconductor processing and a need to devote time and research focus at both the laboratory scale, to address fundamental issues, and on the pilot line, to address equipment and scale-up problems and to validate processes.

From their earliest development, CuInSe₂-based solar cells, along with other thin-film PV materials including Cu₂S, CdTe, and amorphous Si, attracted an interest because of their perceived potential to be manufactured at a lower cost than Si wafer-based PV.

However, after more than 25 years of research and development of CuInSe₂, manufacturing has only recently moved past the pilot-production stage and has not demonstrated any cost advantages. A fundamental question must be asked: what needs to be done to ensure that Cu(InGa)Se₂ solar cell technology reaches its potential for large-scale power generation?

Part of the answer is to address the critical need for the accelerated development of new manufacturing technology including improved deposition equipment and processes based on well-developed engineering models. Also, new diagnostic and process-control tools will have to be developed. This requires fundamental materials and device knowledge to determine what properties can be measured in a cell or module fabrication process that can act as reliable predictors of final performance. Better processes, equipment, and control based on a more solid knowledge base can directly translate to higher throughput, yield, and performance.

There is also a critical need for continued improvement in the fundamental science of the materials and devices [222, 223]. Significant improvements in efficiency will only come from increased V_{OC} so the chemical and electronic nature of the defects that limit it, and their origin, must be understood. This can contribute to a comprehensive model for the growth of Cu(InGa)Se₂, relating processing parameters to defect formation, junction formation, and device limitations. In addition, a fundamental understanding of the role of sodium and the nature of the grain boundaries and free surface needs to be developed. A greater understanding of the role of the CdS layer and the chemical bath process might enable alternative materials that do not contain cadmium and have wider band gap to be utilized with greater efficiency and reproducibility.

A second fundamental question to be asked is: what might be the breakthroughs that could lead to the next generation of thin-film Cu(InGa)Se₂-based solar cells?

Further development of wide band gap alloys to enable cells to be made with $E_g \geq 1.5$ eV without any decrease in performance will have several benefits for module fabrication and performance as discussed in Section 13.5. In addition, development of a cell with $E_g \approx 1.7$ eV is a prerequisite for tandem cells based on the polycrystalline thin films to be developed. A monolithic tandem cell has the potential to attain efficiencies of 25% or more. The CuInSe₂ alloy system is ideally suited for such a structure since a CuInSe₂ cell with $E_g = 1.0$ eV would make an ideal bottom cell with any of the alloys that increase band gap to 1.7 eV for the top cell. Even if a high-efficiency wide band gap cell is developed, such a structure will require the development of a transparent interconnect between the top and bottom cells and improvements in cell structure or low-temperature processes to allow the bottom cell to survive the subsequent processing of the top cell.

Low-temperature processing of the Cu(InGa)Se₂ layer without loss of efficiency in the final solar cell can have significant additional benefits. With lower substrate temperature, alternative substrate materials, like a flexible polymer web, can be utilized. In addition, lower T_{SS} can reduce thermally induced stress on the substrate, allowing faster heat-up and cooldown, and decrease the heat load and stress on the entire deposition system. Similarly, there may be significant cost and processing advantages to a cell structure that enables the use of a Cu(InGa)Se₂ layer much less than 1 μm .

With all these challenges to improve the fundamental knowledge behind Cu(InGa)Se₂ materials and devices and to develop new manufacturing technology and breakthrough advancements, research and development on Cu(InGa)Se₂ and related materials remains exciting and promising. All of the reasons for the initial excitement over the potential for thin-film Cu(InGa)Se₂ remain valid. The high efficiency, demonstrated stability, and tolerance to material and process variations give great hope that it will be a major contributor to our solar electric future.

REFERENCES

1. Contreras M *et al.*, *Prog. Photovolt.* **7**, 311–316 (1999).
2. Tanaka *et al.*, *Proc. 17th Euro. Conf. Photovoltaic Solar Energy Conversion*, 989–994 (2001).
3. Wieting R, *AIP Conf. Proc.* **462**, 3–8 (1999).
4. Burgess R *et al.*, *Proc. 20th IEEE Photovoltaic Specialist Conf.*, 909–912 (1988).
5. Jasenek A *et al.*, *Thin Solid Films* **387**, 228–230 (2001).
6. Hahn H *et al.*, *Z. Anorg. Allg. Chem.* **271**, 153–170 (1953).
7. Shay J, Wernick J, *Ternary Chalcopyrite Semiconductors: Growth, Electronic Properties, and Application*, Pergamon Press, Oxford (1974).
8. Tell B, Shay J, Kasper H, *Phys. Rev.* **B4**, 4455–4459 (1971).
9. Tell B, Shay J, Kasper H, *J. Appl. Phys.* **43**, 2469, 2470 (1972).
10. Wagner S, Shay J, Migliorato P, Kasper H, *Appl. Phys. Lett.* **25**, 434, 435 (1974).
11. Shay J, Wagner S, Kasper H, *Appl. Phys. Lett.* **27**, 89–90 (1975).
12. Meakin J, *Proc. SPIE Conf. 543: Photovoltaics*, 108–118 (1985).
13. Kazmerski L, White F, Morgan G, *Appl. Phys. Lett.* **29**, 268, 269 (1976).
14. Mickelsen R, Chen W, *Proc. 15th IEEE Photovoltaic Specialist Conf.*, 800–804 (1981).
15. Mickelsen R, Chen W, *Proc. 16th IEEE Photovoltaic Specialist Conf.*, 781–785 (1982).
16. Chen W *et al.*, *Proc. 19th IEEE Photovoltaic Specialist Conf.*, 1445–1447 (1987).
17. Potter R, *Sol. Cells* **16**, 521–527 (1986).
18. Hedström J *et al.*, *Proc. 23rd IEEE Photovoltaic Specialist Conf.*, 364–371 (1993).
19. Gabor A *et al.*, *Sol. Energy Mater. Sol. Cells* **4**, 247–260 (1996).
20. Tarrant D, Ermer J, *Proc. 23rd IEEE Photovoltaic Specialist Conf.*, 372–375 (1993).
21. Rocheleau R, Meakin J, Birkmire R, *Proc. 19th IEEE Photovoltaic Specialist Conf.*, 972–976 (1987).
22. Mitchell K *et al.*, *IEEE Trans. Electron. Devices* **37**, 410–417 (1990).
23. Kazmerski L, Wagner S, “Cu-Ternary Chalcopyrite Solar Cells”, in Coutts T, Meakin J, Eds, *Current Topics in Photovoltaics*, 41–109, Academic Press, London (1985).
24. Haneman D, *Crit. Rev. Solid State Mater. Sci.* **14**, 377–413 (1988).
25. Rockett A, Birkmire R, *J. Appl. Phys.* **70**, R81–R97 (1991).
26. Rockett A, Bodegård M, Granath K, Stolt L, *Proc. 25th IEEE Photovoltaic Specialist Conf.*, 985–987 (1996).
27. Rau U, Schock H, *Appl. Phys. A* **69**, 131–147 (1999).
28. Suri D, Nagpal K, Chadha G, *J. Appl. Crystallogr.* **22**, 578 (1989) (JCPDS 40-1487).
29. Ciszek T, *J. Cryst. Growth.* **70**, 405–410 (1984).
30. Neumann H, *Sol. Cells* **16**, 317–333 (1986).
31. Wasim S, *Sol. Cells* **16**, 289–316 (1986).
32. Gödecke T, Haalboom T, Ernst F, *Z. Metallkd.* **91**, 622–634 (2000).
33. Ye J, Yoshida T, Nakamura Y, Nittono O, *Jpn. J. Appl. Phys.* **35**, 395–400 (1996).
34. Zhang S, Wei S, Zunger A, *Phys. Rev. Lett.* **78**, 4059–4062 (1997).
35. Herberholz R *et al.*, *Eur. Phys. J.* **6**, 131–139 (1999).
36. Wei S, Zhang S, Zunger A, *Appl. Phys. Lett.* **72**, 3199–3201 (1998).

37. Schroeder D, Rockett A, *J. Appl. Phys.* **82**, 4982–4985 (1997).
38. Wei S, Zhang S, Zunger A, *J. Appl. Phys.* **85**, 7214–7218 (1999).
39. Ruckh M *et al.*, *Sol. Energy Mater. Sol. Cells* **41/42**, 335–343 (1996).
40. Kazmerski L *et al.*, *J. Vac. Sci. Technol., A* **1**, 395–398 (1983).
41. Rincón C, González J, *Sol. Cells* **16**, 357–362 (1986).
42. Alonso M *et al.*, *Phys. Rev. B* **63**, 075203 1–13 (2001).
43. Alonso M *et al.*, *Appl. Phys. A* **74**, 659–664 (2002).
44. Wei S, Zunger A, *Appl. Phys. Lett.* **72**, 2011–2013 (1998).
45. Noufi R, Axton R, Herrington C, Deb S, *Appl. Phys. Lett.* **45**, 668–670 (1984).
46. Neumann H, Tomlinson R, *Sol. Cells* **28**, 301–313 (1990).
47. Zhang S, Wei S, Zunger A, Katayama-Yoshida H, *Phys. Rev. B* **57**, 9642–9656 (1998).
48. Schroeder D, Hernandez J, Berry G, Rockett A, *J. Appl. Phys.* **72**, 749–752 (1998).
49. Kiely C, Pond R, Kenshole G, Rockett A, *Philos. Mag. A* **63**, 2149–2173 (1991).
50. Chen J *et al.*, *Thin Solid Films* **219**, 183–192 (1992).
51. Wada T, *Sol. Energy Mater. Sol. Cells* **49**, 249–260 (1997).
52. Schmid D, Ruckh M, Grunwald F, Schock H, *J. Appl. Phys.* **73**, 2902–2909 (1993).
53. Gartsman K *et al.*, *J. Appl. Phys.* **82**, 4282–4285 (1997).
54. Kylner A, *J. Electrochem. Soc.* **146**, 1816–1823 (1999).
55. Scheer R, *Trends Vac. Sci. Tech.* **2**, 77–112 (1997).
56. Damaskinos S, Meakin J, Phillips J, *Proc. 19th IEEE Photovoltaic Specialist Conf.*, 1299–1304 (1987).
57. Cahen D, Noufi R, *Appl. Phys. Lett.* **54**, 558–560 (1989).
58. Kronik L, Cahen D, Schock H, *Adv. Mater.* **10**, 31–36 (1998).
59. Niles D, Al-Jassim M, Ramanathan K, *J. Vac. Sci. Technol., A* **17**, 291–296 (1999).
60. Bodegård M, Stolt L, Hedström J, *Proc. 12th Euro. Conf. Photovoltaic Solar Energy Conversion*, 1743–1746 (1994).
61. Bodegård M, Granath K, Rockett A, Stolt L, *Sol. Energy Mater. Sol. Cells* **58**, 199–208 (1999).
62. Shafarman W *et al.*, *AIP Conf. Proc.* **394**, 123–131 (1997).
63. Contreras M *et al.*, *Thin Solid Films* **361–2**, 167–171 (2000).
64. Boyd D, Thompson D, Kirk-Othmer *Encyclopaedia of Chemical Technology*, Vol. 11, 3rd Edition, 807–880, John Wiley (1980).
65. Probst V *et al.*, *Proc. 1st World Conf. Photovoltaic Solar Energy Conversion*, 144–147 (1994).
66. Contreras M *et al.*, *Proc. 26th IEEE Photovoltaic Specialist Conf.*, 359–362 (1997).
67. Jensen C, Wieting R, *Proc. 13th Euro. Conf. Photovoltaic Solar Energy Conversion*, 1631–1633 (1995).
68. Basol B, Kapur V, Leidholm C, Halani A, *Proc. 25th IEEE Photovoltaic Specialist Conf.*, 157–162 (1996).
69. Hartmann M *et al.*, *Proc. 28th IEEE Photovoltaic Specialist Conf.*, 638–641 (2000).
70. Vink T, Somers M, Daams J, Dirks A, *J. Appl. Phys.* **70**, 4301–4308 (1991).
71. Wada T, Kohara N, Nishiwaki S, Negami T, *Thin Solid Films* **387**, 118–122 (2001).
72. Matson R *et al.*, *Sol. Cells* **11**, 301–305 (1984).
73. Mattox D, *Handbook of Physical Vapor Deposition (PVD) Processing*, Noyes Publ., Park Ridge, NJ (1998).
74. Jackson S, Baron B, Rocheleau R, Russell T, *Am. Inst. Chem. Eng. J.* **33**, 711–720 (1987).
75. Shafarman W, Zhu J, *Thin Solid Films* **361–2**, 473–477 (2000).
76. Klenk R, Walter T, Schock H, Cahen D, *Adv. Mater.* **5**, 114–119 (1993).
77. Kessler J *et al.*, *Proc. 12th Euro. Conf. Photovoltaic Solar Energy Conversion*, 648–652 (1994).
78. Gabor A *et al.*, *Appl. Phys. Lett.* **65**, 198–200 (1994).
79. Hasoon F *et al.*, *Thin Solid Films* **387**, 1–5 (2001).
80. Stolt L *et al.*, *Appl. Phys. Lett.* **62**, 597–599 (1993).

81. Stolt L, Hedström J, Sigurd D, *J. Vac. Sci. Technol.* **A3**, 403–407 (1985).
82. Powalla M, Voorwinden G, Dimmler B, *Proc. 14th Euro. Conf. Photovoltaic Solar Energy Conversion*, 1270–1273 (1997).
83. Eisgruber I *et al.*, *Proc. 28th IEEE Photovoltaic Specialist Conf.*, 505–508 (2000).
84. Nishitani M, Negami T, Wada T, *Thin Solid Films* **258**, 313–316 (1995).
85. Negami T *et al.*, *Mater. Res. Soc. Symp.* **426**, 267–278 (1996).
86. Grindle S, Smith C, Mittleman S, *Appl. Phys. Lett.* **35**, 24–26 (1979).
87. Chu T, Chu S, Lin S, Yue J, *J. Electrochem. Soc.* **131**, 2182–2185 (1984).
88. Gay R *et al.*, *Proc. 12th Euro. Conf. Photovoltaic Solar Energy Conversion*, 935–938 (1994).
89. Kapur V, Basol B, Tseng E, *Sol. Cells* **21**, 65–70 (1987).
90. Basol B, Kapur V, *IEEE Trans. Electron. Devices* **37**, 418–421 (1990).
91. Garcia F, Tomar M, *Jpn. J. Appl. Phys.* **22S**, 535–540 (1983).
92. Schulz D *et al.*, *Proc. 27th IEEE Photovoltaic Specialist Conf.*, 483–486 (1997).
93. Knowles A, Oumous H, Carter M, Hill R, *Semicond. Sci. Technol.* **3**, 1143, 1144 (1988).
94. Nadenau V *et al.*, *Prog. Photovolt.* **3**, 363–382 (1995).
95. Pern F *et al.*, *Sol. Cells* **24**, 81–90 (1988).
96. Guillemoles J *et al.*, *J. Appl. Phys.* **79**, 7293–7302 (1996).
97. Sato H *et al.*, *Proc. 23rd IEEE Photovoltaic Specialist Conf.*, 521–526 (1993).
98. Kessler J, Dittrich H, Grunwald F, Schock H, *Proc. 10th Euro. Conf. Photovoltaic Solar Energy Conversion*, 879–882 (1991).
99. Oumous H *et al.*, *Proc. 9th Euro. Conf. Photovoltaic Solar Energy Conversion*, 153–156 (1992).
100. Karg F *et al.*, *Proc. 23rd IEEE Photovoltaic Specialist Conf.*, 441–446 (1993).
101. Mooney G *et al.*, *Appl. Phys. Lett.* **58**, 2678–2680 (1991).
102. Verma S, Orbey N, Birkmire R, Russell T, *Prog. Photovolt.* **4**, 341–353 (1996).
103. Wolf D, Müller G, *Thin Solid Films* **361–2**, 155–161 (2000).
104. Orbey N, Norsworthy G, Birkmire R, Russell T, *Prog. Photovolt.* **6**, 79–86 (1998).
105. Jensen C, Tarrant D, Ermer J, Pollock G, *Proc. 23rd IEEE Photovoltaic Specialist Conf.*, 577–580 (1993).
106. Marudachalam M *et al.*, *Appl. Phys. Lett.* **67**, 3978–3980 (1995).
107. Kushiya K *et al.*, *Proc. 25th IEEE Photovoltaic Specialist Conf.*, 989–993 (1995).
108. Thornton J, Lomasson T, Talieh H, Tseng B, *Sol. Cells* **24**, 1–9 (1988).
109. Talieh H, Rockett A, *Sol. Cells* **27**, 321–329 (1989).
110. Guenoun K, Djessas K, Massé G, *J. Appl. Phys.* **84**, 589–595 (1998).
111. Murali K, *Thin Solid Films* **167**, L19–L22 (1988).
112. Galindo H *et al.*, *Thin Solid Films* **170**, 227–234 (1989).
113. Abernathy C *et al.*, *Appl. Phys. Lett.* **45**, 890 (1984).
114. Kazmerski L, Ireland P, White F, Cooper R, *Proc. 13th IEEE Photovoltaic Specialist Conf.*, 184–189 (1978).
115. Potter R, Eberspacher C, Fabick L, *Proc. 18th IEEE Photovoltaic Specialist Conf.*, 1659–1664 (1985).
116. Mitchell K, Liu H, *Proc. 20th IEEE Photovoltaic Specialist Conf.*, 1461–1468 (1988).
117. Cashman R, *J. Opt. Soc. Am.* **36**, 356 (1946).
118. Kitaev G, Uritskaya A, Mokrushin S, *Sov. J. Phys. Chem.* **39**, 1101 (1965).
119. Kainthla R, Pandya D, Chopra K, *J. Electrochem. Soc.* **127**, 277–283 (1980).
120. Kaur I, Pandya D, Chopra K, *J. Electrochem. Soc.* **127**, 943–948 (1980).
121. Lincot D, Ortega-Borges R, *J. Electrochem. Soc.* **139**, 1880–1889 (1992).
122. Lincot D, Ortega-Borges R, Froment M, *Philos. Mag. B* **68**, 185–194 (1993).
123. Nakada T, Kunioka A, *Appl. Phys. Lett.* **74**, 2444–2446 (1999).
124. Kylner A, Rockett A, Stolt L, *Solid State Phen.* **51–52**, 533–539 (1996).
125. Hashimoto Y *et al.*, *Sol. Energy Mater. Sol. Cells* **50**, 71–77 (1998).
126. Kylner A, Lindgren J, Stolt L, *J. Electrochem. Soc.* **143**, 2662–2669 (1996).

127. Kylner A, Niemi E, *Proc. 14th Euro. Conf. Photovoltaic Solar Energy Conversion*, 1321–1326 (1997).
128. Cherin P, Lind E, Davis E, *J. Electrochem. Soc.* **117**, 233–236 (1970).
129. Grzeta-Plenkovic B, Popovic S, Celustka B, Santic B, *J. Appl. Crystallogr.* **13**, 311–315 (1980).
130. Kessler J *et al.*, *Tech. Digest PVSEC-6*, 1005–1010 (1992).
131. Yu P, Faile S, Park Y, *Appl. Phys. Lett.* **26**, 384, 385 (1975).
132. Tell B, Wagner S, Bridenbaugh P, *Appl. Phys. Lett.* **28**, 454, 455 (1976).
133. Kazmerski L, Jamjoum O, Ireland P, *J. Vac. Sci. Technol.* **21**, 486–490 (1982).
134. Heske C *et al.*, *Appl. Phys. Lett.* **74**, 1451–1453 (1999).
135. Kylner A, *J. Electrochem. Soc.* **143**, 1816–1823 (1999).
136. Ramanathan K *et al.*, *Proc. 2nd World Conf. Photovoltaic Solar Energy Conversion*, 477–482 (1998).
137. Wang L *et al.*, *MRS Symp.* **569**, 127–132 (1999).
138. Leskelä M, Ritala M, *Thin Solid Films* **409**, 138–146 (2002).
139. Kessler J *et al.*, *Proc. 23rd IEEE Photovoltaic Specialist Conf.*, 447–452 (1993).
140. Olsen L *et al.*, *Proc. 26th IEEE Photovoltaic Specialist Conf.*, 363–366 (1997).
141. Sterner J, Kessler J, Bodegård M, Stolt L, *Proc. 2nd World Conf. Photovoltaic Solar Energy Conversion*, 1145–1148 (1998).
142. Bhattacharya R *et al.*, *Sol. Energy Mater. Sol. Cells* **63**, 367–374 (2000).
143. Kushiya K *et al.*, *Sol. Energy Mater. Solar Cells* **49**, 277–283 (1997).
144. Nakada T, Furumi K, Kunioka A, *Trans. Electron Devices* **46**, 2093–2097 (1999).
145. Muffler H *et al.*, *Proc. 28th IEEE Photovoltaic Specialist Conf.*, 610–613 (2000).
146. Ennaoui A, Blieske U, Lux-Steiner M, *Prog. Photovolt.* **6**, 447–451 (1998).
147. Othake Y, Kushiya K, Yamada A, Konagai M, *Proc. 1st World Conf. Photovoltaic Solar Energy Conversion*, 218–221 (1994).
148. Engelhardt F *et al.*, *Proc. 2nd World Conf. Photovoltaic Solar Energy Conversion* (1998).
149. Othake Y *et al.*, *Proc. 25th IEEE Photovoltaic Specialist Conf.*, 793–796 (1996).
150. Othake Y *et al.*, *Sol. Energy Mater. Sol. Cells* **49**, 269–275 (1997).
151. Hariskos D *et al.*, *Proc. 13th Euro. Conf. Photovoltaic Solar Energy Conversion*, 1995–1998 (1995).
152. Guillemoles J *et al.*, *Jpn. J. Appl. Phys.* **40**, 6065–6068 (2001).
153. Gordon R, *MRS Bull.* **25**, 52–57 (2000).
154. Lewis B, Paine D, *MRS Bull.* **25**, 22–27 (2000).
155. Menner R, Schäffler R, Sprecher B, Dimmler B, *Proc. 2nd World Conf. Photovoltaic Solar Energy Conversion*, 660–663 (1998).
156. Ruckh M *et al.*, *Proc. 25th IEEE Photovoltaic Specialist Conf.*, 825–828 (1996).
157. Westwood W, “Reactive Sputter Deposition”, in Rossnagel S, Cuomo J, Westwood W, Eds, *Handbook of Plasma Processing Technology*, Chap. 9, Noyes Publ., Park Ridge, NJ (1990).
158. Tarrant D, Gay R, *Proc. 2001 NCPV Prog. Rev. Meeting*, 113–114 (Nov. 2001).
159. Stolt L, Hedström J, Skarp J, *Proc. 1st World Conf. Photovoltaic Solar Energy Conversion*, 250–253 (1994).
160. Rau U, Schmidt M, *Thin Solid Films* **387**, 141–146 (2001).
161. Kessler J *et al.*, *Proc. 16th Euro. Conf. Photovoltaic Solar Energy Conversion*, 775–778 (2000).
162. Cooray N, Kushiya K, Fujimaki A, Okumura D, *Jpn. J. Appl. Phys.* **38**, 6213–6218 (1999).
163. Lundberg O, Bodegård M, Malmström J, Stolt L, *Prog. Photovolt.* **11** (2002).
164. Fahrenbruch A, Bube R, *Fundamentals of Solar Cells*, 231–234, Academic Press, New York (1983).
165. Shafarman W, Klenk R, McCandless B, *J. Appl. Phys.* **79**, 7324–7328 (1996).
166. Eron M, Rothwarf A, *Appl. Phys. Lett.* **44**, 131 (1984).
167. Ohnesorge B *et al.*, *Appl. Phys. Lett.* **73**, 1224–1227 (1998).

168. Fahrenbruch A, Bube R, *Fundamentals of Solar Cells*, 105–161, Academic Press, New York (1983).
169. Phillips J *et al.*, *Phys. Status Solidi B* **194**, 31–39 (1996).
170. Roy M, Damaskinos S, Phillips J, *Proc. 20th IEEE Photovoltaic Specialist Conf.*, 1618–1623 (1988).
171. Walter T, Menner R, Köble C, Schock H, *Proc. 12th Euro. Conf. Photovoltaic Solar Energy Conversion*, 1755–1758 (1994).
172. Shafarman W, Phillips J, *Proc. 23rd IEEE Photovoltaic Specialist Conf.*, 364–369 (1993).
173. Sah C, Noyce R, Shockley W, *Proc. Inst. Radio Engrs.* **45**, 1228–1243 (1957).
174. Eron M, Rothwarf A, *J. Appl. Phys.* **57**, 2275–2279 (1985).
175. Walter T, Herberholz R, Schock H, *Solid State Phen.* **51**, 301–316 (1996).
176. Rau U, *Appl. Phys. Lett.* **74**, 111–113 (1999).
177. Meyer T *et al.*, *Eur. J. Appl. Phys.* **8**, 43–52 (1999).
178. Walter T, Herberholz R, Müller C, Schock H, *J. Appl. Phys.* **80**, 4411–4420 (1996).
179. Herberholz R *et al.*, *Proc. 14th Euro. Conf. Photovoltaic Solar Energy Conversion*, 1246–1249 (1997).
180. Nishitani M, Negami T, Kohara N, Wada T, *J. Appl. Phys.* **82**, 3572–3575 (1997).
181. Sites J, Mauk P, *Sol. Cells* **27**, 411–417 (1987).
182. Turner G, Schwartz R, Gray J, *Proc. 20th IEEE Photovoltaic Specialist Conf.*, 1457–1460 (1988).
183. Schwartz R, Gray J, Lee Y, *Proc. 22nd IEEE Photovoltaic Specialist Conf.*, 920–923 (1991).
184. Klenk R, *Thin Solid Films* **387**, 135–140 (2001).
185. Niemegeers A, Burgelman M, De Vos A, *Appl. Phys. Lett.* **67**, 843–845 (1995).
186. Liu X, Sites J, *AIP Conf. Proc.* **353**, 444–453 (1996).
187. Minemoto T *et al.*, *Thin Solid Films* **67**, 83–88 (2001).
188. Schmid D, Ruckh M, Schock H, *Sol. Energy Mater. Sol. Cells* **41–2**, 281–294 (1996).
189. Wei S, Zunger A, *Appl. Phys. Lett.* **63**, 2549–2551 (1993).
190. Nelson A *et al.*, *Phys. Rev. B* **42**, 7518–7523 (1990).
191. Löher T, Jaegermann W, Pettenkofer C, *J. Appl. Phys.* **77**, 731–738 (1995).
192. Kronik L *et al.*, *Appl. Phys. Lett.* **67**, 1405–1407 (1995).
193. Morkel M *et al.*, *Appl. Phys. Lett.* **79**, 4482–4485 (2001).
194. Scheer R *et al.*, *Appl. Phys. Lett.* **63**, 3294–3296 (1993).
195. Paulson P *et al.*, *J. Appl. Phys.* **91**, 10153–10156 (2002).
196. Nadenau V, Hariskos D, Schock H, *Proc. 14th Euro. Conf. Photovoltaic Solar Energy Conversion*, 1250–1253 (1997).
197. Siemer K *et al.*, *Sol. Energy Mater. Sol. Cells* **67**, 159–166 (2001).
198. Marsillac S *et al.*, *Appl. Phys. Lett.* **81**, 1350–1352 (2002).
199. Shafarman W, Klenk R, McCandless B, *Proc. 25th IEEE Photovoltaic Specialist Conf.*, 763–768 (1996).
200. Hanna G, Jasenek A, Rau U, Schock H, *Thin Solid Films* **387**, 71–73 (2001).
201. Heath J *et al.*, *Appl. Phys. Lett.* **80**, 4540 (2002).
202. Nadenau V, Jasenek A, Rau U, Schock H, *J. Appl. Phys.* **87**, 584–593 (2000).
203. Hengel I, Neisser A, Klenk R, Lux-Steiner M, *Thin Solid Films* **361–2**, 458–462 (2000).
204. Gray J, Lee Y, *Proc. 1st World Conf. Photovoltaic Solar Energy Conversion*, 123–126 (1994).
205. Topic M, Smole F, Furlan J, *J. Appl. Phys.* **79**, 8537–8540 (1996).
206. Dullweber T, Hanna G, Rau U, Schock H, *Sol. Energy Mater. Sol. Cells* **67**, 145–150 (2001).
207. Dullweber T *et al.*, *Thin Solid Films* **387**, 11–13 (2001).
208. Probst V *et al.*, *Thin Solid Films* **387**, 262–267 (2001).
209. Russell T *et al.*, *Proc. 15th IEEE Photovoltaic Specialist Conf.*, 743–748 (1982).
210. Kessler J, Wennerberg J, Bodegård M, Stolt L, *Sol. Energy Mater. Sol. Cells* **67**, 59–65 (2001).

211. Wennerberg J, Kessler J, Stolt L, *Proc. 16th Euro. Conf. Photovoltaic Solar Energy Conversion*, 309–312 (2000).
212. Alsema E, van Engelenburg B, *Proc. 11th Euro. Conf. Photovoltaic Solar Energy Conversion*, 995–998 (1993).
213. Jester T, *Prog. Photovolt.* **10**, 99–106 (2002).
214. Woodcock J *et al.*, *Proc. 14th Euro. Conf. Photovoltaic Solar Energy Conversion*, 857–860 (1993).
215. Zweibel K, *Sol. Energy Mater. Sol. Cells* **59**, 1–18 (1999).
216. Andersson B, Azar C, Holmberg J, Karlsson S, *Energy* **23**, 407–411 (1998).
217. Thumm W *et al.*, *Proc. 1st World Conf. Photovoltaic Solar Energy Conversion*, 262–265 (1994).
218. Fthenakis V, Moskowitz P, *Prog. Photovolt.* **3**, 295–306 (1995).
219. Steinberger H, *Prog. Photovolt.* **6**, 99–103 (1998).
220. Moskowitz P, Fthenakis V, *Sol. Cells* **29**, 63–71 (1990).
221. Eberspacher C, Fthenakis V, *Proc. 26th IEEE Photovoltaic Specialist Conf.*, 1067–1072 (1997).
222. Schock H, Noufi R, *Prog. Photovolt.* **8**, 151–160 (2000).
223. Birkmire R, *Proc. 26th IEEE Photovoltaic Specialist Conf.*, 295–300 (1997).

14

Cadmium Telluride Solar Cells

Brian E. McCandless¹ and James R. Sites²

¹University of Delaware, Newark, Delaware, USA, ²Colorado State University, Fort Collins, Colorado, USA

14.1 INTRODUCTION

Thin-film cadmium telluride (CdTe) solar cells are the basis of a significant technology with major commercial impact on solar energy production. Large-area monolithic thin-film modules demonstrate long-term stability, competitive performance, and the ability to attract production-scale capital investments. This chapter reviews the status of CdTe thin-film solar cells, with emphasis on the properties that make CdTe a favorable material for terrestrial photovoltaic solar energy conversion, their historical development, methods for device fabrication, analysis of device operation, and the fabrication strategies and technical challenges associated with present and future development of thin-film CdTe cells and modules.

Calculations of the dependence of ideal solar cell conversion efficiency on band gap show that CdTe is an excellent match to our sun, a G2 spectral-class star with an effective black-body photosphere surface temperature of 5700 K, and a total luminosity of 3.9×10^{33} erg/s. CdTe is a group II^B-VI^A compound semiconductor with a direct optical band gap that is nearly optimally matched to the solar spectrum for photovoltaic energy conversion. The direct band gap, $E_g = 1.5$ eV, and high absorption coefficient, $>5 \times 10^5/\text{cm}$, of CdTe means that high quantum yield can be expected over a wide wavelength range, from the ultraviolet to the CdTe band gap, $\lambda \sim 825$ nm. Short-wavelength photons, with energy greater than E_g , are absorbed near the CdTe surface, making CdTe an attractive absorber-layer material for thin-film solar cells. The theoretical solar cell efficiency versus band gap for CdTe and the optical absorption coefficient versus energy for CdTe and other selected photovoltaic materials are compared in Figure 14.1 [1, 2]. The high CdTe absorption coefficient, $>5 \times 10^5/\text{cm}$, for photons with $E > E_g$ translates into 99% absorption of the absorbable AM1.5 photons within 2 μm of film thickness.

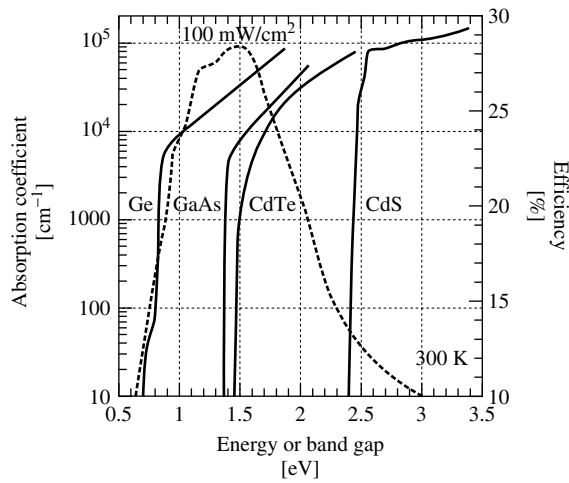


Figure 14.1 Theoretical solar cell efficiency (dotted) for AM1.5 spectral irradiance versus band gap and absorption coefficient (solid) versus energy for different semiconducting photovoltaic materials

CdTe emerged as a new electronic material in 1947 when Frerichs synthesized CdTe crystals by the reaction of Cd and Te vapors in a hydrogen atmosphere and measured their photoconductivity [3]. The early foundation for understanding the electronic nature of CdTe emerged from subsequent studies of single crystals purified by zone refinement. In 1954, Jenny and Bube [4] first reported that *p*-type and *n*-type conductivity could be obtained in CdTe by doping with foreign impurities. Shortly thereafter, Krüger and de Nobel [5] showed that the conductivity type could also be changed by varying the Cd–Te stoichiometry. Cd excess yields *n*-type and Te excess yields *p*-type conductivity, as had been discovered for PbS, PbSe, and PbTe. In 1959, the *p*–*T*–*x* diagram of the Cd–Te system and its relationship to intrinsic conduction and extrinsic conductivity via foreign-atom incorporation was established by de Nobel [6], who proposed the existence of two electronic levels associated with Cd vacancies and one with interstitial Cd to account for the measured changes in conductivity at different temperature and Cd partial pressure. Furthermore, the electronic levels associated with In as an *n*-type dopant and Au as a *p*-type dopant were estimated.

Loferski at RCA first proposed using CdTe for photovoltaic solar energy conversion in 1956 [1]. Although methods for controlling *n* and *p*-type conductivity in CdTe crystals were established by 1960, limited research was directed at the development of *p/n* homojunctions. In 1959, Rappaport, also at RCA, demonstrated single-crystal homojunction CdTe cells with conversion efficiency $\sim 2\%$ fabricated by diffusion of In into *p*-type CdTe crystals, yielding $V_{OC} = 600$ mV, $J_{SC} \sim 4.5$ mA/cm² (73 mW/cm² irradiance), and fill factor (FF) = 55% [7]. In 1979, the CNRS group in France achieved $>7\%$ conversion efficiency for a device made by close-space vapor transport deposition (VTD) of *p*-type arsenic-doped CdTe films onto *n*-type crystals, with $V_{OC} = 723$ mV, $J_{SC} \sim 12$ mA/cm² (AM1 irradiance) and $FF = 63\%$ [8]. Later they reported cells with efficiency $>10.5\%$, with $V_{OC} = 820$ mV, $J_{SC} = 21$ mA/cm², and $FF = 62\%$ [9]. Little subsequent work on *p/n* CdTe homojunctions has been reported.

In contrast to p/n homojunction development, CdTe heterojunction solar cells have been widely investigated since 1960, proceeding along two paths, according to CdTe conductivity type. For n -type CdTe single crystals and polycrystalline films, extensive work was carried out on heterojunctions with p -type Cu_2Te . In the early 1960s, n -type CdTe/ p -type Cu_2Te devices having a structure analogous to the CdS/ Cu_2S solar cell [10] were fabricated, by surface reaction of n -type single crystals or polycrystalline films in acidic aqueous solutions containing Cu salts for topotaxial conversion of CdTe to p -type Cu_2Te [11–15]. By the early 1970s, the best thin-film CdTe/ Cu_2Te cells achieved cell efficiencies $>7\%$, with $V_{\text{OC}} = 550$ mV, $J_{\text{SC}} \sim 16$ mA/cm² (60 mW/cm² irradiance), and $FF = 50\%$, as reported by Justi *et al.* [16]. Interestingly, these cells utilized an underlying 5- μm -thick n -type CdS layer to improve adhesion and electrical contact of the 20- μm -thick CdTe film on molybdenum substrates. Difficulty in controlling the Cu_2Te formation process, poor device stability in CdTe/ Cu_2Te cells, and lack of a transparent p -type conductor ultimately shifted research emphasis to heterojunction structures employing p -type CdTe. Other work with n -type CdTe utilized Schottky barrier devices, formed by heating Pt or Au grids in contact with n -type CdTe single crystals [16] or electrodeposited CdTe thin films, with efficiencies approaching 9% [17].

For solar cells with single-crystal p -type CdTe, heterojunctions using stable oxides, such as $\text{In}_2\text{O}_3:\text{Sn}$ (ITO), ZnO, SnO_2 , and CdS have been more widely investigated. In these devices, the short wavelength spectral response is influenced primarily by the transmission of the heteropartner and low-resistance contact, collectively referred to as the window layer. Solar cells based on p -type CdTe single crystals with electron-beam-evaporated indium–tin oxide (ITO) window layers with efficiencies = 10.5% were developed by the Stanford group, 1977, with $V_{\text{OC}} = 810$ mV, $J_{\text{SC}} = 20$ mA/cm², and $FF = 65\%$ [18]. In 1987, cells made by the reactive deposition of indium oxide, In_2O_3 , on p -type CdTe single crystals yielded total area efficiencies = 13.4%, with $V_{\text{OC}} = 892$ mV, $J_{\text{SC}} = 20.1$ mA/cm², and $FF = 74.5\%$ [19]. In this device, the CdTe crystal had a carrier concentration of $6 \times 10^{15}/\text{cm}^3$ and the CdTe (111) face was etched in bromine methanol prior to loading into vacuum for In_2O_3 deposition. The V_{OC} of this cell remains the highest ever reported for a CdTe device. Solar cells with ZnO window layers on p -type CdTe single crystals yielded poorer junction behavior, with efficiency $<9\%$ and $V_{\text{OC}} = 540$ mV [20].

Cells made by evaporating n -type CdS films onto single-crystal p -type CdTe were first prepared by Muller *et al.* in the mid-1960s [21, 22], yielding conversion efficiencies less than 5%. In 1977, Mitchell *et al.* reported a conversion efficiency = 7.9% with $V_{\text{OC}} = 630$ mV for a cell with 1- μm -thick CdS and an ITO transparent electrode [23]. The highest efficiency for a cell fabricated with thin-film CdS on p -type CdTe single crystal was reported by Yamaguchi *et al.* in 1977. Their cell utilized 0.5- μm -thick CdS deposited by chemical vapor deposition onto the (111) face of phosphorous-doped CdTe single crystals and gave 11.7% efficiency with $V_{\text{OC}} = 670$ mV [24].

Thin-film CdTe/CdS heterojunction solar cells have been fabricated in two different configurations, referred to as *substrate* and *superstrate*. In both configurations, light enters the cell through the transparent conducting oxide (TCO) and CdS films. However, in the superstrate cell, the TCO, CdS, and CdTe layers are sequentially deposited onto a glass superstrate, which also serves as the mechanical support for the cell, and light must pass through the supporting glass before reaching the CdS/CdTe junction. In the substrate configuration, the CdTe film is typically deposited first onto a suitable

substrate, followed by sequential deposition of CdS and the TCO. Novel schemes have also been demonstrated for fabricating *substrate* configuration cells by transferring the entire cell from a disposable superstrate to a substrate (see, for example, Reference [25]). Superstrate polycrystalline CdTe/CdS heterojunction thin-film solar cells were first demonstrated in 1969 by Adirovich *et al.* in a superstrate design with evaporated CdTe on a CdS/SnO₂/glass superstrate, yielding an efficiency >2% [26]. This was followed in 1972 by Bonnet and Rabenhorst, who, in their paper for the 9th European Photovoltaic Specialists Conference, described a 5 to 6% efficient substrate design CdS/CdTe/Mo made by chemical vapor-deposited CdTe and vacuum-evaporated CdS films [27]. This paper delineated the fundamental issues that still influence the development of highly efficient CdTe/CdS thin-film solar cells: (1) the role of Cu in *p*-type doping of CdTe; (2) the controlling role of doping efficiency in CdTe; (3) the effects of abrupt versus graded CdTe–CdS junctions; (4) the effects of active versus passive grain boundaries; and (5) the formation of low-resistance contacts to *p*-type CdTe.

Development of thin-film CdTe/CdS solar cell fabrication processes during the 1980s and 1990s was advanced by refinements in device design, postdeposition treatments, and formation of low-resistance contacts rather than by refinements in specific deposition methods. This is primarily due to the relatively high chemical stability of CdTe compared to the elemental and compound precursors used to prepare it. Thus, numerous film-fabrication techniques have been used to deposit CdTe for moderate- to high-efficiency solar cells, and eight of these are reviewed in this chapter. Surprisingly, CdTe/CdS solar cells having conversion efficiency from ~10 to ~16% have similar photovoltaic behavior. Electrical analysis suggests that device operation is primarily limited by Shockley–Read–Hall recombination in the space charge region [28].

In spite of tolerance to the deposition technique, two enigmatic aspects of processing high-efficiency thin-film CdTe/CdS solar cells persist, that is, the use of superstrate device configuration, with CdTe deposited onto CdS, and the need for processing step(s) that expose the CdTe and CdS films to Cl and O. During the 1980s, significant gains in performance were obtained by empirical optimization of superstrate fabrication processes with respect to processing variables such as the CdTe deposition temperature, postdeposition heat treatment, growth or treatment chemical environment, and CdTe contact formation. For example, the Matsushita Battery Industrial Company reported that for screen-print/sintered CdTe cells, it was critical to control the CdCl₂, O, and Cu concentrations in the structure by adjusting the slurries and the temperature–time sequences of the sintering step [29]. The Monosolar electrodeposition process was optimized to the 10% efficiency level by addition of Cl to the CdTe plating bath and the use of a so-called “type-conversion junction formation” postdeposition treatment to electrically activate the cell [30]. The group at Kodak achieved the 10% efficiency level with close-space sublimation-deposited CdTe by optimizing the CdTe deposition temperature and the oxygen content in the deposition ambient [31]. A turning point for thin-film CdTe cell performance, with a collateral benefit for processing tolerance, was the application of a postdeposition air-heat treatment of CdTe/CdS structures coated with CdCl₂ [32, 33]. Combining the “CdCl₂ treatment” with advancements in low-resistance contact formation led to the achievement in 1993 of a >15% efficient cell with CdTe deposited by close-space sublimation [34]. Refinements in window-layer processing [35] and employing vapor CdCl₂ treatments [36] have led to additional improvements. The record efficiency

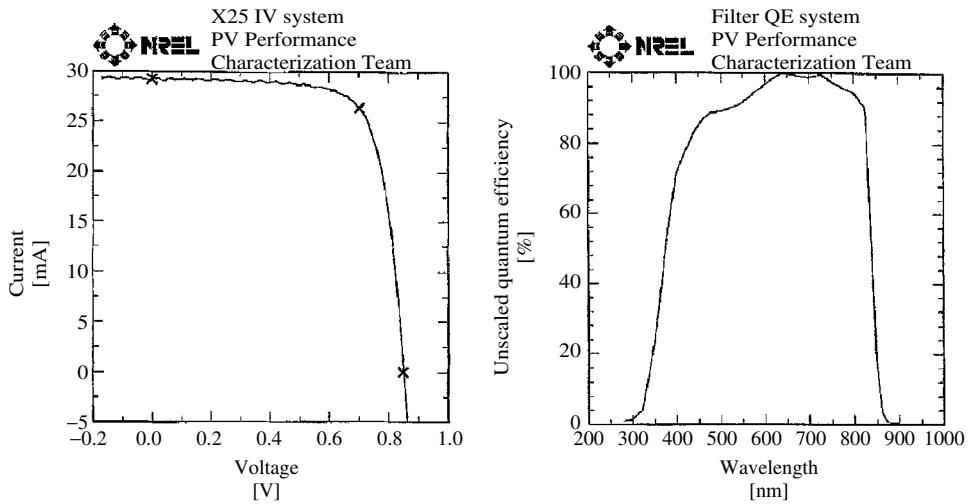


Figure 14.2 Current–voltage and relative quantum efficiency curves for 16.4%-efficient CdTe/CdS thin-film solar cell [37]

to date is 16.5% with $V_{OC} = 845$ mV, $J_{SC} = 25.9$ mA/cm², and $FF = 75.5\%$ [37]. The J – V and quantum efficiency (QE) characteristics of this cell are shown in Figure 14.2.

Superstrate polycrystalline thin-film CdTe/CdS solar cells have received significant R&D attention and have achieved the highest performance among CdTe-based solar cell configurations. Consideration of the cell parameters obtained by devices in all configurations suggests that $V_{OC} = 900$ mV, $J_{SC} = 26$ mA/cm², and $FF = 80\%$, and efficiency approaching 19% are reasonable expectations without major breakthroughs. Translating high-efficiency cells to high-efficiency module fabrication, however, will require the additional understanding of processing tolerances, the effects of thermal and chemical nonuniformities in processing large-area devices, and the effects of cell-area delineation, interconnections, and encapsulants.

14.2 CdTe PROPERTIES AND THIN-FILM FABRICATION METHODS

This section summarizes the fundamental properties of CdTe and describes methods for depositing polycrystalline CdTe thin films. CdTe is unique among the II^B-VI^A compounds, such as ZnS, CdSe, and HgTe, in that it exhibits the highest average atomic number, the least negative formation enthalpy, the lowest melt temperature, the largest lattice parameter, and the highest ionicity. Electronically, CdTe exhibits amphoteric semiconducting behavior, making it possible to intrinsically and extrinsically dope CdTe n and p -type. All these factors complement its nearly ideal optical band gap and absorption coefficient for terrestrial photovoltaic devices, making it a forgiving material to deposit and control in the thin-film form. Table 14.1 presents pertinent physical and optoelectronic data for CdTe.

The synthesis of II^B-VI^A compounds is facilitated by the large negative formation enthalpies (ΔH_f) and correspondingly low vapor pressures (p_{sat}) of the compounds compared to their constituent elements: for CdTe, $\Delta H_f = -22.4$ kcal/mol and $p_{sat}(400^\circ\text{C}) =$

Table 14.1 CdTe optoelectronic and physiochemical properties

Property	Value or range	Reference
Optical band gap; E_g (300 K)	1.50 eV \pm 0.01 eV	Single crystal [38] polycrystalline film [39]
Temperature dep: dE_g/dT	-1.7 meV/K	[40]
Electron affinity: χ_e	4.28 eV	[41]
Absorption coefficient (600 nm)	$6 \times 10^4/\text{cm}$	[38, 39]
Index refraction: (600 nm)	~ 3	[42]
Static Dielectric constant: $\epsilon(\theta)$	9.4, 10.0	[41, 43]
High Freq. Dielectric constant: $\epsilon(\infty)$	7.1	[43]
m_e^*	0.096	[44]
m_h^*	0.35	[44]
μ_e	500-1000	[44]
μ_h	50-80	[44]
Space group	F-43 m	[45]
Lattice parameter: a_0 (300 K)	6.481 Å	[45]
Cd-Te bond length	2.806 Å	Calculated from a_0
Density	~ 5.3	[42]
Heat of fusion: ΔH_f° (300 K)	-24 kcal/mol	[46]
Entropy: S° (300 K)	23 cal/deg-mol	[46]
Sublimation reaction	$\text{CdTe} \rightarrow \text{Cd} + 1/2\text{Te}_2$	[46]
Sublimation pressure: p_{sat}	$\log(P_s/\text{bar}) = -10650/T(\text{K}) - 2.56 \log(T) + 15.80$	[46]
Melting point	1365 K	[44]

10^{-5} Torr and for CdS, $\Delta H_f = -30$ kcal/mol and $p_{\text{sat}}(400^\circ\text{C}) = 10^{-7}$ Torr [46]. The equilibrium reaction for CdTe solid and Cd and Te vapors is



The CdTe temperature versus composition, T - x , atmospheric pressure phase diagram is shown in Figure 14.3(a). The individual vapor-solid equilibria for CdTe, CdS, Cd, Te, and CdCl_2 are shown in Figure 14.3(b) over the temperature range employed for fabricating solar cells, from 100 to 600°C . Congruent evaporation of CdTe facilitates vapor-deposition techniques, and the comparatively high sublimation pressures for Cd and Te ensure single-phase composition in deposits formed in vacuum at temperatures above $\sim 300^\circ\text{C}$. CdTe is also the stable product of cathodic reduction from solutions containing Cd and Te ions due to the reasonably close reduction potentials for Cd and Te and the low solubility product of CdTe.

The T - x phase equilibrium of the CdTe system at atmospheric pressure is characterized by Cd ($x = 0$) and Te ($x = 1$) endpoints and by the compound CdTe (Figure 14.3a). Note that the CdTe melt temperature, $T_m = 1092^\circ\text{C}$, is significantly higher than for either

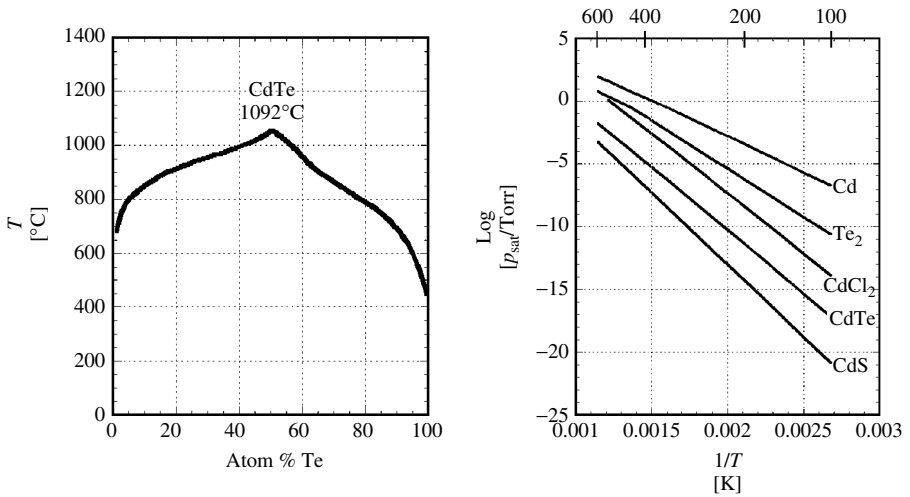


Figure 14.3 (a) CdTe T - x phase diagram (1 atm) [47] and (b) vapor–solid p_{sat} versus $1/T$ diagram for CdTe, CdS, CdCl_2 , Cd, and Te [48]

Cd, $T_m = 321^{\circ}\text{C}$, or Te, $T_m = 450^{\circ}\text{C}$ [49]. A detailed examination of the T - x projection around the CdTe stoichiometric composition indicates a very narrow, $\sim 10^{-6}$ at.%, symmetrical existence region at $T < 500^{\circ}\text{C}$. At higher temperatures, the existence region widens and is asymmetrical on the Cd-rich side up to 700°C and becomes Te-rich at higher temperatures [44]. The existence region and intrinsic defect structure are related by the preparation conditions of the bulk material and have been the subject of intensive investigation from the time since de Nobel [50]. Krüger published a comprehensive review of the defect chemistry in 1977 [51], and recently, theoretical treatments of defect levels in CdTe have extended this basis [52]. A critical topic of study is how the bulk properties transfer to thin-film CdTe.

The solid-state properties of CdTe are derived from the ionic character of the CdTe bond. Among the $\text{II}^{\text{B}}\text{-VI}^{\text{A}}$ compounds, CdTe has the highest value on the Phillips ionicity scale = 0.717, which is below the Phillips' threshold value of 0.785 for octahedral coordination [53]. Geometrical considerations show that tetrahedral coordination is favored in ionic binary compounds having cation/anion radius ratio between 0.225 and 0.732, while octahedral coordination is favored for a ratio greater than 0.732 [54]. In CdTe, the cation/anion radius ratio is $r(\text{Cd}^{2+})/r(\text{Te}^{2-}) = 0.444$, thus favoring tetrahedral coordination.

Tetrahedral atomic coordination, with the four nearest neighbors of the other element and the twelve next-nearest neighbors, leads to diamond structure in monatomic solids and zincblende and wurtzite structures in binary solids. Solid CdTe at atmospheric pressure exists in a face-centered cubic zincblende structure with unit cell dimension of 6.481 Å and CdTe bond length of 2.806 Å. Figure 14.4 depicts two views of the CdTe zincblende structure viewed across the closest-packing (111) plane, with alternating anion and cation planes, and viewed across the (110) plane, with equal numbers of anions and cations in each plane. These are the predominant orientations encountered in CdTe thin films.

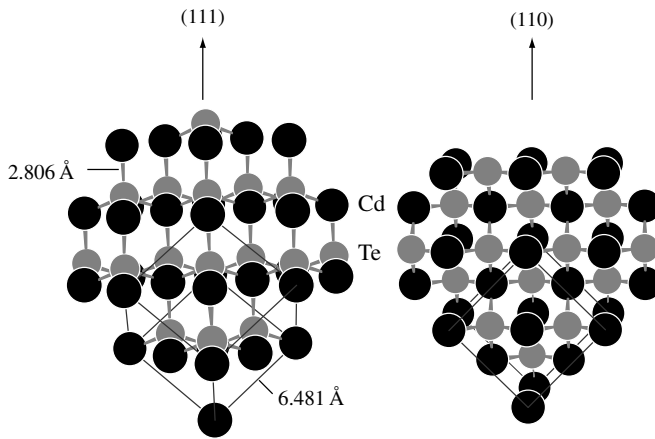


Figure 14.4 Zincblende CdTe crystal structure showing orientation with respect to (111) and (110) planes. The Cd atoms are black and Te atoms are gray. The Cd–Te bonds and F.C.C. unit cells are indicated for each view

CdTe polytypes are also known, depending on the formation pressure [55]. The hexagonal wurtzite structure, typically associated with tetrahedral coordination in predominantly covalent solids, is found in CdTe deposited in vacuum. No pure wurtzite bulk specimens have ever been reported [56]. Octagonal coordination, leading to the halite NaCl structure can be induced in CdTe by subjecting single crystals to high pressure, above 35 kbar. Among II–VI compounds, only CdO, with ionicity = 0.785, occurs with the halite structure at standard pressure and temperature.

The bulk optical and electronic properties of CdTe arise from the electronic-band structure within the periodic lattice near the valence-band maximum (VBM) and the conduction-band minimum (CBM). The VBM and CBM occur at the same momentum position, Γ , within the first Brillouin zone, giving rise to a direct band gap of 1.5 eV at 300 K. The temperature variation of the CdTe band gap is ~ -1.7 meV/K. The band curvature about the extrema represents the effective mass of electrons at the CBM and of holes at the VBM and controls carrier-transport properties and interband density-of-states (see Table 14.1).

Qualitatively, the band structure of CdTe can be understood from its relatively high ionicity, since the parts of the Bloch functions having the same periodicity as the lattice are related to the Cd and Te atomic orbitals. The conduction band arises from the first unoccupied level of the cation, namely, the 5s level of Cd. The uppermost valence band consists of the highest occupied level of the anion, namely, the 5p level of Te. It has been shown that cation *d* and anion *p* coupling reduce valence-band offsets in CdTe [57]. Detailed calculations of the *E*–*k* band structures in cubic CdTe and other II–VI compounds were originally carried out by the local pseudopotential method in the mid-1960s [58] and more recently using the linearized augmented plane-wave method, considering all electrons and relativistic kinematics [59].

Deviations from perfect single crystals cause profound changes in electronic and optical properties. Imperfections or defects disrupt the periodic structure, producing

localized electronic states within the band gap, E_g . It is customary to refer to states having ionization energy $\sim E_g/2$ as “deep” and states having ionization energy near the bands as “shallow.” The types of defects controlling electronic properties include native defects, chemical impurities, and complexes thereof; native defects and impurities can occur substitutionally or interstitially. For example, cadmium vacancy, V_{Cd} , gives rise to shallow acceptor states, while cadmium substitution on a tellurium site, Cd_{Te} , gives rise to shallow acceptor states. Interstitial cadmium, Cd_i , gives rise to a relatively shallow donor state, while tellurium, Te_i , gives rise to deep states. A selected group of native, impurity, and complex defect levels in CdTe is shown in Figure 14.5.

Present-generation high-efficiency CdTe solar cells are based on p -type CdTe and n -type CdS. The desired electrical properties are obtained by activation treatments that incorporate specific impurities into the CdTe and CdS layers such as postdeposition treatments that introduce $CdCl_2$, O_2 , and Cu into CdTe, which may activate or passivate native defects [61]. The specific effects of these agents on grain surfaces and the intragrain bulk properties must be considered separately to account for the enhanced p -type conductivity and the electrical passivation of grain boundaries in films after treatment. A comprehensive review of bulk diffusivities of group I, II, and III impurities in CdTe is given in Reference [62].

The polycrystalline aspect of cell fabrication gives rise to critical challenges for the development of *thin-film* photovoltaics: (1) separating intragrain from grain-boundary

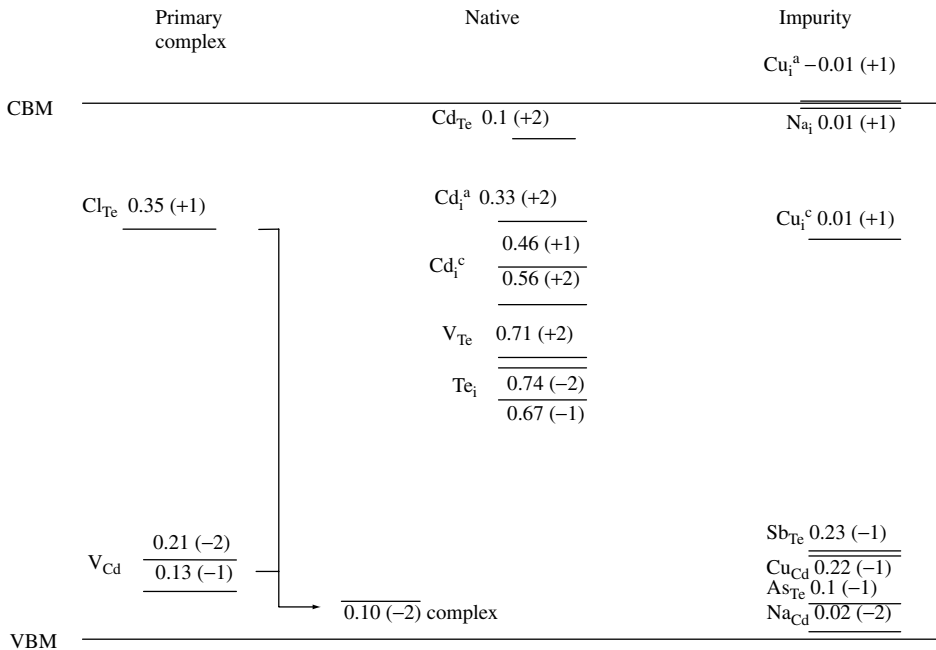


Figure 14.5 CdTe band structure with doping and defect levels. Charge states are in parentheses; energy is in electron volts measured from the conduction band for donor (positive) states and valence band for acceptor (negative) states. The superscripts a and c represent alternative interstitial sites. (Adapted from Wei S, Mtg. Record, National CdTe R&D Team Meeting (2001) Appendix 9 [60])

effects; (2) discovering the effect of grain boundaries on film properties and junction behavior; and (3) controlling film properties over very large area, encompassing $\sim 10^{12}$ grains per square meter for a CdTe module having 1- μm -wide grains. For CdTe/CdS solar cell development, these challenges have been met through advancing characterization techniques and empirical optimization of film deposition and postdeposition treatments.

A detailed review of the analytical techniques employed to probe the microstructure, microchemistry, and electronic properties of thin-film CdTe/CdS solar cells is beyond the scope of this chapter. However, several powerful methods have emerged to provide a quantitative assessment of film properties and are discussed elsewhere generally [63, 64], and specifically in terms of CdTe/CdS solar cells [65–67]. Some of these methods may ultimately find application as diagnostic sensors for in-line process-control feedback during module manufacture. These are listed below, accompanied by one or more references in which the techniques are applied to CdTe/CdS thin-film solar cells.

Morphology and structure:

- Scanning Electron Microscopy (SEM) [68]
- Transmission Electron Microscopy (TEM) [69]
- Atomic Force Microscopy (AFM) [70]
- X-Ray Diffraction (XRD) [71]

Bulk chemical composition:

- Energy Dispersive X-ray Spectroscopy (EDS) [72]
- X-Ray Diffraction (XRD) [73]
- Auger Electron Spectroscopy (AES) [74]
- Secondary Ion Mass Spectroscopy (SIMS) [75, 76]

Surface chemical composition:

- X-ray Photoemission Spectroscopy (XPS) [77]
- Glancing Incidence X-Ray Diffraction (GIXRD) [78]

Optoelectronic properties:

- Optical absorption [79]
- Ellipsometry [80]
- Raman [81]
- Photoluminescence (PL) [82, 83]

Junction analysis:

- Current–voltage versus illumination and temperature ($J-V-T$) [28, 84]
- Spectral response [23]
- Capacitance–voltage ($C-V$) [85]
- Optical Beam Induced Current (OBIC) [86]
- Electron Beam Induced Current (EBIC) [87]
- Cathode Luminescence (CL) [88]

Numerous methods have been employed to deposit CdTe thin films for solar cells, as detailed in the special issue of the *International Journal of Solar Energy* [89] and other review articles [90–92]. We will review eight methods that have demonstrated viability for the commercial manufacture of CdTe solar cells and modules over the past decade. Figure 14.6 presents schematic views of each fabrication procedure, including nominal temperature and pressure conditions, film thickness, and growth rate. The

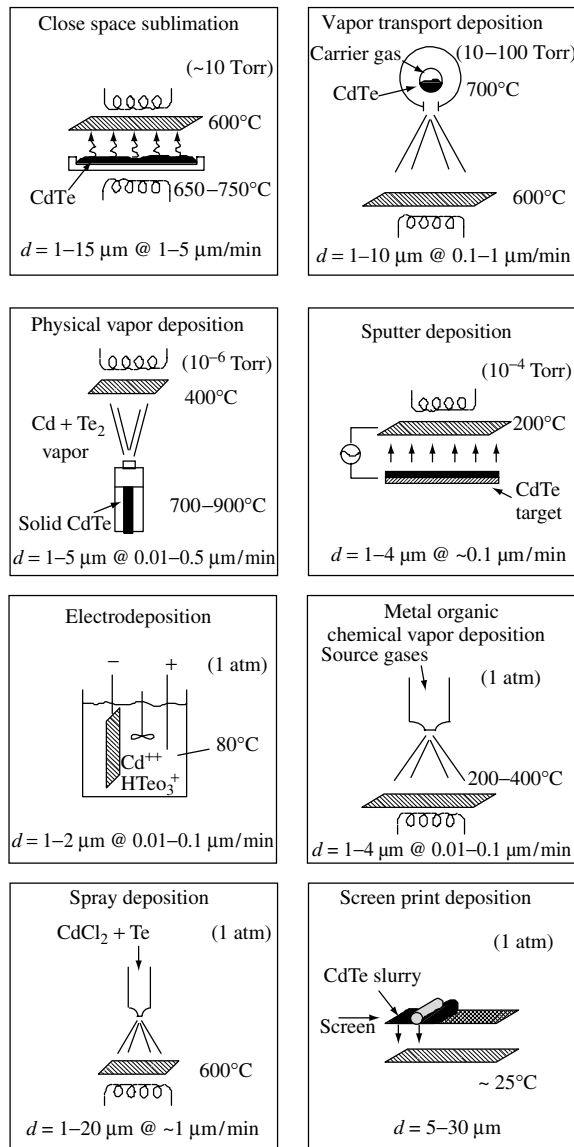


Figure 14.6 Schematic representations of eight CdTe thin-film deposition techniques. The substrate in each view is the cross-lined rectangle. Film thickness, d , and growth rate are shown at the bottom of each panel

presentation is organized by three chemical concepts: (1) condensation/reaction of Cd and Te₂ vapors on a surface (PVD, VTD, CSS, and sputter deposition), (2) galvanic reduction of Cd and Te ions at a surface (electrodeposition), (3) reaction of precursors at a surface [metal-organic chemical vapor deposition (MOCVD), screen-print deposition, and spray deposition].

14.2.1 Condensation/Reaction of Cd and Te₂ Vapors on a Surface

14.2.1.1 Physical vapor deposition (PVD)

The basis for vapor deposition of CdTe is the equilibrium between Cd and Te₂ vapors and CdTe solid, $\text{Cd} + 1/2\text{Te}_2 \rightleftharpoons \text{CdTe}$. As a consequence, CdTe can be deposited by coevaporation from elemental sources, by direct sublimation from a CdTe source or by vapor transport using a carrier gas to entrain and deliver Cd and Te₂ vapors from either elemental or CdTe sources. Congruent sublimation of the CdTe compound fixes the gas-phase composition for deposition from a CdTe source, and the relatively low vapor pressure of CdTe compared to elemental Cd and Te facilitates the deposition of single-phase solid films over a wide range of substrate temperatures (refer to Figure 14.3(b)). Similar considerations allow coevaporation from multiple II-VI binary sources to deposit alloys in pseudobinary systems such as CdZn_{1-x}Te_x and CdTe_{1-x}S_x.

Evaporation can be carried out from open crucibles or from Knudsen-type effusion cells, with the latter providing superior control over beam distribution and utilization. For effusion-cell evaporation, the deposition rate and uniformity of the species arriving at the substrate are controlled by source temperature, effusion-cell geometry, source to substrate distance, and total pressure [93, 94]. Within the effusion cell, mass transport to the nozzle exit occurs in a transitional flow regime, between free molecular flow and diffusion-limited flow. Effusion cells are typically constructed of boron nitride or graphite and are radiatively heated. For deposition in moderate vacuum, $\sim 10^{-6}$ Torr, with a CdTe source effusion cell with 0.5-cm-diameter orifice and a temperature of 800°C, at a source to substrate distance of 20 cm, a deposition rate of ~ 1 $\mu\text{m}/\text{min}$ is obtained on a substrate at a sufficiently low temperature ($\sim 100^\circ\text{C}$) for Cd and Te sticking coefficients to approach unity. At higher substrate temperatures, the sticking coefficients of impinging Cd and Te decrease, resulting in a lower deposition rate, imposing a practical limit to substrate temperature of less than 400°C for modest CdTe utilization. As-deposited films exhibit (111) preferred orientation and normal grain-size distribution with a mean grain diameter that depends on film thickness and substrate temperature; for 2- μm -thick films, the mean grain diameter ranges from ~ 100 nm at 100°C to ~ 1 μm at 350°C. The physical vapor deposition (PVD) process has been investigated by university (Stanford University [95], Institute of Energy Conversion at University of Delaware [96]) and industrial (Canrom and Central Research Laboratory at Japan Energy Corporation [97]) groups.

14.2.1.2 Close-space sublimation (CSS)

To evaporate CdTe films onto substrates at temperatures above 400°C, reevaporation of Cd and Te from the growing CdTe surface limits the deposition rate and utilization. This can be mitigated by depositing at higher total pressure, ~ 1 Torr, but mass transfer from the source to the substrate becomes diffusion-limited, so the source and substrate must be brought into close proximity. For close-space sublimation (CSS), the CdTe source material is supported in a holder having the same area as the substrate; the source holder and substrate cover serve as susceptors for radiative heating and conduct heat to the CdTe source and the substrate, respectively. An insulating spacer allows thermal isolation of the source from the substrate, so that a temperature differential can be sustained throughout the duration of the deposition. The ambient for deposition typically contains a nonreactive

gas such as N₂, Ar, or He. A small partial pressure of O₂ appears to be crucial for obtaining good film density and solar cell junction quality. As-deposited CSS films deposited above 550°C exhibit nearly random orientation and normal grain size distribution with mean grain size that is comparable to film thickness. The CSS process has been intensively investigated by groups at Kodak [98], USF [99, 100], NREL [101], Matsushita [102], and Antec [103, 104] and has yielded the highest small-area cell performance of any process shown in Figure 14.6. Commercial development is presently under way at Antec, GmbH.

14.2.1.3 Vapor transport deposition (VTD)

VTD allows high-rate deposition at high substrate temperature at pressures approaching 0.1 atm onto moving substrates. While CSS is diffusion-limited, VTD works by convective transfer of a vapor stream saturated with Cd and Te to the substrate, where supersaturation of the Cd and Te vapors results in condensation and reaction to form CdTe. The CdTe source consists of a heated chamber containing solid CdTe in which the carrier gas mixes with the Cd and Te vapors and is exhausted through a slit over or under the moving substrate at a distance on the order of ~1 cm. The geometrical configuration of the source influences the uniformity and utilization of the vapors in the carrier gas. The carrier-gas composition can be varied, as with CSS, to include N₂, Ar, He, and O₂. As-deposited VTD films are similar to CSS films, with nearly random orientation and normal grain size distribution with mean grain size that is comparable to film thickness [105]. The VTD process can provide a very high deposition rate onto moving substrates and is currently being investigated by the Institute of Energy Conversion and is under development by First Solar, LLC [106].

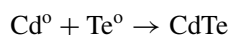
14.2.1.4 Sputter deposition

CdTe films have been deposited by radio-frequency magnetron sputtering from compound targets. Mass transfer of Cd and Te occurs via ablation of the CdTe target by Ar⁺, followed by diffusion to the substrate and condensation. Typically, deposition is carried out at a substrate temperature less than 300°C and at pressures ~10 mTorr. As-deposited films 2-μm-thick deposited at 200°C exhibit mean grain diameter ~300 nm and nearly random orientation. The sputter-deposition technique has been investigated by groups at the University of Toledo [107] and NREL [108].

14.2.2 Galvanic Reduction of Cd and Te Ions at a Surface

14.2.2.1 Electrodeposition

Electrodeposition of CdTe consists of the galvanic reduction of Cd and Te from Cd²⁺ and HTeO₂⁺ ions in acidic aqueous electrolyte. The reduction of these ions utilizes six electrons in the following reactions:



The large difference in reduction potential necessitates limiting the concentration of the more positive species, Te, to maintain stoichiometry in the deposit. In practice, the low Te species concentration (10^{-4} M) limits the CdTe growth rate due to Te depletion in the solution at the growing surface and subsequent mass transport. To overcome this, the electrolyte is vigorously stirred, and different methods of Te replenishment are employed. Thickness and deposition area are limited by the ability to maintain deposition potential over the entire surface of the growing film. As-deposited films can be fabricated as stoichiometric CdTe, Te-rich (by increasing Te species concentration in the bath) or Cd-rich (by depositing at low potentials with limited Te species concentration). As-deposited electrodeposited CdTe films on CdS thin-film substrates exhibit strong (111) orientation with columnar grains having a mean lateral diameter of 100 to 200 nm. The basis for this technology has been formalized in the open literature [109]. Electrodeposition of CdTe has been intensively studied by the group at Monosolar [110], Ametek [111], and the University of Texas [112]. In the 1980s, the Monosolar process was transferred to SOHIO and thence to BP Solar, where commercial development took place at the factory in Fairfield, California. In the early 1990s, the Ametek process was transferred to the Colorado School of Mines in Golden Colorado.

14.2.3 Precursor Reaction at a Surface

14.2.3.1 Metal organic chemical vapor deposition (MOCVD)

MOCVD is a nonvacuum technique for depositing CdTe films at moderately low temperature from organic Cd and Te precursors such as dimethylcadmium and diisopropyltellurium in hydrogen carrier gas. The substrates are supported on graphite susceptors and can be heated radiatively or by coupling to a radio frequency generator. Deposition occurs by pyrolytic decomposition of the source gases and reaction of the Cd and Te species. As a consequence, the growth rate depends strongly on the substrate temperature, which typically ranges from 200 to 400°C. As-deposited films 2- μ m-thick deposited at 400°C exhibit columnar grain structure with lateral grain diameter ~ 1 μ m. The MOCVD process has been investigated by groups at SMU/USF [113] and Georgia Institute of Technology [114].

14.2.3.2 Spray deposition

Spray deposition is a nonvacuum technique for depositing CdTe from a slurry containing CdTe, CdCl₂, and a carrier such as propylene glycol. The slurry can be sprayed onto unheated or heated substrates, after which a reaction/recrystallization treatment is performed. The application of spray deposition to CdTe films was developed by John Jordan (Photon Energy Corporation) during the 1980s. The company was sold to Coors in 1995 and had its name changed to Golden Photon. Cells with >14% efficiency were fabricated, but commercial development ceased in 1997. In this process, the mixture was sprayed onto the substrates at room temperature and baked at 200°C, followed by a bake in the presence of O₂ at 350 to 550°C, a mechanical densification step, and a final treatment at 550°C. Films produced by this method vary in morphology, grain size, and porosity, but films used to make high-efficiency cells exhibited a 1- to 2- μ m-thick dense region near the CdTe–CdS interface, a relatively porous back surface region, and random crystallographic

orientation. A dramatic consequence of the fabrication process was the consumption of the CdS layer, leading to a nearly uniform CdTe_{1-x}S_x alloy throughout the film thickness, which reduced the absorber-layer band gap to ~ 1.4 eV. In the highest-efficiency cells made by spray deposition, CdS diffusion and subsequent alloy formation consumed most of the CdS film, resulting in an enhanced blue-spectral response and correspondingly high short-circuit densities. The method was extensively investigated by the group at Golden Photon [115, 116].

14.2.3.3 Screen-print deposition

Screen-print deposition is perhaps the simplest of the CdTe techniques, combining Cd, Te, CdCl₂, and a suitable binder into a paste that is applied to the substrate through a screen. Following a drying step to remove binder solvents, the layer is baked at temperatures up to 700°C to recrystallize the film and activate the junction. Films fabricated by this method typically have a thickness ranging from 10 to 20 μm with lateral grain dimension of ~ 5 μm and random orientation. Screen-printed CdTe can be traced back to the 1970s with the pioneering work of Matsushita [117] and subsequently by groups at the University of Seoul [118] and the University of Ghent [119].

14.3 CdTe THIN-FILM SOLAR CELLS

All high-efficiency CdTe solar cells to date have essentially the same *superstrate* structure as that successfully demonstrated by Bonnet and Rabenhorst in 1972 [26]. This structure is depicted in Figure 14.7. The alternative *substrate* configuration, with the TCO/CdS/CdTe deposited onto an opaque substrate, has been much less successful, primarily because of poor CdS/CdTe junction quality and poor ohmic CdTe contact, resulting from chemical instability of the back contacts and from copper diffusion out of the back contact toward the CdTe surface during film growth.

The primary photodiode junction occurs between the *p*-type CdTe absorber and the *n*-CdS window layer. There are, however, a number of complicating factors, such as the need for a high-resistance oxide layer when the CdS is thin, the need for a thermal treatment with CdCl₂ and oxygen to improve the CdTe quality, the interdiffusion of CdS and CdTe, and the barrier associated with the back contact. The following sections will address these complications.

14.3.1 Window Layers

The first step in the fabrication of a superstrate CdTe cell is to coat the glass with a transparent conducting oxide (TCO), such as SnO₂, indium–tin oxide, In₂O₃:Sn, referred to as ITO, or cadmium stannate, Cd₂SnO₄, which serves as the front contact. To obtain high current density in the completed cell, the CdS layer needs to be very thin, which, owing to its polycrystallinity, raises the possibility of local shunting or excessive forward current. It has been found that the deposition of a second, highly resistive, transparent oxide layer, referred to as the HRT layer, between the TCO and CdS significantly ameliorates this problem and improves junction quality and uniformity in a manner analogous to

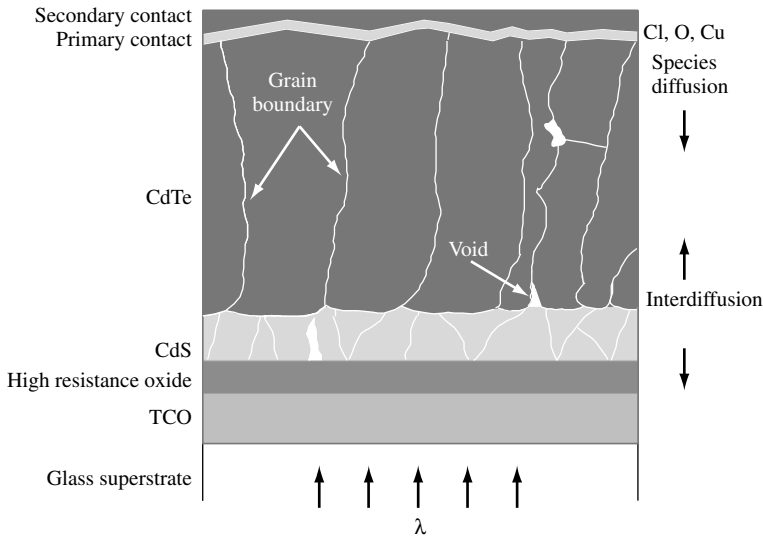


Figure 14.7 Basic CdTe solar cell structure. The polycrystalline nature of the CdS and CdTe layers are indicated schematically and are not to scale

that found for CuInSe₂/CdS and a-Si thin-film cells [120]. Materials used for the resistive layer include SnO₂ [121], In₂O₃ [122, 123], Ga₂O₃ [105], and Zn₂SnO₄ [124].

Most CdTe cells utilize *n*-type CdS for the window layer immediately adjacent to the CdTe. The processing possibilities for depositing good-quality CdS are nearly as varied as those shown in Figure 14.6 for CdTe and include chemical bath deposition, sputter deposition, and physical vapor deposition. The choice is usually driven by compatibility with the other deposition processes in a fabrication line. It is generally desirable to keep the CdS layer as thin as possible to allow a high fraction of the photons with energy above its band gap to reach the CdTe absorber and hence produce a high photocurrent.

In practice, as will be discussed in more detail later, cell-processing conditions often promote interdiffusion between CdTe and CdS. The resulting band gap shift in CdS reduces the window-layer transmission and lowers the short-wavelength quantum efficiency [125, 126]. This effect can be minimized either by heat treatment of the CdS with CdCl₂ to recrystallize the film or by judicious control of device processing to reduce the remaining CdS thickness [124] effectively to zero [116]. Thin-film CdTe cells with the CdS layer omitted altogether, however, have not performed well as of this writing (see, for example, Table 2 in Reference [122]).

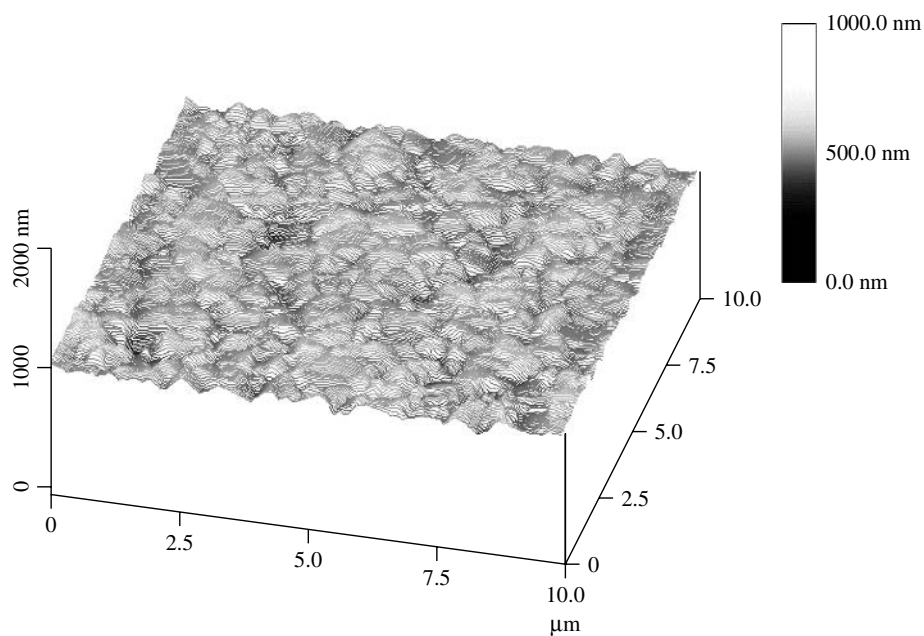
Another strategy to reduce window absorption has been to mix CdS with ZnS to increase the band gap of the layer, and hence the photon transmission, but simple mixing has not produced net performance gains. The highest-efficiency CdTe cells to date have used Cd₂SnO₄ TCO and Zn₂SnO₄ HRT bilayer superstrates to take advantage of their wide optical band gaps and inherent conductive properties, with the Cd₂SnO₄ serving as the TCO layer and Zn₂SnO₄ as the HRT layer. An additional feature of this strategy is that the Zn₂SnO₄ HRT layer contributes to CdS consumption during processing [127].

14.3.2 CdTe Absorber Layer and CdCl₂ Treatment

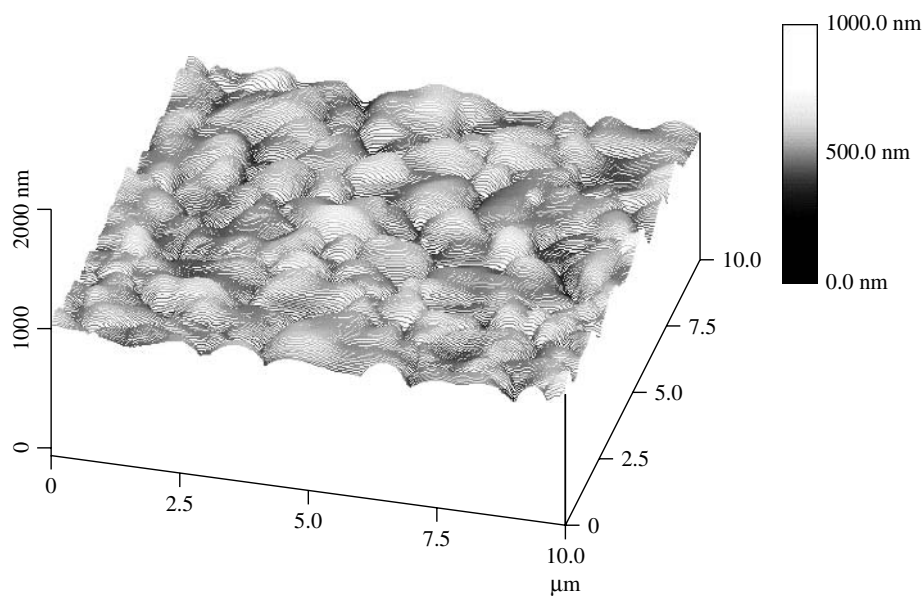
The large number of successful techniques for deposition of device-quality CdTe films was shown schematically in Figure 14.6. However, in cases of chloride-free deposition techniques such as physical vapor deposition (PVD), the actual deposition of the CdTe film has been found to be less critical than the postdeposition processing, which generally involves exposure to a high-temperature processing step followed by exposure to a chlorine-containing species and oxygen at $\sim 400^\circ\text{C}$, referred to as the “CdCl₂ treatment.” The treatment step has been performed in a variety of ways, such as dipping the CdTe layer in a CdCl₂:CH₃OH or CdCl₂:H₂O solution followed by drying to precipitate a CdCl₂ film [128, 129] by treatment in CdCl₂ vapor [130, 131] or by exposure to HCl [132] or Cl₂ gas [133]. Chlorine species may also be incorporated during CdTe film formation, in the form of Cl⁻ ions in an electrodeposition bath [134] or as a component of a screen-printing slurry [68]. The typical temperature–time range for the thermal cycle following chlorine incorporation is from 380 to 450°C for 15 to 30 min, depending on CdTe film thickness, with thicker films requiring longer treatment time.

The changes induced by chlorine incorporation and subsequent heat treatment depend on the prior thermochemical history of the CdTe/CdS structure. For example, the treatment can promote recrystallization and grain growth in films having submicrometer initial CdTe crystallite size [135]. The change in morphology and structure is shown in Figures 14.8 and 14.9. Figure 14.8 shows atomic force micrographs of the surface morphology of PVD CdTe, deposited at 250°C, before and after treatment at 420°C in CdCl₂ and air vapor. Figure 14.9 shows cross-sectional TEM images of changes in grain size and crystallographic defects in the junction region of a CdTe/CdS/ITO structure deposited by PVD onto a smooth Si wafer. Depositing the structure on a Si wafer facilitated the mechanical preparation of the sample for cross-sectional thinning. Table 14.2 more generally compares the changes in grain size, aspect ratio, and crystallite orientation for CdTe deposited by several different methods. For CdTe films having submicrometer initial crystallite size, such as shown in Figure 14.8, significant recrystallization occurs during the CdCl₂ treatment. This takes two forms: (1) intragrain, or primary, recrystallization changes grain orientation from typically (111) to random (see Figure 14.10) and (2) intergrain, or secondary, recrystallization results in grain coalescence. The phrase “fluxing agent” has been coined in reference to the role of CdCl₂ in promoting grain growth, although the secondary recrystallization does not always occur, depending on the thermochemical history of the film and the initial grain size. For films deposited at high temperature, having large initial grain size, annealed prior to CdCl₂ exposure, or containing the native oxide, CdTeO₃, little measurable grain growth (secondary recrystallization) occurs during CdCl₂ treatment. This is because surface energy is already minimized or is pinned by the presence of the oxide. Under these processing conditions, film randomization is the predominant effect, showing that CdCl₂ still exerts an intragrain influence on lattice arrangement.

The postdeposition treatment also modifies the electronic properties. Air-heat treatment alone, at temperatures above $\sim 500^\circ\text{C}$, can reduce the CdTe sheet resistance up to three orders of magnitude [136]. Treatment with CdCl₂ in air likewise reduces resistivity, by the combination of recrystallization and creation of acceptor states. The primary electronic effect of Cl incorporation seems to be the formation of an acceptor complex with Cd vacancies (see Figure 14.5). Both the single-donor and the double-acceptor states are



(a)



(b)

Figure 14.8 AFM images comparing PVD CdTe/CdS thin-film structures (a) before and (b) after heat treatment in CdCl₂ vapor at 420°C for 20 min

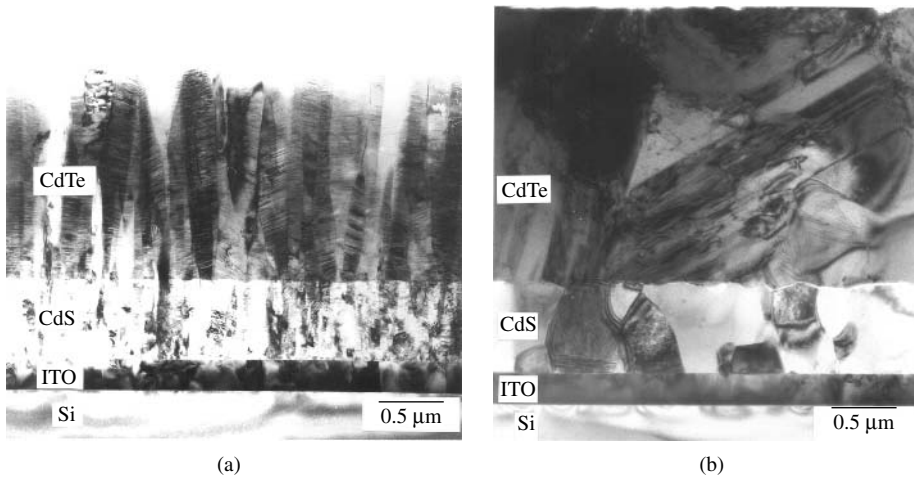


Figure 14.9 TEM images comparing PVD CdTe/CdS thin-film structures (a) before and (b) after CdCl₂ heat treatment at 420°C for 20 min. Average grain size increased from roughly 0.1 to 0.5 μm in both CdTe and CdS

Table 14.2 Structural changes of CdCl₂ HT on CdTe deposited by different methods. Data from films examined by B. E. McCandless. For sprayed and screen-printed cells, random film orientation is obtained as a result of the film formation process

Deposition method	Film thickness [μm]	Mean grain size: D Init → CdCl ₂ HT [μm]	Orientation Init → CdCl ₂ HT
PVD	4	0.1 → 1	(111) → (220)
ED	2	0.1 → 0.3	(111) → (110)
Spray	10	10 → 10	Rand
Screen	12	~10	Rand
VTD	4	4 → 4	Rand → Rand
CSS	8	8 → 8	Rand → Rand
Sputter	2	0.3 → 0.5	(111) → (?)
MOCVD	2	0.2 → 1	(111) → Rand

pushed closer to the band edges, resulting in a single, relatively shallow acceptor state. Although this complex is a more effective dopant than the Cd vacancies alone, excess Cl can lead to compensating Cl_{Te} donors.

The impact of CdCl₂ treatment on cell operation is increased photocurrent and open-circuit voltage, and reduced shunting. Figure 14.11 compares the light $J-V$ behavior of three PVD cells having 4-μm-thick CdTe and 0.2-μm-thick CdS, processed with the same back contact but with no postdeposition treatment, air-heat treatment at 550°C, and optimized CdCl₂ treatment at 420°C for 20 min in air. With no treatment, the device exhibits very low photocurrent and high series resistance. The spectral response is low

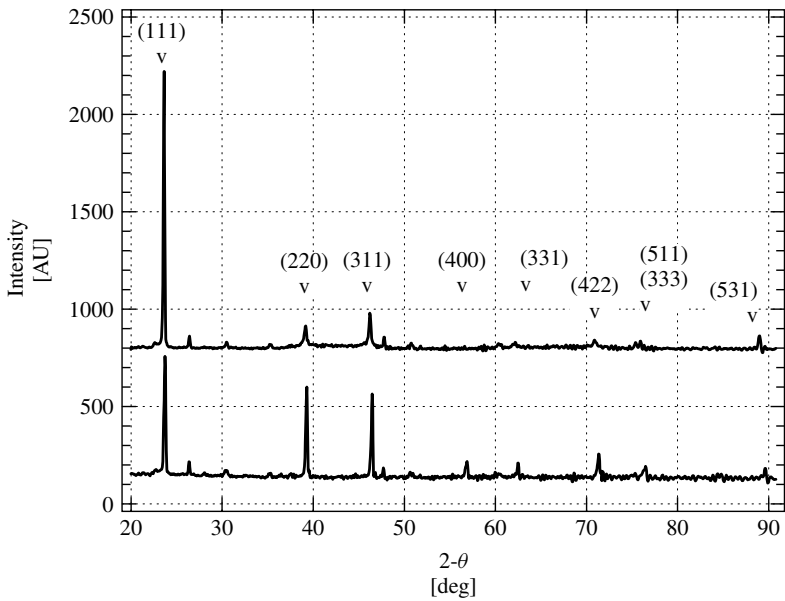


Figure 14.10 X-ray diffraction patterns of PVD CdTe/CdS thin-film structures before and after vapor CdCl₂ heat treatment at 420°C for 20 min, showing randomization of the film orientation. The primary peaks are due to the 1.5- μ m-thick CdTe layer; the other peaks are due to the underlying CdS and ITO films

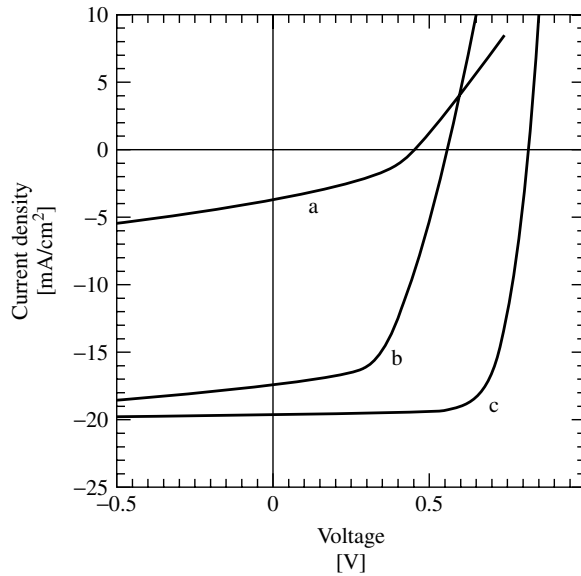


Figure 14.11 Light AM1.5 $J-V$ curves of PVD devices with Cu₂Te/C contacts and different post-deposition processing: (a) no heat treatment; (b) treatment at 550°C for 5 min in air; (c) treatment in CdCl₂ vapor at 420°C for 20 min in air [105]

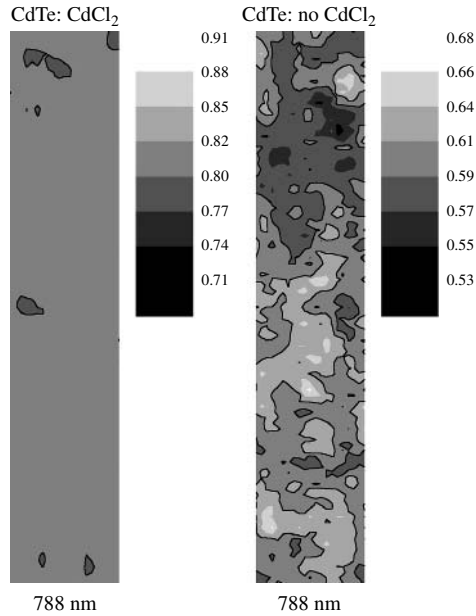


Figure 14.12 Local variations in quantum efficiency with 1- μm beam and $\lambda = 788 \text{ nm}$. Areas shown are $50 \times 10 \mu\text{m}$

overall and exhibits a peak near the CdTe band edge, suggesting *p-i-n* device operation [137]. With either air treatment or vapor $\text{CdCl}_2 + \text{air}$ treatment, the $J-V$ and spectral response behavior correspond to *p-n* device operation, with optimal properties obtained for the vapor $\text{CdCl}_2 + \text{air}$ treatment. For devices made by other methods, similar behavior is obtained, but the starting condition (Figure 14.11a) can be improved by deposition at high temperature in an oxygen-containing ambient.

The effect of the CdCl_2 treatment on photocurrent microuniformity is shown in Figure 14.12, for cells with CdTe deposited by CSS. The QE map on the left was made on a cell following a typical CdCl_2 treatment, and shows spatially uniform collection. The map on the right was for a cell fabricated without the CdCl_2 treatment and exhibits considerable nonuniformity [138]. The light intensity for these maps is nearly 100 mW/cm^2 and the light spot is slightly smaller than $1 \mu\text{m}$. The large local reductions in photocurrent without CdCl_2 treatment are areas of high resistance associated with grain boundaries. With the use of the CdCl_2 treatment, spatial-junction uniformity is improved by the electronic incorporation of Cl and O species and alloy formation by diffusion of CdS into CdTe. The QE of the sample with CdCl_2 treatment is ~ 0.82 over 95% of the measured area, while that of the sample without CdCl_2 treatment ranges from 0.50 to 0.68.

14.3.3 CdS/CdTe Intermixing

All CdS/CdTe cells are exposed to processing temperatures of at least 350°C during CdCl_2 treatment. In some cases, such as spray pyrolysis, much higher temperatures are involved. Hence, a chemical reaction between CdTe and CdS can occur and this is the

driving force for bulk and grain-boundary interdiffusion of CdTe and CdS. It has been widely reported that a continuous CdTe–CdS solid-solution alloy series can be formed by codeposition of CdTe and CdS at temperatures less than 200°C. The optical band gap of these alloys varies with the composition according to $E_g(x) = 2.40x + 1.51(1 - x) - bx(1 - x)$, with bowing parameter, $b \sim 1.8$, as shown in Figure 14.13 [139]. However, thermal treatment of alloy films above 400°C can induce phase segregation, with the miscibility gap found for equilibrated CdTe–CdS mixed crystals.

Numerous references have established the T – x phase relations in CdTe–CdS mixed crystals at temperatures above 625°C, which exceeds the temperatures typically used to deposit and process thin-film CdTe/CdS structures. This has been extended down to 360°C by lattice-parameter determination of equilibrated CdTe_{1–x}S_x alloy films, as shown in Figure 14.14 [146]. Thermodynamic analysis of the asymmetric phase boundaries using nonideal solution thermodynamics reveals positive values of excess-mixing enthalpies $\Delta H^{\text{EX}} = 3.5$ kcal/mol for CdS into CdTe and $\Delta H^{\text{EX}} = 5.6$ kcal/mol for CdTe into CdS. For CdS dissolved in CdTe, the experimentally obtained excess-mixing enthalpy supports those calculated from first principles band structure theory for the CdTe–CdS system [147].

The crystallographic forms of the solid alloys are the zincblende (F-43 m) structure for CdTe_{1–x}S_x and the wurtzite (P6₃mc) structure for CdS_{1–y}Te_y. The zincblende transition to the wurtzite structure in metastable films occurs at $x = 0.3$, and the lattice parameter within each structure type follows Vegard's rule. Metastable and equilibrated CdTe_{1–x}S_x alloy films exhibit the same dependence of E_g , with minimum at 1.39 eV, corresponding to the zincblende–wurtzite transition.

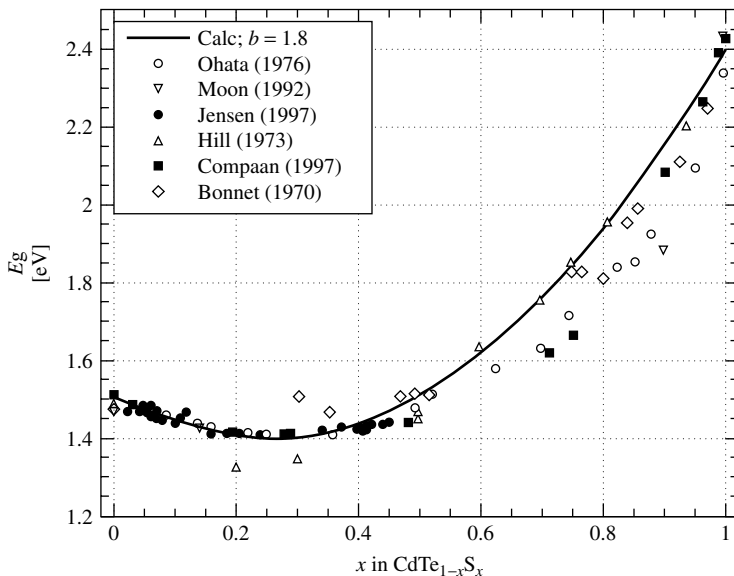


Figure 14.13 Optical band gap of CdTe_{1–x}S_x alloy thin films versus composition. (Data listed in order from References [140–145])

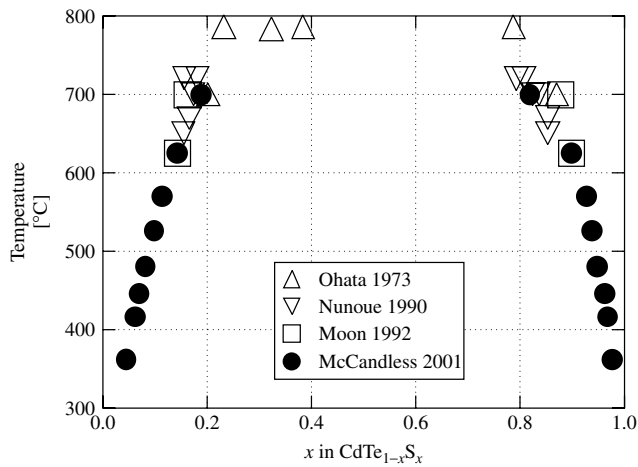


Figure 14.14 CdTe–CdS pseudobinary phase diagram. (Data listed in order from References [73, 140, 145, 148])

The formation of $\text{CdTe}_{1-x}\text{S}_x$ and $\text{CdS}_{1-y}\text{Te}_y$ alloys in the absorber layer occurs by interdiffusion between CdS and CdTe during CdCl_2 treatment in air [135, 204]. Diffusion of CdTe into CdS can reduce the transmissive properties of the window from 500 to 650 nm, but is mitigated by heat treatment of the CdS layer prior to CdTe deposition to increase CdS grain size and density. However, diffusion of CdS into CdTe is a faster process and is more difficult to control, especially for cell structures with ultrathin, <100 nm, CdS films. The progressive diffusion, which creates a distribution of lattice parameters within the film, can be easily detected with X-ray diffraction line-profile analysis (Figure 14.15).

Quantifying the diffusion process for films of a known grain structure showed that the diffusion proceeds via Fickian bulk and grain-boundary diffusion processes having Arrhenius temperature dependence [149] (Figure 14.16). Similar bulk diffusivities were found for CdS/CdTe couples using single-crystal CdTe and thin-film couples in *substrate* and *superstrate* configurations, yielding an activation energy of ~ 3.0 eV, corresponding to Cd self diffusion via Cd interstitials. Likewise, similar grain-boundary diffusivities were obtained for *substrate* and *superstrate* thin-film couples, with an activation energy of ~ 2.0 eV (Figure 14.17). The bulk diffusivity was weakly sensitive to the chemical composition of the treatment ambient, as shown in Figure 14.18. However, the grain-boundary diffusion process is enhanced by the partial pressures of CdCl_2 and O_2 during the CdCl_2 treatment. Finally, it has been demonstrated that grain-boundary diffusion can be retarded by oxidizing grain boundaries prior to exposure to CdCl_2 species [122] or by deposition of CdTe films in an oxygen-containing ambient.

Thus, alloy formation can be more pronounced in films deposited at low temperature having small grains and high grain-boundary density, such as by electrodeposition. In such films, a high partial pressure or concentration of CdCl_2 together with O_2 during CdCl_2 treatment will result in considerable alloy formation. In addition, alloy formation is dramatically enhanced for cells with CdTe deposited at high temperature in the presence of Cl species during growth, such as spray pyrolysis.

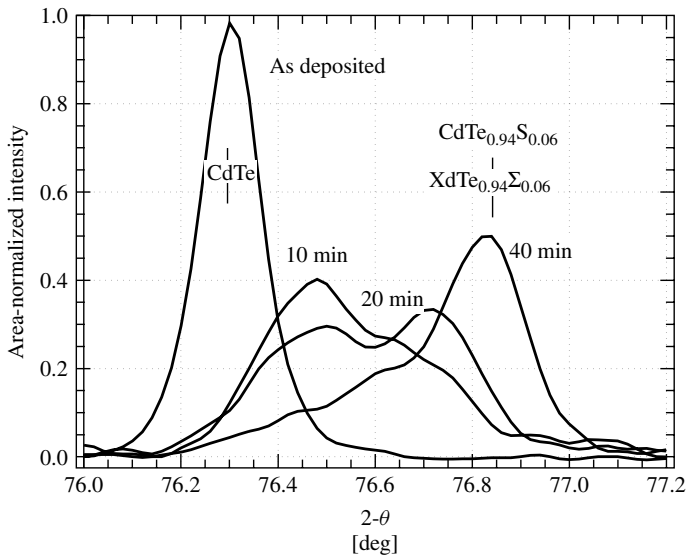


Figure 14.15 Time-progressive X-ray diffraction line profiles for the (511)/(333) reflection for PVD CdTe/CdS thin-film structures deposited at 250°C and treated in CdCl₂:Ar:O₂ vapor at 420°C. Positions of pure CdTe and CdTe_{1-x}S_x alloy with $x = 0.06$ are indicated

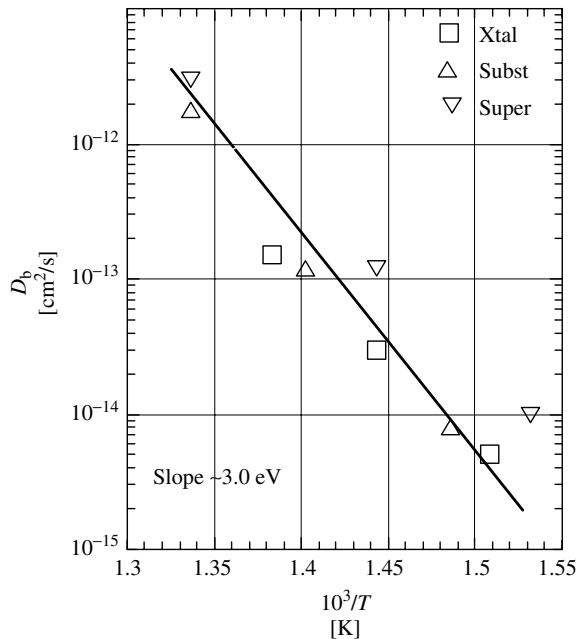


Figure 14.16 Arrhenius plot of bulk-diffusion coefficients versus inverse of treatment temperature for values obtained by modeling XRD line profiles of thin-film CdTe/CdS samples and from AES depth profiling of S distribution in CdTe single crystal [73]

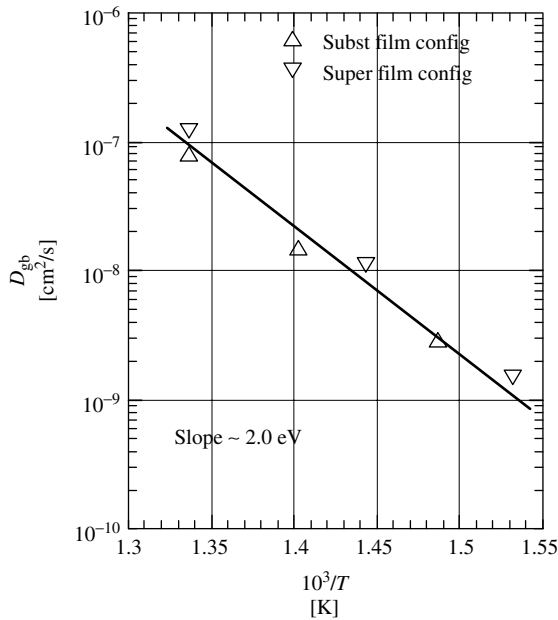


Figure 14.17 Arrhenius plot of grain-boundary diffusion coefficients versus inverse of treatment temperature for values obtained by modeling XRD line profiles of thin-film CdTe/CdS samples [73]

In cells, alloy formation has both beneficial and detrimental effects. The interdiffusion process narrows the absorber-layer band gap, resulting in higher long-wavelength quantum efficiency. Although this gain is somewhat offset by a reduction in the built-in voltage, open-circuit voltages exceeding 820 mV have been obtained in cells having alloyed $\text{CdTe}_{1-x}\text{S}_x$ absorber layers with composition $x > 0.05$, made by spray pyrolysis [150]. Intermixing reduces interfacial strain [68] and may reduce the dark recombination current [78]. The CdS film thickness is reduced, which can be beneficial for window transmission, but nonuniform CdS consumption can result in lateral junction discontinuities. The $\text{CdTe}_{1-x}\text{S}_x$ alloy formation is detected in XRD line profiles of the absorber layer and in the long-wavelength spectral response. This correlation between compositionally broadened XRD line profiles and the long-wavelength QE edge is illustrated in Figure 14.19 for XRD and QE measurements of completed cells. For CSS cells, deposited at high temperature and having large grains, the absorber layer exhibits a narrow (511)/(333) XRD profile at the CdTe position, indicating a negligible degree of alloy formation, and hence low CdS diffusion into CSS-deposited CdTe. This is seen in the QE plot, where the long-wavelength edge occurs at the wavelength expected for CdTe. In contrast, the cell made by spray pyrolysis, with the CdTe film formed at high temperature in the presence of CdCl_2 , exhibits an asymmetrical XRD line profile with its peak near the one expected for the $\text{CdTe}_{0.96}\text{S}_{0.05}$ and a tail extending toward pure CdTe. The XRD line profile thus indicates nonuniform S distribution in the absorber layer, evident in the QE plot as a shallow drop in the long-wavelength response. The PVD case is intermediate to the CSS and spray cases, having smaller grains than CSS films and receiving less exposure to CdCl_2 than sprayed films. Thus, it appears that apart

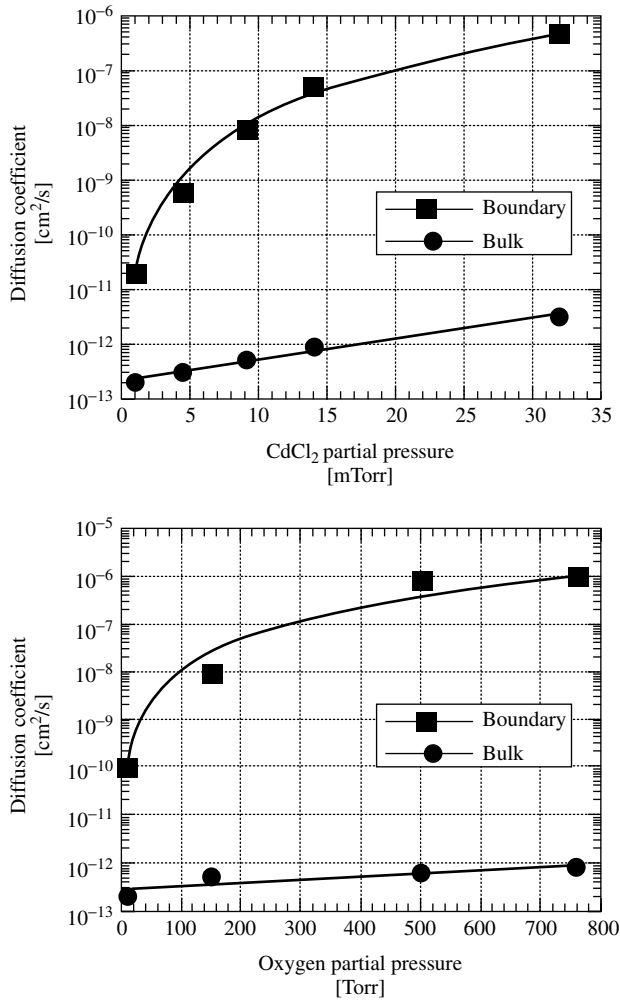


Figure 14.18 Sensitivity of bulk and grain-boundary diffusion coefficients (a) to $p\text{CdCl}_2$ at constant $p\text{O}_2 \sim 125$ Torr, at $T = 420^\circ\text{C}$, and (b) to $p\text{O}_2$ at constant $p\text{CdCl}_2 = 9$ mTorr, at $T = 420^\circ\text{C}$

from the differences in current generation, device operation is fundamentally similar for cells with differing amounts of $\text{CdTe}_{1-x}\text{S}_x$ alloy in the absorber layer.

14.3.4 Back Contact

The top region shown in Figure 14.7 is the back contact, consisting of a primary contact to CdTe, which typically consists of a tellurium-containing p^+ surface, and a secondary contact, which is the current-carrying conductor. As with other p -type semiconductors, there is a tendency to form a Schottky barrier with many metals, and achieving a low-resistance ohmic contact has proven to be challenging. The most common strategy is to form a Te-rich surface by selective chemical etching and then apply copper or a

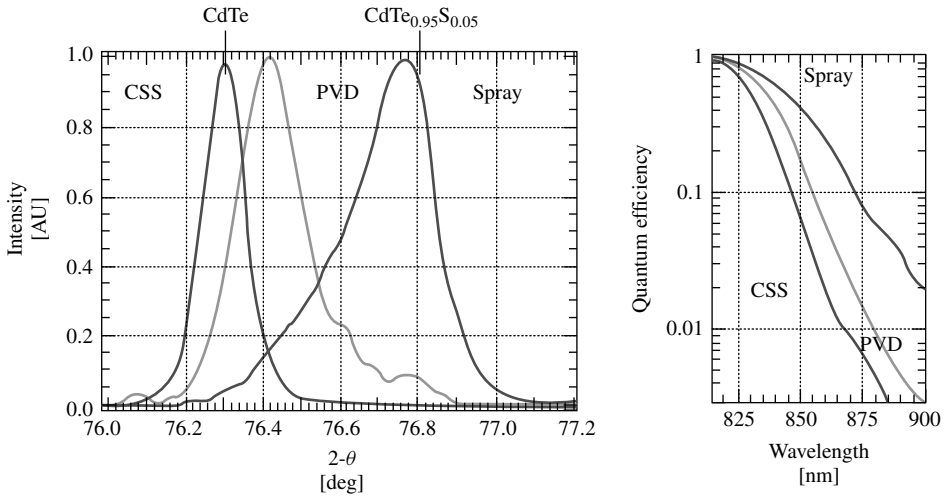


Figure 14.19 Correlation of XRD (511)/(333) reflection with long-wavelength quantum efficiency

copper-containing material. Copper will react with Te to form a p^+ -layer that can then be contacted with a metal or with graphite. The subtelluride Cu_2Te has been directly measured at the back surface using GIXRD methods [151]. Also, Cu acts as a relatively shallow donor in CdTe and can be diffused into CdTe from a doped contact material such as graphite paste [34] or ZnTe:Cu [205].

There are a variety of surface treatments that have been used, prior to formation of the copper layer, to reduce the back barrier. Table 14.3 gives a summary of these surface treatments and the corresponding materials that have typically been used for the back contact. Although fabrication laboratories tend to utilize a single surface treatment and contact material, there is little evidence that the preferred contact process is dependent on the deposition technique.

The high bulk-diffusion coefficient for Cu in CdTe, $3 \times 10^{-12} \text{ cm}^2/\text{s}$ at 300 K [156], coupled with its multiple valence states and weak Cu–Te bond give rise to potential stability issues related to its use as discussed below. Alternatives to the use of copper in the back

Table 14.3 Back-contact formation methods (NP = nitric + phosphoric acid mixture, BDH = sequential reaction in bromine, acidic dichromate, and hydrazine)

CdTe deposition method	Surface treatment	Primary contact	Thermal treatment	Additional contact	Reference
PVD	Te + H ₂	Cu	200°C/Ar	C	[152]
ED	BDH	Cu	None	Ni or Au	[153]
Spray	Etch	C + dopant	None	None	[154]
Screen	None	C + Cu dopant	400°C/N ₂	None	[155]
VTD	BDH	Cu	200°C/Ar	C	[151]
CSS	NP Etch	C + HgTe + Cu	200°C/He	Ag paste	[84]
Sputter	Br Etch	ZnTe:N	In situ	Metal	[156]
MOCVD	Br Etch	ZnTe:Cu	In situ	Metal	[157]

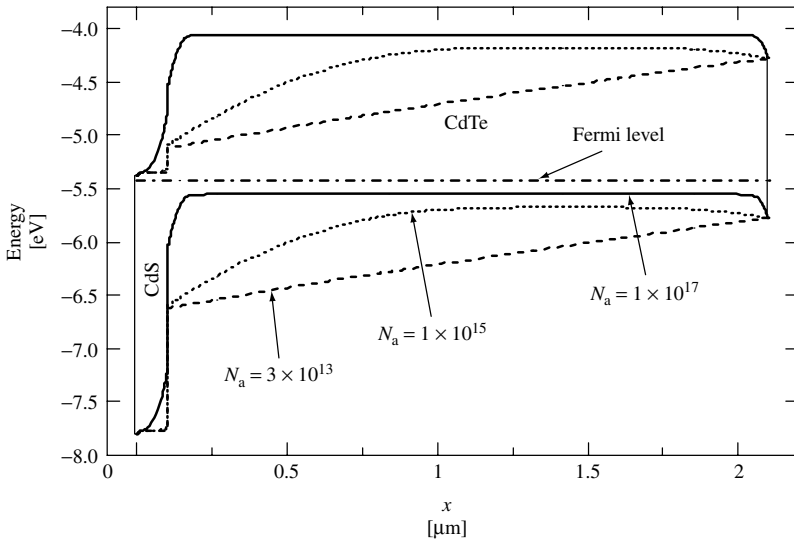


Figure 14.20 CdTe/CdS junction band diagrams at $V = 0$ for three values of CdTe acceptor density and a back-contact barrier = 0.3 eV

contact have generally involved the use of other tellurides, such as ZnTe:N [158] and Sb_2Te_3 [159], that can make reasonable contact to the CdTe and form only modest barriers with an appropriate metal. To date, however, contacts demonstrably free of Cu have not shown significant promise.

One consequence of a back-contact barrier, and the value of keeping it small, can be seen in the band diagrams of Figure 14.20 calculated by Alan Fahrenbruch for a 2- μm -thick CdTe layer [160]. The back contact is essentially a second diode with opposite polarity and smaller barrier than the primary junction. For a thick absorber, or one with reasonably large carrier density (solid curve), the bands are flat over most of the absorber thickness, the primary junction effectively blocks modest forward currents, and the back barrier has only a minor effect on the current–voltage curves. For carrier densities more typical of CdTe (between dashed and dotted lines), however, the depletion widths of the primary and back-contact diodes overlap. The effective reduction in the barrier for electrons means that forward current can flow more easily, reducing the open-circuit voltage.

14.3.5 Solar Cell Characterization

Considerable information about the electrical properties of CdTe solar cells has been deduced from straightforward measurements of current versus voltage (J – V), quantum efficiency (QE) and capacitance versus frequency (C – f) and voltage (C – V). More detailed information can be obtained from the temperature dependence or the time evolution of these curves.

The J – V curve (Figure 14.2) for the record-efficiency cell follows a standard diode equation with additional factors included to take account of circuit resistance and

forward-current mechanisms other than thermionic emission.

$$J = J_0 \exp[(V - JR)/AkT] - J_{SC} + V/r \quad (14.1)$$

For the illuminated $J-V$ curves of the record-efficiency CdTe cell, the prefactor J_0 is 1×10^{-9} A/cm², the series resistance R is $1.8 \Omega\text{-cm}^2$, the diode quality factor A is 1.9, and the shunt resistance r is $2500 \Omega\text{-cm}^2$. The values for R and A were found using the technique described in Reference [161].

The forward-current ($J + J_{SC}$) data for the record-efficiency CdTe cell is replotted in Figure 14.21 using a logarithmic scale, and the analogous data of a high-efficiency GaAs cell [162] is shown for comparison. Since CdTe and GaAs have nearly the same band gap, they should ideally have the same lower limit to J_0 and same V_{OC} and $J-V$ characteristic, if they were both limited by band-to-band recombination. Both curves have had small corrections for series and shunt resistances (R and r). Since the absorber materials have similar band gaps, the CdTe and GaAs cells should have similar $J-V$ curves. The V_{OC} difference shown, however, is nearly 200 mV. At maximum power (MP), the voltage difference is larger yet, approaching 300 mV, because the CdTe A-factor is 1.9 compared to 1.0 for the GaAs. The physical difference is due to the additional recombination-current paths for the CdTe junction. This excess forward current for the CdTe cell is roughly two orders of magnitude greater than that of the GaAs cell under normal operating conditions. The implication is that there is considerable room for improvement of V_{OC} in CdTe cells through reduction in such recombination. Referring to the band diagrams in Figure 14.20, it is apparent that for sufficiently high density of midgap states, low doping levels in CdTe will enhance recombination current. Further, low doping levels and the resulting field profiles are expected to reduce minority transport, resulting in more pronounced voltage-dependent collection, reducing J_{MP} .

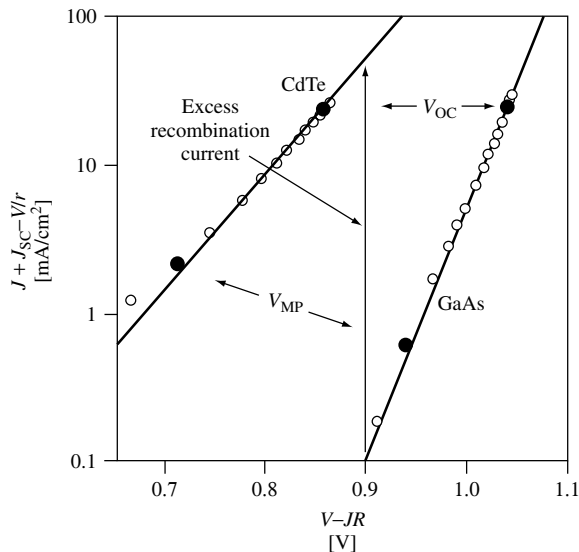


Figure 14.21 Comparison of high-efficiency CdTe and GaAs-illuminated $J-V$ data on a log plot, corrected for resistive effects

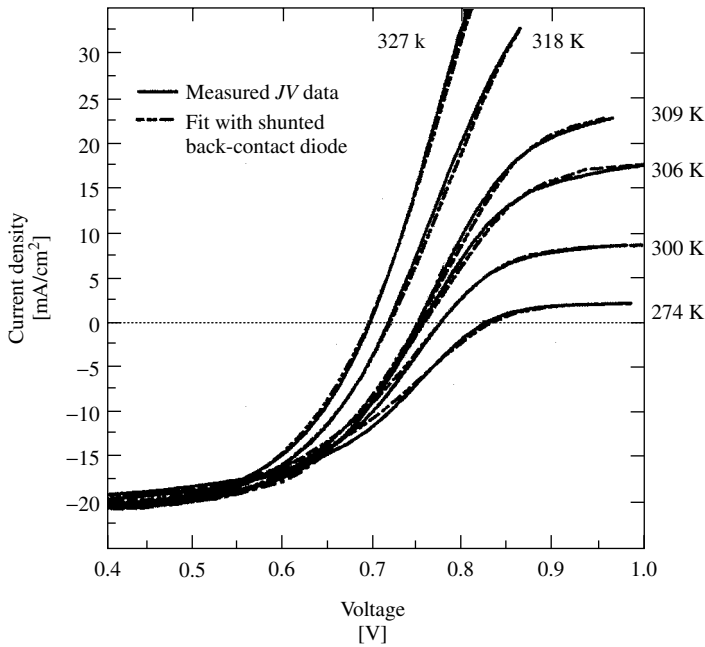


Figure 14.22 Measured and calculated curves for a CdTe cell with a back-contact barrier [162]

The effect of a back-contact barrier on the device band diagram was shown earlier in Figure 14.20. The effect on measured $J-V$ curves is illustrated in Figure 14.22. Assuming the two depletion regions do not overlap, the two diodes can be treated as independent circuit elements. The calculated fit to the curves, with a back-diode barrier height of 0.3 eV, is in fact quite good. The impact of the back barrier becomes larger as the temperature is lowered. This impact is very dramatic in the first quadrant, where the shape of the $J-V$ curves is commonly described as “rollover” [163–165]. The degree of “rollover” of $J-V$ curves such as those illustrated in Figure 14.22 has been shown to be related to the amount of copper used in the fabrication of the back contact [166]. With smaller amounts of copper, “rollover” is observed at higher temperatures implying a larger back-contact barrier, and it has a greater impact on cell performance.

The addition of large amounts of copper to reduce the back-contact barrier, and hence inhibit “rollover”, however, can lead to a decrease in CdTe cell stability, at least for cells held at elevated temperatures. Several authors have seen significant performance changes when CdTe cells were held at high temperatures (typically 60–110°C) for extended periods of time [167–171]. Such studies, often referred to as “stress” tests, generally first see a decrease in fill factor and next in V_{OC} . Only in extreme cases is J_{SC} affected. Figure 14.23 shows the illuminated $J-V$ curves for an NREL-manufactured CdTe cell soon after it was fabricated, and at different periods of time following light soaking at 100°C under open-circuit bias. Such curves are typical of those seen with cells from different manufacturers. The dark $J-V$ curves for these and other CdTe cells also show a progressive increase in “rollover” with continuing temperature stress. Qualitatively similar $J-V$ characteristics are measured for the devices of Figures 14.22 and 14.23,

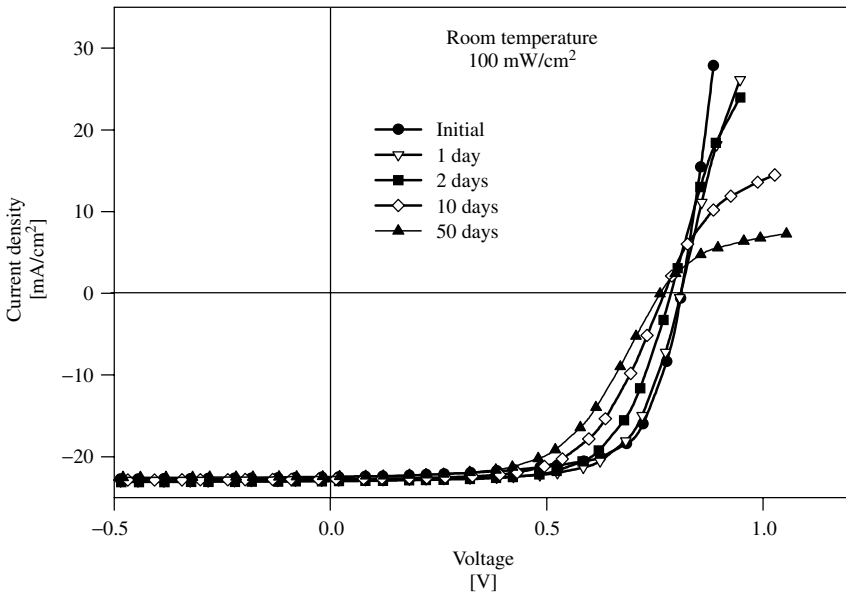


Figure 14.23 $J-V$ of CdTe cells following extended exposure to 100°C at V_{OC} [168]

showing an increase in rollover as temperature is decreased or as time at open-circuit 100°C stress is increased. As the temperature of the $J-V$ measurement is reduced, the acceptor concentration decreases, resulting in the back-barrier height exerting a greater effect, as shown in Figure 14.20. The rollover in the stressed devices could likewise be due to a reduction in carrier density in the CdTe layer.

There is conflicting evidence of the dependence of CdTe cell performance changes with stress temperature, but one study [169] has deduced an empirical activation energy near 1 eV, which predicts that $J-V$ changes at 100°C are accelerated 500 to 1000 times compared to a typical annual range of outdoor temperatures for solar panels. Hence, one would not expect significant performance changes for modules until they had been deployed in the field for many years.

Additional “stress” studies have shown that reductions in cell efficiency are smaller when the voltage bias is held at short circuit or maximum power, rather than at open circuit [169–171], or when less copper is used in the back contact [166]. The movement of copper out of the back-contact region is faster when forward bias reduces the electric field within the cell [169, 171–173], and it has at least two effects on cell performance. One is the increase in back-barrier height, similar to the copper-free case. The second is a detrimental effect on cell performance due to copper movement toward the front junction, probably enhanced by grain-boundary paths. There is no general agreement, however, on whether the copper causes an increase in CdTe recombination states, a change in the CdS layer, or possibly an increased overlap of the front and rear junctions by creating conducting filaments.

There are a variety of possible optical losses before the photons reach a CdTe solar cell’s absorber, and there are additional optical losses due to incomplete absorption of

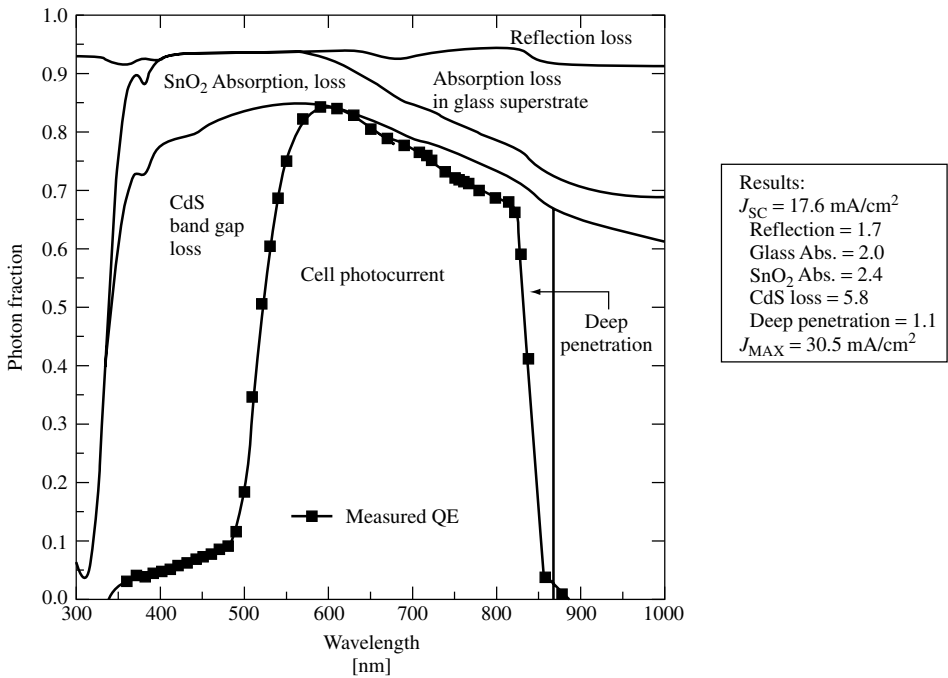


Figure 14.24 CdTe cell photon losses and quantum efficiency versus wavelength [174]

the photons penetrating through the absorber. The QE of a solar cell, especially when combined with independent reflection and absorption measurements of the cell and individual window layers, is a powerful tool to analyze these losses. The data shown in Figure 14.24 are for a CdTe cell with relatively large losses in J_{SC} . This cell, fabricated by Solar Cells, Inc., was deliberately chosen to illustrate the analysis process and is not indicative of the cells currently being manufactured.

To quantify the photon losses in Figure 14.21, the measured QE is multiplied by the light spectrum, in units of photons/cm²/nm, integrated over wavelength, and multiplied by unit electric charge to yield J_{SC} . For comparison, the maximum current density J_{max} is found to be 30.5 mA/cm² for $E_g = 1.5$ eV by a similar calculation up to the band gap cutoff wavelength (vertical line) using unity QE.

The optical regions shown in Figure 14.24 are the reflection from the cell, the absorption of the glass superstrate, the absorption of the SnO₂ conductive contact, and the loss below 500 nm associated primarily with absorption of a ~250-nm-thick CdS window. The separation of individual absorption terms was deduced from the reflection and transmission of partially completed cell structures terminated after each layer. The remaining loss region approaching the band gap is assumed to be due to the photons that penetrated too deeply for complete collection. Integration of these loss spectra, again weighted by the illumination spectrum, gives the current-density loss for each. These losses are listed in the inset to Figure 14.24 for the standard global AM1.5 spectrum [175], normalized to 100 mW/cm². The sum of the losses is the difference between the measured and the maximum current densities.

The inset tells us quantitatively that considerable current enhancement is possible by employing a thinner CdS window, and to a lesser extent with a different glass or improved SnO₂ process. Potential for improvement in J_{SC} with an antireflection coating or from better collection of the deeply penetrating photons would be even smaller. It is certainly possible, however, to reduce the larger losses. The record efficiency cell, for example, has a J_{SC} of 26 mA/cm². Its losses from glass, SnO₂, and CdS absorption are each more than a factor of five less than the cell shown in Figure 14.23, and no single loss factor contributes more than 1 mA/cm².

The capacitance of a solar cell can yield information about extraneous states within the band gap, and it can often give a credible profile of the carrier density within the absorber [176]. Figure 14.25(a) shows the measured capacitance of a CdTe cell as a function of frequency for three biases: 0, -1, and -3 V. The capacitance magnitude is relatively small, corresponding to a small carrier density and a large depletion width. The large depletion width implies that most photons are absorbed in a region with an electric field and hence photocurrent does not vary significantly with voltage [177]. The fact that the curves are relatively flat over nearly three decades in frequency strongly suggests that they are not significantly affected by extraneous states. The upturn at high frequencies is

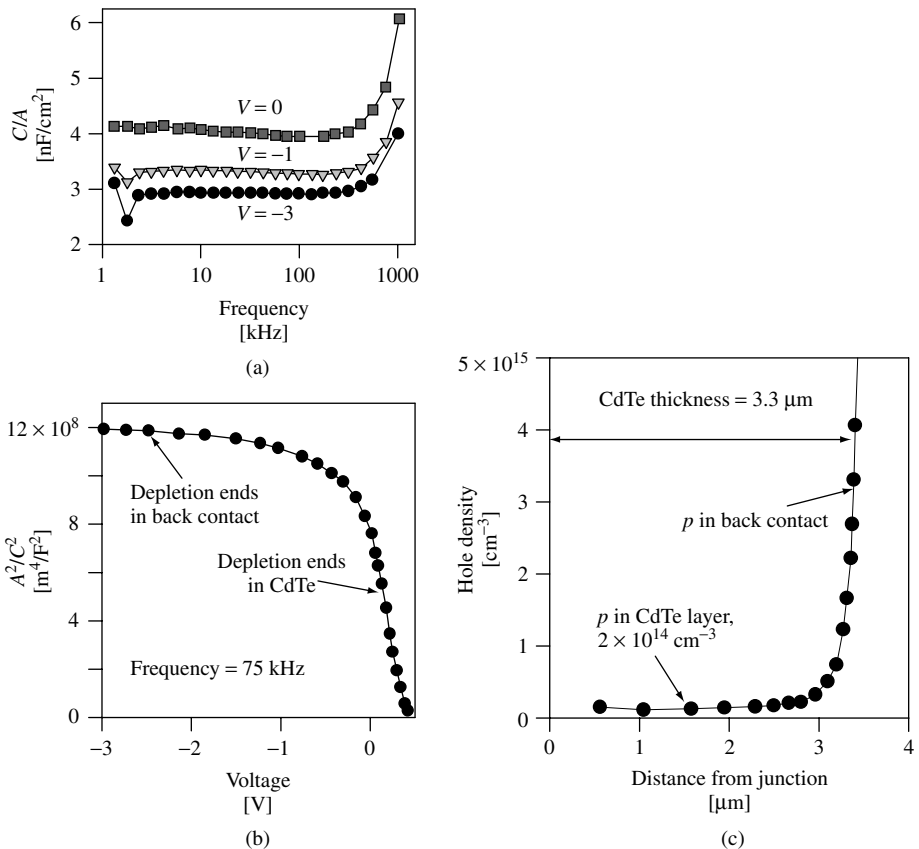


Figure 14.25 Capacitance measurements and hole-density determination for a CdTe solar cell

due to circuit inductance [178], and the points off the curves at low frequencies are due to an apparatus anomaly. Typically, a frequency in the middle of the flat region, in this case 75 kHz, is chosen for subsequent $C-V$ measurements.

Capacitance versus voltage data at 75 kHz is plotted in Figure 14.25(b) in the commonly used C^{-2} versus V format, in which the vertical axis is proportional to the square of the depletion width, w , for a given voltage, since $C/A = \epsilon/w$. The slope is inversely proportional to the carrier density at the depletion edge. In this case, there are two distinct regions. In reverse bias, the C^{-2} , and hence the depletion width, changes very little. Near zero bias and into forward bias, however, the depletion width narrows considerably.

The same data can be plotted (Figure 14.25c) as hole density ρ versus depletion width, which is referred to as the distance from the junction, since the depletion is assumed to be essentially all in the absorber. The two regions suggested by the C^{-2} versus V plot have become extremely clear. For the first 3 μm into the CdTe, the hole density is very low (mid 10^{14} range), but then it increases dramatically. The interpretation is that 3 μm is the thickness of the CdTe layer, and the rapid increase in hole density takes place as the depletion edge enters the back-contact region. In fact, the measured thickness of this particular CdTe was somewhat larger than 3 μm , and in general the electronic thickness is comparable to the physical thickness. The likely explanation is that there are local areas such as grain boundaries and highly defective grains where the back-contact material penetrates into the CdTe and effectively reduces its thickness. Following the elevated temperature cycles that led to Figure 14.23, there can also be a reduction in net CdTe thickness.

CdTe solar cells fabricated by a variety of the techniques illustrated in Figure 14.6 have shown hole densities between 1×10^{14} and $8 \times 10^{14}/\text{cm}^3$ as determined by the capacitance technique. A relatively low carrier density may be an impediment to higher-efficiency cells. It suggests that compensating native donors remain a problem for the CdTe cells made to date. The direct impact of the low hole density is that the Fermi level is 250 to 350 mV from the valence-band maximum, and hence limits the junction barrier, and therefore V_{OC} . A bigger, and probably related, problem is that the low densities are likely to be symptomatic of the excessive recombination states responsible for much of the voltage and fill-factor difference seen in Figure 14.21.

14.3.6 Summary of CdTe-cell Status

During the past 20 years, there has been major progress in refining the basic CdTe cell structure of Bonnet and Rabenhorst. The highest current densities achieved are similar to crystalline GaAs when adjusted for small differences in band gap. Open-circuit voltage and fill factor are limited by excessive forward-current recombination and low carrier density, but have nevertheless achieved values about 80% as large as GaAs, again adjusted for band gap. The recombination current appears to follow the Shockley–Read–Hall mechanism through distributed states in the space charge region [179]. There is some concern about the diffusion of copper atoms, but significant degradation under normal operating conditions for well-fabricated cells is unlikely. Although cell-level basic research should certainly continue, the status of CdTe solar cells is clearly healthy enough to proceed with mainstream commercialization.

14.4 CdTe MODULES

A CdTe photovoltaic module consists of electrically interconnected CdTe cells on a superstrate that serves as the mechanical support. The module's electrical output depends on individual cell output, interconnection scheme, and losses due to nongenerating areas and interconnection-resistive losses. Obtaining high cell efficiency at the module scale depends on the successful transfer of small-area batch processing steps, such as the CdCl_2 treatment, to either large-area batch or continuous processing, and on minimizing dead-area and resistive losses as well as optical losses due to the use of low-cost glass. In effect, the manufacturer's goal is to obtain a series-connected array of large-area CdTe/CdS diodes having spatially uniform physical and electrical properties in a high-throughput fabrication process. This manufacturing orientation is somewhat different from that of integrated-circuit manufacturers, where the challenge lies in minimizing the spatial dimension of each circuit element.

The electrical interconnections between adjacent cells can be made via external contacts or by monolithic integration during deposition and processing. For cost-effective commercial-scale modules, the principle of monolithic integration is often adopted, where the cells on a single large-area substrate or superstrate are isolated and interconnected by scribing through the deposited layers at different stages of fabrication. Scribing can be achieved by mechanical means or, preferably, by laser scribing in which the stopping point is determined by matching the absorption properties of the different layers with the appropriate wavelength and power density [180]. The first scribe isolates the TCO front contact, the second through the CdS and CdTe provides an electrical path from the TCO to the back contact of an adjacent cell, and the third isolates the back contact between cells. A monolithically interconnected module is shown in Figure 14.26. The photocurrent generated by each individual cell flows from one end of the module to the other. The module voltage is simply the sum of the voltages from the series connected individual cells. This monolithic structure and its three laser scribes are very similar to that of amorphous silicon-based PV modules. Significant design analysis of module geometry and lateral-sheet resistances, to minimize resistive and dead-area losses, has been carried out for amorphous silicon PV modules, and is applicable to CdTe PV modules [181, 182].

The structure shown in Figure 14.26 utilizes a sheet of glass as the supporting superstrate. The choice of glass is based on the cost per watt, optical loss, and thermal

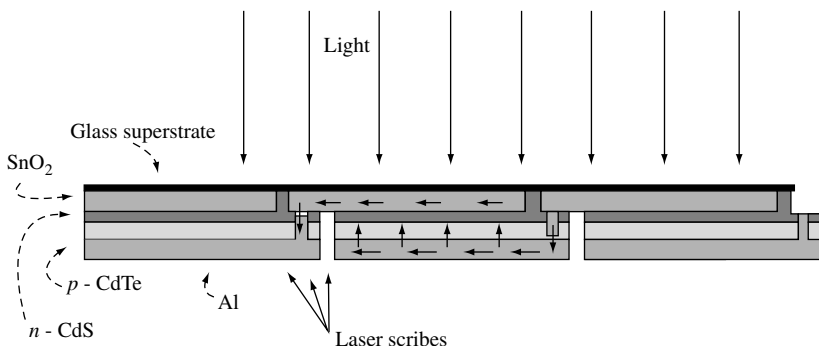


Figure 14.26 Schematic of a series-connected integrated CdTe module having three laser scribes

tolerance of the glass. For example, the light-generated current in CdTe cells deposited on borosilicate glass is 2 mA/cm^2 higher than on soda lime glass, owing to high absorption in the soda lime glass above 600 nm. However, the high-transparency glasses, such as borosilicates, fused quartz, and Vycor, require more refining and are thus significantly more costly than the soda lime glass commonly used for windowpanes. A review of the optical properties of these and other glasses is found in Reference [183]. In addition, low-cost soda lime glass exhibits a lower softening temperature, restricting its application for high-temperature processing. Reducing the iron content in soda lime glasses improves the transparency at wavelengths greater than 600 nm and raises the melt temperature, at a lower cost than borosilicate or other highly refined glass types.

Commercialization of CdTe PV modules will rely on a constant supply of affordable raw materials, especially cadmium and tellurium. In terms of the material requirements, a facility with 1 MW/year manufacturing capacity, with 100% utilization of Cd and Te species using a 2- μm -thick absorber layer, will require approximately 1 metric tons of CdTe, which translates to 0.4 metric ton of cadmium and 0.6 metric ton of tellurium. Both elements are obtained as the by-products in the smelting of ores; cadmium is obtained from zinc, copper, and lead refining, while tellurium is primarily obtained as a product of the electrolytic refining of copper and skimmings from lead production [184]. Tellurium is the scarcer and more costly component, however, tellurium availability is estimated to be ~ 1600 metric tons per year [185]. At present, the costs for $\sim 95\%$ pure cadmium and tellurium are $\sim \$\text{US } 12/\text{lb}$ ($\text{\$US } 24\,000/\text{ton}$) and $\sim \$\text{US } 20/\text{lb}$ ($\text{\$US } 40\,000/\text{ton}$), respectively. Thus, the total cadmium and tellurium costs for the 1-MW capacity plant would be $\sim \$\text{US } 34\,000$, which amounts to less than $\text{\$US } 0.10$ per watt. This is significantly less than the price of the superstrate glass/TCO for the $100\,000 \text{ m}^2$ required for 1-MW capacity, which is currently $\text{\$US } 10.80/\text{m}^2$ [186], equaling $\text{\$US } 1.08$ per watt. A detailed analysis of PV-manufacturing costs is presented in Reference [187].

Present-generation CdTe PV modules are typically $\sim 1 \text{ m}^2$ in area and have achieved efficiencies above 10%, with peak power on the order of 90 W. At the time of this writing, the only commercial CdTe cells are manufactured by Matsushita Battery Company in Japan, with an annual production of 1.2 MW [188]. Three CdTe module manufacturers are entering production: First Solar, L.L.C., in Toledo, Ohio; BP Solar, in Fairfield, California; and Antec Solar GmbH, in Germany. The module dimensions and output of prototype superstrate CdTe modules from these companies are listed in Table 14.4.

The First Solar module utilizes vapor transport deposition of CdTe onto moving substrates to achieve a high growth rate while maintaining high substrate temperature. The

Table 14.4 Summary of CdTe module performance, compiled by Zweibel. Consult the listed references for module fabrication details

Manufacturer	Country	CdTe method	Per-module power [W]	Aperture efficiency [%]	Module size [m^2]	Reference
Antec	Germany	CSS	47	7.0	0.66	[189]
BP Solar	USA	ED	92	11.0	0.84	[4]
First Solar	USA	VTD	67	10.1	0.66	[3]
Matsushita	Japan	Screen	59	11.0	0.54	[190]

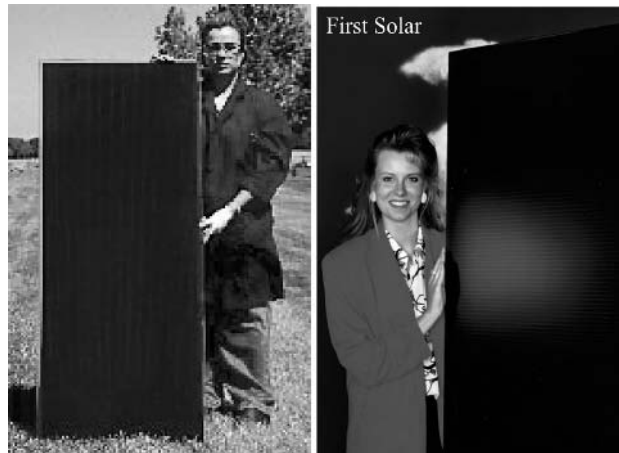


Figure 14.27 CdTe modules made by (a) BP Solar and (b) First Solar. (BP Solar photograph courtesy of D. Cunningham. First Solar photograph courtesy D. Rose)

modules are formed on tin oxide-coated soda lime glass made by Libby Owens Ford. The production line is reported to be capable of 2.9 m^2 per minute throughput [191]. A photograph showing a First Solar module is shown in Figure 14.27(b).

The BP Solar module utilizes electrodeposited CdTe films and overcomes throughput issues associated with low growth rate by simultaneous batch deposition of many modules. The plant has eight identical reaction chambers, or tanks. Each tank is capable of handling 40, 0.55 m^2 ($14'' \times 61''$) substrates or 24, 0.94 m^2 ($24'' \times 61''$) substrates [192]. A photograph of a BP Solar module is shown in Figure 14.27(a).

The Antec module utilizes CSS deposition of the CdTe layer, with a patented source diffuser to improve spatial uniformity during deposition. Spatial uniformity in CSS deposition is an issue because the source and substrate have the same area and are in static relation to each other.

Issues confronting manufacturers of thin-film CdTe solar cells are maintaining small-area efficiencies at the module scale, control of uniformity during growth, reproducibility, and product certification with respect to expected lifetime. Module performance and spatial uniformity are linked to the CdS film thickness; thick CdS films improve processing latitude but reduce light-generated current. With the ultrathin CdS films used to obtain state-of-the-art performance in small-area cells, spatial variations in CdTe-film microstructure can affect the diffusion of CdS into CdTe and the resulting junction structure. Incorporating buffer layers into the window-layer side of the structure, refining the postdeposition treatments, and developing in-line sensing diagnostic tools are viable pathways for widening the tolerance window needed to raise the current density in modules.

14.5 THE FUTURE OF CdTe-BASED SOLAR CELLS

The future of CdTe thin-film photovoltaic devices in energy production and optical sensing is assured by the material properties, laboratory-scale device performance, and photovoltaic module implementation. Enhancing the viability of CdTe/CdS for terrestrial

power generation depends on improving device performance, cost-effective translation of fabrication processes to the module scale, and cell and module stability. In addition to efficiency gains in single-junction devices, band gap tailoring of the absorber by alloying with other group IIB metals can facilitate development of multijunction cells with efficiencies approaching 30%. Translating single-junction efficiency gains from batch processes to continuous module fabrication and developing monolithic multijunction modules on a single superstrate can significantly reduce production costs. Achieving this goal requires greater understanding of the relationship between processing conditions and critical material properties needed for high efficiency and good long-term stability.

Although the fundamental nature of polycrystalline CdTe is not yet fully understood, we have shown that significant progress has been made toward the development of 20% efficient single-junction thin-film cells. In addition, we have seen that several CdTe film deposition techniques yield similar device performance, by a suitable combination of postdeposition processing and back-contact formation. Reaching the 20% efficiency target and translating this to high module performance relies on determining and overcoming the mechanisms that limit the open-circuit voltage and fill factor in present-generation cells. This is simply due to the fact that the current density in champion thin-film CdTe cells has reached 80% of its theoretical maximum for AM1.5 illumination and is primarily limited by optical losses in the glass/TCO/CdS structure. The values of $V_{OC} \sim 850$ mV and $FF \sim 75\%$ appear to represent practical limits, and fall short of the expectations based on band gap. Forward current in present-generation high-efficiency CdTe/CdS devices appears to be controlled by the Shockley–Read–Hall recombination in the space charge region. Many investigations also show a profound influence of back-contact formation on both V_{OC} and FF . For module implementation, obtaining both high J_{SC} and V_{OC} is complicated by large-area control of CdTe–CdS interdiffusion and junction formation between the CdTe absorber and the TCO, since a thin CdS layer is required in the finished device. Thus, critical research directions for improving efficiency in CdTe/CdS cells are (1) identification and reduction of the density of limiting intragrain defect states; (2) increasing the p -type carrier concentration in CdTe; (3) eliminating or controlling parallel junctions that may arise because of pinholes; (4) developing robust manufacturing processes; and (5) defining and overcoming performance limitations related to back-contact formation.

In addition to its basis for single-junction devices, CdTe can be alloyed with other II^B-VI^A compounds to alter its band gap, allowing multijunction cells to be designed. The multijunction cell structures using CdTe-based wide band gap cells in monolithic structures must confront the relationship between cell geometry and both processing temperature and chemical stability. Materials based on alloys between CdTe and other group II^B-VI^A compounds allow a wide range of optoelectronic properties to be incorporated into devices by design.

Semiconducting compounds of the form II^B-VI^A provide a basis for the development of tunable materials, obtained by alloying different compounds in pseudobinary configurations. For photovoltaic heterojunction devices, semiconductors using Cd, Zn, Hg cations and S, Se, Te anions exhibit a wide range of optical band gap, suggesting their potential for use in optimized device designs by tailoring material properties (Table 14.5). The high optical absorption coefficients, $\sim 10^5/\text{cm}$, and direct optical band gaps of many II-VI semiconductors make them suitable for use in thin-film photovoltaic

Table 14.5 Properties of pseudobinary II^B-VI^A alloys suitable for absorber layers

Compound	Single crystal optical E_g range 300 K [eV]	Optical bowing parameter	Stable endpoint structure	Miscibility gap?
Cation substitution				
$Cd_{1-x}Zn_xTe$	1.49–2.25	0.20	ZB–ZB	N
$Hg_{1-x}Cd_xSe$	0.10–1.73	?	ZB–W	N
$Hg_{1-x}Zn_xTe$	0.15–2.25	0.10	ZB–ZB	N
Anion substitution				
$CdTe_{1-x}S_x$	1.49–2.42	1.70	ZB–W	Y
$CdTe_{1-x}Se_x$	1.49–1.73	0.85	ZB–W	?
$CdSe_{1-x}S_x$	1.73–2.42	0.31	W–W	N
$HgTe_{1-x}S_x$	0.15–2.00	?	ZB–ZB	?
$HgSe_{1-x}S_x$	0.10–2.00	?	ZB–ZB	?

devices. For terrestrial photovoltaic applications, in which a band gap of ~ 1.5 eV is desired, considerable progress has been made in the development of solar cells based on the CdS–CdTe heterojunction wherein $CdS_{1-y}Te_y$ and $CdTe_{1-x}S_x$ alloys have been shown to play a role in the device operation. For the development of next-generation, multijunction cells, top cells with an absorber band gap of ~ 1.7 eV are required [193, 194].

The alloy systems shown in Table 14.5, separated by cation and anion substitution in pseudobinary compounds, define a broad range of optical band gap suitable as absorber layers in terrestrial photovoltaic converters. The isostructural systems $Cd_{1-x}Zn_xTe$ and $Hg_{1-x}Zn_xTe$ offer tunable systems with a wide range of band gap and controllable p -type conductivity.

Thin-film solar cells based on $Cd_{1-x}Zn_xTe$ were the subject of study in the late 1980s, by several laboratories, including the Georgia Institute of Technology (GIT) and International Solar Energy Technology (ISET). Two approaches to depositing the $Cd_{1-x}Zn_xTe$ films had been considered in the previous work: synthesis by reaction of sequentially deposited metal layers (ISET) and metal organic chemical vapor deposition (GIT). CdS/ $Cd_{1-x}Zn_xTe$ devices using $Cd_{1-x}Zn_xTe$ films made by the reaction of sequentially deposited metals with $x = 0.1$, corresponding to $E_g \sim 1.6$ eV, yielded 3.8% efficiency and suffered from low V_{OC} and FF [195]. Although little follow-up work was conducted to explain the low performance, for CdS/ $Cd_{1-x}Zn_xTe$ devices made by MOCVD, it was found that the $CdCl_2$ + air treatment step reduced the band gap from 1.7 to 1.55 eV, owing to chemical conversion of the zinc alloy to volatile $ZnCl_2$. The best cells made with the 1.55 eV band gap yielded 4.4% conversion efficiency [196].

CdTe-based thin-film photovoltaic devices are also suited to applications beyond terrestrial power conversion, including space-power generation, infrared detectors, and gamma radiation detectors. Using the current–voltage characteristics of state-of-the-art and realistic devices on rigid glass superstrates, AM0 operation at $60^\circ C$ can be determined by accounting for the temperature dependence of the band gap and differences in irradiance. State-of-the-art cells with 16.5% AM1.5 efficiency at $25^\circ C$ translate to 13.9% AM0 efficiency at $60^\circ C$. Typical cells having 12% AM1.5 efficiency at $25^\circ C$

translate to 10% AM0 efficiency at 60°C. For cells on 0.05-mm-thick polyimide substrate at AM0 conditions, the 12% state-of-the-art and 10% typical cells should yield power-to-weight ratio of 1520 and 1100 W/kg, respectively. CdTe research and development for space applications, in which AM0 power-to-weight ratio greater than 1000 W/kg is desired, has followed three approaches with results as follows: (1) 6 to 7% AM1.5 efficiency for thin-film deposition in the *substrate* configuration on lightweight flexible substrates [25], (2) 11% AM1.5 efficiency for transfer of completed superstrate cells from rigid superstrates to lightweight flexible substrates [197], and (3) 11% efficiency for direct superstrate deposition onto 100- μm thick glass foils [105]. Encouraging results of CdTe/CdS cell stability were obtained under 1-MeV electron bombardment at fluences of 10^{14} to $10^{16}/\text{cm}^2$ [198].

For infrared detection and thermal imaging, devices using $\text{Cd}_{1-x}\text{Hg}_x\text{Te}$ alloys have been investigated intensively since the mid 1960s, leading to a significant technology base of sensor and charge-coupled device (CCD) imaging devices [199]. To achieve good sensitivity at wavelengths of 8 to 10 μm , long minority-carrier lifetime is required in the absorbing $\text{Cd}_{1-x}\text{Hg}_x\text{Te}$. To minimize trapping and Shockley–Read–Hall recombination centers, single crystals are fabricated using either a cast-recrystallization technique or the Bridgman growth technique. Schottky photodetecting arrays are fabricated on polished slices of the single crystals. High-quality $\text{Cd}_{1-x}\text{Hg}_x\text{Te}$ thin films have been deposited by both liquid-phase and vapor-phase epitaxy on CdTe and $\text{Cd}_{1-x}\text{Hg}_x\text{Te}$ single-crystal wafers [200].

Gamma ray detectors for tomographic applications based on CdTe have been investigated using two approaches: (1) direct detection by ionization in CdTe and (2) deposition of a CdTe/CdS thin-film photodetector on a scintillating superstrate such as cadmium tungstenate (CdWO_4). For direct detection, the gamma ray is stopped in CdTe in either a metal–semiconductor–metal or all-semiconductor *p-i-n* structure using CdTe single crystals [201]. In either design, the optimal detector is achieved with devices having the lowest possible leakage current and highest mobility-lifetime product.

Concerns have been raised about cadmium toxicity and the possibility of introducing significant amounts into the environment where the cells are manufactured and deployed. Managing cadmium in the manufacturing environment relies on a combination of appropriate engineering and chemical hygiene practices. Concerns over module deployment are being addressed at technical and policy levels. First, modules are environmentally well sealed, which serves to both protect the cell from environmental deterioration and to contain the semiconducting materials, in the event of mechanical failure. By recycling modules at the end of life in a manner consistent with metal products, it is estimated that nearly all the cadmium in a module can be recycled at a cost of roughly 5 cents/W [202]. Alternatively, module deployment by a leasing arrangement or by confinement to industrially managed energy farms could facilitate total control over installed cadmium distribution. The amount of cadmium used in thin-film CdTe modules is relatively modest. A CdTe module 1 m^2 in area, producing approximately 100 W of power using a CdTe layer less than 2 μm thick, contains less than 10 g of cadmium, or about the same as a single nickel–cadmium flashlight battery [203]. On a larger scale, it would take about 40 000 metric tons of cadmium to switch the entire US power grid to CdTe modules. Assuming a 30-year life cycle, about 7% of the current world output of cadmium would be required.

This chapter has shown the development and present state of CdTe solar cells and modules. Wide-scale commercialization of CdTe technologies hinges on improving performance, understanding stability, developing low-cost consumer products for varying energy and photonic market demands, and managing cadmium. At the cell level, improved performance can be expected as fundamental understanding of the device operation improves. Issues related to stability involve both cell-related mechanisms, linked to cell processing, and module-related mechanisms, linked to encapsulation and environmental conditions. Future CdTe product development hinges on successful marketing of photovoltaics as a viable energy source, which in turn depends on reductions in the cost per installed watt, which, at the time of this writing, makes thin-film CdTe solar cells a leading contender for future power generation.

14.6 ACKNOWLEDGMENTS

Brian McCandless wishes to acknowledge the contributions of the technical staff at the Institute of Energy Conversion, in particular Robert Birkmire, James Phillips, and Steven Hegedus for insightful discussions; Kevin Dobson and Joy Deep Dass for assistance in literature research; and Shannon Fields and Erten Eser for help with figure preparation. James Sites is deeply indebted to many colleagues in the CdTe community, but particularly to the students who have done research with him in this area: Pete Mauk, Hossein Tavakolian, Rick Sasala, Ingrid Eisgruber, Gunther Stollwerck, Nancy Liu, Jennifer Granata, and Jason Hiltner. Both authors gratefully acknowledge long-time research support from the United States National Renewable Energy Laboratory. The comparative nature of this work would not have been possible without access to samples and data generously provided by numerous CdTe research groups.

REFERENCES

1. Loferski J, *J. Appl. Phys.* **27**, 777–784 (1956).
2. Based on Rothwarf A, Boer K, *Prog. Solid. State Chem.* **10**, 71–102 (1975).
3. Frerichs R, *Phys. Rev.* **72**, 594–601 (1947).
4. Jenny D, Bube R, *Phys. Rev.* **96**, 1190–1191 (1954).
5. Krüger F, de Nobel D, *J. Electron.* **1**, 190–202 (1955).
6. de Nobel D, *Philips Res. Rpts* **14**, 361–399 and 430–492 (1959).
7. Rappaport P, *RCA Rev.* **20**, 373–397 (1959).
8. Mimilya-Arroyo J, Marfaing Y, Cohen-Solal G, Triboulet R, *Sol. Energy Mater.* **1**, 171 (1979).
9. Cohen-Solal G, Lincot D, Barbe M, Conf. Rec. 4th ECPVSC, 621–626 (Stresa, Italy, 1982).
10. Fahrenbruch A, Bube R, *Fundamentals of Solar Cells*, Academic Press, New York, 418–460 (1983).
11. Elliot J, Ed, US Air Force ASD Technical Report 61–242 (1961).
12. Cusano D, General Electric Res. Lab. Report, No. 4582 (1963).
13. Bernard J, Lancon R, Paparoditis C, Rodot M, *Rev. Phys. Appl.* **1**, 211–217 (1966).
14. Lebrun J, Conf. Rec. 8th IEEE Photovoltaic Specialist Conf., 33–37 (1970).
15. Justi E, Schneider G, Seredynski J, *J. Energy Conversion* **13**, 53–56 (1973).
16. Ponpon J, Siffert P, *Rev. Phys. Appl.* **12**, 427–431 (1977).
17. Fulop G *et al.*, *Appl. Phys. Lett.* **40**, 327–328 (1982).
18. Mitchell K, Fahrenbruch A, Bube R, *J. Appl. Phys.* **48**, 829–830 (1977).
19. Nakazawa T, Takamizawa K, Ito K, *Appl. Phys. Lett.* **50**, 279–280 (1987).

20. Aranovich J, Golmayo D, Fahrenbruch A, Bube R, *J. Appl. Phys.* **51**, 4260–4265 (1980).
21. Muller R, Zuleeg R, *J. Appl. Phys.* **35**, 1550–1556 (1964).
22. Dutton R, *Phys. Rev.* **112**, 785–792 (1958).
23. Mitchell K, Fahrenbruch A, Bube R, *J. Appl. Phys.* **48**, 4365–4371 (1977).
24. Yamaguchi K, Matsumoto H, Nakayama N, Ikegami S, *Jpn. J. Appl. Phys.* **16**, 1203–1211 (1977).
25. McClure J *et al.*, *Sol. Energy Mater. Sol. Cells* **55**, 141–148 (1998).
26. Adirovich E, Yuabov Y, Yugadaev D, *Sov. Phys. Semicond.* **3**, 61–65 (1969).
27. Bonnet D, Rabenhorst H, Conf. Rec. 9th IEEE Photovoltaic Specialist Conf., 129–132 (1972).
28. Phillips J *et al.*, *Phys. Status Solidi (B)* **194**, 31–39 (1996).
29. Suyama N *et al.*, Conf. Rec. 21st IEEE Photovoltaic Specialist Conf., 498–503 (1990).
30. Başol B, Conf. Rec. 21st IEEE Photovoltaic Specialist Conf., 588–594 (1990).
31. Tyan Y, Perez-Albuerne E, Proc. 16th IEEE Photovoltaic Specialist Conf., 794–800 (1982).
32. Meyers P, Liu C, Frey T, U.S. Patent 4,710,589 (1987).
33. Birkmire R, Conf. Record NREL ARD Rev. Meeting, 77–80 (1989).
34. Britt J, Ferekides C, *Appl. Phys. Lett.* **62**, 2851–2852 (1993).
35. Wu X *et al.*, *J. Appl. Phys.* **89**, 4564–4569 (2001).
36. McCandless B, Hichri H, Hanket G, Birkmire R, Conf. Rec. 25th IEEE Photovoltaic Specialist Conf., 781–785 (1996).
37. Wu X *et al.*, Conf. Rec. 17th European Photovoltaic Solar Energy Conversion 995–1000 (2001).
38. Mitchell K, Fahrenbruch A, Bube R, *J. Appl. Phys.* **48**, 829–830 (1977).
39. Rakhshani A, *J. Appl. Lett.* **81**, 7988–7993 (1997).
40. Fardig D, Masters Thesis, University of Delaware, Department of Electrical Engineering (1991).
41. Fahrenbruch A, Colorado State University subcontract report (2000), unpublished.
42. Hartmann H, Mach R, Selle B, “Wide Gap II-VI Compounds as Electronic Materials”, in Kaldis E, Ed, *Current Topics in Materials Science*, Vol. 9, North-Holland Publishing Company, New York (1982).
43. Madelung O, *Semiconductors Other than Group IV Elements and III-V Compounds*, Springer-Verlag, New York (1992).
44. Aven M, Prener J, Eds, *Physics and Chemistry of II-VI Compounds*, John Wiley and Sons, New York, 211–212 (1967).
45. International Committee for Diffraction Data, Card Number 15–770.
46. Knacke O, Kubaschewski O, Hesselmann K, *Thermochemical Properties of Inorganic Substances*, 2nd Edition, Springer-Verlag, New York (1991).
47. Data from ASM Binary Phase Diagrams (2000).
48. Data from Knacke O, Kubaschewski O, Hesselmann K, *Thermochemical Properties of Inorganic Substances*, 2nd Edition, Springer-Verlag, New York (1991).
49. Hultgren R *et al.*, *Selected Values of the Thermodynamic Properties of Binary Alloys*, American Society for Metals, Ohio, 627–630 (1971).
50. de Nobel D, *Philips Res. Rpts* **14**, 361–399 and 430–492 (1959).
51. Krüger F, *Revue de Physique Appliquée* **12**, 205–208 (1977).
52. Wei S, Zhang S, Zunger A, *J. Appl. Phys.* **87**, 1304–1311 (2000).
53. Phillips J, *Bonds and Bands in Semiconductors*, 42, Academic Press, New York (1973).
54. Huheey J, Keiter E, Keiter R, *Inorganic Chemistry*, 113–126, Harper Collins, New York (1993).
55. Wu W, Gielisse P, *Mater. Res. Bull.* **6**, 621–638 (1971).
56. Myers T, Edwards S, Schetzina J, *J. Appl. Phys.* **52**, 4231–4237 (1981).
57. Wei S, Zunger A, *Appl. Phys. Lett.* **72**, 2011–2014 (1998).
58. Cohen M, Bergstresser T, *Phys. Rev.* **141**, 789–801 (1966).
59. Wei S, Zhang S, Zunger A, *J. Appl. Phys.* **87**, 1304–1310 (2000).

60. Wei S, Mtg. Record, National CdTe R&D Team Meeting (2001) Appendix 9.
61. Başol B, *Int. J. Sol. Energy* **12**, 25–35 (1992).
62. Capper P, Ed, *Properties of Narrow Gap Cadmium-Based Compounds*, INSPEC, London, 472–481 (1994).
63. Kazmerski L, *Sol. Cells* **24**, 387–418 (1988).
64. Mueller K, *Thin Solid Films* **174**, 117–132 (1989).
65. Levi D *et al.*, *Sol. Energy Mater. Sol. Cells* **41/42**, 381–393 (1996).
66. Durose K, Edwards P, Halliday D, *J. Cryst. Growth* **197**, 733–742 (1999).
67. Dobson K, Visoly-Fisher I, Hodes G, Cahen D, *Sol. Energy Mater. Sol. Cells* **62**, 295–325 (2000).
68. Nakayama N *et al.*, *Jpn. J. Appl. Phys.* **15**, 2281 (1976).
69. McCandless B, *Mat. Res. Soc. Symp. Proc.* **668**, H1.6.1–H1.6.12 (2001).
70. Ballif C, Moutinho H, Al-Jassim M, *J. Appl. Phys.* **89**, 1418–1424 (2001).
71. Rogers K *et al.*, *Thin Solid Films*, **339**, 299–304 (1999).
72. Yan Y, Albin D, Al-Jassim M, *Appl. Phys. Lett.* **78**, 171–173 (2001).
73. Nunoue S, Hemmi T, Kato E, *J. Electrochem. Soc.* **137**, 1248–1251 (1990).
74. Martel A *et al.*, *Phys. Status Solidi B* **220**, 261–267 (2000).
75. Dobson K, Visoly-Fisher I, Hodes G, Cahen D, *Adv. Mater.* **13**, 1495–1499 (2001).
76. Wu X *et al.*, *J. Appl. Phys.* **89**, 4564–4569 (2001).
77. Waters D *et al.*, Conf. Rec. 2nd WCPVSEC, 1031–1034 (1998).
78. Oman D *et al.*, *Appl. Phys. Lett.* **67**, 1896–1898 (1995).
79. Rakhshani A, *J. Appl. Phys.* **81**, 7988–7993 (1997).
80. Aspnes D, Arwin H, *J. Vac. Sci. Technol.* **A2**, 1309–1323 (1984).
81. Fisher A *et al.*, *Appl. Phys. Lett.* **70**, 3239–3241 (1997).
82. Grecu D *et al.*, *J. Appl. Phys.* **88**, 2490–2496 (2000).
83. Okamoto T *et al.*, *J. Appl. Phys.* **57**, 3894–3899 (1998).
84. Rose D *et al.*, *Prog. Photovolt.* **7**, 331–340 (1999).
85. Balcioğlu A, Ahrenkiel R, Hasoon F, *J. Appl. Phys.* **88**, 7175–7178 (2000).
86. Dobson K *et al.*, *Mat. Res. Soc. Symp. Proc.* **668**, H8.24.1–H8.24.6 (2001).
87. Galloway S, Edwards P, Durose K, *Sol. Energy Mater. Sol. Cells* **57**, 61–74 (1999).
88. Durose K, Edwards P, Halliday D, *J. Cryst. Growth* **197**, 733–740 (1999).
89. Bonnet D, Ed, *Int. J. Solar Energy*, **12**, Harwood Academic Publishers, Reading, U.K. (1992).
90. Chu T, Chu S, *Prog. Photovolt.* **1**, 31–32 (1993).
91. Birkmire R, Eser E, *Annu. Rev. Mater. Sci.* **27**, 625–653 (1997).
92. Bonnet D, Meyers P, *J. Mater. Res.* **10**, 2740–2754 (1998).
93. Jackson S, Baron B, Rocheleau R, Russell T, *J. Vac. Sci. Technol. A* **3**, 1916–1920 (1985).
94. Jackson S, Baron B, Rocheleau R, Russell T, *AIChE J.* **33**, 711–721 (1987).
95. Fahrenbruch A, Bube R, Kim D, Lopez-Otero A, *Int. J. Sol. Energy* **12**, 197–222 (1992).
96. McCandless B, Youm I, Birkmire R, *Prog. Photovolt.* **7**, 21–30 (1999).
97. Takamoto T, Agui T, Kurita H, Ohmori M, *Sol. Energy Mater. Sol. Cells* **49**, 219–225 (1997).
98. Tyan Y, Perez-Albuern E, Conf. Rec. 16th IEEE Photovoltaic Specialist Conf., 794–800 (1982).
99. Chu T *et al.*, *IEEE Electron. Dev. Lett.* **13**, 303–304 (1992).
100. Ferekides C *et al.*, *Thin Solid Films* **361–362**, 520–526 (2000).
101. Wu X *et al.*, Conf. Rec. 28th IEEE Photovoltaic Specialist Conf., 470–474 (2000).
102. Ohyama H *et al.*, Conf. Rec. 26th IEEE Photovoltaic Specialist Conf., 343–346 (1997).
103. Bonnet D, Richter H, Jaeger K, Conf. Rec. European 13th Photovoltaic Solar Energy Conversion, 1456–1461 (1995).
104. Bonnet D, Conf. Rec. 14th European Photovoltaic Solar Energy Conversion, 2688–2693 (1997).
105. McCandless B, unpublished work.
106. Powell R *et al.*, U.S. Patent 5,945,163 (1999).

107. Wendt R, Fischer A, Grecu D, Compaan A, *J. Appl. Phys.* **84**, 2920–2925 (1998).
108. Abou-Elfoutouh F, Coutts T, *Int. J. Sol. Energy* **12**, 223–232 (1992).
109. Krüger F, *J. Electrochem. Soc.* **125**, 2028–2034 (1978).
110. Başol B, *J. Appl. Phys.* **55**, 601–603 (1984).
111. Fulop G *et al.*, *Appl. Phys. Lett.* **40**, 327–328 (1982).
112. Bhattacharya R, Rajeshwar K, *J. Electrochem. Soc.* **131**, 2032–2041 (1984).
113. Chu T, Chu S, *Int. J. Sol. Energy* **12**, 122–132 (1992).
114. Sudharsanan R, Rohatgi A, *Sol. Cells* **31**, 143–150 (1991).
115. Jordan J, International Patent Application WO93/14524 (1993).
116. Kester J *et al.*, *AIP Conf. Ser.* **394**, 196 (1996).
117. Ikegami S, *Tech. Digest Int'l PVSEC-3*, 677–682 (1987).
118. Kim H, Im H, Moon J, *Thin Solid Films* **214**, 207–212 (1992).
119. Clemminck I, Burgelman M, Casteleyn M, Depuydt B, *Int. J. Sol. Energy* **12**, 67–78 (1992).
120. Bauer G, von Roedern B, *Conf. Rec. 16th European Photovoltaic Solar Energy Conversion*, 173–176 (2000).
121. Jordan J, Albright S, U.S. Patent 5,279,678 (1994).
122. Takamoto T, Agui T, Kurita H, Ohmori M, *Sol. Energy Mater. Sol. Cells* **49**, 219–225 (1997).
123. McCandless B, Birkmire R, *Conf. Rec. 28th IEEE Photovoltaic Specialist Conf.*, 491–494 (2000).
124. Wu X *et al.*, *Conf. Rec. 28th IEEE Photovoltaic Specialist Conf.*, 470–474 (2000).
125. McCandless B, Hegedus S, *Conf. Rec. 22nd IEEE Photovoltaic Specialist Conf.*, 967–972 (1991).
126. Clemminck I *et al.*, *Conf. Rec. 22nd IEEE Photovoltaic Specialist Conf.*, 1114 (1991).
127. Wu X, *J. Appl. Phys.* **89**, 4564–4569 (2001).
128. Meyers P, Leng C, Frey T, U.S. Patent 4,710,589 (1987).
129. McCandless B, Birkmire R, *Sol. Cells* **31**, 527–535 (1990).
130. McCandless B, Hichri H, Hanket G, Birkmire R, *Conf. Rec. 25th IEEE Photovoltaic Specialist Conf.*, 781–785 (1996).
131. Mahathongdy Y, Albin D, Wolden C, Baldwin R, *Conf. Rec. 15th NREL PV Rev. Meeting* (1998).
132. Zhou T *et al.*, *Conf. Rec. 1st WCPVSEC*, 103–106 (1994).
133. Qu Y, Meyers P, McCandless B, *Conf. Rec. 25th IEEE Photovoltaic Specialist Conf.*, 1013–1016 (1996).
134. Başol B, Tseng E, Lo D, U.S. Patent 4,548,681 (1984).
135. McCandless B, Moulton L, Birkmire R, *Prog. Photovolt.* **5**, 249–260 (1997).
136. Birkmire R, McCandless B, Shafarman W, *Sol. Cells* **23**, 115–126 (1985).
137. Birkmire R, McCandless B, Hegedus S, *Int. J. Sol. Energy* **12**, 145–154 (1992).
138. Hiltner J, Sites J, *Mat. Res. Soc. Proc.* **668**, H 9.8, 1–7 (2001).
139. Jensen G, Ph.D. Dissertation, Stanford University, Department of Physics (1997).
140. Ohata K, Saraie J, Tanaka T, *Jpn. J. Appl. Phys.* **12**, 1641–1642 (1973).
141. Moon D, Im H, *Powder Metall.* **35**, 53–58 (1992).
142. Jensen D, McCandless B, Birkmire R, *Mat. Res. Soc. Symp. Proc.* **428**, 325–330 (1996).
143. Hill R, Richardson D, *Thin Solid Films* **18**, 25–28 (1973).
144. Compaan A *et al.*, *Mat. Res. Soc. Symp. Proc.* **428**, 367–371 (1996).
145. Bonnet D, *Phys. Stat. Sol.* **A3**, 913–919 (1970).
146. McCandless B, Hanket G, Jensen D, Birkmire R, *J. Vac. Sci. Technol. A* **20**(4), 1462–1467 (2002).
147. Wei S, Zhang S, Zunger A, *J. Appl. Phys.* **87**, 1304–1311 (2000).
148. Ohata K, Saraie J, Tanaka T, *Jpn. J. Appl. Phys.* **12**, 1198–1204 (1973).
149. McCandless B, Engelmann M, Birkmire R, *J. Appl. Phys.* **89**(2), 988–995 (2001).
150. Albright S *et al.*, *AIP Conf. Ser.* **268**, 17–32 (1992).
151. McCandless B, Phillips J, Titus J, *Conf. Rec. 2nd WCPVEC*, 448–452 (1998).

152. McCandless B, Qu Y, Birkmire R, Conf. Rec 1st WCPVSEC, 107–110 (1994).
153. Szabo L, Biter W, U. S. Patent 4,735,662 (1988).
154. Albright S, Ackerman B, Jordan J, *IEEE Trans. Elec. Dev.* **37**, 434–437 (1990).
155. Matsumoto H *et al.*, *Sol. Cells* **11**, 367–373 (1984).
156. Lyubormisky I, Rabinal M, Cahen D, *J. Appl. Phys.*, **81**, 6684–6691 (1997).
157. Ringel S, Smith A, MacDougal M, Rohatgi A, *J. Appl. Phys.* **70**, 881–889 (1991).
158. Drayton J *et al.*, Compaan, presented at Spring MRS (San Francisco, April 2001).
159. Romeo N *et al.*, *Sol. Energy Mater. Sol. Cells* **58**, 209–218 (1999).
160. McMahan T, Fahrenbruch A, Conf. Rec. 28th IEEE Photovoltaic Specialist Conf., 539–542 (2001).
161. Sites J, Mauk P, *Sol. Cells* **27**, 411–417 (1989).
162. Kurtz S, Olson J, Kibler A, Conf. Rec 23rd IEEE Photovoltaic Specialist Conf., 138–141 (1990).
163. Stollwerck G, Sites J, Conf. Rec. 13th European Photovoltaic Solar Energy Conversion, 2020–2022 (1995).
164. Niemegeers A, Burgelman M, *J. Appl. Phys.* **81**, 2881–2886 (1997).
165. McCandless B, Phillips J, Titus J, Conf. Rec. 2nd WCPVSEC, 448–452 (1998).
166. Asher S *et al.*, Conf. Rec. 28th IEEE Photovoltaic Specialist Conf., 479–482 (2000).
167. Fahrenbruch A, *Sol. Cells* **21**, 399–412 (1987).
168. Meyers P, Phillips J, Conf. Rec. 25th IEEE Photovoltaic Specialist Conf., 789–792 (1996).
169. Hiltner J, Sites J, *AIP Conf. Ser.* **462**, 170–173 (1998).
170. Gupta A, Townsend S, Kaydanov V, Ohno T, Conf. Rec. NCPV Rev. Mtg, 271–272 (2000).
171. Hegedus S, McCandless B, Birkmire R, Conf. Rec. 28th IEEE Photovoltaic Specialist Conf., 535–538 (2000).
172. Dobson K, Visoly-Fisher I, Hodes G, Cahen D, *Sol. Energy Mater. Sol. Cells* **62**, 145–154 (2000).
173. Greco D, Compaan A, *Appl. Phys. Lett.* **75**, 36–363 (1999).
174. Stollwerck G, MS Thesis, Colorado State University (1995).
175. Hulstrom R, Bird R, Riordan C, *Sol. Cells* **15**, 365 (1985).
176. Mauk P, Tavakolian H, Sites J, *IEEE Trans. Electron Dev.* **37**, 1065–1068 (1990).
177. Liu X, Sites J, *J. Appl. Phys.* **75**, 577–581 (1994).
178. Scofield J, *Sol. Energy Mater. Sol. Cells* **37**, 217–233 (1995).
179. Phillips J, Birkmire R, McCandless B, Meyers P, Shafarman W, *Phys. Stat. Sol. (b)* **194**, 31–39 (1996).
180. Matulionis I, Nakada S, Compaan A, Conf. Rec. 26th IEEE Photovoltaic Specialist Conf., 491–494 (1997).
181. Willing F *et al.*, Conf. Rec. 21st IEEE Photovoltaic Solar Energy Conversion, 1432–1436 (1990).
182. van den Berg R *et al.*, *Sol. Energy Mater. Sol. Cells* **31**, 253–261 (1993).
183. *Kirk-Othmer Encyclopedia of Chemical Technology*, Third Edition, Vol. 11, 807–880, John Wiley and Sons, Inc., New York (1980).
184. Brown R, U.S. Geological Survey Minerals Yearbook, (2000) U.S.G.S., 67.1–67.4.
185. Andersson B, *Prog. Photovolt. Res. Appl.* **8**, 61–76 (2000).
186. Gerhardinger P, McCurdy R, *Mat. Res. Soc. Symp. Proc.* **426**, 399–410 (1996).
187. Zweibel K, *Sol. Energy Mater. Sol. Cells* **59**, 1–18 (1999).
188. Maycock P (Ed), *Photovoltaic News*, **20** (Feb, 2001).
189. Green M *et al.*, *Prog. Photovolt. Res. Appl.* **7**, 31–37 (1999).
190. Suyama N *et al.*, Conf. Rec. 21st IEEE Photovoltaic Specialist Conf., 498–503 (1990).
191. Rose D *et al.*, Conf. Rec. 28th IEEE Photovoltaic Specialist Conf., 428–431 (2000).
192. Cunningham D *et al.*, Conf. Rec. 16th European Photovoltaic Solar Energy Conversion, 281–285 (2000).
193. Fan J, Palm B, *Sol. Cells* **11**, 247–261 (1984).

194. Nell M, Barnett A, *IEEE Trans. Elec. Dev.* **ED-34**, 257–265 (1987).
195. Basol B, Kapur V, Kullberg R, Conf. Rec. 20th IEEE Photovoltaic Specialist Conf., 1500–1504 (1988).
196. Rohatgi A, Sudharsanan R, Ringel S, MacDougal M, *Sol. Cells* **30**, 109–122 (1991).
197. Romeo A, Batzner D, Zogg H, Tiwari A, *Mat. Res. Soc. Symp. Proc.* **668**, H3.3.1–H3.3.6 (2001).
198. Zweibel K, Conf. Rec. IECEC (Denver, CO, 1988).
199. Charlton D, *J. Cryst. Growth* **59**, 98–110 (1982).
200. Li T, Conf. Rec. 33rd Electronic Components Conference, 546–551 (1983).
201. Niraula M *et al.*, *Appl. Phys. Lett.* **75**, 2322–2324 (1999).
202. Fthenakis V, Eberspacher C, Moskowitz P, *Prog. Photovolt.: Res. Appl.* **4**, 447–456 (1996).
203. Zweibel K, Moskowitz P, Fthenakis V, NREL Technical Report 520–24057 (Feb. 1998).
204. Herndon M, Gupta A, Kaydanov V, Collins R, *Appl. Phys. Lett.* **75**, 3503–3506 (1999).
205. Gessert T, Duda A, Asher S, Narayanswamy C, Rose D, Conf. Rec. 28th IEEE Photovoltaic Specialist Conf., 654–657 (2000).

15

Dye-sensitized Solar Cells

Kohjiro Hara and Hironori Arakawa

*National Institute of Advanced Industrial Science and Technology (AIST),
Tsukuba, Japan*

15.1 INTRODUCTION TO DYE-SENSITIZED SOLAR CELLS (DSSC)

15.1.1 Background

Photoelectrochemical solar cells (PSCs), consisting of a photoelectrode, a redox electrolyte, and a counter electrode, have been studied extensively. Several semiconductor materials, including single-crystal and polycrystal forms of *n*- and *p*-Si, *n*- and *p*-GaAs, *n*- and *p*-InP, and *n*-CdS, have been used as photoelectrodes. These materials, when used with a suitable redox electrolyte, can produce solar light-to-current conversion efficiency of approximately 10%. However, under irradiation, photocorrosion of the electrode in the electrolyte solution frequently occurs, resulting in poor stability of the cell, so efforts have been made worldwide to develop more stable PSCs.

Oxide semiconductor materials have good stability under irradiation in solution. However, stable oxide semiconductors cannot absorb visible light because they have relatively wide band gaps. Sensitization of wide band gap oxide semiconductor materials, such as TiO₂, ZnO, and SnO₂, with photosensitizers, such as organic dyes, that can absorb visible light has been extensively studied in relation to the development of photography technology since the late nineteenth century. In the sensitization process, photosensitizers adsorbed onto the semiconductor surface absorb visible light and excited electrons are injected into the conduction band of the semiconductor electrodes. Dye-sensitized oxide semiconductor photoelectrodes have been used for PSCs.

Gerischer and Tributsch studied a ZnO electrode sensitized by organic dyes including rose bengal, fluorescein, and rhodamine B [1, 2]. In early studies, however, single-crystal and polycrystal materials, which cannot adsorb a large amount of dye, were used for the photoelectrode, which resulted in low light-harvesting efficiency (LHE) and,

consequently, low photon-to-current conversion efficiencies. Additionally, the organic dyes that were used had a narrow absorption range in visible light, which also contributed to low solar cell performance. Thus, to improve light-harvesting efficiencies and cell performance, researchers used two approaches: developing photoelectrodes with larger surface areas that could adsorb large amount of dye and synthesizing dyes with broader absorption ranges. Significant improvements in the performance of a dye-sensitized solar cell (DSSC, or Grätzel cell) have been mainly due to the development of high-performance nanoporous TiO_2 thin-film electrodes that have a large surface area capable of adsorbing a large amount of photosensitizer, and due to the synthesis of new Ru complex photosensitizers capable of absorbing in the wide visible and near-IR region from 400 to 800 or 900 nm.

Ru bipyridyl complexes are suitable photosensitizers because the excited states of the complexes have long lifetimes and oxidized Ru(III) has long-term chemical stability. Therefore, Ru bipyridyl complexes have been studied intensively as photosensitizers for homogeneous photocatalytic reactions and dye-sensitization systems. An Ru bipyridyl complex, bis(2,2'-bipyridine)(2,2'-bipyridine-4,4'-dicarboxylate)ruthenium(II), having carboxyl groups as anchors to adsorb onto the semiconductor surface, was synthesized and single-crystal TiO_2 photoelectrodes sensitized by the Ru complex were studied in 1979 to 1980 [3, 4].

Recent drastic improvements in the performance of DSSC have been made by Grätzel and coworkers at the Swiss Federal Institute of Technology (EPFL). They achieved a solar energy efficiency, η , of 7 to 10% under AM1.5 irradiation using a DSSC consisting of a nanocrystalline TiO_2 thin-film electrode having a nanoporous structure with large surface area, a novel Ru bipyridyl complex, and an iodine redox electrolyte [5, 6]. They also developed a Ru terpyridine complex that absorbs in the near-IR region up to 900 nm as a photosensitizer for a nanocrystalline TiO_2 photoelectrode: the resulting cell obtained $\eta = 10.4\%$ under AM1.5 with a short-circuit photocurrent density, J_{SC} , of 20.5 mA cm^{-2} , an open-circuit voltage, V_{OC} , of 0.72 V, and a fill factor (ff) of 0.70 [7, 8].

The DSSC is an attractive and promising device for solar cell applications that have been intensively investigated worldwide, and its PV mechanism is well understood [9–18]. Recently, commercial applications of the DSSC have been under intensive investigation. The cost of commercially fabricating DSSCs is expected to be relatively low because the cells are made of low-cost materials and assembly is simple and easy. In this chapter, we describe the DSSC, including its structure, component materials, characteristics, working mechanism, preparation, and long-term stability, and discuss the improvement of its performance and commercial applications.

15.1.2 Structure and Materials

The schematic structure of the DSSC constructed by the Grätzel group is shown in Figure 15.1. The composition of the DSSC is described in this section.

15.1.2.1 Transparent conducting oxide-coated glass substrate

Transparent conducting oxide (TCO)-coated glass is used as the substrate for the TiO_2 photoelectrode. For high solar cell performance, the substrate must have low

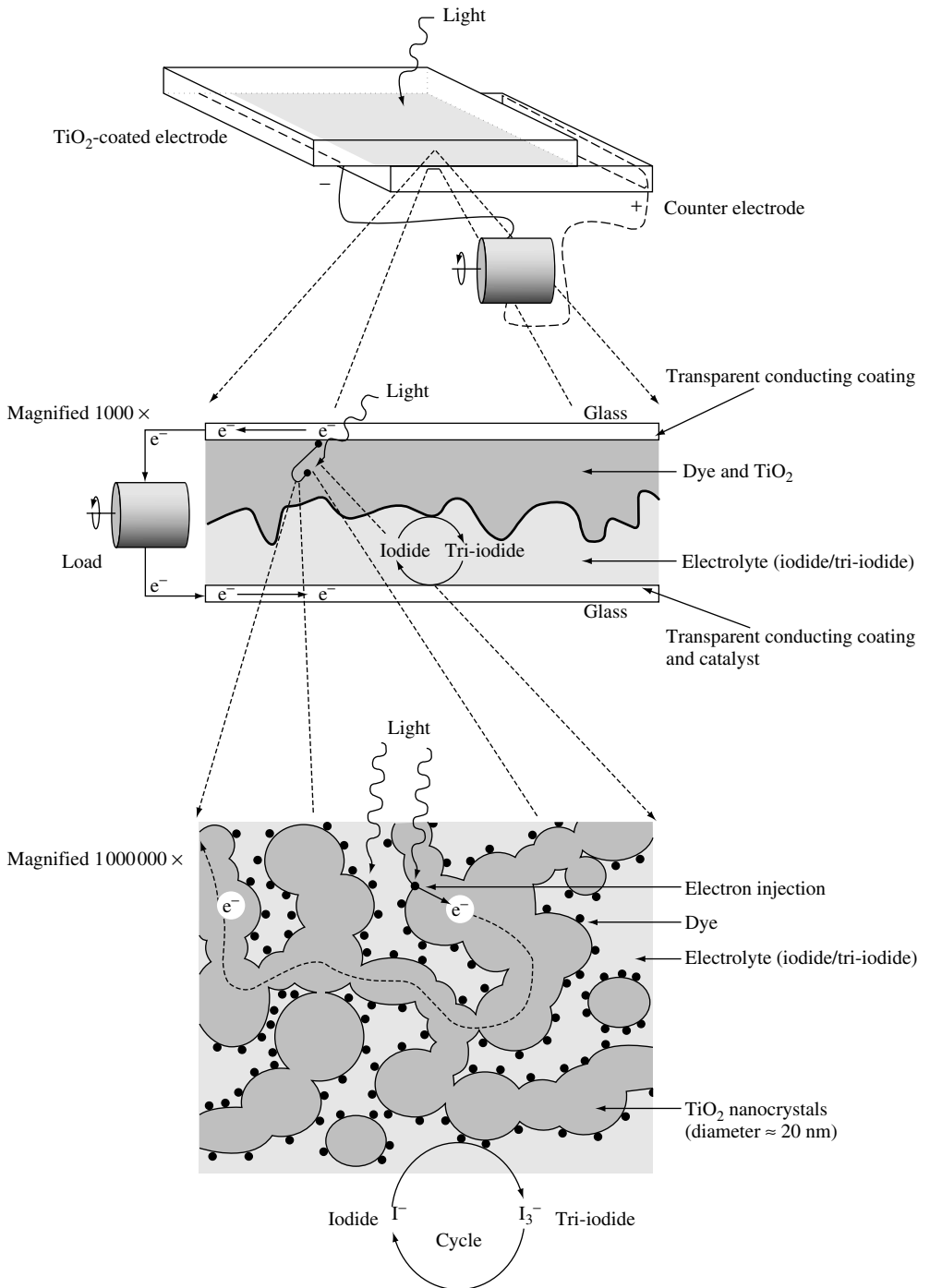


Figure 15.1 Schematic structure of the nanocrystalline dye-sensitized solar cell (DSSC). Reprinted from *Sol. Energy Mater. Sol. Cells*, **55**, Smestad G, 157–178, © 2002, with permission from Elsevier Science [15]

sheet resistance and high transparency. In addition, sheet resistance should be nearly independent of the temperature up to 500°C because sintering of the TiO₂ electrode is carried out at 450 to 500°C. Indium–tin oxide (ITO) is one of the most famous TCO materials. In spite of having low resistance at room temperature, ITO resistance increases significantly at high temperature in air. Usually, fluorine-doped SnO₂ is used as the TCO substrate for DSSCs (e.g. Nippon Sheet Glass Co., $R = 8\text{--}10 \Omega/\text{square}$).

15.1.2.2 TiO₂ photoelectrode

Photoelectrodes made of such materials as Si, GaAs, InP, and CdS decompose under irradiation in solution owing to photocorrosion. In contrast, oxide semiconductor materials, especially TiO₂, have good chemical stability under visible irradiation in solution; additionally, they are nontoxic and inexpensive. The TiO₂ thin-film photoelectrode is prepared by a very simple process. TiO₂ colloidal solution (or paste) is coated on a TCO substrate and then sintered at 450 to 500°C, producing a TiO₂ film about 10 μm in thickness. Because this film is composed of TiO₂ nanoparticles (10–30 nm), giving it a nanoporous structure, the actual surface area of TiO₂ compared to its apparent surface area, roughness factor (rf), is >1000; that is, a 1-cm² TiO₂ film (10 μm thickness) has an actual surface area of 1000 cm². The dye is considered to be adsorbed on the TiO₂ surface in a monolayer. Thus, if the nanoporous TiO₂ film has a high rf, the amount of dye adsorbed is drastically increased (on the order of 10⁻⁷ mol cm⁻²), resulting in an increase of LHE that is near 100% at the peak absorption wavelength of the dye. In comparison, the amount of adsorbed dyes on the surface of single-crystal and polycrystal materials is quite small, with only 1% LHE even at the peak wavelength.

Normally, the TiO₂ film contains large TiO₂ particles (250–300 nm), which can scatter incident photons effectively, to improve the LHE as shown later. The porosity of the film is also important because the electrolyte, which contains the redox ions, must be able to penetrate the film effectively to suppress the rate-determining step via diffusion of redox ions into the film. Appropriate porosity, 50 to 70%, is controlled in the sintering process by the addition of a polymer such as polyethylene glycol (PEG) and ethyl cellulose (EC) into the TiO₂ colloidal solution or paste. Figure 15.2 shows a scanning electron microscope (SEM) photograph of a typical nanocrystalline TiO₂ film. A detailed description of the procedure for preparing the TiO₂ film is given in Section 15.2.2.

15.1.2.3 Ru complex photosensitizer

The Ru complex photosensitizer, which contributes the primary steps of photon absorption and the consequent electron injection, is adsorbed onto the TiO₂ surface. The chemical structure of typical Ru complex photosensitizers developed by Grätzel's group are shown in Figure 15.3 (TBA is tetrabutylammonium cation, (C₄H₉)₄N⁺), and Figure 15.4 shows absorption properties of the complexes in solution. The y-axis is represented by absorbance (A) and $1 - T (= 1 - 10^{-A})$, where T is the transmittance. The *cis*-bis(4,4'-dicarboxy-2,2'-bipyridine)dithiocyanato ruthenium(II) (RuL₂(NCS)₂ complex), which is referred to as N3 dye (or red dye), can absorb over a wide range of the visible regions from 400 to 800 nm. The trithiocyanato 4,4'4''-tricarboxy-2,2':6',2''-terpyridine ruthenium(II) (black dye) (RuL'(NCS)₃ complex), absorbs in the near-IR region up to

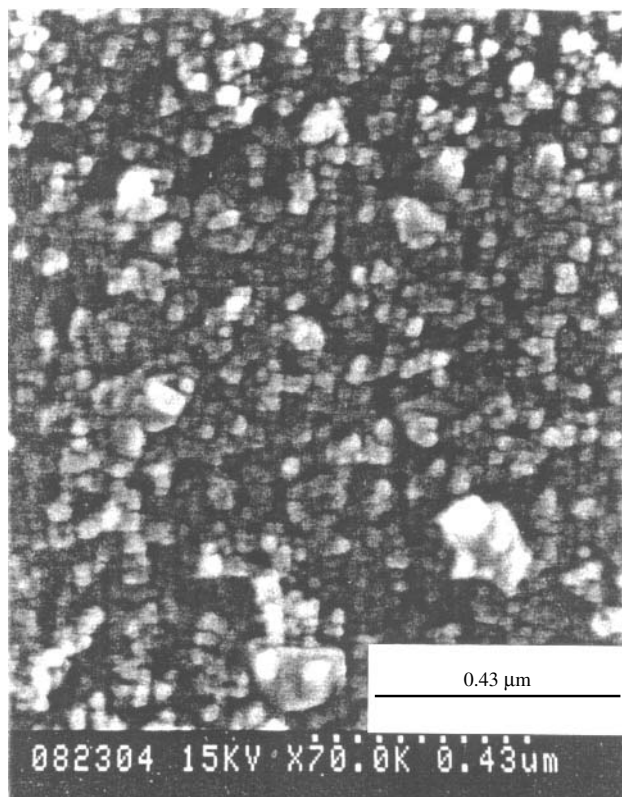


Figure 15.2 Scanning electron microscope photograph of a typical nanocrystalline TiO_2 film: the scale bar corresponds to $0.43 \mu\text{m}$

900 nm. Absorption by these dyes in the visible and near-IR regions is attributed to the metal-to-ligand charge-transfer (MLCT) transition. The highest occupied molecular orbital (HOMO) and the lowest unoccupied molecular orbital (LUMO) are mainly derived from the d-orbitals of the Ru metal and the π^* orbital of the ligand, respectively. The NCS ligand shifts the HOMO level negatively, leading to a red shift in the absorption property of the complex, and also contributes electron acceptance from reduced redox ions (I^-). These Ru complexes have carboxyl groups to anchor to the TiO_2 surface. Anchoring causes a large electronic interaction between the ligand and the conduction band of TiO_2 , resulting in effective electron injection from the Ru complex into the TiO_2 . The Ru complex is adsorbed on the TiO_2 surface via either carboxylate bidentate coordination or ester bonding ($-\text{C}(=\text{O})\text{O}-$) as measured by FT-IR absorption analysis [19–23]. Figure 15.5 shows the anchoring structure of the N3 dye adsorbed on the (101) surface of TiO_2 . The coverage of the TiO_2 surface with the N3 dye reaches near 100% as derived from the surface area of TiO_2 and the amount of the dye.

15.1.2.4 Redox electrolyte

The electrolyte used in the DSSC contains I^-/I_3^- redox ions, which mediate electrons between the TiO_2 photoelectrode and the counter electrode. Mixtures of iodides such as

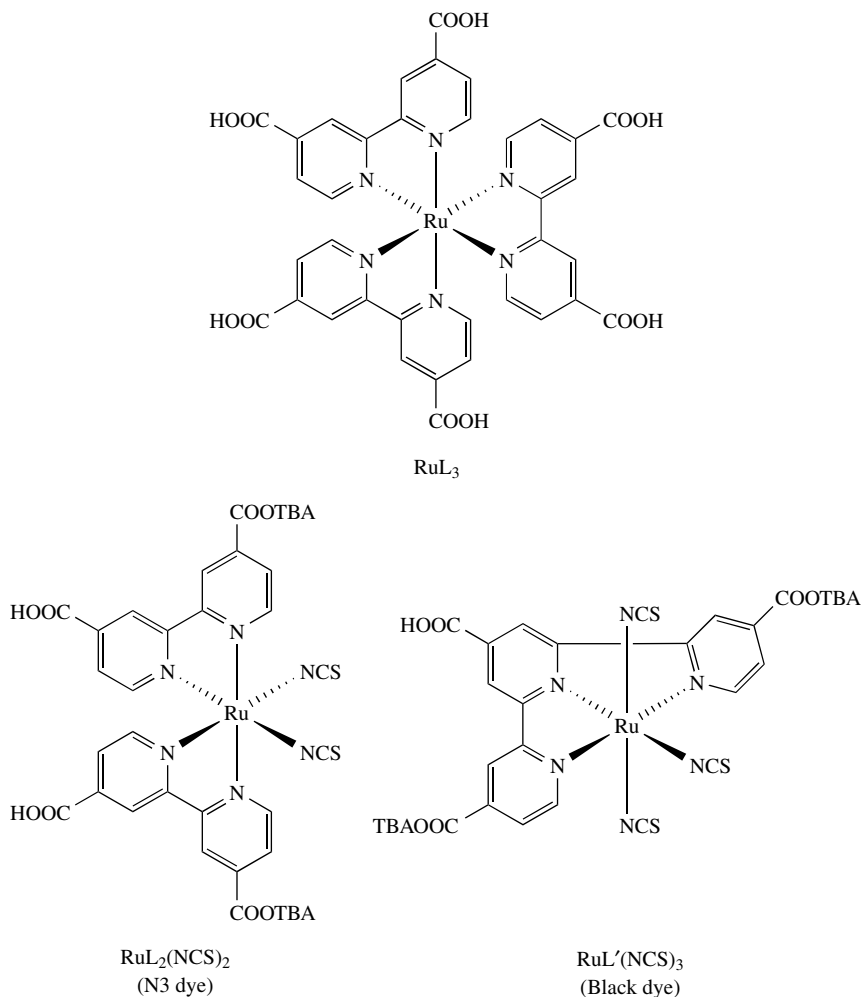


Figure 15.3 Molecular structures of typical Ru complex photosensitizers

LiI , NaI , KI , tetraalkylammonium iodide (R_4NI), and imidazolium-derivative iodides with concentrations of 0.1 to 0.5 M (M: molar concentration) and 0.05 to 0.1 M I_2 dissolved in nonprotonic solvents (e.g. acetonitrile, propionitrile, methoxyacetonitrile, propylene carbonate, and their mixture) are employed. Cell performance of DSSCs depends on counter cations of iodides such as Li^+ , Na^+ , K^+ , and R_4N^+ owing to different ion conductivity in the electrolyte or adsorption on the TiO_2 surface, leading to a shift of the conduction-band level of the TiO_2 electrode [24, 25]. Viscosity of solvents directly affects ion conductivity in the electrolyte, and consequently the cell performance. To improve cell performance, low-viscosity solvents are desired. The diffusion coefficient of I_3^- in methoxyacetonitrile is estimated as $5.4\text{--}6.2 \times 10^{-6} \text{ cm}^2 \text{ s}^{-1}$ [24]. Basic compounds such as *tert*-butylpyridine are added to the electrolyte solution to improve cell performance, as shown later [6]. Br^-/Br_2 and hydroquinone have also been used as redox electrolyte for DSSC [25, 26], but the iodine redox electrolyte gives the best performance.

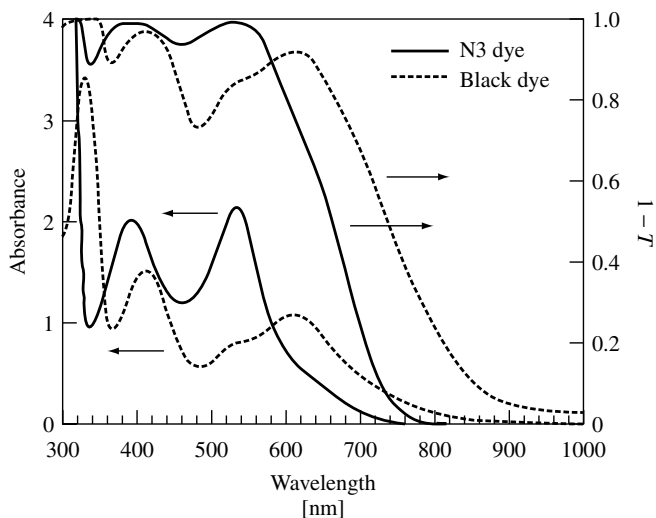


Figure 15.4 Absorption spectra of N3 dye and black dye represented by absorbance and light-harvesting efficiency, $1-T$ (T : transmittance): (—) N3 dye, (---) black dye

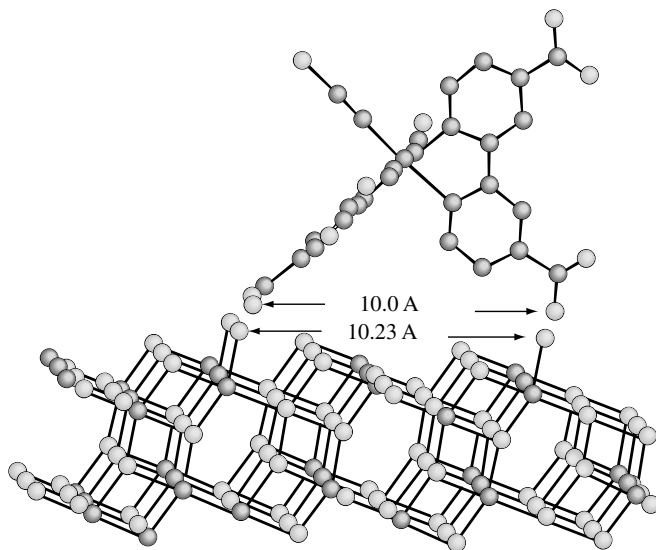


Figure 15.5 Anchoring structure of N3 dye adsorbed on the (101) surface of TiO_2 : the top is N3 dye and the bottom is TiO_2 . Reprinted with permission from © (2002) American Chemical Society

15.1.2.5 Counter electrode

Tri-iodide ions, I_3^- , formed by the reduction of dye cations with I^- ion, are re-reduced to I^- ions at the counter electrode. To reduce the tri-iodide ions, the counter electrode must have high electrocatalytic activity. Pt coated on TCO substrate ($5\text{--}10\ \mu\text{g cm}^{-2}$ or approximately 200-nm thickness) or carbon are usually used as the counter electrode.

15.1.2.6 Sealing materials

A sealing material is needed to prevent the leakage of the electrolyte and the evaporation of the solvent. Chemical and photochemical stability of the sealing material against the electrolyte component, iodine, and the solvent is required. Surlyn (Du Pont), a copolymer of ethylene and acrylic acid, meets these requirements.

15.1.3 Mechanism

This section describes the primary processes that occur in a DSSC and discusses the solar energy-to-current conversion efficiencies of cells.

15.1.3.1 Primary processes

Figure 15.6 is a schematic energy diagram of a DSSC. The following primary steps convert photons to current:

1. Ru complex photosensitizers adsorbed on the TiO_2 surface absorb incident photon flux.
2. The photosensitizers are excited from the ground state (S) to the excited state (S^*) owing to the MLCT transition. The excited electrons are injected into the conduction band of the TiO_2 electrode, resulting in the oxidation of the photosensitizer.

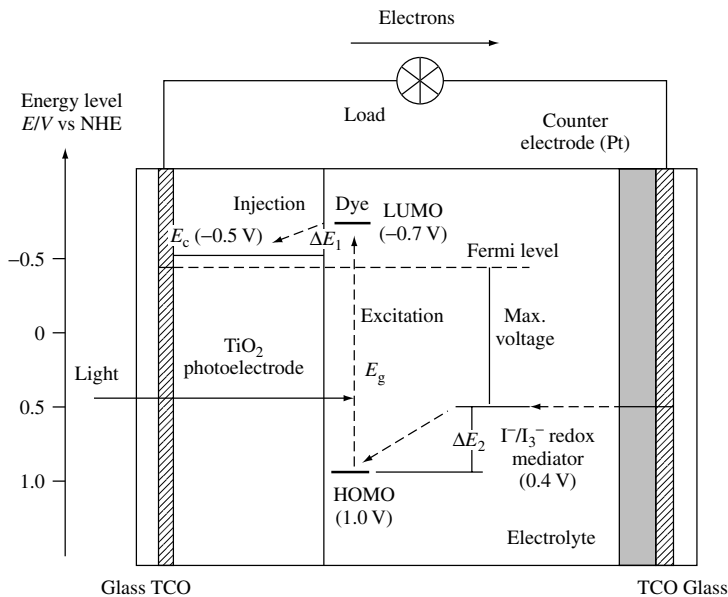


Figure 15.6 Schematic energy diagram and operating principle of DSSC

3. Injected electrons in the conduction band of TiO_2 are transported between TiO_2 nanoparticles with diffusion toward the back contact (TCO) and consequently reach the counter electrode through the external load and wiring.
4. The oxidized photosensitizer (S^+) accepts electrons from the I^- ion redox mediator, regenerating the ground state (S), and I^- is oxidized to the oxidized state, I_3^- .



5. The oxidized redox mediator, I_3^- , diffuses toward the counter electrode and is re-reduced to I^- ions.



Overall, electric power is generated without permanent chemical transformation.

The performance of a DSSC is predominantly based on four energy levels of the component: the excited state (approximately LUMO) and the ground state (HOMO) of the photosensitizer, the Fermi level of the TiO_2 electrode, which is located near the conduction-band level, and the redox potential of the mediator (I^-/I_3^-) in the electrolyte. The photocurrent obtained from a DSSC is determined by the energy difference between the HOMO and the LUMO of the photosensitizer, analogous to the band gap, E_g , for inorganic semiconductor materials. The smaller the HOMO–LUMO energy gap, the larger the photocurrent will be because of the utilization of the long-wavelength region in the solar spectrum. The energy gap between the LUMO level and the conduction-band level of TiO_2 , ΔE_1 , is important, and the energy level of the LUMO must be sufficiently negative with respect to the conduction band of TiO_2 to inject electrons effectively. In addition, substantial electronic coupling between the LUMO and the conduction band of TiO_2 also leads to effective electron injection. The HOMO level of the complex must be sufficiently more positive than the redox potential of the I^-/I_3^- redox mediator to accept electrons effectively (ΔE_2). The energy gaps, ΔE_1 and ΔE_2 , must be larger than approximately 200 mV as driving force for each of the electron-transfer reactions to take place with optimal efficiency [16].

In the case of solid–liquid junction solar cells, PSCs, the voltage is attributed to the energy gap between the Fermi level (near conduction-band level for *n*-type semiconductor) of the semiconductor electrode and the redox potential of the mediator in the electrolyte. As shown in Figure 15.6, the voltage in the DSSC is developed by the energy gap between the Fermi level of a TiO_2 electrode and the redox potential of the I^-/I_3^- in the electrolyte. The conduction-band level of the TiO_2 electrode and the redox potential of I^-/I_3^- were estimated to be -0.5 V versus normal hydrogen electrode (NHE) and 0.4 V versus NHE, respectively, as shown in Figure 15.6 [18] (or -0.7 V versus saturated calomel electrode (SCE) and 0.2 V versus SCE, respectively [12, 16]). Thus, in the case of a DSSC using a TiO_2 electrode and I^-/I_3^- redox mediator, the maximum voltage is expected to be approximately 0.9 V, depending on the electrolyte component because the Fermi level of the TiO_2 electrode depends on the electrolyte components and their concentrations.

In contrast to a conventional *p-n*-type solar cell, the mechanism of a DSSC does not involve a charge-recombination process between electrons and holes because electrons are only injected from the photosensitizer into the semiconductor and a hole is not formed in the valence band of the semiconductor. In addition, charge transport

takes place in the TiO_2 film, which is separated from the photon absorption site (i.e. the photosensitizer); thus, effective charge separation is expected. This photon-to-current conversion mechanism in a DSSC is similar to the mechanism for photosynthesis in nature, in which chlorophyll functions as the photosensitizer and charge transport occurs in the membrane.

In conventional p - n -type solar cells and classical PSCs using polycrystal or single-crystal photoelectrodes, electronic contact between the components that form the photovoltaically active junction, and the equilibrium between the electronic charge carriers in them, leads to space charge formation. Photogenerated charges are separated by the electric field in the space charge layer. In DSSC, however, the individual particle size is too small to form a space charge layer. Charge separation in DSSC has been discussed relative to an electrical field at the electrolyte/semiconductor interface, although not one due to space charge in the semiconductor [27]. Small cations, such as Li^+ , in the electrolyte and H^+ released from the dyes upon binding, can adsorb (or intercalate) on the semiconductor surface. A dipole is formed across the Helmholtz layer between these cations and negatively charged species (iodide ions and the dye). The electrical potential drop across the Helmholtz layer will help separate the charges and reduce recombination with the dye cations or the redox mediator. Under illumination, this potential will decrease, as the electrons injected in the semiconductor will neutralize some of the positive charge at the surface.

15.1.3.2 Photovoltaic performance

Figure 15.7 shows the external spectral response curve of the photocurrent for nanocrystalline TiO_2 solar cells sensitized by N3 and black dyes with an I^-/I_3^- redox electrolyte, where the incident photon-to-current conversion efficiency (IPCE) is represented as a

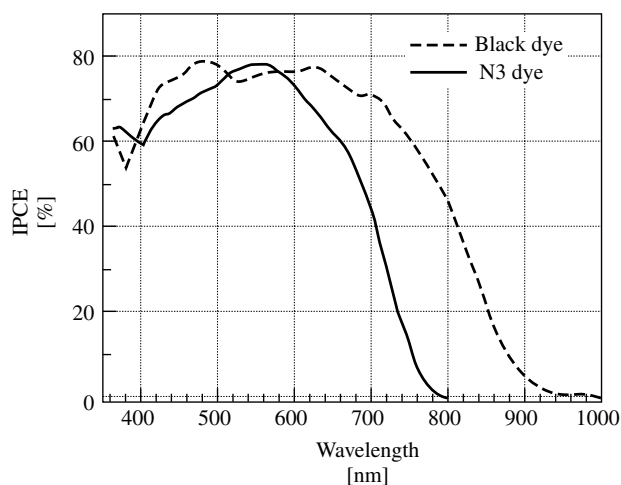


Figure 15.7 Spectral response curve of the photocurrent for the DSSC sensitized by N3 and black dyes: (—) N3 dye, (---) black dye. The incident photon-to-current conversion efficiency (IPCE) is plotted as a function of wavelength. The data is used from Reference [18]

function of wavelength. IPCE is obtained by the following equation:

$$\text{IPCE}[\%] = \frac{1240[\text{eV} \cdot \text{nm}] \times J_{\text{SC}}[\mu\text{A cm}^{-2}]}{\lambda[\text{nm}] \times \Phi[\mu\text{W cm}^{-2}]} \times 100 \quad (15.1)$$

where J_{SC} is the short-circuit photocurrent density for monochromatic irradiation, λ is the wavelength, and Φ is the monochromatic light intensity. As shown in Figure 15.7, solar cells sensitized by the Ru complex photosensitizers can efficiently convert visible light to current. N3 dye ($\text{RuL}_2(\text{NCS})_2$) responds to light from 400 to 800 nm, and black dye ($\text{RuL}'(\text{NCS})_3$) responds to the near-IR region up to 950 nm. The IPCE of the N3 dye-sensitized solar cell reaches 80% at 550 nm and exceeds 70% in the region from 400 to 650 nm. Taking into consideration losses due to light reflection and absorption by the TCO substrate, the internal photon-to-current conversion efficiency is effectively 90 to 100%, indicating high performance of the DSSC. IPCE is also given by the following equation:

$$\text{IPCE} = \text{LHE} \phi_{\text{inj}} \eta_{\text{c}} \quad (15.2)$$

$$\text{LHE} = 1 - T = 1 - 10^{-A} \quad (15.3)$$

where LHE is the light-harvesting efficiency, ϕ_{inj} is the quantum yield of electron injection, and η_{c} is the efficiency of collecting the injected electrons at the back contact. According to equation (15.2), if ϕ_{inj} and η_{c} are almost equal to unity, IPCE is determined by the LHE (i.e. $1 - T$) of the dye adsorbed on the film (shown in Figure 15.4).

Solar energy-to-electricity conversion efficiency, η , under white light irradiation (e.g. AM1.5) can be obtained by the following equation:

$$\eta = J_{\text{SC}} \times V_{\text{OC}} \times ff / I_0 \times 100 \quad (15.4)$$

where I_0 is the photon flux (approximately 100 mW cm^{-2} for AM1.5). A current versus voltage curve obtained for a nanocrystalline TiO_2 solar cell sensitized by black dye is shown in Figure 15.8. Evaluation of the performance was carried out at the National Renewable Energy Laboratory (NREL) operated by the US Department of Energy. An efficiency of 10.4% was obtained (cell size = 0.186 cm^2 , $J_{\text{SC}} = 20.53 \text{ mA cm}^{-2}$, $V_{\text{OC}} = 0.721 \text{ V}$, and $ff = 0.704$) [8, 18].

15.1.4 Charge-transfer Kinetics

15.1.4.1 Electron injection process

Recently, the electron-transfer kinetics in the DSSC, shown as a schematic diagram in Figure 15.9, have been under intensive investigation. Time-resolved laser spectroscopy measurements are used to study one of the most important primary processes, electron injection from photosensitizers into the conduction band of semiconductors [28–47]. The electron-transfer rate from the photosensitizer into the semiconductor depends largely on the configuration of the adsorbed photosensitizer material on the semiconductor surface and the energy gap between the LUMO level of the photosensitizer and the conduction-band

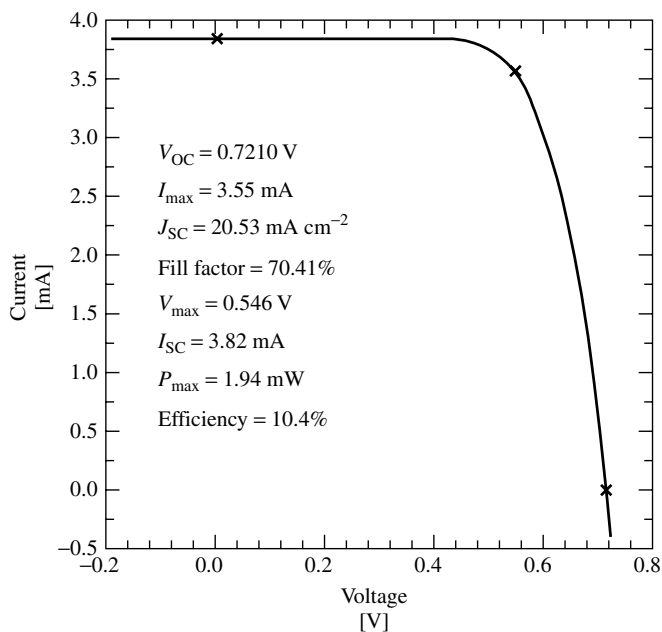


Figure 15.8 Photocurrent–voltage curve obtained for a nanocrystalline TiO_2 solar cell sensitized by black dye. The certified results were obtained at NREL (USA). Reprinted with permission from Hagfeldt A, Grätzel M, *Acc. Chem. Res.* **33**, 269–277 (2000). © (2002) American Chemical Society

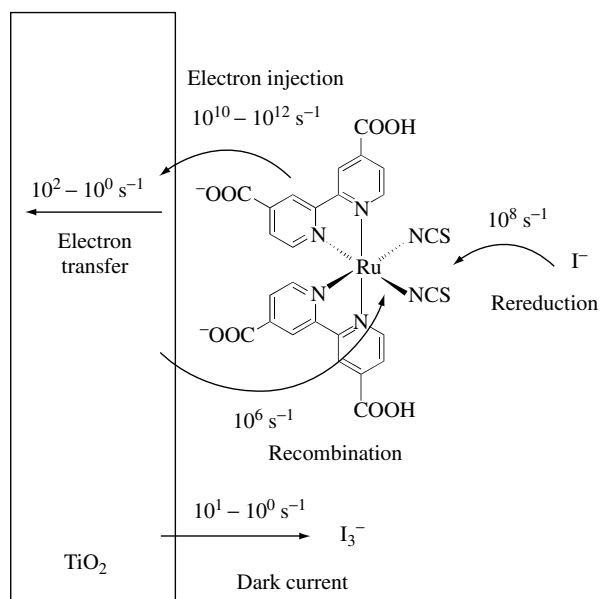


Figure 15.9 Schematic diagram of electron-transfer processes in DSSC

level of the semiconductor. For example, the rate constant for electron injection, k_{inj} , is given by Fermi's golden rule expression

$$k_{\text{inj}} = \left(\frac{4\pi^2}{h} \right) |V|^2 \rho(E) \quad (15.5)$$

where V is the electronic coupling between the photosensitizer and the semiconductor, $\rho(E)$ is the density-of-states of the conduction band, and h is the Planck constant. The value of V is attributed to overlap between the wavefunction of the excited states of the photosensitizer and the conduction band, and it depends largely on the distance between the adsorbed photosensitizer material and the semiconductor surface. In a DSSC, the photosensitizer is strongly adsorbed on the semiconductor surface with carboxyl groups as the anchor, resulting in a very large V between the π^* orbital of the excited state of the photosensitizer and the conduction band of TiO_2 , which consists of the unoccupied 3d orbital of Ti^{4+} . In addition, the conduction band of the semiconductor has a continuous and relatively large density-of-states. Thus, electron injection from the photosensitizer to the semiconductor occurs at a higher rate than does the relaxation from the excited state to the ground state (i.e. relaxation via the emission lifetime). For example, it has been observed that electron injection from N3 dye into TiO_2 occurs on the order of femtoseconds as measured by the time-resolved laser spectroscopy [28, 32]. This ultrafast rate of electron injection contributes to the high energy-conversion efficiencies of the DSSC.

In addition, the rate constant for electron injection depends largely on the semiconductor materials employed. A slower electron injection rate was observed with coumarin dyes and N3 dye injected into ZnO compared to the TiO_2 system [35, 37, 45]. The different rate constant may be caused by the difference in the electronic coupling between the π^* orbital of the dye and the accepting orbitals in ZnO and TiO_2 and/or their density-of-states. The states near the conduction-band edge of ZnO consist of the 4s orbitals of Zn^{2+} , while those of TiO_2 consist of the 3d orbitals of Ti^{4+} , which may result in the observed difference in their electronic coupling with the π^* orbital of the dye.

15.1.4.2 Charge recombination

The charge-recombination process (Figure 15.9) between injected electrons and oxidized dyes must be much slower than electron injection and electron transfer from I^- ion into oxidized dyes (i.e. regeneration of dyes) to accomplish effective charge separation. It was reported that charge recombination between injected electrons on TiO_2 and cations of N3 dye occurs on the order of microseconds to milliseconds, in contrast with ultrafast electron injection [28, 39, 40, 48–50]. The much slower charge recombination compared to electron injection leads to effective charge separation and consequently high cell performance. Charge recombination in the N3 dye/ TiO_2 system is derived from electron transfer from TiO_2 to Ru(III), while electron injection occurs because of electron transfer from the bipyridyl ligand to TiO_2 . Thus, it is considered that long-distance electron transfer from TiO_2 to the Ru metal center leads to a much smaller electron-transfer rate.

15.1.4.3 Regeneration of the oxidized photosensitizers

Electron transfer from the I^- ion into oxidized photosensitizers (cations), or regeneration of photosensitizers (Figure 15.9), is one of the primary processes needed to achieve effective charge separation. The kinetics of this reaction has also been investigated by time-resolved laser spectroscopy [48, 51]. The electron-transfer rate from the I^- ion into cations of the N3 dye was estimated to be 100 ns [48]. This reaction rate is much faster than that for charge recombination between injected electrons and dye cations. Thus, fast regeneration of the oxidized photosensitizer also contributes to the accomplishment of effective charge separation.

15.1.4.4 Recombination between injected electrons and tri-iodide ions (dark current)

Recombination of injected electrons with tri-iodide ions (I_3^-) on a semiconductor as shown in Figure 15.9, corresponding to dark current, is one of the primary processes in a DSSC (reaction [5]).



This reaction can also occur on the SnO_2 surface because the nanocrystalline TiO_2 does not completely cover the TCO substrate, but predominantly occurs on the TiO_2 surface because of the high surface area of the TiO_2 relative to the SnO_2 . This reaction contributes to the loss of PV performance in a DSSC analogous to the forward-bias injection of holes and electrons in a $p-n$ junction. The V_{OC} in DSSC is obtained using the injection current, I_{inj} , as represented by the following equation, as well as $p-n$ junction solar cells:

$$V_{OC} = \frac{kT}{q} \ln \left(\frac{I_{inj}}{I_0} + 1 \right) \quad (15.6)$$

where k is the Boltzmann constant, q is the magnitude of the electron charge, T is the absolute temperature, and I_0 is the dark current. I_{inj} and I_0 are represented by the following equations:

$$I_{inj} = q\eta\Phi_0 \quad (15.7)$$

$$I_0 = qn_0k_{et}[I_3^-] \quad (15.8)$$

where η is the quantum yield for photogenerated electrons, Φ_0 is the incident photon flux, n_0 is the electron density on the conduction band of the semiconductor in the dark, k_{et} is the rate constant for recombination, reaction [5], and $[I_3^-]$ is the concentration of oxidized redox mediator, I_3^- , in the solution. From equations (15.6) to (15.8), we obtain the following equation:

$$V_{OC} = \frac{kT}{q} \ln \left(\frac{\eta\Phi_0}{n_0k_{et}[I_3^-]} + 1 \right) \quad (15.9)$$

Usually, $\eta\Phi_0 \gg n_0k_{et}[I_3^-]$ and equation (15.9) is simplified as follows [6, 12, 52, 53]:

$$V_{OC} = \frac{kT}{q} \ln \left(\frac{\eta\Phi_0}{n_0k_{et}[I_3^-]} \right) \quad (15.10)$$

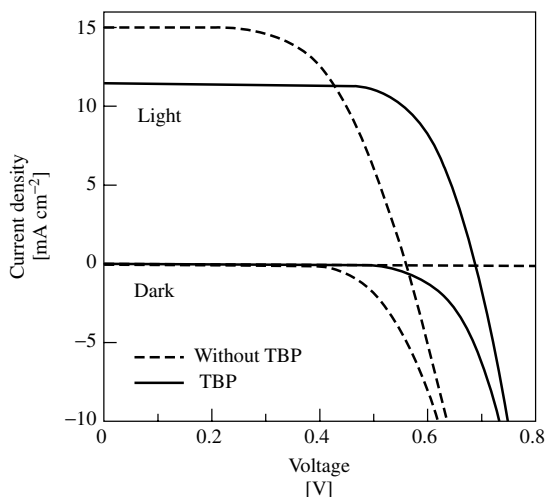


Figure 15.10 Current–voltage characteristics of N3 dye-sensitized TiO₂ solar cells under illumination and darkness using electrolyte with and without TBP: (—) without TBP, (—) with TBP

Dark current is considered to occur at the TiO₂/electrolyte interface where the photosensitizers are not adsorbed. To suppress dark current, pyridine derivatives such as *tert*-butylpyridine (TBP) have been employed as coadsorbates on the TiO₂ surface, resulting in the improvement of photovoltage [6, 52]. TBP is considered to adsorb on the uncovered TiO₂ surface. Figure 15.10 shows the current–voltage characteristics of the N3 dye-sensitized TiO₂ solar cell under illumination and darkness, using electrolyte with and without TBP. This clearly indicates that TBP suppresses dark current, resulting in the improvement of V_{OC} . A decrease of the J_{SC} by addition of TBP is considered to be due to the negative shift of the conduction-band level of TiO₂ owing to adsorption of TBP, which has basic property, leading to suppression of the electron injection from the dye.

The kinetics of recombination, reaction [5], has been investigated and discussed [6, 52, 54–59]. If this reaction occurs predominantly with a large reaction rate, the DSSC does not work. Taking into consideration this and the slow transport of the photoinjected electrons through the nanocrystalline TiO₂ film (described in the next section), the recombination must be extremely slow. In fact, the rate of recombination has been estimated to be on the order of 0.1 s to several seconds [56]. This slow recombination would be due to a low electrocatalytic activity of TiO₂ for the reduction of tri-iodide ions.

15.1.4.5 Electron transport in TiO₂ film

Electron transport in TiO₂ film is an important process related to PV performance in the DSSC (see Figure 15.9) and has been studied by many researchers [60–74]. The electron transport in nanocrystalline TiO₂ film has been discussed with respect to different mechanisms: a diffusion model [60–63], a mechanism that involves tunneling through potential barriers between the particles [63], a trapping/detrapping mechanism [65–68], and an insulator–metal (Mott) transition mechanism [69]. Electron conductivity in TiO₂ is very small, resulting in slow response of the photocurrent. For example, diffusion

coefficients of the electrons in nanocrystalline TiO_2 film have been estimated to be 1×10^{-7} [60] and $1.5 \times 10^{-5} \text{ cm}^2 \text{ s}^{-1}$ [61]. In the DSSC, the electron conductivity of TiO_2 film is significantly increased due to electron injection from photosensitizers under photon irradiation [62, 63]. In addition, conductivity and response of the photocurrent increase with increasing incident light intensity [62, 63]. It has been suggested that when injected electrons fill the trap site and/or surface levels in the TiO_2 film, the diffusion coefficient of the electron increases drastically, leading to elevated electron conductivity and good response of the photocurrent.

15.1.5 Characteristics

As described above, the photovoltaic (PV) mechanism of DSSC is different from that of conventional p - n -type solar cells. The DSSC has other unique characteristics such as the following:

1. *High energy conversion efficiency*: A DSSC efficiency equal to that of the amorphous-Si solar cell has been obtained during laboratory development and efficiencies greater than 10% may be possible.
2. *Low-cost fabrication*: The DSSC is very simple to construct and is made of low-cost materials. Fabrication costs will therefore be less than that for conventional solar cells. For example, US\$0.60/W, which may be competitive for conventional solar cells, has been estimated for a DSSC with 10% efficiency [10, 15].
3. *Abundant supply of component materials*: Oxide semiconductors such as TiO_2 , dye, and iodine are abundantly available. Although metal deposits of Ru are limited, the amount of Ru complex used in the DSSC is only $1 \times 10^{-7} \text{ mol cm}^{-2}$. As discussed in Section 15.3.2.2, organic dye photosensitizers could be used rather than Ru complexes if resource limitation is a problem.
4. *Good potential for colorful, adaptable consumer products*: Colorful and transparent solar cells can be made using various kinds of dyes, depending on the use of the cell. For example, transparent solar cells could be used in place of windowpanes. Additionally, the use of a plastic substrate, rather than glass, is possible if low temperature processing of the TiO_2 film preparation ($<250^\circ\text{C}$) is available and would expand the use of DSSC.
5. *Low potential for environmental pollution*: The TiO_2 , dyes, and iodine used in the DSSC are nontoxic. The only component that could potentially cause harm is the organic solvents used in the electrolyte solution. Future research should be directed toward developing a solid-state electrolyte.
6. *Good recyclability*: The organic dye photosensitizers adsorbed on the electrode can be removed by washing the electrode with alkali solutions or combustion, providing recyclability of the DSSC.

15.2 DSSC FABRICATION ($\eta = 8\%$)

15.2.1 Preparation of TiO_2 Colloid

Commercial powders of TiO_2 , such as P25 (Degussa or Nippon Aerosil [75]), can be used to fabricate the TiO_2 photoelectrode. Colloidal TiO_2 prepared by hydrolysis of Ti(IV)

alkoxides, such as isopropoxide and butoxide, has usually been used to produce high-performance solar cells [16, 76]. Generally, the anatase phase rather than rutile phase of TiO_2 is more suitable for electrodes [77]. Preparation involves the following steps:

1. Precipitation by hydrolysis of Ti alkoxides using 0.1 M HNO_3 .
2. Peptization by heating at 80°C for 8 h, followed by filtering.
3. Hydrothermal growth by autoclaving at 200 to 250°C for 12 h.
4. Sonication with an ultrasonic bath.
5. Concentration with an evaporator.

Precipitation involves controlled hydrolysis of a Ti alkoxide, such as Ti isopropoxide. To obtain monodispersed particles of the desired size, the hydrolysis and condensation kinetics must be controlled. Ti-alkoxides suitably modified with acetic acid or acetyl acetate yield colloids having a large surface area ($>200 \text{ m}^2 \text{ g}^{-1}$) and smaller particle diameter (5–7 nm) [16, 76]. Peptization results in the segregation of the agglomerates to primary particles, after which the large agglomerates are removed by filtration. Autoclaving of the colloidal TiO_2 solution leads to growth of the primary particles to 10–25 nm and also to some extent increases the anatase crystallinity present. At higher autoclaving temperature, more growth of particles and rutile formation occur, particularly at temperatures above 240°C . Electrodes prepared using colloids autoclaved at or below 230°C are transparent, while those made from colloids autoclaved at higher temperatures are translucent or opaque. After autoclaving, the precipitates are redispersed using an ultrasonic processor equipped with a Ti-horn (e.g. Sonics & Materials Inc., 400–600 W [78]). The colloidal solution is then concentrated at 45°C using a rotary evaporator to reach desired concentration of approximately 11 wt% TiO_2 .

15.2.2 Preparation of the TiO_2 Electrode

The TiO_2 thin film is usually prepared by one of the two methods:

(a) Doctor blade technique

To increase the porosity of the film, 0.02 to 0.07 g of polyethylene glycol (PEG, molecular weight 20 000) is added as a binder to 1 mL of the concentrated colloidal TiO_2 solution (TiO_2 , 11 wt%). If a commercial powder such as P25 is used, the powder is dispersed by grinding with water, a particle stabilizer such as acetylacetone, and a nonionic surfactant such as Triton X [6]. The colloidal TiO_2 solution is spread on a TCO substrate and then sintered at 450°C for 30 min under air. The resulting TiO_2 film is transparent.

(b) Screen printing

The TiO_2 colloid is separated from acidified water, washed carefully, and then mixed with EC as a binder and α -terpineol as a solvent in ethanol, yielding an organic TiO_2 paste after evaporating ethanol. The paste is printed on a TCO substrate using a screen printing machine and then sintered at 500°C for 1 h under air. The film thickness is easily controlled in screen printing by the selection of paste composition (i.e. wt% of TiO_2 nanoparticles in the paste), screen mesh size, and repetition of printing.

Films prepared by both methods have film thicknesses of 5 to 15 μm and film mass of about 1 to 2 mg cm^{-2} . The optimum film thickness is 13 to 14 μm . The films have porosity of 60 to 70% [76]. High porosity produces effective diffusion of the redox mediator into the film. The roughness factor (shown above) for a 10- μm film reaches approximately 1000, allowing the adsorption of large amounts of photosensitizer and consequently increased light-harvesting efficiency, as described in Section 15.1.2.2. TiO_2 film prepared from 10 to 20 nm particles of TiO_2 is transparent.

The scattering property of the film is important for the improvement of the LHE of the dye-coated film, resulting in improved IPCE performance of the cell. This effect of the scattering in the TiO_2 film has been investigated in detail [16, 76, 79–82]. The path length of the incident light and therefore the absorption due to the adsorbed dye can be increased by light scattering in the TiO_2 film. This can be achieved by the addition of some larger TiO_2 particles in small TiO_2 particles during film preparation, since larger particles have small surface area and consequently cannot adsorb large amount of the dye. A simulation of light scattering in the TiO_2 electrode of DSSC predicts that a suitable mixture of small TiO_2 particles (e.g. 20 nm diameter) and of larger particles (250–300 nm diameter), which are effective light-scattering centers, have the potential to enhance solar light absorption significantly [80]. Actually, the photocurrent of DSSC increased by using a scattering film compared to that for a transparent film [81]. This improvement in the photoresponse of DSSC due to the scattering effect is observed especially in the low-energy region (e.g. 650–900 nm). As shown in Figures 15.4 and 15.7, the IPCE values obtained in the red region are higher than what is indicated by the absorption spectra of the dyes in solution (Figure 15.4, $1 - T$). On the low-energy side, a significant part of the incident radiation penetrates the layer due to the low absorption coefficient of the dye, while photons of 500 to 650 nm can be mainly absorbed near the TCO/ TiO_2 interface because of the large absorption coefficient. Multiple reflections of the low-energy light in highly scattering films result in increased light absorption and hence increased photoresponse than what the solution absorption spectra indicate.

It has also been reported that TiCl_4 treatment of the film significantly improves cell performance, especially the photocurrent [6]. After printing, the TiO_2 films are immersed in 0.1 to 0.5 M TiCl_4 aqueous solutions at room temperature and then sintered at 450°C for 30 min. It is possible that TiCl_4 treatment improves the photocurrent by improving the connections between TiO_2 particles.

15.2.3 Dye Fixation onto the TiO_2 Film

After preparation of the TiO_2 films, the N3 dye photosensitizer is adsorbed onto the TiO_2 surface. The films are immersed into the dye solution (0.2–0.3 mM in ethanol or *tert*-butanol–acetonitrile, 1:1 mixed solution) followed by storage at room temperature for 12 to 18 h. This treatment produces intense coloration of the film. Before use, the film is washed with alcohol or acetonitrile to remove excess nonadsorbed dyes inside the nanoporous TiO_2 film.

15.2.4 Redox Electrolyte

As described in Section 15.1.2.4, organic solutions containing iodine redox ions have been used as the redox electrolyte. Typical organic solvents are nitrile solvents having relative low viscosity, such as acetonitrile, propionitrile, methoxyacetonitrile, and methoxypropionitrile, which produce a high degree of ion conductivity. It has been reported that imidazolium derivatives, such as 1,2-dimethyl-3-hexylimidazolium iodide (DMHImI) and 1,2-dimethyl-3-propylimidazolium iodide (DMPImI), decrease the resistance of the electrolyte solution and improve photovoltaic performance [83, 84]. A typical electrolyte composition that produces high solar cell performance for the Ru complex photosensitizers reported by Grätzel's group is a mixture of 0.5 M DMHImI, 0.04 M LiI, 0.02 M I_2 , and 0.5 M *tert*-butylpyridine (TBP) in acetonitrile [76]. As discussed earlier, TBP shifts the conduction-band level of the TiO_2 electrode to the negative direction and suppresses the dark current that corresponds to the reduction of I_3^- ions by injected electrons, leading to the improvement of the voltage [6, 52].

15.2.5 Counter Electrode

Sputtered Pt on a TCO substrate ($5-10 \mu\text{g cm}^{-2}$, or 200-nm thickness) has been usually employed as a counter electrode. When Pt is sputtered producing a mirrorlike effect, the photocurrent is slightly increased due to the light-reflection effect. In addition, the electrocatalytic activity of the Pt-sputtered TCO electrode for the reduction of tri-iodide ions is improved by the formation of Pt colloids on the surface [85]. Small amounts of an alcoholic solution of H_2PtCl_6 are dropped on the surface of the Pt-sputtered TCO substrate, followed by drying and heating at 385°C for 10 min, resulting in the formation of Pt colloids on the surface. The properties of the Pt counter electrode directly affect the fill factor of the solar cell. A desirable exchange current density corresponding to the electrocatalytic activity for the reduction of tri-iodide ions is 0.01 to 0.2 A cm^{-2} [16, 85].

15.2.6 Assembling the Cell and Cell Performance

We can easily fabricate an unsealed DSSC and measure its PV performance. A spacer film, such as polyethylene (15- to $30\text{-}\mu\text{m}$ thickness), is placed on the dye-coated TiO_2 photoelectrode and then the electrolyte solution is dropped on the surface of the TiO_2 electrode using a pipette (one or two drops). The counter electrode is placed on top of the TiO_2 electrode, and then the two electrodes are fastened together with two binder clips. If a low melting point polymer film such as Surlyn is used instead of the spacer film, we can fabricate a sealed cell after packaging of the cell using a resin (e.g. ethylene vinyl acetate, EVA) for long-term stability.

Since Grätzel and coworkers reported high performance of a DSSC in 1991, many workers worldwide have tried to reproduce their result. Some reported performances are shown in Table 15.1. These cells were fabricated using a Ru complex photosensitizer, N3 dye, and a nanocrystalline TiO_2 electrode. In many cases, the light condition is AM1.5

Table 15.1 Photovoltaic performance of N3 dye-sensitized TiO₂ solar cells

Institute	Cell size [cm ²]	J_{sc} [mA cm ⁻²]	V_{oc} [mV]	Fill factor	η [%]	Light source	Year
EPFL	0.31	18.2	720	0.73	9.6	AM1.5	1993
EPFL-NREL	0.17	18.6	740	0.73	10.0	AM1.5	1997
Uppsala Univ.	1.0	30.4	610	0.37	6.9	ELH lamp	1994
ISK	0.5	14.2	630	0.71	6.3	AM1.5	1994
Osaka Univ.	0.5	3.9	570	0.67	6.1	21 mW cm ⁻²	1995
NREL	0.44	14.5	730	0.71	7.5	AM1.5	1997
NIMC	0.13	14.5	698	0.71	7.2	AM1.5	1998
EPFL-NIMC	0.21	15.2	780	0.71	8.4	AM1.5	1999
INAP	144	–	–	–	7.0	AM1.5	1997

EPFL: Swiss Federal Institute of Technology, Switzerland

NREL: National Renewable Energy Laboratory, USA

ISK: Ishihara Sangyo Kaisha Ltd

NIMC: National Institute of Materials and Chemical Research, Japan

INAP: Institut für Angewandte Photovoltaik GmbH, Germany

(approximately 100 mW cm⁻²) produced with a solar simulator in the laboratory. Grätzel and coworkers reported $\eta = 9.6\%$ in 1993, and they achieved 10% at NREL in 1997. Other high efficiencies were reported by Lindquist and coworkers, at Uppsala University (6.9%, 1994), NREL (7.5%, 1997), Ishihara Sangyo Kaisha Ltd. in Osaka (6.3%, 1994), and Yanagida and coworkers at Osaka University (6.1%, using 21 mW cm⁻², 1995). Our group achieved 7.2% in 1998, 8.4% in cooperation with EPFL in 1999, and 8.3% in cooperation with Sumitomo Osaka Cement Co. Ltd. in 2000. A venture company, Institut für Angewandte Photovoltaik GmbH (INAP), that has been investigating commercialization of the DSSC in cooperation with EPFL achieved 7% in 1997 using a 144 cm² cell (12 × 12 cm²). Although these groups have reproduced efficiency values greater than 7%, additional studies must be done to reproduce 10% efficiency.

The establishment of standard measurement conditions for cell performance of DSSC is necessary before cell performance can be estimated exactly because performance depends on measurement conditions, such as light intensity and spectrum. Generally, under low light intensity, fill factor of DSSC is improved because of low photocurrent (i.e. low series resistance), resulting in improved cell performance. The light whose intensity and spectrum are close to AM1.5 irradiation should be used as the light source similar to conventional solar cells. Spectral response (IPCE) performance of DSSCs also depends on light conditions [63]. DSSCs show relatively slow response because of low electron mobility of the TiO₂ film, as described in Section 15.1.4.5. Under high-intensity irradiation, the response of DSSCs increase with electron injection and electron trap filling. Therefore, IPCE performance should be measured by a DC method with high-intensity monochromatic light or an AC method using white bias irradiation and low chopper frequencies (e.g. <50 Hz [63]).

15.3 NEW DEVELOPMENTS

DSSCs producing current with 10% efficiency using a Ru complex photosensitizer and a nanocrystalline TiO₂ photoelectrode have been shown to be a significant new type

of highly efficient solar cell in addition to the conventional p - n type solar cells. Basic and theoretical studies of DSSCs and attempts to commercialize them have been intensively pursued. This section discusses recent approaches to improve cell performance and commercialize DSSCs.

15.3.1 New Oxide Semiconductor Film Photoelectrodes

To date, nanocrystalline TiO_2 electrodes have been used predominantly as the photoelectrode in DSSCs, but other oxide semiconductor materials, ZnO [23, 86–92], SnO_2 [23, 51, 91–93], Nb_2O_5 [23, 43, 91, 92], In_2O_3 [23, 91, 92], SrTiO_3 [94], and NiO [95], have also been investigated (Table 15.2). Nevertheless, nanocrystalline TiO_2 electrodes have the best performance, and oxide semiconductor materials exceeding the performance of TiO_2 have not been found. The physical properties of the materials, such as the energy level of the conduction band and the electron conductivity, influence the performance of the photoelectrode significantly, affecting cell performance.

Recently, combined photoelectrodes consisting of two oxide semiconductor materials have also been investigated [96–98]. Tennakone and coworkers reported that a DSSC based on a nanocrystalline SnO_2/ZnO -combined photoelectrode and N3 dye produced a highly efficient cell performance equal to that of the TiO_2 solar cell [96, 97]: 8% η ($J_{\text{SC}} = 22.8 \text{ mA cm}^{-2}$, $V_{\text{OC}} = 0.67 \text{ V}$, and $ff = 0.50$) under 90 mW cm^{-2} and 15% η under 10 mW cm^{-2} [96]. They employed a combined film consisting of small particles of SnO_2 (15 nm) and large particles of ZnO (2 μm , 53 wt%). The performance of the combined photoelectrode was improved drastically compared to that of ZnO and SnO_2 electrodes. It is believed that the Ru complex is adsorbed on SnO_2 nanoparticles, and ZnO contributes to the electron-transfer process. These results indicate the possibility of developing non- TiO_2 , high-performing electrodes for DSSC, although the detailed mechanism of the new electrode has not been elucidated at this time.

The effect on performance of coating the surface of the TiO_2 electrode with other oxide compounds has been investigated by several groups. Zaban *et al.* prepared a nanocrystalline TiO_2 electrode coated with Nb_2O_5 , whose conduction-band level is more negative than that of TiO_2 . They measured cell performance of a DSSC using this photoelectrode and N3 dye [99]; the J_{SC} and V_{OC} were improved compared to those of the TiO_2 electrode. Wang *et al.* studied cell performance of DSSC using a nanocrystalline ZnO -modified TiO_2 photoelectrode and N3 dye [100]. In this study, the J_{SC} and V_{OC} were also improved compared to those of the TiO_2 electrode. They believed that the improvement was caused by a positive shift of the conduction-band level of the photoelectrode and suppression of dark current due to the ZnO coating [100].

15.3.2 New Dye Photosensitizers

15.3.2.1 Metal complex photosensitizers

As described in Section 15.1.2.3, the $\text{RuL}_2(\text{NCS})_2$ complex (N3 dye), and $\text{RuL}'(\text{NCS})_3$ complex (Black dye), were developed and investigated intensively as photosensitizers. Other Ru complex photosensitizers have also been synthesized and characterized, and their

Table 15.2 Photovoltaic performance of dye-sensitized oxide semiconductor solar cells

Reference	Electrode	Dye	Conditions	Performance
[83]	ZnO	N3	56 mW cm ⁻²	$\eta = 2\%$
[87]	ZnO	Mercurochrome	AM1.5 (99 mW cm ⁻²), 0.09 cm ²	$\eta = 2.5\%$ ($J_{SC} = 7.4$ mA cm ⁻² , $V_{OC} = 0.52$ V, $ff = 0.64$)
[87]	SnO ₂	Mercurochrome	AM1.5 (100 mW cm ⁻²), 0.25 cm ²	$\eta = 0.65\%$ ($J_{SC} = 2.0$ mA cm ⁻² , $V_{OC} = 0.58$ V, $ff = 0.56$)
[87]	In ₂ O ₃	Mercurochrome	AM1.5 (100 mW cm ⁻²), 0.25 cm ²	$\eta = 0.38\%$ ($J_{SC} = 5.4$ mA cm ⁻² , $V_{OC} = 0.24$ V, $ff = 0.29$)
[23]	Nb ₂ O ₅	N3	520 nm (4 mW cm ⁻²), 1 cm ²	$\eta = 2.6\%$ ($J_{SC} = 0.29$ mA cm ⁻² , $V_{OC} = 0.61$ V, $ff = 0.58$)
[88]	Nb ₂ O ₅	N3	Xe lamp (100 mW cm ⁻²), UV and IR cut off	$\eta = 1.2\%$ ($J_{SC} = 3.3$ mA cm ⁻² , $V_{OC} = 0.67$ V, $ff = 0.54$)
[90]	SrTiO ₃	N3	AM1.5 (1 sun)	$\eta = 1.8\%$ ($J_{SC} = 3$ mA cm ⁻² , $V_{OC} = 0.789$ V, $ff = 0.70$)
[92]	SnO ₂ /ZnO	N3	90 mW cm ⁻²	$\eta = 8\%$ ($J_{SC} = 22.8$ mA cm ⁻² , $V_{OC} = 0.67$ V, $ff = 0.5$)
[94]	Nb ₂ O ₅ /TiO ₂	N3	Xe lamp	$J_{SC} = 11.4$ mA cm ⁻² , $V_{OC} = 0.732$ V, $ff = 0.564$
[95]	TiO ₂ /ZnO	N3	Xe lamp (81 mW cm ⁻²), UV and IR cutoff	$\eta = 9.8\%$ ($J_{SC} = 21.3$ mA cm ⁻² , $V_{OC} = 0.71$ V, $ff = 0.52$)
[88]	Nb ₂ O ₅ /TiO ₂	N3	Xe lamp (100 mW cm ⁻²), UV and IR cutoff	$\eta = 2.0\%$ ($J_{SC} = 7.1$ mA cm ⁻² , $V_{OC} = 0.68$ V, $ff = 0.42$)
[91]	NiO (<i>p</i> -type)	erthrosin B	68 mW cm ⁻²	$J_{SC} = 0.2$ mA cm ⁻² , $V_{OC} = 0.08$ V
[98]	Y ₂ O ₃ /SnO ₂	N3	AM1.5 (100 mW cm ⁻²)	$\eta = 4.9\%$ ($J_{SC} = 13.8$ mA cm ⁻² , $V_{OC} = 0.61$ V, and $ff = 0.59$)

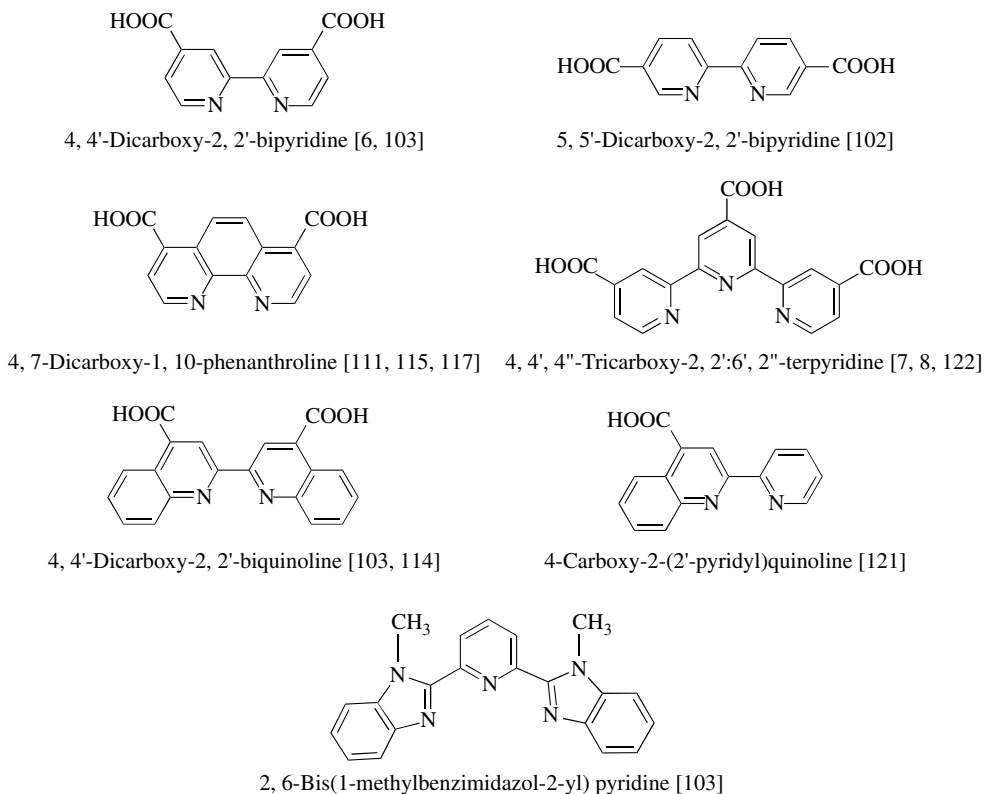


Figure 15.11 Molecular structures of ligands for Ru complex photosensitizers

performances as photosensitizers in the DSSC have been reported by many researchers [101–122]. Several ligands for Ru complex photosensitizers are shown in Figure 15.11 and the structures of new metal complex photosensitizers and their absorption properties are shown in Figure 15.12. The y-axis is represented by molar absorption coefficient, ϵ (i.e. absorption coefficient per M, unit $M^{-1} \text{ cm}^{-1}$).

For example, a Ru phenanthroline complex, *cis*-bis(4,7-dicarboxy-1,10-phenanthroline)dithiocyanato ruthenium(II) ($\text{Ru}(\text{dcphen})_2(\text{NCS})_2$), which has absorption properties due to MLCT transition with a maximum near 520 nm, similar to N3 dye, has been synthesized and characterized [111, 115, 117], and an efficiency value of 6.1 to 6.6% under AM1.5 was obtained using a nanocrystalline TiO_2 solar cell. It has been reported that a Ru bipyridyl complex having an acetylacetonato ligand instead of two thioisocyanato ligands (-NCS) also showed high performance as a photosensitizer [118]. A Ru biquinoline complex, whose absorption due to MLCT transition is red-shifted compared to that of N3 dye, has also been synthesized [114]. Because the LUMO level of this complex is not sufficiently negative to inject electrons effectively, high solar cell performance has not been obtained with a nanocrystalline TiO_2 electrode, although electron injection from this complex into a nanocrystalline SnO_2 electrode, whose conduction-band level is more positive than that of TiO_2 , occurs effectively [114]. Tuning of both the LUMO and the HOMO levels of the complex to inject electrons effectively into the conduction band

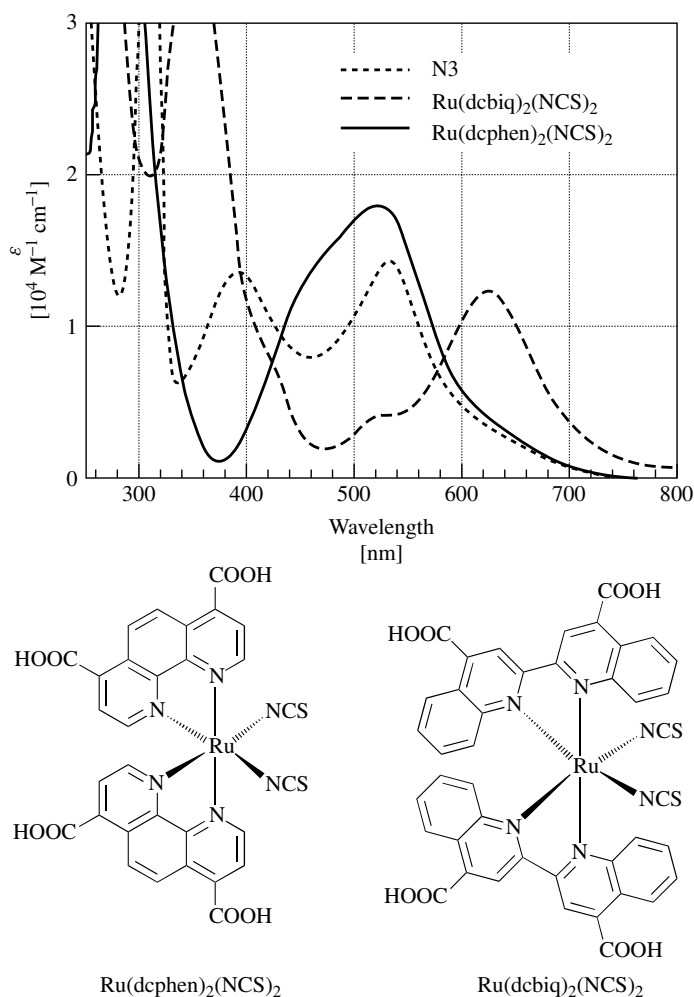


Figure 15.12 Molecular structures of new metal complex photosensitizers, $\text{Ru(dphen)}_2(\text{NCS})_2$ and $\text{Ru(dcbiq)}_2(\text{NCS})_2$, and their absorption properties in ethanolic solution: (---) N3 dye [6, 103], (---) $\text{Ru(dcbiq)}_2(\text{NCS})_2$ [103, 114], (—) $\text{Ru(dphen)}_2(\text{NCS})_2$ [111, 115, 117]. The y-axis is represented by molar absorption coefficient, ϵ

of the semiconductor electrodes and accept electrons from I^- ions, respectively, is very important in developing new efficient photosensitizers.

Metal complexes having metal centers other than Ru have also been synthesized and their performance have been investigated. These include Fe complexes [123, 124], Os complexes [125–128], Re complexes [129], and Pt complexes [130]. A nanocrystalline TiO_2 solar cell sensitized by a square-planar platinum (II) complex containing 4,4'-dicarboxy-2,2'-bipyridine and quinoxaline-2,3-dithiolate ligands showed an efficiency of 2.6% ($J_{\text{SC}} = 6.14 \text{ mA cm}^{-2}$ and $V_{\text{OC}} = 0.60 \text{ V}$) under simulated AM1.5 solar irradiation [130]. However, highly efficient performance exceeding that of the Ru complex

photosensitizers has not been attained. This is believed to be because the HOMO level of Ru complexes derived from the d orbitals of the Ru metal center (i.e. the redox potential of Ru(II)/Ru(III)) is best matched to the iodine redox potential to accept electrons effectively.

Porphyrin [131–134] and phthalocyanine [135] derivatives have also been employed as photosensitizers in the DSSC. A nanocrystalline TiO₂ solar cell sensitized by Cu chlorophyllin produced 2.6% efficiency ($J_{SC} = 9.4 \text{ mA cm}^{-2}$ and $V_{OC} = 0.52 \text{ V}$) under 100 mW cm^{-2} [131]. To develop new efficient metal complex photosensitizers, an increase in the absorption coefficient of the metal complex as well as an increase in the red shift of the absorption region is needed because the absorption coefficient decreases as the red shift increases.

15.3.2.2 Organic and natural dye photosensitizers

Organic dyes whose HOMO and LUMO levels match the conduction-band level of the semiconductor and the iodine redox potential can also be utilized as photosensitizers. As described in Section 15.1.1, organic dyes such as 9-phenylxanthene dyes were used as photosensitizers in early researches. Organic dyes have several advantages as photosensitizers: (1) they have a variety of structures for molecular design, (2) they are cheaper than metal complexes, and (3) they have large absorption coefficients attributed to intermolecular $\pi-\pi^*$ transition. Construction of nanocrystalline DSSCs using organic dye photosensitizers has been reported, and some structures are shown in Figure 15.13 [90, 91, 136–145].

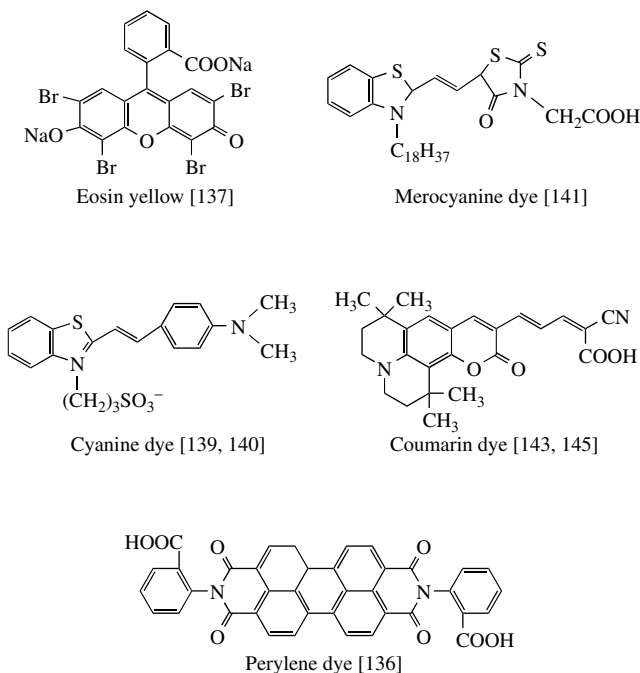


Figure 15.13 Molecular structures of organic dye photosensitizers

A nanocrystalline SnO₂ solar cell sensitized by a perylene derivative produced 0.9% efficiency under AM1.5 ($J_{SC} = 3.26 \text{ mA cm}^{-2}$ and $V_{OC} = 0.45 \text{ V}$) [136]. With a TiO₂ solar cell (1 cm²) sensitized by eosin yellow, one of the 9-phenylxanthene dyes produced 1.3% efficiency ($J_{SC} = 2.9 \text{ mA cm}^{-2}$, $V_{OC} = 0.66 \text{ V}$, and $ff = 0.67$) [137]. A mercurochrome/ZnO solar cell (0.09 cm²) attained 2.5% efficiency ($J_{SC} = 7.44 \text{ mA cm}^{-2}$, $V_{OC} = 0.52 \text{ V}$, and $ff = 0.64$) under AM1.5 irradiation [90, 91].

Cyanine and merocyanine dyes have also been used as photosensitizers [138–142]. A nanocrystalline TiO₂ solar cell based on a merocyanine dye photosensitizer (surface area, 0.25 cm²) produced an efficiency of 4.2% ($J_{SC} = 9.7 \text{ mA cm}^{-2}$, $V_{OC} = 0.62 \text{ V}$, and $ff = 0.69$) under AM1.5 (100 mW cm⁻²) [141]. Aggregates of the merocyanine dye formed on the TiO₂ surface result in expansion of the absorption area, especially in the long-wavelength region, resulting in improvement of light-harvesting performance [141].

We synthesized new coumarin derivatives that can absorb visible light from 400 to 700 nm and prepared nanocrystalline TiO₂ solar cell. Under AM1.5 irradiation, an efficiency of 5.6% was attained (area = 0.25 cm², $J_{SC} = 13.8 \text{ mA cm}^{-2}$, $V_{OC} = 0.63 \text{ V}$, and $ff = 0.64$) [143, 145] (recently we attained 6.0% efficiency). A maximum IPCE of 76% was obtained at 470 nm. The photocurrent performance of this solar cell is almost equal to that of the N3 dye/TiO₂ solar cell, indicating a promising prospect for organic dye photosensitizers. Design and development of new organic dyes with absorption in the near-IR region and large absorption coefficients are needed to improve DSSC performance using organic dye photosensitizers.

In addition to organic dyes, natural dyes extracted from plants can also be used as photosensitizers [34, 146, 147]. A nanocrystalline TiO₂ solar cell using a santalin dye extracted from red sandalwood can produce 1.8% efficiency under 80 mW cm⁻² irradiation [147]. Cherepy *et al.* reported that a nanocrystalline TiO₂ solar cell using flavonoid anthocyanin dyes extracted from blackberries can convert sunlight to electrical power at an efficiency of 0.6% ($J_{SC} = 1.5 - 2.2 \text{ mA cm}^{-2}$ and $V_{OC} = 0.4 - 0.5 \text{ V}$) under AM1.5 [34]. The maximum IPCE was 19% at the peak of the visible absorption band of the dye. They also observed a fast electron injection of <100 fs from cyanin dye into the conduction band of TiO₂ as measured by time-resolved transient absorption spectroscopy [34].

15.3.3 New Electrolytes

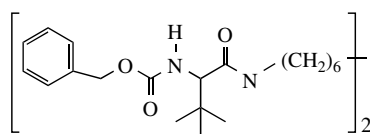
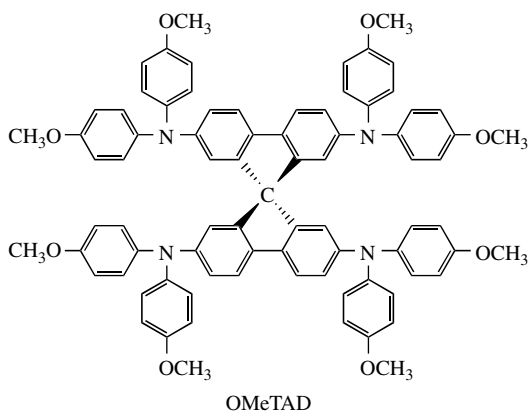
Room-temperature ionic liquids (molten salts) have been extensively studied as replacements for volatile organic solvents in electrochemical devices such as batteries because of their high ionic conductivity, electrochemical stability, and nonvolatility. Of these properties, nonvolatility is the most critical for ensuring the long-term stability of electrochemical devices. Such room-temperature ionic liquids have also been utilized and studied in DSSCs in place of liquid electrolytes [84, 148]. Ionic liquids used in DSSCs include imidazolium derivatives, such as 1-hexyl-3-methylimidazolium iodide (HMImI) [84] and 1-ethyl-3-methylimidazolium bis(trifluoromethylsulfonyl)imide (EMIm-TFSI) [148]. Matsumoto *et al.* reported that an N3 dye-sensitized TiO₂ solar cell using an EMIm salt having hydrofluoride anions, H₂F₃⁻ or H₃F₄⁻, as the electrolyte solvent produced 2.1% efficiency under AM1.5 ($J_{SC} = 5.8 \text{ mA cm}^{-2}$, $V_{OC} = 0.65 \text{ V}$, and $ff = 0.56$) [148]. If the viscosity

of these ionic liquids can be decreased similarly to that of organic solvents, the solar cell performance will be improved as a result of increased ionic mobility of the electrolyte.

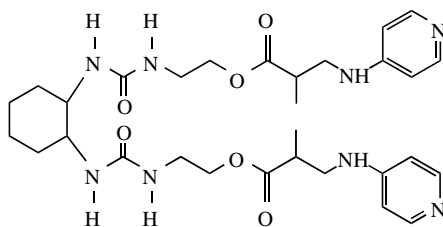
15.3.4 Quasi-solid-state and Solid-state DSSCs

Development of solid-state or quasi-solid-state DSSCs is essential for developing a cell with long-term stability and is critical for commercialization. Because liquid electrolytes using organic solvents are usually utilized in conventional DSSCs, techniques for sealing the cell must be perfectly established to prevent evaporation of components of the electrolyte especially under high temperatures in outdoor applications. In addition, the solid-state DSSC would allow easier interconnection of a cell into a monolithic module.

Grätzel and coworkers studied an N3 dye-sensitized nanocrystalline TiO₂ solar cell using a hole-transport material, 2,2',7,7'-tetrakis(*N,N*-di-*p*-methoxyphenyl-amine)9,9'-spirobifluorene (OMeTAD), as a solid electrolyte (Figure 15.14) [149]. OMeTAD is



L-valine derivative galator



Gelator reported by Toshiba

Figure 15.14 Molecular structures of a solid-state electrolyte and gelator

spin-coated on the surface of the N3 dye/TiO₂ electrode and then Au is deposited by vacuum evaporation as the counter electrode, resulting in a sandwich-type DSSC. The cell efficiency was 0.7% under 9.4 mW cm⁻² irradiation, and a J_{SC} of 3.18 mA cm⁻² was obtained under AM1.5 (100 mW cm⁻²) [149]. The maximum IPCE was 33%. The rate of electron injection from OMeTAD into cations of N3 dyes has been estimated as 3 ps, which is faster than that from I⁻ ions [150].

Tennakone and coworkers utilized a *p*-type semiconductor material, CuI (band gap, 3.1 eV), as a hole conductor and fabricated a solid-state DSSC [147, 151, 152]. Acetonitrile solution of CuI is dropped into the surface of the dye-coated TiO₂ film heated at approximately 60°C and then is diffused inside the film. After evaporation of the acetonitrile, CuI is deposited into nanoporous TiO₂ film. Au-coated TCO substrate as the counter electrode is pressed onto the surface of the TiO₂/dye/CuI film. In a system using santalin dye as the photosensitizer, 1.8% efficiency was obtained under 80 mW cm⁻² irradiation [147] and the efficiency reached 4.5% for the TiO₂/N3 dye/CuI/Au system, suggesting the possibility that a highly efficient solid-state DSSC could be produced [151]. In these systems, CuI is considered to be partially in contact with TiO₂, decreasing cell performance owing to the recombination of injected electrons. To increase cell performance, there must be decreased TiO₂/CuI contact. Solid-state DSSCs have been studied using other organic and inorganic hole conductor materials, *p*-type CuSCN [153, 154], polypyrrole [155], and polyacrylonitrile [97].

Quasi-solidification of the electrolyte using a gelator is another method for replacing liquid electrolytes in a DSSC. Gelation can be accomplished by adding gelator into the electrolyte without other changes in the components of the electrolyte. Yanagida and coworkers studied gelation of the electrolyte using L-valine derivatives (Figure 15.14) as a gelator and measured solar cell performance of DSSCs using gel electrolytes [156]. The gelator was added at a concentration of 0.1 M and then dissolved at 90 to 140°C. The gel solution was poured onto the dye-coated TiO₂ film and then cooled. Interestingly, the performance of DSSCs using a gel electrolyte has been almost the same as that using a liquid electrolyte. Good long-term stability of the sealed cell using the gel electrolyte was obtained compared to that of a sealed cell using a liquid electrolyte.

Recently, Hayase and coworkers (Toshiba Co.) reported constructing a highly efficient DSSC using a gel electrolyte [157, 158]. The chemical structure of one of the gelator materials is shown in Figure 15.14. The gelator was dissolved in the electrolyte at high temperature, and consequently the gel solution was deposited on the dye-coated TiO₂ electrode surface and then cooled. One electrolyte composition they reported is a mixture of a gelator shown in Figure 15.14 (0.1 g), 1-methyl-3-propylimidazolium (10 g), I₂ (0.1 g), and 1,2,4,5-tetrakisbromomethylbenzene (0.1 g). Gelation is caused by polymerization between nitrogen and halogen compounds. A high efficiency, 7.3% ($J_{SC} = 17.6$ mA cm⁻², $V_{OC} = 0.60$ V, and $ff = 0.68$), was obtained for an N3 dye-sensitized TiO₂ solar cell using the gel electrolyte under AM1.5 irradiation, compared to 7.8% for a solar cell based on a liquid electrolyte. They concluded that the resistance of the electrolyte did not increase as a result of the gelation because no change of the fill factor was observed. The photocurrent increased linearly with increasing incident light intensity of up to 100 mW cm⁻², as well as a liquid DSSC. This suggests that gelation of the electrolyte does not suppress diffusion of I⁻ and I₃⁻ ions in the electrolyte.

15.4 APPROACH TO COMMERCIALIZATION

15.4.1 Stability of the DSSC

For commercialization of the DSSC to be successful, the cell and module must have long-term stability. In this section, studies of photochemical, chemical, and physical stability of the component materials of the DSSC and recent investigations concerning long-term stability of the cell will be discussed.

15.4.1.1 Photochemical and physical stability of materials

The photostability and thermal stability of Ru complexes have been investigated in detail [6, 159–162]. For example, it has been reported that the NCS ligand of the N3 dye, *cis*-Ru(II)(dcbpy)₂(NCS)₂ (dcbpy = 2,2'-bipyridyl-4,4'-dicarboxylic acid), is oxidized to a cyano group (–CN) under photo-irradiation in methanol solution, as measured by UV–Vis absorption spectroscopy and nuclear magnetic resonance (NMR) spectroscopy [6, 159]. In addition, the intensity of the IR absorption peak attributed to the NCS ligand starts to decrease at 135°C, and decarboxylation of N3 dyes occurs at temperatures above 180°C [161]. Desorption of the dye from the TiO₂ surface has been observed at temperatures above 200°C.

It has been considered that high stability of the dye can be obtained in a DSSC system by including I[–] ions as the electron donor to dye cations. Degradation of the NCS ligand to a CN ligand due to an intramolecular electron-transfer reaction producing Ru(II) from Ru(III) occurs within 0.1 to 1 s [159], while the rate of reduction of Ru(III) to Ru(II) due to electron transfer from I[–] ions into the dye cations is on the order of nanoseconds [28]. This indicates that one molecule of N3 dye can contribute to the photon-to-current conversion process with a turnover number of at least 10⁷ to 10⁸ without degradation [159]. Taking this into consideration, N3 dye is considered to be sufficiently stable in the redox electrolyte under irradiation.

We must also take into consideration the photoelectrochemical and chemical stability of the solvent in the electrolyte. Organic solvents employed in DSSCs are, for example, propylene carbonate, acetonitrile, propionitrile, methoxyacetonitrile, methoxypropionitrile, and their mixtures. It is known that carbonate solvents, such as propylene carbonate, decompose under illumination, resulting in the formation of a carbon dioxide bubble in the cell. Methoxyacetonitrile (CH₃O–CH₂CN) reacts with trace water in the electrolyte to produce the corresponding amide (CH₃O–CH₂CONH₂), which decreases the conductivity of the electrolyte [163]. Acetonitrile and propionitrile are considered to be relatively stable, giving 2000 h of stability under dark conditions at 60°C [163].

The stability of vapor-deposited Pt electrocatalyst on a TCO substrate used as a counter electrode has also been investigated. It was reported that the electrocatalytically active Pt layer did not seem to be chemically stable in an electrolyte consisting of LiI and I₂ dissolved in methoxypropionitrile [164].

15.4.1.2 Long-term stability of the cell

Professor Grätzel observed that a DSSC using an N3 dye and a nanocrystalline TiO₂ photoelectrode showed good long-term stability, which is due to effective photo-induced

electron transfer from the Ru complex photosensitizer into the conduction band of the semiconductor and from the iodine redox mediator to the photosensitizer. The number of electrons produced by one photosensitizer molecule (turnover number) reaches 500 million, corresponding to continuous stability for 10 years under irradiation.

Long-term stability of the DSSC is currently being investigated for commercial applications at EPFL, Solaronix S.A. in Geneva, the Netherlands Energy Research Foundation (ECN), INAP, and NIMC [6, 13, 159, 163, 165–167], shown in Table 15.3. For example, 7000 h of cell stability, which corresponds to 6 years of outdoor use, has been obtained under 1000 W cm^{-2} with a UV cutoff filter, as shown in Figure 15.15 [159]. Späth and coworkers conducted DSSC stability tests at Solaronix with polymer-sealed devices containing viscous electrolytes with a high boiling point, such as glutaronitrile [165]. They discovered that no significant degradation of stability occurred over a period of 9600 h of continuous illumination at 35°C , indicating chemical stability of components and a physically stable seal using polymer materials. In addition, long-term stability of a small cell for more than 10 000 h has also been accomplished under no UV light conditions at 17°C at 2.5 suns using an electrolyte of 0.5 M LiI, 0.05 M I_2 , and 0.3 M TBP in methoxypropionitrile [163]. Stability tests under UV irradiation have also been carried out [167]. Addition of MgI_2 to the electrolyte can significantly improve stability to UV light, resulting in stable PV performance for more than 1500 h under UV irradiation [167]. A detailed mechanism of the UV-stabilizing effect due to MgI_2 has not been elucidated.

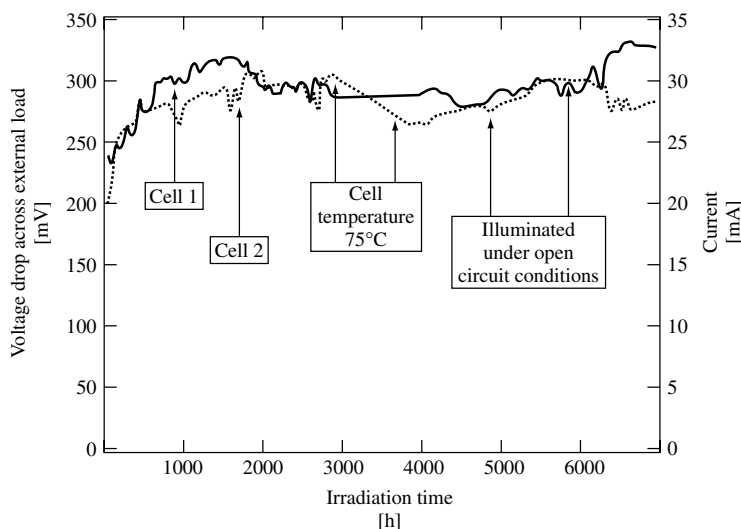


Figure 15.15 Stability test carried out with two sealed DSSCs over 7000 h of continuous illumination with visible light (polycarbonate 395-nm cutoff filter) at 1000 W m^{-2} light intensity. The photocurrent and voltage drop measured across an external load resistor of 10Ω are plotted as a function of irradiation time. Cell 1 (solid line) was continuously illuminated at 35°C ; the same for cell 2 (broken line) except that it was operated for a 700-h period at 75°C and for 1000 h at open circuit. Reproduced from Kohle O, Grätzel M, Meyer A, Meyer T, *Adv. Mater.* **9**, 904–906 (1997) by permission of Wiley-VCH, STM-Copyright & Licenses [159]

Table 15.3 Long-term stability test of dye-sensitized TiO₂ solar cells

Institute and reference	Dye	Test conditions	Components	Term	Results
EPFL [6]	N3	150 W W-halogen lamp UV cutoff, 50°C	Li/LiI ₃ in PC or NMO	10 months	J_{SC} : 20–30% decreased initially. Passed charge: 10^5 C cm ⁻² , 10^7 turnovers.
EPFL [13]	N3	800 W m ⁻² Xe lamp UV cutoff	TBAI, I ₂ in AN Surlyn + waterglass	100 days	J_{SC} increased and V_{OC} decreased for the first 20 days. The efficiency is constant for 100 days.
EPFL [150]	N3	AM1.5 (1000 W m ⁻²), UV cutoff, 35°C	KI, I ₂ in GN	7000 h	J_{SC} increased by 20–30% during the first 1000 h, thereafter reaching a plateau value.
ECN, Solaronix [156]	N3	Fluorescent lamp (1000 W m ⁻²), UV cutoff, 35°C	KI, I ₂ in GN Surlyn 1702	9600 h	J_{SC} increased and V_{OC} decreased for the first 2000 h. Passed charge: $103\,680$ C cm ⁻² .
ECN, INAP, Solaronix [158]	N3	Sulphur lamp (2–3 sun), UV cutoff, 20°C, $\eta = 2\%$	HMIImI, LiI, I ₂ , TBP in MPN Surlyn	8300 h	V_{OC} decreased (50 mV) and J_{SC} increased.
ECN, INAP, Solaronix [158]	N3	UV (10 mW cm ⁻²), 20°C	HMIImI, MgI ₂ , I ₂ , TBP in AN Surlyn	1500 h	J_{SC} and V_{OC} were constant.
INAP [154]	N3	Sulphur lamp (2.5 sun) UV cutoff, 17°C	LiI, I ₂ , TBP in MPN	10 000 h	J_{SC} was constant after initial decrease.
NIMC-SOC	N3	AM1.5 (1000 W m ⁻²) UV cutoff, 20°C, $\eta = 5\%$	DMPImI, LiI, I ₂ , TBP in AN, PN, MPN	4500 h	J_{SC} decreased 5% and V_{OC} was constant. 1.3×10^7 turnovers.
NIMC	Mero- cyanine	AM1.5 (1000 W m ⁻²) UV cutoff, 20°C, $\eta = 3\%$	DMPImI, LiI, I ₂ in MAN	1500 h	J_{SC} and V_{OC} were constant. 1×10^6 turnovers.

PC: propylene carbonate, NMO: 3-methyl-2-oxazolidinone, TBAI: tetrabutylammonium iodide, AN: acetonitrile, PN: propionitrile, GN: glutaronitrile, MAN: methoxy-acetonitrile, MPN: 3-methoxypropionitrile, TBP: tert-butylpyridine, HMIImI: 1-hexyl-3-methylimidazolium iodide, DMPImI: 1,2-dimethyl-3-propylimidazolium iodide
SOC: Sumitomo Osaka Cement Co. Ltd

One of the organic dyes, merocyanine dye, also gave good long-term stability in a preliminary test using a sealed cell under continuous AM1.5 irradiation with a 420-nm cutoff filter, although organic dyes are generally considered to be unstable compared to metal complexes. We obtained stability of cell performance for approximately 1500 h, corresponding to a turnover number of more than 10 million (Table 15.3).

These results strongly indicate that the DSSC shows sufficient physical and chemical stability during the period of illumination. Nevertheless, stability tests at high temperatures and high humidity must be carried out for outdoor applications.

15.4.2 Module Fabrication and Other Subjects for Commercialization

The sheet resistance of TCO substrates (i.e. SnO_2) is relatively high, making the DSSCs resistance-limited if they are larger than about 1 cm^2 . Increased sheet resistance of the TCO substrate on scale-up of the DSSC leads to loss of efficiency, especially fill factor. Therefore, scale-up of the DSSC using a modular approach has been investigated [168, 169]. A module consists of several interconnected basic cells with two TCO substrates coated with TiO_2 or platinum, including the electrolyte inside. The electrolyte contains iodine and iodide, which dissolve metal materials, dissolved in an organic solvent. Therefore, standard conductors like silver will not work or has to be protected by sealing materials. In addition, for having an organic solvent in such a system, one must seal the system carefully also at the outside. To seal the modules, an inert material, glass frit, even for interconnections has been used [168]. An efficiency of 7% was achieved using a module consisting of 12 interconnected cells with a total area of 112 cm^2 (7.6% for a 3-cm^2 cell and 8% for a 1-cm^2 cell) [168]. A continuous process for the fabrication of a monolithic series connecting DSSC modules using laser scribing has been proposed by Kay and Grätzel (Figure 15.16) [13].

Recently, polymer substrates instead of glass have been utilized in constructing DSSCs, expanding possible commercial applications [170–174]. Polymer substrates allow roll-to-roll production, which can achieve high throughput. When a polymer film is used as a substrate, aqueous TiO_2 paste without organic surfactants is sintered at relatively low temperatures, approximately 150°C being sufficient to produce mechanically stable TiO_2 films. Sommeling *et al.* at ECN used an ITO-coated poly(ethylene terephthalate) (PET) film as a substrate and prepared a plastic DSSC [170–172]. A cell performance with a J_{SC} of $15 \mu\text{A cm}^{-2}$, V_{OC} of 0.48 V, and ff of 0.67 was obtained at an illumination intensity of 250 lux. This performance is sufficient to power indoor appliances such as watches and calculators. Under AM1.5 irradiation, a V_{OC} of 0.7 V and J_{SC} of 2 mA cm^{-2} were obtained.

Recently, the DSSC has been used for educational demonstration of solar energy-to-electricity conversion because of its simple fabrication [15, 175]. One can purchase DSSC kits including all components, TCO-coated glass, TiO_2 electrodes, blackberries (i.e. dye), and electrolyte solution [176, 177] and easily demonstrate an artificial photosynthetic process. For detailed studies, one can purchase other materials, including Ru complex photosensitizers, TiO_2 paste, and sealing materials from Solaronix S. A. [178].

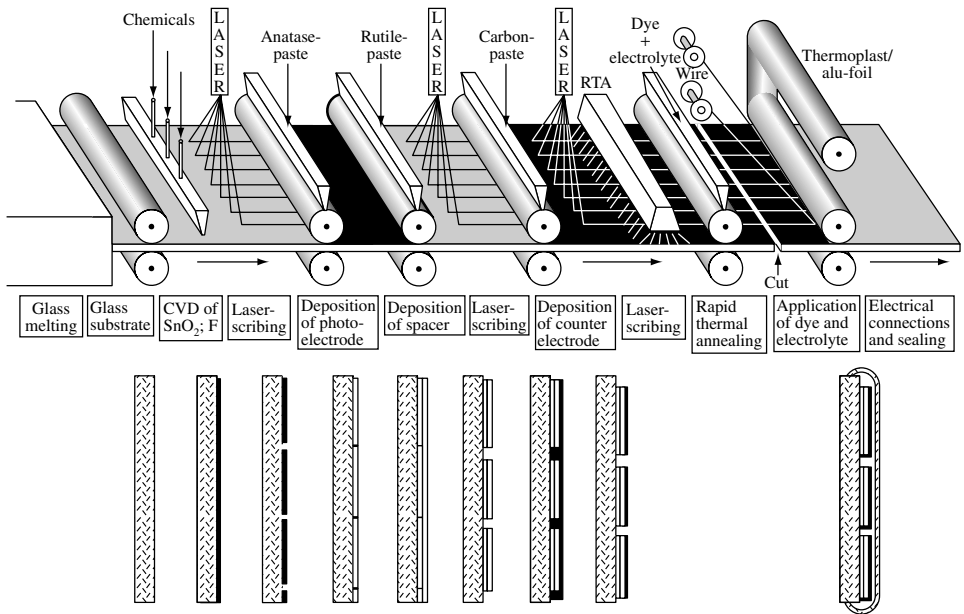


Figure 15.16 Continuous process for the fabrication of monolithic series-connected DSSC modules. Reprinted from *Sol. Energy Mater. Sol. Cells*, **44**, Kay A, Grätzel M, 99–117, © (2002), with permission from Elsevier Science

15.5 SUMMARY AND PROSPECTS

Since 1991, when Grätzel and coworkers reported the development of the highly efficient, novel DSSCs, researchers throughout the world have intensively investigated DSSC mechanisms, new materials, and commercialization. A maximum efficiency of 10.4% has been obtained under AM1.5 in the laboratory. In addition, satisfactory long-term stability of sealed cells has been achieved under relatively mild test conditions (low temperatures and no UV exposure). It will be possible to achieve commercial DSSC production in the near future for indoor applications, such as calculators and several kind of watches. For expanded commercial applications, however, there are several problems that confront us. Overcoming these problems greatly brings DSSC close to expanded commercialization.

(a) Improvement of efficiency

For commercial applications, efficiency higher than 10% (e.g. 15%) is sure to be desired. Expanding the absorption property of the photosensitizer to near IR region is necessary for improved J_{SC} . The absorption property of black dye, whose absorption threshold is close to 920 nm, is expected to be the optimal threshold for single-junction solar cells similar to GaAs. Development of new photosensitizers able to absorb in the near IR region is also desired. Extending of the region of ICPE spectral sensitivity with black dye or other new photosensitizers from the typical 500–600 nm out to 700–900 nm would increase J_{SC} from 20 to 28 mA cm⁻² resulting in an overall efficiency of 15%. The absorption coefficient of the photosensitizers and the light-scattering effect of the

semiconductor film (described in Section 15.2.2) would improve the IPCE performance in the long-wavelength region. In addition, the energy gaps, ΔE_1 and ΔE_2 , as the driving forces for electron-transfer processes (Figure 15.6) are sure to result in energy loss. If we can construct good systems performing with smaller ΔE_1 and ΔE_2 because of molecular design of the photosensitizers, the efficiency can be improved. Improvement of V_{OC} is also important for achievement of higher efficiencies. As shown above, decreased V_{OC} is mainly attributed to recombination between the injected electrons and the redox mediator, I_3^- (dark current). Molecular design of the photosensitizers and/or blocking effect of dark current using adsorbate, such as TBP would improve the V_{OC} . Development of new semiconductor materials, whose conduction-band level is more negative than that of TiO_2 , and the new redox mediator, whose redox potential is more positive than that of the I^-/I_3^- redox, would also increase V_{OC} of DSSC. Presently, however, good semiconductor materials and redox mediators exceeding the combination between the TiO_2 electrode and the iodine redox have not been found.

(b) Long-term stability for outdoor applications

As shown in Section 15.4.1.2, satisfactory long-term stability of sealed cells has already been achieved under relatively mild testing conditions (low temperatures and no UV exposure). For outdoor applications, additional stability testing under more rigorous conditions will be required (e.g. high temperature at near $80^\circ C$, high humidity, and UV exposure).

(c) Solid electrolyte

As shown in Section 15.3.4, development of solid-state electrolytes in DSSCs is essential for developing a cell with long-term stability and is critical for commercialization. Several organic and inorganic materials, such as OMeTAD, polypyrrole, CuSCN, and CuI, have been investigated as solid electrolytes. Presently, however, performance of solid-state DSSCs using these materials are inferior to that of DSSC using liquid electrolytes. It is very difficult to form a good solid–solid interface, which will produce a high solar cell performance because of the large surface area of the nanoporous TiO_2 electrode. On the other hand, liquid electrolytes can easily penetrate into the nanoporous TiO_2 electrode. One of the factors determining high performance of DSSC is the easy formation of solid–liquid interface between the nanoporous TiO_2 electrode and liquid electrolyte. Therefore, electron-transfer processes can occur at most part of the interface. Low electron (or hole) conductivity of the solid electrolyte materials would also determine low performance of solid-state DSSC. CuI is one of the more attractive materials used for solid electrolyte in DSSC and 4% efficiency was attained using TiO_2 /dye/CuI system, as shown in Section 15.3.4. For commercial applications, improvement of the cell performance and long-stability testing of the cell are required because long term stability of the CuI system has not been clarified. Development of new solid electrolyte materials is also desired.

REFERENCES

1. Gerischer H, Tributsch H, *Ber. Bunsen-Ges. Phys. Chem.* **72**, 437–445 (1968).
2. Tributsch H, Gerischer H, *Ber. Bunsen-Ges. Phys. Chem.* **73**, 251–260 (1969).
3. Anderson S *et al.*, *Nature* **280**, 571–573 (1979).

4. Dare-Edwards M *et al.*, *Faraday Discuss. Chem. Soc.* **70**, 285–298 (1980).
5. O'Regan B, Grätzel M, *Nature* **353**, 737–740 (1991).
6. Nazeeruddin Md *et al.*, *J. Am. Chem. Soc.* **115**, 6382–6390 (1993).
7. Nazeeruddin Md, Péchy P, Grätzel M, *Chem. Commun.* 1705–1706 (1997).
8. Nazeeruddin Md, *J. Am. Chem. Soc.* **123**, 1613–1624 (2001).
9. Kalyanasundaram K, Grätzel M, “Metal Complexes as Photosensitizers in Photoelectrochemical Cells”, in Kalyanasundaram K, Grätzel M, Eds, *Photosensitization and Photocatalysis Using Inorganic and Organometallic Compounds*, 247–271, Kluwer Academic Publishers, Dordrecht, Netherlands (1993).
10. Smestad G, Bignozzi C, Argazzi R, *Sol. Energy Mater. Sol. Cells* **32**, 259–273 (1994).
11. Smestad G, *Sol. Energy Mater. Sol. Cells* **32**, 259–288 (1994).
12. Hagfeldt A, Grätzel M, *Chem. Rev.* **95**, 49–68 (1995).
13. Kay A, Grätzel M, *Sol. Energy Mater. Sol. Cells* **44**, 99–117 (1996).
14. Bignozzi C, Schoonover J, Scandola F, “A Supramolecular Approach to Light Harvesting and Sensitization of Wide-Bandgap Semiconductors: Antenna Effects and Charge Separation”, in Meyer G, Ed, *Molecular Level Artificial Photosynthetic Materials*, 1–97, John Wiley & Sons, New York, NY (1997).
15. Smestad G, *Sol. Energy Mater. Sol. Cells* **55**, 157–178 (1998).
16. Kalyanasundaram K, Grätzel M, *Coord. Chem. Rev.* **77**, 347–414 (1998).
17. Grätzel M, *Curr. Opin. Colloid Interface Sci.* **4**, 314–321 (1999).
18. Hagfeldt A, Grätzel M, *Acc. Chem. Res.* **33**, 269–277 (2000).
19. Argazzi R *et al.*, *Inorg. Chem.* **33**, 5741–5749 (1994).
20. Finnie K, Bartlett J, Woolfrey J, *Langmuir* **14**, 2744–2749 (1998).
21. Nazeeruddin Md *et al.*, *Langmuir* **16**, 8525–8528 (2000).
22. Murakoshi K *et al.*, *J. Electroanal. Chem.* **396**, 27–34 (1995).
23. Sayama K, Sugihara H, Arakawa H, *Chem. Mater.* **10**, 3825–3832 (1998).
24. Liu Y, Hagfeldt A, Xiao X, Lindquist S, *Sol. Energy Mater. Sol. Cells* **55**, 267–281 (1998).
25. Hara K *et al.*, *Sol. Energy Mater. Sol. Cells* **70**, 151–161 (2001).
26. Vlachopoulos N, Liska P, Augustynski J, Grätzel M, *J. Am. Chem. Soc.* **110**, 1216–1220 (1988).
27. Zaban A, Ferrere S, Gregg B, *J. Phys. Chem. B* **102**, 452–460 (1998).
28. Tachibana Y *et al.*, *J. Phys. Chem.* **100**, 20056–20062 (1996).
29. Rehm J *et al.*, *J. Phys. Chem.* **100**, 9577–9578 (1996).
30. Kamat P, Bedja I, Hotchandani S, Patterson L, *J. Phys. Chem.* **100**, 4900–4908 (1996).
31. Nasr C, Liu D, Hotchandani S, Kamat P, *J. Phys. Chem.* **100**, 11054–11061 (1996).
32. Hannappel T, Burfeindt B, Storck W, Willig F, *J. Phys. Chem. B* **101**, 6799–6802 (1997).
33. Heimer T, Heilweil E, *J. Phys. Chem. B* **101**, 10990–10993 (1997).
34. Cherepy N, Smestad G, Grätzel M, Zhang J, *J. Phys. Chem. B* **101**, 9342–9351 (1997).
35. Murakoshi K, Yanagida S, Capel M, Castner Jr. E, in Moskovits M, Ed, *Interfacial Electron Transfer Dynamics of Photosensitized Zinc Oxide Nanoclusters*, 221–238, American Chemical Society, Washington, DC (1997).
36. Ellingson R *et al.*, *J. Phys. Chem. B* **102**, 6455–6458 (1998).
37. Asbury J, Wang Y, Lian T, *J. Phys. Chem. B* **103**, 6643–6647 (1999).
38. Heimer T, Heilweil E, Bignozzi C, Meyer G, *J. Phys. Chem. A* **104**, 4256–4262 (2000).
39. Tachibana Y *et al.*, *J. Phys. Chem. B* **104**, 1198–1205 (2000).
40. Huber R *et al.*, *J. Phys. Chem. B* **104**, 8995–9003 (2000).
41. Iwai S *et al.*, *J. Chem. Phys.* **113**, 3366–3373 (2000).
42. Willig F, “Dye-Sensitized Electron Injection into Semiconductor Electrodes”, in Miller R *et al.*, Eds, *Surface Electron Transfer Processes*, 167–309, VCH Publishers, New York (1995).
43. Moser J, Grätzel M, *Chimia* **52**, 160–162 (1998).
44. Asbury J, Hao E, Wang Y, Lian T, *J. Phys. Chem. B* **104**, 11957–11964 (2000).
45. Asbury J *et al.*, *J. Phys. Chem. B* **105**, 4545–4557 (2001).

46. Benkő G *et al.*, *J. Am. Chem. Soc.* **124**, 489–493 (2002).
47. Huber R, Moser J, Grätzel M, Wachtveitl J, *J. Phys. Chem. B* **106**, 6494–6499 (2002).
48. Haque S, Tachibana Y, Klug D, Durrant J, *J. Phys. Chem. B* **102**, 1745–1749 (1998).
49. Haque S *et al.*, *J. Phys. Chem. B* **104**, 538–547 (2000).
50. Kuciauskas D *et al.*, *J. Phys. Chem. B* **105**, 392–403 (2001).
51. Nasr S, Hotchandani S, Kamat P, *J. Phys. Chem. B* **102**, 4944–4951 (1998).
52. Huang S *et al.*, *J. Phys. Chem. B* **101**, 2576–2582 (1997).
53. Kumar A, Santangelo P, Lewis N, *J. Phys. Chem.* **96**, 834–842 (1992).
54. Stanley A, Matthews D, *Aust. J. Chem.* **48**, 1293–1300 (1995).
55. Matthews D, Infelta P, Grätzel M, *Sol. Energy Mater. Sol. Cells* **44**, 119–155 (1996).
56. Salafsky J, Lubberhuizen W, van Faassen E, Schropp R, *J. Phys. Chem. B* **102**, 766–769 (1998).
57. Duffy N, Peter L, Rajapakse R, Wijayantha K, *J. Phys. Chem. B* **104**, 8916–8919 (2000).
58. Cahen D *et al.*, *J. Phys. Chem. B* **104**, 2053–2059 (2000).
59. Gregg B, Pichot F, Ferrere S, Fields C, *J. Phys. Chem. B* **105**, 1422–1429 (2001).
60. Cao F, Oskam G, Meyer G, Searson P, *J. Phys. Chem. B* **100**, 17021–17027 (1996).
61. Solbrand A *et al.*, *J. Phys. Chem. B* **101**, 2514–2518 (1997).
62. Solbrand A *et al.*, *J. Phys. Chem. B* **103**, 1078–1083 (1999).
63. Sommeling P *et al.*, *Sol. Energy Mater. Sol. Cells* **62**, 399–410 (2000).
64. Hoyer P, Weller H, *J. Phys. Chem. B* **99**, 14096–14100 (1995).
65. Schwarzburg K, Willig F, *Appl. Phys. Lett.* **58**, 2520–2522 (1991).
66. de Jongh P, Vanmaekelbergh D, *Phys. Rev. Lett.* **77**, 3427–3430 (1996).
67. de Jongh P, Vanmaekelbergh D, *J. Phys. Chem. B* **101**, 2716–2722 (1997).
68. Könenkamp R, Henniger R, Hoyer P, *J. Phys. Chem.* **97**, 7328–7330 (1993).
69. Wahl A, Augustynski J, *J. Phys. Chem. B* **102**, 7820–7828 (1998).
70. Nelson J, *Phys. Rev. B* **59**, 15374–15380 (1998).
71. van de Lagemaat J, Park N, Frank A, *J. Phys. Chem. B* **104**, 2044–2052 (2000).
72. Kopidakis N *et al.*, *J. Phys. Chem. B* **104**, 3930–3936 (2000).
73. van de Lagemaat J, Frank A, *J. Phys. Chem. B* **104**, 4292–4294 (2000).
74. Kambe S *et al.*, *J. Phys. Chem. B* **106**, 2967–2972 (2002).
75. 2-24-15 Aoyama, Minato-ku, Tokyo 107, Japan, FAX: +81-3-402-4289.
76. Barbé C *et al.*, *J. Am. Ceram. Soc.* **80**, 3157–3171 (1997).
77. Park N, van de Lagemaat J, Frank A, *J. Phys. Chem. B* **104**, 8989–8994 (2000).
78. 53 Church Hill Road, Newton, CT 06470-1614, USA, FAX: 203-270-4610, E-mail: info@sonicsandmaterials.com.
79. Usami A, *Chem. Phys. Lett.* **277**, 105–108 (1997).
80. Ferber J, Luther J, *Sol. Energy Mater. Sol. Cells* **54**, 265–275 (1998).
81. Rothenberger G, Comte P, Grätzel M, *Sol. Energy Mater. Sol. Cells* **58**, 321–336 (1999).
82. Tachibana Y, Hara K, Sayama K, Arakawa H, *Chem. Mater.* **14**, 2527–2535 (2002).
83. Bonhôte P *et al.*, *Inorg. Chem.* **35**, 1168–1178 (1996).
84. Papageorgiou N *et al.*, *J. Electrochem. Soc.* **143**, 3099–3108 (1996).
85. Papageorgiou N, Maier W, Grätzel M, *J. Electrochem. Soc.* **144**, 876–884 (1997).
86. Redmond G, Fitzmaurice D, Grätzel M, *Chem. Mater.* **6**, 686–691 (1994).
87. Rensmo H *et al.*, *J. Phys. Chem. B* **101**, 2598–2601 (1997).
88. Rao T, Bahadur L, *J. Electrochem. Soc.* **144**, 179–185 (1997).
89. Keis K, Lindgren J, Lindquist S, Hagfeldt A, *Langmuir* **16**, 4688–4694 (2000).
90. Hara K *et al.*, *Chem. Lett.* 316–317 (2000).
91. Hara K *et al.*, *Sol. Energy Mater. Sol. Cells* **64**, 115–134 (2000).
92. Equchi K, Koga H, Sekizawa K, Sasaki K, *J. Ceram. Soc. Jpn.* **108**, 1067–1071 (2000).
93. Nasr S, Kamat P, Hotchandani S, *J. Phys. Chem. B* **102**, 10047–10056 (1998).
94. Burnside S *et al.*, *J. Phys. Chem. B* **103**, 9328–9332 (1999).
95. He J, Lindström H, Hagfeldt A, Lindquist S, *J. Phys. Chem. B* **103**, 8940–8943 (1999).

96. Tennakone K, Kumara G, Kottegoda I, Perera V, *Chem. Commun.* 15–16 (1999).
97. Tennakone K *et al.*, *Chem. Mater.* **11**, 2474–2477 (1999).
98. Kay A, Grätzel M, *Chem. Mater.* **14**, 2930–2935 (2002).
99. Zaban A, Chen S, Chappel S, Gregg B, *Chem. Commun.* 2231–2232 (2000).
100. Wang Z *et al.*, *Chem. Mater.* **13**, 678–682 (2001).
101. Heimer T, Bignozzi C, Meyer G, *J. Phys. Chem.* **97**, 11987–11994 (1993).
102. Argazzi R *et al.*, *Inorg. Chem.* **33**, 5741–5749 (1994).
103. Nazeeruddin M *et al.*, *J. Chem. Soc., Dalton Trans.* 4571–4578 (1997).
104. Shklover V *et al.*, *Chem. Mater.* **9**, 430–439 (1997).
105. Argazzi R, Bignozzi C, Hasselmann G, Meyer G, *Inorg. Chem.* **37**, 4533–4537 (1998).
106. Liska P *et al.*, *J. Am. Chem. Soc.* **110**, 3686–3687 (1998).
107. Shklover V *et al.*, *Chem. Mater.* **10**, 2533–2541 (1998).
108. Ruile S, Kohle O, Pettersson H, Grätzel M, *New J. Chem.* 25–31 (1998).
109. Zakeeruddin S, Nazeeruddin Md, Humphry-Baker R, Grätzel M, *Inorg. Chem.* **37**, 5251–5259 (1998).
110. Jing B *et al.*, *J. Mater. Chem.* **8**, 2055–2060 (1998).
111. Sugihara H *et al.*, *Chem. Lett.* 1005–1006 (1998).
112. Lees A *et al.*, *Eur. J. Inorg. Chem.* 2309–2317 (1999).
113. Thompson D, Kelly C, Farzad F, Meyer G, *Langmuir* **15**, 650–653 (1999).
114. Islam A *et al.*, *Chem. Lett.* 490–491 (2000).
115. Yanagida M *et al.*, *J. Chem. Soc., Dalton Trans.* 2817–2822 (2000).
116. Schwarz O *et al.*, *J. Photochem. Photobiol., A: Chem.* **132**, 91–98 (2000).
117. Hara K *et al.*, *Langmuir* **17**, 5992–5999 (2001).
118. Takahashi Y *et al.*, *Inorg. Chim. Acta* **310**, 169–174 (2000).
119. Aranyos V *et al.*, *Sol. Energy Mater. Sol. Cells* **64**, 97–114 (2000).
120. Renouard T *et al.*, *Inorg. Chem.* **41**, 367–378 (2002).
121. Yanagida M *et al.*, *New J. Chem.* **26**, 963–965 (2002).
122. Islam A *et al.*, *New J. Chem.* **26**, 966–968 (2002).
123. Ferrere S, Gregg B, *J. Am. Chem. Soc.* **120**, 843–844 (1998).
124. Yang M, Thompson D, Meyer G, *Inorg. Chem.* **39**, 3738–3739 (2000).
125. Alebbi M *et al.*, *J. Phys. Chem. B* **102**, 7577–7581 (1998).
126. Trammell S, Meyer T, *J. Phys. Chem. B* **103**, 104–107 (1999).
127. Sauvé G *et al.*, *J. Phys. Chem. B* **104**, 3488–3491 (2000).
128. Sauvé G *et al.*, *J. Phys. Chem. B* **104**, 6821–6836 (2000).
129. Hasselmann G, Meyer G, *Z. Phys. Chem.* **212**, 39–44 (1999).
130. Islam A *et al.*, *New J. Chem.* **24**, 343–345 (2000).
131. Kay A, Grätzel M, *J. Phys. Chem.* **97**, 6272–6277 (1993).
132. Kay A, Humphry-Baker R, Grätzel M, *J. Phys. Chem.* **98**, 952–959 (1994).
133. Boschloo G, Goossens A, *J. Phys. Chem.* **100**, 19489–19494 (1996).
134. Tennakone K *et al.*, *J. Photochem. Photobiol., A: Chem.* **108**, 175–177 (1997).
135. Nazeeruddin Md, Humphry-Baker R, Grätzel M, Murrer B, *Chem. Commun.* 719–720 (1998).
136. Ferrere S, Zaban A, Gregg B, *J. Phys. Chem.* **101**, 4490–4493 (1997).
137. Sayama K *et al.*, *Chem. Lett.* 753–754 (1998).
138. Khazraji A, Hotchandani S, Das S, Kamat P, *J. Phys. Chem. B* **103**, 4693–4700 (1999).
139. Wang Z, Li F, Huang C, *Chem. Commun.* 2063–2064 (2000).
140. Wang Z *et al.*, *J. Phys. Chem. B* **104**, 9676–9682 (2000).
141. Sayama K *et al.*, *Chem. Commun.* 1173–1174 (2000).
142. Sayama K *et al.*, *New J. Chem.* **25**, 200–202 (2001).
143. Hara K *et al.*, *Chem. Commun.* 569–570 (2001).
144. Gao F, Bard A, Kispert L, *J. Photochem. Photobiol., A: Chem.* **130**, 49–56 (2000).
145. Hara K *et al.*, *J. Phys. Chem. B* **107**, 597–606 (2003).
146. Tennakone K *et al.*, *J. Photochem. Photobiol., A: Chem.* **108**, 193–195 (1997).

147. Tennakone K *et al.*, *J. Photochem. Photobiol., A: Chem.* **117**, 137–142 (1998).
148. Matsumoto H *et al.*, *Chem. Lett.* 26–27 (2001).
149. Bach U *et al.*, *Nature* **395**, 583–585 (1998).
150. Bach U *et al.*, *J. Am. Chem. Soc.* **121**, 7445–7446 (1999).
151. Tennakone K *et al.*, *J. Phys. D: Appl. Phys.* **31**, 1492–1496 (1998).
152. Tennakone K, Perera U, Kottegoda I, Kumara G, *J. Phys. D: Appl. Phys.* **32**, 374–379 (1999).
153. O'Regan B, Schwartz D, *J. Appl. Phys.* **80**, 4749–4754 (1996).
154. Kumara G *et al.*, *Sol. Energy Mater. Sol. Cells* **69**, 195–199 (2001).
155. Murakoshi K, Kogure R, Wada Y, Yanagida S, *Sol. Energy Mater. Sol. Cells* **55**, 113–125 (1998).
156. Kubo W *et al.*, *Chem. Lett.* 1241–1242 (1998).
157. Mikoshiba S, Sumino H, Yonetsu M, Hayase S, *Proc. 16th European Photovoltaic Solar Energy Conference* (2000).
158. Mikoshiba S, Sumino H, Yonetsu M, Hayase S, Japan Patent, 2001-160427 (2001).
159. Kohle O, Grätzel M, Meyer A, Meyer T, *Adv. Mater.* **9**, 904–906 (1997).
160. Durham B, Casper J, Nagle J, Meyer T, *J. Am. Chem. Soc.* **104**, 4803–4810 (1982).
161. Amirnasr M, Nazeeruddin Md, Grätzel M, *Thermochim. Acta* **348**, 105–114 (2000).
162. Grünwald R, Tributsch H, *J. Phys. Chem. B* **101**, 2564–2575 (1997).
163. Kern R *et al.*, *Opto-Electron. Rev.* **8**, 284–288 (2000).
164. Olsen E, Hagen G, Lindquist S, *Sol. Energy Mater. Sol. Cells* **63**, 267–273 (2000).
165. Späth M *et al.*, *Proc. 14th European Photovoltaic Solar Energy Conference* (1997).
166. Rijnberg E *et al.*, *Proc. 2nd World Conference and Exhibition on Photovoltaic Solar Energy Conversion* (1998).
167. Hinsch A *et al.*, *Proc. 16th European Photovoltaic Solar Energy Conference* (2000).
168. Hanke K, *Z. Phys. Chem.* **212**, 1–9 (1999).
169. Pettersson H, Gruszecki T, *Sol. Energy Mater. Sol. Cells* **70**, 203–212 (2001).
170. Sommeling P, Späth M, van Roosmalen J, “Dye-Sensitized Nanocrystalline TiO₂ Solar Cells on Flexible Substrates”, *Proc. 2nd World Conference and Exhibition on Photovoltaic Solar Energy Conversion* (1998).
171. Sommeling P *et al.*, “Flexible Dye-Sensitized Nanocrystalline TiO₂ Solar Cells”, *Proc. 16th European Photovoltaic Solar Energy Conference* (2000).
172. Sommeling P, Späth M, Kroon J, van Roosmalen J, “Flexible Dye-Sensitized Nanocrystalline TiO₂ Solar Cells”, *Abstract 13th International Conference on Photochemical Conversion and Storage of Solar Energy* (2000).
173. Hagfeldt A, “Research and Development of Dye-Sensitized Solar Cells at the Angstrom Solar Center”, *Abstract 4th NIMC International Symposium on Photoreaction Control and Photo-functional Materials* (2001).
174. Lindström H *et al.*, *Nano Lett.* **1**, 97–100 (2001).
175. Smestad G, Grätzel M, *J. Chem. Educ.* **75**, 752–756 (1998).
176. <http://www.solideas.com/solrcell/cellkit.html>, Sol Ideas Technology Department, P.O. Box 51038, Pacific Grove, California 93950, USA. E-mail: info@solideas.com.
177. <http://www.nisinoda-electronics.co.jp/>, 7-1-3 Ebie, Fukushima, Osaka, Japan. FAX: +81-6-6451-7836.
178. <http://www.solaronix.ch/>, Solaronix SA, rue de l'Ouriette 129, 1170 Aubonne VD. FAX: +41-21-821-22-89.

16

Measurement and Characterization of Solar Cells and Modules

Keith Emery

National Renewable Energy Laboratory, Golden, CO, USA

16.1 INTRODUCTION

Methods of assessing the performance of photovoltaic cells and modules are described in this chapter. The performance of cells and modules can be described by their current versus voltage ($I-V$) and spectral responsivity versus wavelength ($S(\lambda)$) characteristics. Measurement equipment, procedures, and artifacts are discussed for $I-V$ and $S(\lambda)$. The most common performance indicator is the photovoltaic (PV) efficiency under standard reporting conditions (SRC) (temperature, spectral irradiance, total irradiance). The efficiency is the maximum electrical power divided by the total irradiance. Procedures for accurately determining the efficiency or the maximum power with respect to reference conditions are described. Alternatives to the standard peak watt rating and how they compare with actual field performance are discussed. Since photovoltaics must operate for 20 to 30 years, with a degradation of less than 1% per year, procedures for assessing the durability of PV modules are also discussed.

16.2 RATING PV PERFORMANCE

A variety of performance indicators have been employed by the photovoltaic community to rate the performance of PV cells and modules [1–4]. Domestic and international consensus standards have been adopted to rate the performance of PV cells and modules in terms of the output power, or equivalently their efficiency with respect to SRC defined by temperature, spectral irradiance, and total irradiance [5–15]. Modules and systems are rated by their peak power under SRC because manufacturers sell and customers purchase PV modules and systems according to the price per watt of power produced. Other performance indicators may be more appropriate for niche markets, such as aesthetics

for building-integrated photovoltaics, liters per day for water pumping, or low light-level operation for consumer electronics [4].

The actual output of a PV module or system in the field is a function of orientation, total irradiance, spectral irradiance, wind speed, air temperature, soiling, and various system-related losses. Various module- and system-rating methods attempt to ensure that the actual performance is comparable to the rated performance to keep the resulting level of customer satisfaction high.

16.2.1 Standard Reporting Conditions

The PV performance in terms of SRC is commonly expressed in terms of efficiency. At the research level, an internationally accepted set of SRC is essential to prevent the researcher from adjusting the reporting conditions to maximize the efficiency. The procedures for measuring the performance with respect to SRC must be quick, easy, reproducible, and accurate for the research cell fresh out of the deposition system or for the module on a factory floor with production goals. The PV conversion efficiency (η) is calculated from the measured maximum or peak PV power (P_{\max}), device area (A), and total incident irradiance (E_{tot}):

$$\eta = \frac{P_{\max}}{E_{\text{tot}}A} 100 \quad (16.1)$$

The term *reporting*, rather than *reference* or *test*, is used because a measurement can be performed at conditions other than SRC and then carefully corrected to be equivalent to being measured at SRC. The SRC for rating the performance of cells and modules are summarized in Table 16.1 [1, 5–15]. The direct, global, and AM0 reference spectra are summarized in Figure 16.1 and Tables 16.2 and 16.3.

As a matter of shorthand, the global and direct terrestrial reference spectra are often referred to as AM1.5 G and AM1.5 D, respectively. Many groups often just refer to the reference spectrum as AM1.5. This can be confusing without a reference because numerous different AM1.5 reference spectra have been proposed and used in the past. It should be noted that neither the direct reference spectrum nor the global reference spectrum actually integrates to exactly 1000 Wm^{-2} [10, 12, 13, 17]. The global reference spectrum integrates to approximately 963 Wm^{-2} and the direct reference spectrum

Table 16.1 Standard reference conditions for rating photovoltaic cells, modules and systems

Application	Irradiance [Wm^{-2}]	Reference Spectrum	Temperature [$^{\circ}\text{C}$]
Terrestrial			
Cells	1000	Global [5]	25 cell [5, 6, 11]
Modules, systems	1000	Global [11, 13]	25 cell [7] or NOCT [7]
Modules, systems	1000 ^a	Prevailing	20 ambient
Concentration ^b	>1000	Direct [10]	25 cell [5]
Extraterrestrial ^c	1366 [8], 1367 [14]	AM0 [8, 14, 15]	25 [15], 28 cell [16]

^aLinear regression of power to project test conditions, 850 Wm^{-2} with a 5° field of view for concentrator systems

^bAt present, no consensus standards exist although ASTM and the European Community are developing standards

^cAt present no consensus standards exist although there is an ISO draft standard [15]

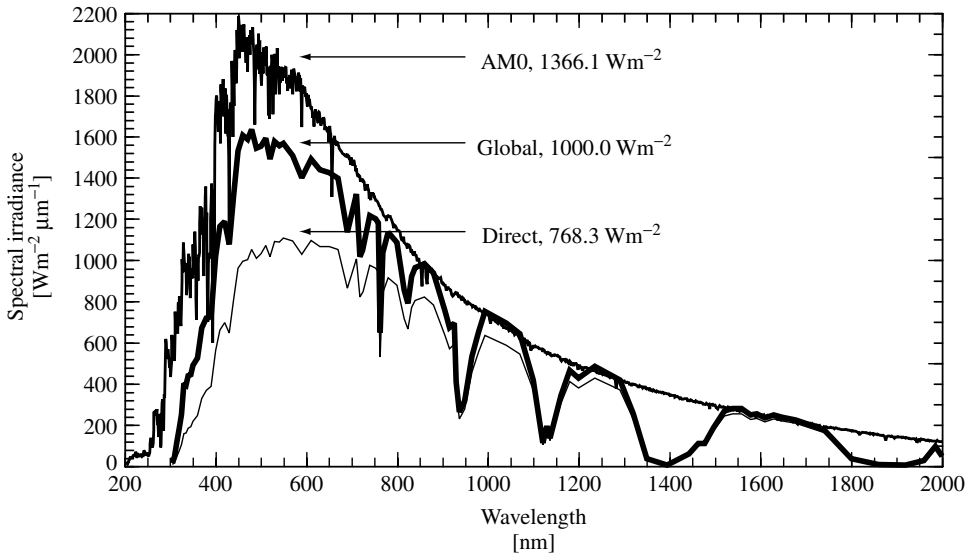


Figure 16.1 Global, Direct, and AM0 reference spectra listed in Tables 16.2 and 16.3. Adapted with permission from the Annual Book of ASTM Standards, Copyright ASTM [10, 12, 13]

integrates to approximately 768 Wm^{-2} . Different numerical integration methods give differences in the integrated or total irradiance of the reference spectra at the 0.1% level because of the relatively small number of data points (120) and the large variations in the spectral irradiance with wavelength. The structure in the spectral irradiance is a function of bandwidth. The bandwidth in the spectral irradiance at any given wavelength is approximately the difference in wavelength between adjacent points. The PV community has arbitrarily taken the term “one sun” to mean a total irradiance of 1000 Wm^{-2} [17]. In fact, the spectral irradiance of the global reference spectrum normalized to 1000 Wm^{-2} in Table 16.2 and Figure 16.1 exceeds the AM0 spectral irradiance in the infrared, which is not physically possible without concentration. The term *global* in Tables 16.1 and 16.2 refers to the spectral irradiance distribution on a 37° tilted south-facing surface with a solar zenith angle of 48.19° (AM1.5). The term *direct* in Tables 16.1 and 16.2 refers to the direct-normal component (5° field of view) of the global spectral irradiance distribution [18]. The term AM1 or AM1.5 is often used to refer to standard spectra, but the relative optical air mass (AM) is a geometrical quantity and can be obtained by taking the secant of the zenith angle (See Section 20.3 for a more complete explanation of AM.). For AM1, the zenith angle is 0° . The relative optical air mass can be pressure-corrected to an absolute air mass by multiplying by the barometric pressure and dividing by the sea level pressure. In outer space the pressure is zero so the absolute air mass is always zero. The internationally accepted global reference spectrum is based upon the 1962 US standard atmosphere with a rural aerosol distribution as input to a sophisticated Monte Carlo ray-tracing model for wavelengths up to 2500 nm and an undocumented simple direct-normal spectral model for the irradiances from 2500 nm to 4050 nm [12, 13, 18]. The fact that the reference spectrum only approximates the “real-world” spectra at solar noon is unimportant as long as the differences between the photocurrents are the same for various PV

Table 16.2 Standard direct and global reference spectra adapted with permission from the annual book of ASTM standards, Copyright ASTM [10, 11]. The global spectrum integrates to 1000.0 Wm^{-2} and the direct spectrum integrates to 768.3 Wm^{-2}

Wavelength [nm]	Global [Wm^{-2} μm^{-1}]	Direct [Wm^{-2} μm^{-1}]	Wavelength [nm]	Global [Wm^{-2} μm^{-1}]	Direct [Wm^{-2} μm^{-1}]	Wavelength [nm]	Global [Wm^{-2} μm^{-1}]	Direct [Wm^{-2} μm^{-1}]
305	9.5	3.4	740	1211.2	971.0	1520	262.6	239.3
310	42.3	15.6	753	1193.9	956.3	1539	274.2	248.8
315	107.8	41.1	758	1175.5	942.2	1558	275.0	249.3
320	181.0	71.2	763	643.1	524.8	1578	244.6	222.3
325	246.8	100.2	768	1030.7	830.7	1592	247.4	227.3
330	395.3	152.4	780	1131.1	908.9	1610	228.7	210.5
335	390.1	155.6	800	1081.6	873.4	1630	244.5	224.7
340	435.3	179.4	816	849.2	712.0	1646	234.8	215.9
345	438.9	186.7	824	785.0	660.2	1678	220.5	202.8
350	483.7	212.0	832	916.4	765.5	1740	171.5	158.2
360	520.3	240.5	840	959.9	799.8	1800	30.7	28.6
370	666.2	324.0	860	978.9	815.2	1860	2.0	1.8
380	712.5	362.4	880	933.2	778.3	1920	1.2	1.1
390	720.7	381.7	905	748.5	630.4	1960	21.2	19.7
400	1013.1	556.0	915	667.5	565.2	1985	91.1	84.9
410	1158.2	656.3	925	690.3	586.4	2005	26.8	25.0
420	1184.0	690.8	930	403.6	348.1	2035	99.5	92.5
430	1071.9	641.9	937	258.3	224.2	2065	60.4	56.3
440	1302.0	798.5	948	313.6	271.4	2100	89.1	82.7
450	1526.0	956.6	965	526.8	451.2	2148	82.2	76.2
460	1599.6	990.8	980	646.4	549.7	2198	71.5	66.4
470	1581.0	998.0	993	746.8	630.1	2270	70.2	65.0
480	1628.3	1046.1	1040	690.5	582.9	2360	62.0	57.6
490	1539.2	1005.1	1070	637.5	539.7	2450	21.2	19.8
500	1548.7	1026.7	1100	412.6	366.2	2494	18.5	17.0
510	1586.5	1066.7	1120	108.9	98.1	2537	3.2	3.0
520	1484.9	1011.5	1130	189.1	169.5	2941	4.4	4.0
530	1572.4	1084.9	1137	132.2	118.7	2973	7.6	7.0
540	1550.7	1082.4	1161	339.0	301.9	3005	6.5	6.0
550	1561.5	1102.2	1180	460.0	406.8	3056	3.2	3.0
570	1501.5	1087.4	1200	423.6	375.2	3132	5.4	5.0
590	1395.5	1024.3	1235	480.5	423.6	3156	19.4	18.0
610	1485.3	1088.8	1290	413.1	365.7	3204	1.3	1.2
630	1434.1	1062.1	1320	250.2	223.4	3245	3.2	3.0
650	1419.9	1061.7	1350	32.5	30.1	3317	13.1	12.0
670	1392.3	1046.2	1395	1.6	1.4	3344	3.2	3.0
690	1130.0	859.2	1443	55.7	51.6	3450	13.3	12.2
710	1316.7	1002.4	1463	105.1	97.0	3573	11.9	11.0
718	1010.3	816.9	1477	105.5	97.3	3765	9.8	9.0
724	1043.2	842.8	1497	182.1	167.1	4045	7.5	6.9

Table 16.3 AM0 standard solar spectrum adapted with permission from the annual book of ASTM standards, Copyright ASTM [8]

λ [nm]	$E(\lambda)$ [Wm ⁻² μm^{-1}]																
119.5	6.30E-2	320.5	820.6	521.5	1939	719.8	1388.0	1088	577.8	1490	296.2	1892	137.0	2294	67.99	4460	5.799
120.5	5.72E-1	321.5	713	522.5	1855	720.7	1385.0	1090	599.3	1492	294.1	1894	135.3	2296	68.52	4480	5.694
121.5	5.00E+0	322.5	701.8	523.5	1927	721.7	1386.0	1092	592.8	1494	296.2	1896	132.5	2298	68.39	4500	5.591
122.5	1.21E+0	323.5	674	524.5	1992	722.7	1383.0	1094	555.9	1496	287.2	1898	137.1	2300	68.75	4520	5.491
123.5	4.86E-2	324.5	775.4	525.5	1963	723.6	1389.0	1096	570.7	1498	291.2	1900	136.0	2302	68.89	4540	5.392
124.5	3.50E-2	325.5	892.6	526.5	1702	724.6	1384.0	1098	569.5	1500	290.7	1902	138.9	2304	68.78	4560	5.296
125.5	2.94E-2	326.5	998.3	527.5	1860	725.5	1372.0	1100	583.2	1502	278.9	1904	135.9	2306	68.64	4580	5.202
126.5	3.59E-2	327.5	971	528.5	1930	726.5	1375.0	1102	570.4	1504	274.6	1906	136.5	2308	68.48	4600	5.110
127.5	2.17E-2	328.5	935.2	529.5	1951	727.4	1374.0	1104	576.9	1506	271.9	1908	135.3	2310	68.08	4620	5.020
128.5	1.76E-2	329.5	1081	530.5	1986	728.4	1347.0	1106	576.0	1508	281.1	1910	136.2	2312	68.00	4640	4.932
129.5	4.07E-2	330.5	1036	531.5	1997	729.3	1332.0	1108	573.2	1510	288.8	1912	133.0	2314	67.98	4660	4.846
130.5	1.23E-1	331.5	984.2	532.5	1801	730.3	1364.0	1110	573.0	1512	283.3	1914	135.5	2316	67.05	4680	4.762
131.5	4.06E-2	332.5	973.2	533.5	1956	731.2	1358.0	1112	564.6	1514	281.1	1916	134.2	2318	66.42	4700	4.680
132.5	4.21E-2	333.5	939.3	534.5	1890	732.2	1360.0	1114	565.3	1516	282.5	1918	133.5	2320	67.15	4720	4.599
133.5	1.71E-1	334.5	977.3	535.5	2024	733.1	1351.0	1116	565.9	1518	283.3	1920	131.1	2322	65.70	4740	4.520
134.5	4.66E-2	335.5	961.4	536.5	1903	734.0	1364.0	1118	563.6	1520	282.2	1922	133.5	2324	64.33	4760	4.443
135.5	3.88E-2	336.5	825	537.5	1914	735.0	1348.0	1120	552.0	1522	274.6	1924	131.4	2326	64.30	4780	4.367
136.5	3.15E-2	337.5	858	538.5	1937	735.9	1335.0	1122	561.0	1524	276.6	1926	132.3	2328	65.51	4800	4.293
137.5	2.98E-2	338.5	939.2	539.5	1864	736.9	1337.0	1124	557.6	1526	280.5	1928	128.8	2330	65.65	4820	4.221
138.5	4.04E-2	339.5	976.5	540.5	1800	737.8	1333.0	1126	543.3	1528	281.0	1930	128.5	2332	64.89	4840	4.150
139.5	7.71E-2	340.5	1026	541.5	1913	738.8	1292.0	1128	550.8	1530	269.3	1932	126.8	2334	65.23	4860	4.080
140.5	6.19E-2	341.5	941.5	542.5	1857	739.7	1309.0	1130	542.6	1532	278.0	1934	128.8	2336	64.33	4880	4.012
141.5	4.29E-2	342.5	1012	543.5	1911	740.7	1295.0	1132	545.9	1534	272.8	1936	128.5	2338	64.06	4900	3.946
142.5	4.77E-2	343.5	968.8	544.5	1911	741.6	1286.0	1134	542.1	1536	276.5	1938	128.9	2340	64.87	4920	3.881
143.5	5.21E-2	344.5	810.9	545.5	1934	742.6	1307.0	1136	546.0	1538	273.3	1940	124.5	2342	64.77	4940	3.817

(continued overleaf)

Table 16.3 (continued)

λ [nm]	$E(\lambda)$ [Wm ⁻² μm^{-1}]																
144.5	5.19E-2	345.5	957.2	546.5	1911	743.5	1324.0	1138	534.1	1540	267.8	1942	126.0	2344	64.61	4960	3.754
145.5	5.64E-2	346.5	944.1	547.5	1865	744.4	1309.0	1140	529.4	1542	270.3	1944	115.2	2346	64.23	4980	3.693
146.5	7.22E-2	347.5	919	548.5	1895	745.4	1324.0	1142	531.8	1544	274.2	1946	113.6	2348	64.24	5000	3.633
147.5	8.65E-2	348.5	914.4	549.5	1928	746.3	1316.0	1144	531.1	1546	273.6	1948	123.7	2350	64.13	5050	3.519
148.5	8.36E-2	349.5	906.9	550.5	1894	747.3	1322.0	1146	538.2	1548	266.0	1950	123.5	2352	61.50	5100	3.387
149.5	8.11E-2	350.5	1070	551.5	1903	748.2	1320.0	1148	533.9	1550	265.4	1952	119.8	2354	61.29	5150	3.261
150.5	8.86E-2	351.5	998.3	552.5	1878	749.2	1297.0	1150	532.2	1552	268.9	1954	125.8	2356	62.34	5200	3.142
151.5	9.44E-2	352.5	925.3	553.5	1914	750.1	1299.0	1152	529.2	1554	260.5	1956	125.0	2358	61.44	5250	3.028
152.5	1.19E-1	353.5	1052	554.5	1931	752.0	1285.0	1154	531.3	1556	262.7	1958	124.7	2360	62.23	5300	2.919
153.5	1.32E-1	354.5	1132	555.5	1930	754.0	1285.0	1156	526.4	1558	263.7	1960	123.7	2362	62.47	5350	2.814
154.5	2.10E-1	355.5	1065	556.5	1853	756.0	1280.0	1158	525.4	1560	262.8	1962	122.6	2364	62.16	5400	2.715
155.5	2.19E-1	356.5	929.8	557.5	1878	758.0	1271.0	1160	513.6	1562	264.5	1964	118.8	2366	62.07	5450	2.620
156.5	1.88E-1	357.5	811.3	558.5	1818	760.0	1257.0	1162	506.8	1564	261.4	1966	120.7	2368	61.96	5500	2.529
157.5	1.75E-1	358.5	706.9	559.5	1839	762.0	1260.0	1164	512.0	1566	257.5	1968	122.9	2370	61.18	5550	2.442
158.5	1.71E-1	359.5	1010	560.5	1875	764.0	1243.0	1166	511.9	1568	256.2	1970	121.7	2372	61.47	5600	2.358
159.5	1.79E-1	360.5	989.4	561.5	1856	766.0	1239.0	1168	513.9	1570	257.5	1972	117.9	2374	59.19	5650	2.279
160.5	1.97E-1	361.5	895	562.5	1882	768.0	1224.0	1170	505.4	1572	258.9	1974	119.8	2376	61.03	5700	2.202
161.5	2.27E-1	362.5	1017	563.5	1893	770.0	1215.0	1172	512.5	1574	253.4	1976	120.6	2378	61.37	5750	2.129
162.5	2.57E-1	363.5	1016	564.5	1886	772.0	1206.0	1174	511.8	1576	244.7	1978	116.9	2380	61.05	5800	2.059
163.5	2.90E-1	364.5	1033	565.5	1829	774.0	1205.0	1176	497.6	1578	241.6	1980	117.9	2382	60.29	5850	1.992
164.5	3.03E-1	365.5	1174	566.5	1861	776.0	1186.0	1178	494.6	1580	256.2	1982	118.0	2384	57.17	5900	1.927
165.5	4.39E-1	366.5	1256	567.5	1920	778.0	1207.0	1180	506.7	1582	246.8	1984	117.9	2386	57.25	5950	1.865
166.5	4.07E-1	367.5	1203	568.5	1841	780.0	1212.0	1182	499.5	1584	250.2	1986	114.4	2388	59.29	6000	1.806
167.5	3.95E-1	368.5	1122	569.5	1892	782.0	1206.0	1184	482.7	1586	251.0	1988	118.6	2390	59.41	6050	1.749
168.5	4.64E-1	369.5	1249	570.5	1800	784.0	1207.0	1186	497.8	1588	240.0	1990	118.2	2392	59.09	6100	1.694
169.5	5.99E-1	370.5	1161	571.5	1855	786.0	1202.0	1188	481.0	1590	228.5	1992	116.4	2394	59.10	6150	1.641
170.5	6.74E-1	371.5	1197	572.5	1925	788.0	1191.0	1190	490.3	1592	243.6	1994	114.1	2396	58.90	6200	1.591

171.5	7.01E - 1	372.5	1074	573.5	1908	790.0	1174.0	1192	494.5	1594	251.3	1996	115.7	2398	59.22	6250	1.542
172.5	7.39E - 1	373.5	937.8	574.5	1899	792.0	1149.0	1194	493.7	1596	241.0	1998	114.5	2400	58.33	6300	1.495
173.5	7.79E - 1	374.5	917.6	575.5	1862	794.0	1166.0	1196	486.2	1598	250.9	2000	115.9	2402	58.82	6350	1.450
174.5	9.24E - 1	375.5	1082	576.5	1878	796.0	1161.0	1198	464.1	1600	243.5	2002	114.6	2404	58.60	6400	1.407
175.5	1.10E + 0	376.5	1106	577.5	1889	798.0	1152.0	1200	476.9	1602	243.9	2004	113.7	2406	58.32	6450	1.365
176.5	1.24E + 0	377.5	1306	578.5	1814	800.0	1143.0	1202	486.2	1604	243.5	2006	113.4	2408	58.21	6500	1.325
177.5	1.43E + 0	378.5	1353	579.5	1860	802.0	1139.0	1204	466.6	1606	242.1	2008	114.5	2410	58.13	6550	1.286
178.5	1.57E + 0	379.5	1087	580.5	1870	804.0	1137.0	1206	480.8	1608	244.3	2010	113.9	2412	58.09	6600	1.249
179.5	1.61E + 0	380.5	1225	581.5	1885	806.0	1130.0	1208	458.7	1610	232.5	2012	113.4	2414	55.61	6650	1.213
180.5	1.87E + 0	381.5	1103	582.5	1905	808.0	1110.0	1210	468.9	1612	237.9	2014	112.5	2416	54.02	6700	1.178
181.5	2.28E + 0	382.5	806.5	583.5	1889	810.0	1095.0	1212	474.0	1614	240.5	2016	112.7	2418	56.76	6750	1.145
182.5	2.29E + 0	383.5	697.2	584.5	1892	812.0	1091.0	1214	474.8	1616	228.9	2018	112.3	2420	56.40	6800	1.112
183.5	2.29E + 0	384.5	978.1	585.5	1814	814.0	1110.0	1216	474.7	1618	240.2	2020	110.7	2422	56.59	6850	1.081
184.5	2.11E + 0	385.5	1028	586.5	1862	816.0	1080.0	1218	471.7	1620	230.9	2022	108.6	2424	56.16	6900	1.051
185.5	2.36E + 0	386.5	1026	587.5	1880	818.0	1076.0	1220	469.4	1622	235.6	2024	110.3	2426	56.11	6950	1.022
186.5	2.75E + 0	387.5	1023	588.5	1780	820.0	1069.0	1222	468.0	1624	238.6	2026	110.3	2428	56.05	7000	0.994
187.5	3.07E + 0	388.5	1003	589.5	1640	822.0	1053.0	1224	465.6	1626	237.7	2028	109.4	2430	56.28	7050	0.967
188.5	3.35E + 0	389.5	1196	590.5	1844	824.0	1072.0	1226	464.8	1628	239.7	2030	106.8	2432	55.96	7100	0.941
189.5	3.64E + 0	390.5	1271	591.5	1818	826.0	1068.0	1228	457.4	1630	235.9	2032	109.4	2434	55.49	7150	0.916
190.5	3.84E + 0	391.5	1367	592.5	1839	828.0	1060.0	1230	461.5	1632	234.7	2034	107.7	2436	54.93	7200	0.892
191.5	4.25E + 0	392.5	1039	593.5	1827	830.0	1033.0	1232	457.9	1634	231.9	2036	107.6	2438	54.89	7250	0.868
192.5	4.19E + 0	393.5	593.4	594.5	1804	832.0	1047.0	1234	457.2	1636	229.0	2038	104.7	2440	55.47	7300	0.845
193.5	3.88E + 0	394.5	1046	595.5	1813	834.0	1028.0	1236	456.4	1638	222.4	2040	107.7	2442	55.25	7350	0.823
194.5	5.31E + 0	395.5	1339	596.5	1836	836.0	1019.0	1238	456.5	1640	221.6	2042	106.9	2444	55.10	7400	0.802
195.5	5.53E + 0	396.5	870.9	597.5	1811	838.0	1038.0	1240	449.7	1642	221.1	2044	107.2	2446	53.86	7450	0.781
196.5	6.12E + 0	397.5	946.6	598.5	1788	840.0	1017.0	1242	448.5	1644	220.7	2046	106.9	2448	53.35	7500	0.761
197.5	6.31E + 0	398.5	1552	599.5	1805	842.0	1020.0	1244	446.4	1646	226.6	2048	105.9	2450	53.20	7550	0.742
198.5	6.31E + 0	399.5	1695	600.1	1786	844.0	990.7	1246	447.5	1648	226.9	2050	105.8	2452	53.13	7600	0.723
199.5	6.79E + 0	400.5	1714	601.1	1762	846.0	1001.0	1248	446.6	1650	222.3	2052	104.3	2454	53.73	7650	0.705

(continued overleaf)

Table 16.3 (continued)

λ [nm]	$E(\lambda)$ [Wm ⁻² μm^{-1}]																
200.5	7.47E + 0	401.5	1780	602.1	1740	848.0	1003.0	1250	446.5	1652	222.8	2054	104.7	2456	52.76	7700	0.688
201.5	8.18E + 0	402.5	1793	603.1	1784	850.0	967.0	1252	439.6	1654	224.8	2056	104.7	2458	52.11	7750	0.671
202.5	8.42E + 0	403.5	1716	604.1	1797	852.0	957.1	1254	441.3	1656	224.5	2058	104.0	2460	53.62	7800	0.654
203.5	9.39E + 0	404.5	1706	605.1	1791	854.0	867.9	1256	438.4	1658	224.3	2060	102.0	2462	53.43	7850	0.638
204.5	10.450	405.5	1699	606.1	1772	856.0	939.2	1258	436.8	1660	221.9	2062	103.9	2464	53.40	7900	0.623
205.5	10.740	406.5	1619	607.1	1776	858.0	984.8	1260	436.9	1662	222.6	2064	99.7	2466	53.12	7950	0.608
206.5	11.290	407.5	1659	608.0	1751	860.0	959.0	1262	433.6	1664	221.1	2066	103.1	2468	53.06	8000	0.593
207.5	12.900	408.5	1768	609.0	1740	862.0	975.9	1264	432.2	1666	217.7	2068	102.3	2470	51.39	8050	0.579
208.5	15.340	409.5	1747	610.0	1728	864.0	912.5	1266	430.7	1668	214.5	2070	100.3	2472	52.84	8100	0.565
209.5	21.790	410.5	1561	611.0	1740	866.0	878.8	1268	424.0	1670	219.8	2072	101.2	2474	51.77	8150	0.552
210.5	28.450	411.5	1849	612.0	1730	868.0	953.1	1270	430.4	1672	210.8	2074	101.7	2476	52.51	8200	0.539
211.5	34.180	412.5	1820	613.0	1720	870.0	951.1	1272	428.7	1674	215.6	2076	101.3	2478	52.12	8250	0.527
212.5	31.900	413.5	1786	614.0	1685	872.0	944.2	1274	424.5	1676	208.5	2078	101.0	2480	49.95	8300	0.514
213.5	33.790	414.5	1766	615.0	1712	874.0	947.1	1276	426.0	1678	211.7	2080	98.7	2482	49.96	8350	0.503
214.5	40.800	415.5	1763	616.0	1661	876.0	949.1	1278	423.6	1680	202.0	2082	99.9	2484	51.60	8400	0.491
215.5	36.840	416.5	1874	616.9	1644	878.0	925.3	1280	416.7	1682	198.6	2084	98.0	2486	49.72	8450	0.480
216.5	32.890	417.5	1693	617.9	1700	880.0	926.3	1282	373.2	1684	207.8	2086	99.5	2488	51.24	8500	0.469
217.5	35.960	418.5	1713	618.9	1699	882.0	914.5	1284	408.6	1686	208.6	2088	99.1	2490	51.23	8550	0.459
218.5	45.220	419.5	1730	619.9	1715	884.0	928.3	1286	413.1	1688	208.3	2090	98.9	2492	51.06	8600	0.448
219.5	47.820	420.5	1788	620.9	1727	886.0	913.5	1288	413.7	1690	206.4	2092	95.6	2494	50.48	8650	0.438
220.5	48.240	421.5	1828	621.9	1698	888.0	915.4	1290	409.5	1692	209.8	2094	96.5	2496	50.64	8700	0.429
221.5	40.330	422.5	1609	622.9	1697	890.0	911.5	1292	412.3	1694	208.4	2096	96.1	2498	50.45	8750	0.419
222.5	50.600	423.5	1740	624.8	1664	892.0	902.6	1294	409.3	1696	207.7	2098	96.8	2500	50.61	8800	0.410
223.5	64.220	424.5	1798	625.8	1662	894.0	905.5	1296	411.4	1698	206.8	2100	96.7	2520	49.22	8850	0.401
224.5	60.100	425.5	1724	626.8	1709	896.0	910.5	1298	406.5	1700	203.4	2102	96.3	2540	47.82	8900	0.393
225.5	53.290	426.5	1727	627.8	1715	898.0	885.7	1300	408.3	1702	201.8	2104	96.4	2560	46.46	8950	0.384
226.5	40.160	427.5	1596	628.8	1712	900.0	880.8	1302	403.2	1704	202.1	2106	96.4	2580	45.15	9000	0.376
227.5	40.690	428.5	1614	629.8	1685	902.0	882.7	1304	400.4	1706	202.4	2108	95.9	2600	43.89	9050	0.368

228.5	52.940	429.5	1501	630.7	1682	904.0	872.8	1306	403.4	1708	199.0	2110	94.0	2620	42.68	9100	0.360
229.5	48.620	430.5	1155	631.7	1649	906.0	872.8	1308	401.6	1710	200.3	2112	95.1	2640	41.50	9150	0.353
230.5	53.120	431.5	1715	632.7	1684	908.0	846.1	1310	399.9	1712	192.3	2114	94.7	2660	40.37	9200	0.345
231.5	51.950	432.5	1674	633.7	1662	910.0	857.0	1312	390.1	1714	201.0	2116	92.9	2680	39.28	9250	0.338
232.5	54.280	433.5	1760	634.7	1673	912.0	864.9	1314	397.3	1716	198.7	2118	93.9	2700	38.22	9300	0.331
233.5	45.600	434.5	1698	635.7	1668	914.0	857.0	1316	384.9	1718	198.0	2120	92.8	2720	37.20	9350	0.324
234.5	39.710	435.5	1752	636.6	1663	916.0	852.0	1318	393.1	1720	195.0	2122	93.0	2740	36.21	9400	0.318
235.5	52.400	436.5	1962	637.6	1688	918.0	853.0	1320	394.2	1722	194.8	2124	91.5	2760	35.26	9450	0.311
236.5	49.520	437.5	1837	638.6	1682	920.0	827.3	1322	391.2	1724	188.4	2126	92.0	2780	34.34	9500	0.305
237.5	49.370	438.5	1594	639.6	1645	922.0	820.3	1324	391.6	1726	192.4	2128	92.6	2800	33.45	9550	0.299
238.5	42.770	439.5	1857	640.6	1633	924.0	826.3	1326	388.0	1728	191.5	2130	92.0	2820	32.59	9600	0.293
239.5	44.970	440.5	1742	641.5	1626	926.0	831.2	1328	386.8	1730	192.5	2132	92.1	2840	31.75	9650	0.287
240.5	40.310	441.5	1964	642.5	1642	928.0	837.2	1330	379.1	1732	188.7	2134	91.7	2860	30.95	9700	0.281
241.5	52.460	442.5	2014	643.5	1635	930.0	832.2	1332	379.5	1734	179.2	2136	89.6	2880	30.17	9750	0.276
242.5	71.960	443.5	1942	644.5	1637	932.0	840.1	1334	385.9	1736	174.6	2138	91.2	2900	29.41	9800	0.270
243.5	67.810	444.5	2007	645.5	1621	934.0	827.3	1336	382.9	1738	180.7	2140	90.6	2920	28.68	9850	0.265
244.5	62.140	445.5	1853	646.4	1622	936.0	812.4	1338	380.5	1740	185.6	2142	90.5	2940	27.97	9900	0.260
245.5	50.340	446.5	1924	647.4	1633	938.0	820.3	1340	375.4	1742	183.9	2144	89.8	2960	27.28	9950	0.255
246.5	51.370	447.5	2112	648.4	1634	940.0	813.4	1342	378.5	1744	186.9	2146	89.0	2980	26.62	10000	0.250
247.5	56.570	448.5	2007	649.4	1570	942.0	798.5	1344	378.5	1746	183.0	2148	89.6	3000	25.97	11000	0.170
248.5	46.530	449.5	2062	650.3	1630	944.0	814.4	1346	375.7	1748	182.2	2150	89.2	3020	25.35	12000	0.119
249.5	57.460	450.5	2180	651.3	1645	946.0	809.4	1348	376.4	1750	182.7	2152	88.5	3040	24.74	13000	8.65E - 2
250.5	61.250	451.5	2145	652.3	1618	948.0	793.6	1350	370.2	1752	181.7	2154	88.3	3060	24.15	14000	6.42E - 2
251.5	46.890	452.5	1974	653.3	1605	950.0	795.6	1352	373.4	1754	183.7	2156	88.1	3080	23.58	15000	4.86E - 2
252.5	42.340	453.5	2004	654.3	1589	952.0	788.6	1354	371.8	1756	182.8	2158	87.8	3100	23.03	16000	3.75E - 2
253.5	52.540	454.5	2013	655.2	1537	954.0	777.7	1356	361.6	1758	182.4	2160	87.0	3120	22.49	17000	2.93E - 2
254.5	60.710	455.5	2069	656.2	1303	956.0	791.6	1358	368.6	1760	181.8	2162	86.0	3140	21.97	18000	2.33E - 2
255.5	80.820	456.5	2112	657.2	1456	958.0	788.6	1360	363.4	1762	176.6	2164	84.2	3160	21.47	19000	1.87E - 2
256.5	103.800	457.5	2136	658.2	1567	960.0	784.7	1362	365.9	1764	179.4	2166	75.6	3180	20.98	20000	1.52E - 2
257.5	127.800	458.5	2005	659.1	1563	962.0	779.3	1364	361.3	1766	180.5	2168	82.6	3200	20.50	25000	6.28E - 3
258.5	127.500	459.5	2043	660.1	1580	964.0	777.2	1366	364.0	1768	178.5	2170	84.7	3220	20.04	30000	3.04E - 3

(continued overleaf)

Table 16.3 (continued)

λ [nm]	$E(\lambda)$ [Wm ⁻² μm ⁻¹]																
259.5	106.000	460.5	2075	661.1	1585	966.0	767.2	1368	358.4	1770	177.1	2172	85.0	3240	19.59	35 000	1.64E - 3
260.5	87.150	461.5	2090	662.0	1597	968.0	771.7	1370	356.4	1772	177.8	2174	85.1	3260	19.15	40 000	9.65E - 4
261.5	91.520	462.5	2140	663.0	1569	970.0	767.5	1372	359.3	1774	177.7	2176	84.1	3280	18.72	50 000	3.97E - 4
262.5	105.600	463.5	2075	664.0	1558	972.0	771.9	1374	357.4	1776	174.3	2178	82.7	3300	18.31	60 000	1.92E - 4
263.5	168.900	464.5	2010	665.0	1575	974.0	754.1	1376	352.6	1778	173.0	2180	84.8	3320	17.91	80 000	6.10E - 5
264.5	254.500	465.5	2077	665.9	1567	976.0	760.4	1378	356.3	1780	173.3	2182	82.9	3340	17.52	1 00 000	2.51E - 5
265.5	257.500	466.5	1954	666.9	1555	978.0	756.1	1380	355.6	1782	172.7	2184	84.1	3360	17.14	1 20 000	1.21E - 5
266.5	254.200	467.5	2049	667.9	1554	980.0	752.4	1382	351.4	1784	172.5	2186	84.0	3380	16.77	1 50 000	4.98E - 6
267.5	255.600	468.5	2028	668.8	1569	982.0	755.1	1384	353.8	1786	171.5	2188	81.2	3400	16.41	2 00 000	1.58E - 6
268.5	248.500	469.5	2024	669.8	1554	984.0	749.2	1386	349.4	1788	173.4	2190	82.7	3420	16.06	2 50 000	6.51E - 7
269.5	243.500	470.5	1909	670.8	1551	986.0	745.6	1388	351.5	1790	171.7	2192	83.2	3440	15.72	3 00 000	3.06E - 7
270.5	272.400	471.5	2052	671.8	1541	988.0	742.9	1390	348.1	1792	170.4	2194	82.8	3460	15.39	4 00 000	1.05E - 7
271.5	228.700	472.5	2076	672.7	1537	990.0	732.0	1392	349.3	1794	168.9	2196	82.5	3480	15.07	10 00 000	3.51E - 9
272.5	201.200	473.5	2025	673.7	1533	992.0	738.7	1394	347.0	1796	168.8	2198	82.5	3500	14.76	10 00 000	3.51E - 9
273.5	200.200	474.5	2086	674.7	1530	994.0	737.6	1396	345.3	1798	168.5	2200	82.1	3520	14.45	-	-
274.5	135.200	475.5	2050	675.6	1527	996.0	733.6	1398	346.8	1800	167.6	2202	81.6	3540	14.16	-	-
275.5	178.500	476.5	1990	676.6	1523	998.0	731.4	1400	339.2	1802	164.5	2204	81.7	3560	13.87	-	-
276.5	247.500	477.5	2110	677.6	1520	1000.0	728.0	1402	340.3	1804	166.6	2206	77.4	3580	13.58	-	-
277.5	238.200	478.5	2043	678.5	1518	1002.0	725.8	1404	338.1	1806	165.5	2208	79.3	3600	13.31	-	-
278.5	162.300	479.5	2111	679.5	1515	1004.0	709.7	1406	337.9	1808	165.3	2210	80.6	3620	13.04	-	-
279.5	87.190	480.5	2070	680.5	1513	1006.0	685.9	1408	338.5	1810	164.9	2212	80.5	3640	12.78	-	-
280.5	96.450	481.5	2126	681.4	1510	1008.0	714.5	1410	338.2	1812	163.1	2214	80.2	3660	12.53	-	-
281.5	212.300	482.5	2058	682.4	1508	1010.0	713.4	1412	329.6	1814	161.3	2216	79.2	3680	12.28	-	-
282.5	299.800	483.5	2053	683.4	1506	1012.0	709.5	1414	330.7	1816	156.9	2218	79.2	3700	12.04	-	-
283.5	319.500	484.5	2003	684.3	1504	1014.0	702.9	1416	333.3	1818	145.6	2220	79.5	3720	11.80	-	-
284.5	239.800	485.5	1862	685.3	1503	1016.0	697.1	1418	332.9	1820	155.8	2222	79.1	3740	11.57	-	-
285.5	166.300	486.5	1653	686.3	1501	1018.0	694.6	1420	329.7	1822	154.6	2224	78.8	3760	11.35	-	-
286.5	328.900	487.5	1862	687.2	1500	1020.0	691.0	1422	321.9	1824	159.4	2226	77.1	3780	11.13	-	-
287.5	342.800	488.5	1947	688.2	1499	1022.0	687.5	1424	325.9	1826	159.3	2228	78.0	3800	10.92	-	-

288.5	328.400	489.5	1994	689.1	1506	1024.0	694.0	1426	320.2	1828	157.1	2230	77.9	3820	10.71	–	–
289.5	481.800	490.5	2041	690.1	1512	1026.0	691.4	1428	319.5	1830	158.5	2232	77.9	3840	10.50	–	–
290.5	612.800	491.5	1929	691.1	1506	1028.0	690.5	1430	321.0	1832	157.0	2234	77.8	3860	10.31	–	–
291.5	592.000	492.5	1929	692.0	1495	1030.0	680.2	1432	322.4	1834	156.1	2236	77.3	3880	10.11	–	–
292.5	531.900	493.5	1921	693.0	1495	1032.0	682.3	1434	321.5	1836	156.1	2238	75.7	3900	9.92	–	–
293.5	545.800	494.5	2093	694.0	1498	1034.0	664.4	1436	322.5	1838	154.0	2240	76.2	3920	9.74	–	–
294.5	518.500	495.5	1959	694.9	1480	1036.0	675.4	1438	323.1	1840	154.3	2242	76.1	3940	9.56	–	–
295.5	563.800	496.5	2051	695.9	1489	1038.0	665.5	1440	308.8	1842	151.3	2244	76.2	3960	9.38	–	–
296.5	519.400	497.5	2052	696.8	1489	1040.0	664.4	1442	314.5	1844	152.5	2246	76.1	3980	9.21	–	–
297.5	517.000	498.5	1898	697.8	1457	1042.0	664.3	1444	311.6	1846	153.5	2248	74.7	4000	9.04	–	–
298.5	474.400	499.5	2004	698.8	1494	1044.0	666.3	1446	317.4	1848	147.2	2250	75.5	4020	8.87	–	–
299.5	493.300	500.5	1889	699.7	1486	1046.0	651.0	1448	314.7	1850	153.0	2252	75.0	4040	8.69	–	–
300.5	428.000	501.5	1843	700.7	1462	1048.0	655.3	1450	312.2	1852	151.8	2254	73.7	4060	8.52	–	–
301.5	464.300	502.5	1927	701.6	1455	1050.0	656.5	1452	308.0	1854	150.5	2256	74.2	4080	8.35	–	–
302.5	498.300	503.5	1967	702.6	1462	1052.0	653.4	1454	307.9	1856	148.0	2258	74.5	4100	8.18	–	–
303.5	632.500	504.5	1901	703.6	1468	1054.0	647.3	1456	306.6	1858	149.8	2260	74.3	4120	8.02	–	–
304.5	614.000	505.5	2027	704.5	1482	1056.0	650.1	1458	311.8	1860	147.2	2262	72.6	4140	7.87	–	–
305.5	606.200	506.5	1995	705.5	1472	1058.0	633.3	1460	309.6	1862	146.0	2264	73.5	4160	7.71	–	–
306.5	566.400	507.5	1939	706.4	1452	1060.0	634.8	1462	306.0	1864	146.6	2266	72.9	4180	7.56	–	–
307.5	626.800	508.5	1952	707.4	1455	1062.0	640.7	1464	305.5	1866	144.1	2268	73.2	4200	7.42	–	–
308.5	623.200	509.5	1949	708.3	1442	1064.0	633.8	1466	303.7	1868	144.1	2270	73.1	4220	7.27	–	–
309.5	506.000	510.5	1980	709.3	1426	1066.0	627.2	1468	304.5	1870	145.4	2272	72.6	4240	7.13	–	–
310.5	634.300	511.5	2031	710.3	1440	1068.0	621.4	1470	302.3	1872	140.7	2274	72.1	4260	7.00	–	–
311.5	743.200	512.5	1899	711.2	1416	1070.0	611.3	1472	300.6	1874	136.6	2276	72.5	4280	6.86	–	–
312.5	668.500	513.5	1893	712.2	1408	1072.0	620.4	1474	295.8	1876	119.0	2278	72.3	4300	6.74	–	–
313.5	713.300	514.5	1906	713.1	1408	1074.0	611.3	1476	296.4	1878	139.0	2280	71.9	4320	6.61	–	–
314.5	675.600	515.5	1933	714.1	1413	1076.0	610.6	1478	294.1	1880	140.3	2282	68.8	4340	6.48	–	–
315.5	645.100	516.5	1697	715.0	1398	1078.0	606.6	1480	300.0	1882	142.1	2284	71.1	4360	6.36	–	–
316.5	645.300	517.5	1755	716.0	1403	1080.0	616.9	1482	297.5	1884	141.3	2286	70.8	4380	6.25	–	–
317.5	788.800	518.5	1682	716.9	1407	1082.0	588.3	1484	293.2	1886	138.5	2288	71.0	4400	6.13	–	–
318.5	677.600	519.5	1860	717.9	1400	1084.0	596.4	1486	296.0	1888	141.4	2290	70.8	4420	6.02	–	–
319.5	724.100	520.5	1863	718.8	1376	1086.0	607.3	1488	273.1	1890	137.6	2292	70.5	4440	5.91	–	–

technologies and as long as methods for the correlation between results using the reference spectrum and results from “real world” spectra is established. The technical basis for the direct spectra has recently been reexamined and found to have a diffuse component that is substantially greater than that concentrators would normally encounter [19, 20]. On examination of the US solar radiation database, it was found that when the global-normal irradiance is near 1000 Wm^{-2} , the direct-normal component is near 850 Wm^{-2} and not the 767 Wm^{-2} that the direct standard spectrum integrates into [20]. This difference has been attributed to an aerosol optical depth at 500 nm of 0.27 in the terrestrial reference spectra [20]. This has not been a problem for single junction PV concentrators in the past because of their relative insensitivity to the specific direct spectra [21]. Recent high-efficiency structures such as the GaInP/GaAs/Ge triple-junction solar cell exhibit a significant difference in the efficiency between the global and direct reference spectrum ($>10\%$ relative) [22, 23] as shown in Figure 16.2. It has been proposed that the direct reference spectrum be modified to have a lower aerosol optical depth of 0.066 broadband or 0.085 at 500 nm to better represent the spectral irradiance in sunny regions (average daily direct-beam energy greater than $6 \text{ kWh/m}^2/\text{day}$) where concentrators might be deployed [22]. This low aerosol optical depth direct beam reference spectrum was generated using the same atmospheric conditions as the current terrestrial reference spectrum [10, 12, 13, 18] and has been adopted at NREL for evaluating concentrators as of January 2003. Tabular values of this direct beam spectrum can be found at the following web sites: <http://www.nrel.gov/highperformancepv/> or <http://rredc.nrel.gov/solar/standards/am1.5/>.

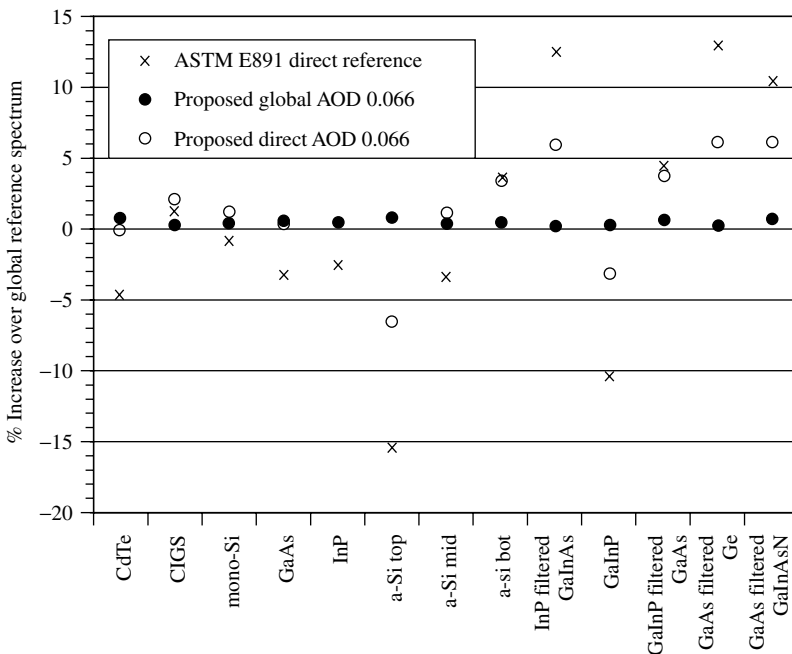


Figure 16.2 Percentage change in the normalized short-circuit current from the normalized global reference spectrum for various state-of-the-art PV technologies compared with the proposed direct reference spectra

The extraterrestrial spectral irradiance distribution at one astronomical unit distance from the sun is commonly referred to as the AM0 spectrum. At present, international consensus standards do not exist for AM0 measurements. Each country's space agency has adopted its own internal procedures. However, an international standard is in the draft stage [15]. Measurements of the total AM0 irradiance used by the aerospace community have varied from 1353 Wm^{-2} to 1372 Wm^{-2} [8, 14, 16, 24, 25]. Many groups still rely on the less accurate value of 1353 Wm^{-2} total AM0 irradiance [16, 24]. Recently, a new ASTM AM0 standard has been adopted that uses more accurate spectral irradiance measurements that are given in Table 16.3 and Figure 16.1 [8]. The best estimate for the solar "constant" is 1367 Wm^{-2} recommended by the World Radiation Center [14] or 1366.1 recommended by ASTM [8]. Both of these values were obtained from long-term monitoring of the solar irradiance with an active-cavity radiometer on the Solar Max and Nimbus 7 and other satellites [26]. Fortunately, the 1353 Wm^{-2} total AM0 irradiance, used by many groups for efficiency measurements and reporting purposes does not enter into the spacecraft PV power measurements. This is because primary balloon or space-based AM0 reference cells are calibrated at whatever irradiance that exists at the time of calibration, corrected to one astronomical unit distance from the sun. This means that numerical values of the AM0 total irradiance and spectral irradiance are not used in calibrating primary AM0 reference cells as discussed in Section 16.3.3.

A variety of definitions for cells and modules have been proposed [1, 5, 27, 28]. A module consists of several encapsulated, environmentally protected, and electrically interconnected cells. The area of a cell is taken to be the total area of the space charge region which includes grids and contacts. The standard cell area definitions replace the term *space charge region* with frontal area, but this term does not adequately account for devices with multiple cells on a single substrate or superstrate. The area of a concentrator cell is based upon the cell area that is designed to be illuminated [5]. This area is taken to be the area of the space charge region minus the area of any peripheral bus bars or contacts. A submodule or minimodule is an unencapsulated module.

The PV efficiency (η) is inversely proportional to the area definition used (equation 16.1). In fact, differences in the area definition often account for the greatest differences in η between various groups and values published in the literature [28, 29]. The largest differences occur when the so-called active area (total device area minus all area that is shaded or not active) is used. The use of an active area in the efficiency neglects the trade-off between lower resistance losses and increased shading. Several thin-film PV device structures do not have any shading losses, so the active and total area is the same. To prevent an artificial increase in the efficiency, care must be taken to ensure that light outside the defined area cannot be collected by multiple internal reflections or that carriers generated outside the defined area are collected due to incomplete electrical isolation. The smaller the cell area, the larger this possible effect. The larger the perimeter-to-area ratio, the greater the effect of the current being collected outside the defined area. This phenomenon is the reason a 1-cm^2 minimum area is required for inclusion in the *Progress in Photovoltaics* efficiency tables [30]. To be sure that the region enclosed by the total area is the only active region, an aperture should be used [30]. At the module level, the total area including the frame is used. For prototype modules, where the frame design is less important than the encapsulation and cell interconnections, an aperture-area definition is often used. The aperture-area definition is the total area minus the frame area.

This aperture area may be defined by opaque tape if there is no frame to eliminate the possibility of the module collecting current outside the defined aperture area by multiple internal reflections or light piping.

The most common performance rating method for modules is the PV power conversion efficiency under SRC (Table 16.1). The power or peak watt rating on the module's nameplate is usually given with respect to SRC, as shown in Table 16.1 using a 25°C module temperature. Unfortunately, prevailing conditions under natural sunlight do not commonly match nameplate conditions. The nameplate rating that the manufacturer assigns to a given module model number is often higher than the measured power output in the field [31–33]. If the nameplate rating is determined at 25°C, then the actual power produced is often less than this because the module will typically run at 40° to 60°C. The temperature coefficient for the peak power is usually negative. The nameplate rating also does not include long-term degradation or system losses. System losses include the power-conditioning unit's efficiency, ability of the power conditioner to operate at the maximum PV power point, orientation, shading, resistance losses in the wiring, and mismatch in the power of different modules.

The nominal operating cell temperature (NOCT) is a rating designed to give information about the thermal qualities of a module and a more realistic estimate of the power in the field on a sunny day at solar noon. The NOCT of a module is a fixed temperature that the module would operate at if it is exposed to the nominal thermal environment (20°C air temperature, 800 Wm⁻² total irradiance, and a wind speed of 1 ms⁻¹) [7, 34]. The term “standard operating conditions” or SOC is sometimes used for flat-plate or concentrator-terrestrial modules operating at NOCT. The actual determination of the NOCT of a module with an uncertainty of less than ±2°C has proved difficult because of difficulties in measuring the temperature of cells in an encapsulated module, uncertainties in the total irradiance, and secondary environmental effects such as wind direction, ground reflections, mounting, and electrical loading [34, 35]. The installed NOCT is up to 15°C warmer for roof-mounted applications than a free-standing module depending on the stand off distance between the module and the roof [34, 35]. The module temperature can be calculated from the NOCT or installed NOCT and air temperature using

$$T = T_{\text{air}} + (\text{NOCT} - 20^\circ\text{C})E_{\text{tot}}/800 \text{ Wm}^{-2}. \quad (16.2)$$

A wind speed correction can also be applied to equation (16.2) [7, 34].

For a fair and meaningful comparison of efficiencies between technologies, the measurements should be performed after any initial degradation. Commercial silicon modules have shown small changes in performance after the first few hours of operation [36, 37]. At the present time, all amorphous silicon PV technologies degrade when exposed to sunlight. Fortunately, this degradation stabilizes at a level of 80% to 90% of the initial value (see Chapter 12). Partial recovery occurs in the field during the summer when the higher module temperature leads to partial annealing or when amorphous silicon modules are annealed in the laboratory at 60° to 70°C [38, 39]. The efficiency continues to decrease after 500 h of light exposure at lower temperatures even if the light level is reduced [38–40]. For a fair and meaningful comparison of improvements in amorphous silicon module development, the performance at SRC is now reported after illumination

of about 1000 Wm^{-2} , at a module back-surface temperature of nominally 50°C , for at least 1000 h, with a resistive load near P_{max} , and low humidity [28, 39]. These conditions were chosen to approximate one year of outdoor exposure without the humidity or temperature cycling. Other thin-film module technologies may undergo reversible and irreversible changes during the first few hours of light exposure [29, 41, 42].

16.2.2 Alternative Peak Power Ratings

A variety of groups have suggested and adopted alternative rating schemes to compare module and system performance between the various PV technologies. These schemes are based on measurements of a module's performance in the field and on performing a regression analysis on the data. The site-specific power production is more relevant for bulk power generation than the power with respect to a particular theoretical reference spectrum and module operating temperature.

One popular method was adopted by Pacific Gas and Electric Company and the Photovoltaics for Utility-Scale Applications (PVUSA) project in California, USA, to rate and purchase PV systems. They perform a linear regression analysis on the actual measured system or module power produced (P), air temperature (T_a), wind speed (S), and total plane-of-array irradiance (E_{tot}) as measured with a pyranometer or radiometer:

$$P = P_{\text{max}}(E_{\text{tot}}, T_a, S) = E_{\text{tot}}(C_1 + C_2 E_{\text{tot}} + C_3 T_a + C_4 S), \quad (16.3)$$

where C_1 , C_2 , C_3 , and C_4 are the regression coefficients [32, 43]. The goal of performing a multiple regression analysis on the measured power to a fixed set of environmental conditions is to accurately represent the average power output under clear-sky conditions near midday at a given site. The power can be measured at the maximum direct-current (DC) power point, or on the DC side of the inverter, or at the alternating-current (AC) power out of the inverter. The last two power measurement locations will include some system losses. This site-specific rating scheme takes into account the different thermal characteristics of modules and spectral sensitivities since it is not referenced to a standard spectrum or module temperature. The power rating is evaluated using equation (16.3) at $T_a = 20^\circ\text{C}$, $S = 1 \text{ ms}^{-1}$, and $E_{\text{tot}} = 1000 \text{ Wm}^{-2}$ for flat-plate collectors. For concentrators, the direct-normal incidence sunlight within a 5° or 5.7° field of view of 850 Wm^{-2} is used for E_{tot} . The difference between the fields of view is because an absolute-cavity radiometer has a 5° field of view and some less accurate but less expensive normal incidence pyrheliometers have a 5.7° field of view.

The primary advantage of basing the reference temperature on the air temperature is that the different thermal characteristics of the module, array, and system are included in the rating, and the power rating is closer to what is actually observed. The different spectral conditions at the different sites are also accounted for by not referencing the performance to a fixed spectrum, but rather, referencing the power to the actual spectrum that was incident on the module. If a PV reference cell is used to measure E_{tot} , then the power would be with respect to a reference spectrum at all light levels. Spectral mismatch issues associated with E_{tot} , measured with a thermal- or spectrally matched detector are discussed further in Section 16.3.1.

16.2.3 Energy-based Performance Rating Methods

Despite its widespread acceptance, the peak power rating (i.e. maximum instantaneous watts) does not capture the differences among the plethora of flat-plate and concentrator-module designs with different total irradiance, diffuse irradiance, spectral irradiance, and temperature sensitivities. Energy-based ratings (i.e. integrated power over time in kWh) capture the module performance in the “real” world. It is easy to integrate the measured PV power produced over a time interval to obtain the total energy produced compared with the incident energy. A variety of rating criteria besides the standard reference conditions listed in Table 16.1 exist, depending on the application in Table 16.4.

The AM/PM method, proposed by ARCO/Siemens Solar Industries, attempts to rate a module in terms of the PV energy produced during a standard solar day with a given reference temperature and total irradiance distribution [44]. The AM/PM method is appealing because it is an energy-rating method that is not site-specific. A variation on the AM/PM energy-rating method was developed in which a regression analysis of the measured power and irradiance data to a nonlinear response function was summed over a standard day defined by a fourth-order polynomial [45].

A rating scheme based on the PV energy delivered over a standard day has been proposed for a small set of standard days [46–49]. These five days were obtained from the typical meteorological year database (http://rredc.nrel.gov/solar/old_data/) corresponding to a hot-sunny, cold-sunny, hot-cloudy, cold-cloudy, and a nice day [49, 50]. The meteorological data for the standard days include latitude, longitude, date, air temperature, wind speed, relative humidity, and direct, diffuse-horizontal, and global-normal irradiances. The direct-beam and plane-of-array spectral irradiances were then computed for hourly intervals throughout the day using a spectral model [51]. The model developed by Nann requires only the meteorological parameters listed in the standard days. Figure 16.3 shows the meteorological characteristics of the hot-sunny standard day [46–49]. The hot-sunny day was taken from the meteorological data for Phoenix Arizona, US, on June 24, 1976 [49, 50].

Other schemes for energy rating based on site-specific conditions instead of standard days have also been developed. In 1990, a rating based on realistic reporting conditions (RRC) was proposed. This method measured the performance of PV modules under different irradiances and temperatures and predicted the module’s output under

Table 16.4 Photovoltaic rating criterion for PV applications

Application	Relevant PV parameter
Grid-connected, hydrogen production	Annual energy delivered
Power for peak utility demand	Power near solar noon
Remote system for cooling	Temperature coefficient and NOCT
Remote system with storage	Energy during cloudy day
Pump system for agriculture	Energy during growing season
Small power consumer products	Efficiency at very low irradiance
High value (Space)	High efficiency, radiation, and thermal stability

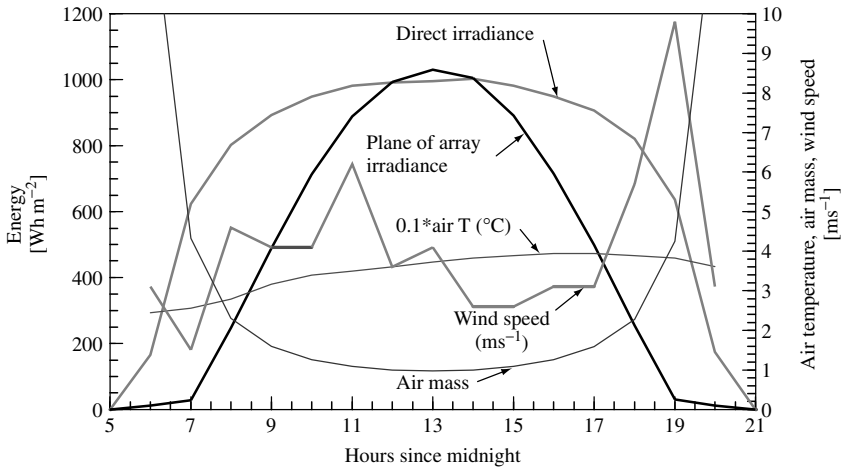


Figure 16.3 Meteorological conditions for the hot-sunny reference day [46–49]

various operating conditions [3, 4, 52–54]. This method has been used to compare commercial modules, highlighting the different dependencies on light level and temperature. Figure 16.4 illustrates the comparative ratings of selected modules for various locations in the United States [52] and Europe [53]. The results in Figure 16.4 indicate that the annual PV efficiency is 2 to 20% less than the efficiency under SRC (25°C , 1000 Wm^{-2} , and the global reference spectrum). The annual PV efficiency is total PV energy divided by the total energy deposited on a south-facing surface tilted to the latitude of the site. Spectral effects were ignored in Figure 16.4 with the global reference spectrum in Table 16.2 used for all calculations, so only temperature and total irradiance effects are included. The solar cell was modeled as described in Chapter 3 with a double exponential with series resistance and shunt resistance to model the performance as a function of total irradiance and temperature. Current state-of-the-art modules may be less sensitive to temperature and irradiance variations because of smaller temperature coefficients, series resistance, dark current, and a larger shunt resistance. The deviation of the annual efficiency from the efficiency under SRC would have been less if two-axis tracking were assumed. However, most flat-plate systems do not employ two-axis tracking. The spectral model developed by Nann was coupled with a PV model to compare the performance of a variety of PV technologies [4]. The PV model used a double exponential with series and shunt resistances to fit to the highest-efficiency cells made at the time of each technology. The environmental conditions include time, date, global-horizontal irradiance, direct-normal irradiance, diffuse irradiance, plane-of-array irradiance, ambient temperature, wind speed, and relative humidity. The results of the study were similar to those summarized in Figure 16.4 and References [52, 53]. The spectral model confirmed that the spectral sensitivity of Si, CdTe, CuInSe₂, and GaAs technologies on the annual energy production is +1% to –3%. The results also show that the efficiency of single- and multijunction amorphous silicon is ~10% less in winter months solely from spectral effects [4].

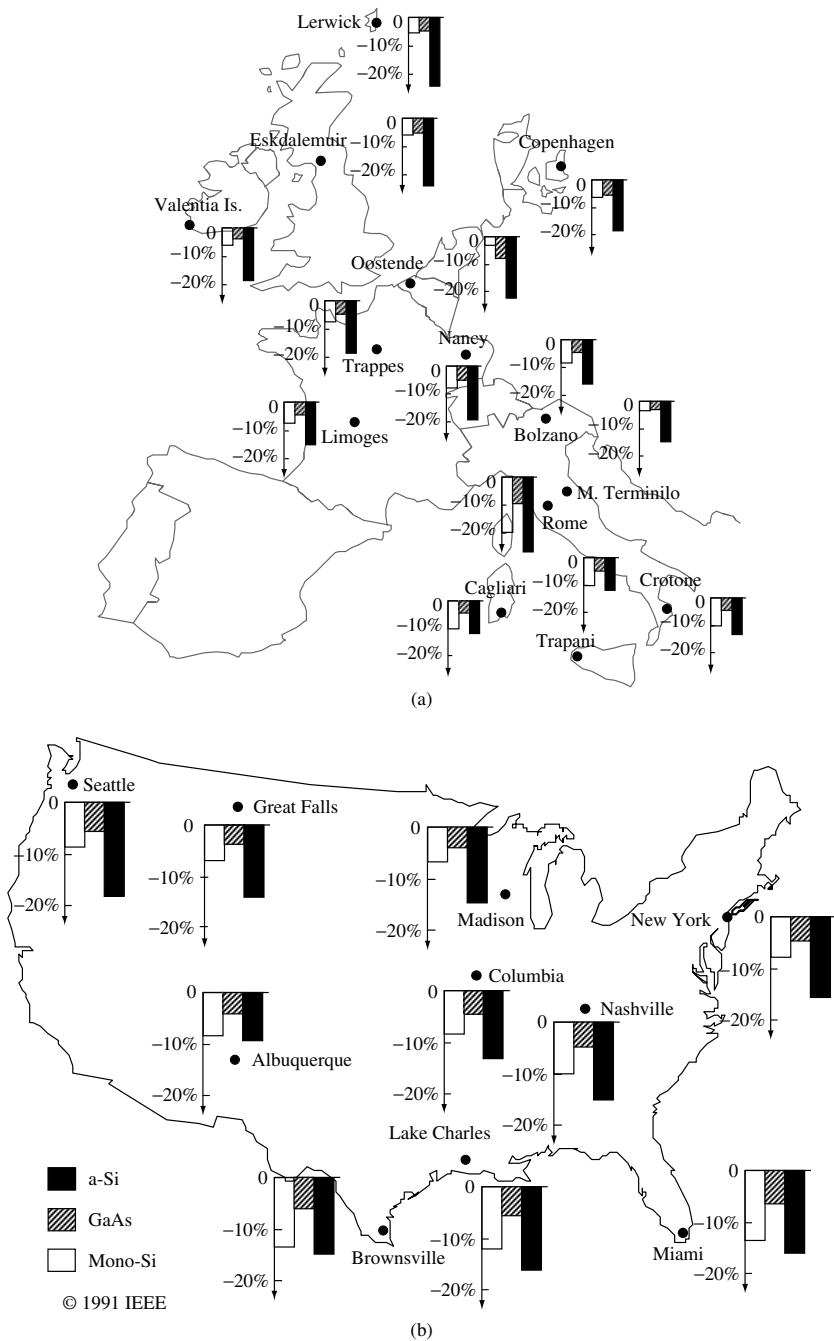


Figure 16.4 Example of PV performance on a yearly basis normalized to standard reference conditions for three different solar cell technologies (a-Si, GaAs, and c-Si) showing the percentage of deviation from standard conditions for a variety of locations in (a) Europe [52] and (b) the United States [53]

16.2.4 Translation Equations to Reference Conditions

The most basic translation equations for a solar cell are based on the diode model with series and shunt resistances discussed in Chapters 3 and 7. This model has been extended to modules by combining them in series and parallel combinations [55].

To a first order, short-circuit current (I_{SC}), open-circuit voltage (V_{OC}), P_{max} , and fill factor (FF) are linear with temperature, whereas the current is linear with E_{tot} [49, 56–60]. These linear translation equations allow the performance under standard reference conditions to be translated to other conditions for energy-based rating methods. Typical temperature coefficients for various PV technologies are summarized in Table 16.5 and Figure 16.5.

A set of translation equations for current and voltage based on the work of Sandstrom has been implemented in consensus standards [61, 62]. These equations translate the entire current versus voltage ($I-V$) curve for temperature and irradiance. Following the notation of the international standard in Reference [62], the following equations allow one to translate the current I_1 and voltage V_1 measured from temperature T_1 to T_2 and irradiance E_1 to E_2 :

$$I_2 = I_1 + I_{SC1} \left(\frac{E_2}{E_1} - 1 \right) + \alpha(T_2 - T_1) \tag{16.4}$$

$$V_2 = V_1 - R_s(I_2 - I_1) - I_2 K(T_2 - T_1) + \beta(T_2 - T_1), \tag{16.5}$$

where α and β are the temperature coefficients, R_s is the series resistance, and K is a curve-shape correction factor. Applying equations (16.4) and (16.5) at a fixed irradiance

Table 16.5 Typical Si solar cell temperature coefficients [57]

Type	$-V_{OC}$ [ppm/°C]	I_{SC} [ppm/°C]	$-FF$ [ppm/°C]	$-P_{max}$ [ppm/°C]
Si cells & modules	2400–4500	400–980	940–1700	2600–5500

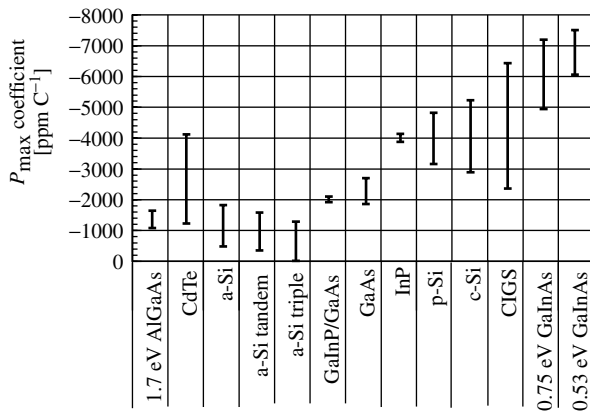


Figure 16.5 Typical P_{max} temperature coefficients of various PV technologies [57]

($E_2 = E_1$) and assuming no series resistance ($R_s = 0$), the value of K that best translates the $I-V$ characteristics for temperature is determined.

Translation equations for I_{SC} , V_{OC} , V_{max} , and I_{max} as a function of E_{tot} , T_c , absolute air mass (AM_a), and angle of incidence (AOI) based on multiple regression analysis of field data have been proposed by King [63]:

$$I_{SC}(E, T_c, AM_a, AOI) = (E/E_0)f_1(AM_a)f_2(AOI)[I_{SC0} + \alpha_{I_{SC}}(T_c - T_0)] \quad (16.6)$$

$$E_e = I_{SC}(E, T_c = T_0, AM_a, AOI)/I_{SC0} \quad (16.7)$$

$$I_{mp}(E_e, T_c) = C_0 + E_{ec}[C_1 + \alpha_{I_{mp}}(T_c - T_0)] \quad (16.8)$$

$$V_{OC}(E_e, i) = V_{OC0} + C_2 \ln(E_e) + \beta_{V_{OC}}(T_c - T_0) \quad (16.9)$$

$$V_{mp}(E_e, T_c) = V_{mp0} + C_3 \ln(E_e) + C_4[\ln(E_e)]^2 + \beta_{V_{mp}}(T_c - T_0) \quad (16.10)$$

$$I_{SC0} = I_{SC}(E = E_0, T_c = T_0, AM_a = 1.5, AOI = 0^\circ) \quad (16.11)$$

$$V_{OC0} = V_{OC}(E_e = 1, T_c = T_0) \quad (16.12)$$

$$V_{mp0} = V_{mp}(E_e = 1, T_c = T_0) \quad (16.13)$$

$$f_2 = \frac{E_0 I_{SC}(AM_a = 1.5, T_c = T_0) - E_{diff}}{E_{dir} \cos(\theta)}, \quad (16.14)$$

where E is the plane-of-array solar irradiance, E_e is the effective irradiance in units of suns, E_0 is the one-sun irradiance of 1000 Wm^{-2} , E_{diff} is the diffuse irradiance in the plane of the module, E_{dir} is the direct-normal irradiance, and AOI is the solar angle of incidence on the module; T_c is the temperature of the cells inside the module, T_0 is the module reference temperature, and $\alpha_{I_{SC}}$, $\alpha_{I_{mp}}$, $\beta_{V_{OC}}$, and $\beta_{V_{mp}}$ are the temperature coefficients of I_{SC} , I_{mp} , V_{OC} , and V_{mp} , respectively. These temperature coefficients are in absolute units so they will vary with the size of the PV device, the number of devices in series, or the number of devices in parallel. The pressure-corrected relative optical air mass AM_a can be written as [64]

$$AM_a = \frac{P}{P_0} [\cos(\theta) + 0.50572(96.07995^\circ - \theta)^{-1.6364}]^{-1}, \quad (16.15)$$

where P is the barometric pressure, P_0 is the pressure at sea level, and θ is the angle between the sun and zenith in degrees. The function $f_1(AM_a)$ is empirically obtained from the temperature- and irradiance-corrected I_{SC} versus air mass and assumes that the only spectral dependence is the zenith angle. Data are collected over a range of irradiances, incident angles, air masses, and temperatures and a multiple regression analysis is applied. These translation equations have been compared with simple linear translation equations derived from simulator-based measurements for several modules using outdoor data [49]. These translation equations give similar results to equation (16.3) when temperature, maximum-power tracking, and spectral issues are considered [48]. Other translation equations for current and voltage are possible [16, 65].

16.3 CURRENT VERSUS VOLTAGE MEASUREMENTS

A solar cell can be modeled as a diode in parallel with a current generator, whereas a module is a series-parallel network of solar cells, as discussed in Chapter 7. Measurements of cell or module $I-V$ behavior allow the diode characteristics to be determined, along with other important parameters including the maximum-power point, P_{\max} . A typical $I-V$ measurement system is composed of a simulated or natural light source, test bed to mount the device under test, temperature control and sensors, and a data acquisition system to measure the current and voltage as the voltage across the device or current through the device is varied with an external load or power supply.

16.3.1 Measurement of Irradiance

Irradiance measurements are made with respect to a reference spectral irradiance or the prevailing solar spectral irradiance. The measurement of the irradiance, E_{tot} , incident on the PV device in equation (16.1) is typically performed with a thermal detector (pyranometer, cavity radiometer) for outdoor measurements and reference cells for simulator-based measurements. If the goal is to determine the PV efficiency or power with respect to standardized or different reference conditions, then a spectral error will exist. Outdoor measurements of PV systems or modules are often made with respect to the prevailing or total irradiance incident on the module. If a broadband thermal detector with a constant spectral responsivity is used, then the spectral error is zero. If a silicon-based pyranometer is used to measure the performance based on the total irradiance, then there will be a spectral error because Si does not respond over the entire spectrum. For PV measurements with respect to a reference spectrum, the spectral error in the measured short-circuit current I_{SC} of a PV device can be written in general as [2]:

$$I'_{\text{SC}} = \frac{I_{\text{SC}}}{M} = I_{\text{SC}} \frac{\int_{\lambda_1}^{\lambda_2} \int_{\theta_1}^{\theta_2} \int_{\phi_1}^{\phi_2} E_{\text{Ref}}(\lambda, \theta, \phi) S_{\text{T}}(\lambda, \theta, \phi) d\lambda d\theta d\phi}{\int_{\lambda_1}^{\lambda_2} \int_{\theta_1}^{\theta_2} \int_{\phi_1}^{\phi_2} E_{\text{Ref}}(\lambda, \theta, \phi) S_{\text{R}}(\lambda, \theta, \phi) d\lambda d\theta d\phi} \times \frac{\int_{\lambda_1}^{\lambda_2} \int_{\theta_1}^{\theta_2} \int_{\phi_1}^{\phi_2} E_{\text{S}}(\lambda, \theta, \phi) S_{\text{R}}(\lambda, \theta, \phi) d\lambda d\theta d\phi}{\int_{\lambda_1}^{\lambda_2} \int_{\theta_1}^{\theta_2} \int_{\phi_1}^{\phi_2} E_{\text{S}}(\lambda, \theta, \phi) S_{\text{T}}(\lambda, \theta, \phi) d\lambda d\theta d\phi}, \quad (16.16)$$

where the spectral responsivity of the device under test (S_{T}), spectral responsivity of the reference detector (S_{R}), reference spectral irradiance (E_{Ref}), and source spectral irradiance (E_{S}) are a function of wavelength (λ) and incident azimuth (ϕ) and zenith (θ) angles. This general form allows the reference detector to be noncoplanar with the device under test and the source angular distribution of the source spectrum to be nearly arbitrary. In practice, the test device and reference detector used to measure the total irradiance are usually coplanar to minimize errors associated with measuring the orientation. The

direct and AM0 reference spectra have no angular dependence, and measurements are normally performed at normal incidence, so the angular dependence in equation (16.16) drops out. If the angular dependence of the reference detector used to measure E_{tot} and the global reference spectra follow an ideal cosine response, then equation (16.16) simplifies to [66, 67]:

$$M = \frac{\int_{\lambda_1}^{\lambda_2} E_{\text{Ref}}(\lambda) S_{\text{R}}(\lambda) d\lambda \int_{\lambda_1}^{\lambda_2} E_{\text{S}}(\lambda) S_{\text{T}}(\lambda) d\lambda}{\int_{\lambda_1}^{\lambda_2} E_{\text{Ref}}(\lambda) S_{\text{T}}(\lambda) d\lambda \int_{\lambda_1}^{\lambda_2} E_{\text{S}}(\lambda) S_{\text{R}}(\lambda) d\lambda}. \quad (16.17)$$

If the reference detector is a thermal detector, S_{R} is independent of the wavelength and drops out. The source spectral irradiance (E_{S}) and spectral responsivity of S_{R} and S_{T} need only be relative in equation (16.17), since any multiplicative error sources will drop out. Ideally, the limits of integration λ_1 and λ_2 in equation (16.17) should encompass the range of the reference detector and reference spectrum, or else an error can arise [68]. If the spectral irradiance of the light source is the same as the reference spectrum or if the relative spectral responsivity of the reference detector matches the relative spectral responsivity of the test device, then M is unity. Manufacturers of PV cells and modules for multimillion dollar satellites require the lowest possible measurement uncertainty; so they require primary balloon or space-calibrated reference cells of the same manufacturing lot, and purchase solar simulators with the closest spectral match to AM0 that is technically possible so that they can assume that M is unity.

The short-circuit current of the reference cell under the source spectrum ($I^{\text{R,S}}$) is used to determine the effective irradiance using the following equation:

$$E_{\text{tot}} = \frac{I^{\text{R,S}} M}{CV} \quad (16.18)$$

where CV is the calibration value of the instrument used to measure the incident irradiance in units of AW^{-1}m^2 . If a thermal detector is used, then CV has the units of VW^{-1}m^2 and $S_{\text{R}}(\lambda)$ is constant.

16.3.2 Simulator-based $I-V$ Measurements: Theory

The short circuit current of a test device ($I^{\text{T,R}}$) at the reference total irradiance (E_{Ref}) can be written as [2, 4, 67]:

$$I^{\text{T,R}} = \frac{I^{\text{T,S}} E_{\text{Ref}} CV}{I^{\text{R,S}} M} \quad (16.19)$$

where $I^{\text{T,S}}$ is the short-circuit current of the test device measured under the source spectrum, M is from equation (16.17), and $I^{\text{R,S}}$ is the measured short-circuit current of the reference cell under the source spectrum. This is the standard simulator-based calibration procedure. Many groups assume M is unity because of the difficulty of obtaining a spectral irradiance of the source spectrum and knowledge of the spectral responsivities of the

test and reference device. Typically, the simulator is adjusted so that E_{tot} is equal to E_{Ref} from equation (16.18) or

$$I = \frac{E_{\text{Ref}}CV}{I^{\text{R,S}}M} = \frac{I^{\text{R,R}}}{I^{\text{R,S}}M} \quad (16.20)$$

where $I^{\text{R,R}}$ is the calibrated short-circuit current of the reference cell under the reference spectral and total irradiance. Typically, a reference cell is made of the same material and technology as the devices that it will be used to test, causing M to be closer to unity since $S_{\text{R}} \approx S_{\text{T}}$. Ideally, the angular response of the reference package should be similar to the device under test. This is essential for outdoor measurements [2, 69–71]. Consensus standards have been developed, giving guidance for reference cells [72–75]. If the detector package has a window and an air gap between the window and cell, then the package should be completely illuminated and used only with simulators to prevent reflection-related artifacts [29, 76]. Recently, the terrestrial community has proposed a standard package design for the World Photovoltaic Scale [74, 75]. This package was designed by international terrestrial PV calibration laboratories to accommodate their various PV calibration equipment, while having standardized connectors to facilitate international intercomparisons.

16.3.3 Primary Reference Cell Calibration Methods

Perhaps the most straightforward method of determining the short-circuit current with respect to a set of reference conditions is to measure the absolute external spectral responsivity of the test device at the reference temperature, $S_{\text{T}}(\lambda)$, and to integrate it with the reference spectrum, $E_{\text{Ref}}(\lambda)$, at the reference total irradiance, E_{tot} , using the following equation:

$$E_{\text{tot}}CV = I_{\text{SC}} = \frac{E_{\text{tot}}A \int_{\lambda_1}^{\lambda_2} E_{\text{Ref}}(\lambda)S_{\text{T}}(\lambda) d\lambda}{\int_{\lambda_1}^{\lambda_2} E_{\text{Ref}}(\lambda) d\lambda}. \quad (16.21)$$

For I_{SC} to be in units of A, wavelength (λ) must be in units of μm , PV area (A) in m^2 , $E_{\text{Ref}}(\lambda)$ in $\text{Wm}^{-2}\mu\text{m}^{-1}$, E_{tot} in Wm^{-2} , and $S_{\text{T}}(\lambda)$ in AW^{-1} . The limits of integration should encompass the range of $E_{\text{Ref}}(\lambda)$. If $E_{\text{Ref}}(\lambda)$ is normalized to integrate to E_{tot} , then the limits of integration should encompass the response range of the device. The relationship between the spectral responsivity and the quantum yield is discussed in 16.4. Equation (16.21) assumes that $S_{\text{T}}(\lambda)$ is uniform over the PV device and that $S_{\text{T}}(\lambda)$ is independent of voltage bias, E_{tot} , and $E_{\text{Ref}}(\lambda)$. These assumptions can be relaxed for single-junction devices by applying an external bias light operating at E_{tot} . Several groups have gone to great lengths to minimize the various errors associated with equation (16.21) [77, 78]. Several intercomparisons show that differences of more than 10% in the absolute spectral response are possible from well-known PV calibration laboratories [74, 79–81]. Accurate spectral response measurements require measuring the

total power incident on a small area of the PV device (or the power density over the entire PV device) and the current produced at that wavelength. The major sources of uncertainty are the detector calibration used to measure the power (typically μW) and the errors in measuring a small AC current (typically μA or less) produced by the chopped monochromatic light, in the presence of a large DC offset (mA to A) from the broadband bias light. Because a reference cell calibrated using equation (16.21) will be fully illuminated when used to set a solar simulator or measure E_{tot} in natural sunlight, variations in the responsivity over the sample surface may result in an error in I_{SC} . Most groups use a high-current, low-noise operational amplifier with a gain of 10 to 10000 as the current-to-voltage converter because commercial current amplifiers saturate around 10 mA. Some groups employ a laser to more accurately measure the absolute response of a reference cell at one wavelength because the light power is in the milliwatt range, instead of microwatt, associated with diffraction-grating or filter-based systems and because reference detectors used to measure the monochromatic light power can be more accurately calibrated for laser lines.

A primary reference cell can be calibrated under natural sunlight using equation (16.19) and a thermal detector [1, 2, 9, 66, 82, 83]:

$$CV = \frac{I^{T,S} \int_{\lambda_1}^{\lambda_2} E_{\text{Ref}}(\lambda) S_T(\lambda) d\lambda}{E_{\text{tot}} \int_{\lambda_1}^{\lambda_2} E_{\text{Ref}}(\lambda) d\lambda} \frac{\int_{\lambda_1}^{\lambda_2} E_S(\lambda) d\lambda}{\int_{\lambda_1}^{\lambda_2} E_S(\lambda) S_T(\lambda) d\lambda} \quad (16.22)$$

where the cell short-circuit current ($I^{T,S}$) the solar spectra ($E_S(\lambda)$), and the total irradiance (E_{tot}) are measured at the same time. The spectral responsivity of the reference detector is constant, so $S_R(\lambda)$ is constant and drops out of equation (16.22). The incident irradiance E_{tot} is measured with a thermal detector that is traceable to the world radiometric reference scale, such as an absolute-cavity radiometer or pyranometer. The solar constant and solar power density in units of Wm^{-2} for solar applications are based on the world radiometric reference scale, which is derived from a family of primary absolute-cavity radiometers that are maintained at the World Radiation Research Center in Davos, Switzerland [84]. The field of view for the cell and spectroradiometer must be matched. Some investigators prefer to use a pyranometer mounted coplanar to the spectroradiometer and solar cell(s) on a horizontal surface [9, 85]. The investigators at the National Renewable Energy Laboratory (NREL) use an absolute-cavity radiometer because it is the primary instrument used to calibrate pyranometers and has a field of view of 5° , minimizing field-of-view-related error sources [1, 68, 82, 86]. A spectral model was developed to extend the measured direct-beam spectrum to encompass the limits of the reference spectra to minimize the errors in equation (16.21) [68, 83, 86]. The pyranometer-based calibration method requires the measurement of the spectral irradiance over a wavelength range of 300 to 2500 nm [9, 85]. Typically, CV is an average of many measurements taken over several days. This method only requires that the relative spectral response and spectral irradiance be known, thereby eliminating all error sources that are not wavelength-dependent.

If the absolute spectral irradiance $E_S(\lambda)$ of the light source in the test plane is known, as is the case for a standard lamp, black-body or absolute spectral irradiance

measurement, then equation (16.18) reduces to [66, 87–89]

$$CV = I^{T,S} \frac{\int_{\lambda_1}^{\lambda_2} E_{\text{Ref}}(\lambda) S_T(\lambda) d\lambda}{\int_{\lambda_1}^{\lambda_2} E_{\text{Ref}}(\lambda) d\lambda \int_{\lambda_1}^{\lambda_2} E_S(\lambda) S_T(\lambda) d\lambda} \quad (16.23)$$

This method is appealing because the reference spectrum may correspond to the black-body spectrum, and it can be readily performed in the laboratory. This method only requires the relative spectral responsivity measurements. If a standard lamp is used and the reference spectrum is the terrestrial reference spectra in Table 16.2, then the spectral correction factor in equation (16.23) is typically 12 [89]. Commercial standard lamps are typically 1000-W tungsten lamps supplied with an absolute spectral irradiance at a 50-cm distance and specific lamp current. This method is sensitive to errors in $S_T(\lambda)$, $E_S(\lambda)$, positioning, and stray light [68, 89]. The sensitivity to positioning is because the light source (i.e. standard lamp or black body) is not collimated and changes in the total irradiance of 1% per mm distance from the source are not uncommon [89]. If a solar simulator is used as the light source in equation (16.23), then the ratio of the integrals involving $S_T(\lambda)$ approach unity minimizing the sensitivity to errors in $S_T(\lambda)$, $E_S(\lambda)$ and positioning errors are reduced to less than 0.1% per mm of distance from the source [87].

Once the short-circuit current is known under a given $E_{\text{old}}(\lambda)$, it can be translated to any other $E_{\text{new}}(\lambda)$ with the following equation:

$$I_{\text{new}} = \frac{I_{\text{old}} E_{\text{tot}}^{\text{new}}}{E_{\text{tot}}^{\text{old}}} \frac{\int_{\lambda_1}^{\lambda_2} E_{\text{old}}(\lambda) d\lambda \int_{\lambda_1}^{\lambda_2} E_{\text{new}}(\lambda) S_T(\lambda) d\lambda}{\int_{\lambda_1}^{\lambda_2} E_{\text{new}}(\lambda) d\lambda \int_{\lambda_1}^{\lambda_2} E_{\text{old}}(\lambda) S_T(\lambda) d\lambda} \quad (16.24)$$

Equation (16.24) assumes that the current is linear with intensity. This method is especially useful for translating the calibration of primary AM0 reference cells to terrestrial reference spectra or vice versa.

The AM0 reference spectrum is by definition the extraterrestrial solar spectrum at one astronomical unit distance from the sun. This means that a small random error will exist because the solar spectrum varies slightly with solar activity. The AM0 community uses this fact to calibrate reference detectors by measuring their response in space or very high altitudes. By definition, there is no spectral error.

Extraterrestrial calibration procedures include using spacecraft, balloons, and high-altitude aircraft [15, 90–96]. There are no spectral corrections for balloon and spacecraft calibrations because the data are taken above the atmosphere. The high-altitude aircraft calibration procedure involves a Langley plot of the logarithm of I_{SC} versus absolute or pressure-corrected air mass over a typical range of 0.25 to 0.5 [92, 93, 95, 96]. The data are collected above the tropopause, thereby eliminating water vapor and most scattering, with the dominant spectral feature arising from ozone absorption [92, 96]. The Jet Propulsion Laboratory (JPL) balloon calibration program requires a custom package design for

standardized mounting, data acquisition system, and thermal considerations [90, 91]. See Chapter 10 for further discussion of calibration of reference cells for testing space cells.

16.3.4 Uncertainty Estimates in Reference Cell Calibration Procedures

All measurements have an uncertainty between the measured or derived value and the true value. In the case of terrestrial PV reference cell calibrations, the true value is the value under reference conditions given in Table 16.1. For extraterrestrial calibrations, the true value is determined by the actual solar spectrum, at the time of calibration and not the tabular reference spectrum, as in the case of terrestrial calibrations. Any variation in the primary AM0 calibration because of the varying solar constant is not considered an error. The spectral responsivity of PV cells change as a function of radiation damage. For an accurate assessment of the performance as a function of radiation damage using procedures that assume the spectral correction factor is unity, at least three matched reference cells are required (beginning of life, midlife, and end of life) to minimize the spectral errors.

The uncertainty that is expected to include 95% of results (U_{95}) in a calibration can be expressed in terms of the random error and systematic error component defined below, through the following equation [97]:

$$U_{95} \equiv \sqrt{B^2 + (t_{95}A)^2} \quad (16.25)$$

where A is the statistical component applied to a series of repeated determinations and is often expressed as a standard deviation. Type B error sources are associated with the instruments used in the measurement process and their associated calibration uncertainties. Student's t value for 95% coverage (t_{95}) is approximately 2.0 for an average of more than 20 measurements. The elemental error sources are composed of J random and systematic error components. The *systematic* error is

$$A \equiv \sqrt{\sum_{i=1}^J (\Theta_i A_i)^2} \quad (16.26)$$

The term *systematic error* is sometimes used synonymously with bias or nonrandom error. The sensitivity coefficient (Θ_i) is obtained by partial differentiation of the result with respect to one of the parameters in the result. If A_i is expressed in units of percent error, then Θ_i is unity. The *random* error is

$$B \equiv \sqrt{\sum_{i=1}^J (\Theta_i B_i)^2} \quad (16.27)$$

An example of an uncertainty analysis of equation (16.22) using the NREL direct-beam calibration method is given in Table 16.6 [98, 99]. Detailed uncertainty analysis using Monte Carlo methods indicates that the uncertainty in the spectral correction factor is 10%

Table 16.6 Uncertainty analysis of the tabular calibration method equation (16.22) [98]

Elemental error source	Systematic [±%]	Random [±%]	Total U_{95} [±%]
I_{SC} ($I^{T,S}$) measurement instrumentation	0.10	0.10	0.22
Absolute-cavity radiometer (E_{tot})	0.37	0.13	0.45
Spectral correction factor	0.20	0.20	0.45
Temperature correction & control @ $\pm 1^\circ\text{C}$	0.15	0.05	0.18
$I^{T,S}$ linearity with varying E_{tot}	0.05	0.05	0.11
Thermal offset voltages	0.05	0.05	0.11
$I^{T,S}$ time constant different from radiometer	0.10	–	0.10
Total	0.47	0.27	0.72

to 20% of the magnitude of the spectral correction factor [68, 99]. A detailed uncertainty analysis of the error in determining the maximum power of a module measured outdoors using the ISO methodology was performed by Whitfield and Osterwald [100]. The ISO methodology has been adopted by all major calibration laboratories and replaces the previous ANSI methodology [101].

16.3.5 Intercomparison of Reference Cell Calibration Procedures

Typically, groups claiming to be able to calibrate primary reference cells with respect to reference conditions claim an uncertainty in the calibration value CV of $\pm 1\%$ [74, 80, 81, 94, 102]. Intercomparisons among the various calibration methods are the best way to determine if the uncertainty estimates are valid. Formal intercomparison of terrestrial calibration procedures sponsored by the Photovoltaic Energy Project (PEP) were conducted in 1985, 1987, and 1993 [74, 80, 81]. The PEP '85 intercomparison involved PV calibration laboratories from the Commission of European Communities, France, Germany, Italy, Japan, United Kingdom, and the United States. The differences in I_{SC} with respect to the global reference spectrum between the laboratories in the PEP '85 intercomparison were almost 8% for single-crystal and multicrystal silicon and 20% for amorphous silicon. However, in the PEP '85 intercomparison, six out of the eight agencies agreed within 3% for the crystalline cells and 6% for the amorphous cells [81]. In the PEP '87 and PEP '93 intercomparisons, the participants provided uncertainty estimates. The level of agreement between the laboratories for the PEP '87 intercomparison was 4% for single-crystal and multicrystal silicon cells and 14% for amorphous silicon [80]. This level of agreement was 2 to 10 times the labs' estimated uncertainties, which ranged from $\pm 0.7\%$ to $\pm 5\%$, indicating that the uncertainty estimates for some of the participants were overly optimistic [80]. Several of the participants based their estimated uncertainties on the standard deviation of repeated calibrations thereby neglecting nonrandom error sources. The PEP '93 intercomparison also showed a rather large spread of 12% for the single-crystal and multicrystal silicon cells, even though the estimated U_{95} uncertainties ranged from $\pm 1.0\%$ to $\pm 2.7\%$, again indicating that several laboratories underestimated their errors [74]. After excluding laboratories whose calibrations were based on reference cells and laboratories that had more than 50% of their calibrations exceed $\pm 2\%$ of the mean, the resultant average

deviation was 1.1% [74]. Because the terrestrial PV calibration laboratories around the world could not agree on a calibration procedure that had a proven U_{95} uncertainty of less than $\pm 2\%$, it was decided to establish a set of reference standards called the World Photovoltaic Scale (WPVS) [74, 75]. The four laboratories from the PEP '93 intercomparison that performed primary calibrations and were within $\pm 2\%$ of the mean were the NREL in the United States, Japan Quality Assurance Organization/Electrotechnical Laboratory in Japan, Tianjin Institute of Power Sources in the Peoples Republic of China, and Physikalisch-Technische Bundesanstalt (PTB) in Germany. A formal mechanism was established to include other laboratories in the future, provided their calibrations agreed with the four established WPVS calibration laboratories. The WPVS reference cells reside with the laboratory that provided them, providing each participating laboratory with reference cells traceable to the WPVS. A set of technical drawings was developed for future WPVS reference cells to prevent the problem with the existing set of 20 WPVS reference cells having incompatible cables, mounting holes, and temperature sensors [74, 75]. Sixteen of the 20 WPVS reference cells were recently recalibrated, along with six new candidate WPVS reference cells [102]. The new WPVS calibration values changed by 0.4% at most, with an average decrease of 0.2% [102]. The results of the PEP terrestrial intercomparisons were much closer than earlier intercomparisons, where deviations of $\pm 3\%$ were common and deviations of 5% from the mean were observed [103]. The year-to-year repeatability appeared to be no better than $\pm 3\%$ [103].

Surprisingly, the spread in I_{SC} temperature coefficients for the laboratories that performed them was greater than 50%, even though the temperature of the cells could be controlled and they had temperature sensors permanently attached to them [74]. This variation in temperature coefficient can be partly understood by noting that the temperature coefficient is a function of the light source that they are illuminated with [57]. For cells having a narrow response range, or for multijunction cells, the sign of the coefficient can even change depending on the light source [57, 104, 105].

The AM0 community has conducted intercomparisons between various groups over the years [90, 94, 106, 107]. In general, the agreement of primary AM0 calibrations on spacecraft, balloon, and high-altitude aircraft calibrations is better than $\pm 1\%$ over many years [90–92]. AM0 calibrations based on terrestrial measurements sometimes agree with primary high-altitude calibrations within 1% [91] and at other times the agreement is poor ($>10\%$) [106].

16.3.6 Multijunction Cell Measurement Procedures

Spectrum-splitting series-connected multijunction devices are critical to achieving high-efficiency III-V-based (Chapter 9) and a-Si-based (Chapter 12) solar cells. The procedures to measure the $I-V$ characteristics of a multijunction device with respect to reference conditions are the same as those for a single-junction device with the added constraint that the simulator should be set such that each junction operates at the proper photocurrent. This is accomplished by satisfying the following j equations for the j junctions in a multijunction PV device [108–111]:

$$I_j^{R,R} = M_j I_j^{R,S} \quad (16.28)$$

$$M_j = \frac{\int_{\lambda_1}^{\lambda_2} E_{\text{Ref}}(\lambda) S_{R,j}(\lambda) d\lambda \int_{\lambda_1}^{\lambda_2} E_S(\lambda) S_{T,j}(\lambda) d\lambda}{\int_{\lambda_1}^{\lambda_2} E_{\text{Ref}}(\lambda) S_{T,j}(\lambda) d\lambda \int_{\lambda_1}^{\lambda_2} E_S(\lambda) S_{R,j}(\lambda) d\lambda}. \quad (16.29)$$

This procedure involves adjusting the simulator in equation (16.28), measuring its spectrum, calculating M_j , and readjusting the simulator. If reference cells are used whose relative spectral responsivity efficiency matches each individual junction, then the spectral correction M_j is unity and only equation (16.27) needs to be satisfied. This is possible for the high-efficiency crystalline material systems in which the other junctions can be shorted out without significantly affecting the relative spectral responsivity [108]. The adjustment of the solar simulator to satisfy equation (16.28) can be problematic. Figure 16.6 illustrates the various approaches that researchers have taken in the past. The first approach illustrated in Figure 16.6(a) involves combining an ultraviolet (UV) light source L_1 and infrared (IR) light source L_2 with a dichroic filter assembly [108, 109, 112, 113]. This approach is particularly useful for two- and three-junction devices in which the top-cell energy gap is around 600 to 700 nm and the middle-cell energy gap is also around 600 to 700 nm. This is because of the relatively limited choices in the transition wavelength for standard dichroic filters. Figure 16.6(b) works for any material system because it uses

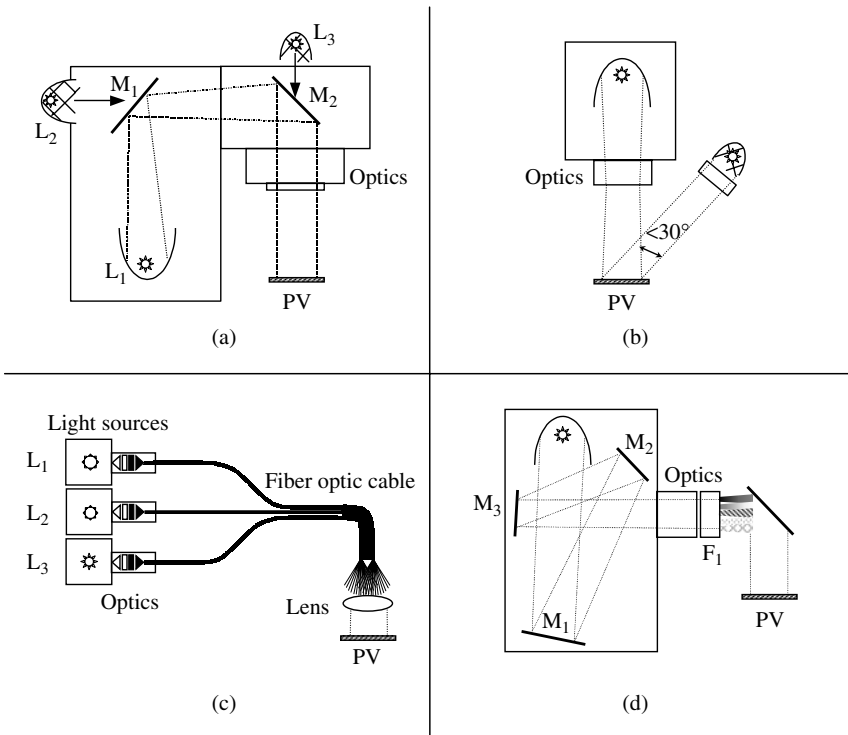


Figure 16.6 Methods of adjusting the spectral content of solar simulators. The light sources are L_1 , L_2 , and L_3 and the mirrors are M_1 , M_2 , and M_3

a simulator whose spectral match is close to the reference spectrum but brings in extra light that can be filtered at will for each junction [114]. The primary disadvantage of this approach is that the supplemental light sources are not collinear with the broadband light, giving the possibility of large variations in the spectral irradiance in the test plane. A fiber-optic solar simulator shown schematically in Figure 16.5(c) is useful because a wide variety of laser and incoherent light sources can be combined into one fiber bundle, which then illuminates the test plane [110, 115, 116]. This approach has the disadvantage of being restricted to small illumination areas, typically less than 2 cm in diameter at one sun. Another approach shown in Figure 16.6(d) is to place filters and apertures close to the integration optics of a large-area solar simulator [110, 114, 115]. This method is particularly useful for large-area ($>100 \text{ cm}^2$) samples. Its primary drawback is that the light sources are not separately adjustable for each junction. This concept can also be applied to pulsed simulators, where the distance between the flash lamp(s) and the test plane is usually large and a wide range of intensities is possible. This method works for any multijunction technology because standard high-pass, low-pass, and band-pass filters are available to cover any combination of band gaps.

An entirely new procedure has recently been developed in which the light sources are set only once [111, 117, 118]. The approach is based on a simulator setup with multiple light sources arranged so that the intensity of each source may be adjusted without causing a change in the relative spectral irradiance. Each light source, $E_{S,i}(\lambda)$ for each junction, j can therefore be characterized by its relative irradiance. The adjustment of the intensity of the i th light source to an absolute level is mathematically described by the scaling factor C_i . Under these premises, the condition $I_j^{\text{T,S}} = I_j^{\text{T,R}}$ yields a system of j linear equations,

$$\sum_i C_i \int E_{S,i}(\lambda) S_{\text{T},j}(\lambda) d\lambda = \int E_{\text{ref}}(\lambda) S_{\text{T},j}(\lambda) d\lambda \quad (16.30)$$

which can easily be solved for the unknown scaling factors C_i . The intensity of the i th light source $E_{S,i}(\lambda)$ for the j th junction of the test device $S_{\text{T},j}(\lambda)$ is adjusted until the measured short-circuit current of reference cell $I_j^{\text{T,R}}$ with an absolute spectral response $S_{\text{R},j}(\lambda)$ is obtained using

$$I_j^{\text{T,R}} = C_i A \int E_{S,i}(\lambda) S_{\text{R},j}(\lambda) d\lambda \quad (16.31)$$

The system of equations requires only relative spectral responses and relative irradiances and is therefore equivalent to the calculation of the mismatch factor in equation (16.29). The equations allow for the same reference cell to be used to set the simulator sources [111, 117, 118]. This procedure only requires one adjustment of each light source. This procedure also requires that the relative spectral irradiance be measured only once for each light source unlike the procedure described by equations (16.28) and (16.29), which requires a spectral irradiance measurement after each simulator adjustment. This allows the performance of a multijunction PV device under varying reference spectra or current-matching conditions to be rapidly determined.

16.3.7 Cell and Module $I-V$ Systems

A wide variety of $I-V$ measurement systems have been developed to measure the performance of PV devices, from 0.01-cm² area cells to multikilowatt arrays [2, 119]. A generic $I-V$ system is shown in Figure 16.7. The voltage across the PV device (from a cell to an array) is biased with a variable load, with the current being sensed by a precision four-terminal shunt resistor or magnetic transducer. (Current through a solar cell should never be measured with a standard ammeter in series because the voltage bias developed across the meter will change the operating point of the cell.) Domestic and international standards have been developed for the minimum characteristics of typical $I-V$ measurement systems [5–7, 9, 11, 13]. The critical parameters on the $I-V$ curve are the open-circuit voltage (V_{OC}), the short-circuit current (I_{SC}), and the maximum-power point (P_{max}). Figure 16.8 shows a typical $I-V$ curve for a 50-W module in the light at SRC and in the dark. The fill factor (FF) is a normalized parameter indicating how ideal the diode properties are, and it is calculated by the following expression:

$$FF = \frac{P_{max}}{V_{OC}I_{SC}} \quad (16.32)$$

The fill factor is often expressed as a percentage by multiplying equation (16.32) by 100.

The open-circuit voltage can be determined from a linear fit to the $I-V$ curve around the zero current point or by measuring the voltage with the load disconnected. The value of V_{OC} is often obtained by linear interpolation of the two $I-V$ points closest to zero current. Performing a linear regression using more than two points can reduce the uncertainty in V_{OC} ; however, care must be taken not to include points resulting from blocking diodes in series with a module or fitting in nonlinear regions. One manufacturer

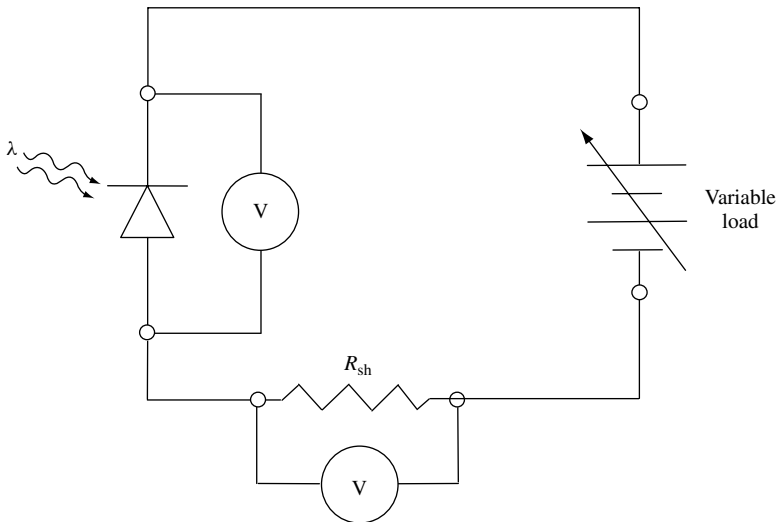


Figure 16.7 Typical current versus voltage measurement system

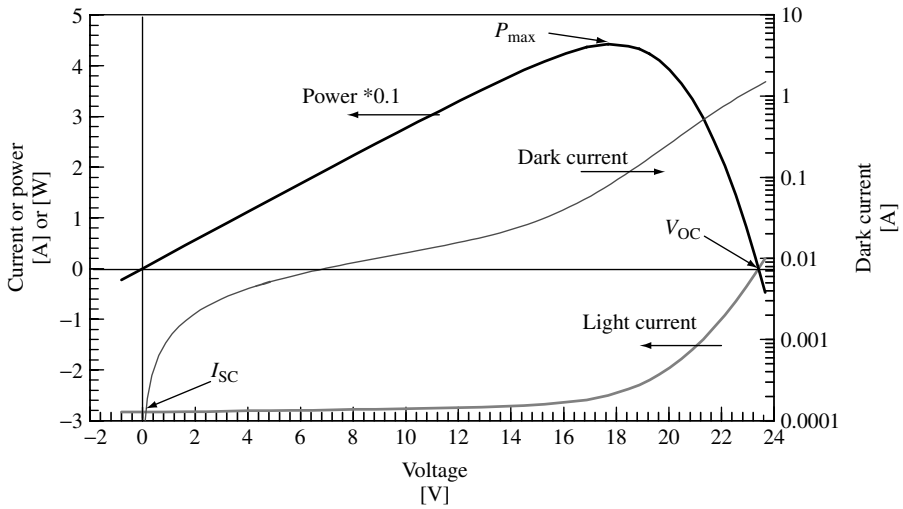


Figure 16.8 Typical light and dark current versus voltage curve of a commercial 50-W PV module

of commercial equipment includes the 20 $I-V$ points in the power quadrant closest to zero current. Another approach that works for all types of cells and modules is to include in the linear regression fit all points that satisfy the constraint that the absolute value of the voltage be less than 10% of the voltage at zero current and the additional constraint that the absolute value of the current be less than 20% of the current at zero voltage.

The value of I_{SC} is usually determined by linear interpolation of the two points closest to zero voltage. Performing a linear curve fit using more than two points can reduce the uncertainty in I_{SC} ; however, care must be taken not to include points resulting from bypass diodes in parallel with a module or fitting in nonlinear regions. One manufacturer includes the 20 $I-V$ points in the power quadrant closest to zero voltage. Another approach that works for a wide variety of cells and modules is to include all $I-V$ points in the linear fit that satisfy the constraint that the current is within 4% of the current at zero voltage and the additional constraint that the absolute value of the voltage be less than 20% of the voltage at zero current. These constraints make no assumptions about the spacing between points (fit to a fixed number of $I-V$ points) or the shape of the curve (avoiding including nonlinear regions) while including as many $I-V$ points in the linear regression as possible.

The maximum power (P_{max}) is often taken to be the largest measured power. A more accurate method is to perform a fourth-order or higher polynomial curve fit to the measured power versus voltage data points within 80% of P_{max} [119]. To prevent erroneous results on low FF devices, the power versus voltage data selected for curve fitting must be restricted to voltages greater than 80% of the voltage at the measured maximum power (V_{max}). This algorithm can be improved by selecting the order of polynomial that gives the best fit to the data up to a fifth order. An approach recommended by American Society of Testing and Materials (ASTM) is to perform a fourth-order polynomial fit to the data where the measured current is greater $0.75I_{max}$ and less than $1.15I_{max}$ and

the measured voltage is greater than $0.75V_{\max}$ and less than $1.15V_{\max}$ [7]. The preceding constraints seem to work for cells and modules with a 40% fill factor to a 95% fill factor [119].

This allows the measured current to be corrected for intensity fluctuations to a constant intensity value. It is best to measure the incident irradiance with a reference cell at each current–voltage point and to use separate meters for the same sampling interval. A less accurate method is to measure the current and voltage sequentially with the same meter and only measure the intensity once. This method assumes that there are no temporal fluctuations in the simulated or natural light intensity during the measurement period and that the voltage is constant. This may not be the case if the bias rate or capacitance is large or if there are transients in the device [29, 119]. One commercial I – V system averages 40 voltage readings and then 40 current readings to obtain a single I – V point. This approach causes problems if the voltage and current are not in equilibrium because of too large a bias rate or other transient phenomena. A better approach would be to take 40 pairs of current and voltage points and then average the voltage and current because this relaxes the assumption that the current and voltage at a given load setting are random with time.

Useful additions that are rarely found in commercial I – V equipment include checking for valid contacts and limiting the maximum current through the device. To prevent damage to PV cells, the resistance between the current and voltage contacts should be measured with manual or automatic measurements prior to the I – V measurement. If the sample is too small for Kelvin contacts, then the current at zero voltage should be monitored while making contact with the cell. Most commercial systems are polarity-dependent because bipolar power supplies or loads are much more expensive. The current near zero volts is obtained by a low-voltage load of opposite polarity. This feature can damage cells and modules with a low reverse-bias breakdown such as amorphous silicon or GaAs if a diode is not placed in parallel with the sample to prevent a reverse-bias voltage from being applied. The polarity can easily be determined from the sign on the voltage near zero current or the sign on the current near zero voltage. This keeps the operator from worrying about which connection is positive and prevents excess bias voltages from accidentally being applied by automatically choosing a safe range for the maximum forward and reverse bias.

Commercial I – V systems developed for the semiconductor industry by Hewlett Packard/Agilent Technologies Inc., Keithley Instruments Inc., and others are readily available. These units can be operated manually or with a computer with a wide range of features and capabilities including bipolar operation. The primary problem with units designed for transistor and diode analysis is the cost and limited maximum current. This limitation is only a problem for groups that need to perform I – V measurements at biases over ~ 100 V and ~ 5 A. These generic I – V systems require software to download the data, save it, and calculate relevant PV parameters. There is also a variety of manufacturers of PV test equipment for I – V measurements including Daystar Inc., Spire Inc., Spectrolab Inc., Pasan Beval S.A., Wacom Electric Co. Ltd, and numerous other small companies. Commercial I – V measurement software is typically designed for industrial applications and lacks the capability to detect bias rate artifacts by changing the bias direction, or variable bias, or load slew rate. Commercial software also has a fixed format for saving the data and plotting the results that may be difficult or impossible for the user to modify.

Most commercial $I-V$ software also measures only the light $I-V$ characteristics in the power quadrant. This is not sufficient for analyzing effects of nonohmic contacts requiring forward bias $I-V$ data beyond V_{OC} or voltage-dependent photocurrent collection requiring reverse bias $I-V$ data.

Many groups have developed custom data acquisition systems with commercial components. These systems are reviewed in Reference [2] and consist of electronics to measure the current and voltage and a power supply [1], operational amplifier [120, 121], capacitor [122], or transistors as the load [123–125]. Ideally, the current sense resistor should have a low temperature coefficient and have a power rating at least six times the maximum expected load power to prevent errors from changing ambient temperature or resistor heating. It should be noted that $I-V$ systems built around custom circuits and software could be difficult and time consuming to maintain when the developer is gone. In determining the most appropriate $I-V$ data acquisition system for devices that may range from single research-level cells to arrays, the present and all possible future applications should be considered. Any group that is considering building their first $I-V$ system, upgrading that old reliable $I-V$ system, or expanding their existing capabilities should consider the following factors:

- Desired outputs from the system – tabular and graphical display and hard copy of data, database or update of a simple directory text file, control over format and content of saved data, meteorological parameters.
- Minimum and maximum current and voltage range.
- Cost in time and money available for design and development.
- Cost in time and money available for maintenance (repairs, enhancements, and expansion).
- Compatibility with existing hardware, software, and databases.
- Flexibility to detect and compensate for artifacts – flexibility in bias direction and bias range, manual control, control over premeasurement illumination and bias state.

Assuming that the PV device is actually at SRC, the error in the FF is primarily affected by the connections to the data acquisition system. First and foremost, four-terminal (known as Kelvin) connections should always be used at the positive and negative terminals of the device. Between the point where positive or negative voltage connections are made and the PV sample, any wire or contact resistance will appear as a series resistance, reducing FF and hence P_{max} and η . At the component level of modules and above, wire resistance losses are included. For cells without wires attached, the goal is to simulate as accurately as possible the module-contacting scheme. This generally means placing a current and preferably a voltage probe contact at each wire bond pad. A temperature-controlled vacuum plate is used for compatible structures in which at least one of the positive or negative contacts is on the front surface (monocrystalline and multicrystalline wafers or thin-film devices deposited on a substrate) to provide a large-area, low-resistance contact. This low but finite contact resistance will appear as a power loss in P_{max} unless a separate voltage contact is used. This voltage contact may be a miniature, spring-loaded, blunt-tipped, gold-plated probe; a patterned, metallized Kapton or ceramic; a printed circuit board placed in a narrow slot in the vacuum plate; or some other method. The surface area of this voltage contact will introduce an error in the voltage when light is incident on the cell because of nonuniform heat transfer to the temperature-controlled

plate. For production PV testers, the ribbons attached to grids on Si cells are simulated by using linear arrays of probes (possibly spring-loaded to a specific force). At the cell level, many PV materials will be damaged if the probe penetrates the relatively thin contact pad or misses the pad and touches the semiconductor. When the contact geometries are small, a micromanipulator and microscope eyepiece may be required, and contacting problems tend to be more difficult. The typical probe contact procedure in the PV performance characterization laboratory at NREL is to choose the appropriately sized Kelvin probe mounted on a three-axis manipulator and make contact with the device, while monitoring the resistance between the voltage and current Kelvin contact. Kelvin probes are used with an attached coaxial cable manufactured by Accuprobe Inc., with CuBe tip diameters between 12.7 μm and 127 μm and contact spacing between 50.8 and 1524 μm . For large-area cells (10 cm by 10 cm or larger) designed to have ribbons attached, differences in fill factors of more than 50% between groups can occur [2, 126]. The source of these differences can be attributed to contacting and spatial nonuniformities in the light source. Contacting-related differences occur when probes are used to simulate the ribbons, because of variations in shadowing, and distributed resistance losses. Differences in I_{SC} of 2% between NREL and other groups have been attributed to light reflected off metal probe(s), nearby operators in white lab coats and fixturing. Custom-fixturing or optics to direct the light upward is often required when both contacts are on the side not being illuminated as is the case for point-contact or wrap-around Si cells, or for superstrate structures like a-Si or CdTe on transparent conducting oxide coated glass. Achieving temperature control and Kelvin-contacting for these structures is problematic. Groups have used patterned circuit boards or Kapton to achieve contacts and temperature control. The contact area is often the junction area for small area thin-film devices on insulating superstrates allowing a metal spool with a vacuum hold down to make thermal, and electrical contact to the metallized cell and a probe or wire to make contact to the transparent conducting oxide layer. Many of the best thin-film devices have a thick layer of In metal bonded to the transparent conducting oxide around the cell border to reduce lateral series resistance losses. High-efficiency research cells on insulating substrates such as Cu(Ga,In)(S,Se) also often have an In border around the cell area to reduce resistance losses.

Evaluating the performance of concentrator cells poses several challenges. As of 2001, there are no consensus standards to evaluate concentrator cells, although ASTM and the Commission for the European Community are developing standards. Issues of temperature measurement and control are aggravated by the large heat load. Typically, concentrator cells are evaluated under flash systems with a 1-ms pulse duration or under continuous illumination. If a continuous light source is used, then the temperature of the space charge region cannot be directly measured – any temperature sensor will affect the temperature because of the small thermal mass and large light level on the sample. There can be large differences in the temperature of the space charge region (i.e. the cell temperature) and the temperature of the vacuum plate or measured front-surface temperature. One approach with the cell in the dark or minimal heat load is to first set the temperature-controlled vacuum plate to a given temperature, and then measure V_{OC} as a function of time as a high-speed shutter is opened, exposing the sample to the full light level [127]. The V_{OC} will rise as the shutter is opened and the cell is exposed to the concentrated light and will go through a maximum as the cell heats up corresponding to the V_{OC} at the known temperature measured with no heat load. The plate temperature can then be reduced until this V_{OC} is obtained. The other primary problem

with concentrators is the measurement of E_{tot} . The simplest approach is to determine the one-sun I_{SC} and assume that this value is linear with light level. Another approach is to use calibrated neutral-density filters [2, 128, 129]. Neutral-density filters can be calibrated to better than 1% at a given wavelength using lasers, but typically they have a $\pm 5\%$ variation in transmissivity with wavelength over a 400- to 1100-nm range, limiting their usefulness to single-junction devices that are insensitive to spectral errors, such as Si and GaAs. The linearity can also be inferred by a series of measurements with aperture or changing flash-lamp voltage [111]. Other approaches to determining the linearity involve exposing the cell to low-level periodic sunlight and concentrated sunlight [130, 131]. Ideally, a calibrated linear reference cell should be used, but spatial nonuniformity of the concentrated beam can lead to a larger error than that if linearity had been assumed. Again, ideally, the spectral responsivity should be measured as a function of bias light level to address the issue that, for nonlinear devices, the spectral error M will change with total irradiance. Groups have developed spectral response systems capable of measuring the responsivity as a function of bias light level to about 200 suns [132, 133].

Concentrator modules cannot normally be measured in solar simulators because the optics are not a point source; the bulb(s) or integration optics will be imaged on the cell, resulting in a much larger spatial variation in intensity than that the module would encounter under natural sunlight. For this reason, concentrator modules are typically evaluated outdoors under natural sunlight over some period of time. There are no standards for concentrator cell, module or system measurements, although the PVUSA method in equation (16.2) has been used to evaluate concentrator systems [32, 43]. Concentrator modules and arrays evaluated at Sandia National Laboratories have consisted of the performance (P_{max} , or $I-V$ characteristics) as a function of direct-beam irradiance and heat sink temperature [129].

16.3.8 Solar Simulators

Solar simulators are used to simulate natural sunlight for repeatable and accurate indoor testing of the $I-V$ characteristics of PV cells or modules. The ideal solar simulator should have less than $\pm 1\%$ variation in the light level during the $I-V$ measurement period, less than a $\pm 1\%$ spatial variation in irradiance in and several cm above the test plane, and introduce less than a 1% spectral mismatch error between the test and reference cell. These constraints are essential to ensure an uncertainty in the efficiency of less than $\pm 2\%$. Solar simulators are classified according to the spatial nonuniformity of the total irradiance, temporal instability of irradiance, total irradiance within a given field of view, and spectral match to the reference spectrum [134, 135]. Groups that evaluate multijunction cells and modules have found that single-source simulators can introduce large errors in I_{SC} , and P_{max} . Multisource solar simulators suitable for evaluating reference cells have been discussed in Section 16.3.6 [108–118, 136].

The temporal variation in light level during the $I-V$ measurement can be corrected if the intensity and device current are measured at the same time for each $I-V$ data point. Most commercial and custom $I-V$ systems for continuous light sources do not correct this temporal variation in the light level, although most groups have procedures in place to correct long-term drift in the simulator total irradiance over a period of hours or longer. The spatial uniformity varying with time for arc lamps cannot be readily

corrected, although placing the intensity monitor as close to the test device as possible can minimize these effects. A spatially nonuniform light source presents a measurement challenge of determining the average illumination level for a cell or the illumination level of the current-limiting cell in a module [126, 137]. The efficiency will always be reduced for nonuniform illumination compared to uniform illumination at the cell [138, 139] or module [140] level.

There are three types of illumination sources typically used for solar simulators: continuous arc, pulsed arc, and filament lamps. The merits and problems of these different simulators have been compared [28, 141–143]. If the distance between the test plane and the nearest optical surface is short, the possibility for reflection-related artifacts may exist [141]. These reflection-related artifacts occur because the field of view of the reference cell and test device are not identical and can occur from reflections off simulator optics, reference cell packages, probe fixtures, the test station enclosure, and the region underneath the test device. Light reflecting from the region under the test device is especially important for bifacial cells and superstrate structures.

With proprietary filters, commercial continuous Xe-arc lamp solar simulators have an excellent spectral match to the AM0 or terrestrial spectrum, and their point source (small arc volume) with integrating optics achieves a ± 1 to $\pm 3\%$ variation in spatial uniformity. The spectrum of these lamps shifts slightly from the blue to the red during the bulb life, with most of the spectral shift occurring in the first 100 h of operation [141]. The intensity of continuous arc lamps is controlled by changing the distance from the lamp to the test plane or by changing the current. Pulsed simulators are especially useful for characterizing concentrator cells and for large-area modules. The intensity of pulsed Xe-arc light sources is adjusted by changing the distance from the lamp to the test plane, by adjusting an aperture near the flash lamp, or by changing the voltage at which the lamp flashes. The spectrum of pulsed lamps shifts from the blue to the red less with the number of flashes of the lamp and is difficult to quantify because of the difficulty in measuring the spectral irradiance of pulsed light sources. The spectral match of unfiltered arc lamps in the UV and visible region is excellent but poor in the red (> 700 nm) because of the numerous Xe emission lines. Custom filters reduce the magnitude of these lines to manageable levels. These emission lines are reduced for pulsed-Xe lamps.

The least expensive small-area light source is a tungsten-halogen lamp with a dichroic filter. These lamps are ideal for quantum efficiency measurements because of their irradiance temporal stability. The lamp spectrum depends strongly on the operating voltage or current [138]. A shift in the spectrum with bulb age has been attributed to tungsten-halogen lamps, but a careful study revealed that although the intensity drops with bulb age at a constant current, the shift with bulb age is less than the variation from bulb to bulb out of the same case [141]. To minimize spectral shifts of filament light sources with bulb age, they should be run at the same current throughout their life. The distance between the bulb and test plane should be varied to maintain the proper light level. There are a wide variety of tungsten-halogen bulbs with different wattage, lifetime, and voltage ratings. The choice of the most appropriate bulb is a compromise; for example, the ELH bulb has one of the highest wattages, but operates at 120 V and has a short lifetime of 35 h. Low-voltage bulbs such as the HLX, ELC, or HMM operate below 40 V, eliminating the safety hazard of higher voltage bulbs, and they have a longer life but a lower wattage. As with continuous arc lamps, the lamp lifetime is reduced by

frequently turning the lamp on and off. At least one module manufacturer uses an array of tungsten-halogen bulbs for production testing of modules in their multi-megawatt plant. They operate the bulbs at a low “simmer” voltage between $I-V$ measurements to greatly increase the lifetime of the bulbs. They use “matched” reference cells to minimize their sensitivity to spectral errors. The spectral irradiance of filament lamps is characterized by a black-body spectrum of 3200 to 3450 K. These lamps are deficient in the blue region of the solar spectrum because the AM0 spectrum can be approximated as a 5900 K black body.

16.4 SPECTRAL RESPONSIVITY MEASUREMENTS

The spectral responsivity ($S(\lambda)$) or quantum efficiency ($QE(\lambda)$) is essential for understanding current generation, recombination, and diffusion mechanisms in photovoltaic devices. PV cell and module calibrations often require a spectral correction factor that uses the spectral responsivity (i.e. equations 16.16–16.22). The spectral responsivity is measured in units of current produced per unit power and can be converted to quantum yield, or electron–hole pairs produced per incident photon through the equation:

$$QE(\lambda) = \frac{qS(\lambda)}{\lambda hc} \quad (16.33)$$

The factor hc/q equals 0.80655 for the wavelength in units of μm and the spectral responsivity in units of A/W. The quantum yield, in units of electron per photon, is often multiplied by 100, giving the quantum efficiency.

Typically, the spectral responsivity is measured at short-circuit current because it is easy to define and usually is the same as the photocurrent except for cells exhibiting voltage-dependent current collection like a-Si devices. PV devices normally operate near their maximum-power point. The spectral responsivity is assumed to be the same at the maximum-power and short-circuit points. Voltage-dependent spectral responsivities have been reported for a-Si [144], CdTe [145], and Cu(Ga,In)(S,Se) [146] material systems. (See Chapters 12, 13, and 14 for further discussion of voltage dependent collection in these types of devices).

The PV community has designed a variety of spectral response measurement systems, including ones based on interference filters, grating monochrometers, and interferometers [74, 77, 80, 81, 147–154]. For a single-junction solar cell, $S(\lambda)$ is determined by illuminating the cell with periodic (i.e. “chopped”) monochromatic light and continuous broadband bias light of much greater intensity. The AC photocurrent from the device due to periodic monochromatic light is converted to an AC voltage and measured with a lock-in amplifier. An AC voltmeter may be used instead of a lock-in amplifier if the AC signal is large compared to the AC noise. The measured photocurrent is often in the μA to mA range with a broadband DC bias light near the device’s intended operating point, for example, 1 sun.

For a two-terminal multijunction device, measuring the spectral responsivity of the individual junctions requires that the junction to be measured is the one which actually determines the photocurrent through the device (e.g. is the current-limiting junction).

Limiting the current is normally achieved by illuminating the other junctions *not* being measured with a DC bias light whose spectral irradiance covers their response range [154]. To measure $S(\lambda)$ for the *top* cell in a two-junction device, the bottom cell must be illuminated with “red” light that is absorbed mostly in the bottom cell. To measure $S(\lambda)$ for the *bottom* cell in a two-junction device, the top cell must be illuminated with “blue” light that is absorbed mostly in the top cell. In practice, the intensity of the bias light is increased until $S(\lambda)$ for the junction being measured is a maximum and $S(\lambda)$ values for the other junctions are minima. If the multijunction device terminals are at zero volts, then the cell being measured is at some reverse-bias voltage since the other junction is forward-biased owing to the bias light [154]. Because $S(\lambda)$ can depend on voltage, the cell being measured should be at zero volts, [154] which is accomplished by forward-biasing the multijunction cell. If each junction of a two-terminal device has about the same V_{OC} , then the cell should be forward-biased to half the V_{OC} of the tandem cell. In practice, the V_{OC} of the individual junctions is not well known; therefore, the forward-bias voltage must be adjusted to maximize the $S(\lambda)$ of the cell being measured and to minimize the $S(\lambda)$ of the other junctions. In practice, for an unknown multijunction device the procedure of increasing the bias light intensity and adjusting the bias voltage to maximize $S(\lambda)$ of the cell being measured while minimizing $S(\lambda)$ of the other junctions is an iterative process.

16.4.1 Filter-based Systems

A filter-based spectral responsivity $S(\lambda)$ measurement system is characterized by shining broadband light through interference filters and directing the light to the device under test, as shown in Figure 16.9 [147]. The filter wheel can be rotated with stepping solenoids controlled by digital logic or stepper motors. The use of the shutter shown in Figure 16.9 is essential when using an AC voltmeter to measure the signal when no monochromatic light is incident on the sample; it is less important though when using a lock-in amplifier to measure the periodic monochromatic signal. The monochromatic beam power is measured with a pyroelectric radiometer and calibrated Si detector. The reference detector can measure the power real time or the power versus wavelength data can be stored in a file. The advantage of real-time calibrations is that intensity fluctuations in the monochromatic beam can be corrected. The advantage of a stored calibration file is that the measured power is much higher, minimizing sensitivity to background light, and polarization effects associated with a beam splitter are not present.

It is often desirable to measure $S(\lambda)$ of modules consisting of multiple cells in series. The simplest approach would be to illuminate the whole module with AC monochromatic and AC broadband light with the module at 0 V, just as in the case of cells. Because of their high monochromatic light power density and large-beam area, filter-based $S(\lambda)$ systems are capable of fully illuminating any commercial module. The problem with this method is that different cells may be current limiting at various wavelengths, and the bias point of the current-limiting cell whose $S(\lambda)$ is being measured is not at 0 V. This problem is solved by voltage biasing, similar to the multijunction $S(\lambda)$ measurements [104, 154]. Figure 16.10 illustrates the geometry for measuring the spectral responsivity of an individual cell in a packaged module in which the individual cells are inaccessible.

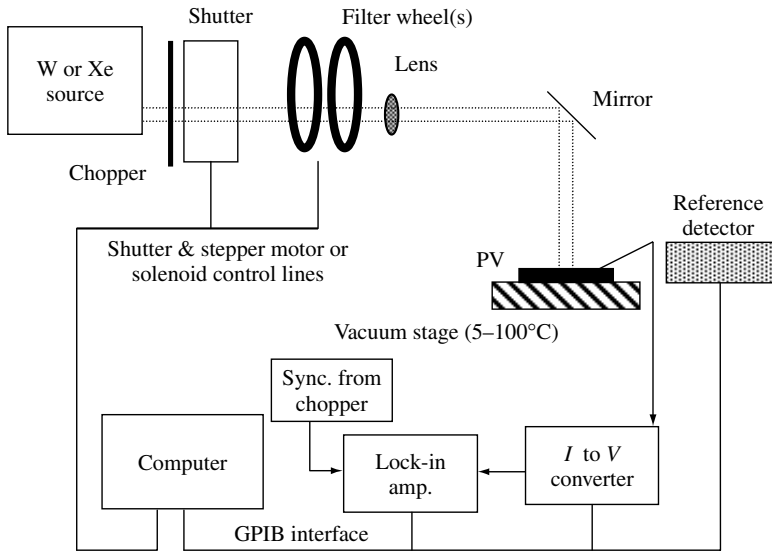


Figure 16.9 Typical narrow-band interference filter-based spectral responsivity measurement system

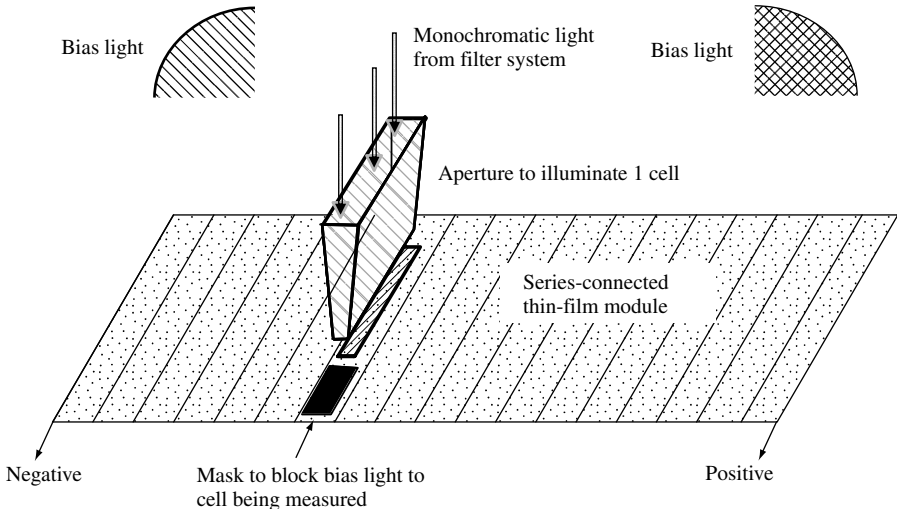


Figure 16.10 Apparatus for measuring the spectral responsivity of a single cell in a multicell module

The solution to the problem of measuring $S(\lambda)$ of a single cell in a module is the following sequence of steps [147]:

1. Bias the module with light to simulate “1 sun.”
2. Forward-bias the module to the measured module open-circuit voltage (V_{OC}) under the bias light in the previous step multiplied by $(n - 1)/n$, where n is the number of cells in series. Another procedure is to apply monochromatic light at a wavelength that the

in the 300- to 600-nm wavelength region to suppress modes at longer wavelengths and shorter wavelengths (e.g. $\frac{1}{2}\lambda$ and 2λ). The light power of the grating-monochrometer-based system can be focused on a rectangular spot of about 1 mm by 3 mm by imaging the monochrometer exit slits onto the test plane with a magnification of less than 1. Chromatic aberrations in the lens(es) cause the beam size to change with wavelength. This effect can be eliminated by eliminating all lenses and using a spherical or, better yet, a parabolic mirror. Typically, grating-based systems have lower optical throughput (lower intensity) but higher spectral resolution than filter-based systems.

16.4.3 Spectral Responsivity Measurement Uncertainty

Spectral responsivity measurements involve the measurement of the photocurrent produced by light of a given wavelength and power. The spectral responsivity is typically measured with bias light simulating reference conditions, because the device may be nonlinear [74, 77, 80, 81, 147–151, 154]. Typically, the spectral correction factor for efficiency measurements is calculated on the basis of $S(\lambda)$ measurements near 0 V and is assumed to be the same as at the maximum-power point. This assumption is valid for most PV systems and results in a negligible error for amorphous silicon, which has a voltage-dependent spectral responsivity [144, 155] assuming a reasonably well-matched reference cell is used such as a Schott KG5 filtered mono-Si cell.

The photocurrent is measured with a current-to-voltage converter. A power operational amplifier (± 40 V, 8 A) with computer-controlled gain resistors (50 to 10 000 Ω) is useful for wide bias ranges and signal levels [147]. A simple current sense resistor may be adequate for systems that measure the same type of PV device all the time. The major limitation is that resistor and thermal noise at the microvolt level limits the measured currents to microamperes. Commercial current preamplifiers typically have a maximum current rating of 1 to 10 mA, limiting their usefulness for measuring the spectral responsivity with bias light (i.e. a 1 cm^2 device with $J_{\text{SC}} = 30 \text{ mA cm}^{-2}$ produces 30 mA of DC bias current with a 1 sun bias light). An operational amplifier configured as a current-to-voltage converter allows the insertion of a power supply in series with the PV device, giving a wide range of bias voltages. This feature is critical when measuring modules, multijunction devices, or devices with a voltage-dependent spectral responsivity [105, 147, 153]. Most groups use a lock-in amplifier to detect the periodic AC signal, but this is not required because the intense monochromatic light afforded with interference filters allows the AC signal to be amplified to the range where AC voltmeters are quite accurate [155]. Modern digital lock-in amplifiers have rapid auto-ranging capabilities and will outperform an AC voltmeter for noisy signals because of their large dynamic range. Error sources related to the measurement of the photocurrent are summarized in Table 16.7. If semiconductor-based calibrations are employed with the same electronics used to measure the test and reference device, then all multiplicative errors drop out. For pyroelectric-radiometer-based calibrations, the absolute photocurrent must be measured for absolute $S(\lambda)$ measurements.

For absolute current measurements, the measured lock-in signal must be multiplied by a waveform correction factor that relates the measured root-mean-square (RMS) signal

Table 16.7 Spectral responsivity error sources for measurement of the photocurrent

-
- I. Electrical instrumentation
 - A. Current-to-voltage (I to V) converter
 - 1. Commercial current amplifier, lock-in amplifier or custom amplifier gain, linearity, noise, offset, shunt resistor, calibration, drift, thermovoltages
 - B. Signal from I to V converter measured with the following:
 - 1. Lock-in amplifier calibration, resolution, accuracy, waveform to sine wave correction factor, overloading, noise, dynamic range, time-constant, procedures for using lock-in amplifier
 - 2. An AC voltmeter gain, offset from noise level, linearity, time-constant
 - II. PV cell or module
 - A. Temperature, response time to periodic light, linearity of PV device, white-light bias spatial uniformity, monochromatic light spatial uniformity, voltage bias of cell being measured, spectral content of bias light, device sensitivity to polarization of light
 - III. Mechanical
 - A. Mechanical movement of optics, mechanical vibration, monochromatic beam wandering with wavelength, chopped stray monochromatic light
-

with the peak signal. This factor is $\sqrt{2}/2$ for a sine wave, $2\sqrt{2}$ for a square wave, and $2\sqrt{2} a \sin(\pi/a)/\pi^2$ for a trapezoid, with the constant π/a being the radian angle at the top of the rising edge of the trapezoidal waveform [156].

The response time of PV devices to chopped light can be a problem for electrochemical cells or those cells with many deep-level recombination centers. Many systems operate with chopping frequencies of 71–93 Hz as a compromise between stability, noise, and deep level response. Chopping frequencies below 4 Hz are required to keep the AC photoresponse independent of frequency [157]. This effect is more pronounced at low light levels and in the infrared. It is important that the light from the bias light source not be allowed to go through the light chopper. A simple procedure to determine if this artifact is present is to turn off the monochromatic light source and measure the test device's response as a function of bias light intensity.

Semiconductor-based calibrations are useful where the photocurrent is known within a multiplicative constant. Their primary limitation is their temperature sensitivity near the energy gap (wavelengths greater than 900 nm for Si) and their limited response range. Calibrated semiconductors are not commercially available for wavelength ranges beyond 300 to 1700 nm (Si-Ge hybrid detector). Accurate calibrations for semiconductor-based detectors are difficult to obtain for wavelengths greater than 1800 nm. If the same amplifier is used to measure the reference and unknown PV devices, then uncertainties in the gain drop out. For semiconductor calibrations, the chopper phase is irrelevant, whereas the electrically calibrated pyroelectric radiometer requires that the chopper be manually adjusted until the phase is correct. Semiconductor-based calibrations allow the test and reference signals to be filtered independently to maximize the signal-to-noise ratio. Various error sources associated with measuring the monochromatic light power are listed in Table 16.8. The measurement of the monochromatic light power can be performed with radiometric detectors or semiconductor detectors. When a quartz slide is used as the beam splitter, errors in the power can arise because of polarization effects. The light off the monochromator is polarized, and the polarization angle can change with a grating change. The band gap, photoluminescence, and

Table 16.8 Spectral responsivity error sources for measurement of the light power

-
- I. Filament or Xe-arc light source
 - A. Intensity fluctuations, change in spectrum with age and current,
 - II. Real-time calibration
 - A. Source-light polarization with a glass beam splitter, signal to noise, detector characteristics, calibration drift with time of monitor detector
 - III. Stored calibration file
 - A. Monochromatic source calibration drift with time
 - IV. Stray light
 - A. Detector sees light that cell does not see, area of detector different from device area, different field of views
 - B. Monochromator – incomplete attenuation of higher and lower grating orders, single versus double grating
 - C. Narrow bandwidth filters – pinholes in the filter, degradation of blocking filter, insufficient blocking of light ($>10^{-4}$)
 - V. Detectors and associated electronics in general
 - A. Calibration, resolution, accuracy, gain, phase, offset, linearity, spatial uniformity of detector element,
 - B. Drift in temperature of room, change in the detector's field of view, degradation of detector,
 - C. Spectral response of detector
 - VI. Pyroelectric detector
 - A. Time constant of detector, microphonics, signal to noise, phase-angle adjustment, waveform factor (square wave assumed)
-

absorption coefficient for PV devices can be sensitive to the polarization angle. The light reflected from a glass surface will have a different polarization than the light reaching the test plane and will be of much lower intensity. These effects are minimized if a calibration is performed with the detector in the test plane and the file is stored to the disk. This procedure is required at least once for real-time calibrations. Real-time calibrations account for the change in spectrum with lamp age, current, and time.

If the beam is larger than the sample, then the spatial uniformity of the monochromatic beam is important. For the NREL filter monochromator system, spatial nonuniformities of $\pm 10\%$ are typical and, more importantly, these errors can change with wavelength because of variations in the transmission of the filter and spatial variation in the output of the Xe-arc lamp. Electrically calibrated pyroelectric detectors are spectrally flat from the UV to far-infrared and have a low broadband error of less than $\pm 2\%$, but are sensitive to microphonics, temperature changes within the detector's field of view, and have noise at the $0.01 \mu\text{Wcm}^{-2}$ level. Semiconductor-based detectors are not sensitive to light outside their relatively narrow response range and can be measured with the same electronics used to measure the test device, eliminating any wavelength-independent multiplicative error sources. Semiconductor-based detectors can drift with age [158] and have temperature coefficients exceeding $1\%/^{\circ}\text{C}$ near their band gap. Table 16.9 summarizes the error in the QE that can occur because of the monochromatic light. The bandwidth of the monochromatic light can contribute to the error near the band gap or when the light transmitted through a band-pass filter is highly asymmetric [156]. These errors have a small effect on the spectral correction factor when the full width at half-maximum bandwidth of the interference filters are less than 10 nm [156], as is commonly found in practice.

Table 16.9 Spectral responsivity error sources related to the monochromatic light

-
- I. Bandwidth, filter defects, polarization variation with wavelength
 - II. Wavelength offset, wavelength error, wavelength variation with room temperature
 - III. Beam wanders with wavelength
 - IV. Beam larger than the test device
 - A. Detector area versus PV area, position of detector and PV different, spatial uniformity of beam
 - V. Beam smaller than detector and device area
 - A. Partially shaded regions, spatial variation in responsivity of PV
-

16.5 MODULE QUALIFICATION AND CERTIFICATION

PV modules are designed to last 20 years or more in the field with no maintenance. Modules are designed to withstand daily thermal cycling, hail, wind, sand and storms, along with prolonged exposure to UV light. For safety reasons, PV cells and wiring must be isolated from the frame, edges, or module surface to prevent a hazardous electrical potential from forming. To verify that a particular product is reliable, domestic and international consensus standards have been developed for the design qualification and type approval of terrestrial crystalline silicon and thin-film modules [159–162].

Ideally, modules should be subjected to long-term exposure under natural conditions. Flat-plate silicon PV modules had poor reliability in the first years of development. An extensive program was conducted in the late 1970s and early 1980s by the JPL for the US government in an effort to improve the reliability of PV modules [163]. The 13 principal flat-plate module degradation mechanisms are open-circuited cell regions, shorted cells, open-circuited interconnects, gradual cell power degradation, optical degradation of the module package, front-surface soiling, glass breakage, open circuits in the module wiring, hot-spot failures of cells in a module, shorted bypass diodes, shorts to the frame or ground, delamination of the module encapsulant, and life-limiting wear out [163].

Accelerated testing procedures have been developed to simulate 20 or more years of exposure in the field and to identify the major failure mechanisms. Accelerated tests have been developed by various governmental organizations such as ASTM [161] or the Commission of European Communities [162, 164–166]. The tests described are from the International Electrotechnical Commission, the international standards organization relevant for photovoltaics [159, 163]. These tests include safety tests, mechanical integrity tests, and thermal cycling. The thermal-cycle test determines the ability of a module to withstand thermal expansion coefficient mismatch, fatigue, and other stresses caused by repeated changes in temperature, and it includes 200 thermal cycles from -40°C to $+85^{\circ}\text{C}$. The damp-heat test, designed to determine the module's ability to withstand the effects of long-term exposure to moisture in high-humidity environments, consists of 1000 h at 85% relative humidity at 85°C . The humidity-freeze test determines the ability of the module to withstand the effects of high temperature and humidity followed by subzero temperatures, and it consists of 10 cycles from 85% relative humidity and 85°C to -40°C . This is not a thermal-shock test because the maximum change in temperature with time above freezing temperatures is $100^{\circ}\text{C h}^{-1}$. This humidity-freeze test reveals the detrimental accumulation of liquid water inside the module under high-humidity

conditions. Because modules can have a substantially inferior performance under low light levels when they have a low shunt resistance, modules are tested at an irradiance of 200 Wm^{-2} (~only 20% of 1 sun). Modules exposed outdoors under short circuit conditions to 60 kWh m^{-2} of total solar irradiation are required to sustain a loss in power of less than 5% to reveal any synergistic degradation effects that may not be detected by other tests. The hot-spot test is designed to ensure that modules will not fail when hot spots occur because of mismatched cells, partial shading, or interconnect failures. A hot spot is a localized region in a module that is operating at a significantly higher temperature ($\sim 5\text{--}40^\circ\text{C}$) than the rest of the module. The hot-spot test consists of five 1-h exposures at 1000 Wm^{-2} irradiance under the worst-case hot-spot condition. The modules must also survive a hail test of 25-mm-diameter ice balls directed at 11 impact locations with a velocity of 23 ms^{-1} [159, 163]. Modules are also subjected to a twist test to detect module defects that might arise when the module is mounted on a nonplanar surface. The twist test consists of supporting the module on three of its corners and deflecting the fourth corner 1.2° with respect to the plane defined by the other three corners [159, 160]. Modules are also expected to withstand wind, snow, or ice loads without mechanical or electrical failure. The static-load test simulates a wind load of 130 km h^{-1} , with a safety factor of 3, and consists of mounting the module in the manner prescribed by the manufacturer and applying a force of 2400 Pa uniformly to the front surface for 1 h and then the rear surface for 1 h. The insulation test is a safety test designed to determine if the current-carrying parts of the module are sufficiently well isolated from the module edges or frame and requires a resistance of greater than $50 \text{ M}\Omega$ at 500 V DC resistance to ground, and less than $50 \mu\text{A}$ current to ground at an applied voltage of 1000 V plus twice the maximum system voltage [159, 160]. For frameless modules, ground is obtained by attaching a metal conductor to the outside perimeter. The wet-leakage-current test is a stringent safety test to ensure that the current-carrying parts are well isolated, preventing a ground-fault condition from occurring even when the module is wet. The wet-leakage test is also designed to verify that moisture does not enter the active part of the module, where it might cause delamination or corrosion. The module is placed in a tank of water with resistivity of $3500 \Omega\text{-cm}$ or less at $22^\circ\text{C} \pm 3^\circ\text{C}$ and a surface tension less than 3 Nm^{-2} and the leakage current at 500 V is measured. The maximum allowed leakage current for the wet-leakage test (sometimes called the wet hi-pot test) is $10 \mu\text{A}$ plus $5 \mu\text{A}$ times the surface area in m^2 . The wet-leakage test is performed before and after the various stress tests. The number of modules, sequence of events, and the pass/fail criteria are specified in the standard documents [156, 157]. Thin-film module testing procedures also require the $I\text{--}V$ characteristics under SRC to be measured periodically during light exposure (between $800\text{--}1000 \text{ Wm}^{-2}$, between $40\text{--}50^\circ\text{C}$) until the module power changes by less than 2% over 3 consecutive periods of at least 48 h [160, 166].

ACKNOWLEDGEMENTS

This work was supported in part under DOE Contract DE-AC36-99GO10337. The authors also wish to acknowledge the support of the National Center for Photovoltaics (www.nrel.gov/ncpv/) and the Measurements and Characterization Division (www.nrel.gov/measurements/). The assistance of D. Gwinner for editing is acknowledged.

REFERENCES

1. Emery K, Osterwald C, *Sol. Cells* **17**, 253–274 (1986).
2. Emery K, Osterwald C, *Current Topics in Photovoltaics*, Vol. 3, Chap. 4 Academic Press, London (1988).
3. Heidler K, Raicu A, Wilson H, *Proc. 21st IEEE Photovoltaic Specialist Conf.*, 1017–1022 (1990).
4. Nann S, Emery K, *Sol. Energy Mater.* **27**, 189–216 (1992).
5. Terrestrial Photovoltaic Measurement Procedures, NASA Tech. Report TM 73702 (June 1977).
6. Standard ASTM E948, *Standard Test Method for Electrical Performance of Non-Concentrator Photovoltaic Cells Using Reference Cells*, American Society for Testing and Materials, West Conshocken, PA, USA.
7. Standard ASTM E1036, *Standard Test Methods for Electrical Performance of Nonconcentrator Terrestrial Photovoltaic Modules and Arrays Using Reference Cells*, American Society for Testing and Materials, West Conshocken, PA, USA.
8. Standard ASTM E490-2000, *Standard for Solar Constant and Air Mass Zero Solar Spectral Irradiance Tables*, American Society for Testing and Materials, West Conshocken, PA, USA.
9. Standard Commission of the European Community, CEC 101, Issue 2, EUR-7078 EN, *Standard Procedures for Terrestrial Photovoltaic Measurements* (1981).
10. Standard ASTM E891-92, *Standard for Terrestrial Solar Direct Normal Solar Spectral Irradiance Tables for Air Mass 1.5*, American Society for Testing and Materials, West Conshocken, PA, USA.
11. Standard IEC 60904-1, *Photovoltaic Devices Part 1: Measurement of Photovoltaic Current-Voltage Characteristics*, International Electrotechnical Commission, Geneva, Switzerland.
12. Standard ASTM E892-92, *Standard for Terrestrial Solar Spectral Irradiance Tables at Air Mass 1.5 for a 37° Tilted Surface*, American Society for Testing and Materials, West Conshocken PA, USA.
13. Standard IEC 60904-3, *Measurement Principles for Terrestrial PV Solar Devices with Reference Spectral Irradiance Data*, International Electrotechnical Commission, Geneva, Switzerland.
14. Wehrli C, *Extraterrestrial Solar Spectrum*, Tech. Report 615, Physikalisch-Meteorologisches Observatorium and World Radiation Center, Davos-Dorf, Switzerland (July 1985).
15. ISO/DIS 15387, draft standard Space Systems – Single-Junction Space Solar Cells – Measurement and Calibration Procedures, International Organization for Standardization, Geneva, Switzerland.
16. *Solar Cell Array Design Handbook*, Tech. Report SP 43-38, Jet Propulsion Laboratory, Vol. 1, Pasadena, CA, USA (Oct. 1976).
17. Bird R, Hulstrom R, Riordan C, *Sol. Cells* **14**, 193–195 (1985).
18. Bird R, Hulstrom R, Lewis L, *Sol. Energy* **39**, 563–573 (1983).
19. Kurtz S *et al.*, *Sol. Energy Mater. Sol. Cells* **62**, 379–391 (2000).
20. Myers D *et al.*, *Proc. 28th IEEE Photovoltaic Specialist Conf.*, 1202–1205 (2000).
21. Osterwald C, *Proc. 18th IEEE Photovoltaic Specialist Conf.*, 951–956 (1985).
22. Emery K, Myers D, Kurtz S, *Proc. 29th IEEE Photovoltaic Specialist Conf.*, 840–843 (2002).
23. Faine P, Kurtz S, Riordan C, Olson J, *Sol. Cells* **312**, 259–278 (1991).
24. Standard ASTM Standard E490-73, *Standard for Solar Constant and Air Mass Zero Solar Spectral Irradiance Tables*, American Society for Testing and Materials, West Conshocken, PA, USA.
25. Makarova Y, Kharitonov A, *Distribution of Energy in the Solar Spectrum*, translated from Russian in NASA Tech. Report TT F-803 (June 1974).
26. Fröhlich C, Lean J, “Total Solar Irradiance Variations: The Construction of a Composite and its Comparison with Models”, *Int. Astronomical Union Symp. 185: New Eyes to See Inside the Sun and Stars*, 89–102, Kluwer Academic Publishers, Dordrecht, The Netherlands (1998).

27. Standard ASTM E1328, *Standard Terminology Relating to Photovoltaic Solar Energy Conversion*, American Society for Testing and Materials, West Conshocken, PA, USA.
28. Emery K, *Sol. Cells* **18**, 251–260 (1986).
29. Emery K, Field H, *Proc. 24th IEEE Photovoltaic Specialist Conf.*, 1833–1838 (1994).
30. Green M *et al.*, *Prog. Photovolt.* **9**, 49–56 (2001).
31. Firor K, *Proc. 18th IEEE Photovoltaic Specialist Conf.*, 1443–1448 (1985).
32. Jennings C, *Proc. 19th IEEE Photovoltaic Specialist Conf.*, 1257–1260 (1987).
33. Taylor R, *Sol. Cells* **18**, 335–344 (1986).
34. Fuentes M, *A Simplified Thermal Model for Flat-Plate Photovoltaic Arrays*, Sandia Tech. Report Sand 85–0330 (May 1987).
35. Koltay P, Wenk J, Bücher K, *Proc. 2nd World Conf. Photovoltaic Solar Energy Conversion*, 2334–2337 (1998).
36. Fisher H, Pschunder W, *Proc. 10th IEEE Photovoltaic Specialist Conf.*, 404–411 (1973).
37. DeWolf S *et al.*, *Proc. 28th IEEE Photovoltaic Specialist Conf.*, 53–56 (2000).
38. Luft W *et al.*, *Proc. 22nd IEEE Photovoltaic Specialist Conf.*, 1393–1398 (1991).
39. Luft W, von Roedern B, *Proc. 24th IEEE Photovoltaic Specialist Conf.*, 850–853 (1994).
40. DelCueto J, von Roedern B, *Prog. Photovolt.* **7**, 101–112 (1999).
41. Meyer T *et al.*, *Proc. 26th IEEE Photovoltaic Specialist Conf.*, 371–374 (1997).
42. Ruberto M, Rothwarf A, *J. Appl. Phys.* **61**, 4662–4669 (1987).
43. Hester S, Townsend T, Clements W, Stolte W, *Proc. 21st IEEE Photovoltaic Specialist Conf.*, 937–943 (1990).
44. Gay C, Rumburg J, Wilson J, *Proc. 16th IEEE Photovoltaic Specialist Conf.*, 1041–1046 (1982).
45. Gianoli-Rossi E, Krebs K, *Proc. 8th Euro. Conf. Photovoltaic Solar Energy Conversion*, 509–514 (1988).
46. Kroposki B *et al.*, *Proc. 25th IEEE Photovoltaic Specialist Conf.*, 1311–1314 (1996).
47. Kroposki B *et al.*, *Proc. 28th IEEE Photovoltaic Specialist Conf.*, 1407–1411 (2000).
48. Whitaker C *et al.*, *Proc. 26th IEEE Photovoltaic Specialist Conf.*, 1253–1256 (1997).
49. Marion B *et al.*, *Validation of a Photovoltaic Module Energy Ratings Procedure at NREL*, NREL Tech. Report NREL/TP-520-26909 (Aug. 1999).
50. Marion W, Urban K, *User's Manual for TMY2s (Typical Meteorological Years) - Derived from the 1961–1990 National Solar Radiation Data Base*, NTIS/GPO Number: DE95004064, NREL Tech. Report TP-463-7688 (1995).
51. Nann S, Riordan C, *J. Appl. Met.* **30**, 447–462 (1991).
52. Raicu A, Heidler K, Kleiss G, Bücher K, *Proc. 11th Euro. Conf. Photovoltaic Solar Energy Conversion*, 1323–1326 (1992).
53. Raicu A, Heidler K, Kleiss G, Bücher K, *Proc. 22nd IEEE Photovoltaic Specialist Conf.*, 744–749 (1991).
54. Bücher K, *Proc. 23rd IEEE Photovoltaic Specialist Conf.*, 1056–1062 (1993).
55. King D, Dudley J, Boyson W, *Proc. 26th IEEE Photovoltaic Specialist Conf.*, 1295–1297 (1997).
56. Green M, *Solar Cells Operating Principles, Technology and System Application*, University of New South Wales, Kensington, Australia (1992).
57. Emery K *et al.*, *Proc. 25th IEEE Photovoltaic Specialist Conf.*, 741–744 (1996).
58. Osterwald C, Glatfelter T, Burdick J, *Proc. 19th IEEE Photovoltaic Specialist Conf.*, 188–193 (1987).
59. Kameda M *et al.*, *Proc. 25th IEEE Photovoltaic Specialist Conf.*, 1049–1052 (1996).
60. Hishikawa Y, Okamoto S, *Sol. Energy Mater. Sol. Cells* **33**, 157–168 (1994).
61. Sandstrom J, *A Method for Predicting Solar cell Current-Versus Voltage Characteristics as a Function of Solar Intensity and Cell Temperature*, JPL Tech. Report TR 32–1142, Jet Propulsion Laboratory, Pasadena, CA, USA (July 1967).

62. Standard IEC 60891, *Procedures for Temperature and Irradiance Corrections to Measured I-V Characteristics of Crystalline Silicon Photovoltaic Devices*, International Electrotechnical Commission, Geneva, Switzerland.
63. King D, Kratochvil J, Boyson W, Bower W, *Proc. 2nd World Conf. Photovoltaic Solar Energy Conversion*, 1947–1952 (1998).
64. Kasten F, Young A, *Appl. Opt.* **28**, 4735–4738 (1989).
65. Hishikawa Y, Imura Y, Oshiro T, *Proc. 28th IEEE*, 1464–1467 (2000).
66. Emery K *et al.*, *Proc. 18th IEEE Photovoltaic Specialist Conf.*, 623–628 (1985).
67. Emery K, Osterwald C, *Sol. Cells* **27**, 445–453 (1989).
68. Field H, Emery K, *Proc. 23rd IEEE Photovoltaic Specialist Conf.*, 1180–1187 (1993).
69. Shimokawa R *et al.*, *Sol. Cells* **19**, 59–72 (1987).
70. Emery K *et al.*, *SERI Results from the PEP 1987 Summit Round Robin and a Comparison of Photovoltaic Calibration Methods*, NREL Tech. Report TR-213-3472 (March 1989).
71. Myers D, Emery K, Stoffel T, *Sol. Cells* **27**, 455–464 (1989).
72. Standard ASTM E1040, *Standard Specification for Physical Characteristics of Nonconcentrator Terrestrial Photovoltaic Reference Cells*, American Society for Testing and Materials, West Conshocken, PA, USA.
73. Standard IEC 60904-2, *Requirements for Reference Cells*, International Electrotechnical Commission, Geneva, Switzerland.
74. Osterwald C *et al.*, *Proc. 26th IEEE Photovoltaic Specialist Conf.*, 1209–1212 (1997) also *Results of the PEP'93 Intercomparison of Reference Cell Calibrations and Newer Technology Performance Measurements: Final Report*, NREL Tech. Report NREL/TP-520-23477 (March 1998).
75. Osterwald C *et al.*, *Prog. Photovolt.* **7**, 287–297 (1999).
76. Shimokawa R *et al.*, *Jpn. J. Appl. Phys.* **28**, L845–L848 (1989).
77. Metzendorf J, *Appl. Opt.* **26**, 1701–1708 (1987).
78. Bruce S, *Optical Metrology and More*, NIST Tech. Report NISTIR 5429, U.S. Department of Commerce, National Institute of Standards and Technology, Gaithersburg, MD, USA (1994).
79. Allison J, Crab R, *Proc. 12th IEEE Photovoltaic Specialist Conf.*, 554–559 (1976).
80. Metzendorf J *et al.*, *Proc. 21st IEEE Photovoltaic Specialist Conf.*, 952–959 (1990), also *The Results of the PEP '87 Round-Robin Calibration of Reference Cells and Modules – Final Report*, PTB Tech. Report PTB-Opt-31, ISBN 3-89429-06706, Braunschweig, Germany (Nov. 1990).
81. Ossenbrink H, Van Steenwinkel R, Krebs K, *The Results of the 1984/1985 Round-Robin Calibration of Reference Solar Cells for the Summit Working Group on Technology, Growth and Employment*, Tech. Report EUR 10613 EN, Joint Research Center, ISPRA Establishment, ISPRA, Italy (April 1986).
82. Osterwald C, *Sol. Cells* **18**, 269–279 (1986).
83. Osterwald C, Emery K, *J. Atmos. Oceanic Technol.* **17**, 1171–1188 (2000).
84. Romero J, Fox N, Fröhlich C, *Metrologia* **32**, 523–524 (1995/1996).
85. Gomez T, Garcia L, Martinez G, *Proc. 28th IEEE Photovoltaic Specialist Conf.*, 1332–1335, (2000).
86. Osterwald C, Emery K, Myers D, Hart R, *Proc. 21st IEEE Photovoltaic Specialist Conf.*, 1062–1067 (1990).
87. Shimokawa R *et al.*, *Jpn. J. Appl. Phys.* **26**, 86–91 (1987).
88. King D, Hansen B, Jackson J, *Proc. 23rd IEEE Photovoltaic Specialist Conf.*, 1095–1101 (1993).
89. Bücher K *et al.*, *Proc. 23rd IEEE Photovoltaic Specialist Conf.*, 1188–1193 (1993).
90. Anspaugh B, Downing R, Sidwell L, *Solar Cell Calibration Facility Validation of Balloon Flight Data: a Comparison of Shuttle and Balloon Flight Results*, JPL Tech. Report 85-78, Jet Propulsion Laboratory, Pasadena, CA, USA (1985).
91. Anspaugh B, *Proc. 19th IEEE Photovoltaic Specialist Conf.*, 542–547 (1987).

92. Brandhorst H, *Appl. Opt.* **4**, 716–718 (1968).
93. Brandhorst H, *Proc. International Colloquium Organized by ECOSEC*, 565–574 in *Solar Cells* (1971).
94. Bücher K, *Prog. Photovolt.* **5**, 91–107 (1997).
95. Emery K, Osterwald C, Kazmerski L, Hart R, *Proc. 8th Photovoltaic Solar Energy Conversion*, 64–68 (1988c).
96. Jenkins P, Brinker D, Scheiman D, *Proc. 26th IEEE Photovoltaic Specialist Conf.*, 857–860 (1997).
97. Standard ANSI/ASME PTC 19.1, *Part 1: Measurement Uncertainty*, American Society for Mechanical Engineers, New York, USA (1985).
98. Emery K, Osterwald C, *Sol. Cells* **27**, 445–453 (1989).
99. Emery K, Osterwald C, Wells C, *Proc. 19th IEEE Photovoltaic Specialist Conf.*, 153–159 (1987).
100. Whitfield K, Osterwald C, *Prog. Photovolt.* **9**, 87–102 (2001).
101. ISO Guide to the Expression of Uncertainty in Measurement, International Organization for Standardization, Geneva, Switzerland, ISBN 92-67-10199-9 (1993).
102. Emery K, *The Results of the First World Photovoltaic Scale Recalibration*, NREL Tech. Report NREL/TP-520-27942 (March 2000.)
103. Treble F, Krebs K, *Proc. 15th IEEE Photovoltaic Specialist Conf.*, 205–210 (1981).
104. Friedman D, *Proc. 25th IEEE Photovoltaic Specialist Conf.*, 89–92 (1996).
105. Virshup G *et al.*, *Proc. 21st IEEE Photovoltaic Specialist Conf.*, 336–338 (1990).
106. Matsuda S, Flood D, Gomez T, Yiqiang Y, *Proc. 2nd World Conf. Photovoltaic Solar Energy Conversion*, 3572–3577 (1988).
107. Bogus K, Larue J, Masson J, Robben A, *Proc. 6th Euro. Conf. Photovoltaic Solar Energy Conversion*, 348–354 (1985).
108. Glatfelter T, Burdick J, Czubytyj W, *Proc. 2nd Photovoltaic Solar Energy Conversion*, 106–109 (1986).
109. Glatfelter T, Burdick J, *Proc. 19th IEEE Photovoltaic Specialist Conf.*, 1187–1193 (1987).
110. Virshup G, *Proc. 21st IEEE Photovoltaic Specialist Conf.*, 1249–1255 (1990).
111. Emery K *et al.*, *Proc. 28th IEEE Photovoltaic Specialist Conf.*, 1126–1130 (2000).
112. Bickler D, *Sol. Energy* **6**, 64–68 (1962).
113. Bennett M, Podlesny R, *Proc. 21st IEEE Photovoltaic Specialist Conf.*, 1438–1442 (1990).
114. Shimokawa R, Nagamine F, Hamyashi Y, *Jpn. J. Appl. Phys.* **25**, L165–L167 (1986).
115. Sopori B, Marshall C, Emery K, *Proc. 21st IEEE Photovoltaic Specialist Conf.*, 1116–1121 (1990).
116. Sopori B, Marshall C, *Proc. 22nd IEEE Photovoltaic Specialist Conf.* (1991).
117. Adelhelm R, Bücher K, *Sol. Energy Mater. Sol. Cells* **50**, 185–195 (1998).
118. Muesel M *et al.*, *Prog. in Photovolt.* **10**, 243–255 (2001).
119. Emery K, Osterwald C, *Proc. 21st IEEE Photovoltaic Specialist Conf.*, 1068–1073 (1990).
120. Schultz P, Meilus A, Hu S, Goradia C, *IEEE Trans. Inst. Meas.* **IM26**, 295–299 (1977).
121. Briskman R, Livingstone P, *Sol. Energy Mater. Sol. Cells* **46**, 187–199 (1997).
122. Cox C, Warner T, *Proc. 16th IEEE Photovoltaic Specialist Conf.*, 277–1283 (1982).
123. Skolnik H, *Sol. Energy* **14**, 43–54 (1972).
124. Kern R, Wagemann W, *Proc. 7th Euro. Conf. Photovoltaic Solar Energy Conversion*, 314–318 (1986).
125. Mantingh E, Zaaiman W, Ossenbrink H, *Proc. 24th IEEE Photovoltaic Specialist Conf.*, 871–873, (1994).
126. Heidler K, Fischer H, Kunzelmann S, *Proc. 9th Euro. Conf. Photovoltaic Solar Energy Conversion*, 791–794 (1989).
127. Moriarty T, Emery K, *Proc. 4th NREL TPV Conf.*, AIP Proceedings Vol. 460, 301–311 (1998).
128. Gee J, Hansen R, *Sol. Cells* **18**, 281–286 (1986).
129. Nasby R, Sanderson R, *Sol. Cells* **6**, 39–47 (1982).

130. Dondero R, Zirkle T, Backus C, *Proc. 18th IEEE Photovoltaic Specialist Conf.*, 1754–1755 (1985).
131. Martin S, Backus C, *Proc. 6th Euro. Conf. Photovoltaic Solar Energy Conversion*, 290–294 (1985).
132. Chambers B, Backus C, *Proc. 3rd Euro. Conf. Photovoltaic Solar Energy Conversion*, 418–422 (1980).
133. Stryi-Hipp G *et al.*, *Proc. 23rd IEEE Photovoltaic Specialist Conf.*, 303–308 (1993).
134. Standard ASTM E927, *Standard Specification for Solar Simulation for Terrestrial Photovoltaic Testing*, American Society for Testing and Materials, West Conshocken, PA, USA.
135. Standard International Electrotechnical Commission IEC 60904-9, *Solar Simulator Performance Requirements*, Geneva, Switzerland.
136. Krut D, Lovelady J, Cavicchi T, *Proc. 2nd World Conf. Photovoltaic Solar Energy Conversion*, 3671–3674 (1998).
137. Cuevas A, Lopez-Romero S, *Sol. Cells* **11**, 163–173 (1984).
138. Dhariwal S, Mathur R, Gadre R, *J. Phys. D: Appl. Phys.* **14**, 1325–1329 (1981).
139. Schönecker A, Bücher K, *Proc. 22nd IEEE Photovoltaic Specialist Conf.*, 203–208 (1991).
140. King D, Dudley J, Boyson W, *Proc. 25th IEEE Photovoltaic Specialist Conf.*, 1295–1297, (1996).
141. Emery K, Myers D, Rummel S, *Proc. 20th IEEE Photovoltaic Specialist Conf.*, 1087–1091 (1989).
142. Seaman C, Anspaugh B, Downing R, Esty R, *Proc. 14th IEEE Photovoltaic Specialist Conf.*, 494–499 (1980).
143. Matson R, Emery K, Bird R, *Sol. Cells* **11**, 105–145 (1984).
144. Hegedus S, *Prog. Photovolt.* **5**, 151–168 (1997).
145. Fardig D, Phillips J, *Proc. 22nd IEEE Photovoltaic Specialist Conf.*, 1146–1150 (1991).
146. Shafarman W, Klenk R, McCandless B, *J. Appl. Physics* **79**, 7324–7328 (1996).
147. Emery K, Dunlavy D, Field H, Moriarty T, *Proc. 2nd World Conf. Photovoltaic Solar Energy Conversion*, 2298–2301 (1998).
148. Standard ASTM E1021, *Standard Test Methods for Measuring Spectral Response of Photovoltaic Cells*, American Society for Testing and Materials, West Conshocken, PA, USA.
149. Bücher K, Schönecker A, *Proc. 10th Euro. Conf. Photovoltaic Solar Energy Conversion*, 107–110 (1991).
150. Hartman J, Lind M, *Sol. Cells* **7**, 147–157 (1982).
151. Stryi-Hipp G *et al.*, *Proc. 23rd IEEE Photovoltaic Specialist Conf.*, 303–308 (1993).
152. Jing-Gui C, Xiong-Jun G, Pei-Neo Y, Yu-Xue W, *Proc. 3rd Photovoltaic Solar Energy Conversion*, 743–748 (1987).
153. Schill C, Bücher K, Zastrow A, *Proc. 14th Euro. Conf. Photovoltaic Solar Energy Conversion*, 309–312 (1997).
154. Burdick J, Glatfelter T, *Sol. Cells* **18**, 301–314 (1986).
155. Shafarman W, Klenk R, McCandless B, *J. Appl. Phys.* **79**, 7324–7328 (1996).
156. Field H, *Proc. 26th IEEE Photovoltaic Specialist Conf.*, 471–474 (1997).
157. Sommeling P *et al.*, *Proc. 14th Euro. Conf. Photovoltaic Solar Energy Conversion*, 1816–1819 (1997).
158. Stock K, Heine R, *Optik* **71**, 137–142 (1985).
159. International Electrotechnical Standard Commission IEC 61215, *Crystalline Silicon Terrestrial Photovoltaic (PV) Modules – Design Qualification and Type Approval*, Geneva, Switzerland.
160. International Electrotechnical Commission Standard IEC 61646, *Thin-Film Terrestrial Photovoltaic (PV) Modules – Design Qualification and Type Approval*, Geneva, Switzerland.
161. Osterwald C, “ASTM Standards Development Status”, *Proc. 18th IEEE Photovoltaic Specialist Conf.*, 749–753 (1985).
162. *Qualification Test Procedures for Photovoltaic Modules*, Commission of the European Communities, Joint Research Center, ISPRA Establishment, Specification 502 (May 1984).

163. Ross R, *Proc. 17th IEEE Photovoltaic Specialist Conf.*, 464–472 (1984).
164. Krebs K *et al.*, *Proc. 5th Euro. Conf. Photovoltaic Solar Energy Conversion*, 597–603 (1983).
165. Dunlop E, Bishop J, Ossenbrink H, *Proc. 2nd World Conf. Photovoltaic Solar Energy Conversion*, 459–462 (1998).
166. Bishop J, Ossenbrink H, *Proc. 25th IEEE Photovoltaic Specialist Conf.*, 1191–1196 (1996).

17

Photovoltaic Systems

Klaus Preiser

Fraunhofer ISE, Freiburg, Germany

17.1 INTRODUCTION TO PV SYSTEMS AND VARIOUS FORMS OF APPLICATION

The modular nature of photovoltaic generators – consisting of photovoltaic modules – means that energy supply systems can be constructed for an extremely wide power range. The power spectrum ranges from a few milliwatts for wristwatches or scientific calculators, to kilowatt systems in remote area power supplies, for example, for mountaineering lodges or water pumps, to large central photovoltaic (PV) power stations in the megawatt range. An overview on the manifold application areas of photovoltaic systems is given in Figure 17.1.

Photovoltaics are generally considered to be an expensive method of producing electricity. However, in off-grid situations photovoltaics are very often the most economic solution to provide the required electricity service. The growing market all over the world indicates that solar electricity has entered many areas in which its application is economically viable. Additionally, the rapidly growing application of photovoltaics in grid-connected situations shows that photovoltaics are very attractive for a large number of private people, companies and governments who want to contribute to the establishment of a new and more environmentally benign electricity supply system. In parallel, considerable cost reductions are envisaged with the mass production of photovoltaic systems, leading to further attractiveness of this technology and its extension to other fields of applications. In Figure 17.2 the market development for photovoltaic modules is shown, indicating outstanding rates of growth of more than 15% per year in the eighties and early nineties cumulating in up to 40% annual increase in the late nineties and the year 2000.

As can be seen from Figure 17.2, about 45% of all modules installed in 2000 have been connected to the public electricity grid. These applications include both smaller decentralised systems, with the solar modules typically installed on rooftops, as well as

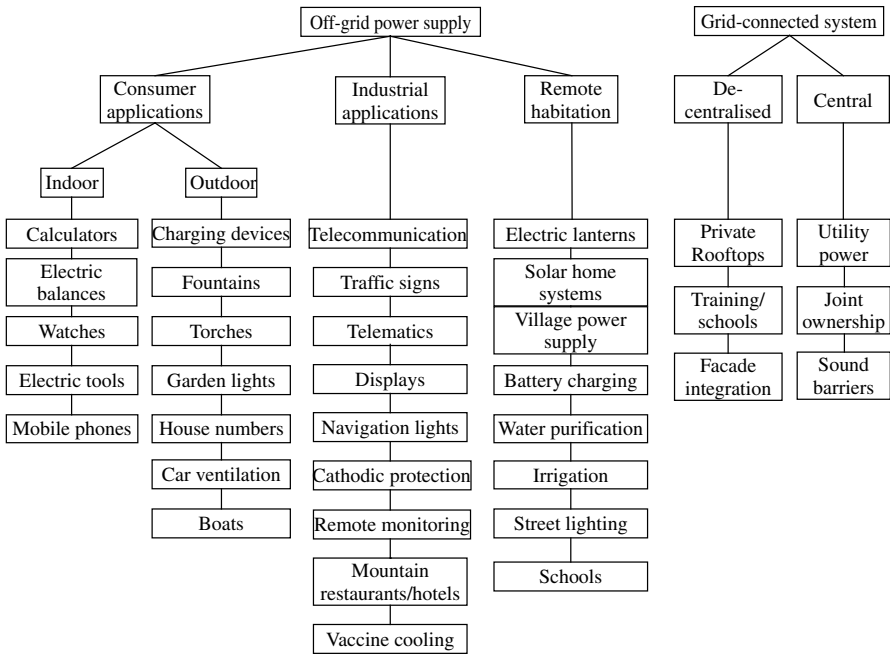


Figure 17.1 Application areas of photovoltaic systems. The applications are subdivided into “off-grid” and “grid-connected” systems

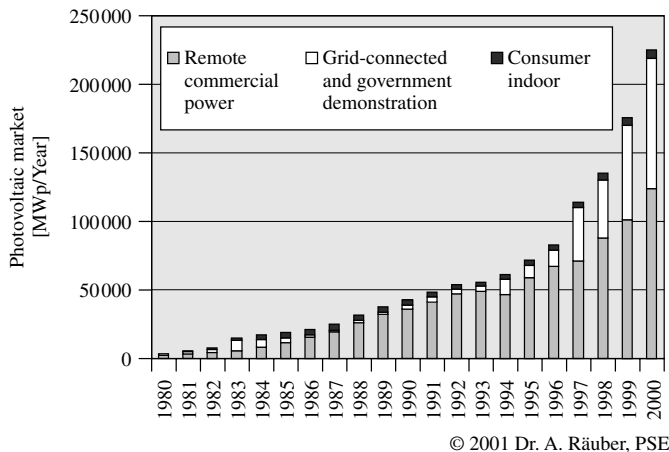


Figure 17.2 Market development of photovoltaic modules in the years 1980 to 2000 [1]

large central systems, with large areas of solar modules usually mounted on dedicated support structures. Still, the majority of the photovoltaic modules are applied in off-grid situations, like consumer products (e.g. camping, caravanning, small appliances), industrial applications (e.g. telecommunication, signalling, cathodic protection, water pumping) and remote habitation (e.g. solar home systems, hybrid systems, village power supply).

17.2 PRINCIPLES OF PHOTOVOLTAIC POWER SYSTEM CONFIGURATION AND THEIR APPLICATION

Photovoltaic systems are solar energy supply systems, which either supply power directly to electrical equipment or feed energy into the public electricity grid. In the following chapters, the most important application areas will be described in detail and pictures of prominent examples will be shown.

17.2.1 Grid-independent Photovoltaic Systems for Small Devices and Appliances

Solar electric power supplies for appliances and small loads in the power range from several milliwatts to several hundred watts are being applied generally because of its cost-effectiveness against a grid connection, in many cases even when the consumer is situated very near to the next grid connection point. Other advantages are their reliability, portability and their environmentally benign production of energy. In very small systems such as wristwatches or scientific calculators, the solar generator consists of one or only a few solar cells. When more power is needed, the individual solar cells are connected together to form solar modules.

An energy storage unit is needed to bridge times when no light or not enough light is available to power the appliance directly. Nickel–cadmium rechargeable batteries are used in most photovoltaically powered appliances, but lead-acid batteries and capacitors (so-called supercaps) can also be used. For caravans, boats and weekend accommodation, special types of car batteries with particularly thick lead plates and special alloys for mobile application can be used. In photovoltaic systems for continuously occupied houses and daily charge/discharge cycles, heavy-duty industrial batteries, the so-called “OpzS” batteries, are most commonly used. They are characterised by very low self-discharge, extremely good tolerance to cycling and thus a long operating lifetime. For small systems, maintenance-free batteries with the electrolyte integrated in matting or in gel form are used. They cannot leak and can thus be operated in any position. As lifetime costs for a stand-alone photovoltaic system are highly dependent on the battery costs, careful selection of the best suited technology for the respective application, operation and battery management schemes are crucial for satisfactory use (see also Section 17.3.1 and Chapter 18 of this book).

A charge controller is included between the solar generator and the battery to prevent it from being overcharged or deep discharged. The charge controller usually has a blocking diode, which prevents the battery from discharging during the night via the solar generator. A good charge controller has very low internal power consumption and includes a load cut-off switch that protects the battery against discharge. Power conditioning may be needed to adapt the voltage level of the photovoltaic system to that of the load. For photovoltaically powered appliances, this is usually a DC/DC converter, which transforms one DC voltage to another. If AC voltage is needed by a consumer, an inverter must be used. This converts the DC voltage delivered by the solar generator or the battery to an AC voltage.

17.2.1.1 Consumer applications

Power systems for appliances and small devices in which the energy supply and demand occur simultaneously do not need an energy storage unit. Pocket Calculators, fans and electric letter balances are examples of such applications [2–4]. As one example of an appliance in the small power range, Figure 17.3 shows an electric balance.

When an electric display is used, these devices are normally powered by dry-cell batteries. As energy demand and photovoltaic energy supply are very well correlated in this application – reading the LCD-display is not possible without light – the system may be designed without any energy storage. Besides environmental aspects, one fact is often neglected – the cost per kWh supplied with dry cells is extremely high – for example, a 1000 mAh dry cell with nominal voltage of 1.5 V contains 1.5 Wh. Its cost of about 1 euro per unit means that the kilowatt hour stored in this way costs about 700 euro/kWh. Not relying on a storage battery means that the system reliability is higher, negative environmental effects are reduced and the comfort in using these systems is increased.

Another example is the fountains that can be found in many public parks, squares, cemeteries and zoos. Usually, the water is recirculated rather than being constantly replenished with fresh water. In general, just a few standard solar modules are sufficient to operate the circulation pump. As circulation during the night or overcast periods is not

Image Not Available

absolutely necessary, a storage element is not needed and the solar generator can be connected directly or via an adaptive converter to the water pump.

17.2.1.2 Photovoltaically powered intelligent emergency telephone

Emergency telephones along motorways and roads across sparsely populated country are necessary, sometimes even life-saving [5]. Extensive cabling can be avoided, both during new road construction and when emergency roadside telephones are subsequently installed, if photovoltaically powered emergency telephones with radio contact to a central receiver station are used (see Figure 17.4).

A solar generator of only a few watts power is sufficient, as the telephones are not used frequently. The “multifunctional emergency call and information system” developed at Fraunhofer ISE does not require external cabling, has an autonomous power supply and



Figure 17.4 Photovoltaically powered emergency telephone (Source: Fraunhofer ISE, Freiburg)

operates reliably. In addition to the original emergency call function, contact can be made to various emergency services and information can be obtained. Furthermore, information such as traffic flows and meteorological data can be recorded at the system location and communicated to predetermined central stations.

17.2.1.3 Solar lantern for rural households in developing countries

A photovoltaic application that is particularly interesting with regard to its ecological and social aspects is the replacement of fossil-fuelled light sources – usually petroleum lamps – in remote regions of developing countries with photovoltaically powered lights.

The robust lighting unit illustrated in Figure 17.5 consists of the light, an electronic ballast, the rechargeable battery and a charge controller. During the day, it is connected

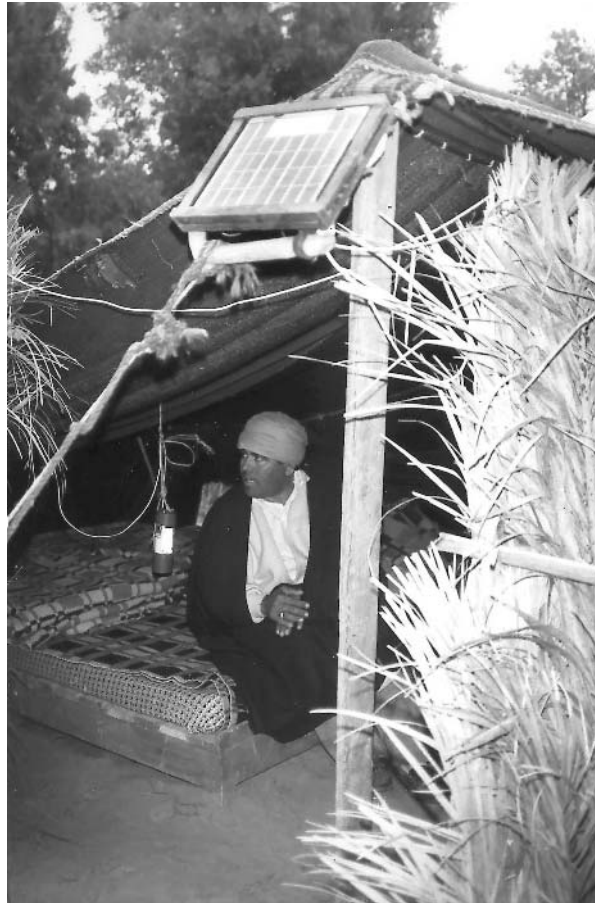


Figure 17.5 Photovoltaically powered light in a hut in Tunisia (*Source:* Ludwig-Bölkow-Stiftung, Ottobrunn)

via a cable and plugged to the permanently mounted solar generator for charging. In the evening it can be used as a portable light inside or outside the dwelling and can be carried and positioned wherever it is most needed. A solar generator with 4 Wp (module size $20 \times 20 \text{ cm}^2$) is sufficient for a daily lighting period of 3 to 5.5 h (depending on the solar radiation). At the same time, the solar-powered light with a luminous flux of about 80 lm is three times as bright as a petroleum lamp.

17.2.1.4 Solar home systems

The designation “Solar Home System” has become a well-defined concept [6–8]. A 50-W photovoltaic module (size about $50 \times 100 \text{ cm}^2$) typically supplies power for three lamps and a black-and-white television set in a single household (Figures 17.6 and 17.7). A lead-acid battery with a charge controller stores the energy from the day for the night and can run alone for two to three overcast days. Depending on the size of the local market, customs duties, taxes and the share of locally manufactured components, the cost of a Solar Home System is between US\$500 and US\$1500.

In many situations, Solar Home Systems (SHS) offer cost advantages over the classic alternative for electrification, which is the extension of electricity grids into sparsely populated regions and connection of power lines to all rural households [9]. The World Bank assesses the average cost worldwide of grid extension to be US\$900 per household. In unfavourable cases, with long distances, difficult terrain and low population density, a power line for one household can cost many tens of thousands of dollars.

The investment needed for this cannot be financed via the low energy consumption of rural households, which ranges between fractions of kilowatt hours and a few kilowatt hours per day. Political decisions to electrify rural areas despite this imbalance have contributed to electricity utilities going into debt in developing and threshold countries, so that necessary investments to modernise distribution grids and power stations cannot be financed. The result is the poor quality of the electric power supply, which can be observed in many regions around the world. Increased privatisation of the power supply is intended to provide a remedy to the described situation [10, 11].

The situation described above is the main reason small diesel generators in the power range of some kilowatts are installed in many remote locations. Because of their low investment costs, they appear economically attractive. However, calculating the lifetime costs shows that the expenses for repair and maintenance of the motor generator and the fuel costs add up to considerably high costs, leading to a situation in which photovoltaics are very often cost-competitive.

Decentralised electrification with privately financed Solar Home Systems fits in perfectly with the aim of sustainable and cost-effective rural electrification. Light that allows information and communication for private users and that lengthens the working time into the evening in farms and shops, schools and community centres cannot be underestimated in its importance. It is therefore actively supported by the energy planning authorities of various countries and by multilateral organisations such as the World Bank [12].

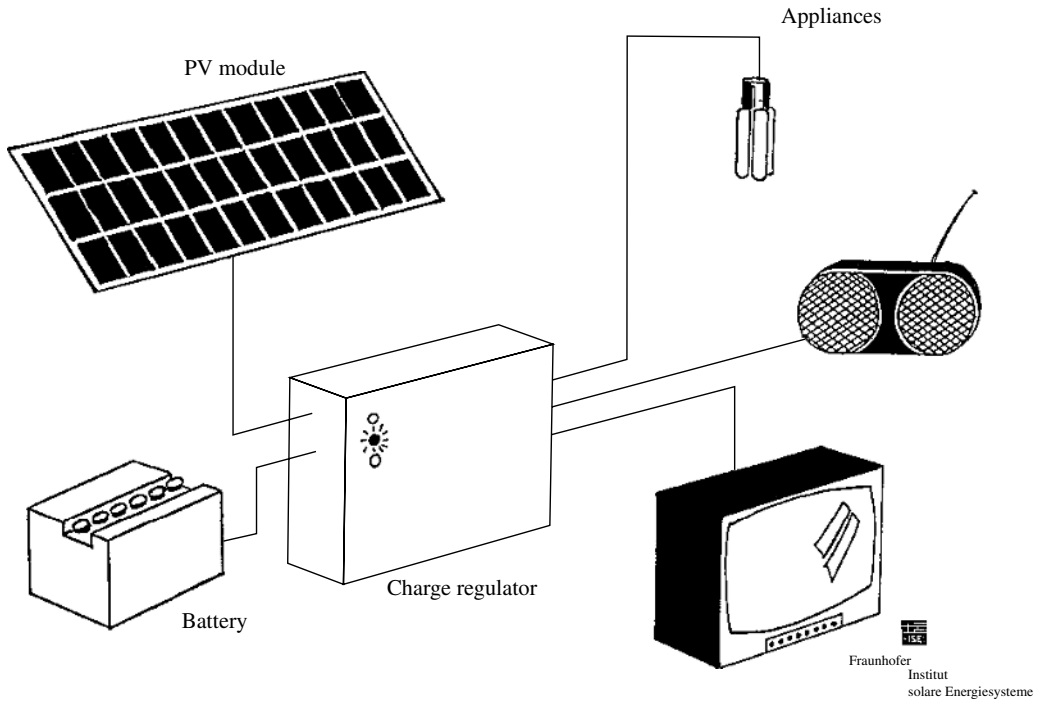


Figure 17.6 Block diagram of a Solar Home Systems to cover the basic electricity demand (lighting and communication) in rural households



Figure 17.7 Sukatani, the first SHS pilot village in Indonesia, was the origin of the currently running rural electrification programme to electrify one million rural households in Indonesia (Source: Fraunhofer ISE, Freiburg)

17.2.2 Photovoltaic Systems for Remote Consumers of Medium and Large Size

Electricity also solves other supply problems. Workshops, food storage and processing, telecommunication, health services and tourism normally demand higher daily amounts of energy and power than can be supplied by a Solar Home System. The usual supply levels, classified according to small and medium loads, and local, regional and national supply with the corresponding voltage levels and power ranges, are illustrated in Figure 17.8. For very low power requirements, pure photovoltaic systems with an appropriate energy storage unit are the best option. With increasing power demands, other electricity generators, like wind turbines and solar thermal generators, become technically and economically attractive. Small stand-alone grids that are supplied by various electricity generators are the next step in remote area power supply. With increasing demands, the connection to the public electricity grids makes good sense. Here, of course, all renewable energy technologies can play a role; the decision on their application, however, has to compete with the energy prices of conventional power stations driven by fossil or nuclear fuels. Because of the price reductions in the last years, photovoltaic power technology is cautiously expanding into the range “supply of small and medium loads” at present.

17.2.2.1 Photovoltaically powered telecommunication system

Owing to their high reliability and low maintenance, photovoltaics are already widely used to power remote telecommunication systems, for example, repeater stations. Repeaters are

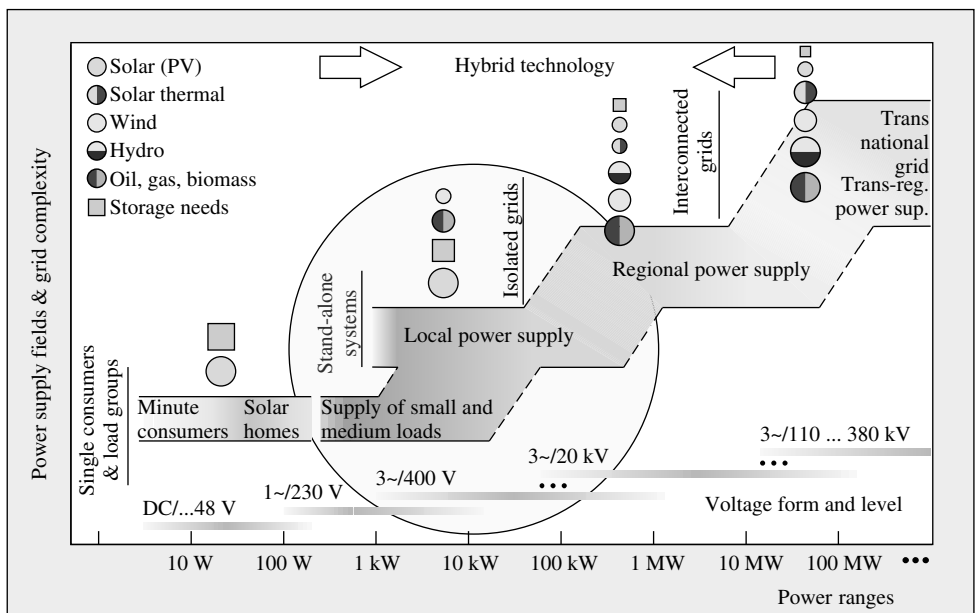


Figure 17.8 Classification of power supply technology for electrification with renewable energy – energy sources, application classes and trends (Source: ISET, Kassel [13])

digital radio signal amplifiers that increase the connection reliability of mobile telephones within radio cells and raise the accessibility level throughout the network. In rural areas and in mountainous regions, repeaters often have to be installed and operated at sites remote from the public electricity grid (see Figure 17.9).

Because of seasonal fluctuations in solar radiation in temperate zones, an exclusively photovoltaic power supply leads to very large and thus expensive systems. In order to avoid these disadvantages, the photovoltaic generator may be combined with other power generators. In Figure 17.10 is shown the prototype of a photovoltaic hybrid system, consisting of a PV generator, a battery and a thermoelectric generator used as auxiliary power source. A micro-controlled energy management system ensures fully automatic operation with minimal consumption of fossil fuel and appropriate battery operation management.

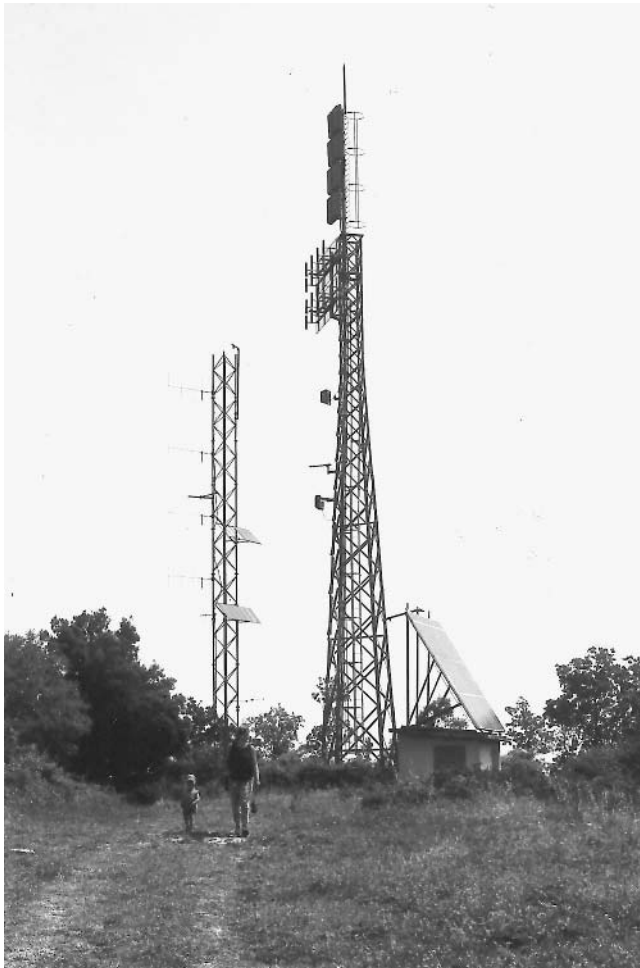


Figure 17.9 PV powered repeater station on a hill in Tuscany, Italy (Source: Fraunhofer ISE, Freiburg)

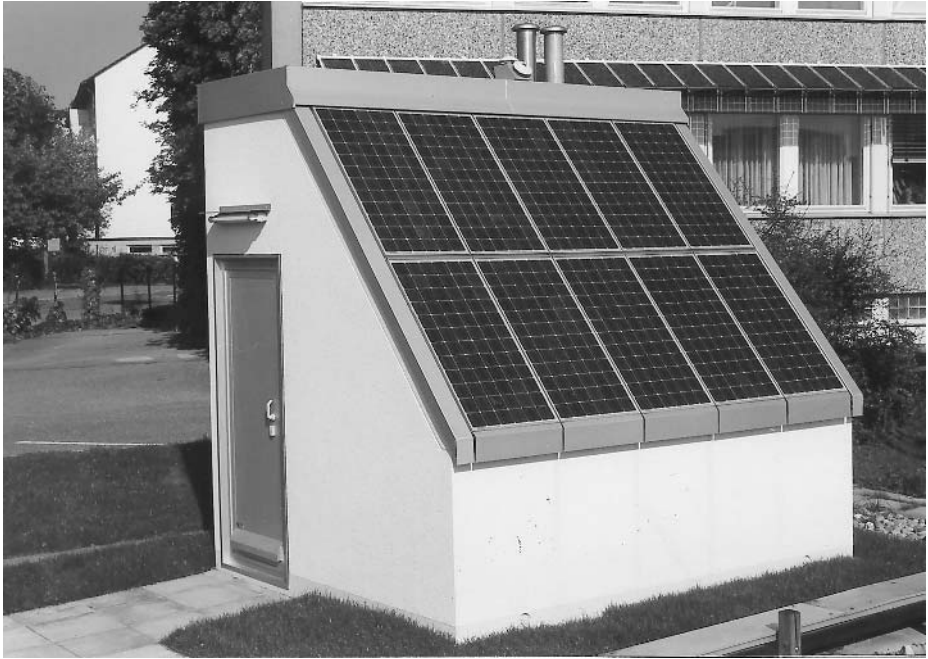


Figure 17.10 Prototype of a hybrid system (photovoltaics and thermoelectric converter) to power a remote repeater station (*Source: Fraunhofer ISE, Freiburg*)

17.2.2.2 PV powered battery-charging stations

Experience with locally centralised battery-charging stations (Figure 17.11) worldwide is by far not as convincing as it is with solar home systems. Normally there is no deep discharge protection (DDP) of the battery foreseen, which besides other effects causes sulphatation of the electrodes and thus an early end of the lifetime of the battery. Using the batteries in a full cycling process means that not the corrosion coefficient but the cycle capability determines the lifetime. Therefore, battery lifetime tends to be very short, only some hundred cycles, especially with locally produced car batteries [14].

Another aspect, which is often neglected with battery-charging station, is that people have to carry a dangerous freight over a quite long distance. In industrialised countries no one would expect this of somebody, even if the means of transport were more comfortable as they are in rural areas of developing countries. The hazard of accidents when transporting batteries, the high risk of wrong connection afterwards and the very poor charge and discharge protection regimes sum up to an unsatisfying operation of this kind of electricity service.

17.2.2.3 Photovoltaic hybrid systems

If higher power is needed or if conventional household appliances and industrial equipment are to be used, a system voltage of 230 or 110 V alternating current is desirable. To increase the reliability of off-grid power supply systems and to reduce the investment

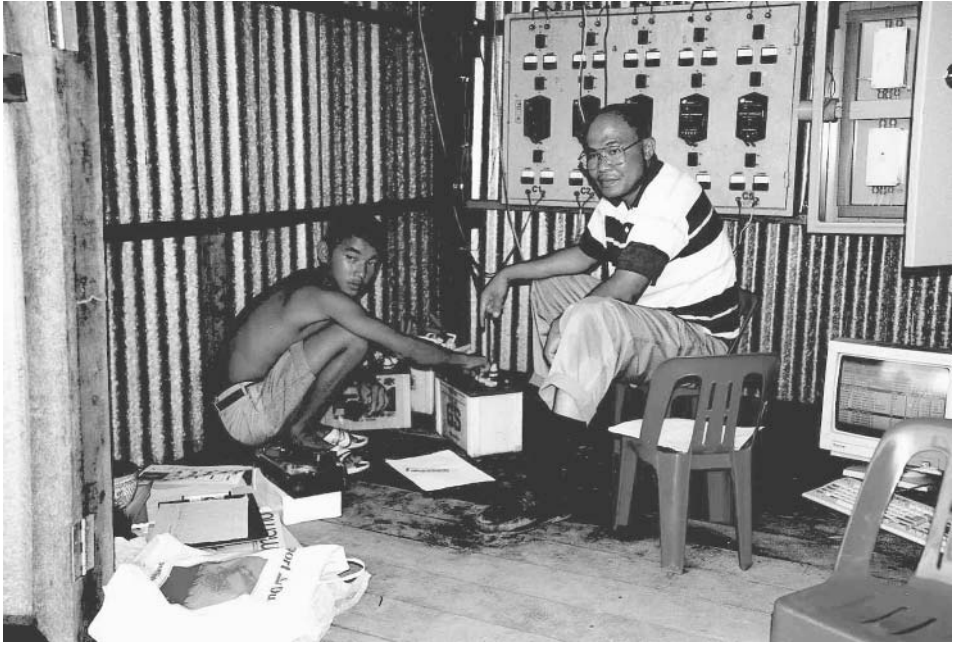


Figure 17.11 A typical PV powered battery-charging station in rural Thailand (Source: Fraunhofer ISE, Freiburg [14])

costs for a certain energy service needed, larger systems (i.e. consumption of several kilowatt hours a day) are typically constructed as “hybrid” systems, that is, the combination of a diesel generator and a photovoltaic generator. Depending on the availability of natural resources, other electricity generators like wind converters or hydroelectric power stations may be used to complement the power supply system. A battery bank ensures that power is available continuously. Under favourable weather conditions, the consumer’s total energy demand is met by the solar generator operating silently and without exhaust gases. Surplus energy is stored in batteries. During the night or unfavourable weather conditions, the energy demand is initially met by the batteries. If there is danger of battery deep discharge, the diesel or gas-fuelled generator provides the electricity and simultaneously charges the battery.

Even in Europe there are still many houses, hikers’ inns and mountaineering lodges that are not connected to the public grid because of the long distances and the resulting connection costs. The only option open to the owners up to now was to install a diesel generator. As they are used to directly supply the consumer load, the diesel generators are often operated in the inefficient partial load range and when they are switched off, no electricity is available at all. However, continuous operation of stand-alone motor generators is undesirable, not only because of the low partial load efficiency, the noise and the exhaust gases but also because of the limited lifetime of combustion motors. Therefore, the Rotwandhaus, a hikers’ inn in the Bavarian Alps, which is open throughout the year, was equipped with a hybrid system consisting of a photovoltaic generator, a wind energy converter and a diesel generator (Figure 17.12).



Figure 17.12 Rotwandhaus with its solar generator and wind energy converter (*Source: Fraunhofer ISE, Freiburg*)

When the wind is strong enough, the wind energy converter supplies the power and charges the battery. As soon as the battery is fully charged, the wind energy converter is throttled. An inverter converts the direct current from the battery to 230 V alternating current so that all conventional electrical appliances can be operated. The necessary supply reliability even during extremely unfavourable weather conditions is guaranteed by the diesel generator. A computer monitors and controls the whole system to ensure that the supplied energy is used as effectively as possible.

Most of the hybrid PV-diesel-battery systems realised worldwide are so-called DC-coupled systems (see Figure 17.13).

Different generators are working via separate charge controllers/rectifiers to the DC storage battery. An inverter generates the desired AC sine wave, it builds the AC grid in frequency and voltage; if power generation and consumption are equal, the battery does not take part in the power flow. Otherwise, the battery stores the surplus of generated power or delivers the additional power that is needed by the load. In order to protect the battery against damage, a charge controller, in most cases the PV charge controller, disconnects the inverter before the battery becomes completely discharged. If there is not enough renewable power and if, at the same time, the state of charge of the battery is low or if the consumers need more power than the inverter can deliver, a back-up generator is started from the control system. In this case, the back-up generator supplies the consumers directly with AC power and charges the battery via its own rectifier.

The big advantage of the DC-coupled system layout is that it is proven in many applications and that reliable components are available on the market. The necessity

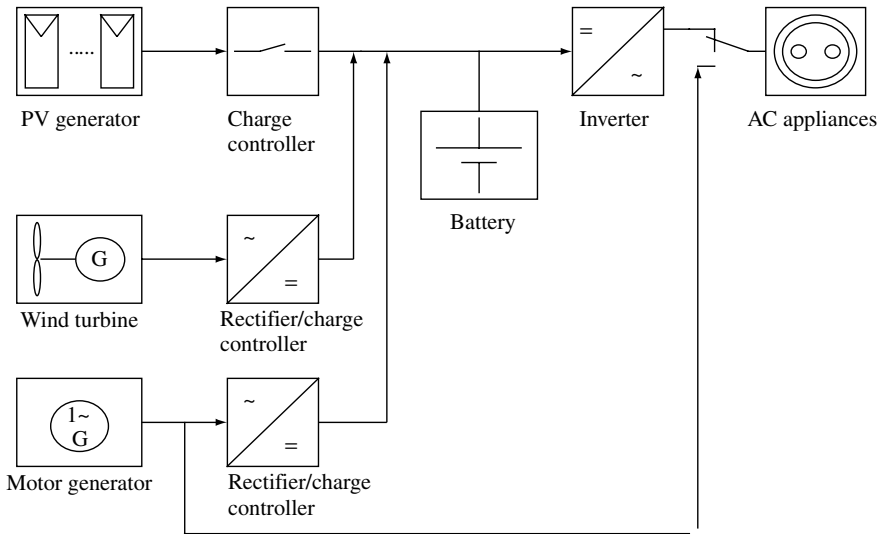


Figure 17.13 “DC coupling” of different electricity generators. Example from the Rotwandhaus, a mountain lodge in the Bavarian Alps

of adapted charge controllers for each generator, however, may lead to systems with relatively high installation costs, which will further increase with the number of the power generators installed.

The other possibility for hybrid system design is the so-called AC-coupled system (Figure 17.14).

The heart of an AC coupled system is a bi-directional inverter. The photovoltaic modules and all the generators are connected to an AC bus bar via suitable inverters. Thus, primarily the AC consumers are supplied with electricity and only the surplus of power is fed back to the storage batteries. Power management is done by only one electronic device, the bi-directional inverter. This may lead to a simplified system concept. The inverter now must be able to work in different modes (charging or discharging the battery), it has to build the local AC-grid in frequency and voltage and it has to be synchronised to any other synchronous electric generator in the system. Because of these high requirements of the inverter, there are only very few bi-directional inverters available on the market, some of which still have prototype character.

17.2.2.4 Village power supply systems

While Solar Home Systems for the decentralised power supply of rural households are considered to be a standard system ready for the market, and while the suitability of PV hybrid systems to power single houses has been proven in various pilot and demonstration programs all over the world, this positive experience is up to now not available for central power stations to supply remote villages with off-grid PV power. Nevertheless, the research and development in rural electrification are increasingly directed towards these systems. The main reason is that with a central system, installation and operation

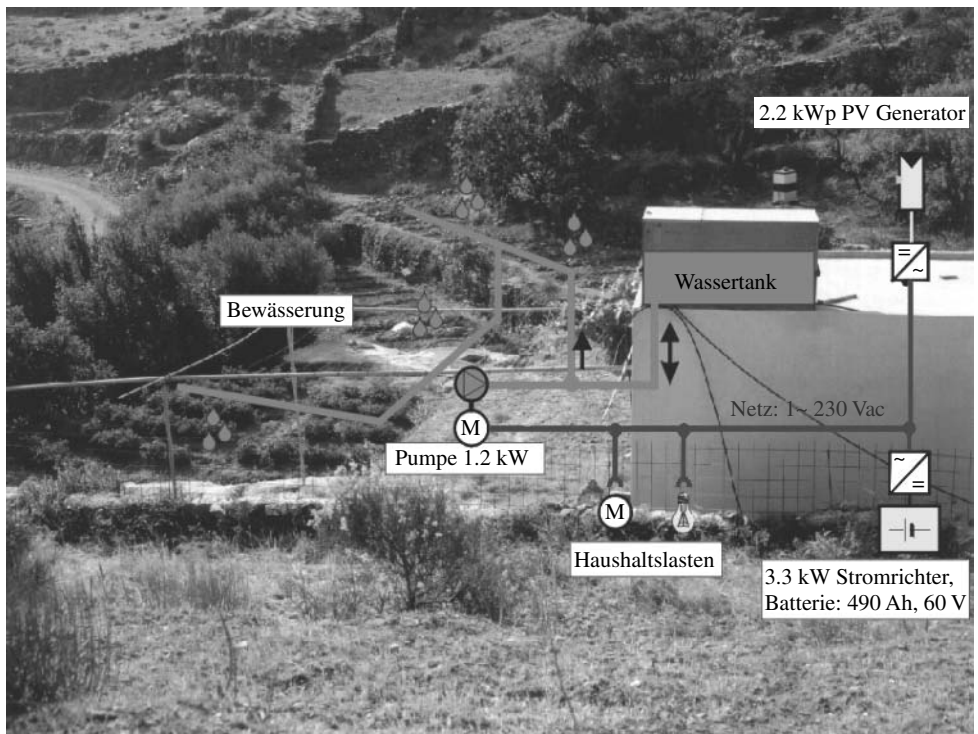


Figure 17.14 “AC coupling” at an example of a three-phase stand-alone power supply system (Source: ISET Kassel)

costs may be lowered compared to the single-house supply option. Today, as more and more electric utilities enter the off-grid market, their interest is to lower the cost as much as possible for operation, maintenance, money collection and so on, which is needed to assure a durable energy service. Experience and reports from those having been involved in PV dissemination programmes for rural electrification confirm that technical problems in the village supply are not the main barrier preventing lasting success. Rather, an appropriate introduction method, user involvement at various levels and planning that allows flexible reaction to the situation as it develops are necessary to achieve optimal joint use of the limited resource.

Today there are technical components, like the inverter, the charge controller, the energy management systems, available in various countries, which are much better suited than they were in the early demonstration projects. The R&D efforts in the development of village power supply systems are now focused on the fair distribution of the energy available, and a suitable limitation of the power consumed by each individual household. Prepayment schemes or energy limiters are in development and demonstrated in several companies and international pilot programs. These systems meter system energy consumption in each individual household and cut the load if the pre-set values or the energy budget has been consumed. A typical representative is the village Llavería, where SEBA, a Spanish user association, together with the Spanish company TTA are operating a hybrid system (Figure 17.15).



Figure 17.15 PV-Diesel-Hybrid system in Llavería (Source: TTA, Barcelona)

17.2.2.5 Photovoltaic pumping systems

An important field of application for battery-free solar electricity systems are water-pumping stations [15]. In this case, water reservoirs serve as product storage devices.

High-power pumps are applied to draw drinking water from great depths for a whole village. The system shown in Figure 17.16 supplies the drinking water for 4000 people on Sumba Island in Indonesia. Using a 6-kWp photovoltaic system, 40 m³ water can be drawn every day.

17.2.2.6 Photovoltaically powered water purification

Besides the water provision, the purification of water also becomes increasingly important (see Figure 17.17; [16–18]). Different technologies exist, like chlorination, UV radiation and ozonisation. From this broad range of purification methodologies, the best-suited system has to be chosen and integrated in a complete photovoltaically powered system for continuous and safe operation.

17.2.2.7 Social aspects in off-grid rural electrification

Providing stand-alone photovoltaic systems for remote locations is often defined and approached as a purely technical matter. However, in numerous applications such as mountaineering lodges, rural households or village power supply systems, it has become clear that other aspects in addition to the technical ones affect the optimum use and effective conversion of solar energy into electricity [8]. There is a danger that expectations of a photovoltaic system will be unrealistically high. It cannot really be compared with the “inexhaustible” supply known from the public grid, but must be placed in a realistic perspective defined by the respective context. This must happen actively and consciously as many users (and also planners) of photovoltaic systems underestimate the amount of redundancy, safety precautions and maintenance work necessary to achieve the high level of safety and reliability afforded by the centrally administrated public grid. This means

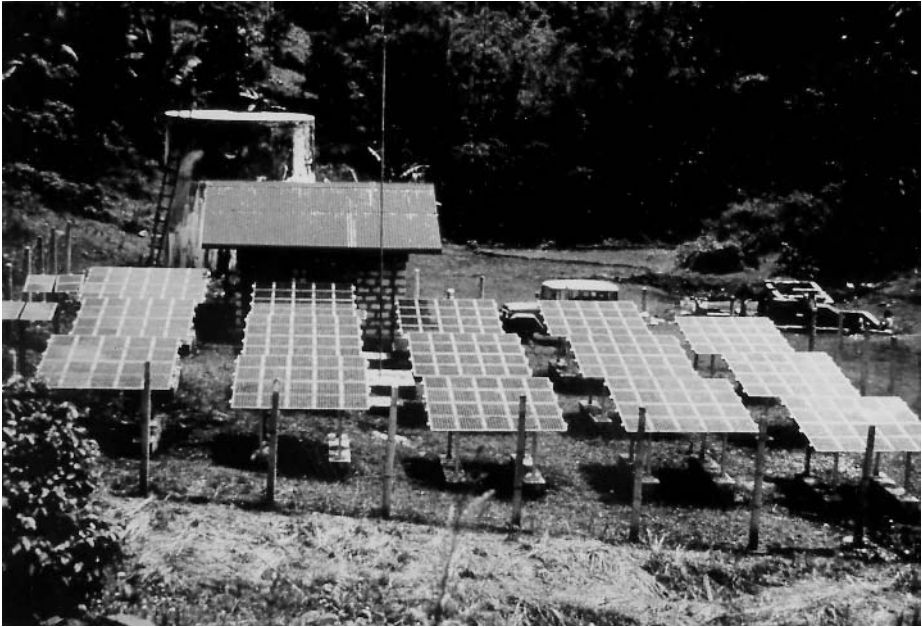


Figure 17.16 Photovoltaically powered system to provide drinking water for 4000 people
(Source: TÜV Rheinland, Cologne)

that the people involved in the whole process must be taken seriously in their ideas about the design, advantages and disadvantages of the PV system. The behaviour of the users influences the system's performance tremendously, because they may purchase components, may install and/or change the system, determine the use of energy, may take over maintenance jobs and even repair the PV system. From this it becomes evident that the functioning of PV Systems can be optimised when the interaction between the new technology and their users can be improved. From this assumption, at Fraunhofer ISE the user-centred approach on rural electrification, called "socio-technical system approach", was developed.

The socio-technical system approach originates from work and organisational psychology and was applied first to labour organisations in Europe. When new technologies were introduced, it was found that not only the technology had to be designed according to the needs of the organisation but also the social organisation needed restructuring to increase the productivity. The approach is based on the open system theory in which the introduction of technology consists not only of hardware and software but also of orgware [19], the human part of the socio-technical system.

"Applied on stand-alone electricity systems" means that a properly reflected energy concept in the planning phase is the basis for the system design. But it is not only the quantity of components and their power consumption that finally determine the energy consumption in the PV system. The users have a decisive influence on the energy consumed, on the energy management carried out to optimise the energy available from the PV generator and to undertake the first level of maintenance (cleaning the PV module,



Figure 17.17 Photovoltaically powered purification unit at a wind powered water pump in Balde del Sur de Chucuma/Argentina (*Source:* Fraunhofer ISE, Freiburg)

re-filling battery water etc.). Therefore, involving them in the operation of the PV system, making them responsible for operation and maintenance is not only a measure to reduce the costs but also to increase their own satisfaction with the energy service provided (see Figure 17.18) [8, 20].

The users also play a decisive role in the evaluation of photovoltaic systems. They make the final decision on whether photovoltaics is a practicable and useful form of electricity generation for them. Satisfaction with the systems is – apart from economic arguments – the factor determining their further dissemination. Only contented operators will recommend this form of electricity generation to further potential users, which is certainly the most effective form of advertisement. In order to best adapt the system to

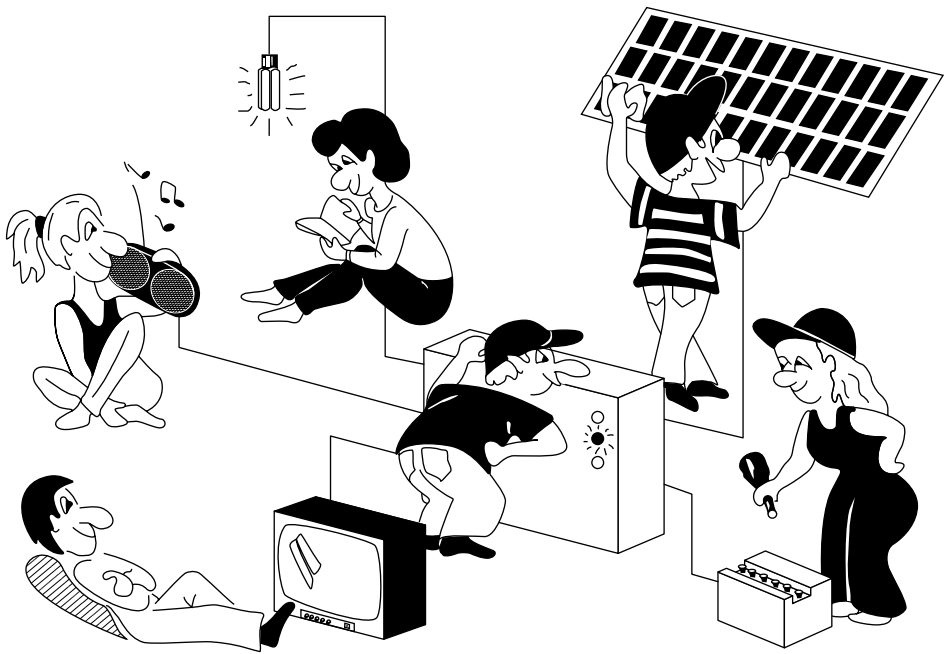


Figure 17.18 A photovoltaic stand-alone system consists not only of technical components but also of the users interacting with the technology on different levels

the particular needs of the intended users, they must be involved from the start in the process of system dimensioning, construction, installation, use and maintenance. The aim of adaptive measures must be to motivate the user to adapt his/her consumption patterns to the electricity generation profile, as one aspect, and at the same time to match the technical system to the demand and usage customs of the users.

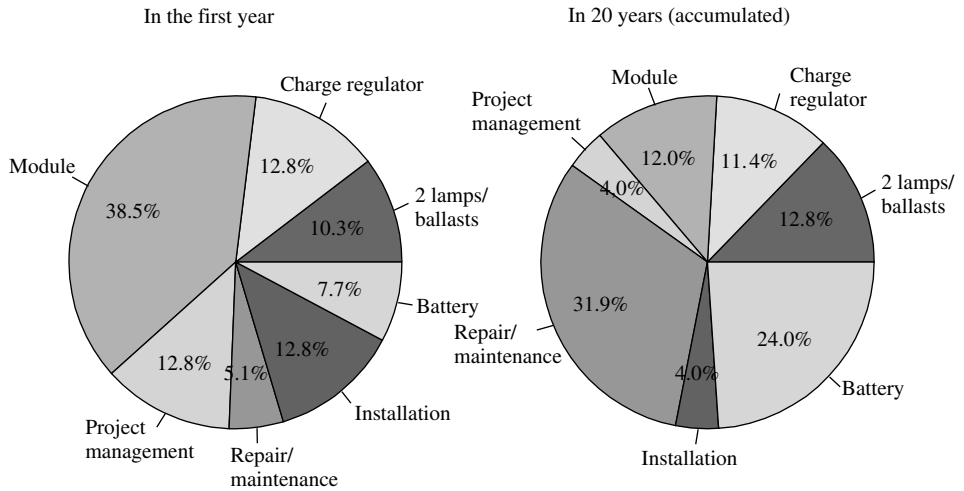
17.2.2.8 Economic aspects in off-grid rural electrification

In Figure 17.19(a) the cost breakdown of a solar home system in the first year is presented on the basis of data available in a project on rural electrification carried out by the German Agency for Technological Co-operation GTZ GmbH. As expected, the purchase costs of the different components are the dominating factor. The photovoltaic module typically represents the major single cost component [9].

However, regarding the lifetime costs of such a system after 20 years of operation shows a completely different picture (Figure 17.19b). The proportion for the PV module decreased to about 12% and the costs for new batteries as well as the efforts for maintenance and repair become the most important factors.

The reason for this shift in the cost distribution is the difference in the quality and reliability of the components. PV modules are highly standardised and worldwide-validated certification procedures have been established, both leading to high-quality components. Up to now, no equivalent standards have been available for the balance

Costs of solar home systems



Tunisia 1993 (no costs for financing)

Figure 17.19 Cost breakdown for Solar Home Systems [7]: (a) year of installation; (b) cumulative costs after 20 years of lifetime

of system components (BOS), that is, battery, charge controller, installation material and the electric appliances.

To achieve highly reliable systems, recommendations for the quality improvement of Solar Home Systems and their components have been prepared in different institutions together with industry partners worldwide and are currently being introduced and implemented in national and international standardisation committees. The guarantee of high-quality standards is seen as the main necessity to bring in financing agencies and companies. Up to now, the risk that is due to the uncertainty about the durability and the handling of PV systems can be identified as one of the main barriers for bank, insurance companies, private fee for service providers, governments and last but not the least, for the users of the systems for becoming involved in this new technology.

The main components of small PV-systems are the PV module, the storage battery, the charge controller, if necessary a DC/AC inverter, the appliances (lamps, radio, TV sets, refrigerators, fans etc.) and the installation material (safety boxes, cables, plugs, sockets etc.). While today and at least in the near future, the PV module will be imported from industrialised countries – in some developing countries the module assembly has already started – all the other components are suited for local production. Of course, these components have to fulfil the high-quality standards as well, which are needed for all components in a PV-system. This is the reason in today's larger PV programmes for rural electrification often components from industrialised countries are used.

However, there are several reasons for the assumption that in the near future – and in reality this development has already started in many countries – good quality

components will be produced locally. The proximity to the markets, that is, close matching with the users' needs and desires, the lower price of the components due to the lower expenses for manpower and the better commercial situation (no import barriers), the ability to repair and replace faulty components very quickly and the promotion by local governments show clearly that there is a large potential for local production.

Today, many local manufacturers work in joint ventures with industrialised countries, which may bring benefits for both sides, quick establishment of a production line of high-quality products for the local partner and increased market shares for the foreign partner. If local producers make wise use of international and national quality rules and quality control bodies, they will increase their market competitiveness considerably [21].

PV-systems have a high investment price, while the running costs are normally lower than those of the conventional alternatives. To overcome the barrier of high price for low-income customers, commercial and to-be-developed financing schemes have to be used. In the following list, the characteristics of the different delivery models applied in rural electrification are given (Figure 17.20).

- **Cash and carry:**
typical: the dealers are based in main cities; customer comes there and pays system cash; ownership is transferred with payment; user is responsible for installation; operation and maintenance is done by the users.
- **Cash sales:**
typical: the dealers are based in main cities and operate a salesmen network; customer pays system cash; system provider installs the system; ownership is transferred with payment; user is responsible for operation and maintenance.
- **Dealer credit:**
typical: dealers with local offices; customer pays system on credit directly offered by system provider (down-payment plus instalments); system provider installs system; ownership is transferred with contract conclusion; user is responsible for operation and maintenance supported by system provider.
- **Instalment credit:**
typical: dealers with micro-finance institutions; customer pays system on credit channelled from financial institution through system provider to customer (instalment =

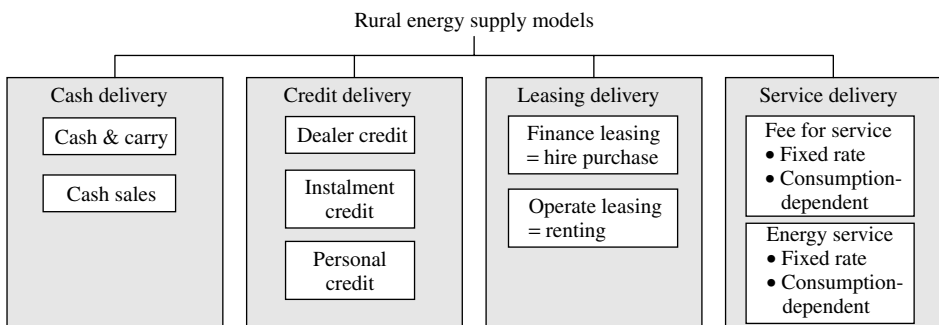


Figure 17.20 Categorisation of different delivery models in off-grid rural electrification

redemption plus interest); system provider installs system; ownership is transferred with contract conclusion; user is responsible for operation and maintenance supported by the system provider.

- **Personal credit:**
typical: customer enters loan agreement with the financial institution of his choice to purchase system from a system provider of his choice; for other characteristics see cash and carry, cash sales.
- **Operate leasing/renting:**
typical: customer rents system for payment of regular leasing fee; system provider is the owner of the system; system provider is responsible for installation and operation and maintenance of the system.
- **Finance leasing/hire-purchase:**
typical: customer leases system for payment of regular leasing fee; system provider owner during basic leasing period; ownership title transferred with payment of remaining amount; system provider installs the system; user responsible for operation and maintenance.
- **Fee-for-service:**
typical: dealer, service company (e.g. utility), customer pays regular service fees for electric service through individual power supply system or village power supply system; service provider is the owner of the system and responsible for installation, operation and maintenance.
- **Energy service:**
typical: ESCO (energy service company), customer pays regular service fees for services such as light, communication, cooling and so on; service provider is the owner of the system and responsible for installation, operation and maintenance.

17.2.3 Decentralised Grid-connected Photovoltaic Systems

17.2.3.1 Rooftop PV generators

Photovoltaic systems can be connected to the public electricity grid via a suitable inverter (Figure 17.21). Energy storage is not necessary in this case. On sunny days, the solar generator provides power for the electrical appliances in a house. Excess energy is supplied to the public grid. During the night and overcast days, the house draws its power from the grid [22, 23].

Photovoltaic systems operating parallel to the grid have a great technological potential [24]. However, without subsidies from government or utilities, they are not yet financially competitive. Therefore, in the last few years in various countries, programmes have been initiated that push the dissemination of grid-connected systems, for example, the 70 000 PV roofs programme in Japan or the 100 000 PV roofs programme in Germany (see Figure 17.22). In addition, national laws on paying higher fees for renewable electricity fed into the grid, like in Germany 99 Pfennig, in Spain 66 Pesetas per kWh, make it more and more attractive for private consumers and investors to become engaged in photovoltaics.

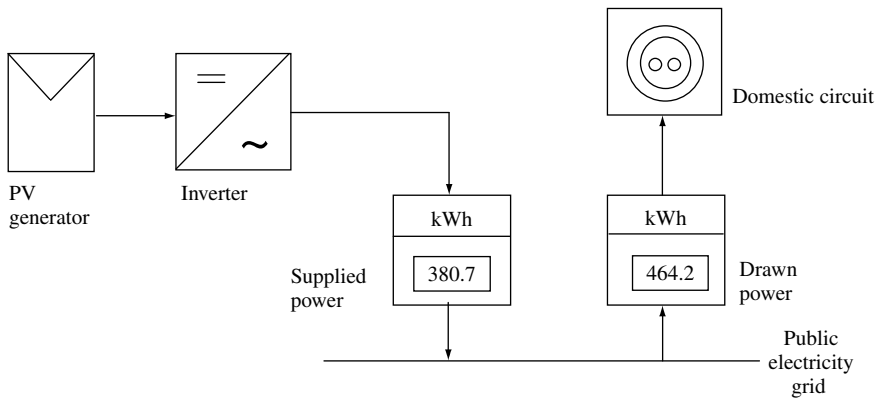


Figure 17.21 Block diagram of a grid-connected photovoltaic generator. The location of the two energy meters may vary depending on the applied payment scheme



Figure 17.22 Grid-connected photovoltaic roof on a private house in Germany (*Source: Fraunhofer ISE*)

17.2.3.2 Building integration

Standard modules are most commonly used for retrofitting buildings with PV systems, as little alteration of the building is required. Usually, they are mounted on the roof using an intermediate, added mounting structure. Integration into the building envelope is more difficult and few examples exist (see Figure 17.23). By contrast, frameless modules, so-called laminates, can replace conventional glass panes and thus allow easy integration.



Figure 17.23 Facade integration on the Mataro Library in Barcelona, Spain (Source: IES-UPM)

They enable the use of a wide product spectrum from the glazing industry. Demands by building owners and architects have stimulated some PV production firms to produce customised modules. These can be “trimmed” for every purpose to a certain extent. Such modules are offered with several options:

- Variable dimensions up to 6 m².
- “Arbitrary” connections of cells.
- Choice of colour.
- Crystalline cells in black, dark blue, light blue, greenish violet and bronze and amorphous modules mostly in brown shades.
- Various inter-cell distance to allow transmission of light (crystalline modules). Amorphous modules can even be made semi-transparent, by incorporating many microscopic holes into the Si layer.
- Rear surface covers can be matched to the colour of cells; they can also be used to influence daylight (e.g. diffusing).
- Cells can be selected to have the same colour.
- The front surface grid can be matched in colour.

By integrating PV cells into conventional double-glazing cells, other functions can be combined with PV (e.g. sound protection). Modules that are to be integrated into a building envelope need to allow enough clearance around the edges. Cells and junction boxes must be placed at an adequate distance to the edge. If not, problems such as partial shading or assembling problems may occur.

17.2.3.3 The Japanese residential PV promotion program

One of the worldwide largest dissemination programs has been launched in Japan in 1994. In the following years the number of small grid-connected systems skyrocketed [25]. This programme was to some extent combined with low-interest consumer loans and comprehensive education and awareness activities for PV. The programme makes blocks of funds available to PV system retailers in a competitive bid programme.

In 1997, the “New Energy Promotion Law” was introduced with subsidies for PV and a target of 400 MW_p by 2000 and 4600 MW_p by 2010. Up to the end of 1998, about 15 000 small grid-connected systems with an average capacity of about 3.6 kW_p have been installed; in 1999 alone, about 18 000 systems were installed. This led to cumulated installed capacity of 200 MW in Japan by the end of the year 1999 (see Figure 17.24).

It appears that the Japanese programme has brought down the PV prices over the last years substantially along with the continuously decreasing subsidies. They were reduced from 50% of the total investment costs in 1994 to about 30% in 1999. The upper limit for rebates has been reduced from 900 000¥ per kW in 1994 to 270 000¥ per kW in 2000 (see Figure 17.25).

A result of this effort is that Japan is now the world leader in the development of grid-connected systems. This success is the direct result of a conscious policy to promote PV technology, both for reasons of national energy security (Japan imports most of its fuels) and for reasons of economic development (Japan aims to dominate PV manufacturing to the same extent as it dominates the production of electronic equipment).

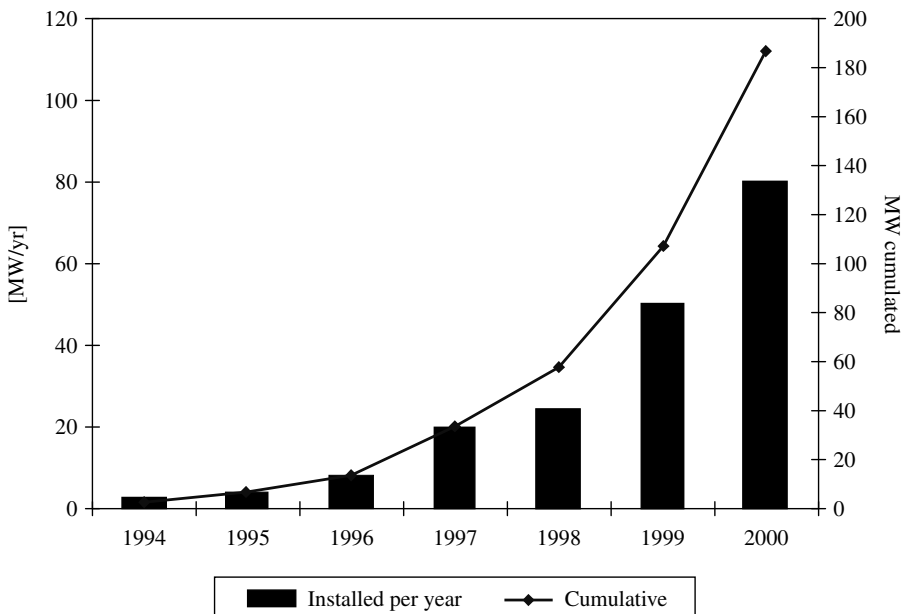


Figure 17.24 Japanese residential PV promotion programme: development of installed capacity and average capacity [25]

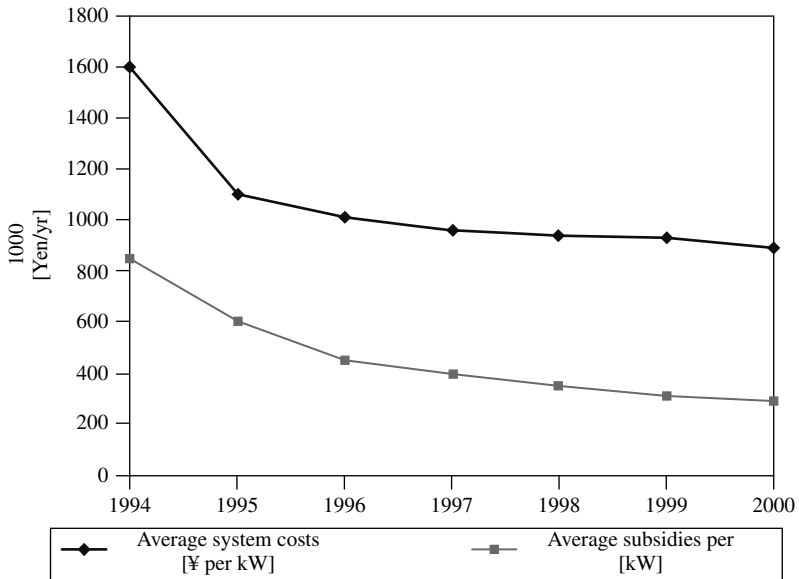


Figure 17.25 Japanese residential PV promotion programme: development of investment costs and rebates 1994–2000 [25]

17.2.3.4 The German 100 000 photovoltaic roofs programme

The German government has made climate protection one of its key policy issues. A 25% carbon dioxide reduction target by the year 2005 compared to 1990 levels was announced. The use of renewable energy sources can help achieve this ambitious goal. By 2010, the German government wants to double the contribution of renewable energies to the total energy demand. In 1998, the use of renewable energies in Germany reached 284 PJ of primary energy demand, which corresponds to a penetration rate of 2% of the total primary energy demand or 5% of the total electricity demand [26].

As the German government and administration are organised in accordance to the federal structure of the country, federal, regional and local authorities are promoting the use of renewable energy sources in many different programmes. The Federal Ministry of Economics and Technology (BMWi) will support within the 100 000 Roofs-PV-Programme the installation of up to 350 MW of photovoltaics (see Figure 17.26). One billion DM will be spent between 1999 and 2004 by giving favourable credit conditions by the government bank KfW, that is, for PV systems between 1 and 5 kW, a soft loan for a 10-year credit is offered with an interest rate that is 4.5% below market conditions.

Since 1991, the “Electricity Feed Law” regulated the input and favourable payment of electricity from renewable energies by the utilities. In 2000 the law was replaced by the “Renewable Energy Law (EEG)” with improved conditions. This law serves as the basis for the implementation of renewable energy technologies in Germany. For electricity generated by photovoltaic generators, the payment amounts to (at least) 99 Pfennig (i.e. about 0.51 €) per kWh for PV systems installed until December 31, 2001. Starting with January 2001 this minimal payment limit will be reduced each year by 5%, that is, for an

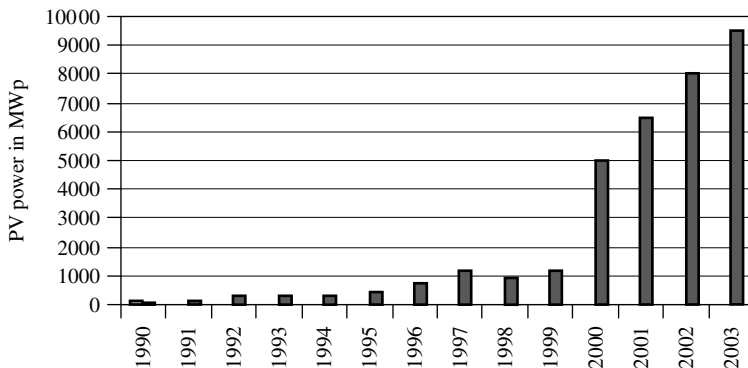


Figure 17.26 Installation already done and prospects of grid-connected photovoltaic systems in Germany (*Source: Deutscher Fachverband Solarenergie DFS*)

installation done in the year 2002 “only” 95 Pfennig will be valid and for an installation finished in 2003 and connected to the public electricity grid 90 Pfennig will be valid. This law expires when a cumulative power of 350-MW photovoltaics has been reached.

17.2.4 Central Grid-connected Photovoltaic Systems

17.2.4.1 Utility systems

Whereas the photovoltaic systems discussed earlier are usually small decentralised systems in the lower kilowatt range, it is also possible to build large central photovoltaic power stations in the higher kilowatt to megawatt range. It is then possible to feed directly into the medium- or high-voltage grid.

One of the most impressive installations done in the late nineties was the megawatt power plant at Toledo in Spain (Figure 17.27).

Another architectural well-designed solution is the megawatt power plant on the roof of the new fair in Munich, installed in 1999 (Figure 17.28).

17.2.4.2 Joint ownership

In Germany, 60% of the total population live in rented apartments. Consequently, they will generally not be able to install grid-connected PV plants on the rooftops of their house. When these people become interested in PV, they can only become PV owners if PV projects are established with “joint ownership”. To create this, a legal entity is set up to deal with the project management as well as with the related financial questions and the distributing scheme of the profits generated through the investment. In most cases, contracts are signed between various project partners to resolve management issues during project realisation (see Figure 17.29).

Contracts contain operational, financial and legal items concerning the collaboration of the different parties in project realisation. Signing parties are mostly the project

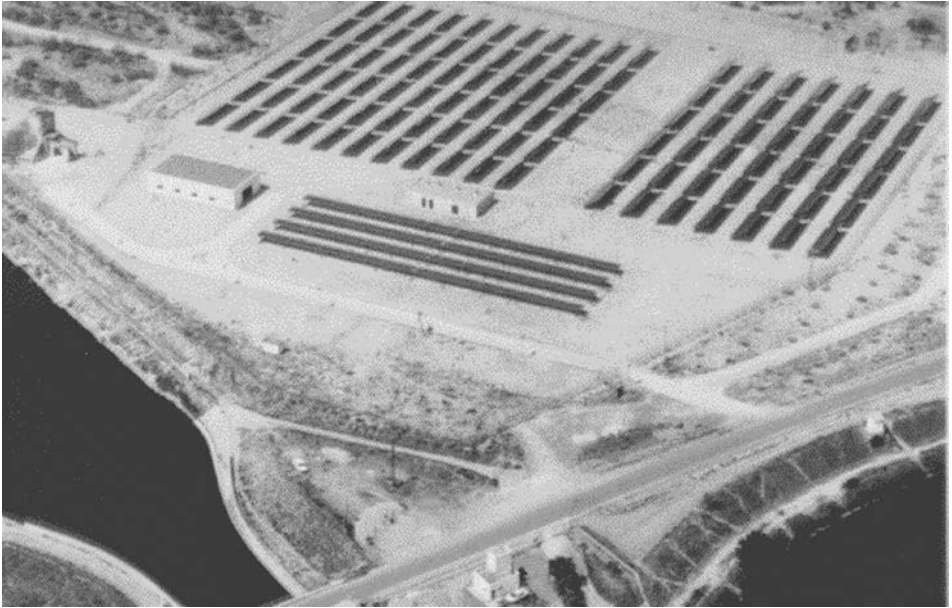


Figure 17.27 Central PV system installed at Toledo (*Source: IES Madrid*)



Figure 17.28 Central PV system installed on the roof of the new fair in Munich, Germany (*Source: Siemens Solar*)

developer, the owner of the electricity grid, the end owner of the PV system and the so-called limited partners. The projects are financed either by purely equity capital of the owners or by a mix of equity and debt capital through credits. The (major) portion of the capital is generated by the project through a public placement. In this case, transaction costs are minimal and risk-funding is supplied by the larger public participating with risk equity (see Figure 17.30).

17.2.5 Space Application

The number of artificial satellites launched by the world's nations exceeds more than 5000. Some of them return to Earth as part of their mission and others fall to Earth after

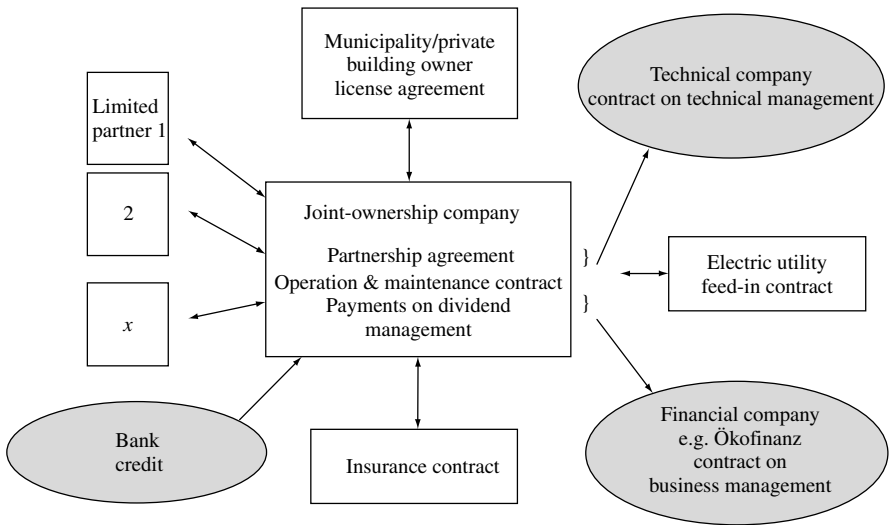


Figure 17.29 Example of the organisational structure of a joint ownership project [27]



Figure 17.30 Joint ownership PV installation of 100 kW on the soccer stadium Freiburg, Germany [27]

their orbits decay. Those that remain in orbit number about 2300 and in addition there are about 5700 items of “space debris”, such as rocket bodies, apogee kick motors and so on, making a total of some 8000 manmade objects currently in orbit around the Earth.

Satellites can be classified by their function since they are launched into space to do a specific job. The type of satellite that is launched to monitor cloud patterns for a

weather station will be different from a satellite launched to send television signals across Canada. Below, the classification into nine different types of satellites is given as well as a prominent representative of each of it:

- Astronomy satellites, for example, Hubble Space Telescope
- Atmospheric studies satellites, for example, Polar
- Communications satellites, for example, Anik E
- Navigation satellites, for example, Navstar
- Reconnaissance satellites, for example, Kennan, Big Bird, Lacrosse
- Remote sensing satellites, for example, Radarsat
- Search and rescue satellites, for example, Cospas-Sarsat
- Space exploration satellites, for example, Galileo
- Weather satellites, for example, Meteosat (see Figure 17.31)

17.2.5.1 The international space station ISS

The International Space Station is the largest and most complex international scientific project in history (Figure 17.32). When it is complete the station will represent a move of unprecedented scale off the home planet. Led by the United States, the International Space Station draws upon the scientific and technological resources of 16 nations: Canada, Japan, Russia, 11 nations of the European Space Agency and Brazil. More than four times as large as the Russian Mir space station, the completed International Space Station will have a mass of about 502 000 kg. It will measure 120 m across and 95 m long. Assembly is planned to be completed by 2004. Most of the 256-kW solar arrays will be delivered by United States; only Russia will provide a science power platform that can supply about 20 kW of electrical power. This PV generator – worth about 450 million US\$ – will be the largest object ever transported by human being into space. Each of the 6560 solar modules consists of 40 8×8 cm² mono-crystalline silicon cells. Cell efficiency will be around 14.5%, which seems to be not very outstanding; however, when the production of the cells started in 1988, the technology of the much more efficient GaAs cells – up to 26% is now possible – was not yet available.

17.2.5.2 The unmanned airplanes “Pathfinder” and “Helios”

The Pathfinder is one of several unpiloted prototypes under study by NASA’s ERAST (Environmental Research Aircraft and Sensor Technology) program, a NASA-industry alliance that is helping develop advanced technologies that will enable aircraft to study the Earth’s environment during extremely long flights at altitudes in excess of 30 km. The Pathfinder is a remotely controlled, solar-powered flying wing, designed and built as a proof of concept vehicle for a much larger aircraft capable of flying at extremely high altitudes for weeks at a time. Pathfinder is constructed of advanced composites, plastics and foam, and despite a wingspan of nearly 30 m, it weighs only about 300 kg. Current from solar arrays provides power during daylight, while stored energy allows flight after dark. The batteries allow an endurance of about 2 h in darkness.

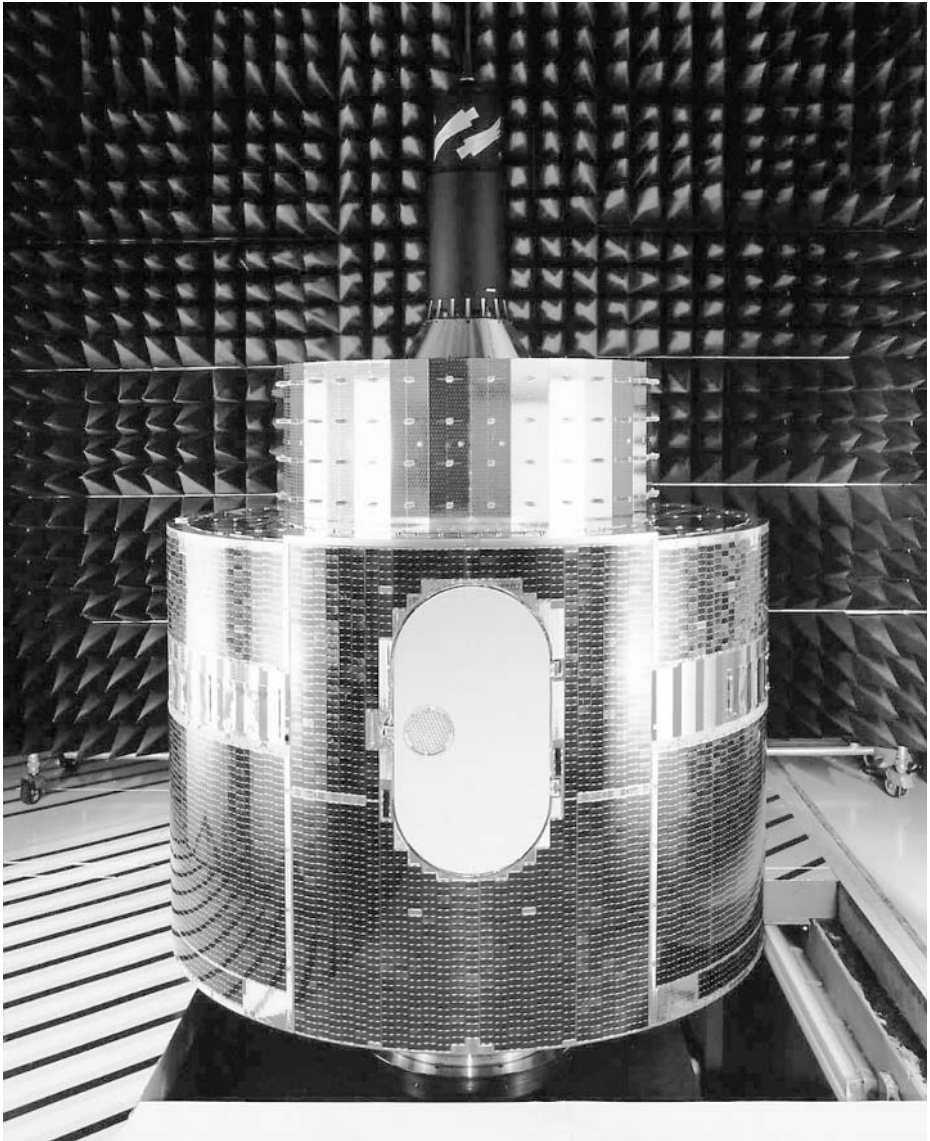


Figure 17.31 The weather satellite Meteosat, developed by the European Space Agency ESA

A further development of the Pathfinder is the Helios Prototype (Figure 17.33). The craft has a wingspan of 80 m, $2\frac{1}{2}$ times that of the solar-powered Pathfinder's flying wing, and longer than the Boeing 747 jetliner. Helios, which is relatively cheap to run and is harmless to the environment, is being developed mainly for commercial uses. Since the plane will be able to observe the Earth from a high-level altitude and will also function as a relay station for radio communications, its potential applications include weather observation as well as a collection of information in case of volcano eruptions and/or earthquakes.



Figure 17.32 The International Space Station

17.3 COMPONENTS FOR PV SYSTEMS

As has been seen in Section 17.2.2.8, the so-called balance of systems play a key role in the lifetime costs of photovoltaic systems. Therefore, the main components will be described as a summary; for more details, see the respective chapters in this book.

17.3.1 Battery Storage

Stand-alone PV systems require energy storage to compensate for periods without or within sufficient solar irradiation, such as during the night or during cloudy weather. In all cases in which electric energy storage is required, the classical electrochemical accumulator battery is the most convenient form of energy storage for a PV system, especially since its DC (direct current) characteristic allows for direct connection between



NASA Dryden Flight Research Center Photo Collection
<http://www.dfrc.nasa.gov/gallery/photo/index.html>
NASA Photo: EC99-45186-3 Date: September 1999 Photo by: Tom Tschida

Helios Prototype in flight over lakebed during second battery-powered flight

Figure 17.33 Helios, an unmanned prototype aircraft for flights at 30 km of altitude

the PV generator and the battery, without need for any conversion or transformation of the supplied PV energy.

Unfortunately experience has shown that in stand-alone PV systems, the battery appears to be the “weakest point” of the system, since its lifetime expectancy is usually an order of magnitude lower than that of all the other PV system components, and thus 30% of the lifetime costs of solar off-grid systems or even more may be attributed to the storage. Although a variety of storage technologies are under development, the lead-acid battery still is, and will be for some years to come, the working horse for electricity supplies in remote areas.

Typically, the storage battery of a stand-alone PV system is dimensioned to ensure, if the solar irradiation is insufficient, that the envisaged loads can be powered for at least 3 to 4 days. The result of such typical dimensioning is that the daily depth of discharge of a PV battery is in the range of about 25 to 30% of its rated (10 h) capacity. Furthermore, the dimensioning of the PV generator may usually be assumed to cover the entire energy

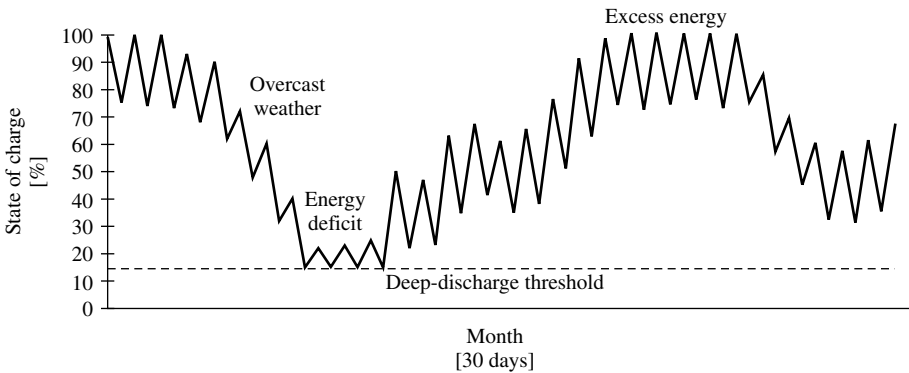


Figure 17.34 Operating conditions of batteries in PV systems

demand of the envisaged loads under average irradiation conditions. These two basic assumptions allow the following points regarding the typical operating conditions of a battery in a stand-alone PV system to be deduced (see also Figure 17.34):

- *Excess energy operation*: In summer, any PV system operates under excess energy operating conditions, since it is designed for lower (average) solar irradiation conditions. As a result, the battery reaches the maximum charge voltage threshold nearly every day at midday or during the early afternoon, and, until evening, it is fully (100%) charged. During the night, the battery discharges and in the morning, at sunrise, it reaches its minimum state of charge, approximately 70% of its rated capacity. During the next day, it repeats the same charge cycle as during the previous day and is again fully charged in the evening. These are optimum operating conditions for a PV battery.
- *Energy deficit operation*: In winter, if not significantly over-dimensioned, the same PV system will encounter energy deficit operating conditions more or less frequently. Each time cloudy weather (without direct sun) persists for some days, the state of charge of the battery will gradually diminish and sooner or later the battery voltage will drop below the minimum discharge voltage threshold. Unless the user reduces consumption voluntarily, the result will be that the DDP cuts off the load. Load cut-off will be maintained by the DDP until the battery is recharged during the next sunny day and reaches a reasonable voltage level, allowing the DDP to switch the load on again. During winter, depending on how carefully the user manages his/her PV system, the battery may very frequently suffer long periods of harmful deep discharge.
- *Float cycling operation*: During those days when the battery reaches neither the 100% full charge condition nor the minimum discharge voltage threshold, it cycles in a semi-charged float condition that is difficult to characterise. However, in comparison to the other two previously described operating conditions, this intermediate operating condition is of little overall significance for the life of the battery since it does not occur nearly as frequently as the other two.

Accordingly, the operating conditions and lifetime of a PV battery are primarily determined by the number of days when the battery reaches 100% full charge condition (which is the optimum) and the number of days when it reaches the minimum discharge

voltage threshold (worst operating condition). If the PV generator has been dimensioned to be too small for the envisaged loads, the battery will reach deep discharge conditions more frequently during the year and its lifetime will be short. If, instead, the PV generator is over-dimensioned, the battery will reach 100% full charge conditions nearly every day of the year, and its lifetime will be longer.

As battery lifetime is one of the key factors that determine lifetime costs of the whole stand-alone Photovoltaic system, one must obey a complex set of rules when aiming for maximum battery lifetime, that is, choose the best suited technology for your application, define properly suited end-of-charge and end-of-discharge thresholds, avoid deep discharge, avoid acid stratification in the electrolyte, avoid high battery temperatures, assure frequent full charging, avoid individualisation of single cells in a series of connected batteries and so on [28, 29]; for more details see Chapter 18.

In Table 17.1 the most important rules to achieve long battery lifetime are summarised.

It must be pointed out that some of the rules are generally in contradiction to each other (e.g. full charging needs high voltages but high voltages accelerate corrosion). In photovoltaic stand-alone systems, it may be difficult to follow these rules at all times. A compromise must be found between the demands of the battery for regular recharging and the investment into expensive photovoltaic generators, so energy may not be available during low insulation periods for recharging of the battery. As the application of the rules is the responsibility of the charge controller, it becomes evident how complex the technical design for this important electronic system component can be.

17.3.2 Charge Controller

Although photovoltaic systems can be used without charge controllers and this practice can be found very often in small PV systems, it has to be stated that while planning the long-term operation of a stand-alone photovoltaic system, it is a must to avoid overcharge and deep discharge. As has been seen in the previous chapter, battery costs over the lifetime of a PV system take the major share of the cost of the system. Battery lifetime again depends to a large degree on its operation strategy.

Table 17.1 Rules for battery management and their positive effects when they are applied

Rule for battery management	Effect when applied
Avoid high voltages during charging on the battery	Less corrosion and loss of water
Avoid low voltages during discharge of the battery	Less corrosion
Avoid extended periods without full charging of the battery	Less sulphatation
Avoid deep discharge	Less sulphatation and growth of dendrites
Avoid reverse charging of the cells	Less degradation of negative electrodes
Avoid stratification of the electrolyte	Less sulphatation
Avoid high battery temperatures	Slower ageing processes
Overcharge the battery slightly once a month	Frequent full charging is assured

The charge controller is the link between the solar generator, the battery and the load. It prevents both overcharging and deep discharging of the battery. A list of the most important requirements of the charge controller follows.

- Low internal consumption (<5 mA).
- High efficiency value (96 to 98%).
- Load disconnection if deep discharge occurs (current-dependent, discharge cut-off voltage, if possible).
- Regular charging at a higher voltage to promote gassing.
- Temperature compensation of the charging cut-off voltage (4 to 6 mV/K).
- Reverse poling impossible.
- Breakdown voltage of the semiconductor components at least twice the open circuit voltage of the solar generator.
- Integrated overvoltage protection (conducting capacity limit by a 8/20 norm impulse: 3 kA per installed kWp of the solar generator).
- Ambient temperature (0 to 50°C standard model).

When system complexity increases, then other aspects have to be considered in designing a stand-alone PV system: with appropriate energy management schemes, the use of the electricity generated and the lifetime of sensitive system components can be further optimised, for example, switching off less priority loads, switching on water pumps to access energy to fill a water storage, starting the back-up generator to avoid critical situations for the battery. These energy management units have to be designed specifically for the foreseen application. As described earlier, it is highly recommended that the system displays units that inform the user about the current status of the system and give them advice about how to react in an appropriate way.

17.3.3 Inverters

Inverters are power electronic devices used in various photovoltaic (PV) system configurations:

- grid-connected systems
- stand-alone systems with rechargeable batteries
- pumping systems without storage batteries.

17.3.3.1 Inverters for grid-connected systems

The planning of a grid-connected photovoltaic system begins with the choice of a suitable inverter. This determines the system voltage on the DC side, and the solar generator can then be configured according to the input characteristics of the solar inverter. The inverter is the second most important component of a grid-connected photovoltaic system (after the solar generator). Its task is to convert the direct current generated by the solar cells to a 50-Hz alternating current conforming to the grid. In contrast to inverters intended only for stand-alone operation, those intended for parallel operation must respond just as

well to the grid characteristics as to the solar generator performance. As all of the solar current flows through the inverter, its properties fundamentally affect the behaviour and operating results of the photovoltaic system.

Apart from the efficient conversion of direct to alternating current, the inverter electronics also include components that are responsible for the daily operation mode. They ensure that operation starts at the right time in the morning as soon as the solar cells deliver enough power. Unsuccessful start attempts require energy from the grid and should be avoided by good controls. During the day, the optimum working point on the I-V characteristic curve shifts according to the fluctuations in solar radiation and module temperature. Intelligent inverter control includes maximum power point (MPP) tracking and continuous readjustment to the most favourable working point. Protective devices are also integrated into the inverter, which automatically disconnect the system if irregularities in the grid or the solar generator occur.

Today most inverter models are additionally equipped with data loggers and measurement computers, which allow the power, voltage, current and other operating parameters to be recorded continuously. These data can be read out at intervals via a serial interface with a laptop computer and analysed.

17.3.3.2 Inverters for stand-alone systems

Because of the specific operating conditions of stand-alone inverters, different design aspects have to be considered.

In a typical domestic power supply, the ratio of the peak power to the average power is about 25:1, so the inverter must have a high efficiency of approximately 90%, particularly in the partial load range (5–10% of the rated power). Only a few inverters satisfy this condition together with a sinusoidal output voltage and the capacity to withstand short-term, double to triple overloading. Depending on the requirements, both sinusoidal and rectangular waveforms can be used.

The most important requirements on inverters for stand-alone photovoltaic systems are summarised in the following list.

- Large input voltage range (–10% to +30% of the rated voltage).
- Output voltage as close to sinusoidal as possible.
- Little fluctuation in the output voltage and frequency.
- $\pm 8\%$ voltage constancy, $\pm 2\%$ frequency constancy.
- High efficiency for partial loading; an efficiency value of at least 90% at 10% partial load.
- Ability to withstand short-term overloading for appliance starting conditions, for example, two to three times the rated current for 5 s for refrigerators and washing machines.
- Lowest possible overvoltages for inductive and capacitive loads.
- Half-wave operation possible, caused by power reduction with a diode, for example, in hair dryers.
- Able to withstand short circuits.

However, the following restrictions apply to the use of inverters with a rectangular waveform:

- Because the voltage level at the zero crossing is not clearly defined, the function of some appliances with electronic controls (e.g. modern washing machines) is affected.
- The steep voltage gradients destroy resistors in simple power supplies (e.g. in freezers) by overloading.
- The steep voltage gradients result in increased noise and heat generation in transformers and motors. Further, a reduction of about 10% in the efficiency value must be expected.

17.3.4 Auxiliary Generators

In general, diesel generators are used today in larger photovoltaic hybrid systems with an energy demand of around 10 kWh/day. For systems with a daily energy demand of a few hundred watt hour up to a few kilowatt hour, small combustion motors, small fuel cells, thermoelectric generators (TEG), thermophotovoltaic generators (TPV) or appropriate thermodynamic converters such as small Stirling motors all come into question in principle. If adequate commercial availability is regarded, at present the choice is narrowed essentially to small combustion motors (diesel, petrol) with a coupled generator, and thermoelectric generators. While the investment costs and the availability in nearly all countries make petrol and diesel generators very attractive, the inherently high reliability, low maintenance and the almost silent operation and simple remote starting facilities speak for the application of thermoelectric generators in small photovoltaic hybrid systems (Table 17.2).

Table 17.2 Comparison of the characteristics of small, commercially available auxiliary generators [30]

	Small combustion motors		Thermoelectric
	Petrol	Diesel	
Electric power range	>0.3 kW	>3 kW	>0.03 kW
Efficiency value at full load	App. 5–15%	App. 20–25%	App. 3%
Adjustability	Good	Good	Limited
Remote starting	Yes, >3 kW	Yes	Yes
Reliability	Medium	Medium	High
Maintenance demand	High	High	Low
Environmental acceptability	Pollution emission CO ₂ emission Noisy	Pollution emission CO ₂ emission Noisy	Pollution emission CO ₂ emission Almost silent
Commercial manufacturers available	Globally	Globally	Few
Fuel:			
Type	Petrol	Diesel	e.g. propane/butane
Availability	Medium	High	Medium
Consumption	0.6–1 l/kWh	0.4–0.5 l/kWh	2–2.5 kg/kWh

A significant disadvantage of combustion motors is their need for regular maintenance. Car manufacturers recommend for diesel motors a change of the lubricant at least every 10 000 km. If we assume an average speed of 50 km/h, this means that after 200 h of operation a complete service is necessary. Keeping in mind that a back-up generator in a stand-alone system is working in optimised systems at least for 2 h and in conventional systems for about 6 to 8 h a day, this means that in optimised systems every 3 months and in conventional systems every 30 days a complete maintenance service has to be calculated. Together with the high costs for fuel transport, this is the main reason for the low attractiveness of combustion motors in off-grid electrification.

17.3.5 System Sizing

In addition to the quality of the system components and the construction of the system, the sizing of the solar generator and the storage battery plays an important role in the operating reliability of a photovoltaic power supply. The dimensions of the solar generator and the storage battery determine what proportion of the consumer's energy demand can be met by the photovoltaically generated electricity. A photovoltaic system should be sized in accordance with the other planning steps:

1. Determination of the energy demand and optimisation of the consumption: This step includes determining the energy demand of the intended consumers as exactly as possible and investigating possibilities for saving energy by reducing the power consumption of the appliances or systems used.
2. Development of the concept: Setting the voltage level (in many cases this is determined by the user) and thus the type of photovoltaic system (DC, AC, combined DC and AC, grid-connected, stand-alone, with or without a back-up generator).
3. Choice and dimensioning of the system components for power conditioning: Converters to match the power generation and consumption sides are chosen according to the system type. The efficiency values of these components often have a decisive influence on the system energy balance and thus must be taken into account when sizing (step 4). This applies particularly to inverters used to supply power to conventional 230-V appliances.
4. Sizing the solar generator and the storage battery.
5. Dimensioning the solar charge controller.
6. Dimensioning the cables: The voltage drops occurring in cables should not be ignored, particularly in larger systems operating at a low voltage level.

It may be necessary to iterate steps 1 to 4 several times. For example, the result obtained in the sizing step 4 may demand a further reduction in consumption or a change in the system concept (e.g. incorporation of an additional generator), for various reasons (insufficient area for the solar generator, system cost etc.).

Generally, several variants are considered during the planning stage, which differ in aspects such as supply reliability, cost, maintenance demand and electrical and structural configuration. The priority given to each aspect depends on the particular application intended for the photovoltaic power supply. For a system that is required to

operate completely autonomously, the supply reliability is decisive, whereas this issue is of secondary importance for a household supply in which a back-up generator is included anyway.

The operation behaviour of the photovoltaic system is characterised and evaluated with the help of a suitable computation procedure. It is particularly important to know the system's operation behaviour with regard to the supply reliability and the effective use of the photovoltaically generated electricity.

The optimal tilt angle for the solar generator depends on the specific conditions under which the system is operated. A clear distinction must be made between grid-connected and stand-alone systems. Grid-connected systems are generally optimised to achieve the maximum possible annual yield. As all of the energy output from the solar generator is used either by direct consumption or by being fed into the public electricity grid, the system yield has the same dependence on the orientation and tilt angle as the solar radiation incident on the solar generator (Figure 17.35).

The optimum tilt angle of about 30° is smaller than the average solar zenith (equal to 90° latitude), as the major share of the solar radiation is incident during the warmer six months for the Central European climate.

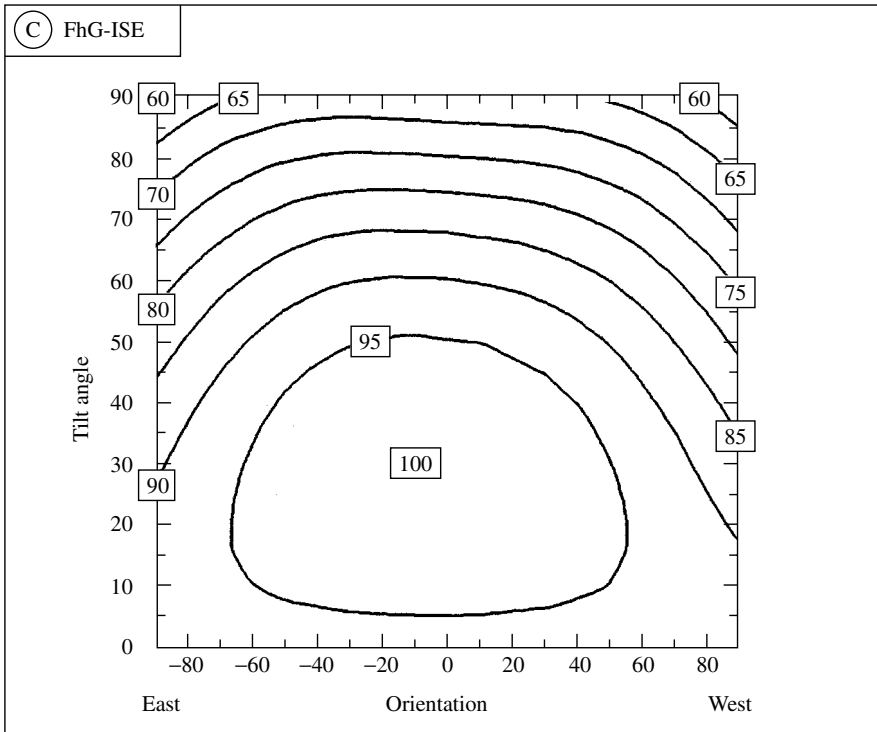


Figure 17.35 Dependence of the annually used solar energy from a grid-connected system dependent on the orientation and tilt angle (percentage values relative to the maximum used solar energy; orientation 0 = south, for the northern hemisphere)

In stand-alone systems, the fundamental difference in operating behaviour as compared to grid-connected systems is due to the storage battery. As stand-alone systems generally have to achieve a certain, pre-determined solar fraction within a given operating period, the decisive time within that period for the system sizing is the one during which the radiation level is lowest. The optimal tilt angle depends not only on the radiation characteristic but also on the system itself. Figure 17.36 shows the optimal tilt angle, for which the solar generator area is minimal for the relevant pre-determined solar fraction, and the corresponding solar generator power.

Whereas in summer, the storage capacity does not have any effect on the optimal tilt angle (solid line), a dependence can be observed in winter (dotted line); higher solar fractions lead to less steep inclinations, particularly for small storage capacities. The explanation for this difference is the variation in the daily radiation in winter. If the storage capacity is small, sunny days lead to surpluses, so that the available radiation cannot be fully used. Thus, on overcast days, the (weak) diffuse radiation must be used optimally, with a less steep slope (smaller tilt angle) as a result.

17.3.6 Energy-saving Domestic Appliances

On average, a four-person household in Germany consumes about 3500 kWh electricity per year, if electricity is used neither for space heating nor for water heating. In order to meet this demand, for example, with a grid-connected photovoltaic system, about 4-kW rated power, that is, a module area of about 40 m², would be needed in Southern Germany. With a module price of about 4 € per watt of rated power, the solar modules alone would cost €16 000. In view of these high investment costs, the potential for saving energy with the appliances used in the household should be exploited as far as possible, rather than investing in a large system.

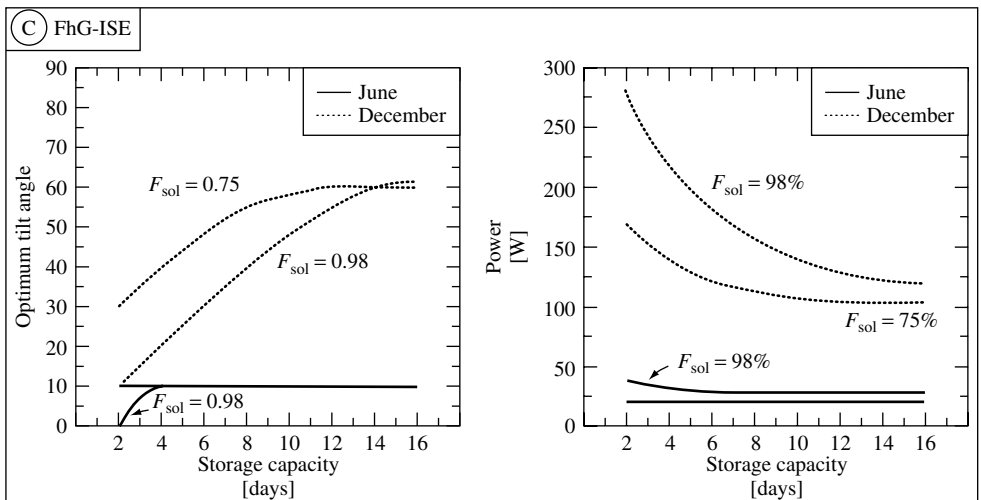


Figure 17.36 Optimal tilt angle for minimising the solar generator size and corresponding values of the solar generator power as a function of the storage capacity

Table 17.3 Electricity consumption (kWh/year) of household appliances

Appliance	Wasteful	Average	Energy saving
Refrigerator (upright, No freezer, 100 liter)	270 (100%)	230 (85%)	87 (32%)
Freezer (upright, 200 liter)	800 (100%)	426 (53%)	168 (21%)
Refrigerator/freezer combination (upright, 200 liter)	625 (100%)	343 (55%)	267 (54%)
Washing machine (without a hot water connection) ^a	522 (100%)	366 (70%)	280 (54%)
Washing machine (with a hot water connection, 60°C) ^b	– –	– –	202 (38%)
Dishwasher (without a hot water connection) ^c	614 (100%)	481 (68%)	296 (48%)
Lighting (5 × 60 W) ^d	438 (100%)	–	87 (20%)

^aUse: 3 full loads per week, each with 5 kg of washing

^bRelative to a machine with 522 kWh/year

^cUse: 5 loads per week with 10 settings per load

^dUse: 4 h per day

Table 17.3 demonstrates how large the potential is for saving energy with household appliances. The absolute electricity consumption is given for a wasteful, an average and an energy-saving appliance in kilowatt hour per year. The table shows that the electricity consumption for some appliances can be reduced by up to 80%, without a loss in convenience, simply by using modern, energy-saving models. It is also evident that connecting the washing machine and the dishwasher to a non-electric hot water supply can reduce the electricity consumption still further.

Refrigerators and freezers, washing machines and dishwashers are purchases that are expected to last for many years. Thus, it is certainly worthwhile investing in energy-saving appliances that have a particularly low electricity and water consumption.

If energy saving is taken seriously, a four-person household can achieve an annual consumption of about 700 kWh, not including electricity for building services (electric doorbell, outside light, heating pump etc.). Even when not completely energy-optimised, a four-person household can manage with an annual consumption of 1500 kWh, including building services.

17.4 FUTURE DEVELOPMENTS IN PHOTOVOLTAIC SYSTEM TECHNOLOGY

17.4.1 Future Developments in Off-grid Power Supply with Photovoltaics

Rural electrification with photovoltaics has become a rapidly emerging market in the last few years. While grid extension is getting more and more difficult because of the high costs of connection in remote households with their relatively low-energy consumption

for lighting and communication, about two billion people worldwide stay without access to electricity as the modern form of energy supply. As the population, especially in rural areas of developing countries, grows rapidly, there are more people each day without access to electricity than the day before!

This is why in many countries rural electrification programmes have been initiated. These programmes explicitly foresee the application of photovoltaic systems to provide electric power to remote rural households and public facilities, for example, Argentina has electrified 300 000 households and 6000 public facilities, in Morocco all villages in rural areas shall be electrified within the year 2010, which takes into consideration that about 200 000 households have to be supplied by photovoltaics; in many other countries such as China, Indonesia, India, Sri Lanka, Philippines, Mexico, Bolivia, Kenya, Uganda or South Africa large programmes do exist or are in preparation for realisation in the near future. The World Bank as one of the major support organisations in rural electrification is involved in more or less all these national programmes, thus helping to cover the high up-front costs of PV rural electrification and establishing innovative financing schemes. Most of these programmes today concentrate on Solar Home Systems, as these systems are relatively easy to install and operate. However, the key for success or failure of these programmes lies in the establishment of appropriate infrastructures for installation, operation and maintenance of these systems as well as in the introduction of schemes for quality certification, microfinancing and adequate involvement of the users [9, 21, 31].

After some disastrous experiences with village power supply systems in the seventies and early eighties, they see today a revival in many rural electrification programmes. The reason for this is that much better suited and more reliable components are available today and that more and more utilities or other energy service companies (ESCO) are starting to enter the market. With these new players a different concept appeared, which is the provision of energy service instead of selling PV systems. In Argentina, for example, the companies getting engaged in rural electrification – and benefiting from the subsidy scheme set-up there – have to sign a contract of serving the rural population with electricity for at least 45 (!) years. Here, often village power supply systems are applied: a small electric grid is created that may be considered as similar to the already existing public electricity grid. However, because of the strong limitation of the resources compared to a large electricity grid, new models have to be developed to plan, market, operate and sell this service. The involvement of the users in these central systems is seen as essential as the behaviour of the whole community does have a major impact on the appropriate use of the limited power and energy provided. Appropriate financing schemes, such as prepayment meters or the involvement of microfinancing institutions in the whole process, are new developments that will have to be elaborated further in the near future.

Today about two billion portable appliances are used worldwide and the market is rapidly growing. In the near future, the doubling of this number is expected. Watches, laptops, mobile phones, palm pilots and so on are characteristic for the new information society. This means the future of information is free of cables. Most of these devices are powered by batteries, but they are often flat and have to be recharged at a grid-based charging station. Photovoltaics are considered to be one of the best solutions to cover the often low-energy demands of these grid-independent devices. First prototypes do exist. The development of the market will be successful if adapted systems can be

developed that can cope with the often extreme restrictions of miniaturisation and the often lacking availability of sunlight or at least of artificial light. Highly efficient solar cell highly miniaturised and also efficient energy conversion and new product design adapted and suited to the energy source will be the key factors of a successful market penetration.

In parallel to the power supply of the appliances themselves, a need arises for repeaters of the signals to be transmitted, which will be lower in its energy and power demands but will have to guarantee permanent availability. As these repeaters will have to be located on peaks or tops of hills and mountains, grid connections will be very often too expensive. Therefore, low-maintenance hybrid systems will gain a natural market where they can compete with the extremely high requirements concerning reliability and ease of operation.

In all stand-alone applications, the storage unit is one of the technical components that still needs the most development. Often described as the weakest link in the chain, it is responsible for a large share of the costs in long-term operation. Thus, optimisation of the interaction of all components in the system with the aim of reducing the overall lifetime costs is today the main issue on this sector. As also the battery industry has recognised, there is a great need for the development of better battery management principles, adaptation of the existing battery technologies to the charging and discharging requirements in photovoltaic systems and the development of completely new and better suited storage units.

17.4.2 Future Developments in Grid-connected Photovoltaic Systems

Today's electricity supply systems in industrialised countries are based on a structure with large central power stations that supply consumers via a dense distribution grid. This structure will suffer increasingly in the liberalised markets, as it is not flexible enough in the choice of primary energy sources to allow energy flows and energy costs to be optimised. In addition, obtaining authorisation for large technological power plants or grid extensions will become more and more complicated. Furthermore, this type of capital-intensive structure could hardly be implemented for comprehensive electrification in developing countries. There are several ongoing approaches to develop novel grid structures, which enable both the optimisation of existing grids in industrialised countries and ecologically acceptable electrification in threshold countries. These approaches aim to help in a transition to a decentralised structure of small and medium sized generators. In these concepts new devices such as cogenerations sets, fuel cells, renewable energy systems, such as photovoltaics, wind, micro hydro, biomass and so on, can play a key role (Figure 17.37).

However, because of specific operational constraints of all these components, new devices have to be incorporated in such a structure to achieve an optimised use of these new technologies. Short-term energy storage consisting of locally installed batteries or flywheels, power quality management (also on the low voltage side to reduce voltage breakdowns and compensate harmonic distortions) and intelligent communication systems between the single components and a central energy management unit have to be applied.

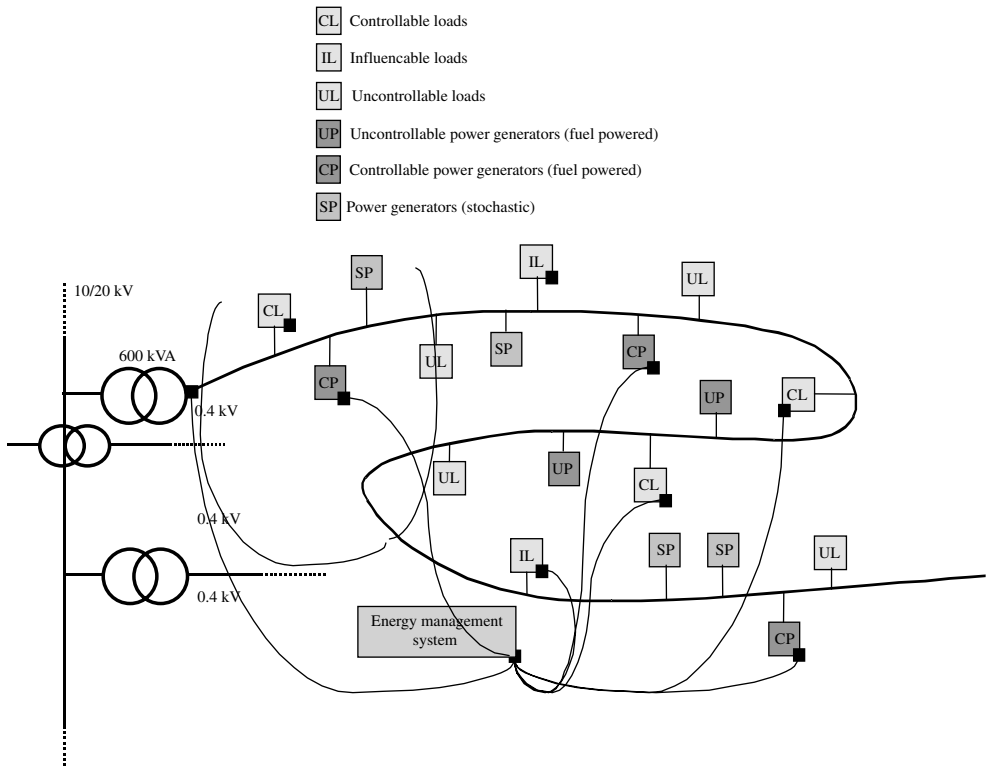


Figure 17.37 Future, decentralised grid structure with superimposed communication network

REFERENCES

1. Räuber A, Wettling W, Die P, "Szene heute – Technologie, Industrie, Markt", 16. *Symposium Photovoltaische Solarenergie*, 14.-16.03.01, Staffelstein (2001).
2. Amann J *et al.*, *Produkte mit integrierter photovoltaischer Energieversorgung*, BMBF-Statusseminar Photovoltaik, Bad Breisig, 23.-25.4.1996, S. 43-1–S. 43-20 (1996).
3. Roth W, Lemmel H, *Elektronik Fachzeitschrift für industrielle Anwender und Entwickler* **18**, S. 84–S. 88 (1: Journalist für Technik und Wissenschaft) (1999).
4. Roth W, Lemmel H, *Elektronik Fachzeitschrift für industrielle Anwender und Entwickler* **20**, S. 40–S. 43 (1: Journalist für Technik und Wissenschaft) (1999).
5. Pfanner N, Roth W, Steinhüser A, "Application of Photovoltaics in the Stationary Sector of Road Traffic", *12th European PV Solar Energy Conference*, 11.-15.4.1994, S. 206 (Amsterdam, 1995).
6. Asia Alternative Energy Unit ASTAE, *Best Practices for Household Electrification Programs: Lessons from Experiences in Selected Countries*, World Bank Technical Paper, Number 324 (1996).
7. Njaimi M, Ounalli A, Ullerich U, "Solar Home Systems: An Alternative to Rural Electrification Programs via the Electric Grid", *11th EC Photovoltaic Solar Energy Conference* (Montreux, Switzerland, 1992).
8. Parodi O, Preiser K, Schweizer P, "Balde de Leyes: The Integrated Way to Electrical Light", *13th EU PV Solar Energy Conference* (Nice, France, 1995).

9. Preiser K, Parodi O, Kuhmann J, "Quality Issues for Solar Home Systems", *13th EU PV Solar Energy Conference* (Nice, France, 1995).
10. Foley G, *Electricity for Rural People*, Panos Publication Lmt., London N1 9PD, UK (1990).
11. Foley G, *Photovoltaic Applications in Rural Areas of the Developing World*, World Bank Technical Paper, Number 304 (1995).
12. The World Bank, *Rural Energy and Development – Improving Energy Supplies for Two Billion People*, ISBN 0-8213-3806-4, The World Bank, Washington, DC (1996).
13. Kleinkauf W *et al.*, "Decentralized Grid-Compatible PV Power Supply – Strategy For Electrification And Integration Concepts with Modular Technology", *2nd World Conference on PV Solar Energy Conversion* (Vienna, Austria, 1998).
14. Wiengmoon B, Wattanapong R, Parodi O, Wiemken E, "PV-Battery Charging in the Huay Dua Village, Thailand", *South-East Asia PV Conference* (Phuket, Thailand, 1997).
15. Mc Nelis B, Barlow R, "Photovoltaic Water Pumping", in Hille G, Roth W, Schmidt H, Eds, *PV Systems*, Seminar Handbook, Fraunhofer ISE, Freiburg, Germany (1995).
16. WHO – World Health Organisation, *Guidelines for Drinking Water Quality*, Volume I: Recommendations, Geneva, Switzerland (1993).
17. UNDP – United Nations Development Programme, *Human Development Report* (1998).
18. Parodi O, Preikschat M, Preiser K, "PV Contra Coli-Bacteria – Suitability of UV-Water Purification Devices for PV Systems", *14th EU PV Solar Energy Conference* (Barcelona, Spain, 1997).
19. Butera F, *Renewable Energy Sources in Developing Countries: Success and Failures in Technology Transfer and Diffusion*, Progetto Finalizzato Energetica, Rome (1989).
20. Parodi O, Preiser K, Schweizer-Ries P, Wendl M, "When Night Falls on Balde de Leyes – The Success story of an Integrated Approach in PV Rural Electrification", *2nd World Conference and exhibition on Photovoltaic Solar Energy Conversion* (Wien, Austria, 1998).
21. Gabler H, Preiser K, *Technical Quality Control for Solar Rural Electrification*, Institutional Cooperation for Solar Energy Activities in Mekong Riparian Countries, Hanoi, Vietnam (1998).
22. Erge Th *et al.*, "The German 1000-Roofs-PV-Programme – a Résumé of the 5 Years Pioneer Project for Small Grid-Connected PV Systems", *2nd World Conference and Exhibition on Solar Energy Conversion*, 6.-10.7.1998, S. 2649–S. 2651 (Wien, Österreich, 1998).
23. Heydenreich W, Wiemken E, Gabler H, Kiefer K, "Correlation Between Photovoltaic Energy Production and Household Electricity Consumption – Evaluation of Data from the German Thousand Roofs Programme", *Proceedings EuroSun '96* (Freiburg, Germany, 1996).
24. Erge Th, Kiefer K, Hoffmann V, *Sol. Energy J.* **70**(6), 479–487 (2001).
25. Haas R, *Marketing Strategies for PV Systems in the Built Environment*, Working Document for Task VII of the IEA-PVPS – Implementing Agreement (2001).
26. Stubenrauch F, *Renewable Energy Policy in Germany*, Projektträger BEO, <http://www.agores.org> (2000).
27. Hille G, Preiser K, "Innovative Financing Scheme: Joint Ownership of Photovoltaics", *ALTENER-Conference 2000* (Toulouse, France, 2000).
28. Bopp G *et al.*, "A Systematic Effort to Define Evaluation and Performance Parameters and Criteria for Lead-Acid Batteries in PV Systems", *13th European Photovoltaic Solar Energy Conference* (Nice, France, 1995).
29. Sauer D *et al.*, *J. Power Sources* **64**, 197–201 (1997).
30. Steinhüser A, Roth W, Schulz W, Schmidt H, "Photovoltaic Power Supply for Telecommunication Network Components in Remote Areas", *Proceedings Telescon 2000–The Third International Telecommunications Energy Special Conference*, 7.-10.5.2000, S. 221–S. 225 (Dresden, 2000).
31. Schweizer P, *Psychologische Faktoren bei der Nutzung regenerativer Energien. Eine Studie zum Einsatz von Solartechnik im zentralen Himalaya*, ISBN 3-931660-51-6, Ph.D. thesis at the University of Heidelberg, Heidelberg, Germany (1995).

18

Electrochemical Storage for Photovoltaics

Dirk Uwe Sauer

Fraunhofer Institute for Solar Energy Systems ISE, Freiburg, Germany

18.1 INTRODUCTION

The availability of solar energy is not only different with respect to the annual yield but varies within the seasons of the year, during day and night and from day to day due to the weather conditions. So do the electrical loads. To balance the differing time patterns of loads and solar energy production, energy storage must be included in almost all autonomous power supply systems. Thirty percent or even more of the lifetime costs of autonomous power supply systems based on solar energy may be attributed to the storage. Only very few autonomous photovoltaic (PV) power supply systems have no battery storage system. These are PV or wind-pumping systems where the difference between water demand and energy supply (solar radiation) is levelled out by means of a water storage tank.

PV-powered autonomous power supplies power the complete range of appliances from very small appliances (watches, calculators) with a few milliwatt power requirements to large village power supply systems with about 10 kW power requirements. This chapter is dedicated to applications of PV generators in the range of approximately 10 W to 10 kW. This excludes very small appliances where different storage concepts are used.

There are a number of technical solutions to the problem of energy storage. Storing energy in the electric field of a capacitor is a solution for storage times ranging from microseconds up to 10 s. Storing energy in the magnetic field of a coil is a technology that has been under development for many years (supraconducting coils). It has, however, until today, not resulted in a product that has entered the commercial market.

Medium and high-speed flywheels are being operated in small numbers in grid support, uninterruptible power supplies and in underground railways or buses to overtake

energy from regenerative braking and to support acceleration. However, storage times are in the range of seconds. Compressed air storage in the MWh range, which after decades of development has not reached the market, and pumped water storage are the other technologies that store the energy mechanically. Pumped water storage shows a pronounced economy of scale, which means that larger systems have lower specific investment costs and better storage efficiencies. This is the reason pumped storage has its application in small grids that supply power in megawatt hours per day rather than in the domain of energy systems based on photovoltaics, which are and will be designed to deliver some 10 kilowatt hours per day.

The most promising storage technologies today for the application of which we are discussing here, are electrochemical systems [1]. Therefore, this chapter is dedicated to electrochemical storage systems only.

Although a variety of storage technologies are under development, for the systems focused in this chapter the lead acid battery still is, and will be for some years to come, the working horse for autonomous power supply systems. The ageing effects that limit battery lifetimes are treated in detail. Optimised control strategies allow increasing the battery lifetime and a considerable reduction of the overall system costs.

For storing large energy quantities with low power requirements, electrochemical storage systems with separate storage and power conversion units are under development. These are namely hydrogen storage systems with an electrolyser and a fuel cell as converters and redox-battery systems. The latter use charged ions from metal salts dissolved in liquids as the storage medium and a converter unit quite similar to a fuel cell. These systems are getting more and more interesting as seasonal storage systems and for balancing power generation and power demand in grids with a high penetration of renewable power sources (mainly wind and sun).

There are numerous requirements for storage systems in autonomous power supply systems. Their importance in different applications is different; some of them are in contradiction to each other and therefore they cannot be fulfilled at the same time. Table 18.1

Table 18.1 Requirements to electrical storage systems in autonomous power supply systems (the order of appearance does not imply any weighting of their importance)

<ul style="list-style-type: none"> ● High energy efficiency ● Long lifetime (years) ● Long lifetime in terms of capacity throughput ● Low costs ● Good charge efficiency even at very low currents ● Low self-discharge rate ● Low maintenance requirements ● High availability worldwide ● High power availability ● Easy estimation of state of charge and state of health 	<ul style="list-style-type: none"> ● Low exposure ● Easy recycling ● Low toxicity of materials ● Fail-safe behaviour at overcharging or deep discharge ● Easy extendibility in voltage and capacity through series and parallel connection ● Low voltage gap between charging and discharging (allows direct connection of loads to the battery) ● Fast charging ability ● No memory effect ● Low explosive potential ● High reliability in operation: high MTBF
--	--

Note: MTBF: mean time between failure

gives an overview of the most important requirements of batteries in autonomous power supply systems.

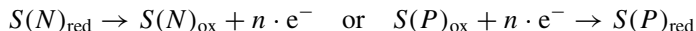
System designs for autonomous power supply systems should track the properties and the requirements of the storage system from the very beginning. Planning of a system and later on just adding the storage will neglect the numerous interactions between the storage, its peripherals and its operation strategy and the overall system design and control. Therefore, only an integrated planning of the system allows to use all synergies and to design systems that can be operated during their lifetime at minimum costs.

18.2 GENERAL CONCEPT OF ELECTROCHEMICAL BATTERIES

18.2.1 Fundamentals of Electrochemical Cells¹

18.2.1.1 *The equilibrium potential*

The basic element of each battery is the electrochemical cell. A positive and a negative electrode are immersed in an electrolyte. The reactive substances (the active materials) are stored in the electrodes.² Chemical and electro chemical reactions, the electrode reactions, occur at both electrodes, which release or absorb electrons according to



N and P indicate negative and positive electrodes, S_{red} and S_{ox} indicate the reduced and oxidised states of the chemical compounds that react and n is the number of electrons involved in the process. The possibility of splitting up the cell reaction into two separate electrode reactions is a decisive prerequisite for the realisation of any electrochemical cell. Only then can the electron exchange connected with the electrode reactions be collected as a current that flows through the consumer (or the charging device), and the energy input or output connected with the chemical reaction be converted into electrical energy. Otherwise, the reaction would occur merely as a chemical reaction. The electrical charge would be exchanged directly between the reacting substances and the released energy would be converted predominantly into heat and to some extent into volume energy.

The electrochemical storage system is based on the conversion of chemical energy into electrical energy and vice versa. The amount of energy that can be stored in a cell is determined by the different energy content of chemical substances that represent the charged and discharged states. Consequently, the characteristic parameters of the system are determined by a number of electrochemical reactions and the energetic changes connected with these reactions. In total, these reactions result in the cell reactions that characterise the battery system.

¹ This section is based on Chapters 2.1, 2.2 and 2.3 from the book of D. Berndt "Maintenance-free batteries" [3] which can be highly recommended for a deeper insight into applied battery technology.

² Please note: the wording used herein is characteristic for classical electrochemical secondary accumulators with solid active masses and a liquid electrolyte. In fact, batteries with solid electrolytes and liquid active masses exist as well. Examples are redox-flow batteries (see Section 18.5.1) or the NaS batteries (liquid Na and S as active masses, solid oxide ceramic as electrolyte).

The laws of thermodynamics generally apply to the equilibrium, which means that all reactions are balanced. In the electrochemical cell, these data can only be measured when no current flows through the cell or the electrodes. On account of this balance, the thermodynamic parameters do not depend on the reaction path; they depend only on the difference between the final and initial components of the electrochemical reaction.

Because of the equilibrium conditions, the laws of thermodynamics describe the possible upper limit of the performance data. As soon as the current flows through the cell, energy losses occur due to kinetic restrictions and ohmic resistance.

The energy exchange, connected with electrochemical reactions, is described by the following thermodynamic parameters. As far as these parameters concern chemical or electrochemical reactions, they actually describe the difference between the parameters before the reaction started and after it was completed. Therefore, they are expressed as the difference between the initial and the final state of the reaction.

- *Enthalpy of the reaction* ΔH , which describes the amount of energy released or absorbed. It is derived from the energy content of the chemical compounds H .
- *Free enthalpy of the reaction* ΔG (also called the Gibbs free energy), which represents the (maximum) amount of chemical energy that can be converted into electrical energy, and vice versa.
- *Entropy* ΔS , which characterises the energy loss or gain connected with the chemical or electrochemical process. The product $T\Delta S$ represents the heat exchange with the surroundings when the process occurs reversibly. This is synonymous with minimal heat loss or gain of the system, which is true only when no current flows through the battery.

T is the absolute temperature. The most important relation among these parameters is given by the following formulae:

$$\Delta G = \Delta H - T \cdot \Delta S$$

As ΔG describes the amount of energy that can be converted into electrical energy, a simple relation between the Gibbs free energy and the equilibrium voltage³ E_0 of the cell can be derived.

$$\Delta G = -n \cdot F \cdot E_0$$

where n is the number of exchanges of electronic charges, F is the Faraday constant (96485 As) and nFE_0 describes the generated electrical energy.

Thermodynamic quantities like ΔH and ΔG depend on the concentration of the reacting components as far as these are dissolved according to the relation

$$\Delta G = \Delta G_S + R \cdot T \cdot \sum_i \ln[(a_i)^{j_i}]$$

³ Occasionally, the equilibrium voltage is called the open-circuit voltage. However, strictly speaking this term only means a voltage without external current flow, and may concern a mixed potential as well. On account of secondary reactions, the rest potential in batteries are usually mixed potentials, but this is not strictly observed in practical languages.

with $a_i = \text{activity}^4$ of the reacting components i (closely related to the concentration),
 $j_i = \text{number of equivalents of this component that take part in the reaction,}$
 $R = \text{molar gas constant for an ideal gas } (R = 8.3413 \text{ J/K/mole}),$
 $\Delta G_S = \text{standard value when all activities are unity.}$

From these equations, the Nernst equation describing the concentration dependence of the equilibrium voltage can be derived, where $E_{0,S}$ is the equilibrium potential in standard conditions.

$$E_0 = E_{0,S} + \frac{R \cdot T}{n \cdot F} \cdot \sum \ln[(a_i)^{j_i}]$$

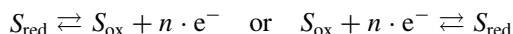
The temperature coefficient of the equilibrium cell potential can be derived from the following thermodynamic relation.

$$\frac{dE_0}{dT} = -\frac{\Delta S}{n \cdot F}$$

Thermodynamic calculations are always based on a complete cell, and the derived voltage refers to the potential difference between two electrodes. The potential difference between the electrode and the electrolyte, the “absolute potential”, cannot be determined. The name electrode potential always refers to a potential difference measured with the aid of a reference electrode. To get a basis for the electrode-potential scale, the zero point was arbitrarily equated with the potential of the standard hydrogen electrode (SHE⁵).

18.2.1.2 Electrode kinetics at current flow

When current flows through a cell, the reaction must take place at a corresponding rate. For each delivered ampere-second, a corresponding number of electron exchanges must have occurred. This means that at the electrodes the elementary processes



must take place $6.42 \cdot 10^{18}/n$ times (reciprocal of one elemental charge). To achieve this current flow, additional forces are required, which intensify the electron and ion flow in the required direction. These additional forces find their expression in deviations from the equilibrium data, which means irreversible energy loss.

⁴ Activity described the “effective concentration”. Thermodynamic rules are derived for dilute solutions. The activity is equivalent to the concentration in very dilute solutions, but the activity can be different at higher concentrations as interactions among the ions in the solution need to be taken into account.

⁵ The standard hydrogen electrode means a hydrogen electrode immersed in acidic solution with H^+ ion activity of 1 mole/dm³ and H_2 pressure of 1 atm. The specification of the electrolyte concentration is required because the potential of the hydrogen electrode depends on the H^+ ion concentration and is shifted by -0.0592 V when the H^+ concentration is reduced by one decade. The potential of the standard hydrogen electrode at 25°C is synonymous with the zero point of the potential scale. The temperature coefficient of the standard hydrogen electrode is $+0.871 \text{ mV/K}$.

Usually, the reaction path consists of a number of reaction steps that precede or follow the actual charge-transfer step, and the rate of each these reaction steps is determined by its kinetic parameters, such as exchange current density, diffusion coefficient or transport numbers. The slowest partial step of this chain is decisive for the rate of the overall reaction. As a consequence, limitations of the reaction rate are often not caused by the electron-transfer step itself, but by preceding or following steps such as the transport rates of the reacting ions to and from the electrode surface.

Transport processes play an important role, because electrochemical conversion can only take place when reaction partners and electrons are available at the same time. Frequently, the reaction substances must be brought to these places or transported away, for example, when the reactions include substances in the dissolved state.

Electrochemical equilibrium is always composed of two reactions, the actual reaction and its reversal. The resulting current/voltage relation is called the “current/voltage curve” or the “current/potential curve”. It is composed of two curves, one for the forward and the other for the reverse reaction. At equilibrium, both reactions are in balance.

The forward and reverse reactions of an arbitrary electrode are shown in Figure 18.1. The horizontal axis represents the electrode potential related to the equilibrium potential E_0 . The vertical axis represents the current density, which is synonymous with the reaction rate.

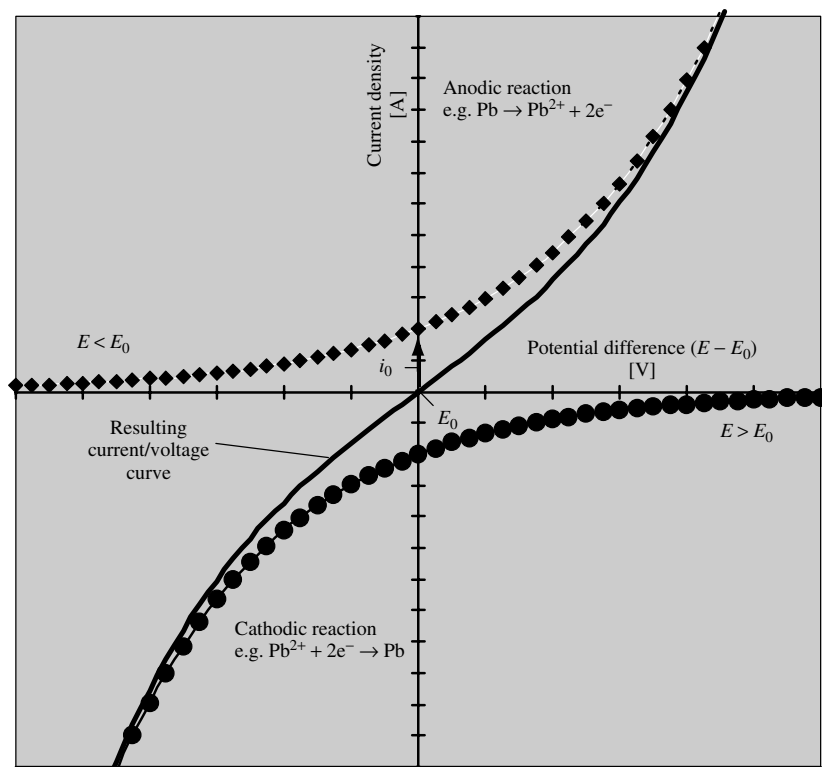


Figure 18.1 Current/voltage curve based on the Butler–Volmer equation (example taken from the lead electrode of a lead-acid battery)

The exponential relation between voltage and current is based on the fact that the charge/discharge reaction, in which the electrons are released or absorbed (the so-called “transfer reaction”) can be approximately described by an exponential law, called the Butler–Volmer equation.

$$i = i_0 \cdot \left\{ \exp \left[\frac{\alpha \cdot F}{R \cdot T} \cdot (E - E_0) \right] - \exp \left[-\frac{(1 - \alpha) \cdot F}{R \cdot T} \cdot (E - E_0) \right] \right\}$$

Therein i is the current density, i_0 the exchange current density, E the actual potential, E_0 the open-circuit electrode potential and α the transfer factor describing the efficiency of the overvoltage on forward and backward reactions. The difference $E - E_0$ is called overvoltage or polarisation. The difference expresses the additional energy voltage required to force the current through the surface. The exponential relation between current and voltage means that the increase in current might be enormous when the overvoltage exceeds certain values.

The equilibrium voltage E_0 is determined by the point at which the forward and reverse reactions are equally fast. In lead acid batteries, this is the point where metal dissolution and deposition balance each other, which means that the current densities of the forward and reverse reaction equal each other. This equilibrium potential represents a dynamic equilibrium: current flow occurs in both directions, but does not appear externally.

The current density for the forward and reverse reactions at the open-circuit potential is called the exchange current density i_0 , which describes the rate at which this equilibrium is adjusted. The exchange current density represents an important kinetic parameter. High exchange current density means that the equilibrium potential is rather stable, while a low exchange current density indicates that the electrode potential will be polarised even when very small current densities flow through the electrode. On the other hand, it is important that unwanted side reactions have rather small exchange current densities. In the lead electrode, the exchange current density for the charge/discharge reaction is of the order of 10^{-5} A/cm² while it is only of the order of 10^{-13} A/cm² for the hydrogen production.⁶ Therefore, the hydrogen evolution at open-circuit voltage is rather small.

In the literature, simplified versions of the Butler–Volmer equation can be found. For high overvoltages caused by the electrochemical charge-transfer (trans) process, the so-called Tafel equation is a proper approximation.

$$(E - E_0)_{\text{trans}} = \frac{R \cdot T}{\alpha \cdot F} \cdot \ln \left(\left| \frac{i}{i_0} \right| \right)$$

Using a semi-logarithmic plot results in straight lines, called the Tafel lines. For mathematical reasons, α is signed positive for positive currents and negative for negative currents.

⁶ It is worth noting that the current density caused by the current flow through the electrode during a charge or discharge of a lead-acid battery (approximately 10 h discharge or charge) is of the order 10^{-5} A/cm² to 10^{-6} A/cm² for the Pb electrode (assumptions: capacity of the lead electrode 3.865 g/Ah, inner surface of Pb active material 0.5 m²/g and discharge current 0.1 A/Ah). This gives a feeling for the very high activity in equilibrium conditions.

For small overvoltage, the first-order approximation of the exponential terms in the Butler–Volmer equation results in the following equation:

$$(E - E_0)_{\text{trans}} = \frac{R \cdot T}{F} \cdot \frac{i}{i_0}$$

Electrochemical reactions, chemical reactions as well as transport processes that precede or follow the charge/discharge step, lead to changes in the concentration of the reacting substances at the electrode surface and thereby may change the current/voltage curves. Each of these steps can cause an overvoltage. If the diffusion of one of the reacting partners to the electrode surface is the slowest partial step, then the concentration of this substance is reduced more and more with increasing overvoltage. A limit is reached when the concentration of the reaction partner is reduced to zero at the electrode surface. From this point, further increase in overvoltage no longer increases the current. In fact, with rising overvoltage typically a side reaction becomes dominant and the current goes into this reaction. This is the case with the hydrogen evolution at the lead electrode. If the electrode is totally charged and the overvoltage is increasing, the current going into the hydrogen-evolution reaction takes over the complete current through the electrodes. This happens even though the current-exchange density for the hydrogen evolution is several decades smaller than that of the lead charging/discharging reaction.

Diffusion processes can be characterised by a limiting current i_{lim} , which describes the maximum flow of charge carriers that can be transferred through diffusion to the reaction site. The overvoltage of this diffusion process (diff) can be described by the following equation.

$$(E - E_0)_{\text{diff}} = \frac{R \cdot T}{n \cdot F} \cdot \ln \left(1 - \frac{i}{i_{\text{lim}}} \right)$$

An effect not often described explicitly is the “production” of the charge carriers from a chemical process. Typically, this is included in the diffusion overvoltage, but for a deeper understanding of the battery processes and the effects of ageing (diffusion itself is not affected directly by ageing) it is worthwhile to separate these effects.

To explain the effect, the lead acid battery is taken as an example. Figure 18.10 in Subsection 18.4.7.1 will describe the process in more detail. From the electrochemical process described by the Butler–Volmer equation or the Tafel equation charged ions are released into the electrolyte during the discharge process. This increases the concentration c of charged ions in the electrolyte above the equilibrium concentration c_0 (defined by the solubility of the ions in the electrolyte) resulting in a concentration (conc) overvoltage. The following equation gives the mathematical formulation of this overvoltage.

$$(E - E_0)_{\text{conc}} = -\frac{R \cdot T}{n \cdot F} \cdot \ln \left(\frac{c}{c_0} \right)$$

As soon as the concentration of any species in a solution deviates from its equilibrium concentration, chemical processes driven by concentration gradients occur. In the case

of the lead electrode, dissolved Pb^{2+} ions form the lead sulphate crystals (PbSO_4) with SO_4^{2-} . The rate of formation of sulphate crystals (and the dissolution of the crystals during charging) determines the concentration of the charged ions in the electrolyte and therefore the concentration overvoltage. The rate of forming and dissolving of sulphate crystals depends strongly on the crystal size, shape and number. These parameters depend on the operating conditions of the battery and on the ageing of the active material. Therefore, battery ageing and active material structure is reflected by the values of the concentration overvoltage and the charge-transfer overvoltage.

The diffusion overvoltage describes the transport of ions that are available in sufficient volume (in the lead acid battery these are the SO_4^{2-} ions), thus a classical transport phenomenon. The concentration overvoltage describes the generation with respect to the absorption of ions from a chemical process.

Chemical processes are always driven by concentration gradients. Electrochemical processes are driven by the external currents. Therefore, the electrochemical process must take place exactly at the rate given by the external current. The rate of the chemical process depends only on ion concentration. With respect to the charge/discharge process in a battery, this means that the electrochemical process follows without delay any changes in the external current flow. Chemical processes have time constants as the rate of the process depends on the concentration in the electrolyte. In steady-state charge and discharge conditions, the rates of the electrochemical process and the chemical process need to be equivalent. This means that the ratio of the ion concentration and the equilibrium concentration in the electrolyte is constant.

All processes strongly depend on the temperature. The temperature dependence of the reaction rate k of a chemical reaction is described by the Arrhenius equation (C is a constant, E_A the activation energy).

$$k = C \cdot \exp\left(-\frac{E_A}{R \cdot T}\right)$$

The activation energy for many processes is of the order of 50 kJ/mole. From this experience, the rule of thumb “*increase of temperature by 10 K increases the reaction rate by a factor of 2*” is derived.

18.2.2 Batteries with Internal and External Storage

Electrochemical accumulators convert electrical energy into chemical energy. The energy is stored in a chemical compound. In secondary electrochemical batteries, this process is reversible. During discharging, the chemical energy is converted back into electrical energy. Thus, the converters determine the charging and the discharging power and the storage determines the energy capacity of the systems. This principle concept is described in Figure 18.2.

In secondary electrochemical batteries with internal storage, the converter and the storage cannot be separated. The interface of the active material to the electrolyte is

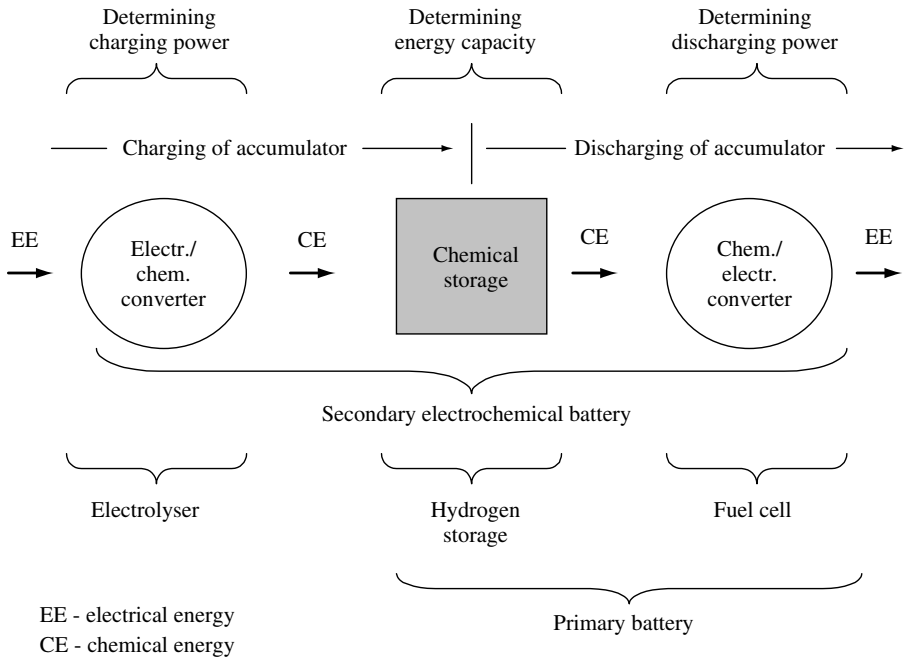


Figure 18.2 Schematics of electrochemical storage systems

equivalent to the converter; the transformed active mass is the storage. In conventional secondary electrochemical batteries, power and capacity depend on each other and cannot be designed independent of each other. In practice, there is a small margin for the design. For high-power and low-capacity requirements, very thin electrodes having a high surface-to-capacity ratio are used. Section 18.4 will go into the details of this type of batteries.

Nevertheless, the margin is limited and this is a drawback for autonomous power supply systems where high energy capacity is required and the power requirement is moderate. Therefore, electrochemical storage systems with separated converters and storage are of interest. The electrolyser/hydrogen storage/fuel cell system is a well-known option for the problem even though it is not yet a common commercially available solution. Details of this system will be discussed in Section 18.5.2.

A second class of storage systems with separated converter and external storage units are electrochemical Redox systems, where the reaction partners like iron and chromium salts or vanadium salts are dissolved in liquids and stored separately in tanks. The converter functions quite similar to a fuel cell. During charging or discharging, the electrolyte is pumped into the converter. These systems are not available in large quantities in the market yet, but there are several R&D activities on these systems. Section 18.5.1 will discuss this technology in more detail.

For a clear understanding of this chapter and to get familiar with the wording used in the “storage community”, the following two sections explain some basics. They are oriented very much on the application of storage systems in autonomous power

supply systems. They are by no means complete but should help to understand this chapter without additional literature. For more information, References [2, 3] are highly recommended.

18.2.3 Commonly Used Technical Terms and Definitions

A battery is made from two or more electrochemical *cells* connected in series. *Primary* and *secondary* electrochemical cells can be distinguished. Secondary batteries – also called accumulators – have reversible reactions and are rechargeable. This chapter is centred around them.

An electrochemical cell consists of two *electrodes*. Commonly, one is called the “positive” electrode and the other, the “negative” electrode. The positive electrode has a more positive potential than the negative electrode with respect to the standard hydrogen electrode.⁷ Each combination of charged and discharged active material has a specific electrochemical potential. The potential difference between the positive and the negative electrode is called the *cell potential* or *cell voltage*. The *equilibrium voltage* of a cell is a function of the electrolyte concentration and the temperature. The *open-circuit voltage* can be measured if no external current flows through the battery. It is identical to the equilibrium voltage if all the internal overvoltages mainly caused by diffusion processes have levelled out. The time until this stadium has been reached depends on the battery technology and the operation condition. It is in the range of some seconds to many hours.

The *capacity* of a cell is measured typically in ampere-hours (Ah). The capacity is determined by a constant current discharge down to a defined *end-of-discharge voltage*. The capacity depends significantly on the discharge current and the temperature. Battery manufacturers can define the discharge current and the end-of-discharge voltage on their own. Therefore, it is very important to check the reference conditions defined by the manufacturer while comparing the capacity of different products.

Typically, nominal cell voltages are in the range between 1.2 and 3.6 V. Therefore, several cells are usually connected in series to build a *string* of higher nominal voltage. The *nominal voltage* of a battery is therefore defined by the number of cells connected in series times the nominal cell voltage of a single cell. Batteries are often sold in so-called blocks or modules. Therein, several cells have been integrated and connected in series with only one set of terminals. A well-known example is the starting, lighting, ignition (SLI) battery for cars where 6 cells are connected in series but are sold as one 12 V block. To increase the capacity of a cell, often several sets of positive and negative electrodes are connected in parallel within a single cell. To increase the capacity even more, two or more strings can be connected in parallel. The *nominal energy* content (Wh or kWh) of a battery is defined by the nominal battery voltage times the nominal battery ampere-hour capacity.

The *state of charge (SOC)* gives the capacity that can be discharged from a battery at a certain moment. Hundred percent state of charge means a fully charged battery, 0% SOC means that the nominal capacity is discharged. State of charge is defined in more

⁷ The standard hydrogen electrode is a platinum electrode rinsed with hydrogen gas in 1 N electrolyte. Its potential is defined as 0 V.

detail in Section 18.2.4. Often, instead of SOC the *depth of discharge (DOD)* is used in the literature or in data sheets. DOD is defined as 0% when the battery is fully charged and as 100% after the nominal capacity is discharged from the battery ($DOD = 100\% - SOC$).

When looking up literature related to autonomous power supply systems, typically a *positive battery current* is defined to increase the SOC of the battery while a negative current decreases the SOC. However, please be aware that some authors use the opposite definition.

A *cycle* refers to a discharge followed by a recharge. Cycles used in data sheets always start from a fully charged battery up to a certain DOD. A nominal *full cycle* is a discharge down to 100% DOD. The *cycle lifetime* for a battery is given by the number of cycles as a function of the DOD. Nevertheless, in autonomous power supply systems cycles as defined above do not occur as can be seen from Figure 18.6. Many *partial cycles* within a *macrocycle* (time between two full charging states) occur, where a partial cycle is defined as the charge transfer within the time of the change of the direction of the battery current. Overall, charge transfer of batteries in autonomous power supply systems can be defined by the *capacity throughput*. It is given by the accumulated ampere-hour discharged from the battery divided by the nominal capacity. The resulting number is formally equivalent to the number of 100% DOD cycles delivered during the battery life. This normalised number will be referred herein as the capacity throughput.

The *ampere-hour efficiency* η_{Ah} is defined as the ratio of the ampere-hours discharged from the battery divided by the ampere-hours charged to the battery within a certain period (typically one month or one year or within a period between two full charging processes). Often the *charge factor* is used instead of the ampere-hour efficiency. It is defined as $1/\eta_{Ah}$. For a sustainable battery operation, charge factors greater than one are necessary.

The *energy efficiency* η_{Wh} is the ratio of the energy discharged from the battery divided by the energy charged to the battery within a certain period (defined as above).

The size of a battery is given by its nominal energy content in the fully charged condition. To express the relative size of a battery concerning the load in autonomous power supply systems, often the term *days of autonomy* is used. The “days of autonomy” is defined by the ratio of the nominal energy content of the battery (kWh) (sometimes the practical capacity according to Figure 18.3 instead of the nominal capacity is also used) to the average energy consumption per day (kWh/day). Therefore, the unit is “days” and expresses how long a system can be supplied only from the fully charged battery.

Battery currents are usually given relative to the battery size. The reason is that the strains and the current-dependent electrical properties are related to the specific current loads to the electrodes with respect to the active materials. For larger capacities just formed from parallel-connected electrodes or cells or from larger electrodes, the normalisation of the current to the capacity is an appropriate measure. Therefore, battery currents are expressed as multiples of the ampere-hour capacity or as multiples of the capacity-defining discharge current. For a battery with a capacity of $C = 100$ Ah, a current of 10 A is defined as $0.1 \times C$. In the example, 100 A is called the *C-rate*. I_{10} is the current that discharges a fully charged battery within 10 h down to the defined end-of-discharge voltage. The typical nomenclature for the capacity is C_x where x is the time in which the battery is

discharged. For example: $C_{10} = 10 \text{ h} \times I_{10}$, or $C_{10} = 100 \text{ Ah}$, $I_{10} = 10 \text{ A} = 0.1 \times C_{10}$. Note that $1 \times I_{10}$ is not equivalent to $10 \times I_{100}$ as the C_{100} capacity is typically larger than the C_{10} capacity. For a more detailed example, see Section 18.4.7.3.

The *end-of-charge voltage* defines an upper voltage limit. Charging of the battery usually is not stopped on reaching the end-of-charge voltage (other than the end-of-discharge voltage), but the charge current is reduced accordingly to maintain the end-of-charge voltage over time.

The *lifetime* of a battery depends very much on the operating conditions and the control strategy. Manufacturers usually define two types of lifetime: the *float lifetime* (calendar lifetime) gives the lifetime under constant charging conditions without cycling (typical applications are uninterruptible power supplies), and for continuous cycling (*cycle lifetime*, typical applications are fork-lift trucks). Sometimes, the *shelf lifetime* is given. It defines the time for which a battery can be stored before usage.

Self-discharge describes the (reversible) loss of capacity on open-circuit conditions. It depends very much on the temperature.

The *state of health* is defined as the ratio of the actual measured capacity and the rated or nominal capacity. The state of health indicates to which extent the battery is still able to fulfil the requirements. According to the norms, lead acid batteries are at the end of their lifetime if the state of health is under 80%. However batteries can be operated significantly longer, but the days of autonomy are reduced accordingly and a system might not fulfill the energy requirements any more in a proper way. Batteries operating at a state of health of 50% are found frequently especially in hybrid systems. As a consequence, the share of the motor generator is increasing.

18.2.4 Definitions of Capacity and State of Charge

For operation and energy management in autonomous power supply systems, the battery capacity and the actual state of charge of the battery are the most important parameters. State-of-charge determination is difficult in autonomous energy supply systems with renewable energies because full charging of the battery as it is done frequently with conventional battery chargers is very unusual.

If state of charge is displayed, the question that arises is, what is the meaning of the specific values. Figure 18.3 shows different definitions of the battery capacity and the corresponding definitions of state of charge. The measured capacity of a battery might be smaller or even higher than the rated capacity given by the manufacturer. During the lifetime, the measured capacity decreases more and more due to ageing effects. The practical capacity is less than the measured capacity. Owing to the special conditions of renewable energy sources, batteries are almost never completely recharged (number of charging hours is limited) [4]. The maximum state of charge that is reached during normal system operation is called a “solar-full state of charge”. Further on, the system defines an end-of-discharge criterion to avoid deep discharging of the battery and therefore accelerated ageing, which usually differs from the end-of-discharge criteria used for capacity tests. Therefore, the practical battery capacity is lower than the measured capacity. In the literature and other publications, no common definition of the state of charge is used. Therefore, any data and results must be handled with care.

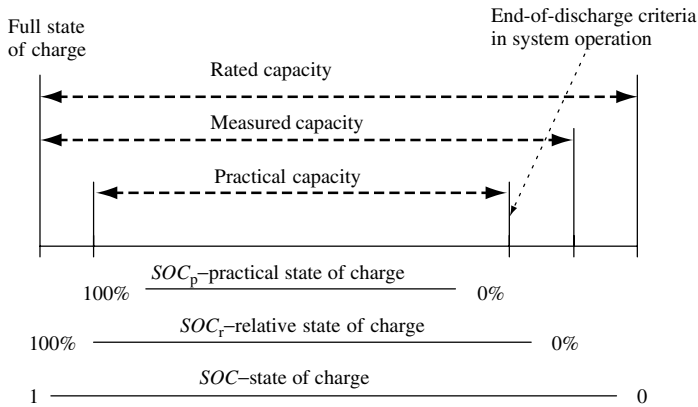


Figure 18.3 A Comparison of the different definitions of battery capacity and the corresponding definitions of state of charge

Within this chapter the following definitions according to Figure 18.3 and [5] will be used.

The rated or nominal capacity is defined as the 10-h discharge capacity C_{10} . This is the basis for the SOC determination. The rated or nominal capacity does not change during the life of a battery whereas the measured capacity changes with time. The state of charge with respect to the measured capacity is called relative state of charge (SOC_r). The practical capacity C_p is always lesser than the measured capacity. The state of charge definition related to the practical capacity is the practical state of charge (SOC_p). SOC_p is 100% if a solar-full state of charge is obtained.

In [5], a complete review of the different definitions for the capacity, state of charge and full state of charge is given. Further on, definitions of open-circuit voltage and state of health are included, because some state-of-charge meters and algorithms use these definitions as well.

18.3 TYPICAL OPERATION CONDITIONS OF BATTERIES IN PV APPLICATIONS

To understand the requirements of storage systems for autonomous power supply systems, an analysis of the typical operating conditions is necessary. The operating conditions vary very much according to the location and application of the system, the load patterns, the installed power generators and the operation strategy.

The most important parameters for the classification of the operating conditions are the charge and discharge currents, the state-of-charge profile and the temperature.

18.3.1 An Example of an Energy Flow Analysis

Photovoltaic stand-alone systems may be roughly separated into two groups. There are systems consisting of the PV modules that charge the batteries. A charge controller prevents

overcharging or deep discharging. The appliances are supplied from the battery either directly or via a DC/AC converter. The typical representative of this first system group is the Solar Home System (SHS), which is operating in hundreds of thousands of rural households. It will supply lights and TV sets and delivers, in a standard version, approximately 0.25 kWh of electricity per day. Larger systems may deliver up to 5 kWh per day.

The second group of systems combine a photovoltaic generator with a diesel gen-set and possibly with additional wind turbines or hydroelectric generators. Including a diesel gen-set as a controllable generator gives an additional degree of freedom to the system sizing.⁸ It allows reducing the battery capacity, especially if the solar radiation undergoes strong seasonal variations. These systems are called hybrid systems. They are designed to deliver from 1 kWh per day to typically between 10 and 100 kWh per day. They may be used to supply power to telecommunication equipment, mountain lodges, hospitals or hotels in non-electrified rural areas and small villages.

A typical hybrid system with a 4.5-kW_p PV generator, a diesel generator and 32 kWh of lead acid battery storage is in operation since 1992 in the Black Forest in Germany. It has to deliver 10 kWh per day to the hikers inn “Unterkrummenhof”. An analysis done in model calculations based on measured data shows the flow of energy in the system and the effect of internal losses (Figure 18.4). Two-thirds of the power delivered (E_{consumer}) is drawn from the battery storage. The numbers given in the diagram are normalised to the nominal energy production of the PV generator under the radiation conditions at the site. A detailed discussion of the energy-flow diagram is given in [6].

Figure 18.4 underlines the key role that battery storage has to fulfil in hybrid systems. More than 80% of the energy used goes via the battery storage. This is a typical value for all hybrid systems and is even higher in many pure PV battery systems.

18.3.2 Classification of Battery-operating Conditions in PV Systems

An intensive study of the operational data of close to 30 batteries in stand-alone PV systems with and without a diesel generator was made. All systems were operated under European radiation conditions [7]. The study resulted in a classification of the battery-operating conditions into four classes. Figures 18.5 and 18.6 show measured data on the annual operating conditions of four systems selected to represent the four different classes. Figure 18.5 shows scatter graphs of the battery current versus battery voltage and Figure 18.6 shows the time series of the state of charge within a complete year.

The hybrid system “Unterkrummenhof”, characterised in Figure 18.4 is a system from Class 2. Class 3 and Class 4 represent systems with an increasing role of the diesel gen-set and relatively smaller PV generators and batteries. The “Class 1” system is a system without a back-up generator, designed to operate with high reliability in Europe.

Solar home systems (SHSs), which were not included in the survey, operating under the favourable conditions of low latitudes would typically be equipped with a three- to five- “day” battery and would not show the pronounced long-lasting period of

⁸ Diesel gen-sets are currently the most common solution for an additional controllable generator. Other solutions like thermoelectric, thermophotovoltaic or fuel cell generators have been developed in many places and might be alternatives in the near future.

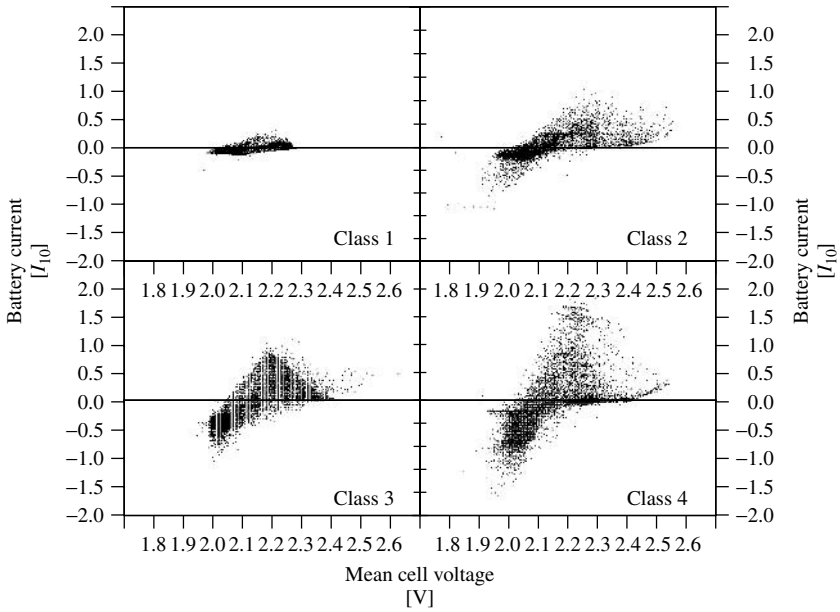


Figure 18.5 Battery current in units of I_{10} versus cell voltage for all data points. For each class, data of a complete year were taken from a representative system

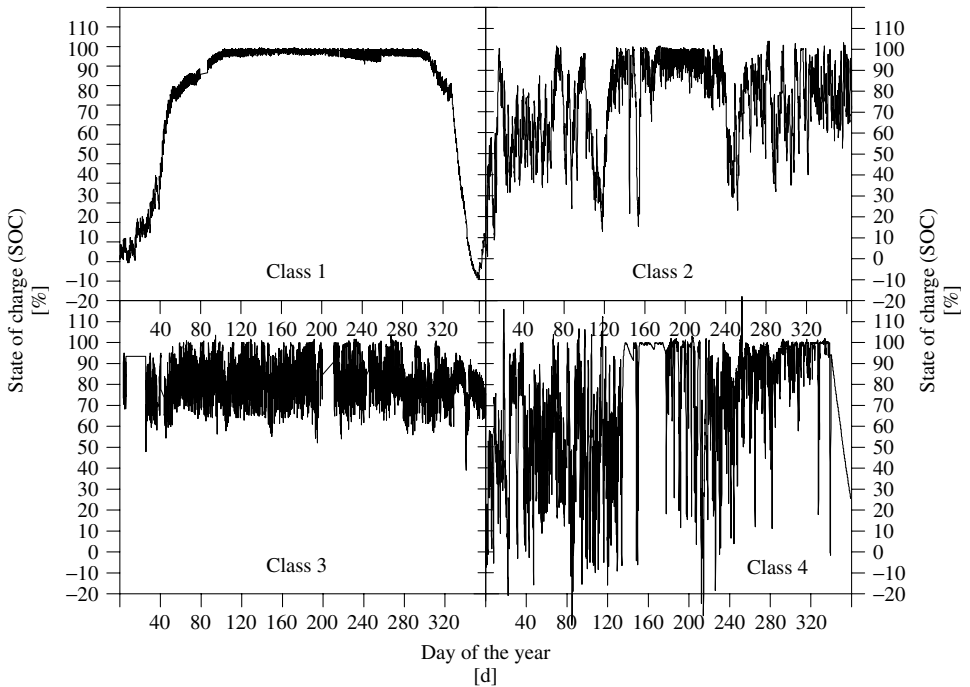


Figure 18.6 Time series of state of charge calculated from current, voltage and temperature using an ampere-hour balance with a voltage and temperature-dependent loss current [5, 8]

- The charging and discharging currents are small compared to the standard 10-h discharging current I_{10} (at least for system Classes 1 and 2).
- For long periods, sometimes weeks or even months, the batteries do not reach a fully charged state (SOC = 100%).

These features are distinct from other battery applications in, for example, uninterruptible power supplies, where the batteries are kept at a full state of charge for the longest time of the year or in vehicle traction applications, for example, fork-lift trucks, where the batteries are fully recharged regularly with high charging current. Figure 18.6 also demonstrates that in systems of Classes 1 and 2 – the same is true for the solar home system application – the daily discharged capacity is between 5% and 30% of the nominal battery capacity. This is equivalent to the annual full cycles between 20 and 100.

Table 18.2 gives a comprehensive view of the requirements of the battery in the different system classes. In Table 18.3, suggestions for the selection of adequate lead acid battery types out of the variety of products available in the market on the basis of this classification are made.

On the basis of this classification, an evaluation of the properties of a battery according to the requirements of the systems is possible. Solar fraction and storage size in days of autonomy are the output of all commercial system design and simulation-software packages. Therefore, the classification allows the system designer to ask the battery manufacturers for an appropriate battery type by showing him the typical operating conditions.

Table 18.2 Identification of classes by typical system indicators (solar fraction, storage size) for the different classes of operating conditions and importance of battery features for the different classes. The storage size is given in units of battery capacity divided by the mean daily load (days of autonomy). The solar fraction is the amount of energy produced by the PV generator divided by the energy produced by all the energy sources within the system (including the diesel generator in hybrid systems) [9]

System indicators	Class 1	Class 2	Class 3	Class 4
Solar fraction	100%	70–90%	About 50%	<50%
Storage size/days of autonomy	3–>10 days	3–5 days	1–3 days	About 1 day
Capacity throughput ⁹	10–25	30–80	100–150	150–200
Necessary battery features				
Number of lifetime cycles ⁹	Low (<300)	—————→		High (>1200)
Capability to withstand long periods in deep discharged states	Important	←————		Less important
Low self-discharge rate	Important (<1% per month)	—————→		Less important (5% per month)
Measures against acid stratification	Important	Very important		Important
Resistance against corrosion	Important	←————		Less important

⁹ The capacity throughput is defined as the number of ampere-hours discharged from the battery divided by the nominal capacity of the battery. The given numbers are typical of the applications in the defined classes of operating conditions. A full cycle with regard to lifetime cycles is defined by a one capacity throughput. This is equivalent to a complete discharge (100% DOD) of a fully charged battery. In data sheets, often the cycle number is given for cycles with a depth of cycle other than 100% (e.g. 80%). This has to be taken into account while comparing the design capacity throughput of different products (see also Figure 18.24).

Table 18.3 Continuation of Table 18.2. Different product groups of lead acid batteries are classified with respect to the different classes as defined in Section 18.3.2 (● optimum, ○ acceptable) table from Reference [9]

Type of battery	Class 1	Class 2	Class 3	Class 4
SLI	–	–	–	–
Stationary	●	●	○	–
Traction	–	○	●	●
Electric vehicle	–	○	●	●
“Solar battery” (from SLI)	●	○	–	–
VRLA	●	●	●	○
Flooded	●	●	●	●

The differences in the operating conditions and the requirements listed in Table 18.2 show clearly that one “solar battery” cannot exist. The range of operating conditions in autonomous power supply systems is very large and requires appropriate individual solutions.

An additional parameter for differentiating the operating conditions of batteries is the amount of capacity throughput caused by an AC ripple. Loads and generators are connected to the battery at the same time. This results, in many cases, in so-called micro-cycles in which the battery current changes from charging to discharging and vice versa with a frequency between 1 and 300 Hz. Measurements and calculation have shown that this can cause an additional capacity throughput of up to 30%. This in fact shortens the lifetime of the batteries. Taking into account the optimum operating strategies, battery ageing is related strongly to the capacity throughput. The amount of this additional capacity throughput depends very much on the system’s sizing and the electrical properties of the loads, the inverters, the converters and the generators [10].

18.4 SECONDARY ELECTROCHEMICAL ACCUMULATORS WITH INTERNAL STORAGE

18.4.1 Overview

There are several secondary electrochemical accumulators available on the market. They differ in parameters concerning the materials of the electrodes and the electrolyte. This results in different electrical properties like energy and power density, efficiency, lifetime, cycle life, operation temperature, inner resistance and self-discharge and last but not the least economic properties like battery costs and maintenance requirements.

Products like lead acid batteries, ZnBr_2 , NiCd, NiFe, NiZn, nickel-metal hydride (NiMH), Zn-air, Li-ion, Li-polymer, Li-metal and rechargeable alkali mangan (RAM) are available. They operate at room temperature, but also high-temperature batteries like NaS and NaNiCl_2 (“ZEBRA”) operating at 300 to 350°C are possible. In addition, there are capacitors storing the energy in an electrostatic field instead of chemical bonds out of which the double-layer capacitors are the most interesting for autonomous power supply systems.

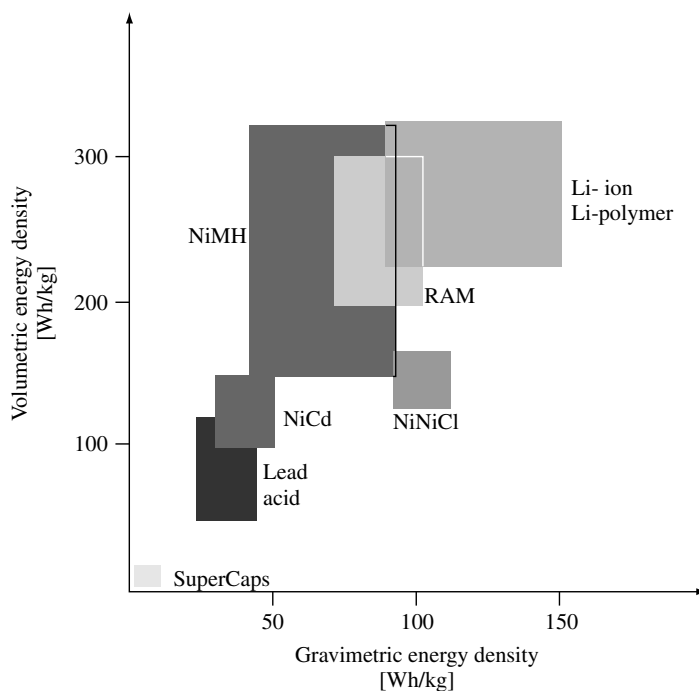


Figure 18.7 Practical specific volumetric energy density (Wh/l) versus specific gravimetric energy density (Wh/kg) for various secondary battery technologies (data from Table 18.4)

The specific energy densities of batteries are an important parameter to characterise the different battery types. For logistic reasons on supplying the batteries to the systems, gravimetric and volumetric energy densities are a relevant cost factor also for autonomous power supply systems. Figure 18.7 shows an overview of the energy densities of different secondary battery technologies based on an analysis of commercially available products. The figure does not show the theoretical limits of the different technologies.

Table 18.4 gives an overview of the most important properties of several secondary electrochemical accumulators. A more detailed description is given on the NiCd (Section 18.4.2), the nickel-metal hydride (NiMH) (Section 18.4.3), the RAM (Section 18.4.4) and the Lithium batteries (Section 18.4.5) as well as on the double-layer capacitors (Section 18.4.6). Lead acid batteries are treated in greater detail in Section 18.4.7. All other battery types have no relevance in the field of autonomous power supply systems. Details on all primary and secondary batteries can be found in [2].

18.4.2 NiCd Batteries

NiCd batteries have been available as a commercial product for many decades and are well-proven products. They have very good properties concerning lifetime and lifetime cycles. They are widely used in heavy-duty applications and in very cold climates. Standard NiCd-battery designs can be operated easily at temperatures of -20°C and specially designed cells can be operated even up to -50°C . Nevertheless, NiCd batteries

Table 18.4 Overview of the technical data of different secondary batteries based on actual available products. All numbers are typical data based on the data sheets of existing products. The data are not the theoretical limits for the different technologies. Products for special applications may have technical parameters outside the ranges displayed in the table

Battery technology	Electrolyte	Energy density [Wh/kg]	Energy density [Wh/l]	Efficiency η_{Wh} [%]	Life-time [a]	Typ. cycle-lifetime [cycles]	Temperature for operation		Typical applications (examples)
							Standard charging [°C]	Discharging [°C]	
Lead acid	H ₂ SO ₄	20–40	50–120	80–90	3–20	250–500	–10 to +40	–15 to +50	Stationary application (UPS, autonomous power supplies), traction, SLI
NiCd	KOH	30–50	100–150	60–70	3–25	300–700	–20 to +50	–45 to +50	Power tools, hobby toys, consumer products, traction, applications as for lead acid batteries with higher power requirements or lower ambient temperature, electrical cars
NiMH	KOH	40–90	150–320	80–90	2–5	300–600	0 to +45	–20 to +60	Laptop, mobile phones, camcorder, electric vehicles, hybrid cars, hobby toys
Li-ion, Li-polymer	Organic, polymers	90–150	230–330	90–95	–	500–1000	0 to +40	–20 to +60	Laptop, mobile phones, Camcorder, smart cards
RAM		70–100	200–300	75–90	–	20–50	–10 to +60	–20 to +50	Consumer products, hobby toys
SuperCaps		1–10	2–15	90–95	~10	500 000	–25 to +75	–25 to +75	For applications with typical cycle periods of less than 10 s at very high power requirements
NaNiCl	β -AlO ₂	~100	~150	80–90	–	~1000	+270 to +300	+270 to +300	Hybrid vehicles, electric vehicles (prototypes available)

have a bad image due to the cadmium content, which is, known to be environmentally incompatible.

Several different types of NiCd batteries are in the market with differences in the plate technologies and the handling of evolved gases.

The basic reaction is the same for all construction types of NiCd batteries.



During discharge, trivalent NiOOH is reduced under consumption of water to divalent Ni(OH)₂. Metallic cadmium is oxidised to Cd(OH)₂. The reversible backward reactions proceed during charging.

The potassium hydroxide electrolyte (KOH) does not undergo a significant change in its concentration or density during charging or discharging. Only water, which is present in high concentrations, participates in the reaction. The electrolyte density is about 1.2 g/cm³.

NiCd batteries are available with liquid electrolyte and as sealed, maintenance-free types [3].

The rated voltage of NiCd cells is 1.2 V. Although the discharge rate and the temperature significantly affect the discharging behaviour of all electrochemical cells, the effect is noticeably less pronounced in NiCd batteries than in lead acid batteries. As a result, NiCd batteries can be discharged at higher rates, without the accessible capacity falling much below the rated capacity. Even for discharge rates of $5 \times C_5$ a high-performance NiCd battery can supply 60 to 80% of the rated capacity. Also, the influence of the temperature on the capacity is comparatively small which is due to the fact that diffusion processes have less impact on the reaction kinetics compared with lead acid batteries.

High temperatures in the range of 40°C and more should be avoided as the charging efficiency is getting very low and the self-discharge rate is increasing significantly. Self-discharge rates at 20°C are in the range of 20%/month. The energy efficiency is in the range of 60 to 70%, which is significantly less compared to lead acid batteries.

A NiCd battery can withstand occasional deep discharge, inverse charging and also freezing of the cells without direct damage.

NiCd cells have a low internal resistance. Typical values for the DC resistance are between 0.4 and 2 mΩ for a fully charged 100 Ah cell. The internal resistance is largely inversely proportional to the cell size for all cell types. Falling temperatures and a decrease in the SOC increase the internal resistance, but the internal resistance remains essentially constant up to a DOD of 60 to 80%, and only increases significantly at higher DODs. Thus, the internal resistance is not a suitable indicator to determine the state of charge.

Under normal operating conditions, a NiCd battery can reach up to 2000 100% DOD cycles even under severe operating conditions. Depending on the application and the operating conditions, the lifetime can be between 8 and 25 years. Starter batteries for diesel generators reach lifetimes of about 15 years, batteries for train lighting achieve 10 to 15 years and stationary batteries have lifetimes of 15 to 25 years. Good charging

(charge factors of approximately 1.2), frequent overcharging and frequent full discharges are necessary to achieve long lifetimes.

A number of factors are responsible for the high reliability and the very long lifetime of NiCd batteries: the design is mechanically very robust, the cells are not easily damaged by incorrect technical handling, such as inverse charging, overcharging and long idling periods at medium or low states of charge and the reactants involved are not very corrosive with regard to the electrodes and other components in the cell.

One drawback is the so-called memory effect, which occurs under some operating conditions. This term is used to describe the tendency of the battery to adapt its electrical properties to the cycling conditions in which it has been operated over a long period of time. This means that a battery that is cycled over prolonged periods up to a certain DOD, tends to limit discharging to this DOD even if a higher discharge at high discharge current is planned. This effect can be resolved by discharging the battery several times with a low current. In modern NiCd batteries, this effect is not very pronounced any more.

Despite the good electrical properties, the market share of NiCd batteries in autonomous power supply systems is not very high due to the high costs. Investment costs for NiCd batteries are round about a factor of 3 higher than lead acid batteries.

18.4.3 Nickel-metal Hydride (NiMH) Batteries

The active material of the positive electrodes of a nickel-metal hydride (NiMeH or NiMH) battery in its charged state is NiOOH, the same material as in a NiCd battery. The negative active material in the charged state is hydrogen, a component of a metal hydride. The metal alloy is subjected to a reversible absorption/desorption process during charge and discharge of the cell. The reaction for the reversible charge/discharge process is indicated below [11].



An aqueous solution of potassium hydroxide is the main component of the electrolyte. Only a small amount of electrolyte is used in sealed nickel-metal hydride cells, most of which is absorbed in the separator and the electrodes. In the cell, oxygen can be transported from the positive to the negative electrode and can recombine there with hydrogen to form water. Thus, the cells can be used like dry cells and can also be installed in any desired position.

The discharge characteristics of sealed nickel-metal hydride cells are very similar to those of sealed NiCd cells. The open-circuit voltage is between 1.25 and 1.35 V/cell, and the nominal voltage is also 1.2 V.

The electrical characteristics are quite similar to NiCd batteries even though their energy efficiency is about 80 to 90% and the maximum power available is less than that in NiCd batteries. The latter is of little relevance in autonomous power supply systems. Memory effects are less pronounced than in NiCd batteries. Self-discharge at 25°C is also in the range of 20%/month, but at 45°C it is as high as 60%/month.

Nickel-metal hydride batteries are not as robust against polarity reversal as NiCd batteries. If the positive electrode gains a negative potential, hydrogen is generated at

the positive electrode. Some of the gas can be absorbed by the metal of the negative electrode, but the rest remains as gas in the cell. If the discharge is continued, oxygen is formed at the negative electrode, which further increases the gas pressure and leads to oxidation of the metal electrode. When the overpressure is large enough, the safety vent opens and the gas pressure falls again. To avoid this, appropriate measures must be taken especially if long series-connected strings are used. References [12, 13], and Chapter 19 of this book discuss a number of possible solutions for this problem.

Nickel-metal hydride batteries have replaced NiCd batteries in the market for portable appliances (e.g. mobile phones, camcorders and power tools) to a large extent due to their better environmental compatibility and their higher gravimetric energy density (Figure 18.7). However, NiMeH batteries are not commercially available in larger capacities as necessary for autonomous power supply systems. The reasons for this are mainly the costs that are actually approximately five times higher than the lead-acid batteries. Currently, there is no evidence that NiMeH batteries will play a major role in storage for autonomous power supply systems except for small technical appliances with some 10 Wp. It is more likely that Lithium batteries may enter this market, but NiMeH batteries are seen as an interim technology between NiCd and Lithium batteries.

18.4.4 Rechargeable Alkali Mangan (RAM) Batteries

Alkali-mangan cells are well known as primary batteries for several decades. Over the past few years this technology has entered the market as a secondary battery. In the beginning, the primary batteries were used and recharged. Meanwhile, rechargeable alkali-manganese (RAM) cells are in the market specially designed as a secondary battery. RAM batteries are gas tight. The nominal voltage is 1.5 V/cell and is therefore 25% higher than that of NiCd or NiMeH batteries. Currently, only small batteries with capacities of up to 5 Ah are in the market. They are significantly less expensive than the NiCd batteries. RAM cells have higher inner resistance than all other batteries discussed here. RAM cells are much more environmentally compatible than NiCd batteries as they contain no heavy metals.

The major drawback is the low deep-cycling lifetime of the RAM cells. Up to now only approximately 20 to 50 full cycles (100% DOD) are available. However, if only very shallow cycles are required (1–5% DOD), several thousands of cycles can be achieved. Even though RAM cells are currently not suited to larger autonomous power supply systems, they are interesting storage systems for small appliances with limited lifetime or usually very shallow cycling like, for example, some kinds of toys. Emergency lighting systems may be another field of application where normally only the surveillance electronics need any power (recharged by a small PV generator) and only in case of an emergency the full capacity is needed.

18.4.5 Lithium-ion and Lithium-polymer Batteries

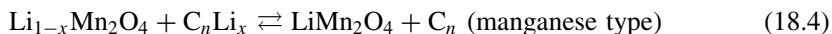
Lithium batteries have been the most emerging battery technology over the last few years. Primary lithium batteries were already well known due to their very high energy density and shelf lifetimes of up to 10 years without any major self-discharge. Nowadays, lithium-ion and lithium-polymer batteries have captured the market for portable applications like

camcorders, mobile and cordless phones and organisers. Even though they are not used in larger autonomous power supply systems today, it is worth having a closer look at this technology. Their electrical properties concerning efficiency and charge/discharge characteristics are very well suited to these applications. At the moment, lithium batteries are by far too expensive for applications where the high gravimetric energy density is of little benefit. However, as this is an emerging technology and cost reductions in the manufacturing process are expected, they might play a role in some autonomous power supply applications in the next few years.

The lithium-ion rechargeable battery's operation is based simply on lithium ions migration between the cathode and anode. Lithium-ion rechargeable batteries are therefore fundamentally different from non-rechargeable lithium and, for example, secondary lead acid or NiCd batteries in that the basic form of the cathode and anode materials does not change.

When the battery is charged, the lithium ions in the cathode material (lithium compound) migrate via a separator into the layer structure of the carbon material that forms the anode, and a charging current flows. During discharging, the lithium ions in the carbon material migrate backwards to the cathode material. This is known as the "rocking-chair" principle. Even though a large number of different material combinations are known under the name of lithium ion batteries, the most important materials for the commercial products are of the LiCo and the LiMn type.

The reactions for the reversible charge/discharge process are indicated below.



Li-ion batteries of the modern types as marketed today have a nominal voltage of 3.6 V. As this is far above the water-electrolysis voltage of 1.23 V, no aqueous electrolytes can be used anymore. The electrolyte here is an organic solvent with dissolved lithium salts. The cathode material is lithium cobaltite (LiCoO_2) or lithium manganese oxide spinel (LiMn_2O_4). The anode material is graphite of coke (graphitised carbon).

Lithium-ion rechargeable batteries have a three-layer structure consisting of a porous separator sandwiched between sheet-like cathode and anode materials, which, in the case of a prismatic cell, are wrapped around in an elliptical form. These materials are impregnated in an electrolyte and sealed in a metal case. This metal case includes a safety vent to protect the battery by releasing gas externally if the pressure inside the cell builds up to extreme levels.

Lithium batteries are potentially risky due to their very high energy density and the reactivity of metallic lithium. Incorrect handling of a lithium rechargeable battery may cause heat, explosion or fire. Therefore, it is even more important with this battery type to assure overcharge protection, over-discharge protection, over-current protection, short-circuit protection and operation at too high temperatures. Today, lithium batteries are only supplied with an integrated control electronic as a protection device. It works independent of all external chargers or monitoring devices and is therefore fully controlled by the battery manufacturer.

The main differences between the lithium-ion and the lithium-polymer batteries can be described as follows. Lithium ion batteries have a fluid organic electrolyte while the negative electrode is made from a lithium/carbon intercalation electrode. The electrolyte has a high conductivity. The non-metal electrode increases the safety in comparison with a Li-metal electrode. What is sold today as lithium-polymer batteries is in fact a combination of a polymer electrolyte and a lithium/carbon intercalation electrode. The use of the polymer simplifies the manufacturing. Strictly speaking the so-called lithium-polymer batteries are polymer lithium-ion batteries.

The lithium-polymer cell is just entering the market. In the long run, it is expected that lithium-polymer batteries can be manufactured at lower costs than lithium-ion batteries. Further, they allow very flexible battery designs. This makes lithium-polymer batteries an interesting solution for chip integration or smart cards, but also larger capacities for power applications are available for field demonstrations now.

Compared to NiCd or nickel-metal hydride batteries, a disadvantage of lithium batteries is that they are less tolerant to operations with high currents, which makes discharge at high currents noticeably more difficult. Also, they currently do not achieve the same cycle life as NiCd or nickel-metal hydride batteries. However, both points are subject to R&D and especially concerning the power rating, significant steps forward have been achieved.

Lithium batteries require constant current/constant voltage charging (Figure 18.23a). The recharge behaviour is very good. Full charging of the battery is not as important as with lead acid batteries to achieve adequate lifetimes. However, the voltage limit must be observed very accurately. The end-of-charge voltage is limited to 4.1 V and must not be extrapolated by more than 50 mV. High voltage causes the formation of metallic lithium. In series-connected cells, it must be assured that the voltage limits are kept within the acceptable limits for each individual cell.

The discharge of lithium batteries must be restricted to the material-specific end-of-discharge voltage. Again, over-discharge leads to the formation of metallic lithium. For the cobalt type, the end-of-discharge voltage is 2.3 V/cell and for the manganese type 2.7 V/cell. Figure 18.8 shows the discharge curves of a lithium-ion battery at different discharge currents. The battery capacity only slightly depends on the discharge current. In addition, Figure 18.9 shows the temperature dependence of the discharge curves. As the ion migration depends strongly on the temperature, the low-temperature performance is not too good.

18.4.6 Double-layer Capacitors

Conventional capacitors have a dielectric between the electrodes. Their capacity is determined by the dielectric number and the area of the electrodes. The so-called double-layer capacitors have an ion-conducting electrolyte between the electrodes. Therefore, an agglomeration of charge carriers at the interface between the electron-conducting and the ion-conducting interface is possible. The interface is called the electrochemical double layer. In contrast to secondary batteries, no chemical reaction and no charge transfer from the electrode to the electrolyte happened. Therefore, no changes in the material structure occur resulting in cycle lifetimes of several hundred thousands. The storing of energy

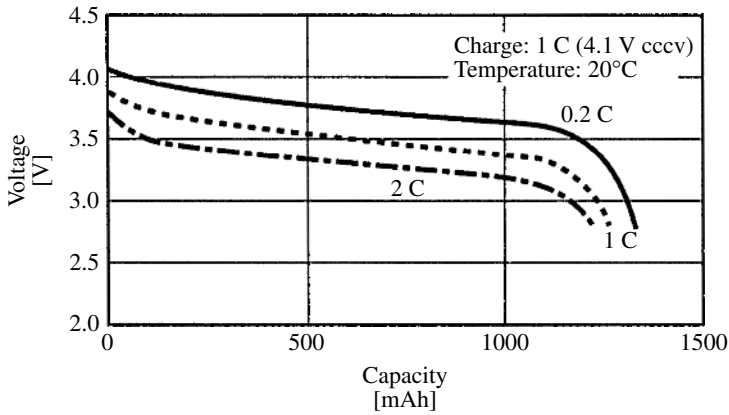


Figure 18.8 Voltage during discharge of a Li-ion battery with $C_5 = 1350$ mAh capacity as a function of the discharged capacity at different discharge currents and a temperature of 20°C. The charging is done with the constant current–constant voltage (cccv or IU, see Sub-section 18.4.7.6.1) regime with a charge current of 1 C and an end-of-charge voltage of 4.1 V [14]

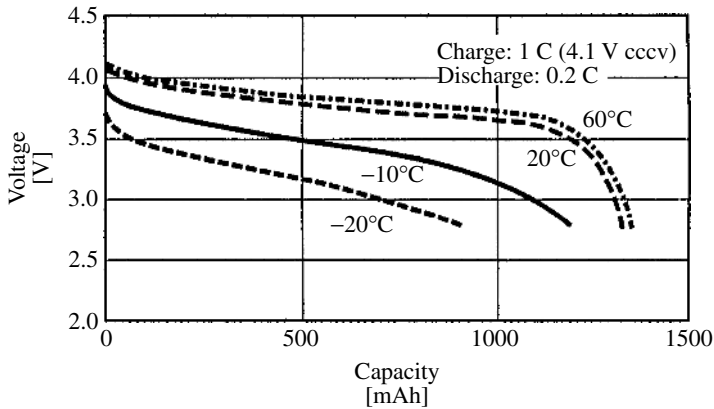


Figure 18.9 Voltage during discharge of a Li-ion battery with $C_5 = 1350$ mAh capacity as a function of the discharged capacity at different battery temperatures at a discharge current of 0.2 C. The charging is done as in Figure 18.8 [14]

only depends on the electrostatic effect. However, in contrast to classical capacitors in which in the dielectric only electrons are moved, in double-layer capacitors a movement of ions and therefore a significant mass movement occurs. This results in diffusion-time constants during charging and discharging in the double-layer capacitor.

Depending on the electrode material, the capacity is approximately 20 to 40 $\mu\text{F}/\text{cm}^2$. The electrode materials are typically made of carbon with very high surface areas of approximately 2000 m^2/g . The number of charge carriers in the double layer is limited because with increasing charge-carrier density the potential increases. If the potential is too high, the charge carriers are forced to penetrate the electrode/electrolyte interface resulting in electrochemical reactions like in secondary batteries. However, in this case

this is an irreversible effect and destroys the double capacitor. An additional problem is that in many double-layer capacitors aqueous electrolytes are used and the gassing must be avoided as well (start of water electrolysis at 1.23 V). Therefore, the maximum voltage needs to be limited to approximately 1.5 to 2.0 V. To avoid the electrolysis problem, organic electrolytes are used which allow maximum voltages of 3 to 4 V, but they have significantly lower conductivity than aqueous electrolytes. Therefore, for applications with very high power requirements capacitors with aqueous electrolytes are used; if higher energy density and lower power is required organic electrolytes can be used. Because overcharging of the double-layer capacitors will destroy them, a careful single-cell control is necessary when they are operated in long strings of series-connected cells.

Double-layer capacitors are often known by their brand names like SuperCaps or GoldCaps. They all are based on the above-described technology.

The self-discharge of double-layer capacitors is in the range of 5%/day at 20°C. Especially at higher temperatures, the self-discharge rate (approximately doubling of the self-discharge rate with a 10-K temperature increase as in all electrochemical systems) is hardly acceptable for autonomous power supply systems.

The electrical characteristics are dominated on one hand by the low inner resistance (resulting in high power) and on the other hand by the linear decrease in voltage with the state of charge. On one hand, this allows easy estimation of the state of charge, but on the other hand the voltage drop is very high and increases the requirements of the electronics or limits the usable energy from the double-layer capacitor (e.g. operation only between 1.7 and 2 volts).

Today, double-layer capacitors are available in units of up to some thousand farads. Their gravimetric and volumetric energy density is very low (Figure 18.7), but they may have power densities up to 5000 W/kg. Therefore, double-layer capacitors are most suited to applications with very high power requirements and low energy demand. As double-layer capacitors are a new and emerging technology, it is difficult to give definite cost figures. For orientation purposes, a cost of approximately 50 000 euro/kWh can be estimated today. However, to supply a current of 200 A at 2 V for 2 seconds the cost is approximately 10 euro for the storage.

For autonomous power supply systems, double capacitors are an interesting technology in applications with peak power demand or for smoothing of power flow. These are, for example, pumping systems where pumps have a very high power demand to overcome the initial inertia. Another application might be grid-connected PV inverters with power quality control functionality. They are more efficient with a milli second storage system. As a rule of thumb, it can be assumed that double-layer capacitors can find their place in applications with discharge times of less than 10 s per cycle (for “power storage”) or in combinations with conventional batteries. The big advantage of the capacitors is their almost unlimited number of cycles until the end of their lifetime (several hundred thousands).

18.4.7 The Lead Acid Battery

Lead acid batteries have been commercially used for more than 100 years for storing electrical energy. It has been the most widely used storage system for electrical energy

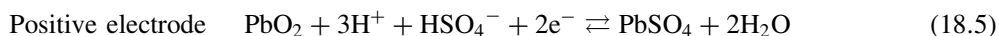
for decades and still remains so. Lead acid batteries cover a wide range of applications from SLI batteries in cars and trucks to uninterruptible power supplies, from load-levelling batteries for grid stabilisation to traction batteries (fork-lift trucks and others) and last but not the least autonomous power supply systems. Different battery designs have been developed for different applications to cover the various requirements.

Lead acid is by far the cheapest battery type in comparison to all other readily available storage systems with appropriate characteristics according to the list given in Table 18.1. A major drawback of the lead acid battery is the low specific gravimetric energy content due to the high molecular weight of lead. However, this is not a parameter of major importance in autonomous power supply systems as the battery is stationary.

It is expected that the lead acid battery will remain as the working horse for autonomous power supply systems for many more years, probably decades. Therefore, this chapter gives a deeper insight into the lead acid battery. The lead acid–battery chemistry, a detailed description of the battery design, ageing effects and recommendations for the operating strategy are the main topic of the following sections.

18.4.7.1 Lead acid–battery chemistry

Lead acid batteries in the charged state consist of a positive electrode with lead dioxide (PbO_2) and a negative electrode with lead (Pb) as the active materials. Both electrodes contain a support grid, which is made from hard lead alloys. Sulphuric acid (H_2SO_4) diluted to 4M or 5M is used as the electrolyte. The following reaction equations describe the main reaction:



PbO_2 and Pb are both converted to lead sulphate PbSO_4 during discharging (double sulphate theory). Sulphuric acid as the electrolyte is used up during the discharging of the battery. Therefore, the concentration of the sulphuric acid decreases linearly with the state of charge. This is an important difference with respect to almost all other battery types, where the electrolyte has only the function of an ion conductor. In lead acid batteries, it is in addition the source for the ions to counterbalance the charge dissolved in the electrolyte from the electrochemical process. Therefore, the electrolyte is subject to “structural” changes like the electrode materials themselves. This is an important reason for several battery characteristics and ageing effects as will be discussed later.

In Section 18.2.1.2, it was described that during charging and discharging not only the electrochemical process described by the Butler–Volmer equation occurs but a chemical process takes place as well. Figure 18.10 shows a schematic of this overall process for the lead electrode which is described by equation (18.6).

The charged electrode consists of lead (Pb) in the solid state. When a discharge current occurs, two electrons are withdrawn from the metallic lead and dissolution of Pb^{2+} ions into the electrolyte occurs. Through diffusion, the charged ions are transported

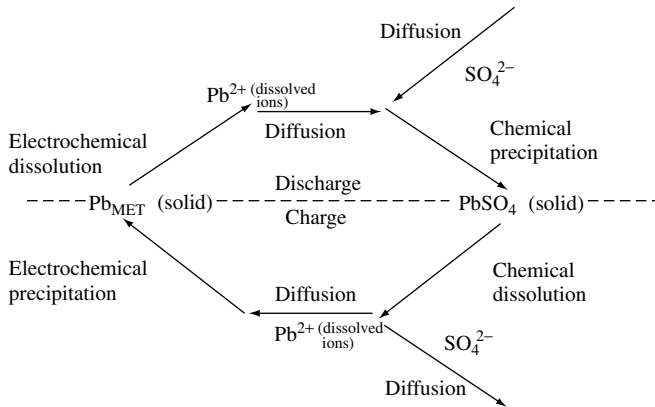


Figure 18.10 Schematic of the charge/discharge process in the lead electrode of a lead acid battery

away from the reaction surface. As the charged ions unbalance the number of positive and negative ions in the electrolyte, negatively charged ions are necessary to counterbalance the positive surplus. They are provided as SO_4^{2-} ions from the sulphuric acid electrolyte. The SO_4^{2-} ions are transported by diffusion from the free electrolyte volume to the reaction site of the electrochemical reaction. There, the Pb^{2+} and the SO_4^{2-} ions meet and form $PbSO_4$ by a chemical precipitation process. This finally results in the formation of $PbSO_4$ crystals.

During charging, the reverse process takes place. Pb^{2+} ions are taken from the electrolyte to form solid Pb during the electrochemical precipitation process. These ions are transported by diffusion processes to the reaction site. To stabilise the Pb^{2+} ion concentration in the electrolyte, a chemical dissolution process of the $PbSO_4$ crystals takes place. Because the positive ions are removed from the electrolyte through the electrochemical precipitation process, the SO_4^{2-} ions need to be transported away from the reaction site to assure electrical neutrality.

All these processes cause overvoltages.

1. Electrochemical dissolution with respect to precipitation described by the Butler–Volmer equation.
2. Transport of Pb^{2+} ions described by the diffusion law resulting in diffusion overvoltages.
3. Transport of SO_4^{2-} ions described by the diffusion law, law of migration of charged ions in an electrical field and fluid dynamics caused by the change in the pore volume during charging and discharging resulting in diffusion overvoltages.
4. Chemical precipitation or dissolution of the $PbSO_4$ crystals forced by deviations of the ion concentration in the electrolyte from the equilibrium concentration resulting in concentration overvoltages.

All processes depend on the temperature. Further, the processes depend on the electrolyte concentration. The concentration influences the equilibrium current density of the Process 1, the diffusion rate of ions in Processes 2 and 3 and it has a strong impact on the

equilibrium concentration of the Pb^{2+} ions and hence on the Process 4. Ageing of the battery and the operating conditions (high currents, small currents and pulse currents) have a significant impact on the overvoltages caused by Processes 1 and 4. This is mainly caused by changes in the inner active surface on the charged active material side (Pb) as well as on the PbSO_4 side.

The nominal voltage of a lead acid battery is 2.0 V; the open-circuit voltage of a charged battery is about 2.1 V, depending on the concentration of the electrolyte.

The open-circuit potential of the positive electrode in a fully charged battery is approximately +1.75 V against the standard hydrogen electrode. The negative electrode potential is approximately -0.35 V against the standard hydrogen electrode. The relationship between the electrolyte concentration and the electrode potential with respect to the cell potential can be seen from Figure 18.14. The dependence of the open-circuit potential on the temperature is as small as 0.2 mV/K. Therefore, it can be neglected for practical reasons.

In addition, there is the main side reaction – the water electrolysis. As the electrolyte is aqueous and the cell voltage is approximately 2 V and can be as high as 2.5 V, water electrolysis takes place continuously. Hydrogen and oxygen are produced at the negative and the positive electrodes, respectively. Hydrogen production starts at electrode potentials more negative than 0 V against the standard hydrogen electrode. Oxygen evolution starts at electrode potentials more positive than 1.23 V. Fortunately, the so-called overvoltages at lead electrodes for the gas production are very high and therefore the gas production is inhibited to a high extent. This allows the lead acid battery to be stable even at the high cell potential of 2 V. The self-discharge rate caused by the gassing is approximately 2 to 5% per month.



Very comprehensive handbooks on lead acid batteries have been written by Bode [15] on the fundamentals and by Berndt [3] on valve-regulated batteries.

18.4.7.2 Lead acid batteries – technology, fundamentals, concepts and applications

All the different types of lead acid batteries discussed in the following text are based on the reaction equation presented above. Whereas Figure 18.11 shows a complete battery system in an autonomous power supply system, Figure 18.12 shows the schematic construction of the electrochemical $\text{Pb}/\text{H}_2\text{SO}_4/\text{PbO}_2$ cell.

Solid lead grids, rods or plates serve to conduct the current (grid) and to mechanically stabilise the porous active mass in both electrodes. Depending on the battery type, different lead alloys for the grid are used to increase the stability, improve the tooling properties and to reduce corrosion. The porous active material is attached to the grid



Figure 18.11 A battery in a photovoltaic system with a rated capacity of $C_{10} = 37.5$ Ah and a rated voltage of 168 V (flat-plate technology, 28 blocks of 6 V connected in series, Picture courtesy Fraunhofer ISE)

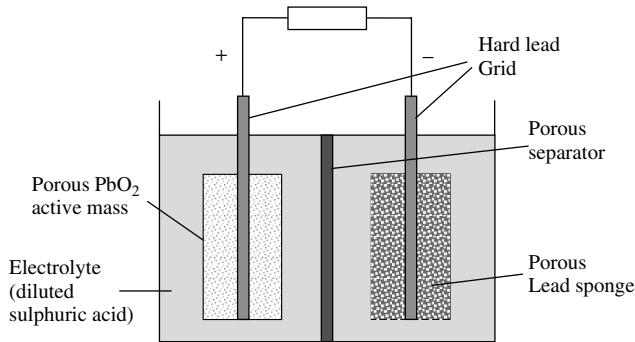


Figure 18.12 Schematic construction of a $\text{Pb}/\text{H}_2\text{SO}_4/\text{PbO}_2$ cell

PbO_2 (lead dioxide) for the positive electrode and to the Pb sponge for the negative electrode. Figure 18.13 shows a more detailed view of the structure of the active material. The active material has an internal surface area of approximately 0.5 to $5 \text{ m}^2/\text{g}$ for the negative and the positive electrode in the fully charged state. The reaction speed and thus the charging and discharging properties are determined by the internal surface. Both electrodes are completely immersed in diluted sulphuric acid (H_2SO_4). As described earlier, the sulphuric acid plays a double role as the ion conductor between the electrodes and a reagent in the charge and discharge reactions. While the battery discharges, the PbO_2 and Pb are converted to PbSO_4 (lead sulphate). The sulphate ions (SO_4^{2-}) are drawn from the electrolyte, causing the electrolyte concentration to fall.

It is worth mentioning that the ratio of the specific volumes of PbSO_4 and Pb is 2.4 and the ratio between PbSO_4 and PbO_2 is 1.96. This means that the solid-phase volume of the active materials increases during discharge. This reduces the free electrolyte volume in the pores and causes mechanical stress on the active material.

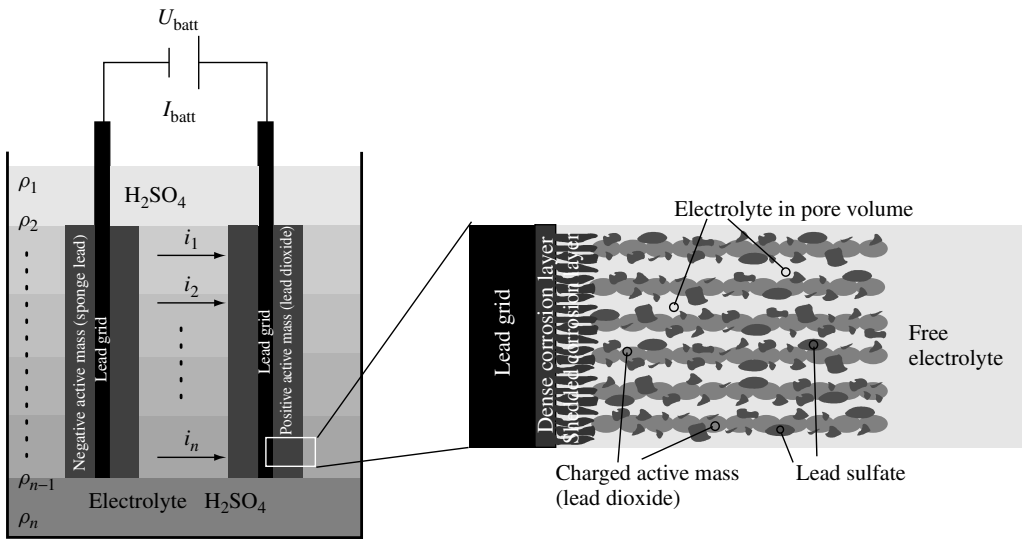


Figure 18.13 A more detailed schematic drawing of the lead acid battery. The left-hand side shows a macroscopic view of the cell including effects like acid stratification represented by the different electrolyte densities in different horizontal heights of the battery followed by inhomogeneous vertical-current distribution within the electrodes. The right-hand side shows a “microscopic” view of the active material in a partial state of charge

A separator is located between the electrodes, intended to prevent short circuits between the electrodes.

The above-described water electrolysis increases significantly as a function of voltage and temperature. As a rule of thumb, an increase in the so-called gassing rate by a factor of two is caused by an increase of 10 K in the temperature and by a factor of 3 by an increase in the cell voltage by 100 mV.

Regarding the hydrogen and the oxygen created as a result of the electrolysis reaction, two different technologies can be distinguished. In so-called flooded batteries, the electrolyte is in the liquid phase. To allow the gases to emerge from the battery, batteries with liquid electrolyte are not sealed gas tight. However, this results in a decrease in the water content of the battery and therefore the electrolyte level decreases and the concentration of the sulphuric acid increases. The water loss needs to be compensated during the maintenance that should take place once or twice a year. Deionised water must be used for refilling and not sulphuric acid or tap water.

The so-called valve-regulated lead acid (VRLA) batteries are sealed gas tight with a valve. The valve allows the release of gas only in the case of overpressure in the battery. In normal operation, the gas is recombined to water within the battery. This effect is achieved by an immobilisation of the electrolyte. Two different techniques are state of the art: the electrolyte is transferred into a viscous gel by adding SiO_2 to the electrolyte or the electrolyte is absorbed within a highly porous glass matt (absorbed glass matt type – AGM). In both cases, the oxygen can pass through the electrolyte to the negative electrode. The recombination of oxygen and hydrogen occurs

at the negative electrode. In VRLA batteries, the electrolyte is not in the liquid phase and therefore no spillage of electrolyte occurs in case of any break of the case or other accidents.

However, if the battery is incorrectly overcharged, more gas is generated than can recombine, so the gas must be able to leave the cell through the valve if an overpressure builds up. At the same time, the valve must prevent ambient air from entering the battery. As these batteries cannot be refilled with water, blowing off the gas from the cell must be reduced to a minimum to prevent the cell from drying out. As a rule of thumb, after more than 10% water loss the battery is at the end of its lifetime. The water loss can be estimated by the weighting of the battery.

To achieve low gassing rates in VRLA batteries, normally lead–calcium alloys are used for the grids. Flooded batteries use mainly lead–antimony alloys with less than 2.5% antimony (Sb). This is a good compromise among the beneficial effects of antimony grids (good grid conditions for casting and good contact of the active material to the grid result in low contact resistance) and the harmful effect of the reduction of the hydrogen overvoltage caused by the antimony. However, as gassing needs to be minimised in VRLA batteries, antimony grids are not an appropriate choice. Especially, in the early days of the VRLA batteries, the antimony-free grids caused a significant reduction in battery lifetime through the so-called antimony-free effect. This effect is described in the literature as premature capacity loss (PCL) [16].

While the rated capacity of a cell depends on the geometry and the number of parallel-connected electrodes, the rated voltage of a cell is 2.0 V. The open-circuit voltage U_0 of the cell depends on the electrolyte concentration as shown in Figure 18.14, but for practical purposes the open-circuit voltage can be determined by the following rule of thumb:

$$\frac{U_0}{\text{V}} = \frac{\rho}{\text{g/cm}^3} + 0.84 \dots 0.86 \quad (18.11)$$

where ρ is the density of the electrolyte. Electrolyte concentration and electrolyte density have an almost linear relation. As the electrolyte density can be easily measured, the electrolyte density is often used to express the electrolyte concentration. At 25°C, 30% H₂SO₄ in H₂O has a density of about 1.22 g/cm³ and 40% H₂SO₄ in H₂O has a density of 1.30 g/cm³. Typical electrolyte densities in fully charged batteries are between 1.22 and 1.32 g/cm³, depending on the application, the technological type and the climatic conditions. The acid density in the discharged state is between 1.18 and 1.05 g/cm³. According to equation 18.11, the open-circuit voltage also varies with the density. It is not a constant by any means.

Figure 18.14 shows the correlation between the electrode and cell potentials and the acid concentration. The acid concentration can be measured by means of the concentration in mol/l, the density in g/cm³ and the percentage of acid in the solution %_{weight}. This allows the translation of all values to one another.

According to equation (18.7), the electrolyte concentration decreases during discharge. According to equation (18.11) the open-circuit voltage decreases in a manner directly proportional to the acid concentration. VRLA (sealed) batteries have less electrolyte per ampere-hour capacity than flooded batteries. Therefore, the open-circuit voltage

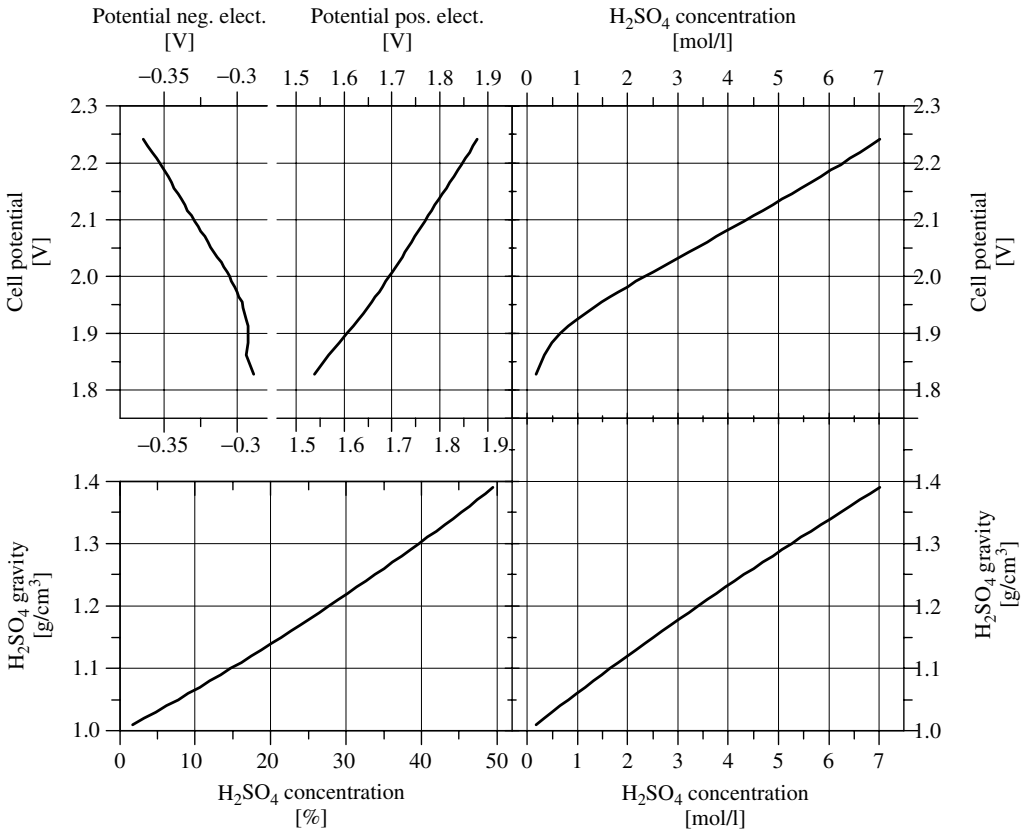


Figure 18.14 Correlation between the acid concentration in percent, mol/l or density and the equilibrium potential of the negative and positive electrodes and the cell potential. The graphs allow converting each value to the other

decreases more rapidly in sealed batteries during discharge than in flooded batteries. This must be taken into account, if the voltage is used as an SOC indicator.

Today, two different plate technologies are commonly used. The most common type of plate is the flat plate (Fauré type). The porous active mass is applied to the hard lead grid as a paste. The flat plate is simple and cheap to produce. The so-called tubular plates¹⁰ are also widespread. A central lead rod, surrounded by active material, is inserted into a protective tube that is permeable to the electrolyte. A plate then consists of a row of adjacent tubes. While flat-plate electrodes have lower internal resistance and therefore higher specific power than tubular plates, the latter show more cycles in their lifetime. Manufacturing of tubular plates is more expensive than the manufacturing of flat plates. Figure 18.15 shows schematics of a flat-plate and a tubular-plate electrode. Currently, wounded lead cells come into the market consisting of a thin lead foil pasted with active material and with a very thin glass-mat separator between the electrodes. These batteries

¹⁰ Tubular-plate electrodes are not very common in North America. Traditionally, tubular-plate batteries are more popular in Europe for cycling applications like, for example, fork-lift trucks.

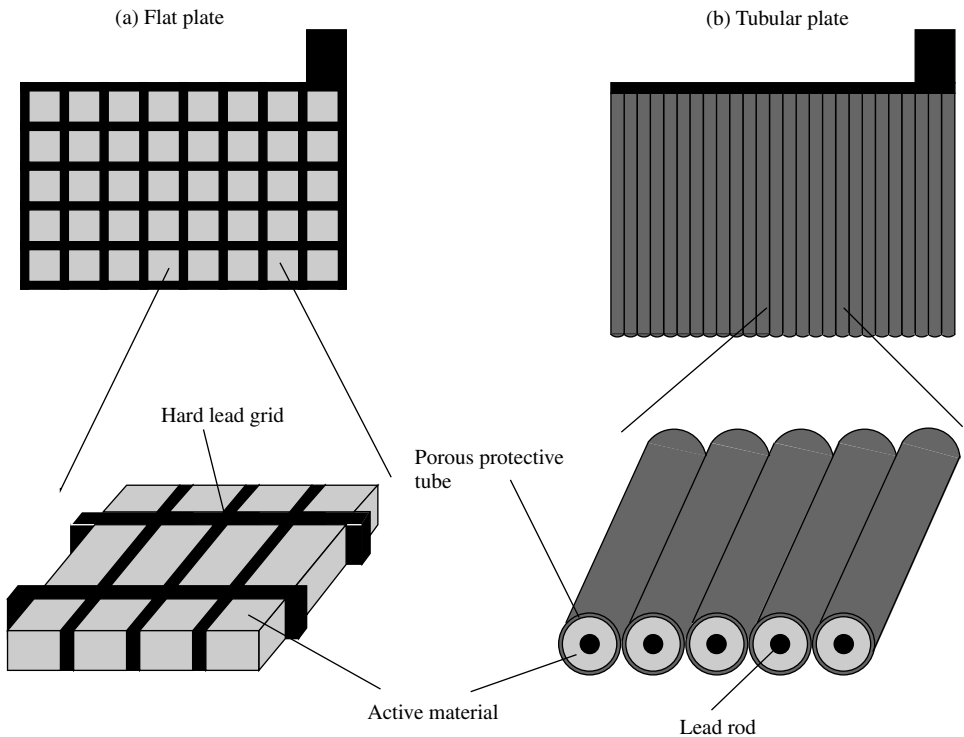


Figure 18.15 Schematic diagram of (a) a flat-plate electrode and; (b) a tubular-plate electrode

are primarily used in high-power applications like the ignition of motors. The first results show good cycle-life behaviour.

Lead acid batteries are used today in many different applications, therefore a large variety of application-specific batteries are in the market. They can be distinguished by their specific power, their cycle life and their float lifetime. Float lifetime is the relevant parameter for batteries in uninterruptible power supplies where the batteries are subjected to only very few cycles in case of failure of the mains, but they should have long operating lifetimes while always being 100% charged. The main battery types for different applications and their typical operating conditions are as follows:

SLI (starting, lighting, ignition) batteries: Used for starting of engines; very high power capabilities even at low temperatures; traditionally only very low capacity throughput; subject to high temperature fluctuations; the largest global market for lead acid batteries with respect to the capacity; production companies in almost all countries throughout the world; the operation profile is changing in modern cars as cars have a very high power demand beside starting owing to numerous electric applications in cars like seat heating, electric window lift or HiFi systems. The batteries are made from very thin flat-plate electrodes to achieve high power. SLI batteries are a mass product, highly automated and are therefore very cheap.

UPS (uninterruptible power supply)/stationary batteries: Long idle periods at full SOC; rapid discharge when required (discharge time in the range of 10 min to 1 h, in some applications even longer); designs for lifetimes of up to 20 years available and market grows strongly in connection with the expansion of telecommunications and computer systems. The electrodes are thicker than for SLI applications to withstand corrosion for long periods.

Traction batteries: Application in fork-lift trucks, traction engines, underground mining vehicles and so on; designed for daily complete cycling with moderate currents and regular and controlled complete charging and cycle lifetimes of 1000 to 2000 cycles with 80% DOD can be achieved. The most common electrode technology in these applications is tubular-plate. Flooded batteries show longer lifetimes than VRLA and are widely used.

Electric-vehicle batteries: Widely fluctuating current profile; partial recharging phases (regenerative braking); inadequate lifetimes to date; expanding market and strong competition from other types of battery technology (see Table 18.3). Low gravimetric energy density is a major drawback in this application. Lead acid batteries based on thin pasted lead foils and wounded design are currently under development and are already available in the market from some manufacturers to serve hybrid vehicles¹¹ that are seen at the moment as a more realistic option than purely battery-powered electric vehicles. Wounded cells have very high power capability and therefore can serve electric motors for accelerating and regenerative braking.

Batteries for photovoltaic systems: Operating conditions corresponding to the load profiles illustrated in Section 18.3; complete charging very seldom and many partial cycles. Two classes of so-called “solar batteries” are in the market. One class is the modified SLI battery with typically thicker grids than those used in SLI batteries, quite cheap (often from local production in developing countries [17]) but with limited lifetime. The other class of “solar batteries” are modifications from high-quality batteries originally used for cycling or standby applications. In general, flooded batteries show better lifetimes in autonomous power supply systems than VRLA batteries. On the other hand, VRLA batteries have significant advantages concerning electrolyte spillage, maintenance and transport and very little release of corrosive and explosive gases. This reduces the requirements on the battery housing significantly. Therefore, a final choice must be made according to the specific application and the boundary conditions.

Operational experience, however, reveals that the lifetime of batteries in stand-alone applications based on solar energy is in general unsatisfactory compared to battery lifetimes in traditional applications. Batteries in solar home systems normally have to be exchanged after 2 to 3 years and batteries in hybrid systems after 3 to 8 years. Lifetime extensions to 5 years in solar home systems and 10 years in hybrid systems are achievable with advanced batteries designed for the purposes of autonomous power supply systems and appropriate system designs and operation strategies.

¹¹ Hybrid vehicles have a conventional motor but with less power than in traditional cars. Acceleration is supported by electric motors powered by the batteries. The batteries are charged during regenerative braking and from the main motor. This concept allows the conventional motor to run with small variations in power and therefore at higher efficiencies. Fuel consumption was reduced with this concept in prototypes down to 2 l/100 km.

18.4.7.3 Discharge capacity

The capacity that can be withdrawn from lead acid batteries depends strongly on the discharge conditions.

For stationary batteries usually the C_{10} or C_8 capacity, for starter batteries usually the C_{20} capacity and for traction batteries usually the C_5 capacity is specified. Solar batteries often are rated as C_{100} and C_{120} at 100 or 120-h discharge current, respectively. Typical end-of-discharge voltage is 1.8 V/cell or 1.85 V/cell for C_{10} , C_{20} and C_{100} . For C_5 , 1.7 V/cell is commonly used. All other ratings and voltage limits can be found as well.

The measured and the practical capacity increase when the discharge current decreases. If a battery is discharged with a lower current than the rated current, a higher capacity than the rated capacity can be withdrawn. If the state of charge is specified with respect to the rated capacity (a reasonable convention), negative values for the state of charge can arise. This is the reason Figure 18.6 displays negative states of charge.

Figure 18.16 shows the voltage during discharge as a function of the discharged capacity at different discharge currents. The lead acid batteries' capacity depends very much on the discharge current.

As a rule of thumb, it can be assumed that a battery with a nominal capacity of 100 Ah at C_{10} has approximately 50 Ah at C_1 and approximately 130 Ah at C_{100} . Please note the fact that the corresponding currents I_1 and I_{100} are not equivalent to $10 \times I_{10}$ res. $0.1 \times I_{10}$. In this example, I_1 is 50 A and I_{100} is 1.3 A.

With respect to the electrical properties, the temperature influences the inner resistance (increasing conductivity of the electrolyte with increasing temperature), the diffusion

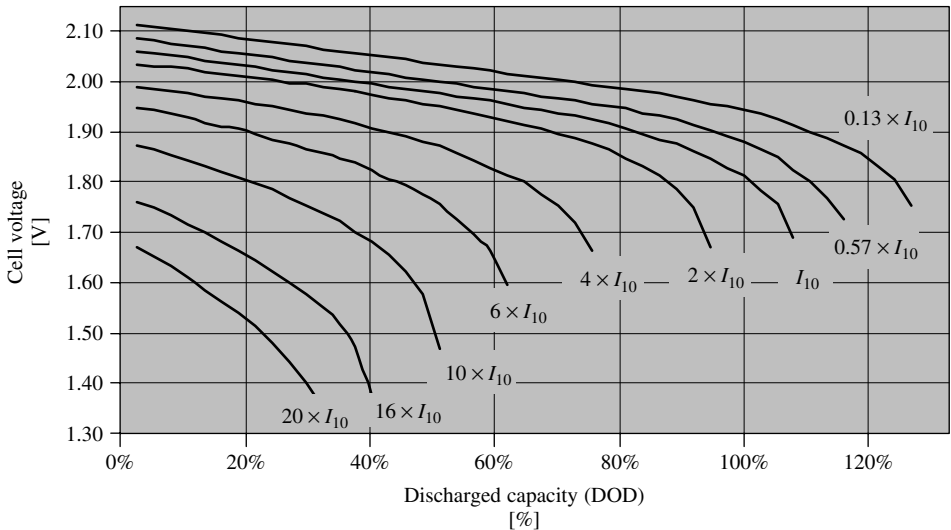


Figure 18.16 Voltage during constant discharge as a function of the discharged capacity at different discharge currents (tubular-plate lead acid battery, C_{10} capacity defined at I_{10} and 1.8 V), data from Berndt D, *Blei-Akkumulatoren (Varta)*, VDI-Verlag, 11. Auflage, Düsseldorf (1986) [18]

processes and the reaction at the electrochemical double layer. Therefore, the capacity of lead acid batteries depends strongly on the temperature. The capacity increases almost linearly by approximately 0.6%/K with an increase in temperature. The capacity decreases in the same way with decreasing temperatures. Depending on the battery technology, the temperature coefficient can be as high as 1.0%/K.

18.4.7.4 Ageing processes and their influence on the battery properties

A comparison with other battery systems, for example, NiCd batteries, reveals that the relatively short lifetime of lead acid batteries is a significant disadvantage. However, the operating behaviour of the batteries is already affected during the lifetime by the processes responsible for ageing. Thus, it is helpful to be aware of the most important ageing processes and to avoid the conditions that accelerate them.

18.4.7.4.1 Acid stratification

Acid stratification is not an ageing process but affects the operating behaviour of the battery. On one hand it reduces the available capacity and changes the current/voltage characteristics. On the other hand it leads to inhomogeneous current distribution at the electrodes. The latter effect accelerates sulphation (Section 18.4.7.4.2), which is a major ageing effect. Therefore, acid stratification is a reason for ageing and not an ageing effect by itself. Acid stratification in flooded batteries can be removed immediately by stirring the electrolyte.

Because the electrolyte functions as an active component of the electrode reaction, local variations in the density can arise, with the result that the acid density decreases in the upper part of the cell and increases in the lower part. The potential difference associated with the concentration difference leads to discharging of the lower section of the electrodes, which can result in irreversible ageing effects (e.g. sulphation).

In batteries with liquid electrolytes, the acid stratification can be eliminated by deliberate overcharging, associated with gas production. The same mixing effect can be achieved by active circulation of the electrolyte. Such electrolyte stirring systems are made from an air bubbling system (Figure 18.22).

Electrolyte stratification can also occur in batteries with immobilised electrolytes. In a gel battery, the effect is very small and therefore is of little relevance. In AGM batteries, the strength of acid stratification depends very much on the quality of the glass mat. Large battery cells from AGM technology are mounted vertically to avoid any acid stratification. While purchasing the batteries, it is important to check the manufacturer's specifications regarding vertical installation of the battery. The problem with VRLA batteries is that an existing acid stratification cannot be removed.

From theoretical consideration [19, 20], it is obvious that small currents in conjunction with acid stratification lead to a significant undercharging of the lower part of the electrodes. This effect is getting more and more pronounced with smaller battery currents. When an acid stratification occurs, the upper part of the electrodes is charge preferential and the lower part is discharge preferential. This results in differences in the local state of charge between the upper and the lower part of up to 30%. During the limited charging

times, the upper part can reach a very high state of charge while the lower part is by far not completely charged. This means, that the lower part of the electrode is cycled in lower states of charge than from the average state of charge of the electrode. Further, the lower part is cycled without a full charge for extended periods.

These findings are confirmed twofold by experimental results. On one hand, it was possible to show experimentally the effect of inhomogeneous current distribution and the state of charge within the electrode as a function of the charge/discharge currents [20]. On the other hand, almost all physicochemical analysis of lead acid batteries from PV systems at the end of their lifetime shows a high degree of sulphation in the lower part of the electrodes [21, 22].

Another problem related to acid stratification in batteries with liquid electrolytes is that a measurement of the acid density, made at the only accessible position above the electrodes, does not give any direct information on the battery's state of charge.

As an example, Figure 18.17 shows the correlation between the acid density above the electrodes in a flooded battery and the battery's state of charge for a battery from a PV system, with a large number of partial cycles.¹² Without acid stratification, a measured acid density of, for example, 1.18 g/cm^3 corresponds to a real state of charge of approximately

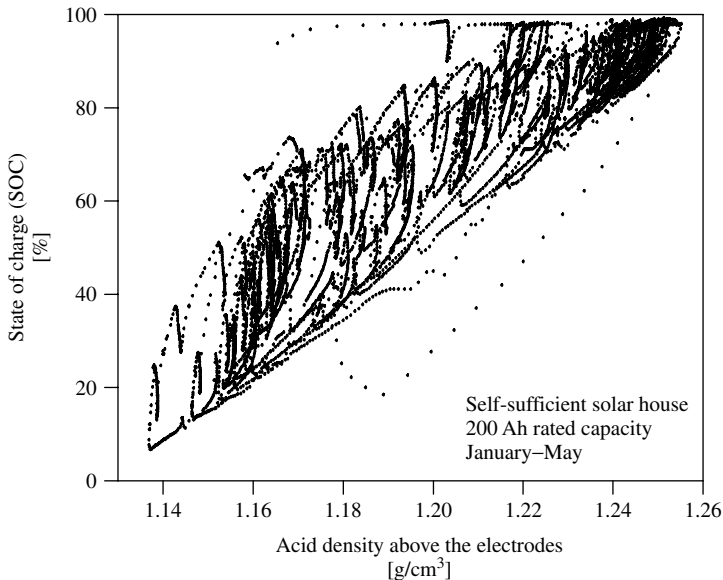


Figure 18.17 Acid density above the electrodes versus the actual state of charge, measured over five months for a battery from a photovoltaic system (200 Ah cells, simulated acid densities based on measured initial data 10-minute average values)

¹² Figure 18.17 is based on a detailed battery model including modelling of the vertical acid-density distribution. The model was verified by measurements in a battery. The model and verification are described in [19]. Therefore, the state of charge and the acid density above the electrode displayed in Figure 18.18 are calculated by the model. The calculations are based on detailed measurements of the battery current, voltage and temperature in the system.

30%, whereas it can range between approximately 30% and 75% if the acid is stratified. This measurement only allows a lower limit to be estimated. A measurement of the acid density above the electrodes can lead to appreciable errors in determining the state of charge and thus in associated operation-management measures.

18.4.7.4.2 Sulphation

When the electrodes are discharged, the active masses, PbO_2 and Pb , are transformed into PbSO_4 . The size of the sulphate formed depends on the strength of the discharge current – high discharge currents result in small sulphate crystals. If a battery is not recharged soon after its discharge, the sulphate crystals grow as a result of recrystallisation processes. The rate of recrystallisation is linearly correlated with the solubility of sulphate ions. Unfortunately, the solubility of sulphate ions increases with decreasing acid concentration [15]. Therefore, periods of low states of charge (and hence low acid concentrations and high sulphate solubility) harm the battery by accelerating the growth of large sulphate crystals. During subsequent charging, large sulphate crystals with their relatively smaller active surface are re-dissolved more slowly than smaller ones, so that sulphate crystals are still present when charging is nearly finished. Figure 18.18 illustrates that for the same volume, small crystals have a larger surface area than large ones (two-dimensional representation of the three-dimensional effect).

During the course of the operation, these remaining sulphate crystals can accumulate, reducing the active mass and thus the accessible capacity [23]. Sulphation can be reduced to a minimum if each discharging process is rapidly followed by sufficiently complete charging. The effect of acid stratification is that complete charging is seldom achieved for the lower part of the electrode, so that strong sulphation occurs there. This sulphation effect can be clearly seen in the cross-sections of Figure 18.19.

As a result of sulphation, the amount of active material available for normal charging and discharging operations decreases. This reduces the capacity, and the voltage during discharge is also shifted to lower values. If sulphation is too pronounced (as in the lower section shown in Figure 18.19), larger areas of the electrodes can become completely inactive.

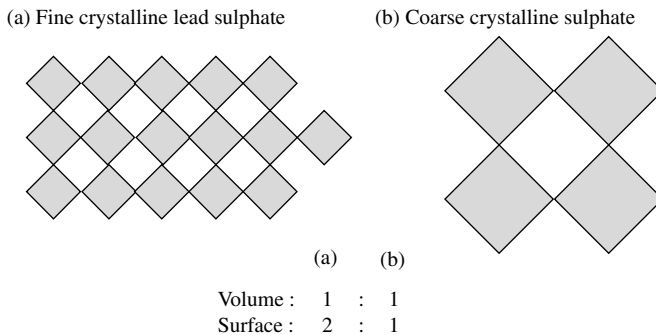


Figure 18.18 An example illustrating the effect of the crystal size on the active surface area of the electrodes. Mass ratio a:b = 1:1, surface area ratio a:b = 2:1

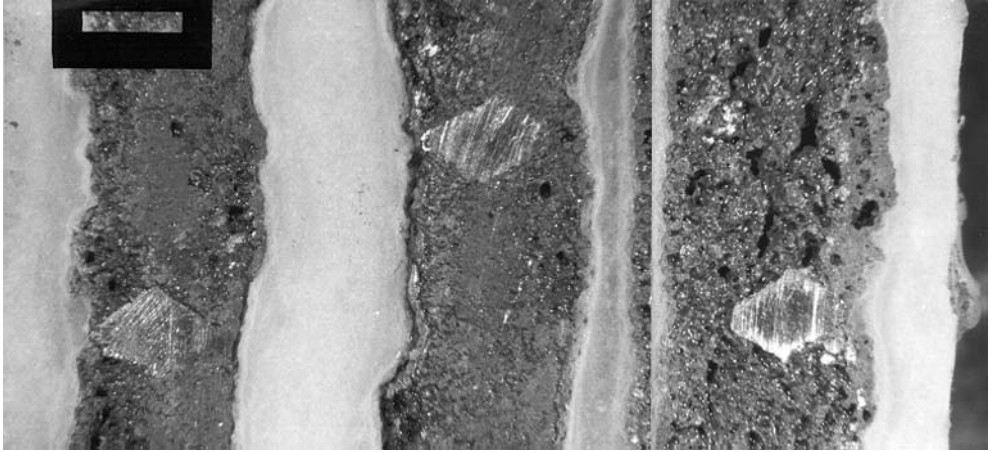


Figure 18.19 Cross-section of a negative flat-plate electrode after 3.5 years of operation in a photovoltaic system. The sections were taken from the upper, central and lower parts of the electrode (from left to right, respectively). Sulphation is clearly indicated in the lower section by the very coarse pores between large crystals, and by the noticeable broadening of the electrode, due to the difference in the specific volumes of Pb and PbSO_4 (Photo source: ZSW)

18.4.7.4.3 Corrosion

The high positive potential at the positive electrode results in the corrosion of the lead grid [24]. On one hand, this causes the cross-section of the grid to decrease, so that the grid resistance increases. On the other hand, a layer consisting of lead dioxide, lead oxide and lead sulphate forms between the grid and the active material, which also raises the contact resistance. This becomes evident during charging and discharging as an increased ohmic voltage drop. Figure 18.20 shows the cross-section of a tubular electrode from a battery after 3.5 years of operation. The lead core (grid rod in the centre of the tube) has almost completely disappeared due to corrosion.

The corrosion rate depends on the acid density, the electrode potential, the temperature, the grid alloy, the active material coverage [25] and a most important factor, the manufacturing quality of the grid. Corrosion is particularly pronounced for cell voltages below 2.0 V and above 2.4 V [24]. Corrosion is minimal for cell voltages around 2.23 V. Corrosion is an irreversible ageing effect and increases the internal resistance of the battery. An indirect consequence is that the current distribution becomes more inhomogeneous in the vertical direction, so that sulphation is accelerated in the lower parts of the electrodes. In batteries for PV systems, thicker grids are used to reduce the effect of corrosion and thus extend the lifetime.

18.4.7.4.4 Erosion

Both electrodes are subjected to strong mechanical loads during cycle operation. The reason is that up to 50% of the active material is converted to lead sulphate during discharge. Lead sulphate has a volume per mole, which is 1.94 times larger than lead dioxide and 2.4 times larger than lead.

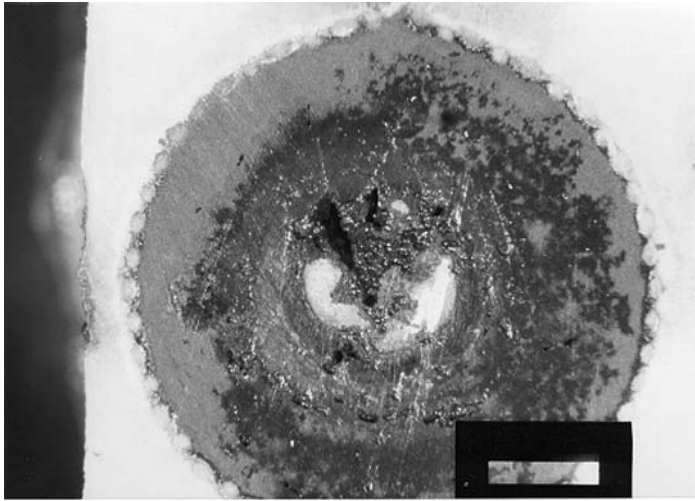


Figure 18.20 Cross-section through a tubular electrode of a battery after 3.5 years of operation. The lead rod (light-coloured area in the centre) has almost completely disintegrated as a result of corrosion. The diameter of the electrode is 8 mm. (Photo source: ZSW)

These large changes in volume act to loosen the active material. This effect increases with increasing depth of discharge. Thus, deep discharge with low currents has an additional negative effect on sulphation. Once the active material has become loose, it can be separated from the electrode, for example, by gas movement, and gathers as sludge at the base of the battery. If the volume below the electrodes that contains the sludge is not large enough, there is a danger of short circuits between the electrodes.

The erosion effect is much less pronounced in sealed batteries, as the electrodes there can be mounted under pressure. The pressure compensates the forces arising from the volume change and increases the stability of the active masses.

The available active mass at the electrodes is reduced by the loss due to erosion. This corresponds directly to a reduction in the accessible capacity. Accordingly, the battery will be discharged earlier.

18.4.7.4.5 Short circuits

In addition to the danger of short circuits in the sludge volume of batteries with liquid electrolytes, there are two further risks for short circuits.

The plate connectors from the positive electrode above the active material are also subject to corrosion. This results in detachment of large corrosion flakes, which can fall onto the electrodes and cause short circuits. This risk can be eliminated by including separators that extend upward well over the electrodes.

Further, there is a risk for all battery types that dendrites (microscopic short circuits) may grow from the positive to the negative electrode through the separators. These dendrites are so fine that they are usually not visible even when the battery is investigated

in the laboratory. Their growth is accelerated by long periods at a low state of charge and thus low acid concentrations. As described in Section 18.4.7.4.2, the solubility of PbSO_4 increases at low acid concentrations. For example, the solubility of PbSO_4 is 2 mg/l at a sulphuric acid density of 1.28 g/cm³, and is already 35 mg/l at a density of 1.02 g/cm³. The higher the solubility the higher is the rate of recrystallisation and hence the rate of formation of large sulphate crystals and dendrites. The danger of dendrite growth can be counteracted by thicker separators and by operating the battery at high states of charge.

In general, a short circuit is a defect that causes a sudden and complete breakdown in the battery. Short circuits can occur from dendrites between the electrodes and the sludge in flooded batteries from active material accumulated as a result of active-material shedding under the electrodes. If the amount of material exceeds the free-electrolyte height under the electrodes, short circuits occur through the “mud”. Microscopic short circuits through the separator affect particularly the self-discharging properties of a battery.

18.4.7.4.6 Reverse charging

If a battery is subjected to a discharging current even after the battery has been fully discharged, the potential changes its sign.

Reverse charging of an individual cell can occur in strings of series-connected cells. The battery voltage and therefore the depth of discharge protection are controlled on the basis of overall string voltage. A single cell within the string may have lower capacity due to manufacturing deviations or due to accelerated ageing. In consequence, the low-capacity cell can be over-discharged resulting in reverse charging.

In case of reverse charging, PbO_2 is formed at the original Pb electrode and vice versa. Although this type of reverse charging can sometimes increase the capacity for a short time, it is certainly detrimental to the cell lifetime in the long term. The main cause of damage is the oxidation of additives in the lead sponge of the negative electrode, which are included to maintain the high porosity of the electrode. If these additives are destroyed, large lead crystals form in the negative electrode resulting in a loss of internal surface area and therefore in an irreversible loss of capacity.

The danger of reverse charging can be reduced if the voltage of the individual cells is monitored and used as the criterion to end discharging (rather than the total voltage of the battery). Alternatively, it can be prevented by allowing charge equalisation between the cells of a series connection [12].

18.4.7.4.7 Ice formation

Figure 18.21 shows the dependence of the freezing point of diluted sulphuric acid on the electrolyte concentration. Ice must be prevented from forming in a battery under all circumstances, as it is then practically impossible to operate the battery (in particular, a frozen battery can hardly be charged) and it is possible that the cell housing may burst (battery breakdown and contamination of the surroundings with sulphuric acid).

For operating modes with very low discharge currents, or if the deep-discharge protection is inactive or non-existent, it is possible to reach extremely deep discharge,

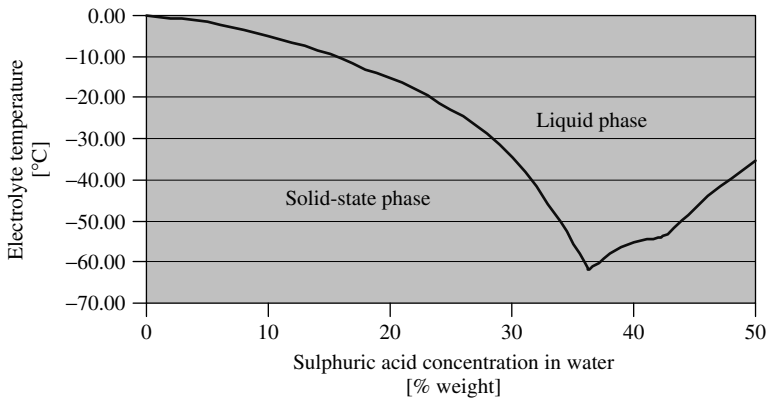


Figure 18.21 Freezing point of diluted sulphuric acid as a function of the acid concentration

as the voltage does not break down until very late in the process. Batteries that are subjected to temperatures below the freezing point should be dimensioned such that after withdrawing $1.3 \times C_{100}$ or $1.7 \times C_{10}$, the acid density is still so high that freezing is not expected, according to Figure 18.21.

18.4.7.5 Battery peripherals

For proper battery operation, several battery peripherals must be used. The following gives a brief description of the most important devices.

Charge controller: Charge controllers are responsible for the charging strategies and the deep-discharge protection. They limit the power from the PV generator if necessary. More details on the operation strategies are given in Section 18.4.7.6 and on the hardware in Chapter 19.

Chargers: Chargers are AC/DC converters that use the power from motor generators to recharge the battery. They need a charge control as well to avoid overcharging of the battery. The charging regime should be the same as for charge controllers.

Charge equaliser: In long strings of series-connected cells, problems with individual cells like overcharging and reverse charging can occur owing to differences in the ageing processes or tolerances in the production. Charge equalisers avoid the detrimental effects by individual treatment of the cells. More details are given in [13] and in Chapter 19.

Monitoring: To get actual information of the state of the battery, monitoring systems can be used. A wide range of commercial products is available. They range from simple voltage monitoring of the complete battery to complete monitoring of temperature, current and voltage of individual blocks and cells as well as impedance of the battery.

State-of-charge meters: For proper battery operation (Section 18.4.7.6) and for the orientation of the user, it is helpful to have proper information on the actual state of charge of the battery. Several devices and algorithms are available, but only very few are really suited to autonomous power supply systems [26].

Electrolyte-agitation systems: To avoid the detrimental effects of acid stratification in flooded batteries, electrolyte-agitation systems are an effective solution. Figure 18.22 shows a battery with an agitation system. Most systems are based on compressed air that is pumped to the bottom of the cells. The ascending air bubbles cause an electrolyte circulation and mixing.

Recombinators: To reduce the loss of water from flooded batteries, recombinators are used. They consist of a catalyser that recombines the hydrogen and oxygen gas evolving from flooded batteries. Figure 18.22 shows a battery with recombinators.

18.4.7.6 Operation strategies

The operation strategy and the charging strategy have an important impact on the battery lifetime. Therefore, in the following paragraphs some ideas on appropriate strategies are discussed.

In most PV systems, the system and the battery control are realised through the charge controllers; in some cases energy management systems take over this job. The battery requires proper handling of frequent full charges, gassing for electrolyte-stirring in flooded batteries, control of end-of-charge voltage and deep-discharge protection.



Figure 18.22 Flooded, tubular-plate battery (2×240 Ah in parallel connection, 12 V) with gas recombinators for reduction of water loss through gassing and an electrolyte-stirring system to avoid acid stratification (only connected to the right hand unit), the membrane air pump is mounted on the wall, operation of the pump: twice a day for 15 min, (Picture courtesy Fraunhofer ISE)

18.4.7.6.1 Charging

As a result of the specific operating conditions, full charging occurs very rarely. Charge and discharge cycles follow each other very frequently. Long charging times at constant power supply as available in grid-connected systems do not occur. Nevertheless, field experience showed that full charging is necessary to achieve long battery lifetimes.

The most common charging strategy is the constant current/constant voltage mode (IU or $cccv$, Figure 18.23(a)). In autonomous power supply systems, this means that the battery is charged with the fully available power until the battery voltage reaches the defined end-of-charge voltage. From this moment, the charging power to the battery is limited in a way that this voltage limit is not exceeded (constant voltage mode). The voltage drops at the moment when the battery charging is not high enough (due to decreasing power generation or increasing load) to maintain the battery voltage at the given limit. Most charge regulators and battery chargers use this charging procedure.

A more advanced charging method is shown in Figure 18.23(b). The charging starts with a constant current/constant voltage charging, but the maximum voltage is reduced after a certain time to a lower limit (IU_0U). This allows higher voltages during the first constant-voltage phase, but avoids negative effects like gassing and corrosion due to long durations of the high voltage. Therefore, this charging method allows overall faster charging but avoids hazardous conditions in the battery. More and more sophisticated charge controllers in the market use this charging procedure.

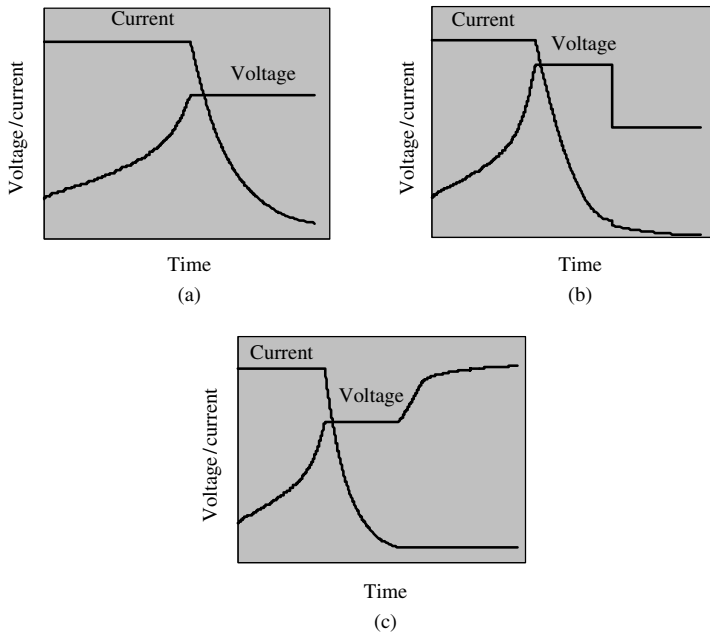


Figure 18.23 Schematics of different charge regimes. (a) Current and voltage during a constant current/constant voltage charge IU or $cccv$; (b) a constant current/constant voltage charge with two end-of-charge voltage limits IU_0U ; and (c) a constant current/constant voltage charge followed by a limited constant current phase IUI_a are shown

Especially for VRLA batteries, it turned out that longer lifetimes can be achieved with the constant current/constant voltage/constant current (IUI_a) charging as shown in Figure 18.23(c) ([4]). After the current drops during the constant-voltage phase below the limit for I_a charging, the charging is continued for a limited time or amount of charge with a constant current. The voltage is not limited during this phase, but the I_a current must be limited in the range of I_{50} to I_{100} . No commercial device in PV applications uses such a scheme these days.

It is necessary to take into account that the batteries in PV systems hardly ever get fully charged due to the limited charging time per day [4]. Therefore, the term full charge has to be distinguished in a real full charge, defined by the point at which the complete active material is converted into charged material, and a practical or solar full state of charge (Figure 18.3). The latter is defined by the maximum state of material conversion that can be achieved during a sunny summer day or the maximum operation time of the back-up generator that is accepted by the system operator. A “solar full charge” requires at least 5 h at a battery voltage of 2.4/cell.

In hybrid systems, a solar full charging can be achieved by operation of the back-up generator or from the PV generator. Full charging every four weeks is recommended. A detailed analysis of the operational data from systems showed that this has little impact on the overall energy balance, but is obviously enhancing the battery lifetime.

For batteries in systems of Class 1, according to Figure 18.6 an end-of-charge voltage of 2.4 V/cell is appropriate. However, the duration per day at this voltage should be limited to two hours. During the rest of the day (if the charging power is available), the battery voltage should be limited to 2.3 V/cell (charging regime as in Figure 18.23(b)).

In systems of Classes 2, 3 and 4, the end-of-charge voltage should be 2.45 V/cell also limited to 2 hours per day. An end-of-charge voltage of 2.35 V/cell for the rest of the day is appropriate (charging regime as in Figure 18.23(b)).

The values are valid for flooded and for VRLA batteries. In addition, for flooded batteries an increase of the end-of-charge voltage up to 2.6 V/cell periodically for a maximum of 5 hours per 14 days is appropriate. This causes gassing and therefore stirring of the electrolyte. Nevertheless, an active electrolyte-stirring system as shown in Figure 18.22 is the best and most efficient solution.

A significant lifetime extension can be achieved if the battery is charged to a really full SOC at least twice a year. This can be achieved by charging the battery normally to a solar-full SOC followed by a complete discharge with approximately I_{10} . The discharge must be followed by a recharge according to the IUI_a charging regime (Figure 18.23c) where the battery gets charged with 110 to 120% of the ampere-hour capacity taken from the battery in the previous discharge or the nominal capacity (whatever value is higher).

The end-of-charge voltage limit depends on the battery-operating condition and on the temperature. All values for the voltage limits given here are for a battery temperature of 25°C. At increasing temperatures, the voltage must be reduced by 4 to 5 mV/(K*cell) but not below 2.25 V/cell. At temperatures below 25°C, the voltage must be increased accordingly but not above 2.6 V/cell. To protect DC loads or electronic devices connected directly to the DC bus bar, it might be necessary to limit the maximum voltage accordingly.

18.4.7.6.2 Deep-discharge protection

Lead acid batteries suffer from deep discharge for several reasons. An increasing depth of discharge results in a decreasing acid concentration and due to the increased sulphate solubility in accelerated sulphation (Section 18.4.7.4.2), corrosion (Section 18.4.7.4.3) and higher sensitivity to freezing (Section 18.4.7.4.7). Further, the mechanical stress is increased because of the changes in the specific volume of the active materials and in long battery strings, the risk of reverse charging of single cells (Section 18.4.7.4.6) increases.

Therefore, the maximum depth of discharge should be limited during normal operation.¹³

While choosing the appropriate DOD for the operation strategy, the data-sheet information given by the manufacturers should be analysed. They often give the number of cycles during the lifetime of a battery as a function of the depth of discharge. However, for the system design the number of cycles is not the most important parameter. The level of capacity throughput that can be realised during the battery lifetime is of more relevance. A cycle with 50% DOD means that only 50% of the capacity is used and therefore the overall capacity throughput for, for example, 200 cycles with 50% DOD is equivalent to 100 cycles with 100% DOD. However, from the point of view of the system design a battery which is limited to 50% DOD during normal operation must have double the size with respect to a battery with 100% DOD during normal operation. This is worthy of mention because batteries are always limited by the capacity throughput on one hand and by operation life on the other hand. Therefore, it makes no sense to operate a battery which is, for example, rated for 10 000 cycles at 20% DOD in autonomous power supply systems even though this might promise the highest capacity throughput. Assuming that on a daily basis 10 000 cycles take place, it would take more than 25 years to achieve this. However, the battery lifetime would not last that long due to other ageing processes.

Figure 18.24 shows for two different batteries the cycle life as a function of the DOD (data taken from data sheets) and the resulting capacity throughput. It is obvious that for the battery Type 2, the capacity throughput is almost independent of the DOD but for battery Type 1 there is a strong dependency leading to higher throughputs at lower DODs.

For practical purposes, the following “rules” can be used, which have proved their suitability in the field. In Classes 1 and 2 (Section 18.3.2), the maximum DOD should be 60 to 70% and in Classes 3 and 4, 80 to 90%. The lower values are for flooded batteries and the higher values are for VRLA batteries. Low-cost “solar batteries” should be operated to a maximum of 50% DOD. It is very important to take into account that the mentioned values for the DOD are given on the basis of the C_{10} capacity. Using, for example, 80% of the C_{100} capacity means using more than 100% of the C_{10} capacity and this is hazardous.

Control of the maximum DOD can be realised either by deep-discharge disconnecting voltage or on the basis of the state of charge. Most commercial charge controllers

¹³ As stated in the subsection on charging, a complete discharge of the battery to 100% DOD twice a year is of benefit to the battery. This is not in contradiction to a limited DOD during normal operation. The defined discharge is done within a short time and is followed directly by complete recharging of the battery. In normal operation, discharge times and duration in deep states of charge can be very long and the next full charging may occur only weeks or month later.

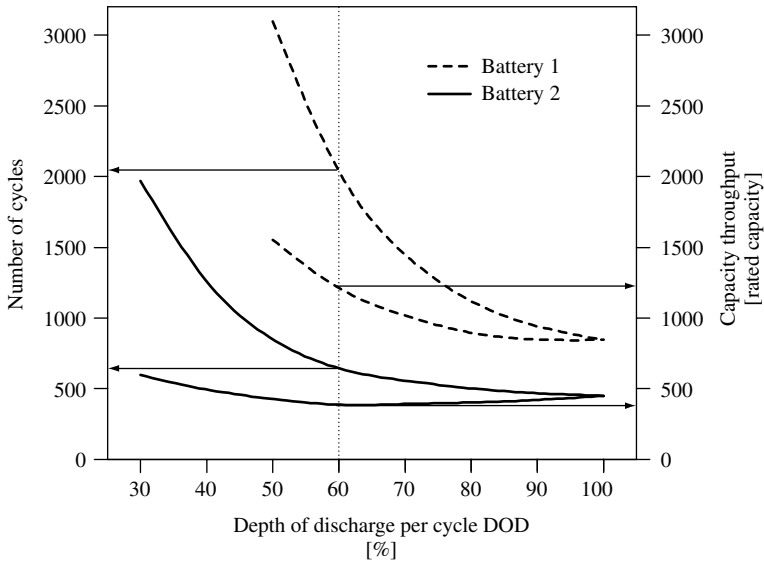


Figure 18.24 Number of cycles and overall charge transfer (capacity throughput) in units of the rated capacity during the battery lifetime as a function of the depth of discharge during cycling. Data from data sheets from battery manufacturers

Table 18.5 Typical end-of-discharge voltages up to which 100% of the C_{10} capacity has been discharged from the battery at different discharge currents at room temperature

$I_{\text{discharge}}$	U [V/cell]
$1.0 \times I_{10}$	1.80–1.85
$0.5 \times I_{10}$	1.85–1.90
$0.2 \times I_{10}$	1.90–1.95
$0.1 \times I_{10}$	1.95–2.00

control the maximum DOD by the voltage. The drawback of this method is that the discharged capacity up to a certain voltage limit depends very much on the discharge current. Table 18.5 shows typical end-of-discharge voltages up to which 100% of the C_{10} capacity has been discharged from the battery. This shows the problem of an efficient DOD control. If the maximum DOD is assured by a high voltage limit even at small currents (e.g. 1.95 V/cell), the available capacity at higher currents is very limited [27]. Figure 18.25 shows a more pronounced version of the problem. A given voltage limit might be appropriate for one battery type, but for another with the same technology (flat plates, lead acid and flooded electrolyte) the discharge curve looks quite different and the same voltage limit results in significant differences in the maximum DOD with respect to the minimum SOC defined to protect the battery as shown in the figure. The difference

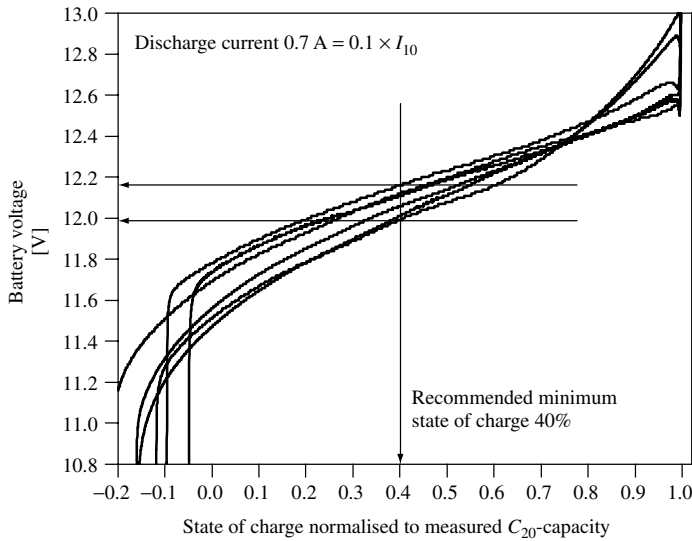


Figure 18.25 Discharge curves of six batteries rated for the same capacity, with the same technology (flat plate, flooded lead acid and all batteries new). The voltage is shown as a function of the state of charge of the batteries. The state of charge is calculated on the basis of the discharge ampere-hour and the nominal (not measured) capacity. Capacity tests were performed with $0.1 \times I_{10}$. The voltage is given for a 12-V block battery made from 6 cells connected in series (a typical design as used for SLI batteries for cars)

in SOC for the same voltage limit could be as high as 25%. Taking into account different battery technologies, the differences in SOC are even higher. In autonomous power supply systems, low and high currents occur (Figure 18.5, [9]).

Two solutions for the problem are available. One is a current-compensated end-of-discharge voltage threshold and the other is the use of state-of-charge determination. The latter solution is the most appropriate for autonomous power supply systems. There are various methods for state-of-charge determination in lead acid batteries, which are appropriate for autonomous power supply systems [26].

18.5 SECONDARY ELECTROCHEMICAL BATTERY SYSTEMS WITH EXTERNAL STORAGE

The secondary batteries described in Section 18.4 use electrodes both as part of the electron-transfer process and to store the energy via electrode solid-state reactions. Consequently, both energy storage capacity and the power rating are intimately related to the electrodes' size and shape.

Electrochemical batteries with external storage overcome this drawback. The reaction occurs within an electrochemical cell and the energy is stored in two tanks separated from the electrochemical cell. The electrochemical cell has two compartments, one for each storage medium, physically separated by an ion-exchange membrane. This allows the designing of the battery power and the energy content separately.

Here, a distinction between the so-called redox-flow batteries in which salts are dissolved in liquid electrolytes and the hydrogen/oxygen storage systems based on the electrolyser and the fuel cell will be made.

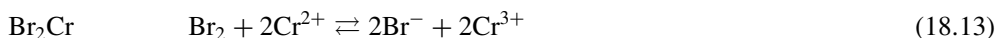
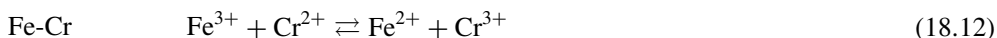
The costs for the converters and therefore the power sizing are independent of the storage size. Therefore, these systems show an economy of scale concerning the energy storage. The larger is the storage, the lower are the specific storage costs. This makes the systems interesting for seasonal storage or other long-term storage applications.

18.5.1 Redox-flow Batteries

In redox-flow batteries, the active material is made from salts dissolved in a liquid electrolyte. The electrolyte is stored in tanks. As the solubility of the salts is typically not very high, the energy density is in the range of lead acid batteries. The electrochemical charge/discharge reactions take place in the converter, which determines the power of the system. Therefore, redox-flow batteries belong to the group of batteries with external storage. Redox-flow batteries were already under investigation for stationary applications in the 1970s and 1980s. An overview of these activities can be found in [28]. Owing to problems with the materials, the investigations were almost stopped but were again started in the last year.

Redox-flow batteries work with electrolytes in two circulations. Each circulation contains a redox system whose valence is changed during charging and discharging. The change in the valence of the two redox systems should take place at preferably high potential difference as this forms the equilibrium voltage of the battery. Figure 18.26 shows the principle of the redox-flow battery with the vanadium battery (equation (18.14)) as an example. The valence of all ions during each step can be seen in the figure.

Several different combinations of salts were and still are under investigation.



Several problems with redox-flow batteries have occurred and are still unsolved. The stability of the separator and the mixing of the electrolytes through the separators are severe problems. Therefore, the vanadium system became the centre of interest in the last few years as the materials and electrolytes are similar for the positive and the negative electrodes. Therefore, a crossing of ions through the separator just causes coulomb losses, but causes no deterioration of the electrolytes.

Defining the specific energy densities is difficult because of the independent sizing of the converter and the storage. Typical values for 20 kW/20 kWh vanadium redox-flow batteries are about 20 Wh/kg and 50 W/kg. For mobile applications in electrical cars, this is not enough, but for stationary, especially in load levelling, applications it is an interesting option. Figure 18.27 shows a prototype of a redox battery at laboratory scale

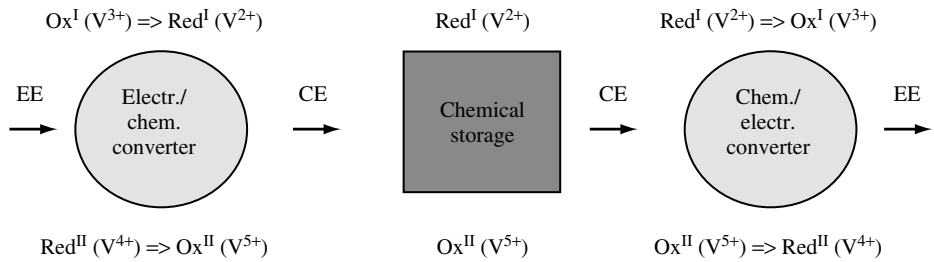


Figure 18.26 General concept of a redox-flow battery with two electrolyte/active mass circulations. The circulation in the upper row is equivalent to the negative electrode, the lower row denotes the positive electrode. In brackets, the vanadium battery is given as an example. The figure is based on an idea from [29] (EE: electrical energy, CE: chemical energy)

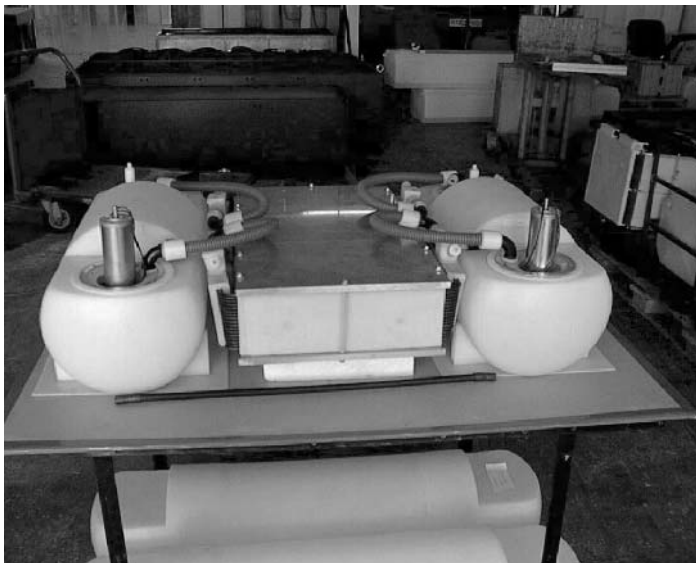


Figure 18.27 Prototype of a vanadium redox-flow battery with 32 cells and 14 Ah (Picture Courtesy by ZSW [29])

and Figure 18.28 shows a schematic of a redox-flow battery in the megawatt hour. As there have been no commercial products in operation for a long time, data on lifetimes are hardly available. Theoretically, long lifetimes can be expected as no part of the system undergoes structural changes as they occur in most other battery technologies. In literature, data for a vanadium battery with more than 13 000 cycles have been reported [30]. In any case, a regeneration of the electrolyte/active mass is possible. The influence of vanadium batteries on the environment is described in [31]. No material loss or “down cycling” of the electrolyte including the vanadium occurs.

What is true for the lifetime is also true for the costs. Rough estimations show, for the vanadium battery, costs of approximately 200 €/kWh for batteries with more than

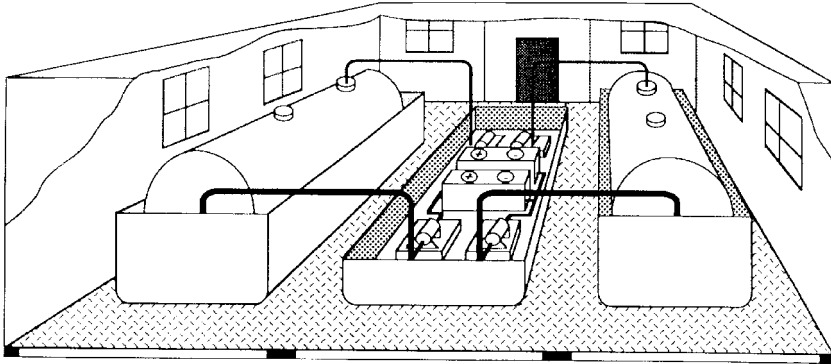


Figure 18.28 Schematic of a redox-flow battery in the megawatt hour range [29]

20 h of discharge time at full power [29]. As no mass production is established, these data are subject to speculations on the mid-term achievable cost figures.

The energy efficiency for the vanadium battery has been demonstrated to be 80 to 85% for the cell itself. As the system requires peripherals (mainly pumps for the electrolytes), the system efficiency can be in the range of 75%, which is considerably better in comparison with the hydrogen system described in Section 18.5.2. No self-discharge of the electrolytes in the tanks occurs. An optimum operation temperature for redox-flow batteries is defined by an optimum of the solubility of all the salts in the electrolyte while avoiding any recrystallisation of a salt.

18.5.2 Hydrogen/Oxygen Storage Systems

The other major technology with external storage is the use of liquid water (discharged state) and its gaseous components hydrogen and oxygen (charged state) [32].

Water can be split into hydrogen and oxygen gas by the fundamental reaction (18.16).



Electrolysis of water starts at 1.23 V/cell. A hydrogen storage system consists of three major components that are listed below:

1. An electrolyser for the production of the gases from electric power,
2. Gas storage for the hydrogen and, depending on the system's design, for the oxygen. Hydrogen is commonly stored either in pressure tanks or metal-hydride tanks.
3. A fuel cell to reconvert the gases into water and electric power. Hydrogen is taken from the storage and oxygen either from gas storage or from air.

Electrolyser/fuel cell systems have been demonstrated; the technology, however, still has to go through a long process of maturation until it reaches the market at acceptable costs and with high reliability.

18.5.2.1 *Electrolyser*

Electrolysers are needed to produce hydrogen and oxygen gas from water by using electric power. Electrolysis is used in many industrial processes apart from hydrogen production. Two technologies for low-temperature water electrolysis are available today:

- Alkaline electrolysers
- Polymer electrolyte membrane (PEM) electrolysers.

In addition, high-temperature steam electrolysers are under investigation, which are in general good for higher efficiencies (see [33]).

Special electrolysers can release the gases already under pressure without using an additional compressor. PEM electrolysers can have efficiencies of 80 to 85%. They are commercially available, but are very expensive because only a few units are sold and expensive materials (membrane, catalysts) are needed. Presently, there is no important market for PEM electrolysers in the kW range. However, larger alkaline electrolysers for use with wind or water power plants are commercial and in operation. Reference [34] gives an overview on a research project on electrolysers operated by wind turbines.

18.5.2.2 *Gas storage*

Three major technologies for hydrogen gas storage are available today:

1. Pressure tanks (low pressure up to 30 bar, medium pressure up to 200 bar and high pressure up to 700 bar).
2. Metal hydrides with adsorption of hydrogen.
3. Liquid hydrogen storage (only for large scale applications).

Low-pressure tanks can be used in conjunction with pressure electrolysers. Specially designed electrolysers [35] produce hydrogen and oxygen at 30 bar without any compressor and therefore a minimum of energy loss due to compression. Medium-pressure tanks or bottles can be fitted to compressors. Today, hydrogen mechanical compressors with a high efficiency for small gas volumes are hardly available. Presently, no compressors for hydrogen with flow rates below approximately 10 Nm³/h are available.¹⁴ Another technology for gas compression is thermal compression with metal hydrides. The pressure in a metal-hydride storage unit increases significantly with an increase in temperature. As different metal alloys have different pressure/temperature curves, gas compression in a multi-stage process is possible. High-pressure gas bottles from composite materials are under development and in operation in R&D and demonstration projects.

Metal hydride is an interesting material for hydrogen storage. The hydrogen is adsorbed within the highly porous metal hydride. In fully loaded metal-hydride tanks, 1 to 2% of the overall weight is hydrogen. The volumetric energy density of metal hydrides is comparable with a 200 bar pressure bottle. The pressure in a metal-hydride tank depends

¹⁴ Nm³ is the typical dimension for a gas amount. It is a gas in a volume of 1 m³ at a pressure of 1 bar and a temperature of 0°C.

on the temperature, the alloy and the state of charge. For outdoor applications, it is important to be aware that the pressure in the metal-hydride tank at constant hydrogen load approximately doubles with an increase of 20 K in temperature.

The energy content of 1 Nm³ of hydrogen gas is approximately 3.5 kWh. Depending on the fuel cell system and power-converter efficiency, between 1 and 1.8 kWh of net energy can be drawn from 1 Nm³ of hydrogen gas.

A standard 200 bar pressure bottle contains 8.8 Nm³ of hydrogen gas. The cost for metal-hydride storage systems is currently in the range of 500 to 1500 € per Nm³.

For oxygen storage, currently only pressure tanks are commercially available. Materials with adsorption properties for oxygen are under investigation. A reduction in volume by a factor of 3 has been achieved.

Nanotubes for hydrogen storage are under investigation. After a very optimistic period some years ago, the optimism has been reduced, but meanwhile there are several activities to investigate this technology which promises very low costs.

18.5.2.3 Fuel cell

As fuel cells can only replace batteries in conjunction with the hydrogen gas generation, only the polymer electrolyte or proton exchange membrane fuel cell (PEMFC) is considered here. A very comprehensive overview of all the fuel cell technologies is given in [36].

The basic reactions are given in equations (18.17) and (18.18).

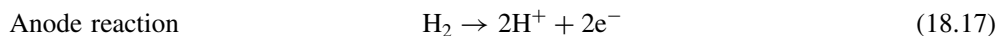


Figure 18.29 shows a schematic of a PEM fuel cell. If hydrogen and oxygen are stored, a closed-loop operation with water and gases can be realised. Then, the water demand for refilling is limited. If air is used instead of pure oxygen, the water produced in the fuel cell process gets lost with the air throughput. The water household of the membrane is one of the most challenging problems in fuel cell operation and control.

PEMFCs operate best at temperatures between 60 and 90°C. The fuel cell stack itself can operate at an efficiency of 50 to 60%. The overall fuel system has additional components beside the stack like air compressors, electronics, valves and security devices. They cause a self-consumption of the fuel cell system and therefore reduce the overall efficiency to 35 to 50%. The efficiency is higher if pure oxygen is used instead of air, but this requires an additional oxygen tank. The stack efficiency is calculated from the ratio of the fuel cell voltage during power generation and the electrochemical potential of the reactants, which is 1.23 V. The coulomb efficiency is considered as 100% even though some gas losses synonymous with coulomb losses due to the penetration of gas through the membrane occur as well.

A big advantage of fuel cells in comparison with motor generators are the high efficiency even at partial loads. Usually the stack efficiency increases with decreasing power output.

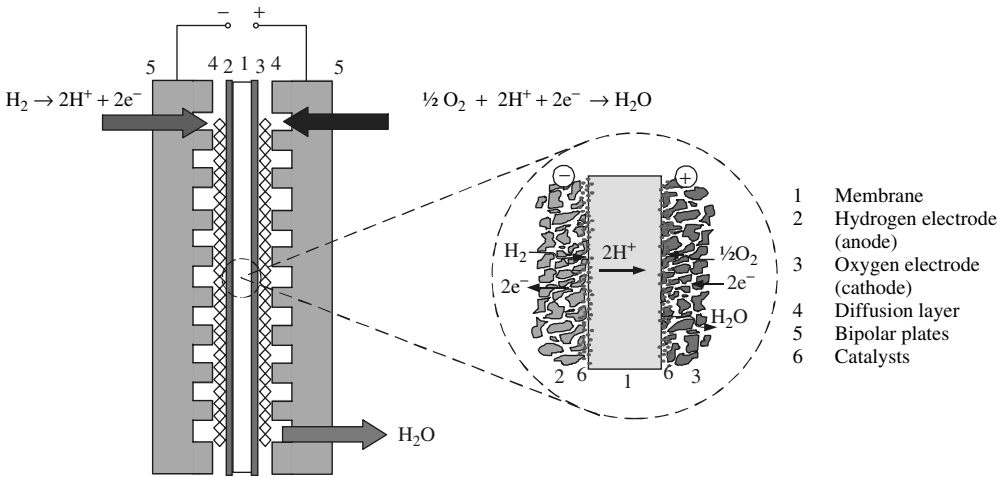


Figure 18.29 Schematic of a polymer electrolyte membrane fuel cell (PEMFC)

The current/voltage characteristic of a fuel cell is quite similar to the characteristic of a PV cell. Unlike secondary electrochemical batteries, the voltage depends very much on the current. To supply a load with a constant voltage, power electronics are necessary. The power electronics are also needed to adjust the point on the I/V curve corresponding to the actual power demand. Therefore, the operation of a fuel cell in applications with varying load demands without power electronics is impossible. Charging of a battery with a fuel cell is in principle possible. However, the fuel cell must not exceed certain current limits for a safe operation. Power electronics that limit current and voltage according to the requirements are highly recommended. Power electronics are necessary in any case if a controlled charge of a battery according to one of the charging regimes given in Figure 18.23 is necessary.

Presently, no cost figures for marketable fuel cells can be given as all available PEM fuel cells are prototypes for R&D and demonstration. However, there is a huge bunch of activities in fuel cell research. They are mainly driven by the automobile industry and by the combined heat and power generation CHP space-heating applications. The target figures for fuel cell systems in these applications are approximately 100 euro/kW for automobiles and 1000 euro/kW for CHP space-heating systems.

18.5.2.4 Applications

Hydrogen storage systems have a low overall efficiency. Even under the assumption of a fuel cell system efficiency of 50%, an electrolyser system efficiency of 85%, no energy losses for the hydrogen storage and efficiencies of 97% each for the two power-converting steps, an overall storage system efficiency of 40% maximum is achievable. Compared with approximately 90% efficiency in lead acid or lithium batteries, this is rather small and rules out the hydrogen system as the principle and only energy storage unit in autonomous power supply systems. This will be the fact as long as the power production is as expensive as it is now. Secondly, the specific storage costs per kilowatt

hour with the hydrogen system must come down to the values of today's lead acid batteries and thirdly, the technical reliability of the complex hydrogen system must be as high as with conventional batteries. The hydrogen storage system is far away from all these goals and these goals will be hardly achieved within the next decade.

One interesting line of development is the reversible fuel cell RFC. RFCs fulfil the functionality of the electrolyser and the fuel cell at the same time. As the process is completely reversible, this is an obvious solution. Technical problems concerning the catalysts and the gas and water management within the cell have to be solved [37]. No commercial products for field applications are available in this technology today.

Applications in autonomous power supply systems will have a combined storage system made from a conventional battery and the hydrogen system. Figure 18.30 shows a principle system design as it is currently under development within an R&D project [38]. The hydrogen system here substitutes the conventional motor generator, which is used today in hybrid systems to bridge the energy gap between summer and winter. A conventional lead acid battery (five days of autonomy) is assisted by the hydrogen storage systems. During summer, the energy excess from the PV generator is used to produce hydrogen in the electrolyser (oxygen is released to the atmosphere). The hydrogen is stored in a metal-hydride tank. During winter, in long periods with low energy supply

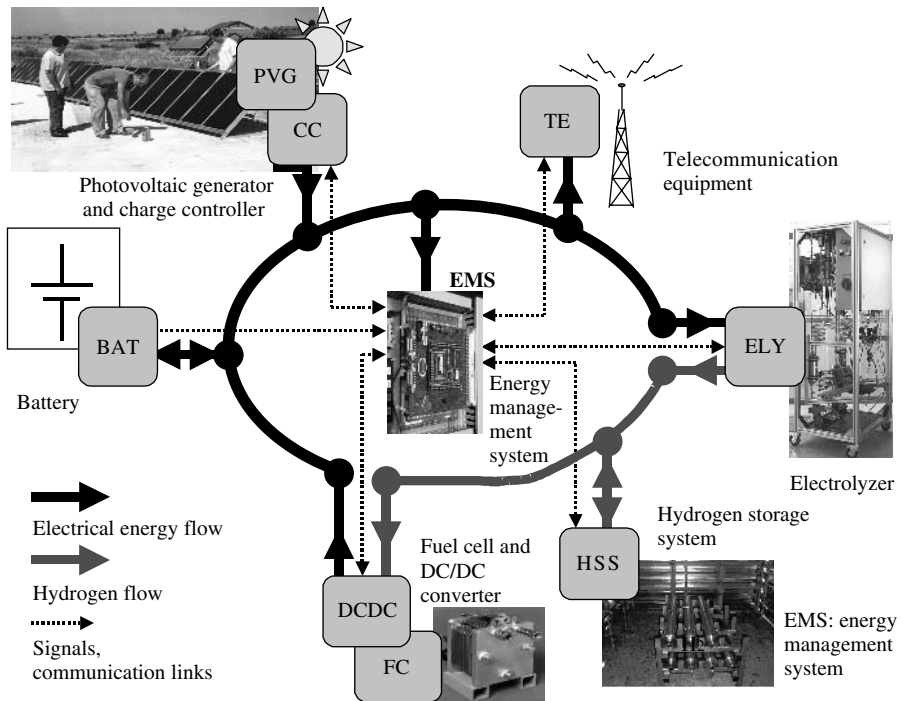


Figure 18.30 Example of an autonomous power supply system for telecommunication with a PV generator, a lead acid battery for short-term storage (five days of autonomy) and a hydrogen storage system for seasonal energy storage. The system and components have been developed by partners in the EC co-financed project FIRST [38]

from the PV generator the fuel cell takes the oxygen from the air and the hydrogen from the tank to produce electrical power.

This concept allows operating the system with very high reliability with respect to the power supply throughout the year without any conventional fuel. The shift of energy from the summer to the winter is beneficial, as, otherwise, in Central Europe a larger PV generator or motor generator would be required to fulfil the energy requirements during winter. Numerous other systems of this type for different applications have been developed and installed by R&D projects within the last decade (e.g. [39–41]).

18.6 INVESTMENT AND LIFETIME COST CONSIDERATIONS

While designing an autonomous power supply system, it is essential to face the lifetime costs rather than looking only into the initial investment costs. The battery has major impacts on the system design, system operation and overall costs.

- The battery causes a considerable part of the initial investment costs.
- The size of the battery influences significantly the solar fraction of the power supply system.
- Typically, more than two-thirds of the energy flow in an autonomous power supply system goes across the storage system. Therefore, the battery acts as an important consumer of electrical energy due to its efficiency of less than 100%.
- The battery voltage influences the selection of the electronic components or vice versa.
- The battery is subject to ageing. Ageing depends very much on the operating conditions of the battery. Operating conditions depend on system sizing and control strategy.
- The lifetime of the battery determines the running costs through the replacement investment.
- The battery needs regular maintenance.
- Depending on the type of the battery, the different requirements of the battery room have to be considered. The requirements are defined in the standards.

These facts are valid for all battery technologies. For the system design, the characteristics of the chosen battery technology must be taken into account. For the following considerations, only lead acid batteries are taken into account.

Investment costs for lead acid batteries depend very much on the technology and the quality of the battery. Typical costs for end users are in the range of 75 to 250 €/kWh. Lifetimes are – depending on the operation conditions – 3 to 8 years. Depending on the sizing of the system (days of autonomy) and the lifetime, the battery will be subjected to 100 to 1000 capacity throughputs. This results in electricity costs of 0.20 to 0.75 €/kWh dedicated to the storage unit. Additional costs occur for the peripherals, the charge controllers res. chargers and maintenance.

Lead acid batteries need maintenance once or twice a year to check the cell connectors, to measure all cell or block voltages to identify weak cells, to clean the tops of the batteries to avoid creeping currents between the poles, to refill water for flooded batteries

and to check the general state of the battery. The set points of the charge controllers or the battery management should be checked. For a 48 V battery system with single cells, 30 to 60 min for the maintenance are necessary.

Figure 18.31 gives an example of the cost share of the battery in a PV battery system. The system is designed to supply power with 100% reliability at a location in Mexico. The left-side graphs show a system that was designed to minimise the initial investment costs under the given boundary conditions. The right-side graphs show the results of a minimisation of the lifetime costs. The calculation includes the initial investment costs, maintenance, repair and replacement of the components, capital costs and other operating costs. It can be seen from the graphs that the lifetime costs are 288% or 248% of the costs for the initial investment. Sizing of the system with respect to lifetime costs resulted, in this example, in an overall cost reduction of 14%. It is interesting to see that this was achieved by approximately 20% higher investments in the PV generator. This allows on one hand a reduction of battery size by approximately 25% and on the other hand the larger PV generator allows a more frequent complete charging of the battery and therefore a lifetime extension. This altogether resulted in a cost reduction for the battery of more than 40% and – as mentioned above – for the overall system of 14%.

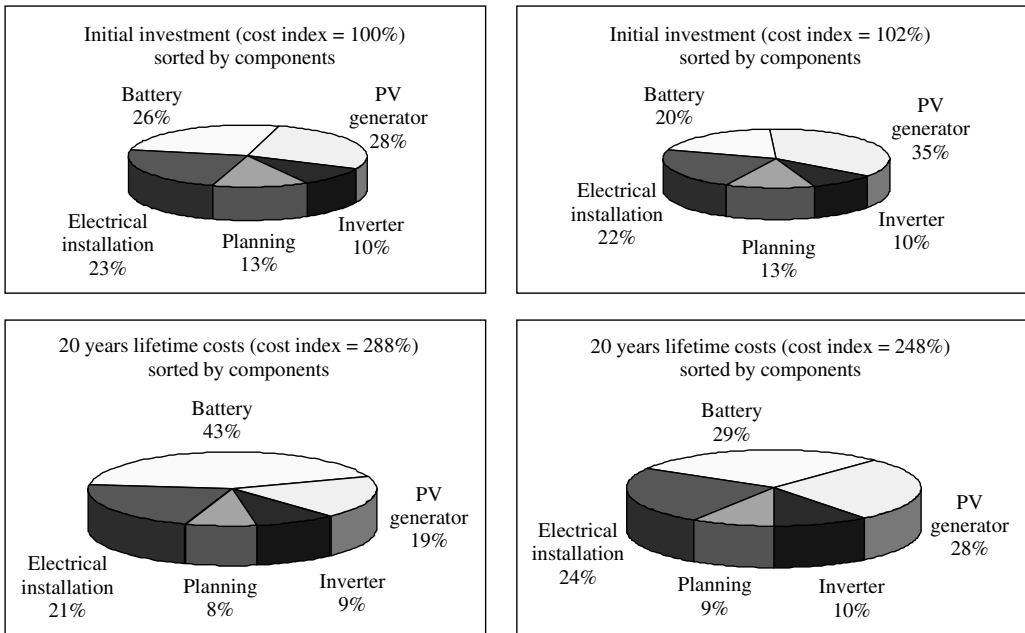


Figure 18.31 Comparison of costs for a PV battery system derived under different assumptions. Left-side graphs show the costs for the system optimised by initial investment costs, right-side graphs show the costs for a system optimised by lifetime costs. The overall costs for the initial investments (upper graphs) and the overall lifetime costs (lower graphs) calculated according to the annuity method are normalised to the initial investment costs for the system optimised by initial investment (cost index = 100%). Location, Mexico; annual power consumption, 1500 kWh; effective interest rate, 6%; lifetime of components: PV generator 20 years, electronic components 15 years, battery according to sizing and operating conditions, calculations and optimisation done with the simulation tool TALCO[42]

This example is just to illustrate the importance of an integrated system planning and design. Powerful tools are necessary and available [42]. The battery is the component with the highest cost share in autonomous power supply systems. Other than in photovoltaics, cost reductions on battery investment costs will be small within the next few years as lead acid batteries are already a commercial product today with a market of more than 10 billion euro per year in the different applications. Cost reductions can occur from improved lifetimes and optimised operation strategies. These figures also show that little tolerance for higher battery costs is given. This is important for the estimation of the market entry of other or new storage technologies. Higher specific costs per kilowatt hour of energy supply and significantly lower efficiency than that achieved today with lead acid batteries will hardly be accepted by a commercial market.

18.7 CONCLUSION

Even though there is a wide range of possible solutions for storage in autonomous power supply systems, the economic boundary conditions focus all solutions on lead acid batteries. This will not change significantly for some years. Their electrical properties are very good. Nevertheless, they have a bad reputation among system designers and operators, which is mainly due to the fact that batteries have a limited lifetime. Owing to their electrochemical nature, they have very complex operation and ageing patterns. Technically speaking, batteries have several time constants. Rapid levelling out of microcycles occurs in the millisecond range, diffusion processes in the seconds and minutes range, state of charge in the hour and day range and ageing effects in the day, month and year range. Batteries have a memory with regard to operation conditions. Faults in the operation can often hardly be repaired, but might show their negative impact much later. Further, currently no method exists that allows a determination of the state of health of the battery within minutes. Nevertheless, it is most likely that lead acid batteries will be the leading storage technologies in autonomous power supply systems for many years to come. This will be especially true if the still available improvements in the lead acid technology concerning lifetime in autonomous power supply systems can be realised.

Mainly lithium batteries have enormous growth rates in the portable market segment. Today, it is difficult to forecast the costs for larger units in terms of capacity for lithium batteries – actual forecasts expect costs in the range of 150 €/kWh and from the technical parameters the lithium batteries are most suited to autonomous power supply systems.

Double-layer capacitors will have their market in applications with very high power demands in the range of a few seconds or less and most probably in combination with an electrochemical battery.

In general, a battery is considered to be “used up” when it has less than 80% of the rated capacity guaranteed by the manufacturer. Nevertheless, this usually does not mean that the battery is completely non-functional. From field experience, it is well known that batteries can be used easily down to 50% of the rated capacity. However, the users must be aware that the days of autonomy are reduced according to the capacity loss and the power available from the battery is reduced due to ageing.

In hybrid systems, the solar fraction reduces with decreasing battery capacity. However, as ageing proceeds, the danger of the so-called “fatal defect” increases. This results in a more or less sudden breakdown of the battery, and can create considerable problems for the user. They are usually due to short circuits, caused by erosion sludge, corrosion flakes from the poles or dendrite growth between the electrodes. This risk should be considered when the decision is made about replacing a battery with clearly reduced capacity.

The operation strategy has a significant effect on the battery lifetime. It is necessary to take this into consideration when planning and designing an autonomous power supply system. Some additional investments in the battery peripherals will result in significant savings within the system lifetime. Frequent additional full charging and deep-discharge protection on the basis of a state-of-charge determination are highly recommended.

Hydrogen storage systems and redox batteries are options for the future, but the hydrogen storage systems have a fundamental drawback concerning the efficiency and the complexity of the system. Nevertheless, important impulses for their development will come from load-levelling applications in grids with a high penetration of renewable energy sources.

Further development on the conventional battery systems is necessary and will happen within the coming years. After almost one century (1880–1980) with no sustainable market entry of different fundamental battery technologies, we have seen within the last decade great achievements with nickel-metal hydride and lithium batteries, which were not expected. Further, improved battery technologies and a more integral system design and operation resulting in longer lifetimes will allow a decrease in the specific costs for electrical energy storage within the next decade by approximately a factor of two. Further cost reduction can hardly be seen from today’s point of view.

REFERENCES

1. Garcke J, Döring H, Harnisch P, *Workshop Fortschrittliche Back-up- und Speichersysteme für regenerative Energieversorgungsanlagen*, Forschungsverbund Sonnenenergie, 51–72 (Köln, 1996).
2. Linden D, *Handbook of Batteries*, 2nd Edition, McGraw-Hill, New York (1995).
3. Berndt D, *Maintenance-Free Batteries – A Handbook of Battery Technology*, John Wiley & Sons, Chichester, UK (1993).
4. Wagner R, Sauer D, *J. Power Sources* **95**, 141 (2001).
5. Sauer D *et al.*, “State of Charge – What do we Really Speak About?” *INTELEC '99*, Electronic proceedings of the conference, Copenhagen (1999).
6. Bopp G *et al.*, “Hybrid Photovoltaic-Diesel-Battery Systems for Remote Energy Supply”, *Proc. NORTH SUN '97* (Espoo, Finland, June 1997).
7. Sauer D *et al.*, *J. Power Sources* **64**, 197–201 (1997).
8. Bopp G *et al.*, *13th European Photovoltaic Solar Energy Conference*, Vol. 2, 1763–1769 (Nice, France, 1995).
9. Sauer D *et al.*, *14th European Photovoltaic Solar Energy Conference*, 1348–1353 (Barcelona, Spain, 1997).

10. Ruddell A *et al.*, *J. Power Sources* **112**, 531–546 (2002).
11. Reilly J, in Besenhard J, Ed, *Metal Hydrid Electrodes in Handbook of Battery Materials*, 209, Wiley-VCH, Weinheim, Germany (1999).
12. Schmidt H, Siedle C, Anton L, Tuphorn H, *Proc. 30th ISATA Conference*, 581–588 (Florence, 1997).
13. Anton L, Schmidt H, 5. Design & Elektronik Entwicklerforum, 103–116 München, Germany, (1998).
14. Maxell Europe GmbH, *Lithium Ion Rechargeable Batteries*, Product explanation.
15. Bode H, *Lead-Acid Batteries*, John Wiley & Sons, New York (1977).
16. Hollenkamp A, *J. Power Sources* **59**, 87–98 (1996).
17. Preiser K *et al.*, *14th European Photovoltaic Solar Energy Conference*, Vol. II, 1692–1695 (Barcelona, Spain, 1997).
18. Berndt D, *Blei-Akkumulatoren (Varta)*, VDI-Verlag, 11. Auflage, Düsseldorf (1986).
19. Sauer D, *J. Power Sources* **64**, 181–187 (1997).
20. Mattered F, Sauer D, Desmettre D, Rosa M, *Acid Stratification and Vertical Current Distribution: An Experimental and Theoretical Explanation of a Major Ageing Effect of Lead-Acid Batteries in PV Systems*, Extended Abstract for LABAT99, Sofia (1999).
21. McCarthy S, Kovach A, Wrixon G, “Operational Experience with Batteries in the 16 PV Pilot Plants”, *9th European Photovoltaic Solar Energy Conference*, 1142–1145 (Freiburg, Germany, 1989).
22. Döring H, Jossen A, Köstner D, Garche J, 10. *Symposium Photovoltaische Solarenergie*, 549–553 (Staffelstein, Germany, 1995).
23. Bohmann J, Hullmeine U, Voss E, Winsel A, *Active Material Structure Related to Cycle Life and Capacity*, Final Report, ILZRO Project LE-277 (1982).
24. Lander J, *J. Electrochem. Soc.* **103**, 1–8 (1965).
25. Garche J, *J. Power Sources* **53**, 85–92 (1995).
26. Piller S, Perrin M, Jossen A, “Methods for State-of-Charge Determination and their Applications”, *Int. Power Sources Symposium* (2001).
27. Kuhmann J, Paradzik T, Preiser K, Sauer D, 13. *Symposium Photovoltaische Solarenergie*, 97–101 Staffelstein (1998).
28. Bartolozzi M, *J. Power Sources* **27**, 219–234 (1989).
29. Garche J *et al.*, *Study on New Battery Systems and Double Layer Capacitors*, Internal study in German language for German project EDISON, Financed by BMWi, Compiled by Centre for Solar Energy and Hydrogen Research Baden Württemberg (ZSW), Ulm, Germany (2000).
30. Tokuda N *et al.*, *SEI Tech. Rev.* **45**, R22-1–R22-7 (1988).
31. Ryhd C, *J. Power Sources* **80**, 21–29 (1999).
32. Rzaeva M, Salamov O, Kerimov M, *Int. J. Hydrogen Energy* **26**, 195–201 (2001).
33. Pham A, “High Efficient Steam Electrolyzer”, *Proc. 2000 DOE Hydrogen Program Review*, NREL/CP-570-28890 (2000).
34. Menzi F, Wenske M, Lehmann J, XII. *WHEC Buenos Aires 1998 Proc.*, 757–765 (1998).
35. Heinzl A, Ledjeff K, in Kreysa G, Jüttner K, Eds, *Elektrochemische Energiegewinnung*, DECHEMA- Monographien, Vol. 128, 595–601, Verlag Chemie, Weinheim, Germany (1993).
36. Fuel Cell handbook, 5th Edition, Online version at <http://216.51.18.233/fchandbook.pdf>, Compiled for the U.S. Department of Energy by EG & G Services (2000).
37. Rau A, Heinzl A, *Reversible Electrolyse-/Brennstoffzellen-System zur Energiespeicherung*, *Tagung der Gesellschaft Deutscher Chemiker e.V.*, Fachgruppe Angewandte Elektrochemie, Ulm, Germany (2000).
38. Vegas A *et al.*, “The FIRST Project-Fuel Cell Innovative Remote Systems for Telecom”, *12th Annual U.S. Hydrogen Meeting* (Washington, DC, 2001).

39. Armbruster A *et al.*, *13th European Photovoltaic Solar Energy Conference*, 360–363 (Nizza, 1995).
40. Brinner A *et al.*, *Int. J. Hydrogen Energy* **17**, 187–198 (1992).
41. Barthels H *et al.*, *Int. J. Hydrogen Energy* **23**, 295–301 (1998).
42. Puls H, Sauer D, Bopp G, *Proc. 17th European Photovoltaic Solar Energy Conference and Exhibition*, 2673–2678 (Munich, Germany, 2001).

19

Power Conditioning for Photovoltaic Power Systems

Jürgen Schmid¹ and Heribert Schmidt²

¹*ISET, Universität Institut für Solare Energieversorgung technik e.V. Kassel,*

²*Fraunhofer Institut für Solare Energiesysteme, Freiburg*

In PV systems, power conditioning units are used to provide a match between the specific characteristics of the PV generator and the connected balance of system (BOS) components. Furthermore, they take over the control of other BOS components, for example, batteries or back-up generators.

In general, the characteristic curve of a PV generator varying with solar radiation and temperature does not match the characteristic curve of the load. In those cases, the power conditioning unit effects a transformation of the load's voltage and current in such a way, that the PV generator is operated at its optimum operation voltage V_{MPP} even under changing boundary conditions.

In the following chapter, the characteristics of the most common power conditioning units – charge controllers, DC/DC converters and inverters – are described.

In almost every stand-alone system, a charge controller is required to optimally operate the storage battery within safe limits as prescribed by the manufacturer.

The matching of PV generator and the load can be achieved by means of DC/DC converters which can be integral part of a charge controller, an inverter or a DC pump, but can also be a separate BOS component.

If in stand-alone systems the load requires an AC voltage, inverters are used to convert the DC power supplied by the PV generator or the storage battery into AC power. Inverters are mandatory in grid-connected PV systems. Here, besides high efficiency, reliability and power quality, safety is an important issue and has to be dealt with.

19.1 CHARGE CONTROLLERS AND MONITORING SYSTEMS FOR BATTERIES IN PV POWER SYSTEMS

In PV-powered systems, batteries are still the component with the lowest average lifetime. Compared to solar modules, which in principle have an infinite economic lifetime and in many cases offer a guarantee period of 25 years, the lifetime of batteries is much lower. The maximum lifetime found in practice is around 8 to 10 years; in most cases it is in the range of 3 to 6 years and in some cases even lower. The upper limit will be determined by normal ageing; the shorter lifetimes are mostly caused by inappropriate treatment or unsuitable control strategies. This topic is discussed in Chapter 18.

Looking at the battery cost in a typical PV diesel system, one can find that its share of the initial costs is around 15%. Because of repeated replacement of exhausted batteries, this initial share grows to more than 35% or even 50% over the expected 25-year service life of the system. Compared to this, the costs for solar modules and other balance-of-system components become small.

To achieve minimum lifetime costs and satisfying operation of the PV system, equipping the battery with appropriate peripherals is money well spent. Some examples, such as systems to automatically mix the electrolyte to prevent acid stratification or automatic water-topping systems, are explained in Chapter 18. Besides this, the application of appropriate operation modes is a crucial factor.

In this chapter, the technical realisation of the key component, the “charge controller”, will be described. Furthermore, a new system to operate long battery strings optimally will be introduced.

19.1.1 Charge Controllers

The fundamental task of a charge controller is to operate the battery within the safe limits defined with respect to overcharging and deep discharging by the battery manufacturer or by the operation mode.

Compared to conventional battery chargers powered by the public grid, the situation is much more complex in PV systems. Here, charging power and energy are limited and depend on the varying insolation and load demand. Well-known charging strategies such as constant-current–constant-voltage charging (CC/CV) or more complex charging strategies, cannot be applied one to one. For example, in PV systems the charging current varies according to the insolation. Nevertheless, the term used is “constant current charging”. Also, regular full charging of the battery – which is very important for a long service life – cannot be guaranteed.

Furthermore, very high energy efficiency is crucial for all balance-of-system components in PV systems. Most grid-powered battery chargers offer only unsatisfactory efficiency values.

In the following sections, the fundamental technical concepts of charge controllers [1, 2] as well as the associated control strategies will be explained. In addition, a list of criteria will be given that should be taken into account when developing or selecting charge controllers.

19.1.1.1 Self-regulating PV systems

In small systems, such as house-number illumination or power supplies for measurement systems, a charge controller can be avoided in special cases.

This is, for example, true for NiCd batteries, when the current provided by the PV module is lower than the continuous charging current accepted by the battery. Also, such “self-regulating” systems have been used in the past for systems in the 50-W range such as light buoys.

In these systems illustrated in Figure 19.1, only a series diode is needed to block reverse currents from flowing into the module at night. To prevent overcharging of the battery, specially tailored PV modules with, for example, 30 crystalline-silicon cells will be used for 12-V lead acid batteries. With this low number of cells, the operating point will move into the steeply sloping part of the module’s $I-V$ curve when the battery is fully charged.

To make this kind of system operate reliably, the load profile as well as the insolation and temperature at the place of operation must be known accurately. Because cheap and reliable charge controllers are available today in the market, such “self-regulating” systems should be avoided.

In all cases, deep-discharge protection according to Section 19.1.1.6 should be implemented.

19.1.1.2 Linear charge controllers

When PV applications commenced, the well-known principles of conventional linear charge controllers were adapted to photovoltaics. These principles do not take advantage of the special properties of solar cells, for example, that they are infinitely tolerant to short circuits. Therefore, the initial linear charge controllers have been replaced by the switching charge controllers described below.

Meanwhile, novel integrated voltage controllers have appeared in the market, which make the principle of linear charge controllers a reasonable option in the power range up to about 50 W like in Solar Home Systems (SHS).

In a linear charge controller, the charging current will be adjusted by a final controlling element that acts continuously and is located either in series or in parallel with

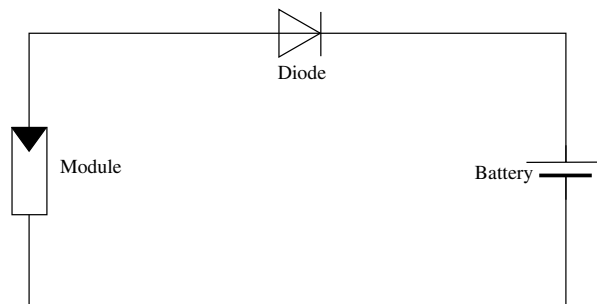


Figure 19.1 “Self-regulating” PV system without a charge controller

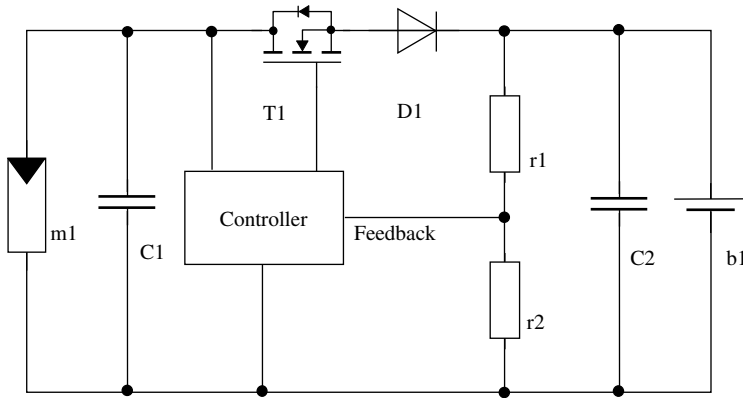


Figure 19.2 Linear charge controller based on the integrated voltage controller MIC 5158 (MICREL) labelled controller with an external power MOS-FET

the solar generator. By driving the controlling element appropriately, the battery voltage can be prevented from exceeding the end-of-charge limit.

Figure 19.2 shows the block circuit diagram of a linear series charge controller. In the constant-current (CC) phase, in which the battery voltage is below the end-of-charge voltage, the control element MOS-FET T1 is fully conducting. The solar generator and the battery are directly coupled via the blocking diode D1. The operating point of the solar generator is determined by the instantaneous insolation and the battery voltage. The power losses inside the control element are almost negligible in this phase. Additional power losses are caused by the voltage drop across the blocking diode D1, which in most cases will be a Schottky diode with a very low forward voltage drop. To minimise the power losses, the blocking diode can be replaced by a second MOS-FET connected back-to-back in series with T1. With such designs, care has to be taken that both MOS-FETs turn off during the night, and that no reverse current flows into the solar generator!

It is important to note that in most cases the energy gained by the reduction of power losses is not relevant for the function of the PV system. In fact, the goal is to reduce the voltage drop across the controller, which finally leads to a saving of one or two solar cells in the module.

As soon as the end-of-charge voltage has been reached, the gate voltage for the MOS-FET T1 will be reduced by the controller. Now, the output voltage is kept constant while the charging current will drop slowly according to the battery's increasing state of charge. In contrast to the first charging phase, now the difference between the solar generator voltage and the battery voltage will occur at the transistor terminals and cause some heat dissipation.

In Figure 19.3, the operating points for three different charging currents are shown as an example. The shaded areas are proportional to the power dissipated in the control element. As can be seen, this power is in the range between approximately one-fourth and one-tenth of the instantaneous maximum power point (MPP) power of the generator. The resulting heat must be dissipated by appropriate heat sinks. This is a clear disadvantage compared to the switching charge controllers described below. On the other hand, there are

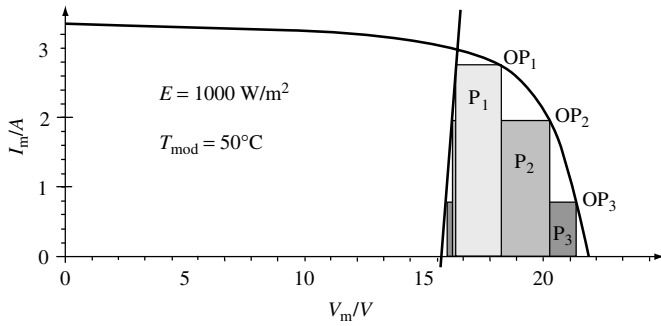


Figure 19.3 $I-V$ curve of a 36-cell PV module and characteristic curve of a 12-V lead acid battery with 3-m input lead (1.5 mm^2 cross-section) for three different charging currents. The shaded areas show the power dissipated in the control element

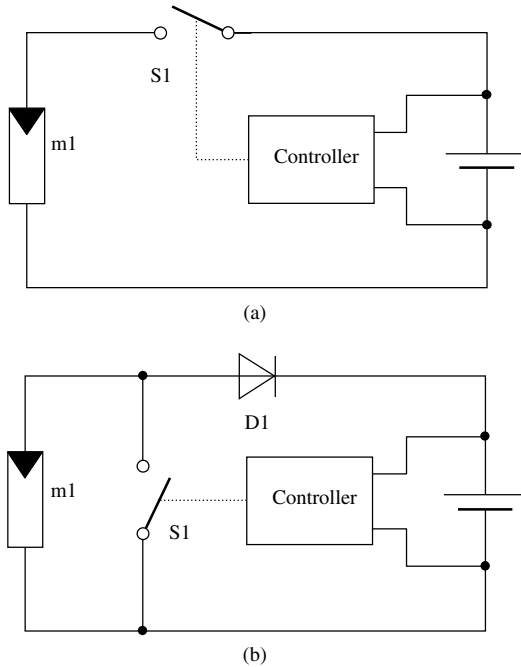


Figure 19.4 Principle of (a) series and (b) shunt controllers

no problems with electromagnetic compatibility (EMC), and the battery will be charged with a life-extending CC without micro-cycles.

19.1.1.3 Switching controllers

The above-mentioned disadvantage of intensive heat dissipation in linear charge controllers can be overcome with switching controllers. In these controllers, the control element is either fully closed (conducting) or fully open (blocking). Under ideal conditions,

the power losses are zero in both cases because either voltage or current at the control element is zero.

Once again, it must be pointed out that the additional energy gained in this way is normally not relevant for the functioning of the PV system. By contrast, the reduction of heat generation leads to savings in component costs (heat sinks) and to an increased reliability due to lower component temperatures.

In a series controller as shown in Figure 19.4(a), the charging current will be controlled by an element switched in series with the solar generator.

In early charge controllers, relays were used as switching elements, but today semiconductor switches like MOS-FETs are used in almost every application.

One advantage of the series controllers is that in addition to PV generators, they can be used for other power sources that are not being tolerant to short circuits such as wind turbines. Furthermore, the voltage stress for the switch is lower compared to the shunt controller described below. With a fully charged battery, the solar generator operates in the open-circuit mode. In this operation mode, no module overloading due to partial shading can occur. On the other hand, the solar generator current is fully turned on and off, which can lead to greater EMC problems compared to shunt controllers.

In the past, the series controller was accused of having fundamentally higher losses. This is no longer true since low-resistive semiconductor switching elements have been used – the losses can be even lower than for shunt controllers. Furthermore, some early series controllers did not start with completely flat batteries because they did not have enough energy to activate the series switch. This problem can easily be solved by powering the controller from the PV module instead of from the battery.

A parallel or shunt controller as shown in Figure 19.4(b) makes use of the electrical characteristic of PV modules that they are infinitely tolerant to short circuits.

In the constant-current charging phase, the module current flows through the blocking diode D1 into the battery. When the end-of-charge voltage has been reached, the PV generator is short-circuited by the switch S1. The blocking diode now prevents the reverse current flowing from the battery into the switch. Furthermore, it suppresses the discharging currents into the PV generator during the night.

In contrast to the series controller, this kind of charge controller will also reliably start charging with a fully discharged battery, because the switch can be energised only when the battery is fully charged.

The hybrid charge controller is a modified shunt controller, in which the blocking diode is bypassed by a second transistor in the charging phase. This reduces the power dissipation in the controller, which leads to smaller heat sinks and lower thermal stress. Furthermore, the reduction of the voltage drop supports the use of cost-optimised PV modules with a smaller number of series-connected cells, for example, 30 to 33 crystalline-silicon cells for 12-V systems.

Another variant of the shunt controller is the partial-shunting controller according to Figure 19.5. Here, only some of the series-connected modules are shunted via taps.

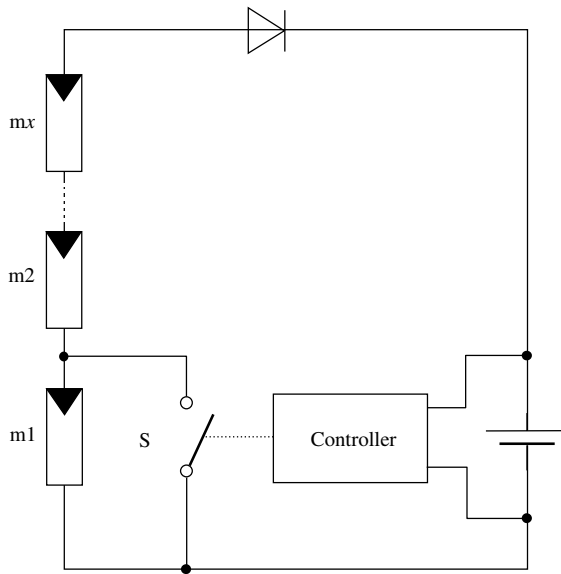


Figure 19.5 Partial-shunting controller for high-voltage systems

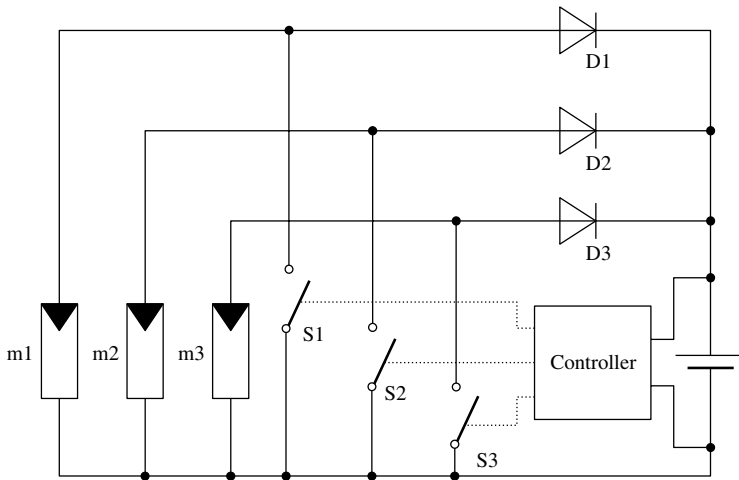


Figure 19.6 Sub-array switching controller for high-power systems

In consequence, the remaining generator voltage is too low to further charge the battery. The advantage of partial shunting is the reduced voltage stress for the switch in high-voltage systems. On the other hand, a tap and additional wiring are needed.

In high-power systems, sub-array switching according to Figure 19.6 is used for charge control. The PV generator is set up as a number of sub-arrays (strings), and each of these strings is connected to the battery via its own control element (e.g. blocking diode and switch).

Two different control strategies are used. The multiple switches can be driven in parallel, turning the full array current on and off in one step. A preferred strategy is to drive the switches in a certain sequence that allows stepwise adjustment of the charging current.

With all of the switching controllers described above, the designer or end user has to be aware that the solar generator is directly coupled with the battery and the load. If the battery connection is interrupted (maintenance work, lead breakage, blowing of the battery fuse etc.), the full open-circuit voltage of the PV generator can be applied to the load and may destroy it! To prevent damage, either the loads must be able to withstand the high voltage or the controller must be designed to avoid voltages higher than the rated output. This can be achieved, for example, by rapid over-voltage detection and load cut-off.

19.1.1.4 Control strategies

When the end-of-charge voltage is reached for the first time, the battery is not yet fully charged. The missing 5 to 10% of charge can be added to the battery by keeping it at the end-of-charge voltage level for a prolonged period. In this constant-voltage (CV) phase, the charging current will slowly decrease. How can such a charging regime be implemented by a series or shunt controller as described above, which can only switch all of the PV generator current on and off? Two techniques are used in practice to approximate the ideal CC/CV charging mode.

In a two-position controller, the charging current is dropped to zero by either opening the series switch or closing the shunt switch as soon as the end-of-charge voltage has been reached. As a result, the battery-terminal voltage decreases. The charging current is enabled again when the battery voltage drops below a threshold that is between 5 and 50 mV/cell lower than the end-of-charge voltage.

This sequence gets repeated periodically and the charging pulses become shorter and shorter, while the intervals in between become longer, as the battery's state of charge increases as shown in Figure 19.7. The average charging current decreases, while the terminal voltage is more or less constant. The period of the cycle described above is

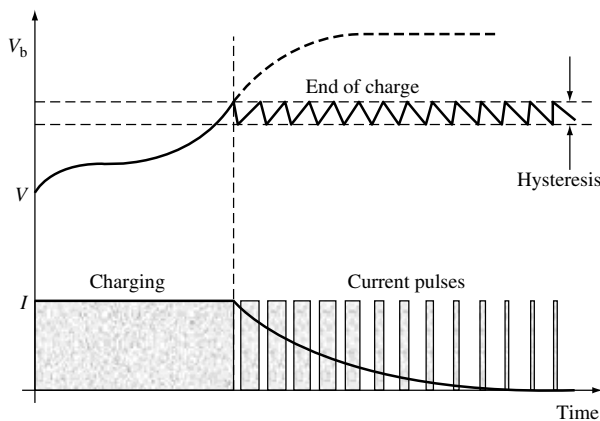


Figure 19.7 Battery voltage and current during charging

not constant and depends on the battery capacity, the state of charge, the charging or discharging current as well as the voltage hysteresis. It can vary from milliseconds to minutes. If mechanical relays are used as switching elements, the period should not be shorter than 1 to 5 min.

The second control regime found in practice is pulse-width modulation (PWM). In principle, it works like the two-step controller described above, but the switching frequency of the control element is fixed and determined by a clock generator. The typical frequency is about 100 Hz. In the CC phase, the switch is permanently closed and the full charging current flows into the battery. When approaching the end-of-charge voltage, the duty cycle (the ratio between the charging time and the cycle period) will be reduced towards zero by the pulse-width modulator. As mentioned above, the average charging current will drop and the battery voltage is kept constant.

One advantage of PWM controllers is that the switching frequency is known and constant. EMC problems can be solved more easily, and also monitoring of the average charging current becomes simpler.

19.1.1.5 Matching DC/DC converter, MPP trackers

Both the battery voltage and the PV generator voltage vary over a wide range during operation due to the changing state of charge and boundary conditions such as temperature and insolation. When directly coupled, this leads to a certain mismatch between the actual and the optimum operation voltage (MPP voltage) of the solar generator and therefore causes energy losses.

The mismatch can be overcome by introducing a matching DC/DC converter (MDC) that de-couples the characteristic curves of the PV generator and the battery. The power stage of these converters corresponds to the well-known topologies such as buck, boost or inverting converters. The control section is specially tailored to the PV conditions and consists of two control loops: one for the input and the other for the output. As long as the end-of-charge voltage has not been reached, the input voltage controller keeps the PV generator voltage at a constant level by appropriate adjustment of the DC/DC converter's switching regime (PWM). The voltage level can either be fixed (CV mode) or can track the actual MPP by an appropriate searching strategy (MPP tracking, MPPT). When the end-of-charge voltage is reached, the output voltage controller takes over and keeps the battery voltage at a constant level. The PV generator's operating point then shifts towards open-circuit conditions.

Numerous strategies and algorithms have been developed to find and track the MPP of a solar generator. They can be grouped into two categories:

- **Indirect MPP trackers**

This type of MPP tracker estimates the MPP voltage by means of simple assumptions and measurements.

Some examples from practice include the following:

- The operating voltage of the solar generator can be adjusted seasonally. Higher MPP voltages can be expected in winter due to lower cell temperatures and vice versa.
- The operating voltage can be adjusted according to the module temperature.

- The operating voltage can be derived from the instantaneous open-circuit voltage by multiplication with a constant factor, for example, 0.8 for crystalline silicon solar cells. The open-circuit voltage is measured periodically (e.g. every two seconds) by disconnecting the load for one millisecond.

The advantage of the above-mentioned procedures is simplicity, but they only give an estimate of the optimum operating point. They are not able to adapt to changing solar generator characteristics due to ageing or soiling.

- **Direct MPP trackers**

In these systems, the optimum operating voltage is derived from measured currents, voltages or the power of the PV generator. Therefore, they are able to react to changes in the generator's performance.

Some examples include the following:

- Periodic scanning of a part of the $I-V$ curve. Here, the operating voltage of the module is varied within a given voltage window by means of the DC/DC converter. The maximum module power is determined and then the operating voltage is adjusted to the corresponding voltage level. In practice, it is much easier to measure the output current of the DC/DC converter and to maximise it. This leads to the same result as above.
- “Mountain-climb algorithm”. Here, the operating voltage is periodically changed in small steps. The increment can either be constant or can be adapted to the instantaneous operating point as shown in Figure 19.8. If the module's power (and therefore the charging current) increases from one step to the next, the search direction is retained; otherwise it is reversed. In this way, the MPP is found and the operating point oscillates around the actual MPP.

The above-mentioned losses due to mismatch are mostly overestimated. Particularly, if the components are chosen properly (e.g. modules with 30 to 33 cells for 12-V systems), the energy losses are on the order of a few percent when using direct coupling

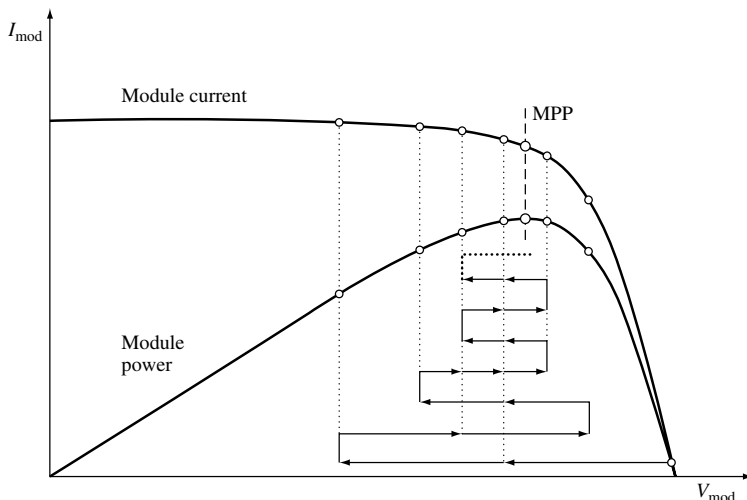


Figure 19.8 Working principle of the “Mountain-climb” MPP-tracking algorithm

instead of ideal matching! Besides this fact, it should be considered whether the additional energy gained by optimum matching is relevant to the function of the system at all. For example, the battery in a typical Solar Home System will be fully charged before noon and the excess solar energy will be dissipated.

In general, caution is indicated if the inventors or the manufacturers claim a tremendous energy gain by the use of MPP trackers!

Nevertheless, there are three advantages in using charge controllers with matching DC/DC converters:

- In the case of long wires from the PV generator to the battery, the generator voltage can be chosen much higher than the battery voltage, resulting in lower currents and therefore lower wiring losses.
- In small applications, the PV module can consist of only a few, large cells instead of numerous small cells connected in series. This reduces production costs, the impact of cell mismatch and the sensitivity to partial shading.
- More complex charging-current profiles can be realised by means of a DC/DC converter.

19.1.1.6 Deep-discharge protection

To achieve a maximum service life, deep discharging of batteries as well as prolonged periods with a low state of charge should be avoided. Therefore, the load has to be disconnected automatically from the battery as soon as the state of charge falls below a certain level. The load should be reconnected to the battery only when a sufficient state of charge has been reached.

Different criteria for detecting the deep-discharge condition have been explained in Chapter 18. In commercial products, the battery voltage will be used as a criterion for load disconnection. As soon as the battery voltage drops below a determined level, the load will be disconnected via a (bi-polar) relay or a semiconductor switch. Also, a control signal can be output to shut down balance-of-system components like inverters.

More complex charge controllers are able to generate a warning signal when the deep-discharge condition is being approached. Also, different loads can be disconnected according to a given priority. Charge controllers including an energy-management systems (EMS) are used to start back-up generators such as diesel or gas generators, depending on the battery's instantaneous state of charge. Additional parameters like load demand, weather conditions and so on can be considered.

There should be an appropriate delay time $t_{d \text{ off}}$ of 10 to 60 s between the undershooting of the end-of-discharge level and the actual disconnection of the load as shown in Figure 19.9. This ensures that undesirable disconnection of loads with large starting currents, for example, motors, refrigerators, washing machines and so on can be avoided. As the end-of-discharge voltage threshold depends on the instantaneous battery current, some advanced charge controllers offer a current-dependent adaptation of the disconnect threshold.

The ideal solution would be deep-discharge protection based on the actual state of charge of the battery. As systems or algorithms for accurately measuring the state of charge

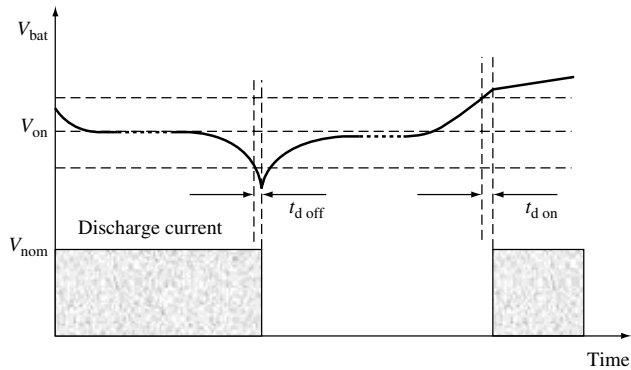


Figure 19.9 Changes in the battery voltage and load current during discharge

under the complex boundary conditions in PV systems are still under development, this type of controller is not yet in the market. For safety reasons, deep-discharge protection systems based on algorithms should be combined with a redundant control system based on simple voltage thresholds as described above!

The voltage threshold for reconnection of the load must be adjusted properly. If it is too low, the battery's open-circuit voltage will overshoot the threshold and the load will be reconnected periodically. In spite of the protection system, the battery will be deeply discharged and damaged. A time delay $t_{d\ on}$ as described above is also appropriate for guaranteeing a minimum state of charge before load reconnection.

In contrast to the end-of-charge threshold, the end-of-discharge threshold should not be temperature-compensated.

19.1.1.7 Monitoring systems and interfaces

Successful functioning of most PV systems strongly depends on the co-operation of the user. Reliable and meaningful information to the user about the current status of the system – the battery in particular – is therefore crucial. It would be ideal to have a “fuel gauge” that enables the system operator to plan the future energy demand. Such systems to monitor the state of charge have been discussed in Chapter 18.

As a minimum, the charge controller should be equipped with a display, for example, a light-emitting diode (LED) that indicates the conditions “Battery can be further discharged (green)” and “Battery is fully discharged (red)”. Other conditions like “Battery close to end-of-discharge” can be helpful. Furthermore, an experienced operator can draw a lot of information from a meter showing the battery's voltage and current as shown in Figure 19.10.

All user interfaces should be ergonomic and provide only that information really required by the operator.

Energy-management systems are equipped with (potential free) inputs and outputs to communicate with external components, for example, to remotely start a diesel generator. In addition, standard interfaces such as RS 232, RS 485 or CAN-Bus can be integrated

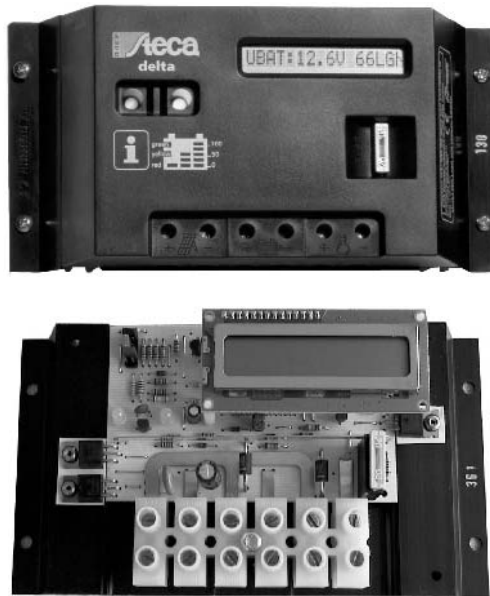


Figure 19.10 Charge controller with integrated voltage and current meter (Courtesy: STECA Solarelektronik, Germany)

to parameterise the controller, to read out the status of the system or to download operation data from the built-in data logger. Another feature is to communicate with external balance-of-system components via power line transmission.

In Solar Home Systems, the charge controller can act as an energy meter or can be used to automatically debit energy costs from a pre-paid card.

19.1.1.8 Design criteria and appraisal factors for charge controllers

The following summary of requirements is intended to support a designer or a purchaser of a charge controller. Which of these requirements must be met has to be decided specifically for each individual application.

The values of voltage thresholds and so on are related to lead acid batteries.

1. Charging phase.

- The end-of-charge voltage threshold should be adjustable according to the battery in use (2.3–2.5 V/cell at 25°C). To prevent extreme misadjustment, the setting range should not extend beyond these limits.
- The end-of-charge voltage can automatically be adapted to the system voltage (e.g. 12 V or 24 V).
- If the battery temperature is expected to deviate more than $\pm 10^{\circ}\text{C}$ from the average temperature under operation, the end-of-charge voltage should have a temperature compensation (approximately -4 to -6 mV/K per cell). If the temperature deviation is smaller, temperature compensation is not mandatory and the threshold should be set

according to the average battery temperature. Fail-safe behaviour is crucial in case of a temperature-monitoring malfunction, for example, due to broken sensor wires.

- The thresholds must be stable over temperature and time.
- If relays are used as control elements, the minimum switching period should be 1 to 5 min.
- The charge controller should be able to charge totally flat batteries. As a minimum requirement, charging should start from a cell voltage of 1.5 V.
- The battery voltage can be monitored by separate sensor wires. This is recommended if the battery wiring is long and of low cross-section. Fail-safe behaviour is crucial in case of broken sensor wires.
- The charge controller should be able to automatically perform gassing charging or equilibration charging according to the manufacturer's recommendations.
- It must be possible to prevent gassing charging in case of valve-regulated batteries (Gel- or AGM-VRLA batteries).
- The output voltage must be limited to safe values in the case of system operation without a battery, for example, due to unintended disconnection of the battery, wire breakage or blowing of the battery's fuse.

2. Deep-discharge protection.

- Deep-discharge protection is mandatory for a long service life. Only when the function of the system is more important than the battery life (e.g. in SOS telephones), deep-discharge protection can be omitted.
- The threshold voltages should be adjustable in a range of 1.5 to 2.0 V/cell. The adjustment range should not extend beyond this range to prevent extremely incorrect settings.
- The threshold should not be temperature-compensated.
- The threshold must be stable over temperature and time.
- The threshold can automatically adapt to the instantaneous battery current.
- The threshold can be based on the battery's actual state of charge.
- A time delay of 10 to 60 s should be implemented between undershooting of the threshold and the actual load disconnection.
- A warning signal can be given out when the deep-discharge condition is approached, for example, switch on a yellow LED 30 min before load disconnection at full load.
- Load disconnection can be performed according to load priorities.
- After load disconnection, only minimum current ($<I_{10,000}$) should be drawn from the battery. This can be achieved by appropriate design, for example, displaying of the current system status only on demand.
- The threshold for load reconnection should be relatively high, for example, >2.1 V/cell.
- A time delay of 10 to 60 s should be implemented between overshooting of the reconnection voltage threshold and the actual reconnection of the load.

3. Efficiency.

- The parasitic consumption of the charge controller should be less than 0.2% of the PV generator's power, for example, <8 mA in a 12-V/50-W controller.

- The voltage drop measured between the PV input terminal and the battery terminal should be less than 4% at full charging current, for example, approximately 0.5 V in a 12-V system.
- The voltage drop measured between the battery terminal and the load terminal should be less than 4% at full load current, for example, approximately 0.5 V in a 12-V system.
- The above-mentioned figures lead to an efficiency of >96% under rated charging as well as discharging conditions.

4. *Safety aspects and compliance to codes.*

- The charge controller must be protected against the reverse polarity of the input voltage and the battery voltage, for example, by a combination of fuses and diodes. Also, interchange of the inputs and outputs must not lead to damage.
- The charge controller must permanently withstand the maximum possible open-circuit voltage of the PV generator. This occurs at maximum insolation and minimum module temperature.
- Inputs and outputs must be protected against transient over-voltages by appropriate voltage arresters, for example, varistors.
- The charge controller must be designed according to the ambient temperatures at the usage site.
- The housing for the charge controller must withstand the environmental stress at the usage site, for example, protection level IP 00 inside a control cabinet, or IP 65 for outdoor applications.
- The electronic components should be protected by lacquer or encapsulation.
- The terminals should be generously dimensioned and robust. Cage clamps are a preferred solution.
- The charge controller must comply with relevant codes concerning electric safety and electromagnetic compatibility (EMC). It must have a Communautés Européennes (CE) label.

19.1.2 Charge Equaliser for Long Battery Strings

19.1.2.1 Introduction

All electrochemical storage systems react sensitively to operating states that do not conform to their specifications, such as overcharging, deep discharge or reversed polarity. The general observations are that the lifetime is shortened, the storage capacity and the efficiency are diminished and more maintenance is required. Further, detrimental conditions can arise with some batteries, for example, lithium-ion batteries, which lead to destruction or even explosion.

Thus, the manufacturers specify the allowable charging and discharging voltages, currents and also temperatures very precisely for individual cells – for the voltages, tolerances on the order of 1% are no exception.

However, on proceeding from the individual cell to series connection of several cells or groups of cells, which are usually needed, a well-known phenomenon is observed: in all applications, from laptops through PV systems and electric vehicles to

un-interruptible power supplies and grid back-up systems, each individual cell in the series connection behaves differently. This individualisation results from differences in cell capacity, self-discharge rate, charging factor and so on. They are determined by production conditions, ageing and temperature and cannot be avoided on principle.

Conventional charge controllers are not able to recognise this variation in the behaviour of the cells, so that the undesirable operating conditions listed above arise. In practice, it is evident that the “weakest link in the chain” determines the quality of the whole string, and that the deviating performance of a single cell can lead to a chain reaction.

The problem of increasing divergence in individual cell properties within a battery has been known since the beginning of battery technology, so that over the years a number of different procedures to solve the problem have been developed. Most of them are based on the dissipation of the surplus energy of fully charged cells in a bypass element. This approach is not suitable for applications in which highest efficiency is crucial, such as PV systems. Furthermore, it is effective only with a fully charged battery – it has no impact when the battery is being discharged.

On the basis of experience with numerous PV systems, active, non-dissipative charge-equalising systems have been developed. In contrast to conventional dissipative systems, here the surplus energy from cells having a higher state of charge is redistributed among the remaining cells. As indicated in Figure 19.11, this redistribution occurs not only during or at the end of charging but also constantly during discharging.

As a result, cells with a lower capacity are supported by the other cells during discharge. Their relative state of charge decreases evenly with that of the cells with higher capacity. In this way, the entire available capacity of all cells can be used. During charging, some of the charging current is redistributed from weaker cells to stronger ones, so that these are charged with a higher current, resulting in faster charging.

The energy redistribution also allows cells with larger capacity tolerances to be connected together in series. Costly selection of matched cells during battery construction can thus be avoided. In extreme cases, it is even possible to sustain operation with a mixture of new cells and old cells after the replacement of defective cells. Additionally,

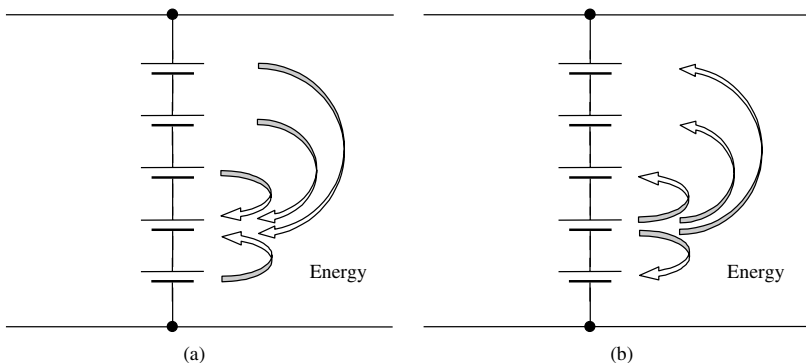


Figure 19.11 (a) Support for a weak cell during discharge by redistribution of energy from stronger cells. (b) Protection against overcharging

it has been shown that the energy efficiency can increase as overcharging or reverse charging is prevented.

19.1.2.2 The T-CHEQ principle

Several different procedures for active charge equalisation were developed and publicised under the name “CHarge EQualizer” (CHEQ) [1].

The “T-CHEQ” principle is based on a multiple-gate forward converter as shown in Figure 19.12. It can be used over a wide power range, but is particularly suited to higher power values. Here, the cells are coupled magnetically via coils, which are wound around a common core. The coils are periodically connected to the single cells with alternating polarity via semiconductor switches. As the same voltage is induced in all the coils due to the tight coupling, an equalising current automatically flows into or out of the cells if there is any deviation from the average cell voltage. It is advantageous that all cells can be treated simultaneously. Furthermore, this device can be extended to a battery charger by feeding energy into an additional coil wound around the core.

19.1.2.3 Operating experience

The working principle of active charge equalisation has been proven in numerous laboratory tests and pilot installations.

A typical charging cycle from a long-term test with a T-CHEQ system is shown in Figure 19.13. The battery was charged according to a CC/CV charging profile with a

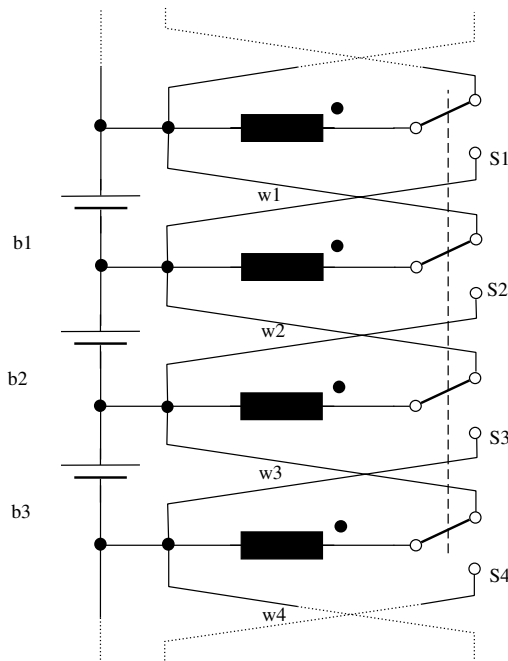


Figure 19.12 CHarge EQualizer with transformer coupling (T-CHEQ)

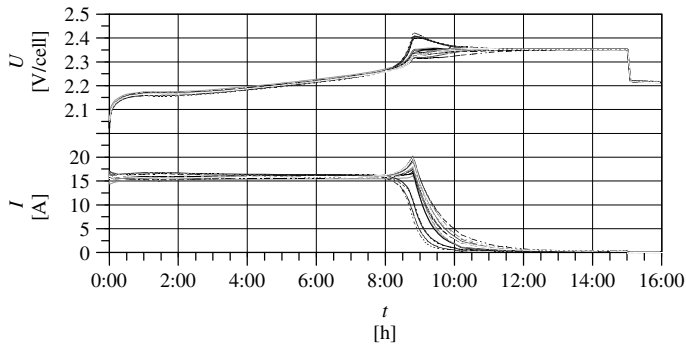


Figure 19.13 Voltages and currents of 16 series-connected cells during charging with an activated T-CHEQ

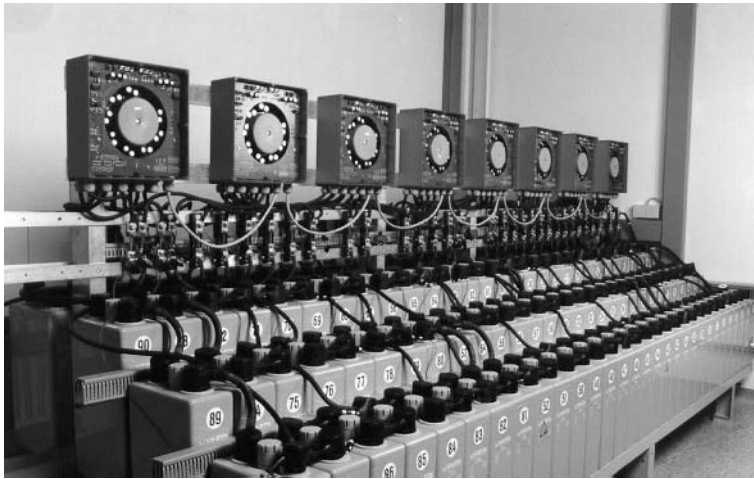


Figure 19.14 Experimental set-up with a 342-V/200-Ah sealed lead acid battery with eight cascaded T-CHEQs

charging current of 16 A and an end-of-charge voltage of 2.35 V/cell. The upper curves in Figure 19.13 show the 16 individual cell voltages and the lower curves show the corresponding cell currents. The cells with a lower capacity are the first to be fully charged – their voltage increases above the average voltage. As a result, the T-CHEQ draws some of the charging current from these cells and directs it to the cells with a lower state of charge. After 9 h, some cells are effectively charged only with 5 to 10 A, whereas the charging current for others is around 20 A. At the end of the charging phase, the T-CHEQ achieves a convergence of all the cell voltages and all the cells are fully charged.

Investigations of a 342-V/200-Ah sealed lead acid battery (VRLA, Gel-type) with eight cascaded T-CHEQs (Figure 19.14) show that such high system voltages can be operated without any difficulties. This type of battery is very sensitive to overcharging due to its demobilised electrolyte.

19.2 INVERTERS

19.2.1 General Characteristics of PV Inverters

Since the production cost of PV electricity is several times more expensive than conventional electric energy, conversion efficiency becomes predominant to the economics of the total PV system. As a consequence extremely high efficiency not only in the nominal power range but also under a part-load condition is a requirement for PV inverters in grid-connected as well as in stand-alone systems. Since some characteristics of both types of applications are different, they will be highlighted separately in the following chapter.

19.2.2 Inverters for Grid-connected Systems

This configuration consists mainly of the following components: the PV generator, the inverter, the safety devices and, in many cases, the electric meter as shown in Figure 19.15.

The actual power fed into the grid can be estimated by multiplying the actual power of the PV generator with the actual efficiency of the inverter if we neglect the losses in the safety device and in the meter. More important is the energy produced by the system after a certain period of time, for example, after one year of operation. In this case the mean efficiency of the inverter taking into account all load conditions throughout the year becomes important. As a first step the inverter must allow the PV generator to operate in the MPP by adjusting the corresponding operation voltage as shown in Figure 19.16.

Many inverters adjust this operation voltage continuously to the actual MPP. This operation is called maximum power point tracking (MPPT). The method most commonly used to perform the MPPT is to change the actual input voltage in such a way that maximum power is obtained (Figure 19.8). The effect of continuous MPPT is often over-estimated. Simulation has shown that for grid-connected PV systems, CV operation leads only to losses between 1 and 2% when properly adjusted [1, 2].

For optimum use of the PV energy, MPPT and CV operation can be seen as equivalent. As a matter of their operation principle, single-phase inverters, which are most common in small-scale PV systems ($P \leq 5 \text{ kW}_P$), lead to deviations from the MPP due to DC ripple, which is explained as follows: when injecting AC power into the grid, the feed-in current should be in phase with the grid's voltage, which means that the power factor equals one as shown in Figure 19.17.

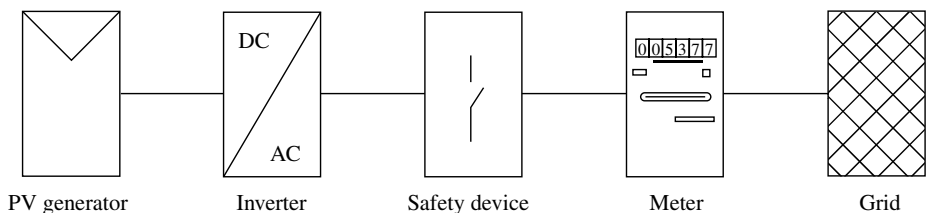


Figure 19.15 General structure of a grid-connected PV system

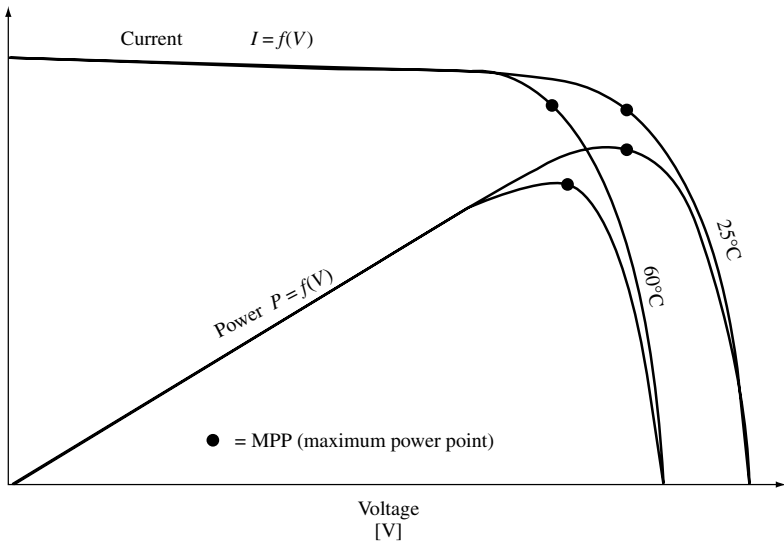


Figure 19.16 Maximum power point (MPP) for different module temperatures

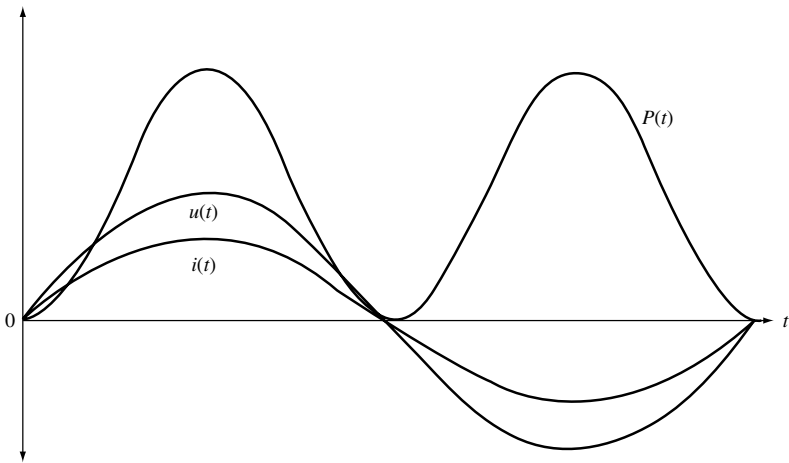


Figure 19.17 Pulsewise injection of power into single-phase grids needs energy storage

As a consequence, the actual power injected into the grid becomes

$$\begin{aligned}
 P(t) &= u(t) \cdot i(t) \\
 &= u_o \cdot \sin(\omega t) \cdot i_o \cdot \sin(\omega t) \\
 &= u_o \cdot i_o \cdot \sin^2(\omega t) \\
 &= ui[1 + \sin(2\omega t)]
 \end{aligned}$$

These power pulses with a frequency of 100 Hz are also shown in Figure 19.17. Since the PV generator provides continuous and quasi-constant power and since power injection

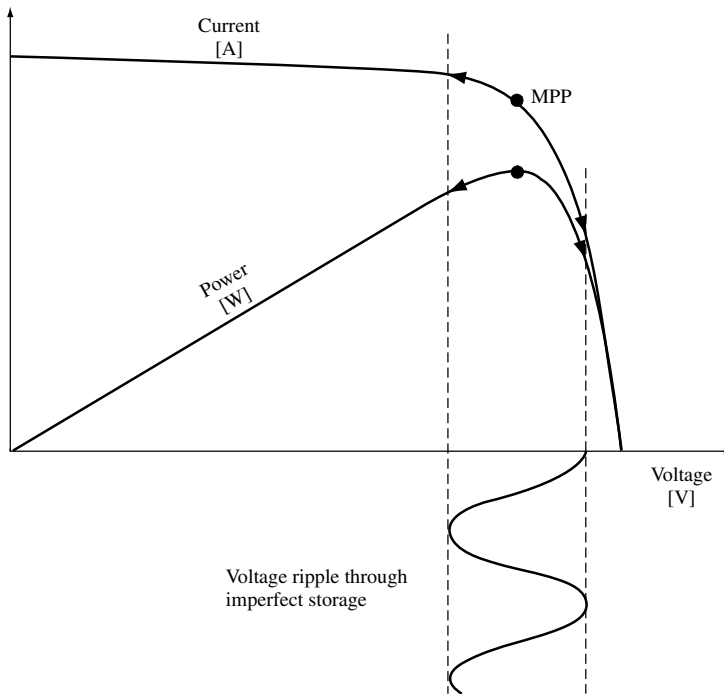


Figure 19.18 Deviations from the MPP through DC voltage ripple caused by the working principle of single-phase inverters

into the grid is pulsewise, each single-phase inverter needs a storage element that can be realised either using a capacitor or an inductor [3]. Since for economic reasons these storage elements must be limited, a voltage ripple can be found with all single-phase inverters at the DC side. This ripple forces the PV generator to deviate from the MPP as shown in Figure 19.18.

Well-designed single-phase inverters show DC voltage ripple with a negligible influence on MPP deviations. It should be noted at this point that three-phase inverters inject a continuous power into the grid, which eliminates the need for this kind of storage.

19.2.3 Inverters for Stand-alone Operation

Typical inverters for this type are often supplied by batteries. They have to provide constant voltage and frequency to the loads irrespective of the actual load profile. In case of reactive loads they have to provide and to absorb reactive power.

In hybrid PV systems, they should be able to operate in a bi-directional mode. This means that they should be able to recharge the battery in case of surplus power at the AC side.

Basically, both inverter types for a grid-connected and stand-alone operation have very similar hardware elements with respect to power electronics. Differences are found in inverter control.

19.2.4 Inverter Principles

19.2.4.1 General aspects

Basically, inverters convert direct current (DC) into alternating current (AC) by inversion of the DC polarity in the rhythm of the desired AC frequency (Figure 19.19). The symbol used to describe an inverter is shown in Figure 19.20.

19.2.4.2 Square-wave-type inverters

A simple version of such an inverter is shown in Figure 19.21.

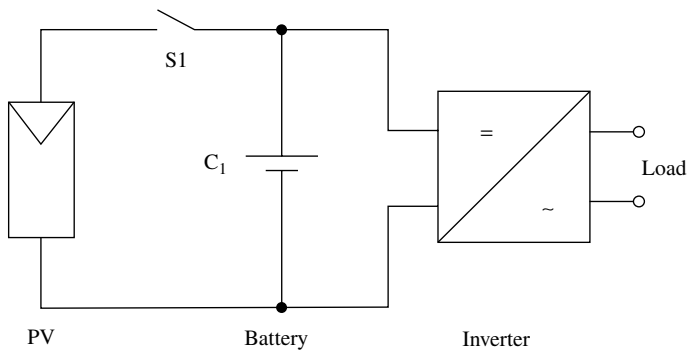


Figure 19.19 Typical configuration for stand-alone AC power supply systems

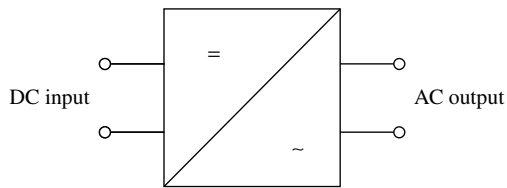


Figure 19.20 Symbol used to describe inverters

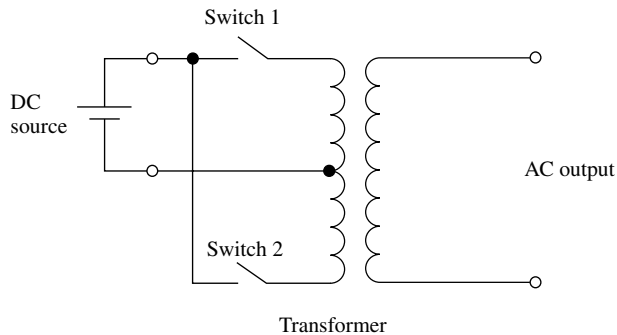


Figure 19.21 Layout of a simple inverter with square-wave AC output

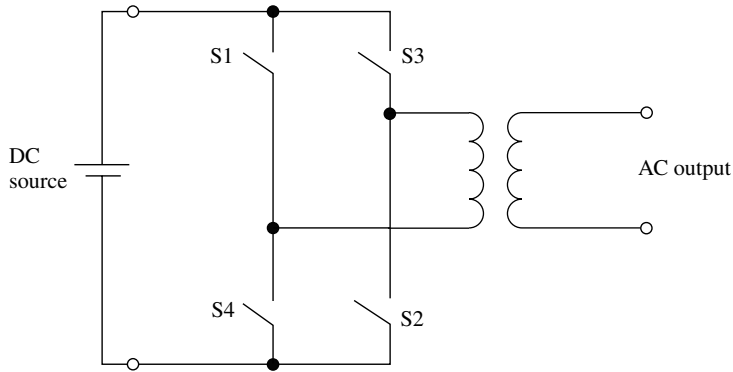


Figure 19.22 H-bridge-type inverter

AC at the primary windings of the transformer is produced by alternatively closing the switches 1 and 2. If switch 1 is closed, switch 2 is open and vice versa. The resulting AC output voltage is of the square-wave type, which may be used for resistive-type loads such as incandescent light bulbs and so on. The two primary windings of the transformer can be reduced to one if two more switches are used as shown in Figure 19.22.

In this configuration, the switches are opened and closed pairwise in such a way that the groups S1 and S2 and the groups S3 and S4 open and close alternately. At the output of the H-bridge formed by the switches S1 through S4, AC is already available. The transformer is only necessary in case of a voltage transformation.

19.2.4.3 Inverters with sinusoidal AC output

Since many consumers and the public grid operate on the basis of sinusoidal voltage, high-quality inverters should also be able to provide this type of AC output. This voltage form can be produced by voltage-transformation principles. Two of the most common transformation principles, namely, the step-down and the step-up converter and a combination of both will be highlighted as well as a digital synthesis one.

19.2.4.3.1 Step-down converter (Buck converter)

With the help of these converters, the input DC voltage, which is, for example, generated by the PV generator (V_{PV}) as represented in Figure 19.23, can be stepped down.

If the switch S_1 is turned on at t_0 , the diode D is reverse-biased and a circuit current arises (Figure 19.24). The current ($= i_L$) does not increase immediately but rather rises with a rate imposed by the inductor L:

$$\frac{di_L}{dt} = \frac{V_{PV} - V_{load}}{L}$$

Meanwhile, the inductor stores energy in a magnetic form. If S_1 is turned off after $t = t_1$, the load is separated from the supplied system. The current is, however, maintained by the stored energy in the inductor L and flows through the freewheeling

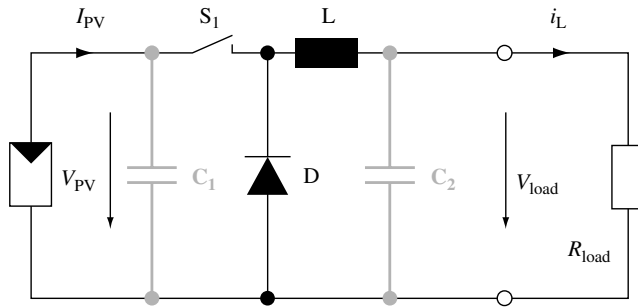


Figure 19.23 Equivalent circuit diagram of a step-down converter

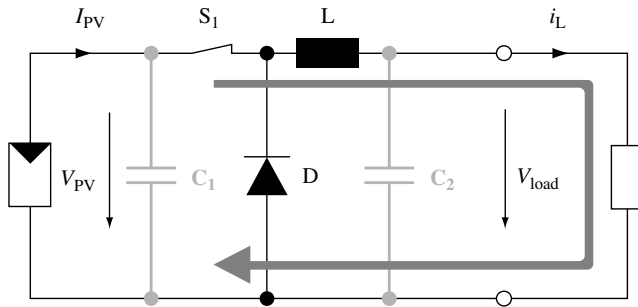


Figure 19.24 Step-down converter during “on” state

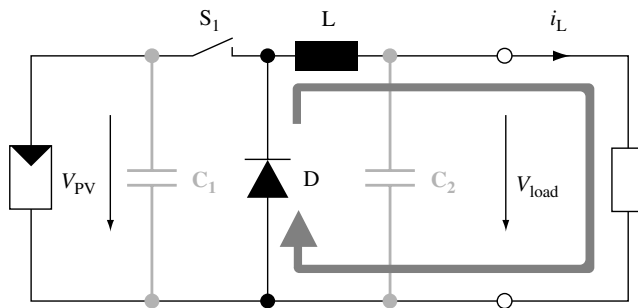


Figure 19.25 Step-down converter during “off” state

diode instead (Figure 19.25). Neglecting the voltage drop across the diode, the current falls down, however, due to the following equation:

$$\frac{di_L}{dt} = -\frac{V_{load}}{L}$$

The capacitor C_1 is used to support the supply voltage (V_{PV}). In principle, S_1 is turned on and off with a switching frequency (i.e. with “ t_{on} ” and “ t_{off} ”). With regard to Ohm’s law, the behaviour of the load voltage can be obtained from the load current ($= i_L$).

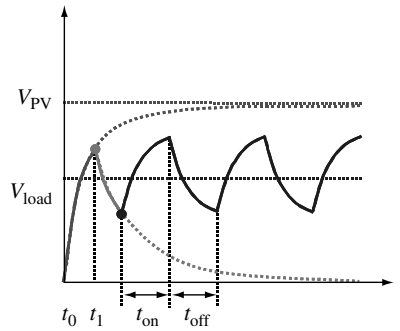


Figure 19.26 Behaviour of the load voltage of a step-down converter

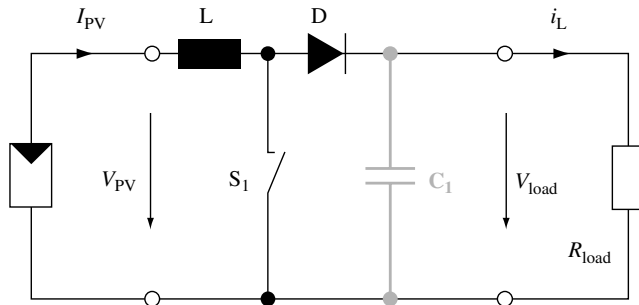


Figure 19.27 Equivalent circuit diagram of a step-up converter

As shown in Figure 19.26, the resulting load voltage obviously has a ripple, which can be smoothed by the additional capacitor C_2 . Anyway, its average value (V_{load}) is lower than V_{PV} . In case the switching frequency is increased, for example, up to the kilohertz range, then the necessary inductance can be reduced considerably.

The resulting voltage transformation can be described by the relation of the switching time as follows:

$$\frac{V_{load}}{V_{PV}} = \frac{t_{on}}{t_{off} + t_{on}}$$

19.2.4.3.2 Step-up converter (Boost converter)

By rearrangement of the components of the step-down converter, a step-up converter can be obtained (Figure 19.27). Contrarily, here V_{PV} is stepped up. At a steady state as S_1 is still “off”, V_{load} is equal to the V_{PV} , neglecting the voltage across diode.

As shown in Figure 19.28, during “on” state, without C_1 the load voltage drops immediately to zero. The circuit current ($= i_L$) flows through the inductor L and S_1 and rises according to the following equation:

$$\frac{di_L}{dt} = \frac{V_{PV}}{L}$$

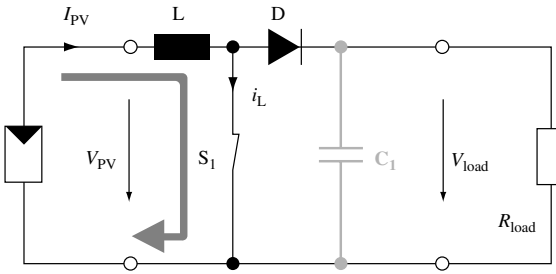


Figure 19.28 Step-up converter during “on” state

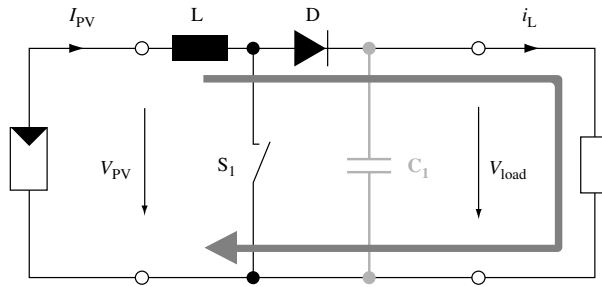


Figure 19.29 Step-up converter during “off” state

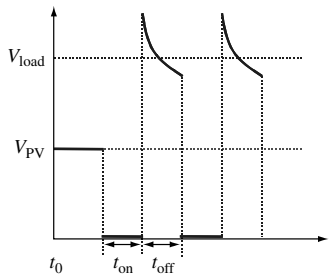


Figure 19.30 Behaviour of the load voltage of a step-up converter

After S_1 is switched off (Figure 19.29), the induced voltage in the inductor adds itself to V_{PV} , which then lies across the load. i_L flows through the inductor and further to the load. Thereby, it falls down gradually because $V_{load} > V_{PV}$:

$$\frac{di_L}{dt} = \frac{V_{PV} - V_{load}}{L}$$

The proceeding of the load voltage is illustrated in Figure 19.30. The diode D protects against a short circuit (i.e. discharge) of the charged capacitor C_1 , which is assumed to be so big that it can smooth the load voltage completely.

The resulting voltage transformation then becomes

$$\frac{V_{load}}{V_{PV}} = \frac{t_{off} + t_{on}}{t_{off}}$$

19.2.4.3.3 Step-down/step-up converter (Buck/Boost or inverting converter)

This circuit (Figure 19.31) enables both step down and step up of a DC voltage. During the “on” state, the energy given by the source (PV generator, in this case) is stored in the inductor L (Figure 19.32). The stored energy in the inductor L is then delivered to R_{load} during the “off” state (Figure 19.33). With the help of the diode D, the current flows through the inductor L only in one direction during both “on” and “off” states. As a result, V_{load} obviously has an opposite polarity to V_{PV} . Therefore, the circuit is also called an inverting converter. Equations describing the proceeding of the circuit currents can be derived in the same way to both converters mentioned before and will not be done here. As stated earlier, the capacitor C_1 supports the supply voltage V_{PV} and C_2 smoothes V_{load} . In conclusion, the amplitude of V_{load} can be either lower or higher than V_{PV} depending on the adjusted t_{on} and consequently t_{off} [4]:

$$\frac{V_{load}}{V_{PV}} = \frac{t_{on}}{t_{off}}$$

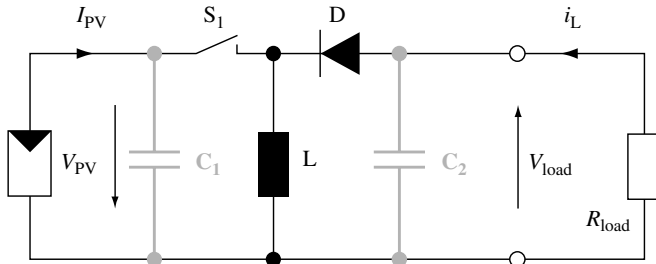


Figure 19.31 Equivalent circuit diagram of a step-down/step-up converter

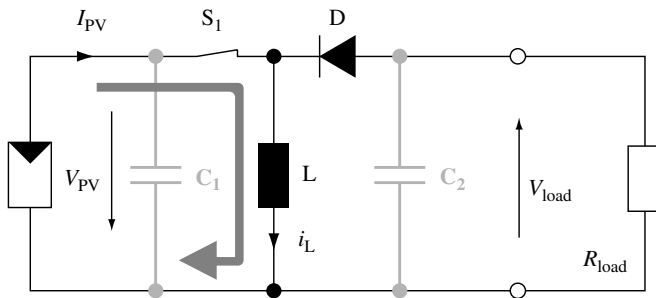


Figure 19.32 Step-down/step-up converter during “on” state

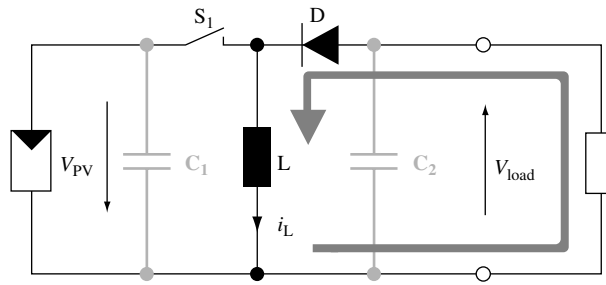


Figure 19.33 Step-down/step-up converter during “off” state

19.2.4.3.4 Combination of a step-down converter with an inverter

The combination of a step-down converter with a voltage inversion is shown in Figure 19.34. It should be noted that in this configuration the voltage of the DC input sources must always be equal to or bigger than the AC peak voltage.

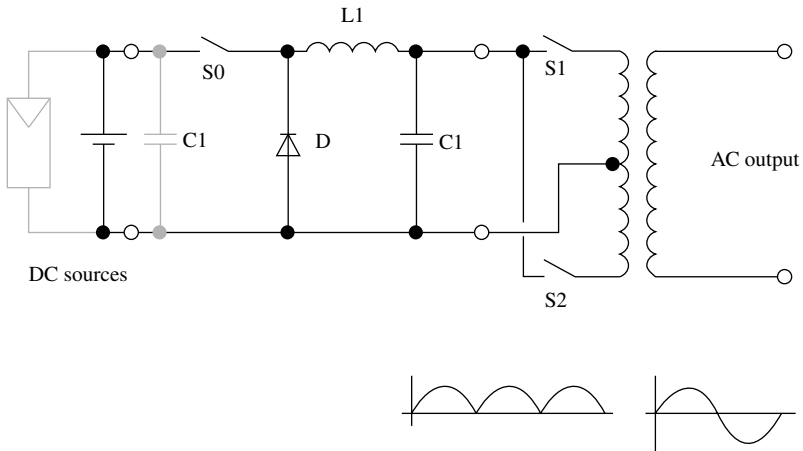


Figure 19.34 The combination of a step-down converter with inverters allows to produce sine-shaped AC output voltage. Wave shapes correspond to the voltage at the terminals over them

19.2.4.3.5 Voltage shaping by digital synthesis

In a further concept, the step-down converter can be replaced by digital synthesis as shown in Figure 19.34. In this concept, the desired voltage is obtained by binary addition of individual voltage sources [5–7]. Depending on the sum of these sources, the sine-shape can be approximated.

When using 5 sources, 32 voltage steps according to 2^5 adjustable levels can be obtained as shown in Figure 19.35. The resulting total harmonic distortion (THD)¹ can be kept well below 5%.

¹ Definition of THD: sum of the amplitudes of all harmonic frequencies compared to the amplitude of the fundamental signal (the 50- or 60-Hz frequency).

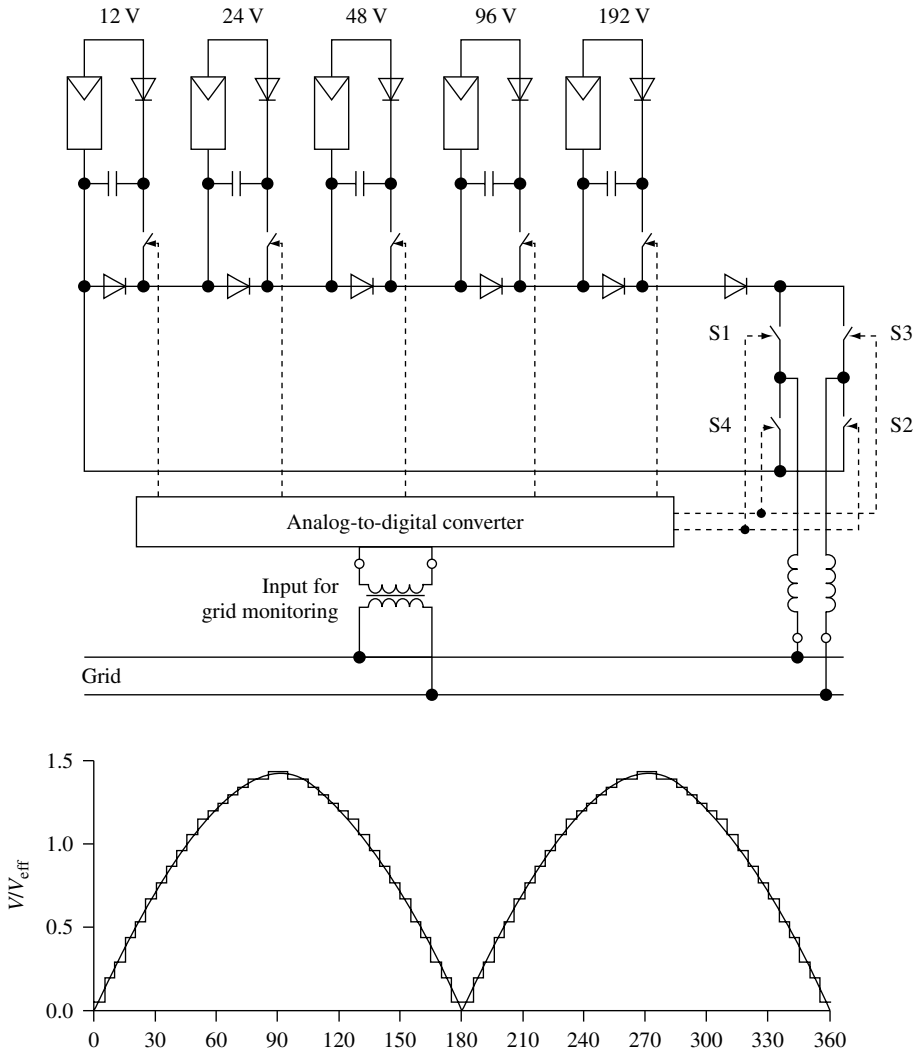


Figure 19.35 Digital waveform synthesis inverter

This concept provides extremely high efficiency since no induction coils or other magnetic elements are required (see Figure 19.35). One disadvantage that can be seen in the use of multiple voltage sources is the increase in cabling needs between the PV generator and the inverter.

In this concept the switches (transistors) S1 through S4 are needed to invert every second sine half-wave to arrive at AC. If using voltage sources with such voltages that they can sum up with the peak voltage of the desired AC output as

$$\sum_{i=1}^n V_i = 1.1\sqrt{2}V_{AC} = 358 \text{ Volts for } 230 \text{ V AC (+10\% tolerance)}$$

no transformer is needed, which increases the efficiency of this concept further, especially under part-load conditions.

19.2.4.3.6 Integration of the step-down principle into the inverting process

The four switches of the H-type bridge itself can also be used to form the desired sine-shape of the AC output. In this case a choke has to be inserted between the bridge and the AC output as shown in Figure 19.36. As has been shown in the concepts before, the switches S1 and S2 and therefore S3 and S4 act synchronously, but their switching frequency becomes very much higher than the desired AC output frequency that is called the fundamental frequency. During the first half-period of the fundamental frequency (10 ms for 50 Hz), the switches S1 and S2 change their on and off state in such a way that the relation t_{on}/t becomes proportional to the actual desired voltage similar to the step-down converter principle shown in Figure 19.23. In fact, the step-down converter principle has been extended to work under both positive and negative polarities.

The configuration shown in Figure 19.36 has become popular since only a very few components are needed, resulting in high efficiency and low cost. One possible disadvantage of this concept is the high DC input voltage necessary for proper working, for example, 358 V DC for 230 V at the AC side. Adding a transformer between the load and the inverter's output allows reducing the DC input voltage according to its transformation ratio. This combination can be found in many products that are in the market today. Compared to the transformer-less version, separation of the potential between source and load becomes feasible. Reduced efficiency and increased investment costs are the consequences, however.

The concept shown in Figure 19.36 allows further operation in a reversed power flow. This situation may occur for inverters in the stand-alone mode if the load is of a reactive type or if surplus power from the AC side is used to charge the battery. In both cases, the variable AC voltage must be transformed to the DC voltage level, which is always higher than any value of the AC voltage as shown in Figure 19.37. By combining S2 and D3 in Figure 19.36, a complete step-up converter can be realised for the positive part of the AC voltage. For the negative part, the combination of S1 and D4 forms the step-up converter for inverse power flow.

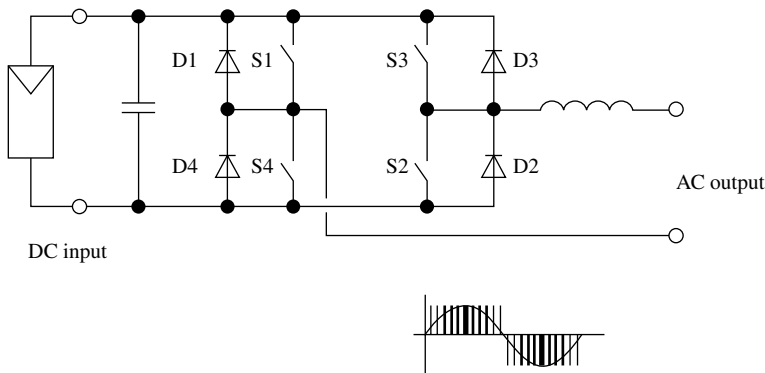


Figure 19.36 Pulse-width modulated (7-phase chopping) H-type bridge inverter

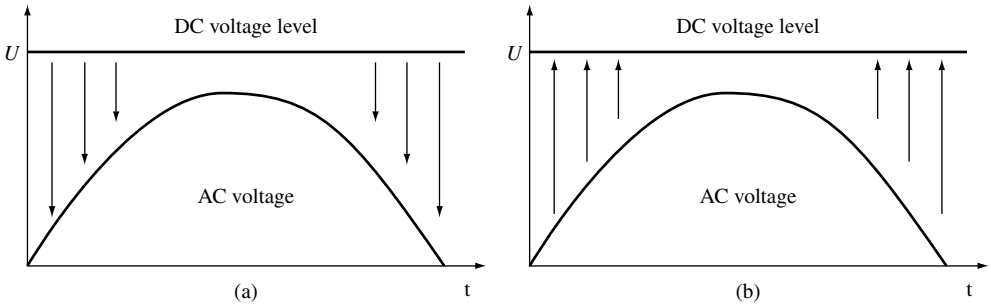


Figure 19.37 (a) Step-down conversion in the forward power-flow mode. (b) Step-up conversion in the reverse power-flow mode

19.2.4.3.7 Bi-directional step-up/step-down conversion

The concept described above allows reversed power flow only in cases in which the DC voltage level is always higher than the peak voltage of the AC side, which means that $U_{DC} \geq 358 \text{ V}$ for 230 V AC. However, there are two possibilities to lower the DC voltage level, that is, to install a transformer at the AC side or to install a bi-directional DC-DC converter at the DC side. Since a conventional step-down converter, as was described earlier, is not able to act as a step-up converter in the reversed power-flow mode, either two converters in anti-parallel mode or a different conversion concept would be necessary. One topology developed by Cuk [8] in 1977, which is able to fulfil these requirements, is given in Figure 19.38.

This conversion principle is in fact able to perform step-up as well as step-down conversion in both directions. The relation between the input voltage U_1 and the output voltage U_2 becomes:

$$U_2 = U_1 \cdot \frac{t_{on}}{(t_{off} + t_{on}) \cdot \left(1 - \frac{t_{on}}{(t_{off} - t_{on})}\right)}$$

Switches S1 and S2 operate complementarily, for example, if S1 is on, S2 is off and vice versa.

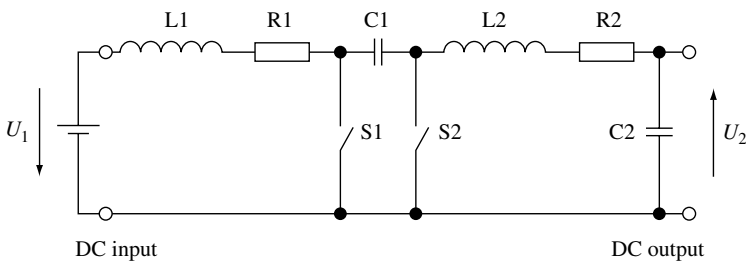


Figure 19.38 Bi-directional Cuk converter

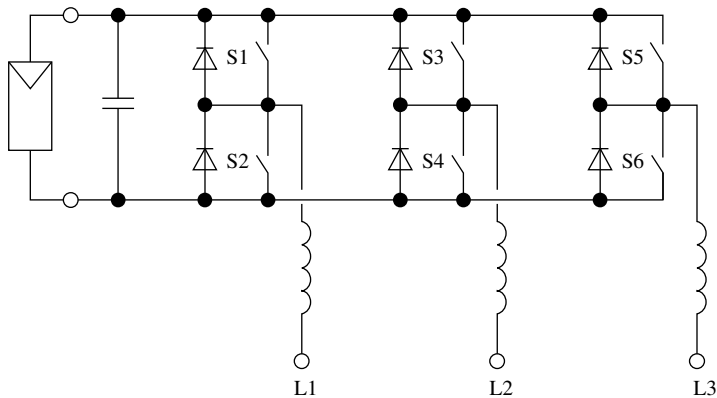


Figure 19.39 Three-phase PWM inverter

19.2.4.3.8 Three-phase configuration

The configuration shown in Figure 19.36 is also very well suited to be expanded into a three-phase version as given in Figure 19.39 [4].

This type of inverter is normally suited to a power range above 5 kW. Connection efforts at the AC side are somewhat higher since three terminals have to be dealt with. The most striking advantage of a three-phase concept can be seen in the fact that the power output and, thus, the power input are absolutely constant. As a consequence, no storage capacitor at the DC input side is needed.

This concept can also be combined with a three-phase transformer in a way as has been described earlier.

This inverter type is most commonly used in PV pumping systems. In contrast to most other applications, PV pump inverters operate with variable frequency and voltage at the AC output side. As an example, a typical characteristic of a centrifugal pump system is given in Figure 19.40.

The figure shows the pump head as a function of mass flow. The parameters are pump speed equivalent to the frequency and system efficiency.

Since the sinusoidal shape is obtained by a step-down process, as was described earlier, lowering of the AC voltage can be easily performed by the same configuration. In addition, MPP tracking can easily be performed by adjusting the frequency and proportionally the AC voltage in such a way that the PV generator can provide maximum power. In Figure 19.41, a typical PV pump system configuration is shown.

19.2.4.3.9 High-frequency concepts

If electric isolation between DC input and AC output is requested and if the bulky 50-Hz transformer should be avoided, high-frequency (HF) transformer concepts may be used. Three topologies using HF concepts will be described in this section.

In the first concept, the configuration as described in Figure 19.34 is used to operate with a high frequency (some 100 kHz) using an HF transformer. The HF square-wave

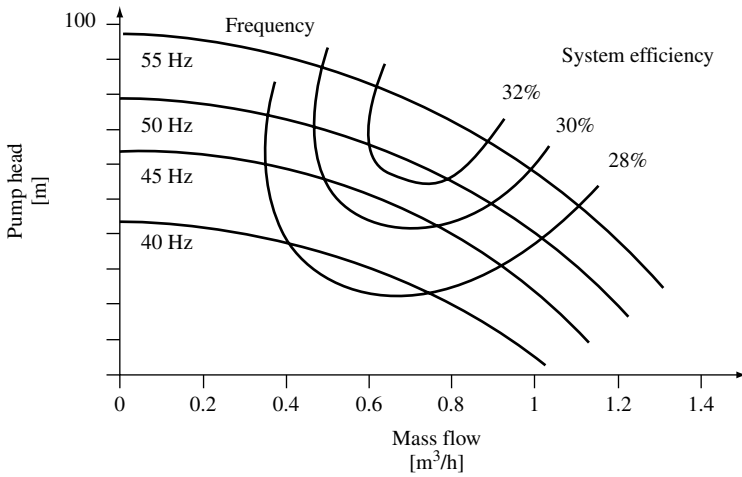


Figure 19.40 Characteristic of a centrifugal pump system

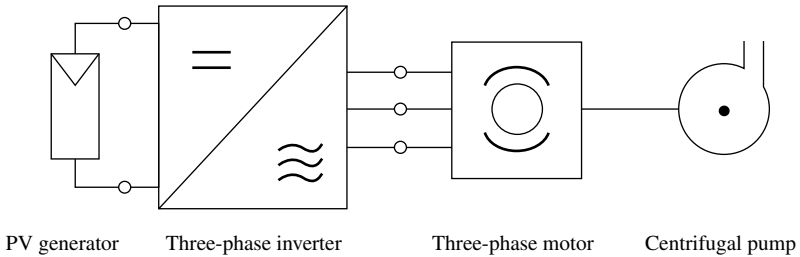


Figure 19.41 Typical layout of an AC PV pumping system

AC output is then rectified as shown in Figure 19.42, providing the desired DC voltage necessary for PWM inversion according to the H-type Bridge explained in Figure 19.36.

Compared to the low-frequency concepts, it becomes obvious that the savings using the HF transformer are widely being compensated by extra components. This might be one of the reasons HF concepts have not widely been used in inverters offered to the market so far.

When operating the high-frequency concept, as described in Figure 19.42, in the PWM mode, in which the desired low frequency is used for modulation, a PWM series of unipolar half-waves result after the rectifier at the secondary windings of the HF transformer. By means of the combination of L and C₂, a unipolar series of sine-shaped half-waves result, which are finally inverted with the H-type bridge as described in Figure 19.43. The 100-Hz pulsewise power injection requests an adequate storage element, which is realized by means of the capacitor C₁. It should be noted that this storage function is realized with C₂ in the topology presented previously in Figure 19.42.

Finally, an HF concept is presented in which AC is directly produced at the secondary side of the HF transformer. In this case, the non-controlled rectifier shown in

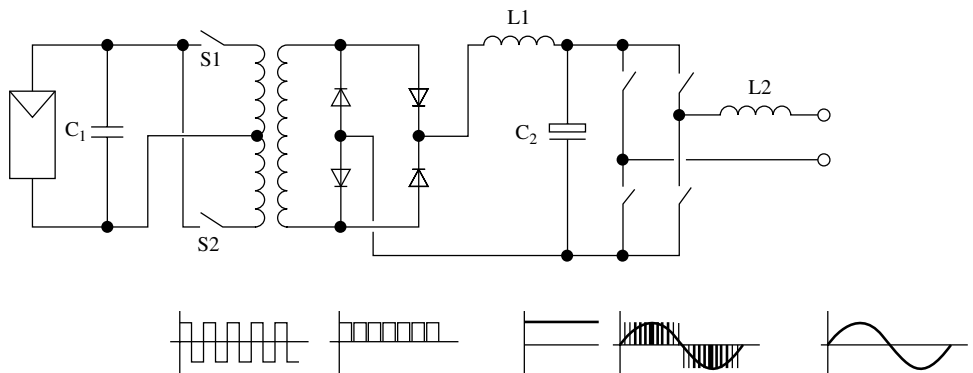


Figure 19.42 HF transformer combined with PWM H-type bridge inverter

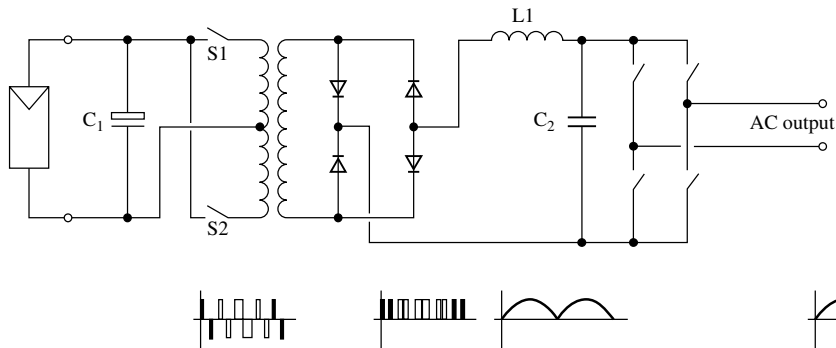


Figure 19.43 HF transformer combined with PWM high-frequency generator at the input side and a low-frequency H-type bridge at the output side

Figure 19.43 has been replaced by active switches combining the functions of rectification and inversion. This configuration is shown in Figure 19.44. It should be noted that in this case, the switches in the H-type bridge have to be operated in the rhythm of the high frequency in contrast to the configuration according to the topology shown in Figure 19.43. Since transistors switched with higher frequencies have higher losses as well as higher investment costs, the benefit of saving the passive rectifier used in the concept given in Figure 19.43 might be compensated by these facts to a certain extent.

19.2.5 Power Quality of Inverters

When dealing with power quality, a distinction has to be made between stand-alone and grid-connected applications.

In a stand-alone operation, the output waveform becomes important for many applications. Square-wave inverters, according to the working principle shown in Figure 19.21 or Figure 19.22, may be used to power resistive-type loads such as light bulbs or similar objects. When feeding power to reactive-type loads such as motors, proper operation

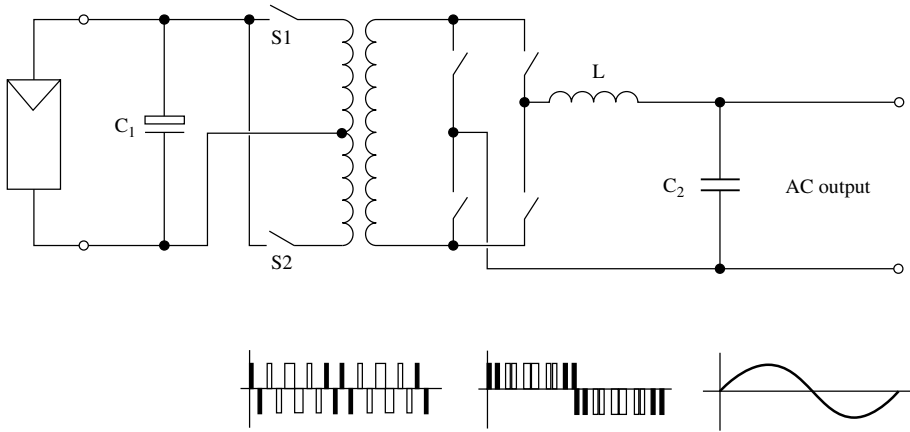


Figure 19.44 Direct AC synthesis at the secondary winding of the HF transformer. The PWM high-frequency signal is inverted in the low-frequency rhythm and smoothed by means of L and C₂. C₁ is needed to store the input energy in the rhythm, which equals twice the low frequency

might become difficult and losses inside the load created by the square-wave character of the supply might occur [9]. For these load-types, ideal sinusoidal voltage supply would be best. In reality, a compromise between this ideal voltage that results in high expenses and a lower quality for cheaper investments must be found.

The deviation from the ideal sinusoidal voltage is normally described as total harmonic distortion (THD). THD is usually defined as the ratio of the square root of the sum of the squares of the rms values of the harmonics to the rms value of the fundamental. This ratio is usually converted to percent or decibels (dB). As an example, the third harmonic and their influence on the shape of the fundamental waveform are given in Figure 19.45.

For high-quality power supply, the THD of the output voltage should be less than 5%, which corresponds with the quality of the public grid.

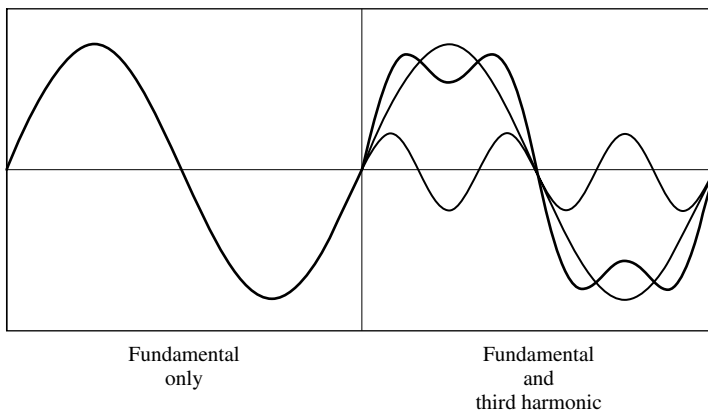


Figure 19.45 Influence of harmonics on the waveform

As a second and very important power-quality element for stand-alone applications, the ability to provide and to absorb reactive power should be mentioned. Typical loads requesting reactive power are electric motors. Under these load conditions, the load current is no longer in phase with the voltage as shown in Figure 19.46.

Proper handling of reactive power is only possible with appropriate topologies as have been described and presented in Figures 19.36 and 19.37. In some inverter designs, handling of reactive power is limited depending on the load type. In this case, the acceptable power factor, which corresponds with the cosine of the phase-angle difference between voltage and current, is defined and the maximum power of the inverter is given in kilovolt amperes (kVA) instead of kilowatts (kW). The energy of the reactive power, which is to be absorbed and afterwards re-injected into the load, is normally stored in capacitors of appropriate size.

If all the elements in the inverter allow for reverse power flow, a bi-directional inverter is obtained, which can be used to charge the battery, when surplus power at the AC side is available. The combination of a Cuk converter shown in Figure 19.38 with a H-type bridge given in Figure 19.22 allows for such a concept.

Finally, stand-alone inverters should also be able to blow fuses in cases in which a short current occurs in loads. This requirement is perfectly fulfilled with only a few inverters. The reason can be seen in the high current needed to blow fuses. Depending on the reaction time, this current can be as high as five times the nominal one as shown in Figure 19.47.

Some inverters produce this high current by reducing the AC output voltage significantly. The resulting flicker observed for loads not to be separated by the fuse in question may be accepted in most cases.

Since the output voltage of grid-connected inverters has to correspond with the grid's voltage, the quality of the current that is to be injected into the grid becomes important. Under ideal circumstances, this current should be in phase with the grid's voltage (power factor = 1). The deviation from this power factor becomes therefore important for the description of the power quality. All modern transistor-based inverters have a power factor near unity at nominal load, with a tendency towards smaller values under part load (Figure 19.48).

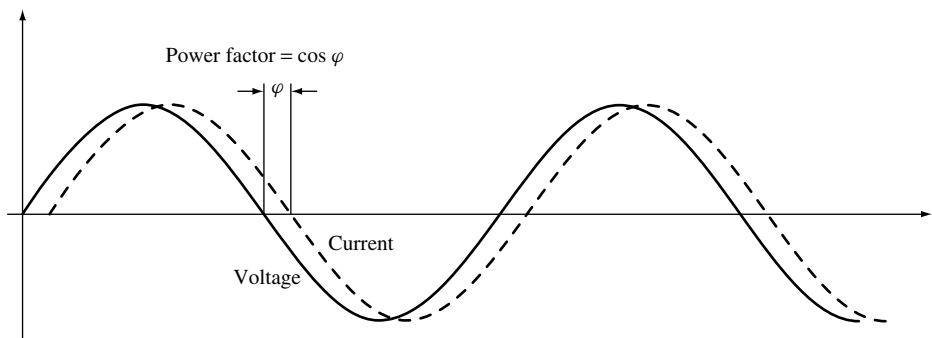


Figure 19.46 Power factors $\neq 1$ produced by reactive (inductive or capacitive) loads

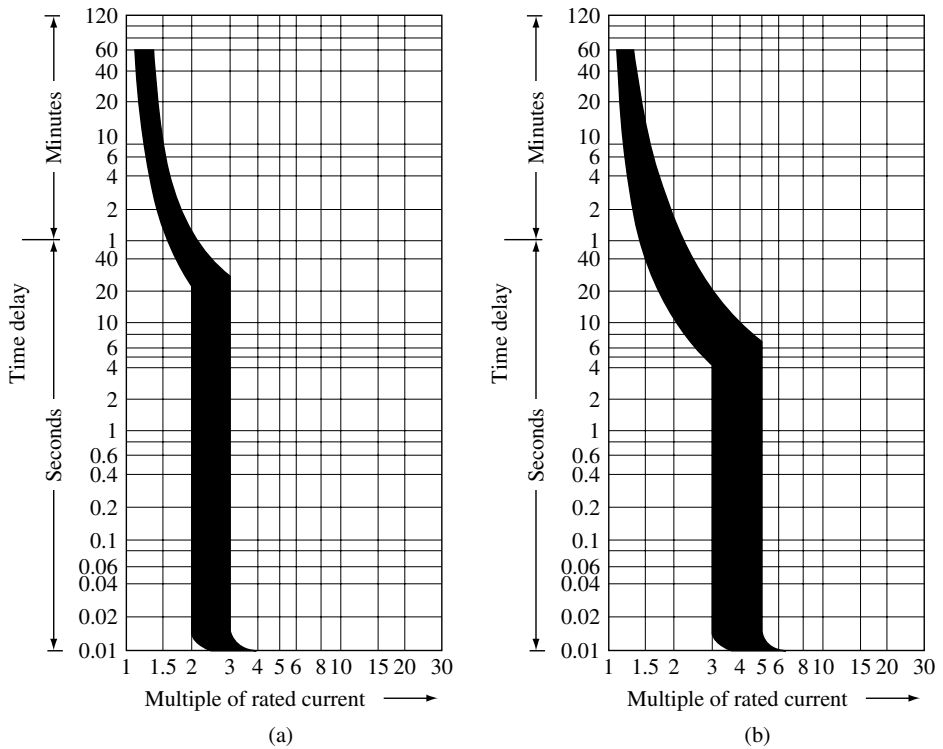


Figure 19.47 Current–time diagram for different fuse types: (a) characteristic left and (b) characteristic right (DIN EN 60898, DIN EN 62019)

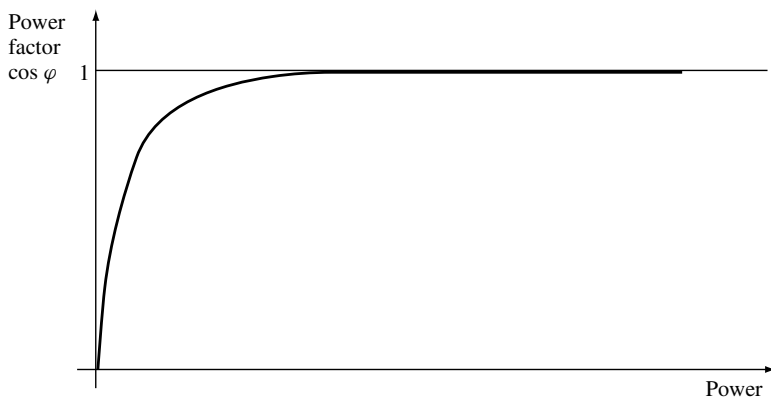


Figure 19.48 Power factor as a function of the output power of a typical grid-connected inverter

For grid-connected inverters’ the THD of the current injected into the grid is used to describe the inverters’ quality. The THD of the injected current, which is defined in the same way as was done for the voltage. A high-quality grid-connected inverter shows a THD in the current that is below 5%.

19.2.6 Active Quality Control in the Grid

Since the power factor in modern grid-connected inverters can be adjusted by internal control, this kind of inverters can be used to compensate reactive power flow in the grid, which otherwise must be performed by extra compensation units such as inductors or capacitors. This ability can either be fixed to a constant value or, in case of an appropriate communication system, be controlled by the grid operator according to the actual needs.

As a further means of power quality improvement, high-quality inverters are able to compensate deviations in the sinusoidal voltage of the grid. As shown in Figure 19.49, the inverter injects surplus power into the grid to compensate for the actual deficit in the voltage.

In a later stage of PV use, inverters will have to prevent grid overloading. Grid-connected inverters can easily handle this kind of power control by changing the DC input voltage from the MPP in such a way that the PV generator reduces power production to the desired level. This request may come in a situation in which several hundreds of megawatts of PV power are fed into a local system. To allow for such ability, the grid operator must be able to communicate with these inverters.

As a consequence, it can be stated that high-quality inverters will be able to improve the power quality in the grid by adjusting the power factor, by reducing the THD and by stabilising power flow through power control. To realise these functions, appropriate control and the availability of a communication element becomes necessary. A few inverters in the market already show these features today.

19.2.7 Safety Aspects with Grid-connected Inverters

An important issue for grid-connected systems is associated with islanding protection. Islanding may occur, if a part of the local grid is switched off, for example, for maintenance reasons and if the injected power is equal to the actual load in the separated part of the grid. This situation is shown in Figure 19.50.

The situation described above becomes very unlikely since not only the effective power but the reactive power as well must be equal between production and consumption.

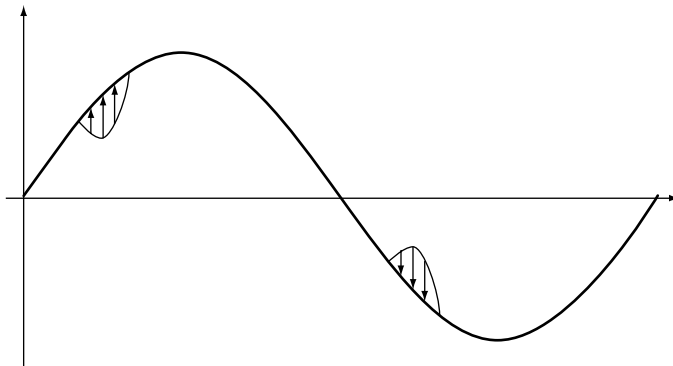


Figure 19.49 Inverter injects surplus power

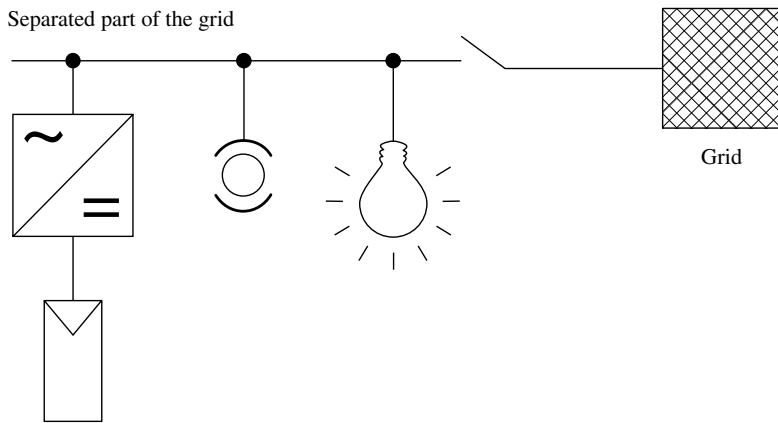


Figure 19.50 After switch-off, the separated part of the grid may continue operation, if the injected power by the PV system equals the actual load

As a first measure, frequency and voltage monitoring will identify by far most situations in grids turned off since the smallest deviations in production or in consumption will lead to changes in frequency or voltage or in both of them. The experience with big wind farms has shown that limitation of voltage or frequency may lead to undesired results, however.

In case of heavy loads on the grid, both the voltage and the frequency may fall below the set point. In this situation, cut-off of power sources takes place when they would be needed urgently to support the grid. As a further method to identify islanding conditions, monitoring of the grid's impedance is being performed by injecting power peaks, which do not correspond with the fundamental frequency (50 or 60 Hz), by the inverter into the grid and by monitoring this influence on the grids voltage shape. This method is currently accepted by German safety code.

This code, which applies to grid-connected single-phase PV systems smaller than 5 kW, requests a separation from the grid, if the impedance of the grid exceeds 1.75 ohms or if a jump in the impedance ≥ 0.5 ohms occurs. Reconnection to the grid is allowed for grid impedance smaller than 1.25 ohms. There are two independent monitoring and switching systems that have been requested. One of the two systems must act on a mechanical switch, for example, a relay, while for the second system, the semiconductors of the inverter output bridge are accepted. Figure 19.51 explains this configuration.

In addition to the monitoring of the grid impedance, frequency deviations above ± 0.2 Hz or voltage differences bigger than -15 or $+10\%$ must lead to a separation of the grid as well. The safety protection device can either be integrated into the inverter or installed separately between the inverter and the grid. The latter may be used preferably in combination with small-scale inverters, for example, module-integrated ones. In these cases, the investment cost for integrating the unit in each of the small inverters with a power of not more than a few hundred watts may not be economic. In case of a separate installation, one supervision unit could be used to protect several small module-integrated inverters. As an alternative, also accepted as a safety device, voltage monitoring of all three phases of the grid, which lead to a separation, if one of the three phases becomes

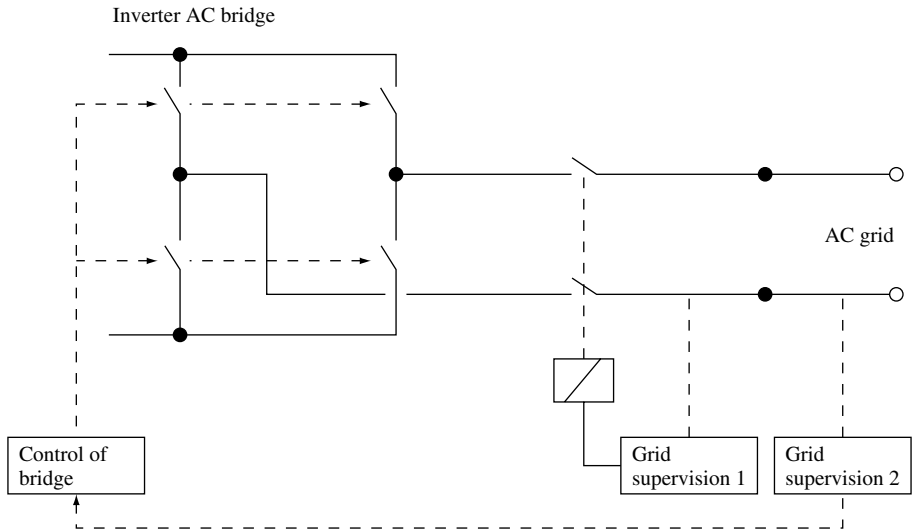


Figure 19.51 Two independent grid-supervision units for safety against islanding (DIN VDE 0126)

zero, can be used in Germany. In case of a single-phase grid, as is the case in many rural areas of the world, this method cannot be applied, however.

There is a limitation to be expected, if a big number of inverters are monitoring the grid in this way. In this case, interference between the different inverters may lead to unspecific interpretation of the grid's response. It might become necessary therefore to equip all inverters with communication capabilities. This feature would allow switching off all relevant inverters by the grid operator if needed. As a further benefit, power-quality improvements controlled by the grid operator will become feasible as well.

19.3 ACKNOWLEDGEMENT

Heribert Schmidt of the Fraunhofer ISE, Freiburg, authored Section 19.1, *Charge Controllers and Monitoring Systems for Batteries in PV Power Systems*. Jurgen Schmidt, of the ISET/Universität Kassel, authored Section 19.2, *Inverters*.

REFERENCES

1. Nekrasov P, "Partial Shunt Regulation", *Proc. 14th Annual Meeting of the Astronautical Society* (May 13–15, 1968).
2. Salim A, "A Simplified Minimum Power Dissipation Approach to Regulate the Solar Array Output Power in a Satellite Power Subsystem", *Proc. 11th Intersociety Energy Conversion Engineering Conference Proceedings*, Vol. II (Nevada, Sept. 12–17, 1976).
3. Siedle Ch, *Vergleichende Untersuchungen von Ladungsausgleichsrichtungen zur Verbesserung des Langzeitverhaltens vielzelliger Batteriebanken (Comparative investigations of CHarge Equalizers to improve the long-term performance of multi-cell battery banks)*, Doctoral thesis, Reihe 21, Nr. 245, ISBN 3-18-324521-3, Düsseldorf VDI-Verlag (1998).
4. Appelbaum J, Gabbray D, *IEEE Trans. Aerospace Electron. Syst.* AES 21, 484–489 (1985).

5. Gonzalez G, Hill G, Ross Jr. R, *Photovoltaic Array – Power Conditioner Interface Characteristics*, DOE/JPL-1012-79, Prepared for U.S. Department of Energy (1979).
6. Schmid J, Schmidt H, “Inverters for Photovoltaic Systems”, *5th Contractors Meeting Commission of the European Communities DG XVII*, ISPRA (Italy, May 22–24, 1991).
7. Schmid J, Schätzle R, “Simple Transformer-less Inverter with Automatic Grid Tracking and Negligible Harmonic Content for Utility Interactive Photovoltaic Systems”, *Proc. 4th EC Photovoltaic Solar Energy Conference*, 316 (Stresa, 1982).
8. Dickerson A, “*Proof of Feasibility of a Novel Inverter for Photovoltaic Power Conditioning*”, draft final report, Contract 21-3517, Received from Cal Poly State University, San Luis Obispo, CA (Sept. 1985).
9. Cuk S, Middlebrook R, “A New Optimum Topology Switching DC-to-DC Converter”, *Power Electronic Specialists Conference* (1977).

This Page Intentionally Left Blank

20

Energy Collected and Delivered by PV Modules

Eduardo Lorenzo

Instituto de Energía Solar – Universidad Politécnica de Madrid, Madrid, Spain

20.1 INTRODUCTION

This chapter deals with two different questions: “How much solar radiation reaches the surface of a photovoltaic (PV) collector?” and “What is the conversion efficiency of this solar radiation into electricity?” Both questions are analysed from the PV-system designer’s point of view, whose ultimate interests, depending on the type of application, are the determination of the PV collector surface needed to provide a certain required service, and the estimation of the average electricity yield from a certain PV array.

The input information available for the PV designer is usually restricted to the 12 monthly mean values of global horizontal irradiation, that characterise the solar climate of the location, and to the electrical characteristics of the PV modules under Standard Test Conditions (STC), as provided by its manufacturers. This chapter contains a whole set of procedures applicable to most PV engineering practical problems using only this input information. In particular, models to predict the long-term evolution of the solar radiation incident over any arbitrarily oriented surface, and also models to anticipate the electricity output of PV arrays operating in other than STC are described. Looking for practical usefulness, the chapter is, as far as possible, self-contained and the formulae are presented in such a way, that they can be applied directly to practical problems, even if sometimes empirical or cumbersome expressions have to be introduced. Some examples intended to clarify the proper use of the formulae have also been included.

The two above-mentioned questions intrinsically differ in nature. The random character of the solar radiation over the Earth implies that answers to the first question are never more than future predictions, unavoidably associated with a degree of uncertainty (even if very good past solar radiation data are available). This uncertainty is more than is commonly assumed, and represents a serious limit to the accuracy (or, more strictly, to

the significance) of the results of any PV design exercise, irrespective of the complexity of the radiation and PV array models supporting the particular design tool. This means that for stand-alone PV systems, reliability can only be properly estimated for Loss of Load Probabilities greater than 10^{-2} . For grid-connected systems, it implies that yield predictions should be understood to have an uncertainty that can reach up to $\pm 30\%$, for monthly values, and $\pm 10\%$ for annual ones.

Regarding the behaviour of PV modules in arbitrary operating conditions, an $I-V$ model based on the incident irradiance and ambient temperature is presented. Particular attention is paid to the consideration of incidence angle effects, which can be significant in several real situations. Further refinements to incorporate the effects of wind speed, solar spectrum and low irradiance effects are also described. These second-order effects help to explain temporary differences between predicted and observed values, but are of minor importance when long-term energy production calculations are considered.

Finally, some problems related to relevant applications are particularly addressed: the reliability of stand-alone PV systems, the case of Solar Home Systems (SHS) (characterised by a large variety of individual real energy consumption values in contrast to only a few standard ones for design purposes), and the energy yield of grid-connected PV systems.

20.2 MOVEMENT BETWEEN SUN AND EARTH

Although the movement of the sun relative to a fixed point on the Earth seems very familiar, because the sun is fortunately there everyday, the mathematics that governs it is surprisingly complex. In fact, the understanding of such movement was among the longest scientific adventures of mankind. It seems that the very first sundials were built in the Babylonian time (1800 BC), and that the attempts to explain the evolution of the “gnomon” shadow led to the first proposed models of the Sun–Earth movement, which in turn led to the beginning of geometry, in Greece [1]. Figure 20.1 pays a fully

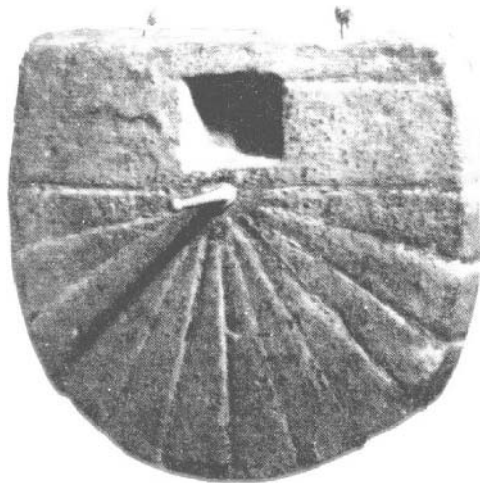


Figure 20.1 Sundial about 2000 years old

deserved homage to such a glorious background. However, it was not until the seventeenth century, when Kepler published *Astronomia Nova* (1609) and *Harmonice mundi* (1618), that such movement was completely explained. And then the explanation spread only very slowly. For example, Galileo in his *Dialogo sopra y due massimi del mundo*, published in 1632 (just one year before the famous ecclesiastic sentence condemning him for publicly defending the heliocentric system formerly proposed by Copernicus), still promoted the idea of the planets revolving around the sun in circular orbits, fully ignoring Kepler's work.

Fortunately for us, such discussions ended a long time ago. Today, it is well established that the Earth goes around the sun in an elliptic orbit with the sun at one of the foci. The plane containing this orbit is called the *ecliptic plane* and the time that the Earth takes to complete this orbit leads to the definition of the year. The distance from the sun to the Earth, r , is given by

$$r = r_0 \left[1 + 0.017 \sin \left(\frac{360(d_n - 93)}{365} \right) \right] \quad (20.1)$$

where d_n is the day number counted from the beginning of the year. It is worth noting that the eccentricity of the ecliptic is only 0.017, that is, very small. Because of that, the deviation of the orbit from the circular is also very small, and it is normally adequate to express the distance just in terms of its mean value r_0 , equal to 1.496×10^8 km, and is usually referred to as *one astronomical unit*, 1 AU. For most engineering applications, a very simple and useful expression for the so-called eccentricity correction factor is

$$\varepsilon_0 = (r_0/r)^2 = 1 + 0.033 \cos \left(\frac{360d_n}{365} \right) \quad (20.2)$$

The Earth also spins once a day on its own central axis, the *polar axis*. The polar axis orbits around the sun, maintaining a constant angle of 23.45° with the ecliptic plane. This inclination is what causes the sun to be higher in the sky in the summer than in the winter. It is also the cause of longer summer sunlight hours and shorter winter sunlight hours. Figure 20.2 shows the Earth's orbit around the sun, with the inclined polar axis; and Figure 20.3 adds some details for a particular day and a particular geographic latitude, ϕ . It is important to note that the angle between the equatorial plane and a straight line drawn between the centre of the Earth and the centre of the sun is constantly changing over the year. This angle is known as the *solar declination*, δ . For our present purposes, it may be considered as approximately constant over the course of any one day. The maximum variation in δ over 24 h is less than 0.5° . If angles north of the equator are considered as positive and south of the equator are considered negative, the solar declination can be found from

$$\delta = 23.45^\circ \sin \left[\frac{360(d_n + 284)}{365} \right] \quad (20.3)$$

On the *spring equinox* (20th/21st March) and the *autumn equinox* (22nd/23rd September), the line between the Sun and the Earth passes through the equator. Consequently, $\delta = 0$, the length of day and night is equal all over the Earth, and the sun rises and sets precisely in the east and west, respectively. On the *summer solstice* (21st/22nd June) $\delta = 23.45^\circ$,

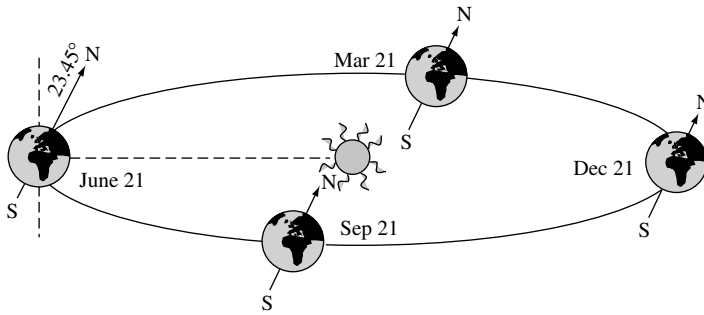


Figure 20.2 The orbit of the Earth around the sun

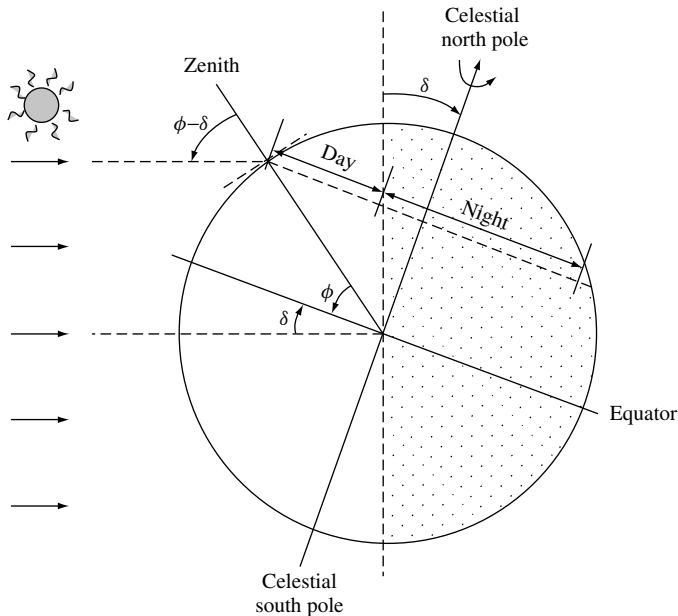


Figure 20.3 Relative Earth–Sun position at noon of a negative declination day (winter in the Northern Hemisphere, and summer in the Southern Hemisphere)

the sun is situated directly above the Tropic of Cancer, and sunrise and sunset are displaced towards the north-east and north-west, respectively. In the Northern Hemisphere, the summer solstice is when the longest day and shortest night of the whole year occur. In the Southern Hemisphere, it is the opposite. On the *winter solstice* (21st/22nd December) $\delta = -23.45^\circ$, the sun is directly above the Tropic of Capricorn, and sunrise and sunset are displaced towards the south-east and south-west, respectively. In the Northern Hemisphere, this is the shortest day and longest night of the whole year, and again, the opposite is true in the Southern Hemisphere.

A classic way of representing the sky is as a sphere centred on a fixed point of the Earth, as indicated in Figure 20.4. This is known as the *celestial sphere*. Each of its

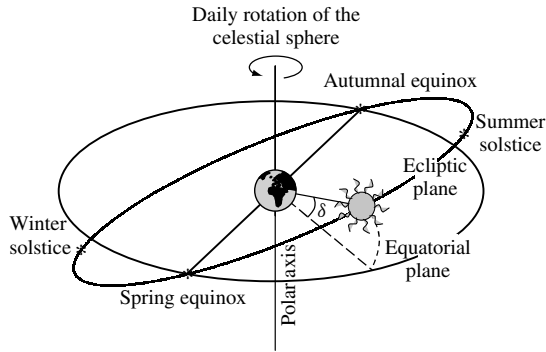


Figure 20.4 The celestial sphere and the ecliptic plane

points represents a direction towards the sky as seen from the Earth. The intersection of the celestial sphere with the equatorial plane defines the *celestial equator*. The points of intersection with the polar axis are called the *celestial poles*. Using this form of representation, the movement of the Earth around the stationary sun may instead be seen as a movement of the Sun with the Earth taken as fixed. The sun then travels through a great circle of the celestial sphere, the *ecliptic*, which forms an angle of 23.45° with the celestial equator. The sun completes this circuit once a year while the celestial sphere rotates once a day around the Earth (regarded as fixed). In this way, the sun marks out a circle around the Earth. The diameter of the circle changes daily, reaching a maximum on the equinoxes and a minimum on the solstices. The rotation of the sun around the ecliptic is in the opposite direction to that of the celestial sphere around the Earth.

Now, landing on a particular location on the Earth's surface, where a PV system is going to be used, it is convenient to specify the position of the sun by means of two angles that refer to the horizontal plane and to the vertical. The vertical intersects the celestial sphere at points known as the zenith and the nadir. Figure 20.5 attempts to visualise these concepts. The *solar zenith angle*, θ_{ZS} , is between the vertical and the incident solar beam; and the *solar azimuth*, ψ_S , is between the meridians of the location and the sun. The complement of the zenith angle is called the *solar altitude*, γ_S , and represents the angle between the horizon and the solar beam in a plane determined by the zenith and the sun. In the Northern (Southern) Hemisphere, the solar azimuth is referenced to south (north) and is defined as positive towards the west, that is, in the evening, and negative towards the east, that is, in the morning.

At any given moment, the angular coordinates of the sun with respect to a point of geographic latitude ϕ (north positive, south negative) are calculated from the equations:

$$\cos \theta_{ZS} = \sin \delta \sin \phi + \cos \delta \cos \phi \cos \omega = \sin \gamma_S \quad (20.4)$$

and

$$\cos \psi_S = \frac{(\sin \gamma_S \sin \phi - \sin \delta)}{\cos \gamma_S \cos \phi} [\text{sign}(\phi)] \quad (20.5)$$

where ω is called the true solar time, or local apparent time, or solar hour, and is the difference between noon and the selected moment of the day in terms of a 360° rotation

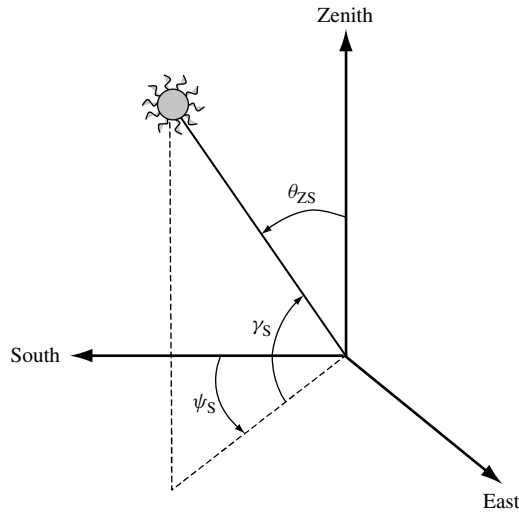


Figure 20.5 Position of the sun relative to a fixed point on the Earth

in 24 h. $\omega = 0$ at the midday of each day, and is counted as negative in the morning and positive in the afternoon. $[\text{sign}(\phi)]$ means “1” for northern latitudes and “-1” for southern latitudes. The true solar time ω is related to the local official time, TO , also called local standard time (the time shown by a clock) by the equation

$$\omega = 15 \times (TO - AO - 12) - (LL - LH) \quad (20.6)$$

where LL is the local longitude and LH is the reference longitude of the local time zone (positive towards the west and negative towards the east of the Greenwich Meridian). AO is the time by which clocks are set ahead of the local time zone. In the European Union, AO is usually one hour during winter and autumn, and two hours during spring and summer. In this equation ω , LL and LH are given in degrees, while TO and AO are given in hours.

Figure 20.6 presents the sun’s trajectory on the celestial sphere for (a) a winter and a summer day and (b) the corresponding plots of solar altitude versus azimuth. We will return to such plots later on.

Equation (20.4) may be used to find the *sunrise angle*, ω_S , since at sunrise $\gamma_S = 0$. Hence

$$\omega_S = -\arccos(-\tan \delta \tan \phi) \quad (20.7)$$

In accordance with the sign convention, ω_S is always negative. Obviously, the sunset angle is equal to $-\omega_S$ and the length of the day is equal to $2 \times \text{abs}(\omega_S)$. In the polar regions, during the winter the sun does not rise ($\tan \delta \tan \phi > 1$) and equation (20.7) has no real solution. However, for computing purposes, it is convenient to set $\omega_S = 0$. Similarly, during the summer, $\omega_S = -\pi$ is a practical solution for the continuous day. It is also interesting to note that just at noon, $\omega = 0$, and the solar altitude is equal to the latitude

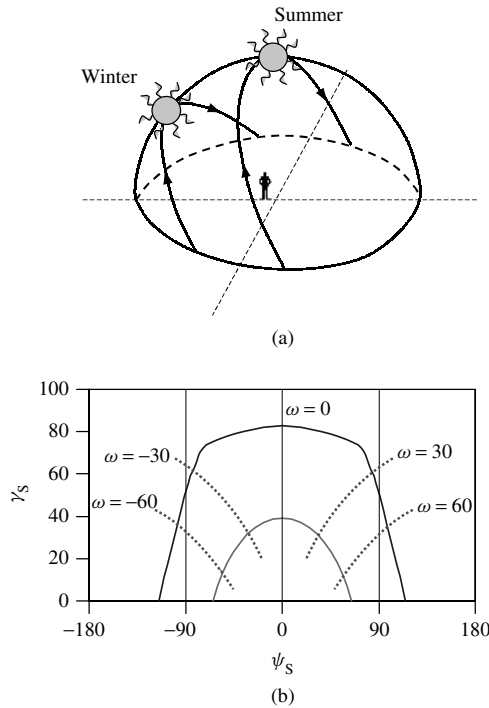


Figure 20.6 (a) Sun's trajectory corresponding to a winter and to a summer day represented over the celestial sphere. (b) The solar altitude γ_S is plotted against the solar azimuth ψ_S . The solar time ω is also shown

complement plus the declination

$$\omega = 0 \Rightarrow \gamma_S = \frac{\pi}{2} - \phi + \delta \quad (20.8)$$

It should be noted that equation (20.5) is indeterminate for $\gamma_S = \pi/2$ and for $\phi = \pi/2$. In the first case, the sun is just on the vertical, so that ψ_S is meaningless. In the second, the sun's position is given by $\gamma_S = \delta$ and $\psi_S = \omega$.

It should now be said that equations (20.1–20.3 and 20.6) derive from considering the angular velocity of the Earth through its elliptic orbit as constant, which is sufficiently accurate for most PV engineering applications. In particular, for all designs involving flat-plate PV modules, typical accuracy is about 1° . However, if desired, more accurate expressions are obtained when taking into account that the well-known Kepler's second law governs this angular velocity [2].

Another word of caution is necessary here. All the above-presented equations refer to a baseline year composed of 365 days, while the time length of the real year is 365 days, 5 h, 48 min and 45.9 s. As is well known, the difference is compensated by adding a day in the leap years. For most PV engineering applications, the same number corresponding to the precedent may be associated to this additional day, that is, $d_n = 59$ for both 28th and 29th of February. However, for some demanding applications, such as

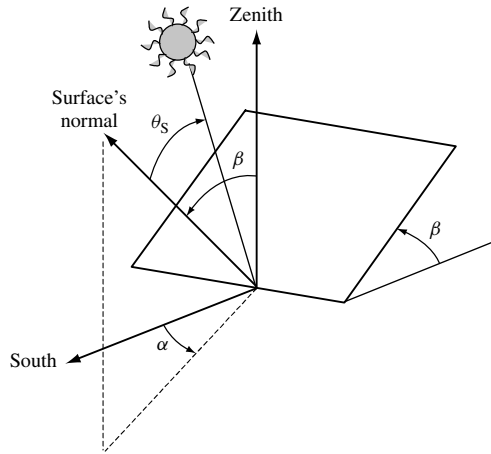


Figure 20.7 Receiver position (slope β and azimuth α) and sun's rays incidence angle θ_S

highly accurate trackers for concentrators, more precise equations may be necessary to calculate the relative Earth–Sun position. The interested reader is encouraged to consult Reference [3]. It describes an accurate algorithm and provides a software file for its implementation.

Equations (20.4) and (20.5) give the angles θ_{ZS} and ψ_S relative to a horizontal surface. However, most practical applications require the position of the sun relative to an inclined plane to be determined. The position of a surface (Figure 20.7) may generally be described by its slope β (the angle formed with the horizontal) and the azimuth α of the normal to the surface. The angle of solar incidence between the sun's rays and the normal to the surface may be calculated from

$$\begin{aligned} \cos \theta_S = & \sin \delta \sin \phi \cos \beta - [\text{sign}(\phi)] \sin \delta \cos \phi \sin \beta \cos \alpha + \cos \delta \cos \phi \cos \beta \cos \omega \\ & + [\text{sign}(\phi)] \cos \delta \sin \phi \sin \beta \cos \alpha \cos \omega + \cos \delta \sin \alpha \sin \omega \sin \beta \end{aligned} \quad (20.9)$$

Although this expression appears quite complicated, it is very convenient to use in most instances. In the case of surfaces tilted towards the equator (facing south in the Northern Hemisphere, or facing north in the Southern Hemisphere), $\alpha = 0$, and it simplifies to

$$\cos \theta_S = [\text{sign}(\phi)] \sin \delta \sin(\text{abs}(\phi) - \beta) + \cos \delta \cos(\text{abs}(\phi) - \beta) \cos \omega \quad (20.10)$$

20.3 SOLAR RADIATION COMPONENTS

Figure 20.8 helps to illustrate the following brief explanation of the different components of solar radiation that reach a terrestrial flat-plate PV surface

To a good approximation, the sun acts as a perfect emitter of radiation (black body) at a temperature close to 5800 K. The resulting power incident on a unit area perpendicular to the beam outside the Earth's atmosphere, when it is 1 AU from the sun, is known as the *solar constant*

$$B_0 = 1367 \text{ W/m}^2 \quad (20.11)$$

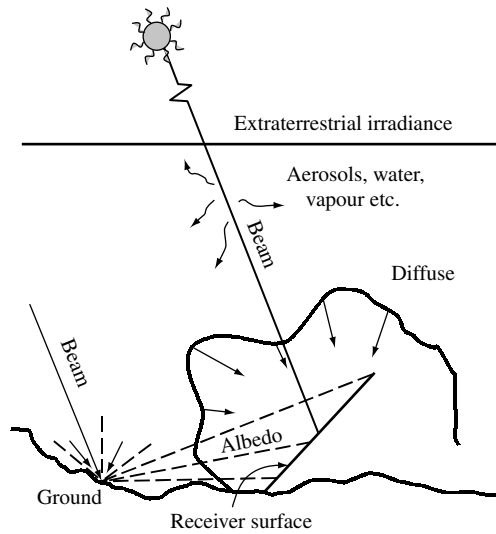


Figure 20.8 Different components of solar radiation

The radiation falling on a receiver situated beyond the Earth's atmosphere, that is, *extraterrestrial radiation*, consists almost exclusively of radiation travelling along a straight line from the sun. Since the intermediate space is almost devoid of material that might scatter or reflect the light, it appears virtually black, apart from the sun and faint points of light corresponding to the stars.

As the solar radiation passes through the Earth's atmosphere, it is modified by interaction with components present there. Some of these, such as clouds, reflect radiation. Others, for example, ozone, oxygen, carbon dioxide and water vapour, have significant absorption at several specific spectral bands. Water droplets and suspended dust also cause scattering. The result of all these processes is the decomposition of the solar radiation incident on a receiver at the Earth's surface into clearly differentiated components. *Direct or Beam radiation*, made up of beams of light that are not reflected or scattered, reaches the surface in a straight line from the sun. *Diffuse radiation*, coming from the whole sky apart from the sun's disc, is the radiation scattered towards the receiver. *Albedo radiation* is radiation reflected from the ground. The total radiation falling on a surface is the sum of these (direct + diffuse + albedo) and is termed *global radiation*.

It is intuitively obvious that the directional properties of the diffuse radiation depend to a large extent on the position, form and composition of the water vapor and dust responsible for scattering. The angular distribution of the diffuse radiation is therefore a complex function that varies with time. Diffuse radiation is essentially anisotropic. The amount of albedo radiation is greatly affected by the nature of the ground, and a wide range of features (snow, vegetation, water etc.) occur in practice.

In the following discussion, the word *radiation* will be used as a general term. To distinguish between power and energy, more specific terminology will be used. *Irradiance* means density of power falling on a surface, and is measured in W/m^2 (or similar); whereas *irradiation* is the density of the energy that falls on the surface over some

period of time, for example, hourly irradiation or daily irradiation, and is measured in Wh/m^2 . Furthermore, only the symbols B_0 , B , D , R and G will be used, respectively, for extraterrestrial, direct, diffuse, albedo and global irradiance, whereas a first subscript, h or d , will be used to indicate hourly or daily irradiation. A second subscript, m or y , will refer to monthly or yearly averaged values. Furthermore, the slope and orientation of the concerned surface are indicated among brackets. For example, $G_{\text{dm}}(20,40)$ refers to the monthly mean value of the daily global irradiation incident on a surface tilted $\beta = 20^\circ$ and oriented $\gamma = 40^\circ$ towards the west. For surfaces tilted towards the equator ($\gamma = 0$), only the slope will be indicated. For example, $B(60)$ refers to the value of the direct irradiance incident on a surface tilted $\beta = 60^\circ$ and oriented towards the south (in the Northern Hemisphere).

An important concept characterising the effect of atmosphere on clear days is the *air mass*, defined as the relative length of the direct-beam path through the atmosphere compared with a vertical path directly to sea level, which is designed as AM . For an ideal homogeneous atmosphere, simple geometrical considerations lead to

$$AM = \frac{1}{\cos \theta_{\text{ZS}}} \quad (20.12)$$

which is generally sufficient for most engineering applications. If desired, more accurate expressions, considering second-order effects (curvature of the Earth, atmospheric pressure etc.), are available [4].

At the standard atmosphere $AM 1$, after absorption has been accounted for, the normal irradiance is generally reduced from B_0 to 1000 W/m^2 , which is just the value used for the standard test of PV devices (see Chapter 16). Obviously, that can be expressed as $1000 = 1367 \times 0.7^{AM}$. For general AM values, a reasonable fit to observed clear days data is given by [5].

$$G = B_0 \cdot \varepsilon_0 \times 0.7^{AM^{0.678}} \quad (20.13)$$

A particular example can help to clarify the use of these equations, by calculation of the sun co-ordinates and the global irradiance on a surface perpendicular to the sun, and also on a horizontal surface, over two geographic positions defined by $\phi = 30^\circ$ and $\phi = -30^\circ$, at 10:00 (solar time) on 14 April, being a clear day. The solution is as follows:

$$14 \text{ April} \Rightarrow d_n = 104; \varepsilon_0 = 0.993; \delta = 9.04^\circ$$

$$10:00 \text{ h} \Rightarrow \omega = -30^\circ$$

$$\phi = 30^\circ \Rightarrow \cos \theta_{\text{ZS}} = 0.819 \Rightarrow \theta_{\text{ZS}} = 35^\circ \Rightarrow \cos \psi_{\text{S}} = 0.508 \Rightarrow \psi_{\text{S}} = -59.44^\circ$$

$$\Rightarrow AM = 1.222 \Rightarrow G = 902.4 \text{ W/m}^2$$

$$\Rightarrow G(0) = G \cdot \cos \theta_{\text{ZS}} = 739 \text{ W/m}^2$$

$$\phi = -30^\circ \Rightarrow \cos \theta_{\text{ZS}} = 0.662 \Rightarrow \theta_{\text{ZS}} = 48.54^\circ \Rightarrow \cos \psi_{\text{S}} = 0.403 \Rightarrow \psi_{\text{S}} = -66.28^\circ$$

$$\Rightarrow AM = 1.510 \Rightarrow G = 846.9 \text{ W/m}^2$$

$$\Rightarrow G(0) = G \cdot \cos \theta_{\text{ZS}} = 561 \text{ W/m}^2$$

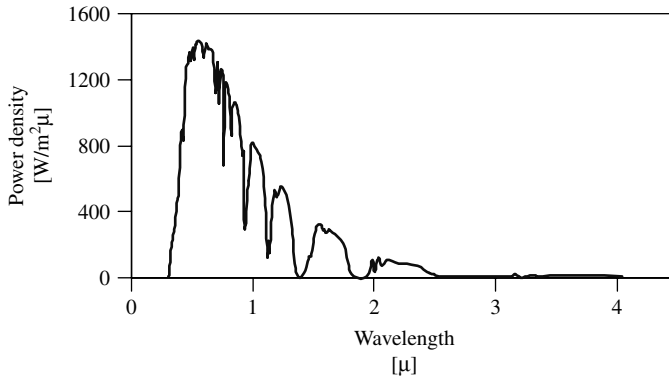


Figure 20.9 AM 1.5 solar spectrum, for an irradiance $G = 1000 \text{ W/m}^2$

When solar radiation enters the Earth's atmosphere, not only the irradiance but also the spectral content is affected. Figure 20.9 shows the AM 1.5 spectrum, which is considered for standard test of PV devices. Figure 16.1 shows other spectra for comparison. In general, increasing air mass displaces the solar spectrum towards the red. This is why the sky becomes so nice at nightfall.

Of course, PV devices are sensitive to the spectrum, as discussed in Chapters 3, 9, 12 and 16. However, this is of little importance from the PV engineering point of view, compared to changes in total radiation incident on the PV modules. Because of that, in what follows, we will omit the detailed treatment of the spectral composition of sunlight. Additional comments will be given later on in this chapter.

20.4 SOLAR RADIATION DATA AND UNCERTAINTY

The amount of global radiation that reaches the receiver is extremely variable. On the one hand, even the extraterrestrial radiation experiences regular daily and yearly variations due to the apparent motion of the sun. These variations are predictable and can be theoretically determined just by geometrical considerations. For example, the extraterrestrial irradiance over a horizontal surface is given by

$$B_0(0) = B_0 \varepsilon_0 \cos \theta_{zs} \quad (20.14)$$

which when integrated over the day, leads to [6]

$$B_{0d}(0) = \frac{T}{\pi} B_0 \varepsilon_0 \left[-\frac{\pi}{180} \omega_S \cdot \sin \delta \cdot \sin \phi - \cos \delta \cos \phi \sin \omega_S \right] \quad (20.15)$$

where T is the day length, that is, 24 h. The monthly average of this quantity, named $B_{0dm}(0)$, is of particular practical importance. Obviously

$$B_{0dm}(0) = \frac{1}{d_{n2} - d_{n1} + 1} \sum_{d_{n1}}^{d_{n2}} B_{0d}(0) \quad (20.16)$$

Table 20.1 Declination and extraterrestrial irradiation values for the characteristic day of each month

Month	Date	d_n	δ [degrees]	$B_{0d}(0) = B_{0dm}(0)$, in [Wh/m ²]			
				$\phi = 30^\circ$	$\phi = 60^\circ$	$\phi = -30^\circ$	$\phi = -60^\circ$
January	17	17	-20.92	5 907	949	11 949	11 413
February	14	45	-13.62	7 108	2 235	11 062	9 083
March	15	74	-2.82	8 717	4 579	9 531	5 990
April	15	105	+9.41	10 225	7 630	7 562	3 018
May	15	135	+18.79	11 113	10 171	5 948	1 225
June	10	161	+23.01	11 420	11 371	5 204	605
July	18	199	+21.00	11 224	10 741	5 530	878
August	18	230	+12.78	10 469	8 440	6 921	2 294
September	18	261	+1.01	9 121	5 434	8 835	4 937
October	19	292	-11.05	7 436	2 726	10 612	8 226
November	18	322	-19.82	6 056	1 114	11 754	10 983
December	13	347	-23.24	5 498	613	12 174	12 177

where d_{n1} and d_{n2} are the day numbers of the first and last day of the month, respectively. It is useful to know that, for a given month, there is a day for which $B_{0d}(0) = B_{0dm}(0)$. It can be demonstrated that this day is the one whose declination equals the mean declination for the month. Table 20.1 shows the day number of this day and the corresponding value of $B_{0dm}(0)$ for each month of the year at several latitudes.

We have also shown that the effect of clear cloudless skies can be predictably accounted for by a single geometrical parameter, namely, the Air Mass (equation 20.12). On the other hand, there are random variations caused by climatic conditions: cloud cover, dust storms and so on so that the PV systems design should rely on the input of measured data close to the site of the installations and averaged over a long time. This is routinely done by the National Meteorological Services (or similar services), which use a variety of instruments and procedures, from direct sunlight measurements (pyranometers, pyrhemometers etc.) to correlations with other meteorological variables (hours of sunshine, cloudiness, tone of satellite photographs etc). Then, they are treated to derive some representative parameters, which are made publicly available by different ways: World radiation databases [7, 8], Regional [9], National [10–12] and local [13] Radiation Atlas, web sites [14, 15] and so on. The 12 monthly mean values of global horizontal daily irradiation, $G_{dm}(0)$, today represent the most widely available information concerning the solar radiation resource, and that is likely to remain in the years to come. It is important to note that solar radiation unavoidably represents a large source of uncertainty for PV systems designers, as revealed by the significant disparity between different information sources. As a representative example, we will consider the case of Madrid.

The Spanish National Meteorological Institute has been recording daily values of hours of sunshine from 1951 to 1980, and hourly global horizontal irradiation data since 1973. This means that the Madrid solar radiation data bank is today composed of more than 50 years of daily indirect observations and more than 25 years of hourly direct ones. Such comprehensive data may appear very gratifying. However, an in-depth examination of the data bank reveals several difficulties: significant data gaps (the most important extends from June 1988 to July 1989); changes of the sensor's calibration constant (in

1977, the IPS-1956 reference was substituted by the WRP); and inconsistencies between global, direct and diffuse irradiation values due to mistakes in graphic record evaluation. All these difficulties must be overcome when computing statistical representative values. Different researchers use different procedures (for example, when considering a set of data of doubtful quality, one can opt to use it directly, or to estimate a best value, or simply to neglect it), arriving at different results. Furthermore, different researchers use different data recording periods for computing representative values (because solar radiation data are being constantly and routinely recorded, this is usually the case). The astonishing result is that a large disparity in representative values is found for the same location, when different publications are consulted. Table 20.2 presents the $G_{dm}(0)$ values for Madrid according to different publications. Large disparities are evident and deserve further comment, because they translate into serious practical consequences. For example, for sizing the PV generator of a stand-alone PV system, it is customary to select the so-called worst month, that is, the month with the lowest value of $G_{dm}(0)$. It is clear that irrespective of the selected sizing methodology, the choice of the particular solar radiation database for Madrid involves PV array size differences up to 12% $[(1.58-1.77)/1.58]$, far beyond the claimed accuracy of most presently available PV sizing methods.

It is important to note that, despite the above-mentioned difficulties, concerning rough solar radiation data, the uncertainty does not derive primarily from a lack of perfect precision in the measuring instruments, but rather from the random nature of the solar radiation, that is, from the overall statistical fluctuations in the collection of finite number of counts over finite intervals of time. This leads us to the question of the real representativeness of the data, or, in more strict terms, to the “confidence” we have that average values, based on past observations of solar radiation, are a correct prediction of the future solar radiation. A close look at the rough recorded data can help to elucidate this question. Figure 20.10 shows the January $G_{dm}(0)$ values corresponding to the years 1979 to 1986, for which very accurate data – let us say, 3% of accuracy – are available, according to Reference [16]. The average value is $\overline{G}_{dm}(0) = 1.99 \text{ kWh/m}^2$. We could then give this value as our estimate for the future. However, if someone now asked the question, “What is the probability that the future $G_{dm}(0)$ will be exactly 1.99 kWh/m^2 ?”, we would have to answer – somewhat uncomfortably – that the probability is no doubt close to zero. However, we would have to hasten to add that if we relax the prediction rigour, just saying that the future $G_{dm}(0)$ values will be within the range of 1.55 to 2.58 kWh/m^2 , as in Figure 20.10, then the probability is high. Note that this range represents $\pm 26\%$ of the

Table 20.2 Values of the mean global daily irradiances $G_{dm}(0)$, in kWh/m^2 , in Madrid according to different publications

Ref	Jan	Feb	Mar	Apr	May	June	July	Aug	Sep	Oct	Nov	Dec	Year
[7]	1.86	2.94	3.78	5.22	5.80	6.53	7.22	6.42	4.69	3.17	2.08	1.64	4.29
[16]	1.99	2.64	4.32	5.32	6.28	7.29	7.47	6.62	5.11	3.40	2.16	1.72	4.53
[94]	2.29	2.81	4.48	5.25	6.60	7.24	7.55	6.33	5.22	3.62	2.10	1.64	4.60
[10]	2.0	2.8	4.4	5.4	6.6	7.4	7.8	7.0	5.4	3.6	2.6	1.8	4.7
[9]	1.73	2.63	4.15	5.45	6.17	6.69	7.22	6.49	4.80	3.16	1.99	1.77	4.36
[95]	2.0	2.91	3.92	5.34	6.31	6.95	7.09	6.31	4.73	3.30	2.18	1.74	4.41
[96]	2.13	2.75	4.55	5.10	6.58	7.43	7.42	6.48	5.00	3.39	2.13	1.58	4.55
[14]	1.94	2.76	4.05	4.84	5.79	6.47	7.05	6.24	4.87	3.07	1.98	1.61	4.23

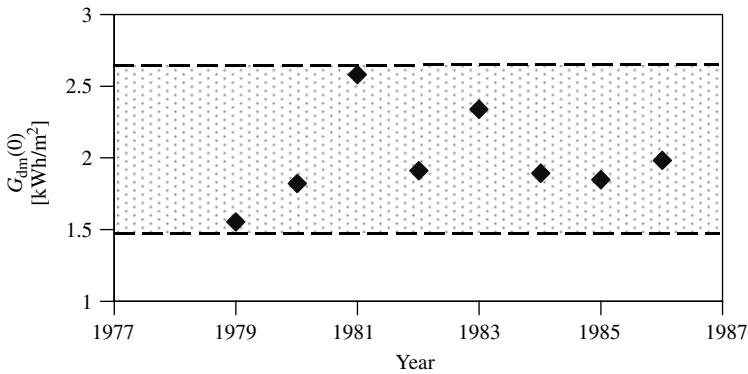


Figure 20.10 January means of the global horizontal irradiation $G_{dm}(0)$ in Madrid, for the years 1979 to 1986, in kWh/m²

average value, much larger than the accuracy of the original data! Then, our questioner's retort would probably be, "How 'high' is the probability and how 'large' is the range?"

Basic statistical theory [17] gives proper answers to this question. For example, if we desire a 99% probability (the *confidence coefficient*) we must keep a $\pm 3\sigma$ range (the *confidence interval*) around the average value, in which σ is the *standard deviation* of the past observed values. In our example, $\sigma = 0.31$ kWh/m², so that $\pm 3\sigma$ represents $\pm 47\%$ of the average value. Still larger than the previously considered range, noted by the band of Figure 20.10! In order to keep on intervals of practical use, a $\pm 2\sigma$ interval is often employed. The corresponding confidence interval is 95%. In our example, $\pm 2\sigma$ represents $\pm 31\%$. Using the 2σ confidence level, the correct way to state the daily global irradiation prediction for the next January would be to say

$$1.37 \text{ kWh/m}^2 \leq G_{dm}(0) \leq 2.61 \text{ kWh/m}^2$$

or

$$G_{dm}(0) = 1.99 \text{ kWh/m}^2 \pm 31\%$$

Probably, surprised by such large uncertainty ($\pm 31\%$ seems badly matched and inconsistent with the "high accuracy" image generally associated with modern computational technology), our questioner would retort, "How can this uncertainty be reduced?" In fact, the only way is by enlarging the number of years of the future for which the prediction applies. That is, to give an estimate not for the next January, but for the average value of the following Januarys. Then, it can be shown that the confidence interval becomes reduced by a factor of $1/\sqrt{N}$, N being the number of future years for which the prediction is extended. Coming back to our example, and considering a future length of 10 years, the correct prediction would be

$$1.79 \text{ kWh/m}^2 \leq G_{dm}(0) \leq 2.19 \text{ kWh/m}^2$$

or

$$G_{dm}(0) = 1.99 \text{ kWh/m}^2 \pm 10\%$$

And still, we are disregarding the instrumental errors – at least $\pm 3\%$ in the best series of solar radiation data – and the causes of variability that can be hidden on a series of only 20 years of data. For example, the ones associated with the Global Climatic Change due to the global emissions of CO_2 . As a matter of fact, it should be noted that some of the $G_{\text{dm}}(0)$ values listed in Table 20.2 for January fall outside this range.

Table 20.3 shows the uncertainty parameters for each month and for the entire year for Madrid, based on data of Reference [16]. It is worth observing that monthly uncertainty is greater in winter than in summer (this is because summer solar radiation is dominated by clear days, essentially governed by the predictable extraterrestrial radiation, while winter solar radiation is strongly influenced by cloudy days, which are governed by random atmospheric phenomena). Besides, uncertainty becomes substantially lower when the whole year is considered (this is because yearly data result from greater aggregates than monthly data, and it is a basic law that the greater the aggregation, the lower the dispersion of the corresponding results). Later on, we will analyse the implications for different PV applications. It should be said that the IES experience in designing PV systems for different locations around the world has led us to believe that the above-described, concerning solar radiation data sources for Madrid, far from being a particular case, is rather representative of a general situation. For example, the December mean daily global horizontal irradiation in New York is $G_{\text{dm}}(0) = 1.36 \text{ kWh/m}^2$ according to Reference [7], 1.47 kWh/m^2 according to Reference [14], and 1.6 kWh/m^2 according to Reference [15]. The interested reader is encouraged to also consult Reference [18].

It is rather obvious that, whatever the detailed methodology, the PV-system design is essentially a prediction exercise extended over the expected system lifetime. From the previous considerations, it follows that such a prediction exercise is unavoidably associated with a rather large degree of uncertainty. Irrespective of whether good historical data are available and whether more complex models are used, any attempt to overcome such uncertainty is simply wrong. We should insist on that because, unfortunately, many authors often forget it when proposing PV-system design tools. This false sense of predictability and regularity in the solar radiation is, to a certain extent, being boosted by the proliferation of software-based tools, that are able to perform extremely detailed simulations with large sequences of solar radiation data. The great “accuracy” of their calculations tends to confer an impressive “scientific” appearance to these tools, and foster the tendency to believe that their results are superior to others. However, the truth is that such great accuracy is statistically meaningless, and that, much more simple design methodologies can yield results of similar confidence. We should keep this idea in mind all through this chapter.

Table 20.3 Solar radiation parameters for Madrid. Mean G_{dm} and standard deviation values σ are given in kWh/m^2 , while $2\sigma/G_{\text{dm}}$ is given in %

	Jan	Feb	Mar	Apr	May	June	July	Aug	Sep	Oct	Nov	Dec	Mean
G_{dm}	1.99	2.64	4.32	5.32	6.28	7.29	7.47	6.62	5.11	3.4	2.16	1.72	4.53
σ	0.31	0.31	0.36	0.39	0.64	0.34	0.31	0.18	0.36	0.39	0.36	0.17	0.08
$2\sigma/G_{\text{dm}}$	31	23	17	15	20	9	8	8	14	23	34	20	4

20.4.1 Clearness Index

The relation between the solar radiation at the Earth's surface and the Extraterrestrial radiation gives a measure of the atmospheric transparency. This way, a *clearness index*, K_{Tm} , is calculated for each month:

$$K_{Tm} = \frac{G_{dm}(0)}{B_{0dm}(0)} \quad (20.17)$$

Note that the clearness index is physically related not only to the radiation path through the atmosphere, that is, with the AM value, but also with the composition and the cloud content of the atmosphere. Liu and Jordan [19] have demonstrated that, irrespective of latitude, the fractional time during which daily global radiation is equal to or less than a certain value is directly dependent on this parameter. Because of that, K_{Tdm} can properly characterise the solar climate of a particular location. This provides the basis for estimating solar radiation on inclined surfaces.

20.5 RADIATION ON INCLINED SURFACES

To eliminate the effects of varying local features, such as obstructions that cast shadows and the specific ground covering, solar radiation is routinely measured on horizontal surfaces free of obstacles. Consequently, solar radiation data are most often given in the form of global radiation on a horizontal surface. Since PV modules are usually positioned at an angle to the horizontal plane, the radiation input to the system must be calculated from the data.

The assessment of radiation arriving on an inclined surface, using as input global horizontal data, raises two main problems: to separate the global horizontal radiation into their direct and diffuse components; and, from them, to estimate the radiation components falling on an inclined surface. In general, these problems may be posed for different time scales, for example, daily irradiation, hourly irradiation and so on. Individual or time-averaged values may be sought. Here, we will first focus on the monthly average daily irradiation values. This is not only convenient for presentation purposes, but also coherent with solar radiation data availability, and particularly suited to afford most PV engineering practical problems. Additional comments for other cases will also be given afterwards.

20.5.1 Estimation of the Direct and Diffuse Components of Horizontal Radiation, Given the Global Radiation

The underlying concept is the one originally proposed by Liu and Jordan [19]. It consists of establishing empirical correlation between the *diffuse fraction of horizontal radiation*, $F_{Dm} = D_{dm}(0)/G_{dm}(0)$, (diffuse radiation/global radiation) and the *clearness index* (global radiation/extraterrestrial radiation) defined in equation (20.17). Note that the clearer the atmosphere, the higher the radiation and the lower the diffuse content. Hence, F_{Ddm} and K_{Tdm} are expected to be negatively correlated. Actual analytical expressions are established from the comparison of simultaneous measurements of global and diffuse radiation

performed in certain places. Liu and Jordan were, in fact, very clever in selecting the clearness index (which they called the cloudiness index) to characterise the solar climate at a particular location, because the division by the extraterrestrial radiation eliminates the radiation variations due to the apparent motion of the sun. This way, the correlation between F_{Dm} and K_{Tm} becomes independent of latitude effects, and, in principle, tends to be of universal validity.

Various empirical formulae are available. Using data from ten locations situated between 40°N and 40°S , Page [20] recommended a liner equation that has been frequently identified as the one giving the best results.

$$F_{Dm} = 1 - 1.13K_{Tm} \quad (20.18)$$

Figure 20.11 plots equation (20.18) and a set of experimental points, obtained in Madrid, from 1977 to 1988.

Example: Determination of direct and diffuse components of the global radiation for the month of June in a location having a latitude $\phi = 30^\circ$ and a mean global horizontal daily irradiation $G_{dm}(0) = 6100 \text{ Wh/m}^2$. The solution is

$$\phi = 30 \text{ and June} \Rightarrow B_{0dm}(0) = 11\,420 \text{ Wh/m}^2 \text{ (See Table 20.1)}$$

$$G_{dm}(0) = 6100 \text{ Wh/m}^2 \Rightarrow K_{Tm} = 0.534 \Rightarrow F_{Dm} = 0.396 \Rightarrow D_{dm}(0) = 2418 \text{ Wh/m}^2 \\ \Rightarrow B_{dm}(0) = 3682 \text{ Wh/m}^2$$

Empirical correlations between the diffuse fraction of the horizontal irradiation and the clearness index can also be derived for an individual day (April 14 is, for example, an individual day, while generic April is a monthly mean day). They should be described here because they have been the object of extensive research in the general solar radiation community and, as a result they have received large attention in the available literature, and they are often employed in today's available PV engineering software tools. However, it should be advised that their advantage for PV design purposes is far from clear. As a matter of fact, the electrical behaviour of PV generators is mainly governed by the linear

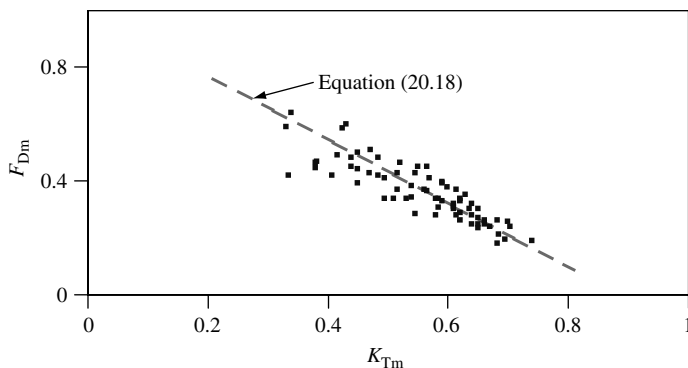


Figure 20.11 The diffuse fraction of the mean daily global irradiation F_{Dm} is plotted against the clearness index K_{Tm} . The cluster of points refers to measured values in Madrid from 1977 to 1988

dependence incident irradiance. It follows that the mean power they deliver during a period of time tends to be equal to the delivered power when they are illuminated with the mean irradiance during such time. Second-order effects, associated to ambient temperature or operation voltage fluctuations, do not significantly alter this idea, provided that they are adequately considered, as discussed afterwards. Because of that, rather few benefits, in terms of long-term performance predictions, should be expected from analysing all the days of a month instead of only the mean day of such a month. The reason for the popularity of individual day analysis in recently available software tools, lies more with fashion and prestige than with increasing energy yield prediction certainty.

Figure 20.12 shows the experimental values of $F_{Dd} = D_d(0)/G_d(0)$ versus $K_{Td} = G_d(0)/B_{0d}(0)$, obtained in Madrid, from 1977 to 1988. Each point derives from the simultaneous measurement of the diffuse and the global horizontal irradiation along a particular day. Note that the general trend is consistent with the principle that the clearer the atmosphere, the lower the diffuse content. A third-order or fourth-order polynomial in K_{Td} is generally used to model the diffuse fraction F_{Dd} . A correlation between F_{Dd} and K_{Td} was first developed by Liu and Jordan [19]. However, it was derived from diffuse radiation data that were not compensated for by shadow-band effects (the shadow band is a device added to a pyranometer, to exclude the direct radiation from the sun. Hence, it allows for the measurement of diffuse radiation. However, the shadow-band screens the sensor not only from the sun but also from a portion of the diffuse radiation coming in from the sky, so that, a correction must be made to the measurement). Not surprisingly, later revisions by other authors concluded that the Liu and Jordan correlation underestimates diffuse radiation.

The most frequently referred correlation for daily values is that put forward by Collares Pereira and Rabl [21], using data from five stations located in the United States. It is expressed as

$$F_{Dd} = 0.99 \text{ for } K_{Td} \leq 0.17$$

$$F_{Dd} = 1.188 - 2.272K_{Td} + 9.473K_{Td}^2 - 21.856K_{Td}^3 + 14.648K_{Td}^4 \quad (20.19)$$

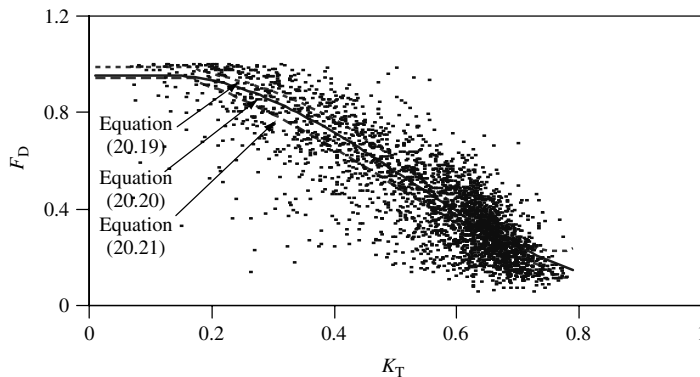


Figure 20.12 The diffuse fraction of the individual daily global irradiation F_{Dd} is plotted against the clearness index K_{Td} . The cluster of points refers to measured values in Madrid from 1977 to 1988

Despite independence of latitude, other second-order factors can affect the observed correlations, leading to a certain site dependence. For example, at very high latitudes, perennial snow cover could significantly increase diffuse radiation caused by multiple reflections between the ground and cloud cover. Also, atmospheric humidity tends to increase scattering, in relative terms. Hence, for a given clearness index, locations with low humidity will tend to have the lowest diffuse radiation content. Because of that, and because radiation data are still being accumulated and revised, new correlations are continuously enlarging the available literature. A recent study [22], devoted to the development of solar radiation models for the Mediterranean area, has found about 250 different correlations in the literature. The same study, extended to more than 150 000 pairs of data from eleven different stations of the European network, has proposed the following expression

$$\begin{aligned}
 F_{Dd} &= 0.952 \text{ for } K_{Td} \leq 0.13 \\
 F_{Dd} &= 0.868 + 1.335K_{Td} - 5.782K_{Td}^2 + 3.721K_{Td}^3 \\
 &\quad \text{for } 0.13 < K_{Td} \leq 0.8 \\
 F_{Dd} &= 0.141 \text{ for } K_{Td} > 0.8
 \end{aligned}
 \tag{20.20}$$

Local correlations that are derived from the data of only one site can also be found. As an example, Macagnan [16] proposed the following for Madrid

$$\begin{aligned}
 F_{Dd} &= 0.942 \text{ for } K_{Td} \leq 0.18 \\
 F_{Dd} &= 0.974 + 0.326K_{Td} - 3.896K_{Td}^2 + 2.661K_{Td}^3 \\
 &\quad \text{for } 0.18 < K_{Td} \leq 0.79 \\
 F_{Dd} &= 0.115 \text{ for } K_{Td} > 0.79
 \end{aligned}
 \tag{20.21}$$

Such diversity of correlations can again perplex our hypothetical questioner, who would ask, “What correlation should I use?” Hence, it is worth to study further the implications of using one or the other.

On the one hand, it should be remembered that the uncertainty associated with the variability of observed individual data, as described in the previous section for global radiation, also applies here. The cluster of (F_{Dd}, K_{Td}) points in Figure 20.12 reveals that, for a given K_{Td} , very different F_{Dd} values can be found in reality. For example, the observed range for $K_{Td} = 0.5$ is $0.1 \leq F_{Dd} \leq 0.7$, that is $\pm 75\%$ around the mean value. In more strict terms, a measure of the dispersion of expected observations around the prediction derived from a particular correlation, is given by the so-called Root Mean Square Error, or Standard Error of Estimate, s_e . As with the standard deviation, $\pm 2s_e$ is the interval, around the predicted value, for 95% confidence. In general, s_e are larger than 25%, which means that, regardless of the selected correlation, we would nearly always expect real values of diffuse irradiation for individual days falling between $\pm 50\%$ of the predictions. It is also interesting to observe that the dispersion associated with individual days (Figure 20.12) is significantly larger than the dispersion associated with monthly means (Figure 20.11).

On the other hand, when long-term performance predictions are concerned – which is the standard case on PV design – the implications of using different correlations are in

fact very modest. As a representative exercise, we have calculated the daily irradiation incident on a surface tilted to the latitude in Djelfa-Algeria ($\phi = 34.6^\circ$), for a winter day ($d_n = 17$) and for a summer day ($d_n = 161$), using the different correlations defined by equations (20.19–20.21). Djelfa and Madrid are relatively similar on geographical altitude and solar climate. Hence, it is reasonable to assume that the same local correlation could be applied to both places. $G_d(0) = 2778$ and 6972 Wh/m^2 for the winter and for the summer day, respectively. This radiation data has been obtained from Reference [7], by assuming that the value of the global irradiation during these days coincides with the corresponding monthly averages. Details of the calculating procedure will be given in the next section, but they are not relevant for the present discussion. The results are as follows:

$$d_n = 17 \Rightarrow B_{0d}(0) = 5177 \text{ Wh/m}^2$$

$$G_d(0) = 2778 \text{ Wh/m}^2 \Rightarrow K_{Td} = 0.537$$

Eq.	F_{Dd}	$D_d(0)$ in [Wh/m ²]	$G_d(\phi)$ in [Wh/m ²]
20.19	0.5301	1472	3946
20.20	0.5067	1408	4008
20.21	0.4351	1209	4185

$$d_n = 161 \Rightarrow B_{0d}(0) = 11\,525 \text{ Wh/m}^2$$

$$G_d(0) = 6972 \text{ Wh/m}^2 \Rightarrow K_{Td} = 0.605$$

Eq.	F_{Dd}	$D_d(0)$ in [Wh/m ²]	$G_d(\phi)$ in [Wh/m ²]
20.19	0.4034	2813	5988
20.20	0.4031	2811	5988
20.21	0.3345	2332	5940

Significant differences are observed in the estimation of the diffuse component of the horizontal irradiation. However, the noticeable key point is that these differences are significantly lessened in the estimation of the global irradiation. For example, for the winter day, differences on the diffuse component reach 22% while differences on the global radiation are lower than 6%.

Now, it is worth noting that, to a certain extent, we can cite a physical reason for the differences, considering the primary role of scattering in the diffusion of solar radiation. Equation (20.19) was derived from northern latitudes, with higher air masses than the Mediterranean region (higher air mass means higher scattering and, consequently, higher diffuse radiation content), and Madrid is a relatively high altitude site (670 m over the sea level) and its climate is essentially dry (both, higher altitude and lesser humidity

means lesser scattering). Note that the correlative order of the results agrees with this physical explanation.

To summarize, an adequate answer to our hypothetical questioner is as follows:

1. Most PV engineering problems are properly solved using a monthly mean analysis. Then, equation (20.18) is the recommended choice.
2. If you require a day-to-day analysis, the choice of a particular diffuse-to-global correlation is not really critical. You can simply adhere to the widely extended practise of trusting on the “universal” character of equation (20.19). But, if you are interested in a specific site, you can perform slightly better by choosing a more site-specific correlation, providing it is derived from solar radiation measurements in a place having a similar climate to the concerned site.
3. Whichever possibility you choose, you must take a very important precaution. If your results are going to be compared with the results of another calculation (for example, comparing different PV module orientations for the same application), then be sure that they both use the same assumptions, correlations, model and data. Otherwise, the differences in the results would be completely meaningless. Although this caveat should be obvious, it still should be mentioned, because the literature contains several examples of different results derived from different correlations that were proposed as the basis of optimisation design exercises [23].

Finally, it should be mentioned that not only daily but also hourly based correlations have been proposed. These are correlations between the diffuse fraction of the hourly horizontal global irradiation, $F_{Dh} = D_h(0)/G_h(0)$, and the hourly clearness index, $K_{Th} = G_h(0)/B_{0h}(0)$. However, none of the hourly based correlations proposed so far is really satisfactory [6, 22], so that the associated complexity is not justified. Hence, they will be not considered here.

20.5.2 Estimation of the Hourly Irradiation from the Daily Irradiation

In some cases, the treatment of solar radiation is more easily understood at the instant time scale, that is, at the radiance level. Because irradiation over an hour (in Wh/m^2) is numerically equal to the mean irradiance during this hour (in W/m^2), irradiance values can be, to a certain extent, assimilated to hourly irradiation values. However, since the availability of hourly irradiation data is limited, the problem is how to estimate the hourly irradiation, given the daily irradiation.

To introduce the solution to this problem, it is highly instructive to observe that, in terms of extraterrestrial horizontal radiation, the ratio between irradiance, $B_0(0)$, and daily irradiation, $B_{0d}(0)$, can be theoretically determined from equations (20.4), (20.14) and (20.15).

$$\frac{B_0(0)}{B_{0d}(0)} = \frac{\pi}{T} \times \frac{\cos \omega - \cos \omega_S}{\left(\frac{\pi}{180} \omega_S \cos \omega_S - \sin \omega_S \right)} \quad (20.22)$$

where the sunrise angle, ω_S , is expressed in degrees and T , the day length, is usually expressed in hours.

From the examination of data from several stations, it has been repeatedly noted [19, 24] that, considering long-term averages of terrestrial radiation, the correspondence between the measured ratio of diffuse irradiance to diffuse daily irradiation, $r_D = D(0)/D_d(0)$, and this theoretical expression for extraterrestrial radiation (equation 20.22) is quite good, while the correspondence between the measured ratio of global irradiance to global daily irradiation, $r_G = G(0)/G_d(0)$, and this expression, although not perfect, is quite close, so that a slight modification is required to fit the observed data. The following expressions apply [21]:

$$r_D = \frac{D(0)}{D_d(0)} = \frac{B_0(0)}{B_{0d}(0)} \quad (20.23)$$

and

$$r_G = \frac{G(0)}{G_d(0)} = \frac{B_0(0)}{B_{0d}(0)}(a + b \cos \omega) \quad (20.24)$$

where a and b are obtained from the following empirical formulae:

$$a = 0.409 - 0.5016 \times \sin(\omega_S + 60) \quad (20.25)$$

and

$$b = 0.6609 + 0.4767 \times \sin(\omega_S + 60) \quad (20.26)$$

Note that r_D and r_G have units of T^{-1} , and that they can be extended to calculate irradiances during short periods centred on the considered instant, ω . For example, if we wish to evaluate the irradiation over one hour between 10:00 and 11:00 (in solar time), we set $\omega = -22.5^\circ$ (the centre time of the considered period is 10:30, i.e. one hour and half, or 22.5° , before noon) and $T = 24$ h. If we wish to evaluate the irradiation over one minute, we just have to express T in minutes, that is, we set it to 1440, the number of minutes in a day.

An example can help in the use of these equations: the calculation of the irradiance components at several moments along the 15 April in Portoalegre–Brasil ($\phi = -30^\circ$), knowing the global daily irradiation, $G_d(0) = 3861 \text{ Wh/m}^2$. The results are as follows:

$$d_n = 105 \Rightarrow B_{0d}(0) = 7562 \text{ Wh/m}^2 \Rightarrow K_{Td} = 0.5106 \Rightarrow F_{Dd} = 0.423$$

$$\Rightarrow D_d(0) = 1633 \text{ Wh/m}^2$$

$$\omega_S = -84.51^\circ$$

$$\frac{\pi}{180} \omega_S \cos \omega_S - \sin \omega_S = 0.8542$$

$$a = 0.6172$$

$$b = 0.4672$$

$$r_D = 0.0922(\cos \omega + 0.0967) \text{ h}^{-1}$$

$$r_G = r_D(a + b \cos \omega)$$

ω°	r_D [h ⁻¹]	r_G [h ⁻¹]	$D(0)$ in [Wm ⁻²]	$G(0)$ in [Wm ⁻²]	$B(0)$ in [Wm ⁻²]
ω_s	0	0	0	0	0
± 60	0.0618	0.0529	100.94	204.25	103.31
± 30	0.1177	0.1211	192.24	467.58	275.34
0	0.1382	0.1508	225.73	582.24	356.51

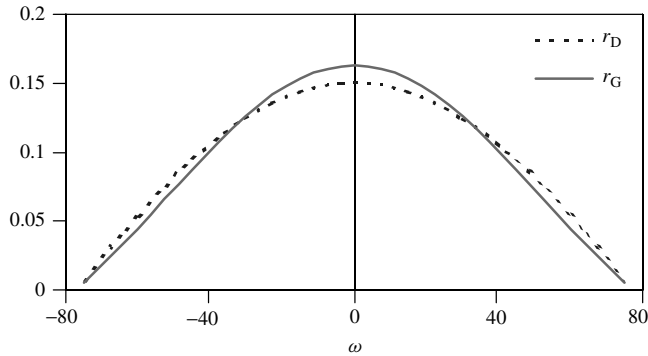


Figure 20.13 Plots of irradiance to daily irradiation ratios, for both diffuse and global radiation, r_D and r_G , along the day at a latitude $\phi = -30^\circ$ for 15 April

Figure 20.13 plots r_D and r_G versus the solar time, along the day. It is interesting to observe that r_G is slightly more sharp-pointed than r_D . This is because, due to air mass variations, beam transmittance is higher at noon than at any other moment of the day. Obviously, integrating the areas below both, r_D and r_G must be equal to one. As already mentioned, for this calculation it can be assumed that the irradiation over one hour (in Wh/m²) is numerically equal to the mean irradiance during this hour and also equal to the irradiance at the instant half way through the hour. For example, the global irradiance at noon, $G(0) = 580.4 \text{ W/m}^2$ can be identified with the hourly irradiation from 11:30 to 12:30, $G_h(0) = 580.4 \text{ Wh/m}^2$. This assumption does not introduce significant errors and it greatly simplifies the calculations by eliminating the need to evaluate integrals with respect to time, which, otherwise, can be quite tedious.

From these equations, it can be deduced that, on any day of the year and anywhere in the world, 90% of the total global horizontal irradiation is received during a period centred around midday and of length equal to two-thirds the total sunlight day length. Consequently, a stationary receiver tilted to the equator ($\alpha = 0$) captures all the useful energy in this period. The same need not be true, however, of receivers that track the sun.

20.5.3 Estimation of the Radiation on Surfaces on Arbitrary Orientation, Given the Components Falling on a Horizontal Surface

The most obvious procedure for calculating the global irradiance on an inclined surface, $G(\beta, \alpha)$, is to obtain separately the direct, diffuse and albedo components, $B(\beta, \alpha)$,

$D(\beta, \alpha)$ and $R(\beta, \alpha)$, respectively. Once these are known

$$G(\beta, \alpha) = B(\beta, \alpha) + D(\beta, \alpha) + R(\beta, \alpha) \quad (20.27)$$

20.5.3.1 Direct irradiance

Straightforward geometrical considerations lead to

$$B(\beta, \alpha) = B \max(0, \cos \theta_S) \quad (20.28)$$

where B is the direct irradiance falling on a surface perpendicular to the sun's rays, and $\cos \theta_S$ is the angle of incidence between the sun's rays and the normal to the surface, given by equation (20.9). B can be obtained from the corresponding value on a horizontal surface

$$B = \frac{B(0)}{\cos \theta_{ZS}} \quad (20.29)$$

Note that when the sun is illuminating the back of the surface (for example, during all morning on a vertical surface oriented to the west) $|\theta_S| > \pi/2$. Then, $\cos \theta_S < 0$ and $B = 0$. This way, the factor $\max(0, \cos \theta_S)$ reflects that the irradiance incident on the back surface of PV modules is normally not utilised.

20.5.3.2 Diffuse irradiance

We can assume that, when the sun is occluded, the sky is composed of elemental solid angles, such as $d\Omega$ (Figure 20.14) from which a diffuse radiance $L(\theta_Z, \psi)$ is emanated towards the horizontal surface. The term radiance is taken to mean the flux of energy per unit solid angle crossing a surface normal to the direction of the radiation. It is expressed in $\text{W/m}^2 \cdot \text{steradian}$.

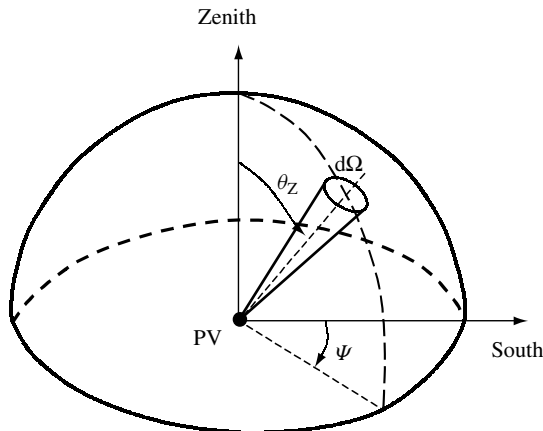


Figure 20.14 Angular co-ordinates, θ_Z and ψ , of an elemental solid angle of the sky

Then, the horizontal irradiance is equal to the integration of the contribution of each solid angle, and can be written as

$$D(0) = \int_{\text{sky}} L(\vartheta_Z, \psi) \cos \vartheta_Z d\Omega \quad (20.30)$$

where the integral is extended to the whole sky, that is, $0 \leq \theta_Z \leq \pi/2$ and $0 \leq \psi \leq 2\pi$.

When we are dealing with an inclined surface, a similar reasoning leads to

$$D(\beta, \alpha) = \int_{\alpha} L(\vartheta_Z, \psi) \cos \vartheta'_Z d\Omega \quad (20.31)$$

where ϑ'_Z is the incident angle from the solid angle element to the inclined surface, and α means the integral is extended to the non-obstructed sky. The general solution of this equation is difficult because, under realistic skies, the radiance is not uniform and varies with the sky condition. For example, the form, brightness and position of clouds strongly affect the directional properties of the radiance.

The distribution of radiance over the sky is not measured routinely. Nevertheless, a number of authors [25, 26] have developed instruments to measure it and have presented results for different sky conditions. Some general patterns may be discerned from these.

With clear skies, the maximum diffuse radiance comes from the parts of the sky close to the sun and to the horizon. The minimum radiances come from a region at an angle of 90° to the solar zenith (Figure 20.15). The diffuse radiation coming from the region close to the sun is called *circumsolar radiation* and is mainly due to the dispersion by aerosols. The angular extent of the sun's aureole depends mainly on the turbidity of

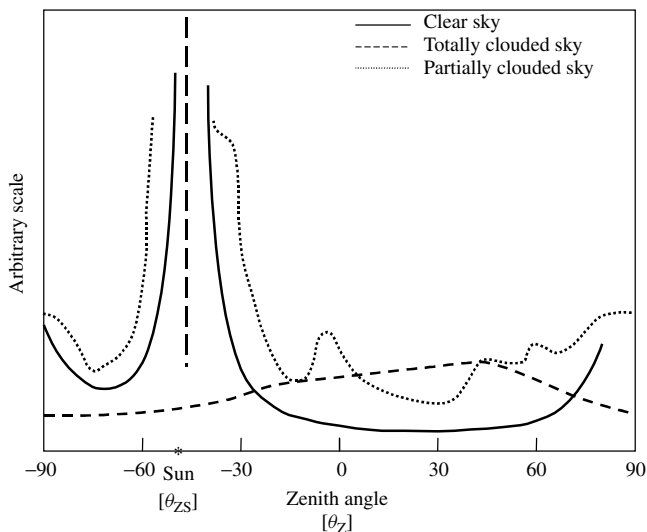


Figure 20.15 Typical angular distribution of the sky irradiance. The values are taken along the length of the meridian containing the sun, $\psi = \psi_S$

the atmosphere and on the zenith angle of the sun. The increase in diffuse radiance near the horizon is due to the albedo radiation of the Earth and is called *horizon brightening*.

The radiance distributions associated with overcast skies are very well described by Kondratyev: “for dense non-transparent cloudiness, the azimuthal dependence of diffuse radiation intensity is very weak. There is a slight monotonic increase of the radiance from the horizon upward towards the zenith” [27].

Some models can be derived from these general ideas. The simplest model makes use of the assumption that the sky radiance is isotropic, that is, every point of the celestial sphere emits light with equal radiance, $L(\theta_Z, \psi) = \text{constant}$. The solution of equations (20.30 and 20.31) leads then to

$$D(\beta, \alpha) = D(0) \frac{1 + \cos \beta}{2} \quad (20.32)$$

Because of its simplicity, this model has achieved great popularity, despite the fact that it systematically underestimates diffuse irradiance on surfaces tilted to the equator.

The opposite approach assumes that all the diffuse radiation is circumsolar, that is, from the sun. This is really a case of treating diffuse radiation as though it were direct, and leads to

$$D(\beta, \alpha) = \frac{D(0)}{\cos \theta_{ZS}} \max(0, \cos \theta_S) \quad (20.33)$$

This model also has the advantage of being very simple to use, but in general it overestimates diffuse irradiances.

In general, better results are obtained with so called anisotropic models. Hay and Davies [28] proposed to consider the diffuse radiation as composed by a circumsolar component coming directly from the direction of the sun, and an isotropic component coming from the entire celestial hemisphere. Both components are weighted according to the so-called anisotropy index, k_1 , defined as

$$k_1 = \frac{B(0)}{B_0(0)} = \frac{B}{B_0 \varepsilon_0} \quad (20.34)$$

The solution of equation (20.31) is now

$$D(\beta, \alpha) = D^I(\beta, \alpha) + D^C(\beta, \alpha) \quad (20.35)$$

where

$$D^I(\beta, \alpha) = D(0)(1 - k_1) \frac{1 + \cos \beta}{2} \quad (20.36)$$

and

$$D^C(\beta, \alpha) = \frac{D(0)k_1}{\cos \theta_{ZS}} \max(0, \cos \theta_S) \quad (20.37)$$

respectively, define the contribution of the isotropic and of the circumsolar components.

Note that k_1 is just the ratio between a pyrheliometer's reading and the solar constant, once corrected by the eccentricity due to the ecliptic orbit of the Earth around the sun. This way, k_1 can be understood as a measure of the instantaneous atmospheric transmittance for direct irradiance. When the sky is completely clouded over, $k_1 = 0$ and the above equation becomes the same as that for the simple isotropic model. This anisotropic model is an excellent compromise between simplicity and precision. It has been well-validated against measurements performed at different worldwide locations, and has been extensively used, for example, for the elaboration of the European Atlas of the Solar Radiation [9].

Also, very commonly employed, in particular with digital machines, is the model that has been put forward by Perez [29, 30]. It divides the sky into three zones acting as diffuse radiation sources: a circumsolar region, a horizontal band and the rest of the celestial hemisphere. The relative contributions of each component is modulated by means of empirical factors determined from the study of data from 18 measurement stations at 15 sites in North America and Europe. The Perez model used to perform slightly better than others [31], because the larger number of modulating factors allows for the consideration of a larger number of different sky conditions.

20.5.3.3 Albedo irradiance

The reflectivity of most types of ground is rather low. Consequently, the contribution of the albedo irradiance falling on a receiver is generally small. (An exception occurs in the case of snow.) There is therefore no point in developing very sophisticated models for albedo. It is usual to assume that the ground is horizontal and of infinite extent and that it reflects isotropically. On this basis, the albedo irradiance on an inclined surface is given by

$$R(\beta, \alpha) = \rho G(0) \frac{1 - \cos \beta}{2} \quad (20.38)$$

where ρ is the reflectivity of the ground and depends on the composition of the ground. When the value of ρ is unknown, it is common to take $\rho = 0.2$

It is now opportune to go forward with the example of the previous section, by calculating the irradiance components over a surface tilted to the latitude, the 15 April in Portoalegre-Brazil. Using equations (20.34) to (20.37) to deal with diffuse radiation and $\rho = 0.2$, the results, expressed in W/m^2 , are as follows:

ω	k_1	$D^I(\phi)$	$D^C(\phi)$	$B(\phi)$	$R(\phi)$	$G(\phi)$
ω_s	0	0	0	0	0	0
$\pm 60^\circ$	0.2205	73.40	31.80	147.56	2.73	255.49
$\pm 30^\circ$	0.3082	124.14	76.94	357.14	6.26	564.48
0°	0.3403	138.97	98.09	455.31	7.80	700.18

It becomes clear that the albedo can be generally neglected in PV calculations.

20.5.3.4 Daily irradiation

The most accurate way of calculating $G_{\text{dm}}(\beta, \alpha)$ from $G_{\text{dm}}(0)$ is, first, to calculate the hourly horizontal irradiation components $G_{\text{hm}}(0)$, $D_{\text{hm}}(0)$ and $B_{\text{hm}}(0)$; second, to transpose them to the inclined surface $G_{\text{hm}}(\beta, \alpha)$, $D_{\text{hm}}(\beta, \alpha)$ and $B_{\text{hm}}(\beta, \alpha)$; and, finally, to integrate during the day.

Such a procedure, summarised in Figure 20.16, allows us to account for the anisotropic properties of diffuse radiation, and leads to good results whatever the orientation of the inclined surface. However, it is laborious to apply and a computer must be used. It is interesting to mention that, for the case of surfaces tilted to the equator ($\alpha = 0$), frequently encountered in photovoltaic applications, if the diffuse radiation is taken to be isotropic, the following expression may be applied

$$G_{\text{d}}(\beta, 0) = B_{\text{d}}(0) \times RB + D_{\text{d}}(0) \frac{1 + \cos \beta}{2} + \rho G_{\text{d}}(0) \frac{1 - \cos \beta}{2} \quad (20.39)$$

where the factor RB represents the ratio between the daily direct irradiations on an inclined surface and on an horizontal surface, and may be approximated by setting it equal to the corresponding ratio between daily extraterrestrial irradiations on similar surfaces. Hence, RB is given as follows:

$$RB = \frac{\omega_{\text{SS}} \frac{\pi}{180} [\text{sign}(\phi)] \sin \delta \sin(|\phi| - \beta) + \cos \delta \cos(|\phi| - \beta) \sin \omega_{\text{SS}}}{\omega_{\text{S}} \frac{\pi}{180} \sin \delta \sin \phi + \cos \delta \cos \phi \sin \omega_{\text{S}}} \quad (20.40)$$

where ω_{SS} is the sunrise angle on the inclined surface, which is given by

$$\omega_{\text{SS}} = \max[\omega_{\text{S}}, -\arccos(-[\text{sign}(\phi)] \tan \delta \tan(\text{abs}(\phi) - \beta))] \quad (20.41)$$

It is interesting to observe that for the equinox days, $\delta = 0 \Rightarrow \omega_{\text{S}} = \omega_{\text{SS}}$ and equation (20.40) becomes $RB = \cos[\text{abs}(\phi) - \beta] / \cos \phi$.

Example: Estimate the average daily irradiation in January at Changchun–China ($\phi = 43.8^\circ$) over a fixed surface facing south and tilted at an angle $\beta = 50^\circ$ with respect to the horizontal, knowing that the mean value of the global horizontal irradiation is $G_{\text{dm}}(0) = 1861 \text{ Wh/m}^2$ and the ground reflection $\rho = 0.2$. The solution is as follows:

$$\text{January} \Rightarrow d_{\text{n}} = 17; \delta = -20.92^\circ$$

$$\phi = 43.8^\circ \Rightarrow \omega_{\text{S}} = -68.50 \text{ and } B_{\text{0d}}(0) = 3586 \text{ Wh/m}^2 \Rightarrow K_{\text{Tm}} = 0.519$$

$$\Rightarrow F_{\text{Dm}} = 0.414$$

$$D_{\text{dm}}(0) = 770 \text{ Wh/m}^2; B_{\text{dm}}(0) = 1091 \text{ Wh/m}^2$$

$$\arccos(-\tan \delta \tan(\phi - \beta)) = -92.38^\circ \Rightarrow \omega_{\text{SS}} = -68.5^\circ \Rightarrow RB = 2.741$$

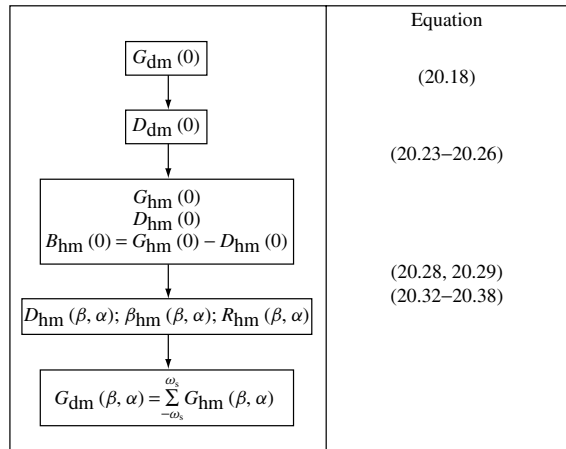


Figure 20.16 Diagram explaining the calculation of the daily irradiation on an inclined surface $G_{dm}(\beta, \alpha)$ from the corresponding horizontal value $G_{dm}(0)$

$$D_{dm}(50) = 633 \text{ Wh/m}^2; B_{dm}(50) = 2990 \text{ Wh/m}^2; R_{dm}(50) = 66 \text{ Wh/m}^2$$

$$G_{dm}(50) = 3689 \text{ Wh/m}^2$$

It is worth mentioning that a more detailed calculation, following the procedure outlined in Figure 20.16, would lead to $G_{dm}(50) = 3956 \text{ Wh/m}^2$. That means the error associated to equation (20.40) is below 8%. This difference is mainly due to the different consideration of the diffuse radiance distribution.

20.6 DIURNAL VARIATIONS OF THE AMBIENT TEMPERATURE

The behaviour of the photovoltaic modules depends, to some extent, on the ambient temperature. Just as it is for solar radiation, sometimes it is necessary to determine how this parameter varies throughout the day. The data available as a starting point for this calculation are, in general, the maximum and minimum temperature of the day, T_{aM} and T_{am} , respectively.

A model that is simple but, nevertheless, gives a good fit to the experimental values is obtained from the fact that the temperature evolves in a similar manner to the global radiation but with a delay of about 2 h. This fact allows the following three principles to be deduced

- T_{am} occurs at sunrise ($\omega = \omega_s$).
- T_{aM} occurs two hours after midday ($\omega = 30^\circ$).
- Between these two times, the ambient temperature develops according to two semi cycles of a cosine function: one from dawn to midday, and the other between midday and sunrise of the following day.

The following set of equations based on the above, permits the ambient temperature throughout a day j to be calculated as follows:

For $-180 < \omega \leq \omega_S$

$$T_a(j, \omega) = T_{aM}(j-1) - \frac{T_{aM}(j-1) - T_{am}(j)}{2} [1 + \cos(a\omega + b)] \quad (20.42)$$

with $a = \frac{-180}{\omega_S + 330}$ and $b = -a\omega_S$

For $\omega < \omega_S \leq 30$

$$T_a(j, \omega) = T_{am}(j) + \frac{T_{aM}(j) - T_{am}(j)}{2} [1 + \cos(a\omega + b)] \quad (20.43)$$

with $a = \frac{180}{\omega_S - 30}$ and $b = -30a$

For $30 < \omega \leq 180$

$$T_a = T_{aM}(j) - \frac{T_{aM}(j) - T_{am}(j+1)}{2} [1 + \cos(a\omega + b)] \quad (20.44)$$

with $a = \frac{180}{\omega_S + 330}$ and $b = -(30a + 180)$

To apply these equations, it is necessary to know the maximum temperature on the previous day, $T_{aM}(j-1)$, and the minimum temperature of the following day, $T_{am}(j+1)$. If these data are unavailable, then it can be assumed, without introducing too much error, that they equal those for the day in question.

20.7 EFFECTS OF THE ANGLE OF INCIDENCE AND OF THE DIRT

The reflectance and transmittance of optical materials depends on the angle of incidence. Glass covers of solar collectors are not an exception and therefore the optical input of photovoltaic modules is affected by their orientation with respect to the sun, due to the angular variation of the glass reflection. Theoretical models, based on the well-known Fresnel formulae, have been developed for clean surfaces. The most popular formulation is from ASHRAE [32]. For a given incidence angle, θ_S , it can be described by the simple expression

$$FT_B(\theta_S) = 1 - b_0 \left(\frac{1}{\cos \theta_S} - 1 \right) \quad (20.45)$$

where $FT_B(\theta_S)$ is the relative transmittance, normalised by the total transmittance for normal incidence, and b_0 is an adjustable parameter that can be empirically determined for each type of photovoltaic module. If this value is unknown, a general value $b_0 = 0.07$ may be used. The effect of the angle of incidence on the successfully collected solar radiation can be calculated by applying equation (20.45) to the direct and circumsolar irradiances, and by considering an approximated value, $FT = 0.9$, for the isotropic diffuse and reflected radiation terms. Figure 20.17 shows a plot of $FT_B(\theta_S)$ versus θ_S . It presents

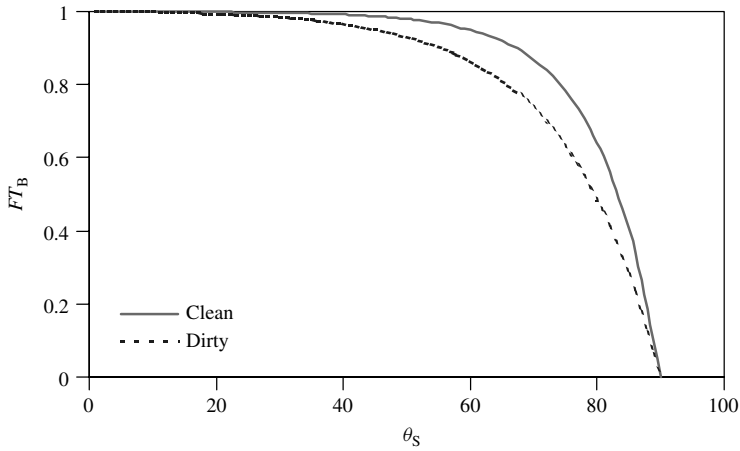


Figure 20.17 The relative transmittance FT_B is plotted against the angle of incidence θ_S , for a clean surface and also for a dust-covered surface

a pronounced knee close to 60° . In practical terms, that means the effects of the angle of incidence are negligible for all the θ_S values well below this figure. For example, $FT_B(40^\circ) = 0.98$.

The ASHRAE model is simple to use but has noticeable disadvantages. It cannot be used for $\theta_S > 80^\circ$, and, still worse, it cannot take into consideration the effects of dust. Dust is always present in real situations, and not only reduces the transmittance at normal incidence but also influences the shape of $FT_B(\theta_S)$. Figure 20.17 shows that the relative transmittance decreases because of dust at angles from about 40 to 80° . Real $FT_B(\theta_S)$ are best described [33] by

$$FT_B(\theta_S) = 1 - \frac{\exp\left(-\frac{\cos \theta_S}{a_r}\right) - \exp\left(-\frac{1}{a_r}\right)}{1 - \exp\left(-\frac{1}{a_r}\right)} \quad (20.46)$$

where a_r is an adjust parameter mainly associated with the degree of dirtiness, as shown in Table 20.4. Note that the degree of dirtiness is characterised by the corresponding relative normal transmittance, $T_{\text{dirt}}(0)/T_{\text{clean}}(0)$. Equation (20.46) applies for direct and circumsolar radiation components. The angular losses for isotropic diffuse and albedo radiation components are, respectively, approximated by [33]

$$FT_D(\beta) = 1 - \exp\left[-\frac{1}{a_r} \left[c_1 \left(\sin \beta + \frac{\pi - \beta \cdot \frac{\pi}{180} - \sin \beta}{1 + \cos \beta} \right) + c_2 \left(\sin \beta + \frac{\pi - \beta \cdot \frac{\pi}{180} - \sin \beta}{1 + \cos \beta} \right)^2 \right] \right] \quad (20.47)$$

Table 20.4 Recommended parameters for angular losses calculation

Dirtiness degree	$T_{\text{dirt}}(0)/T_{\text{clean}}(0)$	a_r	c_2
Clean	1	0.17	-0.069
Low	0.98	0.20	-0.054
Medium	0.97	0.21	-0.049
High	0.92	0.27	-0.023

and

$$FT_R(\beta) = 1 - \exp \left[-\frac{1}{a_r} \left[c_1 \left(\sin \beta + \frac{\beta \cdot \frac{\pi}{180} - \sin \beta}{1 - \cos \beta} \right) + c_2 \left(\sin \beta + \frac{\beta \cdot \frac{\pi}{180} - \sin \beta}{1 - \cos \beta} \right)^2 \right] \right] \quad (20.48)$$

where $c_1 = 4/(3\pi)$ and c_2 is linearly related to a_r . Table 20.4 also presents some values of these parameters for several dirtiness degrees.

It must be noted that $FT_B(0) = 1$. That means, this function does not include the dirt effect on the relative normal transmittance but only the angular losses relative to normal incidence. In other words, the “effective” direct irradiance reaching the solar cells of a PV module, should be computed as

$$B_{\text{eff}}(\beta, \alpha) = B(\beta, \alpha) \times \frac{T_{\text{dirt}}(0)}{T_{\text{clean}}(0)} \times FT_B(\theta_S) \quad (20.49)$$

and similar expressions should be used for the diffuse and albedo irradiance (or hourly irradiation) components.

Following the example of 15 April in Portoalegre-Brazil, we can now calculate the effective irradiances over a surface tilted to the latitude, neglecting the albedo, supposing a medium dirtiness degree and by applying $FT_B(\theta_S)$ not only to the direct radiation but also to the circumsolar component of the diffuse radiation. Obviously, $FT_D(\beta)$ is applied to the isotropic component of the diffuse radiation. The results are as follows:

$$FT_D(\phi) = 0.934$$

ω°	$FT_B(\theta_S)$	$B_{\text{eff}}(\phi)$, [Wm ⁻²]	$D_{\text{eff}}(\phi)$ [Wm ⁻²]	$G_{\text{eff}}(\phi)$ [Wm ⁻²]	ΔG_{eff} [%]
ω_S	0	0	0	0	0
± 60	0.913	80.84	126.39	207.23	-11.3
± 30	0.991	249.63	249.74	499.37	-6.8
0	0.999	332.13	296.37	628.50	-6.1

The last column of this table describes the losses due to both dirt and angular effects. Taking into consideration that dirt reduces normal transmittance by a factor of 3% ($T_{\text{dirt}}(0)/T_{\text{clean}}(0) = 0.97$), it can be noted that pure angular losses dominate for $|\omega| > 30^\circ$.

Finally, it should be stressed that angular-dependent reflection is often neglected in PV simulations. However, they become significant in many practical situations, for example, where vertical (façade-integrated PV generators) or horizontal (N–S horizontal trackers) surfaces are concerned. Furthermore, they help to explain the observed low irradiance effects in PV module performance. This is because low irradiance just happens when the incidence angle is large or when solar radiation is mainly diffuse. In both cases, angular losses are particularly important. As a matter of fact, the failure to consider angular losses has been signalled as the main cause of error in some energy models [34].

20.8 SOME CALCULATION TOOLS

20.8.1 Generation of Daily Radiation Sequences

Long series (many years) of daily irradiation data are sometimes required for particular purposes, for example, when studying the long-term reliability of stand-alone photovoltaic systems. However, long series of historical data are scarce and hard to obtain. This leads to the need for methods that are able to generate a series starting from widely available information, such as the 12 long-term average monthly mean values of the daily irradiation, $G_{\text{dm}}(0)$. The idea is that the generated series must keep some statistical properties believed to be universal, as they are also found in historical data, when available. In particular, the persistence of solar radiation, that is, the dependence of today's irradiation on the irradiation of the precedent days, is adequately described by a first-order autoregressive process [35]. Moreover, the probability function of the daily clearness index for any given period has a form associated with only its average value for the period. Several methods for the generation of daily irradiation sequences are available in the literature [36]. The method proposed by Aguiar [37] is the most widely used today.

20.8.2 The Reference Year

As already mentioned, the most widely available information related to the solar radiation resource at a given location is the set of 12 monthly mean values of global horizontal daily irradiation, $G_{\text{dm}}(0)$. The methods presented above allow estimation of all the radiation components incident on any surface of arbitrary orientation and at any moment of the average year, and even at any moment of a long sequence of years. This can be applied to all the problems related to the design of photovoltaic systems: sizing, prediction of energy yields, impact of shadowing, optimisation of tilt angles and so on.

Nevertheless, the solar radiation is still the object of systematic recording, and more and more irradiance and irradiation data are being accumulated and put at public disposal. Such data whether in the form of crude recorded data or in the form of elaborate mathematical tools, attempt to properly represent the climate of the concerned location. The most widely used is the so-called Reference Year, also called the Typical Meteorological Year [18], *TMY*, or the Standard Year. The *TMY* for a location is a hypothetical

year in which months are real months, but are chosen from different years from the whole period for which data are available. In practice [38], the months are chosen such that the monthly mean of the daily global irradiation on the horizontal represents an average value for all values contained in the database. For example, January of 1986 was chosen for the *TMY* of Madrid, because it had a value of $G_{\text{dm}}(0) = 1.98 \text{ kWh/m}^2$, the closest to the average value of $G_{\text{dm}}(0) = 1.99 \text{ kWh/m}^2$ for all the months of January on record [16].

The most widely used *TMY* for photovoltaic applications is set in a one-hour time scale. Hence, it contains 4380^1 values of global horizontal irradiation. Ambient temperature values are also specified for each hour. This huge number of initial data can lead to the impression that the corresponding results should be much more accurate than those obtained when simply using the 12 $G_{\text{dm}}(0)$ values as input. However, this impression is largely wrong. On the one hand, because the representativeness of any data – it should be again remembered – is limited by the random nature of the solar radiation, small differences in the results are scarcely meaningful. On the other hand, because the results obtained from the 12 $G_{\text{dm}}(0)$ values and from the *TMY* are very similar, provided the initial data are coherent (i.e. the monthly means in the *TMY* coincides with the 12 $G_{\text{dm}}(0)$ values) and that the selected correlations and diffuse radiation models to transpose from horizontal to inclined surfaces are the same. The physical reasons for this lie in the quasi-linear power-irradiance relationship in most PV devices, and in the fact, initially shown by Liu and Jordan [19], that the solar climate of a particular location can be well characterised by only the monthly mean daily clearness index. As already mentioned, they have demonstrated that, irrespective of latitude, the fractional time during which daily global radiation is equal to or less than a certain value depends only on this parameter. Surely, to go into this question in-depth would increase the reader's boredom which is probably already large enough; hence, we will restrict ourselves to describing a representative case from our own experience:

In 1992, the Solar Energy Institute in the University of Madrid, IES-UPM, was involved in the design of the 1 MW PV plant in Toledo, Spain. It was the biggest European PV project at that time, so very careful studies were required at the initial project stage. Fortunately, a large historical database, containing 20 years of hourly irradiation data, was available from a nearby meteorological station, and was directly used to calculate the expected energy yields. Both static and sun-tracked photovoltaic arrays were analysed while taking into account detailed features such as shadowing from adjacent rows, back-tracking features and so on. Moreover, the same calculation was also performed using as input the *TMY*, previously derived from the historical radiation sequence, and also using as the only input the 12 $G_{\text{dm}}(0)$ values and computing for just the mean day of each month. The results from the three calculation procedures never differed more than 2%! As a matter of fact, the results were much more sensitive to the considerations of the solar angle of incidence effects [39] described below.

A clever friend, not involved in this project but being aware of this anecdote, posed the questions: Then why go into such exhaustive detail when they give similar results?

¹ There are 8760 hours per year, and the sun shines exactly half of the year in any location, hence there are 4380 hours of sunshine per year.

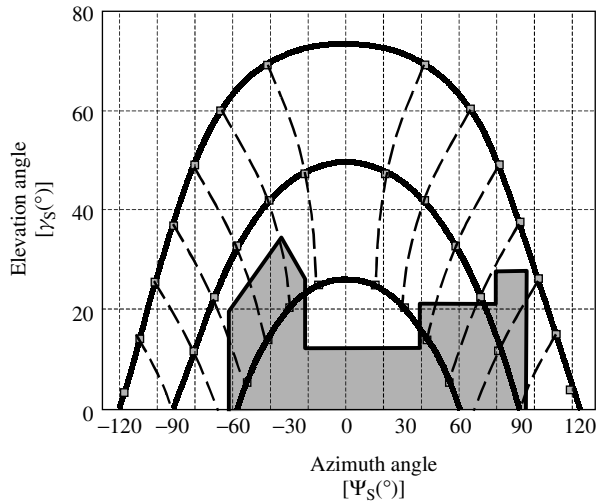


Figure 20.18 Sun's trajectory map corresponding to a latitude $\phi = 40.5^\circ$, with a skyscraper superimposed on the map. For example, on the winter solstice, shadows occur from sunrise to about 10:30 (solar time) and from 14:30 to sunset

Why not just be simple? The proper answers are best found in human psychology. Many people simply desire not to believe in some ideas. Hence, the ones daring to declare them are automatically impelled to provide strong arguments in favour of such ideas. To a large extent, this is usually the case when defending the argument that modern complex software tools do not necessarily yield better results than simple (but judicious) traditional methods. That was the position of the IES-UPM in 1992, and today for the author of this chapter the position remains the same.

20.8.3 Shadows and Trajectory Maps

Surroundings of photovoltaic modules can include trees, mountains, chimneys, walls, other PV modules and so on. Because of that, photovoltaic modules cannot always be positioned entirely free of shadows. This reduces their potential energy yield, and must be taken into account when designing photovoltaic systems. Equations (20.3 to 20.5) allow the plotting of the trajectories of the sun, in terms of elevation versus azimuth angles, as already explained in Figure 20.6.

These types of diagrams are called sun trajectory maps. They are a very useful tool for determining the duration and effect of shadowing cast by any obstacle. A correctly placed theodolite can measure the azimuth and elevation angles of the most relevant points (corners, peaks etc.) of any kind of obstacle. The *local horizon* can then be superimposed on the trajectory map, as Figure 20.18 shows. The effect of the shadow is calculated with the assumption that the direct and circumsolar radiations are zero when the sun is below the local horizon. Unless the shadows are very large, the effect of the local horizon on the diffuse radiation (other than the circumsolar component) can be neglected. Several tools have been proposed [40, 41] to simplify the practise of this calculation.

20.9 IRRADIATION ON MOST WIDELY STUDIED SURFACES

This section analyses some important features of the radiation available on commonly studied surfaces. As already mentioned, the methods presented before conform to a complete package, allowing the calculation of the irradiation incident over any arbitrary surface over any period of time, using the horizontal data as input. This can no doubt be a tedious task, so specific commercial software packages have been developed [42, 43]. However, for many practical engineering problems, more direct and simple tools can be developed. In particular, it is possible to develop analytical expressions that can be simply solved by only hand calculations. In order to apply the discussion in the previous sections, let us analyse the particular case of the yearly mean daily irradiation collected at four different places on a fixed surface, tilted towards the equator ($\alpha = 0$) and inclined at an angle β to the horizontal, $G_{dy}(\beta)$. Figure 20.19 plots, for each place, such value in relation to its maximum and versus the inclination angle referred to as the absolute value of the latitude, that is, $G_{dy}(\beta - |\phi|)/G_{dy}(\beta_{opt})$, being β_{opt} the inclination angle associated to the maximum value of $G_{dy}(\beta)$. The calculation procedure had followed the lines described in Figure 20.16. Solar radiation data has been obtained from Reference [7]. Several aspects need to be outlined.

On the one hand, a great similarity between all the curves is noticeable. Despite large differences in latitude and clearness index of the selected locations, the shape of the curve and also the inclination angle maximising the collection of radiation are very similar for the four selected places. Furthermore, this angle is relatively close to the latitude. It is important to mention that the extension of this exercise to many other places all around the world verifies that this great similarity is nearly universal. In fact, we have performed a specific exercise covering 30 different places distributed from $\phi = 80^\circ$ to $\phi = -78.2^\circ$ (see list in Table 20.5). We limit Figure 20.19 to only four curves for presentation purposes. A physical explanation of this similitude can be argued observing that, irrespective of the latitude, all the surfaces tilted towards the equator and inclined at an angle equal to the absolute value of the latitude are parallel all over the Earth, and also parallel to the Earth's rotation axis. Therefore, in the absence of the atmosphere, on

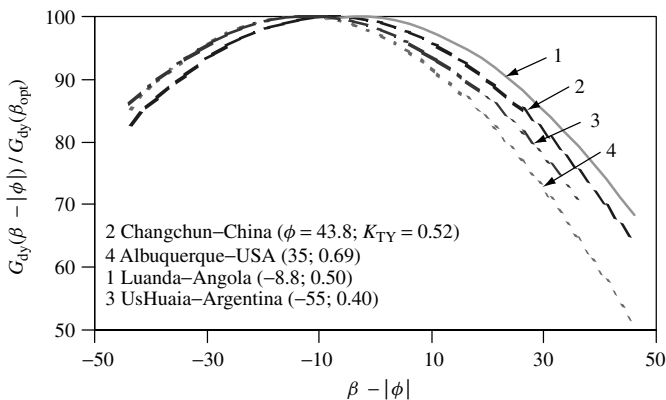


Figure 20.19 Yearly energy collection versus inclination angle for surfaces tilted towards the equator. The percentage of relative collection, with respect to the maximum, $G_{dy}(\beta - |\phi|)/G_{dy}(\beta_{opt})$ is plotted against the difference between the tilt angle and the latitude $\beta - |\phi|$

Table 20.5 Annual radiation availability on different surfaces, for 30 different places all around the world. Various tracking options (1 axis, 2 axis, etc.) described in Section 20.9.2

Location	Lat. ϕ°	$B_{0dy}(0)$ [Wh/m ²]	Clearness index K_{Ty}	Ratios to global horizontal yearly irradiation					
				2 axis	1 Az-axis	1 Ho-axis	1 Po-axis	Fixed β_{opt}	2 axis Conc.
Ice-Island-Arctic	80	4261	0.580	2.75	2.54	1.97	2.60	1.67	2.26
S. Petersburg-Russia	59.9	5703	0.453	1.72	1.64	1.43	1.61	1.18	1.21
Hamburg-Germany	53.6	6437	0.412	1.49	1.42	1.28	1.39	1.11	0.97
Freiburg-Germany	48	7075	0.428	1.42	1.36	1.26	1.33	1.07	0.93
Nantes-France	47.2	7164	0.468	1.50	1.44	1.31	1.41	1.10	1.03
Olympia-USA	46.6	7230	0.437	1.41	1.35	1.27	1.32	1.05	0.93
Changchun-China	43.8	7531	0.510	1.60	1.53	1.35	1.51	1.16	1.13
Sapporo-Japan	43	7615	0.421	1.41	1.35	1.22	1.31	1.09	0.89
Madrid-Spain	40.4	7880	0.544	1.53	1.46	1.36	1.45	1.08	1.12
Seoul-Korea	37.5	8161	0.440	1.39	1.32	1.23	1.30	1.07	0.89
Albuquerque-USA	35	8391	0.687	1.66	1.55	1.47	1.58	1.09	1.37
Djelfa-Algeria	34.6	8427	0.584	1.53	1.44	1.45	1.37	1.06	1.15
El Paso-Mexico	31.5	8691	0.689	1.61	1.49	1.45	1.53	1.07	1.33
Shanghai-China	31.2	8716	0.487	1.36	1.29	1.25	1.27	1.02	0.91
Cairo-Egypt	30.6	8764	0.637	1.53	1.43	1.39	1.46	1.05	1.20
Delhi-India	28.6	8919	0.630	1.56	1.44	1.40	1.47	1.07	1.23
Karachi-Pakistan	24.8	9189	0.560	1.48	1.36	1.35	1.39	1.04	1.13
Morelia-Mexico	19.7	9494	0.415	1.20	1.14	1.14	1.08	0.98	0.70
Dakar-Senegal	14.7	9729	0.599	1.38	1.23	1.31	1.29	0.98	1.04
Bangkok-Thailand	13.7	9768	0.490	1.27	1.16	1.21	1.14	0.98	0.83
Claveria-Philippines	8.6	9924	0.513	1.27	1.13	1.23	1.16	0.95	0.86
Colombo-Sri Lanka	6.9	9961	0.529	1.28	1.12	1.23	1.16	0.96	0.76
Medellin-Colombia	6.2	9974	0.469	1.22	1.08	1.18	1.08	0.95	0.76
Luanda-Angola	-8.8	9918	0.497	1.26	1.12	1.21	1.13	0.95	0.83
El Alto-Bolivia	-16.4	9652	0.579	1.39	1.25	1.31	1.29	0.99	1.04
Sao Paulo-Brazil	-23.5	9267	0.427	1.25	1.19	1.17	1.14	0.99	0.76
Porto Alegre-Brazil	-30	8805	0.505	1.38	1.30	1.26	1.29	1.02	0.93
Bariloche-Argentina	-41.1	7801	0.566	1.58	1.50	1.40	1.50	1.07	1.18
Ushuaia-Argentina	-55	6263	0.402	1.62	1.55	1.30	1.51	1.19	1.07
Little America-Antarctic	-78.2	4306	0.577	2.67	2.48	1.87	2.52	1.55	2.12

the equinox days, they receive identical solar irradiation, $B_{0d}(|\phi|)|_{\delta=0}$. And the same is true for surfaces equally tilted with respect to the latitude angle, $B_{0d}(\beta - |\phi|)|_{\delta=0}$. For other than equinox days, this is not exactly true, because sunrise time (and, therefore, the length of daytime and, in turn, the daily extraterrestrial irradiation) depends on latitude, as described by equation (20.7). However, the yearly ratio between extraterrestrial irradiation collected on both inclinations, $B_{0dy}(\beta - |\phi|)/B_{0dy}(|\phi|)$ tends to remain constant. Now, when accounting for the Earth's atmosphere, such site independence is not necessarily maintained, because of the different climatic conditions, that is, the different annual clearness index K_{Ty} , from one site to another. Obviously, the collection of diffuse radiation is less sensitive to inclination angle variations than the collection of direct radiation. Because of this, the lower the K_{Ty} value (the higher the F_{dy}), the slightly less is sharp-pointed curve that should be expected. Figure 20.19 reveals that this tendency is, in fact, very weak, so that the site independence clearly dominates and the function $G_{dy}(\beta - |\phi|)/G_{dy}(\beta_{opt})$ can be properly considered as being a universal invariant.

On the other hand, the smooth form of the curves of Figure 20.19 suggests that it may be possible to describe them analytically, thus avoiding the need to use a computer each time a particular value is required. A convenient way of doing it is, first, analysing the correspondence between the optimal inclination angle and latitude. It is worth noting that the larger the latitude, the larger the difference between summer daytime and winter daytime and, in turn, the larger the difference between the summer and the winter irradiation. Therefore, it can be anticipated that as latitude increases, the optimal inclination angle should progressively give priority to the collection of summer over the collection of winter. This can be observed in Figure 20.20, where the values of $\beta_{\text{opt}} - |\phi|$ have been plotted against the latitude, for the 30 above-mentioned different locations.

It is useful to fit a linear equation to these values

$$\beta_{\text{opt}} - |\phi| = 3.7 - 0.31|\phi| \quad \text{or} \quad \beta_{\text{opt}} = 3.7 + 0.69|\phi| \quad (20.50)$$

where β and ϕ are given in degrees. It is worth mentioning that the observed dispersion of the cluster of points around equation (20.50) (also depicted in Figure 20.20) is, in fact, of negligible importance, due to the very low sensibility of the energy collection to deviations from the optimal inclination angle. For example, the point corresponding to Delhi ($\phi = 28.6^\circ$) – marked as ♥ in the figure – indicates a value of $\beta_{\text{opt}} = 29.6^\circ$, while equation (20.50) leads to $\beta_{\text{opt}} = 23.4^\circ$. The 6.2° of difference can appear relatively large ($\approx 20\%$), but a detailed simulation exercise would disclose that $G_{\text{dy}}(23.4^\circ)/G_{\text{dy}}(29.6^\circ)$ is 99%, that is, such a difference is irrelevant when translated into energy content. A similar reasoning also justifies the validity of the usual assumption $\beta_{\text{opt}} = \phi$. Now, a second-order polynomial describes very well the curves of Figure 20.19.

$$\frac{G_{\text{dy}}(\beta)}{G_{\text{dy}}(\beta_{\text{opt}})} = 1 + p_1(\beta - \beta_{\text{opt}}) + p_2(\beta - \beta_{\text{opt}})^2 \quad (20.51)$$

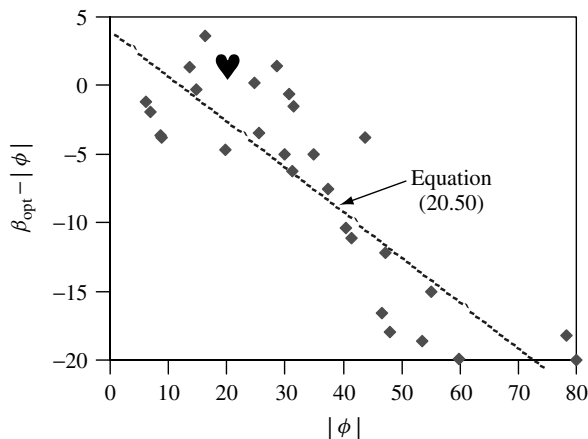


Figure 20.20 Optimal inclination angle versus latitude. The difference between $\beta_{\text{opt}} - |\phi|$ is plotted against the latitude $|\phi|$. The cluster of points corresponds to the different places listed in Table 20.5

where p_1 and p_2 are the adjusted parameters for which values are 4.46×10^{-4} and -1.19×10^{-4} , respectively. The corresponding value of the so-called correlation coefficient, R^2 , is greater than 0.98, indicating that equations (20.50) and (20.51) adjust very well to the simulated values. This way, the results of a rather complex calculation, involving a lot of tedious steps, can be described by means of two simple mathematical expressions. Apart from simplicity and elegance, all the information has been condensed into just four numbers and an equation that have the advantage of having a continuous slope, which can be useful in many calculations. It is worth mentioning that these equations can also be used to calculate the value of $G_{dy}(\beta_{opt})$ from the data corresponding to the horizontal surface, which is the most usually available information.

Example: Estimation of the optimal tilt angle and the corresponding yearly irradiation in Sapporo-Japan knowing the latitude, $\phi = 43^\circ$, and the annual average of the daily global horizontal irradiation, $G_{dy}(0) = 3220 \text{ Wh/m}^2$. The solution is

$$\text{Equation (20.50), } \phi = 43^\circ \Rightarrow \beta_{opt} = 33.37^\circ$$

$$\text{Equation (20.51), } \beta = 0^\circ \Rightarrow G_{dy}(0)/G_{dy}(\beta_{opt}) = 0.8526$$

$$\Rightarrow G_{dy}(\beta_{opt}) = 1.1729 \times G_{dy}(0) = 3776 \text{ Wh/m}^2.$$

The total yearly irradiation is $365 \times G_{dy}(0) = 1379 \text{ kWh/m}^2$.

It is worth mentioning that a more careful calculation, using the 12 values of the monthly mean irradiation and following the procedure described in Figure 20.16, would lead to $G_{dy}(\beta_{opt}) = 3663 \text{ Wh/m}^2$. This means, that the error associated to equation (20.51) is below 3%.

Attempting to help in the following discussion, Table 20.5 presents the results of a detailed simulation exercise devoted to the calculation of the annual radiation availability on horizontal surfaces, optimally tilted fixed surfaces and several types of tracking surfaces. The exercise has been extended to 30 different places distributed around the World. The hope is that the readers could find here a relatively similar location, both in latitude and clearness index, to the location of their interest. The yearly means of the daily global horizontal irradiation, $G_{dy}(0)$, can be obtained by multiplying the corresponding values of the extraterrestrial radiation and the clearness index. (column 3 \times column 4). Then, these horizontal $G_{dy}(0)$ values are used as reference for the irradiation availability in all the other considered surfaces. In particular, column 8 of this table gives the ratio between the global irradiation on a fixed and optimally tilted surface to the global horizontal irradiation, $G_{dy}(\beta_{opt})/G_{dy}(0)$. Hence, the irradiation on the optimally tilted surface is given by the product (column 3 \times column 4 \times column 8).

20.9.1 Fixed Surfaces

The integration of PV generators in buildings, presently in vogue in many industrialised countries, led to the use of a large range of different orientations and tilt angles. PV module orientations from east to west, and tilt angles from horizontal to vertical are found in practise. Then, it is worth extending the previous exercise to surfaces other than those

tilted towards the equator, that is, to $\alpha \neq 0$, and also to dirty surfaces. E. Caamaño [44] has proposed the following solution:

$$\frac{G_{\text{effdy}}(\beta, \alpha)}{G_{\text{dy}}(\beta_{\text{opt}})} = g_1(\beta - \beta_{\text{opt}})^2 + g_2(\beta - \beta_{\text{opt}}) + g_3 \quad (20.52)$$

where

$$g_i = g_{i1} \cdot |\alpha|^2 + g_{i2} \cdot |\alpha| + g_{i3}; i = 1, 2, 3 \quad (20.53)$$

being the values of the coefficients as show in Table 20.6, for medium dirty surfaces. The sub-index “eff” in the left term of equation (20.52) indicates that the dirt effect on the relative normal transmittance is also being included, in order to facilitate the direct application of the equation to real cases.

Let us continue with the example of Sapporo-Japan, by calculating the effective irradiation available on the following surfaces:

1. Optimally oriented, $\alpha = 0$, and optimally tilted, $\beta = \beta_{\text{opt}}$
Equation (20.53), $\alpha = 0 \Rightarrow g_i = g_{i3}$
Equation (20.52), $\beta = \beta_{\text{opt}} \Rightarrow G_{\text{effdy}}(\beta_{\text{opt}}) = 0.9314 G_{\text{dy}}(\beta = \beta_{\text{opt}}) = 3517 \text{ Wh/m}^2$
Note that the total losses due to the optical effects of the angle of incidence ($\approx 7\%$) are larger than pure normal transmittance losses ($\approx 3\%$)
2. Tilted 20° with respect to the horizontal, $\beta = 20^\circ$, and oriented 30° towards the west, $\alpha = 30^\circ \Rightarrow g_1 = -1.032 \times 10^{-4}$; $g_2 = 1.509 \times 10^{-4}$; $g_3 = 0.9057$
 $\beta - \beta_{\text{opt}} = -13.37^\circ \Rightarrow G_{\text{effdy}}(20, 30) = 0.8853 \cdot G_{\text{dy}}(\beta_{\text{opt}}) = 3343 \text{ Wh/m}^2$
It is worth mentioning that a similar calculation, but without considering the angular losses, would lead to $G_{\text{dy}}(20, 30) = 0.936 \cdot G_{\text{dy}}(\beta_{\text{opt}}) = 3533 \text{ Wh/m}^2$
3. A vertical facade, $\beta = 90^\circ$, oriented towards the south-east, $\alpha = -45^\circ$.
 $\alpha = -45^\circ \Rightarrow g_1 = -0.885 \times 10^{-4}$; $g_2 = -2.065 \times 10^{-4}$; $g_3 = 0.8761$
 $\beta - \beta_{\text{opt}} = 56.63^\circ \Rightarrow G_{\text{effdy}}(90, -45) = 0.5806 \cdot G_{\text{dy}}(\beta_{\text{opt}}) = 2192 \text{ Wh/m}^2$

It is opportune to mention again the relatively weak sensitivity of the annual capture of energy to the inclination angle. A value of 0.2% loss for each degree of deviation from the optimum value is a rough approximation. This is true to an even greater extent in the case of azimuthal orientation, where only a 0.08% loss occurs for each degree of deviation from the south. This means that many existing surfaces (roofs, car parks etc.) are suitable for PV modules integration, even if their orientation differs considerably from

Table 20.6 Coefficients used to solve equation (20.52). Values are given for the representative case of medium dirtiness degree ($T_{\text{dirt}}(0)/T_{\text{clean}}(0) = 0.97$)

Coefficients	$T_{\text{dirt}}(0)/T_{\text{clean}}(0) = 0.97$		
	$i = 1$	$i = 2$	$i = 3$
g_{1i}	8×10^{-9}	3.8×10^{-7}	-1.218×10^{-4}
g_{2i}	-4.27×10^{-7}	8.2×10^{-6}	2.892×10^{-4}
g_{3i}	-2.5×10^{-5}	-1.034×10^{-4}	0.9314

the optimum. This also means there is no need to carry out expensive civil works to level the site of PV arrays, despite it being an extended custom in large PV plants.

The case of stand-alone systems designed to feed equipment having a constant consumption throughout the year is an especially interesting one, and deserves particular mention. The design criterion here is to maximise the energy captured during the period of least radiation, rather than throughout the year. As might be expected, such receivers are positioned perpendicular to the winter sunlight, which leads to recommend a tilt angle $\beta \approx \phi + 10^\circ$.

20.9.2 Sun-tracking Surfaces

At the moment, tracking mechanisms are little used in photovoltaics, but in the future they are likely to become much more common, mainly associated with relatively big grid-connected PV plants, where these mechanisms have already demonstrated very high reliability. As a particular example, the 100 kWp tracking system at the Toledo-PV plant [39] is in routine operation with 100% of availability from 1994 (about 66 000 h when writing this chapter).

Tracking about two axes maintains the receiver surface always perpendicular to the sun ($\beta = \theta_{ZS}$; $\alpha = \psi_S$). Hence, it allows collecting the maximum amount of energy possible. Mainly depending on the clearness index, the comparison with an optimally tilted fixed surface leads to the ratio $G_{dy}(2 \text{ axes})/G_{dy}(\beta_{opt})$ varying from 1.25 to 1.55 (column 4 divided by column 8 of Table 20.5). However, it is expensive to implement, because it uses relatively complicated mechanisms and takes up a great deal of space, due to the shadows cast. For these reasons, several types of one-axis trackers are usually preferred.

Azimuthal one-axis trackers rotate around their vertical axis, in such a way that the azimuth of the receiver PV surface is always the same as that of the sun's azimuth. Meanwhile, the tilt angle keeps constant ($\beta = \beta_{cons}$ and $\alpha = \psi_S$). The incidence angle is given by the difference between the surface's tilt angle and the solar zenith angle ($\theta_S = \theta_{ZS} - \beta_{cons}$). Obviously, the amount of collected radiation depends on the inclination of the surface, being the maximum for a value close to the latitude. Again, the sensitivity of the annual capture of energy to this inclination angle is relatively low. A typical value of approximately 0.4% loss from each degree of deviation from the optimum inclination can be assumed. Note that an azimuthal tracker tilted to the latitude collects up to 95% of the yearly irradiation corresponding to the case of two-axes tracking (column 5 divided by column 4 of Table 20.5).

One-axis trackers turning around a single axis-oriented N-S and tilted at an angle β_{NS} to the horizontal are also of great interest. It can be seen that, in order to minimise the solar incident angle, the rotation angle of the axis, $\psi_{NS} - 0$ at noon – must be

$$\tan \psi_{NS} = \frac{\sin \omega}{\cos \omega \cos \beta_{\Delta} - [\text{sign}(\phi)] \tan \delta \sin \beta_{\Delta}} \quad (20.54)$$

where $\beta_{\Delta} = \beta_{NS} - \text{abs}(\phi)$. The corresponding solar incident angle is given by

$$\cos \theta_S = \cos \psi_{NS} (\cos \delta \cos \omega \cos \beta_{\Delta} - [\text{sign}(\phi)] \sin \delta \sin \beta_{\Delta}) + \sin \psi_{NS} \cos \delta \sin \omega \quad (20.55)$$

A common configuration, called *polar tracking*, is when the axis is inclined just to the latitude. Then, the rotation axis is parallel to the rotation axis of the Earth, and the equations (20.54 and 20.55) become reduced to $\psi_{NS} = \omega$, and $\theta_S = \delta$. Because of the variation of the declination during the year, the cosines of the solar incident angle ranges between 0.92 and 1, having an annual mean value of about 0.95. This way, the polar tracker also collects about 95% of the energy corresponding to the two-axes case (column 7 divided by column 4 of Table 20.5). It is interesting to note that a polar tracker turns just at the same angular speed as that of a standard clock.

Another common configuration is when the axis is just horizontal. Horizontal one-axis trackers are of particularly simple construction and do not cast shadows in the N–S direction. This encompasses significant radiation reduction when compared with two-axis tracking (column 6 divided by column 4 of Table 20.5), but still significant radiation increase when compared with optimally tilted fixed surfaces (column 6 divided by column 8 of Table 20.5). Because of this, they are today the most common tracking solution in large PV plants: PVUSA [45], Toledo [39] and so on. And the same is true for solar thermal plants. We should remember that the very first solar tracker used in any significant way for power generation was just a N–S-oriented horizontal one-axis tracker associated to a parabolic reflecting trough, constructed in 1912 by Frank Shumann and C.V. Boys to power a 45-kW steam-pumping plant in Meadi, Egypt [46]. The tracking surface covered an area of 1200 m². The plant was a technical success, that is, reliable trackers existed already at the time, but it was shut down in 1915 due to the onset of World War I and cheaper fuel prices. The world's largest solar plant, at the well-known Luz solar field, erected in California from 1984 to 1986, also employs this type of tracking and, again, with great technical success [47]. The surface position and the solar incident angle are given by

$$\beta = \arctan \left| \frac{\sin \psi_S}{\tan \gamma_S} \right| \quad (20.56)$$

and

$$\cos \theta_S = \cos \delta \cdot [\sin^2 \omega + (\cos \phi \cos \omega + \tan \delta \sin \phi)^2]^{1/2} \quad (20.57)$$

Finally, it is worth commenting that large PV generators have several rows of modules mounted above the ground. The distance between rows affects the energy produced by the PV generator. If the separation is increased, fewer shadows are cast by some rows on the others and more energy is produced. But it also affects the cost, as greater separations lead to more land being occupied, longer cables and more expensive civil works. Therefore, there is an optimum separation, giving the best trade-off between greater energy and lower cost. There is a widely held view that tracking generally requires much more land than static arrangements. However, it should be outlined that this is not necessarily the case when horizontal one-axis tracking is concerned. The interested reader is encouraged to refer to [48], which deals in detail with tracking and shadowing in large PV arrays.

20.9.3 Concentrators

PV concentrators are able to capture only direct-beam solar radiation and require tracking mechanisms to keep in focus the solar cells. Therefore, they are best suited to sunny

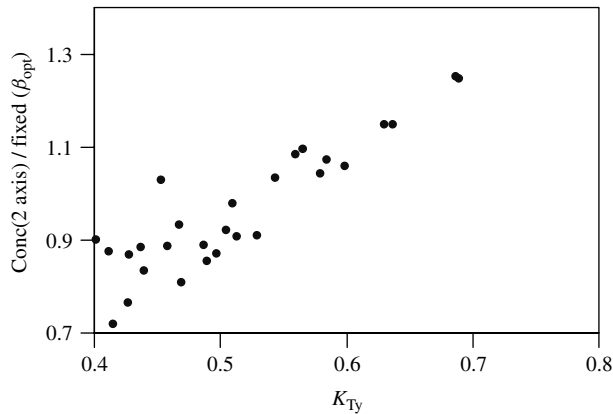


Figure 20.21 Comparison of annual average solar radiation available for fixed flat-plate conventional PV modules, and two-axis tracking PV concentrators. The y-axis is (column 10)/(column 9) and the x-axis column 4 of Table 20.5

sites with low scattering (or low diffuse radiation) and good solar resources. Figure 20.21 compares the amount of normal direct radiation for a PV concentrator mounted on a two-axis tracker, with the amount of global radiation, collected by a conventional flat-plate PV collector, at a fixed optimal tilt. The data represents the 30 locations in Table 20.5. The ratio between both quantities, $B_{dy}(\perp)/G_{dy}(\beta_{opt})$, (column 9 divided by column 8 of Table 20.5) is plotted against the annual clearness index. As a general rule, two-axis tracking concentrators collect more radiation than fixed flat-plate modules in places where $K_{Ty} > 0.55$.

20.10 PV GENERATOR BEHAVIOUR UNDER REAL OPERATION CONDITIONS

A problem that the engineer frequently has to solve is the prediction of the electrical behaviour of a PV generator, given the information about the generator's construction, geographic location, and the local weather. In particular, this represents the base for predicting the generator energy delivery, which is a critical step of any PV-system design. This leads to the question of establishing a PV module rating condition, at which power performance and other characteristics are specified and, defining a method for calculating performance at the prevailing environmental conditions such as solar irradiance, ambient temperature, wind speed and so on.

Traditionally, PV modules are being rated under the so-called Standard Test Conditions (STC) (Irradiance: 1000 W/m^2 ; Spectrum: $AM1.5$; and Cell Temperature: 25°C). In the following, we will use the superscript * to refer to these conditions. The most usual case is to know just the values of the short-circuit current, I_{SC}^* , the open-circuit voltage, V_{OC}^* and the maximum power, P_M^* , which are always included in the manufacturer's data sheets. Furthermore, the characterisation of the PV module is completed by measuring the *nominal operating cell temperature (NOCT)*, defined as the temperature reached by the cells when the PV module is submitted to an irradiance of 800 W/m^2 and

an ambient temperature of 20°C. However, performance predictions based on STC are being continuously questioned, mainly because the resulting annual energy efficiencies are significantly lower than the power efficiencies defined, using STC. Certainly, PV users can be astonished on learning that the real efficiency of the PV module they have purchased, once installed at home, has only about 70% of the STC efficiency they have read in the manufacturer's information. This could lead to a feeling of having been deceived. This frustration can even increase in the case of fraud, that is, if the actual STC power performance of the delivered PV module is below the value declared by the module's manufacturer, which, unfortunately, has sometimes been the case [49, 50].

All together, these facts have stimulated several authors to propose other methods for PV module rating and energy performance estimation, more oriented to give buyers clear and more accurate information about the energy generation of PV modules (see Chapter 16 for a detailed description on rating module performance). This is still an open question, and it is difficult to predict the extent to which these new models would be incorporated in future PV engineering practices. Most of these methods require extending testing to other-than-STC, and rely on a relatively large number of parameters that should be empirically determined. Surely, the use of a large number of parameters would potentially allow for more accurate energy modelling. But it is not clear as to what extent the possible improvements would compensate for the associated increase of complexity derived from the experimental determination of such parameters. The proponents of new methods tend to argue that their procedures can be easily implemented. (Their papers used to include sentences like . . . *the entire test procedure for outdoor measurements, including the set-up, takes approximately three hours* . . . [51]). But, at the same time, the PV module manufacturers are very reluctant to incorporate troublesome novelties into their module characterisation procedures already established at factory PV. This dilemma is, in fact, easily understandable considering the inherent difficulties associated with the adoption of any innovation. This was magnificently explained by Maquiavelo in his famous work *The Prince*, written in 1513:(. . . *There is nothing more difficult to plan, more doubtful of success . . . than the creation of a new order of things* . . .).

Together, claims of low PV modules energy performance, and the flourishing of proposals for new rating methodologies have led, no doubt, to significant confusion in today's PV community, making risky this author's task of selecting a particular methodology for recommending to his PV colleagues. However, it is this author's opinion that, at least in the case of crystalline silicon, energy performance modelling based on only a few parameters obtained at STC, and always included in the manufacturer's data sheets, can lead to adequate predictions, providing that some judicious considerations are made. Obviously, precautions to assure that actual STC power of the purchased PV modules correspond with the manufacturer's declarations are a different matter [52].

It must be remembered that crystalline silicon solar cells remain the workhorse for PV power generation, despite significant advances in other PV devices. For example, c-Si technology increased its world market share [53], from 84.4% in 1999 to 86.4% in 2000. This predominance means that actual information concerning in-field c-Si PV modules performance is particularly consistent, which is not typically the case where other materials are concerned. Because of this, dealing with c-Si PV modules is, by far, the simplest and easiest case for PV designers. This is why, despite the above-mentioned confusion, the

author dares to detail here a rather simple methodology that allows the estimation of the $I-V$ curve of c-Si PV modules operating in any prevailing environmental condition, exclusively using as input the values of I_{SC}^* , V_{OC}^* and P_M^* . In principle, such methodology can be extended to other-than-c-Si materials, and additional comments to do this are also included in the text that follows. However, the reader should be advised that the much less available experience with these materials encompasses significant increase in uncertainty.

20.10.1 The Selected Methodology

In a previous chapter (see Chapter 3), it has been shown that the characteristic $I-V$ of a solar cell can be expressed with sufficient accuracy by

$$I = I_L - I_0 \left(\exp \frac{V + IR_S}{V_t} - 1 \right) - \frac{V + IR_S}{R_P} \quad (20.58)$$

where I_L , I_0 , R_S and R_P are the photo-generated current, the dark current, the series resistance and the parallel resistance, respectively. The voltage V_t equals mkT/e (we recall that for $m = 1$, $V_t \approx 25$ mV at 300 K). This expression gives an adequate representation of the intrinsic behaviour of a typical c-Si solar cell. Nonetheless, it cannot be used directly to obtain the required predictions, because some parameters, I_L and I_0 in particular, cannot be established from the usually available information, often restricted to the values of I_{SC}^* , V_{OC}^* , and P_M^* , which are always included on the manufacturers' data sheets.

This difficulty is effectively overcome when the following assumptions, which are generally valid for c-Si PV cells and modules, are made:

- The effect of parallel resistance is negligible.
- The photo-generated current and the short-circuit current are equal.
- $\exp((V + IR_S)/V_t) \gg 1$ under all working conditions.

This allows equation (20.58) to be written as

$$I = I_{SC} - I_0 \exp \left(\frac{V + IR_S}{V_t} \right) \quad (20.59)$$

which, with $I = 0$, leads to the following expression for the open-circuit voltage:

$$V_{OC} = V_t \ln \left(\frac{I_{SC}}{I_0} \right) \quad (20.60)$$

whence

$$I_0 = I_{SC} \exp \left(-\frac{V_{OC}}{V_t} \right) \quad (20.61)$$

Substituting equation (20.61) in (20.59), we arrive at

$$I = I_{SC} \left[1 - \exp \left(\frac{V - V_{OC} + IR_S}{V_t} \right) \right] \quad (20.62)$$

This is a very useful expression. As we shall see, the values of all the parameters on the right-hand side are easily obtained allowing immediate application of the expression. An inconsistency arises in the sense that $I(V = 0) \neq I_{SC}$. Nevertheless, in all solar cells of practical use, we find that $V_{OC} \gg IR_S \Rightarrow I(V = 0) \approx I_{SC}$, which therefore makes this objection irrelevant. The expression can be inconvenient to use in the sense that I is implicit (it appears on both sides of the equation), theoretically making it necessary to solve the equation iteratively. However, for voltages close to the maximum-power point, a reasonably accurate solution can be obtained with only one iteration by setting $I = 0.9 \times I_{SC}$ in the second term.

The calculation of the maximum power can, in principle, be carried out by considering that the power is given by the product $P = VI$. The values of I_M and V_M , defining the maximum-power operation point, can be obtained from the usual condition for a maximum, $dP/dV = 0$. However, the implicit nature of the resulting expression makes it very cumbersome to use. It would be better to look for a simpler method, based on the existing relationship between the fill factor and the open-circuit voltage. According to M.A. Green [54] an empirical expression describing this relation is

$$FF = \frac{V_M I_M}{V_{OC} I_{SC}} = \frac{P_M}{V_{OC} I_{SC}} = FF_0(1 - r_s) \quad (20.63)$$

where

$$FF_0 = \frac{v_{OC} - \ln(v_{OC} + 0.72)}{v_{OC} + 1} \quad (20.64)$$

and $v_{OC} = V_{OC}/V_t$ and $r_s = R_S/(V_{OC}/I_{SC})$ are defined as the normalised voltage and the normalised resistance, respectively. It is interesting to note that the series resistance at STC can be deduced from the manufacturer's data by the expression

$$R_S = \left(1 - \frac{FF}{FF_0}\right) \frac{V_{OC}}{I_{SC}} \quad (20.65)$$

The values of V_M and I_M are in turn given by [55]

$$\frac{V_M}{V_{OC}} = 1 - \frac{b}{v_{OC}} \ln a - r_s(1 - a^{-b}) \quad \text{and} \quad \frac{I_M}{I_{SC}} = 1 - a^{-b} \quad (20.66)$$

where:

$$a = v_{OC} + 1 - 2v_{OC}r_s \quad \text{and} \quad b = \frac{a}{1 + a} \quad (20.67)$$

This set of expressions is valid for $v_{OC} > 15$ and $r_s < 0.4$. The typical accuracy is better than 1%. Their application to a photovoltaic generator is immediate, if all their cells are supposed to be identical, and if the voltage drops in the conductors connecting the modules are negligible.

Now, for the prediction of the $I-V$ curve of a PV generator operating on arbitrary conditions of irradiance and temperature, a good balance between simplicity and exactness is obtained through the following additional assumptions.

- The short-circuit current of a solar cell depends exclusively and linearly on the irradiance. That is,

$$I_{SC}(G) = \frac{I_{SC}^*}{G^*} G_{\text{eff}} \quad (20.68)$$

where G_{eff} is the “effective” irradiance. This concept must take into consideration the optical effects related to solar angle of incidence, as described in Section 20.7. Effects, as described by equations (20.46–20.59), are as follows:

- The open-circuit voltage of a module depends exclusively on the temperature of the solar cells T_c . The voltage decreases linearly with increasing temperature. Hence,

$$V_{OC}(T_c) = V_{OC}^* + (T_c - T_c^*) \frac{dV_{OC}}{dT_c} \quad (20.69)$$

where the voltage temperature coefficient, dV_{OC}/dT_c is negative. The measurement of this parameter used to be included in PV modules characterisation standards [51, 56] and the corresponding value must, in principle, be also included on the manufacturer’s data sheets. For crystalline silicon cells, dV_{OC}/dT_c is typically -2.3 mV per $^\circ\text{C}$ and per cell.

- The series resistance is a property of the solar cells, unaffected by the operating conditions.
- The operating temperature of the solar cell above ambient is roughly proportional to the incident irradiance. That is,

$$T_c = T_a + C_t G_{\text{eff}} \quad (20.70)$$

where the constant C_t has the value:

$$C_t = \frac{NOCT(^\circ\text{C}) - 20}{800 \text{ W/m}^2} \quad (20.71)$$

The values of $NOCT$ for modules currently on the market varies from about 42 to 46°C , implying a value of C_t between 0.027 and $0.032^\circ\text{C}/(\text{W/m}^2)$. When $NOCT$ is unknown, it is reasonable to approximate $C_t = 0.030^\circ\text{C}/(\text{W/m}^2)$. This $NOCT$ value corresponds to mounting schemes allowing the free air convection in both sides of the PV modules, which cannot be the case on roof-mounting arrays, that restrict some of the airflow. Then, it has been shown [57] that the $NOCT$ increases by about 17°C if some kind of back ventilation is still allowed and up to 35°C if the modules are mounted directly on a highly insulated roof.

Example: To illustrate the use and the usefulness of the equations of the above sections, we shall analyse the electrical behaviour of a PV generator rated at 1780 W (STC), made up of 40 modules, arranged 10 in series \times 4 in parallel. The conditions of operation are $G_{\text{eff}} = 700 \text{ Wm}^{-2}$ and $T_a = 34^\circ\text{C}$. It is known that the modules have the following characteristics under STC: $I_{SC}^* = 3$ A, $V_{OC}^* = 19.8$ V and $P_M^* = 44.5$ W. Further, it is known that each module consists of 33 cells connected in series and that $NOCT = 43^\circ\text{C}$.

The calculations consist of the following steps:

1. *Determination of the characteristic parameters of the cells that make up the generator under STC (equations 20.63–20.67):*

33 cells in series \Rightarrow Per cell: $I_{SC}^* = 3$ A, $V_{OC}^* = 0.6$ V and $P_M^* = 1.35$ W
 Assuming $m = 1$; $V_t(V) = 0.025 \times (273 + 25)/300 = 0.0248$ V $\Rightarrow v_{OC} = 0.6/0.0248 = 24.19 > 15$

Then, $FF_0 = (24.19 - \ln(24.91))/25.19 = 0.833$; $FF = 1.35/(0.6 \times 3) = 0.75$

And $r_s = 1 - 0.75/0.833 = 0.0996 < 0.4 \Rightarrow R_S = 0.0996 \times 0.6/3 = 19.93$ m Ω

$$a = 20.371; b = 0.953 \Rightarrow V_M/V_{OC} = 0.787 \text{ and } I_M/I_{SC} = 0.943$$

It is worth noting that these values lead to a value of $FF = 0.742$, slightly different from the starting value. This error shows the precision available by the method, better than 1% in this instance. Sometimes values of $m = 1.2$ or 1.3 give a better approximation.

2. *Determination of the temperature of the cells under the considered operating conditions (equations 20.70 and 20.71):*

$$C_t = 23/800 = 0.0287^\circ\text{C m}^2/\text{W} \Rightarrow T_c = 34 + 0.0287 \times 700 = 54.12^\circ\text{C}$$

3. *Determination of the characteristic parameters of the cells under the operating conditions being considered (equations 20.68 and 20.69):*

$$I_{SC}(700 \text{ W/m}^2) = 3 \times (700/1000) = 2.1 \text{ A}$$

$$V_{OC}(54.12^\circ\text{C}) = 0.6 - 0.0023 \times (54.12 - 25) = 0.533 \text{ V}$$

With R_S considered constant, these values lead to:

$$V_t = 27.26 \text{ mV}; v_{OC} = 19.55; r_s = 0.0785; FF_0 = 0.805; FF = 0.742; P_M = 0.83 \text{ W}$$

4. *Determination of the characteristic curve of the generator, (I_G, V_G):*

Number of cells in series 330; Number of cells in parallel: 4. Then:

$$I_{SCG} = 4 \times 2.1 \text{ A} = 8.4 \text{ A}; \quad V_{OCG} = 330 \times 0.533 \text{ V} = 175.89 \text{ V}; \quad R_{SG} = 1.644 \Omega; \\ P_{MG}^* = 1095.6 \text{ W}$$

$$I_G(A) = 8.4 \left[1 - \exp \frac{V_G(V) - 175.89 + 1.644 \cdot I_G(A)}{9.00} \right]$$

To calculate the value of the current corresponding to a given voltage, we may solve this equation iteratively, substituting I_G for $0.9 I_{SCG}$ on the first step. Only one iteration is required for $V_G \leq 0.8 V_{OCG}$. By way of example, the reader is encouraged to do it for $V_G = 140$ V and $V_G = 150$ V. The solution is $I_G(140 \text{ V}) = 7.77$ A and $I_G(150 \text{ V}) = 6.77$ A.

5. *Determination of the maximum power point:*

$$a = 17.48; b = 0.9458; V_M/V_{OC} = 0.7883; I_M/I_{SC} = 0.9332$$

$$V_M = 138.65 \text{ V}; I_M = 7.84 \text{ A}, P_M = 1087 \text{ W}.$$

Note that the ratio $P_M/P_M^* = 0.661$, while the ratio $G_{\text{eff}}/G^* = 0.7$. This indicates a decrease in efficiency at the new conditions compared to STC, primarily due to the greater solar cell temperature, $T_c < T_c^*$. An efficiency temperature coefficient can now be

obtained by

$$\frac{1}{\eta^*} \cdot \frac{d\eta}{dT_c} = \left(\frac{P_M}{P_M^*} \cdot \frac{G^*}{G_{\text{eff}}} - 1 \right) \cdot \left(\frac{1}{T_c - T_c^*} \right) = -0.004/^\circ\text{C}$$

This means the efficiency decrease is about 0.4% per degree of temperature increase, which can be considered as representative for c-Si.

It should be noted that, depending on the input data availability, other PV-generator modelling possibilities exist. For example, commonly I_M^* and V_M^* are given in the specifications in addition to their product P_M^* . Then, the series resistance can directly be estimated from equation (20.62). This leads to

$$R_S^* = \frac{V_{OC}^* - V_M^* + V_t \ln \left(1 - \frac{I_M^*}{I_{SC}^*} \right)}{I_M^*} \quad (20.72)$$

20.10.2 Second-order Effects

The model presented in the previous section is based only on standard and widely available information, which is an undeniable advantage, in particular for PV-system design. Furthermore, it is simple to use. However, it can be argued that such simplicity is at the price of neglecting the following:

- The effects of the parallel resistance
- The influence of the cell temperature in the short-circuit current.
- The influence of the irradiance in the open-circuit voltage.
- The non-linearity due to low irradiance.
- The spectral effects.
- The effects of wind.

It should be recognised that differences between expected and real energies delivered by PV modules are often mentioned in the literature [58]. Hence, it is worth reviewing the importance of each one of these previously neglected factors, with the aim of clarifying possible error sources. Many of these factors are discussed further in Chapter 16.

The influence of the parallel resistance is, to a great extent, compensated here, by the particular way of estimating the series resistance of a PV module, which assures that the maximum power of the modelled curve coincides exactly with that corresponding to the real one. Because of this, the accuracy of the model tends to be very good just around the maximum-power operation point, that is, just on the voltage region of interest.

The short-circuit current tends to increase slightly with increasing temperature. This can be attributed, in part, to increased light absorption, since semiconductor band gaps generally decrease with temperature, and, in part, to increased diffusion lengths of the

minority carriers. This can be considered by adding a linear term to equation (20.68). Thus

$$I_{SC}(G, T_c) = I_{SC}^* \cdot \frac{G}{G^*} \cdot \left[1 + (T_c - T_c^*) \frac{dI_{SC}}{dT_c} \right] \quad (20.73)$$

where the temperature coefficient dI_{SC}/dT_c depends on the semiconductor type and on the manufacturing process, but it is always quite small. Typical experimental values are below $3 \cdot 10^{-4}$ (A/A)/°C [51, 59]. For a solar cell operating at 70°C, that represents only 0.13% of I_{SC} increase. Hence, ignoring this dependence has no practical effects, in all the cases.

The open-circuit voltage tends to increase with the illumination level. The ideal diode equation (see equation (20.60)) shows there is a logarithmic dependence. Then, this effect can be considered by adding a logarithmic term to equation (20.69). Thus

$$V_{OC}(T_c, G) = V_{OC}^* + (T_c - T_c^*) \frac{dV_{OC}}{dT_c} + V_t \cdot \ln \left(\frac{G_{eff}}{G^*} \right) \quad (20.74)$$

Note that the relative influence of this new term increases with decreasing irradiance. For example, for $G_{eff} = 500$ W/m² and $G_{eff} = 200$ W/m², it represents about 3 and 7%, respectively. Hence, its importance when predicting the energy delivered by PV modules depends on the irradiance distribution of the irradiation content. Obviously, it is more important for northern than for southern countries. For example, in Freiburg-Germany ($\phi = 48^\circ$) about 50% of yearly irradiation is collected below 600 W/m² and 18% below 200 W/m². Meanwhile in Jaen-Spain ($\phi = 37.8^\circ$) about 30% of yearly irradiation is collected below 600 W/m² and only 6% below 200 W/m². Moreover, it should be understood that very low irradiances are sometimes rejected by PV-system requirements. For example, in grid-connected systems, DC power from PV modules must be large enough to compensate for the inverter losses. Otherwise, the PV system becomes a net energy consumer.

While this logarithmic term does account for some variation in open-circuit voltage as irradiance changes, it does not adequately predict the rapid decrease observed at values of irradiance less than about 200 W/m², which causes a noticeable efficiency decrease below this value. The use of a second logarithmic term has been proposed [60] to also consider this low irradiance effect. Thus

$$V_{OC}(T_c, G) = \left[V_{OC}^* + \frac{dV_{OC}}{dT_c} (T_c - T_c^*) \right] \left[1 + \rho_{OC} \ln \left(\frac{G_{eff}}{G_{OC}} \right) \ln \left(\frac{G_{eff}}{G^*} \right) \right] \quad (20.75)$$

where ρ_{OC} and G_{OC} are empirically adjusted parameters. Values of $\rho_{OC} = -0.04$ and $G_{OC} = G^*$ have proven adequate for many silicon PV modules.

The sun spectrum shifts over time, due to changes in atmosphere composition, and changes in the distance the light has to travel through the atmosphere. This can affect the response of PV devices, especially if they have a narrow spectral response. Martin and Ruiz have proposed [61] a model based on the parameterisation of the atmosphere by means of the clearness index and the air mass, and this considers independently the spectrum of each radiation component: direct, diffuse and albedo. It can be described by

modifying the equation (20.68). Thus

$$I_{SC} = \frac{I_{SC}^*}{G^*} (B_{eff} \cdot f_B + D_{eff} \cdot f_D + R_{eff} \cdot f_R) \quad (20.76)$$

where f_B , f_D and f_R obeys to the general form

$$f = c \cdot \exp[a(K_T - 0.74) + b(AM - 1.5)] \quad (20.77)$$

and a , b and c are empirically adjusted factors, for each module type and for each radiation component. Note that 0.74 and 1.5 are just the values of the atmospheric parameters corresponding to the STC. Table 20.7 shows the recommended values of these parameters for crystalline, c-Si, and amorphous a-Si modules. The usefulness of this table can be extended to other PV materials, by linear interpolation on the energy band gap, E_g , between $E_g(\text{c-Si}) = 1.12$ eV and $E_g(\text{a-Si}) = 1.7$ eV. For example, $E_g(\text{a-SiGe}) = 1.4$ eV \Rightarrow estimated value of c is equal to 0.8.

Spectral effects used to be small on a yearly basis. Spectral losses with respect to STC are typically below 2% with semiconductors with broad spectral sensitivity, and below 4% for the others. However, on an hourly basis, spectral effects up to 8% can be encountered.

The PV module cell temperature is a function of the physical variables of the PV cell material, the module and its configuration, the surrounding environment and the weather conditions. It results from the balance of energy inputs and outputs through radiation, convection, conduction and power generation. Today, the more widely extended model, based on the *NOCT* concept and described by equations (20.70 and 20.71), lump the contributions together in an overall heat-loss coefficient, resulting in a liner relationship between module temperature and irradiance under steady-state conditions. This implies accepting that the heat transfer process between the solar cell and the ambience is essentially dominated by the conduction through the encapsulating materials, and neglecting the wind effects on convection. This model is simple to use and requires only standard available input information, which are undeniable advantages for the PV designer. But it can lead to significant errors in cell temperature estimation for non-steady-state conditions [62] (observed thermal time constant of PV modules is about 7 minutes), and for high wind speeds. That has stimulated several authors to develop new thermal models for PV systems, based not only on irradiance but also on wind speed. For example, Sandia

Table 20.7 Coefficient for spectral response modelling, for c-Si and a-Si modules

	B		D		R	
	c-Si	a-Si	c-Si	a-Si	c-Si	a-Si
c	1.029	1.024	0.764	0.840	0.970	0.989
a	-3.13E-01	-2.22E-01	-8.82E-01	-7.28E-01	-2.44E-01	-2.19E-01
b	5.24E-03	9.20E-03	-2.04E-02	-1.83E-02	1.29E-02	1.79E-02

Table 20.8 Temperature coefficients for module and cell temperature estimation, for two typical module designs

Type	T_1 [°C]	T_2 [°C]	b	ΔT [°C]
Glass/cell/glass	25.0	8.2	-0.112	2
Glass/cell/tehdar	19.6	11.6	-0.223	3

Laboratories proposed [63] a two components thermal model given by

$$T_c = T_m + \frac{G_{\text{eff}}}{G^*} \Delta T, \text{ where } T_m = T_a + \frac{G_{\text{eff}}}{G^*} [T_1 \exp(b \cdot \omega_s) + T_2] \quad (20.78)$$

In this equation, T_m is the back-surface module temperature, in °C; ω_s is the wind speed measured at standard 10 m height, in $\text{m}\cdot\text{s}^{-1}$; T_1 is an empirical coefficient determining the upper temperature limit at low wind speeds; T_2 is an empirical coefficient determining the lower temperature limit at high wind speeds; b is an empirical coefficient determining the rate at which the module temperature drops as wind speed increases and ΔT is also an empirical coefficient related to the temperature gap along the back encapsulation material. Table 20.8 gives the parameters found to have good agreement with measured temperatures, for two different module types.

However, the real usefulness of all these second-order corrections (equations 20.74–20.77) for temperature and wind speed is far from clear, because wind speed is difficult to predict, and also because cell temperature errors becomes more tolerable when translated into PV module power generation. For example, for a solar cell operating around 50°C, an error of 20% on the estimation of its cell temperature ($\approx 10^\circ\text{C}$) reflects in an error of only 0.4% ($\approx 10^\circ\text{C} \times 2.3(\text{mV}/^\circ\text{C})/600 \text{ mV}$) in the estimation of the corresponding power.

20.11 RELIABILITY AND SIZING OF STAND-ALONE PV SYSTEMS

The merit of a stand-alone PV system depends on how reliably it supplies electricity to the load. It is customary to quantify this reliability in terms of the Loss of Load Probability (*LLP*), defined as the ratio between the energy deficit and the energy demand, both referring to the load, over the total operation time of the installation. Thus,

$$LLP = \frac{\int_t \text{energy deficit}}{\int_t \text{energy demand}} \quad (20.79)$$

It should be noted that, because of the random nature of solar radiation, the value of *LLP* is always greater than zero, even if the PV system never actually breaks down. The available literature shows a large consensus over the expression of reliability in terms

of energy shortage probability, but different names can be found for the *LLP*: Deficit of Energy [64], Loss of Power Probability [65] and Loss of Power Supply Probability [66]. Moreover, the Load Coverage Rate [67] or Solar Fraction [68], *SF*, defined as the fraction of energy load covered by the PV system is also used to quantify reliability. Clearly, $SF = 1 - LLP$.

The “size” of a PV system means the size of both the generator (PV modules) and the accumulator (batteries or other storage device). It is useful to relate these sizes to the size of the load, in terms of average daily energies. Thus, the generator capacity, C_A , is defined as the ratio of the average daily energy output of the generator divided by the average daily energy consumption of the load. The accumulator capacity, C_S , is defined as the maximum energy that can be extracted from the accumulator divided by the average daily energy consumption of the load. Thus,

$$C_A = \frac{\eta_G \cdot A_G \cdot \overline{G_d}}{L} \text{ and } C_S = \frac{C_u}{L} \quad (20.80)$$

where A_G and η_G are the area and conversion efficiency of the photovoltaic generator, respectively, $\overline{G_d}$ is the mean value of the daily irradiation on the surface of the generator, L is the mean value of the daily energy consumed by the load and C_u is the useful energy storage capacity of the accumulator. More strictly, η_G should be the path efficiency from the array to the load, and C_u is the product of the nominal capacity (which refers to the whole energy that can be extracted from the accumulator if no particular limitations were imposed) and the maximum allowable depth of discharge. We will deal with the practical meaning of such parameters later. Meanwhile, it is worth pointing out that C_A depends on the local solar climate conditions. Therefore, the same photovoltaic generator, connected to the same load, may seem big in one place and small in another where there is less radiation.

Figure 20.22 shows how the energy generation varies over an assumed period of j days, for a given location and load, and for two different sizes of the generator ($C_{A1} < C_{A2}$). The shaded areas underneath the line $y = 1$, illustrate the temporal deficits of energy generation that need to be compensated by extraction of energy from the accumulator. It can be observed that the larger the generator, the lower the deficit and, hence, the smaller the required accumulator. Two ideas are now intuitively apparent: the first is that it is possible to find different combinations of C_A and C_S that lead to the same value of *LLP*; the second is that the larger the photovoltaic system, the better the reliability, that is, the lower the value of *LLP*, but also the greater the cost.

A certain degree of reliability is (or should be) a requirement depending on the typology of the load. For example, reliability requirements of telecommunication equipment are usually higher than that required by domestic appliances (higher reliability means lower *LLP* values). The problem confronting the PV engineer then takes the following “theoretical” form: Which combination of C_A and C_S achieves the desired *LLP* with minimum cost? Since cost estimation is a classic economic problem discussed widely in the literature, the PV-sizing problem is mainly rooted in the relationship between C_A , C_S and *LLP*. Later, C_A and C_S must be translated into the number and power of PV modules and battery capacity.

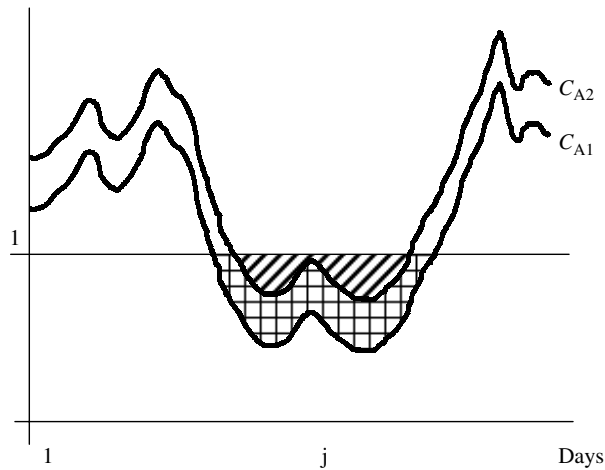


Figure 20.22 Time variation of the generated daily energy, relative to load, for two PV generators for which $C_{A1} < C_{A2}$. The shadowed areas represent the corresponding energy deficits to be covered by the storage device

In essence, any PV- sizing method involves four different steps:

- obtaining solar radiation site information,
- preparation of global horizontal daily irradiation sequences,
- transposition from horizontal to inclined radiation values,
- simulation of PVsystem behaviour, in order to quantify LLP corresponding to pairs of C_A and C_S values.

The first three steps have already been discussed in previous sections of this chapter. We will now deal with the last step, with the following assumptions: first, the daily energy consumption is constant all through the year; second, all the daily consumption occurs at night (i.e. after the energy generation time ends); and, third, the components of the PV system are ideal and can be linearly modelled. This is adequate for analysing the “pure” sizing problem, that is, the relation between C_A , C_S and LLP . Non-linearities and non-ideal effects (for example, battery efficiency) are better taken into account by the use of proper correction factors when translating C_A and C_S values into nominal PV array power and battery capacity. It is interesting to note that short-term (hourly) variations of demanded energy have no effect on LLP [64, 69], provided that $C_S > 2$, which is usually the case. The above- described assumption leads to particularly simple calculations. The state of charge, SOC , of the accumulator at sunset of day j is given by

$$SOC_j = \min \left\{ SOC_{j-1} + \frac{C_A \cdot G_{dj}}{C_S \cdot \overline{G_d}} - \frac{1}{C_S}; 1 \right\} \quad (20.81)$$

where G_{dj} is the total irradiation for day j , and

$$LLP = \frac{1}{N \cdot L} \sum_{j=1}^N E_{LACKj} \quad (20.82)$$

where N is the number of days for which the simulation is carried out, and E_{LACK} is the daily energy deficit, given by

$$E_{LACKj} = \max \left\{ \frac{1}{C_S} - SOC_j; 0 \right\} \quad (20.83)$$

This equation implies that an energy deficit occurs only when the stored energy at the end of the day $SOC_j \cdot C_S \cdot L$ does not suffice to cover the daily load L . Note that $SOC_j \cdot C_S \cdot L < L \Rightarrow (1/C_S - SOC_j) > 0$.

Because information on the daily irradiation used to be expressed in terms of mean monthly values, a different value of C_A may be worked out for each month. In what follows, we shall use for C_A just the value corresponding to the worst month. Thus,

$$\overline{G_d} = \min\{G_{dm}(\beta, \alpha)\}; (m = 1, \dots, 12) \quad (20.84)$$

Computed results can be arranged and presented graphically. Figure 20.23 presents some examples of the so-called “reliability maps”.

The shape of such curves prompts the thought that it should be possible to describe them in an analytical form. Several attempts at proposing analytical methods based on this idea have been made [64, 70–76] allowing sizing of PV systems by means of straightforward, simple calculations. For example, at the IES-UPM we have concluded [76] that all these curves conform to the relationship

$$C_A = f \cdot C_S^{-u} \quad (20.85)$$

where f and u are two parameters that depend on the value of LLP and on the location. These parameters do not have particular physical meaning, and their determination previously requires a lot of simulations to be carried out. However, they allow a large number of simulated results to be condensed into just a few sizing parameters. Advanced simulation software tools have also been developed and are being marketed today [42, 43].

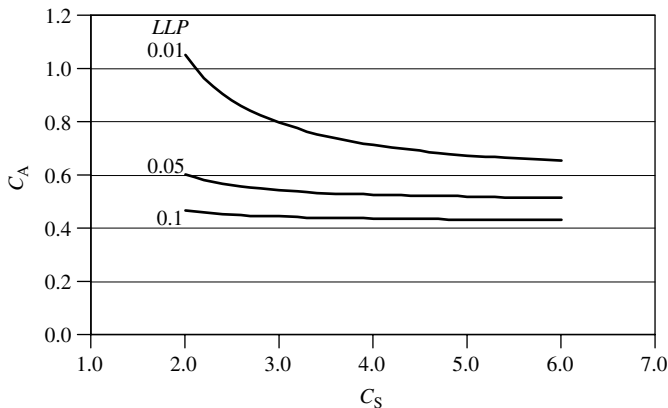


Figure 20.23 Reliability maps: Generator capacity C_A versus storage capacity C_S with the reliability LLP as parameter

It must be stressed that, whatever the detailed methodology, PV-system sizing relies on future prediction (the expected system lifetime) based on past observations of the solar radiation. Basic statistical laws imply that such prediction exercises are unavoidably associated with a degree of uncertainty, as mentioned before. This implies a basic limit of accuracy for PV sizing. We will try to clarify this aspect with an example.

We will suppose that 20 years of daily irradiation data measured in a certain location with a great level of accuracy are available. We will call them the “historical sequence”. This allows us first, to establish the statistical characteristics of the radiation (mean value, standard deviation, etc.); and, second, to make detailed simulations of a PV system’s behaviour over these particular years. Thus, we can map with high precision the reliability associated with different system sizes, for this particular historical sequence. As a simulation exercise, the accuracy of the result is limited only by the precision of the initial measurements, which have been assumed to be very good. However, when using such a sequence for sizing a future system, another limitation arises simply because the solar radiation in the future will not exactly repeat the same pattern as in the past. In fact, it is extremely unlikely in terms of daily sequences. All that can be expected is that the future solar radiation sequence will keep some statistical properties whose validity is known to be general, which opens the door for the generation of a vast collection of hypothetical solar radiation sequences with the same occurrence probability as the historical one. Then, a different reliability map can be associated with each of these radiation sequences, by means of the above-mentioned simulation exercise. Obviously, the similarity between the different maps can be understood as a measure of the uncertainty associated with the prediction. Figure 20.24 shows the result of superimposing such maps. The example is for Madrid, generating different solar radiation sequences following the above-mentioned Aguiar’s method [37]. It is clear that precautions must be taken with predictions for $LLP < 10^{-2}$. For example, for $LLP = 10^{-3}$ and $C_S = 3$, we can find C_A values from 1.1 to 1.5. Other authors [70, 77] have presented similar results. We must conclude that the validity of PV-sizing methodologies is generally restricted to the range $1 > LLP > 10^{-2}$, that is, to solar coverage below 99%. Beyond this limit, sizing results are statistically of doubtful quality, although unfortunately, they are often found in the literature and in simulation software tools marketed today.

It must be stressed that this basic uncertainty cannot be overcome either by reducing the simulation time-step (hourly instead of daily values) or by incorporating more complex models of the elements of the PV systems (non-linear $I-V$ models of PV generators, battery efficiency dependence with SOC etc.). In fact, the reduction of the considered simulation period can only worsen the situation. It can be shown that the validity of sizing results based only on the TMY (avoiding the generation of large-radiation sequences) is restricted to the range $1 > LLP > 10^{-1}$, independent of any other consideration [78]. Appropriately, Marion and Urban [18], when presenting USA TMY s, advises “. . . *Because they represent typical rather than extreme conditions, they are not suited for designing systems to meet the worst-case conditions occurring at a location*”.

On the other hand, such basic uncertainty can help to explain why the result of the different PV-sizing methods can be inconsistent; and also why the accuracy gains associated with the consideration of second-order effects when modelling the PV system are likely to be insignificant. In other words, such modelling can be useful for studying some PV-system features (optimal number of solar cell per module, optimal charge regulation

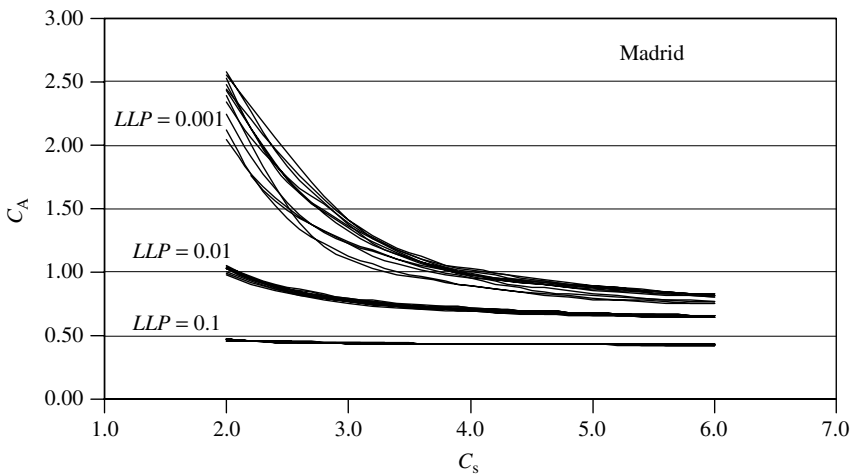


Figure 20.24 Simulated reliability maps, C_A versus C_S , with the historical and with 12 generated solar radiation sequences for three different reliability LLP values

algorithms etc.); but it is of little value when considering the pure size problem, for which a judicious and rather simple hypothesis suffices. A similar conclusion is presented in Kaiser and Sauer [79], from a comparison of the long-term energy yield of stand-alone PV systems simulated with both simple and detailed models. The authors observe that the range of uncertainty due to possible fluctuations of the radiation-time series is significantly larger than the those corresponding to changes in the PV-system component modelling, and conclude “*The results make it clear that exact simulation models can provide exact numbers, but do not automatically allow exact predictions*”.

This can also help explain why PV-system sizing simply based on guesswork remains widely practiced in current engineering practices. This prevents any quantitative relationships between C_A , C_S and LLP being established. The size of the generator is instead chosen to ensure that the energy produced during the design period (most often, the worst month) exceeds the demand of the load by a margin that depends on the designer’s experience. A similar procedure is used to size the accumulator. In summary,

$$C_A = F_{S1} \text{ and } C_S = F_{S2} \quad (20.86)$$

where F_{S1} and F_{S2} are arbitrary factors. For example, $C_A = 1.1$ and $3 \leq C_S \leq 5$ are common values for rural electrification purposes [80]. $1.2 \leq C_A \leq 1.3$ and $5 \leq C_S \leq 8$ are common ranges on the so-called professional market [71]: telecommunication and so on.

It is worth pointing out that this rather unscientific way of proceeding does not necessarily give bad results, in terms of reliability and cost. As a matter of fact, a proper combination of expertise and common sense often leads to very good results. Today, PV systems have the reputation of being reliable, even in those sectors where high reliability is an established requirement, such as telecommunications and cathodic protection. This helps explain why reliability quantification is generally considered irrelevant in real

engineering practice, and mainly good for academic discussion; and why the actual use of PV-sizing methodologies is mainly aimed at giving a pseudo-scientific appearance to commercial activities. Our own experiences at IES-UPM contain several cases of perplexed PV clients requesting our opinion on the big PV-system sizing differences among different PV contractor estimates that they have received for a given location and application. Obviously, simplistic relations like equation (20.86) do not help the PV professional to adopt rigorous sizing procedures. However, we still believe such rigorous procedures should play an important role in future. This is because a professional's credibility benefits from reliability quantification (the use of the Mean Time Between Failures concept in the conventional electricity sector is a good example of this); and also because the usefulness of such methods extends beyond pure sizing problems. Additional comments are given in the following section.

It must be mentioned that in the common case of PV arrays directly coupled to batteries, that is without maximum power-tracking devices, energy balance analysis can be done by means of simple ampere balances, initially supposing that the working voltage is always the nominal one, V_{NOM} , at which it equals the maximum power point voltage of the generator. Therefore,

$$L = V_{\text{NOM}} \cdot Q_L \text{ and } \eta_G \cdot A_G = \frac{V_{\text{NOM}} \cdot I_M^*}{G^*} \quad (20.87)$$

which leads to

$$C_A = \frac{I_M^* \cdot G_{\text{dm}}(\beta, \alpha)}{Q_L \cdot G^*} \text{ and } C_S = \frac{Q_B}{Q_L} \quad (20.88)$$

where Q_L is the amount of charge (expressed in ampere-hours) drawn daily by the load, that characterises the required PV array, and Q_B is the useful ampere-hour capacity of the battery, which is equal to the product of the nominal capacity by the maximum depth of discharge. This approximation, in spite of appearing oversimplified, gives very good results and simplifies the task of deducing the number of PV modules to be installed.

20.12 THE CASE OF SOLAR HOME SYSTEMS

Global market indicators [81, 82] lead to the estimate that about 1.3 million home systems for lighting, radio and television are currently in operation, totalling 40 MWp, and large rural electrification programmes comprising some thousands of SHSs are increasingly becoming a part of the rural market. Thus, SHS represent the most widespread PV application nowadays, and the trend is likely to continue.

Standardisation of equipment and its mass production represent efficient ways to obtain low prices and high technical quality. In consequence, SHS designers have to fix a single "standard" value of energy consumption for a large number of different families. It must be noted that such standardisation is a requirement imposed by the technology itself in order to reduce cost and guarantee quality, but it does not correspond well with the idea of needs at the individual level. PV history shows some interesting cases [83, 84]. For example, in Reference [83] it is stated that "... an interesting aspect,

clearly confirmed by the operating results of ENEL plants, is that the intake power by this type of user . . . is rarely the same on any given day, and it is linked to the particular lifestyle of the people involved, to periods of absence and to the number of occupants of the houses being supplied, and so on". Apart from PV, other types of rural electrification also provide examples. Figure 20.25 shows the distribution of the individual monthly electricity consumption measured along four years in the 63 dwellings of Iferd, a Moroccan village where a small diesel generator set provides 3 h of electricity per day (consumers are metered and pay for their energy use). The large observed spread leads one to question the real meaning of reliability parameters such as LLP , and the real usefulness of rigorous PV-sizing methodologies.

It appears that "standard" LLP values derived from sizing methodologies are scarcely representative of the realities in the field. The relationship between reliability and load, that is, the function $LLP = LLP(L)$ for a given PV system, can be explored just by extending the previously described simulation procedure to a large number of cases. A certain baseline case has been, first, established by fixing the PV array power and the battery capacity values, C_A and C_S , for a given load, L_{BASE} , and a given reliability, $LLP = 0.1$. Then, the load has been varied from $0.8 L_{BASE}$ to $1.2 L_{BASE}$ and the corresponding reliability has been calculated. Figure 20.26 shows the result. Roughly speaking, we can say that an approximately logarithmic relationship exists in such a way that LLP decreases one order of magnitude for each 30% of load reduction. This result, together with the observation that real L values are generally found within the range -50% to $+100\%$ of the mean, let us conclude that real individual LLP values can vary more than three orders of magnitude (for example, from 10^{-1} to 10^{-4}) in the context of the same SHS project. This nullifies any attempt at finding a single representative

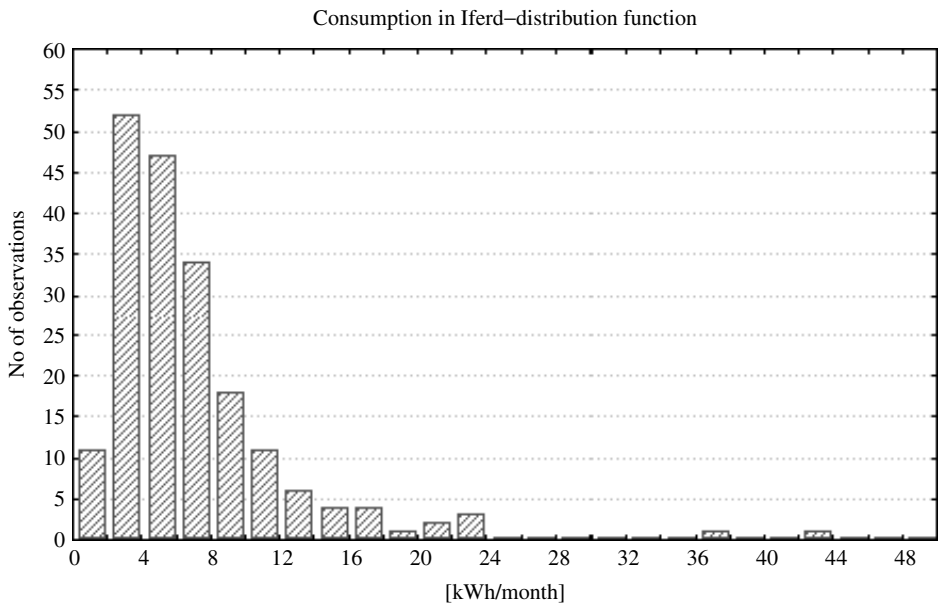


Figure 20.25 Distribution function of monthly electricity consumption in all the Iferd dwellings

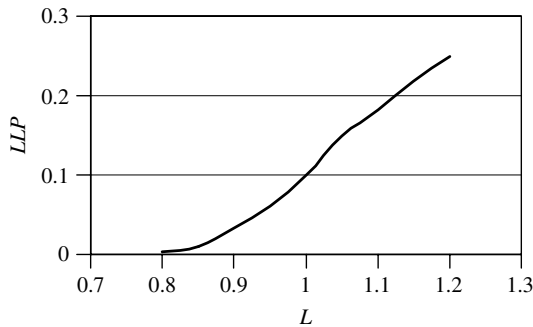


Figure 20.26 Reliability LLP as a dependent variable on the consumption L for a given PV array and capacity values

LLP value. It is worth mentioning that the same is not true when centralised electricity generators are considered (PV or not), because the total energy consumed by all the families involved shows a much lower standard deviation than that corresponding to the individual consumptions (roughly, the standard deviation becomes reduced by a factor of $1/\sqrt{N}$, N being the number of families), so that it is possible to find single L and LLP representative values for the whole served population.

However, even in extremely varying applications, such as SHS, PV-sizing methods based on reliability can be of great help if large-scale programmes become a future reality. This will probably require the development of rigorous engineering: standardisation of different levels of service, technical quality controls and so on. For example, PV-sizing methods based on LLP represent an interesting possibility of comparing different alternatives (different offers from various manufactures) on an objective basis, as the LLP value respectively associated to each alternative, for the same considered energy service [78].

It is worth considering the question: “How much electricity has to be provided to a rural house in a developing country to be socially and economically acceptable?” Although this question is always at the origin of any PV rural electrification programme, its answer in terms of watthour/day, is far from being clear. Energy consumption data, based on practical experience in developing countries, are scarce in the literature [84], which is paradoxical considering that many thousands of SHS are currently operating in developing countries. Instead, there are a great number of consumption scenarios where, although starting from very different hypothesis concerning the number of appliances and the length of time they are in use, the SHSs finally selected have an installed power of about 40 to 50 Wp. This is because past in-field experience has shown PV designers that such systems are generally well accepted by the rural users, while the same is not always the case when small (20–30 Wp) PV modules are concerned. This way, the SHS scenarios elaborated by PV designers must therefore be interpreted as explanation exercises, rather than as designs for systems starting from an evaluation of actual needs (see Chapter 23 for discussion of rural electrification programmes). So, we must conclude that energy scenarios for rural electrification purposes are still an open question, which need to be explored in-depth.

20.13 ENERGY YIELD OF GRID-CONNECTED PV SYSTEMS

The output of grid-connected PV systems is the output from the PV array less the losses in the inverter. The output from the PV array has been considered in detail in this chapter, and the performance of inverters is described in Chapter 19. As far as inverters are concerned, it is important to account for the fact that the instantaneous efficiency, η_y , depends on the ratio between the actual power delivered to the grid P_{AC} , and the rated power of the inverter, P_{IMAX} . This dependence may be represented by [85]

$$\eta_i = \frac{p}{p + k_0 + k_{i1}p + k_{i2}p^2} \quad (20.89)$$

where $p = P_{AC}/P_{IMAX}$ and k_0 , k_{i1} and k_{i2} are parameters characteristic of the inverter defining its electrical behaviour. k_0 is the quiescent power consumption, k_{i1} represents the losses that depend linearly on the current (voltage drop across diodes, etc.) and k_{i2} represents the losses that depend on the square of the current (resistive losses, etc.). These parameters can be obtained from the inverter efficiency curve. Depending on quality level, input voltage and rated power, the loss parameters of existing inverters have a spread of more than a factor of 10. Average values, in percentage, are $k_0 = 2$, $k_{i1} = 2.5$ and $k_{i2} = 8$, leading to 85% typical energy efficiency. Very good inverters reduce these values to $k_0 = 0.35$, $k_{i1} = 0.5$ and $k_{i2} = 1$, leading to 95% typical energy efficiency.

To describe the effect of no-load shut-off, the standby self-consumption k'_0 is used. It is the value to which the operating self-consumption (k_0) is reduced during shut-off ($k'_0 < k_0$). Reduction of self-consumption improves the low- and medium-power efficiency, which is most important for PV applications. The loss fractions due to self-consumption sum up to considerable losses in PV systems. In comparison, the sum of the load dependent losses (due to k_1 and k_2) is 1.5 to 7 times smaller.

Standard methods for performance analysis of PV grid-connected plants have been introduced in the JRC Ispra Guidelines [86] and extended and improved by HTA Burgdorf [87]. Global performance is appropriately described by the so-called *performance ratio* (PR), which is the ratio of AC energy delivered to the grid, E_{AC} , to the energy production of an ideal, loss-less PV plant with 25°C cell temperature and the same solar irradiation. This gives a good indication of how much of the ideally available PV energy has actually been used. It is given by

$$PR = \frac{E_{AC}}{\frac{G_y(\beta, \alpha)}{G^*} \cdot P_M^*} \quad (20.90)$$

Other interesting parameters are the *Reference Yield*, $Y_r = G_y(\beta, \alpha)/G^*$, the *Array Yield*, $Y_a = E_{DC}/P_M^*$, where E_{DC} is the DC energy generated by the PV array, and the *Final Yield*, $Y_f = E_{AC}/P_M^*$. All the three have units of time, and allow us to distinguish between the losses due to the PV array, and the losses associated to the inverter and to the operation of the system. Capture losses, $L_C = Y_r - Y_a$, are defined as the energy losses, expressed in hours per day of PV array operation at STC power output, caused by: cell temperatures

Table 20.9 Power distribution of the yearly irradiation for a low and a high latitude location

Location	$G_y(\beta_{opt})$ [kWh/m ²]	Percent of irradiation in different ranges of irradiance in [W/m ²]				Total
		<200	200–500	500–800	>800	
Jaen	2040	5.8	23.6	44.7	25.9	100
Copenhagen	1190	13.9	30.7	35.7	19.7	100

higher than 25°C, losses in wiring and protection diodes, poor module performance at low irradiance, partial shading, snow and ice coverage, module mismatch, operation of the array at a voltage other than its maximum power point, and spectral and angular losses. System losses, $L_S = Y_a - Y_f$, are the losses due to inverter inefficiencies. It must be noted that $PR = Y_f/Y_r$.

Energy losses in good PV grid-connected systems are about $L_C = 15\%$ and $L_S = 7\%$, which lead to $PR \approx 0.78$. However, reported experimental values have ranged from 0.65 to 0.72. The main reason for such PR reduction is that the actual power of installed PV arrays is often below the rated power declared by the manufactures [88].

The power distributions of solar irradiation are different for varied geographical latitudes. In places of high latitude, with very cloudy weather, the solar irradiation is almost evenly distributed over a wide range of power scale; while in low latitude places, with predominantly clear sky, the higher power range is enhanced. Table 20.9 presents the distribution in different irradiance classes of the total yearly irradiation over an optimally tilted surface, as obtained from the *TMY* of Copenhagen [89] ($\phi = 55.7^\circ$) and Jaen-Spain [90] ($\phi = 37.8^\circ$). Surprisingly, the energy content at low irradiances ($G < 200$ W/m²) is relatively low in both places. This may appear counter-intuitive, but it is easily understood when considering the difference between time and energy distribution. For example, in Copenhagen, the low irradiance (<200 W) accounts for only 13.9% of the total annual irradiation, despite it occurring during 2461 h/year, which represents 55% of the total daily time. That leads one to question the idea, sometimes defended in PV literature [91], that PV module performance at low irradiances is very relevant for cloudy climates. As a matter of fact, empirical evidence that efficiency at low light levels is scarcely relevant is found in the literature [92].

However, because the most commonly occurring irradiation corresponds to medium irradiances, an energetic advantage can be obtained by selecting the inverter size smaller than the PV generator peak power, that is, $P_{IMAX} < P_M^*$. The corresponding reduction of relative inverter self-consumption and losses may compensate the possible energy loss by an inverter power limit lower than the maximum PV output power. Recommended values of P_{IMAX}/P_M^* range from 0.6 (high latitudes) to 0.8 (low latitudes) [85, 93].

20.14 CONCLUSIONS

Methods to estimate all the solar radiation components incident on any arbitrarily oriented surface and at any time of the year have been presented. The only required input

information is the 12 monthly mean values of the daily global horizontal irradiation. Several sources of solar radiation data are available. The corresponding values, for the same location and the same month, can significantly differ from one source to another. The corresponding uncertainty does not derive primarily from a lack of precision in the measuring instruments, but from the random nature of the solar radiation. The intrinsic uncertainty of solar radiation represents an important limit to the significance of the results of any PV design exercise, irrespective of the complexity of the model supporting the particular design tool. Because of this, rather simple design methodologies can yield results of similar confidence that results from sophisticated ones. The annual solar radiation availability on horizontal surfaces, optimally tilted fixed surfaces and several types of tracking surfaces has been calculated for 30 different places distributed all over the world. The hope is that the readers could find here a similar location, both in latitude and clearness index, to the location of their interest.

On the other hand, the PV module's conversion efficiency of solar radiation into electricity has also been considered. A model for predicting the $I-V$ characteristic of a PV generator at any prevailing condition such as solar irradiance, ambient temperature, wind speed and so on, have been described. The only required input data are the short-circuit current, the open-circuit voltage and the maximum power under the STC, and the Nominal Operating Cell Temperature. All these data are commonly found in the manufacturer's standard information. Particular attention has been paid to the consideration of the dust and angle of incidence effects.

Some relevant aspects related to the design of the more important PV applications have been disclosed. It has been stressed that, whatever the detailed methodology, stand-alone PV-system sizing relies on future prediction (the expected system lifetime) based on past observations of the solar radiation data. The corresponding uncertainty, unavoidably associated with the random nature of the solar radiation, encompasses that simulation models can provide exact numbers but not automatically exact predictions. Concerning SHS, by far the most widespread PV application nowadays (in terms of the number of systems currently in operation), the difficulties for deriving representative standard energy consumption values have been pointed out. Finally, energy performance ratios for grid-connected PV systems have been defined.

ACKNOWLEDGEMENTS

Montse Rodrigo has been extremely kind in preparing all the figures. The comments of the editor have been extremely valuable. The writing of this chapter has been at the expense of many hours away from my loved ones. I must thank the large tolerance and patience of Leda and Cristina Celena.

REFERENCES

1. Serres M *et al.*, *Éléments d'Histoire des Sciences*, Chap. 3, Ed Bordas, Paris, 77–117 (1989).
2. Spencer J, *Search* **2**, 172–178 (1971).
3. Blanco M, Alarcón D, López T, Lara M, *Sol. Energy* **70**, 431–441 (2001).
4. Kasten F, *Arch. Meteorol. Geophys. Bioklimatol.* **14**, 206–223 (1966).

5. Meinel A, Mainel M, *Applied Solar Energy, An Introduction*, Addison-Wesley, Reading, MA (1976).
6. Iqbal M, *An Introduction to Solar Radiation*, Academic Press, Ontario (1983).
7. International H-World Database, *Mean Values of Solar Irradiation on Horizontal Surface*, Ed Progenza, Sevilla, Spain (1993).
8. SOLMET, *Solar Radiation-Surface Meteorological Observations*, National Climatic Data Center, TD-9724, Asheville, NC (1979).
9. Palz W, Greif J, *European Solar Radiation Atlas*, Commission of the European Communities, Ed Springer, Germany (1996).
10. Font Tullot I, *Atlas de la Radiación Solar en España*, Ed Instituto Nacional de Meteorología, Madrid, Spain (1984).
11. Capderou M, *Atlas Solaire de l'Algerie*, Ed EPAU, Alger (1985).
12. Colle S, Pereira E, *Atlas de Irradiação Solar do Brasil*, INM, Labsolar EMC-UFSC (1998).
13. *Atlas de radiació solar a Catalunya*, Institut Català d'Energia, Barcelona, Spain (1996).
14. NASA Surface Meteorology and Solar Energy Data Set. Available at eosweb.larc.nasa.gov/sse.
15. National Solar Radiation Data Base. Available at rredc.nrel.gov/solar.
16. Macagnan M, Lorenzo E, Jimenez C, *Int. J. Sol. Energy* **16**, 1–14 (1994).
17. Papoulis A, *Probability, Random Variables and Stochastic Processes*, McGraw-Hill, New York (1965).
18. Marion W, Urban K, *User's Manual for TMY2s*, Report to DOE DE-AC36-83CH10093, NREL (1995).
19. Liu B, Jordan R, *Sol. Energy* **4**, 1–19 (1960).
20. Page J, *Proc. U.N. Conf. New Sources Energy*, 378–390 (1961).
21. Collares-Pereira M, Rabl A, *Sol. Energy* **22**, 155–164 (1979).
22. Miguel A *et al.*, *Sol. Energy* **70**, 143–153 (2001).
23. Egido M, Lorenzo E, *Sol. Energy Mater. Sol. Cells* **26**, 51–69 (1992).
24. Willier A, *Arch. Meteorol. Geophys. Bioklimatol.* **7**, 197–204 (1956).
25. Hopkinson R, *J. Opt. Soc. Am.* **44**, 455–459 (1954).
26. McArthur L, Hay J, *J. Appl. Meteorol.* **20**, 421–429 (1981).
27. Kondratyev K, *Radiation in the Atmosphere*, Academic Press, New York, NY (1969).
28. Hay J, McKay D, *Int. J. Sol. Energy* **3**, 203–240 (1985).
29. Perez R *et al.*, *Sol. Energy* **36**, 481–497 (1986).
30. Perez R *et al.*, *Sol. Energy* **39**, 221–231 (1987).
31. Siala F, Rosen M, Hooper F, *J. Sol. Energy Eng.* **112**, 102–109 (1990).
32. Standard ASHRAE 93-77, *Methods of Testing to Determine the Thermal Performance of Solar Collectors*, American Society of Heating, Refrigeration, and Air Conditioning Engineers, New York (1977).
33. Martin N, Ruiz J, *Sol. Energy Mater. Sol. Cells* **70**, 25–38 (2001).
34. Bottenberg W, “Module Performance Ratings: Tutorial on History and Industry Needs”, *PV Performance, Reliability and Standards Workshop*, 5–42, NREL, Vail, CO (1999).
35. Amato U *et al.*, *Sol. Energy* **37**, 179–194 (1986).
36. Graham V *et al.*, *Sol. Energy* **40**, 83–92 (1988).
37. Aguiar R, Collares-Pereira M, Conde J, *Sol. Energy* **40**, 269–279 (1988).
38. Benseman R, Cook F, *N Z J. Sci.* **12**, 296–708 (1960).
39. Lorenzo E, Maquedano C, *Proc. 13th Euro. Conf. Photovoltaic Solar Energy Conversion*, 2433–2436 (1995).
40. Quaschnig V, Hanitsch R, *Proc. 13th Euro. Conf. Photovoltaic Solar Energy Conversion*, 683–686 (1995).
41. Skiba M *et al.*, *Proc. 16th Euro. Conf. Photovoltaic Solar Energy Conversion*, 2402–2405 (2000).
42. Castro M *et al.*, *Era Sol.* **87**, 5–17 (1998).

43. Kaiser R, Reise C, *PV System Simulation Programmes*, Internal Report for the IEA SHCP Task 16, Fraunhofer-FISE, Freiburg (1996).
44. Caamaño E, Lorenzo E, *Prog. Photovolt.* **4**, 295–305 (1996).
45. Jennings C, Farmer B, Townsend T, Hutchinson P, Gough J, Shipman D, *Proc. 25th IEEE Photovoltaic Specialist Conf.*, 1513–1516 (1996).
46. Butti K, Perlin J, *A Golden Thread: 2500 Years of Solar Architecture and Technology*, Ed Cheshire, Palo Alto, NY (1980).
47. de Laquil III P., Kearney D, Geter M, Diver R, in Johansson T, Kelly H, Reddy A, Williams R, Eds, *Renewable Energy: Sources for Fuels and Electricity*, Chap. 5, Island Press, Washington, DC, 213–236 (1993).
48. Lorenzo E, Macagnan M, *Prog. Photovolt.* **2**, 45–55 (1994).
49. Zilles R, Ribeiro C, Moszkowicz M, *Proc. 2nd WCE Photovoltaic Solar Energy Conversion*, 2009–2012 (1998).
50. Durisch W, Tille D, Wörz A, Plapp W, *Appl. Energy* **65**, 273–284 (2000).
51. Eikelboom J, Jansen M, *Characterisation of PV Modules of New Generations*, ECN-C-00-067, Report to NOVEM Contract 146.230-016.1, Available at www.ecn.com (2000).
52. Caamaño E, Lorenzo E, Zilles R, *Prog. Photovolt.* **7**, 137–149 (1999).
53. Schmela M, *PHOTON Int.* **3-2001**, 32–35 (2001).
54. Green M, *Solar Cells*, Chap. 5, Prentice Hall, Kensington, 95–98 (1982).
55. Araujo G, Sánchez E, *Sol. Cells* **5**, 377–386 (1982).
56. King D, Kratochvil J, Boyson W, *Proc. 26th IEEE Photovoltaic Specialist Conf.*, 1113–1116 (1997).
57. Fuentes M, *Proc. 17th IEEE Photovoltaic Specialist Conf.*, 1341–1346 (1984).
58. Chianese D, Cerenghetti N, Rezzonico R, Travaglini G, *Proc. 16th Euro. Conf. Photovoltaic Solar Energy Conversion*, 2418–2421 (2000).
59. Scheiman D, Jenkins P, Brinker D, Appelbaum J, *Prog. Photovolt.* **4**, 117–127 (1996).
60. Smiley E, Stamenic L, Jones J, Stojanovic M, *Proc. 16th Euro. Euro. Conf. Photovoltaic Solar Energy Conversion*, 2002–2004 (2000).
61. Martin N, Ruiz J, *Prog. Photovolt.* **7**, 299–310 (1999).
62. Jones A, Underwood C, *Sol. Energy* **70**, 349–359 (2001).
63. King L, Kratochvil J, Boyson E, Bower W, *Proc. 2nd World Conf. Photovoltaic Solar Energy Conversion*, 1947–1952 (1998).
64. Gordon J, *Sol. Cells* **20**, 295–313 (1987).
65. Cowan W, *Proc. 12th Euro. Conf. Photovoltaic Solar Energy Conversion*, 403–407 (1994).
66. Abouzahr Y, Ramakumar R, *IEEE Trans. Energy Conversion* **5**(3), 445–452 (1990).
67. Negro E, *Proc. 13th Euro. Conf. Photovoltaic Solar Energy Conversion*, 687–690 (1995).
68. Kaiser R *Photovoltaic Systems*, Chap. Fraunhofer-FISE, Freiburg, Germany (1995).
69. Boland J, Marjolijn D, *Sol. Energy* **71**, 187–198 (2001).
70. Chapman R, *Sol. Energy* **43**, 71–76 (1989).
71. Macomber H, Ruzek I, Costello F, *Photovoltaic Stand-Alone Systems: Preliminary Engineering Design Handbook*, Prepared for NASA, Contract DEN 3-195 (1981).
72. Barra L, Catalanotti S, Fontana F, Lavorante F, *Sol. Energy* **33**, 509–514 (1984).
73. Bucciarelli L, *Sol. Energy* **32**, 205–209 (1984).
74. Bartoli B *et al.*, *Appl. Energy* **18**, 37–47 (1984).
75. Sidrach-de-Cardona M, Mora LI, *Sol. Energy Mater. Sol. Cells* **55**, 199–214 (1998).
76. Egidio M, Lorenzo E, *Sol. Energy Mater. Sol. Cells* **26**, 51–69 (1992).
77. Klein S, Beckman W, *Sol. Energy* **39**, 499–512 (1987).
78. Lorenzo E, Narvarte L, *Prog. Photovolt.* **8**, 391–409 (2000).
79. Kaiser R, Sauer D, *Proc. 12th Euro. Conf. Photovoltaic Solar Energy Conversion*, 457–460 (1994).
80. Universal Technical Standard for Solar Home Systems, Thermie B SUP 995-96, EC-DGXVII (1998).

81. Maycock P, *Renewable Energy World* **2**, 72–76 (1999).
82. Nieuwenhout F *et al.*, *Prog. Photovolt.* **9**, 455–474 (2001).
83. Belli G, Iliceto A, Previ A, *Proc. 11th Euro. Conf. Photovoltaic Solar Energy Conversion*, 1571–1574 (1992).
84. Morante F, Zilles R, *Prog. Photovolt.* **9**, 379–388 (2001).
85. Jantsch M, Schmidt H, Schmid J, *Proc. 11th Euro. Conf. Photovoltaic Solar Energy Conversion*, 1589–1593 (1992).
86. *Guidelines for the Assessment of PV Plants. Document B: Analysis and Presentation of Monitoring Data*, Issue 4.1, JRC of the Commission of the European Communities, Ispra, Italy (1993).
87. Haeblerlin H, Beutler C, *Proc. 13th Euro. Conf. Photovoltaic Solar Energy Conversion*, 934–937 (1995).
88. Rindelhardt U, Teichmann G, Decker B, Grochowski J, *Proc. 14th Euro. Conf. Photovoltaic Solar Energy Conversion*, 2652–2655 (1997).
89. Katic Y, Jensen B, *Proc. 16th Euro. Conf. Photovoltaic Solar Energy Conversion*, 2830–2833 (2000).
90. Nofuentes G, *Contribución al desarrollo de aplicaciones fotovoltaicas en edificios*, Ph.D. thesis, Presented at the Polytechnical University of Madrid, Madrid (2001).
91. Mason N, Bruton T, Heasman K, *Proc. 14th Euro. Conf. Photovoltaic Solar Energy Conversion*, 2021–2024 (1997).
92. Wilk H, *Proc. 14th Euro. Conf. Photovoltaic Solar Energy Conversion*, 297–300 (1997).
93. Macagnan M, Lorenzo E, *Proc. 11th Euro. Conf. Photovoltaic Solar Energy Conversion*, 1167–1170 (1992).
94. Bourges B, *Climatic Data Handbook for Europe*, Ed Kluwer Academic Publishers, The Netherlands (1992).
95. Herrero M, *Soleamiento y Energía Solar*, Ed University of Valencia, Spain (1985).
96. PVSYST 3.1, www.pvsyst.com (2000).

21

Economic Analysis and Environmental Aspects of Photovoltaic Systems

**Richard A. Whisnant¹, Stephen A. Johnston²
and James H. Hutchby³**

¹Parameters, Inc., Cary, North Carolina, ²Research Triangle Institute, Research Triangle Park, North Carolina ³Semiconductor Research Corporation, Research Triangle Park, North Carolina

Photovoltaic (PV) systems provide electric energy, and the range of uses for electricity and the situations in which it is employed are enormous. Moreover, there are numerous other well-developed and widely used technologies for supplying electricity. Conventional fossil-fuel and hydroelectric generation are presently far more widely deployed than PV. The question arises, then, of how PV systems can penetrate the world's electric supply in competition with these alternatives, or, more narrowly, how a PV system can compete with other electricity sources for a specified application. At this point in time, there are many PV systems that do compete successfully in applications for which they are particularly suited. In other applications, PV systems have been deployed with the support of financial subsidies from private or public sources in order to either satisfy defined energy needs or to demonstrate the potential for PV systems. In all cases, it is useful to understand the economic viability, whether present or future, of any PV system in a given application. It is the purpose of this chapter to define and illustrate methods of defining the economics of PV systems as measured by conventional financial criteria and the cost of delivered energy. The cost of delivered energy is a fundamental characteristic of PV systems, and it can be influenced by the design and performance of the system, as well as by the sources and costs of capital to fund the system. The choice to deploy PV in a given situation is also influenced by other issues, including competition from the established electric supply, financial risk, and environmental, political, and humanitarian concerns.

21.1 BACKGROUND

A rational decision to develop, supply, or utilize PV systems calls for consideration of many factors in an organized manner so as to address the broad issue of whether photovoltaics is a good choice for the person or institution making the decision. Electric energy today can be provided from many sources that are both nonrenewable (including coal, oil, natural gas, nuclear) and renewable (such as wind, biomass, hydro, PV). PV systems compete, in the broadest sense of the word, against the other sources. The competition encompasses financial, reliability, environmental, and performance considerations, and the weight given to these factors will depend on the decision maker's priorities. The values of the parameters in the decision process are defined by well-developed and widely available energy-supply technologies. Economic analysis in the developed world usually focuses on which supply technology best meets the well-defined economic criteria for a given application or class of applications. The preponderance of the use of electric energy in the developed world is available from an electric supply grid, and the competitiveness of PV systems is often evaluated in that context. There are some off-grid demands that can be supplied by PV systems, and for which they are technically well qualified. In the United States, such applications include remote vacation homes or public buildings, navigation buoy signals, communications repeaters, outdoor signage, and irrigation pumping.

In less-developed areas of the world, which for the present discussion mean areas without electric-power grids, the context of the decision process is different. PV systems in such areas are often termed *remote* or *village* systems. They may be deployed in individual homes, small businesses, or may serve a community with local distribution of energy. The competition faced by PV systems in these settings is usually from diesel oil-powered generators (nonrenewable source) or from small renewable sources (such as wind, hydro, biomass). The factors in the decision to deploy PV systems may include factors common to developed regions, though there may be fewer energy alternatives, and generally the individual system capacities are much smaller than in developed regions. However, in less-developed regions of the world, certain other factors may assume greater importance. The viability of the systems is a serious issue if the infrastructure for their installation and maintenance is lacking. Conversely, the provision of that infrastructure to provide installation and maintenance may be a more significant concern than in developed regions. It may also vary among energy technologies, and to that extent it is a competitive factor. For example, diesel generators must be supplied with fuel on a periodic basis, and they have moving parts that must periodically be repaired or replaced. PV systems do not require fuel supply and have no moving parts to repair. However, this does not mean that they would never need repair or replacement.

The financial considerations in a decision to deploy PV can be quite different in developed regions than in the undeveloped regions. In a developed country, the economic units (e.g. individuals, families, businesses, government operations) have a cash flow and well-defined energy needs. The question that they must answer periodically is what source of energy will they choose from among competing alternatives that are highly developed and more or less readily available. The question can be addressed in a quantitative fashion, at varying levels of sophistication, and the resources are available to implement the choice. In undeveloped regions, the situation is more likely that the economic units are individuals or very small businesses with little or no cash flow. The question for these regions is whether any electric energy is at all affordable and where do the resources to pay for

it come from. The purely financial comparison of electricity sources by private entities often becomes subservient to public economic-development initiatives, and national and international politics may play a strong role. The choice of electric energy sources for the classes of applications must still be made, and the cost of energy delivered, in the sense employed for developed regions may still be computed, but generally not by individuals or small economic units, because they will not pay for them.

21.2 ECONOMIC ANALYSIS

Once the technical requirements of a PV application have been stated and a PV system design completed, the economic analysis can be carried out. The economic assessment includes both costs and benefits of the system. The methodology for this assessment constitutes a major portion of this chapter.

21.2.1 Key Concepts

The purchase of a PV system represents an expenditure of capital resources at a given time with the expectation of benefits in the form of electric energy delivered over some future period, which is generally the life of the PV system. Other benefits, such as reductions in greenhouse gases, might be quantified. For large systems, the construction expenditures may occur over more than one year. The future benefits, primarily the value of the electricity generated, may be realized over a 10- to 30-year period. Thus, the basic issue is how to measure the value of future benefits from a present expenditure. Further, the issue is how to compare that value for a PV system with a consistently defined value for an alternative system such as a diesel-electric system, a fuel cell, or electricity from the grid. Salvage value at the end of the system life is also a future benefit. In many cases, there will not only be future benefits but future costs as well. The cost of maintenance and the replacement of failed modules are primary examples. In addition, qualitative benefits, such as energy independence or reduction in the risk of future escalation of energy costs, may enter the decision process, although they are not dealt with here.

We generally recognize intuitively that the value of a cost or benefit in the future is not equal to the same cost or benefit today. If we were to receive \$100, we would rather get it today than five years from now. Why? Perhaps because we could buy something today with the money and enjoy its use for the next five years, rather than wait to enjoy it. More practically, we could put the \$100 in a savings account and it would be worth perhaps \$125 in 5 years; so the value of money possessed now as opposed to later can be measured in this simple way. All of this goes to say that there is a “time value of money,” and defining that time value pervades the whole process of economic analysis for PV systems. These expenditures and benefits, as measured in monetary terms, are usually called *cash flows*.

As suggested above, the purchase and operation of a PV system involves a stream of cash flows over a period of years, and economic assessment requires some consistent measure of these cash flows to be made. It may in some instances require the comparison of the value associated with that stream with the value of a different stream for a competing system. For a PV system, such a stream might look like what is shown in Figure 21.1. Outflows, such as the purchase cost and maintenance costs, are shown as negative, while

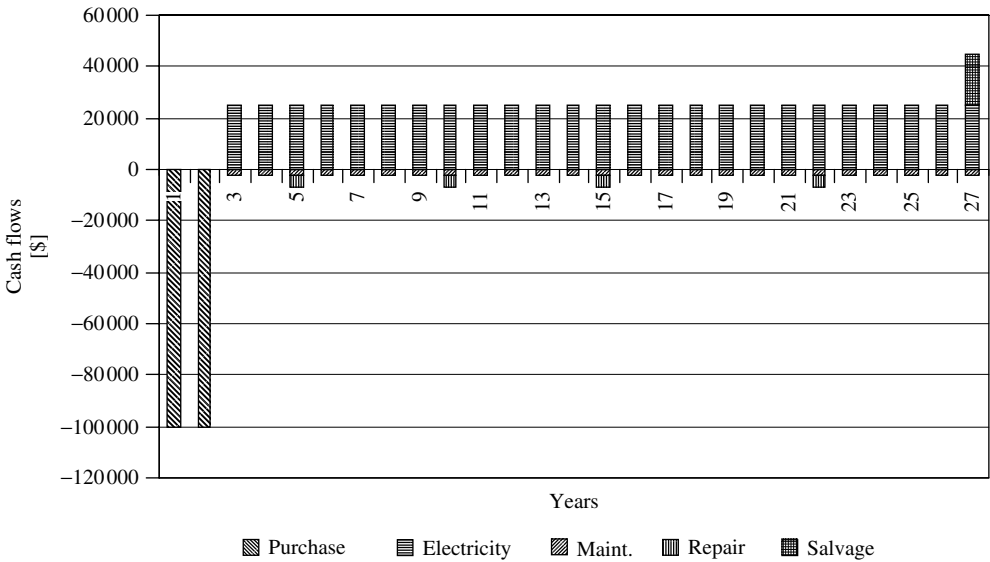


Figure 21.1 Example of PV system cash flows

inflows, such as the value of electricity produced and the salvage value, are shown as positive. In Figure 21.1, it is assumed that the system construction covers 2 years and outlays are \$100 000 in each year; the value of electricity generated is \$25 000 per year for the next 25 years; annual maintenance costs are \$2000; there are replacement costs of \$5000 in Years 5, 10, 15, and 20; and the salvage value is \$20 000 at the end of Year 27. For a PV system, the value of the generated electricity is usually determined by the avoided cost of the electricity that would otherwise need to be purchased. Note that the annual electricity production in kilowatt hour from the PV system is implicitly included in this example through the determination of the electricity cost stream. If the PV system is remotely situated, the PV electricity might alternatively be valued by its contribution to its end-use activity, though this valuation may be easier said than done.

To put a single value on these cost and benefit streams occurring over time, the usual approach is to refer all costs and benefits to a selected point in time, usually the present time, sum the values for the given streams, and compare the sums. These sums are called the *present value* or *present worth* of the systems. To compare two or more systems with one another, the present worth of each is computed to provide an economic comparison.

A sum received or spent at the present time has a present worth, P . A sum spent or received at a future time n years hence has a future worth, F . If P is invested at an interest rate of i percent per year, then its future worth at the end of the first year is

$$F = P + Pi = P(1 + i)$$

The future worth at the end of the second year is

$$F = [P(1 + i)](1 + i) = P(1 + i)^2$$

and the future worth after n years is

$$F = P(1 + i)^n \quad (21.1)$$

Conversely, the present worth of a future sum is given by

$$P = F(1 + i)^{-n} \quad (21.2)$$

Equation (21.2) shows that the present worth of a sum received n years in the future is reduced by the factor $(1 + i)^n$.

When equations (21.1 and 21.2) refer to the money deposited at interest, the factor i is the interest rate offered by the bank, but when an investment in an energy system is being considered, the factor i is referred to as a *discount rate*. The discount rate is the value that the system owner puts on the capital invested in the system, and is often called the opportunity cost of the investor; that is, the rate of return foregone on the next most attractive investment.

In Figure 21.1, the annual delivered energy values of \$25 000 constitute a uniform stream of cash flows. The sum of the future worth of each of these annual amounts, a , is, from equation (21.1)

$$F = a[1 + (1 + i) + (1 + i)^2 + \dots + (1 + i)^{n-1}]$$

This relationship can be shown to be equivalent to [1]

$$F = a[(1 + i)^n - 1] \div i \quad (21.3)$$

By combining equations (21.2 and 21.3), the present worth of a uniform series of amounts a can be stated as

$$P = a \frac{[(1 + i)^n - 1]}{[i(1 + i)^n]} \quad (21.4)$$

Consider the application of equations (21.2–21.4) to the simplified example of cash flows in Figure 21.1. The value of the PV system as measured by present worth at the beginning of Year 3, the time the system begins to produce electricity, is P_s .

$$P_s = P_{\text{investment}} + P_{\text{electricity}} + P_{\text{maintenance}} + P_{\text{replacement}} + P_{\text{salvage}} \quad (21.5)$$

Equation (21.5) implies that each of the components of P_s is referred to the same point in time, beginning of Year 3, and can therefore be summed. Table 21.1 summarizes the computation of P_s . Assume that the two \$100 000 investments are made as of the beginning of Years 1 and 2, and that all other amounts are as of year-end. Assume a discount rate, i , of 8%. Note that in Table 21.1 expenditures, or outflows, are shown as negative numbers and benefits, or inflows, are shown as positive. The appropriate equation for each category is indicated and the value of the exponent, n , required to reference the present-worth values to the beginning of Year 3 is also given. Note that cash flows that occur later in the system life contribute less to the system present worth, relative to their current values, than those that occur earlier.

Table 21.1 Present worth of PV system cash flows shown in Figure 21.1 (discount rate = 8%)

Cash flow		Present worth		
Category	Amount [\$]	<i>n</i>	Equation	<i>P</i> [\$]
Year 1 investment	-100 000	2	(21.1)	$P_{\text{investment}} = -116\,640$
Year 2 investment	-100 000	1	(21.1)	$P_{\text{investment}} = -108\,000$
Annual electricity, Years 3–27	25 000	25	(21.4)	$P_{\text{electricity}} = 266\,869$
Replacement, Year 5	-5 000	5	(21.2)	$P_{\text{replacement}} = -3403$
Replacement, Year 10	-5 000	10	(21.2)	$P_{\text{replacement}} = -2316$
Replacement, Year 15	-5 000	15	(21.2)	$P_{\text{replacement}} = -1576$
Replacement, Year 20	-5 000	20	(21.2)	$P_{\text{replacement}} = -1073$
Annual maintenance, Years 3–27	-2 000	25	(21.4)	$P_{\text{maintenance}} = -21\,350$
Salvage value, Year 27	20 000	25	(21.2)	$P_{\text{salvage}} = 2920$
Total			(21.5)	$P_s = 15\,431$

This PV system present worth is positive, and thus the system can be said to have a net benefit of \$15 431 measured at the beginning of Year 3. Whether this is an acceptable economic choice would depend on the economic criteria of the system purchaser. This subject will be discussed again later.

There are instances when the annual amounts a in equation (21.4) are not uniform (constant) over all periods, but escalate at a constant rate, e . That is, if c is defined as the amount for the first year, the amount for the second year is $c(1 + e)$, and the amount for the third year is $c(1 + e)^2$. An obvious instance of where such a series of cash flows might arise would be in accounting for the effect of inflation on the value of avoided electricity. In this instance, the present worth of the series of cash flows can be expressed [1], when $e > i$, as

$$P = \frac{c}{1+i} \left\{ \frac{(1+x)^n - 1}{x} \right\} \quad (21.6)$$

where x is defined by

$$\frac{1+e}{1+i} = 1+x \quad (21.6a)$$

If the escalation rate is less than the discount rate, $e < i$, then

$$P = \frac{c}{1+e} \left\{ \frac{(1+x)^n - 1}{x(1+x)^n} \right\} \quad (21.7)$$

where x is defined by

$$\frac{1+e}{1+i} = \frac{1}{1+x} \quad (21.7a)$$

If the escalation rate equals the discount rate, $e = i$, then

$$P = cn/(1+e) = cn/(1+i) \quad (21.8)$$

When a financial evaluation of a PV system project is defined, such as the one in Figure 21.1, it is important to be clear about how inflation will be taken into account.

When Figure 21.1 was defined, inflation was not mentioned, and the cash flows shown for the electricity value were constant over a number of years. Such a problem statement is consistent with a “real dollar” or “constant worth dollar” or just “constant dollar” approach. In this view, all monetary values are stated in terms of their purchasing power at the point in time at which the present worth of the system will be calculated. The computation of the present worth is a little simpler for a constant-dollar formulation, but that approach can mask some real-world inflationary effects. For example, the inflation of avoided electricity prices may be different from the inflation of labor required for maintenance or components used in replacing failed modules. When explicitly taking inflation into account, the monetary amounts in the cash flows are stated in terms of the actual dollar transactions at the time at which they occur. These amounts are called *actual dollars*, *then-current dollars*, or just *current dollars*.

Since the calculation of present worth measures is usually carried out for the purpose of comparing system alternatives, it can be argued that useful comparisons can be made in either constant-dollar or current-dollar terms. Where the differences in system measures turn out to be relatively large, that argument is likely to be valid, because the difference in the systems is obvious. However, there may be instances in which the outcome could be skewed if inflation is not properly calculated.

Thus far, the discussion has assumed present worth calculations either on a constant-dollar basis or on a current-dollar basis with inflation at a constant rate. It is also possible that a constant inflation rate does not adequately represent the future. If the inflation rate (or the discount rate) varies over the period of the analysis, then, practically speaking, one is forced to calculate separately the present worth of each future cash transaction and add the terms to get a system present worth.

It needs to be emphasized here that the computation of a present-worth measure for some energy alternatives requires the projection of cash flows (transactions) up to 30 years into the future, and thus the result depends not just on the proper application of computational methods, but on the assumptions and information that go into this projection. The cash flows to be projected include energy prices, materials costs, labor costs, cost of capital, and related factors. This requirement often leads to the parameterization of critical factors and economic analysis under a range of scenarios rather than a single set of assumptions. Fortunately, the effect of the discount rate is to reduce the impact of projections far into the future relative to those in the near term.

Now, let us consider a more general statement of cash flow that supports the definition of additional economic measures of PV systems. The statement assumes that a PV system will be purchased, installed, and operated over a period of years by a profit-making organization. For a given year, n , the net cash flow based on returns to equity capital is [2]

$$X_n = (R_n - C_n - I_n) - (R_n - C_n - I_n - D_n)T - K_n + S_n + B_n - P_n \pm W_n \quad (21.9)$$

The terms of equation (21.9) are as follows.

R_n = gross revenue due to the system in the year n ; typically the value of the electricity generated.

- C_n = cost associated with the operation and maintenance of the system in year n ; including labor, materials, and replacement parts.
- I_n = debt interest paid in year n on funds borrowed (B defined below) to fund the system.
- D_n = tax depreciation in year n for the system, assuming that the taxation applicable to the owner allows deduction of depreciation for tax purposes, calculated as allowed by the tax law.
- T = incremental (marginal) tax rate for the owner; the second term in parentheses in equation (21.9) represents the taxes on income paid by the owner.
- K_n = capital expenditure in year n ; the total amount spent on capital assets.
- S_n = salvage value received in year n .
- B_n = amount of money borrowed in year n from external sources and used to fund capital expenditures.
- P_n = payment of principal on debt capital (B) in year n .
- W_n = net increase in working capital in year n ; has a negative sign if an increase in working capital is required; working capital represents the funds employed for such items as payroll, inventories, and accounts receivable.

The definition of net cash flow on an equity capital basis is used here because profit-making organizations tend to judge their financial performance based on returns on equity capital.

The annual net cash flow in equation (21.9) for each year in a PV project life must be used with equation (21.10) to calculate a system present worth that is comparable to the result P_s shown in Table 21.1.

$$NPW = \sum_{n=0}^L \frac{X_n}{(1+m)^n} \quad (21.10)$$

where

- X_n = annual net cash flow from equation (21.9).
- L = system life or the life of the project for evaluation purposes.
- m = the minimum acceptable rate of return on equity capital.

The quantity m is equivalent mathematically to the discount rate i used earlier (e.g. equations (21.1–21.3)), but m has the additional stipulation that it represents a requirement of the system owner for returns on equity. It may or may not be the opportunity cost. It may represent a hurdle rate set to determine what the owner requires in order to take the financial risk represented by the project.

In Table 21.1, the present worth of each component (investment, annual electricity, replacement, maintenance, and salvage) was calculated over the project life, and the component present worth figures were added to get a system present worth. Equation (21.9) adds the figures for all components (investment, annual electricity, replacement, maintenance, and salvage) in any given year to get the annual net cash flow for that year. Then, the annual net cash flows are discounted in equation (21.10) to get the system

present worth, which is called net present worth (NPW). Thus, the order of computation is different in Table 21.1 from that of equations (21.9 and 21.10), but the result is the same. Equations (21.9 and 21.10) are just a more general expression of the computational process than Table 21.1.

Note also that if the PV system owner is selling electricity and thus has a revenue (income) stream, that revenue is taxable as per equation (21.9). However, if the PV system owner is not selling electricity, then the electricity has a value to the owner and the term R in equation (21.9) can be used in the calculation of the system worth, but the taxation term is zero because $T = 0$. (The case of $T = 0$ is implicit in Table 21.1.)

Several other measures of system worth can be defined using the annual net cash flow defined by equation (21.9).

$$0 = \sum_{n=0}^L \frac{X_n}{(1 + IRR)^n} \quad (21.11)$$

where

IRR = internal rate of return.

Equation (21.11) is solved iteratively for the value of internal rate of return (IRR) that satisfies the equation. To determine if the investment in the PV system is acceptable, the IRR must be compared to a hurdle rate set by the owner. This rate may or may not be the owner's opportunity cost.

A less-sophisticated economic measure is the simple payback period defined by

$$0 = \sum_{n=0}^{PB} X_n \quad (21.12)$$

where

PB = payback period in years.

The payback period is the number of years required for the inflows to equal the outflows. It is the time required to recover the initial investment in the system. This measure is referred to as *simple* because it does not consider the time value of money (there is no discounting). It also does not consider cash flows beyond the time when the investment is recovered. Simple payback is probably more useful, for example, to the homeowner who does not have the same tax and profit considerations as the business owner.

A measure of the intermediate complexity and usefulness is the discounted payback period, defined as

$$0 = \sum_{n=0}^{DPB} \frac{X_n}{(1 + m)^n} \quad (21.13)$$

where

DPB = discounted payback period.

The discounted payback period (DPB) does consider the time value of money, but does not consider the cash flow after the recovery of the initial investment.

Finally, there is another method of valuing PV systems that uses some of the same mathematical techniques as the above measures, but expresses the result differently; namely, the levelized energy cost (LEC) or levelized bus bar energy cost (LBEC). This approach is particularly appropriate to energy providers such as electric utilities. This method provides a unit cost of electricity in \$/kWh that is constant over time (i.e. levelized) and expressed in monetary units at the beginning of a commercial operation. The LEC method is useful to utilities, who sell electricity on a \$/kWh basis, since it is easy to compare the computed LEC to the costs of electricity from other conventional or renewable sources. This method can also be adapted for nonutility system owners.

The LEC method is based on the same discounted cash-flow concepts illustrated by Table 21.1 and equations (21.1–21.8). These latter results represent the total discounted worth of a PV system over its economic life stated in dollars, and these dollars implicitly incorporate the annual PV energy produced. The LEC method, in effect, takes a present worth of the cost (but not revenue) streams as in equation (21.9) and computes a stream of constant annual values having the same present worth. This annual value is divided by the rated annual energy production of the system to get an annualized cost of electricity.

$$LEC = \frac{(NPW_C)(CRF)}{E} \quad (21.14)$$

where CRF is called the capital recovery factor, defined as

$$CRF = \frac{m(1+m)^n}{(1+m)^n - 1} = \frac{a}{P} \quad (21.15)$$

The capital recovery factor (CRF) is the inverse of the present worth of a uniform series defined in equation (21.4). NPW_C is computed from equation (21.10), which, in turn, is based on equation (21.8) with revenues, R , set to zero. The numerator of equation (21.14) is the annualized value of the costs associated with the system construction and operation, that is, it defines a uniform annual series of costs that have the same present value as NPW_C . The term E is the annual energy in kilowatt hour generated by the system.

21.2.2 General Methodology

A general methodology for the economic assessment of PV systems is illustrated in Figure 21.2. The assessment begins in Step 1, system design, which must be done prior to an economic analysis. For an assessment addressing multiple systems and/or applications, the methodology of Figure 21.2 must be carried out for each system of interest and the results summed to determine the economic potential.

Steps 2, 3, 4: system cost. In determining system cost, completeness and accuracy in individual component costs lead to a good estimate of system cost. Figure 21.2 suggests two paths to estimate system cost. If the system design is based on the currently available technology, then defining a complete bill of materials and then obtaining quotations from the vendors is the path to be followed. If the cell/module technology is to be projected into the future, or if a current technology is not in volume production so that its costs are not available, then the price can be predicted from the modeling of the manufacturing process.

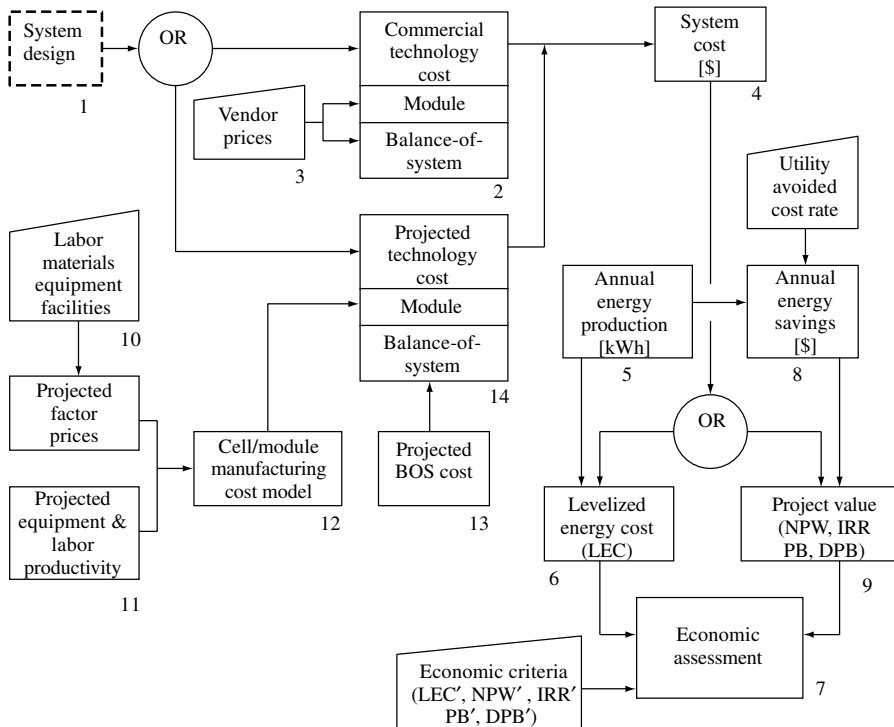


Figure 21.2 Economic assessment

Such a modeling procedure is discussed later in this section. For either path, the system components and materials, aside from the cells and modules, are in general commercially available and the prices can be obtained from manufacturers and distributors. A limited number of cells and modules are also commercially available. System components are particular to the design, and the following list suggests the major components whose costs are required. Detail part specifications and costs are needed in many cases for accurate costing.

- PV cells
- PV modules
- Module support structure
- Tracking structure/drives/controls
- Heliostats
- Foundations and structures
- Cooling system
- Interconnection wiring and terminations
- Power-conditioning unit
- Transfer switching and metering
- Substation equipment
- Land

- Site improvements (grading, roads, fencing, buildings)
- Installation labor and management
- Financing cost during construction
- Shipping
- Taxes
- Licenses, permits.

For large systems whose installation may extend over months or years, a schedule of installation and expenditures will also be needed to properly compute economic measures as defined previously.

Steps 10, 11, 12, 13, 14, 4: system cost (manufacturing-cost modeling). Figure 21.2 shows two paths to determine the system cost. The path utilizing commercial technology has been addressed in the figure. When a PV cell/module technology that is not commercially available is to be considered, predictions of the cell and/or module cost are required. One approach to predicting the cell/module costs is shown in Figure 21.2 (Step 12) as a cell/module-manufacturing cost model. Such a model was developed at the Research Triangle Institute under the sponsorship of the Electric Power Research Institute (EPRI), and was used over a period of years in studies of the cell and module costs [3]. This modeling approach, which eventually came to be called Strategic Analysis of Manufacturing Product and Price (STAMPP), is briefly described here to illustrate how cell/module costs can be predicted.

The objective of STAMPP is to model the operations of a cell- or module-manufacturing firm in such a way that the annual required revenue of the firm is calculated for a specified annual production volume. The required revenue divided by the production volume gives a required unit price for the cell or module. The term *required price* is used because all direct and indirect costs and after-tax profit are included in the revenue. The required price is thus the minimum price for which the product could be sold while returning the specified margin of profit. However, the market would always determine the actual selling price. A further objective of the model is to facilitate the parametric analysis of a wide range of cost factors so that the cost drivers can be identified and their effect on the required price of a cell or module design can be explored for a specified manufacturing process.

The firm is described in the model by a fixed organization whose top management levels are filled by a fixed number of people. The lower levels of the organization, including supervisors, production, and support staff are filled by a number of employees, which is scaled to the manufacturing requirements. Hours of operation, meteorological data for heating/cooling loads, and other firm-level financial and operating data are included among the input.

The physical operations of manufacturing are modeled in STAMPP using the concept of a “workstation”. A workstation is defined as a collection of one or more identical machines, each performing the same operations in parallel. The user specifies the direction of workflow among the workstations.

The user defines the operations performed at a workstation on a per-machine basis. The model calculates the number of machines for each workstation based on a specified

annual volume of the final product and the workstation characteristics. The workstation is characterized by the nominal operating parameters of one of its machines, which are defined as long-term average values. The quantity of work done at each workstation is determined by the model from a process balance using as inputs the total annual product volume from the last workstation, and individual machine parameters including

- form conversion factor (input/output units),
- yield (number of good units out per unit time/ideal production rate),
- machine ideal production rate,
- machine availability.

The quantity of required materials is determined from the workstation-level, per-product-unit consumption factors and the workstation product quantity, and the quantity of labor of specified types is determined from per-machine labor requirements. Total materials, labor, utilities, and floor-space requirements are summed for the firm, and their costs are calculated using these quantities and unit costs input to a cost catalog. Unit costs of process equipment and facilities are used to compute the capital investment for the plant.

Using the calculated production costs, the model produces a corporate income statement and balance sheet. These reports are based on accepted accounting procedures. The income statement provides the revenue to calculate the product cost. The data in both reports can be compared to the data for typical real businesses to assess the appropriateness of the modeling from a business point of view. On the manufacturing side, reports are provided that summarize the equipment, labor, materials, floor space, and utilities required in terms of both quantity and cost. Also reported are personnel and associated costs for administrative functions. The result is a complete picture of all aspects of the cost structure underlying the required product price. In the subsequent section, outputs from the model are shown to illustrate an economic assessment of a PV power plant.

Step 5: annual energy production. Within the assessment framework of Figure 21.2, the annual energy production for the system will be calculated from local solar data and the performance parameters of the system (as described elsewhere). For a private user, the energy considered here is the *useful* energy; that is, the energy actually consumed by the load plus any energy sold back to a utility. For a utility, all of the energy produced is useful.

Step 6: levelized energy cost (LEC). LEC is defined in equation (21.14) as a constant annual cost (\$/kWh) over a specified period of years whose present worth is the same as that of the cost stream associated with its production. The cost stream was defined in equation (21.9). LEC incorporates the cost of capital and the annual energy production. LEC is typically computed by utilities, but could also be used by private PV system owners.

Step 7: economic assessment. The final step in this assessment methodology is to decide if the value of the economic measure computed is an acceptable value when compared to an economic criterion. Where LEC is the economic measure, it is compared with the cost of electricity (LEC') from other sources calculated in the same manner. For a private user, the comparison value might be that of electricity from, for example, a diesel-electric generator or a fuel cell. For a utility, this comparison may entail the consideration of the

system-capacity expansion for a given load growth in order to determine the alternative cost of electricity, or a simpler approach might be just the utility's cost of peaking power. The problem with the simpler approach is that it may not adequately consider issues such as reserve capacity.

Step 8: annual energy value. In order to calculate the project value measures in Step 9, the value of the annual energy production is needed. For grid-connected, customer-side systems, the value is the cost avoided by not purchasing the annual energy produced (Step 5). The value is calculated from the electric utility rate and the energy production. Where the rate is multitiered or has seasonal components, the energy production as a function of time would need to be taken into account in order to value the energy properly.

Step 9: project value. Several financial measures for PV systems have been defined in equations (21.10 to 21.13): NPW(\$), IRR(%), PB(years), and DPB(years). Each one depends on the net equity cash flow, X_n , defined by equation (21.9), which includes a revenue term, R , which is the value of the electricity purchase avoided by the use of the PV system. The annual electric energy produced by the PV system is implicitly included in R .

When the computed economic measure is NPW, IRR, PB or DPB, it is compared to the threshold (NPW', IRR', PB', DPB') values that the owner considers appropriate. If the owner is a commercial firm, the NPW or IRR measures would typically be used. If the decision is between two competing energy sources, say, PV and a fuel cell, the one with the higher NPW or IRR would be preferable. It should be noted that since the fuel-cell system is dispatchable (i.e. provides energy at any time on demand), the PV system is not comparable unless it includes storage. The two systems must be designed to meet the same load profile in order to be compared by a single measure such as NPW or IRR. If the decision for the commercial user is just whether to buy a PV system for a stated purpose, the issue then is whether the NPW or IRR is greater than some threshold value. In this instance, the PV system competes for capital with other capital needs of the firm, and the threshold may be set by considering the NPW or IRR associated with alternative capital expenditures. The firm may even look at the decision in both ways: is the PV system the best choice from among several systems *and* is it a better use of capital than nonenergy expenditures.

The payback (PB) and discounted payback (DPB) measures are more typically appropriate to homeowners or others without tax considerations in the purchase decision, although nothing prevents others from considering these criteria. The payback for the PV system can be compared to the life of the system as a decision criterion. If the payback is shorter than the life, then in a simple view the energy is free after the payback period. Another use of the payback measures is to compare two or more systems by calculating their payback; the one with the shortest payback is preferred.

21.2.3 Case Studies

To illustrate some of the methodologies for the economic analysis of PV systems, brief summaries of three studies in which the authors participated are presented here. Each study considered PV technology operated in a large-scale (25–50 MW) electric-utility setting. The first study [3] compared the required module price in $\$/W_p$ of several Si-cell technologies. The second study [4] covered silicon and copper indium diselenide (CIS)

technology, and the third [5] compared the 500X concentrator systems with Si technology to GaAs technology in plants of the same annual energy capacity. All three studies modeled the cell- and module-manufacturing processes using the STAMPP model, and included both flat-plate and 500X concentrator collectors.

Financial studies of complex systems require extensive data input, and can produce volumes of data output. Restriction of space in this chapter limits the details that can be provided to only a small fraction of what was there in the original studies. The numerical values of inputs and outputs are based on the time at which the studies were performed, so the objective is to illustrate methodology and relative technology comparisons, not to give current quantitative cost results.

21.2.3.1 Module price for silicon technology

From the beginning of the photovoltaic commercialization efforts in the 1970s, crystalline-silicon-cell technology has been dominant. The availability of refined silicon wafers resulting from semiconductor development, the availability of mature processing equipment developed by that industry, and the simplicity of the Si-cell fabrication technology relative to thin-film Si or compound semiconductors such as gallium arsenide or copper indium diselenide were, and still are, major factors that influence the role of silicon in photovoltaics. The first cost analysis conducted by the authors [3], which was also the genesis of the STAMPP program defined earlier, compared silicon-module prices fabricated by several different methods. (In [3], the STAMPP model was called IMCAP, but the model is essentially the same.) While the results discussed here were determined in 1986, there still are some relevant and useful lessons to be learned from the comparison of different cell- and module-fabrication methods, and the focus here is on these rather than on current absolute cost of cells and modules.

Five different cell technologies and modules fabricated from them were examined in this study:

- Flat-plate modules using silicon cells from single-crystal Czochralski wafers.
- Flat-plate modules using silicon cells fabricated on silicon dendritic web substrate.
- Flat-plate modules using single-junction amorphous-silicon cells (a-Si:H) grown on glass.
- Flat-plate modules using tandem-junction amorphous-silicon cells (a-Si:H/a-SiGe:H) grown on glass.
- 500X Fresnel lens concentrator module using high-performance cells from float-zone single-crystal silicon wafers.

The concentrator module incorporated cells under separate development by the study sponsor and the cell fabrication was not modeled with STAMPP. The cells were treated as a purchased item. All of the manufacturing processes were defined to produce annually modules with a total rating of 25 MW.

The module prices computed for this study were intended to give a comparison of significantly different cell technologies and to provide a perspective on how low the prices might fall in the future. The cost of materials and other items for a base case

Table 21.2 Key technical and financial parameters [3]

Parameter	Process case			
	Technology	Base	Pessimistic	Optimistic
Module efficiency (%)	Czochralski	15.0	12.0	17.0
	Dendritic web	15.0	12.0	17.0
	Concentrator	19.42	17.09	21.75
	a-Si:H	10.0	6.0	12.0
Silicon price (\$)	Czochralski	40/kg	75/kg	25/kg
	Dendritic web	40/kg	75/kg	25/kg
	Concentrator	2.00/cell	4.00/cell	1.00/cell
	a-Si:H (silane)	618/kg	2000/kg	150/kg
Glass (\$/m ²)	All	10.76	13.46	8.07
Wafer/Kerf Thk. (mil)	Czochralski	12/10	14/12	10/6
Web pull rate (cm ² /min)	Dendritic web	20	8	30
Plasma deposition rate (Å/s)	a-Si:H	10	2	40
		Financial case		
Return on equity (%)	All	18	22	15
Debt/equity ratio	All	0.3	0.2	0.5
Debt interest rate (%)	All	14	16	12
Average cost of capital (%) (derived from other inputs)	All	17.1	21.0	13.5

Copyright © 2002. Electric Power Research Institute. EPRI AP-4369. Photovoltaic Manufacturing Cost Analysis; A Required Price Approach, Vol. 1, 2. Reprinted with Permission

were selected and reviewed by several organizations involved in the study, and it was recognized that the resulting module-price predictions were lower than those achieved at the time of the study, or, for the most part, even today. They represented a potential level of the price for high volume production with high conversion efficiencies. After determining with the model the key price drivers for each technology, other cases were defined to examine the effect of different values of the key drivers. Two cases, defined as optimistic and pessimistic and shown in Table 21.2, were used to compare with the base case. Base, pessimistic, and optimistic cases relating to material-cost parameters (process case) and cost-of-money parameters (financial case) were defined. Table 21.2 shows only the “key” parameters of the defined cases, that is, the parameters from the cases that had the greatest effect on price.

The range of required module prices associated with the full set of process-case parameters is provided in Figure 21.3 for all of the cell technologies. Within each of the process cases, the spread in module prices among the technologies is about 2:1, so that achievement of important processing parameters and conversion efficiencies has a large impact on their ultimate relative prices.

The effect of the financial case parameters on module price was determined to be in the range of about $\pm 5\%$ of the base case for all of the technologies. For example, Table 21.3 gives the required module prices for the Czochralski modules for each case. The range of prices for the process cases due to variation in material costs (\$3.46–\$1.22) is much greater than the variation due to the financial-case parameters (\$1.98–\$1.80).

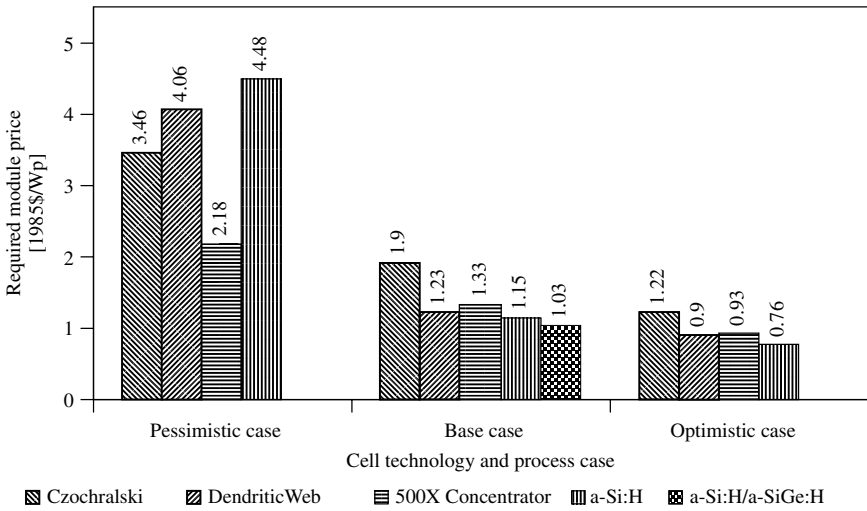


Figure 21.3 Required module price for silicon-cell technologies [3]. Copyright © 2002. Electric Power Research Institute. EPRI AP-4369. Photovoltaic Manufacturing Cost Analysis; A Required Price Approach, Vol. 1, 2. Reprinted with Permission

Table 21.3 Czochralski module prices for process and financial cases (1985\$/W_p)

		Process cases		
		Pessimistic	Base	Optimistic
Financial cases	Pessimistic		1.98	
	Base	3.46	1.90	1.22
	Optimistic		1.80	

This relationship results from the fact that material costs are a large fraction of the required module price, 44.2% for the Czochralski base case, whereas the cost of the required capital for machinery and equipment, which is usable over several years, is a much smaller fraction of the price.

A sensitivity diagram, such as Figure 21.4 for the Czochralski module, illustrates the relative effect of individual process or financial-parameter values on the required module price. Here, the module-price variations for each parameter are plotted with respect to the parameter expressed as a percent of its base-case value. The slopes of the lines are then the price sensitivity to each parameter. For the Czochralski module, the price is most sensitive to the achieved conversion efficiency and the unit cost of the silicon boule. The price is much less sensitive to the unit cost of the glass sheet, wafer thickness, and return on equity (a financial parameter equivalent to the profit for the module manufacturer). Sensitivities for the other cell technologies follow a similar pattern.

One of the most useful results of the study is the illustration of the trade-off between the silicon-utilization and cell-conversion efficiency as reflected in the module price. Figure 21.5 shows the effect of efficiency on the base-case prices for all five cell

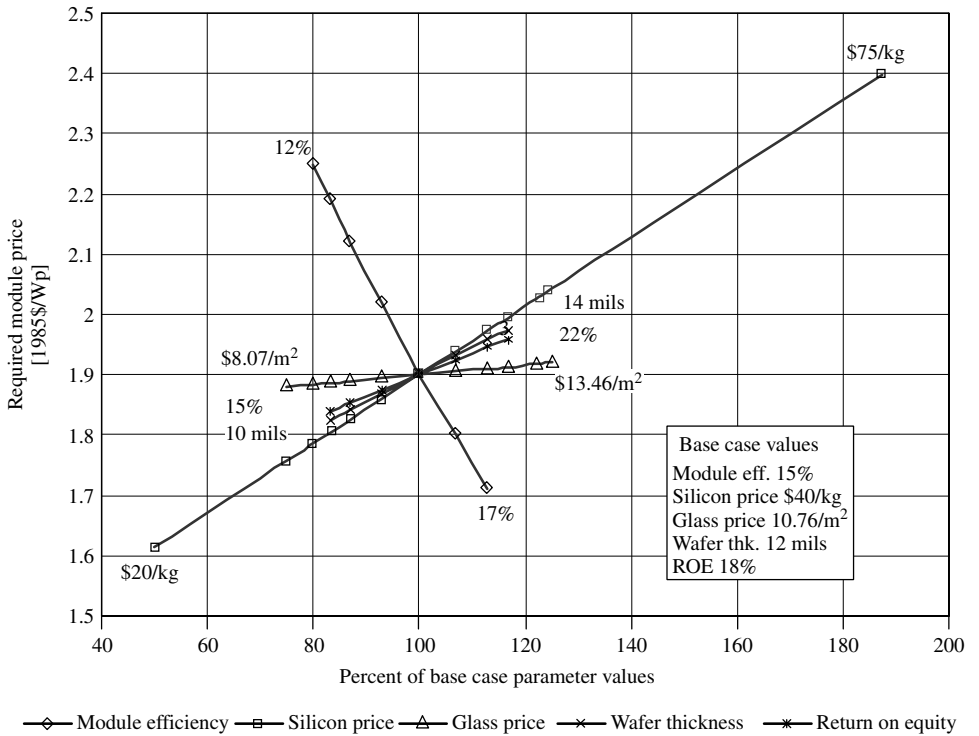


Figure 21.4 Sensitivity of Czochralski required module price to selected parameters [3]. Copyright © 2002. Electric Power Research Institute. EPRI AP-4369. Photovoltaic Manufacturing Cost Analysis; A Required Price Approach, Vol. 1, 2. Reprinted with Permission

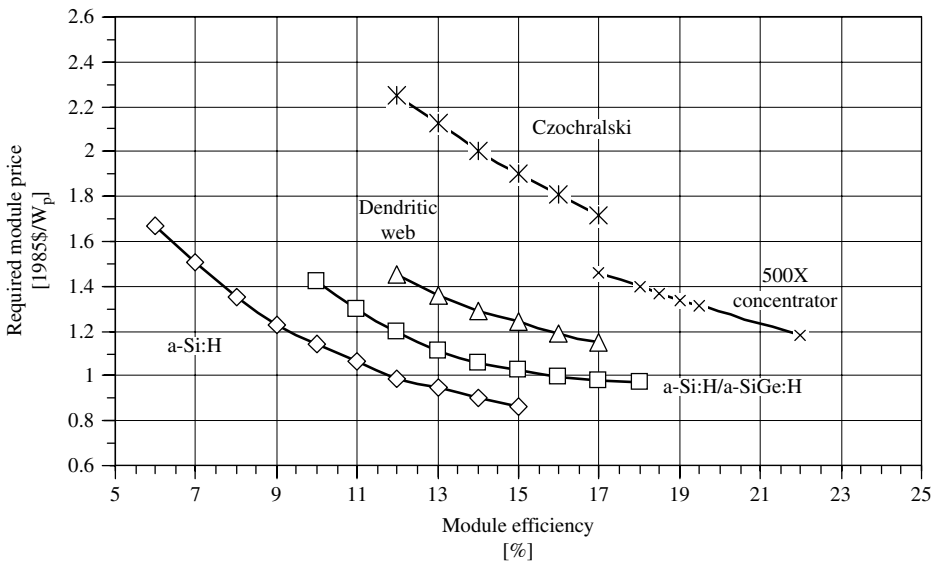


Figure 21.5 Effect of cell technology and efficiency on module price

technologies. Silicon requirements vary significantly with the choice of a cell technology and its associated cell-fabrication process. Cell-conversion efficiency is also significantly different among the cells made by different processes, and these efficiency differences are inherent in the cell structures. For example, the amorphous cells require much less silicon than Czochralski cells, but the latter have higher efficiency and require less module area to achieve the same rated capacity. How the module prices of the two cell technologies compare is also dependent on the cost of their fabrication processes. Some processing steps are unique to each cell or module as required by their structures and materials, but in other steps the processing is essentially the same. For example, the single- and tandem-junction thin-film cells have many common processing steps. Also, the encapsulation steps for several of these modules are the same.

The similarities and differences in the five cell/module technologies have important implications on cost, measured as $\$/W_p$. In the case of cells fabricated from either Czochralski wafers or dendritic web substrates, the use of silicon for dendritic web cells is less than 20% of that used for Czochralski cells, and silicon is the single most costly material in both processes.

The dendritic web thickness was taken as about 5 mils, whereas the wafer thickness was 12 mils, and the wafers must be sawed from a boule with a kerf loss of 10 mils and an area loss because the boule is round. Dendritic webs are formed in a long strip with no kerf loss and very little area loss. The formation of the dendritic web substrate and the wafer is the primary difference in the two cell/module processes; the remaining steps to produce the cells and modules are essentially the same. The cell efficiency was taken as the same for the Czochralski and dendritic web modules.

Amorphous-silicon cells are produced by an entirely different process that results in a silicon cell that is about 1000 times thinner than the other two flat-plate cells. The "silicon" consumption (actually silane gas) is reduced to the point at which the glass substrate on which the cells are grown is the most costly item of material. However, a-Si cell efficiency has proved to be lower than that for the crystalline cells. In this study, base-case module efficiency using crystalline cells was taken as 15%, and the efficiency for the a-Si module was taken as 10%. For the tandem-junction a-Si cell/module, additional film-growth steps are added to the process, which consumes additional silane, but the material cost is still small. The efficiency for the tandem cell was taken as 15%. The module-fabrication steps are also different from the crystalline-cell modules because all of the cells for a module are deposited on one piece of glass, and cell interconnections are defined by scribing rather than soldering copper straps between cells.

For the concentrator module, the cell is fabricated on Si wafers on equipment comparable to the Czochralski flat-plate cell, but its fabrication was not modeled for this study. There are some cell-design differences that change the cell fabrication somewhat. Instead of modeling with STAMPP, a base-case cell cost of \$2/cell was used for a 1-cm square cell. For comparison, the Czochralski and dendritic web cells were 10-cm square. The fabrication of the 48-cell Fresnel module was modeled as an automated parts fabrication and assembly operation. Since the concentration ratio for the module was 500X, the basic trade-off between the concentrator and flat-plate modules is the more complex mechanical structure of the concentrator with much less silicon-cell area compared to the simpler flat-plate structure with more silicon-cell area. The concentrator also had a

base-case conversion efficiency of 19.2%. Inherent in the comparison is also the difference in solar insolation applicable to the two technologies.

The required module prices in Figure 21.5 show a significant overlap of all of the cell technologies except Czochralski, which is consistently higher than the others. It is clear that the module-price, in $\$/W_p$, comparison among any of the four less-expensive modules depends greatly on the efficiency achieved. A horizontal line representing, for example, $\$1.20/W_p$ corresponds to about a 9% efficient single-junction amorphous module, but requires about 12% efficiency for the tandem-junction amorphous module, because the latter is more expensive to produce. The same rationale applies to the dendritic web and concentrator modules. The module price range for the Czochralski single-crystal wafer cells does not overlap the other cells, and, for the input data used in the study, it would always be more costly than the others. In hindsight, single-crystal and polycrystalline cells continue to be the most prevalent commercial technology, which perhaps is due to their having achieved more of their performance potential in volume production than have the other technologies. The wafer-cell technologies have simplicity on their side, even at the disadvantage of higher silicon use.

21.2.3.2 Cost of electricity for utility-scale PV plants

A study by the EPRI [4] encompassed both manufacturing-cost modeling and financial analysis for utility-scale PV plants. The study included three systems: a heliostat field focused on a central receiver incorporating a water-cooled silicon-cell array, a field of Fresnel lens concentrator arrays using silicon cells, and a field of fixed-tilt flat-plate module arrays using CIS cells. Brief results of the Fresnel system are given here to illustrate module-price analysis and system-cost development. Total energy costs for all three plants are also given later to illustrate the economic analysis for the three systems.

An extensive design study defined a 50-MW Fresnel system, and included specifications for a 500X Fresnel concentrator module having 48 Fresnel lenses per module, each lens being about 45-inches square with one back-contact Si cell mounted below it. A glass secondary lens was mounted between the Fresnel lens and the cell. The cell efficiency was taken as 27.4%, and module efficiency as 20.7%. Each cell had a passive heat dissipator on the back surface of the assembly. The basic module structural element was a molded plastic box supporting 4 cell/lens units, and 12 of these were assembled into a module (i.e. 48 cells/module). Sixty of these modules were mounted on a tracking structure to form an array. The total array field had 3390 arrays and the plant covered 700 acres.

Manufacturing of the cell and module assembly was modeled with the STAMPP program described previously. It was assumed that the modules would be produced over two years. The Stanford Advanced Back Contact cells were fabricated on 150-mm silicon wafers using conventional cell-fabrication processes. Table 21.4 summarizes the results of the module-cost modeling for a base case, whose results were input to the plant cost computation. The top section of the table shows some basic operating and financial parameters for the module business, and gives the computed module required price as $\$320.08$ each (1990\$), or $\$1.30/W_p$. Such a cost was indeed optimistic for the time the study was conducted, but it did represent a relatively high annual production volume. A significant amount of automation was employed, especially in the assembly of the module. A breakdown of module cost (taken from the income statement of the business) is shown in

Table 21.4 Fresnel module price summary, base case [4]

Annual plant production (module/year)	101 700
Unit price (1990\$/module)	320.076
Base year	1989
Simulation length (years)	10
Plant capacity factor (%)	100.000
Annual plant operating time (h/year)	8519
Maximum number of shifts per working day	3
Required return on investment (fraction)	0.200
Debt to equity ratio (fraction)	0.250
Combined fed/state income tax rate (fraction)	0.340

*Product price components in first full year of production
(end of year dollars)*

Component	1990\$/module	% of total
Annual sales	320.076	100.00
Annual manufacturing expense	289.366	90.41
Annual direct material expense	219.758	68.66
Annual direct labor expense	14.592	4.56
Annual manufacturing overhead	55.016	17.19
Net annual work-in-process	0.297	0.09
Net finished goods inventory	0.000	0.00
Selling & administrative expense	9.155	2.86
Corporate income taxes payable	6.679	2.09
Excess revenue (interest earned)	12.966	0.50
Annual net income	1.612	4.05

Initial work station equipment cost (\$1989)	4 260 447
Initial facility cost (\$1989)	3 158 375
Total manufacturing area (sq ft)	39 453
Total nonmanufacturing area (sq ft)	11 532
Total facility area (sq ft)	50 985
Total land cost (\$1989)	124 036
Total direct manufacturing labor (# workers)	56
Total indirect manufacturing labor (# workers)	19
Total indirect nonmanufacturing labor (# workers)	43
Total plant labor (# workers)	118

Copyright © 2002. Electric Power Research Institute. EPRI TR-101255. Engineering and Economic Evaluation of Central-Station Photovoltaic Power Plants. Reprinted with Permission

the center section of Table 21.4. Direct manufacturing costs are about 90% of the total cost, with materials accounting for 69%. The 17% contribution of manufacturing overhead is composed of manufacturing supervision labor, equipment and facilities depreciation, plus other smaller items, but about half of the 17% is the R&D budget assigned to the business, which corresponds to 8.5% of sales. In the bottom section of Table 21.4 are the costs of process equipment and buildings, and the number of people employed in the business.

Any study of future costs benefits from an examination of the sensitivity of the result to different values of critical input parameters, because it contributes to understanding the

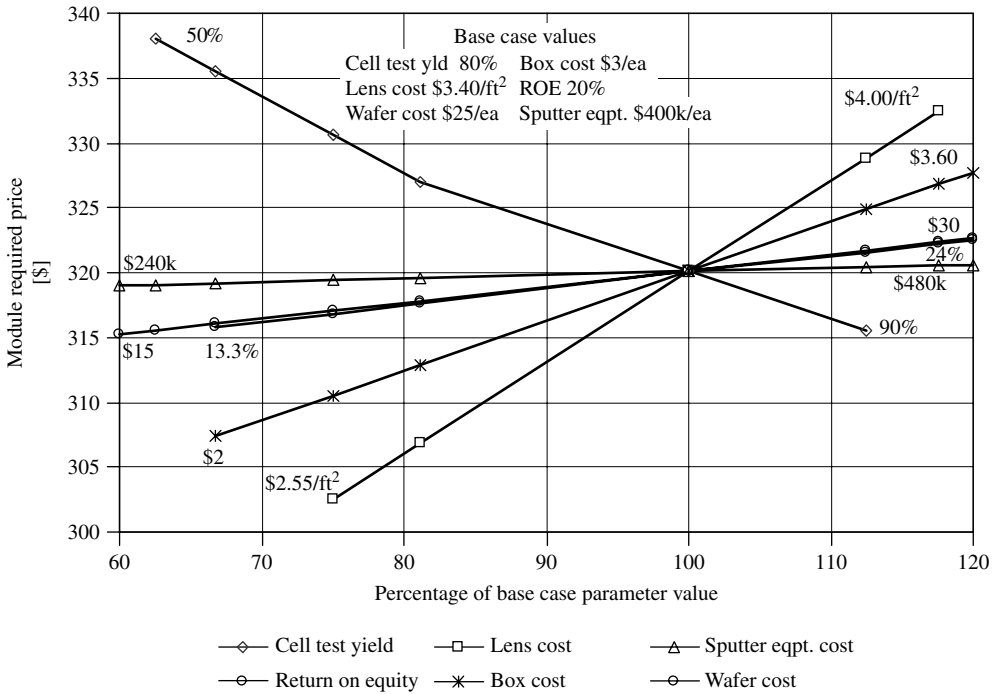


Figure 21.6 Effect of selected parameters on Fresnel module price (1990\$) [4]. Copyright © 2002. Electric Power Research Institute. EPRI TR-101255. Engineering and Economic Evaluation of Central-Station Photovoltaic Power Plants. Reprinted with Permission

risk in the choice of inputs. Figure 21.6 shows the effect of different values of certain materials, equipment, and financial costs on module required price. Cost components are plotted on the abscissa as a percentage of their base case value, which means that the slope of the lines represents a relative sensitivity of module price to the parameter change (absolute values at the extremes are also shown for reference). The output of the STAMPP model identified the Fresnel lens and the molded box as the two largest material costs, at 31% and 17% of material costs, respectively. Silicon wafers, at 5%, were another significant cost. Sensitivities to a fairly wide range of these costs are shown, with the extreme variation in module price being less than 6%. By way of comparison, the price of the most expensive cell-processing equipment, sputtering, had a much smaller impact on module cost. This is a typical result in such studies, resulting from the depreciation of the equipment over several years. Cost of money, represented by return on equity (ROE), has about the same impact as wafer cost. Process yield for each workstation is a parameter in STAMPP. For cell manufacturing, the yield at cell test is critical, and the base case cell yield for the study was 80%. Figure 21.6 shows cell yield to have a large impact relative to some other parameters.

The total capital cost of the Fresnel lens plant in Table 21.5 reflects the accounting system of the study sponsor, EPRI. The \$1.62/W_p cost of the PV modules includes shipping and installation, and is 50% of the total system capital cost. The installed array-structure cost brings the total collector cost to about 73.5% of the system cost. The power conditioning and balance-of-plant costs add another 5.5%, leaving about 20% of the cost

Table 21.5 Total capital requirements for central station plants [4] 3rd Quarter 1990\$, Carrisa Plains Site

	Fresnel lens		Central receiver		CIS flat plate	
	[\$(10 ⁶)]	[\$/Watt]	[\$(10 ⁶)]	[\$/Watt]	[\$(10 ⁶)]	[\$/Watt]
Buildings, site improvement	1.20	0.02	1.9	0.04	1.23	0.02
Array structure	37.92	0.76			13.38	0.27
PV modules	80.80	1.62			66.91	1.38
Heliostat system			53.30	1.07		
Receiver system			18.80	0.38		
Receiver tower			6.30	0.13		
Power conditioning unit	5.92	0.12	4.30	0.09	5.85	0.12
Balance of plant	3.09	0.06	16.40	0.33	7.06	0.14
Master control system	0.12	0.00	0.80	0.02	0.08	0.00
Total field cost	129.10	2.58	101.80	2.04	94.50	1.91
Engineering, & const. Management	5.20	0.10	6.10	0.12	2.80	0.06
Owner's costs	5.40	0.11	5.40	0.11	2.90	0.06
Contingencies	14.20	0.29	19.70	0.39	9.80	0.20
Total plant cost	153.90	3.08	133.00	2.66	110.00	2.22
Escalation (mixed year dollars)	(2.90)	(0.06)	(2.50)	(0.05)	(2.10)	(0.04)
Total cash expended (mixed year dollars)	151.00	3.02	130.50	2.61	107.90	2.18
Allowance for funds during const. (mixed year dollars)	6.80	0.14	5.80	0.12	4.80	0.10
Total plant investment	157.80	3.16	136.30	2.73	112.70	2.27
Preproduction costs	3.20	0.06	2.90	0.06	2.30	0.05
Inventory capital	0.80	0.02	0.70	0.01	0.60	0.01
Land	0.20	0.00	0.30	0.01	0.20	0.00
Total capital requirement	162.00	3.24	140.00	2.80	116.00	2.34

Copyright © 2002. Electric Power Research Institute. EPRI TR-101255. Engineering and Economic Evaluation of Central-Station Photovoltaic Power Plants. Reprinted with Permission

associated with engineering, construction management, cost of money, contingencies, and so on. The contingency item accounts for uncertainties in system performance and unaccounted costs in the design. Later systems of the same design may avoid some of the contingency cost. The total system cost in Table 21.5 is equivalent to the present worth of capital expenditures during the construction of the systems. The central receiver plant and the CIS flat plate plant both turn out to have less-expensive collector costs than the Fresnel lens plant, and the resultant total capital requirements are also less by 14% and 28%, respectively. The central receiver plant has a forced convection, water-cooling system that adds significantly to the system cost relative to the other two plants.

The remaining steps in computing LEC (see equation (21.14)) are summarized in Table 21.6. The typical energy output was calculated from solar-insolation data and the performance parameters of the systems using computer codes. The energy outputs for

Table 21.6 Annual performance and energy cost summary for central station plants [4] Constant 1990\$, Carrisa Plains Site

	Fresnel lens	Central receiver	CIS flat plate
Average annual performance			
Energy output (MWh)	140 100	125 000	112 000
Capacity factor	32.0%	28.5%	25.8%
Annual energy efficiency	18.8%	11.3%	9.9%
Annual expenses (\$10 ⁶)			
Capital charge	16.69	14.42	11.95
Operation & maintenance expense	0.61	1.197	0.18
Total	17.30	16.39	12.13
30-year levelized energy cost (\$/kWh)			
Capital charge	0.119	0.115	0.106
Operation & maintenance costs	0.004	0.016	0.002
Total (\$/kWh)	0.123	0.131	0.106

Copyright © 2002. Electric Power Research Institute. EPRI TR-101255. Engineering and Economic Evaluation of Central-Station Photovoltaic Power Plants. Reprinted with Permission

the systems reflect both the efficiencies and the collector characteristics of the different system designs. The annual capital charge is the annualized amount of the total capital requirement, using a CRF of 10.2%. Levelized energy cost is the total annual expense divided by the annual energy output. It is interesting that the lowest LEC corresponds to the CIS flat-plate system that has the lowest efficiency and incorporates the simplest collector technology. (Cell efficiency for the CIS cell was taken as 15%.) The relationship among the LECs for the systems also points out that cell and module efficiencies, while very important in system performance, do not by themselves determine energy cost. Other system-design factors are also very important, and within limits, override the effect of efficiency on energy cost.

21.2.3.3 Gallium arsenide cells in power systems

GaAs cells have been developed and used extensively for space applications, but traditionally have been considered too expensive for terrestrial applications despite their high efficiency. These compound semiconductor cells are fabricated by epitaxial growth, either on GaAs wafers or on Ge wafers, the latter being a more recent development. The cost of GaAs wafers is a major factor in the cost of cells, and Ge wafers are projected to be less expensive by more than an order of magnitude. The question that arises is whether GaAs cells could be competitive with Si cells for utility-scale terrestrial systems, particularly if grown on Ge wafers. To address this question, the cost study in the previous section, as it relates to the Fresnel lens plant, was extended to determine the cost of energy for the same plant using GaAs cells of several different designs [5].

Two cells were considered: a single-junction GaAs cell, and a tandem-junction GaInP/GaAs cell. These GaAs cells are designed as concentrator cells, and could be considered for the same kinds of applications as the Si concentrator cells in the Fresnel lens

Table 21.7 GaAs cell and module price (1994\$) [5]

Cell/wafer	Cell efficiency	\$/Module (48 cells)	\$/48 cells
SJ/GA-SC	25	741.14	459.94
	30	741.54	460.50
SJ/Ge-SC	25	447.01	156.52
	30	450.40	159.11
SJ/Ge-PC	25	404.19	111.28
	30	407.58	113.79
TJ/GA-SC	30	745.96	464.68
	35	748.56	466.99
TJ/Ge-SC	30	456.33	164.51
	35	456.31	164.90
TJ/Ge-PC	30	413.50	119.11
	35	413.49	119.51

Note: SJ = single junction; TJ = tandem junction; SC = single-crystal; wafer PC = polycrystalline wafer. © 1994 IEEE

module of the prior study [4]. The manufacturing processes for each cell were defined using three different wafers: single-crystal GaAs, single-crystal Ge, and polycrystalline Ge. Modules incorporating each of the six combinations were modeled using the same STAMPP model as for the Fresnel lens module in the prior study. Further, a range of cell efficiencies for the GaAs cells was examined because the GaAs technology was not as well developed as the Si technology. In order to compare the annual energy production from GaAs plants with Si plants, the number of modules required for a 50-MW plant was calculated and the cost of modules computed with STAMPP at the required volume, as shown in Table 21.7. The total capital requirements, as shown in Table 21.5 for the Si plant and adjusted to 1994\$, were then scaled appropriately for the number of GaAs modules.

The price of GaAs cells, whether single- and tandem-junction, shown in Table 21.7 is heavily influenced by the choice of GaAs or Ge substrate. Cells grown on Ge-PC wafers are roughly four times less expensive than cells grown on GaAs-SC wafers. However, the prices of modules incorporating these cells differ by only a little less than a factor of two due to the fact that several substantial module-cost components are the same regardless of the cell structure. The least expensive module cost of \$413.50 in Table 21.7 for TJ/Ge-PC cells compares to the \$328.42 for a module incorporating Si cells (see Table 21.4, escalated to 1994\$). Cell efficiency for the same cell structure in Table 21.7 has little effect on module price. Indeed, module price is, in some cases, just slightly higher for the higher efficiency cell than the lower one (e.g. SJ/Ge-PC at 25% versus 30%). This is a result of the modeling procedure in which the number of modules produced was just sufficient for the 50-MW power plant, being fewer at higher cell efficiency, and the allocation of elements of cost by the STAMPP model to a fewer number of modules.

The reduction in cell and module prices in Table 21.7 reflects a span of about 15:1 in wafer costs between GaAs-SC and Ge-PC wafers, as indicated in Table 21.8. When GaAs cells are grown on the GaAs wafer, the cost of the wafers is almost 60% of the module materials cost, but when a Ge-PC wafer is used, then the wafer contributes to only

Table 21.8 Module materials cost drivers, GaAs tandem-junction cells [5]

	Substrate (GaAs & Ge = 4", Si = 6")			
	GaAs	Single-crystal Ge	Polycrystalline Ge	Si
Wafer cost/each	\$360.46	\$64.37	\$23.62	\$29.94
Material	<i>Percentage of total module materials cost</i>			
Wafer	59.8	20.4	8.6	5.3
Module box (\$3.59/each)	6.9	13.2	15.1	17.4
Heat sink (\$0.52/each)	4.0	7.7	8.8	10.1
Fresnel lens (\$4.07/ft ²)	12.2	23.3	26.8	14.3

Source: © 1994 IEEE

about 9% of the module materials cost. The latter case is very similar to the materials cost contributions for the Si module, where the wafer cost is not the largest single contributor. Using Ge wafers would thus be a major step in making GaAs cells competitive.

When the module prices in Table 21.7 are incorporated into the 50-MW power plant, capital requirements (Table 21.5) by adjusting these costs for the changes in field size resulting from the GaAs conversion efficiencies, the cost of energy generated, expressed as LEC, can be calculated for the various cell structures in Table 21.7 (see Figure 21.7). These GaAs-based energy-production costs are compared to that of Si-based energy-production costs from the previous study [4] as summarized in Table 21.6. Since none of the GaAs module prices, ranging from \$741 to \$413, is as low as the Si module price of \$328, the LECs in Figure 21.7 essentially show the trade-off of the more efficient (27.5% to 35%) but higher cost GaAs modules with the less efficient (27.4%) but lower

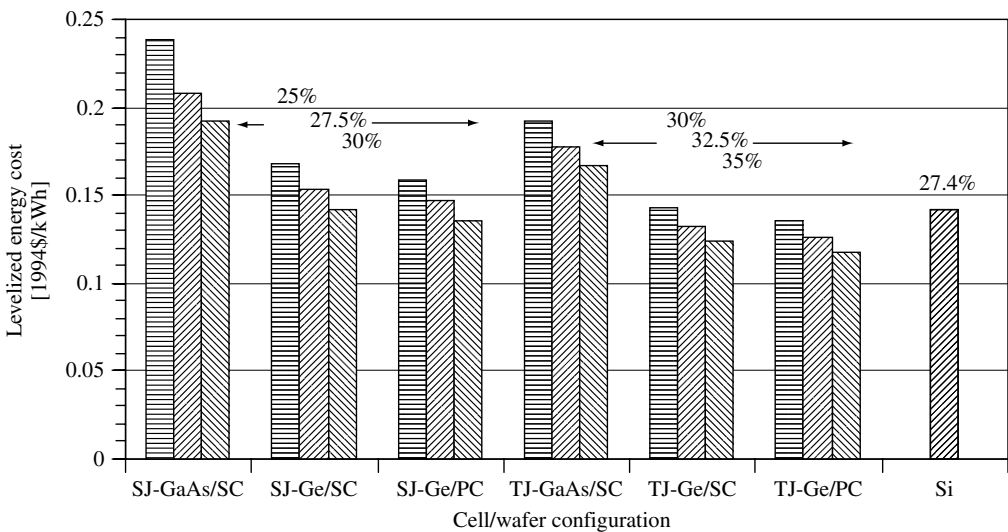


Figure 21.7 Cost of energy produced by 50 MW central station Fresnel lens plants using GaAs cells [5].
© 1994 IEEE

cost Si modules. The most costly GaAs technology (SJ/GA-SC), even at its highest projected efficiency of 30%, has an LEC of \$0.192/kWh compared to the LEC of the Si technology of \$0.142/kWh. The least-costly GaAs technology (TJ/Ge-PC) has an LEC of \$0.118/kWh at its highest efficiency of 35%, which is less than the Si LEC. The slightly more costly TJ/GA-SC technology still has a lower LEC (\$0.124/kWh at 35%) than the Si module, and this GaAs structure using the single-crystal wafer is more likely to achieve the 35% efficiency than the polycrystalline wafer cell.

21.3 ENERGY PAYBACK AND AIR POLLUTION REDUCTION

PV systems convert the free solar energy resource into valuable electric energy. However, it has long been noted that energy is consumed in the manufacture of PV conversion hardware. That is, there is an energy cost to produce energy. The mining, refining, and purification of semiconductor materials is energy intensive, and energy is consumed in the manufacture of all the other materials in a PV system, such as glass, steel, aluminum, copper, and plastic. In addition to the energy content of the materials incorporated directly in the module, support structures, and balance of system (BOS) components, there is an energy content in the equipment that produces all the PV system components. Energy is also consumed in transporting and erecting a PV system at its operating site. During the life of a PV system, usually taken as 20 to 30 years, energy is produced as a return on the energy “invested” in its creation. The long-raised question is: how much more energy does the PV system generate than it takes to produce it; or, is there a net energy benefit to society from PV systems? The answer is usually stated as “energy payback,” which is the number of years that is required to repay the energy content of the PV system with its delivered electricity. Energy payback for PV systems, measured in years, should ideally be a small fraction of the system life in years. In fairness to PV, it should also be noted that fossil energy systems, in addition to the energy consumed as they operate to produce electricity, also have an energy content in their power-plant hardware. In addition, the fuel itself has an energy content associated with the exploration, development, recovery, and transportation to the generation site. Thus, the terms of comparison for energy payback between PV and other systems need to be carefully defined if they are to be meaningful.

The energy-payback question needs to be differentiated from whether a PV system pays for itself economically (financially), which is a primary subject of this chapter. The question of economic benefit is adequately answered when the cost of all materials, equipment of production, and capital are accounted for. These costs include the cost of the energy content of all the elements of the system. Given that economic criteria are met, the energy payback question is essentially an ecological one; that is, does the creation of PV systems that generate substantially more energy than is consumed to produce them represent a wise use of fossil resources? A related issue is the reduction in greenhouse gases that results from the generation of electricity with PV rather than with fossil-fuel-based generation. If governments impose financial penalties on fossil generation or give credits for solar generation, then financial benefits can be introduced into the economic evaluation. To a degree this is implicit in the process when, for example, the cost of exhaust scrubbers for fossil plants is included in the economic comparison. Moreover, if solar energy is the source for producing PV systems, the ecological consequences are

diminished. Given the small amount of PV generation capacity in service today relative to other electric generation capacity, the primary concern for energy payback is in long-term energy planning in relation to ecological impact.

The issue of energy payback has been examined quantitatively, and a good bibliography is given in [6]. Energy payback is determined by the four basic factors mentioned below:

- The design of the PV system, including all components
- The location of the system
- The life of the PV system
- The portion of the manufacturing energy-consumption chain included in the payback.

System design determines the system conversion efficiency and system power level, as well as defining the energy content of the hardware. The system location determines the incident energy for the system, which, coupled with the system life, determines the total energy delivered by the PV system. The total energy content of the PV system depends on just how far back in the energy chain the analysis goes. For example, does the chain go back to the mining, transportation, refining, and fabricating of a material, and include every piece of equipment used at every link of the chain? In most cases, PV material energy content is based on prior studies of the energy content of basic materials. Special considerations are sometimes incorporated; for example, much of the crystalline PV production is currently based on using scrap-refined Si from the microelectronics industry, so it may be reasonable to ignore the energy content of the scrap material.

In a summary of energy payback studies, the US National Renewable Energy Laboratory (NREL), states that “(E)nergy payback estimates for rooftop PV systems boils down to 4, 3, 2, and 1 years: 4 years for systems using current multicrystalline-silicon PV modules, 3 years for current thin-film modules, 2 years for future multicrystalline modules, and 1 year for future thin-film modules.” These data assume a 30-year life. Multicrystalline modules have a longer energy payback because they have a much larger content of silicon than thin-film modules. Shorter payback for future modules is predicated on improved manufacturing processes and higher efficiencies.

NREL credits these results to the Dutch researcher Erik Alsema [7]. His data are based on estimates of 600 kWh/m² for the near-future, frameless, single-crystal silicon PV modules and 420 kWh/m² for multicrystalline modules. With a 12% conversion efficiency and a solar insolation level of 1700 kWh/m²/year, Alsema calculated the 4-year payback for current multicrystalline modules. The future payback of 2 years for multicrystalline modules was based on a 14% efficiency and solar-grade silicon feedstock.

For thin-film modules, amorphous-silicon paybacks are a good proxy for all material systems (including copper indium diselenide, cadmium telluride) because the major energy content is in the substrate, usually glass, and the deposition process plus other facilities. The films are so thin that they have relatively little energy content [8].

Knapp and Jester [6] examine the energy payback for both actual copper indium diselenide (CIS) and single-crystal silicon processes and modules produced using measured data. The data that were collected from plants operated by Siemens Solar Industries and reported in [6] assume that the CIS plant operated at capacity. Energy content of

production equipment, production facilities, and transportation of goods to and from the facility were excluded from the result. Using a solar insolation of 1700 kWh/m²/year, and assuming an 80% correction for the system losses, the single-crystal silicon module had an energy payback of 4.1 years and the CIS module's payback was 2.2 years.

Given the predicted energy paybacks of, say, 1 to 5 years for PV systems, and their life of up to 30 years, payback is not a negligible factor in the overall energy-planning process, but neither is it a prohibitive one. Gradual improvements in conversion efficiency and improvements in manufacturing techniques can further reduce its impact over time.

The literature that addresses energy payback also addresses the contribution of PV systems in reducing greenhouse gases [7, 8]. "An average US household uses 830 kWh of electricity per month. On an average, producing 1000 kWh of electricity with solar power reduces emissions by nearly 8 pounds of sulfur dioxide, 5 pounds of nitrogen oxides, and more than 1400 pounds of carbon dioxide. During its 28 years of clean energy production, a rooftop system with 2-year payback and meeting half of a household's electricity use would avoid conventional electrical plant emissions of more than half a ton of sulfur dioxide, one-third of a ton of nitrogen oxides, and 100 tons of carbon dioxide." (Though not stated, we assume these comparisons are of solar versus coal-fueled generation.) Again, if the cost of removing these from the conventional emissions is quantified, the cost saving can be included in an economic assessment.

21.4 PROSPECTS FOR THE FUTURE

Photovoltaic cells, modules, and systems have undergone intensive development in the 25 years immediately prior to the twenty-first century. Significant improvements in performance and reductions in cost per unit area have been made. The variety of PV cells and module technologies commercially available or under development has expanded greatly, although crystalline-silicon technology still predominates. Cost-effective applications that capitalize on the unique characteristics of PV systems have been implemented. Many other applications have been installed that benefited from subsidies from utilities, government, or economic-development institutions. A lot of progress has been made, and yet PV supplies only a tiny fraction of the electric generation market.

A recent survey [9] by *Photon International* magazine puts the annual worldwide production of Photovoltaics at 401.4 MW_p in the year 2001. There are about 59 PV module manufacturers worldwide. However, the industry has lost more than US\$3 billion over its first 25 years, according to the President and CEO of Siemens Solar in 1998[10]. He further states that two-thirds of the industry is still dependent on some kind of subsidy. Europe, Japan, and the United States each supply major portions of this production. The corporate landscape has been in a constant state of change over these years. Many small companies started up and a few large corporations entered the business. Many of the smaller firms have been absorbed by large corporate conglomerates, but a few have managed to stay in the business and grow. In recent years, some of the world's major corporations have become major players in the PV industry. The top ten producers in 2001 were listed as follows [9]:

1. Sharp (a major Japanese electronic-equipment maker, their solar cells are primarily integral to electronics products) 74.0 MW_p

2. BP Solar (a unit of British Petroleum, that merged with the US firm Solarex and presently has plants in US, Spain, Australia, and India) 54.4 MW_p
3. Kyocera (a major Japanese electronics, equipment, and materials company) 54.0 MW_p
4. Siemens and Shell Solar GmbH (investments by German/Dutch conglomerate Shell and Siemens AG whose main production is in the US) 48.3 MW_p
5. AstroPower (independent US manufacturer) 26.0 MW_p
6. RWE Solar (a unit of the German Utility RWE that merged with ASE Americas) 22.7 MW_p
7. Isofoton (independent Spanish manufacturer of PV and solar thermal technology) 18.7 MW_p
8. Sanyo (a major Japanese maker of electronic consumer products, semiconductors, batteries, etc; PV products made by Solec International division) 16.0 MW_p
9. Mitsubishi (a Japanese conglomerate providing a wide range of products and services) 14.0 MW_p
10. Photowatt (a unit of Matrix Solar Technologies, owned by a Canadian corporation ATS) 13.5 MW_p.

Despite the changes in the makeup of the industry, progress has been sustained by gains in performance and reductions in cost. PV module prices in $\$/W_p$ declined by an order of magnitude over the nearly 20-year period ending in 1994[11]. This experience, shown in Figure 21.8, is based primarily on data for crystalline-silicon modules, but is said to be representative of other flat-plate module technologies as well. The projection beyond 1994 is based on a fit of the data for module price versus cumulative

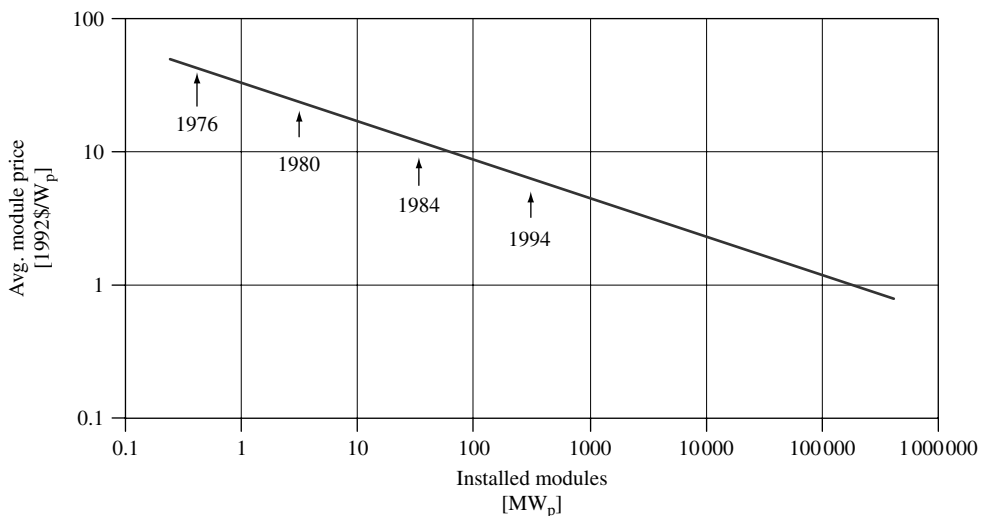


Figure 21.8 PV module price trends. Adapted from [11]. Copyright © 2002. Electric Power Research Institute. EPRI TR-109496. Renewable Energy Technology Characterizations, Topical Report

production. Significant departures from the projection might result from new technological development, such as thin-film modules or concentrator technology.

Some recent experiences [12] with PV systems with capacities in the range of 70 to 236 kW_p showed that system costs dropped by 14% from 1996–1997 to 1998–1999 (\$9.77/W_p to \$8.46/W_p). These systems included both fixed and one-axis tracking systems, which were mounted both on buildings and on the ground, and included modules and inverters from several manufacturers. Three of the most recent projects had installed costs below \$7/W_p.

Siemens has stated [10] that it is planning on a long-term annual growth rate of 15% for installed PV. Their projection is that a 15% to 25% rate would result in PV contributing to 1% of the world's electricity between 2025 and 2040, which they estimate as 300 TWh in 2025. They state that one-third of this energy could provide for the basic needs of two-billion people not served by a grid.

Another view of the potential for PV can be gained from some figures published by the US government. Recent progress and long-term goals for the US PV program [13] are shown in Table 21.9. Meeting these goals would increase cumulative US sales by the year 2030 to 20 times the year 2000 level, and correspond to about a 12% compounded annual rate of sales growth. The average annual sales from 1996 to 2000 would be about 65 MW/year, and from 2001 to 2030 would be roughly 315 MW/year. The US share of the world market for PV was about 41% in 1995[13]. If this share was maintained till 2030, the cumulative capacity would be about 25 GW. Assuming an average of 2000 h/year of sunlight, the annual generated energy would be 50 TWh by 2030. This is substantially lower than the Siemens estimate given above, but the difference is largely explained by the difference in the 12% annual growth rate and the Siemens estimate of 15% to 25%. Starting at the same 500-MW cumulative sales in 2000, using a constant 41% market share and 2000 h/year of sunlight, a 15% growth rate results in about 80 TWh/year of generated energy. Using a 25% growth rate, the energy is about 645 TWh. There is obviously a lot of uncertainty in making such projections, and the truth no doubt lies somewhere in the range of these estimates.

Some additional insight into the potential contribution of PV to the world's electric-energy needs can be had from data published by the US Energy Information Administration [14]. The world's net electricity consumption in 1999 was 12 833 TWh. Of this total, industrialized countries consume 59%, eastern Europe and the former Soviet Union, consume 11%, and developing countries account for 30%. If the cumulative PV capacity

Table 21.9 Photovoltaic progress and program goals (1995\$) US department of energy [13]

	1991	1995	2000	2010–2030
Electricity price (¢/kWh)	40–75	25–50	12–20	<6
Module efficiency ^a (%)	5–14	7–17	10–20	15–25
System cost (\$/W _p)	10–20	7–15	3–7	1–1.5
System lifetime (years)	5–10	10–20	>20	>30
US cumulative sales (MW)	75	175	400–600	>10 000

^aRange of efficiencies for commercial flat-plate and concentrator technologies

in 2000 was 1220 MW (500 MW divided by 41%), an estimate of the energy generated will be 2.4 TWh, or about 0.02% of the world consumption. The projected average annual growth of electricity consumption over the period 1999 to 2020 in [14] is 2.7% worldwide, resulting in consumption of 22 230 TWh in 2020. Extrapolating this to 2025 as 25 398 TWh, the contribution of PV at 300 TWh would be 1.2%. While this is a small fraction, it still could, as the Siemens article points out, make a significant contribution to the lives of people where conventional grid-connected electricity is not available.

Looking at these varied projections of growth in PV sales, it is clear that the penetration of the future electricity market by PV systems is difficult to predict. It depends on many factors whose outcomes are uncertain, among them being the following factors:

- Continued progress in performance and cost reduction of PV systems. This is perhaps the most certain of the factors to be achieved, assuming that the deep-pocket firms now engaged in PV system development continue to be involved. Participation by government and industry associations through support of research and development will also contribute to this factor.
- Increase in the cost of fossil fuels. Numerous predictions made in the past of the cost of oil rising well above US\$30 per barrel have failed to materialize on any consistent basis. The price of oil is a strong determinant of the cost of electricity that competes with PV electricity. The price of oil, largely determined by the international cartel, can only be raised so far without decreasing their market size. Major new fields in the Caspian Sea area or elsewhere will be an influence if they materialize, but such finds will become less likely over time.
- Increases in environmental costs for fossil-fuel-based electricity. Global warming concerns may prompt added costs of production due to greenhouse gas control or regulatory constraints or restrictions on competing uses, especially as the energy use of developing nations goes up. These factors will make PV more competitive.
- Accommodation of users to the variable character of the PV source. PV delivers energy when the sun shines, but there is much demand at other times. This characteristic can be overcome by the integration of PV into utilities, by sharing PV capacity among groups of users (a utility of a different sort), by adding storage to the PV system (e.g. electric storage batteries, hydrogen production and storage, hydroelectric storage), or by lifestyle changes. All of these are possible, but each accommodation has its own barriers.
- The need for off-grid electric power is very large and the capacity required for individual sites is usually small. PV systems are more modular than almost any other source, and they provide insurance against rising fossil-fuel prices. If ways can be found to make them affordable, PV has an enormous off-grid market.

All of these projections suggest that PV systems will continue to increase their market penetration and make a useful contribution to energy supply over the next several decades. The likelihood of their becoming an economically significant fraction of the energy supply, say 5% or more, within the next 20 to 30 years appears to be small at this point. Such an event will require fundamental changes in the way energy is delivered, and those changes will have to be driven by economic and environmental forces beyond the control of the PV industry.

REFERENCES

1. Smith G, *Engineering Economy: Analysis of Capital Expenditures*, 2nd Edition, Chap. 4, The Iowa State University Press, Ames, IA (1977).
2. Stevens Jr. G, *The Economic Analysis of Capita Investments for Managers & Engineers*, Chap. 5, Reston Publishing, Reston, VA (1983).
3. Whisnant R, Wright S, Champagne P, Brookshire K, *Photovoltaic Manufacturing Cost Analysis: A Required Price Approach*, Vol. 1, 2, EPRI AP-4369, Electric Power Research Institute, Palo Alto, CA (1986).
4. Stolte W, *Engineering and Economic Evaluation of Central-Station Photovoltaic Power Plants*, TR-101255, Electric Power Research Institute, Palo Alto, CA (1992).
5. Whisnant R *et al.*, "Silicon and GaAs/Ge Concentrator Power Plants: A Comparison of Cost of Energy Produced", *Proc. IEEE First World Conference on PV Energy Conversion*, 1103–1106 (1994).
6. Knapp K, Jester T, "An Empirical Perspective on the Energy Payback Time for Photovoltaic Modules", *Proc. Solar 2000 Conference* (Madison, WI, 2000).
7. Alsema E, "Energy Requirements and CO₂ Mitigation Potential of PV Systems", *Workshop, Proceedings, Photovoltaics and the Environment* (Keystone, CO, 1998).
8. *Energy Payback: Clean Energy from PV*, NREL Report No. FS-520-24619, National Renewable Energy Laboratory, Golden, CO (1999).
9. Schmela M, *World production for solar cells grew 40% in 2001*, Photon International (magazine), 38–43 (March 2002).
10. Oswald G, "The PV Industry Moving into the Solar Century", *2nd World Congress on Photovoltaic Energy Conversion* (Vienna, Austria, 1998).
11. DeMeo E, Galdo J, *Renewable Energy Technology Characterizations*, Topical Report, TR-109496, U.S. Department of Energy, Electric Power Research Institute, Washington, DC, USA (1997).
12. *Large Systems Cost Report: Cost Analysis for 70 kW and Larger TEAM-UP PV Installations*, Solar Electric Power Association, Washington, DC (2000).
13. *Photovoltaics the Power of Choice: The National Photovoltaics Program Plan for 1996–2000*, U.S. Department of Energy, Washington, DC.
14. *International Energy Outlook 2001*, U.S. Energy Information Administration, Washington, DC (2001).

This Page Intentionally Left Blank

22

PV in Architecture

Tjerk H. Reijenga

BEAR Architecten, Gouda, Netherlands

22.1 INTRODUCTION

22.1.1 Photovoltaics (PV) as a Challenge for Architects and Engineers

What is happening in the built environment around us? We are witnessing an essential change in society. Governments are spending hundreds of millions of dollars on research, development and the demonstration of renewable energy. Big oil companies such as BP Amoco and Shell have invested more than a billion dollars in solar energy. Current developments show that renewables, such as solar energy systems, will be incorporated into our daily life in the near future, as conventional energy sources become depleted and environmental concerns grow [1].

Within a short period of time, solar systems will become an integral part of our society and thus our environment. There are large incentives for urban planners and architects to incorporate these techniques into their design. New products are emerging yet need further development to fully meet the architectural needs of sustainable buildings. Architects therefore need to start thinking about this new Smart Solar Architecture.

The European Commission has issued the “White Paper for a Community Strategy and Action Plan, Energy, for the future: Renewable Sources of Energy” [2]. This White Paper sets a target of 12% for the contribution of renewable energy sources to the total energy consumption in the European Union by 2010. The “Campaign for Take-Off” was launched in 1999 and aims to facilitate the success of the Strategy for Renewable Energy Sources up to the year 2003. One of the proposed key sectors to be promoted during the campaign is PV systems – 1 million systems in total.

The 450 MWp rooftop system campaign in the European Union can be achieved by installing 150 000 systems at an average capacity of 3 kWp each. The 150 MWp

building facades program in the commercial sector can be realized by installing 5000 systems, assuming an average size of 30 kWp per building. With an additional capacity of 50 MWp for stand-alone systems the total target for installed PV for Europe will be 650 MWp (approx. 6 500 000 m²).

22.1.2 Definition of Building Integration

A large part of the future PV market will be associated with building applications, especially in Europe and Japan where the population density is high and the land is valuable [3]. In areas with less population, it will be possible to find land for ground-mounted PV structures (Figure 22.1) [4].

Building-integrated, grid-connected PV systems have the following advantages [5]:

- There is no additional requirement for land.
- The cost of the PV wall or roof can be offset against the cost of the building element it replaces.
- Power is generated on site and replaces electricity that would otherwise be purchased at commercial rates.
- Connecting to the grid means that the high cost of storage is avoided and security of supply is ensured.

Additional benefits of public awareness are [6] as follows:

- Architecturally elegant, well-integrated systems will increase market acceptance.
- Building-integrated PV (BIPV) systems provide building owners with a highly visible public expression of their environmental commitment (Figure 22.2).



Figure 22.1 The 1 MWp ground-mounted system in Toledo, Spain. Reproduced with permission by BEAR Architekten T. Reijenga



Figure 22.2 Integrated façade system with 14 kWp amorphous silicon modules made by Energy Photovoltaics (EPV) in New Jersey, USA on top of a skyscraper at Four Times Square, New York, USA. The PV modules are the dark regions on the facade near the top. Reproduced from Kiss G, *Proc. 2nd WC Photovoltaic Solar Energy Conversion*, 2452–2455 (1998) with permission by Gregory Kiss [7]

The way people deal with photovoltaics in architecture differs from country to country. This depends on the scale, culture and type of financing for building projects. In countries such as Denmark, the Netherlands and the United Kingdom, where public housing is very common, serial production is strongly emphasized in housing projects. Professionals such as project developers and architects implement the housing construction process, in which the main opportunities are for PV roof integration in single-family terraced houses and for façade and roof integration in apartment buildings.

In countries where the government has little influence on house building, the building process is a private initiative. Integration of PV systems in buildings can be carried out by professionals but, on the smaller scale of a single-family house, the motivation must come from the private owner. In these countries, most building-integrated PV systems are found in commercial and industrial buildings in which building professionals are involved. With these types of buildings, PV systems are integrated both into façades and roofs. There is a significant market for private homeowners who buy small-scale (less than 500 Wp) PV systems and mount them somewhere on their house.

The aim of integrating PV systems into buildings is to reduce the requirement for land and the costs [8]. This could be the cost of the support construction and the cost of building elements, such as tiles. It is more efficient to integrate a PV system when constructing the building, rather than mounting it afterwards.

A definition for Building Integration is hard to formulate, as it concerns the physical integration of a PV system into a building, but it also covers the overall image of the PV system in the building. For the architect, the aesthetic aspect, rather than the physical integration, is the main reason for talking about building integration. The optimal situation is a physically and aesthetically well-integrated BIPV system. In fact, many examples of physical integration show a lack of aesthetic integration. Visual analysis of PV systems in buildings shows that the look of a poorly designed building does not improve, simply

by adding a well-designed PV system. On the other hand, a well-designed building with a nicely integrated PV system will be accepted by everybody.

The following section aims to explain some basic thoughts about PV to non-designers, from an architectural and design point of view.

Note: All specified power of PV systems is the power under standard test conditions and tilt which may be greater than the power delivered when installed in nonoptimum orientation required by the BIPV application.

22.2 PV IN ARCHITECTURE

22.2.1 Architectural Functions of PV Modules

Basically there are three locations for integrating PV systems into buildings. The main locations are the roof and façade, with all other locations being known as *building components*.

A PV system can be integrated into the roof in several ways. One choice is for the integrated system to be part of the external skin and therefore be part of an impermeable layer in the construction. In the 1990s, several building projects were constructed on the basis of this principle (Figure 22.3) [9]. The other choice for roof mounting the PV system is above the impermeable layer. This is a more secure option but not without some risk, as the impermeable layer has to be pierced in order to mount the system on the roof. Using PV modules as roof covering reduces the amount of building materials needed, which is very favorable for a sustainable building and can help reduce costs. In addition to covering the complete roof with modules, there are also many products for small-scale use, for example, PV shingles and tiles. The small scale of these products (from 2 cells on a tile to around 20 cells on a look-alike tile) makes them very convenient for use in existing buildings or as do-it-yourself products.



Figure 22.3 Roof integration in a renovation project with the Shell Solar/BOAL profiles in Leiden (NL), providing a 2.1 kWp system per house. The PV roof is an impermeable layer. Reproduced from Maycock P *et al.*, *Building with Photovoltaics*, 78–81, Ten Hagen & Stam, Den Haag (1995) with permission by NOVEM, R Schropp [10]



Figure 22.4 Solar office in Doxford Sunderland (UK) with a transparent double-glazing PV system integrated in the façade. The 73 kWp PV system is manufactured by Saint Gobain and mounted in Schüco window frames. Reproduced with permission by Dennis Gilbert

Transparent PV modules used as roofing materials serve as water and sun barriers and also transmit daylight (see Figure 22.4). In glass-covered areas, such as sunrooms and atriums, sun protection on the roof is necessary in order to avoid overheating in summer. The PV cells absorb 70 to 80% of the sun radiation. The space between the cells transmits enough diffused daylight to achieve a pleasant lighting level in the area. PV cells were used in this way at the Centre for Sustainability De Kleine Aarde in Boxtel (NL) [11] and the Brundtland Centre (DK). Using transparent PV modules in the Solar Office in Doxford (UK), has resulted in a similar contrast in the façade [12]. In order to increase the usage of daylight in the workplaces, transparent PV modules have been used instead of glass.

Of course, PV cells convert sunlight into electricity (with typical efficiencies of 6–15%) with the remainder of the solar energy being converted into heat. At the project “Haus der Zukunft” in Linz (AT), this residual heat is also used to warm the home [13]. An air cavity has been created underneath the PV modules, through which warm air (heated by PV modules) is exhausted. The hybrid collector provides warm air to the heating system in the home, which in this case, makes it a cost-effective use of the collector.

At the Netherlands Energy Research Foundation (ECN) in Petten (NL), Building 42 has a conservatory with 43 kWp BP solar roof-integrated transparent laminates that reduce light and sun transmission by around 70% as compared to glass. The conservatory therefore acts as a big parasol over the offices, protecting them from the sun while still providing enough daylight (Figure 22.5) [14].

Facades are basically constructed using *in situ* bricklaying or concrete constructions, prefab elements or structural metal facades that are mounted in place. Concrete constructions form the structural layer and are covered with insulation and a protective cladding [15]. This cladding can be wood, metal sheets, panels, glass or PV modules. For luxury office buildings, which often have expensive cladding, cladding with PV modules is not more expensive than other commonly used materials, for example, natural stone



Figure 22.5 Interior view of the conservatory with integrated 43 kWp transparent BP solar modules in ECN Building 42 in Petten (NL). Reproduced with permission by BEAR Architecten T. Reijenga

and expensive special glass. This cladding costs around \$1000/m², which is comparable to the cost of the PV module today.

Structural glazing or structural facades are constructed using highly developed profile systems, which can be filled with all types of sheeting, such as glass or frameless PV modules. Facades are very suitable for all types of sunshades, louvers and canopies [16]. There is a logical combination between shading a building in summer and producing electricity at the same time. Architects recognize this and many examples of PV shading systems can be seen around the world (Figure 22.6). A canopy (entrance protection) on the sunny side of a building is a good place for BIPV systems (Figure 22.7) thus providing shade, protection from rain, as well as electricity.

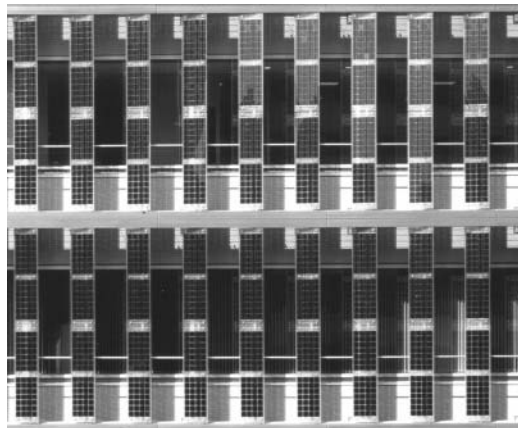


Figure 22.6 Solar shading (PV modules as part of a vertical louver system) on the west façade of the SBIC office building in Tokyo (JA). The transparent vertical louvers, with a total capacity of 20.1 kWp, were manufactured by Atlantis Switzerland. Reproduced with permission by Jiro Ono

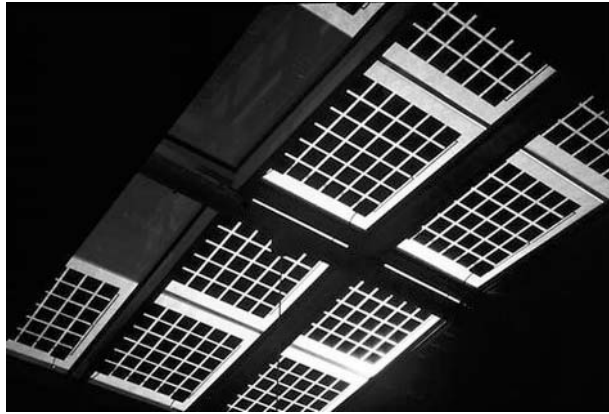


Figure 22.7 This system is the 1.25 kWp canopy with Atlantis transparent modules at the Thoreau Center in San Francisco, CA (USA). The canopy protects the entrance against the rain and wind but daylight is still allowed through via the transparent modules. Reproduced from Eiffert P, Kiss G, *Building-Integrated Photovoltaic Designs for Commercial and Institutional Structures – A Sourcebook for Architects*, 7–10, NREL, Golden, CO (2000) with permission by NREL USA [17]

22.2.2 PV as Part of “Green Design”

The government’s role in promoting and supporting sustainable energy (PV systems) strongly influences the extent to which these systems are used in buildings. In countries with less government intervention, the power companies play a bigger role. Even without financial support, the government can encourage sustainable energy, for example, by demanding better performance for buildings. By introducing certain performance goals, sustainable energy and solar energy PV systems might be considered.

There is a growing interest in “green” products such as organic food, organic fibers as well as green buildings. Insurance companies and financial markets are becoming aware of “green” financing, which requires a different design approach from architects. “Green” design is the basic reason for integrating PV systems into buildings.

22.2.3 PV Integrated as Roofing Louvres, Facades and Shading

For architects, the application of PV systems must be part of a whole (holistic) approach. A high-quality PV system can provide a substantial part of the building’s energy needs if the building has been designed in the right way. In general, the energy consumption of buildings needs to be cut down by at least 50% compared to a typical but inefficiently designed building.

In a holistic approach, integrating a PV system not only means replacing a building material but also aesthetically integrating it into the design. The integration also takes over other functions of the building’s skin. Mounted on a sloped roof, profile systems mean that PV modules can be part of the watertight skin. The system can also be mounted above an impermeable roof foil, thereby protecting the foil against UV light and direct sun. This extends the life span of the foil. This kind of system is also available for flat roofs. The Powerlight Company from Berkeley, CA (USA) introduced a PV system into

the market that is glued on expanded polystyrene (XPS) insulation material. This type of warm roof construction (construction on the warm side of the insulation) system is very well suited to renovating large flat roofs (Figure 22.8).

The designer may well use building elements such as canopies and shading systems to integrate PV systems, but will need to look in detail at shading and PV technology to understand the details of how to design this PV integration. One of the first things that the designer will discover is the fact that an efficient PV system is not automatically a good shading system. In general, a PV system on louvres will need a certain mutual distance between the louvers to prevent shading of the cells, which may let too much sun through at a lower sun angle in spring and fall (Figure 22.9).



Figure 22.8 Powerguard flat-roof PV system including thermal insulation at the Coastguard building in Boston, MA (USA). The 3 kWp system has a special wind-tunnel-tested profile at the edge to keep the system on the roof in heavy winds. Adapted from Eiffert P, Kiss G, *Building-Integrated Photovoltaic Designs for Commercial and Institutional Structures – A Sourcebook for Architects*, 42–44, NREL, Golden, CO (2000). Reproduced with permission by NREL USA [18]



Figure 22.9 Colt shading system that is optimized for sun control. The distance between the louvers with PV modules cause shading on 50% of the PV cells; 47 kWp PV system at Stadtwerke in Winterthur (CH). Reproduced with permission by BEAR Architekten T. Reijenga

Heat load and daylight control systems can be combined with the integration of PV systems. Moreover, when the designer studies these aspects in detail, he or she will discover that PV systems can also be part of the thermal envelope or thermal system (Figure 22.10) [19]. Another example is the refurbishment of Building 31 in Petten (NL) [20]. In this project, the PV system is integrated into a louver system that supports the 35 kWp Shell Solar modules, to keep out the summer heat and give less glare, and improve daylight conditions inside. To prevent shading of the modules by the upper louver, the dimensions of the louvers have to be almost twice the size of the modules (Figure 22.11) (Diagram 1) [21].

Orientation is a major design issue for (green) buildings. The heat load of a building, the need for shading and the design of facades all depend on the orientation.



Figure 22.10 Daylight control at the Kaiser fashion house in Freiburg (D). This 4 kWp PV system on louvers is mounted in front of the glass façade and prevents glare inside. The PV louvers are in the center of the figure. Reproduced with permission by BEAR Architecten T. Reijenga



Figure 22.11 South façade of ECN Building 31 in Petten (NL). The shading structure supports the 35 kWp Shell Solar modules. Reproduced with permission by BEAR Architecten T. Reijenga

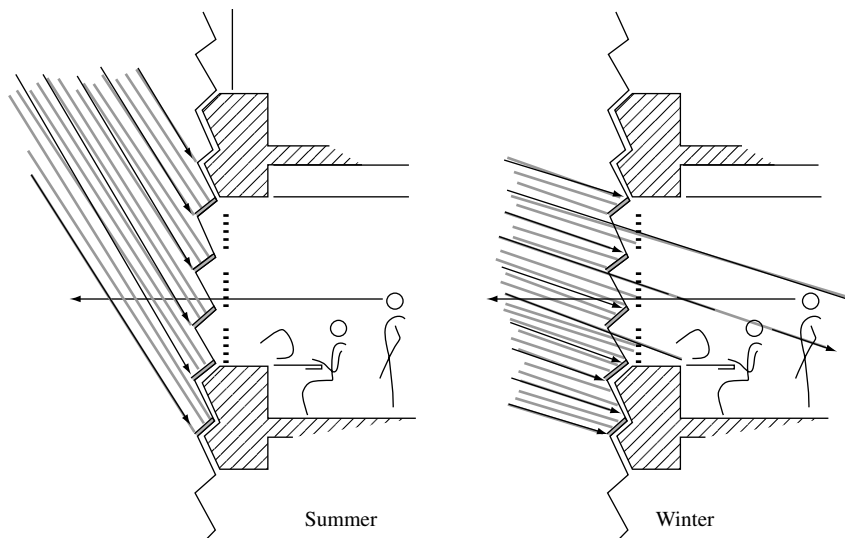


Diagram 1 Shading system with high angle (summer) and low angle (winter). In a fixed position designed for high angle of summer sun the system will be inefficient for the winter period. Reproduced with permission by BEAR Architecten, NL

Orientation is also important for PV systems. Facade systems might be suitable in certain countries, especially at a northern (above 50°N) or a southern (below 50°S) latitude. When shading of the facade cannot be prevented, and for the countries in between these latitudes, sloped surfaces facing the sun or even horizontal surfaces might be more suitable. The designer's final choice will be based on orientation, amount of total annual (sun)light on the PV module, shading from surrounding buildings and the aesthetics of the design. An important issue for the designer is to appreciate the blue, gray or black cells and to become familiar with finding integration opportunities in the first draft design. Ideally, a PV system should not be added to a building but designed as part of the building.

22.2.4 Well-integrated Systems

How can we discuss whether a BIPV system is well integrated? [22] A group of architects within the IEA PVPS (PV Power Systems) Task 7 workgroup discussed this subject and came up with several criteria for judging the aesthetic qualities of BIPV projects [23].

In order to decide which BIPV systems are of a high quality, we need to distinguish between the following:

- technical quality of the BIPV system, that is, the technical aspects of PV, cables and inverters,
- building quality of the BIPV system. Here we look for the quality of the system as a building element (part of the roof or the façade that is replaced by modules). The module and its integration must meet typical building standards, such as an impermeable layer or a structure strong enough to withstand wind or snow loads,

- aesthetic quality of the BIPV system. This is the least scientific and most subjective part of judging BIPV systems. But the reality is that architecturally elegant, well-integrated systems will increase market acceptance.

Both the technical and building qualities of the PV system have been considered as preconditions. All installations in a building must function correctly.

Aesthetic quality is not a precondition. Although the discussion of architectural values is very broad, high-quality architecture or poor architecture is generally recognizable.

The criteria formulated by the IEA PVPS Task 7 workgroup for evaluating the aesthetic quality of building-integrated PV systems are [24, 25]

- natural integration,
- designs that are architecturally pleasing,
- good composition of colors and materials,
- dimensions that fit the gridula,¹ harmony, composition,
- PV systems that match the context of the building,
- well-engineered design,
- use of innovative design.

These architectural criteria need to be explained particularly to nonarchitects and manufacturers developing photovoltaic systems for integration into roofs and façades, who often believe that their systems fit perfectly. Some architectural journals,² however, have criticized PV projects in, for example, the 250 kWp project in Sloten, Amsterdam (NL) [26] and the 1.3 MWp project in Nieuwland, Amersfoort (NL) [27]. The average architect is not yet convinced of the “beauty” of a PV system on his building. All the more reason this book should show appealing examples and critically judge PV products.

The Lafarge Braas PV 700 roof tile system is a good example of how manufacturers look at their product. This system can be placed invisibly in between the flat Lafarge Stonewold tiles (Figure 22.12) [28].

However, in product advertisements, the manufacturer has chosen tiles with contrasting colors instead of harmonious colors, thus ignoring the fact that integration, in most situations, should be discreet. After commercial introduction, the system was prepared for use with a standard roofing tile. This corrugated tile is an even bigger contrast to the flat PV elements. Technically speaking, this high-quality product has been integrated. Aesthetically, however, the product has not been integrated because of the contrast. Therefore, the architect, building inspectors and clients might reject a PV system incorporating this product.

Explanation of the criteria

- *Natural integration*: This means that the PV system seems to form a logical part of the building (Figure 22.13). The system adds the finishing touch to the building. The

¹ Gridula is not a common word outside architectural vocabulary. It means the grid that is used for the design that is a (sometimes hidden) part of the building.

² Archis February 1998.

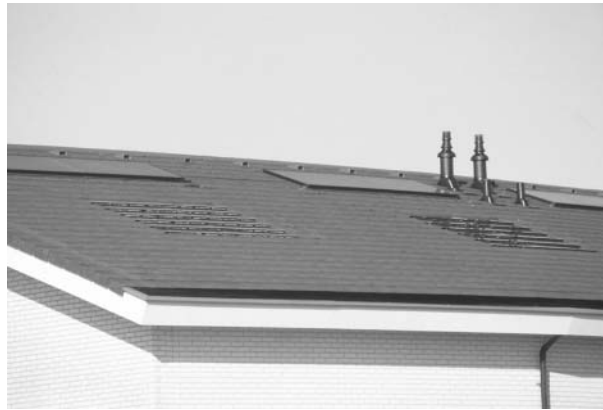


Figure 22.12 This sustainable WWF (World Wildlife Fund) project in Harderwijk (NL) has a roof with a thermal solar collector on top and a 460 Wp PV 700 system underneath. The PV 700 system fits almost invisibly in between the tiles. Reproduced with permission by BEAR Architecten T. Reijenga



Figure 22.13 A naturally integrated PV system that is clearly part of the building. This system is located in Poitiers (FR). Reproduced with permission by ECN J. Beurskens

PV system does not have to be that obvious. In renovation situations, the result should look as though the PV system was there before the renovation.

- *Architecturally pleasing*: The design has to be architecturally pleasing (Figure 22.14). The building should look attractive and the PV system should noticeably improve the design. This is a very subjective issue, but there is no doubt that people find some buildings more pleasing than others.
- *Good composition of colors and materials*: The color and texture of the PV system should be consistent with the other materials (Figure 22.15).
- *Fit the gridula, harmony, and composition*: The dimensions of the PV system should match the dimensions of the building (Figure 22.16). This will determine the dimensions



Figure 22.14 Corridor in the Centre for Sustainability De Kleine Aarde in Boxtel (NL). The space is unheated and naturally ventilated. The 6.7 kWp PV system with transparent modules has a double function and reduces the heat load by around 70%. Reproduced from Reijnga T, Böttger W, *Proc. 2nd WC Photovoltaic Solar Energy Conversion*, 2748–2751 (1998) with permission by NOVEM, R Schropp [11]



Figure 22.15 The 80.5 kWp Atlantis Sunslates on the roof of the historic horse stables in Bern (CH). The color and texture matches so well that this PV system was allowed on a protected historic building. Reproduced with permission by Atlantis Solar Systems Ltd

of the modules and the building grid lines used (grid = modular system of lines and dimensions used to structure the building).

- *Matching the context of the building*: The entire appearance of the building should be consistent with the PV system used (Figure 22.17). In a historic building, a tile-type system will look better than large modules. A high-tech PV system, however, would fit better in a high-tech building.
- *Well engineered*: This does not concern the waterproofing or reliability of the construction. However, it does concern the elegance of the details (Figure 22.18). Did the



Figure 22.16 The cube at the Discovery Science Center in Santa Ana, Los Angeles, CA (USA). The 20 kWp PV system fits the gridula of this huge structure and there is harmony between the PV modules and the structure behind. Some 494 Thin-film Millienna photovoltaic modules from BP Solar were used on the solar cube. Reproduced from Eiffert P, Kiss G, *Building-Integrated Photovoltaic Designs for Commercial and Institutional Structures – A Sourcebook for Architects*, 48, 49, NREL, Golden, CO (2000) with permission by BEAR Architecten T. Reijenga [29]



Figure 22.17 The 180 kWp Sofrel flat-roof system on the UBS Bank near Lugano (CH) matches the context of the roof, which fits between different installations, high-tech chimneys and the tight rhythm of the flat-roof PV system on the roof. Here the BIPV is mainly aesthetically and not physically integrated. Reproduced from Maycock P *et al.*, *Building with Photovoltaics*, 78–81, Ten Hagen & Stam, Den Haag (1995) with permission by UBS Switzerland [10]

designers pay attention to detail? Has the amount of material been minimized? These considerations will determine the influence of the working details.

- *Innovative design*: PV systems have been used in many ways but there are still countless new ways to be developed. This is all the more reason to consider this criterion as well.



Figure 22.18 The Schüco façade in the Solar office in Doxford, Sunderland (UK) is well engineered. Reproduced with permission by BEAR Architecten T. Reijenga

22.2.5 Integration of PV Modules in Architecture

The integration of PV systems in architecture can be divided into five categories:

1. Applied invisibly
2. Added to the design
3. Adding to the architectural image
4. Determining architectural image
5. Leading to new architectural concepts.

These categories have been classified according to the increasing extent of architectural integration. However, a project does not necessarily have to be of a lesser quality just because PV modules have been applied invisibly. A visible PV system is not always appropriate, especially in renovation projects with historic architectural styles. The challenge for architects, however, is to integrate PV modules into buildings properly. PV modules are new building materials that offer new designing options. Applying PV modules in architecture should therefore lead to new designs. In some of the selected projects, the design was based on this principle.

1. *Applied invisibly*: The PV system has been incorporated invisibly (and is therefore not architecturally ‘disturbing’) (Figure 22.19). The PV system harmonizes with the total project. An example is the Maryland project in the USA (Figure 22.20), where the architect tried to integrate PV modules into the design invisibly. This solution was chosen because the entire project concerned historic architecture. A modern high-tech PV module look would not be appropriate for this architectural style.
2. *Added to the design*: The PV system is added to the design (Figure 22.21). Building integration is not really used here, but this does not necessarily mean that architectural

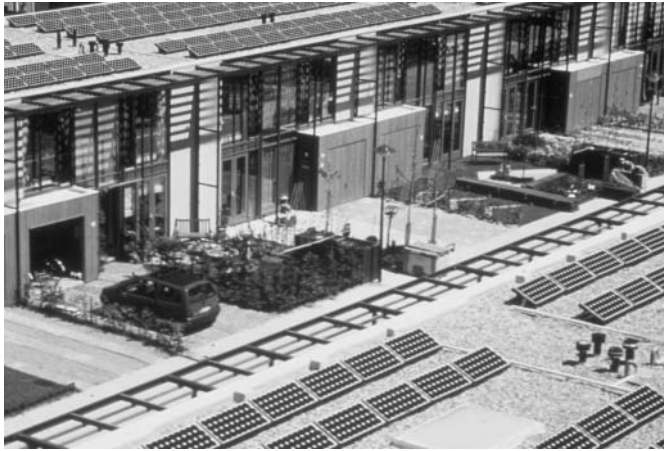


Figure 22.19 Modern style houses in the 1.3 MW project in Amersfoort (NL). The architect thought that the modules did not blend in with the design. He chose an “invisible” solution with a flat-roof system. The PV system is not visible from the surrounding streets. Reproduced with permission by REMU J. van IJken



Figure 22.20 Houses at the National Research Home Park in Bowie, MA (USA) in historic style. The roofs are Unisolar standing-seam roofs with thin film (amorphous silicon). Reproduced with permission by NREL USA

integration is also lacking. The “added” PV system is not always visible either (Figure 22.22).

3. *The PV system adds to the architectural image:* The PV system has been integrated beautifully into the total design of the building, without changing the project’s image (Figure 22.23). In other words, the contextual integration is very good (Figure 22.24).



Figure 22.21 The IES building in Madrid (E) has a 6.6 kWp PV system that was added shortly after the building was finished. The modules are mounted on the façade above the windows and keep out the sun. Reproduced with permission by BEAR Architecten T. Reijenga



Figure 22.22 These houses in Amersfoort Nieuwland (NL) have a roof with a white foil on top. The architect chose a color contrasting with the color of the modules to show that the PV system is an addition to his design. Reproduced with permission by REMU J. van IJken

4. *The PV system determines the architectural image:* The PV system has been integrated into the design in a remarkable and beautiful way and plays an important role in the total image of the building (Figures 22.25 and 22.26).
5. *PV system leads to new architectural concepts:* Using PV modules, possibly in combination with other types of solar energy, leads to new designs (Figure 22.27) and new architecture (Figure 22.28). The integration of PV modules was considered on a conceptual level, which gives the project extra value.



Figure 22.23 The architect integrated the (in total 49 kWp) PV modules into the facades above the windows and produced a combination with the roller blinds. The EMPA office building is located in Sankt Gallen (CH). Reproduced with permission by Electrowatt Eng. Services



Figure 22.24 In this office building in Gouda (NL), the 6.2 kWp PV system is mounted on top of the façade as a canopy that protects the wall. The architect’s intention was to show the PV system to his clients when they visit the office. Reproduced with permission by BEAR Architecten T. Reijenga

22.2.6 Brundtland Centre, Toftlund (DK) – a Case Study

The Brundtland Centre in Toftlund opened in 1995, was developed as an education and demonstration center for Denmark [31]. It is part of the “Brundtlandby Project”, which designated certain towns, such as Toftlund, to put into practice the goals of low energy consumption and environmental impact, as proposed by the Brundtland Report. The Brundtland Centre was built to exhibit and employ the concept of energy-efficient building strategies combined with well-implemented architectural design. Throughout the



Figure 22.25 The dwellings at the 5 MW project in the HAL district of Langedijk (NL) have a large PV roof without any perforations. This strengthens the architectural expression of the roof design. Each roof includes a 5.1 kWp BP Solarex PV system. Reproduced with permission by BEAR Architecten M. van Kerckhoven



Figure 22.26 The canteen at the IMEC in Leuven (B) has an entrance with attractive-looking transparent modules in the roof. Reproduced with permission by IMEC

design process, priority was given to strategies that could be achieved through the design of the building itself – its form, orientation and envelope design – rather than “high-tech” strategies. Where the use of “active systems” was necessary, the design team aimed to develop more energy-efficient ways of operating these technologies.

Early consideration of PV within the design process has resulted in an aesthetically and energetically well-integrated PV system within the architectural design (Figure 22.29). Two types of PV systems are used in the building envelope. A PV array is integrated

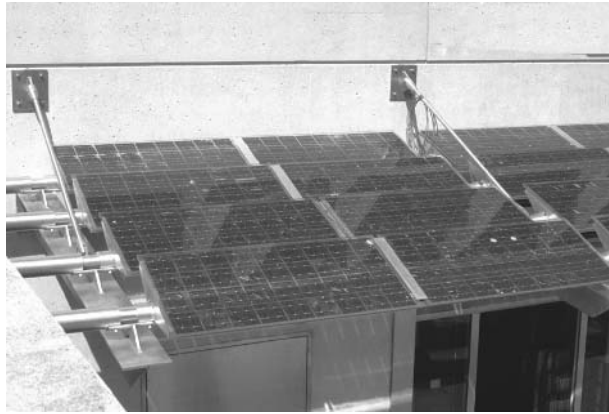


Figure 22.27 This shopping mall in Lausanne (CH), includes a louver system with transparent modules mounted above the shop windows, which results in less reflection of sunlight in the windows, making it easier to look into the shops. Reproduced with permission by BEAR Architecten T. Reijenga



Figure 22.28 This zero-energy project in Etten-Leur (NL) combines different sustainable energy techniques. Each house has a roof structure with 6.2 kWp BP Solar PV modules. The aesthetic integration of the PV system is a completely new concept in housing. Reproduced from Reijenga T, “Energy-Efficient And Zero-Energy Building in the Netherlands”, *Proc. International Workshop on Energy Efficiency in Buildings in China for the 21st Century*, CBEEA (Beijing, December 2000) with permission by BEAR Architecten M. van de Laan [30]

into the roof of the atrium – a central space connecting the adjacent two-storey building sections. Other PV modules are mounted on the southeast façade of the office section (Figure 2.30).

The atrium roof, incorporating the transparent PV modules, stretches out above the entrance of the building, creating a large canopy. Thus, the PV system mounted on the atrium roof is visible from the inside of the atrium as well as from the outside of the building. Mounting the PV system on the roof had a great impact on the architectural expression, the building layout and internal atmosphere of the center (Figure 22.31).



Figure 22.29 Overview of the Brundtland Centre in Toftlund (DK). The glass roof on top of the atrium in the middle of the building has a saw-tooth roof with integrated 9.8 kWp transparent PV modules. Reproduced with permission by BEAR Architecten T. Reijenga



Figure 22.30 PV modules above the windows on the southeast facade. A total of 6 kWp is integrated in the facade. Reproduced with permission by BEAR Architecten T. Reijenga

To achieve the optimum orientation and tilt angle of the PV array (south/ 60°), the atrium roof has been constructed in a saw-tooth shape that runs diagonally across the space. The steel truss roof, combined with the alternating pattern of dark round cells against transparent glazing, gives the atrium a high-tech atmosphere. Special attention has been paid to provide soft diffused quality of daylight in the interior of the atrium. A thin diffusing glass fabric is integrated into the modules so that sharp edges from the circular solar cells are softened.

In energy terms, the integrated PV system in the atrium roof was designed not only to produce electricity but also to provide shading to prevent the atrium from overheating. The transparent modules allow 20% of the available daylight to enter the atrium. The concrete floors and facades accumulate the heat surplus during the day. At night, the atrium is cooled by natural ventilation, while the mechanically assisted ventilation is used to ventilate the adjacent rooms. Automatic controls stop the ventilation when a sufficiently low temperature has been reached.



Figure 22.31 Atrium roof of the Brundtland Centre building from the inside. Because the saw-tooth roof casts a shadow on the modules, some of the cells are fake. This solution achieves a more elegant look from the inside. Reproduced with permission by BEAR Architekten T. Reijenga

22.3 BIPV BASICS

22.3.1 Categories and Type of Buildings

Building-integrated PV systems can be divided into different categories according to

1. cell and module type,
2. architectural integration,
3. type of building,
4. mounting technology, and
5. the function of the integration, and possible additional building and architectural functions of the PV system.

It is important that architects know all these categories and their possibilities. The design process consists of translating the brief (program made by the client) into spaces and enclosures, as well as combining functions and materials into constructions. This process is mainly based on experience and knowledge of constructions and materials. New applications based on existing knowledge or techniques are very important in the creative process. New inventions play a minor role in the process.

22.3.1.1 Categories of cells and modules

There is a wide range of cells and modules in the market. There are various types of cell material, types of modules, framed or nonframed laminates, colors of the cells and colors of back sheets and frames; all provide a wide range of possible surfaces [32]. This is a very basic knowledge for architects. Architects will design BIPV systems with a certain image in mind. The choice of monocrystalline or polycrystalline cells will depend on color and not on efficiency [33].

22.3.1.2 Categories of integration

BIPV systems in projects can be divided according to the location of the application: roof systems, facade systems, glass construction (conservatory/atrium) systems and building components such as shading and canopy systems. The main mounting locations are the roof and the façade. There are also many creative solutions available in designing how PV systems can be integrated. All these solutions are grouped as building components.

22.3.1.3 Types of buildings

Different buildings obviously have very different functions, for example, apartments and family houses, public buildings, commercial and industrial buildings and nonoccupied building structures. These can either be newly constructed or renovated buildings [34]. Nonoccupied building structures include shelters (bus stops, canopies, parking structures), kiosks (newsstands, gazebos, pavilions, phone booths), public toilet buildings, car parks, streetlights, parking meters, screens and barriers (fences, noise barriers), road signs and commercial billboards.

All types of building or nonoccupied building structures are a potential location for BIPV systems.

The various commercially available mounting applications can be grouped into 10 types, and can be found on the on-line PV database (www.pvdatabase.com).

Location on a building:	Building component(s):	Manufacturers such as:
Sloped roof	Tiles and shingles	LaFarge Braas (Figure 22.12), Atlantis Sunslates [35] (Figure 22.15), Japanese tiles (Figure 22.32), UnisolarStanding Seam panels [36] (Figure 22.20).
	Nonintegrated profiles	BP Sunflower (Figure 22.33), Econergy InterSole [37], Alutec profiles (Figure 22.34)
	Integrated profiles	BOAL/Shell Solar profile system (Figure 22.3), Solrif Solar profile system [38] (Figure 22.35)
Flat roof	Roofing element	Powerlight Powerguard® (Figure 22.8), Alwitra Evalon® roofing foil (Figure 22.36)
	Integrated profiles	Schüco profile system (Figure 22.37)
	Independent support structure	Econergy ConSole [39] (Figure 22.19), Solgreen (Figure 22.38), Sofrel [40] (Figure 22.17), Sobac [41]
Facade	Integrated profiles	Schüco façade profile system (Figure 22.39)
	Cladding system	BP Solface [42] system (Figure 22.40)
	Louvers or sun blinds	ADO louver system (Figure 22.41), Colt Shadovoltaic louver system (Figure 22.9)
	Canopy	Donjon canopy system (Figure 22.42)



Figure 22.32 Prefabricated Japanese tilelike roof panel method with CdTe cells in Nie-ken (JA). Capacity of the system is 1.3 kWp. Reproduced with permission by MSK Corporation

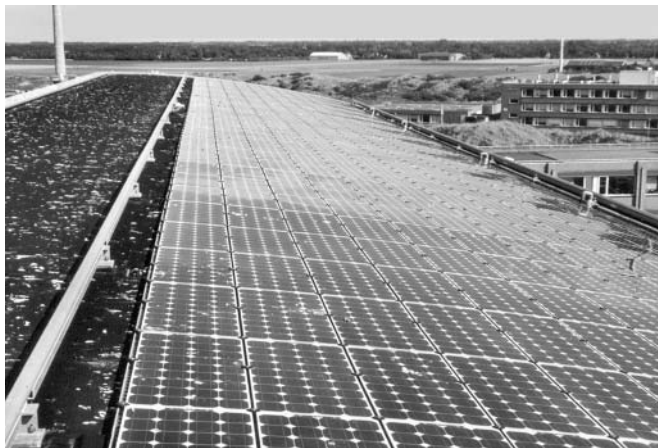


Figure 22.33 BP Sunflower system at the bent roof at ECN building 31, Petten (NL). Capacity 35 kWp. Reproduced with permission by BEAR Architecten H. Lieverse

22.3.1.4 *Function of the integration*

In addition to generating electricity, PV modules are also used as an integral part of the external skin (roof or façade), as sun protection (Figure 22.43) or as a daylight transmitter. Designing double functions and then integrating PV modules into buildings results in cost reductions on the investment in the building. Several buildings have been built that demonstrate PV systems as part of a passive cooling strategy [14].

The advantages in this specific case are

- the PV modules replace building elements,
- the PV modules are very well ventilated at the back,



Figure 22.34 Alutec profile system in a new roof in Langedijk HAL (NL). Capacity of the system is 53 kWp and the project is part of the 5 MW BIPV project. Reproduced with permission by BEAR Architecten M. van Kerckhoven

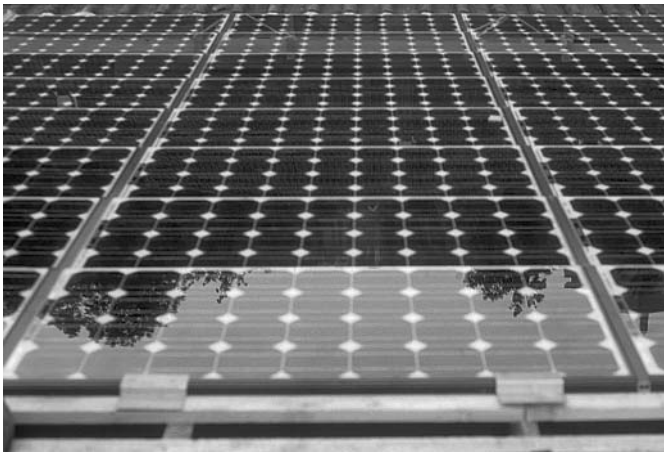


Figure 22.35 Solrif Solar profile system in a roof renovation in Zürich (CH). Capacity of the system is 53 kWp. Reproduced with permission by BEAR Architecten T. Reijenga

- a separate mounting construction is not necessary, and
- the air-conditioning system is eliminated.

22.3.2 Cells and Modules

The PV modules and mounting system are the elements of a PV system that can determine the image of a building. A PV system, particularly the cell material, framing materials, soldering, shape of the modules and the color of cells and back sheets, all influence the image of a building. For architects and designers, these aspects are more important than



Figure 22.36 Alwitra Evalon® roofing foil with amorphous silicon cells. Reproduced with permission by O.Ö. Energiesparverband

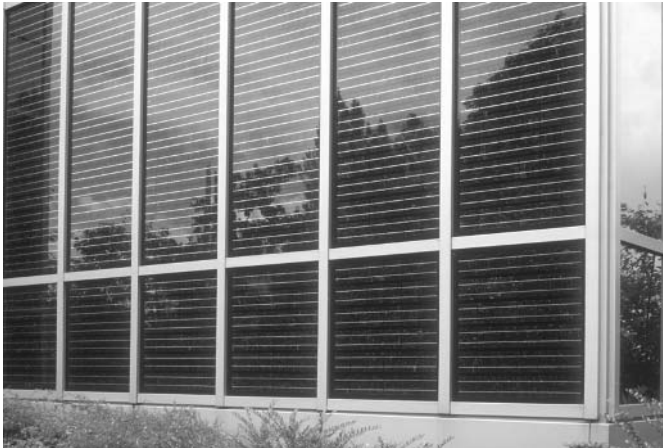


Figure 22.37 Schüco 1.9 kWp roof profile system with transparent modules in the Energy Forum Center in Bad Oeyenhausen (D). This mounting system can also be used in (difficult) horizontal situations. Reproduced with permission by BEAR Architekten T. Reijenga

the electrical efficiency of a system. Typical efficiencies of today's commercially available solar modules are shown in Table 22.1.

22.3.2.1 Solar cell materials

There are several types of solar cell materials: monocrystalline (single crystal) silicon, polycrystalline silicon (both discussed in Chapters 6 and 7), amorphous silicon (Chapter 12), copper indium gallium diselenide (CuInGaSe_2) (Chapter 13), and cadmium

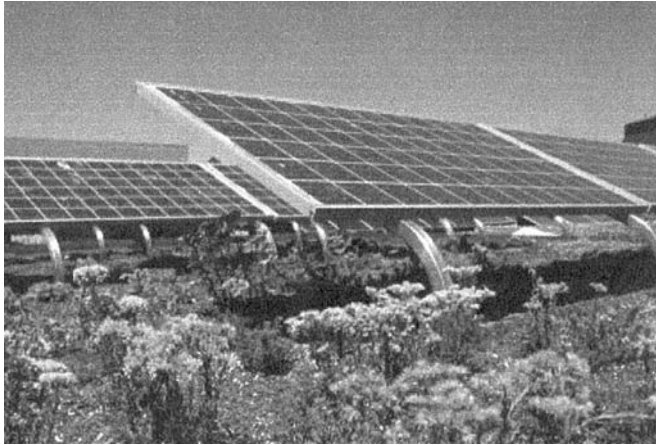


Figure 22.38 Solgreen flat-roof system for green roofs demonstrated on a roof in Switzerland. Reproduced with permission by SOLSTIS



Figure 22.39 Schüco façade profile system in the Doxford building (UK). See also caption at Figures 22.4 and 22.18. Reproduced with permission by BEAR Architecten T. Reijenga

telluride (CdTe) (Chapter 14). Their characteristics that affect their implementation in BIPV applications are briefly presented here.

Monocrystalline Si cells are initially grown as long cylinders, then sliced into thin discs called wafers ($\sim 300 \mu\text{m}$ thick). Initially round, the wafers often have their edges cut to create a nearly square wafer with slightly rounded corners. This increases their packing density on the module. Typical wafers are presently 10×10 or $12.5 \times 12.5 \text{ cm}^2$ but will be increasing as technology develops. Monocrystalline cells have a very uniform appearance. Their color can be varied (see below) but are typically either dark blue or black since this gives the highest efficiency. (The color of the cell is determined by



Figure 22.40 BP Solface vertical wall system at the Demosite in Lausanne (CH). Reproduced with permission by EPFL-LESO-PB



Figure 22.41 ADO louver system with integrated transparent PV modules at an apartment building in Amersfoort Nieuwland (NL). The automatic louvers can switch in two positions. The horizontal position at night (left on the figure) and tilted to the sun by day (right on the figure). Reproduced with permission by BEAR Architecten T. Reijenga

the wavelengths that are reflected. The darker the cell looks, the less light that is being reflected. Therefore darker means more absorption of sunlight by the solar cell.)

Polycrystalline silicon wafers are manufactured with a lower cost process than monocrystalline silicon wafers. They are cast in long square ingots. After slicing, polycrystalline wafers are already in the desired square shape. Compared to monocrystalline cells, polycrystalline cells also typically have a bluish color and are the same size, but are slightly less efficient and slightly of lower cost. The main difference between mono and poly wafers as might affect their application for BIPV is their visual



Figure 22.42 Canopy at the eaves of a roof. 6.2 kWp PV system at an office building in Gouda (NL). Reproduced with permission by BEAR Architecten T. Reijenga



Figure 22.43 This building, at ECN in Petten (NL) has a 43 kWp PV system integrated into the conservatory roof. The conservatory acts as a parasol in front of the offices, thus eliminating the need for air-conditioning in a moderate climate. The building on the right side has a PV shading system (see caption on Figure 22.11). Reproduced with permission by BEAR Architecten T. Reijenga

appearance: monocrystalline cells are uniform while polycrystalline cells have hundreds of reflective facets, of sizes 0.1–1 cm. Each facet is a separate small crystalline region. Both mono and poly cells have metal grids on the front in a rectangular pattern to collect the electricity and to connect to the next cell. These grids are typically not visible from beyond a few meters away.

Amorphous silicon cells (a-Si) are composed of silicon atoms that are in a thin ($\sim 1 \mu\text{m}$) layer and lack crystalline properties. They are commonly referred to as thin film Si PV technology. Amorphous silicon cells are deposited onto substrates like glass window

Table 22.1 Typical efficiencies for modules. These values are obtained under standard test conditions. Different orientation in BIPV applications may result in lower performance

Cell type	Typical efficiencies [%]
Monocrystalline silicon	12–15
Multicrystalline silicon	11–14
Amorphous silicon	6–8
Cadmium telluride	7–10
Copper indium gallium diselenide	8–12

plates or flexible rolls of stainless steel or plastic, giving a wide range of mechanical strength, weight, and flexibility. The substrate is not visible since it is behind the solar cell. The cells have a uniform typically black appearance. These cells have no grids. Flexible substrates are ideal for curved surfaces and rollable “fold-away” modules. Amorphous silicon modules have lower efficiency than mono or poly silicon (Table 22.1) but better performance at higher temperatures [43, Chapter 12] as often occurs in BIPV applications.

Other thin film PV materials presently include CuInGaSe_2 and CdTe . They have a uniform nearly black appearance, indistinguishable visually from amorphous Si modules. They also have lower efficiency compared to mono or poly silicon. CuInGaSe_2 cells can be deposited on flexible plastic or metal foils.

Semitransparent cells for BIPV can be manufactured in two ways. Mono silicon wafers can have a series of deep grooves on the front and back which are perpendicular to one another. Where they intersect, light will be transmitted through the holes. Polycrystalline silicon cells with 2% transmission have been reported [44] but higher values should be possible with larger holes. Another approach is to make very thin amorphous silicon layers on glass with transparent contacts so the entire module is semitransparent. However, the transmitted light will have an orange or red tint because the blue and green portion of the spectrum is absorbed in the silicon layers. Such modules could only be used in applications where this color of light was acceptable such as sun-roofs for automobiles. A better method is to selectively remove part of the amorphous silicon layer using laser ablation. Unfiltered white light transmission of 5–15% have been reported for laser scribed amorphous silicon in BIPV applications [43].

22.3.2.2 Module temperature

Module efficiency, therefore electricity produced, decreases as the temperature increases for mono and poly silicon cells but not for amorphous silicon cells. In many non-BIPV applications, modules are mounted on free-standing frames with ambient air on both sides, allowing for cooling on both sides. In contrast, some BIPV applications install the modules in close contact to building material like roofs or wall insulation. The lack of circulating air increases the module temperature. Relative losses of >5% are possible [45]. A good design criterion for mono or poly silicon applications is to allow as much

cooling as possible by providing for air flow behind the module and minimizing effect of insulation. This is not an issue for amorphous silicon modules [45].

22.3.2.3 *Color of the cells and modules*

Solar cells are basically blue, dark blue or black after processing. Different colors are possible but these are not manufactured as standard. Some manufacturers sell tailor-made cells in special colors (e.g. gold, gray, green, red-orange and yellow). The cell color is varied by changing the thickness of various optical coatings on top of the cell, which changes their reflection. The blue color produces the highest efficiency solar cells. Current literature gives efficiencies for colored cells as 11.8% and 14.5% compared to optimized cell efficiency of 16.8% [46, 47], which corresponds to around 75% of the power of dark-blue cells [48].

Modules have several sections that can be colored. Besides the cells, the frame and the back sheet will also have a certain color. Older modules had natural aluminum frames and a white back sheet. The shape of the cell was very pronounced because of the contrasting color. However, modern modules have colors that are more in harmony: dark-blue cells with a dark back Tedlar® sheet and a dark-colored frame around the module, which produces a very uniform image. A roof or façade containing these uniform-colored modules will be seen as a single surface. The opposite effect is also possible by using modules in striking colors to attract attention and focus on the PV system.

22.3.2.4 *The architecture of modules*

Architects select modules based on their shape and composition possibilities. There is a big visual difference between framed and frameless modules.

Frameless modules look very similar to window glass. A surface with frameless modules with a “hidden” mounting system looks very uniform. The seams seem to be hidden and the individual module is hard to recognize. This smooth surface has a high aesthetic value.

Framed modules give a totally different effect. The frames can be heavy and therefore determine the total impression of the surface. The very visible frames divide the surface into modules and every individual module is very recognizable. This is not always the image envisaged by the architect.

To solve this problem, smaller frames in the same (dark or blue) color as the cells can be used and are less visible. The soldering between the cells is a small detail but is an important part of the image for very visible PV systems. In the older techniques the soldering was very visible and not very smooth. However, new techniques mean that the soldering is hidden better and new types of soldering, for example, ECN cells, can be expected in the future.

Modules vary significantly in size. Standard modules are less expensive than applications using tailor-made modules. However, almost every form, shape and dimension is possible with tailor-made modules. The glazing is available as single and double (insulating) glass. Thin-film modules allow greater freedom to select size and color than c-Si modules.

22.4 STEPS IN THE DESIGN PROCESS WITH PV

22.4.1 Urban Aspects

The aim of integrating PV systems into buildings is to reduce costs. To generate maximum power from building-integrated systems, certain urban and architectural aspects are important.

The main starting point is the maximum power that can be generated by a system. The primary hindrances can be the (partly) shadowing of a system by other buildings or objects, and the nonoptimum orientation relative to the sun. Reflection can also be a problem for the surrounding buildings.

22.4.1.1 Orientation and angle

The amount of irradiance depends on the latitude. The maximum irradiance corresponds to surfaces, tilted at an angle equal to about the latitude minus 10° (see Chapter 20 for calculations on solar irradiance). At 52° north good results ($>90\%$) can be achieved by orienting the modules between southeast and southwest, with system angles between 30° and 50° from the horizontal. Orientations between east and southeast, and between southwest and west, are fairly reasonable with system angles between 10° and 30° from horizontal. The irradiance will be reduced by around 15% of the maximum.

Flat-roof systems with very low angles (between 5° and 10°) can be a good solution for difficult orientations. The loss of irradiance will be between 5% (south) and 20% (north).

22.4.1.2 Distance between buildings

Shadowing is a critical issue for BIPV. In general, designs in which the PV modules are shaded for much of the year should be avoided. For low-rise areas, the problem is easy to solve. The distance between individual houses can be calculated. For mixed height neighborhoods, it will be more difficult. A high-rise apartment building in a low-rise neighborhood can cause a lot of unwanted shading.

The density of an area also has a lot of influence. In high-density areas (cities) the distances between buildings are often so small that there is significant shadowing throughout a large part of the year.

On a general note, it is worth mentioning that facade systems (vertical) are more sensitive to shading and need longer distances from other buildings than tilted systems (roofs). Horizontal systems have a lower irradiance, as previously mentioned, but will be the best solutions for avoiding shadow. Only neighborhoods with a mixture of low- and high-rise buildings might be unsuitable for horizontal systems.

22.4.1.3 Trees

Greening the area around buildings makes the area look very attractive and the microclimate more comfortable for the inhabitants.

The shadowing effect of trees is very important, as the trees will be very dense during the summer. Even during the winter, when trees lose their leaves, the branches give too much shade.

The aspect of growth is sometimes underestimated. Planning for the future growth of trees is very important and must be done carefully to avoid problems a few years after the building has been completed or the PV system has been installed.

Solutions can be to

- only plant trees on the north side of buildings,
- plant only small trees up to two stories high,
- prune trees annually to keep them small.

22.4.1.4 Zoning

In future, a special solar zoning will be needed in urban areas with PV systems. The borders of building areas can be clearly marked on three-dimensional maps to prevent future problems. The amount of sunlight can also be determined on these maps.

22.4.1.5 Reflection

Although not a major problem, under certain circumstances, reflection can occur. In low-rise buildings, there are no significant problems, but in mixed low- and high-rise areas residents in high-rise buildings may experience some annoying reflections if all the surrounding houses have (glass-covered) PV modules. The fact that there are certain distances between buildings (for shadowing) may eliminate most of the potential problems.

22.4.2 Practical Rules for Integration

There are a few important rules for integrating modules into buildings. These rules concern the functioning and maintenance of the system, for example:

1. shadow is not allowed on the module,
 2. ventilation is required at the back of the modules (not as important for thin film a-Si),
 3. make it easy to mount and remove a module,
 4. ensure that the module stays clean or can be cleaned,
 5. make easy electrical connections,
 6. ensure that wiring is sun-proof and weather-proof.
1. As previously mentioned, even partial shadow on the modules will decrease the energy output. Profiled mounting constructions, in particular like awnings, can produce shadows along the edge of the adjacent module that will result in loss of efficiency.
 2. Modules with crystalline cells have a higher output when the temperature is lower. With ventilation at the back of the module it is possible to keep the temperature low

and avoid a decreasing output. However, thin-film amorphous silicon reacts differently. The higher temperature does not influence the efficiency as much as crystalline silicon.³

3. Although the lifetime of modules is proven to be over 20 years, it is better to know how to remove a single module in the middle without removing the whole system. Electrical connections should also be “plug and play”.⁴ Easy electrical connections are needed for fast installation and for easy replacement of modules. Depending on the local safety regulations, precautionary measures should be taken, for example, using lifelines or moveable safety ladders.
4. The surface of the modules should be clean. Tilted modules will be cleaned by rain in most regions. Modules mounted at low angles can be treated with PV-Guard, a treatment that makes the surface smooth and makes cleaning with rain easier. In dry areas, cleaning should be part of the regular maintenance schedule.
5. Protect wiring against the weather. Rain is not the main problem, though all connections must be waterproof. Long-term influence from water should be avoided. Protection against sun and UV light is needed to ensure that the lifespan of the wiring is not reduced. Depending on the area, wiring may also need to be protected from small gnawing animals.

22.4.3 Step-by-step Design

A PV system consists of a number of modules with solar cells, an inverter, batteries or, in most cases, a connection to the grid. A single house with a small installation can be connected through the existing electricity meter. The electricity that is produced will be used primarily in the house. Any surplus will be fed into the grid and the meter will spin backwards. However, not every utility company will allow this and in some cases a second meter is installed. This often happens with larger systems (more than 2 or 3 kWp). Larger systems or combined systems that are maintained by the utilities are connected directly to the grid.

22.4.3.1 Solar design

To design with photovoltaics the first set of questions are, “Why do I want to integrate PV into the building?” and “Is it for general energy supply, to make the building more independent, or to make a statement about the building’s inhabitants?”

Large systems will be used for general energy supply. This means large surfaces that can be treated in an architectural way. Different types of modules, shapes, colors or textures can be used to design the look of the building.

The main issues for a more independent building are the efficiency of the system and the generated yearly output. The size of the PV system will depend on this and the designer has to allow for a certain number of modules. The designer will probably design

³ See Chapter 12.

⁴ “Plug and play” refers to very simple wiring and components that fit together like a computer and can easily be replaced.

the building around the integrated system, otherwise the system will be something that is connected, but not integrated, into the building.

22.4.3.2 Module placement and shadowing

The first step in the design process will be to look at the number of modules, their dimensions and the total dimensions of the system. All these aspects have to be integrated into the roof or facade. Shadowing of the modules is important. A module that is partly shaded will lose more efficiency than expected. If one row of cells in a module is covered or heavily shaded, this can block the output of the entire string.

Small objects that can cause shading, such as chimneys and fans, are less important. The shadow will move during the day and there maybe indirect light available. Some modules have integrated diodes that allow a short break when a row of cells is covered or shaded.

22.4.3.3 Space required for balance of systems and interconnections

Space is also required for the inverters. The modules have junction boxes at the back that are connected by cables to the inverters. For better efficiency, the best place for these inverters is near the modules. An AC cable has to be fed from the inverters into the grid via the meter.

Space is also required for a junction box at the back. Together with the ventilation required at the back of the module, this means a gap between 20- and 50-mm (depending on the size of the junction box) between the back of the module and the mounting surface that can be used for both functions.

Space for a second utility meter may be required near the first meter, unless a double meter can be used. Safety switches are required near the inverters in order to work on the PV system safely.

22.4.4 Design Process: Strategic Planning

A few procedural steps may be necessary to ensure that the PV system is successfully integrated into the design. A common rule is to integrate the PV system into the building process without disturbing that process.

Step 1: The first step is consultation with the authorities about local regulations, building permits and the electrical connection to the grid.

Step 2: The second step is to consult the utility company about the grid connection, electrical diagrams and the metering system.

Step 3: The third step is the internal meeting with all building partners. A kick-off meeting very early in the process may be useful, to discuss the entire integrated PV system with the building contractor, the roofing company, the electrician and the PV supplier.

There are many unique issues to resolve in installing BIPV. The main points in this meeting concern the responsibilities of each party in the building process. Who is

responsible for the waterproofing of the roof – the roofing company or the PV installer? Who is responsible for electrical safety – the electrician or the PV installer? Who is responsible for safety on the site – the general contractor or the PV installer? All these aspects must be clearly defined and noted in advance.

Many PV suppliers offer turnkey contracts. This is easy for clients because they receive a complete working system for their money. However, the client is then responsible for the coordination between PV supplier and building contractor. Placing all responsibility with the building contractor means an extra surcharge of perhaps 10% on the cost of the PV system. A good solution is to make the building contractor (general contractor) responsible for the PV system and negotiate a special fee for coordination and use of equipment (scaffolds and crane) from the building contractor.

22.5 CONCLUSIONS

Building integration aims to reduce costs and minimize the requirement for land. To increase market acceptance it is important to show architecturally elegant, well-integrated systems. Moreover, building owners can show their environmental commitment with highly visible building-integrated PV systems.

This means that there is a large potential for BIPV in the built environment. The main factors for successful integration are suitable buildings [49], (i.e. suitable orientation and lack of shadow) and a reason for building integration. For newly constructed sustainable buildings, BIPV will be part of the energy strategy. However, for existing buildings there must be a valid reason for integrating PV systems. Building renovation, including the roof and façade, often provides an opportune time for selecting BIPV [50, 51].

The building or renovation process plays an important role in the success of BIPV. Can the building owner benefit from BIPV? If so, the owner will be willing to implement PV systems in the building plans. The architect or designer needs to have a good basic knowledge of BIPV and be able to integrate PV into the design. If architects do not understand the basics of PV, they will make mistakes that eventually have to be resolved during the installation process. The worst cases involve mistakes that cannot be resolved at the end of the building process and that result in a lower efficiency and quality of the PV system.

Is the utility company willing to cooperate? If not, the building owner will probably try to avoid difficulties in an already complex construction process.

The architect or designer should use all visible opportunities to integrate PV into the design in a highly aesthetic way. The important issues are the architectural function of a PV module (replacing other building elements) and the visible aspects of modules, such as the dimensions, mounting system, form and color of cells, back sheet and frames.

To recognize these aspects, criteria have been formulated for judging building integration of PV. These criteria are useful for manufacturers and technicians who are involved with building integration from the engineering and technical aspects of the building process.

REFERENCES

1. Reijenga T, "The Changing Cities of Europe", *Proc. Sustain '99* (Amsterdam, 1999).
2. EC DG XVII, "White Paper for a Community Strategy and Action Plan; Energy for the Future: Renewable Sources of Energy", *Proc. Sustain '99* (Amsterdam, 1999).
3. Schoen T *et al.*, *Proc. 14th Euro. Conf. Photovoltaic Solar Energy Conversion*, 359–364 (1997).
4. Kurokawa K, Kato K, Paletta F, Iliceto A, *Proc. 2nd WC Photovoltaic Solar Energy Conversion*, 2853–2855 (1998).
5. Thomas R, Grainger T, Gething B, Keys M, *Photovoltaics in Buildings – A Design Guide*, Report S/P2/00282/REP, ETSU, DTI, London (1999).
6. Strong S, Lloyd Jones D, *A Renewable Future*, IEA PVPS Task7, Final Task (Feb. 2001).
7. Kiss G, *Proc. 2nd WC Photovoltaic Solar Energy Conversion*, 2452–2455 (1998).
8. Muller A, Roecker C, Bonvin J, *Proc. 14th Euro. Conf. Photovoltaic Solar Energy Conversion*, 889–892 (1997).
9. Reijenga T, *Prog. Photovolt.* **4**, 279–294 (1996).
10. Maycock P *et al.*, *Building with Photovoltaics*, 78–81, Ten Hagen & Stam, Den Haag (1995).
11. Reijenga T, Böttger W, *Proc. 2nd WC Photovoltaic Solar Energy Conversion*, 2748–2751 (1998).
12. Lloyd Jones D, Matson C, Pearsall N, *Proc. 2nd WC Photovoltaic Solar Energy Conversion*, 2559–2562 (1998).
13. Wilk H, *OKA-House of the Future*, IEA SHCP Task 19 (1997).
14. Reijenga T, Kaan H, *Proc. 16th Euro. Conf. Photovoltaic Solar Energy Conversion*, 1952–1959 (2000).
15. Hynes K, Pearsall N, Shaw M, Crick F, *Proc. 13th Euro. Conf. Photovoltaic Solar Energy Conversion*, 2203–2205 (1995).
16. Hagemann I, Leppänen J, *Proc. 14th Euro. Conf. Photovoltaic Solar Energy Conversion*, 694–697 (1997).
17. Eiffert P, Kiss G, *Building-Integrated Photovoltaic Designs for Commercial and Institutional Structures – A Sourcebook for Architects*, 7–10, NREL, Golden, CO (2000).
18. Eiffert P, Kiss G, *Building-Integrated Photovoltaic Designs for Commercial and Institutional Structures – A Sourcebook for Architects*, 42–44, NREL, Golden, CO (2000).
19. Pitts A, Tregenza P, Coutts R, *Proc. 16th Euro. Conf. Photovoltaic Solar Energy Conversion*, 1902–1905 (2000).
20. Kaan H, Reijenga T, *Proc. 2nd EuroSun*, V3.2-1–V3.2-6 (1998).
21. Reijenga T, Kaan H, *Proc. 2nd WC Photovoltaic Solar Energy Conversion*, 2740–2743 (1998).
22. Reijenga T, Schoen T, *Proc. 2nd WC Photovoltaic Solar Energy Conversion*, 2744–2745 (1998).
23. Schoen T *et al.*, *Proc. 16th Euro. Conf. Photovoltaic Solar Energy Conversion*, 1840–1843 (2000).
24. Reijenga T, "Photovoltaic Building Integration Concepts – What do Architects need?" *Proc. IEA PVPS Task7 Workshop Lausanne Featuring A Review of PV Products*, IEA PVPS Task7, Halcrow Gilbert, Swindon (2000).
25. Reijenga T, "Photovoltaics in the Built Environment", *Proc. 2nd World Solar Electric Buildings Conference*. ESAA, ANZSES (Sydney, 2000).
26. Cace J, *Proc. 14th Euro. Conf. Photovoltaic Solar Energy Conversion*, 698–700 (1997).
27. Vlek F, Schoen T, Iliceto A, *Proc. 16th Euro. Conf. Photovoltaic Solar Energy Conversion*, 1783–1786 (2000).
28. Reijenga T, *Proc. 16th Euro. Conf. Photovoltaic Solar Energy Conversion*, 1793–1796 (2000).
29. Eiffert P, Kiss G, *Building-Integrated Photovoltaic Designs for Commercial and Institutional Structures – A Sourcebook for Architects*, 48, 49, NREL, Golden, CO (2000).
30. Reijenga T, "Energy-Efficient And Zero-Energy Building in the Netherlands", *Proc. International Workshop on Energy Efficiency in Buildings in China for the 21st Century*, CBEEA (Beijing, December 2000).

31. Reijenga T, Tuyl L, Schneider A, de Vries G, *Smart Architecture for a Sustainable Future*, IEA-EUREC, Brussels (2000).
32. Ito T, Ishikawa N, Nii T, *Proc. 14th Euro. Conf. Photovoltaic Solar Energy Conversion*, 690–693 (1997).
33. Butson J *et al.*, *Proc. 2nd WC Photovoltaic Solar Energy Conversion*, 2571–2574 (1998).
34. Kaan H, Reijenga T, *Proc. ACEEE*, 5.025–5.014 (1998).
35. Posnansky M, Szacsvey T, Dütsch B, Stucki B, *Proc. 14th Euro. Conf. Photovoltaic Solar Energy Conversion*, 1922–1924 (1997).
36. Nath P *et al.*, *Proc. 2nd WC Photovoltaic Solar Energy Conversion*, 2538–2541 (1998).
37. Scheijgrond P *et al.*, *Proc. 16th Euro. Conf. Photovoltaic Solar Energy Conversion*, 2049, 2050 (2000).
38. Toggweiler P, Ruoss D, Brügger U, Haller A, *16th Euro. Conf. Photovoltaic Solar Energy Conversion*, 1972–1975 (2000).
39. Böttger W, Schalkwijk M, Schoen A, Weiden T, *Proc. 14th Euro. Conf. Photovoltaic Solar Energy Conversion*, 2288–2291 (1997).
40. Roecker C, Bonvin J, Toggweiler P, Ruoss D, *Proc. 14th Euro. Conf. Photovoltaic Solar Energy Conversion*, 701–704 (1997).
41. Bonvin J, Roecker C, Affolter P, Muller A, *Proc. 14th Euro. Conf. Photovoltaic Solar Energy Conversion*, 1849, 1850 (1997).
42. Schnaller F, Roecker C, *Proc. 16th Euro. Conf. Photovoltaic Solar Energy Conversion*, 1945–1947 (2000).
43. Arya R, Carlson D, *Prog. Photovoltaics* **10**, 69–76 (2002).
44. Willeke G, Fath P, *Appl. Physics Lett.* **64**, 1274–1276 (1994).
45. Hunter-Fanney A, Dougherty B, Davis M, *J. Solar Energy Engineering*.
46. Mason N, Bruton T, *Proc. 13th Euro. Conf. Photovoltaic Solar Energy Conversion*, 2218, 2219 (1995).
47. Ishikawa N *et al.*, *Proc. 2nd WC Photovoltaic Solar Energy Conversion*, 2501–2506 (1998).
48. Tölle R *et al.*, *Proc. 16th Euro. Conf. Photovoltaic Solar Energy Conversion*, 1957–1959 (2000).
49. Frantzis L, Ghosh A, Rogers M, Kern E, *Proc. 2nd WC Photovoltaic Solar Energy Conversion*, 2799–2801 (1998).
50. Gutchner M, Nowak S, *Proc. 2nd WC Photovoltaic Solar Energy Conversion*, 2682–2685 (1998).
51. Reijenga T, Drok M, Oldegarm J, Kampen J van, *PV Systems and Renovation*, TNO, NOVEM, Delft (2001).

Further Reading

- Humm O, Toggweiler P, *Photovoltaics in Architecture*, Birkhäuser, Basel (1993).
- Lloyd Jones D, Hattersley L, Ager R, Koyama A, *Photovoltaics in Buildings – BIPV Projects*, ETSU, DTI, London (2000).
- Muller A, Roecker C, Bonvin J, *Proc. 14th Euro. Conf. Photovoltaic Solar Energy Conversion*, 889–892 (1997).
- Schoen T, Prasad D, Toggweiler P, Eiffert P, *Proc. 2nd WC Photovoltaic Solar Energy Conversion*, 2447–2451 (1998).
- Strong S, *Photovoltaics in the Built Environment – A Design Guide for Architects and Engineers*, DOE/GO-10097-436, NREL, Golden, CO (1997).
- Photovoltaics in the Built Environment (Special Issue) *Prog. Photovoltaics* **4**(4), 237–320 (1996).

Internet

- www.pyportal.com
www.task7.org
www.pvdatabase.com
www.demosite.ch
www.lafarge.com

23

Photovoltaics and Development

Jorge M. Huacuz¹ and Lalith Gunaratne²

¹*Instituto de Investigaciones Eléctricas, Cuernavaca, México,*

²*Solar Power & Light Co, Ltd, Colombo, Sri Lanka*

23.1 ELECTRICITY AND DEVELOPMENT

23.1.1 Energy and the Early Man

Survival has always been the main preoccupation of mankind. For many thousands of years, food, shelter and protection against harsh weather and wild animals were the primary requirements of early man. In the early days of humanity, people spent most of their time hunting and gathering, and hence, energy cycles in primitive societies were extremely simple: human energy was put into the pursuit of game and the manufacture of tools and weapons; wood collection to keep the fire burning for cooking while at the same time providing warmth and lighting was also an important activity. Food from the hunt was the basic fuel for human energy and the leftover animal grease also contributed to heat and light the shelter to maintain a suitable microclimate.

Over the years, early man incorporated new options to fulfill the basic requirements of survival, and at the same time altered the energy cycles of primitive society. Gardening was added to fishing and hunting as a source of food. Additional human energy had to be put into planting, weeding and harvesting. Products from gardening provided a more predictable source of food energy for humans and the basic feedstock for raising domestic animals, which in turn became the source of high quality protein and eventually an additional source of power. Gardening evolved into agriculture, which, along with animal husbandry, eventually displaced hunting as the main activity for survival. At some point in time, domesticated animals were incorporated to take away from humans the burden of load-pulling and back-carrying.

A time came when technology was developed to simplify everyday productive activities. Along with the dawn of progress came larger and larger requirements for

energy. It is estimated that early man had a daily energy consumption rate of around 2500 kilocalories [1]. Later on, in primitive agricultural societies, which already had some domestic animals, this rate was around five times as large [2]. By the time of the low-technology industrial revolution in the mid-1800s, per capita daily consumption of energy reached 70 000 kilocalories in England, Germany and the United States [3]. During that period fuel wood and coal constituted the main sources of energy with smaller contributions from petroleum and hydropower. In the last quarter of the twentieth century, the dominant energy sources switched to petroleum, natural gas, nuclear energy and coal, while the average per capita consumption of energy in industrialized nations rose to over 230 000 kilocalories per day [3], two orders of magnitude larger than that of primitive man!

23.1.2 Let There be Electricity

With the early studies on electricity in the nineteenth century and the eventual development of the electric power industry, around 1882, the face of the Earth was changed forever. Electric lighting began flooding the cities at night and electric motors became the main source of power in factories. Earlier, in 1846, long distance communication had been made easier and faster with the introduction of the electric telegraph. Over the years, many inventions based on electricity increased the productivity in factories and made life at home easier and more comfortable.

Modern life became an endless chain of activities and events, fuelled by electricity: the alarm clock to wake people up in the morning, followed by the news on television or on the radio, the electric shaver and the hair dryer, the coffee brewer, the blender and the microwave oven or the electric stove, the refrigerator, the air conditioner, the computer, and so on and so forth. Electricity has also been the main element in improving the quality of basic services for the well being of people, such as clean water, education, medical care, entertainment and modern means of information and communication like the Internet.

23.1.3 One Third of Humanity Still in Darkness

Unfortunately, even today, not everybody has the fortune of enjoying all the benefits of progress: about one-third of humanity lacks access to electricity and, therefore, to a large number of electricity-based services and commodities. Around two billion people, mostly in the so-called developing countries, have remained in the earlier stages of human development, and still rely on wood fire, animal grease or kerosene lamps to light their paths and their homes at night. Modern means of communication and entertainment are either not known to them or are a distant possibility. Millions of people die every year from drinking polluted water, while others suffer from the lack of basic medical services. Illiteracy denies millions of people any possibility of gaining access to better opportunities. As hard as it may seem to believe, at the onset of the twenty-first century, with all the technology mankind has been able to create, survival is still the name of the game for millions and millions of people in remote rural areas of the world.

Reasons for such disparity are manifold, but certainly access to reliable, affordable and high-grade energy sources is one of them. The direct relationship between the

per capita energy consumption and human development is well established, as can be observed in a number of studies [4, 5]. What is not too clear is what form of energy, how much of it and for what applications, is required to break the vicious circle of underdevelopment. However, experience shows that a little electricity properly applied could help resolve many of these ailments of society.

23.1.4 The Centralized Electrical System

Electricity is certainly the most sophisticated and flexible form of energy in use today around the world. But it has some drawbacks: electricity has to be used almost immediately after it is generated, as storing it may be expensive, time-limited and inefficient, and in the current scheme of supply, it has to be transported over long distances from the point of generation to the point of use, which can be inefficient and unreliable, especially when these two points are too far apart from each other in places lacking support infrastructure.

In the early days of the electric power industry, electricity was generated right at the point of use. Around 1880, even street lights in places like Paris and London had their own individual generators [6]. Electricity was also then mostly generated using local and renewable sources of energy. Water wheels originally used in the factories to mechanically power process machinery, were later retrofitted into prime movers to turn electric generators, which in turn began powering electric motors in the late nineteenth century.

As the demand for electricity increased because of industrial and urban growth, and the distance between the point of generation and that of use became increasingly large, electric companies searched for new ways to deliver their services within good profit margins. Engineering research focused on alternatives to increase the power and hence the scale of the generating stations and the carrying capacity of transmission lines. Thus, the concept of economies of scale was introduced in the electric power industry, which for over one hundred years has influenced decision making for new investments in electric systems.

Since the generating units grew in size, electric companies oftentimes found themselves with excess generating capacity at the end of the construction of a new plant. The need to recover their investment in this excess capacity frequently motivated them strongly to look for new customers. Transmission and distribution lines were extended to reach the new customers, so an extensive grid was eventually created. Sometimes when demand was nonexistent, it was artificially created. For such purpose, donation of appliances was, at times, made by the electric company to the customer.

23.1.5 Rural Electrification

At some point in time, agricultural processes were identified as potential applications for electricity and, consequently, the lines began to be extended into the rural areas. Here, the density of potential clients and the intensity of electricity use was not as large as in the cities or the industrial centers; therefore investments in grid extensions became hard to recover, so new institutional and financing mechanisms were developed to support the operation. Official rural electrification programs were introduced in the most advanced nations, an initiative that eventually trickled down to the developing countries.

As rural electrification proved beneficial to developed societies, early policy planners felt that the same or similar benefits could be achieved in developing societies. Thus, a major effort was undertaken in the 1960s and early 1970s to extend the electrical lines into the rural areas of developing countries. However, by the end of the twentieth century only a few developing nations had reached an acceptable degree of electric grid coverage in rural areas. The rest could not advance much as a result of a number of problems faced by the electric utilities, including lack of capital to finance additions of capacity and grid extensions. Thus, the process of rural electrification through grid extensions in many developing nations stalled to the point that the problem of rural electrification again became a major political issue around the world.

23.1.6 The Rural Energy Scene

Life in many rural areas of the world is no different today than it was centuries ago. Even energy cycles resemble those of early man, although with the introduction of some modern elements. Firewood remains the main source of fuel in most rural communities, in spite of the alarming deforestation, dangers to health and the amount of work needed to collect it. In most places firewood is used mainly for cooking followed by shelter heating and lighting. A good reference point at hand is the case of Mexico, one of the most advanced economies in the developing world. Here, firewood consumption in 1997 represented around 2.7% of the total energy supply, a share that is larger than that of coal and nuclear electricity taken together and almost equal to that of hydroelectricity [7].

Candles and votive candles are more convenient than firewood for lighting, as they provide a more steady and whiter light, and can easily be carried from place to place, thus serving as a portable means for lighting pathways at night. Candles are frequently available in nearby towns, are not too heavy to carry in moderate quantities for long distances, and can be stored for long periods of time. Almost the same can be said for kerosene, which can be used in rudimentary lamps for lighting, although its availability may be more geographically restricted than that of candles. Getting either candles or kerosene requires money, which imposes an economic burden on poor rural families, while their use poses the risk of fire due to the flammable nature of the materials oftentimes used in the construction of rural houses.

23.2 BREAKING THE CHAINS OF UNDERDEVELOPMENT

23.2.1 Electricity Applications in the Rural Setting

The current patterns of energy use in rural areas show that the provision of small amounts of energy, especially electricity, changes the lifestyles of the rural population significantly. Energy applied to improve quality of life of the population may be a good first step to break the chains of underdevelopment. Applications such as lighting, clean water supply, entertainment and communications, preservation of vaccines and other medical supplies and means for modern education are usually welcome by governments, aid development agencies and the rural communities themselves. A number of tasks at home, mostly done by women, such as the provisioning of water, grain grinding, clothes sewing and others, could be made easier with the provision of small amounts of electricity.

Electricity for the household is at the top of the shopping list of rural communities. A house with electricity is a symbol of status. Beyond that, electrical lighting facilitates movement at night inside the house, helps prevent accidents, eliminates the need for kerosene and other combustible materials for illumination (thus avoiding the risk of fire and health-damaging fumes), helps spot poisonous insects and other wild animals that could be a threat to humans, and helps respond instantly to critical situations in case of accidents or illness. Furthermore, illumination of external areas such as the streets and meeting points also helps promote social interaction and a number of after-hours outdoor activities.

Electricity in the house also makes modern means of entertainment a more realistic possibility. The rural telephone system gives people the opportunity to keep in touch with their families in other parts of the world, and to call for help in case of an emergency. Electricity also gives the opportunity to use modern means of getting information and imparting training, using VCRs, satellite links, computers and even the Internet.

23.2.2 Basic Sources of Electricity

With the introduction of the transistor radio and the handheld flashlight dry cells became a favorite means to provide light and entertainment in rural areas. Dry cells can be purchased in many places and are easy to carry. Thus, many rural families spend substantial amounts of money buying them. Transistor radios play an important role in the life of remote communities, not only because they bring music and entertainment, but also because radio broadcasting in many places carry important messages such as warnings of floods, instructions on health practices and other valuable services, such as family to family message delivery. Some countries have even set up radio stations with regional broadcasting in the locally spoken native language or dialect, when it is different from the official national language.

New forms of entertainment, such as portable televisions, VCRs and tape players, have increased the demand for electricity in many rural communities. Because of this, dry cells prove to be expensive and hence many users in rural areas not connected to the grid have resorted to the car battery as the power source for their needs, including home lighting. Car batteries are widely available in rural areas of many developing countries. They are rechargeable, and because of their relatively larger power capacity, they can be applied to a wider variety of services; they last longer and may turn out to be cheaper per unit of service delivered than dry cells. Recharging car batteries, however, requires a primary source of electricity. Where motorcars or tractors are available, people use them to recharge batteries. Otherwise, they are carried over long distances to the nearest source of electricity for recharging. However, batteries are heavy and burdensome to carry, so transport to the point of recharging is sometimes done on the backs of animals and sometimes on the backs of humans. There have been cases of local entrepreneurs setting up micro businesses to offer battery-recharging service. For this, batteries are collected, taken to the point of recharging, recharged and then returned to the owner. This operation however, requires some infrastructure such as roads and means for transportation, not always available in rural areas.

As the economic power of families increases, so does the need for electricity. Dry cells and car batteries are no longer sufficient, so people in many places put political

pressure on electricity authorities to extend the grid to their communities, or individually resort to the use of small gasoline-fuelled generator sets. Small generator sets have the advantage of supplying alternate current of the right voltage, so that conventional appliances can be used. But their service is usually restricted to a few hours a day, because of the increasing cost of operation and maintenance of the equipment.

Experience shows that even when grid electricity is available, people in rural areas normally use it to light a few bulbs and perhaps to power small radios or typically black and white TV sets. Most people in rural areas lack the money needed to buy larger electric appliances, such as refrigerators and washing machines, or are simply not acquainted with them. Hence, because the number and size of appliances now in use is small, rural electrification represents an important niche of opportunity for the application of photovoltaic technology.

23.3 THE PV ALTERNATIVE

Photovoltaic (PV) technology nowadays is considered one of the most appropriate options to electrify dispersed population in remote places [8]. From an engineering point of view, modularity is perhaps the single most attractive feature of this technology. It allows designers to tailor electricity-generating systems as small in capacity as a few watts, or as large as many megawatts to suit specific needs, just following basic rules of electrical engineering. This feature combined with the suitability of the technology for autonomous operation, producing electricity with locally available sunshine, plus other characteristics such as lightweight, low-maintenance requirements and long useful life, has led people to consider photovoltaics as an attractive option for rural electrification. Ever since the technology was applied to power space satellites in the mid 1950s, the concept of reliable electricity generation for remote applications was firmly established. Terrestrial applications were developed with the basic idea of powering loads in remote places, where the cost of extending the grid was just too high. Today, hundreds of thousands of PV systems have been installed around the world to substitute for candles and kerosene lamps, gasoline- or diesel-powered generating sets, or even for unreliable grid extensions. The types of applications of PV technology in remote areas range from telecommunications, lighthouses and alarm systems in certain industries, to domestic applications and delivery of basic services. Leisure applications, such as sailboats and mountain cottages now carry PV panels to provide the required amounts of electricity, instead of noisy and smoky combustion engines. Even the petroleum industry, which is nowadays the basis for the world's energy supply, is using photovoltaics to supply electricity in offshore rigs or to power remote valve stations in oil and gas ducts.

The advantages of PV technology for rural electrification were demonstrated through a number of early projects in the period between 1968 and 1977 in Niger, Mexico and India. Applications included PV powered educational television, telephones, medical dispensaries and boarding schools for native Indian children. This early work demonstrated not only the technical viability of the systems but also the benefits to the user [9–11]. Some of these installations are still operational and in good condition, although with the limitations of a 30-or-so-year-old technology. Unfortunately, a critical mass of early projects was never achieved as to make a noticeable impact on society, and the lessons derived from the few projects on record have mostly fallen into oblivion. Only the notion that the technology

was too expensive and not too reliable, has prevailed over the years among many decision makers, in spite of the tremendous progress PV technology has made in recent years in terms of cost, efficiency and reliability.

Progress in materials technology, electronics and PV systems engineering, along with a drop in price of the main components of the PV system and a better understanding of the needs and expectations of the rural people, have resulted in a large variety of ideas, proposals and technological schemes to use photovoltaics as a source of electricity to promote human and economic development in rural areas of the developing world. A large number of applications have been identified for PV systems in rural areas, some more mature than others in technical terms, but all facing similar problems to enter the rural market on a massive scale.

23.3.1 PV Systems for Rural Applications

PV systems for remote applications typically include three basic elements: one PV panel that converts solar radiation into electricity, a means to store the electricity produced by the PV panel, which is normally an electrochemical battery, and an electronic device that helps control the flows of electricity within the system, thus protecting the battery by properly dispatching available energy. A variety of devices capable of using electricity to provide comfort, entertainment and other services for the benefit of the user are then attached to the PV system by means of the electronic charge controller (ECC). Figure 23.1 shows a schematic diagram of a general PV system. Depending on the application, some elements of the PV system may not be necessary, as is the case of the battery in water pumping systems.

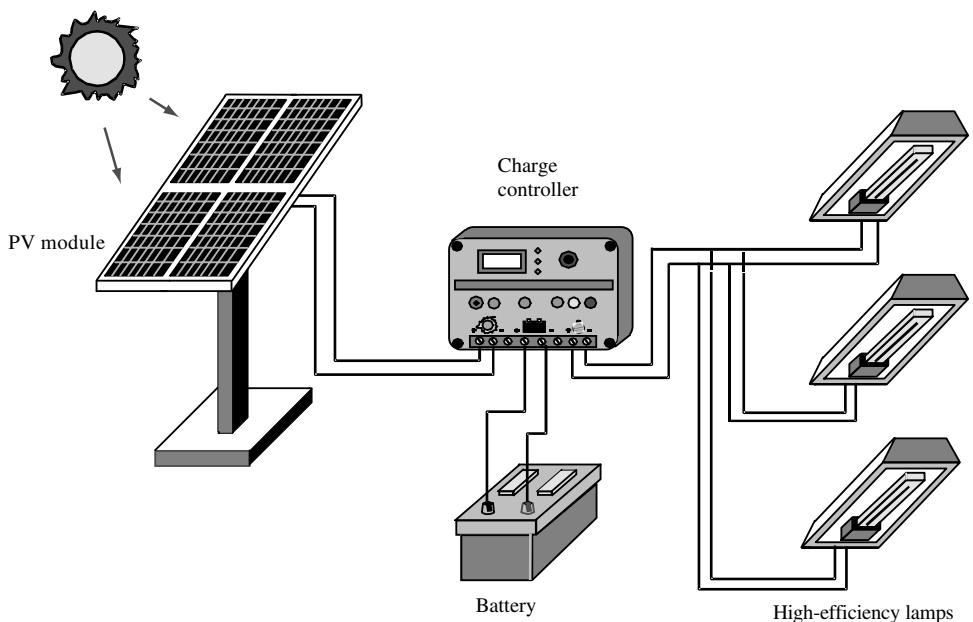


Figure 23.1 Schematic diagram of a general PV system

PV systems can be designed and built in the stand-alone mode, in which photovoltaics is the only source of electricity, or as hybrids, in which photovoltaics is combined with other sources of electricity, such as wind generators, small hydropower stations or combustion generators. PV hybrids are normally built to take advantage of other locally available renewable energy resources while at the same time improving the economics of the application. Photovoltaics can be installed in the so-called “disperse” mode, in which each individual application carries a full PV system as its source of electricity (just as it used to be in the very early stages of the electrification process in the late 1800s). Larger PV systems can be built to feed isolated electric minigrids, as is done today with diesel gen-sets in many parts of the world. Since PV panels produce relatively low-voltage direct-current electricity, a minigrid system requires additional components, such as DC/AC inverters and step-up transformers, to yield the right characteristics of the electricity on the user’s side of the grid. Hybrid systems are also more complex to integrate, since different types of electricity can be produced by the different generating units that are included in the system. Figure 23.2 shows a number of possible configurations of PV systems, for most of which practical examples can be shown.

Solar home systems (SHS) are perhaps the most popular of all the PV applications. An estimated 500 000 to 1 000 000 such systems have been installed in rural communities around the world [12]. Systems for basic lighting generally include one small, 10 to 40 W PV module and a small battery, enough for one to four points of light (normally compact fluorescent lamps). Larger, 50 to 100 W PV panels and batteries of around 100 Ah open the possibility of feeding other electric appliances, such as transistor radios, tape recorders and small TV sets. Even larger PV systems can support complete sets of domestic electric appliances, just as in any urban house, but the price of such systems is at present prohibitively expensive for a poor family. The smallest SHS are direct substitutes for dry cells and other ancient means of lighting a house, and a form of using electrochemical batteries without the need of sending them elsewhere for recharging.

Quality and efficacy of communal services can substantially be increased when relatively small amounts of electricity are available on site. This can be done by photovoltaics. Schools can be supplied with modern audiovisual means, educational television, and even the Internet, as shown by the project *aldea solar* in Honduras, supported by UNESCO, the Honduras Ministry of Education and the Council for Science and technology (COHCYT) of Honduras. In Mexico, over 13 000 PV powered telephones now link tens of thousands of people in remote communities with the rest of the world, through terrestrial PV powered transmitting stations and satellite links [13]. In Cuba, the Ministry of Health has implemented a system of rural clinics powered by photovoltaics, which has been operational for a number of years [14]. PV powered technologies to disinfect water have already been tested and field-demonstrated in countries of Africa and Latin America in a recent project financed by the European Commission [15]. A large number of PV water-pumping projects have been implemented around the world, and many examples of other PV powered communal services and applications can also be found (see for instance: [16–20]).

A large number of possibilities to apply photovoltaics for productive activities in rural areas of the developing countries can also be envisioned. Small irrigation, cattle watering, grain grinding, small handicrafts shops and other similar activities that require

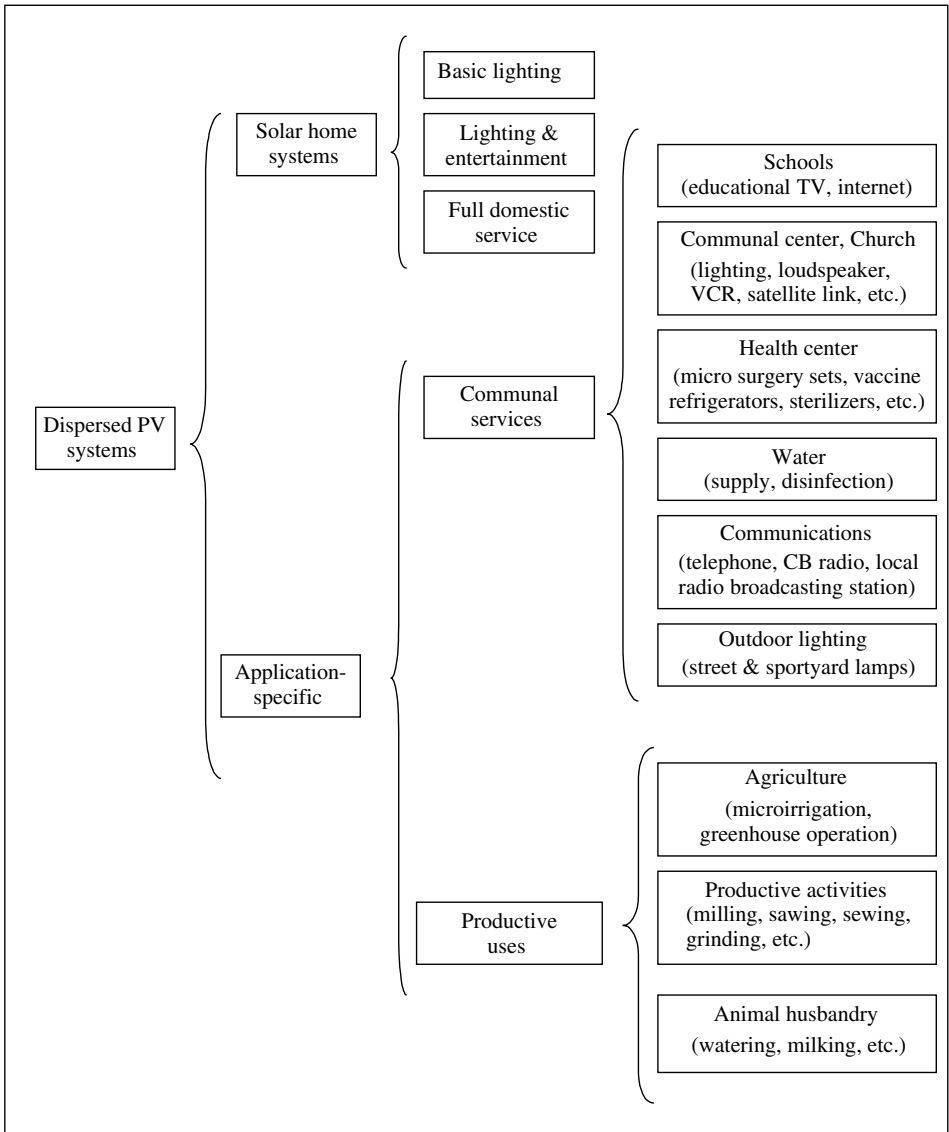


Figure 23.2 Possible configurations of PV systems

relatively small amounts of electricity can now be powered by photovoltaics to increase productivity and foster economic development.

23.3.2 Barriers to PV Implementation

For most urban people around the world, electricity comes into their homes just like magic: it is there, instantly and reliably at the touch of the switch. Few individuals make a conscious connection between their appliances and the electrical pole in the street, so

paying their monthly bills is perhaps the closest they get to the electricity business. But even fewer people realize the technical and administrative complexities behind the process of generation, transmission and distribution of electricity that allows factories to run and people to enjoy the benefits of modern services.

Understanding the physical principles that turn primary energy into electricity belongs to a small group of technical elite in the universities, research centers and electric companies. For the layman, it makes little difference whether primary energy is hydropower, nuclear power, fossil fuels or solar energy. Thus, the fact that electricity can be locally produced using the sunrays as the primary source of energy, with no wires connecting to remote and unknown places and facilities, would be of significance only to the most knowledgeable people. It is interesting to know that PV users in native communities in many parts of the world make a cosmogonist connection between electricity and their ancient god, the Sun. Thus, for most of these people PV technology is an appealing means to get a long-awaited service.

However, after learning about photovoltaics people are inclined to ask why is it that with so many virtues and so many advocates, PV technology has only reached one-tenth of a percent of the world's rural population with no access to the grid? The answer is found in the number of barriers a new technology such as this has to overcome to fully enter the market. In the case of photovoltaics, some such barriers are well known, others still unknown; some technical in nature and others having to do with institutional, social and financing issues. Just as conventional electricity is generated, in large and distant facilities, transmitted and then distributed to reach the individual consumer, so is PV technology produced in a small number of facilities in Europe, Japan and the United States, transported across the continents and distributed to reach the final user in very remote rural areas. And at each step a number of operations need to take place, which involve different degrees of complexity and cost. Therefore, bringing the PV solution to those sites where the grid has not been able to reach can be a very difficult task, unless such barriers are successfully removed.

23.3.3 Technical Barriers

PV systems are claimed to be reliable and long lasting. This is true and proven insofar as the PV module is concerned, but not every component of the system's balance has the same degree of technological maturity. In both, stand-alone and hybrid systems, batteries are perhaps the weakest links. Batteries are exposed to overcharging and over-discharging, which usually reduce their useful lifetime. Batteries also demand a fair amount of attention and regular maintenance, albeit relatively simple. However, even the simplest technical tasks may prove to be complicated in rural areas where a high degree of illiteracy and a lack of familiarity with modern technology, and with electricity in particular, is more the rule than the exception. The problem with batteries arises in part because of the fact that the lead-acid technology now in use, available for over one hundred years, was not specifically designed for use in PV systems. Adaptations of the current technology into what is now called *solar batteries*, and development of new battery types, such as nickel-metal hydride [21], promise to ease many of the current problems.

SHS also face other problems, mostly in the charge controllers and the lamps, basically as a result of an industry that has until now had an uneven degree of development

(for a detailed discussion on charge controllers, see [22]). Two schools of thought seem to underline the issue: simple, sturdy, low-tech, low-purchase-cost devices against high-tech, sometimes a bit complex and perhaps lower life cycle-cost devices. The issue is not easy to resolve, especially with so little systematic information coming from the field on the performance of such devices. Taking into consideration that rural areas in developing countries are far from being mature markets for photovoltaics (and for many other goods) and accounting for the illiteracy of the rural population, consumer choice will hardly be a useful parameter to resolve the issue, especially if one considers that a large number of PV rural electrification projects are still being carried out in the “technology push” mode.

The suitability of photovoltaics as a solution to the rural electrification problem is being taken for granted by many advocates of the technology. Unfortunately, few studies seem to have been carried out to assess the performance of SHS now in the field, in a systematic and comprehensive manner. At this stage of technology implementation, information from the field is vital as a feedback mechanism to gauge the efficacy of the PV solution, to improve the chances of overall success and to assure long-term sustainability. Field surveys, however, tend to be expensive, especially where the most remote and isolated communities are concerned, and availability of funds for monitoring and evaluating SHS projects in the field is not obvious.

A 35-man-month field study was recently completed in Mexico, in which 1740 SHS installations (out of around 60 000 installed with government financing) in most regions and communities included in government programmes were evaluated. The study had a three-fold purpose: to assess the physical and operative condition of the systems, to probe the degree of satisfaction of the users and to evaluate the efficacy of measures previously implemented to make the projects sustainable. Preliminary analysis of the information gathered in the study shows that from the technical point of view things look good with most SHS samples performing well (for more details on these results, see [23]). But there are reasons to believe that as systems age, the results may change, unless corrective measures are taken.

Introducing photovoltaics in rural areas of developing countries is an innovative exercise in society, with the particularity that a space-age technology is being adapted for operation in a sector of society living, in many cases, at least five hundred years in the past. From this perspective, it is hard (and even dangerous for project sustainability) to ignore the strong connection that must be established between the technology (hardware) and the user. For even the most sophisticated, well-designed and perfectly built piece of PV technology is bound to fail sooner than later, if the ground for seeding it is not properly prepared. This means information, training and local capacity building on the user side, as well as user involvement at every step of the process to make them aware of the important role they play in the solution of their own problems. Similar considerations can be made in connection with the environment (social and physical) in which the PV system is bound to be installed. For instance, anecdotic and written information from the field points to the fact that some PV components designed and built with technical criteria prevailing in advanced, cold countries are not performing well in the tropics where it is most needed. Reasons for this are many, but their discussion is outside the scope of this chapter.

Alternative technical schemes to the SHS as a means to provide basic electricity services in rural areas are being tested. Battery-charging stations, where a large central PV array is installed to recharge batteries brought in by the user, who pays a fee for the service, is one such scheme advocated by a number of people. The rationale behind this scheme is that peasants in many parts of the world already use battery-charging points distant from their homes. It is also argued that microbusinesses could develop in remote areas to enhance the chances of sustainability of the electrification process and so, several projects of this kind are underway in various countries. However, recent field studies reveal [24] that this alternative also has several shortcomings, which are forcing project officials and users to switch to SHS as a substitute to the previously used PV battery-charging stations.

The preceding discussion was meant to point out the fact that even though engineers and industries will most likely solve the remaining technical problems facing PV technology for rural applications before this market enters into its mature stage, a number of more complex issues at the technology-user interface remain to be understood and dealt with. The cause-effect diagram of Figure 23.3 is an attempt to show the variety of factors leading to a failed system, and consequently a dissatisfied user. In the long run, the degree of user satisfaction will determine the level of acceptance of PV technology as the solution to the problem of rural electrification.

Technical standards, design guidelines and other elements for quality assurance of PV systems are also important for the sustainability of PV rural electrification projects. A number of these elements are being developed in institutions, professional societies and international organizations around the world. Most of them, however, focus mainly on pure technical (hardware) issues, as is the case of the recommended specifications of the organization Global Approval Program for Photovoltaics (PV GAP) and the standards

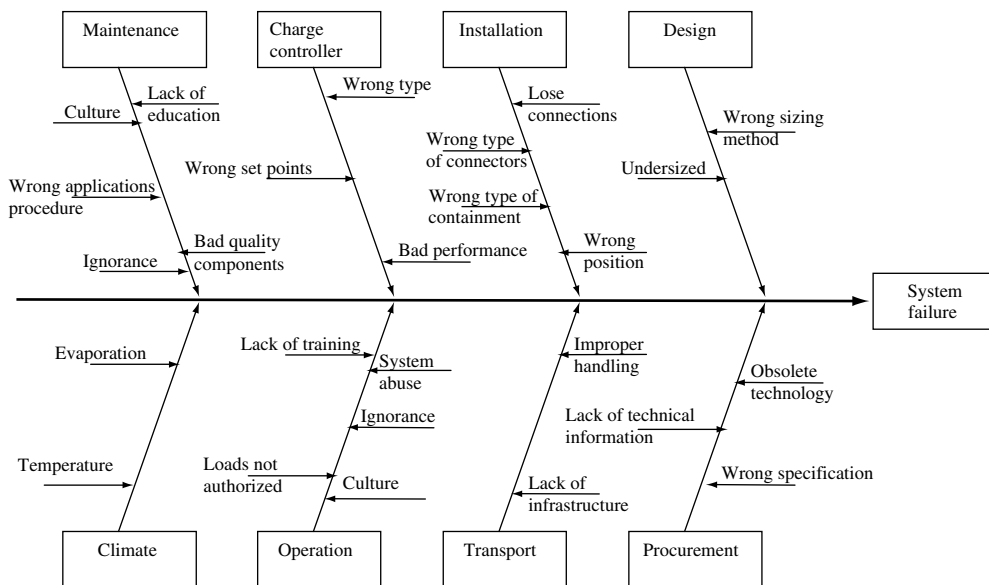


Figure 23.3 Cause-effect diagram showing a variety of factors leading to a failed system

issued by the International Electrochemical Commission (IEC) Technical Committee 82, and little attention is being given to the soft and organizational aspects of the problem dealt with in other works [25, 26].

23.3.4 Nontechnical Issues

23.3.4.1 *Initial cost*

It is common knowledge that for a commercial operation to be sustainable in the modern economy, a flow of goods has to be properly matched by a counter flow of money. Sunrays striking on the roofs of houses are free, but equipments to turn solar energy into electricity, and to transform this electricity into needed services, are not. PV manufacturing companies invest in factories and raw materials, pay wages to their workers and taxes to their governments and are obliged to deliver revenues to their shareholders. All expenses plus profits essentially set the base price of their products. In a second step, PV components from different companies are transported to specific points for systems integration. In turn, packaged systems are fed into the distribution channels for retailing and final installation where the end user wants them.

By the time a PV system is installed on the user's premises, its base price has increased a number of times. So, people need money to get their systems installed. Considering the low capacity of the peasants in rural areas to pay for goods, a set of important questions emerge when one considers photovoltaics as the solution to the rural electrification problem. Are people willing to pay for the system? How much can they afford to pay? What mechanisms can be instrumented to make systems more affordable? If people cannot pay, should they remain in darkness or should somebody come to their rescue? What roles can governments and development agencies play? And even when people can pay, should they bear the full system cost, even at this early stage of technology introduction when many companies are still building their infrastructure and learning how to manufacture, integrate and market the systems, so that their transactions costs are a lot higher than they should be? These are not trivial questions considering that, for the miracle of full-scale rural electrification to happen, around 300 000 million US\$ must, in principle, flow from the poorest regions of the world to the modern sector of society so that PV systems can flow in the opposite direction.

23.3.4.2 *Breaking the initial cost barrier*

Consequently, since solar energy, the fuel used by PV systems is free and systems are, at least theoretically, low maintenance and long lasting, system cost is commonly seen as the main stumbling block for the introduction of photovoltaics. A number of schemes have been tried over the past decade in search of an effective way to remove this barrier. Most of them can be grouped into three categories: the *social route*, in which poverty alleviation programs and other socially driven mechanisms are used by governments and bilateral aid organizations to make funds available for the purchase of PV systems in favor of the least privileged people; the *fiscal route*, in which taxes, import duties and other fiscal levies are removed to lower the local price of the PV system, thus making it somewhat more affordable for the final user, while at the same time facilitating the

creation of a local market; and the *business route*, in which banks, private companies and entrepreneurs are devising and testing a number of schemes to make financing available for the purchase of the PV system, thus helping to create a market for photovoltaics at the same time. One way or another, currently each of these routes somehow benefit from the intervention of governments, multilateral organizations and lending institutions. On the other hand, boundaries between these routes are not necessarily clear-cut, so that combined or coexisting schemes are not uncommon.

Not everyone in rural areas is necessarily poor or totally dispossessed. Some people live in remote places for convenience, either because their source of income is attached to the natural resources locally available, or because they prefer living in a cleaner and quieter environment than in the city. They do not have electricity from the grid, simply because they are too far away, but they usually rely on gasoline or diesel-fuelled gen-sets for their electrical service. These people, however, could easily purchase a PV system without any financial assistance, if one was made available to them. This is already a good market that is being tapped in a number of countries, such as Spain, Colombia, Mexico and others. On the other hand, some estimates indicate that between 25 and 50% of people living in remote places could purchase a SHS provided some sort of financial assistance was available to them [27]. This is a substantial market in its early stages of development; to tap this market a number of schemes are being tried by private entrepreneurs and multilateral development organizations, as is the case in Kenya, Zimbabwe and the Dominican Republic. However, the poorest of the poor, representing the largest portion of the world's rural population, can hardly ever afford to buy their own PV systems.

23.3.4.2.1 *The business route*

For those in need of financial assistance, two alternative models are being tested. One focuses on the sale of the PV system (the sales model), the other on the sale of the electricity produced by the system (the service model). Both models have advantages and shortcomings and both involve flows of money beyond the control of the PV user.

In the sales model, the PV system is purchased on credit by the user, who becomes the owner and takes over the responsibility of system maintenance and replacement of parts. Money for the transaction is usually borrowed by the user from a set of different sources, which may include the system supplier, a finance institution, or any other type of credit organization such as a revolving fund or a local microfinance operation. In any case, money is obtained at a cost, which adds to the cost of the PV system, and is paid back in periodic installments under prearranged terms and conditions. However, this additional cost is what entitles the user to the benefits of electricity, albeit in small quantities. This model is preferred by those who like the social status of system ownership and are willing to assume the task of maintaining the equipment and the responsibility for replacing damaged or worn out parts.

People not willing to take any risks, may opt for the service model, in which the supplier retains ownership of the PV system, or of some parts thereof, and then charges some monthly fee for the electricity delivered to the user. The supplier maintains the system and becomes responsible for providing the user with electricity, according to system capacity. Following the current practice, this kind of service can be provided through a regulated concession, an unregulated open market provider or a community-based provider.

Needless to say, the risk assumed by the service supplier also has a cost, which reflects on the monthly fee charged. According to some estimates, the added monthly fee for service over a period of 10 years could double the life cycle—costs of the same PV system when purchased on credit [27]. Current PV projects in the fee-for-service model show a large dispersion in the amount of the monthly fee charged to individual users. A number of factors may be responsible for this. For instance, some projects may involve some sort of subsidy, and in other cases, service suppliers may not follow the same rules to define the scope of their responsibility: some may retain responsibility over the PV module and charge controller only (the least troublesome parts of a SHS), while dumping on the user the responsibility of replacing the battery (the weakest link in the system) and the lamps.

Selecting a particular route for a given project is not a matter of personal preference only. The landscape is very important and has to be taken into account, since a number of its elements influence this choice, including local social and energy policies officially established in each country. For instance, some countries do not allow private sale of electricity, so that the fee-for-service model could not be applied, unless prevailing laws and regulations are changed as necessary. Low rural population density, difficult access to the communities, long distances from the supply centers and complex logistics to deliver goods and collect fees, can make both fee-for-service and financed sales schemes difficult to implement and geographically limited. In many cases, monthly fee/payment collection may be an expensive task, due to the time and effort it may take for the supplier or the service men to reach the customer. This fact has already been noted by PV companies operating in Sri Lanka, for instance [27]. Timing is another important factor, considering that people may not be home when the fee collector arrives, and that many peasants have money only during the postharvest period. Such difficulties have led some utilities, for many years, to give up on monthly fee collection from remote clients connected to their grids, basically because of very small bills and comparatively larger billing expenditures. Thus, unless fee collection schemes better adapted to the local conditions can be found, one can theorise that the fee-for-service and purchase models will be applicable basically to the most accessible and higher density rural communities. The fraction of the rural population meeting these criteria in many countries seems to be inversely proportional to the degree of rural electrification by grid extensions.

Local culture and idiosyncrasy are two additional elements to be considered for the choice of a delivery model. The notion of common property embedded in many native communities or the lack of familiarity with commercial practices, or even with money, could lead to unsustainable operations in many rural areas. Some academicians studying the process of introduction of PV systems in rural communities, argue that freedom from any financial burden is one of the most cherished values for rural people, and hence could be an important barrier for them to take on any financial obligations. Hence, government intervention may be indispensable at some point to deliver the PV solution in which the business route cannot be applied.

Over the past ten years delivery models in the business route have been tested through a number of projects financed by the GEF and the World Bank in various countries. A recent review [12] of the GEF solar PV portfolio suggests the following emerging lessons, warning that it is still too early to draw definite conclusions:

- Viable business models must be demonstrated to sustain market development for solar photovoltaics.
- Delivery/business model development, evolution and testing require time and flexibility.
- Institutional arrangements for project implementation can greatly influence the value of the project in terms of demonstrating viable business models and thus achieving sustainability.
- Projects must explicitly recognize and account for the high transaction costs associated with marketing, service and credit collections in rural areas.
- Consumer credit can be effectively provided by microfinance organizations with close ties to the local communities if such organizations already have a strong history and cultural niche in a specific country.
- Projects have not produced adequate experience on the viability of dealer-supplied credit under a sales model, and no project in the portfolio appears set to provide such experience.
- Rural electrification policies and planning have a major influence on project outcome and sustainability, and must be addressed explicitly in project design and implementation.
- Establishing reasonable equipment standards and certification procedures for solar home system components that ensure quality service while maintaining affordability is not difficult, and few technical problems have been encountered with systems.
- Substantial implementation experience is still needed before the success of the service approach can be judged.
- Postproject sustainability of market gains achieved during projects has not yet been demonstrated in any GEF project: it is too early in the evolution of the portfolio.

23.3.4.2.2 *The social route*

Governments can act in several capacities along the social route. Financing the purchase of SHS for poor people is perhaps the most critical one, although consumer protection and market regulation are also of importance. Government financing of SHS is seen by some as an unnecessary nuisance that distorts the market and creates dependence in the user's minds (users will not buy once the government has provided systems for free, goes the argument). Most critics of government intervention seem to forget that rural electrification has been historically subsidized by governments not only in developing countries but also in some of the most advanced nations. In that sense, there is no reason to think that PV rural electrification has to be different altogether, as it is only the technology base that is changing; the rest of the landscape remains the same.

Direct government financing of photovoltaics for rural electrification is not necessarily a bad thing. Up to now, the largest volume of SHS installed around the world has been realized through government or donor-led programs. Government intervention may help aggregate markets, reduce transaction costs and, if properly done, can create a better setting for quality assurance and local industry development. At least, this has been the experience with government-financed PV projects in Mexico, where proper institutional mechanisms were implemented for this purpose, and as a result, a local industry has also emerged around government-financed projects, which now produces locally and

exports balance of system components [13, 28–30]. In this case, money provided by the government is seen as an instrument to promote local development. Over 2500 rural communities have been electrified in Mexico with photovoltaics following this model, and it is interesting to note that in many of them people have instrumented a variety of cost-recovery and money-making mechanisms, which allows for system maintenance and additional communal projects.

A number of governments from developing countries are considering the social route to deliver PV-based electricity to rural areas. Policy setting and definition of financing mechanisms are usually the first steps in this direction. Examples can be found in several Latin American countries [31]. Some examples are discussed below.

In Bolivia, Article 61 of the Electrical Law establishes that the State is responsible for the electrification process in smaller localities and in rural areas that cannot be served by private interests. Resources to finance such projects must be provided by the State, through the National Development Fund. The Executive must also propose energy policies and strategies to foster the use of alternative energy sources.

A similar mandate can be observed in Colombia, where Law 143 urges the State to provide basic electrical services to lower-income families in rural areas and to make funds available to cover necessary subsidies in this respect. The Energy and Gas Regulatory Commission is obliged to protect the rights of the lowest-income people, while the Colombian Institute for Electrical Energy has been mandated to prepare the National Energy Plan for regions not served by the grid, including the use of alternative energy systems in substitution of fossil fuelled generating systems.

In Ecuador, the Law of Regime for the Electrical Sector, addresses rural electrification and financing issues for the rural sector. It also assigns priorities for the application of renewable energy in rural electrification projects and describes the structure for project identification, approval, execution and operation. The National Fund for Rural and Urban Marginal Electrification (FERUM) is the body responsible for the administration of financial resources, and is directly regulated by the office of the president.

Similarly, in Nicaragua, the Law for the Electrical Industry holds the State responsible for developing rural electrification in remote areas in lieu of interest from other economic agents. For this, the State must provide the necessary resources through the Fund for Development of the National Electrical Industry. The State is also required by the law to implement policies and strategies for the use of alternative energy sources for electricity generation.

As a last example, in Panama, Article 9 of Executive Decree 22 makes the State responsible for promoting rural electrification and for assigning an annual budget to carry out this task. Consequently, the Office for Rural Electrification was created within the office of the president, and is in charge of promoting the use of renewable energy for rural electrification projects.

23.3.5 Trained Human Resources

Adequate financing and institutional frameworks are necessary but not sufficient conditions to remove the main barriers for PV rural electrification. Properly trained human

resources to develop and operate programs, and to carry out projects, are equally important. PV systems and their implementation in rural areas are frequently looked upon in a very simplistic manner by a number of people. However, disregard for the complexities behind the process has resulted in a large number of failures. One would be surprised to learn how many PV projects in rural areas around the world have not lasted but a few years beyond the inauguration date; or how many others are still not complete because a variety of logistic aspects were not given due consideration at project inception; or even how many others are under-performing as a result of faulty engineering and construction practices. Unfortunately, little reliable information from the field is available in this respect as many projects are in their first years of operation so it would be too early to draw any definite conclusions about them.

PV systems packaging is increasingly being carried out by local companies in the developing countries. This practice has its merits, since it promotes the use of local labor and materials, which benefits the local economy. However, workers are not always properly trained to carry out their duties, so that construction and installation guidelines, no matter how precise and elaborate, are not always followed. Sometimes instruction materials are not in the local language, or are translated incorrectly, and at other times they do not properly match the idiosyncratic framework of the local worker. The benefits of training local workers for industry support cannot be overstressed. An example of how far this training could go can be found in the project carried out by the Spanish Cooperation in Bolivia, where native Aymara Indians were successfully trained to assemble electronic charge controllers for SHS. This project is described in greater detail below [32].

Local distributors and vendors of PV systems frequently lack a proper understanding of the products they sell. This leads more often than not to undersized systems, to make the sale easier, or to overselling the attributes of the PV systems to be sold, creating customer expectations beyond the actual capabilities of the system. In any case, the result is customer dissatisfaction. Thus, for the PV business to grow on solid bases, the front-lines that deal with end users must be properly trained in technical, marketing, selling and business practices. This is easier said than done, as many PV businesses in developing countries are small commercial ventures embedded in other lines of activity, such as hardware stores or cattle feed stores.

Photovoltaics being a novel technology for most people, developing and implementing programs for its massive deployment is not necessarily an easy task for program managers. Assistance is oftentimes required for program formulation, and to establish the proper mechanisms for project financing, implementation and monitoring. Multilateral agencies such as the World Bank, the GEF, UNDP and others, organize workshops and seminars around the globe to disseminate best practices that could help solve this problem. Over the past six years, the Network for Rural Electrification with Renewable Energy (RIER) of the Ibero American Program of Science and Technology for Development (CYTED) has been running courses and workshops on strategies for PV rural electrification throughout Latin America. Attendees usually include officials from government agencies in charge of rural electrification, electric utilities, local financing organizations, PV distributors and salespeople, and university professors. Benefits from such training activities often translate into better-formulated programs and projects, and a more appropriate understanding of the critical elements to make PV rural electrification projects sustainable.

23.4 FOUR EXAMPLES OF PV RURAL ELECTRIFICATION

It is estimated that by the end of the twentieth century, anywhere between 500 000 and one million small PV systems have been installed to power rural homes in developing countries [12]. On top of that, tens of thousands of PV-powered water lifting pumps and other communal services, such as health centers, schools, telephones, street lamps, have been deployed through government programs, donor-led initiatives and entrepreneurial activities. Many such programs have been subject to in-depth reviews as a means to better understand the process that is taking place in the field and to harvest the lessons learned that can be applied to other projects and programs. For details, the reader is encouraged to consult available reports (see for instance, [33–36]). In this section, a few examples of PV rural electrification projects and programs are described.

23.4.1 Argentina

As part of the reform of the electrical sector in Argentina, the provincial electricity markets were divided into centralized and disperse sectors. Each sector has its own structure, its own mission and its own operational form. Then, the program to supply electricity to the rural and disperse population of Argentina (PAEPRA for its name in Spanish) was established by the government in 1994. This program has the goal of providing electricity to 1.4 million people not yet served by the grid, and to electrify around 6000 public services, all this in areas where the low-population density and the long distance to the electric grid makes it too costly to supply electricity by conventional means [37]. PAEPRA operates at the provincial level through concessions to private companies bound by contract to provide electricity services under the supervision and control of the provincial electricity regulatory body [38]. Provincial concessions are awarded through a public bidding process, in which the winning company is the one that requests the least amount of subsidy money on a per customer basis to operate. This subsidy complements the funds collected from the user under a fee-for-service scheme. Participating companies are required to have experience and technical capabilities (1) to operate and maintain electrical systems and other services, such as water supply and telecommunications in a dispersed rural market; (2) to manage electrical systems based on diesel gen-sets, photovoltaics, wind and microhydro turbines; and (3) to manufacture and supply spare parts and components for this type of system. Furthermore, selected companies must be financially healthy.

The PAEPRA program was conceived to operate supported by a loan from the World Bank, but has not moved forward as fast as originally expected for a number of reasons beyond the scope of this work. Since 1986, the Republic of Argentina has a national PV industry with a capacity to produce balance of system components and about 1 MWp per year of PV modules. The current market is based on rural applications for domestic and communal services, water pumping and telecommunications. The presence of this industry is a good element to support the program.

23.4.2 Bolivia

In Bolivia, the National Rural Electrification Program (PRONER) was established to promote and support economic development in rural areas in order to improve the living

conditions and the quality of life of the population. The original objective of the program was to provide electrical services to 100 000 households in a time span of five years by means of renewable energy. The process to carry out this task is based on sustainability, by creating an appropriate institutional, financial and technological framework. This program has been under implementation since 1997, supported by an UNDP-GEF grant. The first phase of the program has the goal of installing 3200 SHS through 22 projects in five municipalities and is aimed at removing financial, institutional, technical and human resource barriers to the massive application of photovoltaics.

Bolivia has been a favorite place for international cooperation in the field of PV rural electrification. In 1988, the Spanish Agency for International Cooperation and the Solar Energy Institute of the Polytechnic University of Madrid launched a PV electrification project to bring electricity to the Aymara community in the high Bolivian plateau. Beyond the traditional objectives of a project of this kind, this particular project attempted to foster the development of a users' organization with capabilities to manage and maintain PV installations, and to be responsible for the proper continuation of the project. At the same time, emphasis was put on the creation of an industrial unit in one of the rural communities to manufacture balance of system components using local manpower and Bolivian components as a basis for future projects [39]. By 1993, a total of 1000 SHS had already been installed and the Association for Solar Electrification (AES) had been created. AES included all PV users and was the owner of all the PV installations. An accounting system was established and a team of installers and maintenance crews was trained. This project has been studied thoroughly and important lessons derived thereof [32]. By the end of its fifth year of operation, a demand for about 30 000 SHS had been created, well beyond the financial capabilities of the project. Unfortunately, several problems in the area of financial management developed within the AES once the main implementing agents pulled out from the country and the project stalled.

In another action, the US-based National Rural Electric Cooperatives Association (NRECA, now an incorporated company) launched several pilot PV projects in Bolivia to test different financial schemes. In cooperation with the local organization Rural Electricity Cooperative (CRE), 90 SHS were installed as a preamble to a further 1300 installations. CRE provided complementary financing for the purchase of the PV systems and managed other aspects of project implementation, including the selection of the users and providing technical training [40]. In cooperation with the Cochabamba Electric Company, a privately owned electricity distribution company, NRECA implemented another project to install 300 SHS in remote rural communities. ELFEC finances the purchase of the equipment and provides installation and maintenance services.

The project INTI K'ANCHAY (light from the sun) has been implemented by the local NGO Energética with financial support from the Netherlands. Five hundred SHS were to be installed in the first phase, to test a financing mechanism that eventually could be extended to cover a larger portion of the 150 000 families without electricity in the province of Carrasco [41]. Companies participating in the process are required, among other things, to supply and install the SHS according to technical norms and specifications issued by Energética, to provide guarantees according to the useful life of the individual components and to build a network of representatives at the microregion level for after-sales service. By July 1999, a total of 200 SHS had already been installed, and applications for 350 more were being processed [42].

On the other hand, the German foreign-aid agency GTZ has promoted and supported several PV projects in Bolivia and has carried out an important promotional campaign in favor of renewable energy through the bilateral program for the diffusion of renewable energy (PROPER). Among other things, PROPER carried out activities to increase the number and capabilities of in-country personnel trained in the field of renewable energy at the professional and technical levels, including microenterprise building [43].

23.4.3 Brazil

PV rural electrification projects in Brazil started around 1992/93 with pilot cooperative projects with Germany and the United States [44]. Around 1500 SHS were installed as part of these projects in Northeast Brazil in cooperation with the local electricity distribution companies, who were responsible for systems installation, maintenance and performance monitoring. In 1994, the Brazilian Government launched an initiative to promote the use of renewable energy and the corresponding *action plan* was established in 1995, with the original goal of installing 50 MWp of PV systems by the year 2005 [45]. The program for energy development in the municipalities and the states (PRODEEM) was also launched in 1994 to deliver electricity by means of renewable energy to rural communities not served by the grid [46]. At the same time, several state governments, including Minas Gerais, Sao Paulo and Parana, launched their own PV rural electrification projects.

The PRODEEM program is coordinated by the National Department for Energy Development of the Ministry of Energy and Mines and is technically supported by the National Center for Electrical Research (CEPEL). Since 1995, three program phases have been implemented [47], with a total number of PV installations close to 2400, basically for water pumping, public lighting and other installations such as communal buildings, schools, health centers and churches. A fourth phase has been under consideration for installing about 1300 additional PV systems [48]. The process for the implementation of PRODEEM is well established and documented in the literature cited here.

The Electric Company of Minas Gerais has been actively involved in deploying PV systems, in spite of owning one of the most extensive electrical grids in Latin America, with a total length of 300 000 km. In 1989, CEMIG launched an experimental project to install PV systems for productive and domestic applications in remote places. Between 1995 and 1997, a demonstration phase of the Program of Assistance for the Rural Development of Brazil took place in cooperation with the US Department of Energy and the US National Renewable Energy Laboratory. PV systems for 70 schools and several pumping systems were installed as part of this program [49]. Plans were made to electrify 2000 regional educational centers and to install about 500 water supply systems, all powered by photovoltaics. By 1987, such pumping systems, with PV capacities between 1 and 2 kW each had already been installed [50]. General criteria for eligibility in the CEMIG program include localities farther than 5 km from the nearest electricity grid and a user density of less than 5 people per kilometer. CEMIG provides financing for 64% of the project cost, the remaining 36% being covered by the community authorities. CEMIG has also established a training center for technicians, who provide regular maintenance of the systems. Monthly salary of the technicians is covered by the municipal authorities of the region they serve [49]. A PV “pre-electrification” program was established by CEMIG in 1998 to stimulate the growth of the electrical demand in remote places, to the point where

grid extensions could become economically viable. Some 500 PV systems were installed for this purpose in 1999 and another 5000 were under consideration for the following years. The rationale of this pre-electrification program is to use photovoltaics as a basis to aggregate electrical demand in rural areas. Once the critical mass has been reached, the grid would be extended to the point of highest demand while the PV installation would be moved to another location for the same purpose.

23.4.4 Mexico

About 5% of the Mexican population (almost 5 million people) has no access to electricity from the grid. A highly dispersed rural population and a rough terrain make grid extensions technically difficult and economically unviable. Several attempts were made in the late 1970s to use photovoltaics to power basic electrical services, as mentioned earlier. In 1989, the Mexican Government launched the PRONASOL program for poverty alleviation, which soon became the platform for a large-scale PV rural electrification activity. Today, over 2500 rural communities have been fully supplied with SHS through government programs, which means there are over 60 000 SHS in the whole territory. It is estimated that another 30 000 SHS have been installed outside government programs on a purely commercial basis. In addition, thousands of other PV-powered rural services have been provided, including rural telephones, schools, health centers and communal buildings.

A distinctive characteristic of the Mexican PV rural electrification program has been the active participation of the national electric utility (CFE) as technical normative agency, a central element for quality assurance and sustainability [29]. Under contract to CFE, the Electrical Research Institute of Mexico developed, in the early 1990s, a set of technical standards and specifications for project implementation. Laboratory testing and field evaluation protocols were also developed and implemented. Government-financed projects are carried out by private companies under the technical supervision of CFE and administered by an implementing agency, usually a government office. Contracts to private companies are awarded through a bidding process within the framework of the law for public works. Companies are required not only to supply the physical equipment but also to install the PV systems and train the user in proper operation and basic maintenance. The winning company must also establish a network of contact points for after-sales services.

Finance to purchase the PV systems has been mostly provided by the Federal Government, with lesser contributions from the state and municipal governments. Communities are requested to contribute to the project according to their own economic capacity. In-kind contributions, such as carrying the PV equipment to the community from the nearest point where vehicles have access, is one of the most frequent services by the community in support of the project. Funds are provided by the government as part of the patrimony for the community and, hence, no *a priori* money repayment mechanisms are established. However, communities are free to implement any fund-raising activities that can help them maintain their systems and purchase additional equipment. A popular mechanism is the so-called communal fund, in which members of the community contribute money or man-hours or both to a common fund managed by the community representatives. The communal fund is then used to maintain the PV installations and/or to implement other projects for the benefit of the community, such as water works repair,

building a new schoolroom and the like. A more detailed description of the Mexican PV rural electrification program can be found in the literature mentioned in References [28, 51, 52].

23.4.5 Sri Lanka

An estimated two million households lack access to grid electricity in this country. Recent studies indicate that at least 10% of these households could afford a SHS at current prices, based on a monthly household income of Rs. 5000 [53]. A market study commissioned by the National Development Bank of Sri Lanka in 1991 indicated that a market of 360 000 households could afford a PV system [54]. However, so far only about 15 000 such systems have been sold commercially for cash through a retail network.

Many reasons have been cited for this low penetration level. As in other places, the biggest barrier for the exploitation of this market has been a lack of consumer financing. Political promises for grid extensions in rural areas and the government sponsored “Electricity for all by the Year 2000” campaign, which was perceived as *grid electricity* for all, have also been major barriers. Lack of government-level endorsement for solar photovoltaics, along with other renewables, was a hindrance to both private sector and NGO promoters. Nevertheless, four companies retail PV systems in Sri Lanka: Shell Renewables, Resco Asia (subsidiary of the US Selco), Alpha Thermal Systems and Access International. Sarvodaya SEEDS, a local NGO, provides microfinancing in partnership with some of these companies.

In the late 1980s, solar PV modules, 12-V lamps and simple electronic charge controllers were assembled in Sri Lanka by Solar Power & Light Company (SPLC), a private venture established as Power & Sun in 1986. However, manufacturing of solar modules ceased as the advantage over imported products was eroded, in part because of the high import duties on raw materials. Thus, SPLC essentially developed into a marketing organization by creating an infrastructure to market, install and maintain PV systems in rural areas. SPLC uses retailers to stock solar home systems; trained technicians and individual agents, called *corresponding agents* (CA), are used to canvass sales, install systems and provide customer service. SPLC, which has just been bought over by Shell International Renewables, has sold over 3000 PV systems directly to consumers, mostly for cash.

Apart from cash sales of SHS, there are examples in Sri Lanka of both successful and “deemed as failed” projects, using loan repayments by the consumer as the measure of success. Projects implemented with total community involvement by NGOs, such as Sarvodaya and Solanka, have been quite successful. Sarvodaya’s already successful microcredit operation was adapted to market SHS, and implemented a pilot project with 250 installations through its Rural Technical Services branch, with assistance from the US-based NGO Solar Electric Light Fund (SELF, now the private company Selco) and a seed fund from a US foundation. Further activities by Sarvodaya using funds from a credit line for renewable energy provided to Sri Lanka by the World Bank, led to the installation of 300 more systems. Plans to install 5000 more within the next five years are already drawn. Sarvodaya SEEDS has become a Participating Credit Institution of the Energy Services Delivery Project. It can now access the fund directly and on-lend to customers. In January 2001, it has been reported that Sarvodaya SEEDS’ lending portfolio exposure is Rs. 89 million (about US \$1 million) for solar photovoltaics.

Solanka Sun Associates, created community level capabilities to do complete projects, including evaluation of potential customers, providing financing; designing, installing and maintaining the solar home systems; collecting repayment and managing the project with the inherent difficulties of managing projects from cities. This model has shown that success can be achieved with proper training and incentives to the operators at the village level. With the lower than commercial rates of interest provided to its customers, Solanka has targeted the lower economic category of the market, having thus far installed two projects, one with 84 solar home systems in the village of Morapathawa, and the other with 77 systems in Thorawa. This has been possible since the funds for lending have been provided as grants. However, it will be difficult to sustain this scheme with commercial level funding, unless interest rates are increased and loan repayment period is reduced. However, this will naturally exclude the current target market of this organization. Thus, the challenge for Solanka is to secure further grant funding to replicate such projects. Its biggest merit has been to prove that the village has the capacity to implement and manage PV electrification projects. Solanka had the provincial government's patronage and support when the selection of areas for implementation was made jointly. The project has an interesting feature in that the 12-V lamp units and the simple electronic controllers are manufactured at the village level. Also, a village level repair unit has been started where defective battery cells can be replaced to lengthen the life of the battery. Loan repayments to date for both projects are 100% due to the grass roots level service that is provided to users. For instance, even when a battery fails, the user immediately gets a replacement while the old one is being repaired or serviced. The Colombo-based head office focuses on long-term strategic planning and also imposes the accounting controls with audits of all accounting operations in the process of selecting recipients and collecting repayments. On the basis of the experience of these two projects, its original promoter has established a commercial solar company called RESCO as a subsidiary of Selco-USA.

A counterexample is the Pansiyagama 1000 homes project, funded by the Sri Lankan and Australian governments, which has a very low repayment rate in spite of the very favorable finance scheme applied. Hence, it can be considered a failure, although technically over 90% of the systems are still operating. This project was politically motivated, and was implemented by the National Housing Development Authority (NHDA) of Sri Lanka, which attempted to implement a "grass roots" level program. However, the top-down manner in which it was done resulted in poor community level involvement and poor management infrastructure. The systems installed were more sophisticated than the normal SHS being installed elsewhere in the country and had a typical cost ranging from Rs. 20 000 (US \$571) to Rs. 32 000 (US \$914), depending on the size of the module and number of lamps. This led to a monthly payment from Rs. 75 (US \$2.14) to Rs. 135 (US \$3.85), depending on the cost of the unit (US \$1 = Rs. 35 in 1990), which turned out to be unrealistically low. According to a socioeconomic survey conducted by the Marga Institute of Sri Lanka, it was found that most households could afford to pay much more for the system. However, since the payments by households were set at nominal terms, their value has been eroding with inflation. At some point in time, the infrastructure for collecting repayments broke down as a result of bureaucratic problems, and some initial technical problems in the systems set a precedent for nonpayment, which was most difficult to break later. Some of these problems have been fixed after the NHDA handed over the maintenance and money collection duties to Power & Sun in 1991. However, the

repayments remain around 50%, as the cost of collecting the money is much more than the actual collections due to the low monthly payment. This means that over-subsidizing solar photovoltaics has a negative effect on the dissemination of solar photovoltaics through the business route. This project has demonstrated that solar photovoltaics is an appropriate technology, but the implementing methodology used for the project was not sustainable and as a result was found detrimental to the commercial dissemination process of solar home systems in Sri Lanka.

23.4.6 Water Pumping in the Sahel

The Regional Solar Programme (RSP) was one of the early systematic programs to apply PV technology to solve pressing problems in the Sahel region of sub-Saharan Africa. Financed by a grant of 34 million ECU from the European Commission, to cover the cost of PV equipment and other procedures such as training, information and public awareness activities, regional coordination and technical assistance, this program was launched in 1989. The goal of the RSP was to install almost 1.4 MWp of PV modules (about 3.5% of the world market at that time) in water-pumping systems, vaccine refrigerators, community lighting and battery-charging stations. At the end of the program, a total of 626 pumping systems and 644 community systems had been installed and a wealth of lessons learned.

The principal objectives of the RSP were [55] to improve the accessibility of water in both quantity and quality, to improve the economic condition of the villagers by development of complementary resources through gardening, to reduce the time spent in procuring drinking water, to train personnel for project management, to create management groups for the solar equipment and to develop and adopt a legal framework for operation of the equipment with contractual structure of the relations between users and private companies.

Not all specific goals and objectives originally planned were fully met, but important lessons were derived. The drinking water component of the program took more than 90% of the installed PV power, so the lessons learned apply basically to this application. Solar pumping was found more affordable than diesel motor pumping, by about a factor of two per cubic meter of water. Compared to the per habitant cost of manual water rising pumps (50 ECU), borehole considered, investment on PV pumping systems was slightly higher (55 ECU), but the service quality of PV pumps was superior. Of the total installed cost, 31% was for the supply of the PV system, 11% for installation, 12% for regional activities (including coordination, quality control, tests, monitoring and the like) and 46% for the distribution network, water tower and other reception infrastructure.

One mode of management of the water supply system used in some communities was directly inspired by the management of water points equipped with manual pumps through a village water committee. This management system, however, was not effective owing to a number of difficulties, including an imperfect mastering of the accounting tools and a quasisystematic confusion of the responsibilities assigned to the principal members of the committee. Other communities preferred delegating the management of the entire system to a private-type body on a fee basis or to a communal-type body. These latter forms of management seemed better suited to the local conditions than the water committee scheme.

The idea of using PV technology to improve productivity of market gardening and farming was finally abandoned, hence the prospects of PV technology in Sahel were found in meeting specific domestic electrical needs (lighting, radios and TV sets), in pumping drinking water and in telecommunications.

23.5 TOWARD A NEW PARADIGM FOR RURAL ELECTRIFICATION

The problem of rural electrification has been traditionally handled by conventional means in a process of successive approximations. In this process, the most remote and dispersed population is attracted to larger population centers, which are then served by a mini electrical local grid, fed by diesel gen-sets or small hydroelectric generators. As the load increases, a point is reached at which extensions of the main grid become economically viable. This process is known as *pre-electrification* among electric companies and has been the basic growth mechanism of the interconnected system in rural areas. Although effective from a purely technical-economic point of view, this pre-electrification process has several downsides. From the social point of view, it forces people to leave their place of origin to create larger population centers, which in turn induces the need for the central provision of other services and puts a larger stress on the environment.

The term pre-electrification is being used nowadays by some authors in reference to PV rural electrification and, in some cases such as the CEMIG example above, the operational scheme is also being transported. However, there are a number of reasons to think that using the term pre-electrification in the context of photovoltaics is not appropriate. Furthermore, transporting the concept is bound to cancel the advantages offered by photovoltaics to create a new path for rural electrification. First, from the purely technical point of view, photovoltaics offers the possibility of supplying high quality electrical services even to the most remote sites, without the need for relocating people or eventually having to resort to grid extensions. Because of its modular nature PV systems can grow in pace with the load. Furthermore, this vision is compatible with current trends in the electrical sector toward distributed generation systems, and is supported by the development of more efficient electrical appliances, the miniaturization of electrical technologies and the progress being made in electronic devices for system supervision and load management. There are also environmental reasons that lead the notion that the local generation of electricity using renewable and nonpolluting energy resources is more convenient than building kilometers of electricity lines across ecologically sensitive areas. Local generation of electricity also offers the possibility for local management and, hence, for active community participation in the process of self-development.

On the other hand, there is evidence that the traditional electrification process based on the old paradigm of *Delivering electricity to rural people* has frequently lent itself mainly to fulfill the political need to improve the electrification statistics rather than to serve the real needs of people. Thus, it is not uncommon to observe rural communities with access to the grid, where a good portion of the households are not connected, usually because of lack of money to pay for the connection fee, or because the secondary distribution network only reaches the center of the community, leaving the rest of the population unserved. Therefore, if electricity supply is to be used as a tool for development, that is understood as increased life expectancy, more knowledge and a better

standard of living [56], then the present rural electrification paradigm must be urgently changed to: “*Increasing the access of the rural poor to electricity-based services*”. This set of services includes health, clean water, education, food preservation, entertainment and the possibility of engaging in productive activities.

Under this perspective, current PV rural electrification activities represent a landmark of the transition period into a new rural electrification scheme to substitute the old one with better results. However, the *new electrification* requires among other things, a new culture for electricity supply and use in rural areas, an *ad hoc* legal framework, new business practices within the electrical sector, innovative financial mechanisms, new and better technologies and appropriate institutional schemes. Thus, the actual value of programs and projects currently underway has to be weighted not only in terms of the number of PV users in rural areas, but also in terms of the benefits PV installations are bringing to the population. Also important to gauge the effectiveness of current PV rural electrification projects is the relevance of the lessons learned from them, which will allow the implementation of improved schemes for successful project replication.

This new paradigm for rural electrification should in turn be embedded in the broader concept of rural energy supply, which calls for a timely supply of useful energy in a variety of forms, so that people can have better opportunities to improve their own quality of life, to foster local economic development and to protect the environment.

REFERENCES

1. Kemp W, *The Flow of Energy in a Hunting Society. Energy and Power*, A Scientific American Book, 55–65, W.H. Freeman and Company, San Francisco, CA (1971).
2. Rappaport R, *The Flow of Energy in an Agricultural Society. Energy and Power*, A Scientific American Book, 69–80, W.H. Freeman and Company, San Francisco, CA (1971).
3. Cook E, *The Flow of Energy in an Industrial Society. Energy and Power*, A Scientific American Book, 83–91, W.H. Freeman and Company, San Francisco, CA (1971).
4. *World Energy Assessment: Energy and the Challenge of Sustainability*, United Nations Development Program, United Nations Department of Economic and Social Affairs, World Energy Council (Sept. 2000).
5. *The Challenge of Rural Energy Poverty in Developing Countries*, World Energy Council, Food and Agriculture Organization of the United Nations (Oct. 1999).
6. Bowers B, *A History of Electric Light & Power*, History of Technology Series 3, P. Peregrinus, The Science Museum, London (1982).
7. National Energy Balance 1997. Energy Secretariat of Mexico.
8. Foley G, *Photovoltaic Applications in Rural Areas of the Developing World*, World Bank Technical Paper Number 304, Energy Series (1995).
9. Lorenzo E, Photovoltaic Rural Electrification, *Prog. Photovolt.: Res. Appl.* **5**, 3–27 (1997).
10. Urbano J, “Introduction to the Design, Operation and Application of Photovoltaic Systems – The CIEA Experience (in Spanish)”, *Proc. 4th Mexican National Solar Energy Society Meeting* (San Luis Potosi, Mexico, Oct. 1–3, 1980).
11. Urbano J, *Rev. Sol.* **16**, 10–13 (1989).
12. Martinot E, Ramankutty R, Rittner F, *The GEF Solar PV Portfolio: Emerging Experience and Lessons*, Monitoring and Evaluation Working Paper 2, GEF pre-publication draft (Aug. 2000).
13. Huacuz J, Agredano J, “Beyond the Gris: photovoltaic rural electrification in Mexico”, *Prog. Photovolt.: Res. Appl.* **6**, 379–395 (1998).

14. Ramos R *et al.*, *Photovoltaic Solar Energy: An Option for Rural Electrification in Cuba (in Spanish)*, Solar Energy Research Centre of Cuba (1995).
15. *Clean Water with Clean Energy: Drinking Water Provision in Remote Regions with Decentralised Solar Power Supply*, INCO-DC Project ERBIC18CT960104, Final Report, European Commission, FhG-ISE, Freiburg, Germany (2000).
16. Sapiain R *et al.*, *Solar Photovoltaic Pumping in Peasant Communities and New Productive Agricultural Applications in Arid Zones in the North of Chile (in Spanish)*, Renewable Energy Centre, Engineering Faculty, University of Tarapaca (Oct. 1997).
17. Ahm P, "Small PV Powered Medical Equipment", *UNESCO World Solar Summit* (July 1993).
18. Muhopadhyay K, Sensarma B, Saha H, *Sol. Energy Mater. Sol. Cells* **31**, 437–446 (1993).
19. *De l'eau solaire pour la Somalie*, Systemes Solaires, No. 100 (1994).
20. *Les lampes portables solaires*, Systemes Solaires, No. 100 (1994).
21. Flores R *et al.*, "Characterization and Evaluation of 30 PV Ovonic-Unisolar Solar Home Systems (in Spanish)". *Proc. ISES Millennium Solar World Forum* (Mexico City, Oct. 2000).
22. Huacuz J, Urrutia M, Eds, *Proceedings of the International Workshop Charge Controllers for Photovoltaic Rural Electrification Systems*, Electrical Research Institute Cuernavaca, Mexico (1998).
23. Nieuwenhout F, *Monitoring and Evaluation of Solar Home Systems: Experiences with Applications of Solar PV for Households in Developing Countries*, Report ECN-C-00-089, Netherlands Energy Research Foundation, Petten (Sept. 2000).
24. dos Santos R, Zilles R, PV Residential Electrification: A Case Study on Solar Battery Charging Stations in Brazil. *Prog. Photovol.: Res. Appl.* **9**(6), 445–453 November/December (2001).
25. European Commission, Directorate General for Energy; Universal Technical Standards for Solar Home Systems. Thermie B: SUP-995-96 (1998).
26. Electrical Research Institute, *Technical Specification for Rural Illumination Photovoltaic Systems (in Spanish)*, Revised Edition. Cuernavaca, Mexico, IIE (1999).
27. Martinot E, Ramankutty R, Rittner F, *Thematic Review of the GEF Solar PV Portfolio: Emerging Experience and Lessons*, Global Environment Facility Working Paper, pre-publication draft (June 2000).
28. Huacuz J, Martinez A, "Renewable Energy Rural Electrification: Sustainability Aspects of the Mexican Programme in Practice", *Nat. Res. Forum* **19**, 223–231 (1995).
29. Huacuz J, Gonzalez C, Uria F, "The role of Comision Federal de Electricidad in the Mexican photovoltaic rural electrification program", *Proc. IERE Workshop Photovoltaic Rural Electrification and the Electric Power Utility*, IIE-EPRI (Cocoyoc, Mexico, May 1995).
30. Flores C, "Expanding PV Rural Electrification with Local Industry and Technology: The Mexican Experience", *Proc. Sustainable Development of the Rural World. Decentralized Electrification Issues* (Marraketch Marruecos, Nov. 13–17, 1995).
31. Huacuz J, "Sustainable Energy in Rural Zones within the Process of Modernization of the Energy Sector in Latin America and The Caribbean (in Spanish)", *Proc. Enerlac '98, IV Energy Conference of Latin America and The Caribbean* (Dominican Republic, 1998).
32. Aguilera T, *Energía Solar Fotovoltaica en el Ambito de la Cooperación al Desarrollo*, Caso de Estudio: El Altiplano Boliviano, Tesis Doctoral, Universidad Politécnica de Madrid, Escuela Superior de Ingenieros en Telecomunicaciones. Madrid (1995).
33. Nieuwenhout F *et al.*, *Monitoring and Evaluation of Solar Home Systems. Experiences with Applications of solar PV for Households in Developing Countries*, Report ECN-C-00-089, Netherlands Energy Research Foundation (Sept. 2000).
34. Hankins M, *Solar Rural Electrification in the Developing World*, Four Case Studies: Dominican Republic, Kenya, Sri Lanka and Zimbabwe. Solar Electric Light Fund (1993).
35. Cabraal A *et al.*, *Best Practices for Photovoltaic Household Electrification Programs*, Lessons from Experiences in Selected Countries, World Bank Technical Paper Number 324, Asia Technical Department Series, The World Bank (1996).

36. Martinot E *et al.*, *World Bank/GEF Solar Home Systems Projects: Experiences and Lessons Learned 1993–2000*. Renewable and Sustainable Energy Reviews, **5**, 39–57 (2001).
37. Fabris A, Sotelino E, *Programas de Electrificación Rural en el Cono Sur de América Latina*, Los Recursos Energéticos Renovables y las Políticas de Electrificación Rural, 109–123 (1997).
38. Frigerio A, “Financiamiento del Programa de Abastecimiento Eléctrico a la Población Rural Dispersa de Argentina”, *Seminario de Inversiones y Negocios para Energías Renovables en América Latina*, (Quito, Ecuador, 14–16 de septiembre, 1998).
39. Castiella H, *Proyecto de Electrificación Rural Mediante Energía Solar Fotovoltaica en Bolivia*, Agencia Española de Cooperación Internacional (La Paz, Bolivia, 1993).
40. Smith P, International Project CRE <http://www.rsvp.nrel.gov> (1996).
41. INTI K’ANCHAY, Informative Bulletin No. 1. Energética (Sept. 1998).
42. INTI K’ANCHAY, Informative Bulletin No. 2. Energética (July 1999).
43. *Renewable Energy Rural Electrification Projects for the Cochabamba-Bolivia Department (in Spanish)*, Comité de Coordinación Interinstitucional (Cochabamba, April 1995).
44. Barbosa E *et al.*, *Toward a Sustainable Future for the Use of SHSs for Rural Electrification in Brazil*.
45. Ribeiro C, Bezerra P, Zilles R, Moskowics M, *Brazilian Strategy on PV Dissemination* (1998) Update.
46. Quintans L, Lima J: *Prodeem: realizações e progressos*, Cresesb Informa, Año III, No. 4 (Diciembre, 1997).
47. Galindo M, Lima J, Quintana L, dos Santos R, *Technical Aspects of the Brazilian PRODEEM Program for Rural Electrification Based on Renewables*.
48. Silva S, *PRODEEM. IV Encontro Forum Permanente de Energias Renovables* (Recife, Pernambuco, Brasil, 6 a 9 de Outubro de, 1998).
49. Diniz A, “Programa de Implantado de Sistemas Fotovoltaicos da CEMIG”, *IV Encontro do Fórum Permanente de Energias Renovaveis* (Recife, Pernambuco, Brasil, 6 a 9 de Outubro de, 1998).
50. dos Santos P, “Programa de Implantação de Bombeamento de Agua FV da COPASA”, *IV Encontro Forum Permanente de Energias Renovaveis* (Recife, Pernambuco, Brasil, 6 a 9 de Outubro de, 1998).
51. Huacuz J, Martínez A, *ATAS Bull.* **8**, 177–194 (1992).
52. Huacuz J, Martínez A, *Mexico: Rural Electrification Program with Renewable Energy Systems*, EDG, No. 5, 15–20 (1996).
53. Gunaratne L, “Funding and repayment management of PV system dissemination in Sri Lanka”, *Proceedings on the Conference on Financial Services for decentralized Solar Energy Applications II*. Harare, Zimbabwe, 20–23 (Oct. 1998).
54. Gunaratne L, Solar PV Market Development in Sri Lanka. GEF Workshop: Making a Difference in Emerging PV Markets. Marrakech, Morocco, September 24–28 (2000).
55. Regional Solar Programme, *Lessons and Perspectives*, European Commission (DGVIII) (Dec. 1999).
56. UNDP, *Human Development Report 2001* (2001).

This Page Intentionally Left Blank

24

Financing PV Growth

Michael T. Eckhart¹, Jack L. Stone² and Keith Rutledge³

¹Solar International Management, Inc., Washington DC, ²National Renewable Energy Laboratory, Golden Colorado, ³Renewable Energy Development Institute, Willits, California

This chapter presents an overview of the financing of photovoltaic PV growth. Solar energy is free, but the equipment to collect it and convert it to electricity is not. PV systems are highly capital intensive, hence the method and cost of financing will affect the economic viability and the affordability of PV systems to the end users (see Reference [1]).

24.1 HISTORICAL DEVELOPMENT OF PV FINANCING

Programs for the financing of photovoltaics began in the late 1980s. The practice of financing photovoltaics has evolved slowly and has not been entirely successful to date:

1987: The Indian Renewable Energy Development Agency (IREDA) was founded; today, it is still the only major national institution that is dedicated solely to the financing of renewable energy.

1989: The World Bank established The Solar Initiative as a way of drawing attention to the environmental and developmental benefits of solar energy (see Reference [2]).

1990: The Solar Electric Light Fund (SELF) began pioneering projects in India, Sri Lanka, Nepal, China, Indonesia, Solomon Islands, Brazil, Zimbabwe, Senegal, Uganda, and South Africa, demonstrating the viability of Solar home systems (SHS) in the developing countries and setting the stage for many PV programs around the world.

1992: The Sustainable Development conference was held in Rio, leading to additional funding of the Global Environment Facility (GEF).

1994: The world's first PV loan program by a bank was established by KM Udupa, chairman of Malaprabha Grameena Bank, the rural lending affiliate of Syndicate Bank, in Hyderabad, India.

- 1995: The Pocantico Conference was convened by the Rockefeller Brothers Fund to debate strategies on mobilizing PV financing in the developing countries.
- 1996: The Japanese government announced a national PV strategy that included a 50% subsidy for residential rooftop applications, substantial increases in government funding of PV R&D, and government subsidies of interest rates to encourage banks to lend for PV applications. In Europe, Triodos Bank established its Solar Investment Fund (SIF), a \$3 million fund focused on end-user financing in the developing countries. In the United States, a joint task force of the World Bank Group and charitable foundations led to plans for the Solar Development Group (SDG) and the proposed SolarBank Program.
- 1997: The Shell–Escom joint venture was established in South Africa, providing nongrid electric service to rural households using a “fee-for-service” strategy. The World Bank closed a GEF-supported PV loan facility in Indonesia and laid out plans for PV loan programs in China, Argentina, and other countries.
- 1998: The PV Market Transformation Initiative (PVMTI) was launched in India, Kenya, and Morocco, sponsored by the International Finance Corporation (IFC) and funded by the Global Environmental Facility (GEF). In the United States, Astropower became the first successful Initial Public Offering (IPO) by a venture capital–backed PV company.
- 1999: Germany launched its 100 000 Roofs PV Program with a “feed-in tariff” for PV electricity and a national program of low-interest loans, which has been successful.
- 2000: The IFC’s Renewable Energy and Energy Efficiency (REEF) Fund, a \$100 million equity fund for such projects in the developing countries, raised its initial capital. In the United States, the Renewable Energy Development Institute (REDI) formalized its PV loan brokerage operation.
- 2001: The Solar Development Group, including the \$20 million Solar Development Foundation (SDF) and the \$29 million Solar Development Capital (SDC) fund, was launched by the World Bank, IFC, GEF, US Foundations, and European governments and donor agencies, to fund PV enterprises in the developing countries.
- 2002: Low-interest loan programs have begun to appear around the world, from California to Kenya.

Historical information from around the world suggests that financing will play a pivotal role in creating and sustaining the growth of PV market demand:

Developing countries: PV companies in India, Indonesia, South Africa, and the Dominican Republic report that only 2 to 5% of prospective purchasers can afford to buy a PV system with cash, while approximately 50% could buy if provided with reasonable third-party financing (please see Section 24.5 for details).

Germany: The KfW made low-interest loans available in conjunction with a DM 0.99 feed-in tariff, igniting a booming PV market that increased from nearly 0 MW in the year 1998, to 40 MW in the year 2000, and an estimated 75 MW in the year 2001 (see Reference [3]).

Indeed, the evidence suggests that market demand for photovoltaics can increase by tenfold with the availability of reasonable end-user credit, from approximately 5% of end users who can pay cash, to 50% of end users who could buy if credit on reasonable terms is made available.

24.2 CAPITAL REQUIREMENTS

The worldwide rate of PV installations grew at approximately 15% per year in the early 1990s, and accelerated to an average growth rate of 30% per year in the late 1990s. What will be the future growth rate of PV markets, and how much capital will be needed to fund the growth of PV markets and industry?

24.2.1 Market Drivers

Photovoltaics are becoming a factor in the development of the rural areas of the world where over 35% of the world's population – 56% of the rural population – live without the benefit of electricity from the utility grid, totaling some 2 billion people or 400 million households (see Reference [4]). There, photovoltaics have energy value.

The second major driver of PV growth is the public policy on environment and sustainable development. Climate Change is driving global action through the Kyoto protocol and the separate US Climate Change Strategy. As a result of environmental concerns, we are seeing accelerated growth of PV markets in Japan, Europe and, to a lesser extent, the United States. Much work still needs to be done to monetize environmental values and turn market potential into reality (see Reference [5]).

24.2.2 Growth Outlook

What level of growth can be expected in the future? Scenarios of 25 and 50% annual growth bracket the likely range of outcomes. As illustrated in Figure 24.1, the difference between 25 and 50% compounded growth is substantial:

25% Growth Rate: At a growth rate of 25% between the years 2000 and 2010, the annual amount of PV installations will reach 2500 MW per year by 2010.

50% Growth Rate: At a growth rate of 50% between the years 2000 and 2010, the annual amount of PV installations will increase to over 16000 MW per year by 2010.

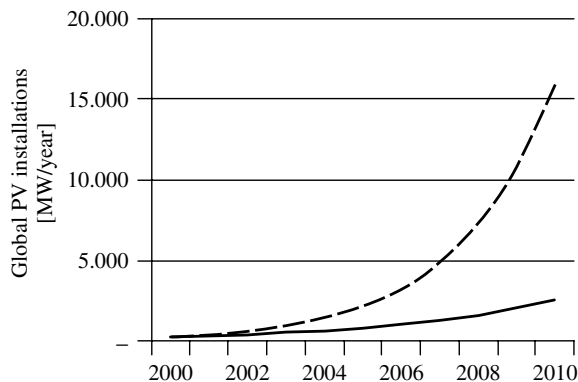


Figure 24.1 PV growth scenarios

24.2.3 Capital Requirements

How much capital will be needed? Table 24.1 presents estimates of the amounts of capital that will be required to support the two scenarios of PV market growth. In the year 2010, modules are assumed to cost \$1.50/Wp, and systems to cost \$3.00/Wp (in 2000 constant dollars). If so, the global PV industry will be doing between \$3.8 and \$23.8 billion of module shipments, and between \$7.7 and \$43.6 billion of system installations in the year 2010, under the 25% and 50% growth rate scenarios, respectively. The amounts of capital that will be required to support these levels of growth are estimated as follows:

PV factory investment requirements: The investment cost of PV factory capacity is on the order of \$2 to \$3 million per MW/year of capacity in the year 2001. This is expected to decline to \$1 million per MW/year of capacity as the scale of the new factories continues to increase (i.e. a 100 MW/year factory will cost \$100 million to build). Assuming that the PV factory capacity will require an investment of \$1 million per MW/year over the next 10 years, the amount of capital to be raised for investment in PV factories will be between \$3.1 and \$19.0 billion.

Working capital requirements: The operations of the factories and sales distribution channels for PV equipment must also be financed, including inventory and receivables. Assuming that 60 days of work-in-process inventory, 60 days of finished goods inventory, and 90 days of receivables need to be financed, the PV industry will require between \$1.9 and \$11.9 billion for working capital financing.

End-user financing requirements: Market indicators suggest that as much as 80 to 90% of the PV market will require end-user financing. Assuming that grid-connected systems represent 50% of the world market, and that 80% of the end users receive an average 80% loan, and assuming that off-grid rural electrification represents 30% of the world market, and that 50% of those end users receive an average 80% loan, then the end-user financing requirement to support PV industry growth will be \$20.6 to \$82.8 billion over the next 10 years.

Table 24.1 Global capital requirements to fund PV growth

	25%/Year growth scenario	50%/Year growth scenario
Annual amounts in 2010:		
PV shipments	2561 MW/year	15 858 MW/year
Module revenues	\$3.8 billion/year	\$23.8 billion/year
System revenues	\$7.7 billion/year	\$43.6 billion/year
Cumulative amounts 2000–2010:		
PV shipments	11 700 MW	47 000 MW
Module revenues	\$23.4 billion	\$94.0 billion
System revenues	\$46.8 billion	\$188.1 billion
Global capital requirements (US \$):		
PV factory investment	\$3.1 billion	\$19.0 billion
Working capital	\$1.9 billion	\$11.9 billion
End-user financing	\$20.6 billion	\$82.8 billion
Total capital required	\$25.6 billion	\$113.7 billion

Source: Eckhart, Overview, 2001

In sum, the PV industry must mobilize at least \$25 billion in capital to support a 25% annual growth rate, and as much as \$114 billion in capital to support a 50% growth rate, over the next 10 years.

24.3 FINANCIAL CHARACTERISTICS OF PV

This section addresses the characteristics of PV that are essential considerations in the financing of end-use applications, over and above standard lending issues like credit worthiness of the borrower.

Geographic location: The average amount of solar energy hitting the Earth is about 1 kW/m². The amount of solar insolation varies by latitude and by regional weather patterns. There is an approximate 2:1 variation in the amount of solar insolation across most of the inhabited world. A 1 kW PV system would generate a 900 to 1000 kWh per year in Germany, and as much as 1800 to 2000 kWh per year in desert locations like Arizona or South Africa. The amount of sunlight varies on an annual cycle, and also as much as $\pm 10\%$ year to year due to atmospheric and weather conditions (see Reference [6]).

Facility design and cost: The cost of a PV system includes the cost of PV modules (typically 40 to 60% of the total), balance-of-system (BOS) equipment (such as batteries, controllers, inverters, switches, fuses, etc.), and services (design, architecture, engineering, procurement, construction, installation, and postinstallation O&M). PV system costs have come down steadily over the past 25 years, and are now typically \$5 to \$15 per installed watt. Financiers should be given evidence that the buyer has shopped for a quality system, from a qualified supplier, at a reasonable price.

System efficiency: System efficiency is the key operational characteristic of a PV system, measuring its conversion of solar insolation at the site to output DC or AC electricity. Most of the publicity about PV efficiencies refers to PV cell efficiencies, typically ranging from 5 to 10% for amorphous silicon, 8 to 12% for CIS and CdTe thin-film technologies, 12 to 18% for crystalline silicon, and 25% and higher for cells that are used in concentrator systems (see Reference [7]). The efficiencies of PV cells in research laboratories are even higher and they are improving steadily. But the key for financing is not the latest development in PV cell research; it is the typical, guaranteed output of an entire PV system in its end-use application. The conversion efficiency of the entire system is affected by the efficiency of the cell, reduced somewhat when placed in a module, then further reduced by losses in the wiring and BOS equipment. Thus, PV system efficiencies are about 60 to 80% of PV cell efficiencies (i.e. the efficiency of a system using 16% efficient cells is likely to be in the range of 10 to 13%).

Useful lifetime: The useful lifetime of a PV system is important because it determines the amount of time a financier can allow for repayment of a loan or lease. PV modules typically come with warranties of 10 to 25 years – assuring the owner of 80% to 90% of the module's rated output over the warranty period. From a lender's point of view this is a positive factor in financing. With such guarantees, the modules will have future value as collateral. The weak link in the financing of PV systems is, however, the fact that the useful life of BOS equipment is much shorter and less predictable. BOS equipment often comes with warranties of 90 days to one year, and useful lives

can range from three to five years for batteries, and from 5 to 10 years for electronic inverters, converters, and controllers. The key to the long life of the full system is therefore ongoing maintenance and repair by a qualified supplier.

Operations and maintenance cost: Whereas photovoltaics have a reputation of being “maintenance free,” this only applies to the PV modules. PV systems actually require regular checking and maintenance like any electrical system. Financing should be contingent on there being a plan and/or contract for ongoing maintenance service by the installer or another qualified electrical contractor.

Residual value: The residual value of a PV system is the amount that it can be sold for (“liquidated”) at the end of the loan or lease. A lender wants assurance that the system’s value is never less than the outstanding balance on the loan. A leasing company needs assurance of good residual value, since this is what the leasing company will own at the end of the lease. Lack of evidence on the collateral/residual value of PV equipment is one of the weak points in PV financing today.

Tax treatment: A key issue for financing is how photovoltaics is treated for tax purposes. This typically includes sales and property tax abatements, income tax deductions and credits, and accelerated depreciation schedules. These factors can be instrumental in determining the economic viability of a PV system and the timing of cash returns to the owner.

Regulatory treatment: A factor that is increasingly important is how photovoltaics is treated in government regulations. A key regulatory issue for grid-connected applications is whether photovoltaics qualifies for net metering. That is, whether electricity generated by the PV system can be applied to offset retail electricity purchases from the utility. If photovoltaics qualifies for net metering, then the value of the PV’s output electricity equals the retail rate, typically 8 to 15 ¢/kWh in Europe and the United States, and over 20 ¢/kWh in Japan. If photovoltaics do not qualify for net metering, then the electricity is only worth the wholesale “avoided cost” rate, which is typically 2 to 5 ¢ per kWh. As of the year 2002, over 30 US states and several countries like Germany and the Netherlands, have adopted net metering or equivalent regulatory treatment.

Economics of the application: The previous factors related to the PV system. But what really separates photovoltaics from other power-generation technologies is the degree to which photovoltaics becomes an essential element of an end-use application – such as providing “essential electricity” for remote telecommunications, water pumping, home lighting, and other off-grid applications, or providing “clean electricity” for homes, commercial buildings, and other on-grid applications. A key question for the financier is whether the end-use application is economically viable, and the degree to which the use of photovoltaics makes it more or less so. Please see Section 24.4 for additional discussions on PV economics.

Codes and standards: Financing should be conditional on a PV system meeting all applicable codes and standards, and this will vary by end-use application, whether the PV system is integrated into the structure of a building, on the roof of a residential home, or in a field serving a remote application. The key US national standards include the National Electric Code and special standards for interconnection to the utility grid that have been promulgated by the Institute of Electrical and Electronic Engineers (IEEE) and Underwriters Laboratories (U/L). There is also a need to meet all applicable local building and electrical codes, which vary by locality (see Reference [8]). European

standards organizations have promulgated a similar set of codes and standards for photovoltaics within the European Union. For solar home systems in the developing countries, the PV Global Acceptance Program (PV/GAP) establishes a testing certification protocol. The adoption of these codes and standards is one of the keys to future financing of PV, as they will build credibility with lenders and investors.

On the basis of the above, one sees that the characteristics of photovoltaics present a complex case. The financial merits of photovoltaics depend on location, cost and quality of the system, efficiency output of the system, useful lifetime, O&M cost, residual value, tax treatment, regulatory treatment, viability of the end-use application, adherence to codes and standards, and credit worthiness of the end user.

24.4 FINANCING PV FOR GRID-CONNECTED RESIDENCES

A major opportunity for PV growth in European, Japanese, and US markets is the grid-connected, residential rooftop system, typically 1.0 to 4.0 kW each. Approximately 110 MW of grid-connected systems were installed in Japan, 75 MW were installed in Germany, and 15 MW were installed in the United States in the year 2001.

24.4.1 Impact of Loan Terms on End-user Cost

Table 24.2 illustrates how the terms of financing can drive monthly payments on a PV system. The example uses a 2.5 kW residential grid-connected PV system costing \$8.00 per installed watt (Wac). Credit card type debt (10 year, 18% interest) on a \$20 000 residential rooftop PV system would yield payments of \$437/month. The monthly payment drops to just \$121/month if the PV system is included in a new home mortgage or financed with a low-interest loan.

It is clear from the above analysis that the preferred way to finance a residential PV system is the primary home mortgage loan, if possible. A longer-term loan results in lower monthly payments, but increases interest paid and hence the total amount of money paid for the system. As a rule of thumb, the cost of money is approximately equal to the cost of the PV system with an 11-year, 11% loan. A longer-term loan or a higher interest rate would cause the interest payments to be more than the cost of the PV system, illustrating once again the impact of financing on the viability of photovoltaics.

Table 24.2 Monthly payments on a 2.5-kilowatt rooftop PV system

Loan type	Term [Years]	Interest rate [%]	Monthly payment [\$/month]
Credit card	7	18	437
Credit line	10	12	295
Home equity loan	15	8	195
Home mortgage	30	6	121

24.4.2 Types of Residential Financing

There are many financing alternatives available in the residential sector that could be applied to the financing of a PV installation:

Unsecured loan: Credit cards have become a significant source of financing, even though interest rates are typically 12 to 24%. Commercial lenders also provide unsecured signature loans and personal lines of credit at interest rates of 10 to 20%. Terms vary from one to ten years.

Equipment secured loan: There is some use of contractor-originated Retail Installment Contracts that hold security on the equipment until the contracts are paid off.

Home mortgage loan: Real estate secured loans are by far the most common and available form of credit to the residential sector. Loan products range from 5- and 10-year home equity loans, to 15-, 20- and 30-year primary mortgage loans, carrying either fixed or variable interest rates.

Energy-efficient mortgage (EEM) loan: In the United States, the EEM is offered by many of the national residential lenders and is designed to allow additional income credit from energy savings to be used in qualifying for a loan. This program is also called Energy Star. Japan and several European countries have similar programs.

Subsidized and targeted loan programs: Certain population groups – including, for example, low-income, minority, and veterans – are eligible for special terms and rates from a variety of specialized lenders. Also, there are special loan programs for designated locations such as rural areas, economically depressed areas, and inner-city urban areas. Government support for these programs ranges from direct loans, to loan guarantees, to interest subsidies.

Utility financing programs: A number of electric utilities have established special loan programs for energy efficiency and renewable energy. In the United States, the Sacramento Municipal Utility District (SMUD), the Los Angeles Department of Water and Power (LADWP), the Long Island Power Authority (LIPA), and the City of Austin Electric Department – all being nonprofit municipal utilities – have established PV financing programs (see Reference [9]). In Austin, the loans are unsecured, ranging from \$1000 to \$9000, with terms of three to ten years, at interest rates of 4.00 to 5.99%. The US cooperative utilities are also looking at PV financing programs. In Germany, municipal utilities created the first real market for photovoltaics between the years 1997 and 1998, applying the “Aachen model” of long-term power purchase contracts.

Government loan programs: A number of states in the United States are establishing clean energy funds, typically administered through the in-state utilities and banks. In New York, a \$130 million fund has been established. Idaho’s Renewable Energy Loan Program finances residential PV in amounts ranging from \$1000 to \$10000, subject to the application having a 10-year payback or less. California has established a special alternative energy financing trust and a new Power and Consumer Finance Authority. This is also happening around the world. In Germany, KfW has established a national loan program for residential installations, offering 10-year loans at a 2% interest rate. In Japan, interest rates on loans for residential PV systems are subsidized. In India, IREDA has an ongoing program of lending for photovoltaics and other renewables.

24.4.3 Lender's Issues

Decisions about whether to make a loan will depend principally on the borrower's ability and willingness to repay the loan, indicated by past credit history and income. Loans secured by appreciating assets, such as real estate, have the longest terms and lowest interest rates, because the value of the collateral serves as additional protection of the loan. Lenders should ask several key questions in qualifying a loan:

- Is this installation economically advantageous for the borrower? The lender should understand whether the borrower is installing the PV system for economic or for environmental reasons.
- Can the system be easily installed by qualified contractors? Does it meet all of the applicable building codes and safety standards?
- How long will the system perform? Is there a warranty on the system? Is there a guarantee on performance over the life of the system?
- What will be the ongoing or recurring costs of operation, maintenance, repairs, and potential removal of the system?
- What are the energy-cost savings that the borrower will receive from owning the PV system? Are these savings certain enough to count as "income" for loan qualification purposes?
- What is the current market value of the system? How does this change over time? What is the likely residual value of the system at the end of the loan period?
- What are the risks on repayment? Technical? Economic? Others? Are the risks well known and understood?

24.4.4 Borrowers' Experience

A market research report prepared by the Regional Economic Research for the California Energy Commission (see Reference [10]) revealed the following:

- The main concerns singled out by residential consumers ranked system reliability, life, safety, and ongoing costs as more important than the initial cost of the system.
- The majority of residential end users (54%) preferred some form of loan financing over investing their savings – with 35% preferring a home equity loan, 22% a personal loan, and 7% a first mortgage.
- Residential end users were more likely to consider installing a solar system when: roofing the home (60%), remodeling (54%), and purchasing a home (50%) – all times when financing is normally utilized. Only 31% stated that they would be more likely to consider installing a solar system as a "stand-alone" purchase.

Market research by the US National Renewable Energy Laboratory (NREL) indicates that 60% of respondents are willing to pay at least \$25 extra per month for a rooftop PV system, 38% are willing to pay an additional \$50 per month, and 15% are willing to pay \$100 more per month. Regarding financing, 46% prefer long-term loans, while 36% prefer short-term loans (see Reference [11]).

24.4.5 Example Calculation

A 2.5-kW rooftop PV system costing \$8.00/Wac installed will cost \$20 000. Assuming an excellent location yielding a 22% capacity factor, the system will produce 1927 kilowatt hours per kW installed, per year, or 4818 kWh/year for the 2.5 kW system. The following is a brief assessment of the financial merits under several cases:

No incentives: If the government does not allow net metering, the value of the electricity will only be the wholesale rate that the utility pays for bulk energy. The PV system is not likely to be given capacity credit, so the value will be energy only, or about 2 to 4 ¢/kWh. The value of the output is therefore \$96.36/year to \$192.72/year. The system will have a simple payback in 103 to 207 years.

Net Metering: If net metering applies, then the value of the electricity is the retail rate (tariff), say, 10 to 15 ¢/kWh. In this case, the value of the output is \$481.80/year to \$722.70/year. The system will have a simple payback in 28 to 42 years.

Subsidy: If the government now provides a subsidy in the amount of \$4.50/Wac, leaving the owner's cost equal to \$3.50/Wac or \$8750, and net metering still applies, then the value of the output is still \$481.80/year to \$722.70/year, and the system will have a simple payback of 12 to 18 years, probably within negotiating range for an environmentally motivated end user.

Low-cost financing: The cost of financing will increase the total cost to the end user, and hence lengthen the payback period or rate of return on investment. A 10-year, 12% loan will add 72% to the total outlay by the owner, increasing system cost from \$8750 to \$15 486. The simple payback will be lengthened from 21 to 32 years. Conversely, if the interest rate is dropped to 5%, the financing will add only 15% to the total outlay by the owner, increasing system cost from \$8750 to \$10 105. Simple payback will be lengthened to 14 to 21 years, much more favorable than the higher-rate financing. While third-party financing lengthens the payback period, it makes the purchase more affordable by more people, based on monthly payments (see Reference [12]).

The analysis has shown that – with net metering, feed-in tariffs, tax credits, capital cost subsidies, and low-interest financing – residential rooftop PV can yield a payback in the range of 10 to 20 years, potentially enough for those who are motivated by the environment and sustainable development.

24.4.6 Improving the Financing of Residential PV

Several things can be done to improve the fit between photovoltaics and the home-mortgage lending industry. First, the debt/equity ratio should be relaxed, allowing a higher fraction of debt on a PV-powered home, reflecting the fact that the owner is prepaying the utility bill for 20 to 30 years. Second, the cost of the PV system should automatically increase the appraised value of the home. Third, the amount of savings on the borrower's utility bill should be added to the income for the purpose of the loan qualification calculation, reflecting the borrower's lower cost of living with the PV option. With these practices, the lending industry would become an enabler of, rather than a constraint on, PV growth.

24.5 FINANCING PV IN RURAL AREAS OF DEVELOPING COUNTRIES

Financing programs for PV in the rural areas of developing countries is the focus of the World Bank, the IFC, aid agencies from the OECD nations, charitable foundations, and a number of special-purpose funds such as the Solar Development Group and the proposed SolarBank Fund.

24.5.1 Rural Applications

There are four principal applications for photovoltaics in the rural areas of developing countries (see Reference [13]):

Solar home systems (SHS): This basic battery-based electrical system with a solar PV charger includes a PV module – typically 20 Wp in Kenya, 35 Wp in southern India, and 50 Wp in Indonesia and the Philippines – plus a battery, charge controller and wiring, receptacles, outlets, and switches for lighting and communications. Financing can be justified on a cost basis, the monthly payments for the SHS are less than a family's existing costs for kerosene, candles, and dry cell batteries (see Reference [14]), but the stronger basis for lending is the upliftment of family lifestyle and income that generally accompanies rural electrification. A 35-W solar home system costs US \$300 to \$750, depending on the manufacture, import duties and taxes (if applicable), the quality of components, and installation. Financing is just beginning to be made available through banks, nonbanking finance companies, microcredit lenders, cooperatives, and other sources. Typical financing for an SHS in a developing country is a 1- to 3-year loan at 18 to 36% interest, or a fee-for-service payment that approximates a lease.

Water pumping for irrigation: The financing of a PV-powered water pump for irrigation can be justified on the basis of the economic impact on the farm, typically the addition of a third crop to what was a two-crop farm, or higher yield per acre as a result of irrigation. A 900-W PV pumping system can cost \$5000 to \$8000, a cost that can be recovered in as little as one year in some extraordinary cases, and can be the least-cost option on a life cycle-basis for many remote farms, especially when compared to the costs of diesel power. PV-powered water pumping is heavily subsidized in most cases today, ranging from 100% grants from European donor agencies to a 50% subsidy from the government of India.

Microenterprise (“Productive Uses”): There are many applications for photovoltaics in small businesses. Financing can be established through microcredit models of group lending, and justified on the basis of the expected cash flows of the microenterprise businesses. PV systems can extend the operating hours with lighting, improve working conditions with lighting and fans, power mechanization and product preservation (drying and refrigeration), and enable communications. PV systems for the microenterprise range in cost from \$300 for a minimal PV lighting system to \$10 000 or more for a system that is capable of running a significant level of factory motors or refrigeration (see Reference [15]).

Institutional uses: Photovoltaics is being applied for lighting, communications, water supply and refrigeration in schools, health/medical clinics, and community services. A 1000-W PV system for a school or clinic can cost \$10 000 or more, fully installed.

Such PV systems are typically paid for by government programs, often supported by grants from donor agencies. These applications will require new forms of institutional financing as PV utilization increases in the future beyond the ability of grant agencies to pay.

24.5.2 Impact of Financing on Market Demand

Evidence from Asia, Africa, and Latin America indicates that market demand for PV systems in the developing countries increases by a factor of ten (10x) with the provision of reasonable levels of end-user financing:

Latin America: The pyramid in Figure 24.2 illustrates an estimate that was made by Soluz Inc., a leading PV company operating in Latin America, suggesting a tenfold increase in market demand if financing is available.

Indonesia: A PV developer in Indonesia estimated that the market would expand from 30% of the population for cash sales to 70% for the fee-for-service option (see Reference [16]).

India: A PV company in India has concluded that 5% of rural people in southern India can afford to pay cash, while 50% could afford to buy a PV system if they had a 1 to 2 year loan at market rates (see Reference [17]).

Sri Lanka: A leading microcredit lender in Sri Lanka concludes that over 50% of the people can afford an SHS with reasonable credit (see Reference [18]).

South Africa: The national utility Eskom conducted a field-survey-based market study in preparation for the Shell–Eskom joint venture and found that nearly 50% of the rural families in the Eastern Cape could afford monthly payments of 47 Rand (then about US \$10.00) per month, whereas very few could afford to pay for the system up front (see Reference [19]).

The findings are consistent around the world, that at least 50% of all rural households can afford to pay for a PV system given reasonable credit terms or the equivalent through a fee-for-service approach.

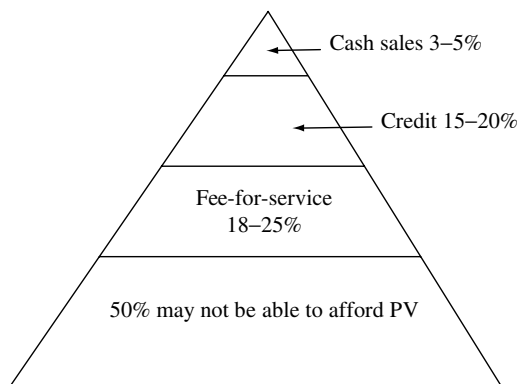


Figure 24.2 Affordability of PV systems by rural people in Latin America

24.5.3 Examples of PV Financing in Rural Areas

The financing of photovoltaics is beginning to occur around the world. The following are some current examples.

Bank Lending: SELCO India (Pty) Ltd, a solar PV installation and service company that has installed over 5000 solar home systems in southern India, has built working relationships with a number of area banks such as Syndicate Bank, and nonbanking finance companies (NBFCs) like Manipal Finance. SELCO has provided cash deposits as partial guarantees to several of the lenders, encouraging them to become involved in PV financing, and has provided interest rate buy-downs in other cases. Loans are typically 80% of the system cost, at 14 to 18% interest, repaid over one to three years. Even such short-term lending has sparked a market in southern India.

Microcredit lending: In Sri Lanka, a microcredit lender named Sarvodaya Economic Enterprise Development Services Limited (SEEDS), has embarked on a successful PV-lending program with its members. SEEDS loans 80% of the cost of the system. Loans are repayable in one to five years. Interest rates are in the mid- to upper-twenties (local borrowing rate plus a spread for SEEDS operation). Repayment is flexible – monthly or seasonal, depending on the income stream of the borrower. The loan recovery rate in SEEDS' program has reached 94%. SEEDS expects to finance as many as 50 000 solar home systems between the years 2001 and 2005. This work in Sri Lanka has built upon and perfected the pioneering work by Grameen Bank in Bangladesh (see Reference [20]).

NGO financing: In Bangladesh, Grameen Shakti, the PV affiliate of the Grameen Bank, is an example of a nongovernment organization that is involved in both the financial and technical aspects of PV dissemination. Grameen Shakti offers three financing options (it charges a “service charge” instead of “interest” because of local custom):

- 85% loan, repaid over a period of three years, having a 12% service charge (interest cost);
- 75% loan, repayable over two years, having an 8% service charge;
- Cash: The buyer receives a 4% discount on the system price by paying cash up front (not taking a loan).

Cooperative financing: In Santa Cruz, Bolivia, Cooperativa Rural de Electrificación (CRE) is a rural electric co-op that began installing PV systems in 1995 for customers who could not be reached by the grid. By 1998, CRE was serving 1300 PV customers, charging a flat monthly electric service fee. CRE owns the PV systems and maintains them.

Fee-for-service model: Several pioneering programs are being implemented using a fee-for-service model – charging a flat monthly fee for the use of a solar home system that is owned and maintained by a service company. Prepayment meters are commonly used on the battery's charge controller, which provides a revenue control mechanism. Users purchase prepayment cards each month at a local shop. In Indonesia, Total Energie, the French PV systems integrator, has completed a fee-for-service trial serving some 5000 customers. In South Africa, Shell-Eskom, a 50/50 joint venture of Shell International and Eskom, the national electric utility in South Africa, has installed 6500 solar home systems and is working toward an initial business trial of 50 000 units when

approved as a “concession” by the central government. The model has been adopted as a national strategy by the South African government. South Africa has set a goal of 100% electrification using grid and nongrid (PV) alternatives by the year 2010. A third major application of the fee-for-service model is in Argentina under a World Bank loan.

Rental/Leasing (Entrepreneurial Model): A variation on the fee-for-service approach is leasing. In the Dominican Republic, Soluz Dominicana, an affiliate of the US-based Soluz, Inc., has established a pioneering model using a leasing approach. Soluz charges \$10 to \$20 per month per SHS. Over 2000 systems are in service. Maintenance is provided by the company.

Tax-driven leasing and other financial engineering: In India, nonbanking finance companies (NBFCs) did some “financial engineering” in the 1997 to 2001 period to create a single-payment lease structure for PV-powered water pumping. The NBFC collected a single, up-front lease payment from the farmer, typically 30% of the system cost. The NBFC then took out a 10-year, 85% loan from IREDA, bearing 2.5% interest. Finally, the NBFC absorbed the 100% first-year depreciation that is available for PV in India, yielding 34% after-tax cash value. The three inflows totaled approximately 150% of the cost of the PV system. The extra 50% was deposited at 12 to 18% interest, from which the IREDA loan is repaid in 6 and 10 years. This model yielded the NBFC a cash-positive deal from day one and a good profit. The net result was a win-win situation: the government’s objectives for additional use of photovoltaics were met, the available incentives were fully absorbed by the financial community, and farmers got water-pumping systems that they otherwise could not afford. Nonbanking finance companies such as Sundaram Finance and Srei International participated in this approach. This example illustrates how governments can mobilize private sector capital through tax and loan policy. It also illustrates how unstable government policy can cripple PV markets – financing of PV water pumps through this technique came to a halt when IREDA stopped making PV loans at the 2.5% rate of interest, thus eliminating the interest arbitrage that the NBFCs had built into the model.

As seen above, the financing of photovoltaics in rural areas of the world’s developing countries is beginning to occur in a number of ways – bank loans, microcredit lending, NGO programs, cooperative financing, fee-for-service models, rental/leasing, and tax-driven leasing. This is a period of renovation. Considerable efforts will be needed to promulgate the use of successful models and build a higher level of acceptance of PV financing by the financial community.

24.6 SOURCES OF INTERNATIONAL FINANCING

24.6.1 International Aid and Donor Funding

In the past, the programs to fund photovoltaics in the developing countries have been sponsored by donors and aid agencies. OECD countries provide about \$50 billion per year in Official Development Assistance (ODA). These amounts include funds channeled by individual countries through multilaterals, such as the United Nations Development Program (UNDP). More recently, in line with GEF grants and World Bank financings, donor agencies have shifted increasingly towards the support of *financing*, rather than

grant *funding*, of solar PV and other renewables. Illustrative examples of such programs include the following:

United States of America: USAID has been funding the Renewable Energy Project Support Operation (REPSO) through Winrock International, resulting in a number of early stage financial support actions in India, Brazil, Indonesia, and elsewhere. USAID explored the possibility of establishing an \$18 million fund in South Africa for the Productive Uses of Renewable Energy (PURE Fund), focused on business uses for photovoltaics. In 1999, the US Export–Import Bank established a \$50 million allocation to China, earmarked for renewable energy exports, including photovoltaics.

Germany: Kreditanstalt für Wiederaufbau (KfW), the German bank for reconstruction, has extended a DM 120 million loan to India’s IREDA including DM 30 million allocation for photovoltaics.

Netherlands: The Ministry of Economic Affairs has supported a number of PV programs around the world, including a 20 000 unit solar home system program in Bolivia and a 30 000 unit program in China, supplied by Shell Solar. A new project in the Philippines is reportedly in the pipeline.

France: The French government had a special tax deduction for investments in the former French colonies, resulting in a subsidized flow of capital to PV projects in such countries. The French electric utility, Electricite de France (EdF) is involved in the financing of fee-for-service programs in Brazil, Indonesia, Morocco, and South Africa.

Spain: In 2001, the Spanish government extended a \$48 million soft loan to the Philippines for the installation of 2 MW of photovoltaics in 100 villages, comprising approximately 150 000 homes, all to be supplied by BP Solar Madrid. One-half of the funds will be loaned under the credit conditions of the OECD: a 10-year loan at just-below market rates. The other half will come from the Spanish Development Aid Fund (FAD): a 30-year loan, with a 10-year grace period, with an interest rate less than 1.0% (see Reference [21]).

Australia: USAID extended a \$30 million soft loan to Indonesia in 1998 for the installation of 50 000 solar home systems supplied by BP Solar Australia.

Japan: The Japanese aid agency, Overseas Economic Cooperation Fund (OECF), was reported to have begun providing aid in support of photovoltaics in developing countries in the year 2000. Reports suggest that the program might be substantial in scope and scale. OECF has prepared a \$100 million funding package for India’s IREDA for renewable energy on lending, including photovoltaics.

Others: The aid agencies of Austria, Denmark, Italy, Sweden, Switzerland, and the United Kingdom have funded a variety of PV programs in the developing countries, generally of the grant-for-demonstration kinds of activities. This kind of aid is being coordinated in Europe by the new EC directorate for international aid.

24.6.2 United Nations

UNDP supported demonstrations of solar home systems, PV water pumping, PV-powered health clinics, and other projects in the developing countries, generally with GEF grant support. UNDP-sponsored projects include

Bolivia: rural electrification with renewable energy

China: renewable energy capacity building

Ghana: renewable energy for rural, social, and economic development

Malawi: barrier removal to Malawi renewable energy

Peru: PV-based rural electrification

Sri Lanka: renewable energy capacity building

Uganda: PV pilot project for rural electrification

Zimbabwe: PV for household and community use.

UNEP has recently sponsored a new PV program in Africa, supporting early-stage financing of solar energy ventures (or, “enterprises”). This program has been funded by the UN Foundation, under the guidance of UNDESA.

The World Health Organization (WHO) funds a program for PV-powered refrigeration for storing medicines in remote areas of Africa.

24.6.3 World Bank Solar Home System Projects

The World Bank, with grant support from the GEF, has funded 12 projects around the world providing basic “energy services” such as lighting, radio, television, and operation of small appliances, using solar home systems in rural households that lack access to electricity grids, including

Argentina: renewable energy in rural markets project

Benin: off-grid electrification project

Cape Verde: energy and water sector reform project

China: renewable energy promotion project

India: renewable resources development project, through IREDA

Indonesia: solar home system project

Lao: PDR rural electrification project

Sri Lanka: energy services delivery project

Togo: off-grid electrification.

There are three more projects pending approval of the World Bank:

Peru: PV-based rural electrification

Guinea: rural energy development

Mexico: renewable energy for agriculture.

Most of the World Bank’s early experience with photovoltaics and other renewables came from its Asia Alternative Energy Unit (“ASTAE”), funded by a number of donor agencies since 1992. A key finding from ASTAE’s early work was that “the lack of term financing was not the sole obstacle to renewable resources or end-use energy efficiency development. The absence of adequate regulatory and institutional arrangements, local technical capacity, and appropriate energy service delivery infrastructure can pose equal or greater barriers to alternative energy development” (see Reference [22]).

On the basis of this experience, the World Bank is concluding that future PV projects will seek to incorporate six elements: support private sector and NGO delivery models, pilot consumer credit delivery mechanisms, pay first-cost subsidies, support policy development and capacity building, enact standards and establish certification, testing, and enforcement institutions, and conduct consumer awareness and marketing programs.

24.6.4 International Finance Corporation (IFC)

IFC, an institution of the World Bank Group, promotes economic development by encouraging private sector investment activities in developing countries. With regard to PV financing, the IFC participates in several PV financing programs:

Photovoltaics Market Transformation Initiative (PVMTI): PVMTI is an initiative of the IFC and the GEF to accelerate the sustainable commercialization and financial viability of solar photovoltaic-based energy services in India, Kenya, and Morocco. The IFC has designated Impax Capital and IT Power Ltd, both of the United Kingdom, as the external management team for PVMTI.

Small and Medium Scale Enterprises (SME) Program: This special unit of the IFC's environmental division makes small loans to entrepreneurial ventures and projects in the developing countries, and has made two financings in photovoltaics, in Vietnam and the Dominican Republic.

Solar Development Capital (SDC): SDC is a 10-year, \$28.75-million fund that makes minority equity, quasi-equity, and debt investments in PV-related businesses in developing nations. SDC seeks to invest in companies involved in distribution, consumer financing or leasing, manufacturing, or other aspects related to accelerated PV use in rural areas.

Solar Development Foundation (SDF): This is an approximately \$19 million nonprofit foundation that provides technical and business assistance to enterprises in preparation for larger-scale private investment, and can provide "seed" finance for business development activities on flexible terms.

Renewable Energy and Energy Efficiency Fund (REEF): REEF was a pioneer financing fund focusing on renewable energy and energy efficiency projects and companies. As of November 2001, REEF was capitalized at a level of \$65 million of equity plus a debt facility from the IFC. The external management team was headed by Energy Investors Funds. REEF was disbanded in late-2002.

24.6.5 Global Environment Facility

The Global Environment Facility (GEF) has been a central source of funding for PV in the developing countries. Since 1991, the GEF has provided grant funding for 25 off-grid PV projects in 20 countries, all through the World Bank Group and the United Nations, accounting for about \$210 million of GEF allocation, and about \$1.4 billion in total project costs, as summarized in Table 24.3. Lessons learned from the GEF's early implementation experience are summarized in a formal review of the program, with several key conclusions (see Reference [23]):

- Local financiers should be encouraged to carry some of the credit risk, not simply act as administrative conduits, in order to increase postproject sustainability and replication.
- Small PV dealers face sufficient business and technology risks that they are reluctant to assume consumer credit risks and incur the costs of credit administration and collections.
- Microfinance may work well in countries that have well-established microfinance institutions, but NGOs do not necessarily have the commercial orientation or business skills for rapid delivery of credit. Scale-up and outreach can become problematic.

Table 24.3 PV projects funded by the Global Environment Facility

Program	Year	Project	Agency	GEF funds [\$ millions]	Total funds [\$ millions]	Status
India	1991	Alternative energy	WB	26.0	186.0	Implementing
Zimbabwe	1991	PV for households and communities	UNDP	7.0	7.0	Completed
Indonesia	1995	Solar home systems	WB	24.0	118.0	Cancelled
Uganda	1995	PV pilot project, rural electrification	UNDP	1.8	3.6	Implementing
Ghana	1996	Renewable energy rural development	UNDP	2.5	3.1	Implementing
Sri Lanka	1996	Renewable energy capacity building	UNDP	1.5	1.5	Implementing
Sri Lanka	1996	Energy services delivery	WB	5.9	55.0	Implementing
Argentina	1997	Renewables energy in rural markets	WB	10.0	120.0	Implementing
Bolivia	1997	Rural electrification with renewables	UNDP	4.5	8.5	Implementing
China	1997	Capacity building for renewable energy	UNDP	8.8	28.0	Implementing
Lao PDR	1997	South provinces renewables project	WB	0,7	2.1	Implementing
Benin	1998	Decentralized rural energy	WB	1.1	5.7	Pending approval
Cape Verde	1998	Energy & water sector reform	WB	4.9	65	Implementing
China	1998	Renewable energy development	WB	35.0	445.0	Implementing
Peru	1998	PV-based rural electrification	UNDP	4.0	9.2	Implementing
Togo	1998	Decentralized energy	WB	1,1	5.7	Pending approval
Guinea	1999	Rural energy	WB	2.0	10.0	Pending approval
Malawi	1999	Barrier removal for renewables	UNDP	3.4	10.7	Pending approval
Mexico	1999	Renewable energy for agriculture	WB	8.7	26.0	Pending approval
SME	1994	Small and medium scale enterprises	IFC	1.6	4.8	Implementing
PVMTI	1996	PV market transformation initiative	IFC	30.0	120.0	Implementing
REEF	1996	Renewable energy & energy efficiency	IFC	30.0	130.0	Implementing
SDG	1998	Solar development group	IFC	10.0	50.0	Implementing

Source: Martinot, E. *et al.*, "The GEF Solar PV Portfolio: Emerging Experience and Lessons," Global Environment Facility, August 2000

- Credit collection can be costly if rural customers are dispersed over large territories with poor transport infrastructure. Businesses organized for marketing, installation, and service may not be well suited for credit collection.
- Some customers with seasonal income (i.e. paddy farmers with semiannual harvests) may require repayment schedules tied to semiannual income rather than to monthly incomes.

In 2001, the GEF broadened its mandate from a source of primarily grant funds through the United Nations and the World Bank Group, to the possibility of providing a broader array of investments, loans, guarantees, and other forms of financial support through a more diverse network of intermediaries.

24.7 FINANCING THE PV INDUSTRY

The PV industry will need to assemble a substantial amount of capital to support its growth. Capital is needed to expand manufacturing capacity and to fund working capital for inventories and receivables, all of which must be financed ahead of sales and profits in a growing industry. There are several sources of financing for the PV industry:

Major corporations: This is a dynamic time in the PV industry. Approximately 75% of worldwide PV market share is held by the operations and subsidiaries of major corporations – Sharp, Kyocera, BP Solar, Siemens, Sanyo, ASE, Shell, and Mitsubishi. It is typical for such large corporations to require a 20% or greater rate of return on internally invested capital, and this has not been achieved in the past. Many PV businesses have lost money, causing companies to quit the business. Companies that have left the PV business include Westinghouse, IBM, Motorola, Xerox, Texas Instruments, Exxon, Shell (US), Arco, Mobil, and others. More recently, with the global movement towards green energy, several major corporations have increased their commitments, including BP in 1996 and Shell International in 1997. The most recent casualty was Siemens, selling its solar division to Shell. Lacking improved profitability, the industry may see a continuation of entries, exits, and reorganizations by major corporations.

Electric utility companies: There has always been an affinity between photovoltaics and the utility companies. For example, Alabama Power was a major investor in Chronar, which closed. Idaho Power acquired a number of PV-systems integration firms between the years 1997 and 1999, only to exit the business and sell the group to Schott in the year 2001. Siemens Solar was half-owned by a German utility, EoN. The former Mobil Solar was acquired by RWE in 1994, a German utility, creating ASE Americas. General Public Utilities established GPU Solar, a joint venture with Astropower, focusing on grid-connected IPP power projects, commercial systems, and residential rooftop systems. The PV industry can expect to receive additional capital investment from the utility industry.

Capital Markets: The public stock markets in Europe and the US began to show interest in clean energy and distributed power generation in the period between 1998 and 2000. The areas of popular stocks in the United States include fuel cells, microturbines, and photovoltaics. In Europe, where the markets reacted earlier, the favorites have included wind power (in which Denmark and Germany lead the world industry), solar photovoltaics, hydropower, and other renewables. There are three publicly traded PV stocks in the United States: Astropower, Evergreen Solar, and Spire Corporation; and several in Europe. The outlook is positive in the near future, as the supply of money for green energy stocks is increasing, including the formation of mutual funds specializing in clean/green energy, such as Winslow's Green Growth Fund.

Venture Capital: The Venture Capital (VC) industry has invested in PV deals over the past 25 years, generally losing their investments, and never achieving their traditionally accepted financial goal of a 40% rate of return. This may be changing in recent years

with successful Initial Public Offerings (IPOs) by Astropower and Evergreen Solar in the United States and Solar World in Germany. Other venture-capital-backed PV companies, not yet publicly traded, include Solar Electric Light Company (SELCO), First Solar, and Global Solar in the United States, Solar Fabrik in Germany, and Solar Century in the United Kingdom. There is a tremendous influx of new venture start-ups in photovoltaics, especially in Europe and Asia where there are booming markets. Venture capital funds that have invested in photovoltaics include Arete Ventures (the Utech Funds) and Nth Power Technologies in the United States; Swiss Re, the Sarasin Fund, and UBS Energy Fund, all in Switzerland; and Gerling Insurance in Germany. Other US VC funds that have expressed interest in new energy technologies include the Commons Fund, Beacon Energy Funds, Energy Ventures Group, Kinetic Ventures, and Perseus Capital.

24.7.1 Financing Working Capital in the Distribution Channels

One of the more challenging aspects of financing PV growth will be how to capitalize the distribution channels to reach the widely dispersed end-use markets. There are several sources of financing for these firms:

Local lenders: Small business financing is inherently a local lending business. The vast majority of funds for financing the working capital requirements of the PV distributors and dealers will be from local banks, NBFCs, and microcredit lenders.

PV manufacturers: Most of the major PV manufacturers have extended credit programs for their best distributors and dealers.

World Bank/IFC: The IFC and GEF have collaborated on the deployment of two programs, PVMTI and SDG, to finance “PV enterprises” in developing countries. Over 200 such businesses have been identified by SDG as of mid-2001. The number of firms that will be required to support worldwide development of PV markets will, according to E&Co, be as high as 16 000 companies.

24.8 GOVERNMENT INCENTIVES AND PROGRAMS

A wide range of government incentives and programs has been adopted for photovoltaics around the world, stimulating demand for PV systems and affecting the financing of photovoltaics.

24.8.1 Potential Impact of Financing as a Government Policy Option

Looking at financing in the context of government policy shows that low-cost financing programs can actually have more impact on PV markets *in the immediate future* than technology research or manufacturing cost reductions. For example, Figure 24.3 illustrates the monthly payments for the 2.5 kW grid-connected, residential rooftop PV system. The PV system is assumed to cost \$8/watt (\$20 000 total cost), with a total system

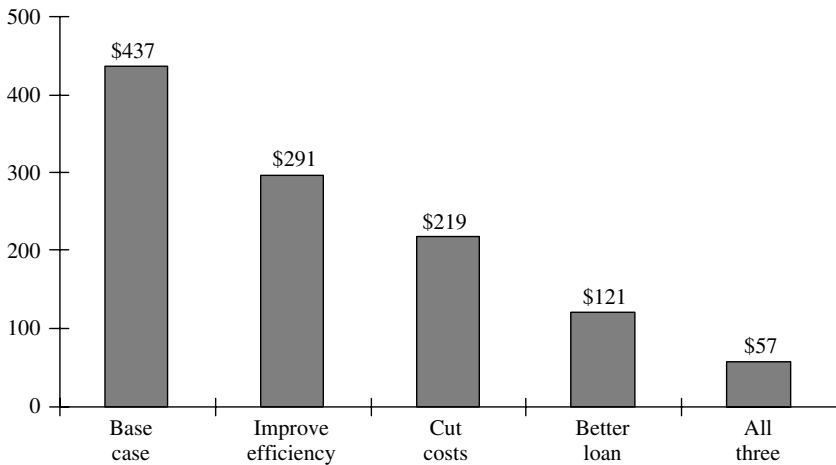


Figure 24.3 Monthly payments on a 2.5 kW residential PV system

efficiency of 10%. In the base case, financing is assumed to be a 7-year 18% loan, resulting in a monthly payment of \$437. Then, three improvements are evaluated (see Reference [24]):

Research programs to improve efficiency: By improving the efficiency of the system, its size can be reduced while still generating the same output, thus reducing the cost. For a 50% increase in system efficiency, from 10 to 15%, the monthly payment will be reduced to \$291 per month. However, it may take ten years or more before technology research can achieve these results in commercial products.

Cost reduction through manufacturing scale-up: By scaling up manufacturing, automating factories, and generally reducing the production cost per unit, total system costs can be reduced. Assuming a 50% reduction in system cost, from \$8.00/Wac to \$4.00/Wac, the monthly payment of the system can be reduced to \$219 per month. Achieving this result might take approximately five years, as new factories are planned, built, and put into operation.

Better financing: A third way of reducing monthly payments is by applying lower-cost, longer-term financing. Here, the 7-year, 18% loan is replaced with a 30-year, 6% loan. Monthly payments come down to \$121 per month, due to the change in financing alone, and this can be done immediately.

All three initiatives: The best public policy will be to accomplish all three cost reductions, but the immediate impact of lower-cost, longer-term financing is apparent.

As shown above, the provision of lower-cost, longer-term financing can have a more immediate impact on the affordability of solar PV systems than research and manufacturing programs, and will probably be the catalyst that creates the jump in demand that, in turn, causes photovoltaics to drive down the learning curve. Thus, financing may be the element that will break photovoltaics out of its long-standing “chicken and egg” dilemma.

24.8.2 Direct Subsidies (“Buy-downs”)

Governments have used different measures to place a value on the public benefits of photovoltaics. Subsidies are tending to be about 30 to 50% of the cost of the PV system. The following is a summary of subsidies that are in use today:

Japan: The program was launched in 1996 with direct subsidies to the amount of 50% of the cost for residential rooftop, grid-connected PV systems. The subsidy is paid to the installation company, not the end user, to foster maximum impact on creating a competitive installation industry and minimum distortion of buyer behavior. The subsidy has since been reduced to 33% in 1999, 25% in 2000, 15% in 2001, and less than 10% in 2002. The Japanese PV market has boomed, reaching over 90 MW or 35% of the world PV market in the year 2000, and there are projections that over 30 000 systems – as much as 130 MW – may be installed in the year 2001 (see Reference [25]).

India: The Ministry of Nonconventional Energy Sources (MNES) has a program in which 10-W to 20-W PV lanterns and 900-W PV water pumps are eligible for a 50% subsidy. The subsidies are distributed through state-level nodal agencies that pass the funds down through the bureaucracy. Thus, it is a matter of working a government “system” to receive the funds. Subsidies are paid only if there is budget available. The net effect has been to create a small market that is “capped” by the availability of subsidy funds. The subsidy program, with its minimum technical specifications, has spawned a subculture PV industry that makes inferior grade equipment just for what is called *the subsidy market*. The Indian subsidy program not only illustrates the power of a subsidy program to create a market but also how to cap it and create distortions (see Reference [26]).

California: The State of California enacted a \$3.00/W “buy-down” for PV systems, initially until the year 2002. The subsidy was subsequently increased to \$4.50/watt and extended for ten years to 2012, but there were still no financing programs. The program had little effect on the market at first; according to the California Energy Commission, only about 235 residential PV systems were installed in the years 1998 to 2000. A power shortage and sharp increase in electric tariffs in the years 2000 to 2001 created a crisis atmosphere, greater public interest in energy and environmental solutions, and, subsequently, renewed demand for PV systems and other power equipment.

Other countries: Many other countries are adopting PV subsidies. Argentina embarked on a concession approach that included embedded subsidies, but the program has not been fully implemented. Mexico adopted a set of programs that added up to a 90% subsidy for rural photovoltaics. Brazil’s PRODEEM program provided massive subsidies, but ended up with a high percentage of nonworking systems. South Africa is considering subsidies as high as 80 to 100% of the cost of a basic 50-W solar home system, in conjunction with the national concession program for nongrid electrification. Morocco’s PV program is delayed, awaiting the resolution of the subsidy amount and distribution method, reportedly about 50% of the system cost.

While PV subsidy programs are being implemented around the world, there is a growing body of evidence and opinion that subsidies ultimately do more harm than good for market development. The common argument in favor of subsidies is that they have an immediate impact on demand – which is the mutual goal of the elected officials who enact

them and the companies that lobby for them. The argument against the use of subsidies is that they create artificial markets and the opportunity for corruption while they are in place, that they cap markets to the level of the subsidy budget each year, and that they eventually bring markets to a halt when they are terminated.

24.8.3 Soft Loans (Interest Subsidies)

The use of interest subsidies has been an effective public policy tool for housing. It might also be used for photovoltaics. These are flexible instruments, allowing the sponsoring government or institutions to correct interest rates without severely distorting market forces. They assure financing while spreading the subsidy over the life of the program. This avoids market manipulation and windfall events often related to direct subsidies. A typical soft loan will have low-interest rates, longer terms than normal, grace periods during which payments need not be made, and other features. There are several examples of soft loan incentives in the PV markets today:

India: The Indian Renewable Energy Development Agency (IREDA) offers favorable loans for photovoltaics: 85% of system cost, 10-year repayment period, 2-year grace period, at 2.5 to 5.0% interest rates. The comparable loan from a national bank would be a 5-year loan at 12.5% interest rate with, no grace period. A comparable loan from a nonbanking finance company would be at 18 to 23% interest rate.

Germany: Kreditanstalt für Wiederaufbau (KfW), the German bank for reconstruction, is providing PV loans as part of the country's 100 000 roofs initiative. Loans can be up to 100% of system cost up to 5 kW, and 50% of cost for larger systems. The interest rate is 4% below prevailing market rates. Combined with the national feed-in tariff of DM 0.99 per kWh, users can make a profit through the use of PV in Germany. The program is highly successful.

Japan: In conjunction with its subsidy program, the government of Japan subsidizes the interest rate on PV loans, with subsidy payments going to the lenders. The resulting net interest rate to the end user is near zero percent.

New York: The New York State Energy Research & Development Administration (NYSERDA) began offering interest subsidies for PV loans made by New York banks in the year 2000. NYSERDA buys down the interest rate on loans by making an up-front payment to the lender to the amount of the present value of lost interest. The amount of the interest subsidy is presently 4.0%, bringing interest rates down from 9.5 to 5.5%.

There are precedents for applying interest subsidies. The use of interest subsidies, soft loans, and third-party (government) guarantees has been used extensively in housing finance programs around the world, lowering the real cost of owning a home while minimizing distortions in the home buyer–seller marketplace.

An interest rate subsidy as low as one-half percent (i.e. lowering the mortgage interest rate from 7.0 to 6.5% on a 30-year mortgage) will actually pay for a residential PV system completely, as reported by Alden Hathaway at the Environmental Resources Trust. For example, for a \$300 000 home mortgage loan, the interest payments will be \$425 277 over 30 years. At the lower rate of 6.5%, total interest payments will be just \$389 197. After taking taxes into account, assuming that the interest is tax deductible and

using a 40% combined federal and state tax rate, the difference in after-tax interest cost is \$21 648, roughly the full cost of a 2.5 kW PV system.

24.8.4 Income Tax Deductions and Credits

Tax incentives are preferred by many government officials because they can get the intended economic benefits to the intended users without the need to establish an implementing bureaucracy. They are opposed by other officials who see the tax system as a method for raising funds to run the government, not as a means of implementing social policy. They can also be written with sunset provisions, ostensibly to protect the budget from runaway spending, but also to provide elected officials with an opportunity to get publicity for enacting it again and again. Tax credits and deductions therefore appear to be less stable and reliable as market incentives or subsidies. Nonetheless, there are several tax-based incentive programs in place today:

India: PV qualifies for 100% depreciation in the first year for corporate (not individual) taxes. This, in conjunction with IREDA's 2.5% loans, created a PV leasing industry in the period between the years 1997 and 2001.

United States of America: The US tax code allows a 10% tax credit against corporate taxes and five-year accelerated depreciation for photovoltaics. The combination of these incentives will drive the preferred financing of photovoltaics in the United States towards leasing. The US Congress is also considering a 15% tax credit on personal income taxes.

Government subsidies and incentives have increased in recent years with tremendous impacts on the immediate size of PV markets in Japan and Germany. The impacts in India appear to be mixed, with subsidies creating markets but also capping them at the levels of the annual budgets. Likewise, subsidies (tax credits) have had mixed results in the United States.

24.9 FUNDING GOVERNMENT RESEARCH AND DEVELOPMENT

Government funding of research and development (R&D) has traditionally been used to bridge the gap between work that is "too high risk for companies to undertake" and "commercial viability."

Photovoltaics present a case study of a successful publicly funded R&D activity. PV R&D efforts were focused on lowering manufacturing costs in volume production, improving the performance (efficiency) of the devices, and extending the operational lifetime of components and systems. Aggressive goals have been set to make photovoltaics economically competitive with traditional sources of electricity (see Reference [27]). Many countries around the world have been involved in such activities in an effort to supplement traditional energy supplies with renewable energy sources.

24.9.1 PV Programs in the United States

US-government programs in photovoltaics originated from the Conference on PV Conversion of Solar Energy for Terrestrial Applications, sponsored by the National Science

Foundation (NSF) held in Cherry Hill, New Jersey in October 1973 (see Reference [28]). The program was the responsibility of the National Science Foundation, and then was transferred to the Energy Research and Development Agency (ERDA), which became part of the US Department of Energy (DOE) in 1977.

The first US program was the Low Cost Silicon Solar Array Project, later renamed the Flat-Plate Solar Array Project. The Jet Propulsion Laboratory was assigned management responsibility based on their long experience with space PV power systems. The newly created Solar Energy Research Institute (SERI) was charged in 1978 with the responsibility for thin-film materials and the Sandia National Labs for the concentrator PV programs. The DOE PV Program features significant cost sharing by its industry partners.

SERI became the National Renewable Energy Laboratory (NREL) in 1990, which has championed such programs as the amorphous silicon partnerships, the Photovoltaic Manufacturing Technology (PVMaT), the Thin-film Partnership, the building-integrated (PV-BONUS) program, the Utility Photovoltaic Group (UPVG), and the Million Solar Roofs (MSR) Program. The National Center for Photovoltaics (NCPV) was established to integrate the programs at NREL and Sandia.

US program funding is shown in Figure 24.4, which indicates the rapid buildup of the program in the 1970s, followed by a sharp reduction in the 1980s, and subsequent increase in the 1990s. As reported by DOE, the government's investment in photovoltaics since 1974 is estimated to be \$1.7 billion.

24.9.2 PV Programs in Japan

From 1974 to 1983, the Japanese R&D program focused on low-cost solar cell production including mass production of raw silicon (Si) material, poly-Si, ribbon crystal, and amorphous silicon (a-Si).

During the second decade of the program from 1984 to 1993, in addition to material R&D efforts, mass production technologies and solar photovoltaic system technology were pursued, together with cell technology such as a-Si-based stacked solar cell and flexible substrate solar cells.

The New Sunshine Project has been in existence since 1993 in which a variety of new programs have been organized on the promotion and cost reductions of PV systems. Examples include field demonstration and testing of PV systems on public facilities and a subsidy program for private houses. The budget for the R&D portion of the Japanese PV Program is shown in Figure 24.4. It should be pointed out that the R&D portion represents only a small portion of the total Japanese PV effort. In FY 2000, the total effort, including subsidies, was approximately six times the R&D portion of the budget.

24.9.3 PV Programs in Europe

The UNESCO conference "The Sun and the Service of Mankind" held in Paris in 1973 was the starting point for the development of renewable energy in Europe (see Reference [29]). The first European Commission technology program for renewable energy was established by the Council of Ministers in 1975. The European Commission's PV program focused

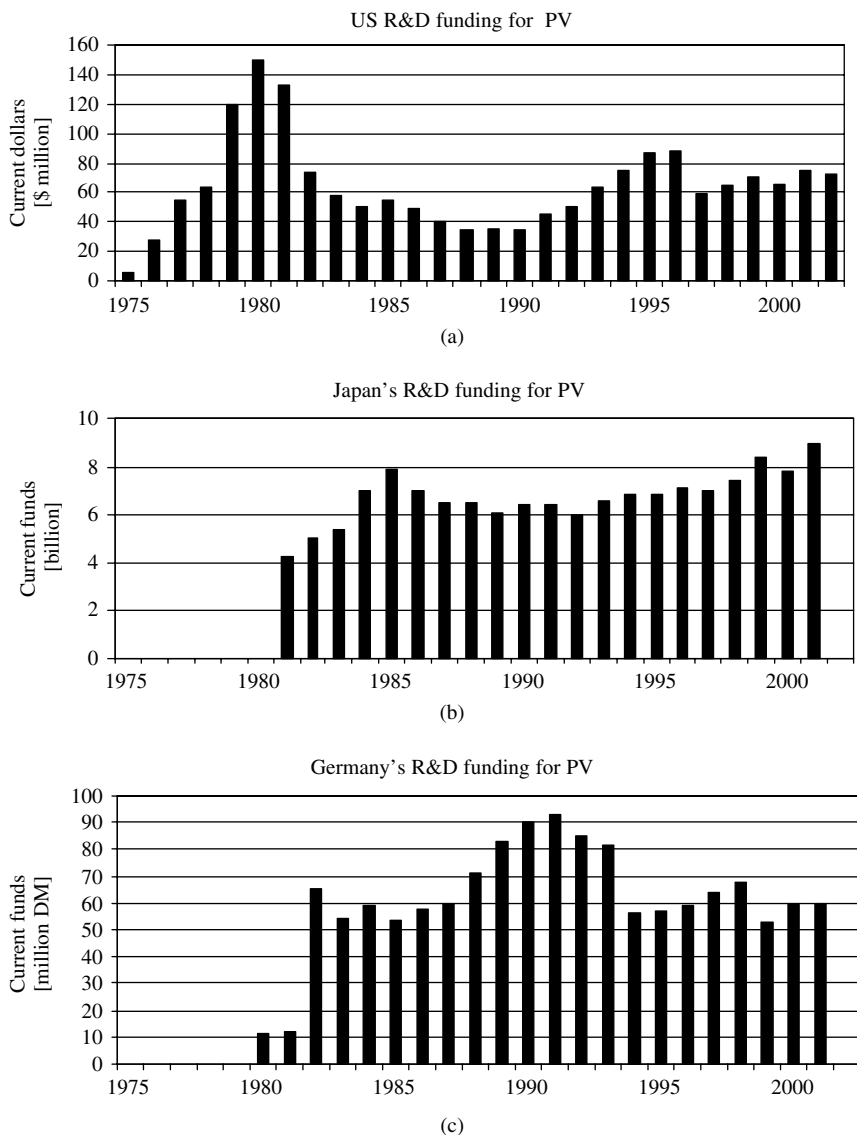


Figure 24.4 Research and development funding for solar photovoltaics. (a) US R&D funding for photovoltaics; (b) Japan's R&D funding for photovoltaics; and (c) Germany's R&D funding for photovoltaics

initially on crystalline silicon and pilot system development. From 1979, the demonstration programs focused on remote and stand-alone applications. Later grid-connected and building-integrated systems were incorporated into the program.

The total budget for EU members on PV R&D between 1974 and the present is about \$1.5 billion. Germany has furnished about 65% of the total. Figure 24.4 shows the recent budgets for the German PV R&D program. Like Japan, Germany also budgeted

commercialization and subsidy programs. Germany's 1000-roofs program was one of the hallmarks of their efforts. Significant efforts in the Netherlands, Italy, Spain, Switzerland, and France have also contributed to the European PV R&D efforts.

24.9.4 Future PV R&D Programs

Predicting the role for public sector funding of R&D is difficult at best. Fortunately, there appears to be good reason to follow the role of other high-technology programs that have come before. Possibly, the best is what has happened with the development of integrated circuits, which had strong government support during its development. Although one could predict that such support would decline and perhaps be phased out as products came out through the end of the development pipeline, the opposite has occurred. Successful research programs breed future successes in terms of new technologies and approaches. Since research is defined as exploring the unknown, there will always be paths to follow for those technologies that have been shown to be useful and successful. Such is the case for photovoltaics.

24.9.5 Sources of R&D Funding

The R&D programs of each country generally only fund organizations within the respective country. The following are the major funding organizations:

United States:

U.S. Department of Energy
Office of Solar Electric Technologies
1000 Independence Avenue, S. W.
Washington, DC 20585

Japan:

NEDO
Solar Energy Department
Sunshine 60 Bldg.
3-1-1 Higashi Ikebukuro
Toshima-ku
Tokyo 170-6028
Japan

Germany:

Bundesministerium fuer Wirtschaft Technologie
53107 Bonn
Germany

The Netherlands:

Novem
P.O. Box 8242

3503 RE Utrecht
The Netherlands

Italy:
ENEA
Renewable Energy Department
CR Casaccia
1300 sp Anguillarese
0006 S M di Galeria (ROMA)
Italy

This chapter has described the financing of PV growth. Financing might be the last “missing link” in the solution to a solar-driven world economy. Our financial systems and practices are built to support a different economic model – central station power plants and the grid system (see Reference [30]). Mobilization of massive amounts of capital to support solar photovoltaics and distributed generation has been, and will for the immediate future be, institutionally complicated. Solutions are coming, though slowly. Now in the year 2002, however, it appears that we are turning the corner towards the financing of a brighter, solar-powered future.

ANNEX

CONTACTS IN PV FINANCING

This Annex exhibit provides a listing of some of the key organizations that are involved in the financing of photovoltaics around the world, by no means covering all, but a list that should prove useful over the coming decade. It is presented by region.

INTERNATIONAL/GLOBAL

Environmental Enterprises Assistance Fund (EEAF)

EEAF, formed in 1990 by USAID, Winrock International and the Rockefeller Foundation, is a specialist in providing debt and equity financing to environmental entrepreneurs in renewable energy and other environmentally beneficial industries.

Contact: Brooks Browne, President
Address: EEAF
1655 N. Fort Myer Drive
Suite 520
Arlington, VA 22209
USA
Phone: 703 522 5928
Fax: 703 522 6450
E-mail: eeaf@igc.apc.org

Global Environment Facility (GEF)

The Global Environment Facility (GEF) is the chief funder of renewable energy in developing countries and, as such, will have a significant impact on expansion of the field. GEF is a major force in promoting renewable energy and the chief driver and catalyst among development agencies.

Contact: Mohamed T. El-Ashry, Chief Executive Officer and Chairman
Address: 1818 H Street, N.W.
Washington, D.C. 20433
U.S.A.
Phone: 202-473-0508
Fax: 202-522-3240
Web site: www.gefweb.org
E-mail: harcher@worldbank.org

International Finance Corporation (IFC)

IFC is an institution of the World Bank Group and promotes economic development by encouraging private sector investment activities in developing countries.

Address: Corporate Relations Unit
International Finance Corporation
2121 Pennsylvania Avenue, NW,
Washington, DC 20433 USA.
Phone: +202-473-7711
Fax: +202-974-4384
E-mail: Webmaster@ifc.org
Web site: <http://www.ifc.org>

Photovoltaics/Market Transformation Initiative (PV/MTI)

PVMTI is an initiative of the International Finance Corporation (IFC) and the Global Environment facility (GEF), to accelerate the sustainable commercialization and financial viability of solar photovoltaic-based energy services in India, Kenya, and Morocco. The IFC has designed Impax capital and IT Power Ltd. as the external management team for PVMTI.

Contact: Vickram Widge
Address: Environment Division
International Finance Corporation
2121 Pennsylvania Avenue, NW
Washington DC 20433

Renewable Energy and Energy Efficiency Fund (REEF)

REEF is a pioneer financing fund focusing on emerging markets, renewable energy, and energy conservation, and efficiency projects and companies. As of April 2001, REEF

was capitalized at a level of \$65 million equity plus debt facility from the International Finance Corporation.

Contact: Kenneth R. Locklin, Managing Director

Address: Energy Investors Fund
727 Fifteenth St, NW
11th Floor
Washington, DC 20005
USA

Phone: 202 783 4419

Fax: 202 371 5116

E-mail: klocklin@eifgroup.com

Solar Development Capital

Solar Development Capital is a 10-year, \$28.75 million fund that makes minority equity, quasi-equity and debt investments in solar photovoltaic (PV) and PV-related businesses in developing nations. SDC seeks to invest in companies involved in distribution, consumer financing or leasing, manufacturing, or other aspects related to accelerated PV use in rural areas. Some senior debt may be placed with microcredit institutions. Offices in the United States, and Netherlands:

US Contact: JD Doliner

Address: Solar Development Capital
1655 North Fort Myer Drive
Suite 520
Arlington VA, 22209-3109

Phone: +1-703-522-5928

Fax: +1-703-522-6450

Web site: www.solardevelopment.org

E-mail: sdcf@mindspring.com

European Contact: Hans Schut

Organization: Solar Development Capital

Address: Utrechtseweg 60
Postbus 55, 3700 AB Zeist,
The Netherlands

Phone: +31-30-693-65-00

Fax: +31-30-693-65-66

Web site: www.solardevelopment.org

E-mail: sdc@triodos.nl

Solar Development Foundation (SDF)

Solar Development Foundation provides technical and business assistance to enterprises in preparation for larger-scale private investment, and can provide 'seed' finance for business development activities on flexible terms. Business development services may include: market research, communications and market testing (pilot-scale operations); training; business planning assistance; development of end-user financing mechanisms, and so on.

SDF provides relatively soft debt and grant funding for its business development services with the expectation that the PV and other off-grid renewable electricity businesses that it assists will to attract follow-on investment.

Contact: Candace Smith, Chief Operating Officer, and Phil Covell, Managing Director
Organization: Solar Development Foundation
Address: 1655 North Fort Myer Drive, Suite 520
Arlington VA, 22209-3109 USA
Phone: +1 703-522-5928
Fax: +1 703-522-6450
E-mail: sdcf@mindspring.com
Web site: www.solardevelopment.org

Solar Electric Light Fund (SELF)

Acting as a catalyst, SELF provides both financial and technical assistance for solar energy and wireless communication systems in the developing world. SELF raises seed funding for in-country NGO's and financial institutions, which provide microloans for the purchase of solar home systems (SHS). SELF has launched solar rural electrification programs and enterprises in India, China, Vietnam, Indonesia, Nepal, South Africa, Brazil, Uganda, Sri Lanka, Tanzania, and the Solomon Islands.

Contact: Robert A. Freling, Executive Director
Address: 1775 K Street, NW Suite 595
Washington, DC 20006
Phone: 202-234-7265
Fax: 202-328-9512
Web site: <http://www.self.org>
E-mail: solarlight@self.org

Solar International Management, Inc. (SolarBank Program)

The SolarBank Program is being developed as a future wholesale capital fund with sub-funds within each country. India and South Africa are the prototype countries. SolarBank Funds will supply capital to banks, nonbanking finance companies, cooperatives, societies, microcredit lenders, NGOs, rural finance groups, and others. It will also provide technical support, training, and special programs to its participating lenders.

Contact: Michael T. Eckhart
Address: Suite 400, 1825 I Street NW
Washington DC, 20006.
Phone: +1 202-429-2030
Fax: +1 202-429-5532
E-mail: info@solarbank.com
Web site: <http://www.solarbank.com>

UNDP Sustainable Energy & Environment Division (SEED)

The Administrator of UNDP made a strategic decision to strengthen UNDP's environment and sustainable development capacity by establishing a new division within the Bureau for

Policy and Programme Support (BPPS): the Sustainable Energy and Environment Division (SEED). Since its origin, SEED has worked to support UNDP's overall efforts to help countries successfully design and carry out programs, which integrate the protection and regeneration of the environment and the use of natural resources. Assistance is provided by means of grant aid for technical assistance and investment projects.

Contact: Mr. Roberto Lenton, Director,
Address: SEED,
304 East 45th Street,
New York, N.Y. 10017, USA.
Phone: +1-212-906-5705
Fax: +1-212-906-6973
Web site: <http://www.undp.org/seed/>

UNEP Collaborating Centre on Energy and Environment

Financing Institution. Promotes and facilitates environmentally conscious energy planning throughout the world and especially in developing countries. UCCEE is funded jointly by UNEP, the Danish International Development Agency (DANIDA), and Risoe National Laboratory.

Contact: Mr. Gordon A. Mackenzie, Senior Energy Planner
Address: UCCEE
Risoe National Laboratory, Bldg. 142, Frederiksborgvej 399,
P.O. Box 49,
DK 4000 Roskilde, Denmark.
Phone: +45-46322288
Fax: +45-46321999
E-mail: gordon.mackenzie@risoe.dk
Web site: <http://www.uccee.org>

Winrock International

Winrock International is a private, nonprofit organization that works with people in the United States and around the world to increase economic opportunity, sustain natural resources and protect the environment.

Contact: Frank Tugwell, President
Address: 1621 North Kent St. – Suite 1200, Arlington, VA 22209-2134
Phone: 703-525-9430
Fax: 703-243-1175
Web site: www.winrock.org
E-mail: information@winrock.org

EUROPE

ASN Bank

Banking for renewable energy projects.

Address: PO Box 30502, 2500 GM Den Haag

Country: Netherlands
Phone: +31 703 569 333
Fax: +31 703 617 948

Clean Energy Fund

Finance for power generation with clean and renewable energy.

Contact: Peter Dunev
Address: 33 St James Street, London SW1A 1HD
Country: UK
Phone: +44 20 7930 1030
Fax: +44 20 7930 1080

D&B Capital

Financial services to the clean and renewable energy sector.

Address: 33 St James's Street, London SW1A 1HD
Country: UK
Phone: +44 20 7 930 1030
Fax: +44 20 7 930 1080

Ernst & Young Renewable Energy Unit

Specialists in RE corporate finance, business planning, taxation, and modeling advice.

Contact: Jonathan H Johns
Address: Broadwalk House, Southernhay West, Exeter EX1 1LF
Country: UK
Phone: +44 1392 284300
Fax: +44 1392 284301

European Bank for Reconstruction and Development

The European Bank for Reconstruction and Development (EBRD) was established in 1991. It exists to foster the transition towards open market-oriented economies and to promote private and entrepreneurial initiative in the countries of central and eastern Europe and the Commonwealth of Independent States (CIS) committed to and applying the principles of multiparty democracy, pluralism, and market economics.

Contact: Beverley Harrison
Address: European Bank for Reconstruction and Development
One Exchange Square
London EC2A 2JN, United Kingdom
Phone: +44 20 7338 6000
Fax: +44 20 7338 6100

E-mail: harrisob@ebrd.com

Web site: <http://www.ebrd.org>

European Commission DG XVII

Funding Organization. Links to EC energy programs. European Union in collaboration with EBRD has produced a useful publication related to funding issues for energy-related projects.

Address: 200 rue de la Loi, B-1049, Bruxelles, Belgique.

Phone: +32 22991111

Fax: +32 22991111

E-mail: ener-info@cec.eu.int

Website: <http://europa.eu.int/en/comm/dg17/dg17home.htm>

European Investment Bank (EIB)

Funding Organization. One of the objectives of EIB is the investment into energy-related projects in Europe as well as in the developing countries outside Europe. Provides funding for assistance with research, development, demonstration, and implementation of projects related to all aspects of renewable energy.

Address: European Investment Bank (EIB),
100 Bd Konrad Adenauer, L-2950 Luxembourg.

Phone: +35-2-43793122

Fax: +35-2-43793189

Web site: <http://www.eib.org>

Impax Capital Corporation Ltd

Finance and strategy for environmental infrastructure and technology. External manager for the IFC's PV market Transformation Program in India, Morocco, and Kenya.

Contact: Melville Haggard

Address: Broughton House, 6–8 Sackville Street, London W1X 1DD

Country: UK

Phone: +44 20 7 434 1122

Fax: +44 20 7 434 1123

IFU

IFU's objective is to promote economic activities in developing countries by promoting investments in these countries in collaboration with Danish trade and industry. IFU participates mostly as a share capital partner holding also a seat on the board of directors together with the Danish company investing in the project company. IFU can also participate as a cofinancing partner, when an existing company is to be expanded or rehabilitated or when state-owned companies are privatized.

Address: Bremerholm 4, DK 1069 Copenhagen K, Denmark.
Phone: +45 33 63 7500
Fax: +45 33 32 2524
E-mail: ifu-cph@inet.uni2.dk
Web site: http://www.ifu.dk/ifu/brief_ifu.htm

ING Bank Nederland

Banking division of ING Group, specialists in renewable energy project finance.

Address: PO Box 1800, Bijlmerplein 888, 1000 BV Amsterdam
Country: Netherlands
Phone: +31 20 652 39 54
Fax: +31 20 652 39 73

New Century Finance Limited

Innovative finance for specific projects and working capital for manufacturers.

Contact: Richard W Price
Address: Pantiles Chambers, 85 High Street, Tunbridge Wells, Kent TN1 1YG
Country: UK
Phone: +44 1892 618461
Fax: +44 1892 618567

New Energies Invest Ltd.

New Energies Invest Ltd. aims to invest into renewable technologies such as solar, wind, geothermal, biomass, small hydro, and fuel cells. The focus is on nonlisted companies, that is, typically New Energies Invest is providing growth capital as private equity. Geographically, New Energies Invest is covering North America and Europe.

Contact: Andreas Knoerzer, First Vice President
Address: c/o Bank Sarasin & Cie., Elisabethenstrasse 62, 4002
BASEL – Switzerland
Phone: +41 61 277 74 77
Web site: newenergies.ch

Rabobank Nederland/Groen Management BV

Specialists in renewable energy project financing. Rabobank is a broad-based financial services provider, founded on cooperative principles. It has been a leading lender to wind power projects and other sustainable development.

Address: PO Box 17100, 3500 HG Utrecht
Country: Netherlands
Phone: +31 302 16 49 83
Fax: +31 302 16 19 76

Triodos Bank NV

Triodos is a social bank with renewable energy, wind, and solar investment funds. Triodos is the leading socially responsible lender in the Netherlands, and is the comanager of Solar Development Capital.

Contact: JF Schut
Address: Postbus 55, 3700 AB Zeist
Country: Netherlands
Phone: +31 30 693 6500
Fax: +31 30 693 6555

VTZ Green Money for the Blue Planet Ltd

Financial services based on environmental, ethical, and financial criteria.

Contact: Martin Brenner
Address: Bahnhofplatz 9, 8023 Zürich
Country: Switzerland
Phone: +41 1 226 45 45
Fax: +41 1 226 45 46

The Wind Fund Plc

Equity investment fund for wind, hydro, and renewable energy projects.

Contact: Simon Roberts
Address: Brunel House, 11 The Promenade, Clifton, Bristol BS8 3NN
Country: UK
Phone: +44 117 973 9339
Fax: +44 117 973 9303

UNITED STATES

ABN Amro Bank NV

Construction and term financing for independent power projects.

Contact: Joseph C Lane
Address: 135 LaSalle Street, Chicago, Illinois 60603
Country: USA
Phone: +1 312 443 2641
Fax: +1 312 750 6387

Commons Capital LP

Commons Capital LP is a venture capital firm investing in private companies, including renewable energy companies that promise strong financial results and significant contributions to a sustainable future.

Contact: William Osborn, Manager
Address: Commons Capital Management LLC
115 Buckminster Road
Brookline, MA 02445
Phone: 617-734-1047
Fax: 617-734-3115
E-mail: *wosborn@aol.com*

E&Co

E & Co was established in 1994 as a nonprofit organization with the strategy of providing enterprise development services and modest amounts of money in the form of grants, loans, and equity investments to economically, socially, and environmentally sustainable energy enterprises in developing countries.

Contact: Michael D. Allen, President
Address: E & Co
383 Franklin Street
Bloomfield, NJ 07003 USA
Phone: 973-680-9100
Fax: 973-680-8066
E-mail: *mike@energyhouse.com*

FAC/Equities A Division of First Albany Corporation

Investment bank specializing in rapidly growing companies including alternative energy firms.

Contact: Eric A Prouty
Address: 53 State Street, 29th Floor, Boston, MA 02109-2811
Country: USA
Phone: +1 617 228 3515
Fax: +1 617 228 3515

GE Capital Corporation

Investor in the alternative energy marketplace providing up to 100% of the requirements for the construction and permanent term financing for projects.

Contact: Craig Reynolds
Address: 1600 Summer Street, 5th Floor, Stamford, Connecticut 06927
Country: USA
Phone: +1 203 357 3872
Fax: +1 203 357 4386

Heller Financial Incorporated

Subsidiary of The Fuji Bank, providing structuring advice and financing for alternative energy and industrial projects.

Contact: Gar Seifullin
Address: 500 West Monroe Street, Chicago, Illinois 60661
Country: USA
Phone: +1 312 441 7616
Fax: +1 312 441 7827

New Alternatives Fund Inc

Mutual fund emphasizing clean energy and the environment.

Contact: Maurice or David Schoenwald
Address: 150 Broad Hollow Road, Melville, New York 11747
Country: USA
Phone: +1 631 423 7373
Fax: +1 631 423 7393

Nth Power Technologies

Nth Power technologies is a leading venture capital fund focusing on high-growth investment opportunities arising out of the restructuring of the global energy marketplace. Nth Power has investments in distributed generation and storage, communications, control technology, transmission system automation, outsourcing, and power quality management.

Contact: Nancy Floyd, Managing Partner
Address: 50 California Street, Suite 840
San Francisco, CA 94161
Phone: 415-983-9983
Fax: 415-983-9984
E-mail: info@NthPowers.com
Web site: www.Nthpower.com

SAM Equity Partners Ltd

SAM Equity Partners is the private equity arm of Sustainable Asset Management. SAM Equity Partners invests in ventures that are commercializing PV-related technologies and which have a significant presence in Europe or North America. The fund does not invest in projects or in emerging market economies.

Contact: Nicholas Parker, Principal
Address: 3rd Floor, 8 Faneuil Hall Marketplace
Boston MA 02109, USA
Phone: (+1 617) 973 5112
Fax: (+1 617) 973 6406
E-mail: nick@sam-group.com
Web site: www.sam-group.com

US Agency for International Development (USAID)

USAID is the international aid agency of the US. government. The energy and environmental technology (EET) division within the environment center (ENV) funds a number of PV-related programs.

Contact: Dr. Griffin M. Thompson, Director, ENV/EET
Address: USAID
1300 Pennsylvania Avenue
Washington DC 20523
USA
Phone: 202 712 1772
Fax: 202 216 3230
E-mail: gthompson@usaid.gov

ASIA

Asian Development Bank (ADB)

ADB is a multilateral development finance institution, engaged in promoting the economic and social progress of its developing countries in the Asian and Pacific region.

Address: 6 ADB Avenue, Mandaluyong,
0401 Metro Manila, P.O. Box 789,
Manila Central Post Office,
0980 Manila, Philippines.
Phone: +632-632-4444
Fax: +632-636-2444
E-mail: adbhq@mail.asiandevbank.org
Web site: <http://www.adb.org/mainpage.asp>

Canara Bank (India)

A public sector bank, it offers loans up to Rs. 25 000, repayment up to 5 years, @ 12.5% p.a.(PRIORITY SECTOR LENDING RATE), for purchase of solar home systems in India, through its branch network. The loan sanctioning authority rests with the branch managers.

Address: H.O. 112, JC Road, Bangalore – 560 002 India
Phone: 91-80-222-1581
Fax: 91-80-229-3517

DFCC Bank (Sri Lanka)

A development bank providing fund and fee based services.

Contact: Mr. Jayantha Nagendran
Address: PO Box 1397, 73/5 Galle Road
Colombo 3 Sri Lanka

Phone: 94 1 440366
Fax: 94 1 440376

IREDA (India)

The financing arm of Ministry of Nonconventional Energy Sources (MNES), Govt. of India, is the principal organization in India, offering a range of services in the renewable energy sector.

Contact: Dr. V. Bakthavatsalam, Managing Director
Address: IREDA-Indian Renewable Energy Development Agency Ltd.,
Core-4A, East Court, 1st floor, India Habitat Center, Lodi Road
New Delhi – 110 003 India
Phone: 91-11-460-1344/66
Fax: 91-11-460-2855.
E-mail: gen@ireda1.globemail.com

Grameen Shakti (Bangladesh)

Grameen Shakti (GS) is a not-for-profit rural power company whose purpose is to supply renewable energy to unelectrified villages in Bangladesh.

Country: Bangladesh
Contact: Mr. Dipal Chandra Barua, Managing Director
E-mail: g_shakti@grameen.net

IT Power India Pvt. Ltd.

A leading renewable energy consultancy with specialist skills in financing of PV projects. ITPI is the local partner organization for PVMTI. In addition, ITPI assists the Indian PV industry develop financing proposals to IREDA. ITPI has been involved in over 50 renewable energy projects in 17 countries. Areas of interest include financing, business packaging, and technical advisory services.

Contacts: Terence J. Hart and Binu K. Parthan
Company: IT Power Pvt Ltd
Address: #6, Rue Romain Roland
Pondicherry, India
Phone: 91-413-342488/227811
Fax: 91-413-340723
E-mail: itpi@itpi.co.in
Web site: www.itpi.co.in

Malaprabha Grameena Bank (India)

A public sector bank, it offers loans up to Rs. 25 000, repayment up to 5 years, @ 12.5% p.a. (PRIORITY SECTOR LENDING RATE), for purchase of solar home systems in India, through its branch network. The loan sanctioning authority rests with the branch managers.

Address: H.O. Post Box No. 111, Belgaum Road, Dharwad – 580 008 India
Phone: 91-836-42861
Fax: 91-836-40393

Manipal Finance Corp. Ltd. (India)

Nonbanking Finance Company (NBFC) offers to lease/finance solar PV systems primarily due to Govt. of India's fiscal incentive of accelerated 100% depreciation on renewable energy systems in the very first year. They are also registered with IREDA as financial intermediaries. The terms of financing vary from project to project and solar PV water pumping systems have particularly benefited from leasing companies.

Address: Manipal House, Manipal – 576 119 India
Phone: 91-8252-70741
Fax: 91-8252-70959.

Nagarjuna Finance Ltd. (India)

Nonbanking Finance Company (NBFC) offers to lease/finance solar PV systems primarily due to Govt. of India's fiscal incentive of accelerated 100% depreciation on renewable energy systems in the very first year. They are also registered with IREDA as financial intermediaries. The terms of financing vary from project to project and solar PV water pumping systems have particularly benefited from leasing companies.

Address: Nagarjuna Hills, Punjagutta, Hyderabad – 500 082, Andhra Pradesh, India
Phone: 91-40-335-4159
Fax: 91-40-335-3805.

Syndicate Bank (India)

A public sector bank, it offers loans up to Rs. 25 000, repayment up to 5 years, @ 12.5% p.a.(PRIORITY SECTOR LENDING RATE), for purchase of solar home systems in India, through its branch network. The loan sanctioning authority rests with the branch managers.

Address: H.O. Manipal – 576 119, D.K. District, Karnataka, India
Phone: 91-8252-70252
Fax: 91-8252-70266.

Winrock International India

Winrock International India (WII) is a nongovernmental organization, an affiliate of Winrock International. WII's mission is to "develop and implement solutions that balance the need for food, income and environmental quality."

Contact: Shyamala Abeyratne, President
Address: 7 Poorvi Marg Vasant Vihar, New Delhi, India 110 057 India
Phone: 91 11 614 2965

Fax: 91 11 614 6004
Web site address: www.winrock.org
E-mail: information@winrock.org

LATIN AMERICA

Inter-American Development Bank (IADB)

The Inter-American Development Bank, the oldest and largest regional multilateral development institution, was established in December of 1959 to help accelerate economic and social development in Latin America and the Caribbean.

Address: 1300 New York Avenue, NW
Washington, DC 20577
United States of America
Phone: 202-623-1000
Web site: <http://www.iadb.org>

AFRICA

African Development Bank

The African Development Bank is the premier financial development institution of Africa, dedicated to combating poverty and improving the lives of people of the continent and engaged in the task of mobilizing resources towards the economic and social progress of its Regional Member Countries.

Address: African Development Bank
01 BP 1387
Abidjan 01, Cote D'Ivoire
Phone: (225) 20.20.44.44
Fax: (225) 20.20.40.06
Web site: <http://www.afdb.org>

REFERENCES

1. Eckhart M, *Financing Solar Energy in the U.S.: Scoping Paper*, REPP (1999).
2. Jechoutec K *et al.*, *The Solar Initiative*, World bank (1995).
3. Sickenberger P, "KfW Support Schemes for PV Financing in Germany", 17th *European PV Conf.*, Munich, Germany (2001).
4. World Bank, *Rural Energy and Development: Improving Energy Supplies to 2 Billion People*, WB Rep No 15912, GLB (1996).
5. Greenpeace, *Solar Generation*, for the European PV Industries Assoc (2001).
6. Ball T, Applied Power Corp., Personal Communication (2001).
7. NREL, *PV Technology Performance* (2001).
8. Wiles J, *PV Power Systems and the National Electric Code: Suggested Practices*, SAN2001-0674, Sandia Nat Labs, Albuquerque, NM, USA (2001).
9. Osborn D, *Sustainable Orderly Development: The SMUD Experience*, UPEX (2001).

10. Regional Economic Research, *Market Research on Energy*, CEC (2001).
11. NREL, *Renewable Energy Market Survey* (2001).
12. Rutledge K, *Financing Solar Energy CD-ROM*, NREL (2001).
13. Gregory J *et al.*, *Financing Renewable Energy Projects: A Guide for Development Workers*, Stockholm Environmental Inst. (1997).
14. Cabraal A *et al.*, *Best Practices for Photovoltaic Household Electrification Programs*, WB Paper No 324 (1996).
15. Alderslice A, Rogers J, *Renewable Energy for Microenterprise*, NREL (1999).
16. DeLange R, Sudimara P, Indonesia, Personal Communication (1997).
17. Hande H, SELCO India, Personal Communication (2001).
18. Saliya S, *SEEDS Solar Lending Programme*, Shell Solar, Mumbai (2001).
19. Eskom, *Market Research for Solar PV Rural Electric Service* (1998).
20. Wimmer N, "Financing Renewable Energies Through Microcredit", *Financing Renewable Energies*, Eurosolar, Bonn (1999).
21. *Photon Int.* **6**, p. 16 (2000).
22. Cabraal A, Cosgrove-Davies M, Schaeffer L, *Prog. PV Res. Appl.* **6**, 297–306 (1998).
23. Martinot E *et al.*, *The GEF Solar PV Portfolio: Emerging Experience and Lessons*, GEF (2000).
24. Eckhart M, *The Solar Bank*, Solar Intl. Mgt. Inc. (1996).
25. Ikki O, *The Current Status of PV Development in Japan*, IRENA, Berlin (2001).
26. Bonda J, *Financing Solar Energy in India*, WIP and TERI for the EC (2000).
27. NREL, *U.S. PV Roadmap* (2000).
28. Donovan P *et al.*, *An Assessment of Solar Energy as a National Energy Resource*, NSF/NASA (1972).
29. Palz W, *The Photovoltaic Power and Its Applications in Space and on Earth, Sun in the Service of Mankind*, Paris (1973).
30. Scheer H, *A Solar Manifesto*, James & James Publishers, London, UK (2001).

This Page Intentionally Left Blank

Index

- a-Si *see* amorphous silicon
- a-Si/a-SiGe tandem solar cells 546–51
- a-Si/a-SiGe/a-SiGe triple-junction solar cells 546–51
- a-Si:H 29
- a-Si:H solar cells, optical design 537–40
- ABAQUS 245
- ABN Amro Bank NV 1108
- absorber layer design of *pin* solar cell 533–4
- absorber region 87
- absorption coefficient 70, 72–4, 341, 507
- absorption coefficient spectra 519
- acceptors 69–70
- accumulator capacity 957–62
- activation energy 807
- ADO louver system 1032
- Advanced Photovoltaic Solar Array (APSA) 435
- Advanced Photovoltaics Systems, Inc. 512
- African Development Bank 1114
- Air Mass 62–3, 914, 916
- Air Mass Zero (AM0) spectrum 417
- air pollution 997–9
- albedo-collecting modules 472
- albedo irradiance 931
- AlGaAs 360
- AlGaAs/GaInP TJIC 397
- AlInP window layers 391–2
- alternating current (AC) 34
- alternative peak power ratings 715
- aluminothermic reduction of silica 201
- aluminum alloys 158
- aluminum back surface field 281
- aluminum industry 158
- Alwitra Evalon roofing foil 1030
- AM/PM method 716
- ambient temperature, diurnal variations of 933–4
- ambipolar diffusion coefficient 108
- Amonix Inc 496
- amorphous silicon (a-Si) 21, 27–9, 153, 176, 505
 - alloying 518–20
 - atomic structure 513–14
 - defects 514–15
 - deposition, miscellaneous methods 526
 - deposition techniques 520–1
 - metastability 514–15
 - optical properties 518–20
- amorphous silicon (a-Si)-based photovoltaics, critical issues for further enhancement and future potential 559
- amorphous silicon (a-Si)-based solar cells
 - continuous roll-to-roll manufacturing on stainless steel substrates 553–5
 - module manufacturing 553–8
- amorphous silicon (a-Si) module 955
 - manufacturing cost, safety, and miscellaneous issues 556–7
 - performance 557–8
 - production on glass superstrate 555–6
- amorphous silicon (a-Si) photovoltaics, status and competitiveness 558
- amorphous silicon (a-Si) *pin* cells 528–41
- amorphous silicon (a-Si)/single-crystalline silicon 176
- amorphous silicon (a-Si) solar cells 505–65, 1033–4
 - designs for 508–13
 - overview 505–13
 - substrate and superstrate designs 509–10

- ampere-hour efficiency 810
 - angle of incidence
 - effects 934–7
 - relative transmittance plotted against 935
 - angular distribution of sky irradiance 929
 - angular losses calculation 936
 - annealing 343–4
 - annual energy production, economic analysis 983
 - annual energy value, economic analysis 984
 - annual performance and energy cost
 - summary for central station plants 36
 - annual radiation availability 941
 - ANSYS 245
 - antireflection (AR) coatings 205, 268–9, 274, 283, 307, 326
 - and encapsulation 287
 - antireflective (AR) coatings, high-efficiency III–V multijunction solar cells 375–6
 - aperture efficiency 322
 - Apollo Telescope Mount array 414
 - Applied Solar Energy Corporation (ASEC) 466
 - architecture 1005–42
 - challenge of photovoltaics 1005–6
 - functions of PV modules 1008–10
 - see also* BIPV
 - Argentina, rural electrification 1061
 - Array field 965
 - ASHRAE model 934–5
 - Asian Development Bank (ADB) 1111
 - ASN Bank 1104–5
 - aspheric lens 486
 - astronomical unit 907
 - Atlantis sunslates 1017
 - atmospheric pressure chemical vapor deposition (APCVD) 547
 - Auger recombination 76
 - Australian National University (ANU) 496
 - autonomous emergency phone and information system 58
 - autonomous power supply systems 799, 808
 - applications 856
 - energy-flow diagram 814
 - for telecommunications 856
 - investment and lifetime costs 857–9
 - requirements to electrical storage systems 800
 - system designs 801
 - autumn equinox 907
 - auxiliary generators 790–1
 - back reflectors 537, 539
 - back-surface field (BSF) 88, 258, 281
 - recombination velocity 98
 - balance equation 120
 - balance of system (BOS) 5, 11, 14, 32–7, 863
 - Ballistic Missile Defence Organization (BMDO) 416
 - band diagram of solar cell 120
 - band gap 37–8, 99–100, 132–4, 516–17, 540
 - a-Si alloys 546
 - as function of lattice constant 361
 - cell efficiencies as function of 415
 - grading 546
 - narrowing (BGN) 70, 73
 - silicon alloys 544–6
- bandedges 516–17, 528–9
 - bandtails 516–17
 - batteries 33, 54, 1052
 - capacity 811–12
 - classification of operating conditions 813–17
 - for photovoltaic systems 835
 - further developments 860
 - general concept 801–12
 - lifetime 787, 811, 860
 - operating conditions 786–7, 811–12
 - secondary electrochemical systems with external storage 849–57
 - state of charge 811–12
 - state of health 811
 - system indicators 816
 - technical terms and definitions 809–11
 - with internal and external storage 807–9
 - see also* lead acid batteries and specific types
 - battery chargers 843
 - battery charging 56
 - battery charging stations 763
 - battery currents 810
 - battery storage 784–7
 - battery voltage and current during charging 870
 - beam radiation 913
 - beginning-of-life (BOL) output 419
 - belt furnaces 274
 - bi-directional step-up/step-down conversion 893
 - bifacial modules 294
 - BIPV 15, 294, 775–6, 1006, 1014
 - basics 1026–35
 - categories and type of buildings 1026–35
 - categories of cell and modules 1026
 - categories of integration 1027

- cells and modules 1029–35
 design process 1036–40
 distance between buildings 1036
 function of integration 1028–9
 module temperature 1034–5
 orientation and angle 1036
 practical rules 1037–8
 reflection 1037
 solar cell materials 1030–4
 space required for balance of systems
 and interconnections 1039
 step-by-step design 1038–9
 strategic planning 1039–40
 trees 1036–7
 types of buildings and functions 1027
 urban aspects 1036
 zoning 1037
 black body, radiation spectrum for 63
 block-casting process 215
 body-mounted arrays 432
 Bolivia, rural electrification 1061–3
 boron back surface field 281
 boron-doped *p*-type material 216
 Bose–Einstein function 122
 boundary condition 338–41
 BP Solar 496
 BP Solface vertical wall system 1032
 Bragg reflectors 124
 Brazil, rural electrification 1063–4
 Bridgman technology 214–16
 Brundtland Centre, Toftlund (DK), case
 study 1022–6
 BSF 266–7, 288
 Buck converter 885–7
 building integration
 definition of 1006–8
 well-integrated systems 1014–18
 building-integrated PV systems *see* BIPV
 built-in voltage 83, 85
 bulk multicrystalline silicon 214–23
 bulk *p*-type material lifetime 419
 bulk silicon crystallization, simulation of
 247–9
 buried contact solar cell process 289–91
 Butler–Volmer equation 804–6

 calibration of space solar cells 424–5
 Canara Bank (India) 1111
 capacitance–voltage (*C*–*V*) characteristics
 398
 carbon
 as impurity in silicon 187
 in multicrystalline silicon 221
 carbon dopant 391
 carbothermic reduction of quartz 167
 carbothermic reduction of silica 161–3,
 198

 Carnot efficiency 125, 131–2, 148
 carrier–carrier scattering 81
 carrier mobility 78–9
 carrier transport 81
 cash flows 974
 casting alloys 158–9
 cause–effect diagram for failed system
 1054
 CdCl₂ treatment 633–7
 CdS/CdTe couples
 bulk diffusivities 639
 grain-boundary diffusion process 639
 CdS/CdTe intermixing 637–42
 CdTe 21, 27, 30–1, 64
 absorber layer 633–7
 band structure 625
 cell photon losses and quantum
 efficiency versus wavelength 648
 close-space sublimation (CSS) 628–9
 condensation/reaction of Cd and Te
 vapors on a surface 628–9
 crystal structure 624
 deposition methods 626–7
 electrodeposition 629–30
 galvanic reduction of Cd and Te ions at
 a surface 629–30
 high-efficiency 645
 material properties and thin-film
 fabrication methods 621–31
 metal organic chemical vapor deposition
 (MOCVD) 630
 optoelectronic properties 622
 phase diagram 623
 physical vapor deposition (PVD) 628
 physiochemical properties 622
 potential toxicity 10
 precursor reaction at a surface 630–1
 screen-print deposition 631
 spray deposition 630–1
 sputter deposition 629
 thin-film deposition techniques 627
 vapor transport deposition (VTD) 629
 CdTe modules 651–3
 CdTe thin-film solar cells 617–62
 back contact 642–4
 basic structure 632
 capacitance measurements and
 hole-density determination 649
 characterization 644–50
 development overview 617–21
 future 653–7
 J–*V* curves 647
 summary of status 650
 window layers 631–2
 CdTe/CdS 28
 bulk-diffusion coefficient versus inverse
 of treatment temperature 640

- CdTe/CdS (*continued*)
 grain-boundary diffusion coefficient
 versus inverse of treatment
 temperature 641
- CdTe/CdS heterojunction solar cells 619
- CdTe/CdS junction band diagrams 644
- CdTe/CdS solar cells
 current-voltage and relative quantum
 efficiency curves 621
 quantitative assessment of film
 properties 626
- CdTe/CdS thin-film structures,
 time-progressive X-ray diffraction line
 profiles 640
- CdTe-CdS pseudobinary phase diagram
 639
- CdTe_{1-x}S_x alloy thin film optical band
 gap versus composition 638
- celestial equator 909
- celestial poles 909
- celestial sphere 908-9, 911
- cell potential 809
- cell technology and efficiency, effect on
 module price 36
- cell voltage 809
- Central and Southwest Services (CSW)
 467
- Centre for Sustainability De Kleine Aarde
 in Boxtel 1017
- centrifugal pump system 894
- chalcopyrite lattice structure 571
- characteristic curve 952
- characteristic parameters 951-2
- charge controllers 33, 787-8, 843,
 864-77
 appraisal factors 875-7
 compliance to codes 877
 design criteria 875-7
 efficiency 876-7
 linear 865
 safety aspects 877
 self-regulating PV systems 865
 with integrated voltage and current
 meter 874
see also T-CHEQ system
- charge equaliser 843
 for long battery strings 877-80
- charge transfer between molecular orbitals
 39
- chemical etchants 397
- chemical leaching, post-treatment by
 195-6
- chemical potential 134, 140, 142, 145
- chemical processes 807
- chemical texturing 285-7
- chemical vapor deposition (CVD) 284,
 315
- Cherry Hill Conference 13
- CHP space-heating applications 855
- CIS flat-plate 36
- Clean Energy Fund 1105
- clearness index 920, 945
- close spaced sublimation (CSS) 30
- cloudiness index 921
- CO₂ emissions 48-9
- CO₂ reduction 22
- Cold Wall process 246
- Colt shading system 1012
- Commons Capital LP 1108-9
- Communication/Navigation Outage
 Forecast System (CNOFS) 440
- Composited Optics Incorporated (COI)
 440
- compound parabolic concentrator (CPC)
 454, 482-3
 concentrating arrays 436-8
 concentration PV systems 31-2
 concentration ratio 450, 455, 484
 concentrator cell and module efficiencies
 473
- Concentrator Initiative 465-6
- concentrators 106-7, 124, 376-80,
 406-7, 449-503, 946-7
 basic types 452-60
 compound parabolic (CPCs) 454,
 482-3
 current activities 495-500
 D-SMTS 494
 development dilemma 450-2
 dielectric-filled 491-2
 early demonstration projects 466-7
 historical overview 460-74
 history of performance improvements
 472-4
 innovative 492-4
 literature 450
 market barriers 449-503
 marketing 451
 miscellaneous programs 471-2
 optics 452-5, 474-95
 parabolic 479-82
 reflection and refraction 478
 reflective trough 494
 research 449-503
 RXI 494
 Sandia National Laboratories program
 461-2
 schematic representation 475
 secondary optics 489-91
 static 456-60, 470, 491-2
 two-stage 473
 types of tracking 456-60
 V-trough 483-5

- conduction band (CB) 4, 66–7, 74, 119–21, 129, 144–5, 536
- confidence coefficient 918
- confidence interval 918
- conservation of energy 71
- consumer products 57–9
- control strategies 870–1
- cost break down of solar home system 56
- cost distribution for modules and silicon wafers 223
- cost model 35
- cost of electricity for utility-scale PV plants 990–4
- cost projections 50
- costs 15–19
 - for TFSC 34
 - for very high-efficiency 1000 suns-concentrating systems 38
 - of construction of PV central plant 35
 - of small professional autonomous photovoltaic systems 55
 - of stand-alone PV installation 33
 - see also* economic analysis; system cost
- covalent bonds 183
- crystal defects 217–19
- crystal growth techniques, numerical simulations of 244–51
- crystal imperfections, effect of 182–5
- crystalline silicon 21, 27–8, 176, 230
 - bulk properties 257
 - contacting structures 260
 - contacts 257–8
 - progress and challenges 23–7
 - surfaces 256–9
 - wafer material for 245
- crystalline silicon Cz module 35
- crystalline silicon noncontacted surfaces 258–9
- crystalline silicon photovoltaic modules 291–302, 948–9, 955
 - cell matrix 291–2
 - electrical characteristics 295–7
 - fabrication spread 297
 - field performance 301–2
 - lamination and curing 293
 - layers of the module 292–3
 - lifetime 301
 - local shading and hot spot formation 297–9
 - mismatch losses 297
 - optical properties 300
 - postlamination steps 294
 - qualification tests 301–2
 - special modules 294–5
 - thermal characteristics 295–7
 - with back contact cells 295
- crystalline silicon solar cells 255–91, 948
 - back contact print and dry 275
 - back surface 266
 - back surface passivation 281
 - cell structure 259–60
 - cofiring of metal contacts 275
 - front contact print and dry 274–5
 - front surface 263–6
 - manufacturing process 271–80
 - materials and processing 260–2
 - performance comparison 270
 - process flow 271–6
 - size effects 266–8
 - substrate 260–3
 - substrate thickness 263
 - testing and sorting 275
 - throughput and yield 279–80
 - variations to basic process 280–3
- crystalline silicon technology 40
- crystalline silicon wafer PV technology 28
- crystallization 193–4, 216–17, 219, 223
 - from aluminum melt 194
 - from silicon-melt 194
 - heat flow in 247
 - thermal modeling of 245–7
- Cu₂S/CdS thin-film solar cells 568
- Cu–In–Se system 571–2
- CuIn_{1-x}Ga_xSe₂, complex refractive index 575
- Cu(InGa)Se₂ 21, 27, 29, 31, 35
- Cu(InGa)Se₂ solar cells 567–616
 - absorption of light with different wavelengths 595
 - alternative buffer layers 588–90
 - back contact 580
 - buffer layers 591–2
 - chemical bath deposition (CBD) 585–6
 - coevaporation 580–3
 - commercial development 570
 - composition 571–3
 - critical materials with respect to primary supply 608
 - current loss 594
 - deposition methods 578–84, 587–8
 - device completion 592
 - device operation 592–602
 - efficiency 590, 593
 - electrical properties 574–6
 - environmental concerns 608–9
 - equipment 602–4
 - evolution of device record efficiencies 605
 - future outlook 609–11
 - grain boundaries 576–7
 - interface effects 586–7
 - junction and device formation 584–92

- Cu(InGa)Se₂ solar cells (*continued*)
 lack of comprehensive scientific base 570
 light-generated current 593
 manufacturing issues 602–9
 material properties 570–8
 module fabrication 604
 module performance 604–7
 optical properties 574
 outdoor testing results 606
 processes 602–4
 production costs 607
 quantum efficiency 593
 recombination 595–8
 scanning electron microscopy image 577
 schematic cross section 569
 structure 571–3
 substrates 578–9
 surface 576–7
 TEM cross section 569
 thin films 570
 transparent contacts 590–1
 two-step processes 583–4
 wide and graded band gap devices 600–2
- Cu(InGa)Se₂/CdS 28
 current–voltage (*J*–*V*) behavior 595–6
- Cu(InGa)Se₂/CdS interface 599–600
- Cu(InGa)Se₂/CdS solar cells
 quantum efficiency curves 596
 temperature dependence 597
- CuInSe₂ 570
 absorption coefficient 574
 complex refractive index 575
 electronic levels of intrinsic defects 576
 intrinsic defects 576
 selected properties 572
- CuInSe₂ solar cells 567, 569
 current density 82, 805
 versus voltage 506
 current flow, electrode kinetics at 803–7
 current matching 548
 current–voltage (*I*–*V*) characteristics 92–5, 103–4, 122, 335, 701
 current–voltage (*I*–*V*) measurements 721–38
- CVD 321, 343
- Czochralski (Cz) cell technology 24, 989–90
- Czochralski (Cz) crystal-pulling technique 205, 246
- Czochralski (Cz) flat-plate cell 989
- Czochralski (Cz)-grown crystalline silicon 206, 261
- Czochralski (Cz)-grown crystals and wafers 207–11, 989
- Czochralski (Cz) module 987
- Czochralski (Cz) web modules 989
- daily energy deficit 959
 daily irradiation 932–3
 on inclined surface 933
 daily radiation sequences 937
 dangling bonds 514–15, 517
 dark saturation current 91–2, 96
 daylight control 1013
- D&B Capital 1105
- DC–AC conversion 37
- declination 916
- deep discharge protection (DDP) 763, 873–6
- Deep Level Transient Spectroscopy (DLTS) 221
- Deep Space 1 spacecraft 416, 437
- deep trapping 531
- defect clustering 334
- defect levels 517–18
- demand side management options 15
- dendritic web (WEB) cells 989
- dendritic web (WEB) production 231
- dendritic web (WEB) technology 35, 232–5, 239–43, 288
- density of state 66–7
- depletion approximation 84
- depletion region 83–5, 88, 90–1
- depth of discharge (DOD) 810, 847–8
- developing countries 1074
 lack of electricity 1044–5
see also remote areas; rural areas
- development 1043–71
- device diagnosis 401–3
- DFCC Bank (Sri Lanka) 1111–12
- diamond lattice 64
- diesel generator sets 54
- diffuse fraction
 of horizontal radiation 920–5
 of individual daily global irradiation 922
 of mean daily global irradiation 921
- diffuse irradiance 928–31
- diffuse radiation 913
- diffusion 78, 80
- diffusion coefficient 81, 185
- diffusion length 212–13, 263
- diffusion overvoltage 807
- diffusion processes 806
- digital synthesis, voltage shaping by 890–2
- diode ideality factor 103
- direct band gap materials 73
- direct band gap semiconductors 71, 76

- direct current (DC) 3, 5, 34
 direct irradiance 928
 direct irradiation 913
 direct subsidies (buy-downs) 1094–5
 dirt effects 934–7
 dirty surfaces 944
 Discovery Science Center, Santa Ana, Los Angeles 1018
 dislocations 184–5, 218
 dispersion parameter 532
 dispersive transport 532
 displacement current 81
 distributed power generation 53
 distribution coefficients 182
 distribution function of monthly electricity consumption 963
 diurnal variations of ambient temperature 933–4
 divergence operator 116
 doctor blade technique 679
 domestic appliances, energy-saving 793–4
 donor funding 1086–7
 donors 69–70, 186, 220
 doping 69, 216, 518
 silicon alloys 528
 doping level and type 262–3
 double-layer capacitors 824–6, 859
 double-sided textured (DT) cells 329, 331
 drift 78–9
 of electrons 534
 of holes 531, 534
 dummy wafers 178
 dust-covered surface 935
 dye fixation onto TiO₂ film 680
 dye-sensitized solar cells (DSSC)
 663–700
 approach to commercialization 691–4
 background 663–4
 cell assembly 681–2
 cell performance 681–2
 characteristics 678
 charge recombination 675
 charge-transfer kinetics 673–8
 counter electrode 669, 681
 efficiency improvement 695–6
 electron injection process 673–5
 fabrication 678–82
 materials 664–70
 metal complex photosensitizers 683–7
 module fabrication 694
 natural dye photosensitizers 687–8
 new developments 682–90
 new dye photosensitizers 683–8
 new electrolytes 688–9
 new oxide semiconductor film photoelectrodes 683
 operating principle 670
 organic dye photosensitizers 687–8
 photovoltaic performance 672–3
 primary processes 670–2
 prospects 695–6
 quasi-solid-state 689–90
 recombination between injected electrons and tri-iodide ions (dark current) 676–7
 redox electrolyte 681
 regeneration of oxidized photosensitizers 676
 sealing materials 670
 solid electrolyte 696
 solid-state 689–90
 stability 691–4
 structure 664–70
 E&Co 1109
 Earth–Sun position 912
 ecliptic plane 907, 909
 ecological dimension 48–54
 economic analysis 971–1003
 annual energy production 983
 annual energy value 984
 capital recovery factor (CRF) 980
 case studies 984–97
 cash flows 973, 977
 discount rate 975
 discounted payback (DPB) 979, 984
 energy payback 997–9
 financial evaluation of system 976
 general methodology 980–4
 inflationary effects 977
 internal rate of return 979
 key concepts 973
 key technical and financial parameters 986
 levelized bus bar energy cost (LBEC) 980
 levelized energy cost (LEC) 980, 983
 net cash flow 978
 overview 972–3
 payback 984
 payback period in years 979
 present value or present worth 974–7
 return on equity (ROE) 992
 total capital requirements for central station plants 993–4
 value of system 975
 see also cost(s); financing of PV growth
 Edge-defined Film-fed Growth (EFG) 230, 232, 234–5, 239–41, 244–5, 251, 288
 Edge-Stabilized Ribbon (ESR) 231
 Edge-Supported Pulling (ESP) 231
 effective concentration 803

- effective distribution function 182
- effective recombination velocity 87
- efficiency of photovoltaic conversion
 - 113–51
 - very high efficiency concepts 132–48
- efficiency calculation 125
- efficiency forecasts 113
- efficiency limit 113, 122–3
- efficiency upper limit of solar cell 120
- Einstein relationship 80–1, 86
- electric current 4
- electric field 86
- electric field profile 532
- Electric Power Research Institute (EPRI)
 - 467–71, 982, 992
- electric-vehicle batteries 835
- electricity
 - and development 1043–6
 - applications in rural setting 1046–7
 - basic sources 1047–8
 - centralized system 1045
 - future 2
 - lack in developing countries 1044–5
 - see also* photovoltaic electricity
- electricity consumption of household appliances 794
- electricity generation 45
 - photovoltaics as long-term substitute 48–54
- electricity production scenarios 52
- electrochemical cells 809
 - fundamentals 801–7
- electrochemical equilibrium 804
- electrochemical potential 122, 143
- electrochemical processes 807
- electrochemical reactions, energy exchange 802
- electrochemical storage 799–862
 - schematics 808
- electrode kinetics at current flow 803–7
- electrodeposition (ED) 30
- electrodes 809
- electrolyte-agitation systems 844
- electrolytic transfer of silicon 201
- electromagnetic compatibility (EMC) 867
- electromagnetic radiation 61
- electron beam-induced current (EBIC) 193
- electron behavior 531
- electron cyclotron resonance CVD (ECRCVD) 341
- electron effective mass 65
- electron fluence for silicon solar cell 421
- electron-hole pairs 62, 70, 74, 122, 143, 257
- electron parameters 531
- electron wave function 65
- electronic density-of-states 515–16
- electronic devices 59
- electronic modeling, thin-film silicon solar cells 333–41
- electrons
 - drift of 534
 - thermodynamic function of 119
- electrostatic potential difference 84–5
- electrostatically clean arrays 439–40
- ELYMAT 212–13
- emergency telephones 757–8
- emitter front 281–2
- emitter sheet resistivity 335
- emitter structures 264
- emitters 87, 93, 258
 - homogeneous 264–5
 - point 265
 - selective 265
- end-of-charge voltage 811
- end-of-discharge voltage 809
- energy and Early Man 1043–4
- energy band diagram 66
- energy band model 339
- energy band structure 65–6
- energy collection versus inclination angle 940
- energy conversion, characteristics of 45–8
- Energy Conversion Devices, Inc (ECD) 553–4
- energy efficiency 810
- energy flow analysis 812–13
- energy gap 516
- energy losses in grid-connected systems 966
- energy-management systems (EMS) 873, 875
- energy market, liberalization 52
- energy payback 997–9
- energy-saving domestic appliances 793–4
- energy storage 55, 799
- energy yield of grid-connected systems 965–6
- Entech Inc 497
- Entech linear-focus Fresnel system 463–5
- enthalpy 802
- entropy 802
- entropy production 116–17, 128
 - in Shockley–Queisser solar cell 129–31
- environmental considerations 997–9
- Environmental Enterprises Assistance Fund (EEAF) 1100
- environmental monitoring 10
- epilayers, characterization 398–400
- epilift technique 320–1

- EPRI 467–71, 992
 equilibrium carrier concentration 67–70
 equilibrium energy band diagram 86
 equilibrium potential 801–3
 equilibrium voltage 805, 809
 Ernst & Young Renewable Energy Unit 1105
 Ethyl Corporation process
 for semiconductor grade silicon 173–5
 simplification 198–201
 Euclides linear trough system 497
 Europe, PV programs 1097–9
 European Bank for Reconstruction and Development (EBRD) 1105–6
 European Commission DG XVII 1106
 European Investment Bank (EIB) 1106
 exchange current density 805
 excimer laser annealing (ELA) 350
 excimer laser recrystallization (ELR) 350
 experience curve 50–1
 experience factor 17, 38
 Explorer I 414
 extensive variables 114
 external collection efficiency 95
 extraction metallurgy in ladle,
 post-treatment by 196–8
 extraterrestrial applications 59–60
 extraterrestrial irradiance 915–16
 extraterrestrial radiation 913, 926

 FAC/Equities A Division of First Albany Corporation 1109
 facade systems 1014
 failed system, cause–effect diagram for 1054
 Fast Auroral Snapshot (FAST) solar array 440
 Fermi energy 68–9, 83, 88, 518
 Fermi function 68
 Fermi level 119, 529, 535
 figures of merit 444–6
 fill factor (*FF*) 309
 Final Yield 965
 financial characteristics 1077–9
 financing of PV growth 1073–115
 borrowers experience 1081
 capital requirements 1076–7
 example calculation 1082
 grid-connected residences 1079–82
 growth outlook 1075
 historical development 1073–4
 lenders issues 1081
 market drivers 1075
 organizations involved in 1100–14
 residential sector 1082
 rural areas 1083–6
 financing the PV industry 1091–2

 financial-support mechanisms 50
 fixed surfaces, irradiation on 943–5
 Flat Plate Array Project 230
 flat-plate, CIS 36
 flat-plate conventional PV modules 947
 flat-plate solar cells 268, 989
 flexible fold-out arrays 433–5
 flexible roll-out arrays 435–6
 float zone (FZ) monocrystals 205
 floating-zone technique 207
 flooded batteries 844
 flywheels 799
 foil *see* silicon ribbon and foil production
 forecasts 15–19
 long-term 18
 four-junction III-V cells 417
 Fourier Transform Infrared Spectroscopy (FTIR) 219
 Franz Keldysh effect 73
 Fraunhofer-Institut für Solare Energiesysteme 497–8
 free-carrier absorption 74
 free enthalpy 802
 Fresnel lens 36, 452–3, 462, 464, 466, 474, 485, 487–9, 496
 Fresnel module price 992
 Fresnel system 990
 front-polished and back-textured (FPBT) 329
 front-surface recombination velocity 97
 front-textured and back-polished (FTBP) 329, 331
 fuel cells 854–5
 fumed silica 159, 170
 functional silanes 160
 fundamental absorption 70

 GaAs 5, 20, 27, 60, 64, 123–4, 360, 426, 472
 back-surface fields 394
 optical properties 394
 properties at 298K 386
 window layers 394
 see also GaInP/GaAs; GaInP/GaAs/Ge
 GaAs cells 393–4, 994–7
 Ge(100) substrates 393–4
 GaAs tandem-junction cells 996
 GaAsP 360
 GaInAs 360
 GaInP 5, 20–1, 40, 426, 472
 absorption coefficient 388–9
 optical properties 387–9
 ordering in 387
 properties at 298K 386
 GaInP solar cells 383–93
 back-surface barrier 392–3
 characteristics 393

- GaInP solar cells (*continued*)
 doping characteristics 389–91
 lattice matching 383–7
 window layers 391–2
- GaInP/GaAs cell efficiencies 361
- GaInP/GaAs multijunction solar cell 360
- GaInP/GaAs tandem solar cells 360, 362
- GaInP/GaAs/Ge concentrator cell 379–80
- GaInP/GaAs/Ge solar cells 361, 363
 materials issues 382–98
 MOCVD 382
 refinements to 403–4
- GaInP/GaAs/Ge tandem cell 359
- Galaxy XI spacecraft 438
- gap states 517–18
- GaSb 472
- GE Capital Corporation 1109
- generator capacity 957–62
 versus storage capacity 959
- Geospace Electrodynamic Connection (GEC) projects 440
- geosynchronous Earth orbits (GEO) 420
- German 100 000 photovoltaic roofs programme 778–9
- germanium
 optical properties 394
 properties at 298K 386
see also GaInP/GaAs/Ge
- germanium cells 394–6, 426–7
 III-V heteroepitaxy 395–6
 junction formation 394–5
- germanium substrates 393–4
- Germany 1074
- gettering 262, 283
- Global Approval Program for Photovoltaics (PV GAP) 1054
- Global Environment Facility (GEF) 1089–91, 1101
- global horizontal irradiation 918
- global irradiance on inclined surface 927–33
- global radiation 913, 920–5
- global trends in performance and applications 20–3
- global warming 48
- glow discharge deposition at different frequencies 523–5
- goals of current solar cell research and manufacturing 19
- government funding of research and development 1096–100
- government incentives and programs 1092–6
- grain boundaries (GB) 183, 185, 217, 310, 333, 337
 categorization 337–8
- grain boundary interface recombination velocities 342
- grain enhancement, thin-film silicon solar cells 343–50
- grain growth 349
- grain size 217–18, 340
- grain size distribution 349
- grains, categorization 337–8
- Grameen Shakti (Bangladesh) 1112
- grand canonical potential current density 129
- grand canonical potential flow for electrons 130
- grand potential 115
- green design, PV role in 1011
- grid-connected systems 754, 779–80
 block diagram 775
 decentralized 774–9
 dependence of annually used solar energy from 792
 energy losses in 966
 energy yield of 965–6
 future developments 796–7
 inverters 788–9, 881–902
 joint ownership 779–80
- grid-independent systems, for small devices and appliances 755–9
- Group IB formation in QD arrays 147
- Group IB material 144–5
- Group IB solar cell
 limiting efficiency 147
 structure 146
- Group III-V semiconductor compounds and alloys 362
- Group III-V solar cells, space applications 426–31
- Group VB 120–1, 129, 144–5
- H-type bridge 892, 895–6
- H-type bridge inverter 892
- hazard classification 10
- Heat Exchange Method (HEM) 246
- heat flow in crystallization 247
- heat load and daylight control systems 1013
- Helios unmanned prototype aircraft 783, 785
- Heller Financial Incorporated 1109–10
- heterojunction with intrinsic thin-layer (HIT) solar cells 271, 288–9
- high-efficiency III-V multijunction solar cells 359–411
 antireflective (AR) coating effects 375–6
 cell configuration 365–6
 chromatic aberration 375
 concentration 376–80

- concentration dependence of efficiency 378
- current matching 376
- current-matching effect on fill factor and V_{OC} 373
- efficiency 382
- efficiency versus band gap 370–2
- fill factor 382
- four-terminal connection 365
- growth on other substrates 405–6
- implementation into terrestrial systems 406–7
- materials availability 398
- metallization 378–9
- multijunction J - V curves 368–70
- overview 359–63
- physics of 363–5
- series-connected device performance 366–82
- series resistance 378–9
- single-junction solar cells, physics of 363–5
- space applications 363
- spectral effects 374–5
- spectral fluctuations 374–5
- spectrum 377
- spectrum splitting 364–5
- temperature dependence 380–2
- terrestrial energy production 363
- theoretical limits to multijunction efficiencies 364
- three-terminal voltage-matched interconnections 366
- top and bottom subcell QE and J_{SC} 367–8
- top-cell thinning 372–3
- troubleshooting 398–403
- two-terminal series-connected (current matched) 366
- high-efficiency multijunction solar cells 551
- high-efficiency silicon (HES) cells 415, 426
- high-level injection 107–9
- high-radiation environment solar arrays 443–4
- high specific power arrays 443
- high-temperature/intensity arrays 438–9
- holes, drift of 531, 534
- horizontal radiation, diffuse fraction of 920–5
- hot electron solar cells 141–4
 - band structure 143
- hot-wire chemical vapor deposition (HWCVD) 341, 345–7, 525–6
- household appliances, electricity consumption of 794
- housing projects 1020–1, 1023
- HS601 spacecraft 426
- HS702 spacecraft 426
- Hubble space telescope 436–7
- human development index (HDI) 2
- hybrid systems 763–6, 768, 860
- hydrogen, passivation with 283–5
- hydrogen dilution 526–7
- hydrogen/oxygen storage systems 852–7
 - applications 855–7
 - electrolysers 853
 - gas storage 853–4
- hydrogen storage systems 860
- hydrogenated amorphous silicon 507
- IFU 1106–7
- IMCAP 985
- impact ionization 76
- Impax Capital Corporation Ltd 1106
- impurities 219–23
- inclination angle versus latitude 942
- inclined surface
 - daily irradiation on 933
 - global irradiance on 927–33
 - solar radiation on 920–33
- income tax deductions and credits 1096
- indirect band gap semiconductors 72, 76
- indium-tin-oxide (ITO) layer 547
- ING Bank Nederland 1107
- ingot fabrication 214–16
- In_2Se_3 - Cu_2Se equilibrium phase diagram 573
- inside efficiency 322
- institutional uses 1083–4
- integrated power systems 442–3
- integrated PV building *see* BIPV; building integration
- intensive variables 114
- Inter-American Development Bank (IADB) 1114
- interest subsidies 1095–6
- interface condition 338–41
- intermediate band (IB)
 - concept 39
 - solar cell band diagram 145
- internal gettering 351
- international aid 1086–7
- International Finance Corporation (IFC) 1089, 1101
- international financing sources 1086–91
- International Panel on Climate Change 48–9
- International Space Organization 422
- International Space Station (ISS) 415–16, 434, 782, 784
- interstitial impurities 184
- interstitial oxygen 219

- intragrain defects 333
 inverters 5, 788, 881–902
 active quality control in the grid 900
 combination of step-down converter with 890
 general characteristics 881
 grid-connected systems 788–9, 881–902
 H-bridge-type 885
 high-frequency concepts 894–6
 power factor as function of output power 899
 power quality 896–9
 principles 884–96
 safety aspects for grid-connected systems 900–2
 square-wave-type 884–5
 stand-alone operation 883
 stand-alone systems 789–90
 three-phase PWM 894
 with sinusoidal AC output 885–96
 Ioffe Physical-Technical Institute 498
 ionizing radiation 419
 IREDA (India) 1112
 iron concentration 222
 irradiance 913, 915
 irradiance measurements 721–2
 irradiance to daily irradiation ratios 926
 irradiation 913
 of most widely studied surfaces 940–1
 on fixed surfaces 943–5
 IT Power India Pvt. Ltd. 1112
I–V characteristics 92–5, 336
I–V curves 275–6, 299, 867, 949–50
I–V measurements
 cell and module systems 731–6
 multijunction cells 400–1
 simulator-based 722–3
I–V performance 548–9

 Japan, PV programs 1097
 Japanese residential PV promotion program 777
 Jet Propulsion Laboratory (JPL) Flat Plate Array Project 230
 joint ownership project 781
 JRC Ispra guidelines 965
 junction isolation 274
J–V characteristics 544
J–V curves 341–2, 368–70
 for series-connected subcells 369

 Kyoto Protocol 22

 Lafarge Braas PV 700 roof tile system 1015
 Lagrange invariant 118

 Landsberg efficiency 148
 laser-grooved buried-grid (LGBG)
 industrial cells 264
 laser-grooved buried-grid (LGBG) solar cell process 290–1
 laser-induced recrystallization 350
 laser-pulse time-of-flight measurements 531
 law of the junction 88
 lead acid batteries 806, 817, 826–49, 856
 acid stratification 837–9
 ageing processes and their influences of properties 837
 applications 829–35
 charge/discharge process in lead electrode 828
 charging 845–6
 chemistry 827–9
 concepts 829–35
 corrosion 840
 deep-discharge protection 847–9
 discharge capacity 836–7
 discharge curves 849
 erosion 840–1
 fundamentals 829–35
 ice formation 842–3
 operation strategies 844–9
 peripherals 843–4
 reverse charging 842
 short circuits 841–2
 sulphation 839
 technology 829–35
 voltage thresholds 875–6
 lead sulphate crystals 807
 Legendre's transformation 114–15
 less-developed areas 972
 light absorption 70–4
 light emitting diode (LED) 76, 137–8, 148
 light-induced degradation (LID) 212–13
 light-soaking effects 541
 light-trapping 269–70, 320, 325–7, 333, 537–8
 lithium batteries 859
 lithium-ion batteries 822–4
 lithium-polymer batteries 822–4
 local apparent time 909
 local horizon 939
 long-base approximation 96
 Loss of Load Probability (LLP) 956–7, 960–1, 963–4
 low intensity low temperature (LILT) cells 441–2
 low pressure chemical vapor deposition (LPCVD) method 213
 low-Earth orbit (LEO) 414, 420

- MACD 307–8, 311, 327–31
 influence of bottom angle of texture pits 331–2
 influence of density of texture pits 332
 influence of texture height 331
- magnesium dopant 391
- Malaprabha Grameena Bank (India) 1112–13
- Manipal Finance Corp. Ltd. (India) 1113
- MARC 245
- market demand 1084
- market distribution by technologies 21
- market evolution 47
- market expansion 39–40
- market growth rates 50
- market share of monocrystalline and multicrystalline solar cells 256
- market volume 56
- markets 15–19
- Mars Pathfinder Sojourner Rover 432
- Mars solar arrays 440
- Mars solar electric propulsion (SEP) vehicle 428
- Martin Marietta point-focus Fresnel system 462–3
- Mataro Library, Barcelona, Spain 776
- matching component cells in multijunction designs 550
- matching DC/DC converter (MDC) 871
- Mathiessen's rule 79
- maximum achievable current density *see* MACD
- maximum power calculation 950
- maximum power point (MPP) 93–4, 866, 881–2, 900, 952–3
 deviations 883
- maximum power point tracking (MPPT) 871–3, 881, 894
- mean global daily irradiations 917
- mechanical stacks 404–5
- mechanical texturing 285–6
- median cracks 228
- MESSENGER Discovery mission 439
- metal-induced crystallization (MIC) 344–9
- metal-insulator-semiconductor (MIS) contacts 258
- metallization techniques 263–4
- metallurgical grade silicon 24, 157–8, 161–7, 176–7
 casting 166
 crushing 166
 economics 167
 furnace for production of 164
 refining 163–6
 upgrading purity 194–8
- metalorganic chemical vapor deposition (MOCVD) 360
 GaInP/GaAs/Ge solar cells 382
- Meteosat weather satellite 783
- Mexico, rural electrification 1064–5
- microcrystalline silicon solar cells 551–2
- microenterprise 1083
- micromorph devices 552–3
- microwave glow discharge deposition 525
- micro-X-ray 347
- mid-Earth orbits (MEO) 420
- Miller indices 65
- minority-carrier diffusion equation 82–3, 89
- minority-carrier diffusion length (MCDL) 307, 351
- minority-carrier lifetime 77
- minority-carrier recombination 185
- mobility edges 517
- modularity 56
- module aperture area 35
- module manufacturing, a-Si-based solar cells 553–8
- module price for silicon cell technology 985–90
- module temperature, BIPV 1034–5
- monitoring systems and interfaces 843, 874
- monochromatic cell 124–6
- monochromatic cell efficiency versus photon energy 125
- monocrystalline float zone (FZ-Si) material 260
- monocrystalline Si cells 1031–2
- monoenergetic membrane 144
- morphological defects 401
- MOS-FETs 866, 868
- multicrystalline silicon (mc-Si) 21, 26, 206
- multicrystalline solar cells 256, 283–7
- multicrystalline wafers 285
- multijunction designs, matching component cells in 550
- multijunction III-V cells 427–8
- multijunction solar cells 20, 38, 132–5, 510–11, 542–53
 advantages 542–4
I-*V* measurements 400–1
 measurement procedures 728–30
 principles and operation 362
 quantum efficiency measurements 549
- multilinear Lagrange invariant 118
- multi-wire sawing technique 224
- n*-type material 77, 83
- n*-type semiconductors 76
- n*-type side 25

- n*-type silicon 184
- Nagarjuna Finance Ltd. (India) 1113
- nanotechnology 39
- National Meteorological Services 916
- National Renewable Energy Laboratory (NREL) 323, 360, 498
- natural integration 1015
- NEDO process 198
- Nernst equation 803
- New Alternatives Fund Inc. 1110
- New Century Finance Limited 1107
- New Energies Invest Ltd. 1107
- NiCd batteries 818–21
- nickel-metal hydride (NiMH) batteries 821–2
- Ni-Si phase diagram 190
- nominal operating cell temperature (NOCT) 714, 947, 951, 955
- noncrystalline semiconductors 517, 532
- n-p* junction 340
- Nth Power Technologies 1110
- nucleation 349
- numerical modeling of solar cells 109–10
- numerical simulations of crystal growth techniques 244–51
- off-grid energy supply systems, characteristics of 55
- off-grid power supply systems 54–7, 754
 - future developments 794–6
 - prerequisites 57
- off-grid rural electrification 768–71
 - categorization of delivery models 773–4
 - economic aspects 771–4
 - see also* rural electrification
- open-circuit voltage 309, 529, 534–7, 809, 951, 954
- optical confinement 285
- optical design, a-Si:H solar cells 537–40
- optical generation rate 89
- optical properties
 - crystalline silicon photovoltaic modules 300
 - GaAs 394
 - GaInP 387–9
 - germanium 394
 - thin-film silicon solar cells 328
- optics 268–70, 326–36
 - concentrators 452–5, 474–95
- optimal tilt angle for minimizing solar generator size 793
- Orbital Workshop array 414
- Ostwald ripening 185
- overcast skies, radiance distribution associated with 930
- overvoltage 806
- oxygen as impurity in silicon 187–8
- oxygen segregation 220
- p*-type material 77, 83
- p*-type multicrystalline silicon 217, 220
- p*-type semiconductors 76
- p*-type side 24
- pair formation 185
- parallel resistance 953
- parasitic power loss 37
- parasitic resistance effects of solar cell 102
- partial-shunting controller 869
- passivated emitter rear contact (PERC) cell 466
- passivated emitter rear floating junction (PERF) cells 266
- passivated emitter rear locally diffused (PERL) cells 261, 263, 266, 270–1, 314–15, 469
- passivated emitter rear totally diffused (PERT) cell 266, 314
- passivation with hydrogen 283–5
- Pathfinder unpiloted prototype 782
- Pb/H₂SO₄/PbO₂ cell 830
- PC1D 334
- peak load 51
- peak-load-reduction technology 14
- performance rating methods, energy-based 716–17
- performance ratio (PR) 965
- periodic table of elements 64
- personal digital assistant 58
- phonon absorption 72
- phonons 72
- phosphorus diffusion 273
- phosphorus doping 518
- photocurrent drift in absorber layers 530–3
- photoconductivity 505
- photoluminescence (PL) intensity 400
- photon absorption 71–2
- photon conversion efficiency, wavelength dependence of 363–4
- photon energy 61, 70, 73, 130
 - monochromatic cell efficiency versus 125
- photon flux 74, 121
- photon flux absorption 313
- photons 3, 5, 61, 117–18, 127–8, 142, 144
- photosynthesis 39
- photovoltaic cells 57
 - and BIPV modules 1029–35
 - manufacturers 22
 - measurement and characterization 701–52

- Photovoltaic Concentrator Applications
Experiments 462
- photovoltaic concentrators *see*
concentrators
- photovoltaic conversion, efficiency of
113–51
- photovoltaic converters 59, 120–31
- photovoltaic-diesel-hybrid system 768
- photovoltaic efficiency 701
annual 717
- photovoltaic electricity 39
contribution of 40–1
technical potential 54
- Photovoltaic Energy Project (PEP) 727
- photovoltaic engineering problems 925
- photovoltaic generator behavior under real
operation conditions 947–56
- photovoltaic industry 153
- photovoltaic integrated as roofing louvres,
façades and shading 1011–14
- photovoltaic module cell temperature 955
- photovoltaic module orientations 925
- photovoltaic module placement and
shading 1039
- photovoltaic modules 5, 7, 34, 46, 60
BIPV 1029–35
certification 745–6
energy collection and delivery 905–70
I–*V* curve 867
integration in architecture 1019–21
measurement and characterization
701–52
net energy loss 10–11
qualification 745–6
rating 947
solar radiation available for fixed
flat-plate conventional 947
transparent 1009
world production 22
- photovoltaic performance, annual 718
- photovoltaic performance rating 701–20
- photovoltaic rating criterion 716
- photovoltaics 753–98, 972
advantages and disadvantages 3
and all of the world's needs 7
and development 1043–71
areas of application 45, 754
as empowering technology 1–2
as environmentally clean and green
technology 9
as long-term substitute for electricity
generation 48–54
as small-scale cottage industry 7
basic R&D 19
components 784–94
consumer applications 756–7
development dimension 54–7
economic assessment 980–4
experience curve for 1976 to 1998 17
funding 8–9
future developments 794–6
future of emerging technologies 37–9
future potential 40
future prospects 999–1002
history 11–15
immediate and exclusive use 7
land area requirement 6–7
motivation for application and
development 45–60
myths of 5–11
notable events in history of 12
overview 753–4
public funding for R&D 9
public support 8
rational decision to develop 972
status 1
trend in worldwide applications 8
use of term 3–5
Utility-Scale Applications (PVUSA)
project 467, 715, 736
- Photovoltaics/Market Transformation
Initiative (PV/MTI) 1101
- pin* device, electronic structure 528–30
- pin* photodiodes 508–9
- pin* solar cell 109
absorber layer design 533–4
band diagram 110
power output 533
- planar cell structures 310
- plant cost 34
- plasma-deposited silicon thin film 527
- plasma-enhanced chemical vapor
deposition (PECVD) 28, 243, 258,
284–5, 314, 324, 341, 353, 520–1
- pn* junction 5, 24–5, 29
n-type 30
p-type 30
- PN*-junction diode electrostatics 83–7
- point-contact cell design 469
- point defects 184
- point-focus Fresnel modules and systems
462
- point-focus optics 456
- Poisson's equation 81, 83
- polar tracking 946
- polycrystalline silicon 21, 26, 310
- polycrystalline silicon wafers 1032–3
- polymethyl methacrylate (PMMA) 453,
495
- polysilicon 24, 161
historical processes to manufacture 199
rejects 178–9
research projects 199
see also semiconductor grade silicon

- Polytechnical University of Madrid
 496–9
 porous-Si layer on single-crystal substrate
 317
 post-treatment
 by chemical leaching 195–6
 by extraction metallurgy in ladle
 196–8
 power conditioning 863–903
 power distribution of solar irradiation 966
 Power Management and Distribution
 (PMAD) 441
 powerguard flat-roof PV system 1012
 precipitates in silicon 190–3
 precipitation 185
 pre-electrification 1068
 premature capacity loss 832
 price–experience curve 47–8
 primary reference cell calibration methods
 723–6
 Production of High Silicon Alloys 167
 professional industrial systems 57
 proton exchange membrane fuel cell
 (PEMFC) 854
 pumping stations 56
 pumping systems 768
 PVUSA 467, 715, 736
 PWM controllers 871, 895
 pyrogenic silica 170
- QD arrays, IB formation in 147
 quality-assurance and quality-control
 (QA/QC) evaluation 555
 quantum dot (QD) arrays 148
 IB formation in 147
 quantum dot (QD) solar cells 442
 quantum efficiency 538
 quantum efficiency measurements,
 multijunction cells 549
 quantum efficiency spectra 545
 quartz, carbothermic reduction 167
 quartz-furnaces 273
 quasi-Fermi energy 535–6
 quasi-Fermi levels 119–20, 122, 126, 145
 quasi-neutral region 83
- R&D
 funding sources 1099–100
 future programs 1099
 government funding 1096–100
 Rabobank Nederland/Groen Management
 BV 1107
 radiance distribution associated with
 overcast skies 930
 radiation, use of term 913
 radiation spectrum for black body 63
- Radio Corporation of America (RCA)
 506
 rapid thermal processes (RTP) 282–3,
 314, 350, 353
 reactive ion etching (RIE) 286–7
 realistic reporting conditions (RRC) 716
 receiver position 912
 rechargeable alkali mangan (RAM)
 batteries 822
 recombination current 339
 recombination mechanisms 113
 recombination process 74–7, 121
 recombination sites 185
 recombinators 844
 redox batteries 860
 redox electrolyte 667–8
 redox-flow batteries 850–2
 reference cell calibration procedures
 intercomparison 727–8
 uncertainty estimates 726–7
 Reference Year 937
 Reference Yield 965
 reflective concentrator configurations 454
 reflective secondary concentrators 463
 refractive lenses 485–9
 Regional Solar Programme (RSP) 1067
 relative transmittance plotted against angle
 of incidence 935
 reliability, stand-alone systems 953–6
 reliability maps 959, 961
 remote areas 57, 761–74, 1048
 see also rural electrification
 remote low power systems 57
 remote (or village) systems 972
 renewable energies 54
 Renewable Energy and Energy Efficiency
 Fund (REEF) 1101
 renewable energy sources 45
 current use and current potentials 46
 repeater station 762–3
 residential sector
 financing for 1079–82
 financing of PV growth 1082
 rooftop system 1079
 reverse bias 139
 RF glow discharge deposition 521–3
 Ribbon Growth on Substrate (RGS)
 231–2, 236–41, 246, 249–50
 RIGES 17
 rigid panel planar arrays 432–3
 rolling-grain model 227
 roof-integrated photovoltaic system 53,
 1008
 rooftop PV generators 774
 Rossi X-Ray Timing Explorer (XTE) 433
 Ru complex photosensitizers 666–7,
 685–6

- rural areas 56–7, 1049–51, 1053, 1083–6
 - financing PV 1083–6
- rural electrification 14, 1045–6
 - advantages of PV technology 1048–9
 - applications 1046–7
 - Argentina 1061
 - barriers to PV implementation 1051–60
 - Bolivia 1061–3
 - Brazil 1063–4
 - initial cost 1055–60
 - Mexico 1064–5
 - nontechnical issues 1055–9
 - Sri Lanka 1065–7
 - toward a new paradigm 1068–9
 - trained human resources for 1059–60
 - see also* off-grid
- rural energy scene 1046
- safety procedures 9–10
- Sahel, water pumping 1067–8
- SAM Equity Partners Ltd. 1110
- Sandia Baseline III point-focus module design 465
- Sandia National Laboratories Concentrator Program 461–2
- satellites 59–60, 363
- SAVANT radiation degradation modeling computer 420
- saw damage 271–2
 - and wafer quality 229–30
- Scanning Electron Microscopy (SEM) 193, 221
- SCARLET arrays 416, 427–8, 437
- Scarlet Deep Space One Satellite 59
- scattering mechanisms 79
- Schrödinger equation 65
- Schüco façade profile system 1031
- Schüco roof profile system 1030
- screen printing 261, 265, 275–9, 679–80
- SEA Corporation 466
- second-order effects 953–6
- secondary electrochemical accumulators
 - with internal storage 817–49
- secondary optical element (SOE) 454
- segregation coefficient 219
- selenium 505
- selenium dopant 389–90
- selenization 29
- self-discharge 811
- self-interstitial 184
- self-regulating PV system 865
- semiconductor band gap 121, 153
- semiconductor equations 81–2
- semiconductor grade silicon 24, 176–7
 - economics and industry 175
 - Ethyl Corporation process for 173–5
 - production 167–75
 - Siemens process for 168–72
 - Union Carbide process for 172–3
- semiconductor lasers 76
- semiconductors 5
 - crystal structure 64–5
 - electronic grade 64–5
 - fundamental properties 64–83
 - n*-type 69–70
 - nondegenerate 68
 - p*-type 69–70
- semitransparent cells 1034
- series resistance 951
- shading structure 1013
- shading system 1014
- shadows and trajectory maps 939
- Shell Solar/BOAL profiles 1008
- Shockley–Queisser cell
 - entropy production in 129–31
 - thermodynamic consistence of 126–9
- Shockley–Read–Hall (SRH) lifetimes 257, 261
- Shockley–Read–Hall (SRH) recombination 75, 620
- shopping mall, Lausanne 1024
- short-circuit current 92, 422, 540, 951, 953
- short-circuit current density 536
- shunt resistances 102–4
- SiC 163
- SiC bond 156
- SiC formation 221
- Siemens process for semiconductor grade silicon 168–72
- Siemens Solar Back Surface Field (BSF) process 213
- SiGe alloys 519
- silica
 - aluminothermic reduction of 201
 - carbothermic reduction of 161–3, 198
- silicon 5, 154–61, 182
 - bulk monocrystalline material 206–13
 - carbon as impurity in 187
 - cell technology, module price for 985–90
 - chemical properties relevant for photovoltaics 156
 - crystalline 153–4
 - current feedstock to solar cells 175–9
 - dopant 390
 - effect of various impurities 186–93
 - electrolytic transfer of 201
 - feedstock for crystalline cells 178
 - group IIIA impurities 186–7
 - group VA impurities 186–7
 - health factors 156–7

- silicon (*continued*)
- history 157–61
 - impurities 155
 - mechanical properties 155
 - miscellaneous applications 161
 - multicrystalline wafers 176
 - occurrence 154
 - oxygen as impurity in 187–8
 - physical properties relevant for
 - photovoltaics 154–5
 - precipitates in 190–3
 - refractive index 155
 - requirements for crystalline solar cells
 - 179
 - semiconductor material 160–1
 - single-crystal wafers 154, 176
 - solar grade feedstock 153–204
 - solidification 179–82
 - thermal properties 155
 - transition-metal impurities in 188–90
 - ultra-pure 160–1
 - see also* metallurgical grade silicon;
 - semiconductor grade silicon; solar grade silicon routes
- silicon alloys 157
- band gaps 544–6
 - doping 528
- silicon applications 157–61
- in aluminum industry 158–9
 - in chemistry 159–60
- Silicon Film (SF) 230, 239–42, 244, 251
- silicon metal 157–8, 161
- silicon monoxide 163
- silicon multicrystalline sawn wafers 154
- silicon nitride 243, 283
- passivation 281
- silicon ribbon crystal growth technology,
 - productivity comparisons 238–9
- silicon ribbon/foil growth techniques 232
- silicon ribbon/foil production 230–44
- manufacturing technology 239–40
 - process description 232–8
- silicon ribbon/foil technology 231
- future directions 243–4
- silicon ribbon material properties and solar cells 240–3
- silicon ribbon/multicrystalline film 176
- silicon ribbon wafer/foil technologies 251
- silicon ribbons 288
- silicon solar cells 240–3
- power density 421
 - space applications 425–6
 - temperature coefficients 719
- silicon tetrachloride 159, 171
- silicon-wafer-based PV module costs 25
- silicones 159
- SIMS (secondary ion mass spectroscopy) 347
- simulation of bulk silicon crystallization 247–9
- simulation of silicon ribbon growth 249–51
- simulation tools 245
- single level trap (SLT) 75
- single-crystal silicon 207
- single-crystalline solar cells 256
- single-junction solar cells 37, 74
- physics of 363–5
- sizing
 - stand-alone systems 953–6
 - system 791–3
- sky irradiance, angular distribution of 929
- Skylab 1 414
- SLI (starting, lighting, ignition) batteries 809, 834
- small area champion cells 20
- smart cut method 317
- Sofrel flat-roof system 1018
- soft loans 1095–6
- solar altitude 909
- solar arrays, space applications 431–41
- solar azimuth 909
- solar batteries 1052
- solar cell 3, 5
- spectral response of 100–2
- solar cells
 - back-contact 108
 - band diagram of 120
 - basic structure 87
 - boundary conditions 87–9
 - circuit model 92, 102
 - color 1035
 - cost 26
 - current-voltage characteristic of 103
 - design 62
 - efficiency 99–100, 362
 - efficiency levels 242
 - efficiency versus impurity concentration 192
 - efficiency versus thickness 242
 - equilibrium conditions 86
 - fabrication 26
 - fundamentals 87–99
 - future-generation 403–6
 - higher-than-one quantum efficiency 140–1
 - intermediate band 144–8
 - lifetime 96–7
 - manufacturing 26
 - materials, BIPV 1030–4
 - model parameters 94
 - numerical modeling of 109–10
 - operation 63, 84, 98–9

- parasitic resistance effects of 102
- performance 62, 96–8
- physics 61–112
- power density as function of time 422
- properties of 95–6
- schematic 4, 62
- short-circuit current versus open-circuit voltage 105
- silicon current feedstock to 175–9
- technology 14
- temperature effects on 104–6
- Solar Cells and Optics for Photovoltaic Concentration 492, 498
- solar constant 912
- solar converters, technical efficiency limit for 131–2
- solar declination 907
- solar design 1038–9
- Solar Development Capital 1102
- Solar Development Foundation (SDF) 1102–3
- solar electric farms 23
- Solar Electric Light Fund (SELF) 1103
- solar electricity, *see also* photovoltaic electricity
- solar energy, availability 799
- solar grade silicon 359
- solar grade silicon routes 193–201
- solar home systems (SHS) 56, 759–60, 813–14, 865, 873, 962–4, 1052, 1054, 1083, 1088
 - cost breakdown 56, 772
- solar hour 909
- solar illumination 540
- Solar International Management Inc. (SolarBank Program) 1103
- solar irradiation, power distributions of 966
- solar lantern for rural households in developing countries 758–9
- solar modules
 - architecture 1035
 - color 1035
 - shipment by technology 176
- solar office, Doxford, Sunderland 1019
- solar radiation 6
 - and uncertainty 915–20
 - available for fixed flat-plate conventional PV modules 947
 - components 912–15
 - estimation of hourly irradiation from
 - daily irradiation 925–7
 - on inclined surfaces 920–33
 - on surfaces on arbitrary orientation 927–33
 - parameters 919
- Solar Research Corporation Pty Ltd 499
- solar shading 1010
- solar simulators 736–8
- solar spectrum 915
- Solar Terrestrial Probe (STP) Program Magnetospheric Multiscale (MMS) 440
- solar time 911
- solar zenith angle 909
- SOLERAS 466–7
- Solgreen flat-roof system 1031
- solid-phase crystallization 343
- solid solutions 184
- solidification, silicon 179–82
- Solidification by Planar Interface (SOPLIN) processes 246–7, 249
- Solrif solar profile system 1029
- space applications 780–3
 - high-efficiency III-V multijunction solar cells 363
 - silicon solar cells 425–6
 - solar arrays 431–41
 - thin-film solar cells 428
- space charge region (SCR) 83, 339
- space environment 417–20
- space solar cells 413–31
 - calibration and measurement 424–5
 - challenge for 416–25
 - history 413
 - performance 416
 - technology requirements 418
- space vehicles 363
- spacecraft 59–60
- Spanish National Meteorological Institute 916
- specialty markets 7
- spectral effects 955
- spectral response 100–2
 - modeling 955
- spectral responsivity, versus wavelength characteristics 701
- spectral responsivity error sources
 - for measurement of light power 744
 - for measurement of photocurrent 743
 - for monochromatic light 745
- spectral responsivity measurements 738–44
 - filter-based 739–41
 - grating-based systems 741–2
 - uncertainty 742–4
- Spectrolab Spectrosun Large Area Pulsed Solar Simulator 425, 466, 499
- spectrum-splitting 364–5, 406, 510, 543
- spherical radiator 476
- spray pyrolysis (SP) 30
- spring equinox 907
- Sri Lanka, rural electrification 1065–7
- Staebler–Wronski effect 511–12

- STAMP program 982, 985, 989–90, 992
 stand-alone systems 39, 937, 945
 inverters 789–90, 883
 reliability 956–63
 sizing 956–63
 standard hydrogen electrode (SHE) 803
 standard reporting conditions (SRC)
 701–15
 standard test conditions (STC) 905, 947,
 950, 955
 Standard Year 937
 Stanford Advanced Back Contact cells
 990
 STAR 496
 starting, lighting, ignition (SLI) battery
 809, 834
 state of charge (SOC) 809, 849
 state-of-charge meters 843
 stationary batteries 835
 Stefan-Boltzman law 119
 step-down converter 885–7, 889
 combination with inverters 890
 step-down principle, integration into
 inverting process 892
 step-up converter 887–9
 Strategic Analysis of Manufacturing
 Product and Price *see* STAMP
 program
 String Ribbon (STR) 230, 232, 235–7,
 239–40, 243, 245, 288
 structural façades 1010
 structural glazing 1010
 sub-array switching controller 869
 substitutional impurities 184, 186
 substrate texturing 537
 summer solstice 907–8
 Sun–Earth movement 906–12
 Sun–Earth position 910, 912
 Sun-tracking surfaces 945–6
 sunlight 5, 40
 SunPower Corporation 466, 496,
 499–500
 sun's rays incidence angle 912
 Sun's trajectory maps 939
 surface recombination 77, 96–7
 surface recombination velocity (SRV)
 258–9, 338
 Surface Texture and enhanced Absorption
 with a back Reflector (STAR) cell
 321
 surface texturing 269
 surface to volume relation (SV) 246
 Survivable COncentrating Photovoltaic
 Array (SCOPE) 439
 SURvivable PowER System (SUPER) 439
 switching controllers 867–70
 Syndicate Bank (India) 1113
 synthetic silica 159–60
 system cost 980–4
 manufacturing-cost modeling 982–3
 system-mounting structure 34
 system sizing 791–3
 Tafel equation 805
 Tafel lines 805
 tandem cells 134
 T-CHEQ 879
 experimental set-up 880
 operating experience 879
 voltages and currents of 16
 series-connected cells during
 charging 880
 technical efficiency limit for solar
 converters 131–2
 telecommunications 761–2
 autonomous power supply system for
 856
 Telstar 414
 temperature coefficients 423
 for module and cell temperature
 estimation 956
 temperature dependence, high-efficiency
 III-V multijunction solar cells 380–2
 temperature determination under
 considered operating conditions 952
 temperature effects on solar cells 104–6
 terminal characteristics 89–92
 terrestrial applications 363
 terrestrial concentrator systems,
 implementation of multijunction III-V
 cells 406–7
 terrestrial energy production,
 high-efficiency III-V multijunction
 solar cells 363
 terrestrial spectrum 407
 texturing 269, 273, 539
 thermal environment 420–3
 thermal modeling of crystallization
 techniques 245–7
 thermionic emission model 537
 thermodynamic consistence of
 Shockley–Queisser photovoltaic cell
 126–9
 thermodynamic converters 790
 thermodynamic current densities 115, 117
 thermodynamic currents 117
 thermodynamic efficiency 125
 thermodynamic fluxes 119
 thermodynamic functions of electrons 119
 thermodynamic functions of radiation
 117–19
 thermodynamic variables 117–19
 thermodynamics
 background 114–19

- basic relationships 114–16
- laws of 116, 130
- thermoelectric generators (TEG) 790
- thermophotonic (TPH) converter 136–40
- thermophotovoltaic (TPV) conversion 135–6, 468–9
- thermophotovoltaic (TPV) generators 790
- thin-film progress and challenges 27–31
- thin-film PV materials 1034
- thin-film PV modules 53
- thin-film silicon solar cells 307–57
 - carrier collection 316
 - carrier generation 316
 - deposition techniques 341
 - design concepts 324–53
 - electronic modeling 333–41
 - generic device structure 325
 - grain enhancement 343–50
 - mechanical support 316–17
 - multicrystalline-Si substrates 320
 - non-Si substrates 321–4
 - optical properties 328
 - overview 307–10
 - processing considerations 350–3
 - review of current position 310–24
 - single-crystal Si substrates 317–20
 - summary from optical modeling 333
 - summary of types 318–19
 - surface structures 312
 - surface texture 311–12
 - thermodynamic considerations 311
- thin-film solar cells 27–9
 - CdTe *see* CdTe thin-film solar cells; silicon thin-film solar cells
 - space applications 428–31
- thin-film technology 40
- thin-film transistor (TFT) 350
- third generation PV converters 148
- time variation of generated daily energy 958
- TiO₂ 274
 - colloid preparation 678–9
 - dye fixation onto film 680
 - electrode preparation 679–80
 - electron transport 677–8
 - photoelectrode 666
 - solar cell, photocurrent–voltage curve 674
- Tokyo A&T University 500
- total harmonic distortion (THD) 890, 897, 899
- total irradiation 958
- TPH converter 148–9
- TPV converter 139, 148–9
- trackers *see* concentrators
- traction batteries 835
- transition metals (TM) 351
 - impurities in silicon 188–90
- translation equations to reference conditions 719–20
- transmission line measurements 400
- transparent conducting oxide (TCO) 440, 509–10, 539–40, 555
- transparent conducting oxide (TCO)-coated glass substrate 664–6
- travel time of electron under short-circuit conditions 531
- trichlorosilane 168
- tri-crystalline silicon (tri-Si) 211–13, 251
- Triodos Bank NV 1108
- triple-junction cells 426, 506
- triple-junction III-V semiconductor cells 416
- triple-junction module 512
- triple-junction *nip* substrate-type solar cells 547
- Tropical Rainfall Measuring Mission (TRMM) 433
- true solar time 909
- TU Electric Power Park 467
- tubular-plate battery 844
- tunnel junction 548
- tunnel-junction interconnects (TJICs) 379, 396–7
- twin boundaries 183
- Typical Meteorological Year (TMY) 937–8, 960
- uncertainty
 - and solar radiation 915–20
 - spectral responsivity measurements 742–4
- uncertainty estimates, reference cell calibration procedures 726–7
- uncertainty parameters 919
- underdevelopment, breaking the chains of 1046–8
- UNDP 1087–8
 - Sustainable Energy & Environment Division (SEED) 1103–4
- UNEP 1088
 - Collaborating Centre on Energy and Environment 1104
- uninterruptible power supplies (UPS) 34, 835
- Union Carbide process
 - for semiconductor grade silicon 172–3
 - simplification 198–201
- United States, PV programs 1096–7
- University of New South Wales (UNSW) 324

- University of Reading 500
US Agency for International Development (USAID) 1111
utility systems 779
- vacancies 184
valence band (VB) 4, 66–7, 74, 119
valve-regulated lead acid (VRLA) batteries 831–2, 846
Vanguard I 413–16
vapor deposition (VD) 30
VHF glow discharge deposition 524–5
village power supply systems 766–7
vision or view factor 118
volatiles 169
voltage shaping by digital synthesis 890–2
VTZ Green Money for the Blue Planet Ltd. 1108
- wafer cost 206xx
wafer material for crystalline silicon 245
wafer quality 205
 and saw damage 229–30
wafering 223–30, 280–1
 cost and size considerations 230
 microscopic process 226–8
 multi-wire technique 224–6
- water pumping
 for irrigation 1083
 Sahel 1067–8
water purification systems 768
wavelength dependence of photon conversion efficiency 363–4
WEB *see* dendritic WEB
well-integrated systems 1014–18
Wind Fund Plc, The 1108
window layer 530
Winrock International 1104, 1113–14
winter solstice 908
World Bank solar home system projects 1088
World Photovoltaic Scale (WPVS) 728
wrought alloys 159
- xerography 505
X-ray diffraction 345–8
- Zentrum fur Sonnenenergie und Wasserstoff Forschung Baden Wurttemberg (ZSW) 500
zero-energy project, Etten-Leur 1024
zinc dopant 390–1
zincblende lattice 64
zone-melting recrystallization (ZMR) 315, 350

Index compiled by Geoffrey Jones.